IMPROVING THE LONGER-TERM RECORD OF EXPLOSIVE VOLCANISM IN THE MEXICO CITY REGION: IMPLICATIONS FOR UNDERSTANDING VOLCANIC HAZARDS FROM DIVERSE ERUPTIONS

by

ALASTAIR GRAHAM EDWARD HODGETTS **MSc, BSc (Hons)**

A thesis submitted to the University of Birmingham for the degree of

DOCTOR OF PHILOSOPHY

June 2022

Department of Earth Sciences
School of Geography, Earth and Environmental Sciences
College of Life and Environmental Sciences
University of Birmingham

UNIVERSITY OF
BIRMINGHAM

University of Birmingham Research Archive

e-theses repository

This unpublished thesis/dissertation is copyright of the author and/or third parties. The intellectual property rights of the author or third parties in respect of this work are as defined by The Copyright Designs and Patents Act 1988 or as modified by any successor legislation.

Any use made of information contained in this thesis/dissertation must be in accordance with that legislation and must be properly acknowledged. Further distribution or reproduction in any format is prohibited without the permission of the copyright holder.

IMPROVING THE LONGER-TERM RECORD OF EXPLOSIVE VOLCANISM IN THE MEXICO CITY REGION: IMPLICATIONS FOR UNDERSTANDING VOLCANIC HAZARDS FROM DIVERSE ERUPTIONS

Alastair G.E. Hodgetts

ABSTRACT

Eruption records are crucial to understanding volcanic output and eruptive processes over time. However, due to a diminishing longer-term record of explosive eruption deposits, often due to burial, erosion and cover, volcanic histories are regularly incomplete thus limiting our understanding of eruptions and their effects through time. This is particularly detrimental for densely populated regions at risk from volcanic activity.

Mexico City is one of the largest populations in the world and sits within one of the major intracontinental volcanic arcs. Risk from diverse eruptions is high, however eruption records are limited due to poor exposure. This thesis, therefore, improves upon these records by combining stratigraphic, geochemical, and geochronological results.

To achieve this, a c.500 m lacustrine core from Lake Chalco, Mexico City is probed in order to construct a detailed tephrastratigraphy and volcanic stratigraphy of the succession. It is found that volcanic deposits account for 59.81% of the composite core, comprising a maximum of 603 tephra layers, along with laharic and coarser-grained volcaniclastic facies and lavas. Volcanic output is assessed using a novel methodology and reveals that the frequency of explosive eruption deposits in the lake has generally waned over time.

Fieldwork was conducted at several volcanoes, including Popocatépetl, Iztaccíhuatl, and Tláloc-Telapón, in order to sample and obtain glass geochemical data to fingerprint possible

volcanic sources of explosive eruption deposits at Lake Chalco. All three volcanoes revealed distinct fingerprints and supplementary $^{40}Ar/^{39}Ar$ dates extend the older eruptive histories of these volcanoes.

Core tephras were also geochemically investigated, with 137 layers analysed for major element glass geochemistry. It is revealed that Nevado de Toluca and La Malinche volcanoes are not chemically distinct from Iztaccíhuatl, so the three volcanoes have to be grouped for correlation with the core. Of the 137 tephras analysed at Lake Chalco; 35 are from Popocatépetl, 43 from either Iztaccíhuatl, Nevado de Toluca or La Malinche; 1 from Tláloc-Telapón; 17 from the nearby monogenetic Sierra Chichicnautzin Volcanic Field; 3 from Los Humeros caldera, Mexico and 1 from Atitlán caldera, Guatemala.

Amongst the analysed tephras, two well-dated and widespread eruptions (isochrons) are correlated into the Chalco succession: (1) the Xáltipan ignimbrite from Los Humeros and (2) the Los Chocoyos (LCY) eruption from Atitlán. Further to these chronological markers, 12 samples (plagioclase and groundmass separates) have been submitted for $^{40}Ar/^{39}Ar$ dating, although results are yet to be finalised.

This study significantly builds upon the eruptive history of the Mexico City region, identifying and characterising many newly identified eruption layers as well as correlating others. The results of this thesis are of direct relevance to hazard assessment for Mexico City, providing a longer-term assessment of explosive volcanism that has directly impacted the region in the past. The methodology used in this study may also be replicated in other regions, and sedimentary successions containing volcanic deposits.



Popocatépetl, 5th April, 2019

SE dispersal, c.2 km plume

Dedicated to the memory of

Olive and Graham Cooksey

for all your love, support and encouraging my interest in the natural world

ACKNOWLEDGEMENTS

This thesis represents just a small proportion of my PhD. A few written lines are often the result of many long days and nights travelling backwards and forwards between Birmingham and Oxford for probe analyses, sampling tephra in Minnesota and logging core section after core section usually into the early hours of the morning. However, although I have experienced some extremely busy and stressful times along the way, the skills I have learnt on this journey have been invaluable. I have also spent time in amazing places, done amazing things and spent time with some amazing people.

First and foremost, I am extremely grateful to my primary supervisor, Sebastian Watt. Seb has been the best supervisor that I could have hoped for. He has always gone above and beyond to help and he has taught me a great deal. Seb is one of the most brilliant scientists with whom I have had the privilege to work, and he is also the nicest of people to know. Thank you Seb for your inspiration, advice and faith in my abilities over these past few years! I am also incredibly grateful to Victoria Smith who has also taught me some important skills. Before embarking on my PhD, I knew next to nothing about glass geochemistry so the fact that I only had a few disasters with the probe was an overall success!

From the day I started at the University of Birmingham, I was warmly welcomed by everyone in the Earth Sciences Department. In particular, Dan and Davey, (as the only other igneous geologists), became great friends, leading to us setting up the *Birmingham Igneous Group*, or 'meet up for a curry and chat' in short. Support from the whole PhD cohort in Birmingham has been incredible, including the support from Gretchel Coldicott, Aruna Mistry and Mica Jones since their number one priority has always been the postgraduates. I am very grateful

for the friendship of everyone in the Earth Sciences Department including Alan and Ully, always on hand to provide a welcome distraction from work and find the time for laughter.

I have also been fortunate to build strong friendships with researchers outside Birmingham, including Gregor and Yannick with whom I helped to conduct fieldwork in Pantelleria and Taal in the Philippines. I have many fond memories from these trips and from our weekly catch-ups and volcanology chats. Thank you both for all of your support.

In 2019, I undertook a research placement at Mount St. Helens volcano, based at the Cascades Volcano Observatory where I worked with inspired volcanologists. Taking a ride in a helicopter for fieldwork was certainly a highlight. Following such an experience however does mean that previous enjoyable hikes now just seem that little bit more mundane! Thank you to Alexa, Larry, Mike, John and Britta (and all at CVO) for teaching me an incredible amount and for providing me with some unforgettable experiences and opportunities.

The wider MexiDrill Project, of which my PhD has been part, has given me the opportunity to belong to a community of scientists. The LacCore team in Minnesota treated me like a colleague rather than a visitor. Thank you to all of you for some memorable times and for not getting too annoyed with me for taking all of the deposits! Thank you also to Erik Brown for travelling from Duluth to meet me and for taking me and Vicki back to Duluth to show us around. I would also like to thank Mike and Kristin, who I met in Minnesota in 2018, for kindly allowing me to stay with them for the duration of my next visit in 2019.

Whilst on the topic of the MexiDrill Project, it was fantastic to have Ivan join the project. We got to know each other fairly well through our mutual fear of the probe as we learnt how it worked, and in Mexico we had some good times and consumed many, many tacos. Muchas

gracias amigo! Also, to all those I met in Mexico, thank you for your kindness and hospitality. Mexico City is a wonderful place and where I have been very privileged to be able to work. Our colleagues in Mexico have been the backbone of this project, in particular J.L. Arce, Giovanni and Claus: their knowledge and support with the fieldwork has been invaluable. In addition, the support from our field assistants, Miguel, Jesus, Kai and Ainhoa was greatly appreciated.

The wider volcanology community has been a fantastic group to join and it has been brilliant to be part of VMSG and CoV. Whilst expanding my professional network, I have also made many friends along the way.

I have missed a lot of people off this list of thanks for which I can only apologise. I am incredibly grateful to everyone, during my time as a PhD researcher, who has given me support during this project. You have all made it incredibly worth it!

My final thanks go to my family who have supported me throughout my PhD. Thank you to my parents, Lorna and Andrew, for always putting me first and for looking out for me and encouraging me throughout everything I have done. Also, to my brother, Calum, who, whilst teasing me about all of my 'holidays' when I am away on fieldwork, has always been proud of me and my 'schoolwork'. And finally, my thanks go to Maria-Angela whose continued love throughout my studies has meant such a lot, particularly during the long times apart. A massive thank you also for helping me to collate this giant document! I am looking forward to us having some well-deserved time together.

Which brings me to Sam Engwell and Marco Maffione. Thank you for taking the time to read this thesis!

TABLE OF CONTENTS

CHAPTER 1 ..... **1**

1. BACKGROUND 3

1.1. Volcanic eruptions 4

2. MOTIVATION 9

CHAPTER 2 ..... **13**

1. STUDY AREA 17

1.1. Geology and volcanism in Mexico 17

1.2. Volcanology of the Mexico City Region 18

1.2.1. Popocatépetl 21

1.2.2. Iztaccíhuatl 21

1.2.3. Tláloc-Telapón 23

1.2.4. Sierra Chichinautzin Volcanic Field 25

1.2.5. Nevado de Toluca 26

1.2.6. La Malinche 26

1.3. Distal volcanoes (>100 km from Mexico City) 28

1.3.1 Ceboruco 28

1.3.2. La Primavera 30

1.3.3. Los Humeros 30

1.3.4 Atitlán, Guatemala 31

2. LAKE CHALCO, MEXIDRILL PROJECT 32

CHAPTER 3 ..... **36**

1. INTRODUCTION 38

1.1. Improving eruption records 39

1.2. Typical drilling projects 41

1.3. Lake Chalco, Mexico City 42

2. GEOLOGICAL SETTING....43

2.1. Volcanic sources around Mexico City....44

2.2. Drilling and production of composite spliced stratigraphy....49

3. STRATIGRAPHIC METHODS....51

3.1. Identification of visible Volcanic Deposits and production of a detailed volcanic stratigraphy....51

3.2. Description of visible Volcanic Deposits and the development of a volcano stratigraphic framework....57

3.3. Determination of the types of volcanic deposit....58

3.4 Dealing with artefacts and drilling imperfections....61

3.5. Calculating depths within the spliced stratigraphy from depths in individual core sections....63

3.6. Projecting off-splice volcanic layers onto the splice....68

3.7. Calculating event-free depth....71

3.8. Assessing the volcanological record of the core....72

4. ANALYTICAL METHODS....73

4.1. Laser Diffraction Particle Size Analysis....73

4.2. Whole Rock Geochemistry....74

4.3. Thin Sections....74

5. VOLCANIC STRATIGRAPHY OF LAKE CHALCO....75

5.1. Stage I: Lava-dominated deposits (448.86 – 553.93 mc) 75

5.1.1. Lavas and flow boundaries....77

5.1.2. Geochemistry and petrology....79

5.2. Stage II: Pre-lacustrine deposits (293.71 - 448.86 mc) 82

5.2.1. Types of deposits....87

5.2.2. Petrology....88

5.3. Stage III: Lacustrine-dominated deposits (0 – 293.71 mc) 88

5.3.1. Quality of the core recovery in Stage III....94

5.3.2 Grain size vs. depth....99
5.3.3. Thicknesses of TFDs....103
5.3.4. Frequency and tempo of explosive volcanism....104
6. OTHER EVENT LAYERS IN LAKE CHALCO....108
7. DISCUSSION....108
7.1. Implications of this study at Lake Chalco....108
7.2. Physical volcanological importance of volcanic deposits in cores....111
7.3. Limitations....114
7.3.1. Core site and environmental limitations....114
7.3.2. Data collection limitations....119
7.4. Implications for Mexico City hazard assessment....119
8. CONCLUSIONS....124
CHAPTER 4....127
1. INTRODUCTION....129
2. GEOLOICAL FRAMEWORK AND VOLCANIC EVOLUTION OF THE SIERRA NEVADA VOLCNAIC RANGE....131
2.1. Sierra Nevada Volcanic Range (SNVR) 132
2.1.1. Tláloc-Telapón....133
2.1.2. Iztaccíhuatl....134
2.1.3. Popocatépetl....136
2.1.4. Summary of the SNVR state-of-the-art....138
3. METHODS....138
3.1. Fieldwork....138
3.2. Glass chemistry....139
3.3 Argon-Argon geochronology....140
4. FIELD TEPHRASTRATIGRAPHY....141
4.1 Characterisation of previously identified proximal deposits of the SNVR volcanoes....141

4.1.1. Tláloc-Telapón....142

4.1.2. Popocatépetl and Iztaccíhuatl....142

4.2 Nepopualco and Xalitzintla sites....144

4.2.1 Nepopualco tephra sequence....146

4.2.1.1. Lower Nepopualco tephras....147

4.2.1.2. Middle Nepopualco Tephras....148

4.2.1.3. Upper Nepopualco tephras....150

4.2.2. Xalitzintla....152

4.2.2.1 East of the Restaurant....154

4.2.2.2. West of the Restaurant....156

4.2.2.3. Fork in the road: 158

4.2.2.4. Xalitzintla Quarry....160

5. GLASS CHEMSITRY AND TEPHRA CORRELATION....162

5.1. Glass compositional fields of Tláloc-Telapón, Iztaccíhuatl and Popocatépetl....164

5.2 Composition of Nepopualco tephras and correlation to their volcanic source....168

6. NEW 40Ar/39Ar DATES....173

7. TEPHRA CORRELATIONS....177

7.1 Tephra correlations between the Xalitzintla and Nepopualco sequences....177

7.2 Chronological order of the Xalitzintla outcrops....182

8. CHEMICAL VARIATIONS THROUGH THE NEPOPUALCO TEPHRA SEQUENCE AND ITS IMPLICATIONS FOR THE VOLCANIC HISTORIES OF POPOCATEPETEL AND IZTACCIHUATL....183

9. INSIGHT INTO THE GENERAL VOCLANIC HISTORY, MAGNTIUDES, AND TEPHRA DISTRIBUTION IN THE MEXICO BASIN....184

10. OTHER VOLCANOES IN THE MEXICO CITY REGION....188

11. CONCLUSIONS....192

CHAPTER 5.....194

1. INTRODUCTION.....196

1.1. Importance of tephrochronology in volcanology.....196

1.2. Use of tephra glass geochemistry at Lake Chalco.....197

2. GEOLOGICAL SETTING.....199

2.1. Volcanism in the Mexico City region and its vulnerability to explosive volcanism.....199

2.2. Proximal polygenetic volcanic sources.....200

2.3. Proximal monogenetic volcanic sources.....204

2.4. Distal volcanic sources.....204

3. METHODS.....205

3.1. Proximal volcanic field methods.....205

3.2. Core methods.....205

3.3. Sub-sample selection and extraction.....206

3.4. Sample preparation for electron probe microanalysis (EPMA) analysis.....208

3.4.1. Sieving and cleaning.....208

3.4.2. Sample mount creation.....209

3.5. EPMA analysis.....211

3.6. Data analysis and filtering of glass geochemical data.....215

4. SOURCE GLASS GEOCHEMISTRY.....216

4.1. Group 1: Proximal polygenetic source.....223

4.2. Group 2: Distal sources.....226

4.3. Group 3: Proximal monogenetic sources.....229

5. CORE GLASS GEOCHEMISTRY.....232

5.1. Stratigraphic correlations.....233

5.1.1. Felsic correlations.....233

5.1.2. Mafic correlations.....235

5.1.3. Ghost correlations....237
5.2. Variability in glass chemistry....238
5.2.1. Glass composition variability in correlated deposits....238
5.2.2. Variation in glass chemistry through tephra units....242
5.3. Laharic Volcaniclastic units....245
5.4. Chemical assignments from visual characteristics....248
5.5. Bimodal eruptions and reworking....251
5.6. Source volcanoes and determination of provenance....255
5.6.1. Popocatépetl....256
5.6.2. Iztaccíhuatl, La Malinche and Nevado de Toluca....259
5.6.3. Sierra Chichinautzin Volcanic Field (SCVF) 262
5.6.4. Tláloc-Telapón and caldera-forming eruption sources....263
5.7. Other sources....269
5.8. Spread though the core....272
5.9. New glass geochemical fields using core analyses....273
6. GEOCHRONOLOGICAL MARKER ERUPTIONS....278
6.1. Los Humeros caldera, Mexico....280
6.2. Atitlán caldera, Guatemala....284
7. DISCUSSION....287
7.1. Frequency of explosive eruptions recorded at Lake Chalco....287
7.2. Exotic source volcanoes and implications for further tephrostratigraphic investigations....291
7.3. Revised estimated eruption volumes/magnitude for correlated eruptions..292
7.4. Hazard implications....294
8. CONCLUSIONS....294
CHAPTER 6....298
1. INTRODUCTION....300

1.1. 40Ar/39Ar Dating....301
1.2. Current age-depth model for Lake Chalco....302
2. IMPROVING THE CHRONOLOGY OF LAKE CHALCO....302
3. METHODOLOGY....306
3.1. Sample selection....306
3.2. Preparation of volcanic units for 40Ar/39Ar dating....308
3.2.1. Sieving and drying....308
3.2.2. Magnetic separation....310
3.2.3. Acid leaching....311
3.2.4. Picking and high grading....311
3.2.5. Picking under clove oil....312
3.3. Groundmass preparation: Lavas....312
4. ANALYSIS....314
CHAPTER 7....315
1. SYNTHESIS AND CONCLUSIONS....317
2. SUGGESTIONS FOR FUTURE STUDY....324
3. SUMMARY....327
REFERENCES....329
APPENDICES....356
C1....356
C2....368
C3....370
C4....378
C5....382
E1....385
E2....466
E3....481

E4.....**483**

E5.....**485**

P1.....**488**

P2.....**510**

P3.....**540**

LIST OF FIGURES

CHAPTER 1

Fig.1. Schematic diagram of an explosive eruption.....7

Fig.2. Examples of volcanoes with recent eruptions.....10

CHAPTER 2

Plate i Geological Map of Mexico.....16

Fig. 1. Location map showing major volcanoes which could impact Mexico City.....19

Fig. 2. Volcanic histories of Popocatépetl and Iztaccíhuatl volcanoes.....22

Fig. 3. Volcanic histories of Tláloc-Telapón and the SCVF.....24

Fig. 4. Volcanic histories of Nevado de Toluca and La Malinche volcanoes.....27

Fig. 5. Summary of the sedimentology of Lake Chalco.....34

CHAPTER 3

Fig.1. Location map of Lake Chalco in relation to Mexico City and Popocatépetl.....45

Fig.2. Schematic indicating how a composite stratigraphy is constructed.....50

Fig. 3. Types of volcanic deposits in Lake Chalco and grain size characteristics.....56

Fig. 4. Classification of different eruption styles identified to be represented in Chalco.....60

Fig.5. Graphic representation of different levels of preservation in Chalco.....62

Fig.6. Schematic indicating what ghost layers are and how they occur.....67

Fig.7. Summary of the volcanic stratigraphy of Lake Chalco.....76

Fig. 8. Stratigraphy and petrology of Stage I deposits.....78

Fig. 9. Geochemistry of the lavas in Stage I and II.....83

Fig. 10. Stratigraphy and petrology of Stage II deposits.....85

Fig. 11. Stratigraphic placement of types of volcanic deposit against sediments.....93

Fig. 12. Stratigraphic positions of different assessed parameters within the core.....97

Fig. 13. Grain size vs. thickness of tephras of different compositions in the core.....100

Fig. 14. Volcanic output rates of different composition tephras in the core.....105

Fig. 15. Physical characteristics of thick tephras.....112

Fig. 16. Modelled eruption scenario from Nevado de Toluca demonstrating the effect of dispersal direction on the thickness of deposits at one location.....117

Fig.17. An analysis of the thickest tephras in Chalco, compared with their grain sizes.....123

CHAPTER 4

Fig. 1. Map of the Trans Mexican Volcanic Belt and location of the Sierra Nevada Volcanic Range.....130

Fig. 2. The Nepopualco sequence 135

Fig. 3. The stratigraphy of the Nepopualco lower tephras.....145

Fig. 4. The stratigraphy of the Nepopualco middle tephras.....151

Fig. 5. The stratigraphy of the Nepopualco upper tephras.....153

Fig. 6. The stratigraphy of the East of the Restaurant site in Xalitzintla.....157

Fig. 7. The stratigraphy of the West of the Restaurant site in Xalitzintla.....159

Fig. 8. The stratigraphy of the Fork in the road site in Xalitzintla.....161

Fig. 9. The stratigraphy of the Xalitzintla of the Restaurant site in Xalitzintla.....163

Fig. 10. Glass compositional fields for the Sierra Nevada Volcanic Range.....167

Fig. 11. Glass chemistry of the Nepopualco tephras.....172

Fig. 12. Glass chemistry of the Xalitzintla tephras.....174

Fig. 13. Chemical correlations between the Xalitzintla sand Nepopualco sequences.....178

Fig. 14. Stratigraphic and geochemcial correlations between the Xalitzintla sand Nepopualco sequences.....180

Fig. 15. Summary of volcanic activity over time at the Sierra Nevada Volcanic Range.....186

Fig. 16. Examples of caldera collapse and hydromagmatic activity from Nevado de Toluca, as seen in the Zinacantepec quarry.....190

CHAPTER 5

Fig. 1 Location of major volcanoes which are likely to have eruption deposits in the Chalco core.....198

Fig. 2. Summary of the tephra preparation stages for electron microprobe analysis.....210

Fig. 3. The anatomy of an electron microprobe.....212

Fig. 4. Glass-shard morphologies of the deposits analysed in chapter 5.....214

Fig. 5. Major element glass compositions and field of major polygenetic volcanoes surrounding the Basin of Mexico.....224

Fig. 6. Major element glass compositions/fields of distal volcanoes to the Basin of Mexico.227

Fig. 7. Major element glass compositions/fields of cones of the Sierra Chichinautzin Volcanic Field.....230

Fig. 8. Correlations between felsic units.....234

Fig. 9. Correlations between mafic units.....236

Fig. 10. Correlations between ghost layers.....239

Fig. 11. Correlations between tephras that also contain variation in glass chemistry.....241

Fig. 12. Variation in glass chemistry of tephras in the core.....243

Fig. 13. Volcaniclastic (laharic deposit) glass chemistries.....247

Fig. 14. Glass geochemistries of tephras of various visual chemical assignments.....249

Fig. 15. Bimodal and reworked deposits throughout the core.....253

Fig. 16. Popocatépetl core correlations.....258

Fig. 17. IMT combined group core correlations.....261

Fig. 18. Sierra Chichinautzin Volcanic Field correlations with the core.....264

Fig. 19. Different evolutionary trends across different volcanic sources.....266

Fig. 20. Correlations in the core with High SiO_2 volcanoes.....268

Fig. 21. Exotic tephra compositions plotting away from the main trends.....271

Fig. 22. Spread in glass chemical data throughout the core.....274

Fig. 23. Glass compositional fields extended by correlated eruption deposits in the core....276

Fig. 24. Correlation of the Xaltipan Ignimbrite from Los Humeros in the core.....281

Fig. 25. Correlation of the Los Chocoyos eruption form Atitlan in the core.....285

Fig. 26. Summary of the spread of eruptions through the core from volcanic sources.....288

CHAPTER 6

Fig. 1. The current age-depth correlation for the core.....303

Fig.2 Stratigraphic position and characteristics of deposits submitted for geochronology in this study.....307

Fig. 3. Summary of the methodology adopted for the geochronology.....309

Fig. 4. Examples of plagioclase crystals under clove oil under different optical views.....313

LIST OF TABLES

CHAPTER 2

Table 1. Summary of the major explosive eruptions of threat to Mexico City throughout the Pleistocene to Holocene.....**29**

CHAPTER 3

Table 1. Types of volcanic and stratigraphic data collected in this study.....**52**

Table 2. Core terminology used in Chapter 3.....**64**

Table 3. Lithologies and depths of Stage I and Stage II deposits.....**80**

Table 4. Key statistics and volcanic data from the Chalco core.....**90**

Table 5. Whole-rock geochemical data from lavas within Chalco.....**95**

CHAPTER 4

Table 1. Description of proximal deposits.....**143**

Table 2. Description of the Nepopualco tephras.....**149**

Table 3. Description of the Xalitzintla tephras.....**155**

Table 4. Major element glass data for the Sierra Nevada Volcanic Range.....**165**

Table 5. Major element glass compositions of the Nepopualco tephras.....**169**

Table 6. Major element glass compositions of the Xalitzintla tephras.....**171**

Table 7. New $^{40}Ar/^{39}Ar$ ages reported in this study.....**176**

CHAPTER 5

Table 1. Summary of key eruptions likely to have impacted Mexico City in the past.....**201**

Table 2. Characteristics of the geochemically analysed tephra layers from the Chalco core (this study) split into 50 m sections of core.....**217**

CHAPTER 6

Table 1. Summary of the samples submitted for $^{40}Ar/^{39}Ar$ dating in chapter.....**305**

CHAPTER 1

BACKGROUND AND MOTIVATION

"If you put your mind to it, you can accomplish anything"

Marty McFly/George McFly, Back to the Future Part I

Contribution statement: This introductory chapter has been written by the author of this thesis.

1. BACKGROUND

The science of volcanology advances through various means, including via the development of new technologies, construction of new methodologies and often by observing new eruptions, which frequently reveal insights into eruptive processes and dynamics, often not preserved or accurately represented in the geological record. Seminal eruptions, e.g., the May 18th, 1980, activity at Mount St. Helens, USA or the June 3rd, 1991, eruption of Mount Unzen, Japan (e.g., Glicken, 1986; Yamamoto et al., 1993) revealed respective lateral collapse and pyroclastic density current (PDC) processes only theorised prior to these events. Since, the worlds' volcanologists have continued to improve upon our understanding of volcanoes as a natural phenomenon, making significant academic and applied contributions. Many of these contributions span multiple scientific disciplines, with cross-disciplinary approaches regularly broadening and strengthening research.

It is estimated that c.800 million people live within 100 km of an active volcano worldwide (Loughlin et al., 2015). Often, these volcanoes are beneficial to the communities that live around them (e.g., bringing nutrient-rich soils or generating volcano tourism) and are contributing factors in the reason some of these communities exist where they do (e.g., Erfurt-Cooper et al., 2015). It is estimated volcanic soils are crucial to c.10% of the world's population (Delmelle et al., 2015) and volcanoes can also provide plentiful water resources and geothermal power (Loughlin et al., 2015; Eggertsson et al., 2020). For the majority of the time, volcanoes are undergoing periods of background quiescence or dormancy (e.g., Carlino et al., 2008). However, active volcanoes pose risks that require management and, in turn, study.

1.1. *Volcanic eruptions*

Volcanic eruptions occur when a volcano ejects material in the form of gases, magma or both, in various forms. Eruptions can be either: (1) phreatic (gas or steam-driven eruptions) typically depositing only lithic clasts, i.e., non-juvenile rocks; or (2) magmatic (magma-generated eruptions) often depositing both juvenile, magmatic material and non-juvenile material, expelled from the vent(s) together. Phreatic eruptions are typically produced by magma at depth coming into close contact with groundwater, superheating it to a critical state, and generating steam (Büttner et al., 2002). The exact timing of these eruptions can be difficult to predict, as demonstrated by the Whakaari (White Island), New Zealand phreatic eruption in 2019, which tragically took the lives of 22 people and injured 25 others (e.g., Kilgour et al., 2019; Ardid et al., 2022). Magmatic eruptions also pose challenges with prediction, although comparatively, typically display a greater number of precursors to an eruption than phreatic events (e.g., Francis and Oppenheimer, 2004). For example, these precursors may include ground deformation and/or an increase in seismic activity or chemical changes in fumarolic gases or ground and spring waters due to changes in the magmatic plumbing system beneath the volcano (Barberi et al., 1992; Xu et al., 2012).

A magmatic eruption occurs when magma reaches the surface, where it is either erupted effusively, explosively or as a hybrid explosive-effusive event (e.g., Schipper et al., 2013). The control on the behaviour of the eruptive style is typically due to the volatile content (e.g., H_2O, CO_2, SO_2, H_2S), rheology and composition of the magma. For an explosive, tephra (magmatic ejecta) forming eruption, magma undergoes bubble nucleation (formation) at a sub-surface level within the plumbing system. These bubbles grow by either diffusion, decompression or

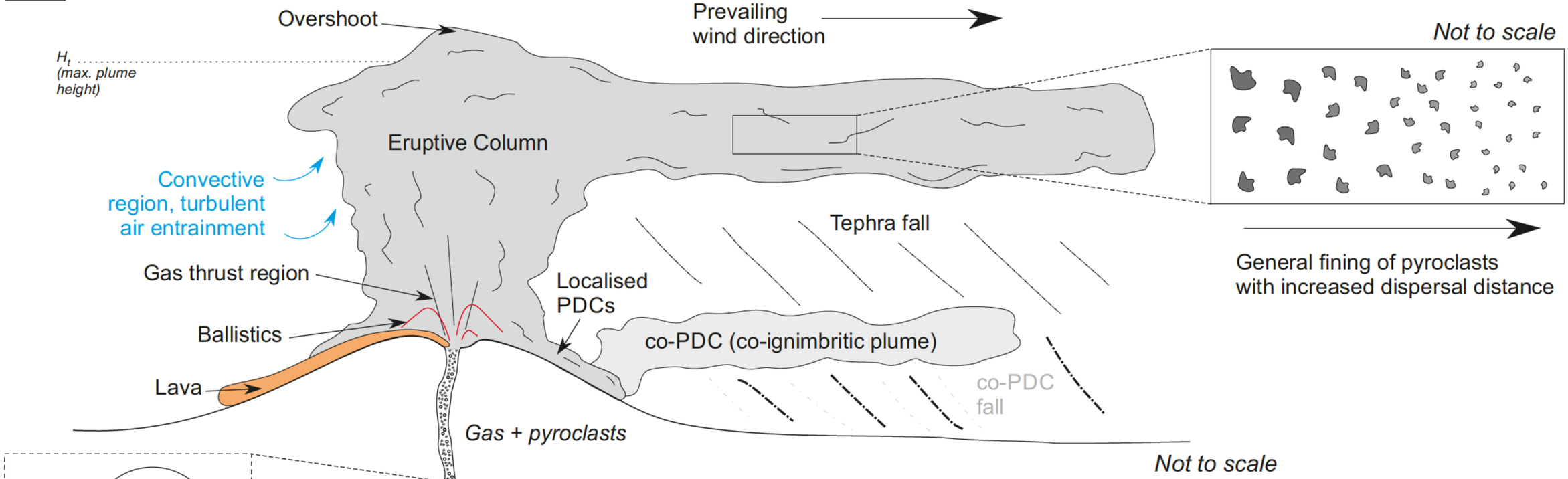
coalescence until a point of supersaturation within the magma. With decreasing pressure, a reduction in the solubility of volatiles occurs, driving further exsolution. This exsolution, coupled with bubble crowding, leads to the disaggregation of the magma at the fragmentation level within the conduit, marking a shift in state from a bubbly magma (liquid), containing gas, to a continuous gas phase, now containing clots of magma (i.e., tephra, e.g., Wilson and Sparks, 1980; Mastin and Ghiorso, 2000; Cassidy et al., 2018). Higher silica (SiO_2) magmas usually demonstrate more explosive eruptions, due to the prevention of gas escape and subsequent increase in bubble overpressure over time. Basaltic volcano systems (lower SiO_2 magmas) permit the escape of volatiles through buoyant ascent of bubbles (degassing), often resulting in less explosive eruptions (e.g., Walker, 1993). Fig.1a schematically displays this process within the sub-surface.

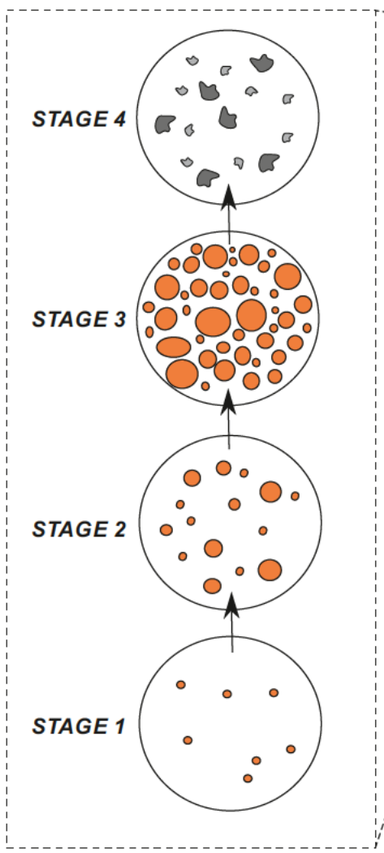
Following the initiation of an eruption, the magma supply controls the duration of the eruption (e.g., Scandone et al., 2007). At the surface, varying eruption processes and eruption dynamics can occur, depending upon numerous sub-surface and surface parameters. Fig.1a schematically represents a typical Plinian eruption, triggered by decompression-driven fragmentation. Minor lava flows may occur, during periods of more effusive activity or through a hybridised eruption scenario, such as the 2011-12 sub-Plinian to Plinian eruption of Cordón Caulle, Chile (Schipper et al., 2013). As tephra leaves the vent(s), the *gas thrust region* vertically carries material upwards. Due to high temperatures and the turbulent entrainment of air from the atmosphere, pyroclasts are further carried vertically through the atmosphere due to the effects of buoyancy. Continued expansion and ambient air entrainment in this *convective region* of the plume permits further rising. When the plume reaches a maximum

plume height (H_t) at neutral buoyancy, the plume spreads outwards into an *umbrella cloud* where prevailing wind controls the dispersal of pyroclasts. As wind carries the tephra laterally away from the eruption site, and buoyant gravity currents at often lower atmospheric heights, the pyroclasts (and lithics) with the greatest mass and highest settling velocities fall first, resulting in a coarser and thicker pyroclastic deposit closest to the volcano. With increased dispersal distance, pyroclasts become progressively finer, depositing thinner and finer-grained deposits at more distal locations. If the mass flux of the volcano is unstable, waxing and waning in the eruptive energy may occur (e.g., Branney and Kokelaar, 2002). If the mass flux is high, the density of pyroclastic material will be too high to rise ambiently above the vent(s) and will fountain down the slopes of the volcanoes, following topography. Aided by gravity, localised pyroclastic density currents (PDCs) will form as ground-hugging clouds of gas, juveniles and lithics (comprised of material from inside the vent(s) and erosion during transportation). PDCs deposit by progressive aggradation (Branney and Kokelaar, 1992), resulting in the sedimentation of ignimbrites (PDC deposits) during depositional phases of the current. At the top of PDCs, where finer and less dense material occurs, similar processes occur to the eruptive plume, with particles rising buoyantly due to the entrainment of ambient air and expansion due to heating. When enough denser material has been removed by sedimentation, the finest pyroclasts within the current also rise ambiently to form a co-ignimbritic plume, which is subject to similar processes to the main eruptive plume.

The style of volcanic eruptions can typically be characterised by the dispersal index of tephra (i.e., distance from source) compared with the fragmentation index (i.e., the degree of magmatic fragmentation that occurs, Walker, 1973). Fig.1b displays this classification by

A





STAGE 1 = *Older bubbles nucleate*

STAGE 2 = *Bubble growth occurs by diffusion and decompression. Further nucleation of bubbles*

STAGE 3 = *Bubbles become crowded leading to wall collapse*

STAGE 4 = *Bubble walls fully collapse at fragmentation converting magma from a gas containing pyroclasts (clots of liquid magma)*

B

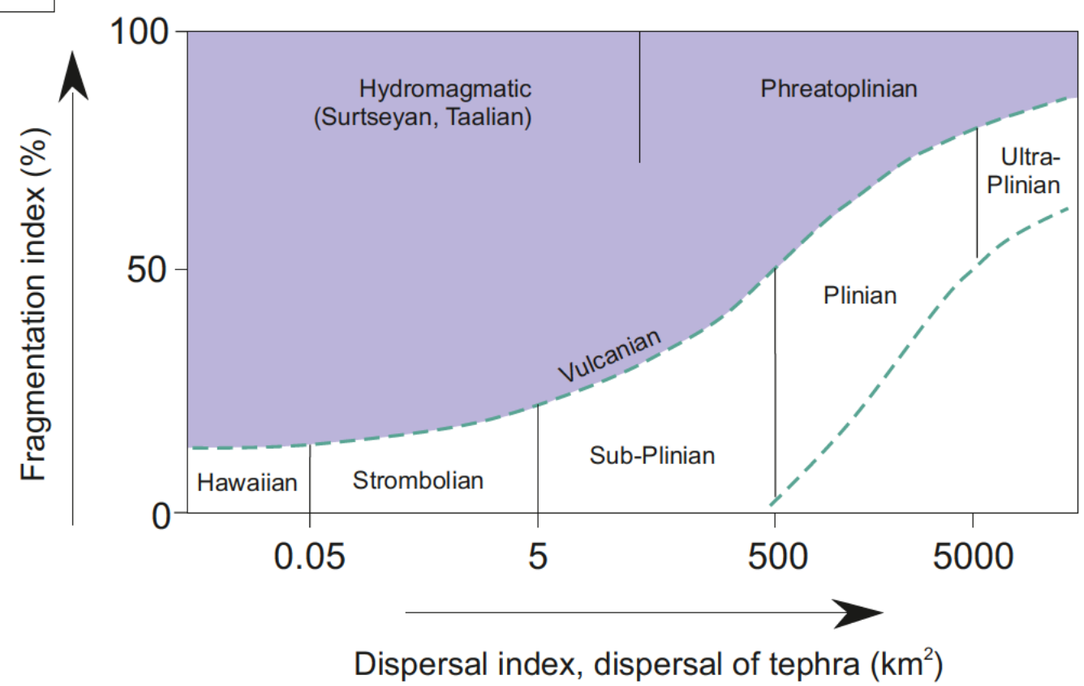


Fig. 1. (a) Schematic diagram representing the surface and sub-surface anatomy and processes often involved in an explosive eruption. Eruptive column regions are after Sparks et al. (1997). (b) Eruptive style classification diagram using fragmentation index vs. dispersal index. The purple areas include eruption styles influenced by magma-water interaction and the white areas are indicative of magmatic eruption styles. Vulcanian eruptions span both water-influenced and non-water-influenced eruption styles. Modified from Walker (1973).

Walker (1973) where it can be seen that hydromagmatic and phreatoplinian eruptions have an increased fragmentation index, by up to 75%. This is due to the addition of water (from external sources, e.g., marine or lake waters, for hydromagmatic eruptions and groundwater sources for phreatomagmatic eruptions, Kokelaar, 1983). Vulcanian eruptions may be hydromagmatic, phreatomagmatic or magmatic.

In order to determine if an eruption is likely, it is important to establish the background activity from the volcano(es) in question. This can be conducted in real-time, often built up over many years, by obtaining geophysical data where average ('normal') activity can be established (e.g., Pan et al., 2021). This data is often enhanced by observations from geologists or local people and communities that live/work on or near the volcano(es) on a daily basis, thus integrating citizen science practices with monitoring efforts (e.g., Duncan et al., 2019; Hicks et al., 2019). Additionally, studying past events and non-events (hiatus') from a volcano's geological record can aid in the establishment of its eruptive capabilities (i.e., the best and worst case eruptive scenario) and its most common style of activity (i.e., the most likely).

Traditionally, the long-term eruptive record of a volcano is grounded in field observations through the description and interpretation of geological products (as outlined above), supplemented by quantitative analysis. From highly explosive magmatically-derived

eruptions, tephra layers can be traced for many tens to hundreds of kilometres and across continents (e.g., Abbott and Davies, 2012). However, the completeness of volcanic eruption records deteriorates rapidly beyond recent historical records, with often only the largest events represented in the geological record over longer timescales (e.g., Crosweller et al., 2012). This presents one the largest challenges for volcanology, resulting in many eruption records being highly incomplete, thus preventing accurate hazard assessments, with the tempo of volcanism being unclear at many volcanoes around the world (e.g., Watt et al., 2013).

2. MOTIVATION

Throughout the course of this PhD, the world has experienced several volcanic eruptions which have severely impacted (and continue to impact) peoples' lives and livelihoods, displacing, injuring and killing thousands. These have occurred in a variety of locations and geological settings, however effects have been greater and lasted for longer in the developing world. Fig.2. displays some of these volcanoes: Anak Krakatau, Indonesia (2018); Volcan de Fuego, Guatemala (2018); Cumbre Vieja, La Palma (2021); Fagradalsfjall, Iceland (2021) and summarises the primary hazards and effects of these volcanoes. Fagradalsfjall, Iceland is included as a 'tourist eruption', demonstrating that when eruptive styles are generally effusive and occur within remote locations, far from populations and infrastructure, they can generate huge economic benefits for the region and are generally considered low risk (Erfurt-Cooper, 2014).

As with any natural hazard-related science, it is easy to become enveloped within the data. However, the news of an eruption triggers a response from the international volcanology community through organisations such as the Volcanic Disaster Assistance Program (VDAP,

ANAK KRAKATAU, INDONESIA (2018)



PRIMARY HAZARDS:

- Lateral collapse
- Tsunami generation
- Pyroclastic (tephra) hazards

EFFECTS:

- 437 deaths
- 2,752 homes destroyed

VOLCAN DE FUEGO, GUATEMALA (2018)



PRIMARY HAZARDS:

- Pyroclastic (tephra) hazards
- Pyroclastic density currents (PDCs)
- Lahars

EFFECTS:

- 190 (confirmed), 2900 (unconfirmed) deaths
- 12,823 people evacuated

CUMBRE VIEJA, LA PALMA (2021)



PRIMARY HAZARDS:

- Pyroclastic (tephra) hazards
- Ballistic hazards
- Lava

EFFECTS:

- 0 deaths
- 7,500 people evacuated

FAGRADALSFJALL, ICELAND (2021)



PRIMARY HAZARDS:

- Gas hazards
- Ballistic hazards
- Lava

EFFECTS:

- 0 deaths
- 0 people evacuated

Fig. 2. Four volcanoes that have erupted during the completion of this PhD: Anak Krakatau, Indonesia (2018); Volcan de Fuego, Guatemala (2018); Cumbre Vieja, La Palma (2021); and Fagradalsfjall, Iceland (2021). The primary hazards and effects are noted indicating the recent-current effects of volcanism around the world. Image credits: Anak Krakatau: Edo Marshall/UKRI (accessed June 2022); Volcan de Fuego: Coordinadora Nacional para la Reducción de Desastres de Guatemala (CONRED, accessed March 2022); Cumbre Vieja: Dougal Jerran [twitter] (accessed January 2022); Fagradalsfjall: Tim Dawson [twitter] (accessed February 2022).

Lowenstern and Ramsey, 2017) and via scientific communication (Williams and Krippner, 2018). By synthesising volcanology with social sciences, hazard and risk, resilience can be strengthened and disaster risk reduction (DRR) improved (e.g., Barclay et al., 2008).

Central Mexico is home to several volcanoes, due to the position of the Trans-Mexican Volcanic Belt (TMVB), a volcanic alignment that results from the subduction of the Riviera and Cocos plates under the North American plate (see chapter 2 onwards and references therein). Resultantly, Mexico City is surrounded by several explosive polygenetic volcanoes (e.g., Popocatépetl, Fig. 1 in Chapter 2) and a monogenetic volcanic field, the Sierra Chichinautzin Volcanic Field (SCVF), as well as being vulnerable to eruptions from more distal sources throughout Central America (e.g., Kutterolf et al., 2016).

Mexico City is home to over 25 million people, who are at risk from effusive and explosive volcanism from any of the surrounding active volcanoes. Due to the city comprising one of the largest populations in the world, geological exposures are limited and sparse, resulting in poorly constrained eruption records for the region (e.g., Bloomfield, 1974; Arce et al., 2020).

This thesis focuses on the improvement of the longer-term record of explosive volcanism in the Mexico City region through the investigation of a deep lacustrine sediment core from Lake Chalco, on the SE edge of the city (e.g., Brown et al., 2019) supplemented by detailed fieldwork. This research is part of a collaborative continental drilling project: MexiDrill, funded by the

International Continental Scientific Drilling Program (ICDP, see Chapter 2). This thesis significantly improves upon the eruptive record of explosive volcanism in the Mexico City region, providing constraints on the frequency, physical parameters and sources of eruptions impacting the region.

This work can be used to better understand volcanic hazards from diverse eruptions in central Mexico and presents a first step in the assessment of a unique and exceptional archive of explosive volcanic activity in a continental arc setting.

CHAPTER 2

STUDY AREA

"Roads? Where we're going, we don't need roads."

Dr. Emmett Brown, Back to the Future Part I, II

This chapter contains elements published in Journal of International Earth Sciences[1], Limnogeology: Progress, Challenges and Opportunities[2] and Journal of Volcanology and Geothermal Research[3].

These papers are provided in Appendices P1, P2 and P3, respectively.

Contribution statement: For [1] and [2] my involvement included contributing to the scientific methodology, analysis and writing, review, and editing.

For [3] my involvement included all aspects of the study (see contribution statement for chapter 4, in which this paper is presented).

---

[1]Martínez-Abarca, R., Ortega-Guerrero, B., Lozano-García, S., Caballero, M., Valero-Garcés, B., McGee, D., Brown, E.T., Stockhecke, M. and **Hodgetts, A.G.E.**, (2021). Sedimentary stratigraphy of Lake Chalco (Central Mexico) during its formative stages. *International Journal of Earth Sciences*, pp.1-21.

[2]Valero-Garcés, B., Stockhecke, M., Lozano-García, S., Ortega, B., Caballero, M., Fawcett, P., Werne, J.P., Brown, E., Najera, S.S., Pearthree, K. and McGee, D., **Hodgetts, A.G.E.**, Martínez-Abarca, R., (2021). Stratigraphy and Sedimentology of the Upper Pleistocene to Holocene Lake Chalco Drill Cores (Mexico Basin). *Limnogeology: Progress, Challenges and Opportunities: A Tribute to Elizabeth Gierlowski-Kordesch*, p.415

[3] Sunyé-Puchol, I., **Hodgetts, A.G.E**, Watt, S.F.L, Arce, J.L., Barfod, D.N., Mark, D.F., Sosa-Ceballos, G., Siebe, C., Dymock, R.C., Blaauw, M. and Smith, V.C., 2022. Reconstructing the middle to late Pleistocene explosive eruption histories of Popocatépetl, Iztaccíhuatl and Tláloc-Telapón volcanoes in Central México. *Journal of Volcanology and Geothermal Research*, *421*, p.107413.

MAPA GEOLÓGICO DE MÉXICO

ESTADOS UNIDOS DE AMÉRICA

GOLFO DE CALIFORNIA
(Mar de Cortés)

OCÉANO PACÍFICO

GOLFO DE MEXICO

SONDA DE CAMPECHE

MAR CARIBE
(Mar de las Antillas)

GOLFO DE TEHUANTEPEC

GUATEMALA

BELIZE

HONDURAS

TRÓPICO DE CÁNCER

-117° -114° -111° -108° -105° -102° -99° -96° -93° -90° -87°

30° 27° 24° 21° 18° 15°

UNIDADES CRONOESTRATIGRÁFICAS: ERA	SISTEMA	SERIE	PISO	AMBIENTES GENÉTICOS: SEDIMENTARIAS CONTINENTALES	SEDIMENTARIAS MIXTAS	SEDIMENTARIAS MARINAS	ÍGNEAS VOLCANOSEDIMENTARIAS CONTINENTALES	ÍGNEAS VOLCANOSEDIMENTARIAS MARINAS	ÍGNEAS VOLCÁNICAS CONTINENTALES	ÍGNEAS INTRUSIVAS GRANÍTICAS Y GABROIDES	METAMÓRFICAS REGIONALES
CENOZOICO	CUATERNARIO			Qc Qe		Q					
CENOZOICO	TERCIARIO	PLIOCENO			Tpmx	Tm N	Tvsc	Tovs	Nmv Nmb Qtpv Mc	Ngr	Tmet
CENOZOICO	TERCIARIO	MIOCENO		Csc	Nmx				Peov Tv	Tgr Pegr	
CENOZOICO	TERCIARIO	OLIGOCENO			Tomx	To					Tgb
CENOZOICO	TERCIARIO	EOCENO		Pgc		Te					
CENOZOICO	TERCIARIO	PALEOCENO			Tpamx	Tpa					
MESOZOICO	CRETÁCICO	Superior		Kgc	Ksmx	Ks				Kgr	Kmet
MESOZOICO	CRETÁCICO	Inferior				KJs Ki K		Kivs	Kiv		
MESOZOICO	JURÁSICO	Superior		Jc	Jmx	Js J		Mvs	Jv	Jgr	Mmet
MESOZOICO	JURÁSICO	Medio			Jmmx			Mlvs Jlvs			Mlmet
MESOZOICO	JURÁSICO	Inferior			Mimx	Ji					
MESOZOICO	TRIÁSICO					TR				TRgr	TRmet
PALEOZOICO	PÉRMICO			Psc	Psmx	Ps		Pvs		Pgr	Pmet
PALEOZOICO	CARBONÍFERO					P					
PALEOZOICO	DEVÓNICO										Pmet
PALEOZOICO	SILÚRICO					Pi					
PALEOZOICO	ORDOVÍCICO										Emet
PALEOZOICO	CÁMBRICO										
PROTERO-ZOICO	Superior					PTs				PTgr	PTmmet
PROTERO-ZOICO	Medio										PTimet1 PTimet2
PROTERO-ZOICO	Inferior										

Actualización y adaptación de la Carta Geológica de la República Mexicana, escala 1:2,000,000 publicada por el Instituto de Geología de la UNAM y el Consejo de Recursos Minerales (Ortega-Gutiérrez et al., 1992)

Realizado por: Luca Ferrari-Pedraglio, Dante Morán-Zenteno y Enrique Alejandro González-Torres

Procesamiento digital y edición cartográfica: Laura Luna-González

Proyección	Cónica Conforma de Lambert
Elipsoide	Clarke de 1866
Datum	Norteamericano de 1927
Meridiano central	-102° 00'
Paralelos base	17° 30' y 29° 30'
Latitud de origen	14° 00'
Falso este	2,500,000 m
Falso norte	0.0 m

Escala 1:4,000,000

0 75 150 300 km

Plate i. Geological Map of Mexico. From Ortega-Gutiérrez et al. (1992)

1. STUDY AREA

1.1. *Geology and volcanism in Mexico*

The geology of Mexico is dominated by volcanic sedimentary rocks, extrusive volcanic rocks, magmatic intrusions and continental-derived sedimentary rocks (see Plate i). Volcanic lithologies typically crop out throughout central Mexico, extending E-W from the Pacific Ocean to the Gulf of Mexico, and dated between the Quaternary and Miocene (c. 23 Ma to present, predominantly light brown lithologies in Plate i). These lithologies define the position of the Trans-Mexican Volcanic Belt (TMVB, Fig. 1), a major intracontinental volcanic arc, where >40% of the population of Mexico lives (e.g., Varley, 2012, Fig. 1). This volcanic arc is 1000 km in length, 160,000 km^2 in area and lies above the subduction of the northern segment of the Cocos plate and Rivera microplate beneath the North American plate (Ferrari et al., 2012). Subduction initiated c.20 Ma, leading to four stages in the development of the TMVB, which overlies Cretaceous and Cenozoic basement (Ferrari et al., 2012). Continued subduction, with convergence rates up to 17 cm/yr (Mori et al., 2007), leads to a continued magma supply along the whole length of the belt.

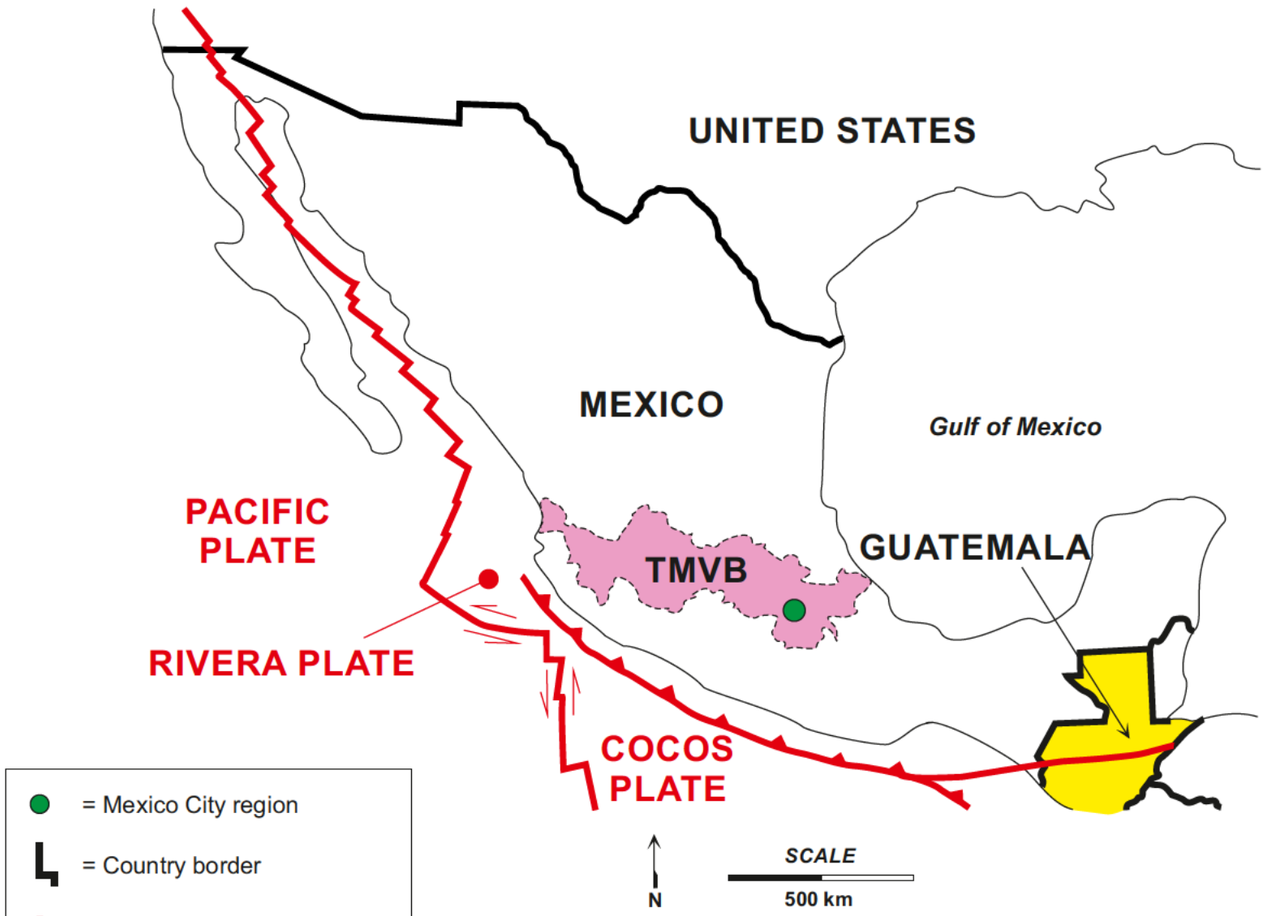
Active volcanoes within the TMVB have erupted in recent times, including polygenetic volcanoes such as Volcán de Colima and Popocatépetl which have been active in present-day and historical times, and for much of the Holocene (e.g., Crummy et al., 2019; Mangler et al., 2019). Monogenetic eruptions have also occurred within the TMVB, including Parícutin volcano, which erupted both explosively and effusively from 1943-1952 (e.g., Pioli et al., 2008). Volcanic fields (i.e., collections of smaller-scale, monogenetic, volcanoes) are common across the TMVB, including the Sierra Chichinautzin volcanic field (SCVF), Mexico's second largest

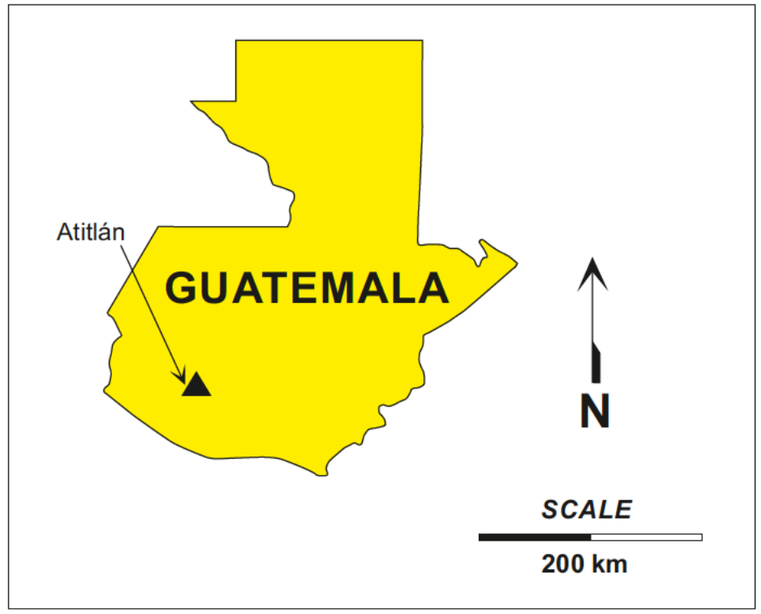
active field, which lies within and south (up to 40 km) of Mexico City (e.g., Del Pozzo, 1982; Robidoux et al., 2020; Guilbaud et al., 2022). Additionally, Mexico contains large caldera volcanoes, which have produced caldera-forming eruptions (up to Volcanic Explosivity Index, VEI, 8) in the past, including Los Humeros, La Primavera, Acoculco, Los Azufres, Las Cumbres and Citlaltépetl (e.g., Varley, 2012). The largest eruption of the TMVB was from Los Humeros at 164 ± 4.3ka, which emplaced the Xáltipan ignimbrite (e.g., Cavazos-Álvarez and Carrasco-Núñez, 2020; Pinti et al., 2021).

The people of Mexico are exposed to volcanoes, their products and their benefits, including fertile soil boosting agricultural yields (e.g., Covaleda et al., 2006, Chapter 1). However, risk from volcanic activity is high and due to densely populated regions surrounded by active volcanoes, such as Mexico City, a better understanding of their eruptive histories is essential to inform the present and future hazard and risk.

1.2. *Volcanology of the Mexico City region*

As discussed above, the Basin of Mexico, in which Mexico City and its metropolitan area (home to c.25 million people) sits, is surrounded by Pleistocene-Holocene volcanoes (e.g., Sunyé-Puchol et al., 2021). Volcanic ranges also surround the city: (1) to the east, the Sierra Nevada Volcanic Range (SNVR, e.g., Mora-Alvarez et al., 1991; Arce et al., 2019); and (2) to the west, the Sierra de Las Cruces Volcanic Range (SLCVR, e.g., Nixon, 1989; Cadoux et al., 2011; Macías et al., 2012). The SNVR is a N-S range comprised of two stratovolcanoes, Popocatépetl and Iztaccíhuatl and a compound volcano, Tláloc-Telapón, from S-N, respectively (e.g., Macías et al., 2012). Other minor vents are also present, including El Papayo which erupted effusively


UNITED STATES
MEXICO
Gulf of Mexico
PACIFIC PLATE
RIVERA PLATE
COCOS PLATE
TMVB
GUATEMALA
= Mexico City region
= Country border
= Tectonic boundary
= Tectonic movement
= Subduction zone
= Trans Mexican Volcanic Belt
N
SCALE
500 km


Atitlán
GUATEMALA
N
SCALE
200 km

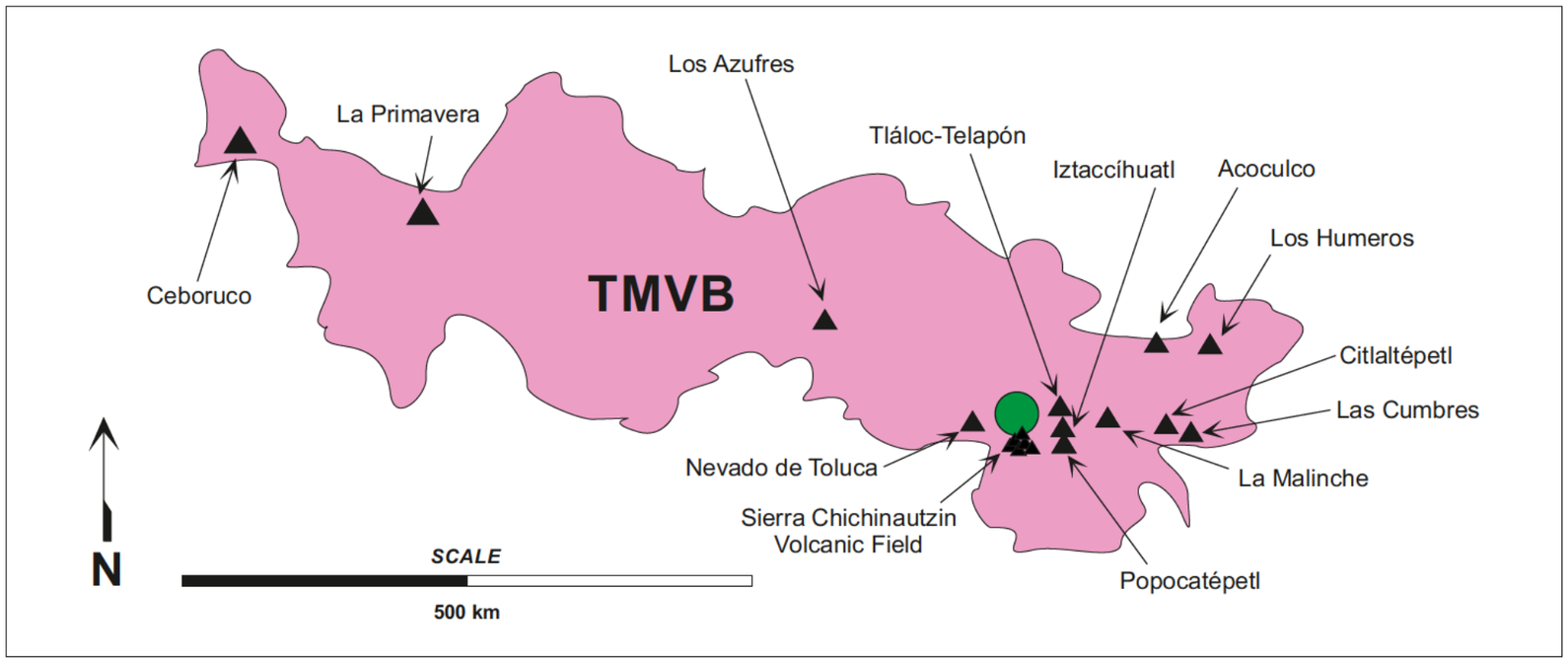

Los Azufres
La Primavera
Tláloc-Telapón
Iztaccíhuatl
Acoculco
Los Humeros
Ceboruco
TMVB
Citlaltépetl
Las Cumbres
Nevado de Toluca
La Malinche
Sierra Chichinautzin
Volcanic Field
Popocatépetl
N
SCALE
500 km

Fig. 1. Location map of the volcanoes described in this chapter and identified as a possible threat to Mexico City. Enlarged sections include a higher resolution for the Trans Mexican Volcanic Belt and Guatemala.

---

c.118 ka (Macías et al., 2012). Activity is thought to young towards the south, following dated lava blocks (c.1.82 Ma) within ignimbrites, inferred to be sourced from Tláloc-Telapón (Cadoux et al., 2012). Palaeo-Iztaccíhuatl (Llana Grande) is dated at c.1.09 Ma (Cadoux et al., 2021) and the earliest Popocatépetl ages are from the Tlamacas edifice c.538 ka (e.g., Gisbert et al., 2022). Activity in the SNVR is fairly well constrained for the past c.30 ka, and these volcanoes are considered the most recently active volcanoes in immediate proximity to Mexico City, with paroxysmal activity from Popocatépetl occurring in the present day (e.g., Love et al., 1998; Sunyé-Puchol et al., 2021).

The SLCVR comprises 8 overlapping edifices as well as smaller volcanic structures that are Pliocene to Pleistocene in age (e.g., Garcia-Palomo et al., 2008; Arce et al., 2019). They are not thought to be currently active. However, their eruptive histories are poorly constrained, with analysis mainly from satellite imagery due to poor exposures (e.g., Garcia-Palomo et al., 2008). Due to limited eruption histories and an absence of well described and mapped pyroclastic deposits, the SLCVR has been omitted from this study, with no reference samples or data to usefully compare with the record at Lake Chalco (see section 2).

Other polygenetic sources which are near to Mexico City include Nevado de Toluca (c.85 km W) and La Malinche (c.95 km E). Although limited eruption histories also exist for these volcanoes, recent (<13 ka) explosive and widespread deposits can be traced across the region, and they are considered active polygenetic stratovolcanoes.

Below, the proximal (<100 km from Lake Chalco, Mexico City) volcanoes are introduced. Further information is provided in chapters 3, 4 and 5.

1.2.1. Popocatépetl

At 5,452 m amsl., Popocatépetl is the second highest point in Mexico. Since 1994, activity was renewed and the volcano has been in an eruptive state, following c.70 years of quiescence (Sunyé-Puchol et al., 2021). Throughout its lifetime it has undergone several collapse and building cycles, with Popocatépetl being the newest edifice, formed c.23.5 ka (c.27.8 cal. ka, Mangler et al., 2022). Older edifices have included Ventorrillo (c.23.5-98 ka); Nexpayantla (c.98-330 ka) and Tlamacas (330->538 ka, Gisbert et al., 2022). Since the formation of the Popocatépetl edifice, which also coincided with a Plinian eruption (depositing the White Pumice), six Plinian eruptions have occurred, on average every 1000-3000 years (Siebe et al., 1998; Sunyé-Puchol et al., 2021). The largest documented eruption since the most recent sector collapse is the Tutti Frutti Plinian eruption (c.17 cal. ka BP), which produced a small caldera and erupted a tephra volume of 3 km^3 (DRE, Sosa-Ceballos et al., 2012). Fig.2a displays some of the largest eruptions since 27.8 cal. ka from Popocatépetl.

1.2.2. Iztaccíhuatl

Sitting c.16 km north of Popocatépetl, Iztaccíhuatl is 5,286 m amsl. Less is known about its eruptive history; however, the younger phase of this volcano is c.600 ka in age (Nixon, 1988; Nixon, 1999; Sunyé-Puchol et al., 2021). The collapse of the Los Pies cone, early in its younger

A



Name: Popocatépetl

Height (m amsl): 5,452

Location: 19.02231, -98.62793

Age: c.538 ka

Last known eruption: in eruptive state

Major eruptions:

Eruption	Deposits	Volume DRE (km³)	Age (ka)	References
Pink Pumice	Fall	2.5	1.1	Siebe et al., 2017
Lorenzo Pumice	Fall	2	2.15	Siebe et al., 2017
Ochre Pumice	Fall	2	4.95	Arana-Salinas et al., 2010
Tutti Frutti Pumice	Fall	3	17	Sosa-Ceballos et al., 2012
White Pumice	Fall	1.9	27.8	Siebe et al., 2017

B



Name: Iztaccíhuatl

Height (m amsl): 5,286

Location: 19.17025, -98.63755

Age: c.600 ka (younger phase)

Last known eruption: c.8 ka

Major eruptions:

Eruption	Deposits	Volume DRE (km³)	Age (ka)	References
NT-13	Fall	-	<606	Sunyé-Puchol et al., (2021)
NT-11/FRT-1	Fall	-	-	Sunyé-Puchol et al., (2021)
NT8**	Fall	-	-	Sunyé-Puchol et al., (2021)
NT-4/XQT-3	Fall	-	-	Sunyé-Puchol et al., (2021)
NT-3	Fall	-	-	Sunyé-Puchol et al., (2021)
Nepopualco Ignimbrite	Ignimbrite	-	631 ± 44	Sunyé-Puchol et al., (2021)
Los Pies	Block and ash flow and Fall	-	440 ± 190	Macias et al., 2012

Fig. 2. (a) Summary fact file of the key characteristics of Popocatépetl volcano, with major pyroclastic eruptions presented. (b) Summary fact file of the key characteristics of Iztaccíhuatl volcano, with major pyroclastic eruptions presented.

---

phase, formed the Los Pies Debris Avalanche Deposit (LPDAD), which covered an area of 550 km^2 and had an estimated volume of c.1.5 km^3 (García-Tenorio, 2008; García-Tenorio et al., 2012; Macias et al., 2012), from an eruption triggered by the collapse. Iztaccíhuatl's older history (Palaeo-Iztaccíhuatl) is estimated at c.1.09 Ma. Fig.2b displays some of the largest eruptions from Iztaccíhuatl during its younger phase. Many of these eruptions are from deposits described in this study (chapter 4) and Sunyé-Puchol et al. (2021).

1.2.3. Tláloc-Telapón

Tláloc-Telapón refers to two peaks/craters that this volcanic complex comprises. The highest is Monte Tláloc at 4,120 m amsl., which is c.28 km NNE of Iztaccíhuatl. This compound volcano began construction at c.0.94 Ma, building by the effusion of dacitic lavas (e.g., Sunyé-Puchol et al., 2021). This activity is thought to have dominated for much of its earlier history, constructing lava domes (e.g., Cadoux et al., 2011; Macias et al., 2012; Rueda et al., 2013). Explosive, pyroclastic eruptions have also been mapped and documented, the oldest being the San Valentin ignimbrite, previously thought to be c.45 ka (Macias et al., 2012). This deposit is re-dated by $^{40}Ar/^{39}Ar$ methods in this study (chapter 4) and Sunyé-Puchol et al. (2021) and is revised to be an age of 102 ± 2 ka. Since c.102 ka, at least five Plinian eruptions have occurred, outlined in Fig.3a.

A



Name: Tláloc-Telapón

Height (m amsl): 5,286

Location: 19.41351, -98.71347

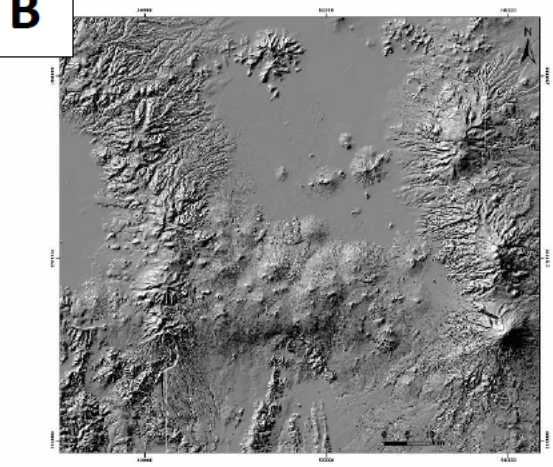
Age: 0.94 Ma

Last known eruption: c.30 ka

Major eruptions:

Eruption	Deposits	Volume DRE (km^3)	Age (ka)	References
Cuauhtemoc	Ignimbrite	c.1.5	29.9-30.1	Rueda et al., 2006; Rueda et al., 2007
Multilayered White Pumice	Ignimbrite	1.58	35.6-36.1	Rueda et al., 2013
P-Mex	Ignimbrite	c.1.5	36.5-39.3	Meier et al , 2007
La Joya	Ignimbrite	c.1.5	40.6-42.8	Huddart and González, 2004; Huddart and González, 2006
San Valentin	Ignimbrite	c.1.5	102 ±2	Rueda et al., 2006; Rueda et al., 2007; Sunyé-Puchol et al., (2021)

B



Name: Sierra Chichinautzin

Location: 19.09122, -99.08706

Age: c.1.3 Ma

Last known eruption: c.1.6 ka

Major eruptions:

Cone	Deposits	Volume DRE (km^3)	Age (ka)	References
Chichinautzin	Scoria Fall and Lava	0.6	1.8	Siebe et al., 2004; Siebe et al., 2005
Pelado	Scoria Fall and Lava	0.9	10	Lorenzo-Merino et al., 2018
Teuhtli	Scoria Fall and Lava	0.5	>14	Siebe et al., 2004; Siebe et al., 2005

Fig. 3. (a) Summary fact file of the key characteristics of Tláloc-Telapón volcano, with major pyroclastic eruptions presented. (b) Summary fact file of the key characteristics of the Sierra Chichinautzin Volcanic Field, with three well documented explosive eruptions presented.

1.2.4. Sierra Chichinautzin Volcanic Field

The Sierra Chichinautzin Volcanic Field (SCVF) lies within Mexico City and extends for up to 40 km south of the city limits (e.g., Del Pozzo, 1982). The field currently comprises c.200 monogenetic cones, which have been the focus of many recent studies (e.g., Alcalá-Reygosa et al., 2018; Lorenzo-Merino et al., 2018; Jaimes-Viera et al., 2018; Guilbaud et al., 2022). Eruptions are fairly well constrained for the past c.40 ka, (see Nieto-Torres and Del Pozzo, 2019) and age information has been extended by the morphometric analysis of cones (e.g., Agustín-Flores et al., 2011). Jaimes-Viera et al. (2018) suggest that volcanism is c.1.3 Ma and that the field is comprised of four smaller fields, active at different times, with the majority of cones <35 ka in age. Portions of the SCVF which are within the Mexico City limits include the Sierra Santa Catarina, an ENE-trending cluster of 7 cones which is thought to have originated at Volcan Xaltepec in the west at c.132 ± 70 ka and migrated east to Tetecón and an older NE-SW trending cluster of eroded cones further north, at c.1.3 Ma (Jaimes-Viera et al., 2018). All current cones in the SCVF currently display subaerial features/morphometries, (e.g., Bischoff et al, 2019), although a tuff cone is also present, Xicotencatl, characterised by its wide aspect ratio. This tuff cone lies within the Chalco basin, c.2 km from Lake Chalco. Some of the major eruptions from the SCVF are outlined in Fig.3b.

1.2.5. Nevado de Toluca

Nevado de Toluca volcano sits towards the SW of the Basin of Mexico and is c.80 km from Mexico City. Its peak is at 4,680m amsl., and the summit contains a 2 km wide crater with a crater lake containing a dacitic dome, El Ombligo (e.g., Capra et al., 2006; Capra et al., 2008). Activity from the Paleonevado stage was lava-dominated and began c.2.6 Ma, ceasing c.1.2 Ma to be succeeded by dome growth and destruction, some producing syn-explosive activity (De Beni, 2001; Garcia-Palomo et al., 2002; Capra et al., 2008). Nevado de Toluca has been in quiescence for c.3 ka (e.g., Macias et al., 1997). Since c.42ka, the volcano has experienced five dome collapses, and four Plinian eruptions, the largest being the Upper Toluca Pumice which emplaced 8 km^3 Dense Rock Equivalent (DRE) of tephra and formed a plume >40 km in height, which dispersed tephra over Mexico City, depositing up to 40 cm of material (Bloomfield et al., 1977; Arce et al., 2003; Capra et al., 2006). These four Plinian events are outlined in Fig.4a.

1.2.6. La Malinche

La Malinche volcano lies within the Puebla Basin and sits c.95 km from Mexico City. It is an isolated stratovolcano with a summit of 2,250 m amsl., which is dominated by dacitic lava domes, leading to interpretations that it is extinct (e.g., Castro-Govea and Siebe, 2007). However, investigations into the eruptive deposits of the volcano have indicated that the volcano has been active throughout the Holocene and is currently in a period of dormancy (e.g., Nelson, 1990; Castro-Govea and Siebe, 2007). Castro-Govea and Siebe (2007) conducted the first detailed stratigraphic investigation into La Malinche, subdividing the Malinche stage into three periods: (1) c.45 – c.23 ka deposits, mostly comprising block and ash flows, and the Humantla Pumice eruption; (2) c.21 – c.16 ka, comprising debris avalanches, block and ash

A



Name: Nevado de Toluca

Height (m amsl): 4,680

Location: 19.10812, -99.75969

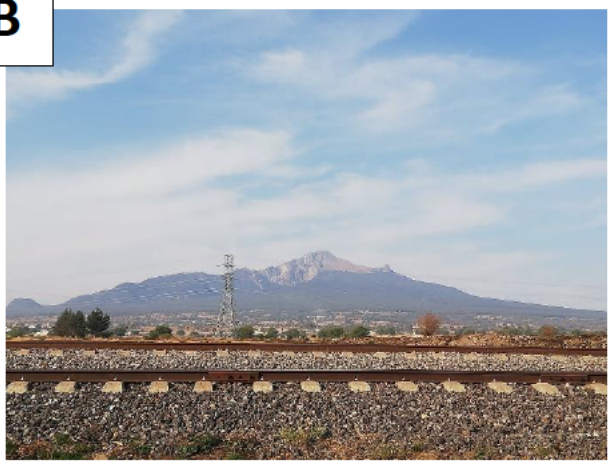
Age: c.2.6 Ma

Last known eruption: c.12 ka

Major eruptions:

Eruption	Deposits	Volume DRE (km³)	Age (ka)	References
Upper Toluca Pumice	Fall	8	12.1-12.8	Arce et al., 2003
Middle Toluca Pumice	Fall	.8	12.1	Arce et al., 2005
Lower Toluca Pumice	Fall	1.5	21.7	García-Palomo et al., 2002; Arce et al., 2005; Capra et al., 2006
Ochre Pumice	Fall	-	36	Capra et al., 2006

B



Name: La Malinche

Height (m amsl): 2,250

Location: 19.23107, -98.03227

Age: >45 ka

Last known eruption: c.8 ka

Major eruptions:

Eruption	Deposits	Volume DRE (km³)	Age (ka)	References
Altamira Pumice	Fall	-	7.82 1 ± 0.11	Castro-Govea and Siebe, 2007
Malinche Pumice II	Fall	-	12.1 ± 0.16	Castro-Govea and Siebe, 2007
Malinche Pumice I	Fall	-	25.7	Castro-Govea and Siebe, 2007
Huamantla	Fall	-	>45	Castro-Govea and Siebe, 2007
Baquedano	Fall	-	>45	Castro-Govea and Siebe, 2007

Fig. 4. (a) Summary fact file of the key characteristics of Nevado de Toluca volcano, with major pyroclastic eruptions presented. (b) Summary fact file of the key characteristics of La Malinche volcano, with major pyroclastic eruptions presented.

---

flows and lahars as well as the Malinche Pumice I eruption; and (3) c.12 -c.3 ka, comprising block and ash flows and lahars, as well as the Malinche Pumice II eruption and Altamira Pumice. These explosive eruptions are further outlined in Fig.4b.

1.3. Distal volcanoes (>100 km from Mexico City)

Explosive volcanoes, outside of the Mexico City region, are often still a threat to Mexico City, (in addition to their nearby communities), if eruption magnitudes are large enough and dispersal directions are directed towards the city. There are too many volcanoes with the potential to impact Mexico City to be described here, so caldera volcanoes or volcanoes which have had caldera-forming eruptions throughout the Pleistocene to Holocene are briefly described below. The major eruptions from each of these volcanoes are also presented in Table 1.

1.3.1 Ceboruco

Ceboruco lies c.615 km NW of Mexico City towards the west of the TMVB. It has an elevation of 2,164 m amsl., and last erupted in 1870, with moderate fumarolic activity continuing within the crater today (Sieron and Siebe, 2008). Since c.1 ka, the crater has constructed several domes which are largely fresh in appearance with little to no vegetation, indicating they are active (Sieron and Siebe, 2008). The onset of volcanism is poorly constrained, although stages of its growth are assumed to be relatively short in duration (Chertkoff and Gardner, 2004). The most

Table1. Major pyroclastic eruptions from distal caldera volcanoes (>100 km) from Mexico City, identified in this study as a possible volcanic threat to the Mexico City region.

Volcano	Eruption	Deposits	Tephra volume (km^3 DRE)	Dispersal	Age (ka)	Distance to Mexico City (km)	References
Ceboruco	Jala Pumice	Falls and ignimbrites	c.3-4	NE	1	c.960	Sieron and Siebe, 2008
La Primavera	Tala Tuff	Falls and ignimbrites	20	Radial (distal to ENE)	95 ± 5	c.500	Mahood, 1981; Walker et al., 1981
Los Humeros	Zaragoza Tuff	Falls and ignimbrites	15	N (poorly constrained)	69 ± 16	c.160	Carrasco-Núñez et al., 2018
Los Humeros	Faby Tuff	Falls and ignimbrites	10	-	70 ± 23	c.160	Carrasco-Núñez et al., 2018
Los Humeros	Xáltipan ignimbrite	Falls and ignimbrites	290	Radial (distal component to SW)	164 ± 4.2	c.160	Carrasco-Núñez et al., 2018; Cavazos-Álvarez and Carrasco-Núñez, 2020
Atitlán	Los Chocoyos	Falls and ignimbrites	510	NW	75 ± 2	c.970	Kutterolf et al., 2016; Cisneros De Leon et al., 2021
Atitlán	L-Fall	Falls and ignimbrites	-	N	191	c.970	Kutterolf et al., 2016
Acoculco caldera	Tecoloquillo Ignimbrite	Falls and ignimbrites	11	S	762 ± 9	c.100	Avellán et al., 2020
Azufres caldera	Cieneguillas ignimbrite	Falls and ignimbrites	12	S	300 ± 7	c.180	Pradal and Robin, 1994
Citlaltepetl	Quetzalapa Pumice	Falls and ignimbrites	c.2	NNE/SSW	20.4 - 19.6	c.190	Rodríguez et al., 2002
Las Cumbres	Las Cumbres collapse	Falls and ignimbrites	9	WNW	16.9 ± 0.8	c.190	Höskuldsson, 1992

well-known and described eruption from Ceboruco is the Jala Pumice caldera-forming eruption, which occurred c.1 ka (e.g., Nelson, 1980; Sieron and Siebe, 2008). This eruption was a VEI6, with a tephra volume of 10.7 km^3 (3-4 km^3 DRE, Sieron and Siebe, 2008), making it one of the largest eruptions in Mexico in the last millennium. With a dispersal to the NE (e.g., Sieron and Siebe, 2008), it is possible that this eruption was dispersed as far as Mexico City.

1.3.2. La Primavera

La Primavera is a large silicic caldera volcano which sits c.500 km to the NW of Mexico City. The onset of volcanism was between c.145 and c.100 ka characterised by the emplacement of lavas in a pre-caldera stage (e.g., Mahood, 1981). Following this, at c.95 ka, a caldera-forming eruption occurred, emplacing the Tala Tuff, which had a tephra volume of c.20 km^3 DRE and formed an 11 km-wide caldera (Mahood, 1981; Sourisseau et al., 2020). Since, the volcano has been in a post-caldera stage dominated by lava effusion, central dome growth and the eruption producing the Giant Pumice Horizon, an important stratigraphic marker for the volcano thought to have accumulated within a caldera lake (Walker et al., 1981). Walker et al. (1981) recognised ten major fall deposits which considering dispersal patterns are often consistent with being sourced from the San Miguel and Planillas satellite vents.

1.3.2. Los Humeros

Los Humeros is the largest active caldera in Mexico (e.g., Carrasco-Núñez et al., 2018). This volcano lies c.160 km NE of Mexico City and is Pleistocene to Holocene in age (e.g., Ferriz and Mahood, 1984). Volcanic basement is as young as c.1.44 Ma with the pre-caldera stage consisting of mostly lava-dome building, continuing until c.270 ± 17 ka (e.g., Cavazos-Álvarez and Carrasco-Núñez, 2020). During the caldera stage, three major eruptions occurred: (1) the

Xáltipan ignimbrite (164 ± 4.2 ka), the largest eruption of the TMVB, with a tephra volume of 290 km^3 DRE; (2) the Faby Tuff (70 ± 23 ka), an eruption with a tephra volume of 10 km^3 DRE; and (3) the Zaragoza ignimbrite (69 ± 16 ka), an eruption with a tephra volume of 15 km^3 DRE (Cavazos-Álvarez and Carrasco-Núñez, 2020). The Xáltipan ignimbrite tephra fall has a radial dispersal with the distal component confirmed to have been dispersed towards the SW (Cavazos-Álvarez and Carrasco-Núñez, 2020), possibly reaching and depositing tephra over the Mexico City region.

1.3.2 Atitlán, Guatemala

Atitlán, although not in Mexico, is considered a threat to Mexico City due to the magnitude of some of its past eruptions. This volcano is responsible for the Los Chocoyos (LCY) eruption at 75 ± 2 ka, which had a tephra volume of c.510 km^3 DRE and a fall deposit, estimated from isopach mapping, to be between 6 and 9 cm at Mexico City (Kutterolf et al, 2016). This eruption is one of the largest in Central and North America and is the third largest eruption globally of the Quaternary (e.g., Paine et al., 2022). Additionally, other explosive events (although typically smaller in magnitude than the LCY eruption), have occurred including the L-Fall at c.191 ka, W-Fall at 158 ± 3 ka and the I-Fall dated to be >40 ka (Kutterolf et al, 2016; Cisneros de León et al., 2021). From isopach maps presented in Kutterolf et al (2016) the L-Fall is the only other eruption which has dispersed tephra towards and possibly over the Mexico City region.

In addition to the volcanoes outlined above, and in section 1.2, multiple other sources are likely to have impacted Mexico City in the past and are likely to impact the region again in the future. These may also include other caldera volcanoes such as Acoculco, Los Azufres, Las Cumbres

and Citlaltépetl. Major eruptions from these volcanoes are outlined in Table 1. It must also be noted that very small thicknesses of ash fall are important to understand as their impact can be substantial (e.g., Wilson et al., 2012; Deligne et al., 2021).

2. LAKE CHALCO, MEXIDRILL PROJECT

As mentioned in Chapter 1, this thesis aims to improve upon the eruptive history of the Mexico City region by combining stratigraphic, glass geochemical and geochronological data. A primary investigation in this thesis is the sedimentary record of Lago Chalco (Lake Chalco), an endorheic lake on the south-eastern edge of Mexico City (Fig. 1). Lake Chalco is part of the wider Basin of Mexico, a collection of five lakes, including Texococo and Xochimilco (e.g., Martínez-Abarca et al., 2022). Following draining of the lake, the area and volume of Chalco has been significantly reduced (see chapter 3).

Due to Lake Chalco providing a large depocenter for sedimentation, recovery of the sedimentary succession has been a focus of several projects in recent years (e.g., Ortega-Guerrero et al., 2018; Brown et al., 2019). In 2008 and 2011, drilling/coring projects were undertaken, with the former recovering the deepest material at c.122 m below-surface (Ortega-Guerrero et al., 2017). In 2012, scientific planning to recover a deeper succession from Lake Chalco began, with the aim to recover the full sedimentary sequence from the lake as part of a multidisciplinary investigation (Brown et al., 2019). The project was funded by the International Continental Scientific Drilling Program (ICDP) and in 2016 was drilled for 6 weeks, day and night, reaching a depth of c.520 m below-surface. Drilling was conducted as part of the MexiDrill Project (https://www.arch.ox.ac.uk/mexidrill), involving scientists from multiple countries and disciplines. Three parallel boreholes (A, B and C, Fig. 1b1 in Chapter 3)

were drilled to maximise recovery of the succession. Rotational techniques were employed using a truck-mounted Boart Longyear LF90 drilling rig with standard Boart Longyear HQ3 wireline diamond-rotational-drilling coring tools (Brown et al., 2019; Martínez-Abarca et al., 2021). Additionally, a fourth borehole was cored (Hole D) which was recovered by hand to 19 m below-surface using a Usinger-type piston corer with percussion, to enhance the recovery of the uppermost softer sediments (Valero-Garcés et al., 2021). Further methods, related to the recovery and processing of core samples, is provided in chapter 3.

Following the drilling, sedimentological descriptions were completed and a composite sequence (splice) was created, which seeks to provide a single sedimentological sequence which minimises the effect of poorly preserved/recovered sections (see chapter 3). The composite stratigraphy is published in Valero-Garcés et al. (2021), and graphically summarised in Fig. 5.

In Fig. 5 the main sediment types of Lake Chalco are presented, as well as drilling gaps and disturbance. The core is subdivided into numbered sections relating major lithostratigraphic units within the composite core. These are presented in Valero-Garcés et al. (2021), Appendix P1. The sedimentology of Lake Chalco comprises mostly diatomaceous, carbonated, silty clay and organic-rich sediment types, with numerous volcanic layers between these lacustrine sediments (see Fig. 4). Towards the base of the core, below c.300 m, the core is dominated by volcanic lithologies, including lavas and volcaniclastic deposits. The volcanic stratigraphy of this succession is presented in detail in chapter 3. The transition from these volcaniclastic lithologies to lacustrine sediments (which account for the majority of the upper c.300 m) is

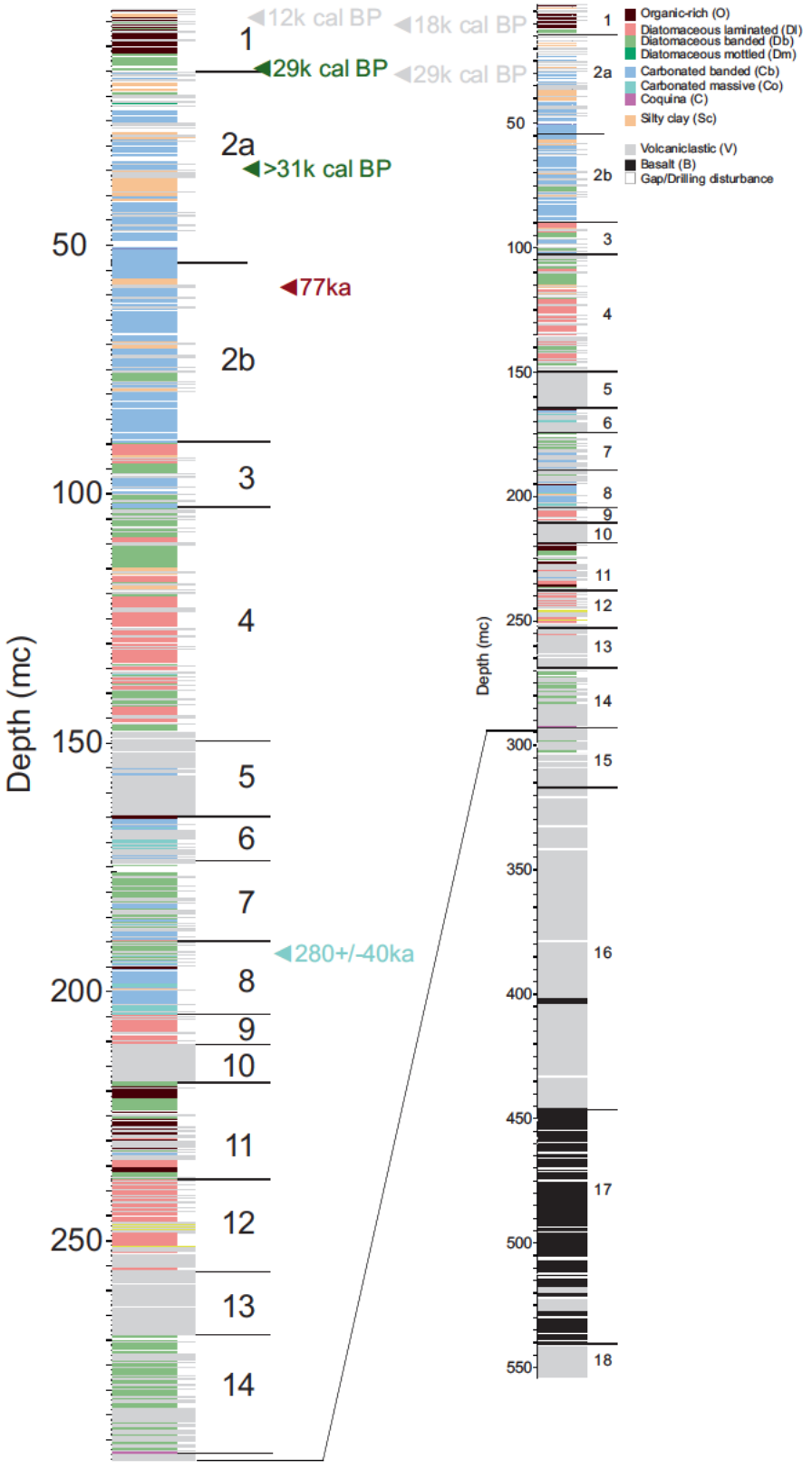

12k cal BP
18k cal BP
29k cal BP
29k cal BP
>31k cal BP
77ka
280+/-40ka
Depth (mc)
50
100
150
200
250
1
2a
2b
3
4
5
6
7
8
9
10
11
12
13
14
Depth (mc)
50
100
150
200
250
300
350
400
450
500
550
1
2a
2b
3
4
5
6
7
8
9
10
11
12
13
14
15
16
17
18
Organic-rich (O)
Diatomaceous laminated (Dl)
Diatomaceous banded (Db)
Diatomaceous mottled (Dm)
Carbonated banded (Cb)
Carbonated massive (Co)
Coquina (C)
Silty clay (Sc)
Volcaniclastic (V)
Basalt (B)
Gap/Drilling disturbance

Fig. 5. Complete lithostratigraphy of the composite sequence at Lake Chalco, including 2016 MexiDrill core sections supplemented by 2008 core sections. The higher resolution section is from the lacustrine sequence in the upper c.300 m of composite core. Some dates are provided, with their origin reported in Valero-Garcés et al. (2021). From Valero-Garcés et al. (2021).

explored in Martínez-Abarca et al. (2021), Appendix P2. In that study, four stages in the development of Lake Chalco are proposed. From earliest to latest, these are: (1) an alluvial deltaic environment characterised by debris flows and hyperconcentrated streamflows; (2) a fluvio-deltaic environment characterised by turbulent flows; (3) a fluvio-lacustrine environment characterised by the transition into a lake basin, forming Paleo-Chalco-I; and (4) a eutrophic lake environment, forming Paleo-Chalco-II.

The sedimentology and stratigraphy of Lake Chalco is of wide interest to many scientific disciplines, with aims to address multiple research questions in the region, such as hydrological balances, palaeoclimatology and glacial cycles, and the pattern of regional volcanic activity through time (e.g., Brown et al., 2019). This thesis investigates the volcanic record at Lake Chalco through time, supplemented by field and chemical studies conducted at some of the potentially hazardous volcanoes discussed in section 1, with the aim to improve upon the current knowledge of volcanism in the region, providing a context for understanding future volcanic hazards.

CHAPTER 3

CONSTRUCTING EXPLOSIVE ERUPTION RECORDS TO PROBE LONG-TERM OUTPUTS OF AN ARC SEGEMENT: A DEEP SEDIMENTARY ARCHIVE FROM MEXICO CITY

"Whoa! This is heavy, Doc"

Marty McFly, Back to the Future Part II (c.f. variations in Part I and III)

This chapter has been written in the style of a paper with the intention to submit to a journal soon.

'We' is therefore used throughout and there has been input into parts of the text by Dr. Sebastian Watt and Prof. Victoria Smith during editing stages of the manuscript.

1. INTRODUCTION

One of the most crucial datasets characterising a volcano is its eruptive history, which provides insight into the styles, frequencies and magnitudes of eruptions, and sets individual events within a longer-term context (e.g., Brown and Branney, 2004; Sisson and Vallance, 2008; Tuffen et al., 2008; Maeno et al., 2016; Marshall et al., 2022). Constructing volcanic stratigraphies is not a trivial task, but such records allow us to evaluate fundamental patterns governing the long-term development of volcanic systems and the hazards they pose. Records of this type show that eruptive behaviour varies across contrasting tectonic settings, magmatic compositions and eruptive environments (e.g., terrestrial, marine, lacustrine, subglacial; Van Eaton et al., 2013; Scarpatti et al., 2020; Hodgetts et al., 2021; Brenna et al., 2022). The quality of these stratigraphic records is also variable and influenced by the dispersal and preservation potential of products – in turn affected by eruptive environment, climatic conditions and anthropogenic influences – alongside the challenges of accessing buried or incompletely exposed stratigraphic sequences (e.g., Watt et al., 2009; Dávila-Harris and Carrasco-Núñez, 2014). Constructing long-term records of past volcanic activity remains one of the greatest challenges for volcanologists in many regions, despite being traditionally grounded in field-based observations. Prior to historical records of observed eruptions, reconstructions of volcanic activity are generally derived from explosive eruption deposits, particularly events producing widespread tephra fall deposits. They do not therefore provide a comprehensive record of all activity, and their completeness also tends to deteriorate rapidly with time. Records of past activity are generally limited to large explosive eruptions for the Holocene (Crosweller et al., 2012; Watt et al., 2013), with very limited records for earlier times. However,

records spanning longer time periods are important for understanding the output of volcanoes on timescales that are comparable to their individual lifetimes (e.g., averaging c.10^5 years for arc-volcanoes (cf. Singer et al., 1997; Bacon et al., 2006; Sunyé-Puchol et al., 2022). Theoretical studies suggest long-term eruption rates at individual volcanoes follow broadly cyclic patterns during edifice growth and the maturation of an upper-crustal magma reservoir, possibly divided into discrete episodes by major disruptive events (e.g., caldera-forming eruptions or large-scale sector collapses; Pinel et al., 2010). This is difficult to test in detail as most field datasets span much shorter timescales. However, in recent years, lake sediment cores have been used to reconstruct higher-resolution and longer timescale records of past volcanism than can be obtained from terrestrial exposures (e.g., McNamara et al., 2018; McLean et al., 2020).

1.1. Improving eruption records

Cores (including sediment cores from marine or lacustrine settings) are often crucial to understanding subsurface geology, and an invaluable technique for scientific advancements including paleoclimatic reconstructions and synthesising archaeological archives (e.g., Smith et al., 2011; Lane et al., 2014). In addition to sediment or basin-based research, such records can provide stratigraphically constrained volcanic records (e.g., Austin et al., 2014; Cassidy et al., 2014). Tephra (volcanic ash, <2 mm, to block/bomb, >64 mm, sized clasts) fall deposits are the most common volcanic deposit within sediment cores, as they are generally the most widely dispersed volcanic product, with ash-sized material commonly transported for tens to hundreds of kilometres from source. For some of the largest known eruptions in the geological record (e.g., the VEI 8 Younger Toba Tuff (YTT) eruption of Lake Toba, c.75 ka) visible tephra (macroscopic deposits visible to the naked eye) up to 30 cm in thickness has been identified

900 km from source (Matthews et al., 2012). Visible tephra on millimetre scales can be found much further from source and cryptotephra (microscopic tephra visible only by a microscope) can be found at even greater distances (e.g., glass from YTT is present in lacustrine sediments in the east coast of Africa (Lane et al., 2013; Costa et al., 2014). Tephrostratigraphic and tephrochronological reconstructions, using such deposits, can allow for these records to be synthesised with other stratigraphic records to either better constrain the eruptive volume, magnitude or timing of an eruption or to understand more about the impacts of an eruption on the environment.

Pyroclastic density current (PDC) deposits (ignimbrites), laharic material, volcanic collapse-derived breccias and lavas may also be present within cores, generally appearing at sites drilled proximal to a volcano. For cores collected in volcanically active regions, these types of deposits also provide an insight into a volcano's eruptive history, particularly in conjunction with relative or absolute chronological data. Any discrete volcanic layer within a core is typically thought to resemble an 'event' assumed to have been deposited instantaneously on geological timescales (e.g., Shane et al., 2006; McLean et al., 2018). The majority of these will have a close temporal connection to an associated volcanic eruption, and many will be primary deposits from that event. Some volcaniclastic deposits, however, may represent secondary erosion and/or reworking of older material, and care is therefore required in interpreting the nature of volcaniclastic deposits when constructing eruption records. It is known from historical explosive and effusive eruptions that primary deposits can accumulate quickly, and their internal stratigraphies can be complex due to the dynamic and rapidly evolving nature of volcanic eruptions. For a volcanic layer to be conceived as having accumulated over larger

timescales, radiometric dating or clear breaks in times (hiatus periods) would need to be recognised, typically by unconformable contact relationships, palaeosol development or a shift in bounding sediment types indicative of different environmental or geological conditions (e.g., Branney and Kokelaar, 2002). For the most part, cores (hard rock or sediment) should be approached with the same geological methodology as a field exposure or outcrop, with stratigraphic relationships and geological principles (such as superposition and uniformitarianism) being applied.

1.2. Typical drilling projects

Lacustrine cores from freshwater lakes within a few tens of kilometres of active volcanoes provide good potential for reconstructing long-term volcanic records at a relatively high resolution. Such lakes occur in a variety of terrestrial environments and are often considered stable systems with regular sediment input. They can also be varved, allowing chronological assessments to be made, irrespective of radiometric dating methods (e.g., Nakagawa et al., 2012). Depending upon the proximity to the volcanoes, different processes within a particular eruption(s) can be investigated, such as the recycling of clasts in crater lakes (e.g., Smith et al., 2019) or volcano-climate interactions in glaciated regions (e.g., Thomas et al., 2021). In contrast, marine archives are typically limited to a minor proportion of tephra fall deposits (depending upon their proximity to volcanoes), derived from large explosive eruptions (Lowe, 2014). These are often large-scale events, such as the c.39 ka Campanian Ignimbrite-forming (CI) eruption from Campi Flegrei, Italy, and may be composed of predominantly co-ignimbritic ash fallout (i.e., the finest ash from the eruption which has been transported the furthest distances (Engwell et al., 2014). These deposits are important, as they permit more accurate

estimations of eruptive volumes and magnitudes for extreme events. However, distal marine cores are not a comprehensive source of data about a particular volcano's eruptive past (Mahoney et al., 2016). Freshwater lakes, closer to volcanic sources, thus provide a complementary archive of past activity, containing higher-frequency input of material from a wider range of eruption magnitudes and types, but generally from a more localised source region. Despite the value of such records, most continental drilling projects are focused on collecting relatively short cores (< 50 m; e.g., Child et al., 1998), and there are few examples of long lake sediment cores that can be used to construct longer-term eruptive histories and that provide opportunities for answering cross-disciplinary research questions (e.g., Brown et al., 2019).

1.3. Lake Chalco, Mexico City

Lago Chalco (Lake Chalco) on the south-eastern boundary of Mexico City, Mexico is an endorheic lake towards the SW of the wider Basin of Mexico (Martínez-Abarca et al., 2021), that has been a site of scientific interest for a number of years (e.g., Ortega-Guerrero et al., 2018; Ortega-Guerrero et al., 2020; Chávez-Lara et al., 2022). At present, following significant anthropogenic modifications and drainage since the Spanish conquest of the Aztec empire in the 16th Century, Lake Chalco is less than 40 km^2 in area and averages a water depth (z_{max}) of c. 3 m, with $CaCO_3$ and Na-rich waters (Caballero et al.,2019; Valero-Garcés et al., 2021). Multiple coring projects (2008, 2011 and 2016) have recovered a near-continuous record from Lake Chalco and have been used to investigate a variety of scientific questions (Brown et al., 2019). The most recent project, in 2016 (MexiDrill Project), was funded by the International Continental Scientific Drilling Program (ICDP). Four parallel cores (Holes 1A, 1B, 1C and 1D)

were extracted from Lake Chalco, reaching a depth of c.520 m below-surface, significantly building upon the c.122 m depth reached by earlier drilling campaigns (Brown et al., 2019; Valero-Garcés et al., 2021). The 2016 cores are assumed to comprise the entire lacustrine history of Lake Chalco and from initial stratigraphic assessments by Valero-Garcés et al. (2021) are assessed to be a near continuous record of sedimentation into the basin. The volcanic record at Chalco is therefore likely an accurate representation of the deposits which have been dispersed or emplaced within the modern Mexico City limits since c.350 ka (Martínez-Abarca et al., 2021).

Here, we present a detailed volcanic stratigraphy of Lake Chalco from the 2016 core, supplemented by earlier cores, to (1) construct a record of eruptions which have affected Mexico City over the lifetime of Lake Chalco; (2) assess the eruptive processes responsible for emplacing volcanic material in the Mexico City region; (3) better understand the eruptive frequency and volcanic output rates over time using this unique core; (4) evaluate eruption source parameters in relation to environmental conditions, and (5) provide a methodological framework for reconstructing activity within an arc segment which can be reproduced using any core containing volcanic material.

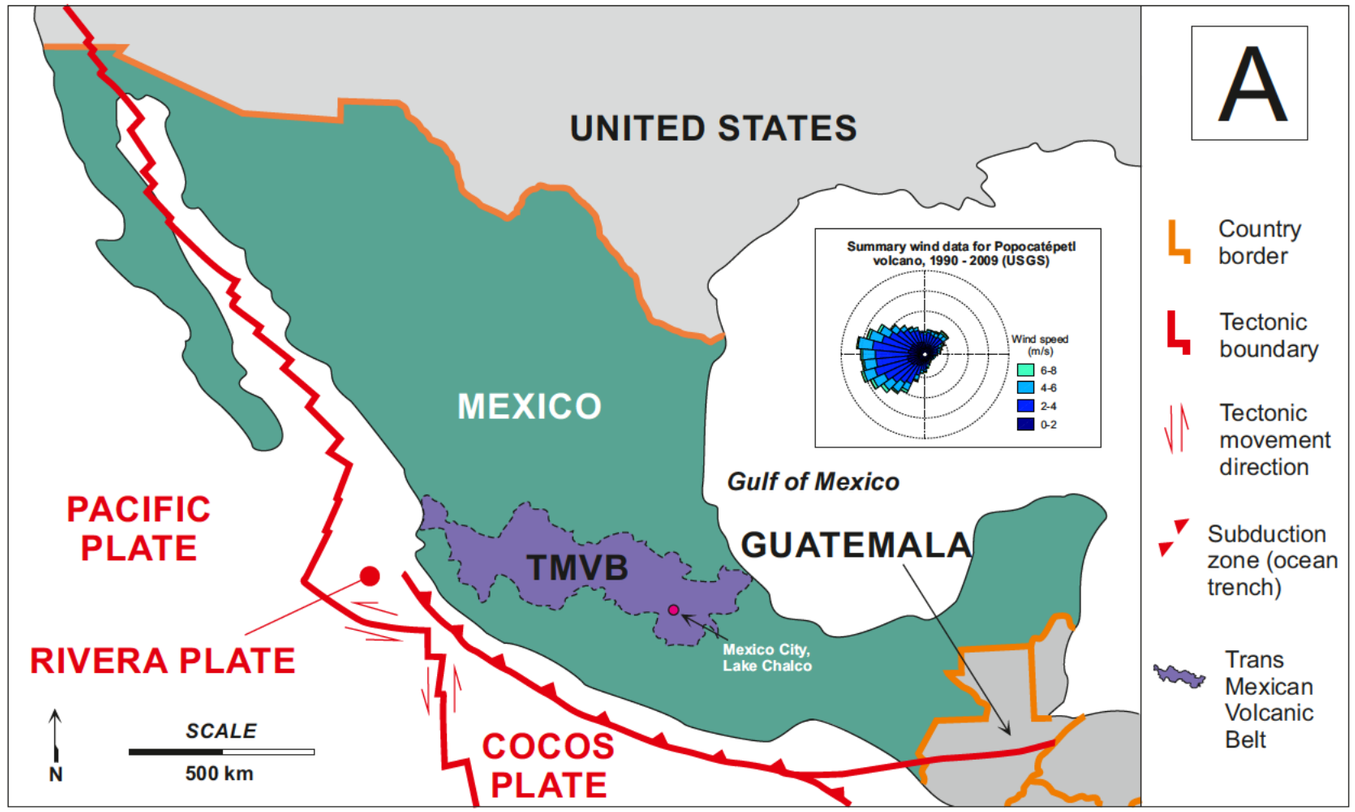
2. GEOLOGICAL SETTING

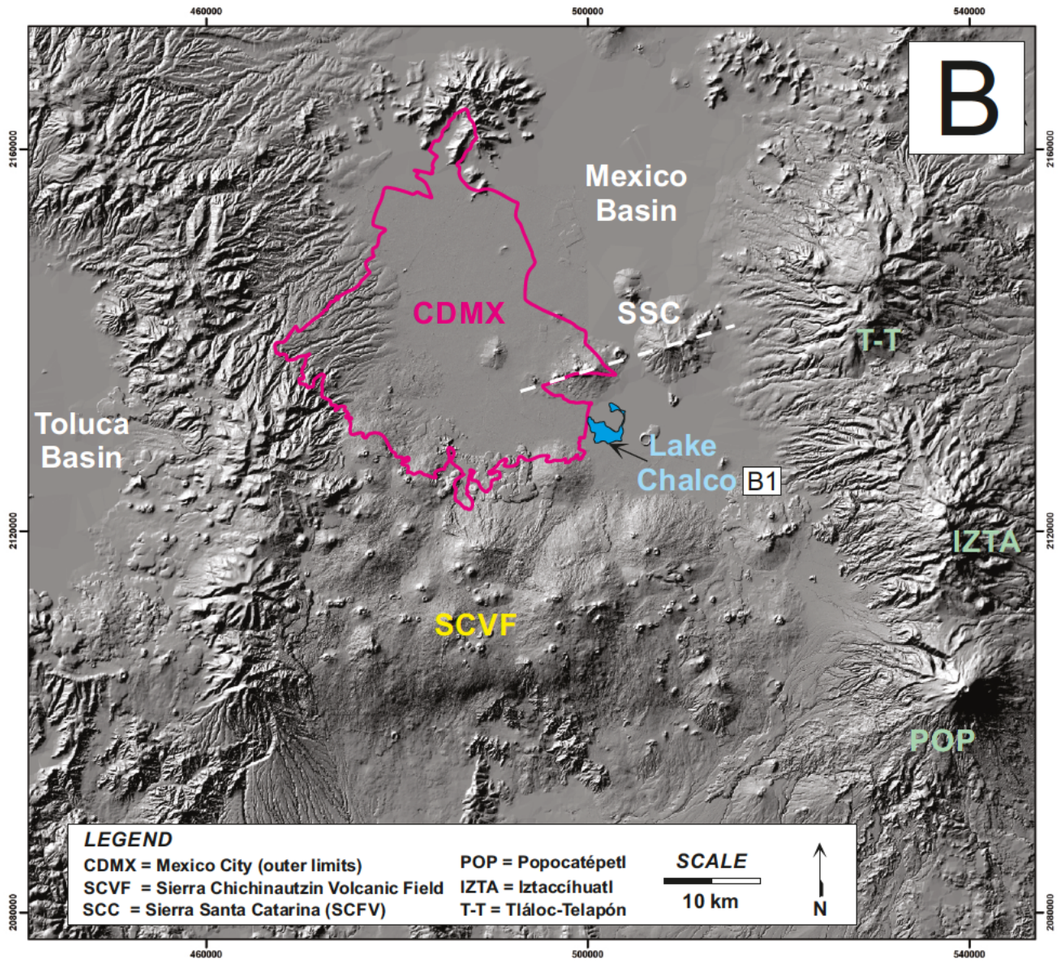
Mexico City and its suburbs are home to c.25 million people. Built upon the lacustrine sediments of the Basin of Mexico, the bedrock lies several hundreds of metres below the surface. Due to groundwater extraction for its inhabitants (the 5th largest population in the world), subsidence rates are high and have accelerated over the past c.70 years, now exceeding 200 mm/yr at Lake Chalco (Valero-Garcés et al., 2021). The origin of the lake is the result of

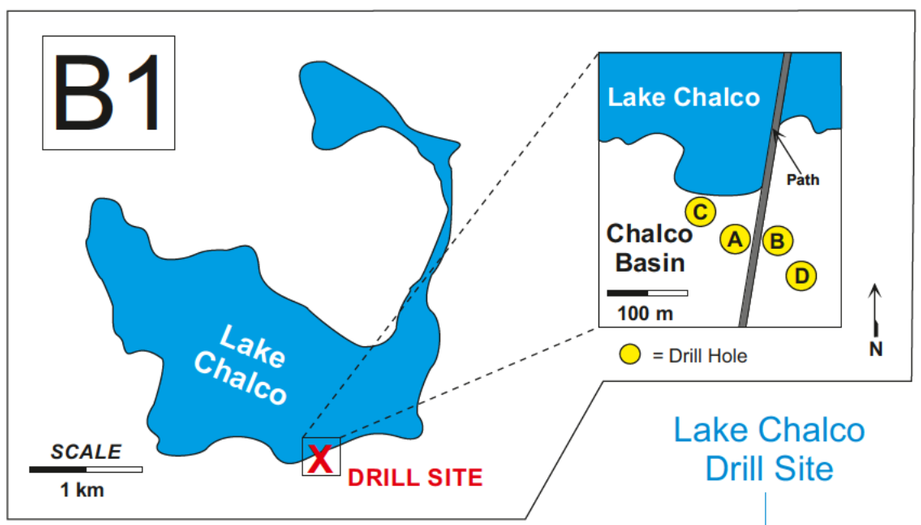
tectonic and magmatic processes within the wider Trans Mexican Volcanic Belt (TMVB; Fig. 1), a volcanic arc that extends W-E across Mexico, formed by the subduction of the Rivera and Cocos plates under the North American plate (Ortega-Guerrero et al., 2018). Consequently, Mexico City is bound by various volcanoes and volcanic ranges, including to the W the Sierra de Las Cruces Volcanic Range (SLCVR), to the E the Sierra Nevada Volcanic Range (SNVR) and to the S the Sierra Chichinautzin Volcanic Field (SCVF, e.g., Fig. 1; Nixon, 1989; Mora-Alvarez et al., 1991; Cadoux et al., 2011; Macías et al., 2012; Siebe and Macías, 2004; Arce et al., 2017; Jaimes-Viera et al., 2018; Sunyé-Puchol et al., 2022). Volcanic activity from the SCVF are thought to have prevented a southern drainage pathway, resulting in the origin of the lake basin c. 1 Myr ago (Mooser, 1963; Martínez-Abarca et al., 2021). Today, over 220 monogenetic cones comprise the SCVF. The close proximity of this volcanic field to Mexico City poses a risk to lives and infrastructure from a range of styles of volcanism, including effusive emplacement of lavas and explosive eruptions (Arce et al., 2015). Hazards from renewed activity at the SCVF are considered to be the most likely scenario for volcanic disruption to Mexico City (particularly to the southern limits of the city, e.g., Nieto-Torres and Del Pozzo, 2019). However, the potential for larger-scale explosive eruptions from nearby stratovolcanoes of the TMVB also forms part of the city's vulnerability to volcanic activity (Espinasa-Pereña and Granados, 2013).

2.1. Volcanic sources around Mexico City

The volcanoes immediately around Mexico City comprise two types: the vents of the SCVF, dominated by mafic magmas, and polygenetic volcanoes (e.g., Toluca, Popocatepetl; Fig. 1) of


A
UNITED STATES
MEXICO
Gulf of Mexico
GUATEMALA
PACIFIC PLATE
RIVERA PLATE
COCOS PLATE
TMVB
Mexico City, Lake Chalco
Summary wind data for Popocatépetl volcano, 1990 - 2009 (USGS)
Wind speed (m/s)
6-8
4-6
2-4
0-2
N
SCALE
500 km
Country border
Tectonic boundary
Tectonic movement direction
Subduction zone (ocean trench)
Trans Mexican Volcanic Belt


B
460000
500000
540000
2160000
2130000
2090000
Mexico Basin
CDMX
SSC
T-T
Toluca Basin
Lake Chalco
B1
IZTA
SCVF
POP
LEGEND
CDMX = Mexico City (outer limits)
SCV = Sierra Chichinautzin Volcanic Field
SCC = Sierra Santa Catarina (SCFV)
POP = Popocatépetl
IZTA = Iztaccíhuatl
T-T = Tláloc-Telapón
SCALE
10 km
N


B1
Lake Chalco
SCALE
1 km
DRILL SITE
Lake Chalco
Path
Chalco Basin
C
A
B
D
100 m
= Drill Hole
N

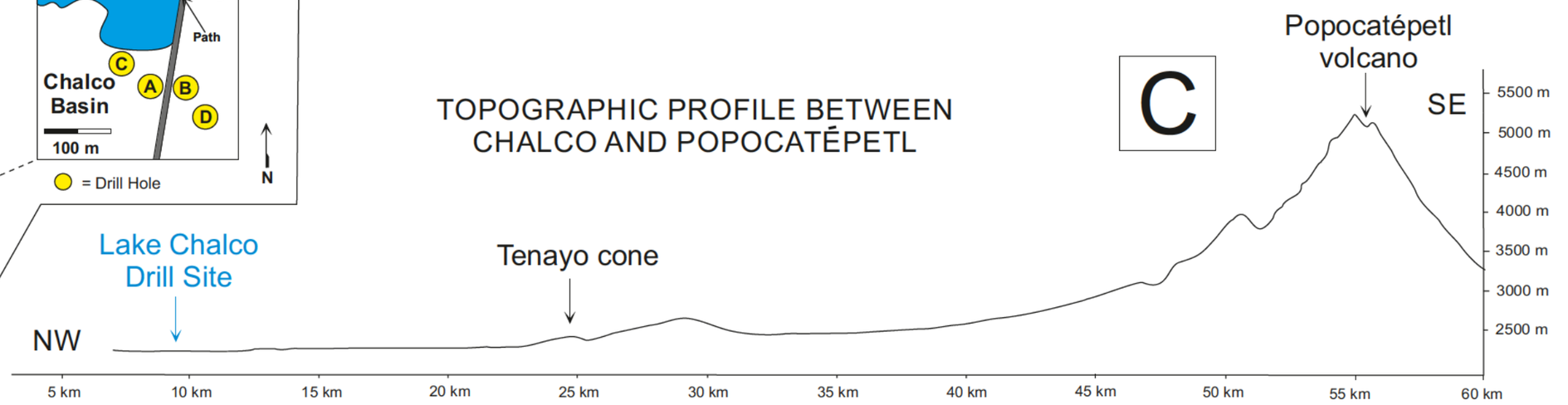

C
TOPOGRAPHIC PROFILE BETWEEN CHALCO AND POPOCATÉPETL
Popocatépetl volcano
SE
NW
Lake Chalco Drill Site
Tenayo cone
5500 m
5000 m
4500 m
4000 m
3500 m
3000 m
2500 m
5 km
10 km
15 km
20 km
25 km
30 km
35 km
40 km
45 km
50 km
55 km
60 km

Fig. 1. (a) Map of Mexico displaying major tectonic boundaries and the location of the Trans Mexican Volcanic Belt (TMVB) as outlined in Arce et al. (2019). Summary wind data file for Popocatépetl volcano from 1990 – 2009 (USGS). (b) Digital Elevation Model (DEM) of the Basin of Mexico with major surrounding volcanoes and volcanic fields (e.g., Sierra Nevada Volcanic Range (SNVR) and Sierra Chichinautzin Volcanic Field (SCVF)). Lake Chalco and the outer limits of Mexico City (CDMX) are also marked. (b1) Map of Lake Chalco and the drilling sites (boreholes A-D). (c) Topographic profile from Popocatépetl volcano to Lake Chalco displaying a relatively smooth and concave geometry from a topographic high to a topographic low. This topography indicates that Lake Chalco lies at the foothills of the surrounding volcanoes and is up to 50 km away from the vent of Popocatépetl.

---

the TMVB. The volcanoes comprising the SCVF are thought to be monogenetic, with the deposits constructing their cones presenting no evidence (e.g., palaeosol development) for more than one eruption. They are therefore considered to be extinct following a single eruption (e.g., Németh and Kereszturi, 2015). The majority of these vents produced both tephra and lavas (e.g., Bertotto et al., 2006). PDCs are not typical of these eruptions, which are generally restricted to Strombolian eruptive styles. Tephra fall deposits from SCVF eruptions are likely to have formed macroscopic tephra deposits at distances of tens of kilometres. For example, ash deposits from the comparable 1943-53 eruption of Paricutín, further west in Mexico, had a thickness of 25 cm at distances of 6-12 km (in all directions) around the vent (Pioli et al., 2008). We thus expect many of the SCVF eruptions to be represented within the Chalco core.

The nearest polygenetic volcanoes (volcanoes that erupt multiple times) to Chalco and the Mexico City region are those of the SNVR (a chain including Popocatépetl, Iztacchihuatl and Tláloc-Telapón). Additionally, Nevado de Toluca to the W and La Malinche volcanoes to the E are large stratovolcanoes with the potential to pose significant risk to the city. Large explosive eruptions from any of these volcanoes, particularly those producing widespread tephra fall deposits from Plinian (or larger) eruptions, would impact the city depending on the

dispersal direction, and we expect all these sources to be represented in tephra fall deposits within the Chalco core.

Volcanic stratigraphy and geochronology show that the most recently active stratovolcanoes surrounding Mexico City, producing pyroclastic eruptions, are Popocatépetl, Tláloc-Telapón, Nevado de Toluca and La Malinche (e.g., García-Palomo et al., 2002; Arce et al., 2003; Arce et al., 2005; Castro-Govea and Siebe, 2007; Sunyé-Puchol et al., 2022), which have all erupted within the last 30 ka. Popocatépetl is the most active of these sources and due to its proximity to Mexico City it is perceived as one of Mexico's most hazardous volcanoes (Macías et al., 2020; Sunyé-Puchol et al., 2022). Popocatépetl has been in a new eruptive phase since 1994, regularly expulsing gas and tephra in paroxysmal episodes (Love et al., 1998; Stremme et al., 2011). Generally, these have been a VEI 3 or lower. However, higher energy eruptions have occurred throughout the Holocene and Pleistocene, including the largest known Plinian eruption at c.16.7-18.2 cal. kyr BP, known as the Tutti Frutti caldera-forming eruption (e.g., Siebe et al., 2017) and estimated to have deposited c.10 cm of tephra on Mexico City (Siebe et al., 1999; Sosa-Ceballos et al., 2012; Sunyé-Puchol et al., 2022). It is the larger eruptions that are most likely to be preserved at Chalco, because the smaller, more typical activity will not produce macroscopic tephra deposits at this distance.

In addition to surrounding polygenetic stratovolcanoes, Mexico City is also vulnerable to volcanic hazards from more distal sources right across the TMVB and beyond (c.f. chapter 2). Within the TVMB lie caldera volcanoes, such as Los Humeros and La Primavera, which are known to have produced >VEI 6 eruptions with widespread tephra deposits, including the Zaragoza Tuff (69 ± 16 ka) and Tala Tuff (95 ± 5 ka) from each of these volcanoes respectively

(Mahood, 1981; Walker et al., 1981; Carrasco-Núñez et al., 2018). Although caldera-forming eruptions only occur at intervals on the order of 10^4 years, the population of Mexico City is exposed to these hazards. For example, Los Humeros has had three very large explosive eruptions in the past c.165 ka, the oldest being the Xáltipan Ignimbrite eruption at 164 ± 4.2 ka kyr, known to have produced radial PDCs and tephra fall deposits with a dispersal axis to the SW, where Mexico City now lies (Carrasco-Núñez et al., 2018; Cavazos and Carrasco-Núñez, 2020).

Furthermore, very large eruptions further afield may also result in tephra deposition in Mexico City, including those in nearby volcanically active countries, such as Guatemala. Atitlán caldera, Guatemala is known to have produced Ultra-Plinian eruptions, including the Los Chocoyos (LCY) eruption at 72 ± 2 ka (Kutterolf et al., 2016; Cisneros De Leon et al., 2021). Isopach maps presented by Kutterolf et al. (2016) estimate the fall thickness of the LCY tephra to be between 6 and 9 cm in Mexico City, which if deposited today would result in widespread disruption, airport closures and a significant risk to human health and infrastructure.

In summary, the geology of the Mexico City region is dominated by lacustrine sediments and volcanic deposits from nearby and more distal sources. Mexico City is vulnerable to many different styles of volcanism, from effusive lava-dominated hazards to explosive pyroclastic processes. Understanding the past eruptive activity in the region can lead to better preparedness and risk management which has the potential to save lives in the event of a future eruption from any volcanic source.

2.2. Drilling and production of composite spliced stratigraphy

Four parallel cores (Holes 1A, 1B, 1C and 1D) were extracted from Lake Chalco as part of the ICDP-funded MexiDrill project in 2016. The drilling campaign reached a depth of c.520 m below-surface with rotational drilling of holes 1A, 1B and 1C conducted using a truck-mounted Boart Longyear LF90 drilling rig with standard Boart Longyear HQ3 wireline diamond-rotational-drilling coring tools (Brown et al., 2019; Martínez-Abarca et al., 2021). Hole 1D was recovered by hand to 19 m depth using a Usinger-type piston corer with percussion, to enhance the recovery of the uppermost softer sediments (Valero-Garcés et al., 2021). Sediment cores were recovered in 1.5 m polycarbonate liners with diameters of 6.1 cm and magnetic susceptibility was recorded following recovery with a Geotek MSCL-S loop sensor (Brown et al., 2019; Martínez-Abarca et al., 2021). All core sections were transported to the National Lacustrine Core Facility (LacCore) at the University of Minnesota, USA for splitting, data collection, subsampling and archiving. High resolution photographs were obtained of all archive halves using a DMT CoreScan digital linescan camera. Geophysical downhole logging was conducted on Hole 1A, using spectral gamma ray (SGR), magnetic susceptibility (MS), focused electric resistivity (Fel), dipmeter (caliper and resistivity), acoustic borehole televiewer, sonic velocity (vp), salinity and temperature tools (Brown et al., 2019). MS values were collected using a Bartington MS2E sensor and all core datasets (images and quantifiable measurements) were uploaded into the free distribution CoreWall software, Corelyzer (http://www.corewall.org/), to make preliminary sediment descriptions and correlations using key marker horizons and visible sediment changes (e.g., Martínez-Abarca et al., 2021). From this, a composite sequence (splice) was compiled to create a single sequence

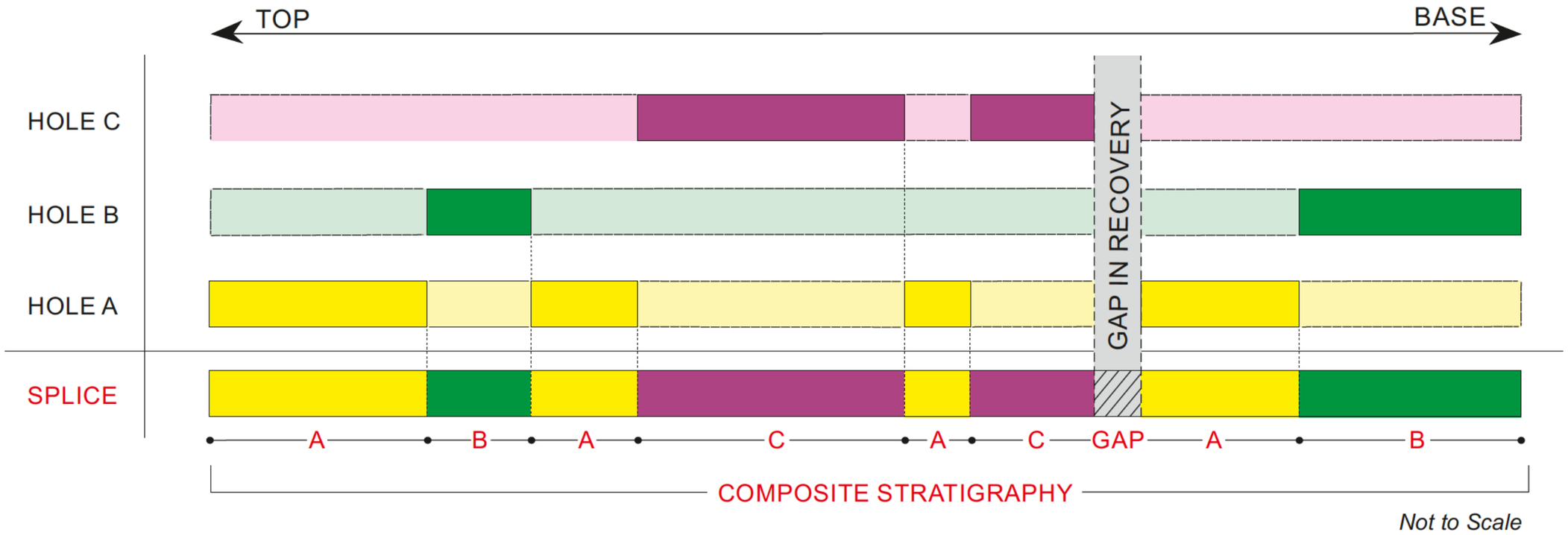

TOP
BASE
HOLE C
HOLE B
HOLE A
SPLICE
GAP IN RECOVERY
A
B
A
C
A
C
GAP
A
B
COMPOSITE STRATIGRAPHY
Not to Scale

Fig. 2. Schematic diagram (not to scale) graphically representing how a composite stratigraphy (splice) is constructed. For the purposes of the diagram, three holes (A-C) are displayed with stronger-coloured segments indicating the best-preserved material for inclusion in the splice.

---

that sought to minimise gaps and to eliminate as far as possible the use of sections with evidence of disturbance or artefacts (Fig. 2). This splice has been published in Valero-Garcés et al. (2021).

3. STRATIGRAPHIC METHODS

3.1. Identification of visible Volcanic Deposits and production of a detailed volcanic stratigraphy

In order to evaluate the record of volcanic activity preserved in the Chalco core, our approach was to distinguish all volcanic deposits from other sediment types. Because volcaniclastic grains are a major component of background terrigenous sediment input to the Chalco basin, we have focused only on macroscopic units (rather than cryptic volcanic deposits, i.e., cryptotephra), identifiable by having visually distinctive properties from the bounding sediment, with sharp upper and lower contacts. These macroscopic beds are interpreted as representing "events" that mark a departure from the background sedimentation (but without any implication on the nature of that event or the transporting sedimentary process), whose emplacement can be considered instantaneous on geological timescales. In some instances where the volcanic nature of a bed was ambiguous, microscopic examination of grains using smear slides was used to determine the predominance of volcanic clasts (see Table 2, Appendix C5).

Visible volcanic deposits, defined in this way, include any deposit containing clasts that have originated from a volcano and which forms a layer (or disturbed layer) that can be seen with

Table 1. Table of data types recorded for each volcanic layer in Stage III. Units, notation and explanation, purpose, associated equations, and additional remarks are also provided.

Data Type	Units	Notation and explanation	Purpose	Equation	Additional remarks
Deposit type	-	TFD – Tephra VC - Volcaniclastic L – Lava C – Fine clayey layer	To distinguish between types of event layer within the core.	-	Interpretative notations based off descriptions that match their criteria.
Composition	-	F – Felsic I - Intermediate M - Mafic	An assignment of relative compositional categories based on colour to discern likely eruptive sources.	-	Composition is only recorded for TFD deposit types.
Top depth	m	Value calculated using Eqs. 1,4.	For stratigraphic placement within the core.	Eq.1, Eq.4	-
Bottom depth	m	Value calculated using Eqs. 2,3.	For stratigraphic placement within the core.	Eq.2, Eq.3	-
Splice section(s)	-	Core section name assigned from LacCore (see Appendix C1).	To examine, view or subsample the event layer.	-	Event layers also likely found in off-splice sections.
On-splice thickness	cm	Value calculated using depths or measured thickness data.	For stratigraphic placement within the core.	-	-
Ghost section(s)	-	Core section name assigned from LacCore (see Appendix C1).	Off-splice sections which contain event layers not represented in the splice.	-	Ghost horizon sections include the best-preserved version of the layer(s).
Ghost depth	m	Value calculated using Eqs. 5,6.	For stratigraphic placement within the core.	Eq.5, Eq.6	These are collapsed to zero thickness on the splice.
Combined basal depth	m	Basal depth values of all event layers (on-splice and off-splice (ghost)) layers in stratigraphic order.	For stratigraphic placement within the core.	-	-
Event-free depth	m	Value calculated using Eq. 7.	Calculated depths minus all interpreted event layers for assessment of output rates and for age-depth modelling.	Eq.7	-
Average ghost thickness	cm	Mean thickness of ghost layers preserved in off-splice core sections.	To record the deposit thicknesses of ghost events.	-	An accurate thickness for the layers compared to the zero-thickness recorded for ghost layers on-splice.
Combined thickness	cm	Thickness values for all layers on-splice with the addition of off-splice ghost events.	For assessments of event layer thicknesses within the splice and including off-splice ghost events.	-	Limited to the composite sequence and ghost layers.

Preservation (thickness reliability)	n	1 – Well preserved 2- Moderately preserved 3 – Poorly preserved	For assessing the reliability of thickness data for a given layer.	-	This can be used to determine overall preservation of the core but is not regarded accurate as sections of core may be better preserved in parts compared to others. Additionally, a higher number of layers may skew to an inaccurate sense of overall preservation.
Grain size	φ	Values from -4 φ to ≤3 φ	For assessing the maximum size of pyroclastic deposits at Chalco.	-	Only interpretated TFDs have assigned grain size values. Grain size values <3 φ cannot be distinguished by eye, as seen by analytical grain size data.
Fine ash component	-	Comments on whether TFDs contain a fine ash component.	To determine if a deposit is likely to be distal, has a co-ignimbritic component or has had a higher degree of fragmentation.	-	Fine ash at Chalco may indicate a range of possible physical volcanological processes and/or explanations and present the largest respiratory hazard for humans.
Structures	-	Comments on any internal structure within event layers.	To determine if any mass flux or fluctuations in prevailing transportation directions are detectable for further investigation.	-	Structures often record changes in the energy levels of an event or their transportive processes.
Possible reworking	n	1 – Deposits are likely primary 2- Deposits may be reworked Assessments made due to sorting, rounding and association to nearby deposits.	For assessing a maximum and minimum number of events which have deposited material at Chalco.	-	Data is based off visual characteristics alone.
Top/Base	-	Comments on the nature of the top and base of each event layer.	For assessing whether events are well preserved or are possibly gradated or in sharp contact with bounding sediments.	-	-
Span cores	-	Comments on whether the event layer spans multiple core sections or can be found in its entirety within a single core section.	To determine which equations are needed for calculating an accurate depth and which events can be considered a minimum thickness due to multiple drives within the layer.	-	-
Confidence volcanic	n	1 – High degree of confidence the event layer is volcanic in origin.	To determine which layers can be considered for an assessment of the eruptive	-	Data is mostly based off visual assessments with some aided by smear slides (see Appendix C5).

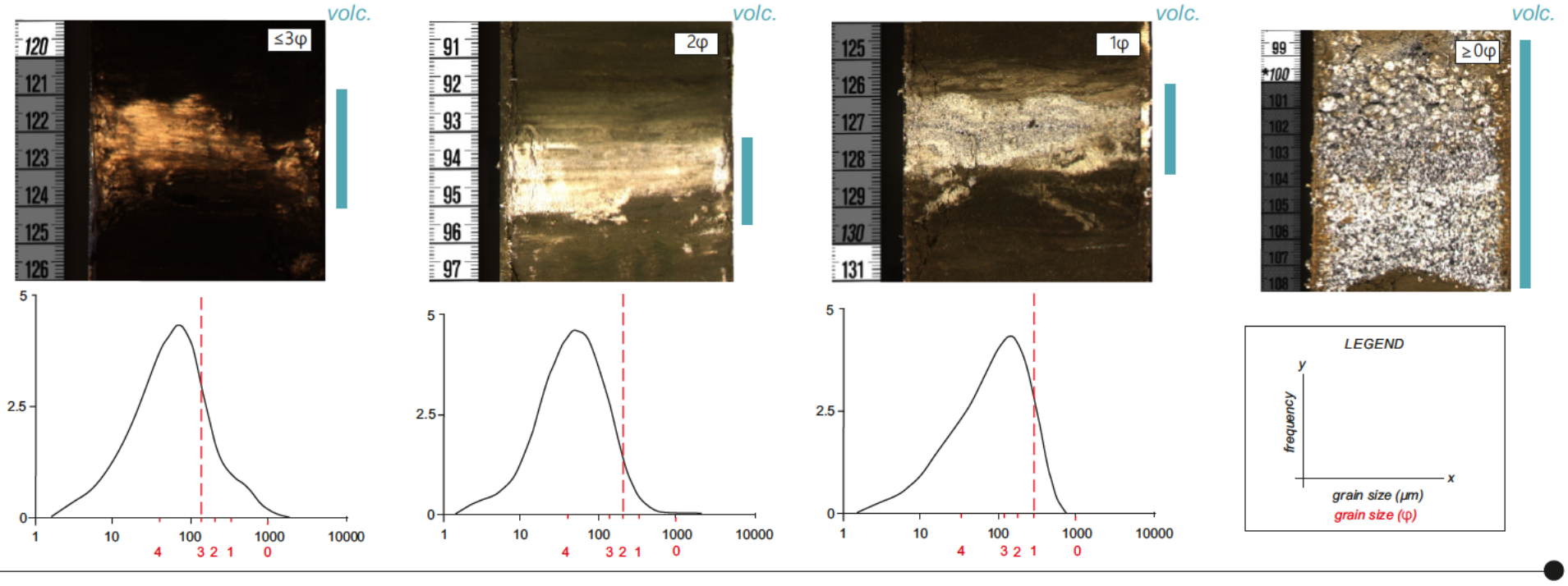
		2 - Moderate to low degree of confidence the event layer is volcanic in origin.	history of the region and to provide minimum and maximum values.		
Section description is based off	-	Core section name assigned from LacCore (see Supplementary Material A).	To examine, view or subsample the event layer.	-	-
Thickness from described section	cm	An alternative thickness value that is ascribed from the described section alone (irrespective of the section(s) used for the splice).	To provide a more accurate thickness of event layers, using better preserved event layers off-splice when they occur.	-	-
Combined thickness with described sections substituted	cm	A collection of the most accurate thickness values for each event layer combining splice, off-splice and ghost event layers.	For the most accurate assessment of event layer thickness for the whole core.	-	-
Description	-	Comments on the physical characteristics of the event layers within the core. Descriptions are made from the best-preserved layer in the core (irrespective of splice sections).	For understanding the nature of the deposit and the reasoning it has been recorded as an event layer.	-	-
Splice and/or ghost section	-	Core section names assigned from LacCore (see Appendix C1).	A collection of all core sections in the splice and recorded as ghost horizons to be cross referenced with descriptions.	-	-

the naked eye. These layers range from millimetre to decimetre scale and may contain vesiculated magmatic fragments (i.e. pumice or scoria), denser crystalline or glassy clasts, or crystal fragments (Fig. 3). Each volcanic layer has been transported and deposited into the lake by eruptive processes (primary volcaniclastic deposits) or subsequent environmental processes (secondary volcaniclastic deposits) following an event. In addition, dense crystalline igneous rocks are present within the lower part of the core, forming further volcanic units (Fig. 3).

The upper and lower boundaries of visible volcanic deposits were noted using high-resolution photographs viewed in Corelyzer, in all core sections (across holes A to D), including those not used in the composite splice (cf. Valero-Garcés et al., 2021). By working through all the parallel holes in stratigraphic order, marker horizons (e.g., clear background sediment changes or distinctive volcanic horizons) were identified. From this, a complete sequence of inferred volcanic deposits was compiled, in an approach that mirrored that used to produce the composite splice, but that also sought to identify any volcanic deposits that may be better preserved in off-splice core sections.

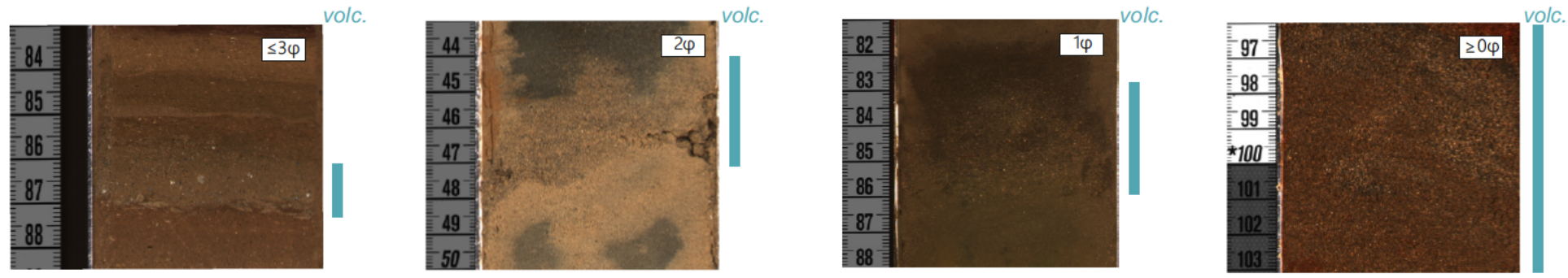
To aid with the identification of volcanic units, MS data was plotted against core section photographs in Corelyzer. MS acts as a non-destructive tool for aiding the identification of volcanic layers within sediment cores (e.g., Hodgson et al., 1998; Rasmussen et al., 2003, Kutterolf et al., 2008; Cassidy et al., 2014). As MS signifies the volume of magnetic minerals present within a deposit (Blum, 1997), magnetic signals are typically higher in mafic deposits when compared with felsic layers. Also, finer deposits (especially those transported from more distal eruptions, in explosive eruptions with increased fragmentation or from co-ignimbritic

A



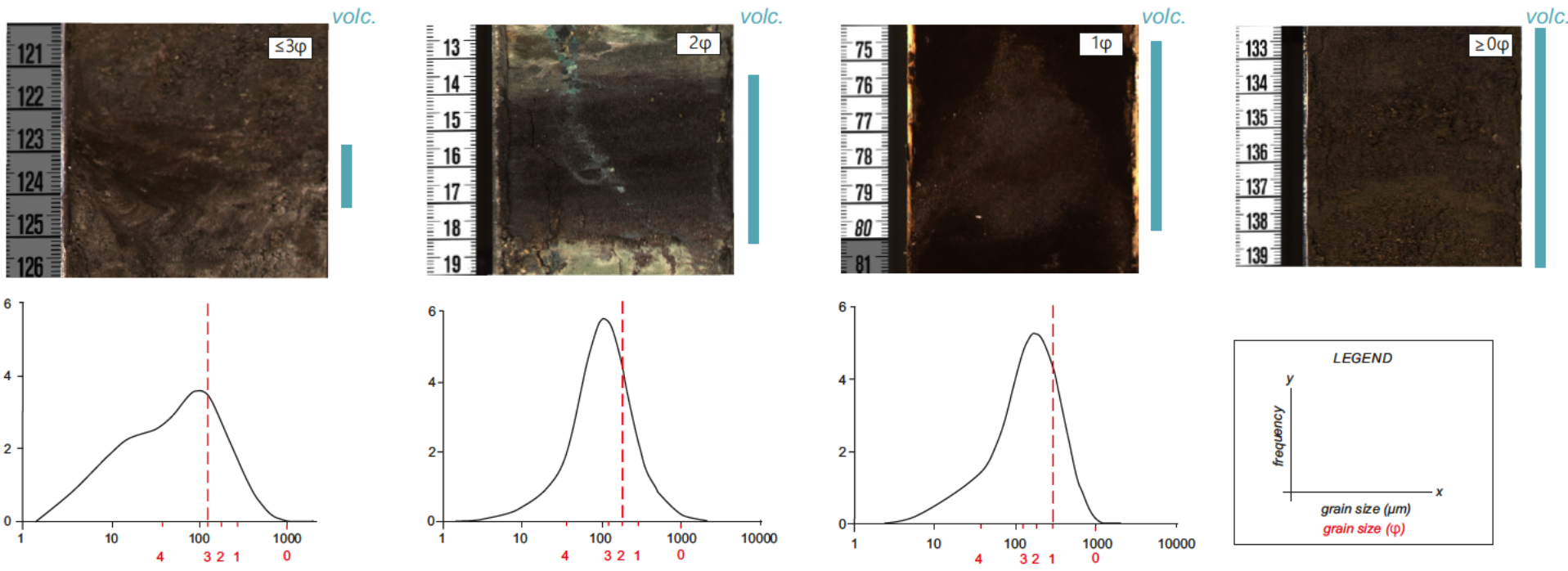
FELSIC TFDs

B



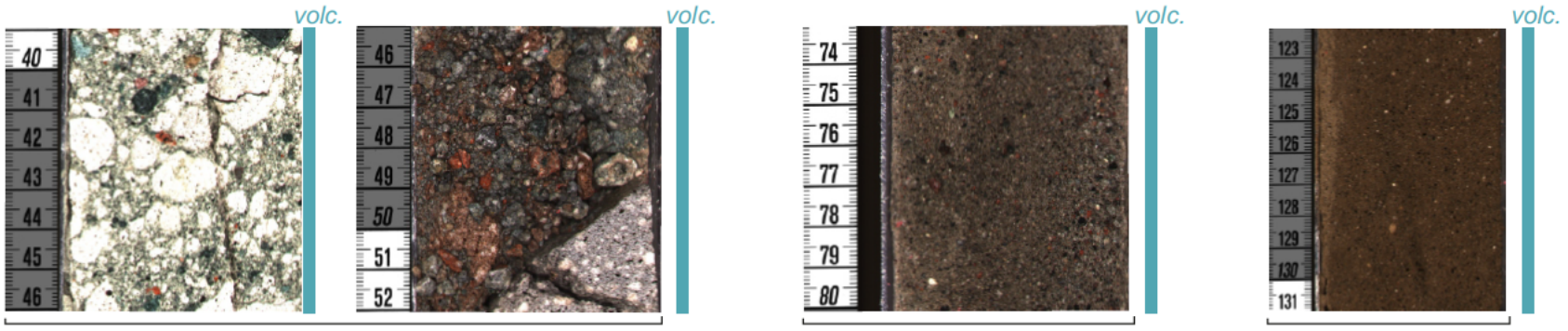
INTERMEDIATE TFDs

C



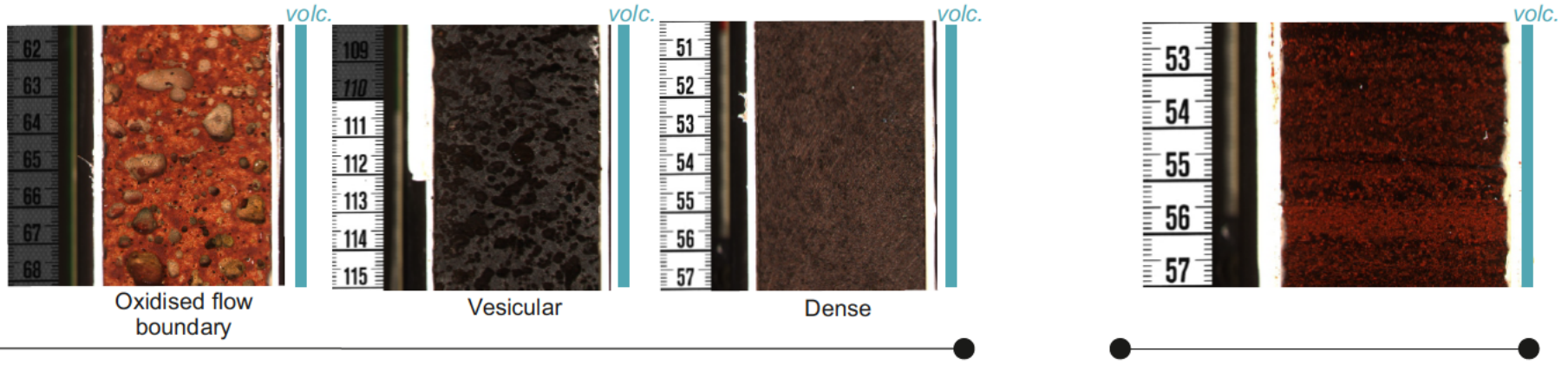
MAFIC TFDs

D



VOLCANICLASTICS

E



LAVA

SCORIA

Fig. 3. (a,c) Representative photographs of felsic and mafic tephras, respectively from the MexiDrill cores of varying maximum grain sizes (≤3 φ, 2 φ, 1 φ and ≥0 φ). Bars indicate where the volcanic layer is in the photograph and average grain size charts are provided for the three finest grain size categories (≤3 φ, 2 φ and1 φ), calculated from an average of the analytical lazer-diffraction values stated in Appendix C2. Photographs provided of the three finest grain sizes include tephra which was analysed by lazer diffraction particle size analysis. (b) Examples of representative intermediate tephras of varying maximum grain sizes (≤3 φ, 2 φ, 1 φ and ≥0 φ). Bars indicate where the volcanic layer is in the photograph. (d) Representative photographs of type 1, type 2 and type 3 volcaniclastic deposits, based on grain size and matrix-abundance. Bars indicate where the volcanic layer is in the photograph. (e) Representative photographs of lavas (including oxidised flow boundaries, vesicular lava and dense lava) as well as a scoria deposit within Stage I of the core. Bars indicate where the volcanic layer is in the photograph.

---

fallout), are typically dominated by glass shards (e.g., Engwell et al., 2014) and have a lower concentration of magnetic minerals, producing a weaker MS signal. Despite this, MS in background sediment is typically very low in the Chalco core, and MS was a valuable tool to highlight potential volcanic layers, particularly those without a strong colour contrast from the bounding sediment. At some points in the core, where dark background sediments occur (e.g., sapropels), MS spikes were almost exclusively used to identify a possible mafic volcanic layer. It must however be noted that MS data was recorded systematically at 0.5 cm intervals, and volcanic layers with <5 mm thickness may not have been captured in the MS dataset.

3.2. Description of visible Volcanic Deposits and the development of a volcano stratigraphic framework

All core sections were logged and described using the freely distributed software PSICAT (http:// www.corewall.org/). As major sedimentological changes had already been identified by Valero-Garcés et al., (2021), focus was directed towards inferred volcanic layers, including any layers whose origin was initially uncertain, which were described in detail to interpret their depositional process. A combination of quantitative and qualitative and descriptive and interpretative data was recorded for each of these layers. Table 1 presents some of the key

types of data recorded, notations and purposes of this data with all data presented in Appendix C1. This built upon the methodology of Mahony et al. (2014).

3.3. *Determination of the types of volcanic deposit*

Volcanic deposits may be produced by explosive or effusive eruptions. The majority of volcanic deposits within the MexiDrill cores are dominated by vesiculated, angular to sub-angular clasts with similar visual characteristics in any individual layer, forming homogenous, well-sorted beds with sharp boundaries, generally up to a few centimetres in thickness. These characteristics are typical of volcaniclastic deposits generated by air fallout from explosive eruptions and can be termed *tephra fall deposits (TFDs)*. TFDs may have been transported large distances depending on wind direction, wind speed and eruption column atmospheric height (e.g., Walker et al., 1971; Sparks et al., 1997). TFDs may also be derived from a more local source. In general, characteristics such as a higher concentration of lithics and/or larger grain size are typical of a more proximal eruption source, and finer ash deposits are typical of more distal sources, but a relatively coarser deposit can also reflect elevated column heights (i.e., a relatively more intense eruption) or an axial downwind position on the dispersal pattern of the TFD. TFDs encompass all volcanic deposits which are derived from primary fallout from an explosive plume, irrespective of their grain size (e.g., well-sorted, clast-supported pyroclastic deposits from very fine ash (>3 φ) to blocks and bombs (-6 φ)).

Other volcanic layers present within the MexiDrill cores are interpreted to have formed by current input to Lake Chalco (i.e., transported by lahars and/or subaqueous sediment density flows). These deposits can be generally sub-divided into two categories: (1) very fine ash-grade repeated sequences with or without internal structure, with rounded clasts and grains; and (2)

poorly-sorted volcaniclastic deposits (i.e., composed of mostly volcanic clasts, Branney et al., 2021) with variable textures ranging from clast-supported and matrix-supported coarse polylithologic conglomerates to matrix-supported sand deposits. This latter type of volcaniclastic deposit may be comprised of multiple structureless beds, with variable grain size, and we interpret their poor sorting to indicate rapid deposition by high-energy events. Changes in grain size and sorting between individual beds is likely to be the result of varying concentration ratios of sediment (i.e., volcanic clasts) to water, with clast-supported deposits more indicative of a debris avalanche/debris flow emplacement mechanisms and finer, matrix-supported deposits of hyperconcentrated flow to dilute streamflow emplacement (e.g., Smith and Lowe, 1991).

Additionally, towards the base of the cores, dense to vesicular microcrystalline rocks were recovered. These are interpreted to be lavas, rather than intrusive rocks, as: (1) regions are oxidised, interpreted to be weathered surfaces of individual flows. *n.b.* These are generally more vesicular than other parts of the lava; (2) there is a lack of peperitic contact at the interaction between the dense rock and overlying volcaniclastic deposits; and (3) the overlying volcaniclastics often contain clasts of lava, resembling that of the rock below, which is to be expected if these lavas cropped out at the contemporaneous ground surface. It must however be noted that with a single core, <10 cm in diameter, internal structures typical of lavas (e.g., flow bands and kinematic indicators) cannot be seen. Fig. 3 provides examples from the MexiDrill cores which act as 'type sections' for the different volcanic deposits within the cores and Fig. 4 summarises the descriptions and interpretations of these.

VOLCANIC PROCESS

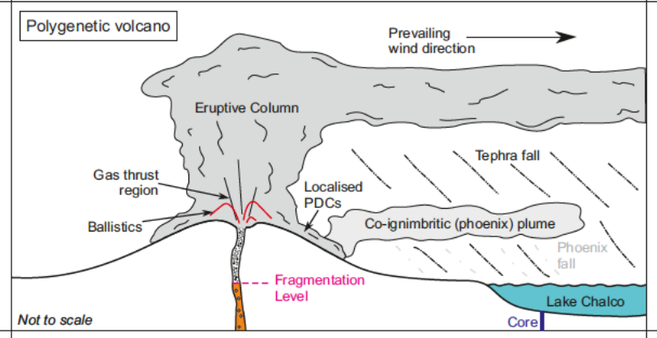
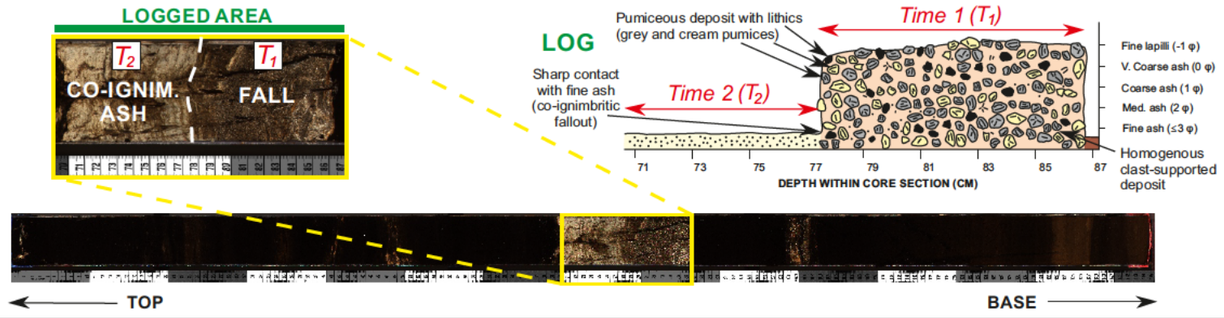
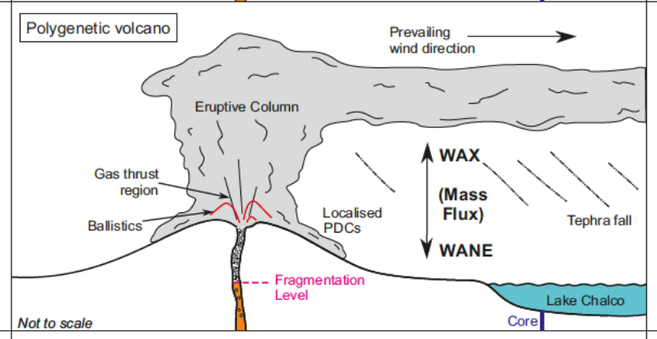
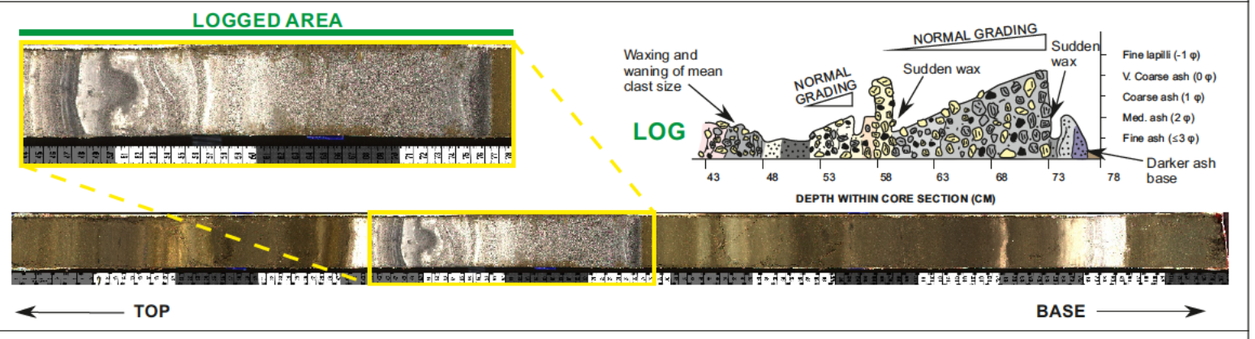
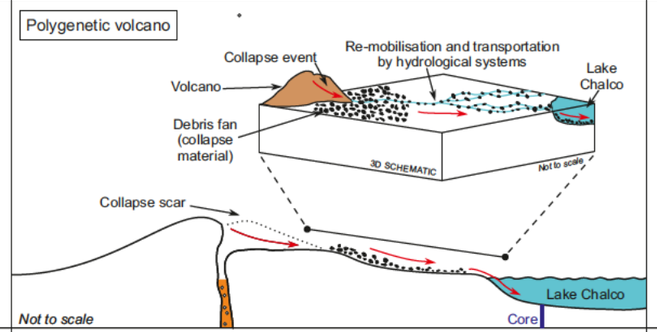
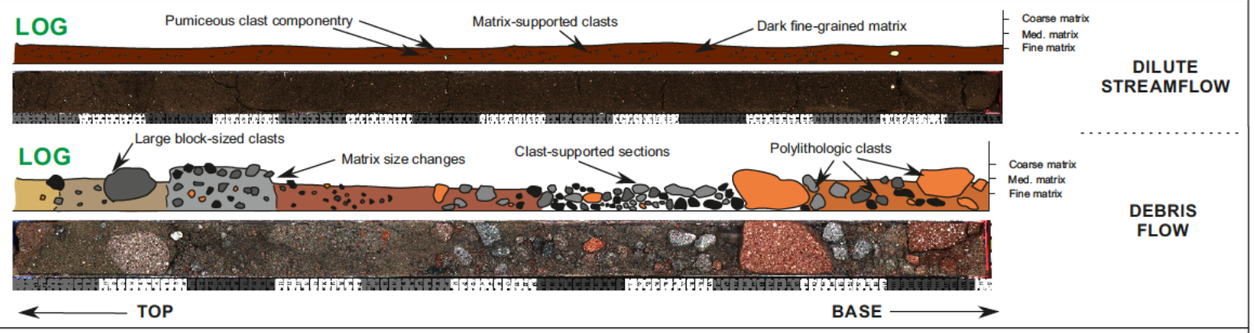
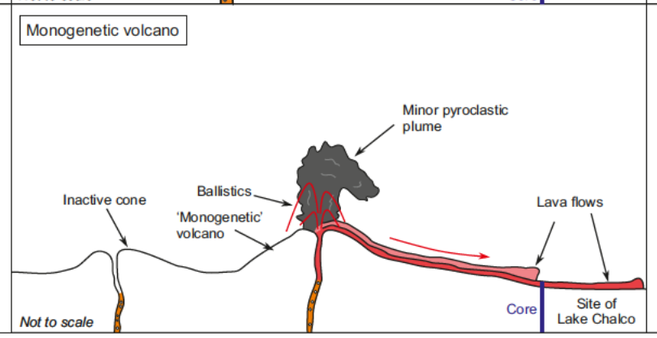
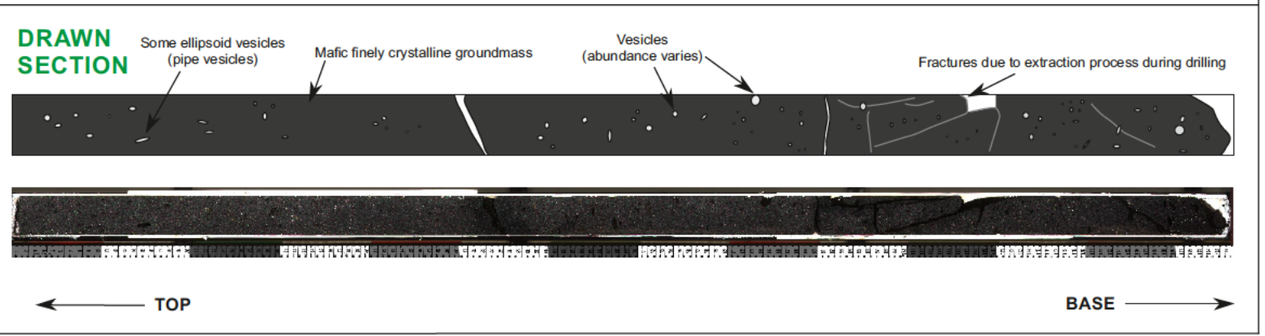
	SCHEMATIC DIAGRAM	EXAMPLE CORE PHOTO AND STRATIGRAPHIC LOG
STEADY COLUMN		
TRANSIENT COLUMN		
LAHAR (COLLAPSE-ORIGIN)		
EFFUSIVE		

Fig. 4. A classification diagram of the general types of volcanic deposits within the Chalco core and their interpreted volcanic processes responsible. A schematic diagram of the eruption process is provided and presented alongside a representative core section photograph(s) and stratigraphic log.

3.4 Dealing with artefacts and drilling imperfections

As discussed in sections 1.1 to 1.3, efforts were made to mitigate the effects of drilling artefacts and gaps, via the production of a splice (e.g., Valero-Garcés et al., 2021). When interpreting the nature of the events that generated the volcanic deposits, the most valuable information aside from the physical and compositional characteristics of the sediment (which identifies the emplacement mechanism and the magma type) is the thickness and the stratigraphic position. Coupled with grain size, this allows an estimation of source proximity and magnitude, and an accurate temporal analysis to be conducted, should a reliable chronology exist for the record. These key data can be used (alongside analytical methods) to estimate the eruption source parameters for individual layers, and to interpret how frequently the region that the core was extracted from experiences deposits from volcanic events of different type, size or composition.

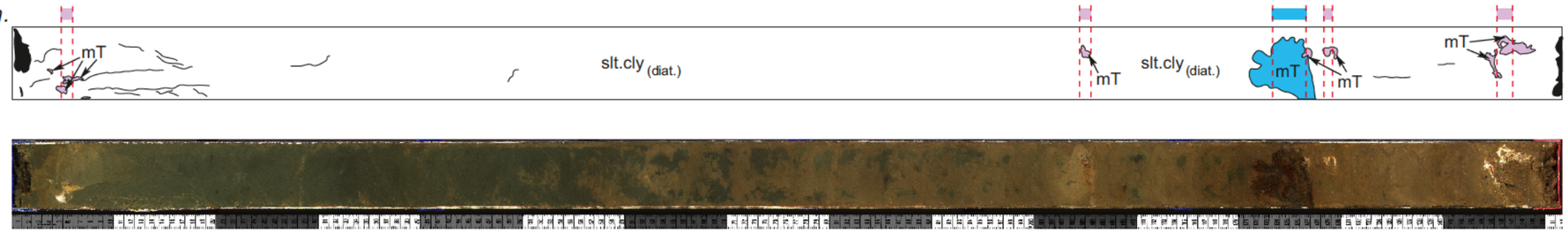
Because the volcanic deposits were emplaced into an often shallow lacustrine system (e.g., Valero-Garcés et al., 2021), minimal erosion and/or reworking of volcaniclastic deposits in the lake is likely to have occurred. Valero-Garcés et al. (2021) concluded these cores provide a continuous lacustrine record, theoretically implying the succession should be complete for volcanic events depositing sediment at this specific site, above a primary deposit thickness sufficient to avoid destruction by bioturbation or lake-current reworking (a point we return to below). Beyond this, the only other factors affecting record completeness are gaps in core recovery or imperfections and disturbances from drilling, and these must therefore be

PRESERVATION VALUE 3

Measured Thickness

DRAWN SECTION

CORE SECTION PHOTO

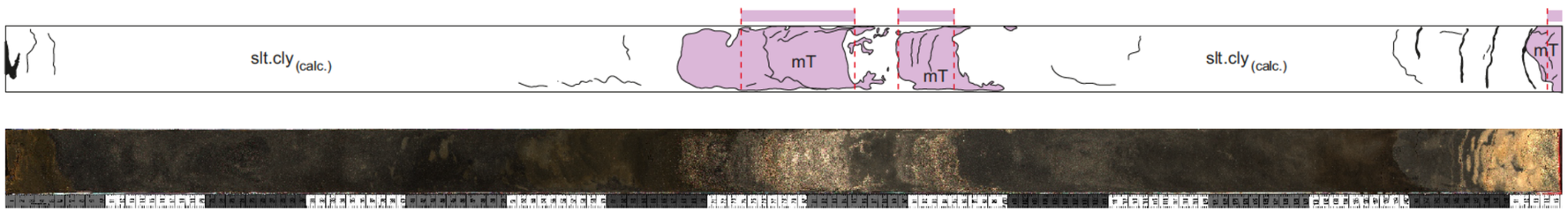


PRESERVATION VALUE 2

Measured Thickness

DRAWN SECTION

CORE SECTION PHOTO

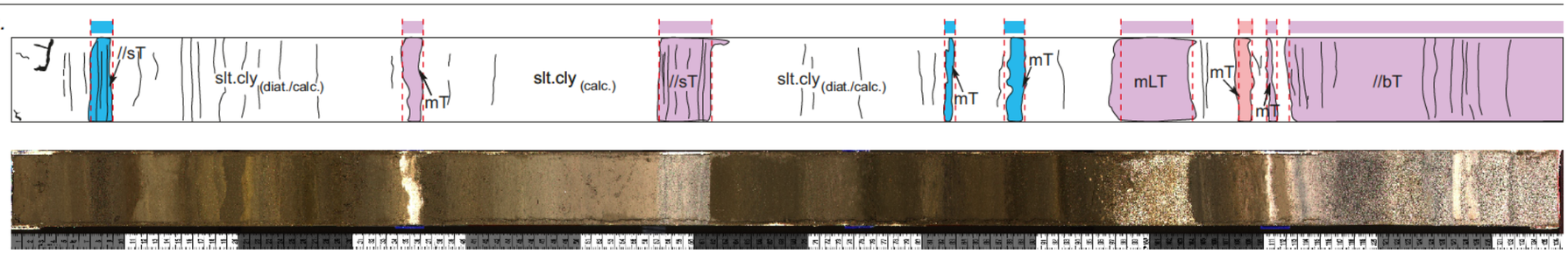


PRESERVATION VALUE 1

Measured Thickness

DRAWN SECTION

CORE SECTION PHOTO



TOP

BASE

Volcanic layers

- TFD (Felsic)
- TFD (Intermediate)
- TFD (Mafic)

Volcanic facies codes

- mT = massive tuff
- mLT = massive lapilli tuff
- //bT = parallel bedded tuff
- //sT = parallel stratified tuff

Sedimentary facies codes

- slt.cly (calc.) = calcareous silty clay
- slt.cly (diat.) = diatomaceous silty clay

Symbols

- = laminations/sediment orientation
- = major cracks/gaps in sediment

Fig. 5. Photographic examples of core sections containing tephra deposits of varying levels of preservation. Schematic, redrawn examples of the core sections are provided alongside the photographs and a bar is presented with dashed lines to show the recorded thickness in this study. Sedimentary lithologies are also noted and different colours are used to display the composition of the tephras.

---

understood and mitigated as much as possible to achieve the most accurate and reliable record.

As mentioned in Table 1, a confidence scale for thickness reliability and preservation quality was assigned to each volcanic unit. Fig. 5 shows the variation in preservation between TFDs and the approach taken to record their thicknesses as accurately as possible. If a layer displayed bioturbation (e.g., bioturbated though the base) but the thickness of the deposit was still well preserved, with a clear upper and lower contact, the tephra was assigned a high preservation value (i.e., 1). This ensured that sections which were well preserved however contained minor bioturbation were not marked as lower quality preservation which would lead to a false assessment of the overall quality of the core. To evaluate preservation values assigned, data regarding the upper and lower contacts of each deposit is also recorded in Table 1 and Appendix C1.

3.5. *Calculating depths within the spliced stratigraphy from depths in individual core sections*

When working with cores, each contact or layer should be assigned a unique identifier that includes both the depth within the section and the section name. This allows each contact/layer to be uniquely referenced to the original cores or core photographs and/or associated metadata. However, for the assessment of the overall record, which requires interpretations of all layers in a stratigraphic sequence, each contact must also have an *on-splice identifier (OSI)*. Table 2 provides an explanation for all core terminology that can be cross-referenced with the

Table 2. Table of core terminology used in this chapter and their definitions and abbreviations.

	Core terminology	Abbreviation	Definition
Drilling and Recovery	Drive	-	The 'push'' or associated drilling attempt to recover a section of core.
	Gap	-	A portion where no core recovery has been achieved.
	Borehole	hole	The continuous location of drilling hole often duplicated to ensure maximum recovery in areas where drilling gaps occur.
	Core section	-	A segment of the core recovered from a borehole. Drives are usually split into 1.5 m segments.
	Core catcher	-	A drilling component that grips the base of the core and ensure minimum sediment is lost during extraction. Often catches material that has fallen which is usually in stratigraphic order.
	Short core	-	Any core that is typically shorter than then drive length, due to loss of recovery during extraction (not captured by the core catcher).
Stratigraphic and sampling	Splice/composite sequence	-	An artificial core comprised of the best-preserved sections of core from multiple boreholes. This is often the working basis for the scientific team to use (see Fig. 2).
	Splice table	-	The table of data compiled during the splice production by the stratigraphy team. Contains information about the core sections used, depth information and drilling gaps. May also contain notes from the drilling process that are relevant to the splice production.
	Core depth below seafloor	CSF-A	Distance from the seafloor (lakebed) to the target in the recovered drive.
	Composite depth scale	CCSF-A	Distance from the seafloor (lakebed) to the target in the recovered drive using splice depth (e.g., adjusted depths to resolve gaps in core recovery and depth inconsistencies). A type of composite depth.
	Top offset	Δo_t	The depth in the core section at which a core section is begun to be used within the splice.
	Bottom offset	Δo_b	The depth in the core section at which a core section is stopped being used within the splice.
	Composite depth	e.g., m_c	A depth of any layer which is converted to splice/composite depth.
	Event-free depth	efd	The depth within the splice that a stratigraphic boundary or layer sits when all instantaneously deposited layers (i.e., events) have cumulatively been removed.
	On-splice identifier	OSI	When using a section that is not within the splice, this refers to a layer that is within the off-splice section(s) that can be correlated to a layer that is on-splice.
	Off-splice identifier	OFSI	When using a section that is within the splice, this refers to a layer that is within an off-splice section(s) that can be correlated to the layer that is on-splice.
	Ghost	g	An off-splice layer or deposit that is not represented within the splice but is required to have an on-splice position for a scientific reason (e.g., tephra). This can be projected artificially onto the splice and have thickness and physical characteristic descriptions recorded off-splice but must be collapsed to zero thickness on-splice to avoid interfering with the splice depth scale (Fig. 6).
	Smear slide	-	A very small sub-sample of sediment taken from a core and dispersed on a glass slide for microscopic examination. This can aid in rapid identification of the composition and/or origin of a deposit within the core (Appendix C5).

terms used in this paper. OSIs can be determined by referring to the splice table, typically compiled during splice production. Firstly, contacts/ layers (in this case, volcanic layers) identified across all core sections were checked against the splice table to ascertain which volcanic layers were present within the splice. For layers present within on-splice and off-splice sections, it was important to only use the thickness and stratigraphic position from the corresponding on-splice section for determination of the layers' on-splice position to avoid creating overall splice thickness discrepancies. Depth position and thickness data was therefore taken from on-splice layers (even if better preserved in off-splice sections) to avoid this problem. Once all possible volcanic layers that have an OSI have been identified, their on-splice top depth can be calculated from the splice table using the following equation:

(Eq. 1)

$$d_t = \frac{cd_{b\ (prev.)} + v_t - \Delta o_t}{100}$$

(where: d_t is the top depth (m) of the volcanic unit in the splice; $cd_{b\ (prev.)}$ is the bottom depth of the preceding section in the splice (cm) - often referred to as CCSF-A; v_t is the top depth of the volcanic layer in the core section (cm) and Δo_t is the top offset (cm) - stated in the splice table).

The bottom depth (m) of the volcanic unit in the splice can be calculated by:

(Eq. 2)

$$d_b = d_t + \frac{t_v}{100}$$

(where: d_b is the bottom depth (m) of the volcanic unit in the splice; d_t is the calculated top depth (m) from Eq. 1 of the volcanic unit in the splice and t_v is the thickness (cm) of the volcanic unit in the corresponding core section that is on-splice).

The above equations (Eqs. 1 and 2) provide each on-splice volcanic layer with an absolute depth for their top and bottom contacts, providing the volcanic units' upper and lower contacts are present within the same core section. For any deposit spanning core sections that have been recovered in the same drive (i.e., core catcher material or segments of the same drive), the following equation (Eq. 3) can be used:

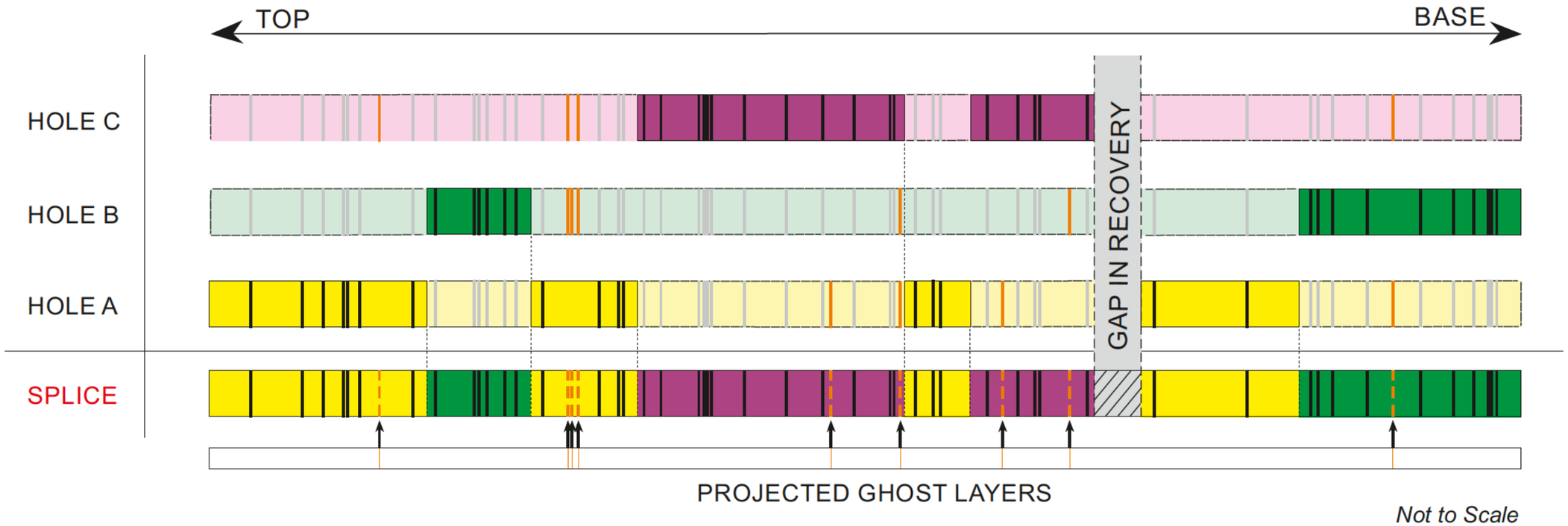
(Eq. 3)

$$d_{b\ (span)} = \frac{cd_{b\ (prev.)} + v_b + ps_{full} - \Delta o_t}{100}$$

(where: $d_{b\ (span)}$ is the depth (m) of the base of the volcanic unit that spans two sections; $cd_{b\ (prev.)}$ is the bottom depth of the preceding section in the splice (cm) - often referred to as CCSF-A; v_b is the basal depth (cm) of the volcanic layer in the core section; ps_{full} is the full length (cm) of the previous section and Δo_t is the top offset (cm) - stated in the splice table).

It must be noted that ps_{full} is a length recorded by eye from the core section photographs. This may differ slightly (on a millimetre scale) from the lengths of core sections used in the splice table, which are often not recorded as metadata.

If volcanic layers span entirely different core section drives (with different identifier numbers) Eq. 1 can be used to calculate an on-splice depth for the top and bottom of the layer. An


TOP
BASE
HOLE C
HOLE B
HOLE A
SPLICE
GAP IN RECOVERY
PROJECTED GHOST LAYERS

Not to Scale

Fig. 6. Schematic diagram containing information on splice production, as seen in Fig. 4. Artificial layers (representing tephra deposits) have been drawn onto the diagram which show that some tephras are only preserved in off-splice sections. The diagram shows how these tephras are projected onto the splice as 'ghost layers' which are collapsed to zero thickness on the splice but contain a thickness in off-splice sections of core.

---

accurate on-splice thickness can be calculated from subtracting the calculated top depth from the bottom depth.

Additionally, for any volcanic layer that is only present within secondary or tertiary segments of a drive (e.g., core catchers) Eq. 4 must be used:

(Eq. 4)

$$d_{sc} = \frac{cd_{b\ (prev.)} + v_t + ps_{full} - \Delta o_t}{100}$$

(where: d_{sc} is the top depth (m) of a volcanic unit that is present in a short core; $cd_{b\ (prev.)}$ is the bottom depth of the preceding section in the splice (cm) - often referred to as CCSF-A; v_t is the top depth (cm) of the volcanic layer in the core section; ps_{full} is the full length (cm) of the previous section and Δo_t is the top offset (cm) - stated in the splice table).

Eq. 4 can be used to calculate the top and the basal depth of this layer with an accurate on-splice thickness calculated by subtracting the top depth from the bottom depth.

3.6. *Projecting off-splice volcanic layers onto the splice*

As described in section 3.6, many volcanic layers within the MexiDrill cores were represented within the splice. However, as the volcanic stratigraphy was determined to millimetre-scale accuracy and at points some layers are only preserved in one or two holes (due to drilling

artefacts and lateral discontinuity), some volcanic and probable volcanic units could not be correlated with any identifiable macroscopic deposit within the splice. As each potential volcanic layer (primary or reworked) represents some form of volcanic event, their exclusion from our analysis would be a source of undersampling in terms of volcanic deposition in Lake Chalco. We have therefore projected these layers onto the splice as *ghost horizons* – extrapolated layers with a defined depth on the splice, but zero on-splice thickness (see Fig. 6). For analyses involving event frequencies or age, temporal or stratigraphic information is assigned to ghost horizons in this way. For analyses involving other volcanological metadata (e.g., thickness, grain size, etc.), this information is taken from the core section where these horizons are best preserved. This approach is also followed for any volcanic layer where preservation is poor on-splice, but where a preservation is better in an off-splice section, using an *off-splice identifier (OFSI)*.

For ghost horizons, the nearest on-splice volcanic layers (above and below) were utilized to extrapolate a projected depth onto the splice, with the ghost horizon sitting within the midpoint between the two surrounding volcanic layers. This was the simplest and most systematic approach to take, because the precise stratigraphic positioning is ambiguous for many ghost layers (i.e., how close they sit above or below known layers, because they most often occur in artefact-rich sections and/or regions of the core with a higher proportion of drilling gaps). Ghost horizon depth(s) can be calculated using Eq. 5:

(Eq.5)

$$g = \frac{\left(\frac{(d_{t\,(succ.)} - d_{b\,(prev.)})}{2} + d_{b\,(prev.)}\right)}{100}$$

(where: g is projected ghost depth (m) of a volcanic unit that is not present in the splice; $d_{t\ (succ.)}$ is the top depth (cm) of the next calculated volcanic layer below which is present in the splice; $d_{b\ (prev.)}$ is the basal depth (cm) of the first layer above which is present in the splice).

Eq. 5 works only if there is one ghost horizon between two on-splice volcanic layers. However, if there is a group of two or more consecutive ghost layers, ghost horizons must be calculated using the following:

(Eq. 6)

$$g_n = g + \frac{\left(\frac{(d_{t\ (succ.)} + d_{b\ (prev.)})}{ng + 1}\right)}{100}$$

(where: g_n is the depth of the second ghost layer and onwards in a group of successive ghost layers; g is the calculated value in Eq. 5; $d_{t\ (succ.)}$ is the top depth (cm) of the next calculated volcanic layer below which is present in the splice; $d_{b\ (prev.)}$ is the basal depth (cm) of the previous calculated above which is present in the splice; ng is the number of ghost layers to be calculated between calculated volcanic layers within the splice).

Eq. 6 ensures that all ghost horizons in a cluster of two or more are calculated at equal spacing between the nearest on-splice volcanic layers above and below, so that these projected volcanic layers (ghosts) are systematically spaced between the bounding on-splice deposits. It must be noted that projections of ghost layers are made irrespective of sedimentological changes within the core, and potential sedimentation rate changes occurring between two on-splice volcanic layers, where ghosts are present, are not considered when estimating the stratigraphic placement of ghost layers.

3.7. Calculating event-free depth

Following depth calculations for all layers within the core (on-splice or off-splice ghost horizons) we have also converted the position of each volcanic layer to an event-free depth. This is based on the assumption that any volcanic layer is an event with near-instantaneous deposition, but that the intervening sediment represents gradual, continuous deposition, and is thus broadly equivalent to time (notwithstanding longer-term variations in sediment accumulation rate). With an established chronology, event free depths allow for more meaningful age-depth modelling, frequency analysis of volcanic events, and sedimentological analysis to be conducted. To calculate event-free depth from the above equations (Eqs.1-6) the thickness represented within the splice must always be used (i.e., including zero thickness for ghosts). Eq. 7 should therefore be used to calculate event-free depths:

(Eq. 7)

$$d_{ef} = d_b - \left(\frac{\Sigma(\Pi t_s)}{100}\right)$$

(where: d_{ef} is event-free depth (m); d_b is the calculated basal depth of the volcanic layer by Eq. 2, ; g is the basal depth (m) or ghost depth calculated from in Eqs. 1-5; $\Sigma(\Pi t_s)$ is the sum of the cumulative splice thickness values up to and including the volcanic layer which event-free depth is being calculated for).

In summary, Eqs.1-7 permit any volcanic layer present within the cores (on or off-splice) to be represented as accurately as possible within the already established splice for the cores. By

using these equations, each volcanic event identified within the record can be ascribed a position within the core, which can be used in conjunction with the physical characteristics of the deposits to obtain a consistent volcanological record.

3.8. *Assessing the volcanological record of the core*

With all potential volcanic layers accounted for, and the metadata (Table 1) recorded for each layer, the sequence can be assessed for the following: (1) identification of clustering patterns (both respective and irrespective of composition); (2) determination of thickness and grainsize (magnitude) of deposits and their eruptive styles; (3) understanding thickness and grain size relationships in relation to depth; (4) estimations of completeness, uncertainty and bias; and (5) implications for hazard assessment for potential future events. Throughout this paper, the volcanic record of the MexiDrill core (supplemented by earlier drilled cores) is assessed from these perspectives to combine analysis of the record from both an eruptive history and physical volcanological perspective. We wish to emphasise that this paper aims to assess patterns of volcanic deposition at the Chalco site irrespective of their source volcanoes. Further analysis and the determination of potential source volcanoes using chemical data and age information, is the focus of chapters 4 and 6. Here, we present the overall volcanic stratigraphy of the MexiDrill cores to provide a long-timescale assessment of the volcanic hazards in a densely populated area.

4. ANALYTICAL METHODS

4.1. Laser Diffraction Particle Size Analysis

Samples for grain size analysis were selected at random from TFDs with ascribed mafic and felsic compositions at varying depths throughout the core to test the accuracy of our qualitative grain-size estimations, which were based on visual inspection of the core. The maximum ascribed grain size analysed was 1 phi, because anything above this size category can be accurately measured directly from the core photographs. For samples with flocculated grains due to residual moisture, a drying step in an incubator was conducted. Average grain size distribution data and red-dashed lines, indicating grain-size estimations, are plotted in Fig. 3 for selected deposits and raw data is presented in Appendix C2.

Grain size analyses were gathered using a Malvern Mastersizer 2000 with Hydro 2000MU attachment. Deionised (DI) water was used as a dispersant with a refractive index of 1.33. For analytical purposes, sample material was input as Silica into the instrument software representing grains with a refractive index of 1.544. The instrument was flushed at least 3 times between samples with DI water to ensure all piping was free of residual material. If water was not clear following 3 flushes, additional flushes were conducted until water was free of any material. Background measurements were collected prior to adding sample material with measurements lasting 12 seconds and a collection of 12000 snaps. The same conditions were applied to sample measurements which were collected after auto alignment of the instrument. Measurement cycles included 3 measurements per aliquot with a delay of 10 seconds between data collection. All pump and stir speeds were set to 2000 RPM. Each analysis was run in ideal

and optimum analytical conditions for the instrument, falling between 10 and 30% obscuration levels.

4.2. Whole Rock Geochemistry

Whole rock major and trace element analyses were conducted on a small number of samples (3 lavas, depths presented in Fig. 8 and Table 3) using inductively coupled plasma emission spectroscopy (ICP-OES) and inductively coupled plasma mass spectrometry (ICP-MS) at Activation Laboratories Ltd (Actlabs) in Canada using the 4Litho Actlabs package (https://actlabs.com/geochemistry/lithogeochemistry-and-whole-rock-analysis/lithogeochemistry/). The accuracy and precision of the calibration was evaluated using secondary standard analyses. The standards used included United States Geological Survey (USGS) reference samples: DNC-1 (dolerite), W-2b (diabase), BCR-2 (basalt), BIR-1a (basalt), W-2a (diabase) with preferred values and their standard deviation presented in Flanagan (1984) and Jenner et al., (1990). All major elements were normalised to 100% (anhydrous) for comparative purposes and raw data (major and trace elements) and secondary standard analyses are presented within Table 5 and Appendix C3. The aim of these analyses was to geochemically characterise lavas within the core and test their variability (see section 5.1.2).

4.3. Thin Sections

Eleven polished thin sections from indurated volcaniclastic material and lavas beneath the lacustrine section of core (293.71 m_c) were also prepared for textural and petrological analysis, complementing the whole rock chemistry. Thin section descriptions are presented in Appendix C4.

5. VOLCANIC STRATIGRAPHY OF LAKE CHALCO

The stratigraphy of the MexiDrill cores comprises various sediment types from organic-rich sapropels to carbonate muds (Valero-Garcés et al., 2021), interbedded with volcaniclastic material, which becomes more dominant with depth, before volcanic rocks predominate in the deepest part of the core. Lacustrine sediment types all occur within the upper c.300 m of core (cf. Valero-Garcés et al., 2021), and this portion is referred to as the *lacustrine-dominated* stage. Below this, the cores are exclusively volcanic in origin, containing fine to coarse grained volcaniclastics and lavas. Most lavas are present between c.400 and c.500 m, (the lowermost section of core). However, minor volcaniclastic material is also present below this, <20 m total thickness. Resultantly, within this chapter three stages of core are referred to (from base to top, Fig. 7): (I) Lava-dominated section (448.86 – 553.93 m_c); (II) Pre-Lacustrine deposits (293.71 - 448.86 m_c); and (III) Lacustrine-dominated deposits (0 – 293.71 m_c).

5.1. Stage I: Lava-dominated deposits (448.86 – 553.93 m_c)

Description

This stage of core is dominated by (c.82 %) dense to vesiculated finely crystalline rocks, recovered as hard rock cores (Fig. 3; Fig. 7). The lithologies are generally grey to black, massive, and lack internal structure. Some parts are vesiculated and many of these are red and oxidised. The rock is aphanitic with a pervasive groundmass texture. Two minor deposits of polylithologic igneous clasts within an indurated fine-grained matrix, alternating with very fine beds also occur as well as c.2 m of scoriaceous deposits which are well bedded.

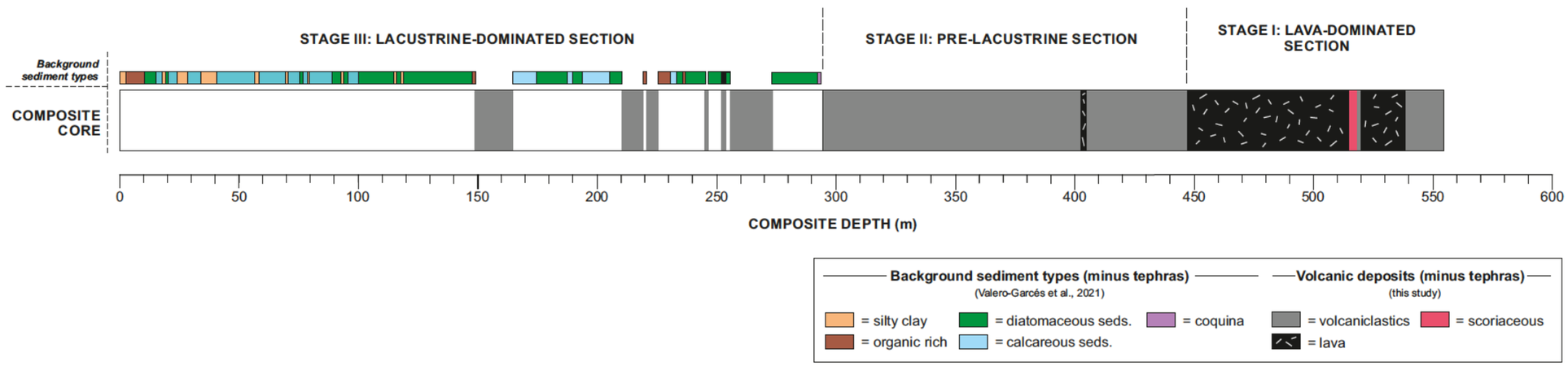

STAGE III: LACUSTRINE-DOMINATED SECTION
STAGE II: PRE-LACUSTRINE SECTION
STAGE I: LAVA-DOMINATED SECTION
Background sediment types
COMPOSITE CORE
0
50
100
150
200
250
300
350
400
450
500
550
600
COMPOSITE DEPTH (m)
Background sediment types (minus tephras)
(Valero-Garcés et al., 2021)
= silty clay
= diatomaceous seds.
= coquina
= organic rich
= calcareous seds.
Volcanic deposits (minus tephras)
(this study)
= volcaniclastics
= scoriaceous
= lava

Fig. 7. Schematic section displaying the whole core as composite sequence with a composite depth scale provided. All volcanic lithologies are represented on the diagram except for tephra layers (due to the low-resolution scale of the diagram). Tephra layer stratigraphic positions can be graphically seen in Fig. 11. The lava displayed in Stage II is a large block (c.2 m thick) within coarse (type 1) volcaniclastics. It has been shown here as a lava lithology as geochemical data is provided for this sample (ARL3, Fig. 9, Table 5) and a thin section and photograph is provided in Fig. 10. Background sediment types in Stage III are also presented (from Valero-Garcés et al., 2021).

Interpretation

These rocks are interpreted as lavas of a basic composition (see section 5.2.2.), with flow boundaries represented by reddened, oxidised and often vesiculated regions. These flow boundaries are likely to have been exposed at the surface (prior to lake formation) and would have undergone chemical and physical weathering. Minor volcaniclastic deposits, interpretated to have originated from erosion or collapse of a polygenetic volcano(es) and transported into the lake by secondary deposition, are also present alongside a well bedded scoriaceous deposit interpreted to be a preserved proximal deposit from a small eruptive centre (i.e., the distal flank of a now buried and/or eroded scoria cone). Fig. 8a displays a stratigraphic column through the deposits of Stage I and with Fig. 8b including photographs of core sections from this stage and the variation in the types of deposits.

5.1.1. Lavas and flow boundaries

A total of 8 lavas (I-VIII, depths in Table 3) have been interpreted and any given lava is no thicker than 20 m (Fig. 8a). The tops of oxidised horizons have been identified as the boundary between flows and where oxidised flow tops are lacking, a sharp contact between two contrasting lava textures and colours has also been interpretated as a contact. There is no

A

B

C

COMPOSITE DEPTH (m)

440

457.5

475

492.5

510

527.5

545

LAVA VIII

LAVA VII

LAVA VI

LAVA V

LAVA IV

LAVA III

LAVA II

SCORIA
VOLCANICLASTICS

LAVA I

VOLCANICLASTICS

AH2

THIN SECTION

AH2

BASE

AH3

THIN SECTION

AH3

BASE

AH7

THIN SECTION

AH7

BASE

Minerals

Ol = olivine
Gl = glass
Pl = plagioclase
Alt. = alteration
Qz = quartz

Groundmass

GM_f = groundmass (fine)
GM_c = groundmass (coarse)

AH2

PPL

Pl
Ol
Alt.
Alt.
Pl
200 µm

XPL

AH3

PPL

Qz
Pl
Gl
Gl
Pl
Qz
200 µm

XPL

AH7

PPL

GM_c
GM_f
GM_f
Ol
GM_c
Pl
Pl
Ol
200 µm

XPL

Fig. 8. (a) Stratigraphic column displaying the composite depths and thicknesses of the lithologies of Stage I. (b) Representative core section photographs from sections that also contain thin sections. Their stratigraphic position is also noted in a. Thin section photographs are also displayed showing the section of core of which the thin section relates. (c) Photomicrographs of the thin sections displayed in b. Images are presented in plane polarised light (PPL) and cross polarised light (XPL) with key minerals and features annotated.

reason to conclude large gaps in time have occurred between flows as no palaeosol development is present above interpretated flow surfaces. It is possible erosion of lavas have occurred where volcaniclastic material overlies (e.g., Lava I, see Table 3). This erosion is inferred by the inclusion of fragments of lava in the overlying volcaniclastic componentry.

5.1.2. Geochemistry and petrology

In order to characterise the lavas and assess variability between flows, we obtained whole-rock major and trace element analysis of three lava samples (ARL 1 and 2 from primary lava VII and lava V, respectively in Stage I; and ARL 3 from a suspected included lava block in the overlying Stage II volcaniclastic deposits, see Fig. 8 for their stratigraphic positions) using inductively coupled plasma (ICP) techniques.

ICP analysis reveals that the lavas are basaltic andesite to andesite with SiO_2 of 55.41 wt.% to 57.33 wt.% (Fig. 9a, Table 5). All samples are similar in terms of rare earth element (REE) concentrations with a Eu anomaly supporting a subduction setting (Fig. 9b,c). It must be noted however that several trace elements were below detection thus affecting overall trends of the data (see Table 5). It can be seen from the Total Alkali Silica (TAS) plot in Fig. 9a that these analyses are consistent with data reported in Jaimes-Viera et al., (2018) from the SCVF.

Furthermore, it is reasonable to assume that these are multiple stacked flows/lobes from the same event and the subtle variation in geochemistry (particularly between ARL1 and ARL3,

Table 3. Lithologies, basal composite depths, descriptions, and interpretations of all volcanic deposits in Stage I and II.

Stage	Lithology	Basal composite depth (mc)	Description	Interpretation
Stage III (Lacustrine-dominated)	Varied	293.71	Lacustrine sediments intercalated with volcaniclastic and tephra fall deposits (see Fig.11 and Appendix C1).	
Stage II (Pre-lacustrine)	Volcaniclastics (Type 2)	297.88	Coarse (type 1), medium (type 2) and fine grained (type 3) volcaniclastic rocks of varying induration. Relative grain size refers to the clasts within the sediments. Clasts are generally polylithologic and volcanic in origin, often containing phenocrysts. Pumiceous core sections are also present and the componentry of small clasts within finer grained volcaniclastic deposits is often pumiceous. Varying structure types are present including cross-stratification. Secondary brittle deformation can be seen in some deposits, which are often more indurated. Colours vary however the matrix is often dark brown in type 2 and type 3 deposits. Type 1 deposits contain some matrix (also often dark brown in colour) however, are more clast supported, with clasts up to c.2 m in size. Clasts are typically rounded throughout. See Fig.10.	Originated from a mass-wasting event from a nearby polygenetic volcano and transported to the lake via drainage pathways (i.e., laharic). Coarser deposits are more indicative of the primary collapse deposit and finer grained deposits have been input into the lake by more dilute streamflow processes (see Smith and Lowe, 1991).
	Volcaniclastics (Type 3)	299.40		
	Volcaniclastics (Type 1)	300.64		
	Volcaniclastics (Type 3)	303.31		
	Volcaniclastics (Type 2)	304.06		
	Volcaniclastics (Type 1)	305.11		
	Volcaniclastics (Type 3)	306.14		
	Volcaniclastics (Type 2)	307.05		
	Volcaniclastics (Type 3)	308.01		
	Volcaniclastics (Type 2)	329.00		
	Volcaniclastics (Type 1)	332.84		
	Volcaniclastics (Type 2)	334.87		
	Volcaniclastics (Type 1)	336.52		
	Volcaniclastics (Type 3)	337.82		
	Volcaniclastics (Type 1)	344.43		
	Volcaniclastics (Type 2)	348.21		
	Volcaniclastics (Type 1)	363.28		
	Volcaniclastics (Type 2)	366.65		
	Volcaniclastics (Type 3)	379.81		
	Volcaniclastics (Type 2)	383.46		
	Volcaniclastics (Type 1) – contains large lava clast	446.18		
	Volcaniclastics (Type 2)	447.03		
	Volcaniclastics (Type 3)	448.87		

Stage I (Lava-dominated)	Lava VIII	456.61		Lavas are interpreted to have originated from nearby small eruptive centres and are formed by effusive volcanism. Scoria is interpreted to represent the distal flank of a nearby scoria cone and volcaniclastic deposits are likely reworked deposits from a mass-wasting event or ignimbrite/lahar deposit (given their thicknesses).
	Lava VII	462.66		
	Lava VI	469.08	Eight lavas, finely crystalline and dark in colour. Some are dense and others contain numerous vesicles. Most lavas exhibit oxidised flow tops which are often also vesiculated. Volcaniclastic deposits are generally matrix-supported but with polylithologic clasts. Clasts are well rounded. Scoria is well bedded and indurated/sintered. These clasts are well indurated and comprised of varying grain sizes from fine to medium ash to lapilli. See Fig.8.	
	Lava V	480.66		
	Lava IV	491.46		
	Lava III	510.93		
	Lava II	515.74		
	Scoria	518.00		
	Volcaniclastics	520.42		
	Lava I	539.44		
	Volcaniclastics	553.93		

Fig. 9) is consistent with analyses from a single source (e.g., Hodgetts et al., 2021). Nevertheless, without a stratigraphic control in which to compare, and/or reference samples, it cannot be concluded whether these lavas were emplaced from the same eruption.

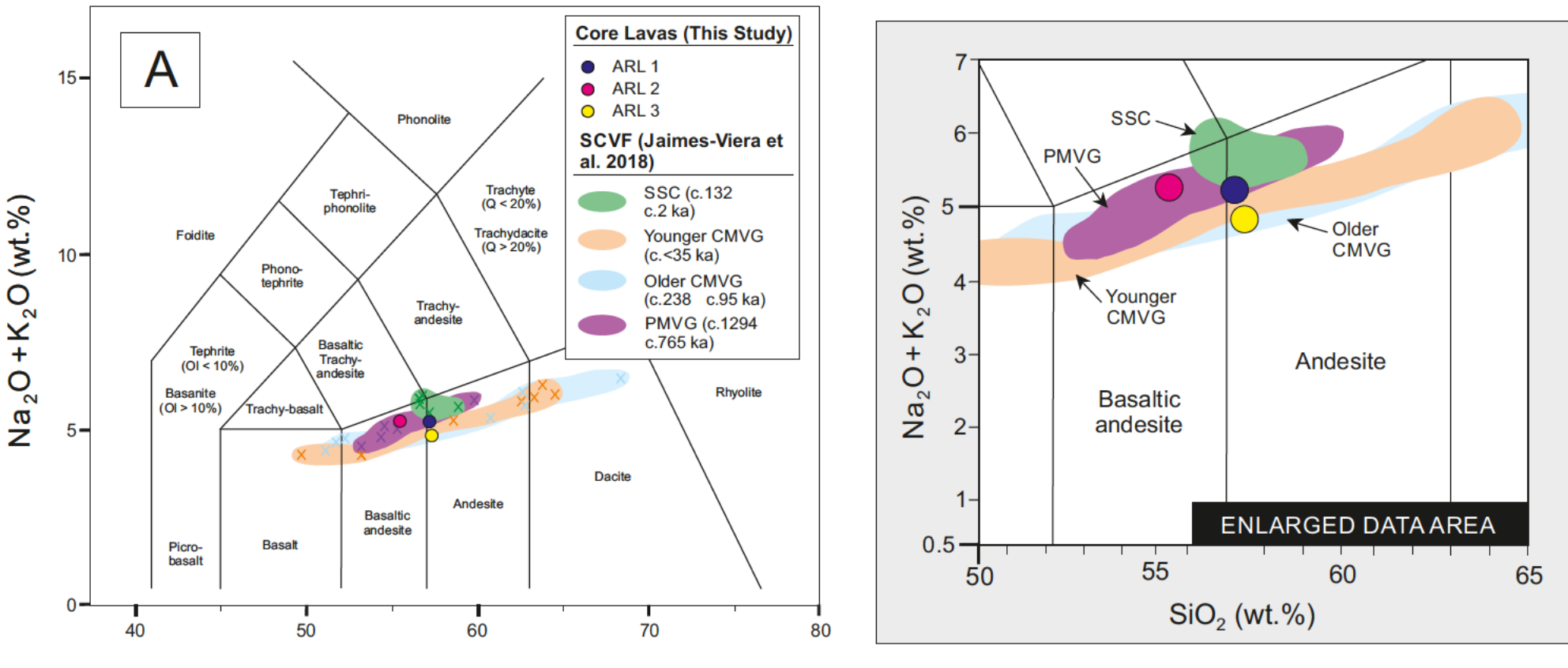
Petrographic analysis of thin sections of the lavas reveals feldspar (plagioclase) laths dominate the groundmass. These are typically twinned however a low abundance (c.5 %) are zoned. Olivine and pyroxene are also present although not pervasive throughout. Chemical alteration can also be seen under thin section in parts. The thin sections are consistent with typical lavas of basaltic andesite to andesitic compositions and the associated mineralogies are typical of these lithologies. Full thin section descriptions are provided in Appendix C4.

In summary, we infer lavas to have been sourced locally to the core site and likely to have originated from a nearby eruption in the SCVF. Compositionally, our analyses are consistent with this as a source and geographically, the core site is within the SCVF. The exact volcanic source (i.e., cone) cannot be ascertained due to the depth of the lavas within the core (>400 mc). We therefore conclude that the volcanic source, likely including a pyroclastic cone around the vent site as well as stacked peripheral lava flows, is now entirely buried under Lake Chalco/ Basin of Mexico sediments.

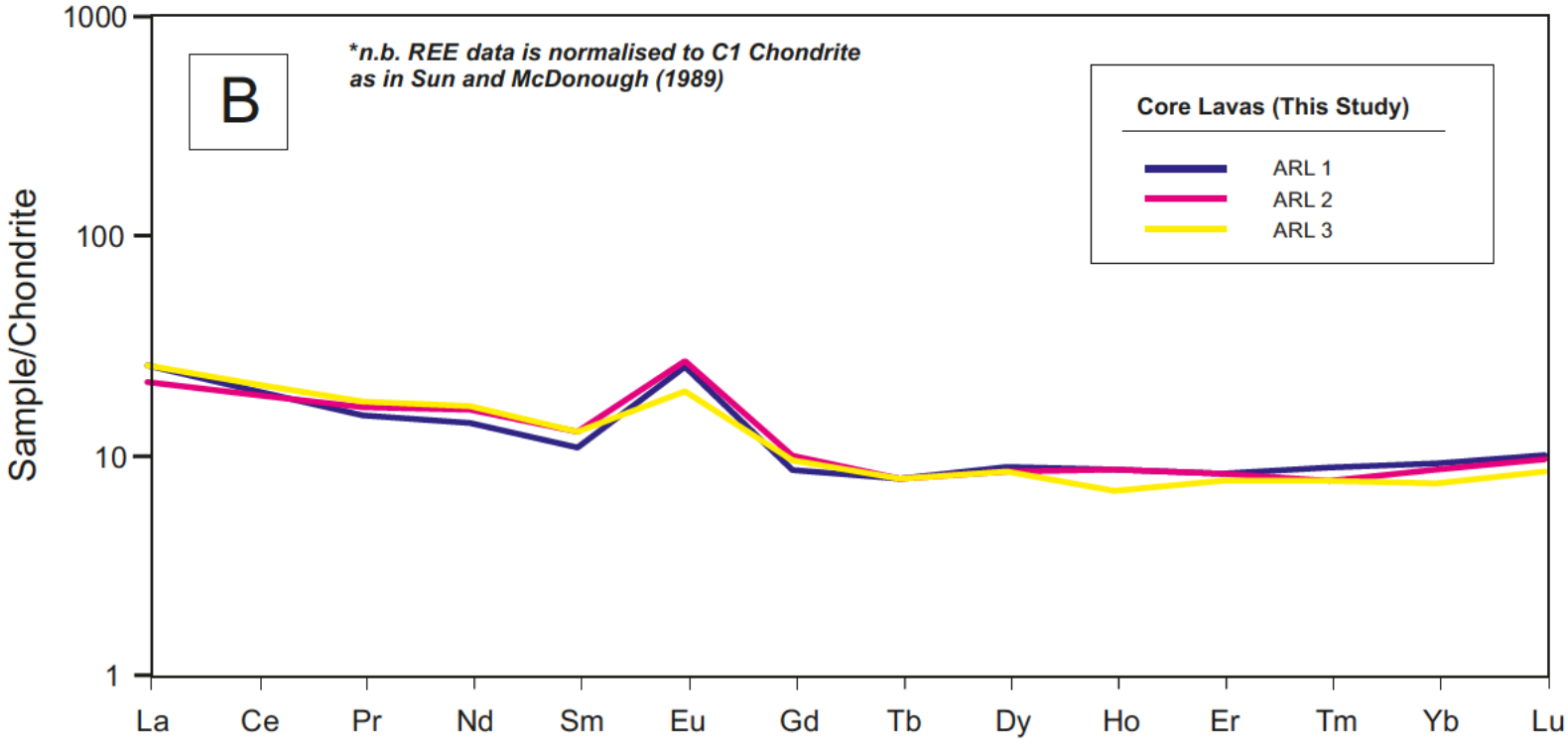
5.2. Stage II: Pre-lacustrine deposits (293.71 - 448.86 m_c)

Description

The time gap between Stage I and Stage II is unconstrained. Stage II lithofacies are variable with different levels of induration, clast to matrix concentrations and components. They have therefore been subdivided into three types: Type 1 – coarse deposits (dominated by at least


A
Core Lavas (This Study)
ARL 1
ARL 2
ARL 3
SCVF (Jaimes-Viera et al. 2018)
SSC (c.132 c.2 ka)
Younger CMVG (c.<35 ka)
Older CMVG (c.238 c.95 ka)
PMVG (c.1294 c.765 ka)
Phonolite
Tephri-phonolite
Trachyte (Q < 20%)
Trachydacite (Q > 20%)
Foidite
Phono-tephrite
Trachy-andesite
Tephrite (Ol < 10%)
Basaltic Trachy-andesite
Basanite (Ol > 10%)
Trachy-basalt
Rhyolite
Dacite
Andesite
Basaltic andesite
Basalt
Picro-basalt
Na2O + K2O (wt.%)
SiO2 (wt.%)
0
5
10
15
40
50
60
70
80

SSC
PMVG
Older CMVG
Younger CMVG
Andesite
Basaltic andesite
ENLARGED DATA AREA
Na2O + K2O (wt.%)
SiO2 (wt.%)
0.5
1
2
3
4
5
6
7
50
55
60
65


B
*n.b. REE data is normalised to C1 Chondrite as in Sun and McDonough (1989)
Core Lavas (This Study)
ARL 1
ARL 2
ARL 3
Sample/Chondrite
1000
100
10
1
La
Ce
Pr
Nd
Sm
Eu
Gd
Tb
Dy
Ho
Er
Tm
Yb
Lu

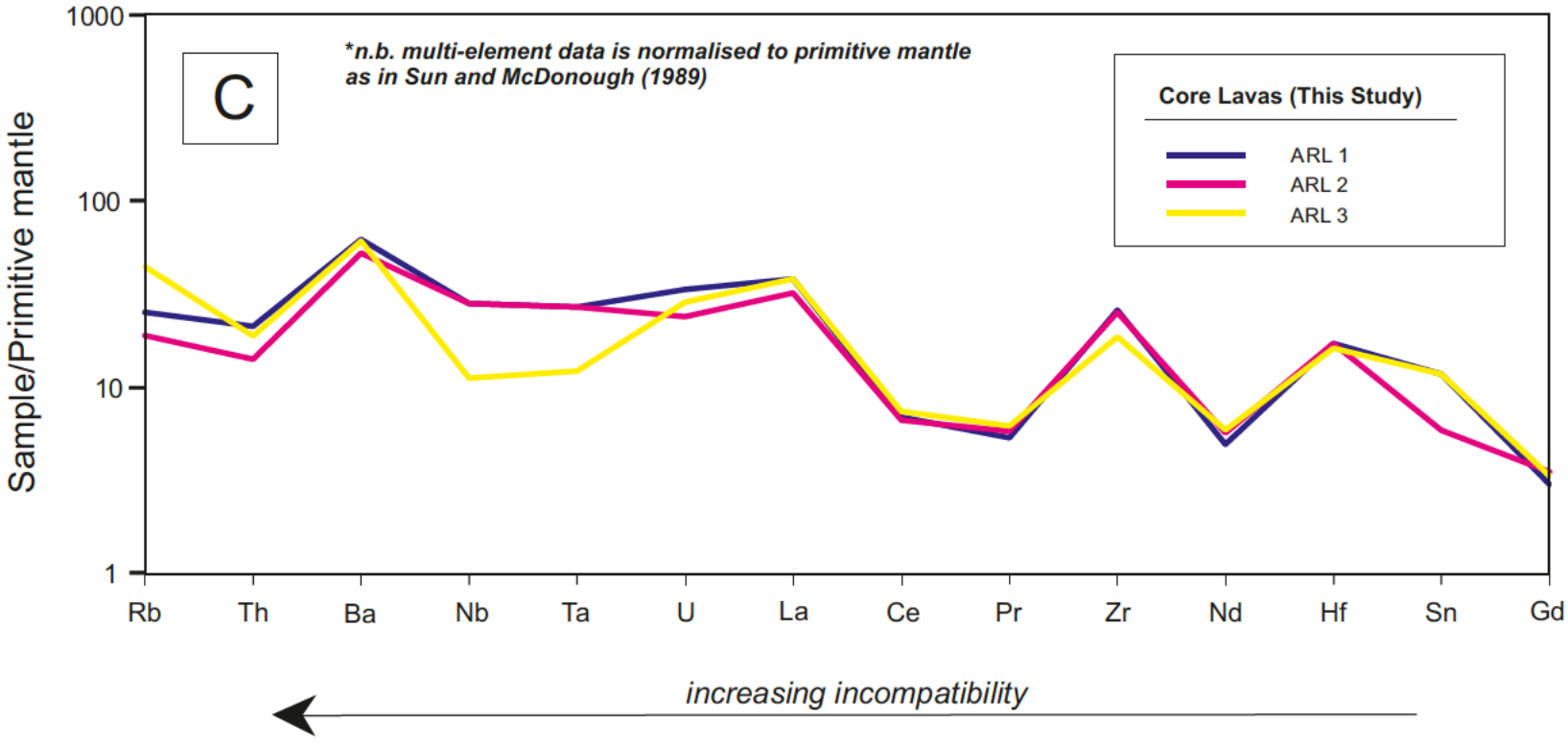
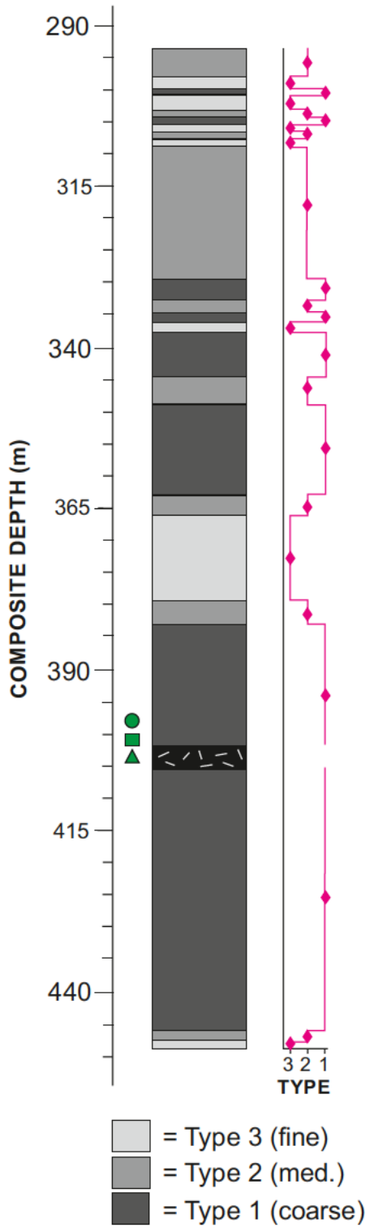

C
*n.b. multi-element data is normalised to primitive mantle as in Sun and McDonough (1989)
Core Lavas (This Study)
ARL 1
ARL 2
ARL 3
Sample/Primitive mantle
1000
100
10
1
Rb
Th
Ba
Nb
Ta
U
La
Ce
Pr
Zr
Nd
Hf
Sn
Gd
increasing incompatibility

Fig. 9. (a) Total Alkali vs. Silica (TAS) diagram displaying the geochemical composition and lithological classification of the lavas analysed in this study. Lavas are of basaltic andesite and andesite compositions. Data is plotted alongside SCVF data from Jaimes-Viera et al., (2018) where data is provided for four interpreted separate fields within the SCVF: (1) SSC (2) Younger CMVG (3) Older CMVG and (4) PMVG. Geochemical fields have been defined using this data and it can be noted that our data spans several of these fields, however, is consistent with a SCVF geochemical fingerprint. (b) Rare Earth Element (REE) plot of trace element data from lava samples normalised to C1 Chondrite values as in Sun and McDonough (1989). Samples display a Eu anomaly supporting a subduction signature. (c) Multi-element plot (with below detection elements removed). Data has been normalised to primitive mantle as in Sun and McDonough (1989). A subduction signature is also noted however the lack of a notable negative Nb-Ta anomaly shows this to be a weak signal.

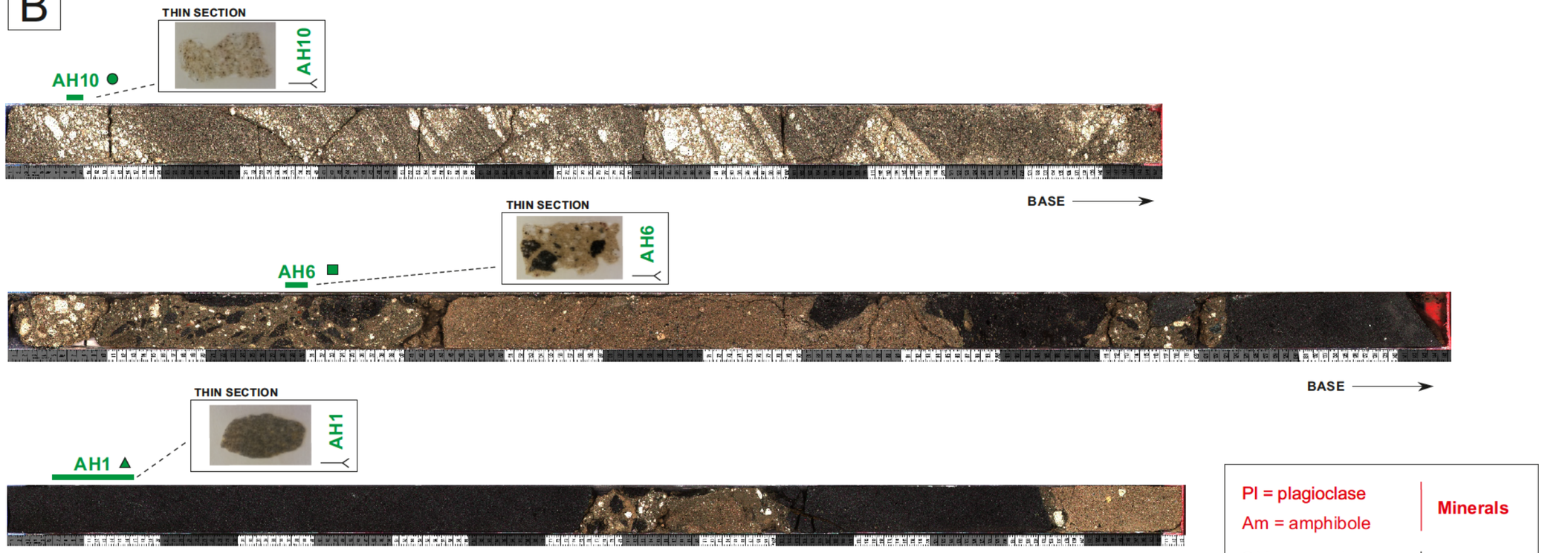
40% lapilli to block/bomb sized clasts often clast-supported with some matrix); Type 2 – medium deposits (generally containing lapilli-sized clasts in a high concentration (20-40%) either clast-supported or matrix-supported and Type 3 – fine deposits (mostly matrix-dominated with minor clasts dispersed amongst the matrix. Fig. 10a displays the different types of volcaniclastic deposits and their stratigraphic placement within Stage II.

These deposits, particularly Type 1, often include more complex internal textures and primary features, such as cross-stratification and secondary brittle deformation structures. They are also massive in parts. Sorting is generally poor overall; however, sections within the deposits are often well sorted with certain clast types dominating in different parts of the stratigraphy. Features such as imbrication are difficult to note as no orientation (other than top and base) can be established. Clasts (from Type 1-3) range in size from <1 cm to >2 m and are often polylithologic (i.e., comprising different rock types). Lava clasts are present within the deposits (see Fig. 10a with a lava clast >2 m noted on the stratigraphic column and Fig. 10b,c for photographs on different scales). Above the large clasts, smaller fragments of lava are in higher concentration for the immediate c.1 m above (Fig. 10b,c). Overall colour is also variable,

A



B



Pl = plagioclase	Minerals
Am = amphibole	
GM = groundmass	Clast type
PC = pumice clast	
LC = lava clast	

C

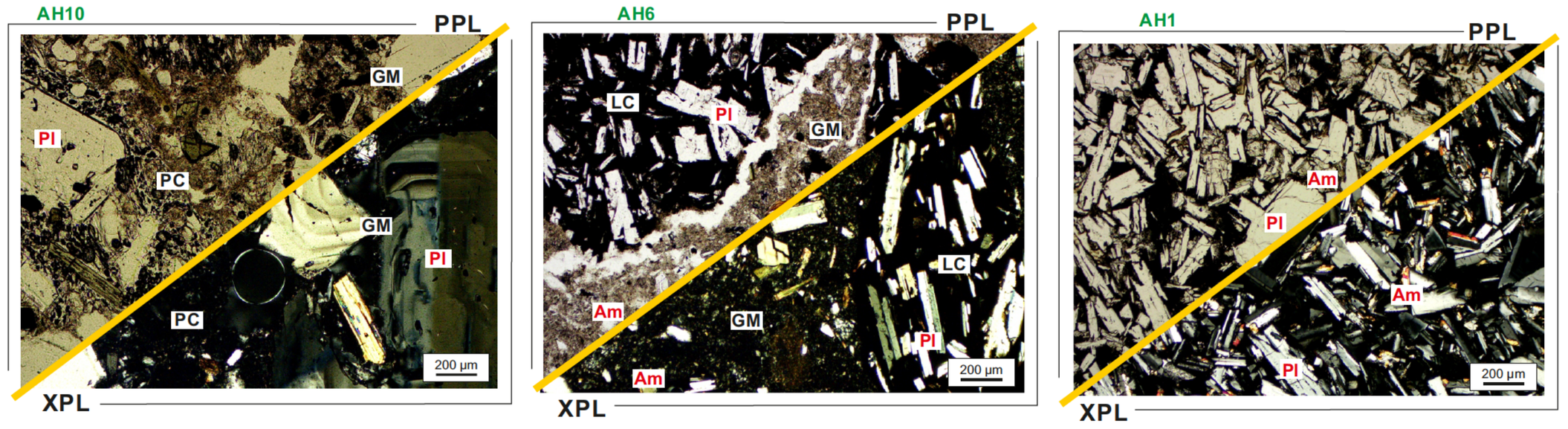


Fig. 10. (a) Stratigraphic column displaying the composite depths and thicknesses of the lithologies of Stage II. Different shades of grey relate to the type of volcaniclastic deposit interpreted and a graph showing the abundance and relative overall occurrence of these deposits is also provided. As mentioned in the caption of Fig. 7, the interpreted block of lava at c.402 mc has been shown here as a lava lihtology as geochemical data is provided for this sample (ARL3, Fig. 9, Table 5) and a thin section and photograph is provided in Fig. 10b,c. (b) Representative core section photographs from sections that also contain thin sections. Their stratigraphic position is also noted in a. Thin section photographs are also displayed showing the section of core of which the thin section relates. (c) Photomicrographs of the thin sections displayed in b. Images are presented in plane polarised light (PPL) and cross polarised light (XPL) with key minerals and features annotated.

---

ranging from brown muds to grey conglomerates. Most clasts are rounded to well-rounded, and MS is typically and consistently very high, and much higher than the younger lacustrine sediments.

Interpretation

Given the highly mixed lithologies and that the bulk of this sequence appears to have been emplaced relatively rapidly, without intervening palaeosols or fine-grained lake sediment, we infer that these deposits originated via a major mass-wasting event that transported large volumes of coarse-grained and heterogeneous volcaniclastic sediment to the margins of the Chalco basin. Large-scale sector collapses are capable of mobilising many cubic kilometres of material, and such events are known from the past history of Popocatépetl (e.g., Robin and Boudal, 1987). The pre-lacustrine sequence is consistent with being derived from remobilisation of marginal deposits from an event of this type (most likely from the SNVR). Its lithological heterogeneity, rounding of clasts, large scale layering, variable modal grain sizes (from muds to conglomerates), cross-stratification, and well sorted sections of the deposits support this interpretation. A large-scale sector collapse deposit between the core site

and the SNVR would have altered the local hydrology and the availability of sediment to the basin and may have been followed by secondary mass transport events triggered by rainfall and/or lake-dam breakout floods (cf. Capra and Macias, 2002), giving rise to the repetitive laharic/debris-flow characteristics of the sequence. As well as transporting the mixed volcanic lithologies provided by such a collapse, secondary transportation may have incorporated local surficial lithologies, such as the underlying lavas that would have formed the pre-Stage II local ground surface. The variable grain size between layers in this sequence is likely to have been caused by fluctuations in water availability and flow energy (see section 5.2.1).

5.2.1. Types of deposits

For depositional process-related purposes, and considering fluctuations in water availability and flow energy, the three sediment types described above are interpreted to be representative of changes along the lahar spectrum (e.g., Smith and Lowe, 1991). This classification permits depositional energy levels to be assessed, with type 1 deposits resembling a high-energy environment and type 2 and 3 deposits resembling increasingly lower energy environments, respectively. The stratigraphic column and abundance graph of these types in Fig. 10a are consistent with this model, as the coarsest deposits are generally found in the lower 40% of the Stage. The upper sections of this Stage are more varied with fluctuations between fine, medium and coarse deposits, suggesting there is more reworking and more extreme fluctuations in energy levels and water availability. This would suggest that the lower c.40% of this Stage perhaps represents immediate reworking of a primary collapse deposit and the upper c.60% is more indicative of longer timescale reworking of this deposit.

Pumiceous horizons within these deposits are possibly sourced by explosive eruptions occurring simultaneously with reworking and being carried as flotsam, or alternatively from reworking of discrete older explosive eruption deposit layers, transported as wholesale blocks from the source volcano within the collapse deposit. These pumice rich sequences are internally stratified and in some instances faulted and/or tilted, with repetition of units with very similar visual appearance, supporting the transportation of large blocks within a primary collapse-derived deposit. The coarse grain size of these pumiceous sequences, coarser than any tephra deposit in the overlying lacustrine sequence, also support the lateral transportation of more proximal volcanic stratigraphies, rather than these pumiceous sequences being primary fallout at the core site.

5.2.2. Petrology

Petrological analysis of thin sections from Stage II deposits (Appendix C4) further supports that the deposit is volcanic in origin. Most matrix material is composed of free crystals and finer-grained interstitial glass, consistent with the abrasion of volcanic material. Crystals are dominated by plagioclase which is often zoned or twinned. Other minerals, such as amphibole and olivine are present but in lower quantities. Lava clasts reveal a similar texture to lavas from Stage I, are dominated by plagioclase laths with amphibole and other inosilicate and nesosilicate minerals. Pumice clasts are also dominated by glass. See Fig 10c for photomicrographs and Appendix C4 for thin section descriptions.

5.3. Stage III: Lacustrine-dominated deposits (0 – 293.71 m_c)

In total the maximum number of potential TFDs is recorded as 603, all occurring within Stage III. These can be further categorised as 266 felsic, 57 intermediate and 280 mafic layers (cf. Fig.

3 and Table 1 for composition category definitions and see Table 4 for a statistical breakdown of volcanic data from the core). A further 46 layers have not been ascribed a compositional identifier due to their resemblance to event layers which are non-volcanic in origin (e.g., flood event layers, Schlolaut et al., 2014). These are recorded as fine clay-rich layers and are ascribed a composition notation of 'C' in Appendix C1 and described in Appendix C5. A minimum number of TFDs is also recorded, which only includes tephras with the highest confidence and primary values (i.e., if a deposit is likely to represent a fall deposit) ascribed (cf. Table 4). The minimum number of TFDs are therefore recorded as 450, with 205 layers being felsic, 40 intermediate and 205 mafic. In total there is 71.06 m (on-splice maximum thickness of volcanic material within Stage III of the core accounting for 24.19% of this section of core being volcanic in origin.

Description

The largest portion of core is Stage III (the lacustrine-dominated deposits) at c.300 m in thickness. As shown in Valero-Garcés et al. (2021), sediment types are variable, fluctuating between organic-rich, diatomaceous sediments, carbonate muds, coquina, silts, sands and gravels. The sediments are intercalated with volcaniclastic material of various types, thicknesses, and compositions. For the purpose of this paper, the term *volcaniclastics* refers to variable deposits containing clasts and matrix, displaying similar characteristics to the deposits in Stage II and well sorted clast-supported deposits interpreted to be TFDs are referred to as tephras. Fig. 11 summarises the volcanic stratigraphy of stage III of the Chalco core plotting all interpreted volcanic horizons alongside sediment types. Tephras are split into felsic, intermediate, and mafic TFDs with their basal depths plotted against composite depth

Table 4. Key statistics and volcanic data from the core for assessing the volume of volcanic material and comparison between different deposit types.

Count (TFDs)		
Composition	**Minimum n (highest confidence and likely primary deposits)**	**Maximum n (all possible layers)**
F	205	266
I	40	57
M	205	280
Total	450	603
Maximum TFDs (all possible layers)		
1 (likely primary)		
Reworking		
Composition	**n**	
F	240	
I	50	
M	254	
Total	544	
2 (possibly reworked)		
Composition	**n**	
F	26	
I	7	
M	26	
Total	59	
Confidence Volcanic		
1 (confident)		
Composition	**n**	
F	230	
I	45	
M	228	
Total	503	
2 (not confident)		
Composition	**n**	
F	36	
I	12	
M	52	
Total	100	
Ghost layers		
Composition	**n**	
F	40	
I	17	
M	37	
Total	94	

Minimum TFDs (highest confidence and likely primary deposits				
TFD Thickness (combined with substitute off-splice thicknesses)				
Composition	**≤5 cm**	**5-9.99 cm**	**10-14.99 cm**	**≥15 cm**
F	162	23	7	13
I	30	7	3	0
M	161	21	11	12
Total	353	51	21	25
TFD Grain Size				
Composition	**≤2 φ**	**1 φ and 0 φ**	**-1 φ and -2 φ**	**≥-3 φ**
F	118	54	31	2
I	19	21	0	0
M	138	67	0	0
Total	275	142	31	2
Structures				
Composition	**No structures (massive)**	**Structured**	**Unsure**	
F	194	11	0	
I	36	4	0	
M	184	17	4	
Total				
Overall core statistics				
Stage III: Lacustrine-dominated section				
Deposit type	**Total splice thickness**			
TFD	21 66 m			
Volcaniclastics	49.40 m			
Total	71 06 m			
Percentage of Lacustrine-dominated section that is volcanic in origin	24.19%			
Total thickness of volcanics including ghosts and off-splice thicknesses	73.73 m			
Whole core				
Deposit type	**Percentage of core**			
TFD	3.91%			
Volcaniclastics	39.98%			
Lava	15 51%			
Scoria	0.41%			
Total (percentage of whole core splice that is volcanic in origin)	59 81%	19.83		

(m_c) and volcaniclastics are presented as lithologies with their thicknesses displayed. Statistics regarding volcanic layers in Stage III can also be seen in Table 4. This section of core likely represents by far the longest time period and a larger number of discrete volcanic events than earlier sections of core, so is thus the focus of the rest of this chapter.

Interpretations

As concluded by Valero-Garcés et al. (2021) the core presents no evidence for a significant break in time and/or exhumation of the lakebed above the water level, thus representing a continuous lake depositional environment. We therefore conclude that the volcanic record in the lacustrine section at Lake Chalco is as complete as possible (minus drilling gaps and artefacts/lower levels of preservation) for airborne volcanic deposits in the region. The lacustrine section conformably overlies the pre-lacustrine section, and we define the boundary between them as a sharp contact, where the change in environment appears to have been rapid, with a sudden onset of fine-grained sediment accumulation. Lake formation may itself have been influenced by hydrological changes following the inferred sector collapse (and subsequent reworking) that led to the pre-lacustrine sequence. The thinner volcaniclastic layers of pre-lacustrine character continue into the lacustrine sequence and may represent periodic reworking of the terrestrial debris-fan deposits by flood events. There is no indication of a time gap between the lacustrine and pre-lacustrine sections, but the time gap between the lavas and the pre-lacustrine section is unconstrained.

Lake Chalco will not contain a complete record of all explosive eruptions from nearby stratovolcanoes, given that only events above a certain magnitude and directed by certain

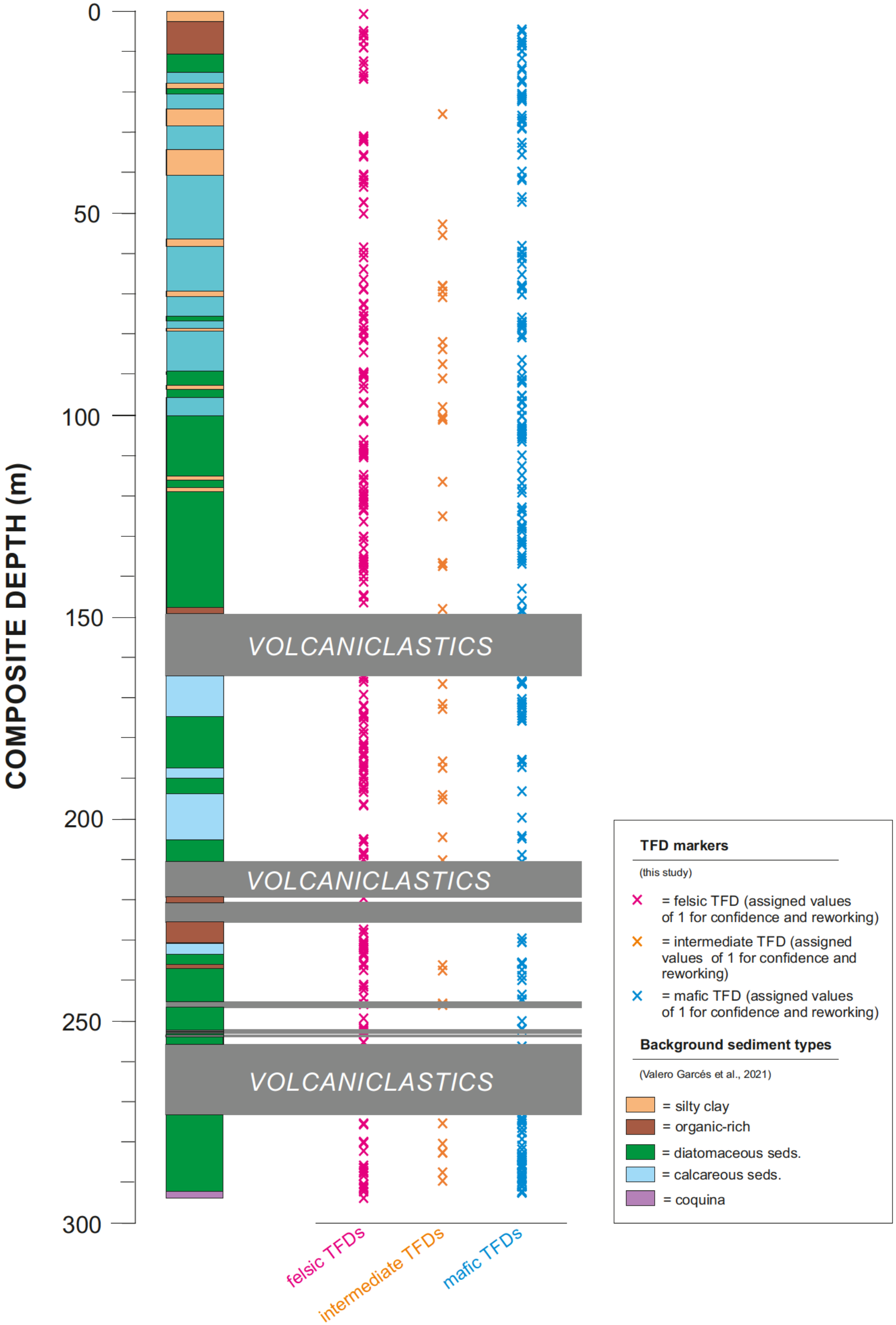

COMPOSITE DEPTH (m)
0
50
100
150
200
250
300
VOLCANICLASTICS
VOLCANICLASTICS
VOLCANICLASTICS
felsic TFDs
intermediate TFDs
mafic TFDs
TFD markers
(this study)
= felsic TFD (assigned values of 1 for confidence and reworking)
= intermediate TFD (assigned values of 1 for confidence and reworking)
= mafic TFD (assigned values of 1 for confidence and reworking)
Background sediment types
(Valero Garcés et al., 2021)
= silty clay
= organic-rich
= diatomaceous seds.
= calcareous seds.
= coquina

Fig. 11. Stratigraphic column displaying background sediment types (from Valero-Garcés et al., 2021). Depths are plotted as meters composite (mc) with volcaniclastic lithologies also displayed. Tephras are presented as markers alongside the stratigraphic column and are divided into felsic, intermediate and mafic layers. Thicknesses of tephras are not shown, and the stratigraphic placement of the layers is plotted from their basal depths.

---

wind directions will have produced macroscopic tephra deposits (and that these in turn can be modified by lacustrine processes) and that dispersal is dependent on wind direction. However, we can be confident that the record provides a relatively complete archive of all explosive volcanic eruptions that have deposited cm-scale (and potentially finer; see discussion below) tephra on the Chalco region, thus reflecting an important archive for understanding the impacts and hazards of volcanic eruptions in Mexico City.

5.3.1. Quality of the core recovery in Stage III

Drilling gaps are inevitable during core recovery as multiple drives (sections of core) are recovered, and particularly affected Stage III due to the highly variable nature of sediment types and properties being drilled. These gaps are appended and accounted for in the splice table/splice thus unaffecting splice positioning of sedimentological and volcanological layers. However, quality of cores is also determined by factors such as the core recovery and the type of drilling/sedimentological properties and behaviour in relation to this drilling. From core section description alone, the lithologies of layers cannot always be determined, hence the stratigraphic methodology and data collection undertaken, outlined in section 3 and Table 1. As smear slides need to be prepared during sub-sampling, for large drilling projects, such as MexiDrill, it is not feasible to obtain smear slides of every layer. Resultantly, the quality of the volcanic stratigraphy for Stage III has been assessed in four ways: (1) by assessing the confidence whether a layer is likely volcanic or possibly volcanic (see Table 1); (2) what the

Table 5. Whole-rock (ICP) major and trace element compositions of lavas emplaced at Lake Chalco. To account for a variety in hydration and for comparative purposes, major elements concentrations are normalised to 100% anhydrous.

ICP (Whole-rock analyses)												
	Major elements (wt.%)											
Sample ID	**SiO_2**	**TiO_2**	**Al_2O_3**	**$Fe_2O_{3\,(t)}$**	**MnO**	**MgO**	**CaO**	**Na_2O**	**K_2O**	**P_2O_5**	**LOI**	**Total [Analytical Total]**
ARL 1	57.19	16.27	7.32	0.12	4.57	7.74	3.99	1.20	1.59	b.d[a]	0.34	100 [110.7]
ARL 2	55.41	17.00	8.08	0.12	4.45	7.70	4.15	1.11	1.94	0.04	0.41	100 [99.42]
ARL 3	57.33	17.15	7.35	0.14	4.06	7.75	3.65	1.16	1.32	0.09	0.27	100 [100.5]

	Trace elements (ppm)											
Sample ID	**Sc**	**Be**	**V**	**Ba**	**Sr**	**Y**	**Zr**	**Cr**	**Co**	**Ni**	**Cu**	**Zn**
ARL 1	22	2	170	432	475	11	290	170	19	60	50	70
ARL 2	23	2	173	365	492	11	282	170	21	70	20	70
ARL 3	23	1	174	423	400	9	208	100	18	b.d[a]	b.d[a]	70
	Ga	**Ge**	**As**	**Rb**	**Nb**	**Mo**	**Ag**	**In**	**Sn**	**Sb**	**Cs**	**La**
ARL 1	19	1	b.d[a]	16	20	b.d[a]	b.d[a]	b.d[a]	2	b.d[a]	b.d[a]	6.2
ARL 2	20	1	b.d[a]	12	20	b.d[a]	b.d[a]	b.d[a]	1	b.d[a]	b.d[a]	5.2
ARL 3	21	1	b.d[a]	28	8	b.d[a]	b.d[a]	b.d[a]	2	b.d[a]	0.8	6.2
	Ce	**Pr**	**Nd**	**Sm**	**Eu**	**Gd**	**Tb**	**Dy**	**Ho**	**Er**	**Tm**	**Yb**
ARL 1	12.3	1.48	6.7	1.7	1.5	1.8	0.3	2.3	0.5	1.4	0.23	1.6
ARL 2	11.8	1.61	7.7	2	1.59	2.1	0.3	2.2	0.5	1.4	0.2	1.5
ARL 3	13.2	1.71	8	2	1.16	2	0.3	2.2	0.4	1.3	0.2	1.3
	Lu	**Hf**	**Ta**	**W**	**Tl**	**Pb**	**Bi**	**Th**	**U**			
ARL 1	0.26	5.3	1.1	b.d[a]	b.d[a]	6	b.d[a]	1.8	0.7			
ARL 2	0.25	5.3	1.1	b.d[a]	b.d[a]	b.d[a]	b.d[a]	1.2	0.5			
ARL 3	0.22	5	0.5	b.d[a]	b.d[a]	5	b.d[a]	1.6	0.6			

[a] b.d. = below detection. All Fe values ($Fe_2O_{3\,(t)}$) are reported as total (t). Secondary standard and original datasets are provided in Appendix C3.

preservation of the layers are (see Table 1 and Fig. 5); (3) if a layer is likely primary or possibly reworked (see Table 1); and (4) how many projected ghost layers there are (i.e., possible volcanic layers not represented in the splice). Fig. 12 displays the quality of the Chalco core from these perspectives. It can be noted from Fig.12 and Table 4 that the majority of Stage III of the core from a volcanic perspective (in part mitigated by the stratigraphic methods applied in section 3) is largely well preserved. Fig. 12a demonstrates the majority (450 out of 603) of volcanic layers are recorded as the highest degree of confidence when determining if they are volcanic in origin. 153 layers have ambiguity from core description alone. Most of these lower confidence layers are found towards the base of the of Stage III deposits (>150 mc) however clusters occur evenly spaced throughout the rest of the Stage. A slightly higher proportion of mafic vs. felsic layers have ambiguity (52 vs. 36, respectively) which is mostly due to the occurrence of dark, black tephra occurring within dark sediments. In these cases, MS spikes has indicated there may be a tephra, but visually from photographs this has been difficult to verify, thus imposing a lower ascribed confidence values to these layers. Generally, confidence values are high throughout the core with confidence increasing with stratigraphic height.

Fig. 12b displays the stratigraphic placement of tephras with different levels of preservation levels ascribed. All possible layers (603 tephras) were assessed for comparison. It can be noted that preservation of the tephras generally displays an opposite trend to confidence values ascribed, with preservation quality, (particularly from preservation values of 3, the lowest), being in higher concentrations with stratigraphic height. This mimics a trend seen in the quality of core recovery and sedimentological preservation noted through logging all c.1500 m of core (across all holes). Moderately preserved tephras are generally spread evenly

A

B

C

D

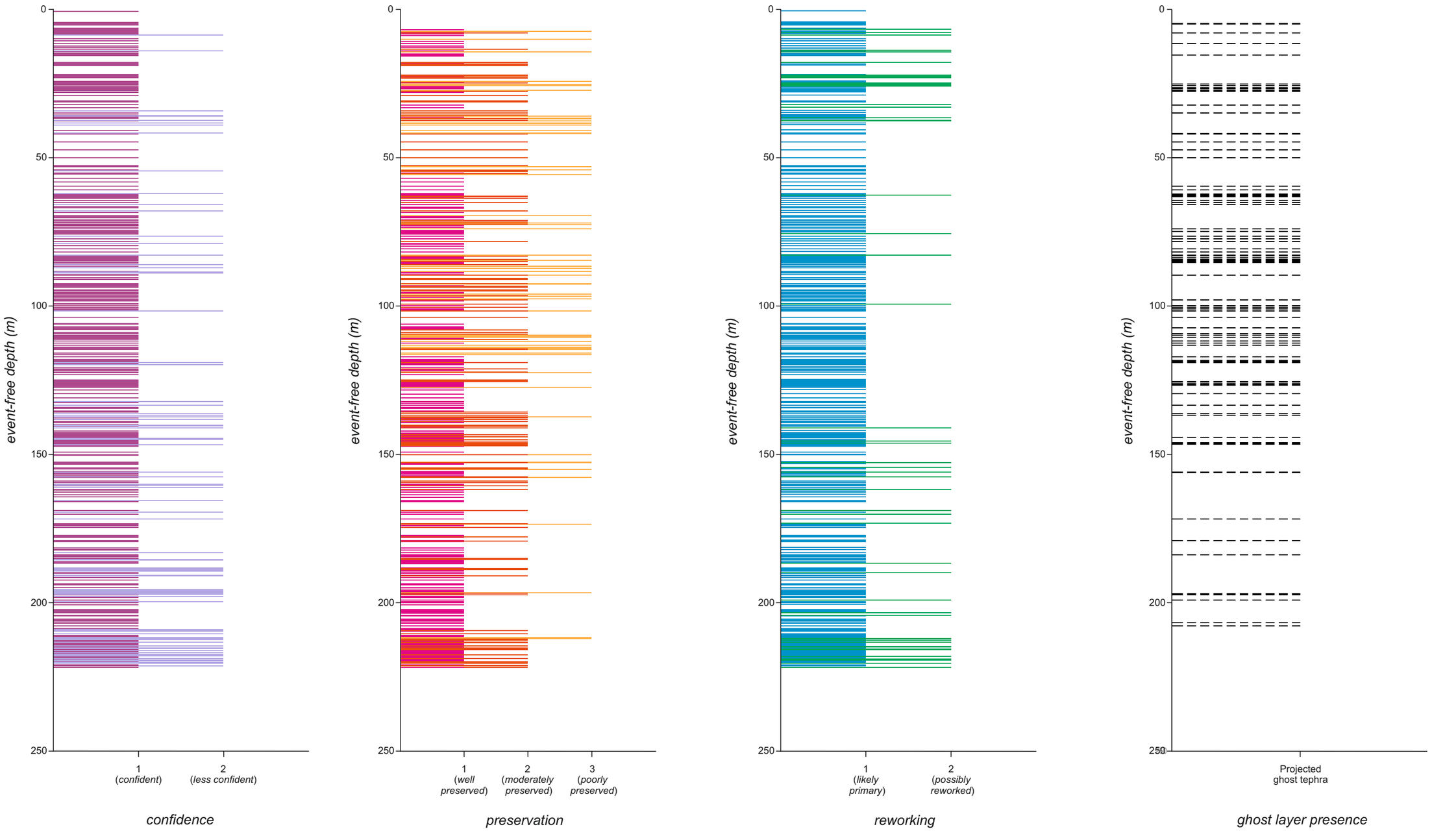

0
50
100
150
200
250
event-free depth (m)
1
(confident)
2
(less confident)
confidence
1
(well preserved)
2
(moderately preserved)
3
(poorly preserved)
preservation
1
(likely primary)
2
(possibly reworked)
reworking
Projected ghost tephra
ghost layer presence

Fig. 12. (a) Bar chart plotted from the basal event-free depth of potential tephras that display different ascribed levels. (b) Bar chart plotted from the basal event-free depth of potential tephras that display the preservation of each layer with respect to depth. (c) Bar chart plotted from the basal event-free depth of potential tephras that display the stratigraphic placement of likely primary and possibly reworked layers. (d) Bar chart plotted to show the projected stratigraphic placements of all ghost tephras recorded in this study.

---

throughout the core with higher density clusters around c.140 mc and c.220 mc.

Fig. 12c graphically displays the same tephra layers in relation to ascribed reworking values (i.e., likely primary values of 1 and possibly reworked values of 2). The majority of possible tephras, 544 layers, are ascribed a highly likely value, with only 59 layers ascribed a possibly reworked status. Two main clusters occur toward the base and the top of Stage III deposits, c. 220 mc and c.25 mc, respectively. It is likely that these clusters are artificially pronounced due to a higher frequency of tephras in these two parts of core (see section 5.3.4).

Ghost horizons are not so much an indication of the preservation quality of the core, (although in parts they challenge the lateral continuity assumption about some layers), but indicate the quality of the splice for accounting for all possible volcanic layers present. Fig. 12d shows the general stratigraphic placement of all ghost layers projected onto the splice. In total 94 ghost tephras have been recognised for the Chalco core. These again indicate some clustering where several ghost tephras occur in succession, however generally the number of ghost tephras increases with stratigraphic height with the highest density occurring between c.50 mc and c.150 mc. This loosely correlates with the poorest preservation of core, where sections in the upper portion of Stage III deposits have more drilling artefacts and sedimentological disturbances. Due to an increased difficulty in stratigraphic correlation in this part of core, it is not surprising that the frequency of ghost layers is higher.

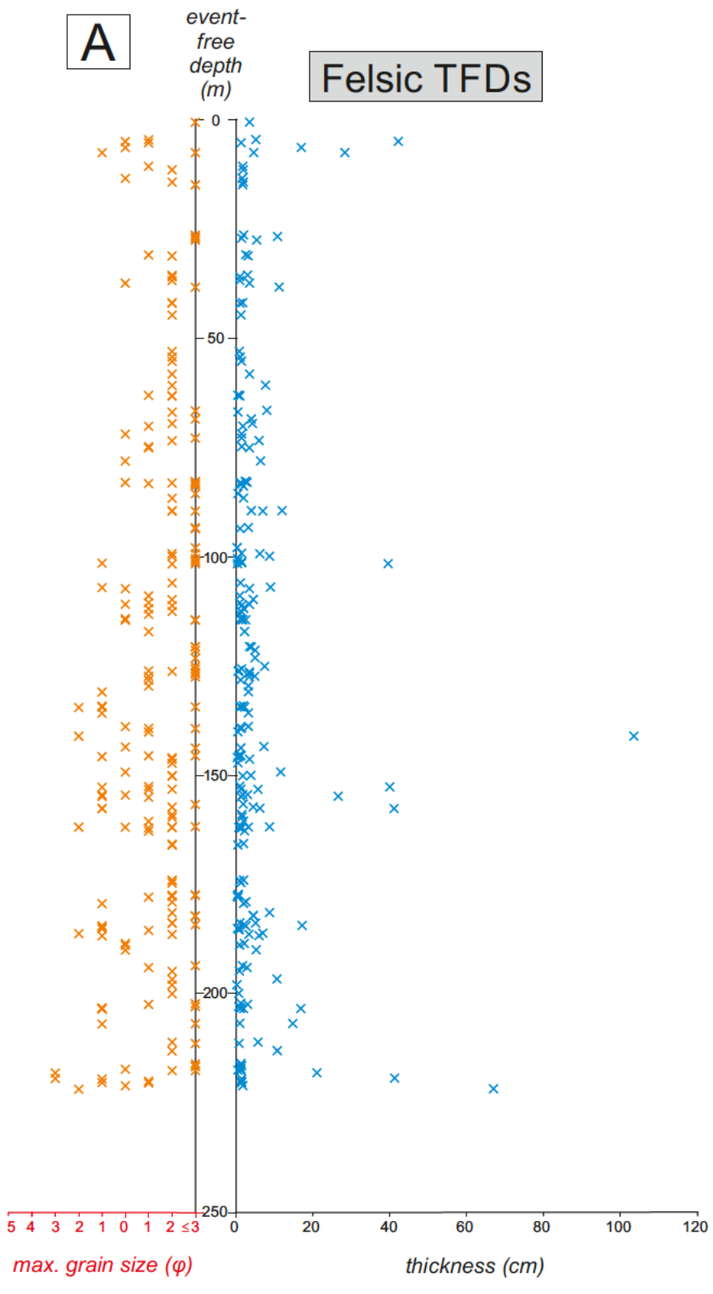
5.3.2 Grain size vs. depth

Grain size provides key information in tephra fall deposits, and reflects the combined effects of column height, wind field and distance from source. Maximum grain size measurements (in phi, φ) derived from core photographs are accurate for clast sizes over 0 φ, since they could be measured directly (note, this is a *maximum* grain-size value, not a modal value), and were estimated based on visual characteristics of finer grained layers. For these finer layers, lazer-diffraction particle size analysis was conducted on a random sub-set of samples taken throughout the core, to test the accuracy of these estimates. This showed the maximum measured grain size of these layers were consistent with those ascribed by eye, down to a size of 3 φ. Below this, we cannot estimate grain size from visual descriptions alone (see Fig. 3 and Appendix C2).

To further assess grain size patterns in Stage III of the core, we only draw on tephras with the highest ascribed volcanic confidence level and those judged to be primary deposits (i.e., the minimum number of tephras). Fig. 13 displays the grain size of tephras vs. event-free depth for felsic (Fig. 13a), intermediate (Fig. 13b), and mafic layers (Fig. 13c). Each composition displays a modal grain size of 2 φ (a fine to medium ash); however, maximum grain size for each composition is variable, at -3 φ, 0 φ and 0 φ, respectively. The scatter within grain size against stratigraphic position is much greater in the felsic and intermediate tephras with mafic tephras generally displaying very consistent grain size. This likely reflects the similar eruptive styles of the events producing the mafic deposits, the majority of which we interpret to be

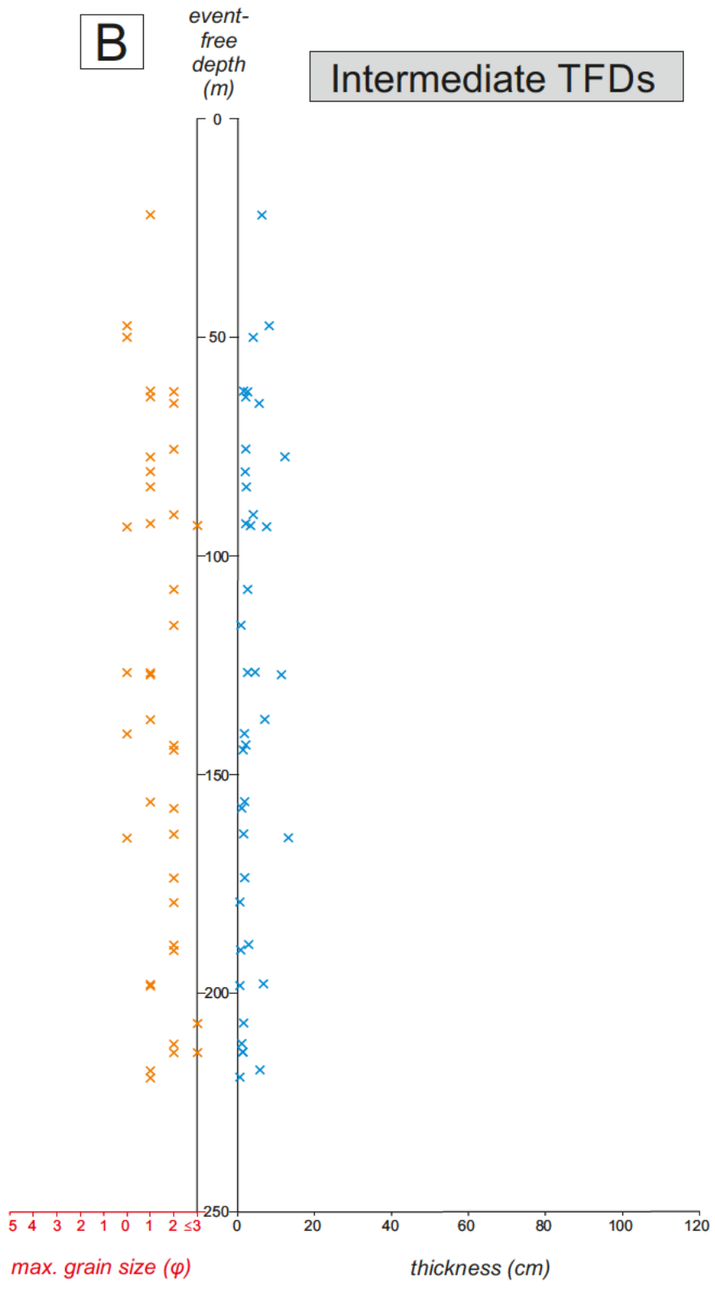
A

Felsic TFDs



B

Intermediate TFDs



C

Mafic TFDs

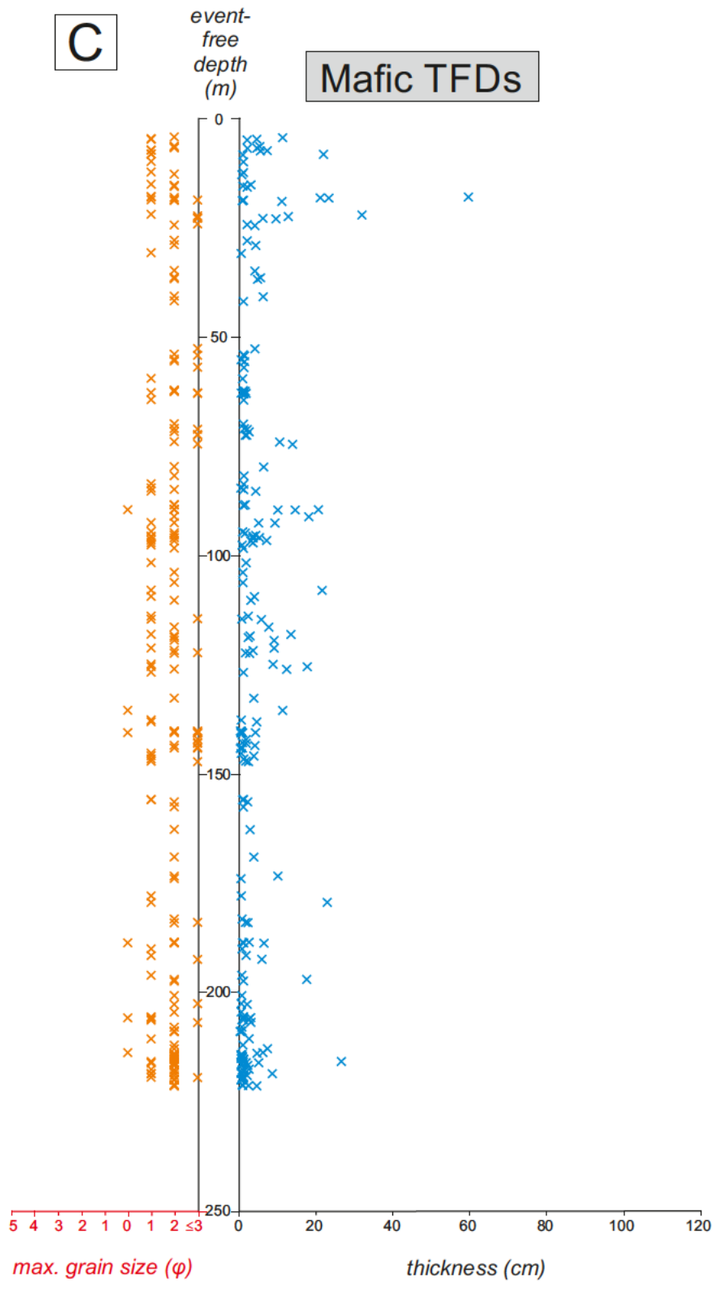


Fig. 13. (a-c) Scatter plot vs. event free depth showing the stratigraphic placement of all felsic, intermediate, and mafic tephras, respectively that have the highest level of confidence that the layer is volcanic in origin and that it is a primary deposit. Layers are plotted with regards to thickness and grain size. Basal event-free depth has been used for the stratigraphic positioning.

---

relatively local (i.e. relatively small, monogenetic Strombolian eruptions from the SCVF), whereas the more evolved units are likely sourced from a much broader area, spanning a wider range of eruption styles and magnitudes. There is some clustering in the mafic grain size data, particularly evident in the finest grain sizes (for example, several very fine mafic ash deposits appearing in quick succession). This suggests that eruption sites for the mafic tephras are not randomly scattered, but may be concentrated in a small spatial areas at different points in time, due to magma supply being focused by tectonic controls (e.g., Cembrano and Lara, 2009), and migrated across the SCVF over longer timescales.

Felsic TFDs extend to the coarsest grain sizes in Stage III, with some visual evidence of clustering and a general pattern, particularly after a relatively coarse set of tephra in the uppermost 20 m, of becoming coarser with depth. Clustering would tentatively suggest that polygenetic sources may erupt cyclically and produce several similar magnitude events closely spaced in time. This hypothesis needs testing by examining whether the chemistry of clustered groups of tephra is consistent with a single source volcano, but the observation has potentially important implications for assessing the repeat time of large magnitude explosive eruptions. The observation of a greater frequency of coarse felsic tephras with depth (for example, the majority of 0 φ deposits occur below 100 m_c; and all but one of the 25 coarser deposits occur in the same interval, with the very coarsest deposits right at the base of Stage III) is intriguing. These coarsest deposits likely have a relatively local source, either from the SNVR, Toluca, or other polygenetic volcanoes around the Basin of Mexico. The broad trend is

not consistent with a long term shift in prevailing wind direction, which might favour Chalco lying on the axial plane of deposits, given that these sources are distributed around the basin and that we wouldn't expect wind patterns to vary in this manner on such long timescales (but to align more closely with climatic patterns that are evident in the nature of background lacustrine sediments in the core; cf. Valero-Garcés et al., 2021). The pattern thus implies either that very large explosive eruptions were more prevalent in central Mexico in the past, and gradually decreased in time; or that the dominantly active polygenetic sources in the vicinity have gradually moved further away from the Chalco core site. The former interpretation would imply a long-term relationship between magma production and storage and arc-scale tectonics, perhaps linked to subduction parameters, but this is hard to test, and we suggest that the latter interpretation is more likely. Activity along the SCVF, for example, has gradually shifted southward in time (although not in an entirely uniform manner; cf. Sunyé-Puchol et al., 2022), with Tlaloc-Telapon being the oldest centre, and Popocatépetl being the youngest. The northern end of the chain is slightly closer to Lake Chalco (Fig. 1) and also more aligned with the prevailing E-W wind axes (Fig. 1a), and the long-term pattern may therefore reflect the gradual migration of activity southward along the SNVR across the lifetime of the core. Again, this hypothesis requires further testing, and would imply that the dominant source of coarse grained felsic deposits in the core is from the SNVR. This is plausible, since the SNVR volcanoes are the closest large polygenetic edifices, with a recognised history of explosive volcanism (Sunyé-Puchol et al., 2022). Many of the finer-grained felsic deposits may also be from the SNVR, but it is likely that they also reflect a range of additional and more distal volcanic sources.

5.3.3. Thicknesses of TFDs

Fig. 13 also displays the thickness of TFDs against event-free depth and grain size, using measured thicknesses for ghost tephras and the best-preserved thickness measurement for on-splice tephras (i.e. some of these thickness values are taken from core sections off the splice; see Table 1 and Appendix C1). A weak positive correlation exists for thickness against grain size, for all tephra compositions, which is to be expected given that for any single source, larger magnitude eruptions are likely to produce both thicker and coarser deposits (notwithstanding variations in wind field).

When thickness vs. event-free depth (i.e. as a proxy for time) is considered alone, most tephras of all compositions are <5 cm. Thicker deposits occur across all compositions, extending to >20 cm for both felsic and mafic TFDs. Mafic tephras proportionately have more deposits between 5 and 20 cm than felsic layers. This is consistent with our inference of the mafic deposits being derived from Strombolian eruptions of the SCVF. Although such eruption styles do not produce particularly widely dispersed fall deposits, because of their low column height, their repetitive nature and long duration can produce thick and relatively fine-grained deposits at distances up to tens of km (e.g., Pioli et al., 2008). Very thick (> 50 cm) tephras from felsic eruptions occur twice at Chalco, both within the lower half of Stage III, and once for a mafic deposit, in the upper part of Stage III. The broad pattern of coarser felsic deposits being more prevalent deeper in the core is replicated in the thickness data, but less strongly. For mafic tephras, thick deposits are relatively evenly distributed throughout the core. Without source information, we assume that in a broad sense finer layers are from more distal sources and thicker layers from more proximal. The observations are therefore consistent with a slightly

higher frequency of proximal large-magnitude felsic eruptions earlier in Stage III, as discussed above from the grain size data. For the mafic tephras, the lack of any strong temporal trend suggests that there is not a consistent direction to any migration of activity across the SCVF through time, although in certain periods (dominated by finer layers) this activity may have been relatively further from Chalco, and at other times, relatively closer.

5.3.4. Frequency and tempo of explosive volcanism

One of the most important insights from the Chalco tephrostratigraphy is the overall frequency of TFDs. Fig. 14 shows event-free depth against the frequency of tephras, binned at 10 m intervals and plotted as a continuous moving average at 1-m increments. This has been plotted for all tephras (Fig. 14a), as well as felsic (Fig. 14b), intermediate (Fig. 14c) and mafic (Fig. 14d) layers separately. Each dataset is further sub-divided into: (1) all possible tephras, (i.e., the maximum number of tephras); (2) tephras with the highest degree of confidence of a volcanic origin (i.e., anything with ascribed confidence value of 1); and (3) events with only the highest ascribed volcanic confidence level and inferred to be primary fall deposits (i.e., the minimum number of tephras (c.f. Table 1 for data value explanations)). This imitates a typical volcanic scenario model of a 'best', 'likely' and 'worst-case' scenarios for the frequency of explosive eruptions that have deposited material within Mexico City in the past.

Fig. 14a generally shows there to be a higher frequency of all tephras towards the lower part of Stage III sediments (>200 m in event-free depth, efd). Other peaks are evident (e.g., between 140 and 150 m (efd)) and there is a gradual overall decrease in frequency with stratigraphic height within the core. These general patterns remain the same across the maximum to minimum tephra datasets.

A

All TFDs

LEGEND

= all possible layers

= all possible layers with confidence values of 1

= all possible layers with a confidence and reworking values of 1

frequency per 10 m (*n*)

0 10 20 30 40 50 60 70 80 90 100

0 50 100 150 200 250

event-free depth (m)

B

Felsic TFDs

n

0 10 20 30 40 50 60

0 50 100 150 200 250

event-free depth (m)

C

Intermediate TFDs

n

0 10 20 30 40 50 60

0 50 100 150 200 250

event-free depth (m)

D

Mafic TFDs

n

0 10 20 30 40 50 60

0 50 100 150 200 250

event-free depth (m)

Fig. 14. (a-d) Cumulative frequency diagram of all, felsic, intermediate and mafic tephras, respectively against event-free depth, binned at 10 m intervals and plotted as a continuous moving average a 1-m increments. Data is provided for: (1) all possible tephras, (i.e., the maximum number of tephras); (2) tephras with the highest degree of confidence that it has a volcanic origin (i.e., anything with ascribed confidence value of 1) and (3) events with only the highest ascribed volcanic confidence level and reworking level (i.e., additionally with all tephras recorded as likely primary deposits), the minimum number of tephras.

When splitting this data further into felsic, intermediate and mafic tephras, again the pattern for each is consistent across the maximum to minimum datasets, suggesting there is little influence of general trends when including more poorly preserved or ambiguous tephra deposits. Despite this, we consider the minimum-tephra plots (with a confidence and reworking score of 1) to be the most reliable, and use these in subsequent interpretations.

For both felsic and mafic tephras, a peak in event frequency early in Stage III is evident, but in other parts of the core the trends are distinct from each other (trends are harder to deduce for intermediate tephras, given the small number of events). For felsic deposits, there is a general decrease in frequency with stratigraphic height (i.e., time; Fig. 14b). This mimics the broad grain size and thickness trends, implying that felsic deposits occur more frequently lower in the core, as well as extending to coarser and thicker values. Such a pattern is consistent with our interpretation of the dominant polygenetic source volcanoes being in the SNVR, and being nearer to Lake Chalco at that time. This is not a simple pattern, and there are additional peaks at c. 10 m and 40 m (efd), with similar values from 80-130 m (efd), and higher event-frequency peaks at c.160 m and 180 m (efd). Prominent troughs (i.e., gaps in activity) occur at c. 20 m, 50 m and 170m (efd).

The frequency pattern of mafic tephras (Fig. 14d) differs from the felsic trends, and displays a more prominent set of peaks and troughs. A large peak occurs towards the base of Stage III,

with strong peaks also between c.180 m (efd) and c.190 m (efd); c.140 (efd) and c.150 m (efd); c.110 m (efd) and c.120 m (efd); c.80 m (efd) and c.90 m (efd); c.60 m (efd) and c.70 m (efd); and c15m (efd) and c.20 m (efd). This pattern suggests that mafic output in the region (and by inference, in the SCVF) is strongly episodic over the period of time represented by the core. This is consistent with observations from monogenetic volcanic fields in general (e.g., Nemeth, 2010; Jaimes-Viera et al., 2018) which typically form clusters of cones due to spatial and temporal links between magma supply to different parts of the field. The peaks do not map closely onto the occurrence of the thickest and coarsest mafic tephras (Fig. 13), and we therefore infer that the frequency pattern is not simply a reflection of changes in the distance of activity from Chalco, but that it indicates absolute variation in output from the monogenetic field, with this output being episodic rather than steady (cf. Jaimes-Viera et al., 2018). The decoupling of the felsic and mafic tephra frequency patterns suggests that there is no common tectonic control on magmatic output from local monogenetic and polygenetic volcanic centres, and that output patterns are more likely influenced by factors (potentially ranging from magma productivity through to crustal storage conditions) local to individual volcanic systems. The decoupling also implies no common climatic influence on tephra dispersal and the likelihood of tephra deposition on Lake Chalco. If the dominant control on tephra accumulation was wind-related, then we would expect more similar patterns across the felsic and mafic deposits (although it could be argued that the different dominant column heights would complicate any such trend); and in addition we'd expect a correlation between eruption frequencies and dominant lacustrine sediment types (Fig. 7), since the latter reflect climatic conditions. There is no clear relationship between the sediment type and the peaks in volcanic activity.

6. OTHER EVENT LAYERS IN LAKE CHALCO

As mentioned in section 5, a further 46 event layers (not characterised as TFDs) have been described in Appendix C1. These layers are generally very fine grained, grey to brown in appearance and occur between c.254 mc and c.229 mc in organic-rich and diatomaceous sediments (Valero-Garcés et al., 2021). Their occurrence within only c.25 m of core suggests these deposits are not volcanic in origin, unless there was a very different style of volcanism responsible during this interval. The MS in these core sections is often at background levels, however as most of these layers are very thin (millimetre scale), it is possible they avoided detection at the 0.5 cm measured MS intervals. This section of core is generally well preserved, but not exclusively so, and the same interval still contains some poorly preserved tephras. We thus infer that the process(es) responsible for these layers were constrained to this time interval and reflect specific environmental conditions. Comparison with Schlolaut et al., (2014) and the flood event layers described therein lead us to conclude that these events are non-volcanic, floods and we have therefore excluded them from our analysis. Examples and further descriptions of these layers are provided in Appendix C5.

7. DISCUSSION

7.1. Implications of this study at Lake Chalco

Knowledge about past volcanic activity (particularly from explosive eruptions) in the Mexico City region is sparse due to a lack of exposure and difficulty in correlating deposits between outcrops. Various recent studies (e.g., Lorenzo-Merino et al., 2018; Arce et al., 2020; Sunyé-Puchol et al., 2022) have significantly increased our knowledge of eruptions, but are principally limited to very large explosive eruptions, to individual volcanoes, and to later

Pleistocene or Holocene periods. The succession at Lake Chalco provides a unique opportunity to probe the explosive record of volcanism in the Mexico City region over a long-timescale, assumed to be a minimum of c.400 ka at the base of Stage III, based on a preliminary age-depth model (Martínez-Abarca et al., 2021), and not on the basis of examining an individual volcano, but in terms of considering an entire region and its exposure to explosive volcanic hazards from multiple sources.

Given that it spans c.400 ka, the eruptive record at Lake Chalco likely extends across the lifetime of proximal polygenetic volcanoes, which in arc settings are typically active on 10^5 years (e.g., Singer et al., 1997; Bacon et al., 2006). Indeed, as noted above, the frequency and grain-size patterns in the felsic tephra records are consistent with gradual migration of activity along the SNVR, potentially marking the successive activity of Tlaloc-Telapon, Iztacchihuatl and, finally, Popocatépetl. In total, at least 450 explosive deposits (with a visible thickness) across the studied time period have deposited material over Lake Chalco, and within the limits of Mexico City and surrounding municipalities, which is important for understanding present-day risk and hazards to one of the world's largest populations.

Long-term eruptive histories can only be obtained from a continuous sedimentary sequence of the type used in this study. There are very few such examples, globally, and the methodology developed here provides a basis for similar approaches that may be made elsewhere to assess the frequency of explosive eruptions, vulnerability to volcanic hazards, style and potential magnitude of events and the diversity of volcanic processes that have impacted a given region in the past.

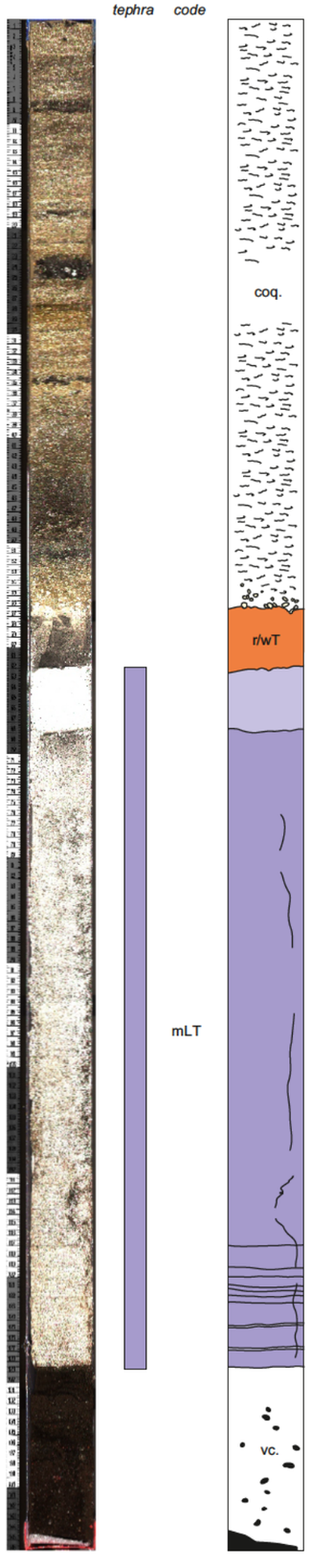
The volume of data obtained from the physical characteristics of a deposit and the stratigraphic placement and preservation within the core can be used to complete a rapid assessment about the volcanology of the region. Parameters such as thickness, grain size and frequency of layers, in conjunction with assessments of the overall quality of the volcanic layers, are the most beneficial datasets that can be acquired and assessed. The lake environment in which the cores have been obtained should also be carefully considered, as outlined in McNamara et al., (2019), avoiding lacustrine environments that are influenced by fluvial input (e.g., from sediment fans at river mouths and/or river inflows) which will transport a higher number of reworked deposits and likely influence the thickness of primary TFDs.

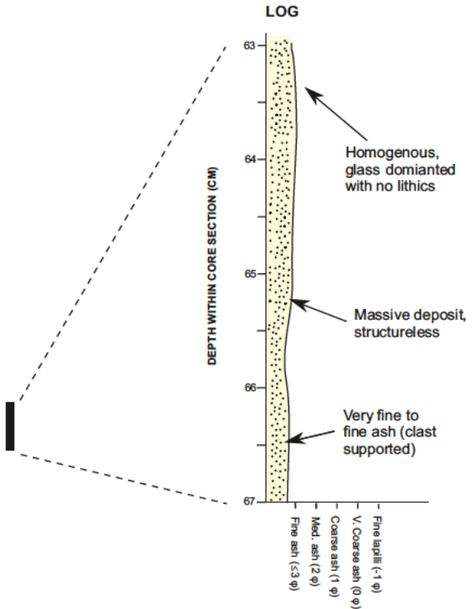
Additionally, McNamara et al., (2019) suggest that lakes with shallow water depths are ideal for preserving deposits that contain information on the temporal evolution of an eruption, due to pyroclasts settling as individual particles through the water column and not as density plumes. Lake Chalco has been an often-shallow lake with stable sedimentation (Valero-Garcés et al., 2021), and the succession is ideal for preserving volcanic layers that we deem to be accurate in terms of grain size, thickness and structures. The thickest tephras in the core support this, often displaying complex internal structures, indicative of the mass flux and eruptive energy of the eruption (see section 7.2). Thinner tephras, which are often fine grained (<1 φ) are generally homogenous and massive at the macroscopic scale. We interpret this to be a feature of distal TFDs, which typically do not record eruptive complexities and display glass-dominated componentry (e.g., Pyle et al., 2006; Engwell et al., 2014).

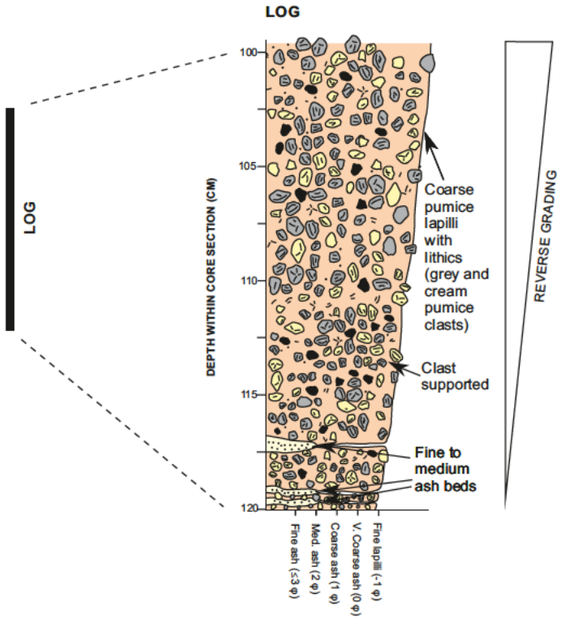
7.2. Physical volcanological importance of volcanic deposits in cores

Internal structures within TFDs, when deposited in a stable environment, can preserve an accurate record of the temporal evolution of an eruption, with structures and grain size changes reflecting the plume dynamics of the eruption. Thicker tephras (indicating a larger magnitude event and/or a more proximal eruption) often preserve such structures (Fig. 15). This type of information may be overlooked in favour of more analytical methodologies (e.g., major and trace element geochemistry to assess provenance). While these methodologies are crucial from a volcanological and/or paleoenvironmental or archaeological perspective, detailed examination of individual deposits can inform assessment of past eruption styles and be an important data source for hazard preparedness. Fig. 15a displays a felsic TFD at c.293 mc with an on-splice thickness of 67 cm. This tephra can be sub-divided into two sections: (1) lower 60.6 cm (composite thickness) which is largely a cream to grey massive lapilli tuff (mLT) with reverse grading and finer ash beds in the lowermost 20 cm; and (2), upper 6.4 cm (composite thickness) which is a very fine grained, white ash with no internal structure, composed of 100% juvenile material. Stratigraphic logs through these two sections highlight the differences in grain size, componentry and colour and are interpreted to represent a primary fall from the eruptive column (section 1) and a co-ignimbritic (phoenix) layer from the ambient lofting of subsequent settling of fine ash from associated PDCs (section 2). Engwell et al., (2014) recognised similar features in distal and (relatively) proximal marine cores containing the CI eruption from Campi Flegrei caldera, Italy. The overall structure suggests that the early stages of the eruption involved an unsteady mass flux, transitioning to a steady column with a gentle overall increase in eruptive energy (the reverse graded section),

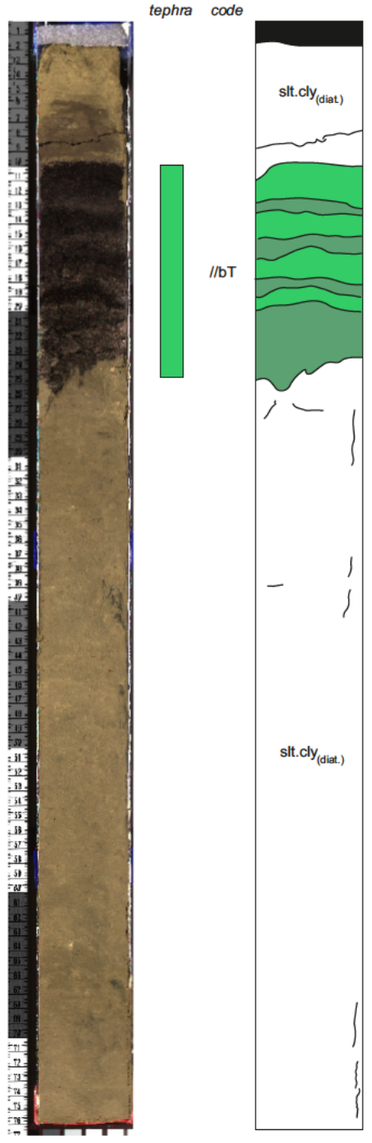
A

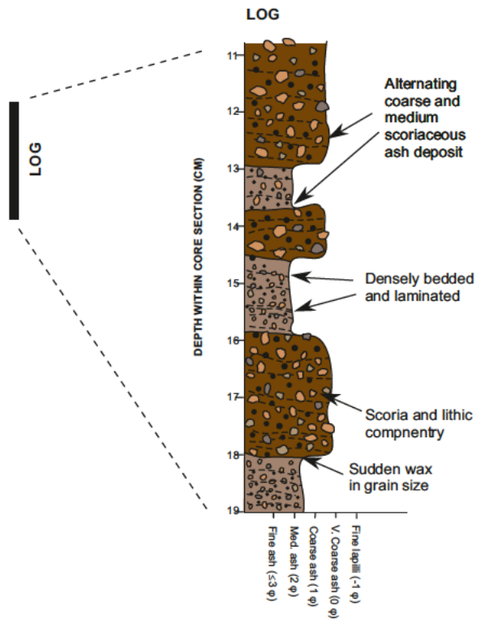






B





Volcanic facies codes

mLT = massive lapilli tuff

//bT = parallel bedded tuff

vc. = volcaniclastic

r/wT = reworked tephra

Sedimentary facies codes

slt.cly (diat.) = diatomaceous silty clay

coq. = coquina

Symbols

= laminations/ sediment orientation

= major cracks/ gaps in sediment

= grading triangle (widest is equal to coarsest)

Fig. 15. (a) Core section photograph alongside a redrawn section displaying the lithologies and stratigraphic placement of a thick and structured felsic tephra. Stratigraphic logs through two contrasting parts of the deposit are provided, interpreted to be the primary fallout from the plume and a secondary fallout from a co-ignimbritic plume. (b) Core section photograph alongside a redrawn section displaying the lithologies and stratigraphic placement of a thick and structured mafic tephra. A stratigraphic log through the tephra shows a deposit with alternating grain sizes, interpreted to be related to paroxysmal bursts typically occurring in an Strombolian eruption.

producing over 30 cm of lapilli, accompanied by large-volume PDCs (forming the phoenix layer). The uppermost ash may alternatively represent a very sharp weakening in eruptive energy and/or change in wind direction, but our interpretation of a co-ignimbrite fall deposit is consistent with the dynamics of very large explosive silicic eruptions from polygenetic volcanoes (e.g., Sparks et al., 1997). Overall, it can therefore be deduced that this eruption was an ignimbrite-forming event, likely of Plinian style, with generally increasing eruptive energy through time. This is one of the thickest and coarsest deposits in the record, and we infer that it represents one of the largest eruptions in the history of the polygenetic volcanoes surrounding the Basin of Mexico. Such events are rare, but would have regionally damaging impacts.

In contrast, Fig. 15b displays a thick (13.38 cm) mafic tephra at c.127.24 m_c. This tephra has internal stratification with sharp contacts between medium and coarse/very coarse ash. The deposit is parallel bedded and records abrupt waxing and waning of the mass flux of the eruptive column. As noted above, we assume that the majority of mafic TFDs are assumed to be sourced from the SCVF, and the internal stratification is consistent with the expected pulsatory Strombolian eruption system of small monogenetic eruptive centres (e.g., scoria cones). This pulsatory style is characterised by sudden fluctuations in eruptive energy driven

by varying gas contents, typically referred to as gas slugs which can be up to metre-sized bubbles (e.g., Lautze and Houghton, 2005).

The two examples provided in Fig. 15 display different eruptive styles from (assumed) different sources. Descriptions provided in Appendix C1 include further information for other tephras which can be used to deduce eruptive style. To avoid over-interpretation regarding fine ash and its origin, data is recorded as to whether the TFD has a fine ash component, allowing tephras to then be examined further for interpretations regarding physical volcanology (e.g., whether this likely represents a mass flux change, co-ignimbritic fall layer, an ash venting phase or remobilised ash etc.).

7.3. Limitations

7.3.1. Core site and environmental limitations

Although we consider the Chalco core to provide an exceptional record of eruptive activity for the Mexico City region, and the methodology applied in this paper to be effective at better understanding the volcanological history of the region, with reproducible approaches that can be applied to other sedimentary archives, there are limitations which must be considered. Firstly, the Chalco core is unique to the region with no nearby cores for comparison and correlation. Parallel holes have all been extracted within c.300 m of each other, to obtain a continuous record of the lake succession from 'one site'. A core from another part of the Chalco Basin or Basin of Mexico would allow the accuracy and precision of the data recorded in the succession to be assessed independently and a constraint on the dispersal axes of some tephras to be determined. This would also provide multiple thickness data points and the construction of approximate isopachs, to better constrain eruption magnitudes. Nevertheless, a deep

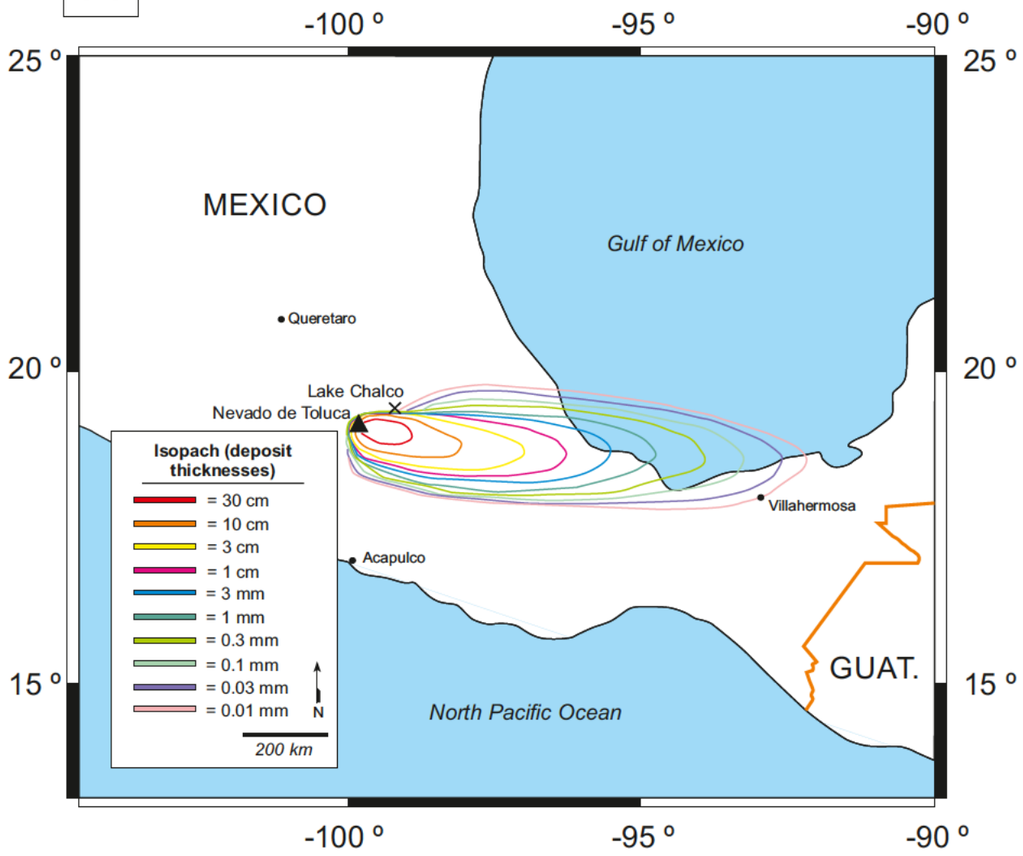
sediment core of this type provides a significant increase on current volcanological understanding within the region, with many of the deposits identified in the core being from eruptions that have not been observed elsewhere.

With a single core site, dispersal axes of tephras are unknown. Bonasia et al., (2014) suggest that the prevailing wind direction in the Mexico City region is towards the NE/E. However, alternate dispersal directions also occur, e.g., the c.14 ka Tutti Frutti Pumice eruption from Popocatépetl had a NW dispersal direction. It is likely that tephras within the core represent different dispersal directions, particularly as source volcanoes are presumably varied The dominant wind direction is also highly seasonal and different sources within the core support that wind direction has been varied over time. It is likely that the majority of tephras represented within the succession are from fallout on or near the dispersal axis of their parent eruption, although for larger magnitude events, deposits can be expected to be found several kilometres from the source in upwind scenarios (e.g., Mastin et al., 2014), a result of material reaching higher altitudes and dispersal being less controlled by tropospheric wind patterns (e.g., Carey et al., 1995). Additionally, duration of the eruption coupled with magnitude and column height may affect where material is deposited and which part of the eruption is represented by the deposit. Long-lived eruptions (spanning weeks to months) are much more likely to have experienced variable wind fields and thus have a larger footprint in terms of their tephra fallout (e.g., Rolandi et al., 2008; Watt et al., 2009; Johnston et al., 2012). It is important to note that many large explosive eruptions from nearby polygenetic volcanoes (e.g., Toluca, Popocatépetl), and likely even the major proportion of such events, will not have formed a deposit in the Chalco core due to tephra dispersal directions which are away from

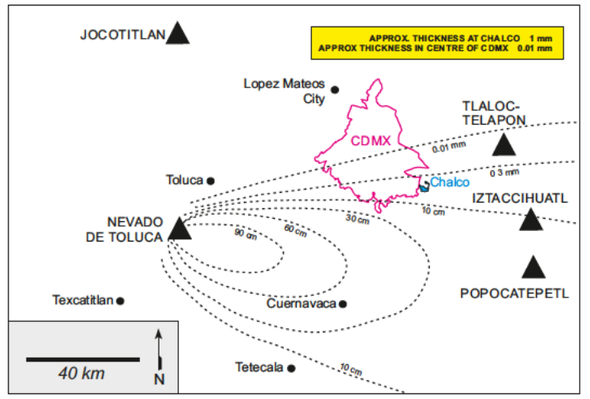
the core site. As an absolute record of activity at these volcanoes, an individual core record will therefore be highly incomplete (and even more incomplete when smaller magnitude explosive eruptions and effusive eruptions are accounted for). However, as a record of explosive volcanic eruptions that impacted the Mexico City region, the Chalco core record can be considered to be much closer to a complete record. From a hazards perspective, this is arguably a more valuable source of information, since it provides information not simply based on the frequency of activity at an individual volcano, but on the frequency of events that impacted a specific site, from all volcanic sources collectively. In contrast to the region's polygenetic volcanoes, the Chalco core is likely much more complete for explosive eruptions of the SCVF. These source vents are not only more local to the core site, but because such eruptions typically have a long duration (up to several months, or even years), ejecting products at low altitude into variable tropospheric wind fields, their tephra dispersal axes tend to be more concentric and can extend in all directions from the vent, forming cm-scale deposits at distances of tens of kilometres (e.g., Pioli et al., 2008).

For any individual eruption or deposit, it remains important to consider dispersal axis when interpreting a deposit. To demonstrate this, Fig. 16 presents a modelled eruption scenario using the USGS volcanic ash dispersion model, Ash3d (e.g., Mastin et al., 2013). The model (Fig. 16a,b) simulates deposit characteristics from an eruption from Nevado de Toluca volcano. Input parameters included 1.5 km^3 DRE of erupted magma, similar to estimates of the c. 25.7 cal. kyr BP Lower Toluca Pumice (LTP) Plinian eruption, with an estimated VEI of 5.4 (García-Palomo et al., 2002; Arce, et al., 2005). Model default values of a 3 hour eruption duration and 16 km plume height (above sea level) were used, with a randomly selected wind profile (from

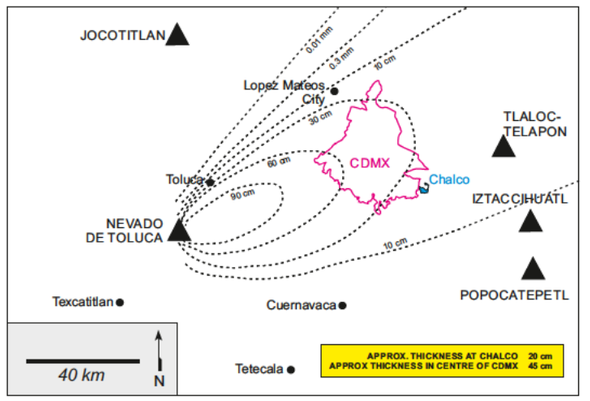
A


-100 º
-95 º
-90 º
25 º
20 º
15 º
MEXICO
Gulf of Mexico
Queretaro
Lake Chalco
Nevado de Toluca
Villahermosa
Acapulco
GUAT.
North Pacific Ocean
Isopach (deposit thicknesses)
= 30 cm
= 10 cm
= 3 cm
= 1 cm
= 3 mm
= 1 mm
= 0.3 mm
= 0.1 mm
= 0.03 mm
= 0.01 mm
N
200 km

B


JOCOTITLAN
APPROX. THICKNESS AT CHALCO 1 mm
APPROX THICKNESS IN CENTRE OF CDMX 0.01 mm
Lopez Mateos City
TLALOC-TELAPON
CDMX
0.01 mm
0.3 mm
Toluca
Chalco
IZTACCIHUATL
NEVADO DE TOLUCA
90 cm
60 cm
30 cm
10 cm
POPOCATEPETL
Texcatitlan
Cuernavaca
40 km
N
Tetecala
10 cm

C


JOCOTITLAN
0.01 mm
0.3 mm
10 cm
Lopez Mateos City
30 cm
TLALOC-TELAPON
CDMX
90 cm
Toluca
Chalco
IZTACCIHUATL
NEVADO DE TOLUCA
10 cm
POPOCATEPETL
Texcatitlan
Cuernavaca
40 km
N
Tetecala
APPROX. THICKNESS AT CHALCO 20 cm
APPROX THICKNESS IN CENTRE OF CDMX 45 cm

D

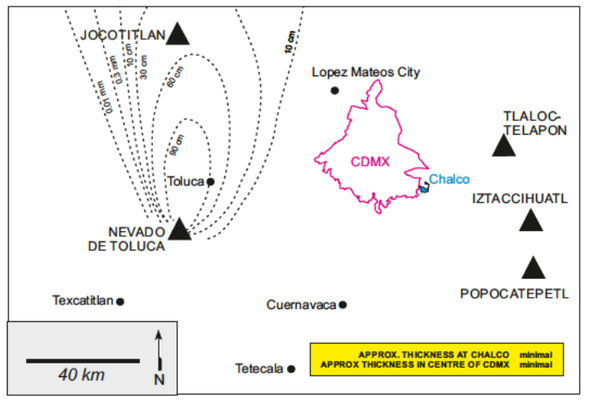

JOCOTITLAN
0.01 mm
0.3 mm
1 cm
10 cm
30 cm
60 cm
90 cm
10 cm
Lopez Mateos City
TLALOC-TELAPON
CDMX
Toluca
Chalco
IZTACCIHUATL
NEVADO DE TOLUCA
POPOCATEPETL
Texcatitlan
Cuernavaca
40 km
N
Tetecala
APPROX. THICKNESS AT CHALCO minimal
APPROX THICKNESS IN CENTRE OF CDMX minimal

Fig. 16. (a) Country-scale modelled eruption scenario at Nevado de Toluca volcano using the USGS volcanic ash dispersion model, Ash3d (e.g., Mastin et al., 2013). A 1.5 km^3 DRE of erupted volume of magma was input to mimic the Lower Toluca Pumice (LTP) eruption (García-Palomo et al., 2002; Arce, et al., 2005). Other input parameters included a 3 hour eruption duration, 16 km plume height (above sea level) and a wind file from February 1st 2022 at 12:00 (local time). The simulation duration was over 24 hours. (b) Basin of Mexico and surrounding source volcano-scale of the modelled scenario in a. (c) Basin of Mexico and surrounding source volcano-scale of the modelled scenario in a with a modified dispersal axis to the NE. (d) Basin of Mexico and surrounding source volcano-scale of the modelled scenario in a with a modified dispersal axis to the N.

February 1st 2022 at 12:00 (local time)). The model simulation was set to 24 hours. The modelled deposit can be seen in Fig. 16a and 16b. In this scenario, a very large eruption, even with a dispersal axis that is broadly towards Lake Chalco, only produces c.1 mm of tephra at the core site (and c.0.01 mm of tephra in the centre of the Mexico City (CDMX) limits). The same scenario model (in relation to Basin of Mexico and surrounding source volcanoes) has been rotated to resemble a NE dispersal axis (Fig. 16c) and N dispersal axis (Fig. 16d), with the NE scenario depositing very thick tephra at Lake Chalco (c. 20 cm), but the N scenario producing no deposition. Although this modelled eruption scenario is simplistic and does not consider more sophisticated plume dynamics (e.g., complexities regarding different phases of the eruption or the buoyant transport of ash), it demonstrates how an unknown dispersal direction and unknown source of individual deposits from one core site limits our physical volcanological understanding of these eruptions. To improve upon this, deposits within the core would need to be correlated to other cores or sedimentary successions, and/or terrestrial exposures of the same eruption layers. Nevertheless, the explosive eruption record at Chalco is accurate for events that have deposited visible thicknesses of tephra in the region, and there is a strong likelihood that these eruptions also deposited tephra within the Mexico City limits.

7.3.2. Data collection limitations

We have attempted to mitigate limitations within the data collection phase of this study to provide the most accurate record of volcanism at Lake Chalco as possible, by projecting ghost layers to account for unrepresented eruptions in the splice, by assigning degrees of confidence with regards to thickness, whether a layer is volcanic in origin and if a deposit is reworked, and by drawing on data from all core sections, including off-splice information. Additionally, we have drawn on analytical grain size methods to test the accuracy of visual assignations. We suggest replicating this methodology with similar core datasets to produce consistent records that are as accurate as possible. However, there remains some subjectivity and potential for human error within any observation-based dataset of this type. It is possible that some volcanic layers may have been missed or interpreted incorrectly, and thickness values for poorly preserved layers have inherent uncertainty (e.g., Fig. 5 presents one way of determining the thickness of layers, but alternatives could be considered). Despite this, our volcanic stratigraphy has been derived from multiple techniques (e.g., numerical plotting of depths and visual checks through core section images), and we deem the results to be as accurate as possible when based on predominantly visual observations. We recommend when replicating this methodology that similar checks are conducted to ensure the highest quality output is used for analysis.

7.4. Implications for Mexico City hazard assessment

As mentioned above (sections 7.1, 7.2 and 7.3) this study has direct relevance for assessing the hazards, risks, and vulnerability of Mexico City to volcanism from diverse eruptions. The Chalco core contains: (1) lavas from localised effusive-style activity; (2) complex volcaniclastic

deposits, interpreted to be sourced from a major mass-wasting event(s) from a nearby polygenetic volcano(es) and subsequent reworking of these; and (3) tephra fall deposits (TFDs) from multiple sources. The stratigraphic placement of lavas and volcaniclastic deposits suggest these processes dominated in the earliest stages of Lake Chalco's evolution. The upper c.150 m_c of core (and most of the upper 300 m_c) is exclusively lacustrine sediments intercalated with TFDs. Nevertheless, volcanic mass wasting events are likely to occur again, as volcanoes undergo collapse and rebuilding throughout their lifetimes (Watt, 2019). It is possible, due to modern-day and future drainage pathways, that these processes may not affect Mexico City itself, but nearby populations and infrastructure closer to the SNVR and other polygenetic volcano(es) are at a higher risk from such events. Additionally, lava flow hazards present a major challenge to Mexico City, particularly from the SCVF. Renewed activity in the SNVF could occur anywhere within the volcanic field, and lavas flows are likely to travel for hundreds of meters to kilometres. This type of volcanic hazard is therefore still a possibility for modern-day Mexico City (see Arce et al., 2015; Nieto-Torres and Del Pozzo, 2019), and the frequency patterns in Fig. 14d suggest that the SCVF is in a relatively elevated period of activity, in the context of the lifetime of the field.

The upper c.300 m_c of the Chalco core provides an exceptional record of explosive volcanism for the Mexico City region, with a minimum of 450 TFDs. Of these, at least 205 are felsic layers, and we infer that the majority of these were erupted from polygenetic centres surrounding the basin of Mexico. As noted above, the long term trend of these deposits is consistent with the SNVR being the dominant source of these deposits. There are, however, likely thinner and finer-grained deposits within the core that were sourced from more distal composite volcanoes

in the TMVB and from caldera systems to the north; and potentially fine ash deposits from Central American caldera systems. The 205 mafic layers were most likely erupted from small monogenetic centres of the SCVF. The thickness and grain-size pattern of the deposits (relatively thick but relatively fine-grained, when compared with the felsic deposits) is consistent with this more localised source and with the expected eruption style of these events. However, some of these layers may be derived from relatively powerful mafic explosive eruptions from polygenetic volcanoes of the SNVR. As a general rule though, since mafic explosive eruptions tend to be less intense and disperse their products over smaller distances, we do not expect the polygenetic volcanoes around the Basin of Mexico to be a major source of such deposits at the Chalco site. There are c.220 cones identified at the surface in the SCVF (Jaimes-Viera et al., 2018). However, morphometric analysis and direct dating of cones suggests that many of these are ≤40 ka (e.g., Niero-Torres and Del Pozzo, 2019). Furthermore, our observations in Stage I suggest that many older cones (and lavas) may be deeply buried beneath younger volcanic and lacustrine deposits. It would therefore be too simplistic to suggest that most of the 220 cones are represented by the 205 mafic tephra layers in the core. Many of the cones are well over 30 km from Chalco, and at these distances, would only be expected to form very thin ash deposits at the core site. We therefore conclude that many of the older mafic TFDs are potentially sourced from buried cones which now lie below several meters to hundreds of meters of sediment. It is also possible that volcanoes of the SCVF are only monogenetic in a 'volcanic architecture sense' and not in a 'petrogenic sense' (cf. Smith and Nemeth, 2017), and that some of these vents may have experienced multiple, closely space eruptions (forming several discrete layers in the core). Further investigation into the mafic deposits in the core, and from successions nearby to other volcanic fields, may permit further

understanding of the long-term eruptive behaviour of volcanic fields and individual cones within them. This approach provides a unique opportunity to understanding monogenetic field development, that cannot be obtained by ground-based characterisation alone.

Regardless of source volcano, every TFD in the Chalco succession is representative of an eruption which has deposited visible tephra in the Chalco region, and at least on part of the Mexico City (CDMX) region. From a hazard perspective, volcanic source is not relevant, as the population would have to adapt to, evacuate or take other significant measures to respond to a similar event today. All tephra deposition poses a risk to human health by inhalation of microscopic volcanic particles (e.g., Damby et al., 2013). Precautions can be taken, such as covering the nose and mouth, which residents of CDMX are often advised, following renewed explosive activity at Popocatépetl since 1994 (e.g., Love et al., 1998; Macias et al., 2020). In addition to the number of times that CDMX has been affected by visible tephra falls, the Chalco succession can be assessed to determine the frequency and tempo of eruptions that produce thicker deposits, which often result in different impacts (e.g., Wilson et al., 2012; Jenkins et al., 2015; Deligne et al., 2021). Fig. 17 displays the stratigraphic position in event-free depth of all TFDs regardless of their composition that are ≥5 cm. These are binned in 5 cm intervals until 25cm, with two bins thereafter (25 to 49.99 cm, and≥50 cm). Generally, frequency decreases with deposit thickness, as expected for general eruption-magnitude frequency relationships. This record of thicker deposits helps evaluate the frequency of eruptions that are likely to cause a higher level of damage to infrastructure and pose a larger risk to life, as thick tephra deposition generally has the highest potential to collapse roofs of buildings e.g., Pomonis et al., 1999; Macedonio and Costa, 2012; Wilson et al., 2012; Hampton et al., 2015;

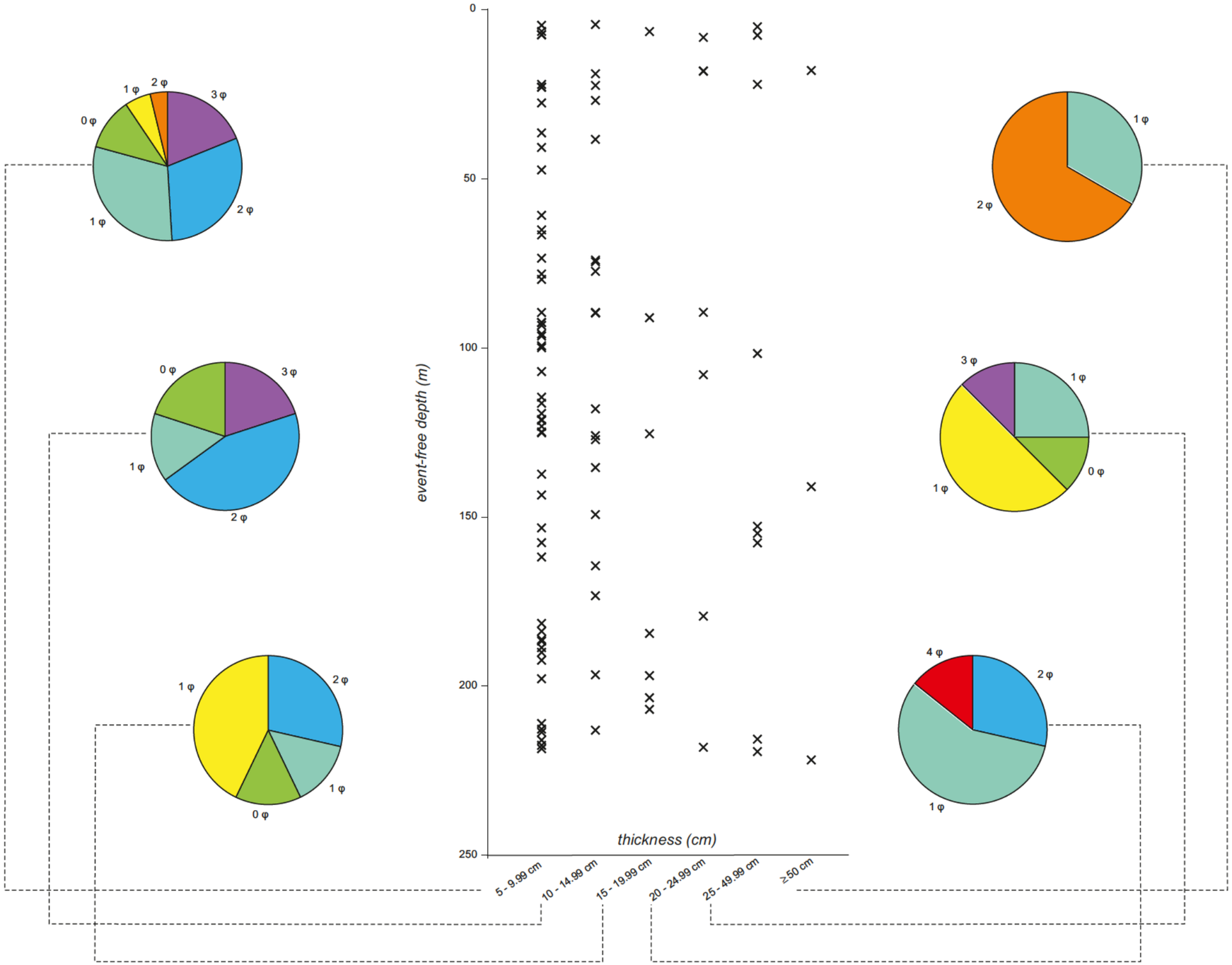

event-free depth (m)
0
50
100
150
200
250
thickness (cm)
5 - 9.99 cm
10 - 14.99 cm
15 - 19.99 cm
20 - 24.99 cm
25 - 49.99 cm
≥50 cm
0 φ
1 φ
2 φ
3 φ
4 φ

Fig. 17. Scatter plot showing the stratigraphic placement of tephras over 5 cm in thickness in the Chalco core. These are further sub-dived into separate bins each increasing in thickness. Grain size data is presented as proportionate pie charts for each bin range.

Blong et al., 2017). The frequency of these events within the Chalco core shows little variability (Fig. 17). Additionally, Fig. 17 presents grain size proportions of the tephra in each bin. Generally, the thicker the tephra, the coarser the deposit, although this isn't always the case and it must be noted that for the thickest tephras, there are very few data points. All deposits contain particles with a maximum grain size coarser than 1 φ. They are ash-dominated deposits, and would likely also contain much smaller ash size fractions. They would therefore also all likely pose human health hazards, and such an eruption occurring in present-day would present a major health and logistical crisis for the city.

8. CONCLUSIONS

1. The Chalco core (MexiDrill project, supplemented by earlier cores) contains a variety of volcanic deposits and lithologies derived from multiple sources and eruptive styles. The majority of the core (59.81% of material in the splice) is volcanic in origin.
2. The Chalco succession can be subdivided into:
    - Stage I (Lava-dominated section, 448.86 – 553.93 mc): 8 stacked lava flows occasionally bound by minor scoria (cone flank) and volcaniclastic deposits.
    - Stage II (Pre-Lacustrine deposits, 293.71 - 448.86 mc): volcaniclastic deposits interpreted to have been formed from a mass-wasting event and subsequent reworking.
    - Stage III (Lacustrine-dominated deposits, 0 – 293.71 mc): various lacustrine sediments intercalated with volcaniclastic material and tephra fall deposits.

3. A unique stratigraphic methodology has been applied to obtain the most complete eruptive record of the Mexico City region, including identifying, defining and projecting off-splice 'ghost' layers onto the splice to account for all possible volcanic events recorded across several boreholes. A variety of metadata about each volcanic layer has been recorded.
4. Preservation of the succession is generally of a greater quality with depth, however, off-splice sections for volcanic layers, where appropriate, has been used to obtain the most meaningful volcanological data from the succession.
5. From a tephrastratigraphic perspective, a maximum of 603 explosive eruption layers have been identified with a minimum (including the most likely to be primary and the highest degree of volcanic origination) of 450 layers. These are subdivided in felsic, intermediate and mafic tephras accounting for 45.5˙%, 8.8˙% and 45.5˙%, respectively.
6. The Chalco core contains a high number of felsic and mafic tephras throughout Stage III deposits which can be seen to be gradually decreasing over time and erupting in clusters, respectively.
7. Most tephra layers are fine grained (containing ash-sized pyroclasts) and are <5 cm in thickness. There is a greater spread between the thickness of tephras for felsic and mafic events towards the upper and lower sections of Stage III.
8. Thicker tephra deposits often preserve internal structure interpreted to be representative of changes in the plume dynamics of an eruption and different eruptive processes throughout the eruption (e.g., co-ignimbritic plumes).
9. The succession at Lake Chalco is an accurate record of volcanic eruptions which have deposited tephra over the Mexico City region in the past, therefore providing an important

and useful archive of volcanic data from a hazard perspective. Mexico City is vulnerable to tephra deposition from a variety of volcanic sources, which poses a risk to human health. There have also been numerous eruptions that deposited material thick enough to collapse roofs and severely damage infrastructure if such an eruption were to occur in present times.

10. This chapter provides an easily reproducible methodology as a tool for volcanologists and sedimentologists to apply to a sedimentary succession containing volcanic material in order to better understand the eruptive history of a region where eruptive records are scant.

CHAPTER 4

RECONSTRUCTING THE MIDDLE TO LATE PLEISTOCENE EXPLOSIVE ERUPTON HISTORIES OF POPOCATEPETL, IZTACCIHUATL AND TLALOC-TELAPON VOLCANOES IN CENTRAL MEXICO

"You can't keep a good scientist down"

Dr. Emmett Brown, Back to the Future Part III

The bulk of the chapter is published in Journal of Volcanology and Geothermal Research[1].

This paper is provided in Appendix P3.

Contribution statement (published with the paper):

Ivan Sunyé-Puchol: Conceptualization, Investigation, Methodology, Project administration, Formal analysis, Validation, Visualization, Writing – original draft, Writing – review & editing. **Alastair G.E. Hodgetts: Conceptualization, Investigation, Methodology, Project administration, Formal analysis, Validation, Visualization, Writing – original draft, Writing – review & editing.** Sebastian F.L. Watt: Conceptualization, Investigation, Funding acquisition, Methodology, Project administration, Validation, Visualization, Writing – original draft, Writing – review & editing. José L. Arce: Investigation, Resources, Methodology, Validation, Visualization, Writing – review & editing. Dan N. Barfod: Investigation, Methodology, Resources, Formal analysis, Validation, Visualization, Writing – review & editing. Darren F. Mark: Funding acquisition, Methodology, Resources, Project administration, Validation, Visualization, Writing – review & editing. Giovanni Sosa-Ceballos: Investigation, Methodology, Resources, Validation, Visualization, Writing – review & editing. Claus Siebe: Investigation, Methodology, Validation, Resources, Visualization, Writing – review & editing. Ross C. Dymock: Methodology, Validation, Visualization, Formal analysis, Writing – review & editing. Maarten Blaauw: Funding acquisition, Methodology, Resources, Project administration, Formal analysis, Validation, Visualization, Writing – review & editing. Victoria C. Smith: Conceptualization, Data curation, Investigation, Funding acquisition, Resources, Methodology, Project administration, Supervision, Formal analysis, Validation, Visualization, Writing – original draft, Writing – review & editing.

---

[1] Sunyé-Puchol, I., **Hodgetts, A.G.E**, Watt, S.F.L, Arce, J.L., Barfod, D.N., Mark, D.F., Sosa-Ceballos, G., Siebe, C., Dymock, R.C., Blaauw, M. and Smith, V.C., 2022. Reconstructing the middle to late Pleistocene explosive eruption histories of Popocatépetl, Iztaccíhuatl and Tláloc-Telapón volcanoes in Central México. *Journal of Volcanology and Geothermal Research*, *421*, p.107413.

1. INTRODUCTION

The metropolitan area of Mexico City and its c.25 million inhabitants sits within the Mexico Basin, which is surrounded by several Pleistocene-Holocene volcanoes of the Trans-Mexican volcanic belt (TMVB; Fig. 1). These volcanoes include Popocatépetl, Iztaccíhuatl, and Tláloc-Telapón, which constitute the Sierra Nevada Volcanic Range (SNVR) to the east of the city. Their explosive activity, as well as those of volcanoes west of the Mexico Basin, is fairly well-constrained for the last 30 ka, as the associated deposits are clearly visible in some accessible exposures (e.g., Ortega-Guerrero et al., 2018; Arce et al., 2003; Sosa-Ceballos et al., 2012; Rueda et al., 2013; Siebe et al., 2017). However, their longer-term eruption history is poorly understood, due to burial and erosion of older deposits, and challenges with correlating the available isolated exposures based on the deposit physical characteristics alone. These isolated exposures have not been studied in detail but contain valuable information that permits reconstruction of a longer and more complete record of explosive volcanism from the SNVR. This is important for evaluating the frequency of large-magnitude explosive eruptions in the region, and for improving our knowledge of the temporal and spatial development of the major volcanic centres in the area.

Here we present detailed chronostratigraphic logs and the glass chemical composition of tephras recorded in two extensive exposures (Nepopualco and Xalitzintla sites), supplemented by a small number of shorter sequences, along the SNVR (Fig. 1b and c). We use these to characterize the proximal pyroclastic products of Iztaccíhuatl, Popocatépetl and Tláloc-Telapón volcanoes (the three main edifices of the SNVR), and to extend and develop

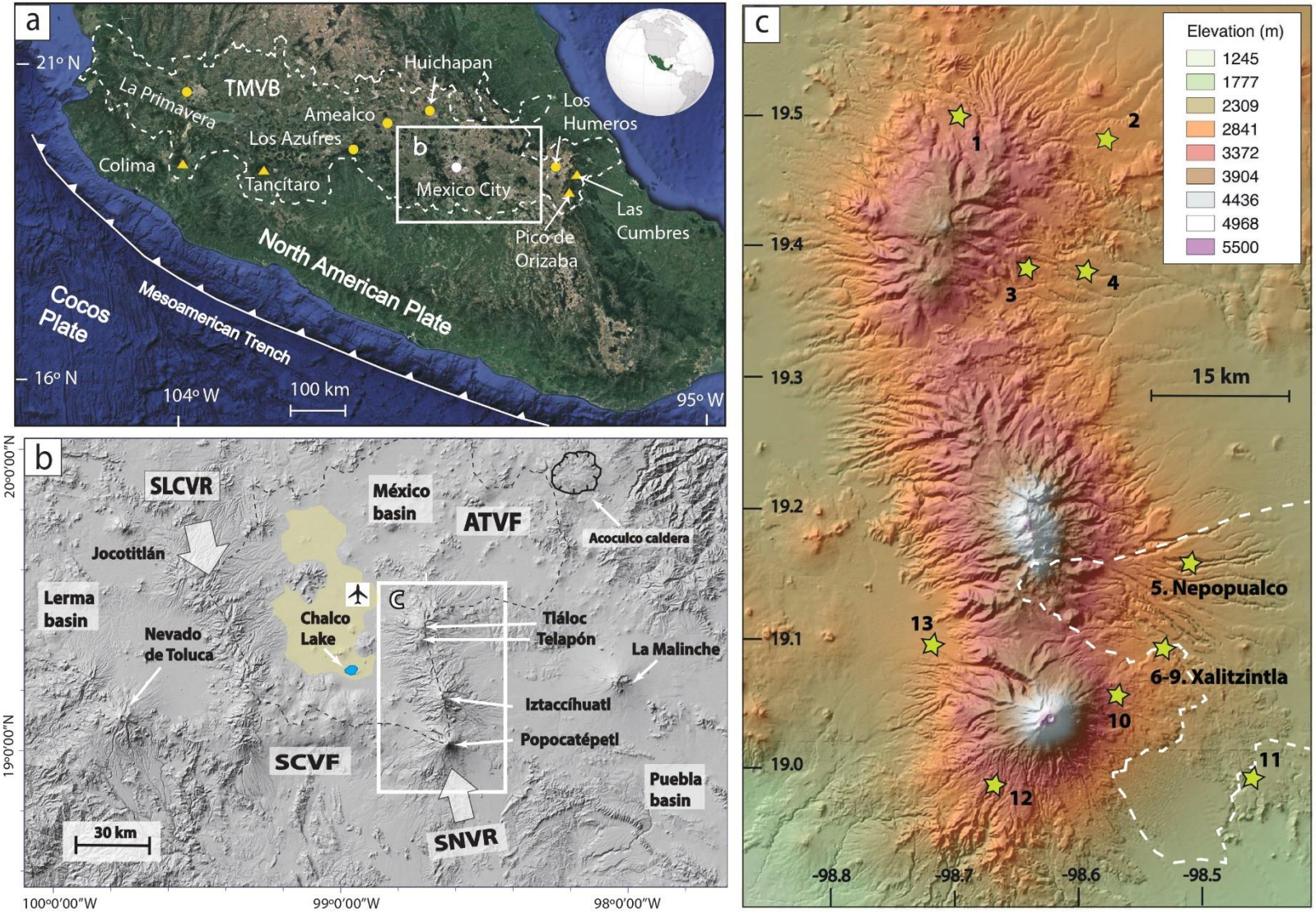

a
21° N
16° N
104° W
95° W
100 km
TMVB
La Primavera
Huichapan
Amealco
Los Azufres
Colima
Tancítaro
Los Humeros
Las Cumbres
Pico de Orizaba
Mexico City
b
North American Plate
Cocos Plate
Mesoamerican Trench
b
SLCVR
México basin
ATVF
Acoculco caldera
Jocotitlán
Lerma basin
Nevado de Toluca
Chalco Lake
Tláloc
Telapón
La Malinche
Iztaccíhuatl
Popocatépetl
SCVF
Puebla basin
SNVR
30 km
20°0'00"N
19°0'00"N
100°0'00"W
99°0'00"W
98°0'00"W
c
Elevation (m)
1245
1777
2309
2841
3372
3904
4436
4968
5500
19.5
19.4
19.3
19.2
19.1
19.0
15 km
1
2
3
4
5. Nepopualco
13
6-9. Xalitzintla
10
11
12
-98.8
-98.7
-98.6
-98.5

Fig.1. (a) Map of the Trans-Mexican Volcanic Belt (TMVB, area within white dashed lin(e) showing main Quaternary stratovolcanoes (yellow triangles) and calderas (yellow dots), as well as Mexico City (white dot); (b) map of the metropolitan region of Mexico City (yellow area in the central TMVB, with the principal volcanic centres marked, including Popocatépetl, Iztaccíhuatl, and Tláloc-Telapón volcanoes along the Sierra Nevada Volcanic Range (SNVR). SCVF = Sierra Chichinautzin Volcanic Field, SLCVR = Sierra Las Cruces Volcanic Range, ATVF = Apan-Tezontepec Volcanic Field; and (c) Digital elevation model (DEM) of the SNVR, showing the location of the studied outcrops (yellow stars; see Table 1 for outcrop locality details), including Nepopualco (n.5) and Xalitzintla sites (n.6-9). The white dashed line shows the limit of Los Pies Debris Avalanche Deposit (LPDAD; Macías et al., 2012).

---

our understanding of their explosive eruption histories. These SNVR volcanoes have been the most active stratovolcanoes near the Mexico basin during the middle to late Pleistocene (Cadoux et al., 2011; Macías et al., 2012). Our geochemical and geochronological data from Nepopualco and Xalitzintla constrain the range of magma compositions erupted from Popocatépetl and Iztaccíhuatl, and the timing of their eruptions over the last c.600 thousand years (ka) and constitute the first step to establishing a long-term record of the medium to large explosive eruptions from the volcanoes surrounding Mexico City.

2. GEOLOICAL FRAMEWORK AND VOLCANIC EVOLUTION OF THE SIERRA NEVADA VOLCANIC RANGE

The Mexico Basin (Fig. 1b) is an endorheic basin closed by the Sierra de Las Cruces Volcanic Range (SLCVR, Mora-Alvarez et al., 1991; Arce et al., 2017) to the west, the SNVR to the east (Nixon, 1989; Cadoux et al., 2011; Macías et al., 2012), and the Sierra Chichinautzin Volcanic Field (SCVF, Siebe et al., 2004; Jaimes-Viera et al., 2018) to the south. The basin closed c.1 Ma ago, when monogenetic cones and lavas of the SCVF blocked drainage to the south resulting in the lower Mexico Basin gradually filling with water (Mooser, 1963; Arce et al., 2013), and

facilitating the rapid accumulation of lake sediments (e.g., Martínez-Abarca et al., 2021). The present magmatism around the Mexico Basin is related to the 3rd phase of the TMVB (Fig. 1a), a 1000 km-long Neogene continental arc related to the subduction of the Cocos and Rivera plates beneath the North American plate (Ferrari et al., 2012), active since 20 Ma. The locus of the TMVB migrated towards the trench at c.7 Ma, coinciding with an increase in silicic volcanism along the arc (Gómez-Tuena et al., 2007).

2.1. Sierra Nevada Volcanic Range (SNVR)

The SNVR forms a N-S oriented range (Fig. 1c) that divides drainage between the Mexico Basin to the west and the Puebla basin to the east (Fig. 1b). There are four large volcanic edifices in the range (Fig. 1b and c); from north to south they are: Tláloc (the "Aztec's God of Rain" in the Náhuatl language) - Telapón ("flat mountain" in Spanish), Iztaccíhuatl ("the woman in white" in Náhuatl), and Popocatépetl ("smoking mountain" in Náhuatl). In this paper we group Tláloc and Telapón volcanoes following the criteria of Macías et al. (2012), as they are perceived to be a single volcanic complex (i.e., compound volcano; Fig. 1c). Minor monogenetic vents are also present along the SNVR, such as El Papayo that emitted lava flows c.118 ka ago (Macías et al., 2012). The volcanic activity of the SNVR is thought to have commenced at its northern tip at Tláloc-Telapón volcano at c.1.82 Ma (García-Palomo et al. 2002; Cadoux et al. 2011; Macías et al., 2012). This age is based on dated lavas, which occur as blocks within pyroclastic density current (PDC) deposits, inferred to have originated from a Paleo-Tláloc edifice (Cadoux et al., 2011). Subsequent activity migrated to the south and emplaced the Paleo-Iztaccíhuatl volcano (Llano Grande, c.1.09 Ma; Cadoux et al., 2011) and then further south again, at the Paleo-Popocatépetl volcano (Tlamacas/Nexpayantla, c.538 ka;

Robin and Boudal, 1987; Conte et al., 2004; Sosa-Ceballos et al., 2015; Delgado-Granados et al., 2017). Although Tláloc-Telapón is the site of the oldest activity of the SNVR, its eruptive history has continued until the very late Pleistocene, evidenced by deposits of ignimbrite-forming eruptions that are < 50 ka (e.g., Macías et al., 2012), indicating possible coeval activity with Iztaccíhuatl and Popocatépetl volcanoes (Rueda et al., 2013).

2.1.1. Tláloc-Telapón

This volcanic complex comprises the lowest elevation edifices of the SNVR, at 4,120 (Tláloc crater) and 4,080 (Telapón crater) meters above sea level (m.a.s.l.). Located c.40 km east from the centre of Mexico City, Tláloc-Telapón is primarily composed of dacitic domes and lava flows, and surrounded by ignimbrites and lahar deposits (Cadoux et al., 2011). Radiometric dates of Paleo-Tláloc lavas yield ages that extend to 1.82 Ma (González and Huddart, 2004; Rueda et al., 2007; García-Tovar and Martínez-Serrano, 2011; Cadoux et al., 2011 Macías et al., 2012). The modern Tláloc-Telapón volcano began its construction at c.0.94 Ma by the effusion of dacitic lavas. This constructional phase ended with the extrusion of the summit lava flows and domes between 0.64 – 0.27 Ma (Cadoux et al., 2011; Macías et al., 2012). Activity at the Tláloc crater appears to have resumed at 129 ka with the emission of rhyolitic lava flows and domes, that are distributed to the east of the present summit dome and within a 2.5-km-wide horseshoe-shaped collapse structure (Macías et al., 2012; Rueda et al., 2013).

Several authors have identified and characterized numerous pyroclastic deposits exposed proximally to Tláloc-Telapón, which have been ascribed to that volcano (e.g., Cornwall, 1971; Huddart and González, 2004; Rueda et al., 2006; Meier et al. 2007; Macías et al., 2012). The youngest deposits include at least five Plinian eruptions that produced PDCs ranging in age

from 44,000 to 21,000 14C yr BP (Macías et al., 2012). They are, from oldest to youngest: San Valentín (45,990-46,895 cal. yr BP, 95% probability [2σ]; 44,195 + 2020/-1615 yr BP), La Joya (40,668-42,807 cal. yr BP, 2σ; 37,220 ± 890 yr BP), P-Mex (36,498-39,375 cal. yr BP, 2σ; 33,180 ± 550 yr BP), Multilayered White Pumice (MWP, 35,578-36,137 cal. yr BP, 2σ; 31,490 +1995/–1595 yr BP) and Cuauhtémoc (29,909-30,065 cal. yr BP, 2σ; 25,640 +275/–265 yr BP) ignimbrites. A relatively recent lava covers the crater at the summit of Tláloc (Rueda et al. 2013), and this is overlain by the c.5.4 cal. ka BP Ochre Pumice eruption deposit from Popocatépetl volcano (Siebe et al., 1996; Arana-Salinas et al., 2010). This indicates that the last known activity at the volcano was pre-5 ka but given the occurrence of multiple late-Pleistocene explosive eruptions and limited exposure in the region, Tláloc-Telapón should still be considered an active volcano.

2.1.2. Iztaccíhuatl

The morphology of Iztaccíhuatl volcano has been likened to a woman lying on her back along a NNW–SSE direction with her head to the north (Figs. 1c and 2a; Macías et al., 2012). This volcano is located c.47 km ESE from the international airport of Mexico City (Fig. 1b), and consists of four peaks (Macías et al., 2012): La Cabeza (the head), El Pecho (the breast), Las Rodillas (the knees) and Los Pies (the feet). El Pecho is the highest peak and reaches 5286 m.a.s.l. The evolution of Iztaccíhuatl is divided into two main phases of cone growth: first, the Older Volcanic Series, including the activity of Paleo-Iztaccíhuatl and the construction of Llano Grande, a shield volcano c.1.09 Ma (Nixon, 1989; Cadoux et al., 2011); and second, the Younger Volcanic Series, represented by lavas and domes emplaced between 600 and 80 ka (e.g., the El Solitario or Téyotl dacite flow; Nixon et al. 1988; Nixon, 1989; Macías et al., 2012).

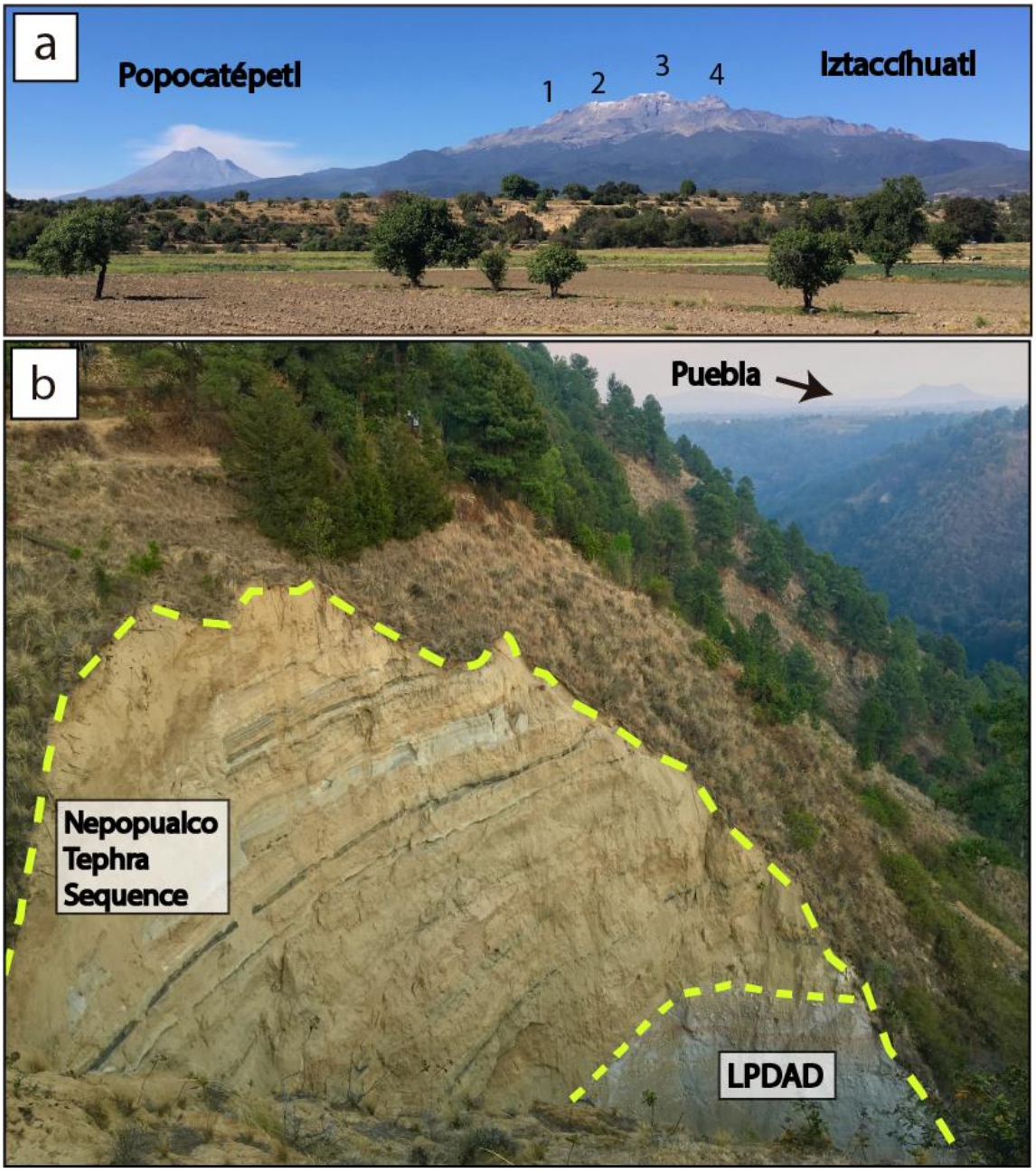

a
Popocatépetl
1
2
3
4
Iztaccíhuatl
b
Puebla
Nepopualco
Tephra
Sequence
LPDAD

Fig. 2. (a) Panoramic view of Popocatépetl and Iztaccíhuatl volcanoes (1 = Los Pies; 2 = Las Rodillas; 3 = El Pecho; and 4 = La Cabeza craters), located in the southern portion of the Sierra Nevada Volcanic Range (SNVR). (b) Tephra layers exposed by a landslide in the Nepopualco gully (outcrop 5 in Fig. 1c). This tephra sequence is interbedded by several remobilized volcanoclastic units and overlies the Los Pies Debris Avalanche Deposit (LPDAD) from Iztaccíhuatl volcano.

A major event in the evolution of modern Iztaccíhuatl involved a sector collapse of the Los Pies cone (Siebe et al., 1995; García-Tenorio, 2008). The volume of the debris avalanche deposit is estimated to be c.1.5 km^3, and the deposits cover an area of 550 km^2 on the SE flank of the volcano (Fig 1c). Los Pies Debris Avalanche Deposit (LPDAD) is overlain by a sequence of PDCs – block & ash-flow type deposits associated with an eruption that followed the sector collapse (Macías et al., 2012; García-Tenorio et al., 2012). An $^{40}Ar/^{39}Ar$ date on plagioclase from juvenile pumices of these PDCs yielded an age of 440 ± 190 ka for the LPDAD (Macías et al., 2012). All of these deposits are towards the base of Nepopualco gully, a key outcrop in this study and site of preliminary description by García-Tenorio et al. (2015).

2.1.3. Popocatépetl

Popocatépetl is the most active volcano of the SNVR and considered one of Mexico's most dangerous volcanoes (e.g., Macías et al, 2020), posing significant risk to the densely populated region as more than 25 million people who live within 100 km of its vent. Located c.45 km SE from Mexico City, Popocatépetl volcano is 5452 m.a.s.l, forming the highest peak of the SNVR, and the second highest in Mexico. After c.70 years of inactivity, Popocatépetl erupted again in 1994. This new activity typically comprises pulsating emissions of tephra and fumarolic gases (Love et al., 1998; Goff et al., 1998; Stremme et al., 2011), associated with subsequent episodes of rapid lava dome growth at the summit crater (Macías and Siebe, 2005; Gómez-Vázquez et

al., 2016), as well as some Vulcanian-style explosions that emplace PDCs and lahar deposits (e.g., the 2001 explosion; Macías et al., 2020).

The modern edifice of Popocatépetl (Fig. 2a), which is mostly comprised of andesitic to dacitic lava flows (Robin, 1984), is constructed over the remnants of previous edifices (c.538 ka; Conte et al., 2004; Sosa-Ceballos et al., 2015; Delgado-Granados et al., 2017). A sector collapse produced an extensive debris avalanche deposit to the south at c.27.8 cal. ka BP (c.23.5 ka BP; Siebe et al., 2017). This was accompanied by the Plinian White Pumice fallout, also dispersed to the south (Robin and Boudal, 1987; Siebe et al., 1993, 1995, 2017). Since then, Popocatépetl has produced at least six Plinian eruptions, including the 16,796-18,201 cal yr BP Tutti Frutti caldera-forming eruption (2σ; recalibrating dates of Siebe et al., 2017 and references therein using the northern hemisphere calibration curve IntCal20 (Reimer et al. 2020) and OxCal (Bronk Ramsey, 2009), which is assumed to be the largest eruption from Popocatépetl based on its widespread distribution and distal thickness (e.g., 10 cm in modern Mexico City, Siebe et al., 1999; Sosa-Ceballos et al., 2012). Three Plinian eruptions have been identified during the Holocene: the 5,333-5,509 cal. yr BP Ochre Pumice (2σ; recalibrating dates of Robin and Boudal 1987; Siebe et al., 1997; Arana-Salinas et al., 2010), 2,150 yr Lorenzo Pumice (Siebe and Macias, 2006), and 1,100 yr BP Pink Pumice (Siebe et al., 1996). These eruptions had dispersal axes to the NE (Panfil et al., 1999; Siebe and Macías, 2006). Siebe et al. (1996) noted that these three Holocene eruptions began with the emplacement of dilute PDCs, followed by extensive pumice fallouts, and ended with the emplacement of dense PDCs.

2.1.4. Summary of the SNVR state-of-the-art

The eruptive history of the SNVR, and particularly the record of the middle to late Pleistocene explosive activity of the stratovolcanoes, is still poorly constrained. For Tláloc-Telapón, five late Pleistocene ignimbrites have been identified and dated (Cornwall, 1971; Huddart and González, 2004; Rueda et al., 2006; Meier et al., 2007; Macías et al., 2012), but the only radiometric ages available are radiocarbon ages, and the glass chemistry of the units have not yet been characterized. For Iztaccíhuatl, only the collapse of Los Pies Cone and its associated avalanche and ignimbrites are dated by $^{40}Ar/^{39}Ar$ (Macías et al., 2012). Other pyroclastic deposits attributed to Iztaccíhuatl have been recognised in the Nepopualco gully (Section 4.1.2; García-Tenorio et al., 2012), but no chemical, stratigraphic or chronological results have been previously published. Popocatépetl has been the subject of several geological studies in the last three decades (e.g., Siebe et al., 1995; 1996; 2017; De la Cruz-Reyna et al., 1995; Espinasa-Pereña and Martín-Del Pozzo, 2006; Arana-Salinas et al., 2010; Sosa-Ceballos et al., 2012), resulting in the stratigraphy of explosive eruptions for the last c.30 ka being fairly well-constrained. However, there is a lack of detailed tephrostratigraphic studies, including glass chemistry, for older sequences, which are likely to date back to around 540 ka when the construction of the Paleo-Popocatépetl is estimated to have commenced (e.g., Delgado-Granados et al., 2017).

3. METHODS

3.1 Fieldwork

Logging and sampling of the middle to late Pleistocene tephras from the SNVR volcanoes was carried out in March 2019. Published volcanological data was reviewed (e.g., Macías et al.,

2012; Rueda et al., 2013; Sosa-Ceballos et al., 2015; Siebe et al., 2017) and the fieldwork was supported by researchers from the National Autonomous University of Mexico (UNAM). Fieldwork was undertaken in accessible, well-exposed outcrops, near the villages of Nepopualco and Xalitzintla (Fig. 1). Roadcuts, deep gullies and quarries, that display multiple tephra units, bound by palaeosols often developed on top of reworked volcanoclastic materials (remobilized products of preceding eruptions that we have interpreted to have been redeposited by dilute lahars, or by other non-volcanic processes) were the focus for this study. Thickness and grain size were measured for each tephra layer, and the textures, colour and concentration of lithics were described. Samples of all units were taken for glass chemical analysis and thick and coarse tephras were sampled for $^{40}Ar/^{39}Ar$ dating. Localities are mapped on Figure 1c (DEM of 15 x 20 m precision downloaded from INEGI-Mexico: https://www.inegi.org.mx), and described in Tables 1 – 3, including locality names and GPS coordinates. All tephra samples were given a unique sample number that was prefixed with 'MXC-' in the field, while individual eruption units (comprising a single event) were given a name that related to the specific site once determined, counting upwards from the base of the exposure (e.g., NT-1, for the oldest exposed tephra in the Nepopualco sequence).

3.2 Glass chemistry

Representative samples of multiple pumice clasts or of bulk ash were collected, depending on the grain-size of the tephra layers, for glass chemical analysis. Tephras were sampled vertically across the deposit to provide a compositionally representative sample and include possible internal compositional variations. Samples were cleaned, crushed, sieved, dried, and mounted in epoxy resin. Mounts were polished and photographed with a petrographic microscope to

assess shard morphology and mineralogy (Tables 1, 2, and 3). These mounts were then carbon-coated prior to measuring the major element concentrations of glass shards using a JEOL JXA-8200 electron microprobe (EMP) equipped with five wavelength-dispersive spectrometers, Research Laboratory for Archaeology and the History of the Art (RLAHA), University of Oxford (UK). A beam accelerating voltage of 15 kV was used with a 6 nA current and a beam diameter of 10 μm. A narrower beam of 5 μm was used for a few highly vesicular samples. The EMP was calibrated using a suite of mineral standards. This calibration was verified using a range of secondary glass standards (ATHO-G, StHs6/80-G and GOR128-G; see Supplementary Material 1 in Sunyé-Puchol et al. (2021); Jochum et al., 2006). Approximately 25 glass analyses, from separate glassy fragments derived from the crushed and sieved samples, were obtained for each of the 71 samples. This includes 25 previously undescribed tephra deposits from Nepopualco, 27 from Xalitzintla, and new characterisation of 13 previously identified and named tephra deposits known to originate from Tláloc-Telapón, Popocatépetl and Iztaccíhuatl (e.g. Macías et al., 2012; Siebe et al., 2017), sampled from other sites around the SNVR (Fig. 1c; and listed as the 13 non-Nepopualco tephras in Table 1). All glass compositions were normalized to 100% for comparative purposes.

3.3 Argon-Argon geochronology

Samples for $^{40}Ar/^{39}Ar$ dating were taken from the thickest and coarsest tephras with large phenocrysts (including hornblende, plagioclase and sanidine). These samples were collected from units in the Nepopualco Sequence and the various Xalitzintla outcrops. The stratigraphically oldest Tláloc ignimbrite was also sampled for dating. Clean pumice clasts were separated from bulk samples and crushed to obtain juvenile-hosted mineral

concentrations. Crushed samples were sieved to 250-500 μm fractions then washed using an ultrasonic bath to remove adhering dust particles. Bulk feldspar was magnetically separated from amphiboles and pyroxenes and subsequently separated into sanidine and plagioclase fractions using lithium metatungstate (LMT) heavy liquid (density c.3.7 mg/l). Feldspars and amphibole were acid-leached following methods of Siegburg et al. (2018) prior to being hand-picked under binocular microscope to avoid inclusion-rich or altered crystals. Samples were irradiated at the Oregon State University (OSU) Irradiation Center using the CLICIT facilities and analysis was carried out in the NEIF Argon Isotope Laboratory at SUERC. Single crystals of sanidine were fused at c.7 W in a single step. Plagioclase and hornblendes were analysed in multigrain aliquots of c.30 crystals that were heated in two-steps: a low power (0.6W) degassing step followed by a fusion step at c.7 W. Sample aliquots with high-age uncertainties (>100%) or negative ages were rejected; this resulted in < 5% of the analyses being removed from the data set. The remaining data were then filtered principally against MSWD criteria (see Supplementary Material 2 in Sunyé-Puchol et al. (2021)). Approximately 25 analyses of aliquots were plotted together (see Supplementary Material 3 in Sunyé-Puchol et al. (2021) in order to achieve a precision of c.10% (2σ) for each sample.

4. FIELD TEPHRASTRATIGRAPHY

4.1 Characterisation of previously identified proximal deposits of the SNVR volcanoes

Several sites around the SNVR (Fig. 1) were visited in order to sample deposits of large explosive eruptions from previously identified exposures. These samples were analysed to provide insights into the glass compositional range of each SNVR volcano, which could be

used to interpret the origin of other previously undescribed tephras from our study sites (Table 1).

4.1.1. Tláloc-Telapón

The fieldwork around Tláloc-Telapón was focused on sampling the deposits of previously identified late Pleistocene ignimbrites (Rueda et al., 2007; 2013; García-Tovar and Martínez-Serrano, 2011; Macías et al., 2012) to chemically characterize their glass chemistry (outcrops 1 to 4 in Fig. 1c). Three separate ignimbrites (MWP, San Valentín, and Cuauhtémoc) were sampled from several sites. The oldest of these, the San Valentín Ignimbrite, was sampled for both radiocarbon and $^{40}Ar/^{39}Ar$ dating to corroborate the previously published radiocarbon age of c. 46 cal. ka BP (Macías et al., 2012), particularly because the age is close to the upper limit of the radiocarbon method and may thus be less reliable. Details of the Tláloc PDCs and the physical parameters of the associated eruptions (e.g., distribution, column height, and magma volume) are documented in Macías et al. (2012) and Rueda et al. (2013).

4.1.2. Popocatépetl and Iztaccíhuatl

Four previously described pumice fall deposits (Pink, Lorenzo, White and Tutti Frutti) from < 30 ka Plinian explosive eruptions of Popocatépetl (e.g. Sosa-Ceballos et al., 2012; Siebe et al., 2017), were sampled from four separate sites around the volcano (Fig. 1). Two subunits from the Tutti Frutti and Pink Pumice deposits were analysed (Pink 1 and 3 from the Pink Pumice; and the Milky and Grey Pumice units from the Tutti Frutti eruption; Table 1). Due to limited exposures, challenging access, and the close spacing between volcanic sources, only one pyroclastic deposit has been previously described and categorically ascribed to Iztaccíhuatl,

Table 1

a) Description of some of the previous identified late Pleistocene pyroclastic deposits of Tláloc volcano

Unit		Description				Location				Age (ka)
Name	Sample	Deposit type	T (m)	Shard morphology	APCS (cm)	North	West	Locality	Outcrop	^{14}C* and Ar/Ar**
Cuauhtémoc Ign.	MXC-91	Poorly sorted pumice and lithics in a fine-medium ash matrix	24	PU, poor but large V	7.5	19.387378°	98.574229°	San Juan C.	4	25.6 ka BP *
MWP Ign.			33							31.5 ka BP *
	MXC-68	Large pumice and lithics-rich in a fine-medium ash matrix	4	PU, elongate V, MI	8	19.497127°	98.715072°	G. Amanalco	1	
	MXC-67	Poorly sorted pumice and lithics in a fine-medium ash matrix	25	PU, BW, elongate V	3	19.497127°	98.715072°	G. Amanalco	1	
	MXC-66	Stratified pumice fall-out/base	2.3	PU, rich in large V	2	19.497127°	98.715072°	G. Amanalco	1	
San Valentin Ign.			29.5							44.2 ka BP *
	MXC-50	Stratified pumice fall-out	2	PU, large V, BW,	1.5	19.477587°	98.575406°	Nanacamilpa	2	101 ± 2 ka **
	MXC-90	Pumice fall-out at the top of the sequence	28	PU, V, BW, CU	2	19.395989°	98.624235°	San Juan C.	3	
	MXC-88	Poorly sorted pumice and lithics in a fine-medium ash matrix	1.5	PU, large rounded V	4.5	19.396556°	98.624861°	San Juan C.	3	103 ± 3 ka **

b) Description of some of the previous identified late Pleistocene - Holocene pyroclastic deposits of Popocatépetl volcano

Unit		Description				Location				Age (ka)
Name	Sample	Deposit type	T (m)	Shard morphology	APCS (cm)	North	West	Locality	Outcrop	C14
Pink-3 Pumice	MXC-118	Sub-unit of coarse non-graded pumice fallout with large lithics	45	SC, BW, large V, CU	2.2	18.987954°	98.453027°	Tianguismanalco	11	1.1 ka BP α
Pink-1 Pumice	MXC-114	Sub-unit of coarse angular, non-graded pumice fallout	18	SC, BW, V, CU	1.5	18.987954°	98.453027°	Tianguismanalco	11	1.1 ka BP α
Lorenzo Pumice	MXC-115	Yellowish pumice fallout of medium lapilli	80	SC, CU, V, BW, MI	1.1	19.040076°	98.563864°	Xalpilcayatl	10	2.1 ka BP β
Milky Pumice	MXC-120	Reversely graded, well-sorted, milky pumice fallout	55	PL, CU, rounded V, MI	2.1	19.075599°	98.731117°	S.P. Nexapa	13	14.3 ka BP γ
White Pumice	MXC-116	Massive whitish pumice fallout, bedded toward the top	110	SC, BW, large V, MI	1.6	18.962417°	98.663488°	Apatlahuaya	12	23.5 ka BP δ
Grey Pumice	MXC-121	Finely laminated beds of grayish pumice fallout rich in lithics	62	SC, BW, CU, large V, MI	2.4	19.075599°	98.731117°	S.P. Nexapa	13	14.3 ka BP γ

c) Description of the previous identified late Pleistocene pyroclastic deposits of Iztaccíhuatl volcano

Unit		Description				Location				Age (ka)
Name	Sample	Deposit type	T (m)	Shard morphology	APCS (cm)	North	West	Locality	Outcrop	Ar/Ar ages (2σ)
Los Pies B&A flow	MXC-02	Reverse grading pumice fall deposit	0.85	SC, rich large/rounded V	2.5	19.149749°	98.508040°	Nepopualco	5	631 ± 44 ka **
Nepopualco dry PDCs	MXC-03	Cross-Stratification ash flows (wet surges)	0.15	2 types? 1 PL and 1 SC	1.5	19.149749°	98.508040°	Nepopualco	5	
Nepopualco wet PDCs	MXC-04	Interbedded medium to coarse ash flows	0.06	2 types? 1 PL and 1 SC	0.1	19.149749°	98.508040°	Nepopualco	5	
Nepopualco fall	MXC-05	Block and ash flow deposit (PDC sequence)	>30	SC, PL, CU, BW, MV	5	19.149749°	98.508040°	Nepopualco	5	440 ± 190 ka ***

T = Thickness, PU = Pumiceous, PL = Platy, CU = Cuspate, BW = Bubble-Walled, F= Fluted, V = Vesicular, MV = Microvesicular, MI = Microlite Inclusions (McLean et al., 2018; and Smith et al., 2019)

APCS = Average Pumice Clast Size (approximate); MWP = Multilayered White Pumice (Rueda et al., 2013);

* ^{14}C ages from Macias et al., 2012; ** Ar/Ar ages from this study; *** Ar/Ar ages from Macias et al., 2012

α= Siebe et al., 1996; β = Siebe and Macias, 2006; γ = Sosa-Ceballos et al., 2012; δ = Siebe et al., 2017

The mineral assemblage of Tlaloc deposits is quartz + sanidine + plagioclase + biotite, with some hornblende and Fe-Ti oxides

The mineral assemblage of Popocatépetl deposits is plagioclase + pyroxene and Fe-Ti oxides

The mineral assemblage of Iztaccíhuatl deposits is plagioclase + hornblende + pyroxene + Fe-Ti oxides and some biotites

the Los Pies B&A Flow (Table 1; Macías et al., 2012; García-Tenorio et al., 2012; 2015). As multiple eruptions help to better classify the compositional range of the deposits of a volcano, we have included an additional, previously undescribed deposit towards the base of the Nepopualco sequence: the Nepopualco Ignimbrite (Table 1, Fig. 3). This deposit is comprised of dilute PDC deposits and a pumice fall (Nepopualco Fall, Table 1, Fig. 3), interpreted to have been produced in a single eruptive event (i.e. in conformable contact and not separated by a paleosol and/or reworked deposits). The following observations suggest Iztaccíhuatl was the source: (1) The geomorphology of the gully lies within a deep fan to the East of Iztaccíhuatl (see section 4.2 and Fig. 1c). Topographically, due to PDCs being gravity-driven currents, the location of this primary ignimbrite deposit implies emplacement from the west, and the local terrain of the Puebla basin does not feasibly support a transport direction from any other volcano in the SNVR (Fig. 1c); (2) Glass data from these deposits are similar to the underlying Los Pies B&A Flows (documented below; Fig. 10, Table 4); (3) $^{40}Ar/^{39}Ar$ Ages from the Nepopualco Ignimbrite, 631 ± 44 ka [2σ], are consistent with known activity from Iztaccíhuatl, and older than any dated deposits of Paleo-Popocatépetl (c.538 ka; Robin and Boudal, 1987; Conte et al., 2004; Sosa-Ceballos et al., 2015; Delgado-Granados et al., 2017).

4.2 Nepopualco and Xalitzintla sites

The remainder of our fieldwork concentrated on the numerous additional well-preserved tephra units in the Nepopualco exposure, and at the additional site of Xalitzintla (outcrops 6-9 in Fig. 1c), c.10 km to the SSW. These two sites lie roughly at the same distance from Iztaccíhuatl and Popocatépetl (c.20 km), so the tephra at Nepopualco and Xalitzintla outcrops could be from either volcano.

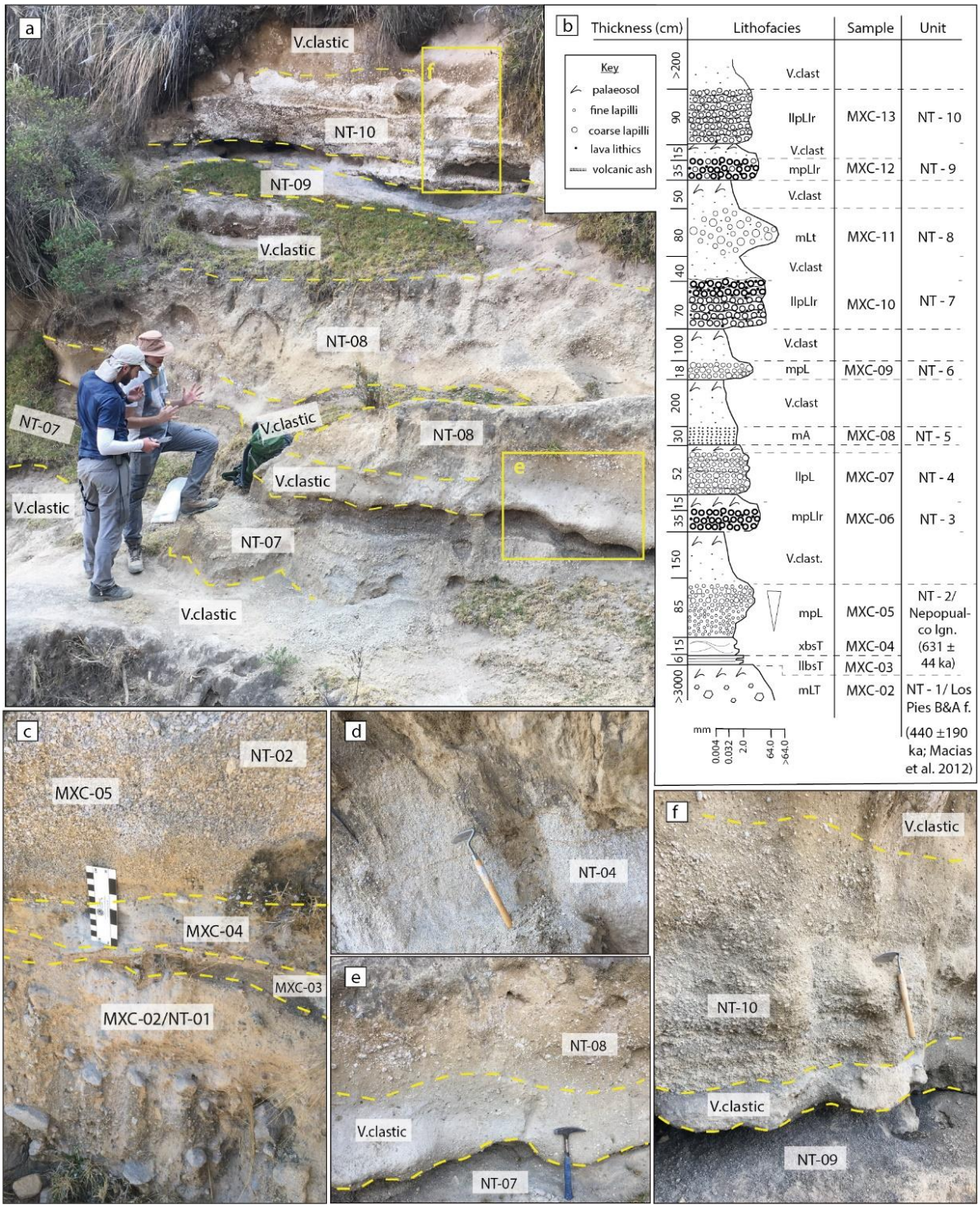

a
V.clastic
NT-10
NT-09
V.clastic
NT-08
NT-07
V.clastic
NT-08
V.clastic
V.clastic
NT-07
V.clastic
b
Thickness (cm)
Lithofacies
Sample
Unit
Key
palaeosol
fine lapilli
coarse lapilli
lava lithics
volcanic ash
>200
V.clast
90
IIpLlr
MXC-13
NT - 10
15
V.clast
35
mpLlr
MXC-12
NT - 9
50
V.clast
80
mLt
MXC-11
NT - 8
40
V.clast
70
IIpLlr
MXC-10
NT - 7
100
V.clast
18
mpL
MXC-09
NT - 6
200
V.clast
30
mA
MXC-08
NT - 5
52
IIpL
MXC-07
NT - 4
35
15
mpLlr
MXC-06
NT - 3
150
V.clast.
85
mpL
MXC-05
NT - 2/ Nepopual-co Ign. (631 ± 44 ka)
15
xbsT
MXC-04
6
IIbsT
MXC-03
>3000
mLT
MXC-02
NT - 1/ Los Pies B&A f. (440 ±190 ka; Macias et al. 2012)
mm
0.004
0.032
2.0
64.0
>64.0
c
NT-02
MXC-05
MXC-04
MXC-03
MXC-02/NT-01
d
NT-04
e
NT-08
V.clastic
NT-07
f
V.clastic
NT-10
V.clastic
NT-09

Fig. 3. (a) Outcrop displaying several units of the lowermost part of the Nepopualco gully sequence. **(b)** Stratigraphic log of the Lower Nepopualco Tephras (Legend: mLT = massive Lapilli Tuff, llsT = parallel-stratified tuff, xsT = cross-stratified tuff, mpL = massive pumice Lapilli, V.clast = volcanoclastic, mpLlr = mpL lithic-rich, llpL = parallel stratified pumice lapilli, mA = massive Ash and llpLlr = llpL lithic-rich; nomenclature based on Branney and Kokelaar, 2002). V.clast in the photographs/logs indicates a reworked (non-primary) volcanoclastic unit, bounding the units that are interpreted as primary eruption deposits. Details of: **(c)** the first pyroclastic layers (MXC-3 to 5 of NT-2) above the Los Pies PDCs (NT-1), **(d)** the NT-4 white fallout, **(e)** the NT-8 above reworked volcaniclastic materials deposited on top of NT-7, and **(f)** the layered NT-10 fallout above the mafic NT-9 fall with reworked materials in-between.

4.2.1 Nepopualco tephra sequence

The Nepopualco site is located c.14 km east of Iztaccíhuatl and 19 km NE of Popocatépetl (outcrop 5 in Fig. 1c) and preserves pyroclastic deposits of at least 25 different eruptive events within a 150-m-deep gully (Table 2; Fig. 2b). The Nepopualco tephra sequence overlies the LPDAD (MXC-01, Fig. 2b), which forms an extensive, low-gradient and elevated debris fan, onto which the thick pyroclastic deposits have accumulated. The fan is deeply incised by numerous gullies, and a recent landslide in the northern wall of the Nepopualco gully (triggered by the 2017 M 7.1 earthquake with an epicentre c.40 km south of Popocatépetl volcano; Mirwald et al., 2019; Fig. 2b) exposes a horizontally stratified sequence of the pyroclastic deposits. The sequence was described from several exposures observable along a footpath that goes from Nepopualco town to the river that drains at the bottom of the gully. All tephra deposits are separated by palaeosols that have developed at the top of each tephra unit, or by layers of reworked volcanoclastic material that often overlie erosive surfaces at the top of the underlying tephra. These volcanoclastic layers commonly also display palaeosols

developed at their tops (see stratigraphic logs in Fig. 3b, 4b and 5c). Apart from the stratigraphic and textural characteristics of the tephra units, the glass compositions, mineralogy and chronological information (Section 5 and 6) have been used to distinguish the tephra units. As this section is mainly focused on the hitherto undescribed Nepopualco pyroclastic deposits, we direct the reader to Figures 3, 4 and 5 for further details regarding the reworked volcanoclastic deposits and palaeosols between tephras. Additionally, for simplicity, primary pyroclastic deposits with angular pumice, which are well-sorted and clast-supported, are interpreted as tephra fallouts deposits, while primary pyroclastic deposits with sub-angular to sub-rounded pumice, poorly sorted in a matrix of volcanic ash, are interpreted as PDC deposits (ignimbrites). Given the large number of tephra units in the Nepopualco sequence, the stratigraphy has been divided in three subgroups: Lower, Middle and Upper Nepopualco tephras. The limit between subgroups was defined by the presence of particularly thick (up to 3 m) reworked units with palaeosols developed at the top (see logs in Figs. 3, 4, and 5), possibly indicating long hiatuses of volcanic activity.

4.2.1.1. Lower Nepopualco tephras

The lowermost pyroclastic unit in the Nepopualco sequence is the Los Pies B&A Flows deposit (ignimbrite related to the LPDAD; Macías et al., 2012; García-Tenorio et al., 2012; 2015). This thick unit (up to 30 m), is labelled as NT-1 (all tephras are numerically named with increase in stratigraphic order from base to top, Fig. 3b and c; Table 2). The next unit (NT-2, which we have named here Nepopualco Ignimbrite as described in section 4.1.2 and attributed to Iztaccíhuatl volcano) is a 6-cm-thick unit comprised of multiple brown laminated PDCs of coarse to medium ash (MXC-03; the Nepopualco dry PDCs), followed by 15 cm of cross-

stratified white PDCs (MXC-04; Nepopualco wet PDCs), and a 85-cm-thick reversely graded pumice fallout of fine to medium lapilli (MXC-05; Nepopualco Fall; Fig. 3b and c). NT-3 is a 35-cm-thick pumice fallout of medium lapilli that is yellowish in colour (MXC-06, Fig. 3b) and rich in lithics. NT-4 is a fallout unit that is 52-cm-thick and comprised of white fine to medium pumice lapilli (MXC-07, Fig. 3b and d), which is diffusely laminated and crystal-rich. NT-5 is a 30-cm-thick fallout unit of dark grey coarse ash, and comprised of clasts that are poorly vesicular with large phenocrysts (MXC-08). NT-6 is an 18-cm-thick fallout deposit of medium to coarse grey pumice lapilli (MXC-09). NT-7 is a 70-cm-thick bedded fallout deposit (MXC-10, Fig. 3a, b, and e) of grey coarse lapilli pumice and rich in lithics (especially in the upper 20 cm). NT-8 is a lens of ignimbrite up to 80 cm in thickness, with large white pumice clasts (up to 10 cm) in a brown ash matrix (MXC-11, Fig. 3b and e). NT-9 is a 35-cm-thick, lithic-rich fallout deposit of scoria and orange crystal-rich pumice (MXC-12, Fig. 3 b and f). The uppermost tephra of this Lower Nepopualco sequence (NT-10) is a bedded 90-cm-thick fallout of lithic-rich, coarse pumice lapilli with darker ash layers in the uppermost part (MXC-13, Fig. 3 b and f).

4.2.1.2. Middle Nepopualco Tephras

The first tephra unit of this subgroup (NT-11) is a 70-cm-thick fallout unit of a bedded white pumice that is normally graded, with clasts ranging from coarse to medium lapilli and rich in fine lithics (<0.5 mm), larger near the top, that grades into a 25-cm-thick ignimbrite (MXC-14, Fig. 4a, b, and c). NT-12 is a 55-cm-thick fallout deposit of coarse orange pumice lapilli (MXC-15, Fig. 4a, b, and d), rich in coarse lithics (0.5 – 2 cm, especially in the upper 20 cm). NT-13 is

Table 2
Description of tephras recorded in Nepopualco sequence (outcrop 5 in Fig. 1c), located 14 km East of Iztaccíhuatl and 19 NE of Popocatépetl (19.149749° N, 98.508040° W)

Tephra unit	Sample	Deposit type	T (m)	Shard morphology	Mineralogy	APCS (cm)	Volcanic Source	$^{40}Ar/^{39}Ar$ ages (2σ)
NT-25	MXC-48	Well-sorted medium ash fall rich in biotite	0.15	PU, BW, rich elongate V, F,	plag, hbl, px, ox, bi, qz	0.05	Uncertain	
NT-24	MXC-47	Well-sorted fine coignimbritic ash	0.1	PU, large V, BW,	qz, san, bi, hbl, ox	0.01	Tláloc-Telapón	
NT-23	MXC-46	White fallout unit of fine to medium lapilli pumice	1.6	PL, BW, CU, large V,	plag, px and ox	1.6	Popocatépetl	369 ± 22 ka
NT-22	MXC-45	Well-sorted orange pumice fall rich in lithics	0.77	SC, PL, CU, BW, MI	plag, hbl, px, ox	3.7	Popocatépetl	
NT-21	MXC-44	Lithics-rich orange pumice fallout of coarse lapilli	0.35	PL, CU, large V, BW, MI	plag, px and ox	3.5	Popocatépetl	
NT-20	MXC-43	Dark fallout unit of fine lapilli rich in lithics (70%)	0.08	PL, large/rounded V, MV, CU	plag, px and ox	0.5	Popocatépetl	
NT-19	MXC-42	Well-sorted white pumice fall poor in lithics	0.3	SC, BW, large V, MI	plag, hbl, px, ox	1.8	Popocatépetl	
NT-18	MXC-41	Normal graded and layered pumice and ash fall	0.9	SC, high V, CU, BW,	plag, px and ox	2.9	Popocatépetl	
NT-17	MXC-39/40	Pumice fall with two ash layers in the middle	0.51	SC, PL, elongate V, CU, rich MI	plag, px and ox	2.8	Popocatépetl	
NT-16	MXC-38	Reverse graded of white ash to fine lapilli	0.27	PU with MV, and SC, large V	plag, px and ox	0.8	Popocatépetl	
NT-15	MXC-37	Lithic-rich massive pumice fallout	0.15	PL, MV, CU, BW, MI	plag, hbl, px, ox	1.4	Popocatépetl	620 ± 52 ka
NT-14	MXC-36	Reverse grading pumice fall deposit	0.08	2 types: 1 PL and 1 SC	plag, hbl, px, ox	1.5	Popocatépetl	
NT-13	MXC-35	Normal graded pumice fall with ash fall at top	0.25	PL, BW, CU, V, MI	plag, hbl, px, ox, qz	1.2	Iztaccíhuatl	
NT-12	MXC-15	Coarse pumice fallout lithic-rich	0.55	SC, BW, rich V, MI	plag, hbl, px, ox	3	Popocatépetl	
NT-11	MXC-14	Normal graded white pumice with PDC at top	0.7	BW, CU, rich V	plag, hbl, px, ox	2.5	Iztaccíhuatl	
NT-10	MXC-13	Bedded pumice fall lithic-rich	0.9	SC, large V, CU, BW, MI	plag, px and ox	2.8	Uncertain	
NT-9	MXC-12	Mafic scoria and ochre pumice fallout	0.35	SC, PL, CU, BW, MI	plag, px and ox	2.7	Popocatépetl	
NT-8	MXC-11	Lenses of PDC deposit	0.8	SC, CU, elongated V, MV	plag, hbl, px, ox, qz	3.2	Iztaccíhuatl	
NT-7	MXC-10	Bedded pumice fall rich in lithics	0.7	SC, BW, CU, rich V, MI	plag, hbl, px, ox, bi	2.8	Uncertain	
NT-6	MXC-09	Grey pumice fallout	0.18	PL, SC, large/elongated V, BW	plag, hbl, px, ox	2.4	Popocatépetl	
NT-5	MXC-08	Well-sorted dark coarse ash	0.3	PL, large/poor V, MI	plag, px and ox	0.2	Mono. Cone?	
NT-4	MXC-07	Well-sorted white pumice fall	0.52	SC, PL, BW, elongated V, MI	plag, hbl, px, ox, bi, qz	1.6	Iztaccíhuatl	
NT-3	MXC-06	Well-sorted lithic-rich yellow pumice fall	0.35	SC, PL, CU, BW, high V, MI,	plag, hbl, px, ox	1.3	Iztaccíhuatl	
NT-2/ Nepopualco	MXC-05	Reverse grading pumice fall deposit	0.85	SC, rich large/rounded V,	plag, hbl, px, ox	2.5	Iztaccíhuatl	631 ± 44 ka
Ignimbrite (dry/wet	MXC-04	Cross-Stratification ash flows (wet surges)	0.15	2 types? 1 PL and 1 SC	plag, hbl, px, ox, qz	1.5	Iztaccíhuatl	
PDc's and fallout)	MXC-03	Interbedded medium to coarse ash flows	0.06	2 types? 1 PL and 1 SC	plag, hbl, px, ox	0.1	Iztaccíhuatl	
NT-1 / Los Pies B&A	MXC-02	Block and ash flow deposit (PDC sequence)	>30	SC, PL, CU, BW, MV	plag, hbl, px, ox, bi	5	Iztaccíhuatl	*440 ± 190 ka
LPDAD	MXC-01	Debris Avalanche with large blocks	>10	PL, big/poor V, MI	plag, hbl, px, ox, qz	20	Iztaccíhuatl	

PU = Pumiceous, PL = Platy, CU = Cuspate, BW = Bubble-Walled, F= Fluted, V = Vesicular, MV = Microvesicular, MI = Microlite Inclusions (McLean et al., 2018; and Smith et al., 2019)
APCS = Average Pumice Clast Size (approximate, as a guidance), LPDAD = Los Pies Debris Avalanche deposit (Macias et al., 2012), T = Thickness, * Age from Macias et al. (2012)

a 25-cm-thick orange pumice fallout consisting of a 10-cm-thick sub-unit of medium lapilli with fine lithics at the base (MXC-35) and a 15-cm-thick sub-unit of fine lapilli in a dark matrix at the top. NT-14 is an 8-cm-thick medium lapilli pumice fallout (MXC-36, Fig. 4e). NT-15 is a 15-cm-thick lithic-rich fallout comprised of fine to medium lapilli pumice (MXC-37, Fig. 4g). The NT-16 tephra layer is a 27-cm-thick reverse graded fallout unit of white coarse ash to fine lapilli pumice (MXC-38). NT-17 is a 51-cm-thick fallout sequence that starts with 4 cm of dark ash followed by 20 cm of medium to fine pumice lapilli (normally graded) rich in lithics (MXC-39), with another 3-cm-thick layer of dark ash, followed by 24 cm of coarse orange pumice with few coarse lithics (0.5 – 2 cm) at the top (MXC-40; Fig. 4 b). NT-18 is a 90-cm-thick pumice fallout with a couple of fine ash layers in the middle (Fig. 4f): the first 30 cm are a coarse orange fallout deposit (rich in lithics towards the top), followed by a thin layer (3 cm) of fine and hardened white ash, 39 cm of bedded pumice (MXC-41), another fine ash layer (2 cm), and a 16-cm-thick unit of medium to fine pumice lapilli.

4.2.1.3. Upper Nepopualco tephras

The first tephra of this subgroup (NT-19) is a 30-cm-thick white pumice fallout with medium lapilli and small lithics (MXC-42, Fig. 5a and c). NT-20 is an 8-cm-thick dark fallout unit comprised of lithics (> 70%) and a few fine lapilli pumices and coarse ash (MXC-43, Fig. 5a and c). NT-21 is a 35-cm-thick fallout of weathered orange pumice, comprised of coarse lapilli rich in lithics (MXC-44, Fig. 5a and c). NT-22 is a 77-cm-thick fallout unit of coarse orange lapilli rich in lithics (MXC-45, Fig. 5b and c). NT-23 is a 160-cm-thick, medium to coarse white lapilli fallout unit (MXC-46, Fig. 5b and c). At the top of the Nepopualco outcrop are two zones of white ash pods within 2 m of soil developed in reworked deposits: the first pod (NT-24) is a

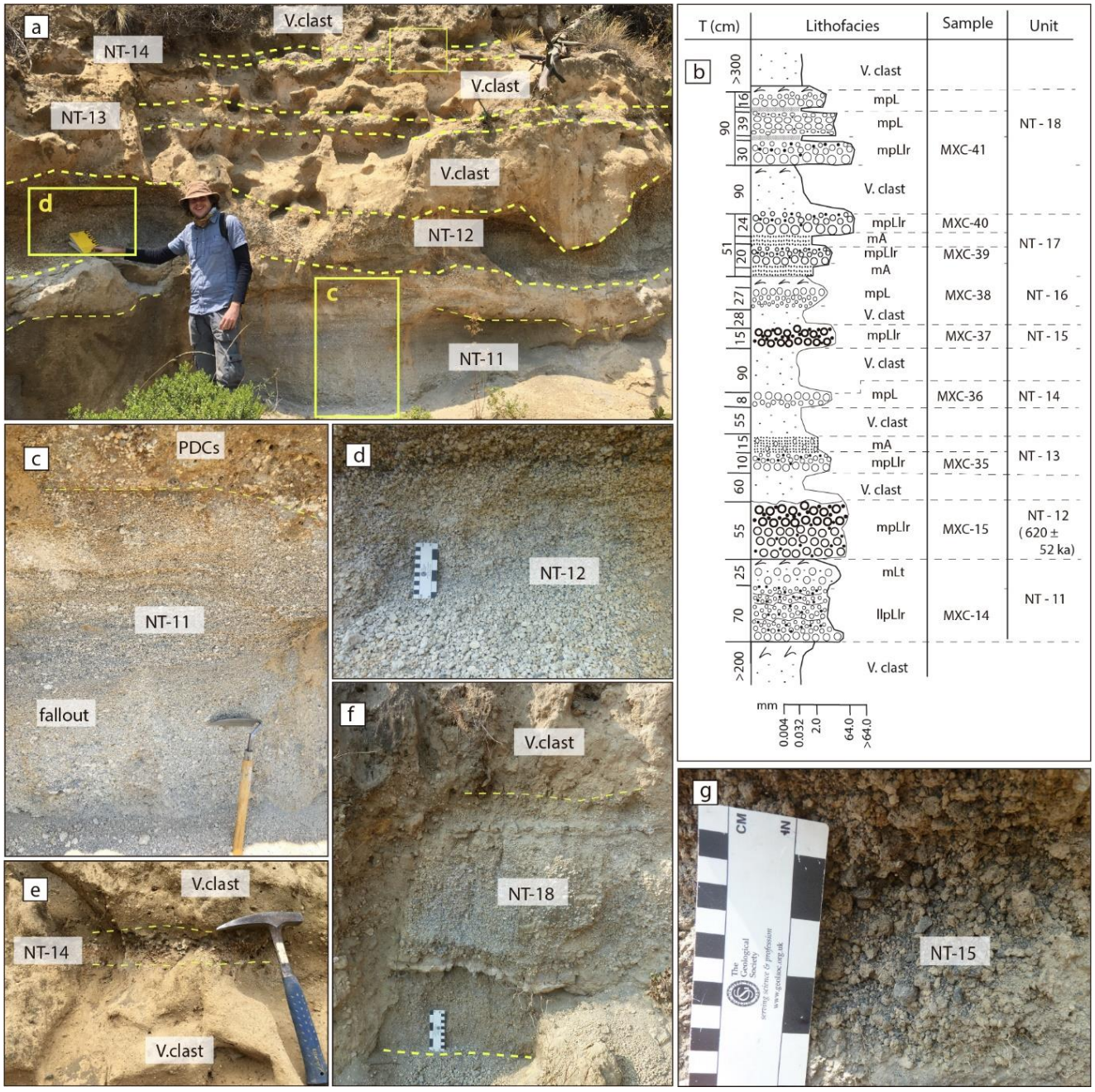

a
V.clast
NT-14
V.clast
NT-13
V.clast
d
NT-12
c
NT-11
b
T (cm)
Lithofacies
Sample
Unit
>300
V. clast
16
mpL
90
39
mpL
NT - 18
30
mpLlr
MXC-41
90
V. clast
24
mpLlr
MXC-40
mA
20
mpLlr
MXC-39
NT - 17
51
mA
27
mpL
MXC-38
NT - 16
28
V. clast
15
mpLlr
MXC-37
NT - 15
90
V. clast
8
mpL
MXC-36
NT - 14
55
V. clast
10
mA
15
mpLlr
MXC-35
NT - 13
60
V. clast
55
mpLlr
MXC-15
NT - 12
(620 ±
52 ka)
25
mLt
NT - 11
70
llpLlr
MXC-14
>200
V. clast
mm
0.004
0.032
2.0
64.0
>64.0
c
PDCs
NT-11
fallout
d
NT-12
f
V.clast
NT-18
e
V.clast
NT-14
V.clast
g
CM
IN
NT-15

Fig. 4. **(a)** Outcrop and **(b)** stratigraphic log of the Middle Nepopualco Tephras (see caption of Fig. 3 for the legend). Details of: **(c)** the thick pumice fallout at the base of NT-11 and the overlaying PDCs, **(d)** the coarse pumice from NT-12, **(e)** the thin NT-14 fallout interbedded within reworked volcanoclastic materials, **(f)** the stratified NT-18 fallout with two interbedded dilute PDCs deposits, and **(g)** the lithic-rich NT-15.

---

fallout unit up to 10 cm thick and comprised of very fine ash (MXC-47, Fig. 5d and e), and the second fallout (NT-25) is comprised of medium ash that is rich in biotite (MXC-48, Fig. 5d and f). Overlying NT-25 is the present-day soil.

4.2.2. Xalitzintla

Tephra layers deposited in the Xalitzintla region are exposed in roadcuts and quarries along the Paso de Cortés road (outcrops 6-9, Fig. 1c and 6a) and within Xalitzintla town. The town is located in a wide valley between the southern margin of the LPDAD and the NE limits of Popocatépetl's flank (Fig. 1c and 6a). The Xalitzintla exposures are located on the northern side of this valley. The sequences described here are from four separate exposures (Table 3): 1) East of the Restaurant, 2) West of the Restaurant, 3) Fork in the road, and 4) Xalitzintla Quarry. The chronostratigraphic order of these sites will be discussed later in section 7, and cannot be determined from field characteristics or topographic relationships, due to discontinuous exposures and an absence of visually correlatable horizons. The Xalitzintla tephras are all fallouts and commonly bound by reworked volcanoclastic materials with palaeosols at the top (see stratigraphic logs in Figs. 6c, 7c, 8c, and 9b).

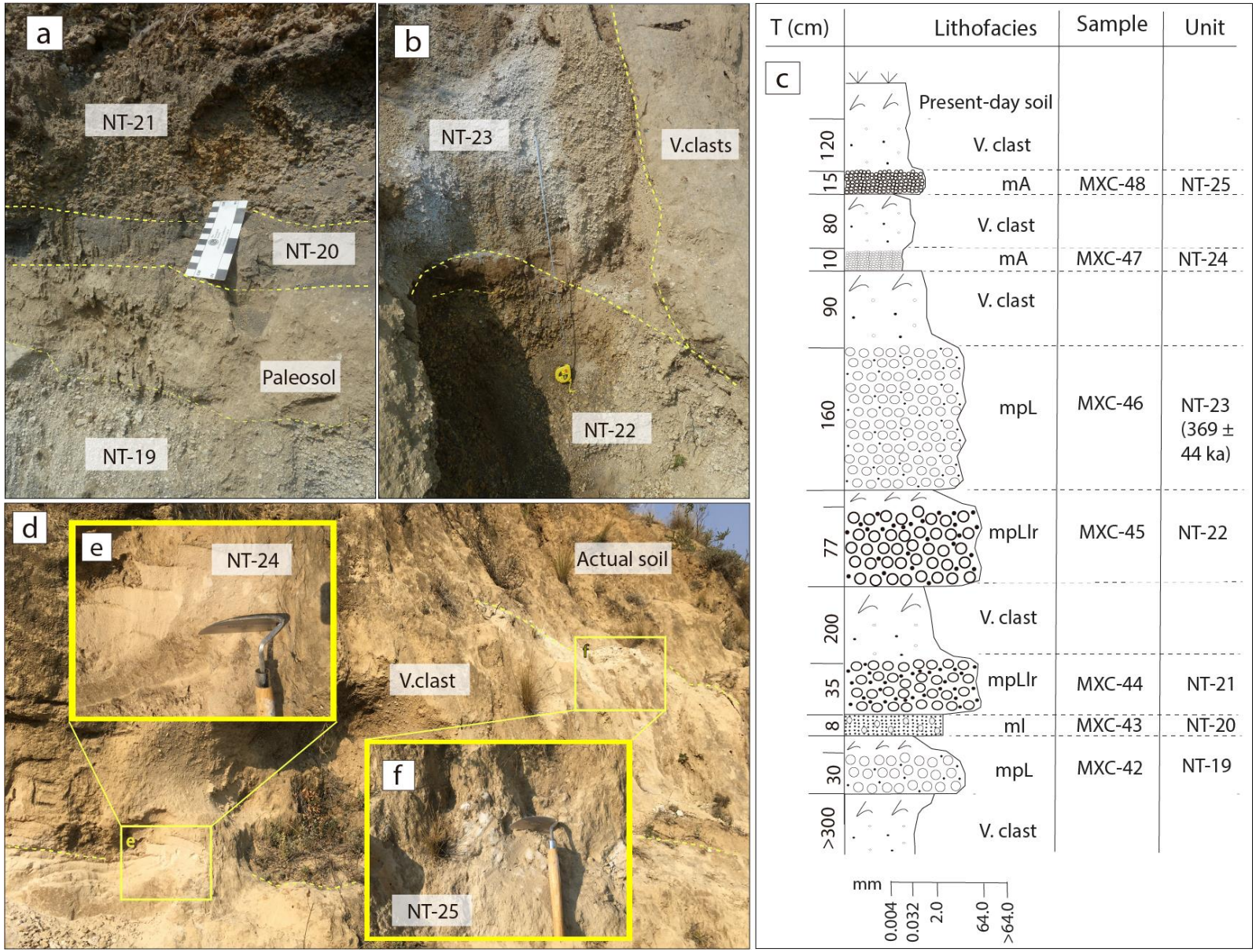

a
NT-21
NT-20
Paleosol
NT-19
b
NT-23
V.clasts
NT-22
d
e
NT-24
Actual soil
V.clast
f
e
f
NT-25
c
T (cm)
Lithofacies
Sample
Unit
Present-day soil
120
V. clast
15
mA
MXC-48
NT-25
80
V. clast
10
mA
MXC-47
NT-24
90
V. clast
160
mpL
MXC-46
NT-23 (369 ± 44 ka)
77
mpLlr
MXC-45
NT-22
200
V. clast
35
mpLlr
MXC-44
NT-21
8
ml
MXC-43
NT-20
30
mpL
MXC-42
NT-19
>300
V. clast
mm
0.004
0.032
2.0
64.0
>64.0

Fig. 5. Detail of: **(a)** the mafic NT-20 and the coarse orange pumice from NT-21 above the palaeosol on top of the white NT-19 pumice fallout, and **(b)** the 1.6-m-thick NT-23 white fallout above the orange NT-22. **(c)** Stratigraphic log of the Upper Nepopualco Tephras (see caption of Fig. 4 for the legend). **(d)** Uppermost part of the Nepopualco sequence with two zones of fine ash pods: **(e)** the NT-24 and **(f)** the NT-25.

4.2.2.1 East of the Restaurant

At least seven different pyroclastic deposits are preserved in this outcrop (ERT-1 to 7, numerically named in stratigraphic order from base to top, as in Nepopualco; Fig. 6b and c), which is located east of the Montaña Fresca Burger restaurant (point 6 in Fig. 6a). The lowermost tephra (ERT-1) is a 43-cm-thick, normal graded, orange weathered pumice fallout (sample MXC-16; Fig. 6c and d) displaying coarse to medium lapilli. Two types of pumice comprise this deposit: one is grey exhibiting felsic phenocrystals and the other is pink with occasional mm-sized mafic crystals. ERT-2 is a 37-cm-thick, lithic-rich fallout unit, which consists of two normally graded subunits of coarse pinkish pumice lapilli to coarse ash at the top (MXC-17 and 18, Fig. 6e), that are separated by a thin layer of lithics. ERT-3 is a distinctive 78-cm-thick fallout sequence made up of several horizontally bedded sub-units separated by lithic-rich horizons (MXC-19 and 20, Fig. 6c and f). The base of this sequence is a 7-cm-thick coarse ash fall with a 0.5-cm-thick lithic-rich layer at the top, followed by eight c.10-cm-thick (each) layers of white medium lapilli pumice. ERT-4 is a grey 5-cm-thick ash fallout layer (MXC-21) and ERT-5 a 20-cm-thick medium to coarse pumice lapilli fallout layer (MXC-22). ERT-6 is a 35-cm-thick fallout unit of medium pumice lapilli (MXC-23). The uppermost tephra

Table 3

Description of Xalitzintla tephras by outcrops (6 to 9 in Fig. 1c and 6a): East of the Restaurant (19.078794° N, 98.506966° W), West of the Restaurant (19.080099° N, 98.507531° W), Fork in the Road (19.084910° N, 98.514919° W) and Xalitzintla Quarry (19.084671° N, 98.520788° W). Tephras and outcrops are in stratigraphic order, from oldest at the base to youngest at top.

Outcrop	Unit	Sample	Deposit type	T (m)	Shard morphology	Mineralogy	APCS (cm)	Volcanic source	$^{40}Ar/^{39}Ar$ ages (2σ)
East of Restaurant									
	ERT-7	MXC-24	Well-sorted pumice fallout of coarse lapilli	0.30	SC, BW, large V, CU	plag, px, ox	2.2	Popocatépetl	
	ERT-6	MXC-23	Fallout of medium pumice lapilli	0.35	SC, CU, rich V, BW, rich MI	plag, hbl, px, ox	1.5	Popocatépetl	
	ERT-5	MXC-22	Medium to coarse pumice fallout	0.20	BW, CU, elongate V, MI	plag, px, ox	2	Popocatépetl	
	ERT-4	MXC-21	Grey layer of coarse ash	0.05	PL, CU, rounded V, MI	plag, px, ox	0.5	Popocatépetl	
	ERT-3	MXC-20	Laminated pumice fallout sequence with nine sub-units	0.78	SC, BW, large V, MI	plag, px, ox	1.6	Popocatépetl	
		MXC-19	Coarsest sub-unit at the base of the fallout sequence		SC, BW, CU, large V, MI	plag, px, ox	2.4	Popocatépetl	236 ± 24 ka
	ERT-2	MXC-18	Uppermost sub-unit of a normal-graded pumice fallout	0.22	SC, BW, CU, large V, MI	plag, px, ox	1	Popocatépetl	
		MXC-17	Lowermost sub-unit, normal graded with a lithic-rich top	0.15	SC, large V, MI, MV	plag, px, ox	2.3	Popocatépetl	
	ERT-1	MXC-16	Normal graded orange fallout with two types of pumice	0.43	PL, CU, BW, elongate V,	plag, px, ox	1.8	Popocatépetl	
West of Restaurant									
	WRT-8	MXC-34	Medium to coarse fallout with a basal grey ash layer	0.55	SC, BW, rich V, large MI	plag, px, ox	2.4	Popocatépetl	
	WRT-7	MXC-33	Massive white yellowish medium lapilli	1.10	BW, CU, V, MI	plag, px, ox	1.2	Popocatépetl	354 ± 58 ka
	WRT-6	MXC-32	Light-grey laminated sequence of pumice fallouts	1.20	SC, BW, large V, MI	plag, hbl, px, ox	1.3	Popocatépetl	431 ± 40 ka
	WRT-5	MXC-31	white medium lapilli pumice fallout finer at top	0.35	BW, CU, rich V, rich MI	plag, px, ox	1.9	Popocatépetl	
	WRT-4	MXC-30	Lithic-rich fallout unit of coarse grey pumice	0.35	PL, large rounded V, MV	plag, px, ox	2.8	Popocatépetl	
	WRT-3	MXC-29	Well-sorted reddish coarse ash fall	0.10	SC, BW, large V, MI, few MV	plag, px, ox	0.3	Popocatépetl	
		MXC-28	Dark-grey medium pumice lapilli fallout	0.40	SC, PU, BW, CU, large V, MI	plag, hbl, px, ox	1.4	Popocatépetl	
	WRT-2	MXC-27	Medium pumice lapilli fall with a lithic-rich basal layer	0.05	SC, BW, V, rich in MI	plag, px, ox	1.5	Popocatépetl	
		MXC-26	Reverse graded pumice medium-to-coarse lapilli	0.25	SC, BW, V, MV, MI	plag, px, hbl, ox	2	Popocatépetl	
	WRT-1	MXC-25	Scoria fallout layer	0.03	SC, BW, CU, V, rich MI	plag, px, ox	1.5	Popocatépetl	
Fork in the Road									
	FRT-6	MXC-107	Coarse grey ash layer with coarse sub-rounded pumices	0.12	PL, elongate V, MI	plag, px, ox, qz	0.4	Popocatépetl	
	FRT-5	MXC-106	Reverse graded yellowish pumice fallout lithic-rich	0.23	PL, PU, large V, MV, MI	plag, px, ox	2.2	Uncertain	
	FRT-4	MXC-105	Brown pumice fallout of coarse lapilli and lithic-rich	0.10	SC, BW, V, MV, rich MI	plag, px, ox	2.7	Popocatépetl	
	FRT-3	MXC-104	Grey bedded pumice fallout sequence with granoclassified	1.20	PU, rich V, rich MI	plag, px, ox	1.2	Popocatépetl	
	FRT-2	MXC-103	Pumice fallout of medium to coarse sub-angular lapilli	0.15	SC, BW, C, large/rounded V	plag, px, ox, qz	2.1	Uncertain	
	FRT-1	MXC-102	Normally graded pumice fallout with lithic layer at top	1.00	SC, large/rounded V, rich MI	plag, px, ox, hbl	1.5	Iztaccíhuatl	
Xalitzintla Quarry									
	XQT-7	MXC-101	Dark brown coarse pumice fallout rich in lithics	0.19	PU, rounded V, MI	plag, px, ox	2.4	Popocatépetl	
	XQT-4	MXC-100	Dark pumice fallout, granoclassified, rich in fine lithics	0.08	SC, PL, BW, larg V, rich MI	plag, px, ox	1.1	Mono. Cone	
	XQT-3	MXC-99	White pumice fallout, lithic-poor and inverse gradation	0.39	BW, large V, some MV, MI	plag, px, ox	1.8	Iztaccíhuatl	
	XQT-2	MXC-98	Dark coarse ash fall	0.26	PL, CU, large V, MI	plag, px, ox	0.3	Uncertain	
	XQT-1	MXC-97	Dark-grey scoria of medium lapilli size	0.22	PL, CU, poor/large V , rich iMI	plag, px, ox	1.5	Mono. Cone	

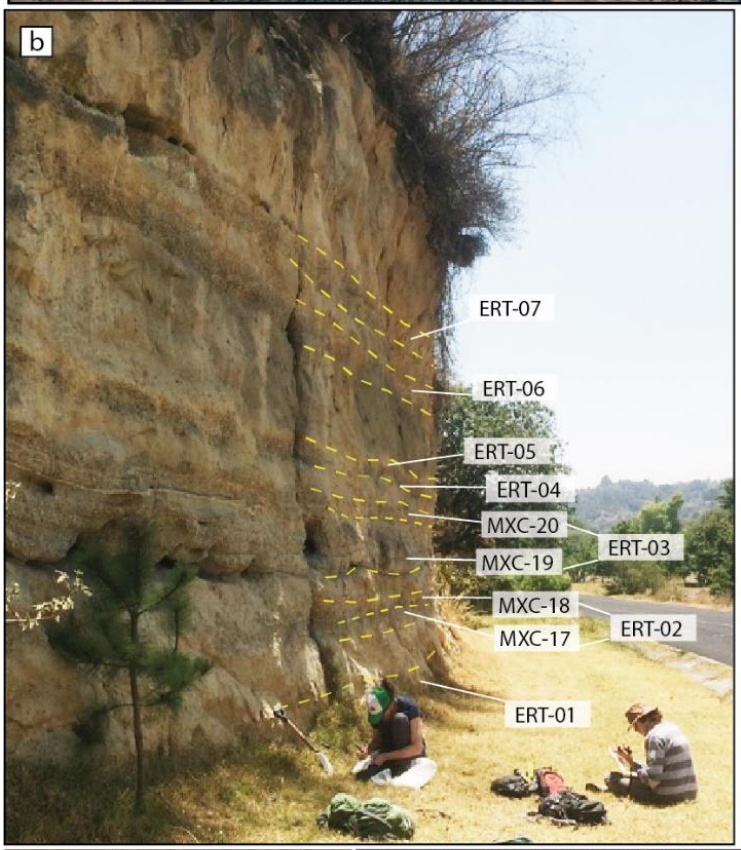
PU = Pumiceous, SC = Scoriaceous, PL = Platy, CU = Cuspate, BW = Bubble-Walled, F= Fluted, V = Vesicular, MV = Microvesicular, MI = Microlite Inclusions (McLean et al., 2018; and Smith et al., 2019);
APCS = Average Pumice Clast Size (approximate), T = Thickness,

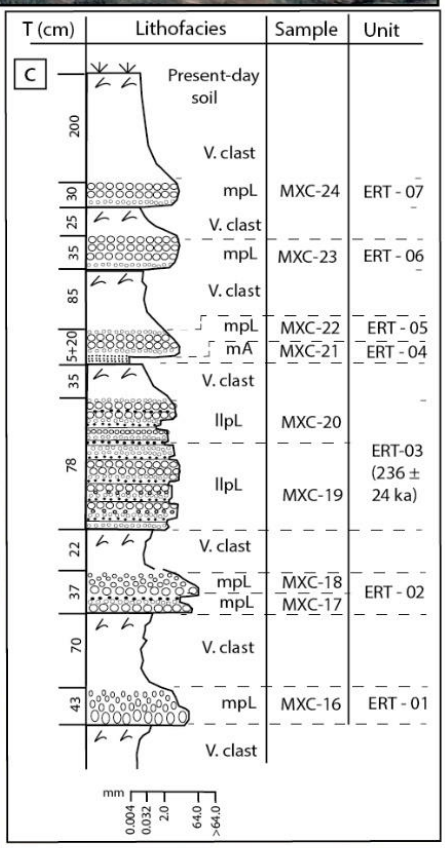
of this outcrop (ERT-7) is a 30-cm-thick pumice fallout of coarse lapilli (MXC-24). Lying above ERT-7 are 2 m of reworked volcanoclastic material with the present-day soil developed above.

4.2.2.2. West of the Restaurant

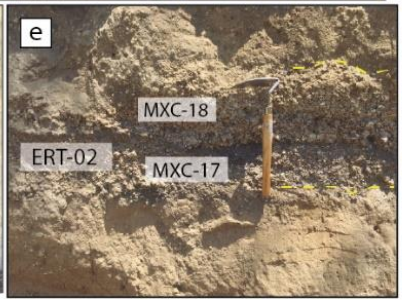
On the western side of the restaurant (point 7 in Fig. 6a) is a small quarry where at least eight pyroclastic units are preserved (WRT-1 to 8; Fig. 7). This sequence sits on a topographic high and dips c.20º towards the road, from where there is a panoramic view of Popocatépetl volcano (Fig. 7a). The lowermost tephra layer of this sequence (WRT-1) is a 3-cm-thick fallout unit of dark pumice (sample MXC-25, Fig. 7b and c). WRT-2 is a 25-cm-thick pinkish fallout of reversely graded medium to coarse pumice lapilli (MXC-26), which is rich in mafic crystals (orthopyroxene and hornblende) and interbedded in its upper portion with a layer of hydrothermally altered lithics. At the top is a 5 cm pumice lapilli fall (MXC-27), which is laterally discontinuous and eroded in some parts of the outcrop. It is discordantly overlain by WRT-3, a 40-cm-thick dark fallout unit composed of grey fine-to-medium lapilli pumice with abundant lithics (MXC-28), which grades into a 10-cm-thick fallout unit of reddish coarse ash (MXC-29). WRT-4 is a 35-cm-thick lithic-rich fallout of coarse grey pumice (MXC-30, Fig. 7 d). WRT-5 is a 35-cm-thick white medium to coarse lapilli pumice fallout (MXC-31), which is slightly finer at the top. WRT-6 is a light-grey, laminated pumice fallout that is 120 cm thick (MXC-32). The basal sub-unit of this deposit is a bedded, 30-cm-thick, coarse ash to fine lapilli fall that is topped brown, lithic-rich horizons. The next sub-unit is structureless, 40-cm-thick, and comprises fine to medium pumice lapilli fall, with a higher concentration of lithics towards the top. The top sub-unit comprises 40 cm of pumice fall interbedded with brown lithic-rich horizons. WRT-7 is a 110-cm-thick fallout unit, which is massive with white to


a
8
9
7
6
N
500 m


b
ERT-07
ERT-06
ERT-05
ERT-04
MXC-20
MXC-19
MXC-18
MXC-17
ERT-03
ERT-02
ERT-01


T (cm)
Lithofacies
Sample
Unit
c
Present-day soil
V. clast
mpL
MXC-24
ERT - 07
MXC-23
ERT - 06
MXC-22
ERT - 05
mA
MXC-21
ERT - 04
IIpL
MXC-20
MXC-19
ERT-03 (236 ± 24 ka)
MXC-18
MXC-17
ERT - 02
MXC-16
ERT - 01
200
30
25
35
85
5+20
78
22
37
70
43
mm
0.004
0.032
2.0
64.0
>64.0


d
ERT-01


e
MXC-18
ERT-02
MXC-17

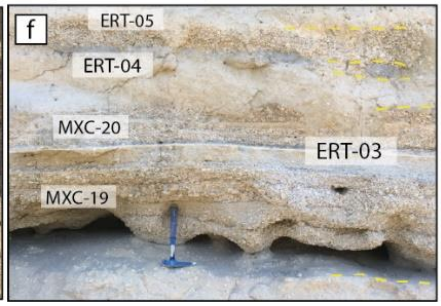

f
ERT-05
ERT-04
MXC-20
ERT-03
MXC-19

Fig. 6. (a) Map of the Xalitzintla region with the location of the four study sites (yellow stars). **(b)** East of Restaurant (ER) outcrop exposed along the Paso de Cortés road (site number 6 in **(a)**; **(c)** stratigraphic log displaying the seven pyroclastic units interbedded with reworked material and palaeosols (see caption of Fig. 4 for the legend); **(d), (e)** and **(f)** field photos showing textural characteristics of tephra layers described in the text (ERT-1 to 5).

---

yellowish medium lapilli and pink coarse pumice clasts that are up to 4 cm in diameter (MXC-33). The uppermost tephra of this sequence (WRT-8) starts with 10 cm of medium dark grey ash followed by 45 cm of a medium to coarse lapilli pumice fallout, which is rich in lithics (MXC-34, Fig. 7e) and grades into c.2 m of reworked volcanoclastic material with the present-day soil at the top.

4.2.2.3. Fork in the road:

Six more tephra layers are exposed in another small quarry along the Paso de Cortés road (FRT-1 to 6; Fig. 8; point 8 in Fig. 6a). The lowermost unit (FRT-1) is a 100-cm-thick, normal graded, white pumice fallout, with clasts ranging from coarse to medium lapilli, and a lithic-rich layer at the top comprising up to 70% lithics (MXC-102, Fig. 8a, b, and c). FRT-2 is a 15-cm-thick pumice fallout of medium to coarse sub-angular lapilli (MXC-103, Fig. 8c). FRT-3 is a distinctive 120-cm-thick, dark grey, normal graded and thinly bedded pumice fallout, with clasts ranging from medium to fine lapilli to coarse ash, that transitions into a lithic-rich (>45%) layer with medium lapilli pumice at the top (MXC-104, Fig. 8d and e). FRT-4 is a 10-cm-thick lithic-rich fallout of brown pumice comprised of coarse lapilli (MXC-105; Fig. 8d and e). FRT-5 is a 23-cm-thick yellowish pumice fallout inversely graded with clasts ranging from medium

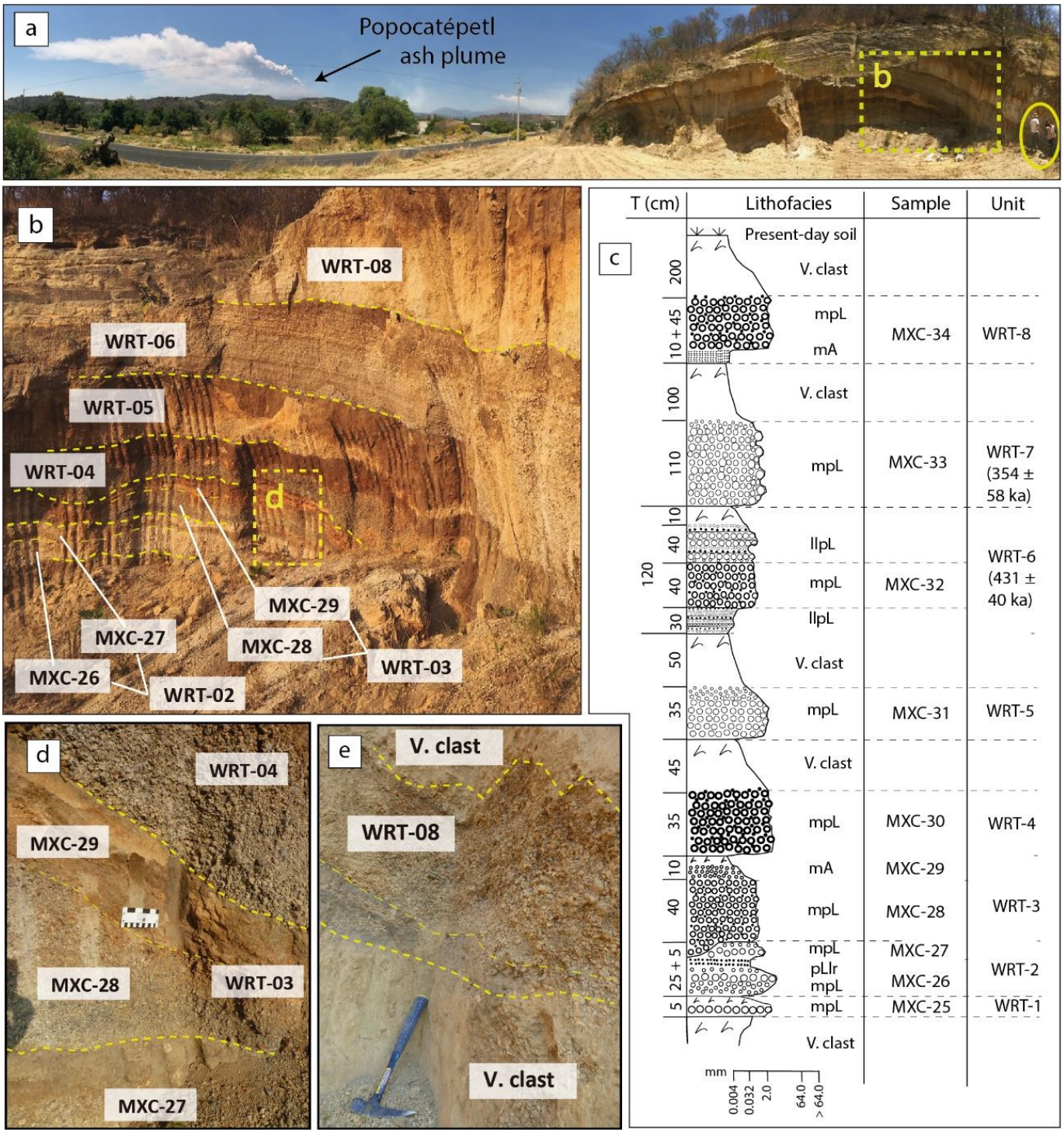

a
Popocatépetl
ash plume
b
b
WRT-08
WRT-06
WRT-05
WRT-04
d
MXC-29
MXC-27
MXC-28
MXC-26
WRT-03
WRT-02
c
T (cm)
Lithofacies
Sample
Unit
Present-day soil
V. clast
mpL
mA
MXC-34
WRT-8
V. clast
mpL
MXC-33
WRT-7 (354 ± 58 ka)
IIpL
mpL
MXC-32
WRT-6 (431 ± 40 ka)
IIpL
V. clast
mpL
MXC-31
WRT-5
V. clast
mpL
MXC-30
WRT-4
mA
MXC-29
mpL
MXC-28
WRT-3
mpL
MXC-27
pLlr
MXC-26
WRT-2
mpL
mpL
MXC-25
WRT-1
V. clast
200
10 + 45
100
110
10
40
40
30
120
50
35
45
35
10
40
5
25 + 5
5
mm
0.004
0.032
2.0
64.0
> 64.0
d
WRT-04
MXC-29
MXC-28
WRT-03
MXC-27
e
V. clast
WRT-08
V. clast

Fig. 7. (a) Panoramic view of Popocatépetl volcano from the West of the Restaurant (WR) site near Xalitzintla (outcrop 7 in Fig. 6a during a small explosive eruption (c.2-km-high plume on the 5th of April, 2019) with an ash cloud moving towards the SE. Note the geologist in the bottom-right of the photo (within yellow ellipsoid) for scale of the outcrop; **(b)** tephra sequence exposed in a quarry of this WR-site; **(c)** stratigraphic log showing the eight pyroclastic units interbedded with reworked material and palaeosols (see caption of Fig. 4 for the legend; **(d)** and **(e)** field photos showing textural characteristics of the tephra layers described in the text.

---

to coarse lapilli, with a lithic-rich layer in the middle (MXC-106, Fig. 8f). FRT-6 is a 12-cm-thick coarse grey ash fallout layer with sub-rounded and embedded orange coarse pumice clasts (mostly at the base of the unit; MXC-107, Fig. 8f). At the top of the sequence there are 100 cm of reworked volcanoclastic material that grades into the present-day soil.

4.2.2.4. Xalitzintla Quarry

At least eleven tephra layers are preserved in a large quarry located NW of Xalitzintla (point 9 in Fig. 6a). Unfortunately, the upper 4 pyroclastic units were out of reach and could not be sampled or described in detail (Fig. 9a and b). The lowermost pyroclastic deposit of this sequence (XQT-1) is a lithic-poor dark-grey scoria fallout that is 22-cm-thick and comprised of medium lapilli clasts (sample MXC-97, Fig. 9c). XQT-2 is a 26-cm-thick fallout unit comprised of dark coarse ash (MXC-98, Fig. 9 d). XQT-3 is a 39-cm-thick white pumice fallout that is lithic-poor (<5%) and slightly inversely graded, with clasts ranging from fine to medium lapilli and the occasional clast that is up to 3 cm in diameter (MXC-99, Fig. 9e). The next four tephra layers are within a 78-cm-thick sequence interbedded by thin layers of reworked material (Fig. 9f).

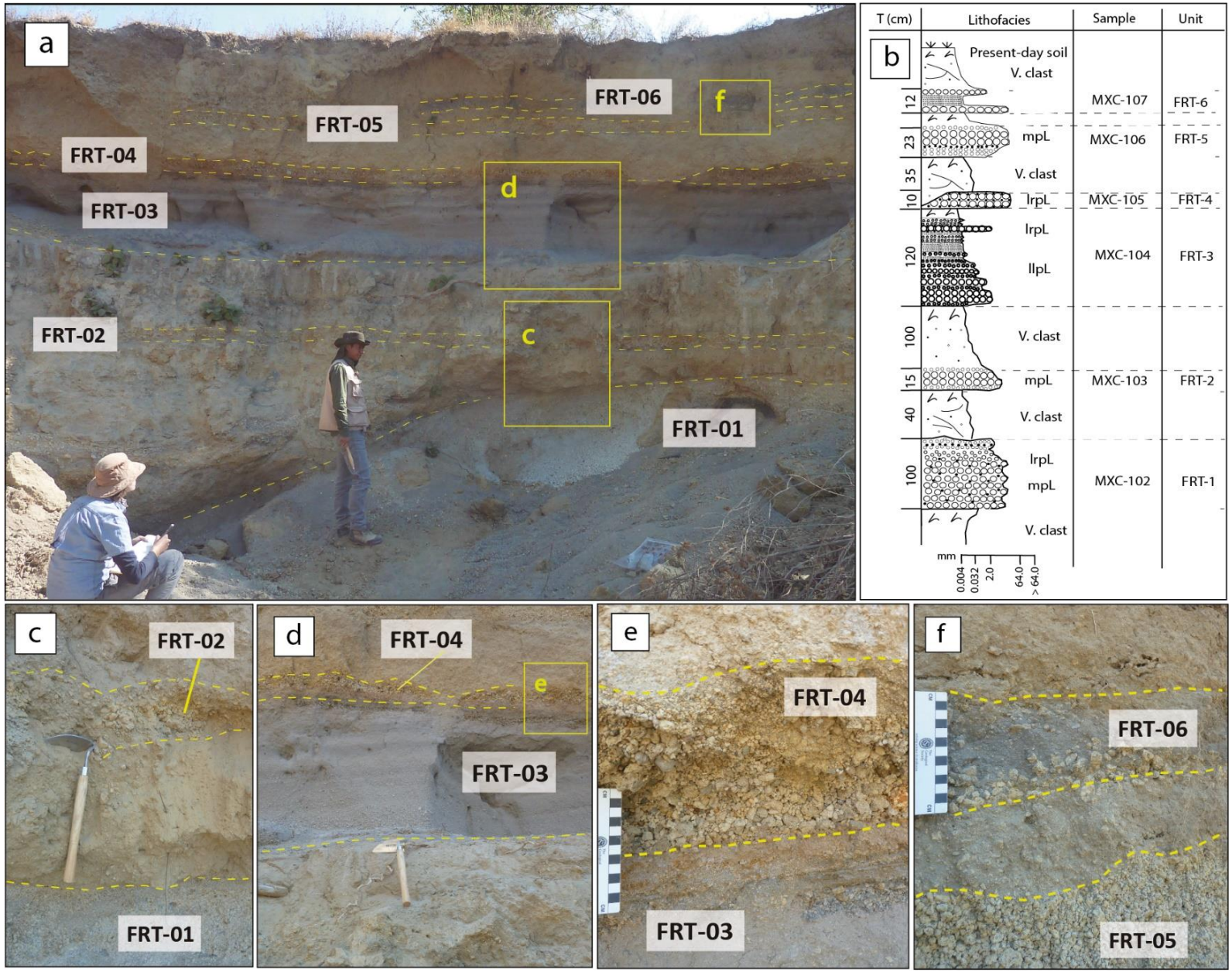

a
FRT-06
f
FRT-05
FRT-04
d
FRT-03
c
FRT-02
FRT-01
b
T (cm)
Lithofacies
Sample
Unit
Present-day soil
V. clast
12
MXC-107
FRT-6
mpL
23
MXC-106
FRT-5
V. clast
35
lrpL
10
MXC-105
FRT-4
lrpL
120
IIpL
MXC-104
FRT-3
V. clast
100
mpL
15
MXC-103
FRT-2
V. clast
40
lrpL
mpL
100
MXC-102
FRT-1
V. clast
mm
0.004
0.032
2.0
64.0
> 64.0
c
FRT-02
FRT-01
d
FRT-04
e
FRT-03
e
FRT-04
FRT-03
f
FRT-06
FRT-05

Fig. 8. (a) Small quarry at the Fork in the Road (FR) site near Xalitzintla (outcrop 8 in Fig. 6(a), **(b)** stratigraphic log displaying six identified fall layers recorded in this site, (**c – f)** field photos showing textural characteristics of the tephra layers described in the text.

XQT-4 is a normally graded 8-cm-thick dark pumice fallout, with fine to medium lapilli to coarse ash, and rich in fine-to-medium lava lithics (MXC-100, Fig. 9g). XQT-5 is a 10-cm-thick yellowish fallout unit of medium lapilli pumice with few coarse clasts up to 2 cm in diameter. XQT-6 is a dark 12-cm-thick normally graded fallout unit, from coarse to medium pumice lapilli and rich in fine-to-medium lithics. XQT-7 is a dark brown 19-cm-thick coarse pumice fallout rich in medium to coarse lava lithics (MXC-101, Fig. 9h). The tephra layers of the uppermost part of the outcrop could not be reached and were not sampled and include: XQT-8, a c.50-cm-thick dark pumice fallout unit with a lithic-rich layer; XQT-9, a c.80-cm-thick light-grey layered pumice fallout of fine to medium lapilli interbedded with thin layers of coarse ash (Fig. 9a and b); XQT-10, a c.50-cm-thick brown pumice fallout unit; and XQT-11, the uppermost tephra recorded in this outcrop, is a c. 2-m-thick orange coarse pumice lapilli deposit (Fig. 9a and b) into which the present-day soil has been developed.

5. GLASS CHEMSITRY AND TEPHRA CORRELATION

The glass compositions of all the tephra layers identified in the outcrops described above were analysed in order to build a tephrostratigraphy that could be used to correlate sites around the SNVR volcanoes, to identify the source of the tephras exposed at Nepopualco and Xalitzintla,

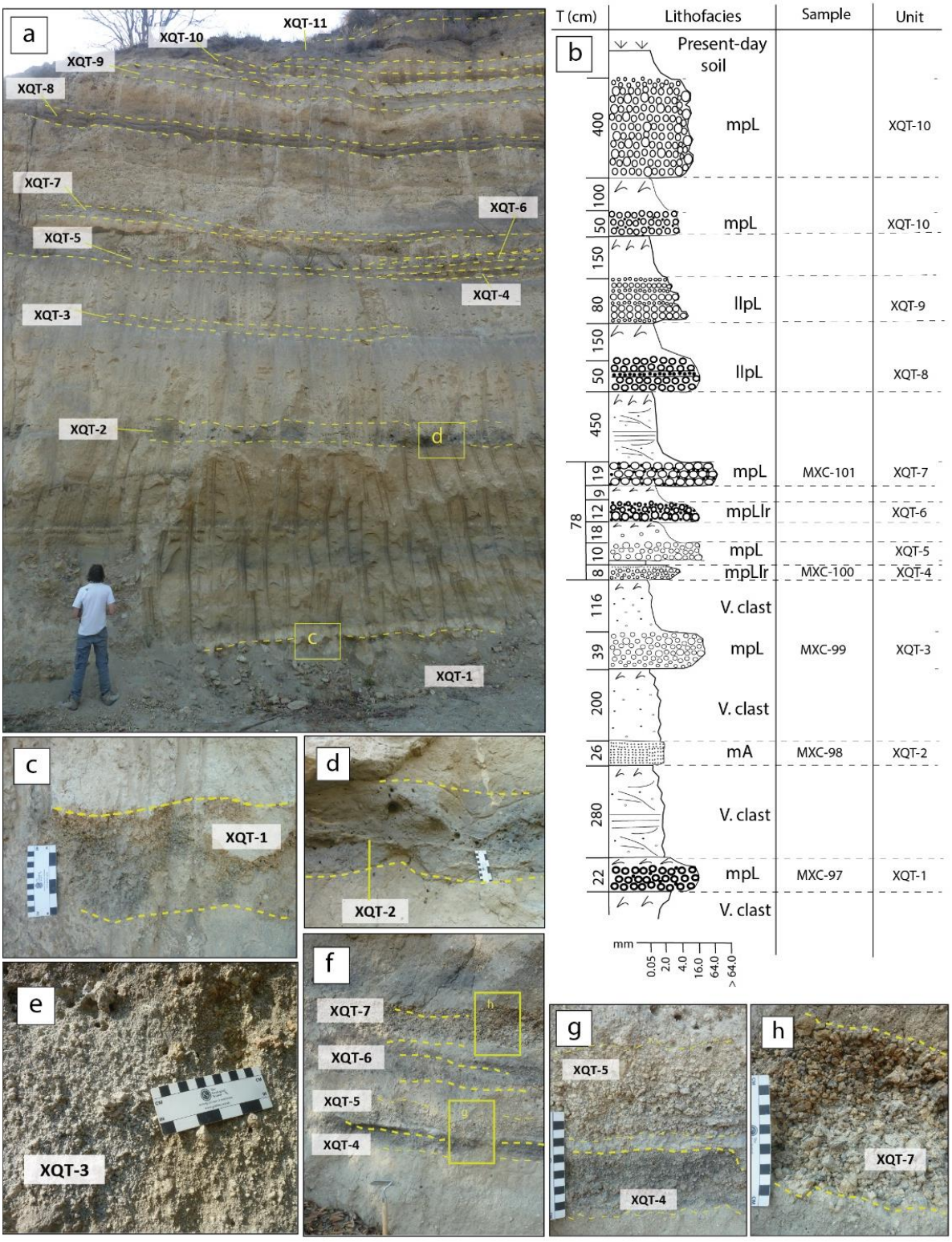

a
XQT-11
XQT-10
XQT-9
XQT-8
XQT-7
XQT-6
XQT-5
XQT-4
XQT-3
XQT-2
d
c
XQT-1
b
T (cm)
Lithofacies
Sample
Unit
Present-day soil
400
mpL
XQT-10
100
50
mpL
XQT-10
150
80
IIpL
XQT-9
150
50
IIpL
XQT-8
450
19
mpL
MXC-101
XQT-7
9
12
mpLlr
XQT-6
78
18
10
mpL
XQT-5
8
mpLlr
MXC-100
XQT-4
116
V. clast
39
mpL
MXC-99
XQT-3
200
V. clast
26
mA
MXC-98
XQT-2
280
V. clast
22
mpL
MXC-97
XQT-1
V. clast
mm
0.05
2.0
4.0
16.0
64.0
> 64.0
c
XQT-1
d
XQT-2
e
XQT-3
f
XQT-7
XQT-6
XQT-5
XQT-4
h
g
g
XQT-5
XQT-4
h
XQT-7

Fig. 9. **(a)** Xalitzintla Quarry, **(b)** stratigraphic log displaying eleven pyroclastic units recorded in this site and interbedded with thick reworked volcanoclastic material units and palaeosols, **(c – h)** field photos showing textural characteristics of the tephra layers described in the text.

---

and to develop the longer-term explosive eruption history of the SNVR. Given that some of the units have been dated here and in other studies (e.g. Macías et al., 2012), this tephrostratigraphy can be used to constrain the chronology at other sites and help evaluate the explosive eruptive history of the volcanoes (e.g., as marker horizons in other regional stratigraphic records; Brown et al., 2019).

5.1 Glass compositional fields of Tláloc-Telapón, Iztaccíhuatl and Popocatépetl

As explained in Section 4.1, we analysed glass from pyroclastic deposits that had been previously attributed to Tláloc-Telapón, Iztaccíhuatl, or Popocatépetl (Table 4; secondary standards in Supplementary Material 1 in Sunyé-Puchol et al. (2021)) in order to establish the compositional fields of the potential source volcanoes of the newly described tephras in the Nepopualco and Xalitzintla sequences.

Major element abundances displayed in a total alkali vs. silica diagram (TAS, Fig. 10a) and bivariate plots (Fig. 10b-e) show that the glass compositions of the late Pleistocene ignimbrites erupted from Tláloc-Telapón are relatively K-rich and rhyolitic. The deposits are compositionally homogenous and plot within a narrow cluster (green area in Fig. 10). They have 74.93-77.66 wt.% SiO_2, 0.27 - 1.60 wt.% CaO, 3.68-4.96 wt.% K_2O, 12.86-14.20 wt.% Al_2O_3, and up to 0.31 wt.% MgO. The products of known eruptions from Iztaccíhuatl and

Table 4

a) Major element composition (average and *standard deviation)* of the matrix glass (anhydrous) from the Tláloc volcano proximal deposits

Sample	MXC-91		MXC-68		MXC-67		MXC-66		MXC-50		MXC-90		MXC-88	
Eruption	Cuauhtémoc Ign.		MWP Ign.		MWP Ign.		MWP Ign.		San Valentin Ign.		San Valentin Ign.		San Valentin Ign.	
n	24		21		22		23		28		27		22	
SiO_2	77.14	*0.18*	77.07	*0.22*	77.05	*0.35*	77.09	*0.21*	77.06	*0.28*	77.16	*0.22*	77.21	*0.31*
TiO_2	0.03	*0.02*	0.03	*0.02*	0.03	*0.02*	0.03	*0.03*	0.03	*0.03*	0.02	*0.02*	0.03	*0.03*
Al_2O_3	13.45	*0.08*	13.49	*0.14*	13.47	*0.25*	13.27	*0.17*	13.55	*0.16*	13.43	*0.19*	13.42	*0.18*
FeOt	0.56	*0.05*	0.58	*0.03*	0.58	*0.05*	0.59	*0.04*	0.57	*0.04*	0.58	*0.04*	0.56	*0.04*
MnO	0.09	*0.02*	0.09	*0.02*	0.09	*0.01*	0.09	*0.02*	0.10	*0.02*	0.08	*0.02*	0.08	*0.02*
MgO	0.03	*0.02*	0.02	*0.02*	0.02	*0.02*	0.04	*0.02*	0.03	*0.02*	0.04	*0.03*	0.04	*0.02*
CaO	0.32	*0.02*	0.31	*0.02*	0.34	*0.05*	0.36	*0.03*	0.31	*0.02*	0.36	*0.03*	0.34	*0.02*
Na_2O	3.77	*0.12*	3.90	*0.13*	4.07	*0.19*	4.04	*0.14*	4.02	*0.13*	3.80	*0.25*	3.77	*0.17*
K_2O	4.56	*0.10*	4.45	*0.08*	4.31	*0.11*	4.44	*0.12*	4.26	*0.11*	4.47	*0.25*	4.49	*0.15*
P_2O_3	0.03	*0.02*	0.01	*0.01*	0.02	*0.01*	0.02	*0.02*	0.03	*0.02*	0.02	*0.02*	0.02	*0.02*
Cl	0.03	*0.01*	0.03	*0.01*	0.03	*0.01*	0.03	*0.01*	0.03	*0.02*	0.03	*0.02*	0.03	*0.02*

Average and standard deviations (italics) for tephra deposits recorded through the Nepopualco sequence. Compositions in weight percent (wt%) were determined using a wavelength-dispersive EMP (see Section 5). n = number of analyses. See Supplementary material for the raw data and secondary standards. * For bimodal samples it is showed a representative composition of each group of plots instead than the general average and standard deviation.

b) Major element composition (average and *standard deviation)* of the matrix glass (anhydrous) from the Popocatépetl volcano proximal deposits

Sample	MXC-118 Pink-3 Pumice		MXC-114* Pink-1 Pumice		MXC-115 Lorenzo Pumice		MXC-120 Milky Pumice		MXC-116 White Pumice		MXC-121 Grey Pumice	
Eruption	15		18		25		17		4		18	
n												
SiO_2	68.45	*0.57*	68.10	71.52	66.58	*0.31*	63.11	*0.54*	69.64	*0.49*	62.15	*1.92*
TiO_2	0.79	*0.03*	0.86	0.72	1.08	*0.04*	0.67	*0.04*	0.48	*0.01*	0.61	*0.17*
Al_2O_3	15.47	*0.22*	15.15	14.29	15.77	*0.11*	18.00	*0.49*	15.99	*0.55*	19.38	*2.15*
FeO*	3.26	*0.13*	3.38	2.62	3.82	*0.12*	4.23	*0.23*	2.52	*0.18*	3.44	*0.81*
MnO	0.07	*0.03*	0.05	0.06	0.05	*0.04*	0.09	*0.03*	0.06	*0.01*	0.06	*0.04*
MgO	1.00	*0.08*	1.12	0.60	1.38	*0.07*	2.01	*0.09*	0.68	*0.04*	1.58	*0.57*
CaO	3.01	*0.20*	3.07	1.90	3.70	*0.16*	5.19	*0.46*	2.66	*0.43*	5.79	*1.31*
Na_2O	4.58	*0.15*	4.87	4.35	4.74	*0.14*	4.39	*0.20*	4.47	*0.24*	4.80	*0.37*
K_2O	3.09	*0.09*	3.14	3.80	2.58	*0.05*	1.91	*0.11*	3.24	*0.21*	1.81	*0.51*
P_2O_3	0.17	*0.05*	0.15	0.05	0.21	*0.03*	0.26	*0.02*	0.12	*0.01*	0.26	*0.08*
Cl	0.10	*0.02*	0.11	0.09	0.07	*0.03*	0.16	*0.06*	0.14	*0.02*	0.13	*0.04*

c) Major element composition (average and *standard deviation)* of the matrix glass (anhydrous) from Iztaccíhuatl proximal deposits.

Sample	MXC-02 Los Pies B&A flow		MXC-03 Nepopualco dry		MXC-04 Nepopualco wet		MXC-05 Nepopualco fall	
Eruption	PDCs				PDCs			
n	21		15		13		21	
SiO_2	76.71	*0.20*	74.80	*2.08*	75.36	*2.44*	71.65	*0.20*
TiO_2	0.21	*0.03*	0.17	*0.03*	0.18	*0.04*	0.28	*0.04*
Al_2O_3	13.09	*0.14*	14.49	*1.38*	14.26	*1.76*	16.22	*0.14*
FeO*	0.95	*0.10*	1.14	*0.30*	0.80	*0.18*	1.69	*0.06*
MnO	0.03	*0.02*	0.05	*0.02*	0.04	*0.02*	0.05	*0.03*
MgO	0.20	*0.02*	0.32	*0.13*	0.22	*0.09*	0.51	*0.03*
CaO	1.08	*0.05*	1.67	*0.65*	1.58	*0.76*	2.54	*0.04*
Na_2O	3.58	*0.16*	4.39	*0.53*	4.24	*0.79*	4.59	*0.16*
K_2O	4.06	*0.17*	2.82	*0.54*	3.19	*0.63*	2.22	*0.04*
P_2O_3	0.02	*0.02*	0.06	*0.03*	0.06	*0.03*	0.08	*0.03*

Popocatépetl are quite variable in composition, and two slightly different evolutionary trends can be discerned (red and blue areas in Fig. 10). The middle Pleistocene Iztaccíhuatl deposits have lower K and Mg (red area in Fig. 10) and higher Ca and Al at given SiO_2 content than deposits from Popocatépetl (blue area in Fig. 10). Glass compositions of the Iztaccíhuatl deposits are rhyolitic with 71.30-78.92 wt.% SiO_2, up to 0.56 wt.% MgO, 0.46-2.65 wt.% CaO, 2.15-4.41 wt.% K_2O, and 11.68-16.61 wt.% Al_2O_3. In contrast, the late Pleistocene - Holocene Popocatépetl eruption deposits have glass compositions that extend from andesite to rhyolite, with ranges of 58.82-71. 84 wt.% SiO_2, 0.58-2.61 wt.% MgO, 1.78-8.13 wt.% CaO, 0.85-3.76 wt.% K_2O, and 14.05-22.73 wt.% Al_2O_3.

Although Popocatépetl's products fall within a consistent linear trend, which implies that the melts have evolved along the same fractionation trend in the past 24 ka, we cannot be certain that all melts erupted from this volcano followed the same fractionation trend during the earlier stages of its history. Our studied tephra deposits span an older time interval (Section 6), but it is notable that many of these deposits overlap compositionally with our defined post-24 ka Popocatépetl field. This suggests that magmas of a similar composition have been erupted over a long-time interval from the SNVR, and in the absence of conflicting information, we attribute all magmas that plot along the higher-K fractionation trend to the Popocatépetl source. Temporally, our known Iztaccíhuatl samples are much closer in age to the stratigraphic interval that is being studied, but as discussed in section 4.1.2, the limitation of these is that our compositional field is only based on two closely spaced eruptions. Nevertheless, these Iztaccíhuatl samples define a distinct linear compositional trend from the post-24 ka Popocatépetl field, with lower K_2O at given SiO_2 contents, and we use this to define

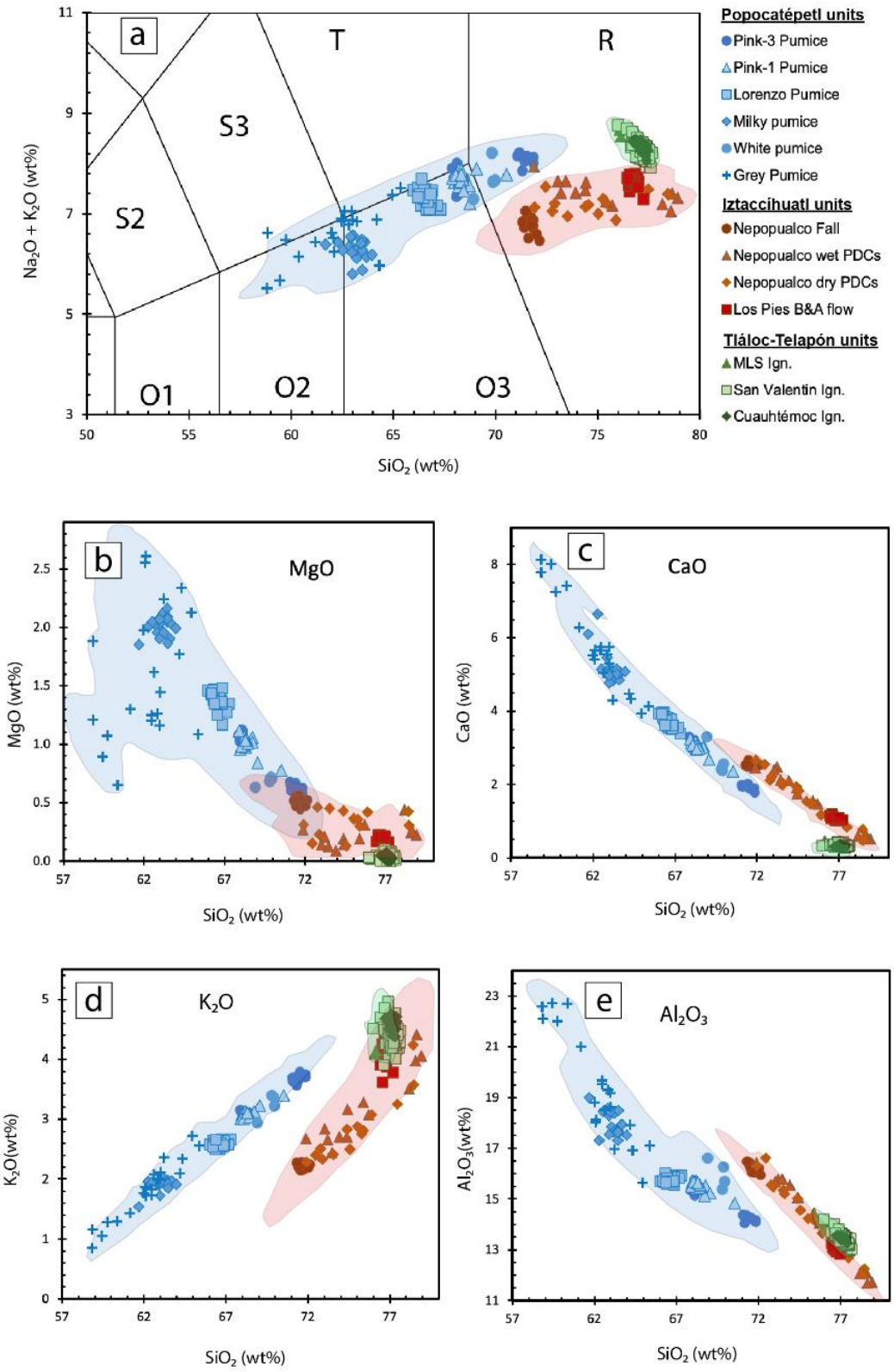

a
T
R
S3
S2
O1
O2
O3
Na2O + K2O (wt%)
SiO2 (wt%)
Popocatépetl units
Pink-3 Pumice
Pink-1 Pumice
Lorenzo Pumice
Milky pumice
White pumice
Grey Pumice
Iztaccihuatl units
Nepopualco Fall
Nepopualco wet PDCs
Nepopualco dry PDCs
Los Pies B&A flow
Tláloc-Telapón units
MLS Ign.
San Valentin Ign.
Cuauhtémoc Ign.
b
MgO
MgO (wt%)
SiO2 (wt%)
c
CaO
CaO (wt%)
SiO2 (wt%)
d
K2O
K2O(wt%)
SiO2 (wt%)
e
Al2O3
Al2O3(wt%)
SiO2 (wt%)

Fig. 10. Glass chemistry of previously described pyroclastic deposits erupted by Popocatépetl, Iztaccíhuatl, and Tláloc-Telapón volcanoes, with the addition of an ascribed Iztaccíhuatl deposit (see Section 4.1.2) plotted in: **a.** Total alkalis vs silica (TAS diagram) of the tephra units; and bi-variate plots of **(b)** SiO_2 vs MgO, **(c)** SiO_2 vs CaO, **(d)** SiO_2 vs K_2O and **(e)** SiO_2 vs Al_2O_3 (selected bivariate plots). Compositional fields of Popocatépetl (blue area Iztaccíhuatl (red area, and Tláloc (green area volcanoes estimated with OxCal/RESET software (Bronk Ramsey et al., 2015).

---

an Iztaccíhuatl compositional field. Although it is possible that the melt compositions erupted by both Popocatépetl and Iztaccíhuatl varied between these low-K and high-K trends over time, we do not consider this likely, given that fractionation trends at other closely-spaced volcanoes are observed to be stable over prolonged periods of time (e.g. Daisen and Sambe volcanoes in Japan; Albert et al., 2019). In the absence of further source compositional constraints, we adopt the simplest interpretation and attribute the two low-K and high-K compositional types that occur within our dataset, to Iztaccíhuatl and Popocatépetl respectively.

5.2 Composition of Nepopualco tephras and correlation to their volcanic source

The tephra layers in the Nepopualco site have a wide range of sub-alkaline glass compositions, from andesites to rhyolites (Fig. 11 and Table 5; secondary standards in Supplementary Material 1 in Sunyé-Puchol et al. (2021)). These major element glass compositions of the Nepopualco tephras (Fig. 11 b-e) partially plot within the two defined compositional fields of Iztaccíhuatl and Popocatépetl. For example, the andesitic to dacitic glass compositions of NT-6, 9, 12, and NT-16 to 23 (concentrations of 61.40-69.61 wt.% SiO_2, 0.92-2.54 wt.% MgO, 2.93-6.07 wt.% CaO, 1.62-2.48 wt.% K_2O, and 18.72-14.91 wt.% Al_2O_3) plot within the high-K

Table 5
Major element composition (average and *standard deviation)* of the matrix glass (anhydrous) from the Nepopualco tephra sequence.

Sample	MXC-02		MXC-03		MXC-04		MXC-05		MXC-06		MXC-07		MXC-08		MXC-09		MXC-10**	
Eruption	NT-1 (L. Pies B&A)		NT-2 (Nepopualco Ign: Dry and wet PDC's and fallout)						NT-3		NT-04		NT-05		NT-06		NT-07	
n	21		15		13		21		24		27		22		23		24	
SiO_2	76.71	*0.20*	74.80	*2.08*	75.36	*2.44*	71.65	*0.20*	73.26	*1.04*	72.13	*1.17*	69.26	*1.51*	67.94	*0.40*	73.95	66.27
TiO_2	0.21	*0.03*	0.17	*0.03*	0.18	*0.04*	0.28	*0.04*	0.31	*0.07*	0.29	*0.06*	1.04	*0.20*	0.90	*0.05*	0.18	0.50
Al_2O_3	13.09	*0.14*	14.49	*1.38*	14.26	*1.76*	16.22	*0.14*	14.65	*0.49*	15.44	*0.57*	14.51	*1.23*	15.52	*0.27*	14.56	17.95
FeOt	0.95	*0.10*	1.14	*0.30*	0.80	*0.18*	1.69	*0.06*	1.86	*0.26*	1.96	*0.28*	3.79	*0.71*	3.68	*0.19*	1.34	2.80
MnO	0.03	*0.02*	0.05	*0.02*	0.04	*0.02*	0.05	*0.03*	0.04	*0.02*	0.06	*0.02*	0.06	*0.02*	0.07	*0.02*	0.07	0.06
MgO	0.20	*0.02*	0.32	*0.13*	0.22	*0.09*	0.51	*0.03*	0.45	*0.12*	0.56	*0.11*	0.74	*0.30*	1.19	*0.09*	0.48	0.91
CaO	1.08	*0.05*	1.67	*0.65*	1.58	*0.76*	2.54	*0.04*	1.96	*0.31*	2.11	*0.31*	3.05	*0.72*	3.47	*0.22*	1.57	4.62
Na_2O	3.58	*0.16*	4.39	*0.53*	4.24	*0.79*	4.59	*0.16*	4.77	*0.22*	4.61	*0.11*	4.52	*0.24*	4.68	*0.20*	4.90	4.79
K_2O	4.06	*0.17*	2.82	*0.54*	3.19	*0.63*	2.22	*0.04*	2.56	*0.17*	2.63	*0.14*	2.75	*0.36*	2.20	*0.13*	2.80	1.85
P_2O_3	0.02	*0.02*	0.06	*0.03*	0.06	*0.03*	0.08	*0.03*	0.07	*0.03*	0.10	*0.04*	0.19	*0.07*	0.19	*0.02*	0.06	0.19
Cl	0.08	*0.02*	0.09	*0.02*	0.07	*0.05*	0.17	*0.09*	0.08	*0.04*	0.11	*0.02*	0.09	*0.07*	0.16	*0.19*	0.10	0.07

Average and standard deviations (italics) for tephra deposits recorded through the Nepopualco sequence. Compositions in weight percent (wt%) were determined using a wavelength-dispersive EMP (see Section 5). N = number of analyses. See Supplementary material for the raw data and secondary standards. * Bimodal samples are shown as selected representative compositions for each sub-component instead of by the average and standard deviation.

Table 5 *(continued)*

Sample	MXC-11*		MXC-12		MXC-13*		MXC-14		MXC-15		MXC-35		MXC-36		MXC-37		MXC-38	
Eruption	NT-08		NT-09		NT-10		NT-11		NT-12		NT-13		NT-14		NT-15		NT-16	
n	16		5		21		16		10		25		25		23		17	
SiO_2	74.25	70.66	62.47	*0.31*	73.15	68.22	71.86	*0.34*	64.34	*0.31*	76.30	*1.39*	64.93	*0.33*	62.36	*0.34*	68.34	*0.99*
TiO_2	0.28	0.65	1.27	*0.09*	0.53	0.83	0.41	*0.03*	0.88	*0.05*	0.30	*0.07*	1.00	*0.12*	1.08	*0.03*	0.77	*0.07*
Al_2O_3	14.39	15.35	16.80	*0.26*	13.99	15.55	15.07	*0.21*	17.32	*0.38*	13.12	*0.75*	16.57	*0.34*	17.07	*0.14*	15.82	*0.36*
FeOt	1.67	2.75	5.52	*0.11*	2.39	3.61	2.29	*0.11*	3.99	*0.26*	1.33	*0.26*	4.08	*0.23*	5.12	*0.18*	3.27	*0.17*
MnO	0.03	0.03	0.11	*0.01*	0.02	0.06	0.04	*0.02*	0.06	*0.02*	0.03	*0.02*	0.07	*0.02*	0.09	*0.02*	0.07	*0.02*
MgO	0.26	0.71	2.13	*0.29*	0.59	1.17	0.60	*0.04*	1.80	*0.24*	0.21	*0.06*	1.87	*0.16*	2.34	*0.07*	1.14	*0.25*
CaO	2.05	2.65	4.71	*0.18*	2.11	3.38	2.29	*0.09*	4.52	*0.23*	1.18	*0.31*	4.55	*0.16*	5.27	*0.19*	3.41	*0.34*
Na_2O	4.14	4.06	4.70	*0.12*	4.39	4.69	4.62	*0.13*	4.86	*0.18*	3.79	*0.18*	4.63	*0.16*	4.61	*0.13*	4.46	*0.23*
K_2O	2.88	2.94	1.94	*0.11*	2.72	2.22	2.63	*0.06*	1.93	*0.15*	3.62	*0.18*	2.02	*0.09*	1.79	*0.08*	2.42	*0.12*
P_2O_3	0.00	0.12	0.28	*0.08*	0.05	0.18	0.08	*0.03*	0.22	*0.03*	0.05	*0.03*	0.20	*0.04*	0.20	*0.04*	0.21	*0.06*
Cl	0.04	0.08	0.07	*0.03*	0.06	0.09	0.13	*0.09*	0.08	*0.01*	0.07	*0.02*	0.07	*0.03*	0.08	*0.02*	0.15	*0.08*

Table 5 *(continued)*

Sample	MXC-39		MXC-41*		MXC-42		MXC-43		MXC-44		MXC-45		MXC-46		MXC-47		MXC-48	
Eruption	NT-17		NT-18		NT-19		NT-20		NT-21		NT-22		NT-23		NT-24		NT-25	
N	20		21		22		25		20		16		23		27		15	
SiO_2	63.83	*0.93*	66.54	63.58	66.09	*0.84*	61.40	*0.30*	61.88	*0.30*	66.56	*0.59*	69.14	*0.31*	76.79	*0.25*	77.03	*0.78*
TiO_2	1.04	*0.09*	0.87	0.95	0.72	*0.04*	1.02	*0.05*	1.04	*0.04*	0.69	*0.04*	0.61	*0.04*	0.09	*0.02*	0.17	*0.03*
Al_2O_3	16.84	*0.46*	15.63	17.09	17.42	*0.62*	17.80	*0.16*	17.58	*0.12*	16.97	*0.47*	15.89	*0.18*	12.59	*0.18*	13.19	*0.45*
FeOt	4.82	*0.38*	3.97	4.36	3.33	*0.20*	5.00	*0.18*	5.04	*0.13*	3.58	*0.21*	2.93	*0.09*	1.04	*0.04*	0.87	*0.14*
MnO	0.09	*0.02*	0.05	0.06	0.05	*0.02*	0.09	*0.02*	0.08	*0.02*	0.07	*0.02*	0.06	*0.02*	0.03	*0.02*	0.04	*0.02*
MgO	1.70	*0.19*	1.51	1.99	1.20	*0.18*	2.50	*0.09*	2.43	*0.10*	1.16	*0.14*	0.97	*0.12*	0.04	*0.02*	0.22	*0.06*
CaO	4.73	*0.33*	4.01	4.82	4.16	*0.43*	5.43	*0.20*	5.37	*0.16*	3.73	*0.30*	3.07	*0.18*	0.41	*0.02*	1.16	*0.20*
Na_2O	4.83	*0.28*	4.31	4.60	4.79	*0.22*	4.79	*0.16*	4.53	*0.11*	4.90	*0.19*	4.68	*0.18*	4.01	*0.18*	4.06	*0.19*
K_2O	1.81	*0.14*	2.29	2.20	1.97	*0.22*	1.71	*0.11*	1.79	*0.05*	2.06	*0.15*	2.39	*0.04*	4.85	*0.20*	3.12	*0.23*
P_2O_3	0.22	*0.04*	0.17	0.27	0.16	*0.04*	0.20	*0.04*	0.19	*0.03*	0.21	*0.04*	0.14	*0.02*	0.01	*0.01*	0.04	*0.03*

Popocatépetl compositional field (blue area in Fig. 11), and most likely were sourced from Popocatépetl. The rhyolitic glasses of NT-2 to 4, and NT-8, 11 and 13 (concentrations of 70.52-78.91 wt.% SiO_2, 0.12-0.75 wt.% MgO, 0.46-2.85 wt.% CaO, 2.28-4.46 wt.% K_2O, and 11.67-16.43 wt.% Al_2O_3) plot within the low-K Iztaccíhuatl compositional field (red area in Fig. 11). NT-24, which is a K-rich rhyolitic white fine-ash fallout (75.65-77.04 wt.% SiO_2, 0.36-0.47 wt.% CaO, 4.63-5.43 wt.% K_2O, 12.39-13.40 wt.% Al_2O_3, and up to 0.09 wt.% MgO), plots partially within the compositional field defined by the known Tláloc-Telapón pyroclastic deposits, and is distinct from all other tephras in the Nepopualco sequence (orange dots and green area in Fig. 11).

Three tephras in Nepopualco do not plot clearly into any of our defined compositional fields. The NT-5, 7, and 10 units (grey and blue diamonds, and yellow square in Fig. 11) have a bimodal glass composition, which overlap with both the Popocatépetl and Iztaccíhuatl fields.

5.3 Composition of Xalitzintla tephras and correlation to their volcanic source

Major element glass compositions of the tephras around Xalitzintla also span a wide range of sub-alkaline compositions (Table 6; secondary standards in Supplementary Material 1 in Sunyé-Puchol et al. (2021)), but mostly plot within the Popocatépetl compositional field (andesite-dacite units within and close to the blue area in Fig. 12; 59.61-68.47 wt.% SiO_2, 0.84-2.83 wt.% MgO, 2.86-6.03 wt.% CaO, 1.42-3.28 wt.% K_2O, and 15.42-18.28 wt.% Al_2O_3), with only two units within the Iztaccíhuatl field (XQT-3 and FRT-1 within the red area of Fig. 12; 71.38-75.34 wt.% SiO_2, 0.13-0.67 wt.% Mg, 1.23-2.48 wt.% CaO, 2.50-3.16 wt.% K_2O, and 13.92-15.61 wt.% Al_2O_3). None of the Xalitzintla tephras plot into the Tláloc-Telapón compositional field (no plots within green area, Fig. 12), but several tephras plot outside our defined

Table 6

Major element composition (average and *standard deviation)* of the matrix glass (anhydrous) from the tephras recorded in Xalitzintla region by outcrops

a) East of the Restaurant site

Sample	MXC-16**		MXC-17		MXC-18		MXC-19		MXC-20		MXC-21*		MXC-22		MXC-23		MXC-24	
Eruption	ERT-1		ERT-2		ERT-2		ERT-3		ERT-3		ERT-4		ERT-5		ERT-6		ERT-7	
n	29		23		14		13		13		10		21		25		26	
SiO_2	68.12	65.72	62.37	67.53	*0.26*	67.10	*0.23*	67.93	*0.28*	67.43	*0.42*	70.05	67.77	66.05	*0.27*	64.92	*0.38*	66.64	*0.32*
TiO_2	1.00	0.92	0.84	0.92	*0.05*	0.97	*0.04*	0.87	*0.03*	0.90	*0.04*	0.88	1.08	1.04	*0.03*	1.09	*0.05*	0.94	*0.03*
Al_2O_3	14.66	16.16	17.20	15.85	*0.22*	15.99	*0.13*	15.74	*0.18*	15.90	*0.13*	14.69	15.20	16.02	*0.13*	16.05	*0.13*	15.81	*0.11*
FeOt	3.75	3.81	4.66	3.35	*0.09*	3.50	*0.12*	3.30	*0.09*	3.46	*0.14*	3.22	3.94	4.01	*0.15*	4.31	*0.16*	3.73	*0.12*
MnO	0.08	0.07	0.05	0.05	*0.02*	0.05	*0.01*	0.04	*0.01*	0.05	*0.02*	0.06	0.03	0.06	*0.02*	0.08	*0.02*	0.07	*0.02*
MgO	1.11	1.52	2.53	1.21	*0.05*	1.30	*0.06*	1.08	*0.07*	1.22	*0.09*	0.92	1.21	1.44	*0.04*	1.77	*0.05*	1.54	*0.06*
CaO	2.95	4.13	5.75	3.26	*0.12*	3.42	*0.14*	3.08	*0.14*	3.29	*0.20*	2.62	3.20	3.65	*0.14*	4.23	*0.15*	3.89	*0.20*
Na_2O	4.93	4.67	4.49	4.48	*0.20*	4.45	*0.13*	4.65	*0.11*	4.55	*0.14*	4.38	4.47	4.78	*0.15*	4.93	*0.27*	4.82	*0.21*
K_2O	3.11	2.62	1.91	3.02	*0.08*	2.94	*0.07*	3.04	*0.09*	2.94	*0.07*	3.02	2.76	2.60	*0.05*	2.31	*0.04*	2.32	*0.06*
P_2O_3	0.22	0.29	0.14	0.18	*0.04*	0.18	*0.04*	0.17	*0.03*	0.17	*0.02*	0.13	0.21	0.26	*0.02*	0.23	*0.03*	0.20	*0.03*
Cl	0.07	0.09	0.06	0.16	*0.16*	0.09	*0.02*	0.09	*0.04*	0.08	*0.01*	0.03	0.11	0.09	*0.05*	0.07	*0.02*	0.05	*0.01*

Table 6 *(continued)*

c) Fork in the Road site

Sample	MXC-102		MXC-103		MXC-104		MXC-105		MXC-106*		MXC-107	
Eruptio	FRT-1		FRT-2		FRT-3		FRT-4		FRT-5		FRT-6	
n	25		14		13		19		28		19	
SiO_2	72.09	*0.21*	70.80	*0.62*	63.80	0.76	63.21	*0.35*	73.21	68.09	*66.02*	*0.62*
TiO_2	0.42	*0.03*	0.78	*0.04*	0.79	0.08	0.66	*0.04*	0.49	0.91	*0.98*	*0.06*
Al_2O_3	15.14	*0.15*	14.47	*0.30*	17.51	1.08	17.96	*0.22*	14.39	15.49	15.92	0.20
FeOt	2.19	*0.09*	2.99	*0.22*	4.23	0.54	4.31	*0.18*	1.92	3.47	*3.96*	*0.13*
MnO	0.04	*0.02*	0.06	*0.02*	*0.07*	*0.02*	0.08	*0.02*	0.02	0.07	0.06	0.02
MgO	0.57	*0.03*	0.75	*0.07*	1.65	0.46	2.02	*0.08*	0.47	1.11	*1.59*	*0.13*
CaO	2.28	*0.06*	2.37	*0.18*	4.39	0.63	5.04	*0.22*	1.79	3.01	*3.93*	*0.21*
Na_2O	4.45	*0.16*	4.77	*0.12*	4.75	0.48	4.37	*0.19*	3.82	4.65	4.80	0.28
K_2O	2.63	*0.05*	2.74	*0.09*	2.38	0.37	1.91	*0.07*	3.72	2.98	2.47	0.07
P_2O_3	0.08	*0.02*	0.16	*0.11*	0.27	0.06	0.22	*0.04*	0.10	0.16	0.20	0.04
Cl	0.11	*0.07*	0.13	*0.01*	0.17	0.19	0.24	*0.25*	0.06	0.07	*0.06*	*0.02*

Average and standard deviations (italics) for tephra deposits recorded through the Nepopualco sequence. Compositions in weight percent (wt%) were determined using a wavelength-dispersive EMP (see Section 5). N = number of analyses. See Supplementary material for the raw data and secondary standards. Bimodal* and trimodal** samples are shown as selected representative compositions for each sub-component instead of by the average and standard deviation."

Table 6 *(continued)*

b) West of the Restaurant site

Sample	MXC-25**		MXC-26		MXC-27		MXC-28		MXC-29		MXC-30		MXC-31		MXC-32		MXC-33		MXC-34	
Eruption	WRT-1		WRT-2		WRT-2		WRT-3		WRT-3		WRT-4		WRT-5		WRT-6		WRT-7		WRT-8	
n	23		14		11		26		15		21		22		12		23		12	
SiO_2	71.80	66.79	60.19	67.56	*0.36*	66.60	*0.52*	61.35	*0.34*	60.81	*0.21*	61.70	*0.23*	68.49	*0.62*	66.92	*0.41*	68.95	*0.46*	65.02	*0.59*
TiO_2	0.76	1.00	1.05	0.51	*0.04*	0.81	*0.07*	1.03	*0.04*	1.04	*0.03*	1.04	*0.03*	0.75	*0.06*	0.67	*0.04*	0.61	*0.04*	0.96	*0.11*
Al_2O_3	14.07	15.29	17.56	16.87	*0.27*	16.73	*0.49*	17.83	*0.21*	18.04	*0.16*	17.53	*0.15*	15.96	*0.31*	16.63	*0.28*	15.92	*0.34*	16.72	*0.80*
FeOt	2.86	4.85	5.95	3.13	*0.18*	3.61	*0.18*	5.00	*0.23*	5.26	*0.16*	5.19	*0.12*	3.16	*0.19*	3.65	*0.15*	2.97	*0.08*	4.02	*0.45*
MnO	0.04	0.06	0.12	0.05	*0.02*	0.06	*0.02*	0.09	*0.02*	0.08	*0.02*	0.09	*0.02*	0.05	*0.02*	0.07	*0.02*	0.05	*0.02*	0.08	*0.02*
MgO	0.55	1.65	3.62	1.06	*0.10*	1.22	*0.11*	2.54	*0.11*	2.69	*0.10*	2.46	*0.08*	1.04	*0.07*	1.19	*0.09*	0.95	*0.05*	1.53	*0.27*
CaO	2.01	3.87	6.50	3.64	*0.22*	3.66	*0.22*	5.52	*0.18*	5.55	*0.16*	5.25	*0.10*	3.20	*0.20*	3.49	*0.18*	3.11	*0.25*	4.34	*0.48*
Na_2O	4.72	3.04	3.27	4.65	*0.31*	4.86	*0.17*	4.67	*0.11*	4.59	*0.09*	4.69	*0.09*	4.55	*0.32*	4.95	*0.15*	4.78	*0.17*	4.71	*0.28*
K_2O	3.05	3.18	1.57	2.01	*0.17*	2.18	*0.20*	1.71	*0.11*	1.65	*0.06*	1.79	*0.06*	2.49	*0.11*	2.14	*0.16*	2.36	*0.09*	2.24	*0.19*
P_2O_3	0.09	0.25	0.11	0.16	*0.03*	0.17	*0.04*	0.19	*0.04*	0.21	*0.02*	0.20	*0.03*	0.16	*0.04*	0.20	*0.04*	0.14	*0.04*	0.26	*0.03*

Table 6 *(continued)*

d) Xalitzintla Quarry site

Sample	MXC-97		MXC-98*		MXC-99		MXC-100		MXC-101	
Eruptio	XQT-1		XQT-2		XQT-3		XQT-4		XQT-7	
n	20		20		22		25		11	
SiO_2	57.48	*0.65*	70.13	56.84	74.89	*0.27*	60.43	*0.46*	62.06	*0.32*
TiO_2	1.19	*0.07*	1.14	1.01	0.29	*0.04*	1.32	*0.06*	1.04	*0.04*
Al_2O_3	16.57	*0.42*	13.60	16.39	14.12	*0.22*	17.07	*0.14*	17.45	*0.25*
FeOt	6.99	*0.37*	4.31	3.61	1.42	*0.13*	6.57	*0.27*	5.70	*0.19*
MnO	0.13	*0.02*	0.08	0.04	0.03	*0.02*	0.12	*0.02*	0.11	*0.03*
MgO	4.82	*0.25*	0.79	0.77	0.34	*0.07*	2.43	*0.13*	2.04	*0.08*
CaO	8.00	*0.32*	2.67	3.95	1.62	*0.08*	5.41	*0.19*	4.89	*0.21*
Na_2O	3.44	*0.24*	5.20	4.80	4.12	*0.20*	4.33	*0.16*	4.67	*0.21*
K_2O	1.15	*0.10*	1.83	2.31	3.02	*0.06*	1.94	*0.08*	1.75	*0.13*
P_2O_3	0.18	*0.03*	0.21	0.20	0.04	*0.03*	0.29	*0.04*	0.24	*0.05*

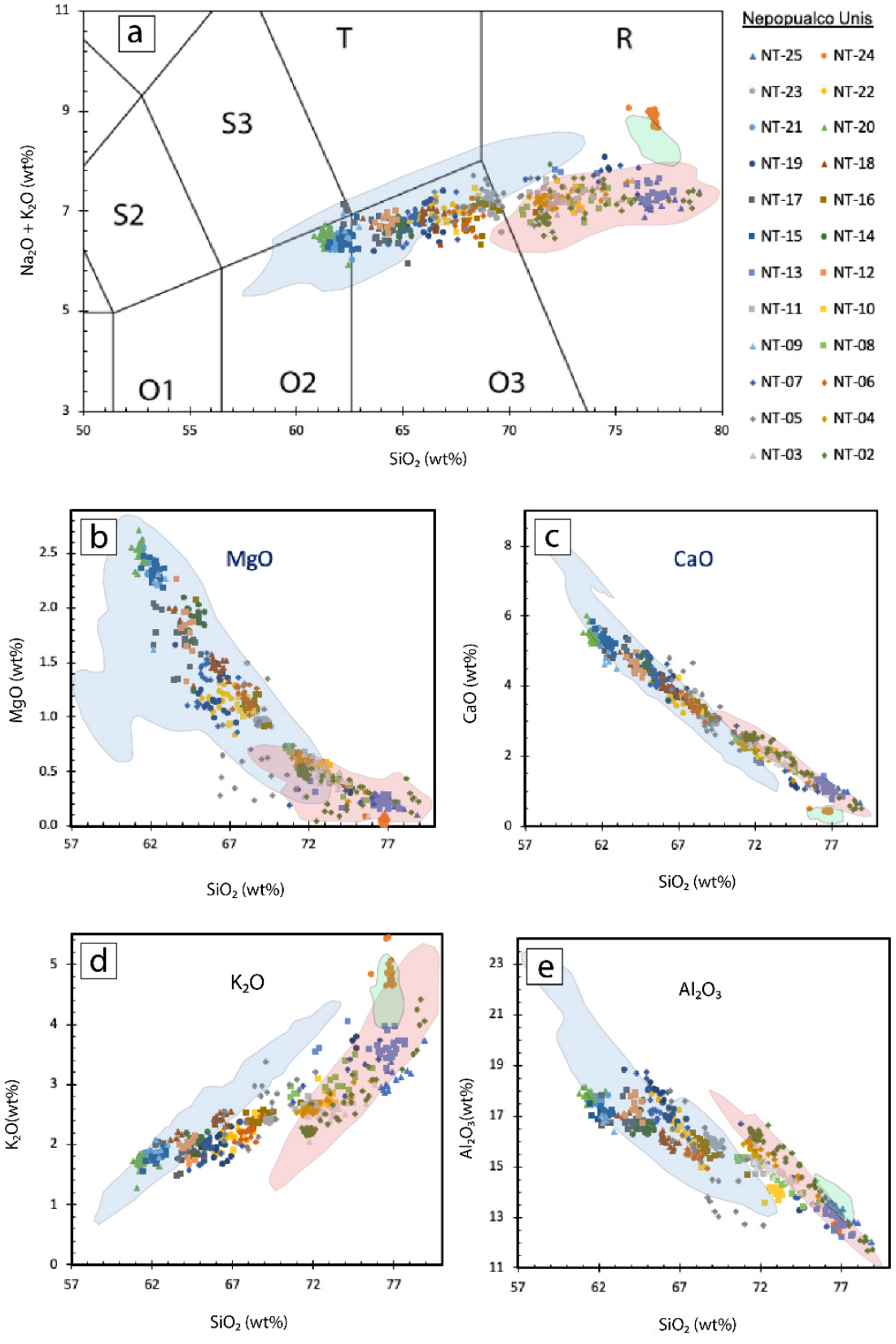

a
T
R
S3
S2
O1
O2
O3
Na2O + K2O (wt%)
SiO2 (wt%)
Nepopualco Unis
NT-25
NT-24
NT-23
NT-22
NT-21
NT-20
NT-19
NT-18
NT-17
NT-16
NT-15
NT-14
NT-13
NT-12
NT-11
NT-10
NT-09
NT-08
NT-07
NT-06
NT-05
NT-04
NT-03
NT-02
b
MgO
MgO (wt%)
SiO2 (wt%)
c
CaO
CaO (wt%)
SiO2 (wt%)
d
K2O
K2O(wt%)
SiO2 (wt%)
e
Al2O3
Al2O3(wt%)
SiO2 (wt%)

Fig. 11. (a) Total alkalis vs silica (TAS) of 24 analysed pyroclastic deposits through the Nepopualco gully; and bivariate plots of **(b)** SiO_2 vs MgO, **(c)** SiO_2 vs CaO, **(d)** SiO_2 vs K_2O and **(e)** SiO_2 vs. Al_2O_3, displayed together with the compositional field of Popocatépetl (blue area, Iztaccíhuatl (red area), and Tláloc-Telapón (green area) volcanoes.

Popocatépetl field (yellow diamonds, Fig. 12a). Other tephra layers outside the fields include XQT-4 (blue diamonds in Fig. 12) and WRT-1 (red square in Fig. 12), which are andesites with slightly lower CaO and Al_2O_3 glass compositions relative to the Popocatépetl trend.

6. NEW $^{40}Ar/^{39}Ar$ DATES

Various deposits from the studied outcrops were $^{40}Ar/^{39}Ar$ dated in this study. These new $^{40}Ar/^{39}Ar$ age ranges are reported at 2σ. From these, two analyses related to the San Valentín Ignimbrite (samples MXC-50 and MXC-88 from sites 2 and 3 respectively in Fig. 1c), that erupted from Tláloc-Telapón volcano, were previously dated by radiocarbon to c. 46 cal. ka BP (around the limit of the technique; Rueda et al., 2007; García-Tovar and Martínez-Serrano, 2011; Macías et al., 2012). Analyses on single sanidine crystals yielded ages of 101 ± 2 ka (MXC-50; 2σ) and 103 ± 3 ka (MXC-88; 2σ), indicating that this ignimbrite is substantially older than previously inferred from radiocarbon dating (Table 7). Moreover, new radiocarbon dates obtained from large charcoal pieces found within this deposit were beyond the upper limit of this method (>50 ka; Supplementary Material 2 in Sunyé-Puchol et al. (2021)).

Three $^{40}Ar/^{39}Ar$ ages were obtained from the Nepopualco sequence. Unfortunately, no sanidines were found in the tephras so the resulting ages were determined from plagioclase and hornblende concentrates, producing ages with larger errors. Analyses on hornblendes

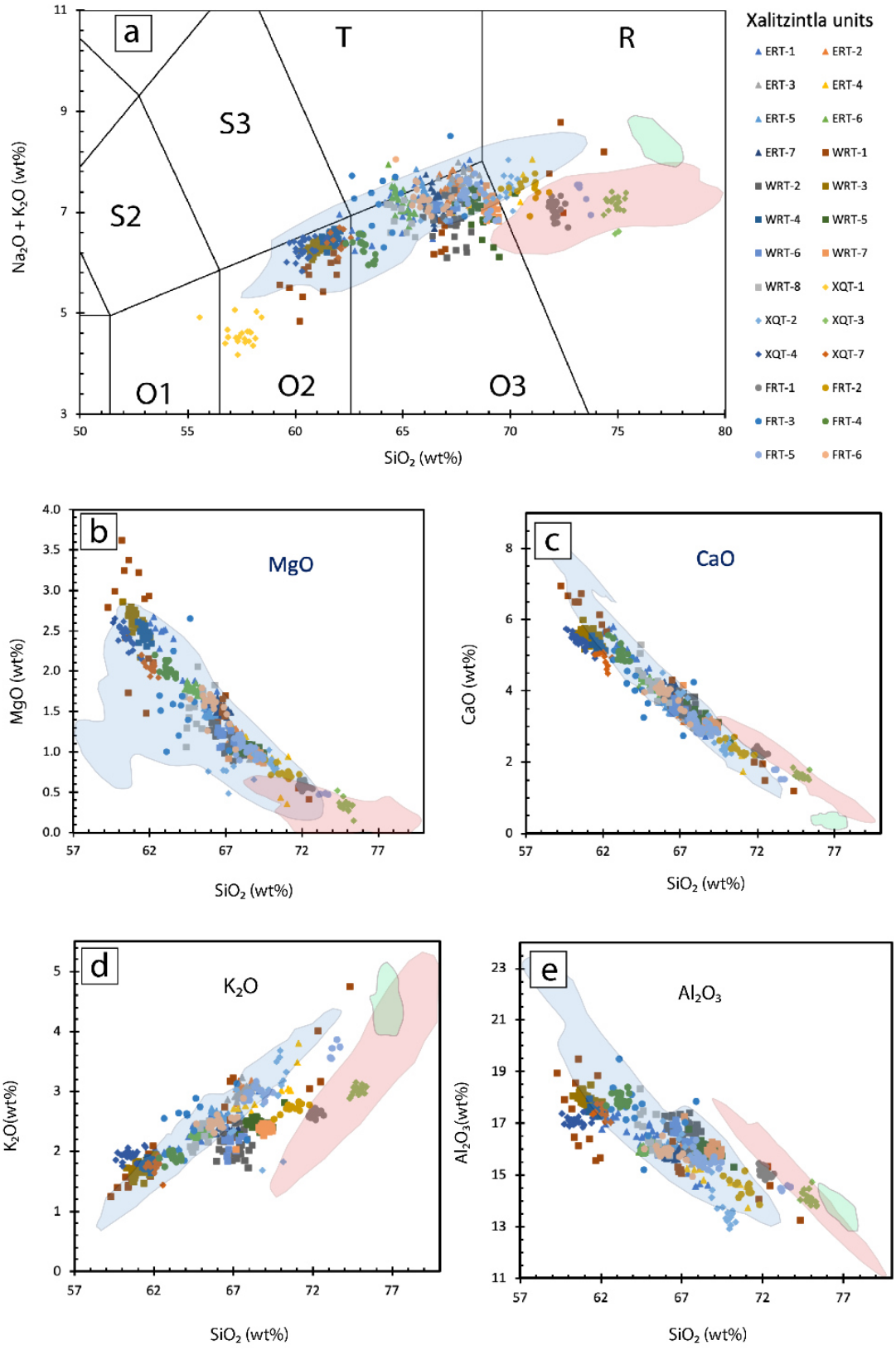

a
T
R
S3
S2
O1
O2
O3
Na2O + K2O (wt%)
SiO2 (wt%)
Xalitzintla units
ERT-1
ERT-2
ERT-3
ERT-4
ERT-5
ERT-6
ERT-7
WRT-1
WRT-2
WRT-3
WRT-4
WRT-5
WRT-6
WRT-7
WRT-8
XQT-1
XQT-2
XQT-3
XQT-4
XQT-7
FRT-1
FRT-2
FRT-3
FRT-4
FRT-5
FRT-6
b
MgO
MgO (wt%)
SiO2 (wt%)
c
CaO
CaO (wt%)
SiO2 (wt%)
d
K2O
K2O(wt%)
SiO2 (wt%)
e
Al2O3
Al2O3(wt%)
SiO2 (wt%)

Fig. 12. (a) Total alkalis vs silica (TAS) of 26 tephras identified in the Xalitzintla region (shown in **Fig. 6(a)**; and bivariate plots of **(b)** SiO_2 vs MgO, **(c)** SiO_2 vs CaO, **(d)** SiO_2 vs K_2O and **(e)** SiO_2 vs Al_2O_3, displayed together with the compositional field of Popocatépetl (blue area), Iztaccíhuatl (red area), and Tláloc-Telapón (green area) volcanoes.

(sample MXC-05) from NT-2 (the Nepopualco Ignimbrite), which is the lowermost tephra of this sequence, yielded an eruption age of 631 ± 44 ka (2σ). This new date is consistent with the underlying LPDAD age range but suggests that the DAD is older than the median age previously reported (440 ± 190 ka; Macías et al., 2012; Fig. 3). Analyses on plagioclase from the NT-12 fallout unit (sample MXC-15), located in the Middle Nepopualco Tephras (Fig. 4), yielded an eruption age of 620 ± 52 ka (2σ). This age is very similar to that of NT-2, but based on their error averages, a time interval of up to c.100 ka could have elapsed between the NT-2 and NT-12 eruptions. At least nine additional explosive eruptions occurred during this period based on the Nepopualco stratigraphy (Table 2). Analyses on plagioclase from the NT-23 (sample MXC-46), located in the Upper Nepopualco Tephras (Fig. 5), yielded an eruption age of 369 ± 22 ka (2σ). Several eruption deposits occur between the two dated horizons (NT-12 and NT-23).

Three additional reliable ages were obtained from the Xalitzintla Restaurant sites: one from a tephra exposed in the easternmost outcrop (ERT-3 unit) and two from tephras in the westernmost outcrop (WRT-6 and 7). Unfortunately, tephras from the other two Xalitzintla sites (Quarry and Fork in the road) did not yield suitable results due to the absence of appropriate minerals (e.g., sanidines or hornblendes, and inclusion-free plagioclases). All $^{40}Ar/^{39}Ar$ dates for these Xalitzintla tephras were from aliquots of plagioclase crystals. ERT-2

Table 7
Summary of 40Ar/39Ar dates reported in this chapter

Unit	Sample	Mineral	Location		Locality	Outcrop	Age (ka;2σ)	MSWD
			North	West				
NT-2	MXC-05	Hornblende	19.149749°	98.508040°	Nepopualco	5	630 ± 44	1.49
NT-12	MXC-15	Plagioclase	19.149749°	98.508040°	Nepopualco	5	619 ± 52	1.19
ERT-3	MXC-19	Plagioclase	19.078794°	98.506966°	Xalitzintla	6	236 ± 24	1.08
WRT-6	MXC-32	Plagioclase	19.080099°	98.507531°	Xalitzintla	7	431 ± 40	1.50
WRT-7	MXC-33	Plagioclase	19.080099°	98.507531°	Xalitzintla	7	353 ± 58	1.54
NT-23	MXC-46	Plagioclase	19.149749°	98.508040°	Nepopualco	5	368 ± 22	1.35
SVI	MXC-50	Sanidine*	19.477587°	98.575406°	Nanacamilpa	2	101 ± 2	1.20
SVI	MXC-88	Sanidine*	19.396556°	98.624861°	San Juan C.	3	103 ± 3	1.30

SVI = San Valentin Ignimbrite; NT = Nepopualco Tephras; ERT = East of the Restaurant Tephras; WRT = West of the Restaurant Tephras; ka = thousand years; 2σ = two sigma; MSWD = Mean Squared Weighted Deviation

yielded a 2σ eruption age of 236 ± 24 ka (Fig. 6), WRT-6 an age of 431 ± 40 ka (Fig. 7) and WRT-7 an age of 354 ± 58 ka (Table 7). A summary of the $^{40}Ar/^{39}Ar$ dates is reported in Table 7 (raw data and age plots in Supplementary Material 3 and 4 in Sunyé-Puchol et al. (2021)).

7. TEPHRA CORRELATIONS

7.1 Tephra correlations between the Xalitzintla and Nepopualco sequences

In order to complement the chemical characterization and the correlation of the studied tephras, we plotted the abundance of TiO_2 vs SiO_2 for the Xalitzintla and Nepopualco tephras (Fig. 13). The data are distributed into two well-defined fields, which largely coincide with the defined compositional fields of Popocatépetl and Iztaccíhuatl volcanoes (blue and red areas in Fig. 13a). Because these plots do not follow a narrow trend (as generally is the case in the other bivariate plots of MgO, CaO, K_2O, and Al_2O_3; Figs. 11 and 12), but are more spatially separated, it is possible to infer some tephra correlations between these two sites. For example, the rhyolitic FRT-1 tephra (yellow triangles in Fig. 13e) recorded in Xalitzintla is very similar to the NT-11 (solid green diamonds in Fig. 13e) in its glass composition (rhyolitic), both forming tight clusters with limited overlap with any other units. Both deposits share a similar mineralogy (e.g. both contain hornblende; Tables 2 and 3) and physical characteristics, being c.1 m-thick, normal graded, white pumice fallout deposits that are lithic-rich at the top (see section 4 for more details and Fig. 14). We infer that these pyroclastic deposits (FRT-1 and NT-11) are associated to the same explosive eruption and were most likely produced by Iztaccíhuatl volcano. Another rhyolitic tephra recorded in Xalitzintla, XQT-3 (empty red diamonds in Fig. 13e), partially overlaps the compositional field of NT-3, NT-4, and NT-8 (empty green triangles and diamonds, and green dashes in Fig. 13e), but based on its overall

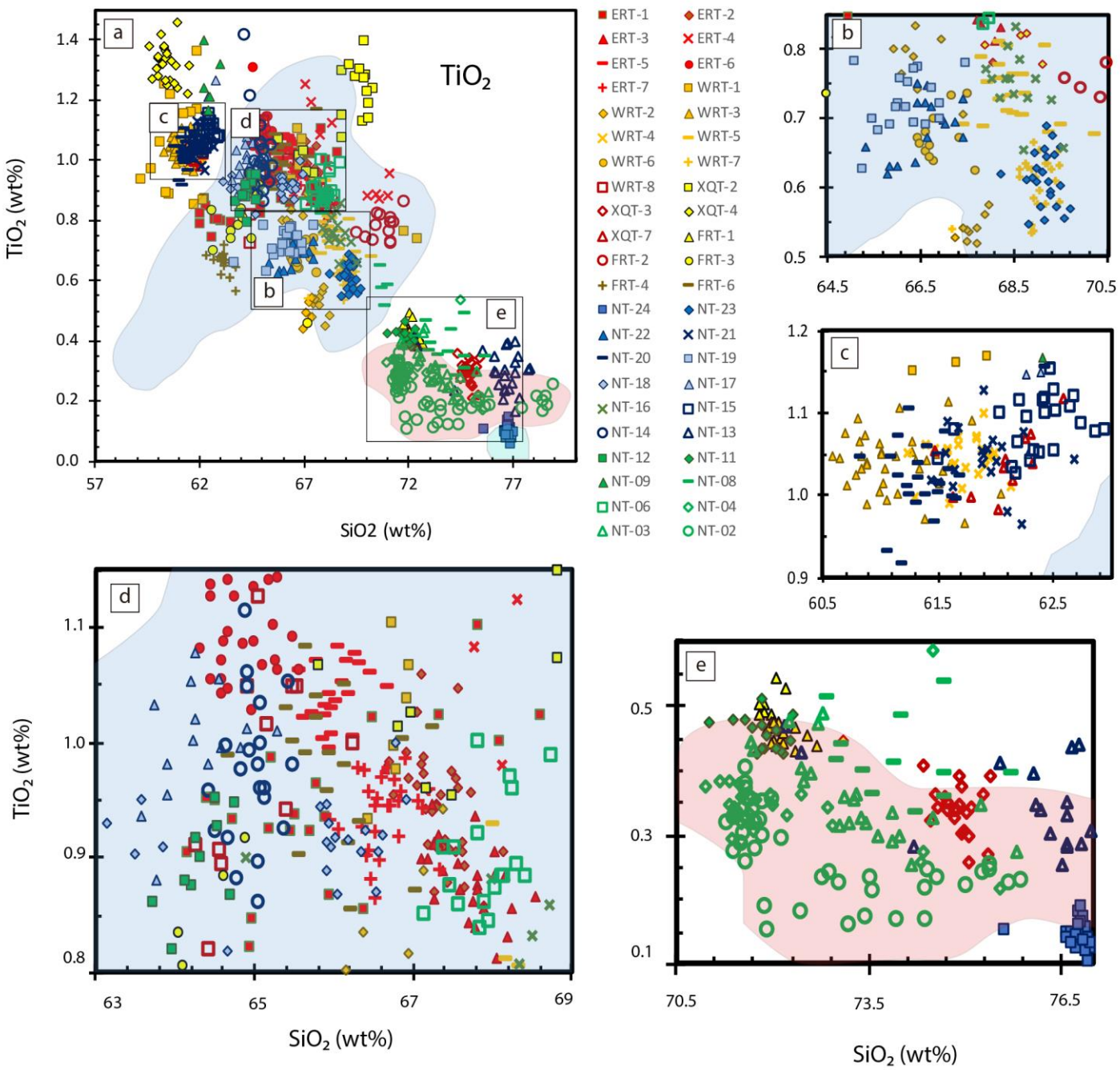

a
b
c
d
e
TiO2
TiO2 (wt%)
SiO2 (wt%)
ERT-1
ERT-2
ERT-3
ERT-4
ERT-5
ERT-6
ERT-7
WRT-1
WRT-2
WRT-3
WRT-4
WRT-5
WRT-6
WRT-7
WRT-8
XQT-2
XQT-3
XQT-4
XQT-7
FRT-1
FRT-2
FRT-3
FRT-4
FRT-6
NT-24
NT-23
NT-22
NT-21
NT-20
NT-19
NT-18
NT-17
NT-16
NT-15
NT-14
NT-13
NT-12
NT-11
NT-09
NT-08
NT-06
NT-04
NT-03
NT-02

Fig. 13. TiO_2 vs SiO_2 plots of: **(a)** tephras from East of the Restaurant (ERT, blue colours) in front of the West of the Restaurant tephras (WRT, red colours) of Xalitzintla; **(b)** tephras from WR in front of tephras from Xalitzintla Quarry (XQ, yellow colours) and Fork in the Road tephras (green colours); **(c)** tephras recorded in Nepopualco region (NT, green and blue colours) in front of Xalitzintla tephras (ERT, WRT, XQT and FRT, red and yellow colours), displayed together with the compositional fields of Popocatépetl (blue area, Iztaccíhuatl (red area, and Tláloc (green area) volcanoes; **(d)** and **(e)** details of two extended areas of the graph in **(c).**

---

physical and sedimentological characteristics, it could only be potentially correlative with NT-4. Both XQT-3 and NT-4 are white pumice fallouts that are 39 and 52-cm-thick respectively (see section 4 and Fig. 14), while NT-8 is an ignimbrite without any associated fallout, and NT-3 is a 35-cm-thick, lithic-rich, coarse lapilli fallout. NT-04 is compositionally diverse and although most of the glass chemical analyses are scattered, there are some analyses that plot within the XQT-3 field, which suggests they could correlate.

Some andesite-dacite tephras at Xalitzintla, which plot within the Popocatépetl compositional field (blue area in Fig. 13), are chemically similar to some Nepopualco units. WRT-7 (yellow plus sign in Fig. 13b) appears to correlate with NT-23 (solid blue diamonds in Fig. 13c), as the glass chemistry is similar. They are both thick white pumice fallout units (1.6 and 1.1 m respectively, Fig. 14) comprising medium to coarse lapilli, and the same mineralogy (plagioclase, orthopyroxene, and oxides; Tables 2 and 3). Moreover, their $^{40}Ar/^{39}Ar$ ages also support this correlation - NT-23 is dated to 369 ± 11 ka and WRT-7 is 354 ± 29 ka. These data suggest that WRT-7 correlates to NT-23 and both stem from the same Popocatépetl eruption. Although less clear, there is some compositional overlap between WRT-6 (solid orange dots, Fig. 13b) and NT-19 (solid sky-blue squares, Fig. 13b) as well as NT-22 (solid marine-blue

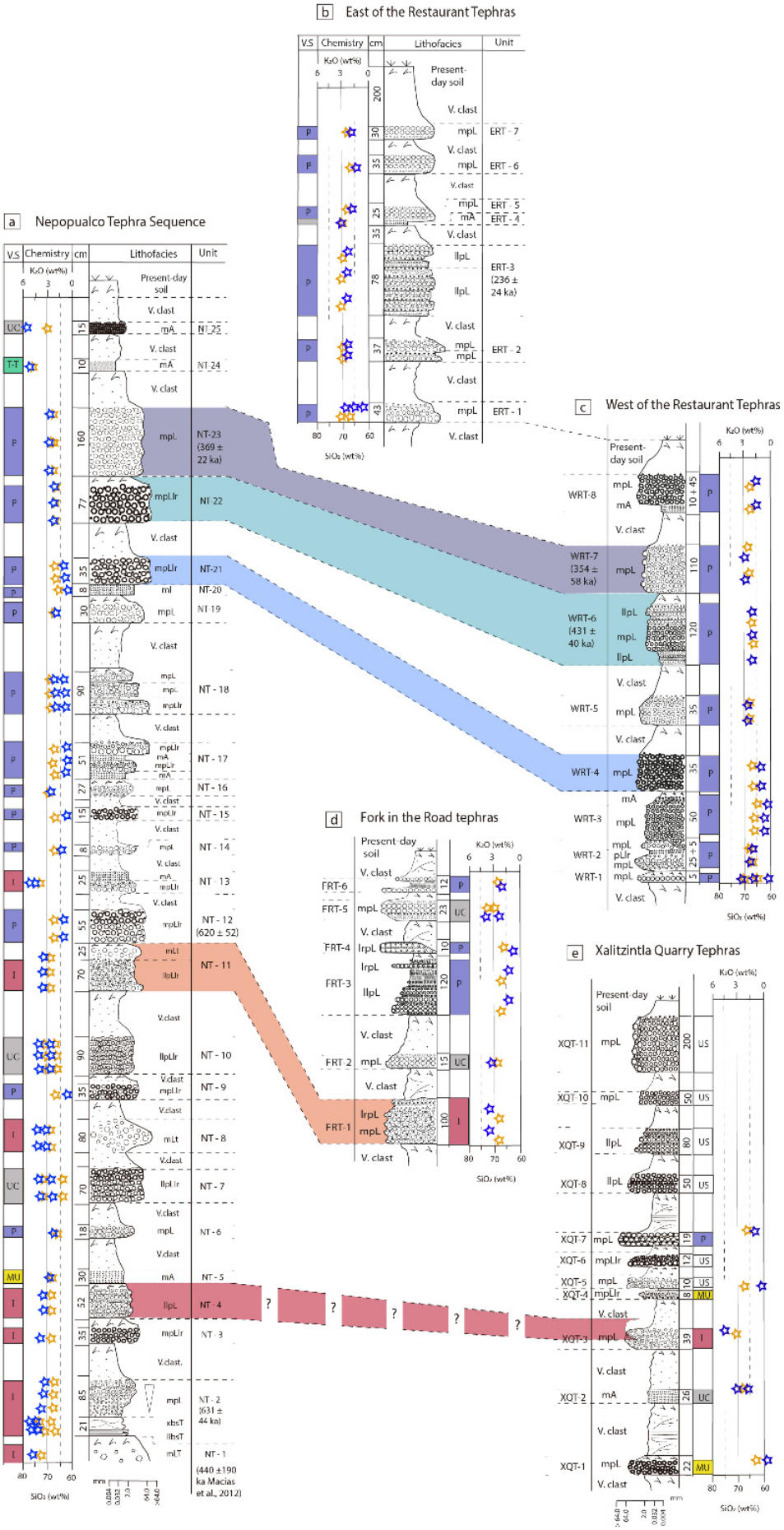

a Nepopualco Tephra Sequence
b East of the Restaurant Tephras
c West of the Restaurant Tephras
d Fork in the Road tephras
e Xalitzintla Quarry Tephras
V.S
Chemistry
cm
Lithofacies
Unit
K2O (wt%)
SiO2 (wt%)
Present-day soil
V. clast
mpL
mA
mpLlr
ml
mLt
llpL
llpLlr
lrpL
xbsT
llbsT
mLT
NT-25
NT-24
NT-23 (369 ± 22 ka)
NT-22
NT-21
NT-20
NT-19
NT-18
NT-17
NT-16
NT-15
NT-14
NT-13
NT-12 (620 ± 52)
NT-11
NT-10
NT-9
NT-8
NT-7
NT-6
NT-5
NT-4
NT-3
NT-2 (631 ± 44 ka)
NT-1 (440 ±190 ka Macias et al., 2012)
ERT-7
ERT-6
ERT-5
ERT-4
ERT-3 (236 ± 24 ka)
ERT-2
ERT-1
WRT-8
WRT-7 (354 ± 58 ka)
WRT-6 (431 ± 40 ka)
WRT-5
WRT-4
WRT-3
WRT-2
WRT-1
FRT-6
FRT-5
FRT-4
FRT-3
FRT-2
FRT-1
XQT-11
XQT-10
XQT-9
XQT-8
XQT-7
XQT-6
XQT-5
XQT-4
XQT-3
XQT-2
XQT-1
mm

Fig. 14. Stratigraphic correlation of **(a)** Nepopualco and **(b)** – **(c)** Xalitzintla tephra layers (East and West of the Restaurant, Fork in the road and Xalitzintla Quarry). The blue stars indicate the SiO_2 (wt.%) composition, and the orange stars the K_2O (wt.%). V.S = volcanic source, P = Popocatépetl (in blue), I = Iztaccíhuatl (in red), T-T = Tláloc-Telapón (in green), MU = mafic unknown (in yellow), UC = uncertain (in grey), and US = unsampled pyroclastic deposits (white).

---

triangles, Fig. 13b). Differences in the deposit characteristics and stratigraphy of the deposits do not support a correlation between WRT-6 and NT-19, but a correlation with NT-22 is supported: NT-22 is a 78-cm-thick pumice fallout of medium to coarse lapilli, rich in lithics and similar to the medial part of the WRT-6 deposit (Fig. 14). The mineralogy (hornblende, plagioclase, orthopyroxene, and oxides; Tables 2 and 3) and stratigraphy order further support that WRT-6 and NT-22 could have been produced by the same explosive eruption. The similar glass compositions, deposit characteristics, mineralogy, and stratigraphic positions of NT-21 (blue crosses in Fig. 13c) and WRT-4 (yellow crosses in Fig. 13c) also suggest that they correlate. Both are 35-cm-thick lithic-rich, coarse lapilli pumice fallout units (see section 3 and Fig. 14). Finally, NT-20 (blue dashes in Fig. 13c) shows similarities to WRT-3 (solid orange triangles in Fig. 13c) based on the glass chemistry (Figs. 11 and 12), mineralogy (plagioclase, orthopyroxene, and oxides; Tables 2 and 3) and chronostratigraphy (Fig. 14). However, the WRT-3 deposit is a 50-cm-thick dark unit composed of grey fine-to-medium lapilli pumice with abundant lithics, and is lithologically different from NT-20, which is an 8-cm-thick dark unit of lithics (> 70%) with a few fine lapilli pumices and coarse ash. This correlation is thus less certain, although both deposits could stem from the same eruption if the Nepopualco site was located at the fallout margin with respect to the dispersal axis of the deposit. There are

other units with similar glass geochemistry (Fig. 13d) but their mineralogy (see Tables 2 and 3) and chronostratigraphy (Fig. 14) do not feasible correlations.

Despite both sequences spanning comparable age ranges, several other tephra units recorded in Xalitzintla cannot be correlated to any of the Nepopualco tephras based on glass compositions (Fig. 13a). These include: XQT-2 (solid yellow squares), XQT-4 (solid yellow diamonds), WRT-2 (solid orange diamonds), FRT-4 (brown plus signs), ERT-5 (red dashes), FRT-6 (brown dashes), and ERT-7 (red plus sign). Thus, these deposits appear to represent additional explosive eruptions to the 25 units already recorded at Nepopualco. Their absence in Nepopualco may either be related to the dispersal axis not overlapping with Nepopualco, due to the primary deposits being too thin to be preserved as discrete, visible horizons. Nevertheless, the matching characteristics of multiple tephras within a continuous stratigraphic section at both Nepopualco and Xalitzintla (particularly WRT), supported by $^{40}Ar/^{39}Ar$ ages, allow for a robust correlation between these two sites.

7.2 Chronological order of the Xalitzintla outcrops

The Xalitzintla outcrops had not been previously studied and given the limited lateral continuity of the field exposures, it was not possible to correlate any single tephra unit across all of the four sites. However, the new $^{40}Ar/^{39}Ar$ dates and glass chemical analyses provide preliminary chronostratigraphic constraints. ERT-3 preserved in the sequence exposed at the East of the Restaurant site (Fig. 6) has been dated to 236 ± 12 ka, and the WRT-7 tephra exposed at the West of the Restaurant (Fig. 7) has an age of 339 ± 16 ka, suggesting that the western outcrop comprises an older segment of the stratigraphy. In addition, we infer that tephras exposed at the Xalitzintla Quarry and Fork in the Road (Figs. 8 and 9) are older than those at

the restaurant sites (Fig. 14) because the lowermost units include rhyolitic tephras (FRT-1 and XQT-3, Fig. 12 and 13) that correlate to the Nepopualco Lower Tephras erupted from Iztaccíhuatl volcano (NT-4 and NT-11, Fig. 14). Iztaccíhuatl is thought to have been largely active before activity commenced at Popocatépetl c.540 ka (e.g. Cadoux et al., 2011; Delgado-Granados et al., 2017; see also section 2.1). These observations suggest the Xalitzintla exposures are separate stratigraphic sections and do not overlap (Fig 14).

8. CHEMICAL VARIATIONS THROUGH THE NEPOPUALCO TEPHRA SEQUENCE AND ITS IMPLICATIONS FOR THE VOLCANIC HISTORIES OF POPOCATEPETEL AND IZTACCIHUATL

Considering the geochemical compositions of the tephra layers in the Nepopualco sequence, and the possible correlation of tephras to their volcanic sources using glass chemistry (see Fig. 11), we propose that Iztaccíhuatl is the source of the rhyolitic tephras recorded near the base of the gully since at least 631 ± 44 ka ($^{40}Ar/^{39}Ar$ age of Nepopualco Ignimbrite or NT-2; Fig. 3 and Table 1), while Popocatépetl started its eruptive activity later, erupting generally andesite-dacite tephras (Table 2). It appears that there was a period of coeval activity between Iztaccíhuatl and Popocatépetl volcanoes, when rhyolitic and andesite-dacite tephras were deposited contemporaneously. The oldest Popocatépetl unit that we recognise is NT-6. Although this is not directly dated, it lies well below NT-12 (also attributed to Popocatépetl; dated at 620 ± 52 ka). This suggests that Popocatépetl was active prior to 600 ka. Between the NT-6 and NT-14 eruptions (both attributed to Popocatépetl and representing c.100 ka considering the new $^{40}Ar/^{39}Ar$ ages of NT-2 and NT-12; Table 2), we identify several explosive eruptions from Iztaccíhuatl, but no more after this point. This is inferred from the absence of

younger pumice fallouts with glass compositions that plot along the Iztaccíhuatl fractionation trend in the younger stratigraphy. Meanwhile, most of the deposits recorded in the Middle and Upper Nepopualco Tephras plot along the Popocatépetl fractionation trend, indicating that it has continued to periodically erupt and distribute tephras over the region up until the present day (Figs. 4, 5, and 11; Table 2).

The fine ash layer (NT-24) deposited at the top of the sequence (Fig. 5) may have been produced by Tláloc-Telapón (for example, from a co-ignimbritic ash plume of one of the late-Pleistocene Tláloc-Telapón ignimbrites; Fig. 11).

The Nepopualco tephra sequence contains evidence for at least 25 explosive eruptions produced during the last c.650 ka: at least 13 are from Popocatépetl and 6 are from Iztaccíhuatl. But explosive eruptions from other sources are also recorded in Nepopualco, including one from the Tláloc-Telapón and one from an unknown mafic source (possibly a nearby monogenetic cone). There are two units near the base of the Nepopualco sequence with an uncertain source, and at least three in the older Xalitzintla sequences (XQT and FRT) that we are unable to attribute. It is possible that these events, which would overlap with both the earliest stages of Popocatépetl's explosive eruption history, or the final stages of Iztaccíhuatl's explosive eruption history (based on the inferences we make above), represent more compositionally diverse magmatism during this transitional phase of SNVR development.

9. INSIGHT INTO THE GENERAL VOCLANIC HISTORY, MAGNTIUDES, AND TEPHRA DISTRIBUTION IN THE MEXICO BASIN

The chronological, chemical, and stratigraphic correlation between Xalitzintla and Nepopualco tephras (including NT-23 to WRT-7 and WRT-8 to ERT-1, Fig. 14) allows us to

establish that at least 7 explosive eruptions from Popocatépetl are recorded at Xalitzintla in addition to the 13 eruptions registered in Nepopualco. These are associated with the 7 tephras recorded in the East of the Restaurant site (ERT-1 to ERT-7, including the 236 ± 12 ka ERT-3), which is the youngest unit from Popocatépetl that we document. The late Pleistocene – Holocene Plinian deposits studied previously by other authors (e.g. the Grey, White or Tutti Frutti pumices) have not been observed in these Xalitzintla tephra sequences we have studied, and fall within a younger stratigraphic interval than is exposed in our study area.

During the middle to late Pleistocene, our new observations imply that the SNVR produced widespread tephra deposits from at least 20 medium-to-large explosive eruptions from Popocatépetl volcano, 6 from Iztaccíhuatl, 1 from Tláloc-Telapón, and 2 eruptions from nearby unknown mafic sources. At least 5 further eruptions, based on their location, physico-chemical characteristics and stratigraphic position, are also likely to have been erupted from either by Popocatépetl or Iztaccíhuatl. The results of this tephrostratigraphic work considerably extend the longer-term understanding of the explosive volcanic history of the Popocatépetl, Iztaccíhuatl and Tláloc-Telapón volcanoes (Fig. 15).

Comparing the recorded thicknesses in these tephra sequences with those of the most recent Popocatépetl eruptions (e.g. the c.27.8 cal. ka BP White Pumice, Siebe et al., 2017; or the 16,796-18,201 cal. yr Tutti Frutti Pumice, Sosa-Ceballos et al., 2012) and considering the prevailing winds of the region (Bonasia et al., 2014), most of the middle to late Pleistocene explosive eruptions identified in the Nepopualco and Xalitzintla outcrops are likely to have distributed tephra over the Mexico and/or Puebla basins. For example, previous studies on the Tutti Frutti eruption estimated that the Mexico City area was covered with at least 10 cm of tephra (Siebe

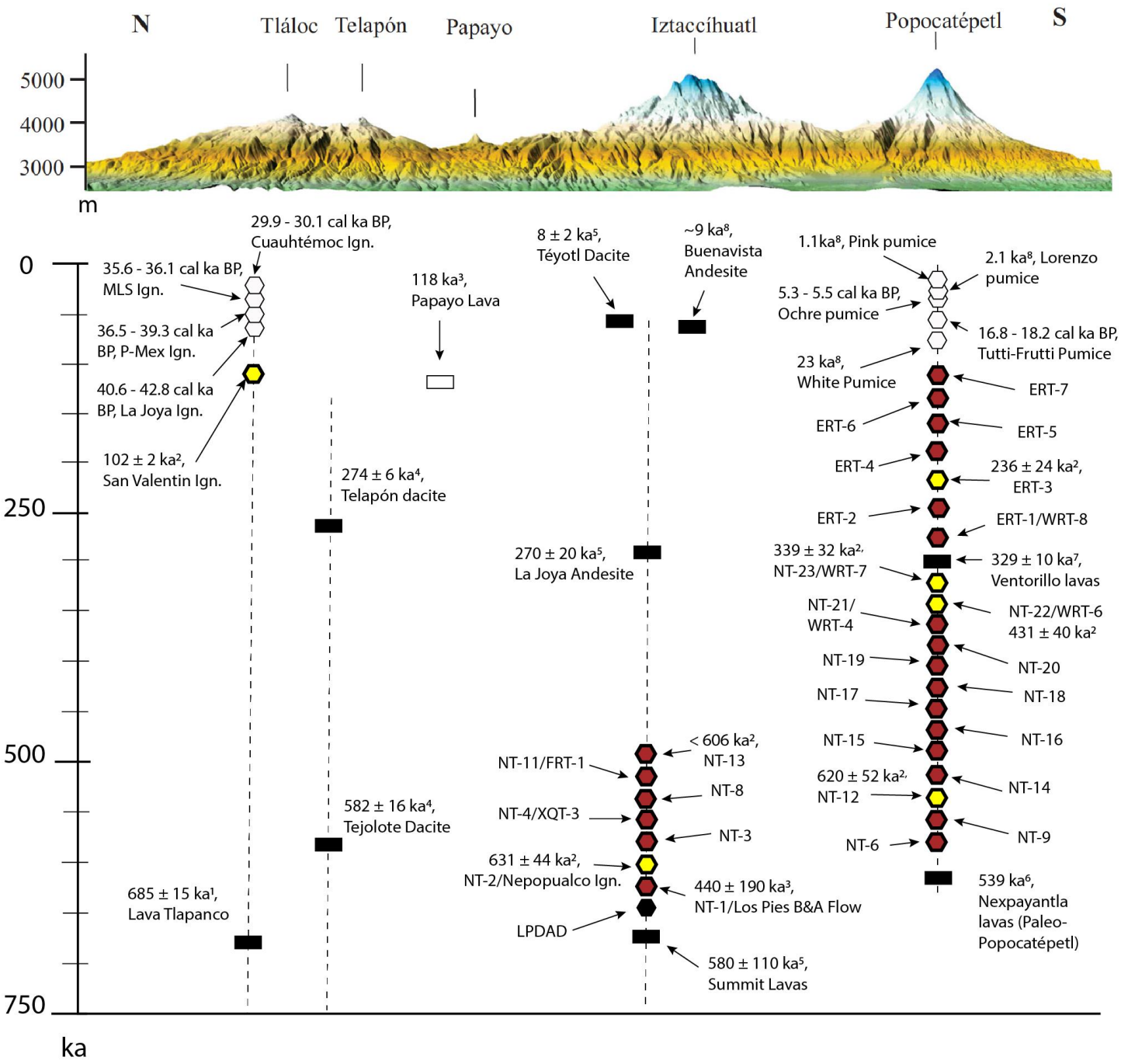

N
Tláloc
Telapón
Papayo
Iztaccíhuatl
Popocatépetl
S
5000
4000
3000
m
0
250
500
750
ka
29.9 - 30.1 cal ka BP, Cuauhtémoc Ign.
35.6 - 36.1 cal ka BP, MLS Ign.
36.5 - 39.3 cal ka BP, P-Mex Ign.
40.6 - 42.8 cal ka BP, La Joya Ign.
102 ± 2 ka², San Valentin Ign.
685 ± 15 ka¹, Lava Tlapanco
118 ka³, Papayo Lava
274 ± 6 ka⁴, Telapón dacite
582 ± 16 ka⁴, Tejolote Dacite
8 ± 2 ka⁵, Téyotl Dacite
~9 ka⁸, Buenavista Andesite
270 ± 20 ka⁵, La Joya Andesite
< 606 ka², NT-13
NT-11/FRT-1
NT-8
NT-4/XQT-3
NT-3
631 ± 44 ka², NT-2/Nepopualco Ign.
440 ± 190 ka³, NT-1/Los Pies B&A Flow
LPDAD
580 ± 110 ka⁵, Summit Lavas
1.1ka⁸, Pink pumice
2.1 ka⁸, Lorenzo pumice
5.3 - 5.5 cal ka BP, Ochre pumice
16.8 - 18.2 cal ka BP, Tutti-Frutti Pumice
23 ka⁸, White Pumice
ERT-7
ERT-6
ERT-5
ERT-4
236 ± 24 ka², ERT-3
ERT-2
ERT-1/WRT-8
339 ± 32 ka², NT-23/WRT-7
329 ± 10 ka⁷, Ventorillo lavas
NT-21/ WRT-4
NT-22/WRT-6 431 ± 40 ka²
NT-19
NT-20
NT-17
NT-18
NT-15
NT-16
620 ± 52 ka², NT-12
NT-14
NT-6
NT-9
539 ka⁶, Nexpayantla lavas (Paleo-Popocatépetl)

Fig. 15. Topographic profile of the Sierra Nevada Volcanic Range (SNVR), which illustrates chronologically the new identified explosive eruptions from Popocatépetl and Iztaccíhuatl, as well as the new $^{40}Ar/^{39}Ar$ age for the San Valentín Ignimbrite from Tláloc-Telapón together with other relevant eruptive episodes during the formation of the range (after García-Tovar and Martínez-Serrano, 2011). The dashed lines indicate the inferred time of activity for each volcano. The black rectangles are lavas with published $^{40}Ar/^{39}Ar$ or $^{40}K/^{40}Ar$ ages, the black hexagon is the debris avalanche deposit related to Los Pies collapse (LPDAD), the red and yellow hexagons are relative and absolute ages of the pyroclastic deposits characterized for the first time in this study, and the empty symbols are published C^{14} ages (rectangles for lavas and hexagons for tephras). 1 = Cadoux et al., (2011; 2σ); 2 = This study ($^{40}Ar/^{39}Ar$; 2σ); 3 = Macías et al. (2012; 1σ); 4 = García-Tovar and Martínez-Serrano (2011; 2σ); 5 = Nixon (1989; assuming 2σ); 6 = Conte et al. (2004; assuming 2σ); 7 = Sosa-Ceballos et al. (2015; 1σ); 8 = Siebe et al. (1996; assuming 2σ).

---

et al., 1999; Sosa-Ceballos et al., 2012), with thicknesses of c.150 cm in the Xalitzintla region (Siebe et al., 2017). If we assume at least some of the eruptions, especially those with thicknesses of c.1m, documented above had a similar NW dispersal axis, these eruptions could have also deposited tephra across the Mexico Basin and the area occupied today by Mexico City. The eruption related to the WRT-7/NT-23 tephra (354 ± 29 ka old), deposited 1.1 m of pyroclastic material in Xalitzintla and 1.6 m in Nepopualco (Fig. 14). It could have deposited several cm of tephra across the Mexico Basin and the area occupied today by Mexico City. If the dispersal axis for the WRT-7/NT-23 eruption was the same as that for the Tutti Frutti event, its thickness at out study sites suggests an eruption of similar magnitude (VEI c. 6; involving 5 km^3 of tephra and an estimated 44 km high eruption column; Sosa-Ceballos et al., 2012).

Recent studies on lacustrine sediments in Lake Chalco, which lies in the southern part of Mexico Basin, east of SNVR (e.g., Ortega-Guerrero et al., 2018) have correlated several tephra

layers to eruptions of nearby stratovolcanoes, including the Tutti Frutti Pumice from Popocatépetl (Siebe et al., 1999; Sosa-Ceballos et al., 2012), the MWP tephra from Tláloc (Rueda et al., 2013) and the Upper and Lower Toluca Pumice deposits from Nevado de Toluca volcano (Arce et al., 2003, 2013). However, these studies have only considered sediments from the uppermost 122 m of the Chalco sequence that spans c.140 ka (Lozano-García et al., 1994, 2015; Caballero and Ortega-Guerrero, 1998; Ortega-Guerrero et al., 2017). Older tephras recorded in deeper sections of Lake Chalco sediments cores (520 m) drilled in 2016 by the International Continental Scientific Drilling Program (ICDP) MexiDrill project (Brown et al., 2019; Valero-Garcés et al., 2021). These will provide a more complete and long-term record of the explosive volcanism around the Mexico Basin, from which eruption frequencies, styles, and magnitudes can be ascertained. The tephrostratigraphy, ages, and glass compositions presented here will be of significance in reliably correlating newly identified tephras to their volcanic sources.

10. OTHER VOLCANOES IN THE MEXICO CITY REGION

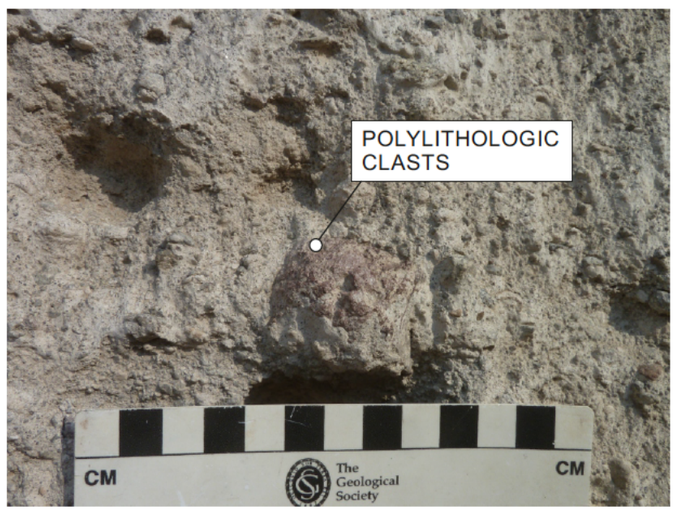
Although the focus of this chapter is on the Sierra Nevada Volcanic Range (SNVR), fieldwork was also conducted at Nevado de Toluca and La Malinche volcanoes (see chapters 2 and 5). As discussed in chapter 2, these stratovolcanoes are considered active and have been responsible for multiple explosive events, including the 8 km^3 DRE Upper Toluca Pumice eruption, from Nevado de Toluca, and the Humantla Pumice eruption from La Malinche (e.g., Bloomfield et al., 1977; Arce et al., 2003; Castro-Govea and Siebe, 2007). Similarly to SNVR volcanoes, fieldwork at Nevado de Toluca and La Malinche was conducted in accessible locations, often utilising gullies, road cuts and quarries.

Without traceable eruption layers as stratigraphic markers, stratigraphic placement between field sites is tricky. An example of this includes a quarry at Zinacantepec, 14Q 041767, 2126670 (Fig. 16), c.13 km north of Nevado de Toluca volcano, which has no identifiable eruption layers to understand its stratigraphic placement. The quarry consists of c.30 m of pyroclastic deposits, containing two eruption units separated by a palaeosol. The ignimbrite associated with the upper eruption unit is c.20 m thick. Within this are polylithologic clasts (subangular to subrounded) up to 1 m in size and imbricated towards the N, away from Nevado de Toluca. These are concentrated in layers and are traceable laterally across the ignimbrite by up to 25 m. At least three layers occur, separated by 5 m of ignimbrite between each layer. Clast size is progressively smaller within each successive (stratigraphically higher) layer, with the uppermost layer comprising mostly clasts up to 10 cm in diameter. Due to these characteristics, these deposits are interpreted to be lithic lag breccias (e.g., Branney and Kokelaar, 2002), which indicate a caldera collapse, with clasts being sourced from the collapse region. The progressively smaller clasts are interpreted to represent different stages in the formation of the caldera, with smaller lithics representative of smaller collapse stages (e.g., Branney et al., 1992; Simmons et al., 2016).

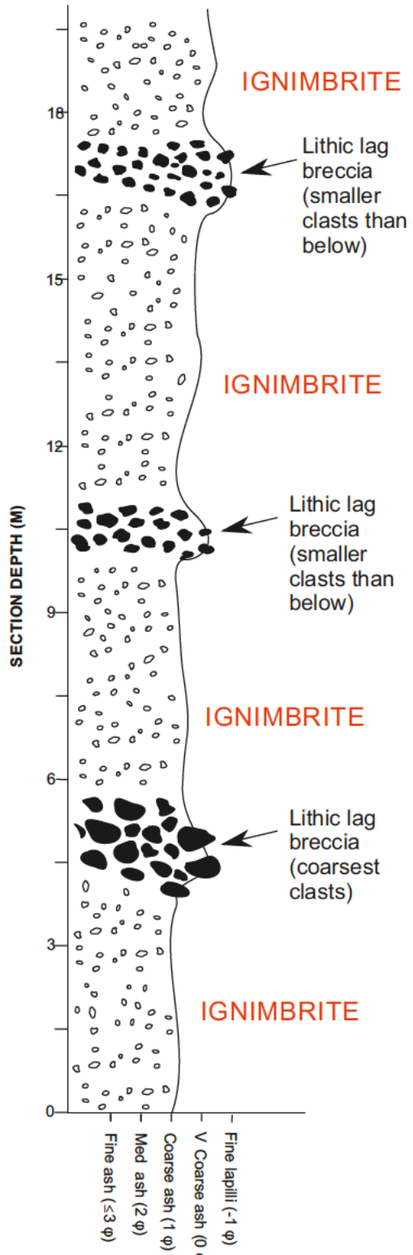
Additionally, at the base of the lowermost eruption unit at Zincantepec, a very fine ash deposit displaying some stratification is observed. This ash is 20 cm thick and is overlain conformably by cross-stratified fine to medium ashes. These deposits are white to light grey in colour and are 50 cm thick. Their upper contact is in sharp contact with an ignimbrite, containing pumice lapilli. Considering the close proximity (c.13 km) to the assumed vent, the fine ash is unexpected. The cross-stratification in the upper unit is consistent with hydromagmatic surge

A

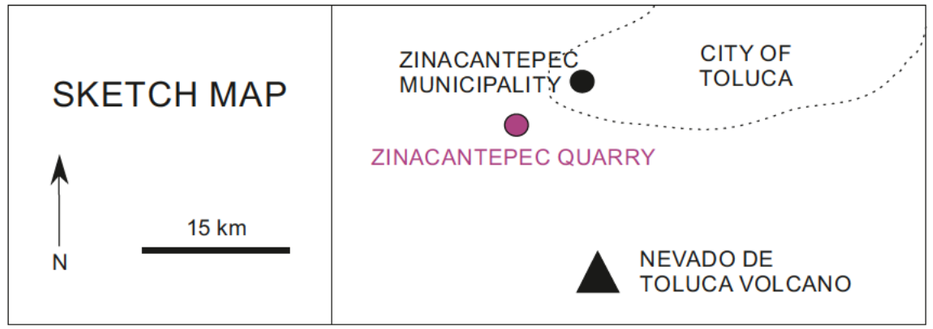




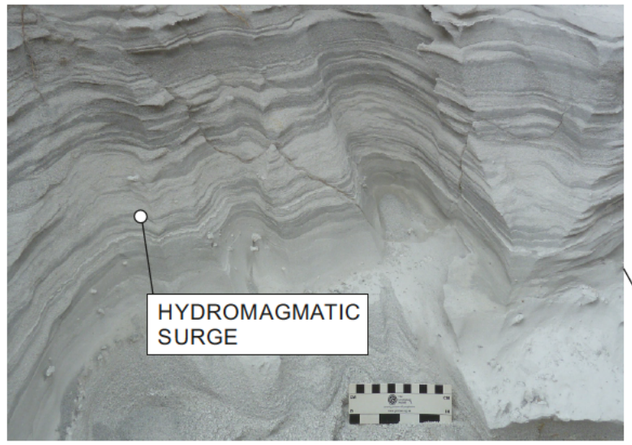
SKETCH LOG



SKETCH MAP



B





SURGE

FALL

SKETCH LOG

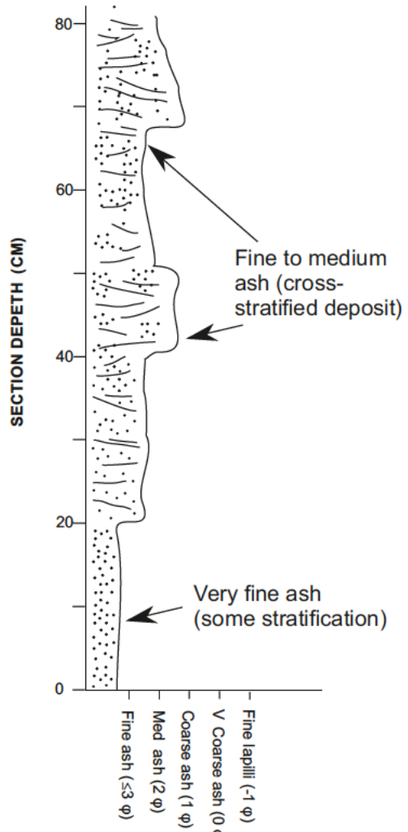


Fig. 16. (a) Example photos of the interpreted lithic lag breccias in the Quarry at Zinacatepec alongside a sketch log through the deposits. (b) Example photos of the interpreted hydromagmatic/phreatomagmatic ash and surge deposits in the Quarry at Zinacatepec alongside a sketch log through the deposits.

---

deposits (e.g., Liu et al., 2017), with the fine ash fall deposit below due to increased fragmentation as a result of magma-water interaction (e.g., Walker, 1973; Kokelaar, 1983). It is therefore interpreted that this eruption began explosively as either a phreatomagmatic or hydromagamtic event, which transitioned into a magmatic eruption when the water had been completely utilized (e.g., Kokelaar, 1983). The source of water (i.e., ground or surface water) is unknown; however, it is possible that the water was sourced from a crater lake, which Nevado de Toluca currently contains. Alternatively, ash venting or resuspended ash could also be responsible as the site is <30 km from the vent(s).

Neither hydromagmatic/phreatomagmatic activity or caldera collapse have been noted from Nevado de Toluca in the literature. Although these are isolated deposits with no stratigraphic context, the eruption source is inferred to be from Toluca due to its close proximity and palaeo-directional indicators (indicating a southern source) in both deposits (e.g., imbrication in lithic lag breccias and cross-stratification in surges). These deposits indicate that Toluca has generated hydromagmatic eruptions and caldera collapse in the past, and that these hazards should be considered in hazard assessments of the volcano. Fine ash presents a major risk to human health, aviation, and water/energy supplies (e.g., Wilson et al., 2012), and due to its low density can travel for large distances, thus increasing the chance of further-reaching eruption effects. Fig. 16 displays these two deposit characteristics from Nevado de Toluca.

11. CONCLUSIONS

1. This work provides a deeper insight into the explosive volcanic histories of the Sierra Nevada Volcanic Range (SNVR), in particular of Popocatépetl and Iztaccíhuatl volcanoes, and characterizes many previously unidentified Late Pleistocene pyroclastic deposits in the SNVR.
2. This chronostratigraphic and geochemical study of the Xalitzintla and Nepopualco tephra sequences in the SNVR provides new insights into the middle to late Pleistocene explosive history of volcanoes surrounding the Mexico basin
3. Major element glass compositions determined by electron microprobe analysis have defined glass compositional fields for Popocatépetl, Iztaccíhuatl, and Tláloc-Telapón volcanoes, and permitted the correlations of tephra layers exposed in the Nepopualco and Xalitzintla sequences to their volcanic source. The Neopopualco and Xalizintla sequences contain deposits representing 20 Popocatépetl and 6 Iztaccíhuatl explosive eruptions, 5 deposits of uncertain source but likely originating from these two volcanoes, and five deposits from more distal vents. This includes one tephra from Tláloc-Telapón volcano related to one of the 5 late Pleistocene ignimbrite-forming eruptions, including the San Valentin Ignimbrite, recently $^{40}Ar/^{39}Ar$ dated in this study at c.102 ka).
4. Since the lateral collapse of Iztaccíhuatl's Los Pies Cone (LPDAD event), dated in this study to c. 631 ± 44 ka (2σ), Iztaccíhuatl has produced at least 6 explosive eruptions that have deposited c.1-m-thick pyroclastic deposits, pumice fallout units and/or ignimbrites that are rhyolitic in composition (e.g., Nepopualco ignimbrite or FRT-1/NT-11 fall).

5. After a period of coeval activity with Popocatépetl volcano, explosive activity at Iztaccíhuatl ceased (probably between 500 and 400 ka) while Popocatépetl continued its explosive activity until today.
6. In addition to the 7 known Plinian eruptions in the last c.24 ka, Popocatépetl has produced at least 20 additional explosive eruptions during the Late Pleistocene. The Popocatépetl eruption deposits identified in Nepopualco and Xalitzintla sites are consistent with Plinian to sub-Plinian eruptive columns, which deposited pumice fallout units with thicknesses of up to 1.6 m.
7. Popocatépetl deposits are predominantly andesitic to dacitic in composition with a few samples extending to more evolved rhyolitic compositions, and plot along a fractionation trend that is displaced to higher K_2O relative to the deposits of Iztaccíhuatl. Some of these eruptions (e.g., NT-23/WRT-7) are likely to have deposited centimetres of ash on the area that is now Mexico City.
8. The glass compositions of the well-known Popocatépetl, Iztaccíhuatl and Tláloc-Telapón deposits, together with the classification of Nepopualco and Xalitzintla tephras, provides a chemical database for future correlations between the Chalco tephras (chapter 5) and their volcanic sources (chapter 5).

CHAPTER 5

GLASS CHEMISTRY OF TEPHRA LAYERS IN LAKE CHALCO: A STUDY INTO THE PROVENANCE OF EXPLOSIVE ERUPTIONS IMPACTING MEXICO CITY, MEXICO

"Actually, I'm a student of all sciences"

Dr. Emmett Brown, Back to the Future Part III

This chapter has been written in the style of a paper with the intention to submit to a journal soon.

'We' is therefore used throughout and there has been input into parts of the text by Dr. Sebastian Watt and Prof. Victoria Smith during editing stages of the manuscript.

1. INTRODUCTION

Tephrochronology is of value to various scientific disciplines, permitting the correlation and dating of geological, paleoenvironmental and archaeological archives (e.g., Shane, 2000; Turkey and Lowe, 2002; Lowe, 2011; Smith et al., 2011; Davies et al., 2012; Dugmore et al., 2013; Riede et al., 2013; Fontijn et al., 2016; Albert et al., 2017; Lane et al., 2017; Jensen et al., 2021). To construct tephrochronological frameworks, glass geochemistry is a useful method in correlating and grouping explosive eruption products to their eruptive source, and in the case of well characterised eruptions, fingerprinting a deposit to a particular eruptive event (e.g., Ponomareva et al., 2015; Foo et al., 2020; Neall et al., 2021; Tomlinson et al., 2022). If a deposit is well dated, this correlation permits the projection of a particular eruptive event as a known point in time into an environmental archive, providing temporal constraint on the sequence (e.g., Smith et al., 2011; Albert et al., 2018). In many cases major elements display sufficient differences in composition to provide a characteristic fingerprint (e.g., Sunyé-Puchol et al, 2021), although trace element geochemistry and mineral compositions may also be used to determine chemical fingerprints from volcanoes and/or eruptions (e.g., Smith et al., 2011; Harangi et al, 2020).

1.1. Importance of tephrochronology in volcanology

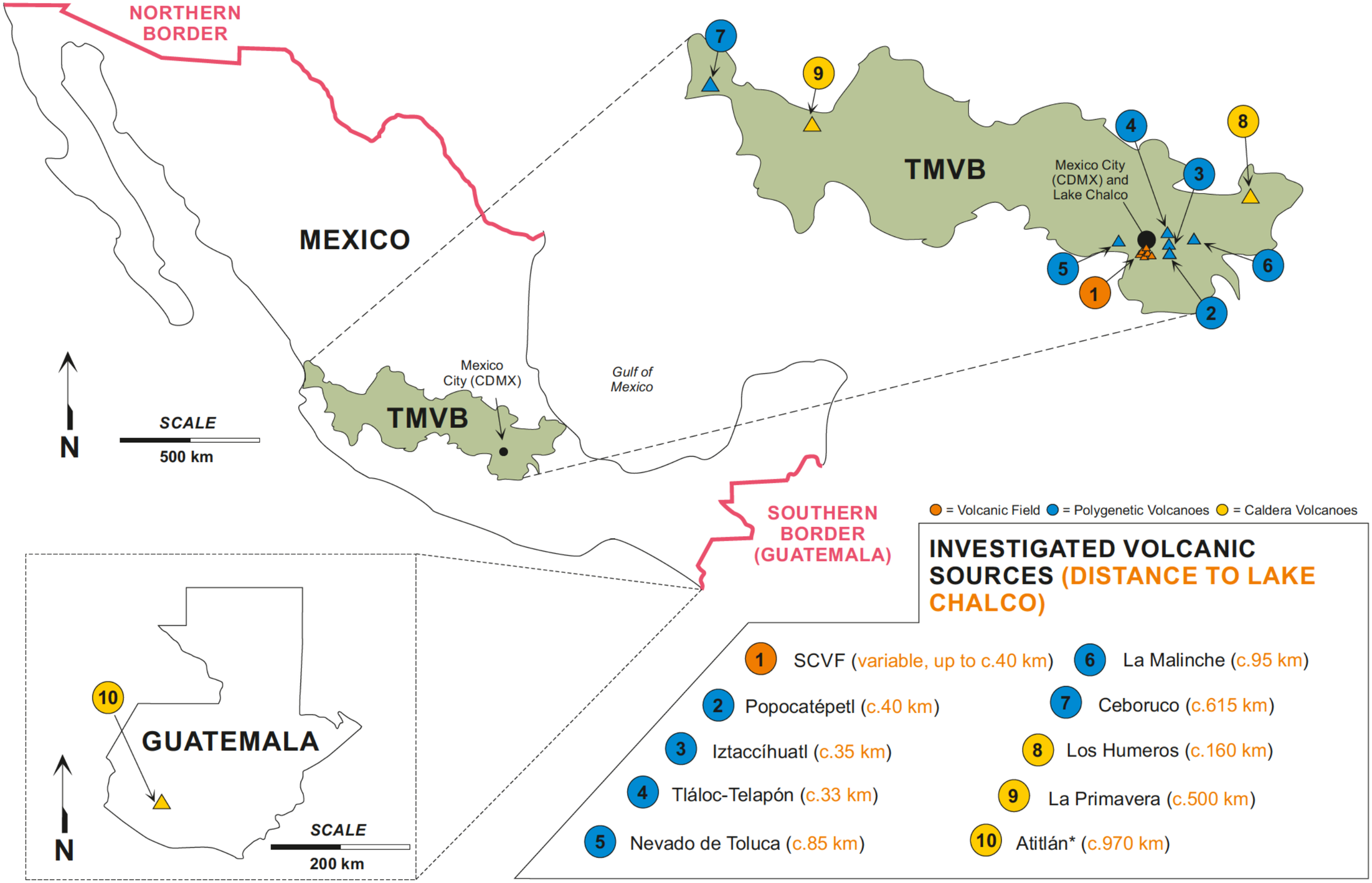
As described above, glass geochemistry (including major element concentrations) can be used effectively to discern between eruptive sources and/or specific eruptions. Volcanology relies heavily upon understanding the eruptive history of a volcano to inform what the volcano may do in the future and when (e.g., Crandell and Mullineaux, 1977; Lockwood and Lipman, 1987; Larsen and Eiríksson, 2008). Tephrochronology is paramount to this, allowing records to be

synthesised, chronologies to be improved and the distances, thicknesses and characteristics of eruption layers to be combined with that observed from the proximal record from a given volcano (e.g., Wulf et al., 2018). Through detailed analysis, eruptive volumes and magnitudes may be revised following the positive identification of an eruption layer, and plume dynamics can be further investigated (e.g., Engwell et al., 2014; Plunkett et al., 2022).

In regions where surface exposures of deposits are lacking, cores (e.g., marine, lacustrine, peat, ice etc.), can help to resolve the poor spatial resolution of eruptive records (e.g., Giaccio et al., 2019; Harning et al., 2019). In Mexico City, older eruptive sequences from nearby volcanoes are difficult to obtain due to the expansion of the city and poor surface preservation (e.g., Sunyé-Puchol et al, 2021). This study therefore draws primarily upon a lacustrine sediment core from Lake Chalco, as mentioned in earlier chapters.

1.2. Use of tephra glass geochemistry at Lake Chalco

Glass chemistry at Lake Chalco is important in determining the source of explosive eruption deposits within the succession. Earlier attempts from shorter cores from the lake (e.g., Ortega-Guerrero and Newton, 1998; Ortega-Guerrero et al., 2018) have been hindered by the lack of well-established glass chemical fields from source volcanoes for comparison. This study significantly builds upon the source chemistries of the source volcanoes and investigates 137 tephra layers within the Chalco core with three key aims of: (1) assigning an eruptive source to as many layers as possible; (2) testing the volcanic stratigraphic methods and correlations, outlined in chapter 3 and (3) to correlate well dated eruption units to provide chronological constraints in the succession. All glass chemistry presented in this study is obtained from



* Source volcano is in Guatemala. *n.b.* all other sources are within the country of Mexico.

Fig. 1. Map of Mexico and Guatemala displaying the volcanoes investigated in this study and their location in relation to Lake Chalco. Approximate distances from the lake are provided in the legend and volcanoes are colour coded in accordance with their volcano type: volcanic field volcanoes = orange, polygenetic stratovolcanoes = blue and caldera volcanoes = yellow.

---

visible units within the core and is exclusively limited to major elements. The methodological approach taken is outlined below.

2. GEOLOGICAL SETTING

2.1. Volcanism in the Mexico City region and its vulnerability to explosive volcanism

As explored in earlier chapters (2 and 3), Mexico City is vulnerable to diverse eruptions and eruptive processes from multiple volcanic sources (e.g., Siebe, 2000; Arce et al., 2003; Martin-Del Pozzo et al., 2008; Donovan et al., 2018). To better understand the impact of proximal and distal volcanoes, defined here as ≤100 km and ≥100 km from Lake Chalco, respectively, each source investigated in this study is considered separately to understand the potential hazards to the city, home to c.25 million people. The locations of these volcanoes and distances from Lake Chalco can be seen in Fig. 1 and major, known eruptions from these volcanoes which have the possibility of being present in the form of tephra deposits within the Chalco core are presented in Table 1.

Tephra hazards are considered to be the greatest volcanic threat to Mexico City as these are possible from multiple sources and are controlled by wind, which increases the distance over which these hazards apply. Volcanic ash (pyroclasts ≤2 mm) can travel large distances downwind, particularly if fine grained (e.g., Walker, 1981; Stevenson et al., 2015), with the largest events affecting areas over 50,000 km^2 (Walker, 1973). Hazards such as pyroclastic

density currents (PDCs) are generally controlled by topography (e.g., Andrews and Manga, 2011; Brand et al., 2016) and typically exhibit runout distances of up to 10-15 km from source, although this can be up to 100 km depending upon the magnitude of the eruption (Loughlin et al., 2015). The nearest polygenetic volcanoes to Mexico City are located in the Sierra Nevada Volcanic Range (SNVR) to the east of the city. These are typically between c.30 and c.40 km from Lake Chalco, so it is unlikely PDC deposits (ignimbrites) would be found at Lake Chalco. This was confirmed by the volcanic stratigraphic assessment of the cores in chapter 3. Laharic (volcaniclastic) deposits are found at Lake Chalco (chapter 3), and the glass chemistry of some of these units is also presented in this study. However, the focus of this chapter is to determine the origin of explosive eruption deposits (tephras) within the core, as well as to test the quality, accuracy and reliability of the core volcanic stratigraphic methodology presented in chapter 3.

2.2. Proximal polygenetic volcanic sources

As mentioned above, proximal volcanoes are here defined as eruptive sources that are ≤100 km from Lake Chalco (See Fig. 1). The proximal volcanic sources investigated in this study include Popocatépetl, Iztaccíhuatl, Tláloc-Telapón, Nevado de Toluca and La Malinche. These volcanoes all have previously known explosive eruptive histories (as outlined in chapter 2). Other proximal polygenetic sources, such as Jocotitlán (c.97 km from Lake Chalco) have been omitted from this study due to limited fieldwork capabilities and time to obtain reference glass samples. Specific polygenetic source information is provided below (section 4.1) and the reader is directed to chapter 2 for a summary of the known eruptive histories of these volcanoes.

Table 1. Summary of key eruptions from proximal and distal volcanoes which have been recognised as potentially being present in the Chalco core.

Volcanic Source	Eruption	Deposit types	Eruptive magnitude (VEI)	Tephra Volume (km^3)	Tephra volume DRE (km^3)	Dispersal direction	Age (ka), method (if reported) *	Known thickness near Lake Chalco (cm)	Approximate from Mexico City (km)	References
Distal caldera sources (Mexico)										
Los Humeros	Zaragoza Tuff	Fall, PDC, co-PDC	6.3	24	15	N (*n.b.* poorly constrained)	69 ± 16, $^{40}Ar/^{39}Ar$	-	160	Carrasco-Núñez et al., 2018
Los Humeros	Faby Tuff	Fall, PDC, co-PDC	6.1	18	10	-	70 ± 23, $^{40}Ar/^{39}Ar$	-	160	Carrasco-Núñez et al., 2018
Los Humeros	Xáltipan Ignimbrite	Fall, PDC, co-PDC	7.8	340	290	Radial, distal component to SW	164 ± 4.2, $^{40}Ar/^{39}Ar$ and U/Th	-	160	Carrasco-Núñez et al., 2018; Cavazos-Álvarez and Carrasco-Núñez, 2020
La Primavera	Tala Tuff	Fall, PDC, co-PDC	6.5	45	20	Radial, distal to ENE	95 ± 5, $^{40}Ar/^{39}Ar$	-	500	Mahood, 1981; Walker et al., 1981
Distal stratovolcanoes experiencing recent caldera-forming eruptions (Mexico)										
Ceboruco	Jala Pumice	Fall, PDC, co-PDC	6	-	3-4	ENE	1, C^{14}	-	615	Chertkoff and Gardner, 2003; Sieron and Siebe, 2008
Distal caldera sources (Guatemala)										
Atitlán	I-Fall	Fall, PDC, co-PDC	-	-	7	-	>40	-	970	Kutterolf et al., 2016; Cisneros De Leon et al., 2021
Atitlán	Los Chocoyos (LCY)	Fall, PDC, co-PDC, surge	8	1220	510	Radial	75 ± 2, (U/Th)/He	6 - 9	970	Kutterolf et al., 2016; Cisneros De Leon et al., 2021
Atitlán	W-Fall	Fall, PDC, co-PDC	-	-	83	NW	158 ± 3, K/Ar	<1	970	Rose et al.,1999; Cisneros De Leon et al., 2021

Atitlán	L-Fall	Fall, PDC, co-PDC	-	-	-	N	191	2	970	Kutterolf et al., 2016
Proximal polygenetic stratovolcanoes										
Nevado de Toluca	Upper Toluca Pumice (UTP)	Fall	6.2	18	8	ENE	12.8 - 12.1, C^{14}	10	85	Arce et al., 2003
Nevado de Toluca	Middle Toluca Pumice (MTP)	Fall	5.6	6	1.8	ESE	~12.1, C^{14}	-	85	Arce et al., 2005
Nevado de Toluca	Lower Toluca Pumice (LTP)	Fall	5.4	4	1.5	ENE	21.7, C^{14}	-	85	García-Palomo et al., 2002; Arce et al., 2005
La Malinche	Malinche Pumice II (MP-II)	Fall	-	-	-	NE	12.1 ± 0.16, C^{14}	-	95	Castro-Govea and Siebe, 2007
La Malinche	Malinche Pumice I (MP-I)	Fall	-	-	-	NW	25.7, C^{14}	-	95	Castro-Govea and Siebe, 2007
La Malinche	Huamantla	Fall	-	-	-	NE	>45 ka	-	95	Castro-Govea and Siebe, 2007
La Malinche	Baquedano	Fall	-	-	-	N	> 45 ka	-	95	Castro-Govea and Siebe, 2007
Iztaccíhuatl	Los Pies PDC	Fall, PDC	-	-	-	E	440 ± 190 ka, K/Ar	-	35	Macias et al., 2012
Popocatépetl	White Pumice	Fall	5.5	5	1.9	S	27.8, C14	-	40	Siebe et al., 2017
Popocatépetl	Tutti Frutti Pumice	Fall	5.8	9	3	NW	17, C^{14}	10	40	Sosa-Ceballos et al., 2012
Popocatépetl	Ochre Pumice	Fall	5.5	4.9	2	N	4.95, C^{14}	-	40	Arana-Salinas et al., 2010
Popocatépetl	Lorenzo Pumice	Fall	5.5	5	2	NE	2.15, C^{14}	-	40	Siebe et al., 2017
Popocatépetl	Pink Pumice	Fall	6	7	2.5	NE	1.10, C^{14}	-	40	Siebe et al., 2017

Tláloc-Telapón	San Valentin	PDC	>5	Similar to MWP	Similar to MWP	E	44.195 +2.02/−1.615, C^{14}	-	33	Rueda et al., 2006; Rueda et al., 2007
Tláloc-Telapón	Cuauhtemoc	PDC	>5	Similar to MWP	Similar to MWP	ESE	25.640 +0.275/−0.265, C^{14}	-	33	Rueda et al., 2006; Rueda et al., 2007
Tláloc-Telapón	P-Mex	Block and ash flow	>5	Similar to MWP	Similar to MWP	NNE	33.180 ± 0.550, C^{14}	-	33	Meier et al., 2007
Tláloc-Telapón	Multilayered White Pumice (MWP)	PDC	5.5	4.68	1.58	NNW	31.490 + 1.995/ −1.595, C^{14}	-	33	Rueda et al., 2013
Tláloc-Telapón	La Joya	PDC	>5	Similar to MWP	Similar to MWP	NW	37.220 ± 0.890, C^{14}	-	33	Huddart and González, 2004; Huddart and González, 2006

*C14 dates are calibrated ages, unless stated otherwise. If this is not stated in the literature, the date is assumed to be calibrated.

2.3. Proximal monogenetic volcanic sources

Here, proximal monogenetic sources investigated are all included within the Sierra Chichinautzin Volcanic Field (SCVF) a volcanic field currently comprising c.220 cones which sit directly within and south of Mexico City, up to 40 km from the core site (Mazzarini et al., 2010; Nieto-Torres and Del Pozzo, 2019; Zarazúa-Carbajal et al., 2021). Other smaller-scale eruptive centres are omitted from this study due to the greater distances these lie from Mexico City, because they are assumed to have a much lower probability of producing explosive pyroclastic deposits which are in the Chalco Core. This is due to the typically small eruptive volumes and magnitudes of eruptions in monogenetic fields, in turn resulting in smaller depositional radius from source, when compared with polygenetic stratovolcanoes (e.g., Valentine and Connor, 2015). Further information regarding the eruptive history of the SCVF is provided in chapter 2 and specific information to this study in section 4.3.

2.4. Distal volcanic sources

Distal volcanic sources identified in this study include the Mexican calderas, Los Humeros and La Primavera; the Mexican stratovolcano, Ceboruco; and Guatemalan caldera, Atitlán, These sources are investigated due to a known prior history of very explosive and high magnitude eruptions (Table 1 and references therein). Other distal sources, such as the active Mexican stratovolcanoes of Colima, Orizaba and El Chichon, have been omitted due to a limited glass geochemical database for the region and/or a lack of evidence for prior eruptions that dispersed macroscopic tephra deposits to the Mexico City region. It is, however, possible that these additional sources were minor contributors to deposits within the Chalco core.

Specific distal source information is provided below (section 4.2) and the reader is directed to chapter 2 for a summary of the known eruptive histories of these volcanoes.

3. METHODS

3.1. Proximal volcanic field methods

In March 2019, fieldwork was conducted in central Mexico with the aim to stratigraphically log and sample explosive pyroclastic eruptions from local source volcanoes to Mexico City, and to use these to characterise the glass geochemical composition of these sources. These included polygenetic composite volcanoes of the Sierra Nevada Volcanic Range (SNVR): Popocatépetl, Iztaccíhuatl and Tláloc-Telapón, as well as Nevado de Toluca and La Malinche and three cones of the Sierra Chichinautzin Volcanic Field (SCVF): Volcán Xicotencatl, Volcán Yuhalizqui and Volcán Teuthli. All field methods are outlined in chapter 4 and Sunyé-Puchol et al. (2021).

3.2. Core methods

The cores used in this study were drilled in 2016 as part of the International Continental Scientific Drilling Program (ICDP) MexiDrill project and were extracted from Lake Chalco from four parallel boreholes (Holes 1A, 1B, 1C and 1D). The cores reached a depth of c.520 m below-surface. Extraction methodologies are outlined in chapter 2,3 and Brown et al. (2019), Martínez-Abarca et al. (2021) and Valero-Garcés et al. (2021). This drilling project is supplemented by other earlier coring projects from Lake Chalco, which reached shallower drilling depths in 2008 and 2011 (see chapter 2,3). All MexiDrill (2016-drilled) cores are stored and archived at the National Lacustrine Core Facility (LacCore) at the University of Minnesota, USA.

3.3. Sub-sample selection and extraction

In 2016, following the splitting, cleaning, imaging and data collection from the cores (see Brown et al., 2019) sub-samples from working halves of the core were collected from discrete stratigraphic units by the MexiDrill project sampling party. Material was extracted using clean spatulas and placed into plastic sample pots (polycons) for safe storage and transportation. The samples taken were recorded and polycons were labelled with the core section name and depth (in centimetres) from which they were taken.

In the summers of 2018 and 2019 additional sub-sampling was undertaken for this study with the focus of: (1) collecting tephra for glass geochemical analysis (this study); (2) obtaining thick (≥5 cm) tephras for $^{40}Ar/^{39}Ar$ geochronology (chapter 6); (3) sampling indurated volcaniclastic deposits for textural and geochemical analysis (chapter 3, this study) and (4) sampling lava for $^{40}Ar/^{39}Ar$ geochronology and geochemical analysis (chapter 3, 6).

Core sections were requested from the repository prior to arrival at LacCore, University of Minnesota to ensure they were temporarily stored at the laboratory for sub-sampling. In the laboratory, the cores were kept in a cold storeroom refrigerated at 4 ℃, simulating optimum core preservation conditions. Sub-samples were taken using a clean spatula cleaned thoroughly between samples to ensure there was no cross-contamination. Depending upon the reason for sampling, an appropriate volume of material was removed. This was typically a 1 cm^3 volumetric sample for geochemical analysis; and a greater quantity, taking the majority of available material but leaving behind a 2 cm wide strip of material covering the full thickness of the target layer, for $^{40}Ar/^{39}Ar$ geochronological analysis. Samples were extracted from the middle of layers and spanning the bulk of the layer thickness, except in some

instances where samples were also taken internally to a layer (e.g. at internal structural boundaries or to systematically test compositional variability). The upper and lower boundaries of deposits were avoided to ensure that samples were not contaminated by other deposits or included background sediment mixed in with the volcanic layer lithological contacts. For poorly preserved/recovered core sections, discretion was used depending upon the appearance of the tephra. Sampled material was stored in polycons or sample bags for smaller and larger volume samples, respectively. Following sampling, foam was cut to size to replace the removed sediment from the core in order to maintain the stratigraphy of the core section. Samples were recorded and described (and in some cases stratigraphically logged and photographed), and a label was printed and applied to the sample polycon/bag. Following this, core sections were wrapped a minimum of two times in acid-free plastic wrap and sealed within core boxes with electrical tape to ensure the end cap of the core box was secured safely, minimising the likelihood of the core separating from its box during transportation back to the repository.

For samples that were ambiguous as to whether they contained volcanic material (e.g., diatomaceous layers sometimes visually appearing as tephras), smear slides were made following the methodology outlined in Appendix C5. Slides were viewed under a petrological microscope for determination of the componentry of the layer. If glass shards were positively identified, a sample was taken following the methodology above.

For more indurated samples, depths within the section containing material desired from the core were identified. Samples were removed using a chisel and geological hammer to ensure a clean break at the intended depths. Samples were then labelled using a marker pen with an

arrow in the direction of younging strata to ensure the correct way up was identified during analytical preparation procedures. Succeeding procedures, following the removal of material, (e.g., core section stratigraphic order maintenance, labelling and wrapping and storage methods) were followed as above.

3.4. *Sample preparation for electron probe microanalysis (EPMA) analysis*

Following the safe arrival of samples in the UK, tephra samples were prepared for Electron Probe Microanalysis (EPMA) at the University of Birmingham and the University of Oxford.

3.4.1. Sieving and cleaning

Samples were placed into a clean, dry beaker labelled with the sample name. Coarse samples (containing very coarse ash to lapilli) were crushed using a pestle and mortar until ash grade. If necessary, lithics and visible organic matter was removed using clean tweezers. Tephra was then added (in small amounts) to sieves containing 80 μm nylon mesh (or 25 μm meshes for thin or fine tephra layers). Samples were passed through the sieve with a pressure hose until finer clayey sediment had been removed and only clean juvenile material remained. This material was then poured into a labelled beaker aided by deionised water to transport the sample form the sieve to the beaker. Here, excess water was carefully poured away, along with floating organic material. Beakers were then placed in an oven at 60 ˚C for 24 hours, checked on after c.12 hours to stir the samples to stop them from sticking to the base of the beaker. Between samples, everything was washed thoroughly with water and soap using a cleaning sponge. All items, (e.g., 80 μm mesh, sieves, beakers, pestle and mortar) were rinsed until clean and confident there was no chance of contamination with the previously prepared sample. All

apparatus was then dried. If 25 μm mesh was used, this was discarded after a single use, as it couldn't be verified that all mesh holes were sufficiently clean.

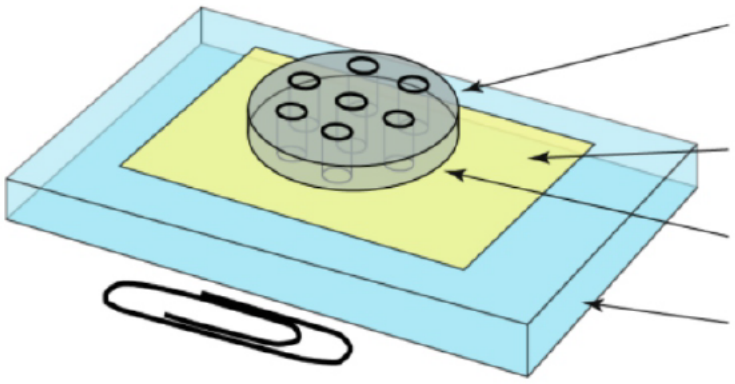
3.4.2. Sample mount creation

Sample mounts can be subdivided into four stages: (1) mounting; (2) grinding; (3) polishing and (4) carbon coating (e.g., Lowe, 2011). Fig.2 schematically depicts the methods involved in these stages with steps 1-3 from the mounting stage and steps 4 and 5 from the grinding, polishing and carbon coating stage.

Resin blocks (2.5 cm in diameter) were made using *SpeciFix 20* (cold mounting) resin and curing agent. After curing for 7 days, 7 holes were drilled into the mounts and they were cleaned in an ultrasonic bath to remove any fine dust (e.g., Froggatt and Gosson, 1982). An arrow (direction of way up) was engraved onto the side of the block, and along with the block name and the mounts were stuck to a glass plate using double sided tape. Six of the seven holes were covered with masking tape to prevent contamination and each hole was successively filled with a different tephra sample by using a folded piece of paper to guide the material in. Sample notes and a map of the mounts were recorded. After all holes were filled, *SpeciFix 20 (*cold mounting) resin and curing agent was applied after being mixed for several minutes. A clean wooden stick was used to place drops of resin into each hole, with each sample being stirred with a paperclip to displace bubbles from the sample. Samples were left for 1 week to cure before grinding.

After removal from the glass plate, samples were ground by hand using silicon carbide grinding papers and progressively finer grit pads (P800, P1200, P2500 and P4000, the latter equivalent to c.6 μm). Sample grinding was lubricated with water and grinding was done in

1. Block positioning

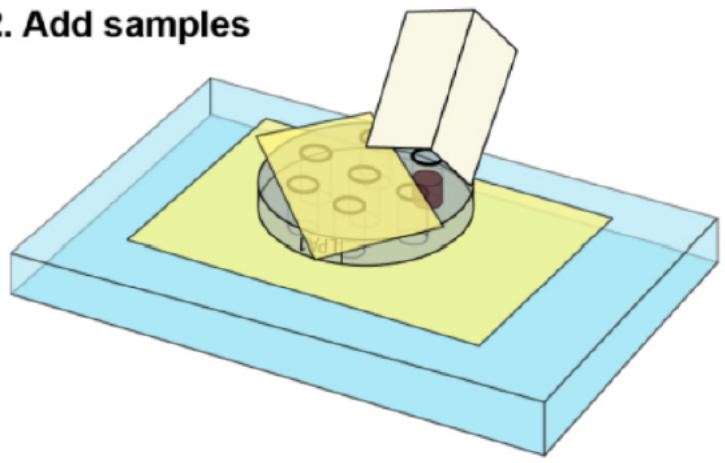


Block made from *SpeciFix* resin (holes drilled through, but number is dependable on sample type/personal preference)

Double-sided sticky tape

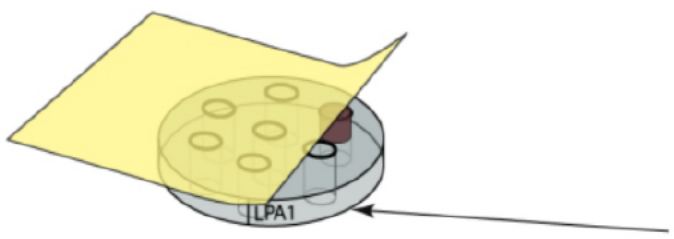
Stick block to tape

2. Add samples



1. Label block/write up marking
2. Add sample to hole using folded paper - cover other holes with sticky tape and be aware of static
3. Back-fill holes with cold-mounting EpoFix resin and remove bubbles by stirring with pin
4. Leave for 24 hours on glass plate

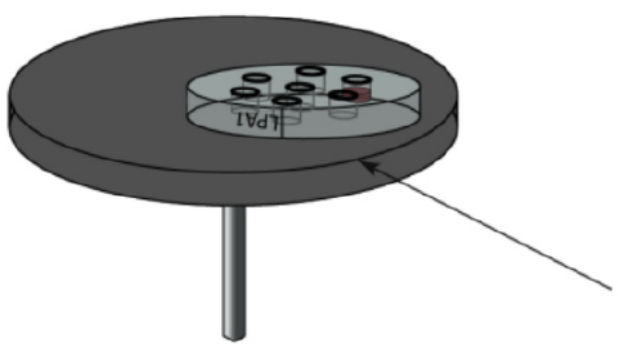
3. Invert and remove tape from base of block



1. Pull block from glass plate to expose glass shards

Bottom of block

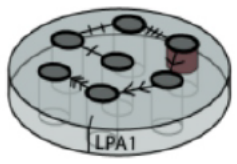
4. Section/polish



1. Section blocks using hand grinders to expose grains (20-30 grains)
2. Polish using machine techniques - sample should be on the bottom of the block

Polisher/grinder

5. Polished surface



max: 1” (25 mm)

1. Map the surface to aid identification of hole
2. Clean block in Petroleum Ether and wipe with blue roll
3. Coat with carbon for EPMA

From Smith, 2019

Smith, R., 2019. Assessing the composition and timing of Late Quaternary volcanic eruptions in southern South America using tephra layers from lacustrine and peat sequences (Doctoral dissertation, University of Oxford).

Fig. 2. Diagrams illustrating the main stages in the preparation of tephra for EPMA analysis, from the mounting of resin blocks (steps 1-3) to the grinding, polishing and carbon coating stages (steps 4 and 5). From Smith (2019).

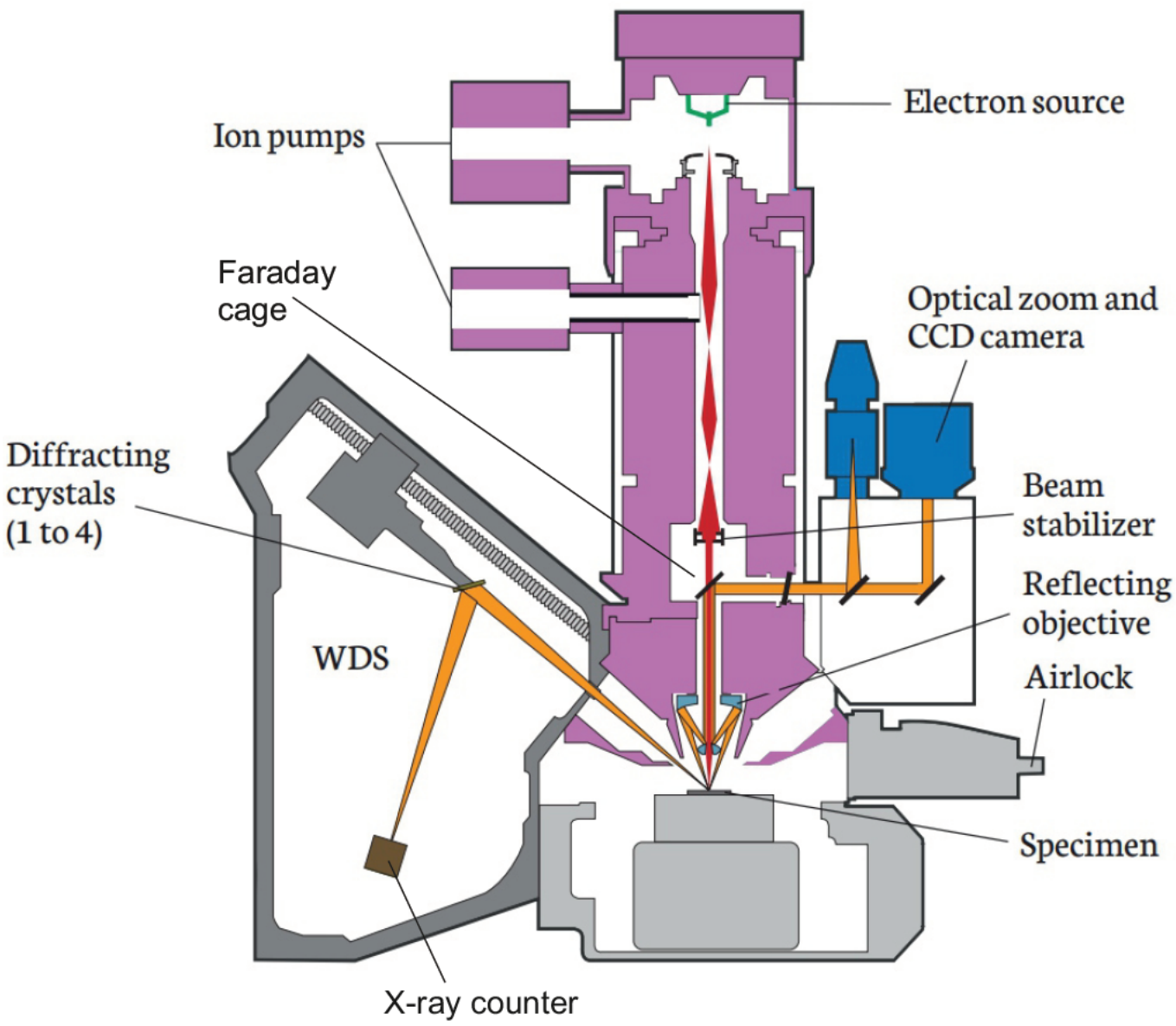
---

figure of eight motions to create an even cross section through the mounts. Samples were checked under a binocular microscope to check for minimal scratches and grooves and well exposed glass shards. All mounts were then cleaned in an ultrasonic bath (facing up) for 5 minutes, to remove any loose ground powders.

Following grinding, samples were polished, secured by weights to a polishing plate. Samples were polished using 3 μm diamond solutions for 40 minutes, followed by 1 μm diamond solutions for 5 minutes, on separate pads, to avoid contamination. Between each diamond polishing stages, samples were checked under a binocular microscope to see the quality of the glass shards and to check that scratches were barely visible, due to a good and even polish. After, samples were cleaned in an ultrasonic bath for 5 minutes and a map was etched into the surface of the mount between the sample holes, to allow navigation around the mount on the electron microprobe (EMP). The final stage was to clean the samples with Petroleum Ether and carbon coat the samples using graphic rods, for EMP analysis (e.g., Hunt and Hill, 1993).

3.5. EPMA analysis

Analysis was conducted at the Research Laboratory for Archaeology and History of Art (RLAHA), University of Oxford using JEOL 8600 and JEOL JXA-8200 wavelength-dispersive electron microprobes. Fig. 3 illustrates the major components of a wavelength-dispersive electron microprobe including spectrometers that use synthetic crystals (e.g., PET, LIF and



Modified from Heath and Taylor, 2015

Heath, J. and Taylor, N., 2015. Electron probe microanalysis. John Wiley & Sons Ltd, West Sussex, UK, pp.1-34.

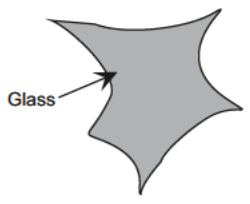
Fig. 3. Illustration of the major elements of a wavelength-dispersive electron microprobe. Modified from Heath and Taylor, 2015.

TAP) to diffract X-rays. All analyses used an accelerating voltage of 15 kV (thus not to irradiate glass due to high Na loss), 6nA beam current and a 10 μm beam diameter (e.g., Morgan and London, 1996). Elemental peaks were counted for 12 seconds (s) for Na, 50 s for Mg, Mn, Cl, P, and 30 s for Si, Ca, K, Al, Ti and Fe. Before analysis began, the instrument was calibrated for each element using primary mineral standards. The accuracy and precision of this calibration was assessed using secondary standard analyses, determined throughout the analytical run. The secondary standards used were MPI-DING reference glasses, covering a range of compositions, e.g., ML3B-G (basalt), StHs6/80-G (andesite), GOR132-G (komatiite), ATHO-G (rhyolite), from the Max Planck Institute (Jochum et al., 2006) with all analyses lying within the standard deviation of the preferred values. All data used in this study, including units from volcanoes and core tephra, as well as secondary standard analyses, are presented in the Appendix E1.

Glass-shard morphologies were noted throughout analysis (Fig. 4) and microlite-rich samples were avoided where possible. If it was not feasible to avoid analysing samples rich in microlites, the electron beam was positioned carefully on glass larger than the beam itself thus to minimise the likelihood of obtaining low totals should the beam move slightly off a shard during analysis. The backscatter electron (BSE) image was used for all samples to see relative compositional changes in the glass (e.g., minerals) and avoid these where possible. It must

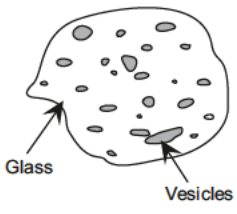
GLASS-SHARD MOPHOLOGIES

Cuspate (CU)



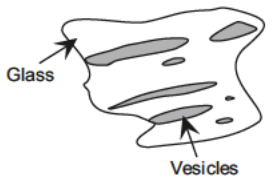
NOT TO SCALE

Pumiceous (PU)



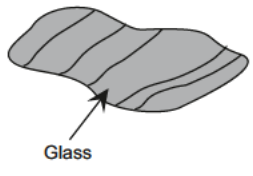
NOT TO SCALE

Vesicular (V)



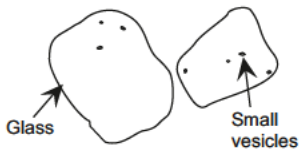
NOT TO SCALE

Fluted (F)



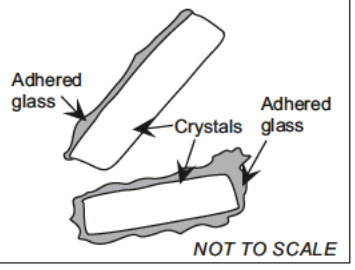
NOT TO SCALE

Blocky (B)



NOT TO SCALE

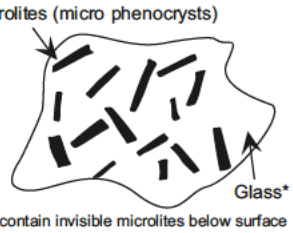
Crystal-adhered glass (C)



NOT TO SCALE

OTHER GLASS CHARACTERISTICS

Microlite-rich



*may contain invisible microlites below surface

NOT TO SCALE

Small shards (S)



= 10 µm electron beam for scale

Fig. 4. Schematic diagrams of the glass-shard morphologies of the samples analysed in this study. Other characteristics are also noted, including the appearance of microlite-rich glass and small shards, which are typically ≤10 μm, the electron beam size. Codes are presented alongside the glass morphologies and characteristics (where appropriate) which relate to the shard shapes displayed in Table 2.

---

however be noted that electrons are generated below the surface of the sample (e.g., Stormer et al., 1993) where the BSE image doesn't reach, resulting in microlites below the surface being unavoidable. Additionally, plagioclase (the mineral in highest abundance in these samples, see chapter 4 and Sunyé-Puchol et al., 2021) is often difficult to distinguish from glass from a BSE image due to a similar elemental componentry.

3.6. Data analysis and filtering of glass geochemical data

For comparative purposes, and to account for variety in hydration, all glass data has been normalised to 100%, and data has been rejected where low analytical totals occurred (<92 wt.%) or where non-glass analyses (e.g., microlites) had been gathered (as judged by anomalous analytical compositions). Care was taken when filtering data, as many of the samples in this study are microlite-rich (see Table 2). Filtering was conducted in several stages, initially removing apparent mineral analyses through stoichiometry (e.g., Deer et al., 1992). To aid in the identification of mineral or partial mineral analyses, data with a >2 wt.% difference between CaO and FeO_t were flagged for investigation. Following the removal of these non-glass analyses (as well as samples with low analytical totals), data was plotted in the OxCal/RESET software (https://c14.arch.ox.ac.uk/resetdb/db.php) for visualisation (Bronk Ramsey and Lee, 2013; Bronk Ramsey et al., 2015). Here, outliers or 'points of interest' were noted for further investigation. In most cases, these points had higher Ca and Al and lower Fe,

Ti and Mn when compared with glass. This is often the case for feldspar and in many cases included partial analyses of feldspar microlites, slightly skewing data towards these differences in elemental concentrations. Data points with higher Ca and Al and lower Fe, Ti and Mn were removed. It is important to note that where ambiguity occurred as to whether a mineral or partial mineral analysis had occurred, these data points were not removed, so as not to over-filter the data. All data presented in this study have undergone this filtering methodology.

4. SOURCE GLASS GEOCHEMISTRY

Building upon chapter 4 and Sunyé-Puchol et al. (2021), volcanoes suspected of producing tephra deposits likely to be in Lake Chalco were geochemically characterised using their glass compositions. This included analysing known eruption units from these sources as well as newly identified deposits attributed to the volcanoes by field methods. All of the tephra preparation methods and analytical procedures were conducted as outlined in section 3.2, 3.3 and 3.4. To supplement our fieldwork at Popocatépetl, Iztaccíhuatl, Tláloc-Telapón, Nevado de Toluca, La Malinche and SCVF, samples were also obtained from Los Humeros and Ceboruco (Fig.1) and published glass data was used from La Primavera (Sourisseau et al., 2020) and Atitlán, Guatemala (Cisneros de León et al., 2021). The eruptions used to construct glass chemical fields from all volcanoes are presented in Table 2.

Data is split into three groups, following categories outlined in section 2: (1) potential proximal polygenetic sources, including Popocatépetl, Iztaccíhuatl Tláloc-Telapón, Nevado de Toluca and La Malinche volcanoes; (2) potential distal sources, including Mexican caldera volcanoes,

Table 2. Characteristics of the geochemically analysed tephra layers from the Chalco core (this study) split into 50 m sections of core.

			Glass Shards						
Tephra Name (Composite Depth)	**Best-preserved thickness (cm)**	**Grain size (φ)**	**Microlite-rich**	**Microlite-poor**	**Shape ***	**Volcanic Source**	**Possible reworking [chemical]**	**n. of analyses**	**Correlated eruptions**
0.585	3.5	3		x	CU	Popocatépetl		13	
5.593	42.25	0	x		PU, C	Iztaccíhuatl, La Malinche and Nevado de Toluca		27	
8.851	28.3	-1	x		CU, C	Ambiguous (central TMVB signature)		9	
8.898	4.63	3	x		CU, C	Popocatépetl		18	
11.542	1	1	x		CU, C	SCVF		26	
15.113	1.63	0	x		CU, V	Ambiguous (central TMVB signature)		32	
16.946	3	1	x		CU	SCVF		9	
20.357	59.5	1			-	SCVF		27	
21.172	23.25	2	x		CU, V	SCVF		18	
22.14	11	2			-	SCVF		8	
31.307	10.8	3	x		CU	Iztaccíhuatl, La Malinche and Nevado de Toluca		8	
31.698	1.5	3			S	Popocatépetl		26	
32.089	5.4	3			S	Ambiguous (central TMVB signature)		3	
35.864	3.13	2			-	Ambiguous (central TMVB signature)		16	
43.419	11.25	3	x		PU	Ambiguous (central TMVB signature)		21	

			Glass Shards						
Tephra Name (Depth)	**Best-preserved thickness (cm)**	**Grain size (φ)**	**Microlite-rich**	**Microlite-poor**	**Shape ***	**Volcanic Source**	**Possible reworking [chemical]**	**n. of analyses**	**Correlated eruptions**
60.799	1.4	2	x		CU, B	Ambiguous (central TMVB signature)		42	
75.335	4.25	2		x	CU, V	Atitlán		26	Los Chocoyos (LCY) eruption, 75 ± 2 ka
78.815	1.5	3		x	V, S	Tláloc-Telapón		55	
79.48	6	2			V, S	Popocatépetl		22	
89.3	2.5	3		x	CU, V	Exotic		24	

89.56	2.88	0		x	C, S	Iztaccíhuatl, La Malinche and Nevado de Toluca		24	
89.658	1.2	2	x		B, V, S	Popocatépetl		14	
92.194	0.5	3		x	CU, C, F	Exotic		28	
93.259	2	2		x	S	Ambiguous (central TMVB signature)		19	
96.71	12	2	x		CU, C	SCVF		12	
96.806	10	0	x		V, CU	SCVF		34	
96.884	7	3			-	Iztaccíhuatl, La Malinche and Nevado de Toluca		10	
100.176	5	1	x		B	SCVF		12	

			Glass Shards						
Tephra Name (Depth)	**Best-preserved thickness (cm)**	**Grain size (φ)**	**Microlite-rich**	**Microlite-poor**	**Shape ***	**Volcanic Source**	**Possible reworking [chemical]**	**n. of analyses**	**Correlated eruptions**
101.141	3.25	3	x		S	Exotic		50	
101.408	1.1	3	x		F, CU, S	Popocatépetl		41	
105.169	3.5	1	x		CU	SCVF		27	
105.721	0.7	1	x		CU	SCVF		21	
107.565	6.25	3			-	Ambiguous (central TMVB signature)		9	
108.14	8.75	2	x		V, PU, C, S	Iztaccíhuatl, La Malinche and Nevado de Toluca		35	
110.312	39.6	2		x	CU	Los Humeros		236	Xaltipan Ignimbrite, 164 ± 4.2 ka
115.775	9	-1	x		F, V, C	Popocatépetl		21	
118.2	3.88	1	x		B, V	Ambiguous (central TMVB signature)		11	
118.63	4.5	2			-	Iztaccíhuatl, La Malinche and Nevado de Toluca		33	
119.807	3.5	0			-	Popocatépetl		6	
120.108	1.5	2	x		CU, B, S	Exotic		28	
123.113	1.3	0	x		F, C, V, S	Popocatépetl		65	
123.478	1.8	0	x		V	Popocatépetl		16	
124.916	0.8	2			-	Ambiguous (central TMVB signature)		4	
130.06	4	3			S	Popocatépetl		6	
131	5	3				Exotic		6	

134.623	8.75	1	x		CU	Ambiguous (central TMVB signature)		16	
136.533	4.5	0			S	Popocatépetl		6	
136.783	3.5	3		x	CU	Los Humeros		56	
137.244	11.3	1	x		CU	SCVF		47	
137.544	4.9	1			V, F, S	Popocatépetl		26	
138.422	1.2	1	x		B	Popocatépetl		20	
141.188	3.25	-1			PU, C, S	Popocatépetl		22	
144.464	1.9	-1	x		B	Popocatépetl		15	
144.654	1	3			-	Los Humeros		19	
144.722	1.25	-1			F, C, S	Popocatépetl		19	
144.809	2.25	-2	x		PU, CU, C	Popocatépetl		29	
146.2805	3.25	-1		x	CU, V	Popocatépetl		23	

			Glass Shards						
Tephra Name (Depth)	**Best-preserved thickness (cm)**	**Grain size (φ)**	**Microlite-rich**	**Microlite-poor**	**Shape ***	**Volcanic Source**	**Possible reworking [chemical]**	**n. of analyses**	**Correlated eruptions**
164.575	3.25	0		x	F	Iztaccíhuatl, La Malinche and Nevado de Toluca		26	
165.047	1.5	3	x		C, PU	Popocatépetl		10	
168.105	116	-4	x		CU, V, C	Iztaccíhuatl, La Malinche and Nevado de Toluca	x [x]	38	
169.145	103.5	-2			-	Iztaccíhuatl, La Malinche and Nevado de Toluca		12	
171.633	4	2	x		V	Popocatépetl		14	
171.779	7.25	0	x		V, C	Iztaccíhuatl, La Malinche and Nevado de Toluca		6	
172.069	1.25	3	x		V, CU, B	Iztaccíhuatl, La Malinche and Nevado de Toluca		28	
172.339	0.75	2	x		CU	Popocatépetl		22	
173.914	1.38	1	x		V	Iztaccíhuatl, La Malinche and Nevado de Toluca		34	
174.244	3.75	1	x		CU	Popocatépetl		20	
178.667	3.88	2	x		CU	Ambiguous (central TMVB signature)		4	
181.723	40	-1		x	F	Iztaccíhuatl, La Malinche and Nevado de Toluca		25	
182.165	1.25	2		x	CU	Popocatépetl		23	
182.311	5.75	1		x	CU	Exotic		49	
183.588	1.75	-1		x	CU	Iztaccíhuatl, La Malinche and Nevado de Toluca		25	

184.224	26.6	-1		x	V, S	Exotic		56	
184.394	1.38	1		x	V, F	Popocatépetl		21	
186.124	1.88	3		x	V, B	Popocatépetl		18	
186.807	4.5	2	x		B	Ambiguous (central TMVB signature)		20	
187.227	6.25	-1	x		V, C, S	Iztaccíhuatl, La Malinche and Nevado de Toluca		44	
187.723	41.15	-1		x	V, C	Iztaccíhuatl, La Malinche and Nevado de Toluca		46	
189.09	1.5	2			S	Ambiguous (central TMVB signature)		4	
189.682	1.63	2		x	C, B, V, PU	Popocatépetl		26	
190.682	2	1	x		S	Iztaccíhuatl, La Malinche and Nevado de Toluca		18	
191.917	1.25	3	x		CU, V, C	Popocatépetl		25	
192.137	8.75	-2		x	PU, S	Iztaccíhuatl, La Malinche and Nevado de Toluca		24	
192.397	1.5	1		x	B, C	Iztaccíhuatl, La Malinche and Nevado de Toluca		30	
193.032	2.75	2	x		V	Iztaccíhuatl, La Malinche and Nevado de Toluca		24	
193.172	2.25	1	x		B	Ambiguous (central TMVB signature)		4	
194.977	13.1	0				Ambiguous (central TMVB signature)		3	

			Glass Shards						
Tephra Name (Depth)	**Best-preserved thickness (cm)**	**Grain size (φ)**	**Microlite-rich**	**Microlite-poor**	**Shape ***	**Volcanic Source**	**Possible reworking [chemical]**	**n. of analyses**	**Correlated eruptions**
204.114	10	2	x		B, CU	SCVF		25	
204.869	2	2		x	CU	Exotic		84	
205.524	1.25	2		x	CU, S	Popocatépetl		12	
209.916	2.63	2	x		V	Popocatépetl		16	
228.011	4.5	3	x		V, C, S	Iztaccíhuatl, La Malinche and Nevado de Toluca		21	
228.071	4.5	3	x		V, CU, B	Iztaccíhuatl, La Malinche and Nevado de Toluca		27	
230.208	1	2		x	PU	Exotic		23	
230.23	5.13	2		x	CU, F	Iztaccíhuatl, La Malinche and Nevado de Toluca		64	
230.407	2.2	3	x		CU	Exotic		9	
230.638	2.1	3		x	CU	Iztaccíhuatl, La Malinche and Nevado de Toluca		30	
231.048	17.2	-1		x	PU, C, S	Iztaccíhuatl, La Malinche and Nevado de Toluca		23	
232.159	0.8	1	x		S	Iztaccíhuatl, La Malinche and Nevado de Toluca		15	

232.194	0.9	3		x	PU, CU, S	Iztaccíhuatl, La Malinche and Nevado de Toluca		32	
233.055	7	-2		x	PU	Iztaccíhuatl, La Malinche and Nevado de Toluca		26	
233.286	3.38	2	x		S	Iztaccíhuatl, La Malinche and Nevado de Toluca		13	
233.661	6	-1		x	PU,CU	Iztaccíhuatl, La Malinche and Nevado de Toluca		54	
233.726	1.75	-1		x	V, C	Iztaccíhuatl, La Malinche and Nevado de Toluca	x	23	
237.208	0.6	2	x		V	Exotic	x	33	
240.957	1.73	3	x		C, S	Popocatépetl		8	
241.429	2.88	1		x	V,S	Popocatépetl		13	
243.414	0.6	1	x		F, V, C	Exotic		16	
243.444	0.8	2	x		V	Iztaccíhuatl, La Malinche and Nevado de Toluca		13	
244.238	10.7	2	x		C, CU, V	Ambiguous (central TMVB signature)		11	

			Glass Shards						
Tephra Name (Depth)	**Best-preserved thickness (cm)**	**Grain size (φ)**	**Microlite-rich**	**Microlite-poor**	**Shape ***	**Volcanic Source**	**Possible reworking [chemical]**	**n. of analyses**	**Correlated eruptions**
251.779	0.5	3		x	PU, F	Popocatépetl		23	
255.175	16.88	-1	x		C, S	Ambiguous (central TMVB signature)		81	
256.12	6.63	-1	x		V, F, S	Iztaccíhuatl, La Malinche and Nevado de Toluca	x	16	
275.23	1.5	3	x		V, CU, C	Exotic		29	
275.25	1	3	x		CU, F, V	Exotic		28	
275.48	14.8	-1		x	CU, C	Iztaccíhuatl, La Malinche and Nevado de Toluca		28	
279.811	5.75	2		x	V, F, CU	Iztaccíhuatl, La Malinche and Nevado de Toluca		26	
280.114	0.8	3	x		V, S	Iztaccíhuatl, La Malinche and Nevado de Toluca		16	
281.395	1.25	0		x	C	Ambiguous (central TMVB signature)	x	20	
281.657	7.25	2	x		B	SCVF		17	
282.057	10.75	2		x	PU, CU, C	Iztaccíhuatl, La Malinche and Nevado de Toluca		72	
283.562	0.5	2	x		V	Ambiguous (central TMVB signature)		11	
283.788	0.63	3	x		F, C	Popocatépetl		31	
283.802	1.5	2		x	F, V, CU	Iztaccíhuatl, La Malinche and Nevado de Toluca		25	
285.315	26.5	1	x		V	SCVF		25	
285.7	5	1	x		V	SCVF		13	

287.02	1.25	0	x		V, C	Ambiguous (central TMVB signature)		24
287.253	0.3	2	x		B	Ambiguous (central TMVB signature)		24
287.321	2.5	1	x		F, CU	Popocatépetl		16
287.396	5.75	1	x		F, CU	Iztaccíhuatl, La Malinche and Nevado de Toluca		18
287.481	1.25	3		x	V, B	Iztaccíhuatl, La Malinche and Nevado de Toluca		26
287.536	0.75	2	x		V, CU	SCVF		21
287.608	1.5	2	x		V	SCVF		13
290.296	41.25	-3			-	Ambiguous (central TMVB signature)		4
290.428	1.5	-1	x		F	Iztaccíhuatl, La Malinche and Nevado de Toluca		15
291.513	4.13	-2	x		V, CU	Iztaccíhuatl, La Malinche and Nevado de Toluca	x	6
293.706	67	-2			V, F, S	Iztaccíhuatl, La Malinche and Nevado de Toluca		34

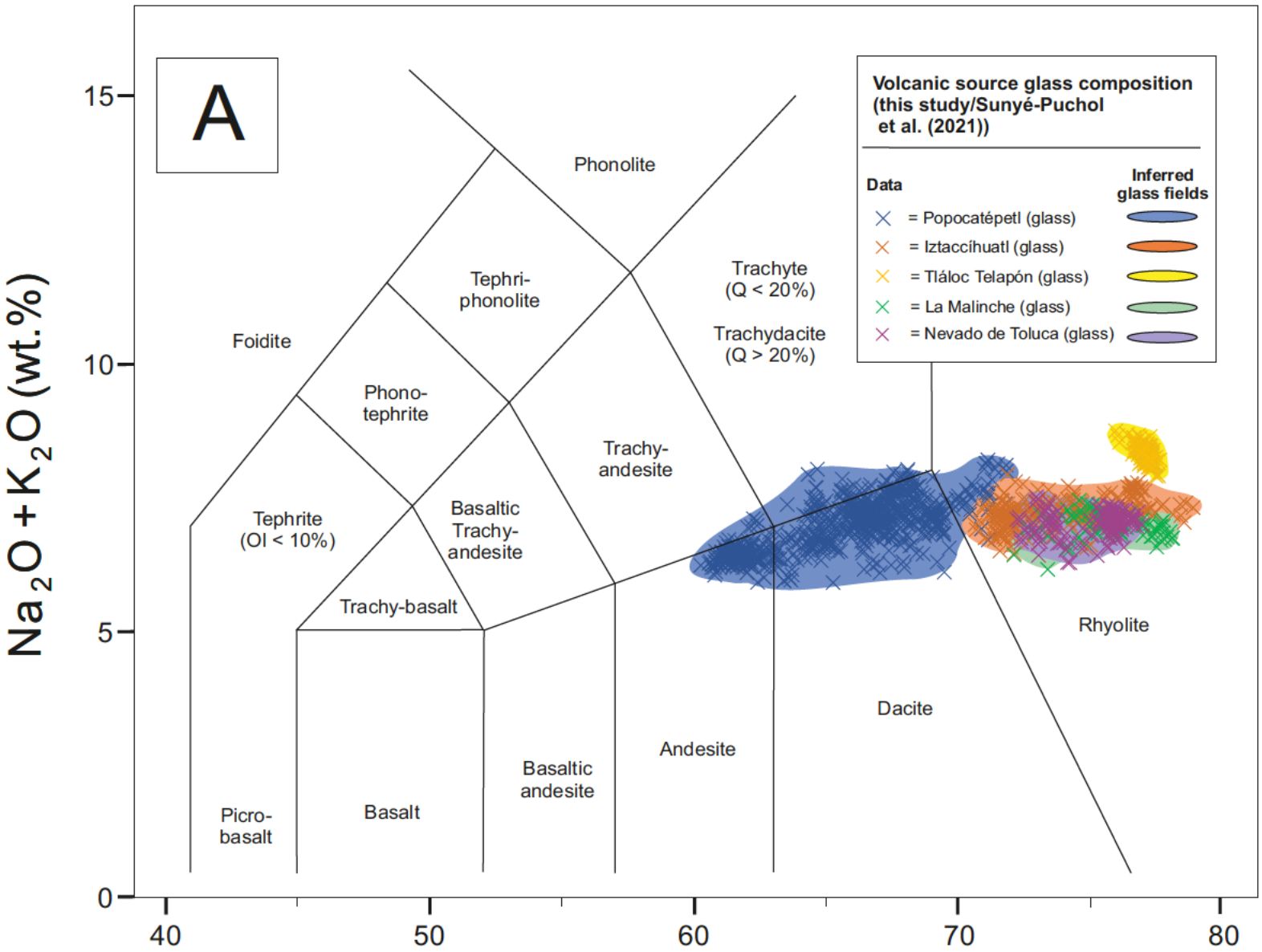
* Glass shapes: CU = cuspate; PU = pumiceous; V = vesicular; F = fluted; B= blocky; C = crystal-adhered glass; S = small shards. Explanations of morphologies are displayed in Fig. 4.

La Primavera and Los Humeros , Ceboruco, which produced the youngest caldera (c.1 ka) in Mexico (Chertkoff and Gardner, 2003; Sieron and Siebe, 2008) and the Guatemelan caldera, Atitlán which has had several large eruptions including the Los Chocoyos (LCY) eruption 75 ± 2 ka (e.g., Cisneros de León et al., 2021), suspected to have a fall deposit between 6 and 9 cm at Lake Chalco, see Fig.11 of Kutterolf et al. (2016); and (3) proximal monogenetic sources, including eruptions from the Sierra Chichinautzin Volcanic Field (SCVF). Geochemical data is presented for these three groupings in Fig. 5, Fig. 6 and Fig. 7, respectively.

4.1. *Group 1: Proximal polygenetic source*

Group 1 consists of major element glass data and geochemical fields from Popocatépetl, Iztaccíhuatl, Tláloc-Telapón, Nevado de Toluca and La Malinche. Fig. 5a displays the glass fields defined in this study on a Total Alkali vs. Silica (TAS) diagram. Three broad calc-alkaline groupings can be noted, with data from Popocatépetl and Tláloc-Telapón generally forming their own clusters at 60.3 – 71.8 wt.% SiO_2 and 76.0 – 77.7 wt.% SiO_2, respectively. Popocatépetl includes glass compositions that span andesite, trachyandesite, trachyte, dacite and rhyolite, with the majority of analyses being dacitic in composition. In contrast, all other volcanoes in Groups 1 – the potential polygenetic source volcanoes in the central TMVB - contain exclusively rhyolitic glass compositions. On the TAS, analyses that are richest in SiO_2 from Popocatépetl (rhyolitic glass) overlap slightly with Iztaccíhuatl glass anlayses. However, Tláloc-Telapón has a distinctive and discrete population. Nevado de Toluca, La Malinche and Iztaccíhuatl all overlap, with the Iztaccíhuatl population having a greater spread, (70.7 – 78.9 wt.% SiO_2) than the other two volcanoes. This however may be due to a greater number of

A


Volcanic source glass composition (this study/Sunyé-Puchol et al. (2021))
Data
Inferred glass fields
= Popocatépetl (glass)
= Iztaccíhuatl (glass)
= Tláloc Telapón (glass)
= La Malinche (glass)
= Nevado de Toluca (glass)
Phonolite
Tephri-phonolite
Foidite
Phono-tephrite
Tephrite (Ol < 10%)
Basaltic Trachy-andesite
Trachy-basalt
Trachyte (Q < 20%)
Trachydacite (Q > 20%)
Trachy-andesite
Rhyolite
Dacite
Andesite
Basaltic andesite
Basalt
Picro-basalt
$Na_2O + K_2O$ (wt.%)
SiO_2 (wt.%)

B

CaO (wt. %)
FeO_t (wt. %)
Al_2O_3 (wt. %)
TiO_2 (wt. %)
Na_2O (wt. %)
K_2O (wt. %)
SiO_2 (wt. %)

Fig. 5. (a) Total alkali vs. silica (TAS) diagram displaying the volcanic source glass compositions of the proximal polygenetic source volcanoes analysed in this study and Sunyé-Puchol et al. (2021). Inferred glass fields have been drawn around the data points. (b) selected bivariate plots showing the data in a.

---

analyses (224) when compared with Nevado de Toluca and La Malinche, with 164 and 74 analyses, respectively.

In Fig. 5b, bivariate plots allow the chemical relationships of major elements to be compared with SiO_2. Tláloc-Telapón can be seen to overlap with data from Iztaccíhuatl, Nevado de Toluca and La Malinche in Al_2O_3, FeO_t and Na_2O, although distinct fields are present in CaO, K_2O and TiO_2. We therefore conclude that Tláloc-Telapón has a distinct glass geochemistry (fingerprint) and thus defines a unique compositional field when compared with other proximal polygenetic sources, permitting comparison and correlation with core tephra analyses. It is also concluded from bivariate plots, that Popocatépetl defines a unique glass compositional field in almost all major elements, most clearly observable in Al_2O_3, TiO_2 and K_2O (versus silica). Popocatépetl can be seen to display a slightly different evolutionary trend to Iztaccíhuatl, as discussed in chapter 4 and Sunyé-Puchol et al. (2021). In this study, it can also be noted that Nevado de Toluca and La Malinche display similar and overlapping evolutionary trends with Iztaccíhuatl, thus confirming Popocatépetl provides the most distinctive fingerprint for correlative purposes.

Consequently, glass data show that of the polygenetic potential source volcanoes proximal to Chalco, only Popocatépetl and Tláloc-Telapón are chemically distinct in major elements, and that Iztaccíhuatl, La Malinche and Nevado de Toluca should be grouped together from a major

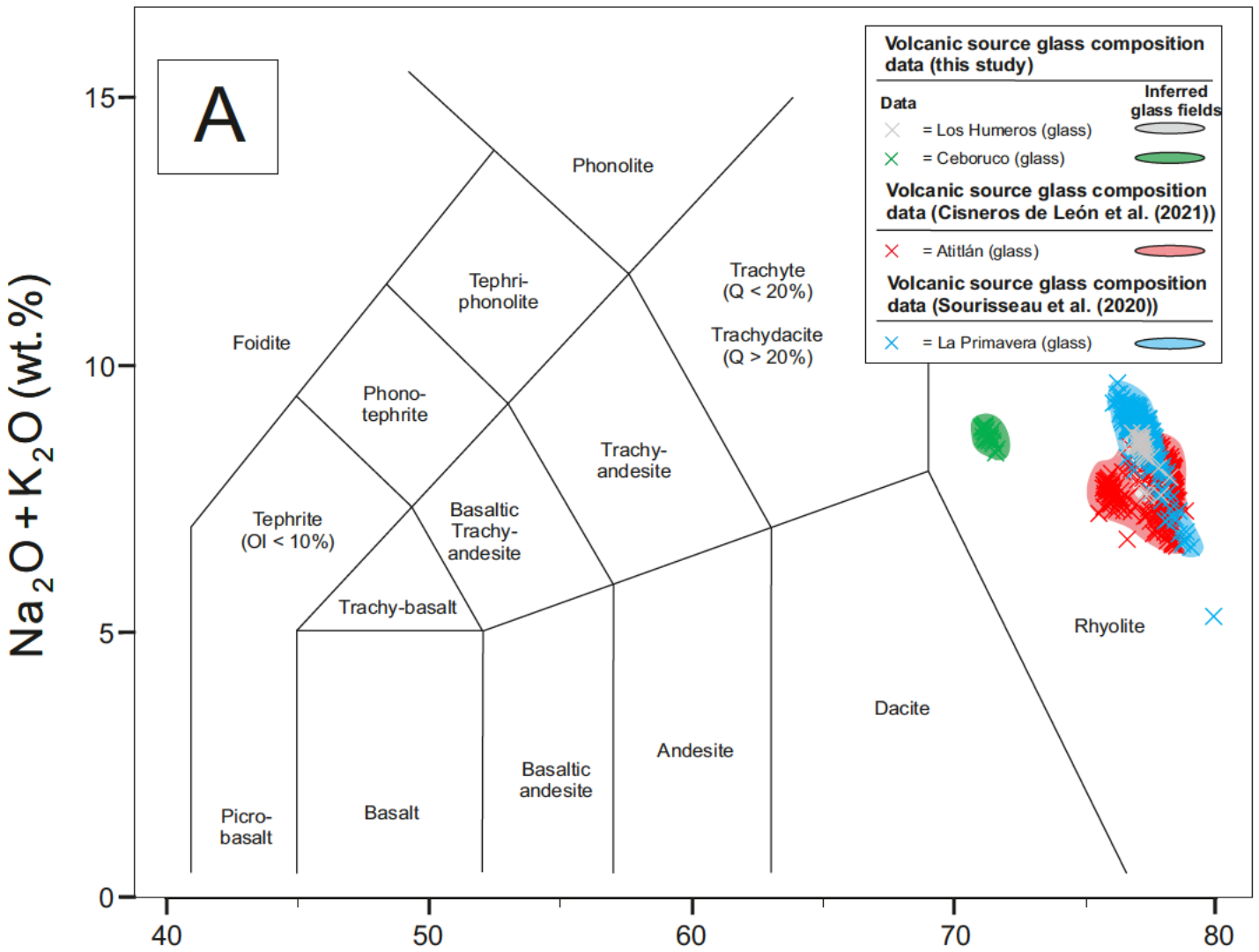
element glass geochemical perspective as they, together, define a unique field with distinctive evolutionary trends, seen in all major elements. Resultantly, for comparative and correlative purposes, these three volcanoes are grouped in terms of their glass geochemistry. No other connection is suggested between these three volcanoes, and they are widely spatially separated, but based on glass chemistry they cannot be separated.

4.2. *Group 2: Distal sources*

As discussed above, potential distal sources of tephra to Chalco include Mexican caldera volcanoes (Los Humeros and La Primavera) and Ceboruco (e.g., from the c.1 ka Jala Pumice caldera-forming eruption). Additionally they include the Guatemala caldera volcano, Atitlán, responsible for one of the largest eruptions (Los Chocoyos, LCY) in Central America in the last c.1 Ma and the third largest eruption of the Quaternary (e.g., Drexler et al., 1980; Newhall, 1987; Rose et al., 1987; Paine et al., 2021). The eruptions from each volcano used to construct glass chemical fields are outlined in Table 2. There are likely a number of other possible volcanic sources for Chalco tephra, in both Mexico and nearby volcanically active areas. These are not examined inidiviually though, and only those sources considered to have the strongest potential for input based on known large explosive eruptions have been selected here for further investigation.

Group 2, the distal potential source volcanoes, is presented on the TAS in Fig. 6a, alongside defined compositional fields. All samples have high SiO_2 contents, with all glass analyses displaying rhyolitic compositions. Ceboruco has a narrow and distinctively lower SiO_2 content (71.1 – 71.6 wt.%) than the other sources. Los Humeros also forms a tight cluster with limited spread in SiO_2 (76.5 – 78.2 wt.%), although both Ceboruco and Los Humeros fields are only

A


Volcanic source glass composition data (this study)
Data
Inferred glass fields
= Los Humeros (glass)
= Ceboruco (glass)
Volcanic source glass composition data (Cisneros de León et al. (2021))
= Atitlán (glass)
Volcanic source glass composition data (Sourisseau et al. (2020))
= La Primavera (glass)
Phonolite
Tephri-phonolite
Trachyte (Q < 20%)
Trachydacite (Q > 20%)
Foidite
Phono-tephrite
Trachy-andesite
Tephrite (Ol < 10%)
Basaltic Trachy-andesite
Trachy-basalt
Rhyolite
Dacite
Andesite
Basaltic andesite
Picro-basalt
Basalt
$Na_2O + K_2O$ (wt.%)
SiO_2 (wt.%)

B

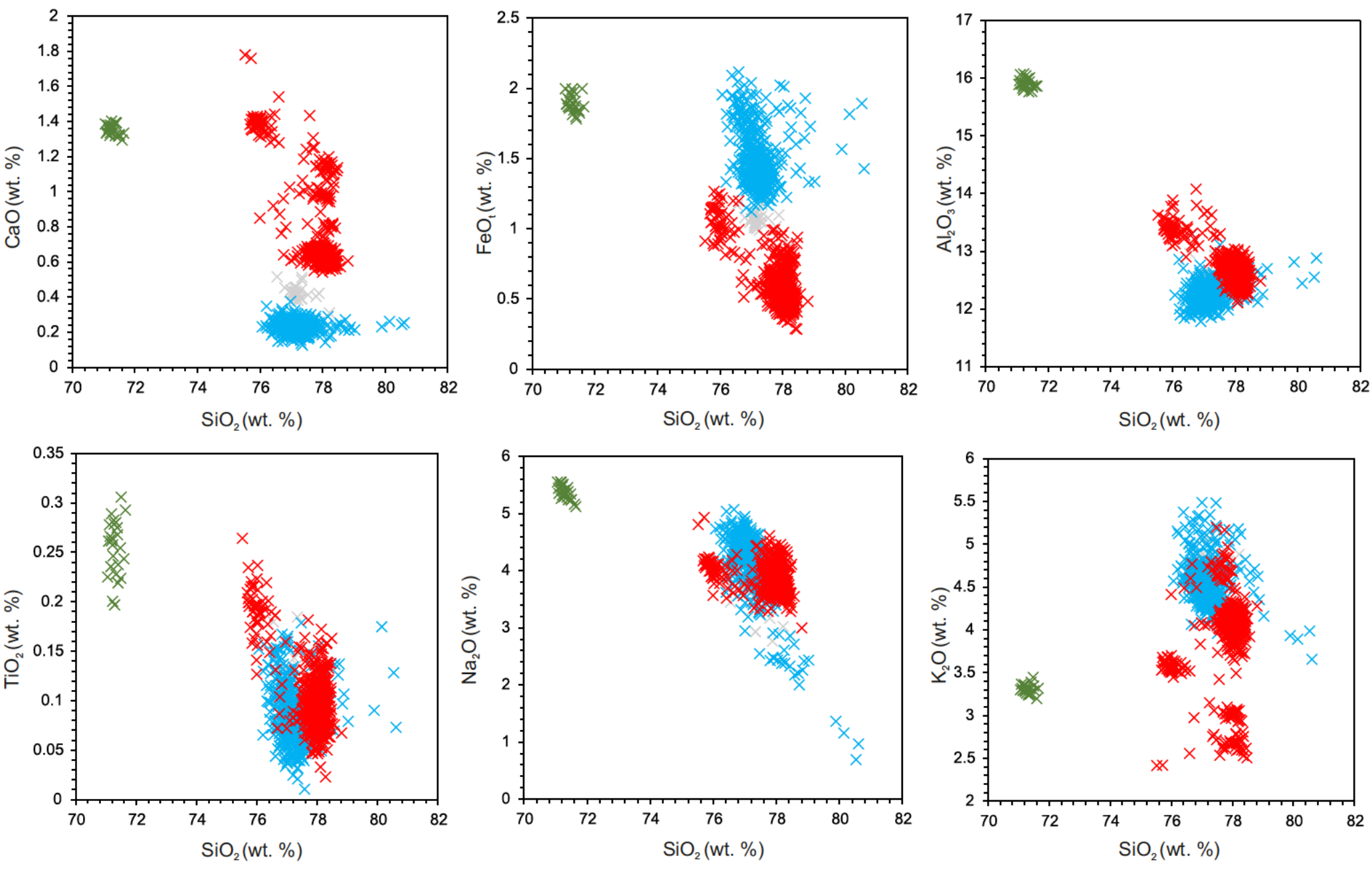

CaO (wt. %)
FeO_t (wt. %)
Al_2O_3 (wt. %)
TiO_2 (wt. %)
Na_2O (wt. %)
K_2O (wt. %)
SiO_2 (wt. %)

Fig. 6. (a) Total alkali vs. silica (TAS) diagram displaying the volcanic source glass compositions of the distal sources investigated in this study. Data has been collected in this study and is supplemented by data presented in Sourisseau et al. (2020) and Cisneros de León et al. (2021). (b) Selected bivariate plots showing the data in a.

---

constructed using one eruption: the Jala Pumice and Xaltipan Ignimbrite, respectively (c.f. Table 2). La Primavera and Atitlán, both have a greater spread in SiO_2 and $Na_2O + K_2O$. From the TAS alone, only Ceboruco can be seen to form a distinct geochemical field, with data from Los Humeros, La Primavera and Atitlán all overlapping.

Fig. 6b (bivariate plots) permit further investigation into the glass chemistry of these distal sources, where it can be concluded that all of the analysed deposits of the volcanoes display chemically distinct compositions in one or more major element. La Primavera is depleted in Ca and enriched in Fe, compared to the other calderas and Atitlán has generally higher Ca and lower Fe. There is an overlap in data for La Primavera, Atitlán and Los Humeros in Na_2O, Al_2O_3, TiO_2 and K_2O, although geochemical independence is best observed in CaO and FeO_t, e.g., CaO concentrations of La Primavera, Los Humeros and Atitlán are 0.13 – 0.37 wt.%, 0.31 – 0.52 wt.% and 0.54 – 1.78 wt.%, respectively.

We are confident that all potential distal sources analysed in this study are sufficiently geochemically distinct in one or more major element and their glass compositions can be used effectively to compare and correlate to core tephra analyses to determine likely source volcanoes.

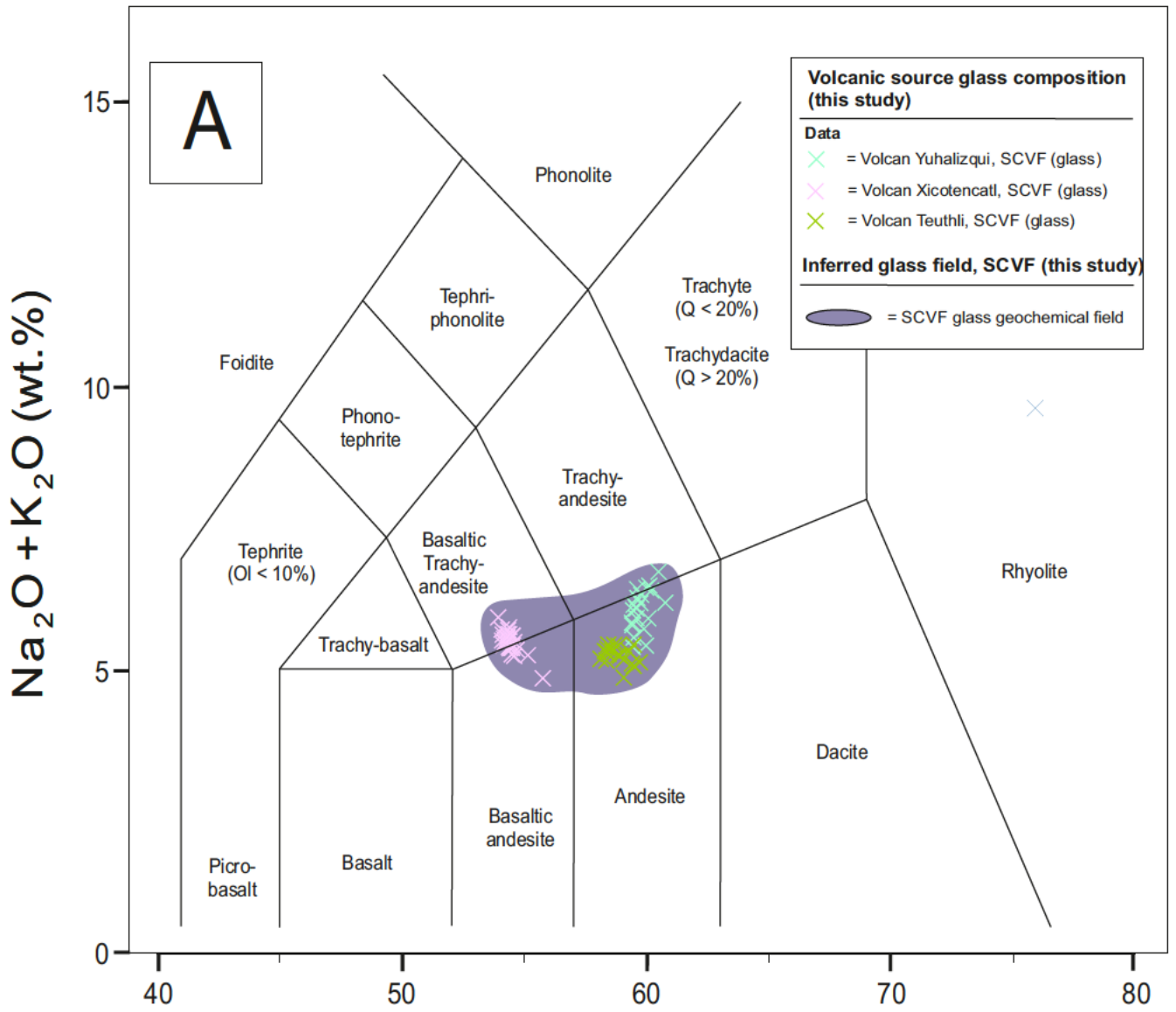
4.3. Group 3: Proximal monogenetic sources

Similarly to group 1 and 2 sources, group 3 (proximal monogenetic volcanoes of the SCVF) are investigated separately. As discussed in section 2, the term monogenetic is used here to refer to small-scale volcanism (e.g., ≤VEI 4), which near Chalco is likely dominated by input from the SCVF, a field comprised of shield volcanoes, scoria/cinder cones and a maar crater (Volcán Xicotencatl). While it is assumed that the volcanoes are monogenetic in an 'eruptive sense' (i.e., erupting only once), our data does not focus on the eruptive history of individual cones/volcanoes, so the term is used to describe the sources from a 'petrogenic sense' to indicate a more simplistic plumbing system, supplied by more basic and less evolved magmas (Smith and Németh, 2017). The volcanoes form the SCVF that have been analysed to determine a glass geochemical field are provided in Table 2.

Fig. 7a (TAS plot) shows data from the SCVF to span basaltic andesite, basaltic trachyandesite, trachyandesite and andesite glass compositions. This variety in glass chemistry is also seen in the whole rock analyses of lavas from the SCVF, presented in chapter 4. As this field is defined using 3 cones (Volcán Xicotencatl, Volcán Yuhalizqui and Volcán Teuthli), the field defined here for the SCVF is assumed to be a limited portion of the wider likely SCVF field, with an expectation that with more volcanoes analysed, the larger and greater the spread of data in the field would be. Nevertheless, these 3 sources define a field which spans SiO_2 concentrations of 54 – 60.8 wt.%. The spread of data in $Na_2O + K_2O$ is more constricted with concentrations ranging from 4.9 – 6.7 wt.%.

Fig. 7b (bivariate plots) again confirm that each volcano analysed for glass chemistry has a distinct geochemical fingerprint. This may however not be the case if more cones were

A


Volcanic source glass composition (this study)
Data
= Volcan Yuhalizqui, SCVF (glass)
= Volcan Xicotencatl, SCVF (glass)
= Volcan Teuthli, SCVF (glass)
Inferred glass field, SCVF (this study)
= SCVF glass geochemical field
Phonolite
Tephri-phonolite
Foidite
Phono-tephrite
Trachyte (Q < 20%)
Trachydacite (Q > 20%)
Trachy-andesite
Tephrite (Ol < 10%)
Basaltic Trachy-andesite
Trachy-basalt
Rhyolite
Dacite
Andesite
Basaltic andesite
Picro-basalt
Basalt
$Na_2O + K_2O$ (wt.%)
SiO_2 (wt.%)

B

CaO (wt. %)
FeO_t (wt. %)
Al_2O_3 (wt. %)
TiO_2 (wt. %)
Na_2O (wt. %)
K_2O (wt. %)
SiO_2 (wt. %)

Fig. 7. Total alkali vs. silica (TAS) diagram displaying the volcanic source glass compositions of local monogenetic cones of the Sierra Chichinautzin Volcanic Field (SCVF), analysed in this study. (b) Selected bivariate plots showing the data in a.

---

analysed (of which there are up to 220, e.g., Guilbaud et al., 2022), and unique groupings based on major element glass chemistry alone may be possible. It can also be noted that there is a fairly close geochemical relationship (e.g., with overlapping Ca and Na) between Volcán Yuhalizqui and Volcán Teuthli, despite being from different parts of the volcanic field: the Sierra Santa Catarina and Chalco region, respectively. Curiously, the lowest silica material is that erupted from Volcán Xicotencatl, which is the only maar crater in the SCVF and is the nearest volcano to the Chalco core site (c. 4 km).

In summary, all sources analysed are calc-alkaline and many exhibit similarities to one another, with regards to evolutionary trends, with some overlapping of glass fields. Despite this, the chemistry from all sources analysed is distinct in one or more element and can thus be used for comparative and correlative purposes, except for Iztaccíhuatl, La Malinche and Nevado de Toluca, which must be grouped together. Thickness and grain size information have not been used as a correlative tool, because the dispersal axes and magnitudes of all events depositing tephra in the core are unknown. It cannot therefore be inferred that the thickest and coarsest deposits (c.f. chapter 3) would be from the nearest source (although they're not likely to be from distal sources); and conversely, fine grained deposits could still originate from local sources.

5. CORE GLASS GEOCHEMISTRY

In total, 137 separate tephra layers have been analysed for major element glass geochemistry from the Chalco core. Additionally, 6 volcaniclastic deposits (see chapter 3 for explanation) have been analysed to determine the heterogeneity of their glass. All analysed tephras have been selected from an even spread of depths throughout the core. Priority was given to felsic layers with the assumption that they are from polygenetic or caldera sources thus allowing us to extend the eruptive histories of poorly understood stratovolcanoes as well as aiming to provide chronological constraints by correlating well known and well dated large magnitude events. Despite this, a small number of mafic layers (26 out of 137, (c.19%) analysed tephras) were selected to understand if they were consistent with a SCVF source. Table 2 presents all analysed tephras (named using their basal m_c depth from chapter 3) and provides information on the thickness, maximum grain size, and shard characteristics of the samples. It also indicates ascribed volcanic sources, based on correlations outlined below, comments on reworking, and the number of analyses (after filtering to remove poor quality data) per tephra.

Principally, glass chemistry has been used to determine the origin of the eruption deposits in the core. Additionally, these analyses permit: (1) the stratigraphic correlations between parallel drill holes (in chapter 3) to be checked; (2) variation in glass chemistry throughout an individual tephra to be investigated; (3) generalised chemical assignments (mafic, intermediate and felsic) in chapter 3 to be tested using quantifiable chemical data, (4) the prevalence of reworking throughout the core to be assessed; (5) complex magmatic histories of individual eruptions to be determined (i.e., with regards to magma mixing and mingling); (6) for chemical fields of individual source volcanoes to be expanded, for those sources where

assignments can be confidently made based on their chemical evolutionary trends defined above; and (7) for well dated and widespread eruptions to be identified in the core, providing geochronological constraints and additional information on the volumes, magnitudes and dispersal of these eruptions. Each of these are explored below.

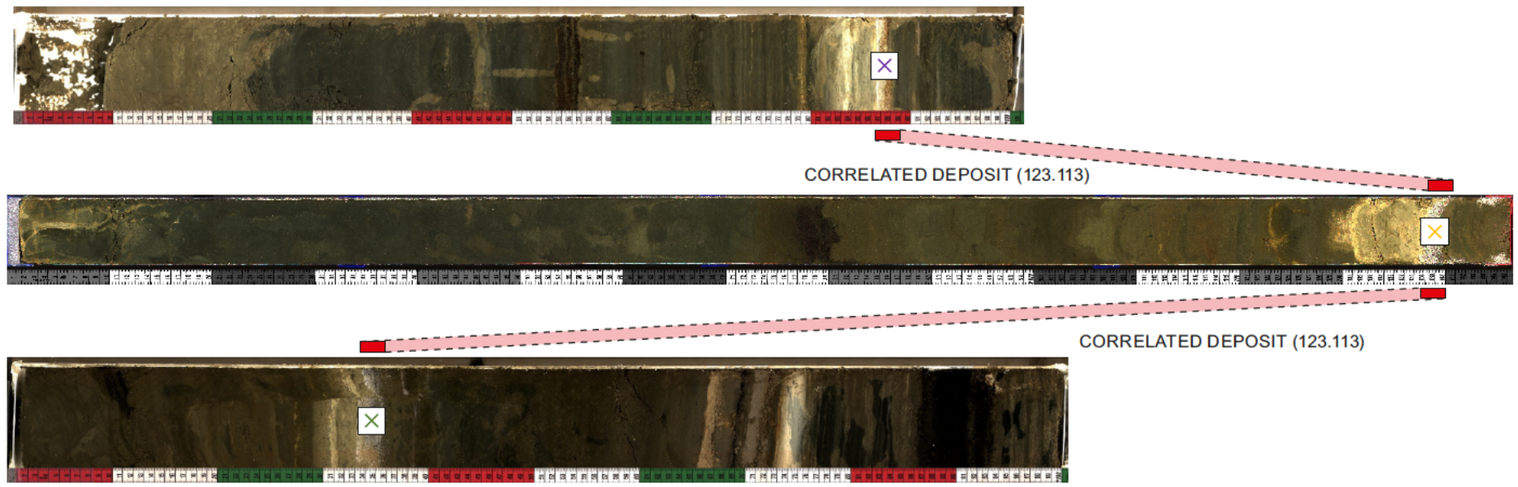
5.1. Stratigraphic correlations

As discussed in chapter 3, stratigraphic correlations across boreholes for the Chalco core were determined based on visual characteristics, identifiable marker horizons (stratigraphic tie points) and depth information, with some support from smear slide analysis (e.g., Valero-Garcés et al., 2021). Through stratigraphic logging of over 1500 m of core, a detailed volcanic stratigraphy was produced for the Chalco core (chapter 3). Due to preservation quality, and drilling artefacts, parts of core were particularly difficult to correlate by eye or magnetic susceptibility, therefore in order to assess the quality of these correlations, checks were made using glass chemistry. These checks were done for both mafic and felsic tephras, as well as on ghost layers with no on-splice identifier (chapter 3) and tested at a range of depths within the core to ensure that correlations were robust at several points. The results are as follows.

5.1.1. Felsic correlations

In most cases, the light coloured felsic eruption layers are generally the easiest to identify as a high percentage of sediments throughout the core are dark in colour. Nevertheless, poor preservation and drilling artefacts resulted in correlations that were based off only one characteristic, e.g., either colour, stratigraphic position, grain size or componentry. An example of a more ambiguous correlation is tephra 123.113, presented in Fig. 8a with on-splice and two off-splice sections. Ambiguity across all 3 boreholes is due to the contrasting distances

A


CORRELATED DEPOSIT (123.113)
CORRELATED DEPOSIT (123.113)

B

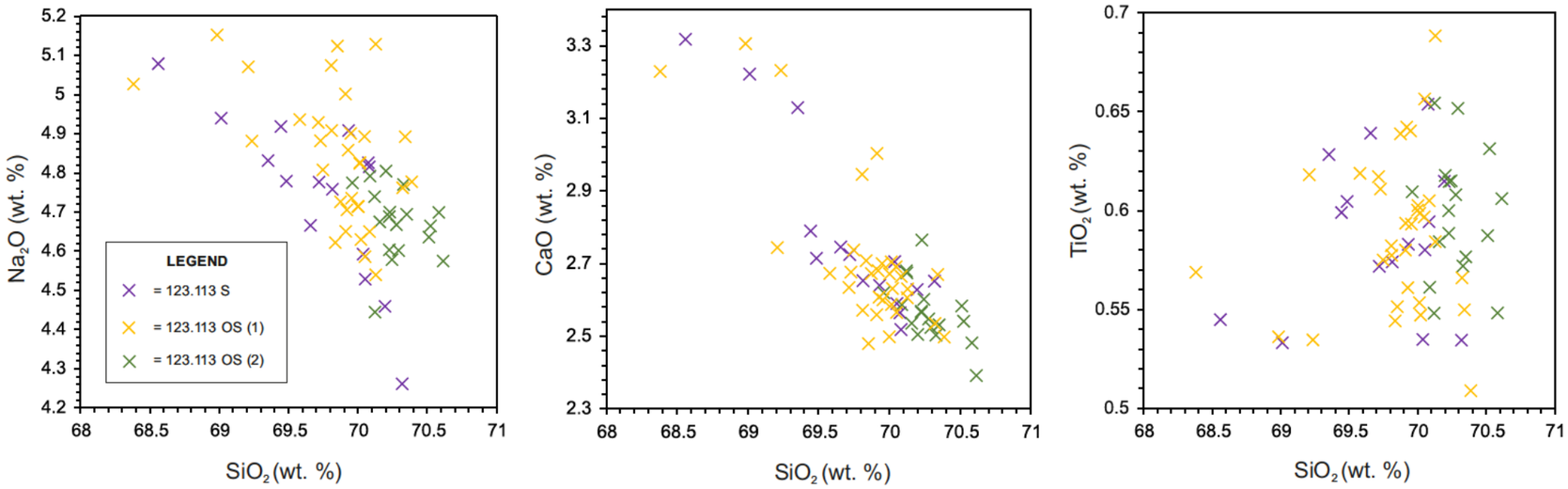

LEGEND
= 123.113 S
= 123.113 OS (1)
= 123.113 OS (2)
Na2O (wt. %)
CaO (wt. %)
TiO2 (wt. %)
SiO2 (wt. %)
SiO2 (wt. %)
SiO2 (wt. %)

Fig. 8. (a) Core section photographs displaying the 'felsic' tephra 123.113 correlated visually and chemically across boreholes and coring projects. Core sections include MEXI-CHA16-1B-71Y-1 (sampled from 137.5 – 140 cm), CHALCO-CHA08-6A-15S-1 (sampled from 87 – 88 cm) and CHALCO-CHA08-4A-22S-1 (sampled from 33 – 36 cm). Crosses are colour coded to the data shown in b and are placed at the mid-point of the depths outlined above. (b) Selected bivariate plots showing the overlap in major element glass analyses supporting a positive correlation.

---

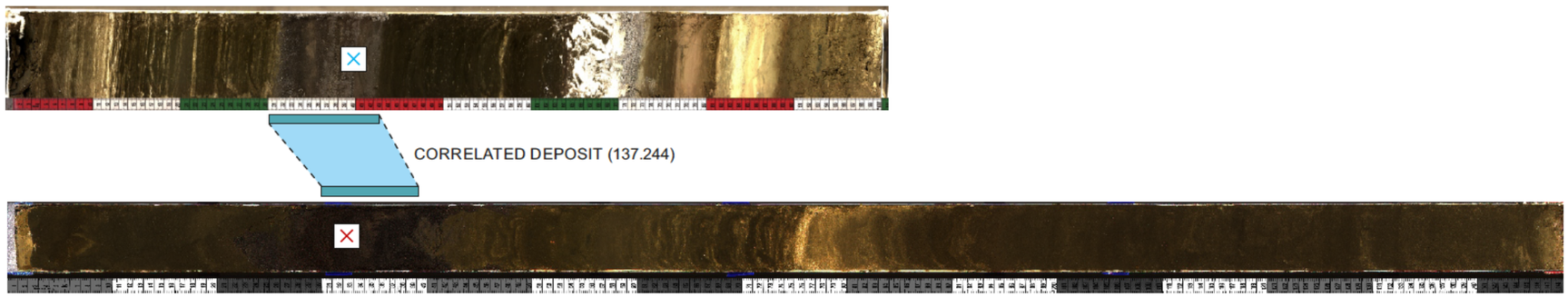
to nearby event layers and differences in the visual characteristics (e.g., colour) of the bounding sediments.

Selected bivariate plots in Fig. 8b confirm that these deposits are the same and the correlation is robust with all analyses falling within <1 wt.% Na_2O and CaO and <0.2 wt.% TiO_2. The spread of data can be seen in all analyses and the correlation has a high degree of confidence. Other felsic units tested chemically for cross-hole correlations were also deemed to reveal robust correlations. No correlations were rejected thus overall lending a high degree of confidence to the stratigraphic approach for felsic tephras. Additional plots displaying these chemical correlations are presented in Appendix E2.

5.1.2. Mafic correlations

Making correlations across the individual cores for mafic deposits is generally more difficult based on visual characteristics, particularly when bounding sediment types are also dark in colour. As discussed in chapter 3, some mafic deposits were identified using magnetic susceptibility values, due to typically being higher in magnetic elements (e.g., Fe). In these cases, visual characteristics were often very difficult to see from core section images, creating ambiguity in the robustness of the correlation.

A


CORRELATED DEPOSIT (137.244)

B

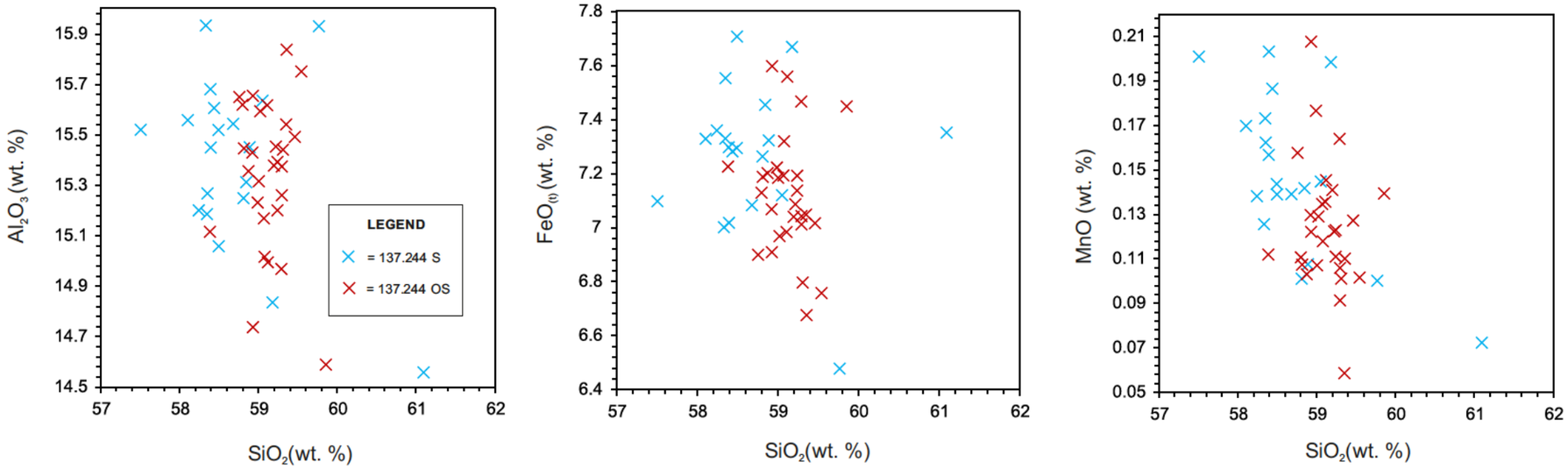

LEGEND
= 137.244 S
= 137.244 OS
Al_2O_3 (wt. %)
SiO_2(wt. %)
$FeO_{(t)}$ (wt. %)
SiO_2(wt. %)
MnO (wt. %)
SiO_2(wt. %)

Fig. 9. (a) Core section photographs displaying the 'mafic' tephra 137.224 correlated visually and chemically across boreholes and coring projects. Core sections include MEXI-CHA16-1C-74Y-1 (sampled from 30 -35 cm) and CHALCO-CHA08-6A-27S-1 (sampled from 40 cm). Crosses are colour coded to the data shown in b and are placed at the mid-point of the depths outlined above. (b) Selected bivariate plots showing the overlap in major element glass analyses supporting a positive correlation.

Fig. 9a is an example of a mafic tephra (137.244) where visual correlation was difficult. As for the felsic eruption, mentioned above, surrounding sediment characteristics differed and marker horizons were lacking in off-splice sections due to poor preservation and poor core recovery. Fig. 9b displays selected bivariate plots presenting the on-splice and off-splice tephra correlated by visual characteristics in Fig. 9a (137.244). From a glass geochemical perspective, these two deposits overlap in all elements and contain the same spread of Al, Fe, Mn and Si compositions. Resultantly, the correlation of 137.244 is deemed to be robust from a glass chemical perspective, corroborating the visual correlation in chapter 3. Further mafic correlations have been tested using glass geochemistry and are presented in Appendix E3. All chemical correlations support the visual correlations.

5.1.3. Ghost correlations

Ghost horizons (tephras) defined in chapter 3 as not containing an on-splice identifier, and therefore missing from the composite stratigraphy are still often preserved in multiple off-splice boreholes. As these sections or portions of core are not included in the composite stratigraphy, the sections in which they are present are often of low preservation quality and contain drilling artefacts. This frequently creates ambiguity over their correlation, which needs to be accurate so that the total number of ghost layers is not overinterpreted, and additional

sediment or repeated tephra sequences are not inadvertently added into the final tephra stratigraphy.

An example of a ghost horizon in poorly preserved core sections is tephra 108.14, displayed in Fig. 10a. Both off-splice sections displayed contain core disturbance and the colour of sediments differ in parts. Tephra 108.14 was correlated visually by colour, stratigraphic position and grain size. However, a lower degree of confidence in this visual correlation was noted, due to differences in the appearance of surrounding sediment. Fig. 10b displays selected bivariate plots that reveal that this correlation is robust and corroborates the visual correlation of these units. In all elements there is a strong overlap with glass chemistry and the spread of data, e.g., in Mg, Ti, Ca and Si is consistent in the two holes. Furthermore, all other ghost tephras analysed from multiple holes display consistent glass chemistries, thus supporting the correlations made. Appendix E4, presents other ghost tephras and plots, corroborating their correlations.

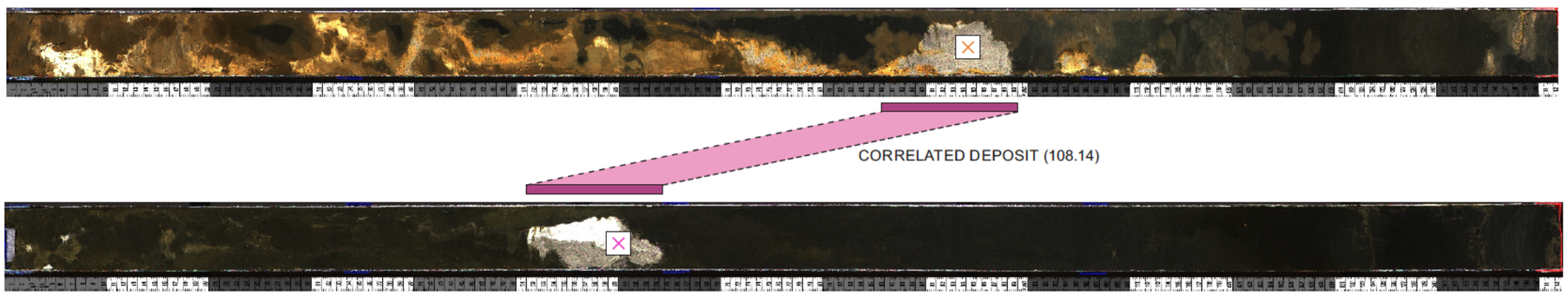
In summary, all tephras containing glass data from multiple boreholes were deemed to contain strong and reliable overlap between data, thus supporting and confirming all correlations to be accurate where these tests were undertaken. This implies that the overall volcanic stratigraphy, developed principally based on visual characteristics, is as robust as it can be.

5.2. Variability in glass chemistry

5.2.1. Glass composition variability in correlated deposits

Variation in glass chemistry throughout an individual tephra deposit must be considered when using tephra deposit chemistry for correlative purposes, because if units are internally

A


CORRELATED DEPOSIT (108.14)

B

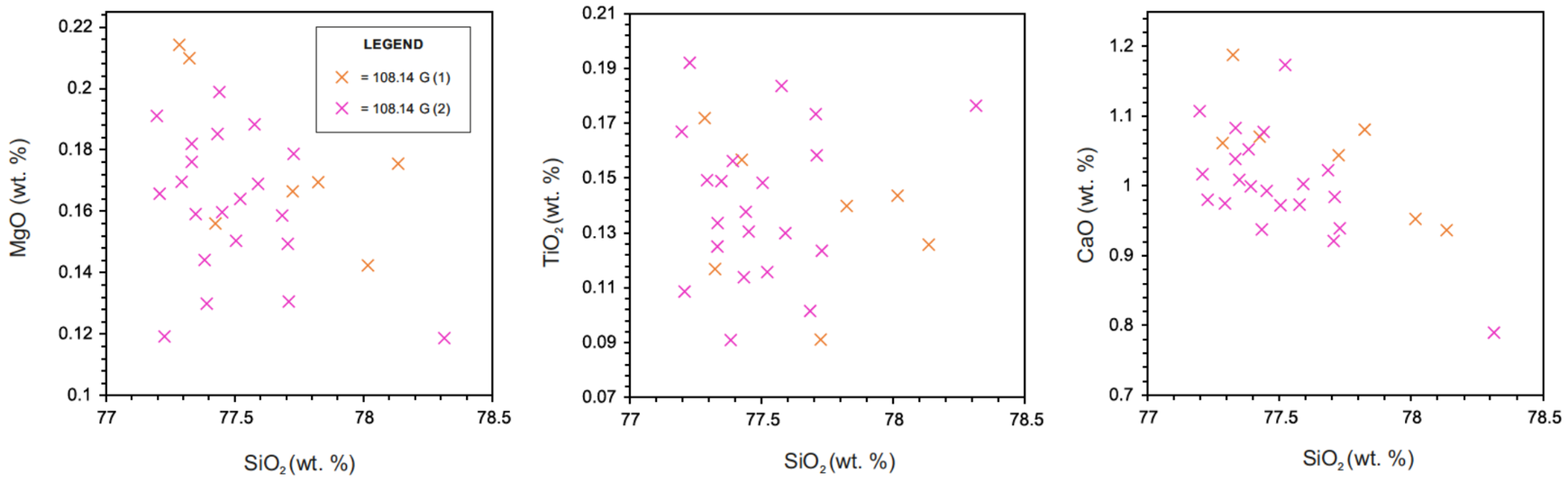

LEGEND
= 108.14 G (1)
= 108.14 G (2)
MgO (wt. %)
SiO2 (wt. %)
TiO2 (wt. %)
SiO2 (wt. %)
CaO (wt. %)
SiO2 (wt. %)

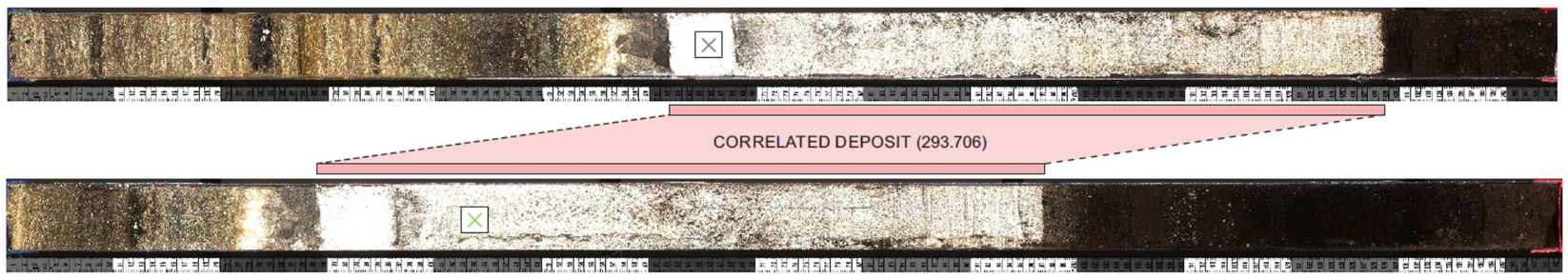
Fig. 10. (a) Core section photographs displaying the 'ghost' tephra 108.14 correlated visually and chemically across boreholes. Core sections include MEXI-CHA16-1C-57Y-1 (sampled from 60 - 61 cm) and MEXI-CHA16-1B-62Y-1 (sampled from 94 - 99 cm). Crosses are colour coded to the data shown in b and are placed at the mid-point of the depths outlined above. (b) Selected bivariate plots showing the overlap in major element glass analyses supporting a positive correlation.

---

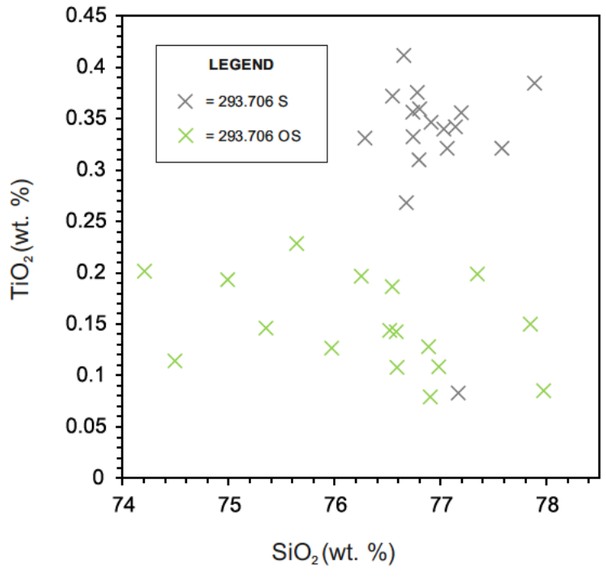
variable then correlation is likely to be poor without samples being taken from across the vertical extent of the deposit (and even this assumes that all parts of the deposit were deposited at all sites). This is exampled in Fig. 11a showing the lowermost tephra in the lacustrine sediments at Lake Chalco, tephra 293.706. This tephra (as outlined in chapter 3) is interpreted as a fall deposit with an upper co-ignimbrite ash. Visually, on-splice and off-splice deposits of the tephra are identical, with the same grain size changes, components, colour, structure, and thicknesses. Both sections also have the same upper and lower bounding sediments and the structure of these are also consistent across holes. However, different parts of the deposit were sampled from the on- and off-splice sections. Selected bivariate plots presenting the glass chemistry of these two samples, from the fall and co-ignimbritic phases (Fig. 11b), show that two distinct groups can be seen, particularly in TiO_2 and Al_2O_3 (e.g., TiO_2 analyses for the off-splice fall phase are <0.25 wt.% and the majority of on-splice co-ignimbritic analyses are >0.25 wt.%). The interpreted co-ignimbritic (finer) ash at the top of the layer is higher in Al and lower in Ti than the interpreted fall (lapilli).

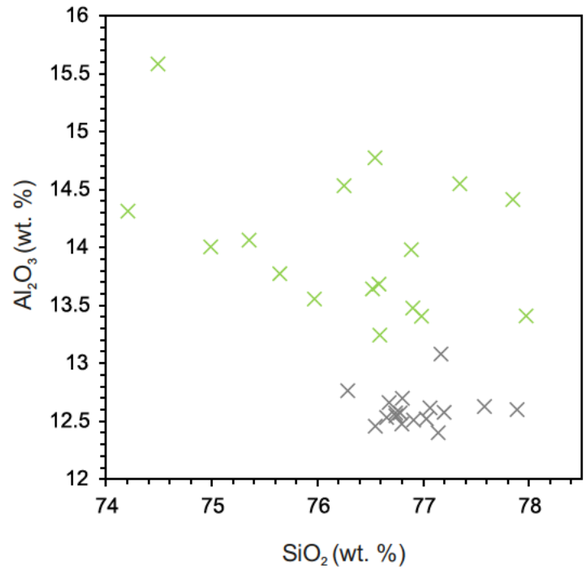
This example highlights that glass chemistry should always be used in conjunction with stratigraphic context and visual characteristics, and highlights the importance and value of visual characteristics for correlation, supplemented by analytical and quantifiable chemical data. If the glass data would have been considered irrespectively of the stratigraphic data it

A


CORRELATED DEPOSIT (293.706)

B


LEGEND
= 293.706 S
= 293.706 OS
TiO2 (wt. %)
SiO2 (wt. %)


Al2O3 (wt. %)
SiO2 (wt. %)

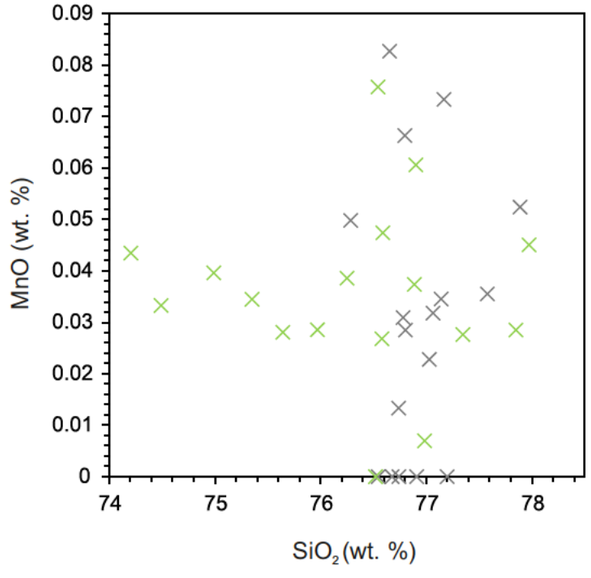

MnO (wt. %)
SiO2 (wt. %)

Fig. 11. (a) Core section photographs displaying the 'felsic' tephra 293.706 correlated visually yet chemically displaying variation across boreholes due to different areas of the tephras being sampled. Core sections include MEXI-CHA16-1A-175Y-1 (sampled from 65 - 67 cm) and MEXI-CHA16-1B-181Y-1 (sampled from 42 - 46 cm). Crosses are colour coded to the data shown in b and are placed at the mid-point of the depths outlined above. (b) Selected bivariate plots showing the overlap in major element glass analyses supporting a positive correlation.

---

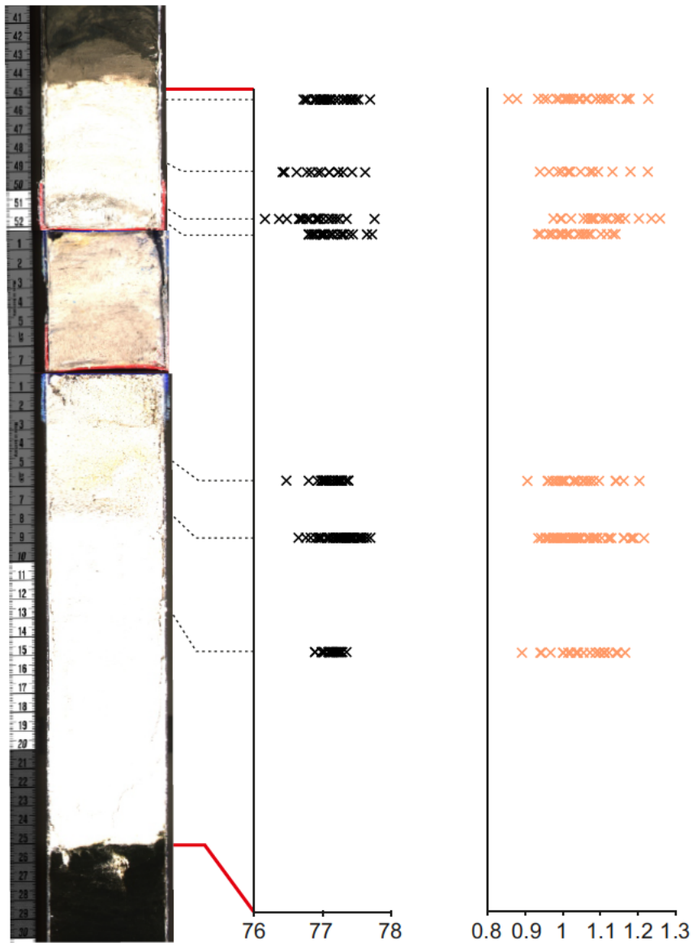
may have been concluded that the two tephras were different. Variation in glass chemistry is further investigated in section 5.2.

5.2.2. Variation in glass chemistry through tephra units

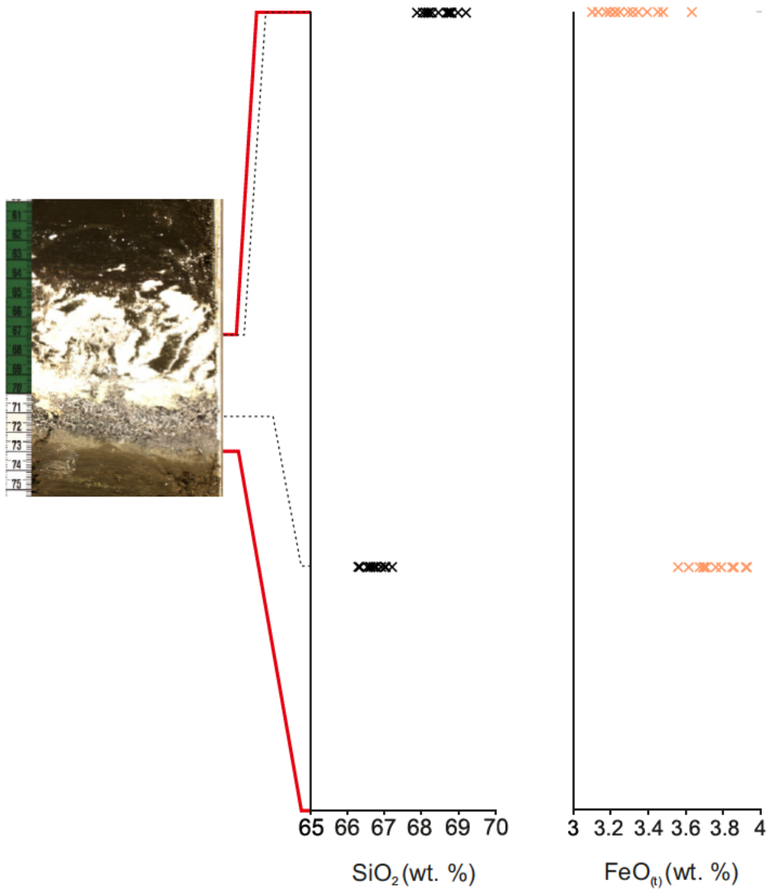
As mentioned above, variability in glass compositions may occur within individual tephras, as eruptions may be chemically zoned (e.g., Tamburrino et al., 2012; Smith et al.,2016). Here, a subset of tephra of various thicknesses were sub-sampled at various stratigraphic positions within their deposit, often spanning grain size changes and analysed to understand the internal variation in glass chemistry.

Fig. 12 displays tephras that show minimal variation and variation in glass chemistry. Tephra 110.312 is provided as an example of a relatively thick (39.6 cm) felsic tephra with 7 separate analyses at different stratigraphic levels within the deposit. As seen in Fig. 12, SiO_2 concentrations are consistent, all between 76 – 78 wt.%, and the spread in FeO_t is fairly constrained, between 0.8 – 1.3 wt.%, with most analyses at each stratigraphic position plotting along the full analytical range. Tephra 110.312 has a maximum grain size of medium ash (2 φ) although is mostly comprised of fine ash (≤3 φ, Chapter 3). All bivariate plots are provided in Appendix E5 for comparison, although it can be concluded that this relatively thick tephra has minimal variation in major element glass geochemistry.

MINIMAL VARIATION



VARIATION IN GLASS CHEMISTRY



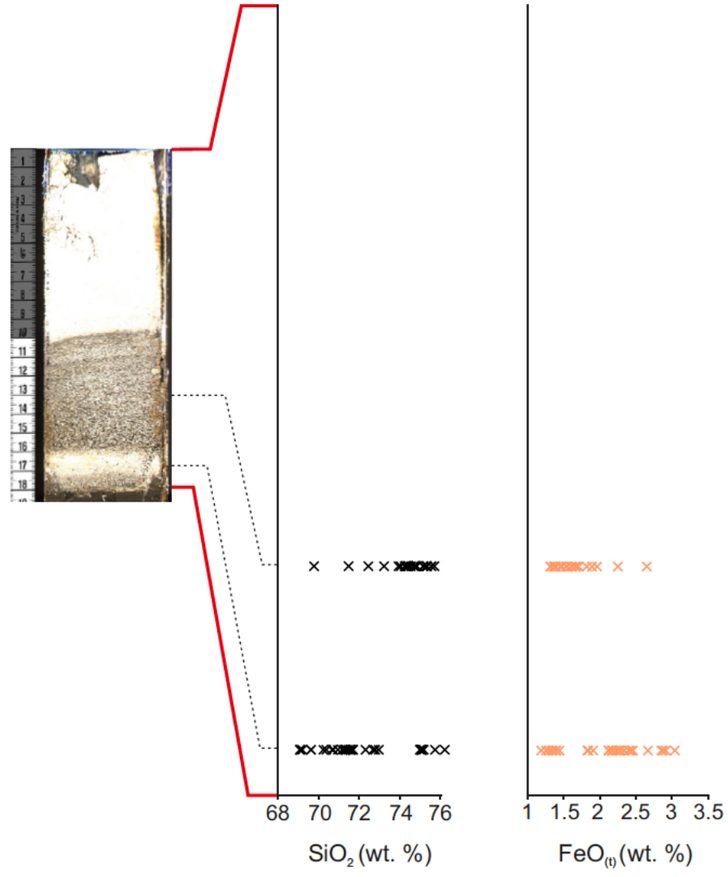


Fig. 12. Examples of the glass geochemical variation (exampled by SiO_2 and FeO_t) throughout individual tephras analysed at different intervals (stratigraphic heights). Photographs are provided of an example of a tephra with minimal variation (110.312), sections MEXI-CHA16-1A-50Y-1, MEXI-CHA16-1A-50Y-2 and MEXI-CHA16-1A-51Y-1.

In contrast, tephras 137.544 and 184.224 (Fig. 12) each have two analyses at different positions within their deposits. These deposits are thinner at 4.9 cm and 26.6 cm, respectively. Similarly to tephra 293.706 (section 5.1.4), tephra 137.544 is sub-sampled from an interpreted fall deposit (a coarse ash) and an interpreted co-ignimbritic ash (a fine ash top). Comparably, the finer ash top is more SiO_2 rich (67.88 – 69.20 wt.%) than the coarser ash base (66.3 – 67.2 wt.%). Furthermore, FeO_t concentrations demonstrate the reverse relationship with the finer ash top being more FeO_t enriched (3.10 – 3.63 wt.%) than the coarser ash base (3.56 – 3.93 wt.%). It can be concluded that these tephras have typically more Si rich and Fe poor co-ignimbritic ash components than the primary fall deposits from the eruptions.

Additionally, Fig. 12 presents a tephra displaying a finer ash base overlain by a coarser (lapilli) phase of the deposit. SiO_2 and FeO_t abundances are shown vertically through the tephra, and a spread can be seen in both elements. Under closer inspection, it can be seen that the majority of SiO_2 analyses in the finer ash base are more Si-poor (70 -72 wt.%) than the lapilli phase stratigraphically above (73 -76 wt.%). While there is also a spread in FeO_t content, the finer ash base covers the full analytical range (with values between 1 and 3.5 wt.%) but the majority of lapilli analyses are towards the lower concentration end of the spectrum (with most values between 1 and 2.5 wt.%). All bivariate plots are displayed in Appendix E5.

In summary, clear and sharp contrasting grain sizes (e.g., transitions between interpreted primary fall deposits and interpreted co-ignimbritic ash) often seem to display some variation in glass geochemistry, based on the examples analysed here. These are not major compositional shifts (i.e the compositions fall within the same broad compositional field (rhyolite, dacite etc.), but two clear populations can often be identified. It is therefore important to consider that finer ashes in the core, without coarser components, may be entirely comprised of co-ignimbritic ash from distal sources, and they may not be perfectly correlated with proximal fall-deposit equivalents. Based on analyses undertaken here, we conclude that thicker tephras (from proximal sources or large explosive eruptions) don't typically display internal variation in glass chemistry.

5.3. Laharic Volcaniclastic units

As described in chapter 3, sedimentologically varied, often heterogeneous volcaniclastic deposits are calculated to comprise 39.98% of the total core, including several discrete layers (totalling 49.4 m) within stage III (lacustrine-dominated section, chapter 3). In chapter 3, these volcaniclastics are defined as poorly sorted volcanic-dominated deposits which are interpreted to have been laterally emplaced, often enhanced by water (i.e., laharic processes).

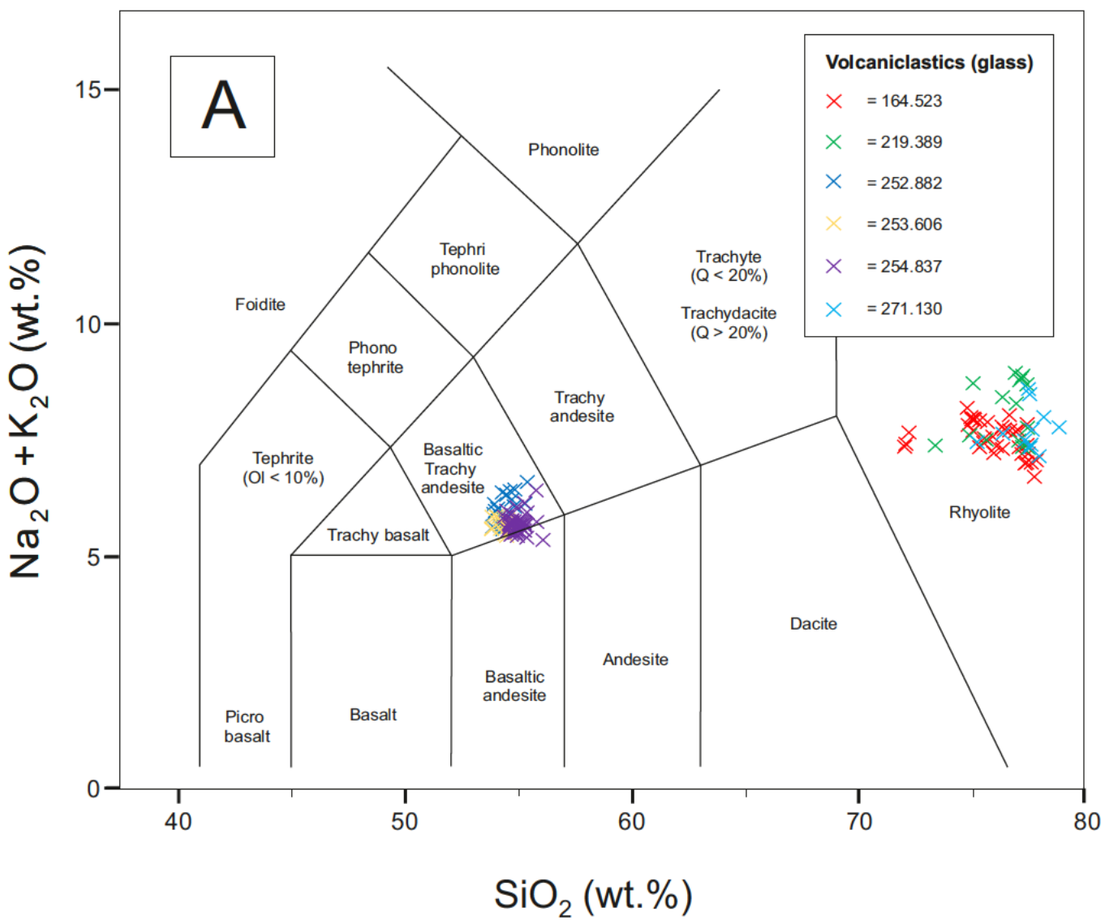
While these deposits are not inferred to be comprised of pyroclastic airfall material, glassy volcanic clasts are a component of the matrix to these layers. To establish the compositional heterogeneity of these deposits, 6 volcaniclastic units with the Stage III lacustrine section of the core (164.523, 219.389, 252.882, 253.606, 254.837, 271.130) were analysed to determine the nature of their matrix in terms of major element glass compositions. These deposits tend to have a matrix of relatively homogeneous appearance, even if the sorting is poor and they

contain a more heterogeneous mixture of coarser clasts. The matrix, therefore, can be ascribed a compositional indicator (mafic; felsic) on the basis of visual appearance, in the same way that this approach has been applied to interpreted tephra fall deposits. Out of the 6 volaniclastic deposits analysed for glass chemistry, 3 fell within 'mafic' ascribed deposits and 3 within 'felsic' (chapter 3). Sources cannot be determined here due to possible mixing with other volcanic deposits from other sources.

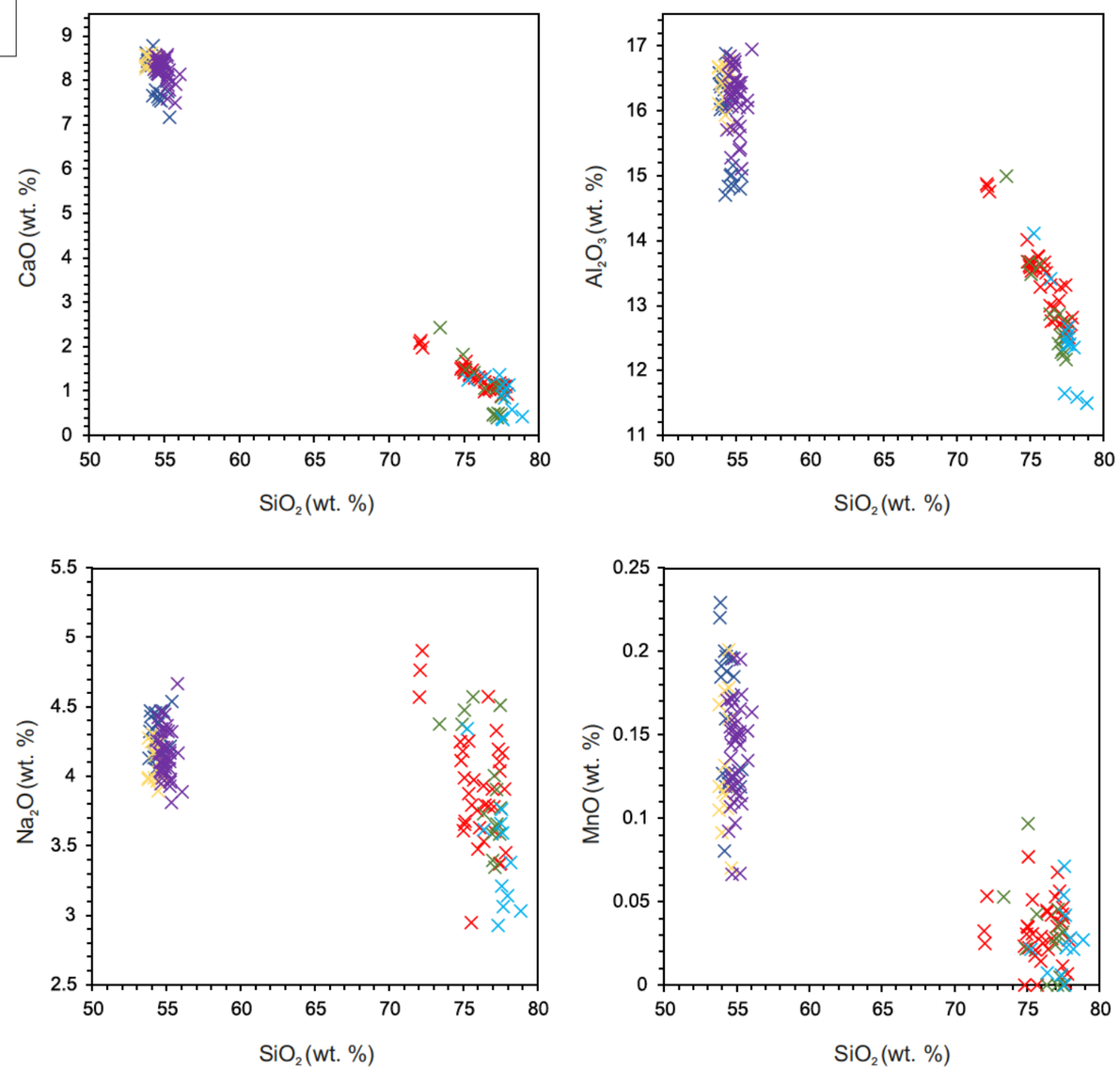
Fig. 13a displays all 6 analysed volcaniclastic deposits on a TAS plot. Initially, from this plot alone, mafic and felsic ascribed compositions can be seen to be consistent with relative SiO_2 contents, e.g., all mafic ascribed volcaniclastics contain between 50 and 60 wt.% SiO_2 and are basaltic-trachyandesite and basaltic andesite and all felsic ascribed volcaniclastics are above 70 wt.% SiO_2 and rhyolitic in composition. Fig. 13a (TAS plot) and Fig. 13b (bivariate plots) reveal that the matrix to all the laharic volcaniclastic layers are fairly homogenous with limited spread in any element, mimicking the spread of compositional analyses that typifies tephra fall deposits. Additionally, each laharic volcaniclastic deposit is clustered and defines a discrete chemical fingerprint, although there is some overlap between fields for the mafic and for the felsic layers.

The relatively narrow and discrete compositional fields of the matrix in each laharic volcaniclastic horizon suggests that they predominantly reflect the mobilisation of loose volcaniclastic material derived from a single eruptive event. Although the coarser components of these deposits suggest some entrainment of more mixed lithologies, material from these parental eruptive events dominates the matrix, suggesting limited incorporation of fine sediment from along the transportation pathway. This is consistent with a laharic source,

A


Volcaniclastics (glass)
= 164.523
= 219.389
= 252.882
= 253.606
= 254.837
= 271.130
Phonolite
Tephri phonolite
Foidite
Phono tephrite
Tephrite (Ol < 10%)
Basaltic Trachy andesite
Trachy basalt
Trachy andesite
Trachyte (Q < 20%)
Trachydacite (Q > 20%)
Rhyolite
Dacite
Andesite
Basaltic andesite
Basalt
Picro basalt
$Na_2O + K_2O$ (wt.%)
SiO_2 (wt.%)

B


CaO (wt. %)
Al_2O_3 (wt. %)
Na_2O (wt. %)
MnO (wt. %)
SiO_2 (wt. %)

C

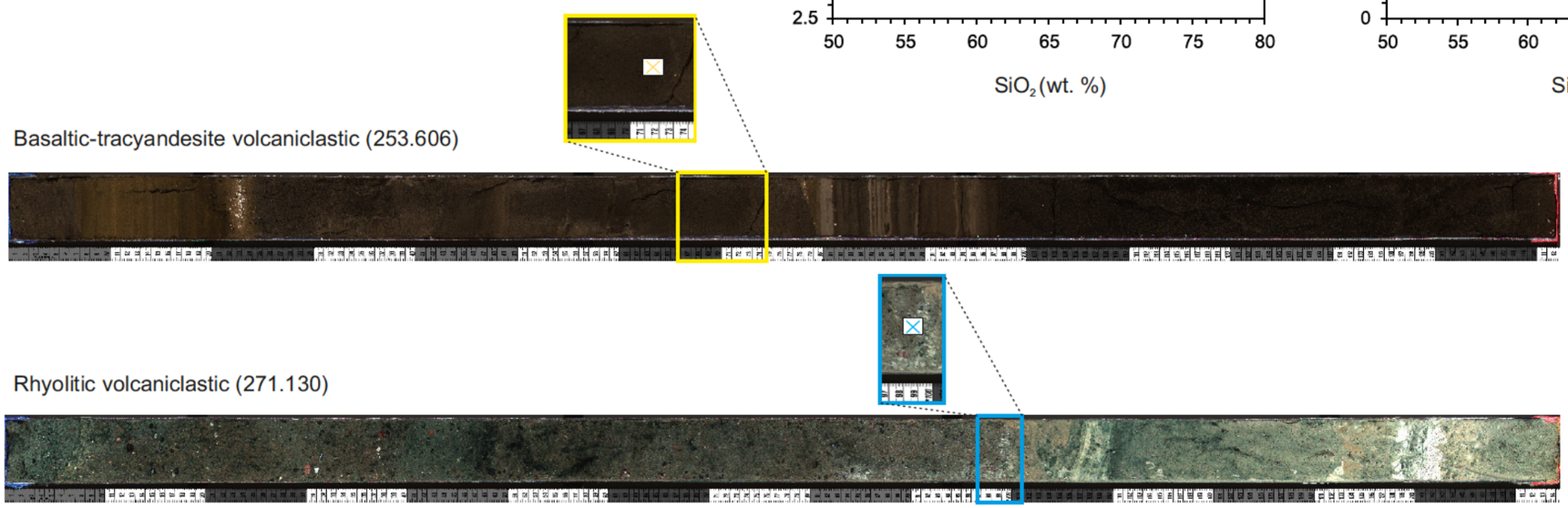

Basaltic-tracyandesite volcaniclastic (253.606)
Rhyolitic volcaniclastic (271.130)

Fig. 13. (a) Total alkali vs. silica (TAS) diagram displaying the glass compositions of six volcaniclastic layers within the Chalco core. (b) Selected bivariate plots of the data in a. (c) Examples of two volcaniclastic layers with contrasting glass compositions, 253.606 and 271.130. These are within core sections MEXI-CHA16-1C-145Y-1 and MEXI-CHA16-1C-158Y-1, respectively.

---

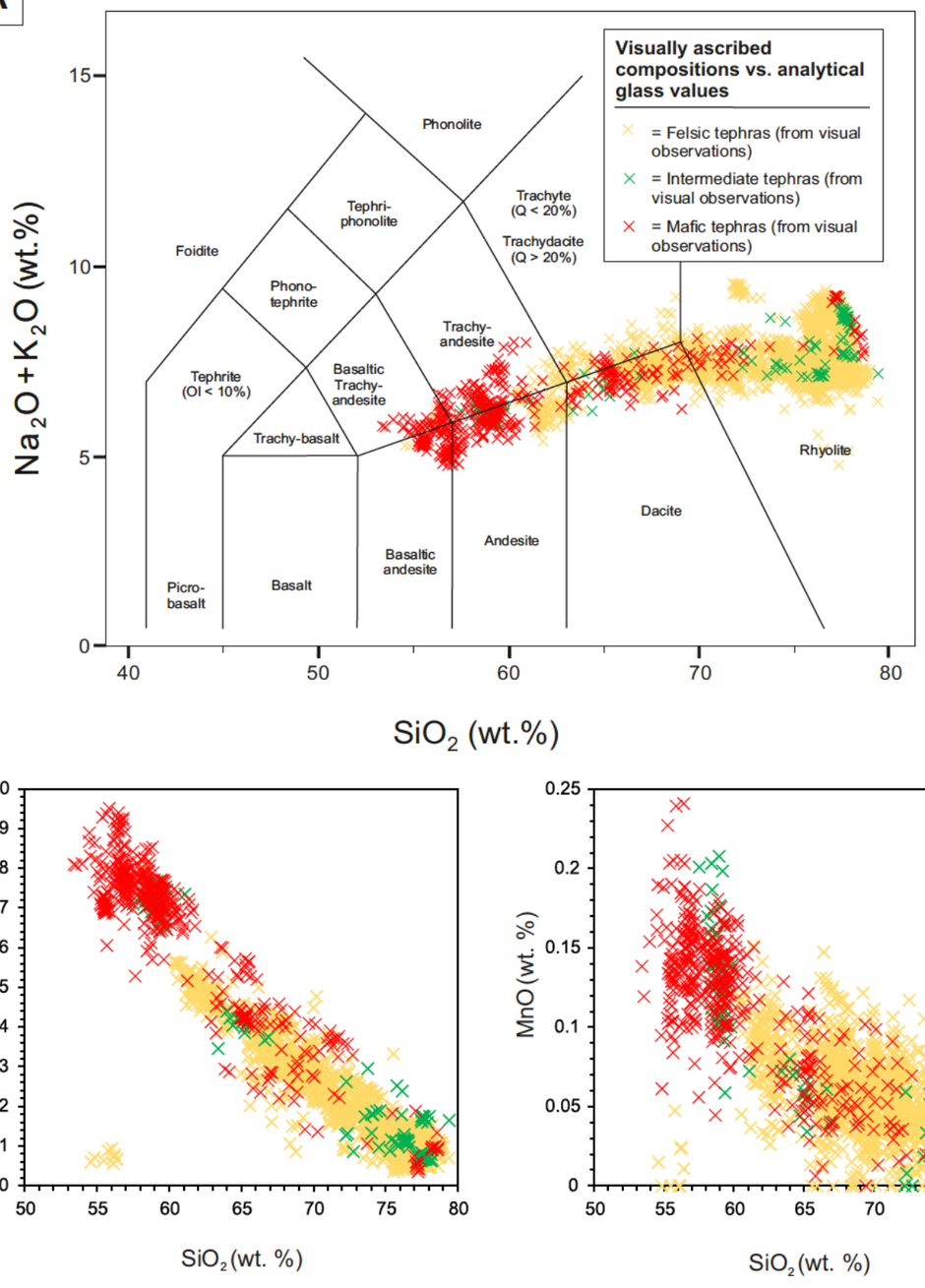
whereby an explosive eruptive event has blanketed the local environment with loose sediment that has then been remobilised and had input to the lake core site. Fig. 13c provides examples of the physical characteristics of a mafic ascribed volcaniclastic unit (253.606) and a felsic ascribed volcaniclastic deposit (271.130).

5.4. Chemical assignments from visual characteristics

Chemical assignments in chapter 3 were based off colour, with darker, more 'mafic' units assumed to be from local smaller-scale monogenetic volcanism (e.g., SCVF) and lighter, 'felsic' deposits assumed to be sourced from more explosive polygenetic and/or caldera volcanoes. Intermediate compositions were ascribed to layers that were grey or brown in colour, without the distinct pale appearance of the felsic units, but distinct from dark mafic layers. The provenance of these deposits was not speculated upon.

Glass compositional analysis allowed testing of the visual assignation. Fig. 14a includes all tephra analyses form the core, with bimodal eruptions spanning two or more volcanic source fields (e.g., Popocatépetl and the SCVF) omitted. It can be seen in Fig. 14a that all ascribed compositional fields overlap. However, the bulk of analyses for mafic ascribed units are towards more SiO_2 poor compositions (e.g., <60 wt.% SiO_2) and the bulk of analyses for ascribed felsic tephras are towards more evolved (SiO_2 richer) compositions (e.g., >70 wt.% SiO_2). Despite this, the overlap between the fields and glass compositions of ascribed mafic

A


Visually ascribed compositions vs. analytical glass values
= Felsic tephras (from visual observations)
= Intermediate tephras (from visual observations)
= Mafic tephras (from visual observations)
Phonolite
Tephri-phonolite
Foidite
Phono-tephrite
Tephrite (Ol < 10%)
Basaltic Trachy-andesite
Trachy-basalt
Trachyte (Q < 20%)
Trachydacite (Q > 20%)
Trachy-andesite
Rhyolite
Dacite
Andesite
Basaltic andesite
Basalt
Picro-basalt
$Na_2O + K_2O$ (wt.%)
SiO_2 (wt.%)
FeO_t (wt. %)
MnO (wt. %)
SiO_2 (wt. %)

B

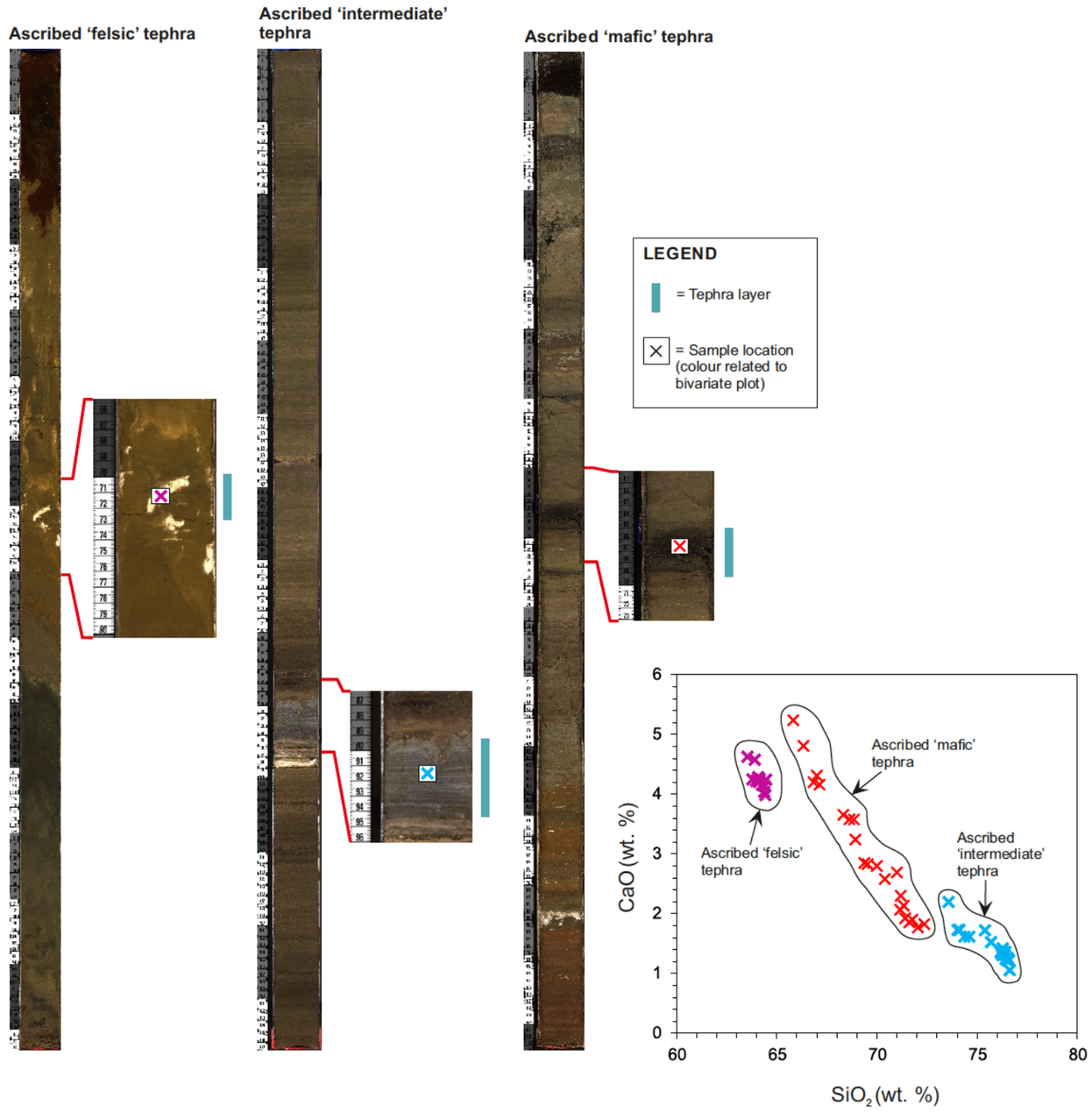

Ascribed 'felsic' tephra
Ascribed 'intermediate' tephra
Ascribed 'mafic' tephra
LEGEND
= Tephra layer
= Sample location (colour related to bivariate plot)
Ascribed 'mafic' tephra
Ascribed 'felsic' tephra
Ascribed 'intermediate' tephra
CaO (wt. %)
SiO_2 (wt. %)

Fig. 14. (a) Total alkali vs. silica (TAS) diagram and selected bivariate plots displaying the glass compositions all tephras in the core, against the relative compositions ascribed in chapter 3. (b) Examples of three anomalous tephras responsible for outliers in a. The geochemical data from these layers is displayed on a CaO vs. SiO_2 bivariate plot.

---

units which are very high SiO_2 (≥75 wt.%) suggest that some eruption deposits are darker in colour despite their evolved glass compositions and vice versa. It should be noted that glass compositions are not the same as bulk chemistry, and that a highly microcrystalline groundmass (as many mafic tephras have) will inevitably have more evolved glass.

Intermediate ascribed tephras, as expected, have a spread throughout all compositions, between 55 wt.% and 80 wt.% SiO_2, however the range is wider than anticipated, with the mode of analyses falling above 70 wt.% SiO_2, suggesting that most ascribed intermediate tephras contain more evolved glass compositions than assumed from visual characteristics. As above however, it is important to note that visual characteristics are completed from the bulk deposit and not the glass, in which the chemistry between the two differs.

Some tephras that do not display expected glass compositions, as ascribed in chapter 3, are presented in Fig. 14b. In this case, it can be seen that ascribed felsic, intermediate and mafic ashes are cream/white, medium grey and black in colour, respectively. However, the CaO vs. SiO_2 bivariate plot displays their analytical glass compositions. Here, the intermediate tephra can be seen to have the most evolved SiO_2 composition (between 73 and 78 wt.%), the mafic tephra occupies the middle SiO_2 field (between 65 and 73 wt.%) and the assigned felsic tephra is the most SiO_2 poor (<66 wt.%). It must however be noted that these eruptions account for many of the outliers in Fig. 14a and are generally anomalous. It is possible that these eruption

deposits are highly crystalline, including within the groundmass. Additionally, the preservation/recovery of the core section containing the ascribed felsic tephra is poor and therefore may contain material from other nearby tephra deposits (a point we return to below).

In summary, intermediate tephras generally contain more evolved glass compositions than expected however, as other factors, including increased microlite or phenocryst contents will lead to more evolved glass. The general composition categories assigned in chapter 3 are therefore deemed to be representative of the bulk deposit (crystals + glass) and are not directly comparable with purely glass analyses.

5.5. Bimodal eruptions and reworking

It is possible that the mixing of magmas can trigger eruptions (e.g., Sparks et al., 1977; Synder, 1997; Morgavi et al., 2017). Evidence for magma mixing and mingling can be observed within individual pyroclasts (e.g., pumice lapilli) if displaying banded/streaky textures from different magma batches, mafic magmatic enclaves or mineral disequilibria within the glass framework (e.g., Rosa et al., 2003; Carrasco-Núñez et al., 2012). Additionally, heterogenous glass compositions may also indicate the mixing of magmas which may display as bimodal (i.e., two varying glass composition populations) from an analysed tephra (Smith et al., 2011). For the majority of tephras within the Chalco core, pyroclasts are ash sized, making mingling textures difficult to observe. Units with identified bimodal glass compositions are indicated in Table 2.

Fig. 15a displays two tephras (43.414 and 281.395) which have bimodal glass compositions (see Fig. 15a1). Tephra 43.414 is interpreted to be a primary fall deposit, with an ascribed felsic composition. In the bivariate plots in Fig. 15a1 two clusters of data can be seen. One cluster is more evolved with SiO_2 compositions between 70 wt.% and 80 wt.% and the other population

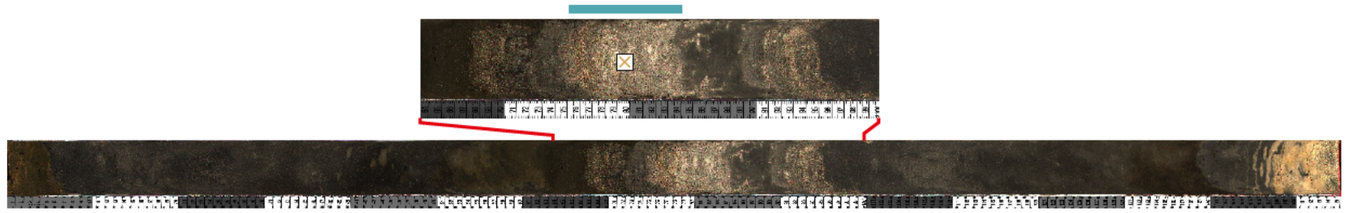
is more basic, between 55 and 58 wt.% SiO_2. Most other elements also contain two populations, e.g., MgO has c.3 wt.% between the two populations. This bimodal glass chemistry is assumed to be representative of the juvenile componentry of eruption, as the tephra is massive and assumed to be primary.

In contrast, tephra 281.395 is potentially reworked (see chapter 3). Two populations in glass chemistry can be seen in Fig. 15a1 again containing more evolved (>70 wt.%) and less evolved (<60 wt.%) SiO_2 populations. These two populations are also chemically distinct in other major elements, including MgO, with a difference in over c.4 wt.%, and K_2O with a difference in c.2 wt.%. The physical characteristics of tephra 281.395 (e.g., rounded grains) have led to the interpretation that this tephra could be reworked. It therefore cannot be ruled out that two populations of glass chemistries are due to the incorporation of material from two or more eruptions comprising the layer.

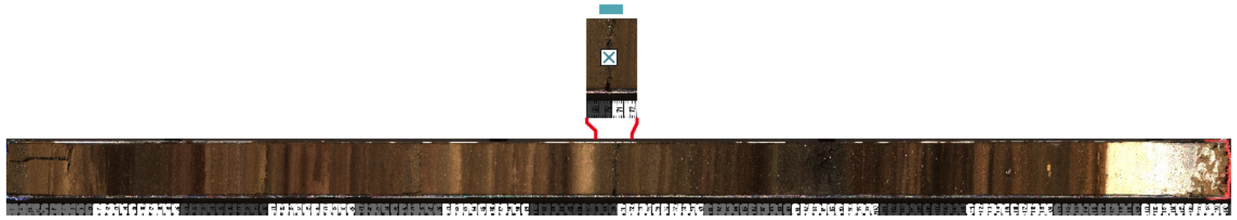
To test if reworking of a deeper layer potentially produced a subsequent geochemically bimodal deposit, we have used glass geochemical analyses to contrast adjacent layers. For all chemically analysed layers, information on a potentially reworked (i.e., non-primary) origin is provided in Table 2, based on both visual characteristics (c.f. chapter 3) and glass geochemistry. To judge chemical evidence of potential reworking, all pairs, or groups of chemically analsyed tephras that stratigraphically lie directly next to one another, with sediment in between, were plotted alongside each other, totalling 77 deposits. This was to examine if there was significant overlap of all major elements. Here, it is assumed that two consecutive eruptions from the same magmatic system are to be chemically distinct from each other, however it is possible that consecutive eruptions from the same magmatic system may

A

Bimodal tephra, 43.414 (not reworked):



Bimodal tephra, 281.395 (reworked):

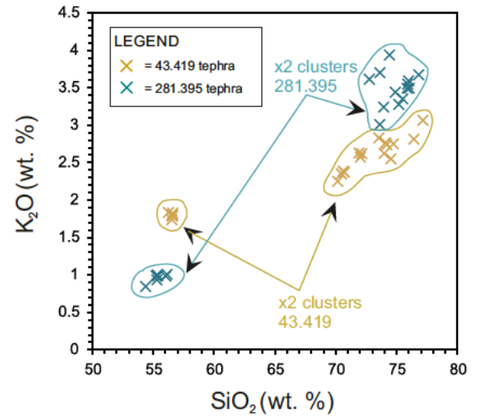


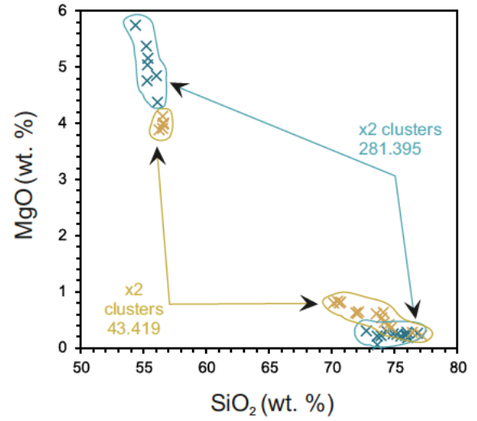
LEGEND

= Tephra/ reworked tephra layer

= Sample location (colour related to bivariate plot)

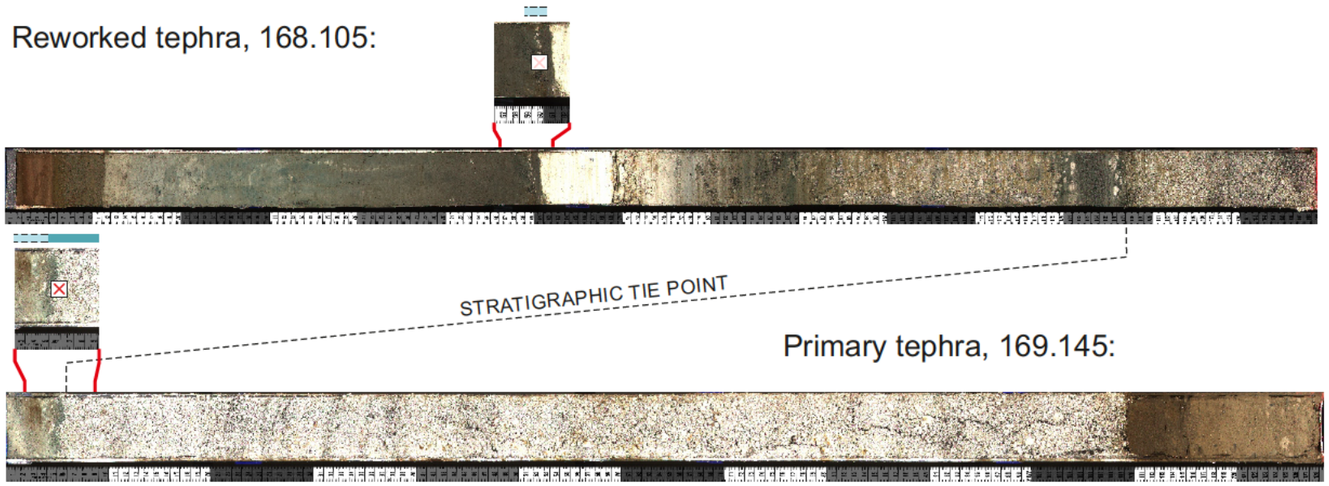
A1





B

Reworked tephra, 168.105:



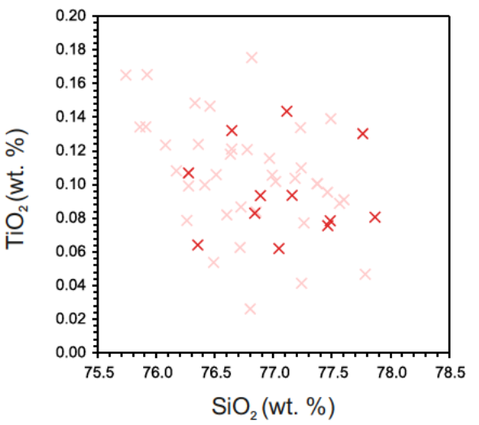
LEGEND

= Tephra layer

= Reworked tephra layer

= Sample location (colour related to bivariate plot)

B1



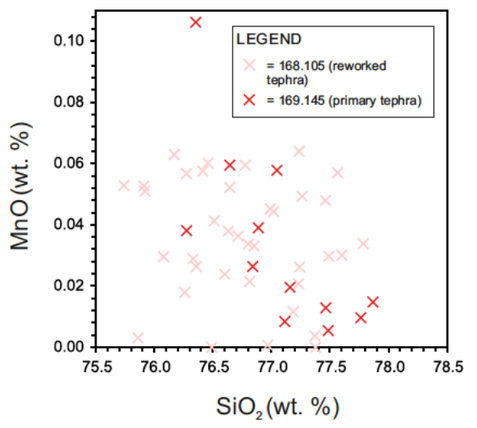


Fig. 15. (a) Examples of bimodal tephras within the core, with tephra 43.414 an example of a likely primary fall deposit, and tephra 281.395 an example of a possibly reworked layer, by visual characteristics. (a1) Selected bivariate plots displaying the geochemical bimodality of the eruptions in a. (b) Examples of a reworked tephra, 168.105 (by visual and chemical characteristics) and its primary deposit from which it is interpreted to have derived, 169.145. (b1) Selected bivariate plots from the layers shown in b, displaying the geochemical homogeneity between the two samples, thus corroborating the reworking of material.

---

produce consecutive deposits with extremely similar compositions. A total of 7 tephra pairs were deemed from glass chemistry alone to possibly comprise a lower primary deposit and an overlying reworked equivalent deposit. These pairs were then compared based on visual deposit and shard characteristics and components to mitigate the point above. Following this, only 1 pair was considered likely to be reworked: Fig. 15b displays the primary tephra (169.145), a pumice lapilli fall, 103.5 cm in thickness and the highly likely reworked deposit (168.105) stratigraphically above. Fig. 15b1 shows the chemical homogeneity in selected bivariates between the two layers, with data overlapping in major elements. When working with cores that contain a high number of artefacts and poor preservation/recovery, physical repetition of layers due to disturbance and mobilisation during the coring and extraction process must also be considered as a potential source of unit duplication. This may not only occur from tephras below, but also above, due to the fluidisation of sediments in the core liner. For this reason it is therefore recommended that when investigating a deposit for unit repetition (whether via natural reworking or artificially introduced by the coring process), any analyses from deposits that stratigraphically lie next to each other in the volcanic stratigraphy are checked against each other, as conducted here. In the case of 168.105, reworking must have been from the lower deposit and via natural reworking processes (e.g., a flood within the catchment), as the cores are well preserved and the characteristics of the deposits (i.e., a fall

deposit containing angular pyroclasts overlain by rounded and poorly sorted deposits containing material from below) are consistent with this process.

It must be noted that all other identified potentially reworked deposits from visual characteristics (chapter 3) containing glass data (Table 2), were unable to be chemically checked for reworking due to a lack of analyses from the possible primary deposit in which they may have been derived.

5.6. Source volcanoes and determination of provenance

The source volcanoes investigated in section 4 largely comprise major element glass fields that are geochemically distinct. As discussed, Popocatépetl, Sierra Chichinautzin Volcanic Field (SCVF), Tláloc-Telapón, Atitlán, Los Humeros, La Primavera and Ceboruco display geochemical signatures (fingerprints) in one or more major element permitting the correlation to core deposits. Unfortunately, Iztaccíhuatl, Nevado de Toluca and La Malinche overlap in all elements although together, they form a distinct fingerprint along a different evolution trend to the other volcanoes, (see section 4, chapter 4 and Sunyé-Puchol et al. (2021)). For the purpose of this study, Iztaccíhuatl, Nevado de Toluca and La Malinche are grouped together in terms of their glass geochemistry with eruptions displaying a chemical signature that overlaps with this being attributed these three volcanic sources simply as a collective group. Efforts to discriminate between the three volcanoes using glass shard characteristics and/or the physical characteristics of known (proximal) deposits from these volcanoes also provided no distinctive signature for the individual volcanoes. Further analysis (e.g., trace elements or Fe-Ti oxide fingerprinting, e.g., Shane, 1998) would need to be conducted to determine if chemically it is possible to tell these sources apart.

In order to assign tephra deposits in the core to eruptive sources, each tephra was plotted individually alongside the source data presented in section 4. By using a series of element pairs, unlikely sources (plotting the furthest from the core tephra analyses) were rejected, to determine if a single likely source could be identified for a deposit, based on compositional overlap in multiple major elements (plotted against silica). Tephra were only assigned to a source volcano (a) if data points overlapped with the defined source-volcano compositional fields in all major elements; (b) if all data fell within the ascribed field or strongly on evolutionary trends; and (c) there were ≥5 analyses for the core tephra on which to base this interpretation.

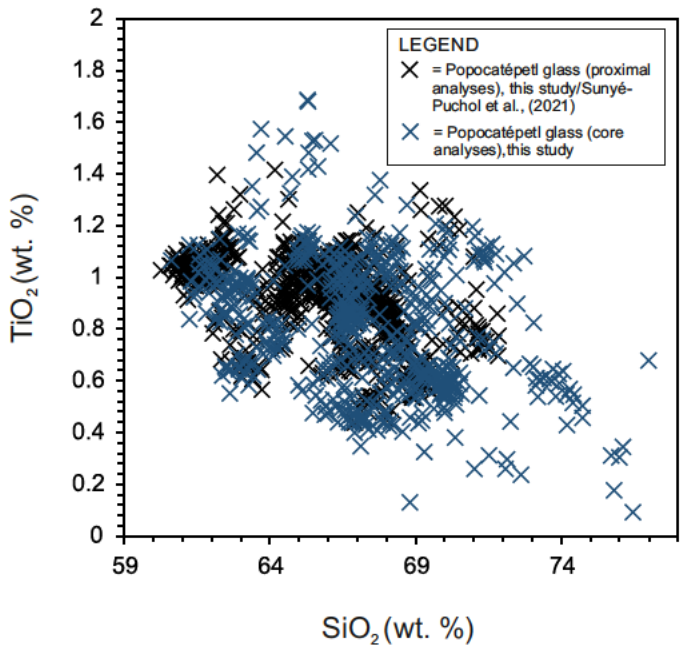
5.6.1. Popocatépetl

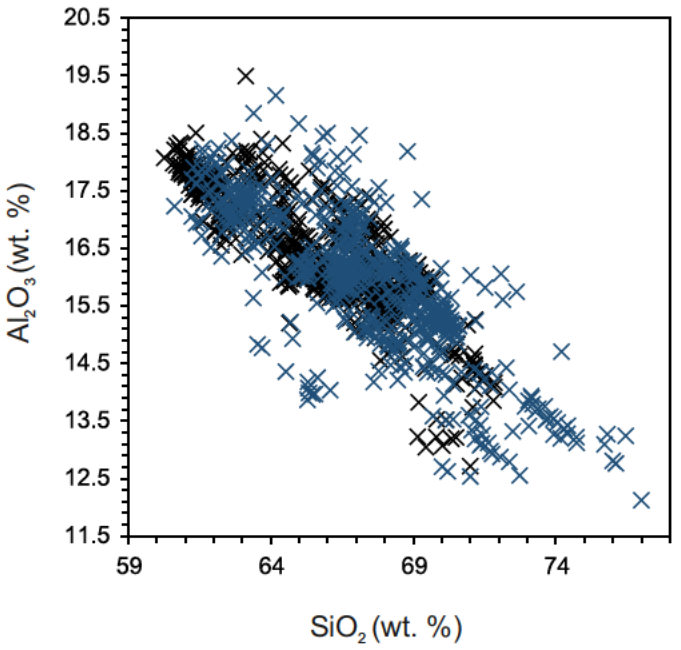
Popocatépetl, at c.40 km from Lake Chalco, is one of the closest polygenetic source volcanoes to the core site. Since 1994, eruptive activity has resumed at Popocatépetl (e.g., Siebe et al., 1996; Witter et al., 2005; De la Cruz-Reyna et al., 2008) thus presenting one of the major natural hazards to Mexico City in recent years. Additionally, due to its present-day activity it is often presumed that this volcano has long been a major source of volcanic activity in the region, and as its name translates to "smoking mountain" in the Náhuatl language, it can be assumed that this volcano has been active at various points in historical times, (e.g., the 16th century, during the Spanish conquest of the Aztec Empire, Tyce, 2018). In chapter 4 and presented in Sunyé-Puchol et al. (2021) the oldest date obtained in this study from Popocatépetl was 619 ± 52 ka (2 σ) from a coarse pumice fall exposed within the Nepopualco sequence, c.19 km from the volcano.

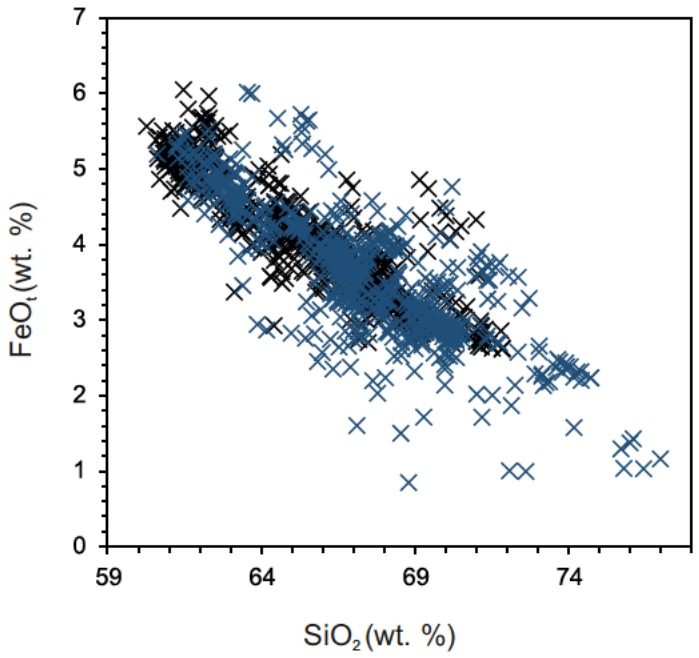
By understanding which deposits in Lake Chalco are sourced from Popocatépetl a more detailed understanding of the frequency of explosive eruptions from this volcano can be constructed. In total, out of 137 analysed layers, 35 (25.5%) have been assigned to Popocatépetl as a likely source (Table 2). These deposits are at various depths within the core from 0.59 m_c to 287.32 m_c suggesting Popocatépetl has produced explosive eruptions throughout the whole timescale of the lacustrine sedimentation at Lake Chalco. The thicknesses of the deposits vary from 0.5 cm to 9 cm. Five eruptions have bimodal glass chemistries that fall within the assigned Popocatépetl glass field and glass is generally microlite-rich, however some (eight layers) in the lowermost half of Chalco core are microlite-poor, containing more cuspate to vesicular shards.

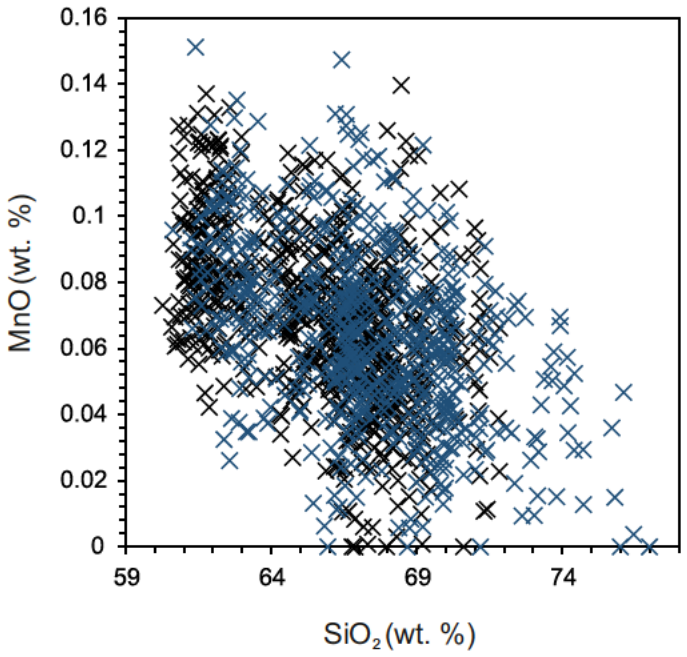
Fig. 16 displays all data points from the 35 layers assigned to Popocatépetl overlain on our previously defined Popocatépetl compositional field (section 4). In all bivariate plots, a clear overlap between the two data sets can be observed. Generally, the core analyses are consistent with the proximal data, with a slightly greater spread in SiO_2 seen in all plots. These higher Si eruptions are generally from the deepest units in the core, suggesting Popocatépetl erupted more SiO_2 rich glasses in its earlier history.

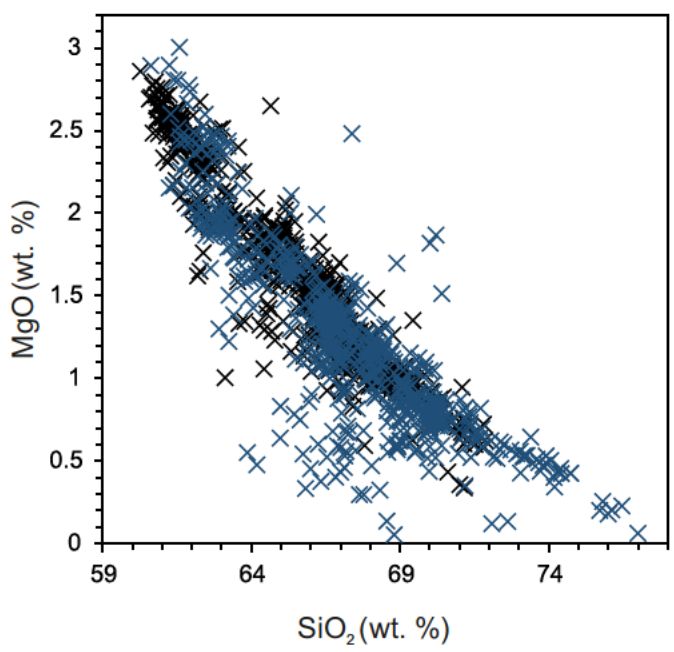
It is with a high degree of confidence that all 35 eruptions assigned to Popocatépetl were sourced from this volcano as the proximal eruptions used to construct the Popocatépetl compositional field (Table 2) span a long-timescale, currently assumed to be close to that of the time represented by the Lake Chalco lacustrine succession (Martínez-Abarca et al., 2021). Minimal variation in glass chemistry from the youngest to oldest eruptions analysed in the core suggests that throughout major stages in Popocatépetl's eruptive history (e.g., its

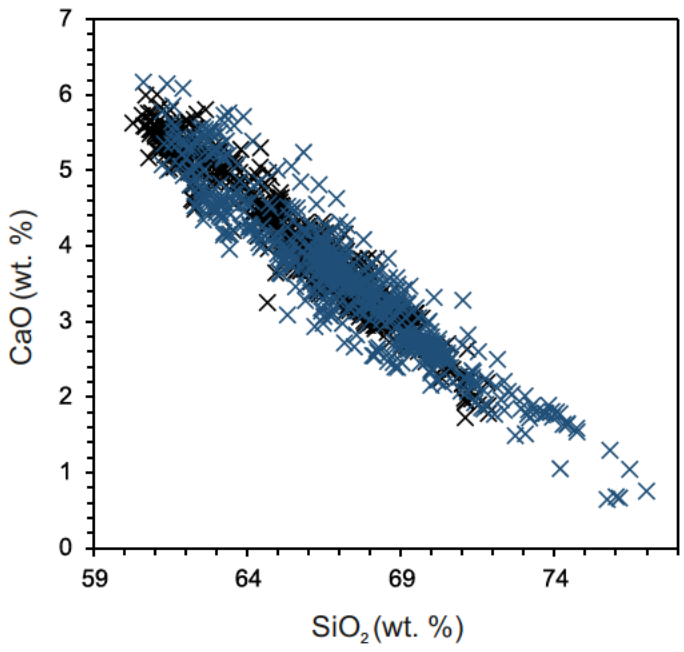

LEGEND
= Popocatépetl glass (proximal analyses), this study/Sunyé-Puchol et al., (2021)
= Popocatépetl glass (core analyses),this study
TiO2 (wt. %)
SiO2 (wt. %)

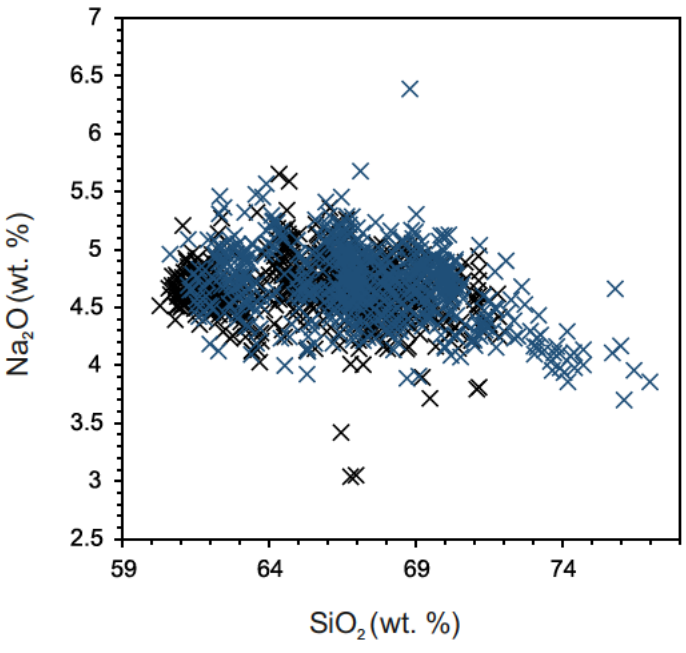

Al2O3 (wt. %)
SiO2 (wt. %)


FeOt (wt. %)
SiO2 (wt. %)


MnO (wt. %)
SiO2 (wt. %)


MgO (wt. %)
SiO2 (wt. %)


CaO (wt. %)
SiO2 (wt. %)


Na2O (wt. %)
SiO2 (wt. %)

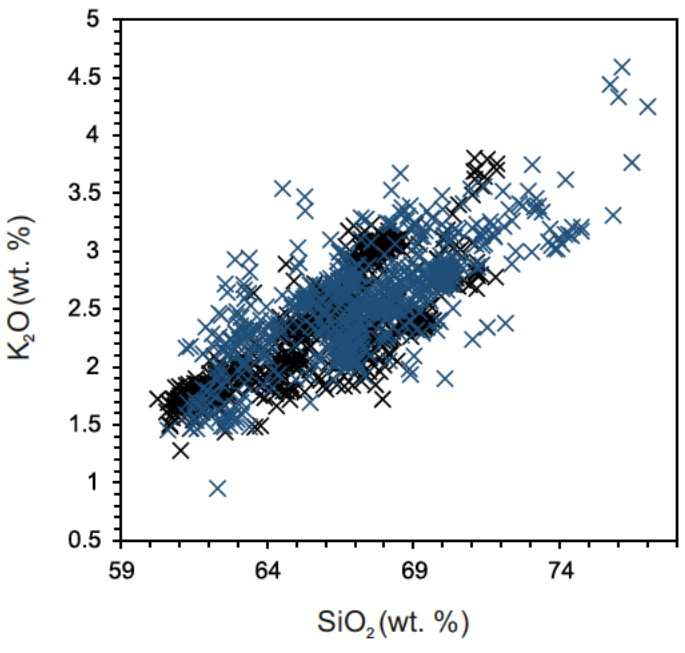

K2O (wt. %)
SiO2 (wt. %)

Fig. 16. Selected bivariate plots showing the overlap and positive correlation between proximal source glass data from Popocatépetl volcano and tephras assigned to this volcano from the Chalco core.

successive volcanic edifices, separated by three major sector collapses, Gisbert et al., 2022), juvenile glass chemistry from the volcano has remained within a consistent evolutionary trend and has occupied a broadly consistent range of silica contents.

5.6.2. Iztaccíhuatl, La Malinche and Nevado de Toluca

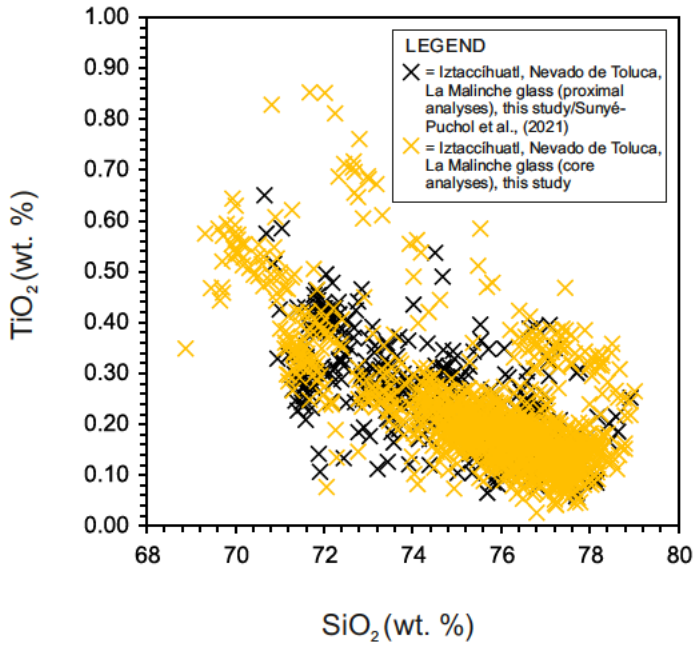
As noted above, for the purpose of defining a glass geochemical field, Iztaccíhuatl, Nevado de Toluca and La Malinche volcanoes are grouped together due to their similar glass chemistries and deposit and glass-shard characteristics. These volcanoes sit at distances of c.35 km, c.85 km and c.95 km from Lake Chalco, respectively and generally lie along an E-W orientated trend across the TMBV. All three volcanoes are major polygenetic stratovolcanoes (e.g., Capra et al., 2006; Castro-Govea and Siebe, 2007; Macías et al., 2012) with explosive eruption histories. As discussed in chapter 4 and Sunyé-Puchol et al. (2021), Iztaccíhuatl appears to display a different evolutionary trend to Popocatépetl, with lower K and Mg and higher Ca and Al, at given SiO_2 concentrations. The Nevado de Toluca (e.g., Upper Toluca Pumice) and La Malinche (e.g., Humantla Pumcie) tephra analysed also plot along this 'Iztaccíhuatl' trend (c.f. Appendix E1).

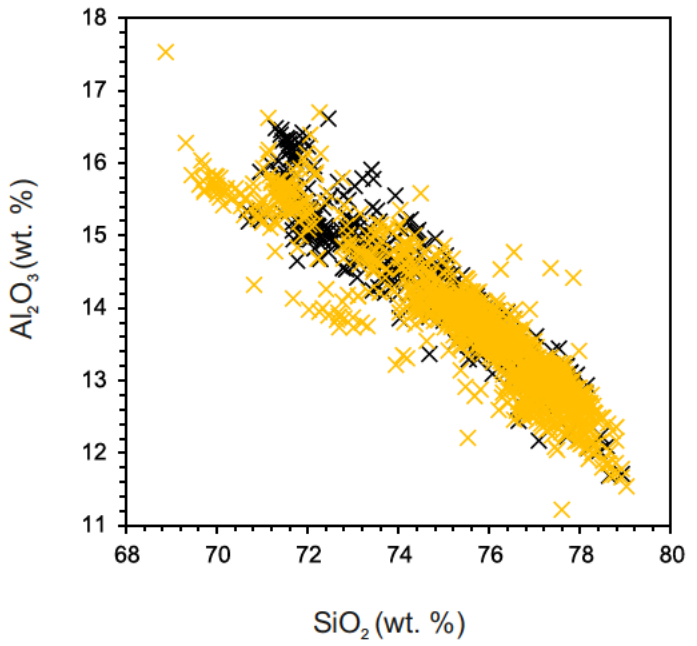
In total, out of 137 analysed layers, 43 (31.4%) have been assigned to Iztaccíhuatl, Nevado de Toluca and La Malinche. Similar to deposits from Popocatépetl, these deposits are spread throughout the length of the lacustrine-dominated section of core (see chapter 3), ranging from 5.59 m_c to 293.71 m_c depths. Thicknesses of the deposits vary from 0.8 cm to 103.5 cm thickness. The thickest fall deposits in the Chalco core are attributed to this volcano-compositional group.

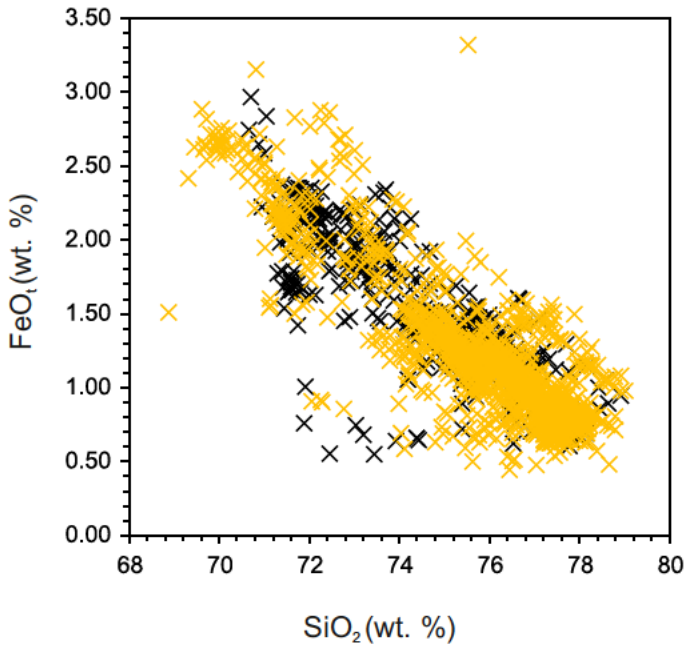
None of the 43 assigned layers display bimodal glass compositions, and glass is both microlite-rich and microlite-poor at various depths within the core. All glass-shard characteristics are presented in Table 2.

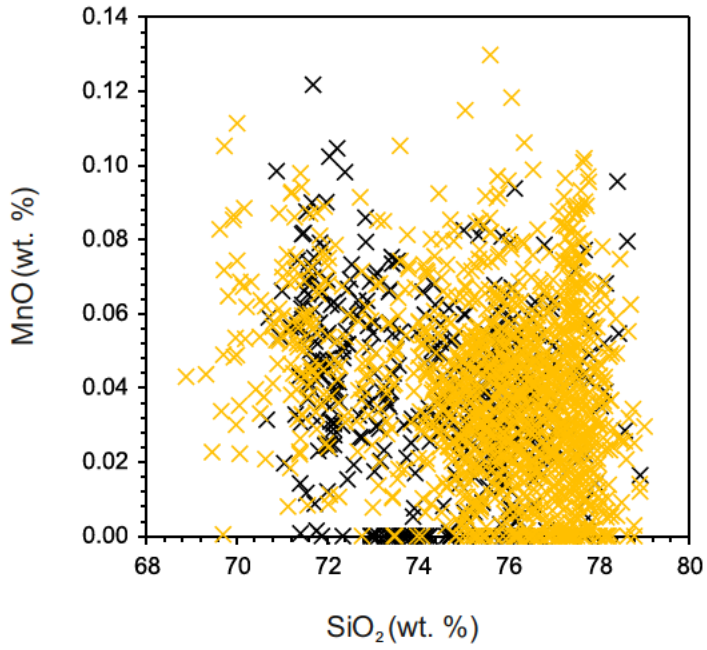
Fig. 17 displays the Iztaccíhuatl, Nevado de Toluca and La Malinche compositional field (ITM) with all assigned data points from the 43 layers overlain. In all elements there is strong overlap between the two datasets. Core analyses have a slightly greater spread (c.0.2 wt.%) within TiO_2, although this is within error and the datasets are typically accordant with one another, with the majority of core analyses slightly skewed towards the high SiO_2 end of the compositional field.

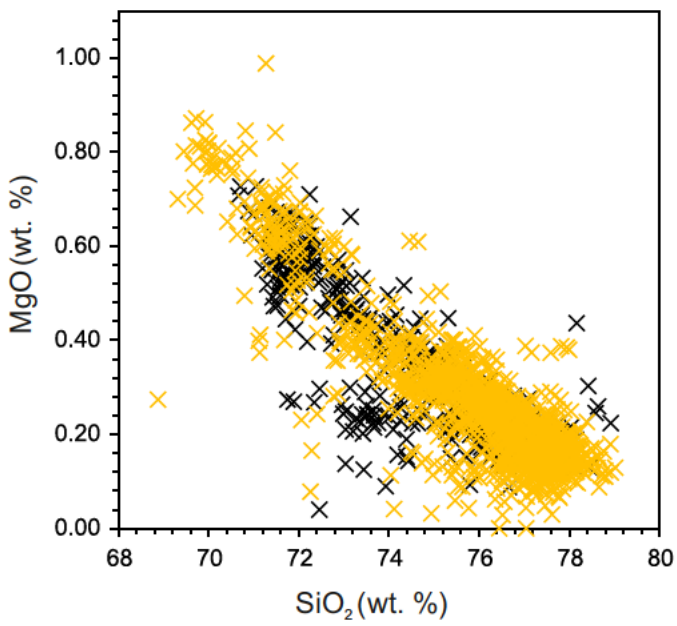
It is with a high degree of confidence that the assigned 43 core layers are sourced from this combined set of three volcanoes, but for any one layer we cannot determine which of these was the source. Proximal deposits from Iztaccíhuatl, presented in chapter 4 and Sunyé-Puchol et al. (2021), suggests that multiple explosive episodes from this volcano took place c.600 ka, with more sparsely distributed eruptions since. If this is correct, then the distribution of the ITM-assigned tephras within the core, which is relatively consistent through to the present day, would suggest a substantial proportion of Toluca and Malinche sourced deposits in the upper parts of the Chalco core. Despite this, a number of deposits (e.g., 25% in the upper 200 m of the composite core) from the ITM-assigned tephras are coarse grained (containing coarse ash/lapilli) and thick (≥10 cm), including tephras 5.593; 168.105 ,169.145; 181.723; 187.723 which are 42.25 cm; 116 cm; 103.5 cm; 40 cm and 41.15 cm, respectively. As Iztaccíhuatl is considerably closer to Chalco than Nevado de Toluca and La Malinche (by c.50 km, Fig.1), it

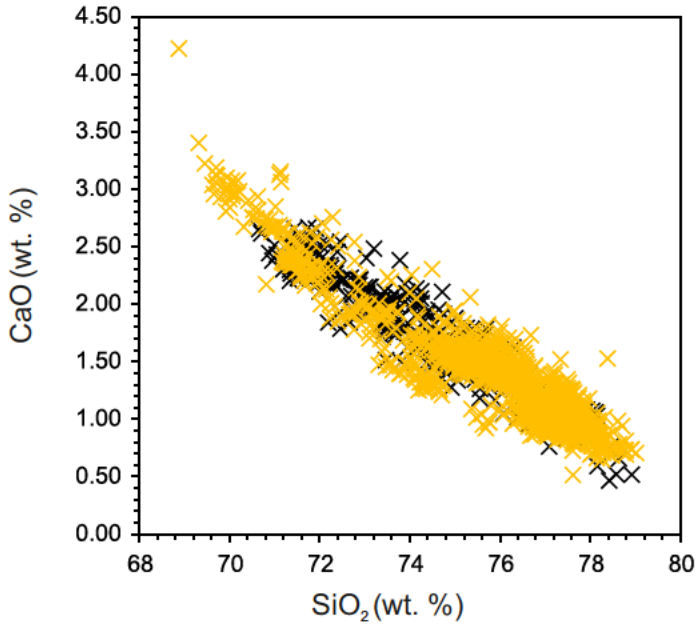

LEGEND
= Iztaccíhuatl, Nevado de Toluca, La Malinche glass (proximal analyses), this study/Sunyé-Puchol et al., (2021)
= Iztaccíhuatl, Nevado de Toluca, La Malinche glass (core analyses), this study
TiO2 (wt. %)
SiO2 (wt. %)

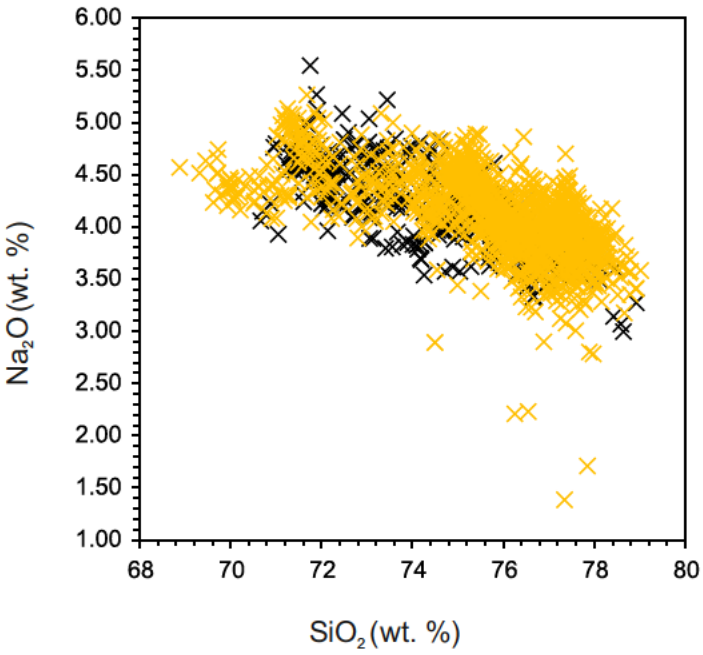

Al2O3 (wt. %)
SiO2 (wt. %)


FeOt (wt. %)
SiO2 (wt. %)


MnO (wt. %)
SiO2 (wt. %)


MgO (wt. %)
SiO2 (wt. %)


CaO (wt. %)
SiO2 (wt. %)


Na2O (wt. %)
SiO2 (wt. %)

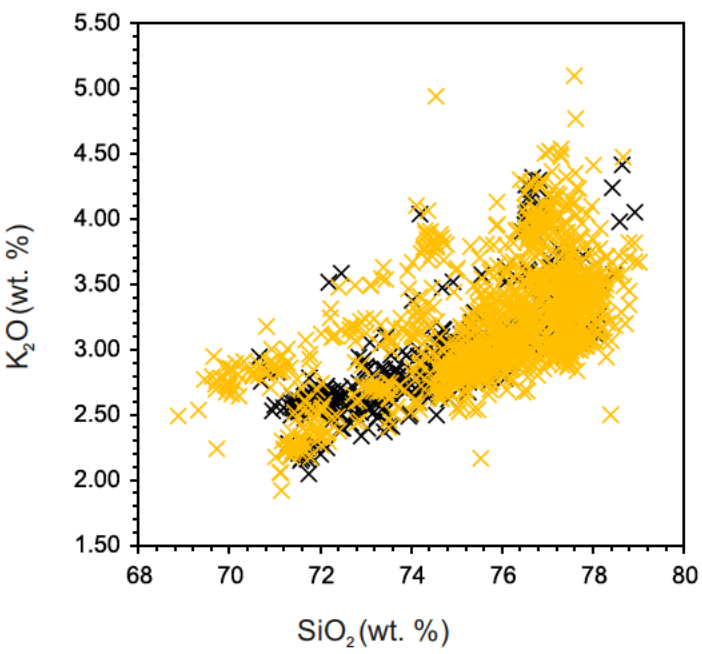

K2O (wt. %)
SiO2 (wt. %)

Fig. 17. Selected bivariate plots showing the overlap and positive correlation between proximal source glass data from Iztaccíhuatl, Tláloc-Telapón and Nevado de Toluca volcanoes and tephras assigned to these volcanos from the Chalco core. The three volcanoes have been grouped together due to overlapping geochemical compositions in major element glass geochemistry.

seems likely that these have been sourced from this volcano. The more recent deposit is anomalous to the cluster at c.168-187 m in the composite core, which if this is accurate, may indicate that activity at Iztaccíhuatl is possibly resuming. This is sceptical however, without a stronger and more reliable method for discriminating between ITM-assigned units.

5.6.3. Sierra Chichinautzin Volcanic Field (SCVF)

The SCVF has been active for c.1.2 Ma (e.g., Jaimes-Vierra et al., 2018). Due to monogenetic volcanoes generally exhibiting lower magnitude eruptions (e.g., maximum VEI 4-5, Van Otterloo and Cas, 2013) it is possible only the most proximal sources to Lake Chalco have produced visible eruption layers within the core (dependent upon dispersal direction).

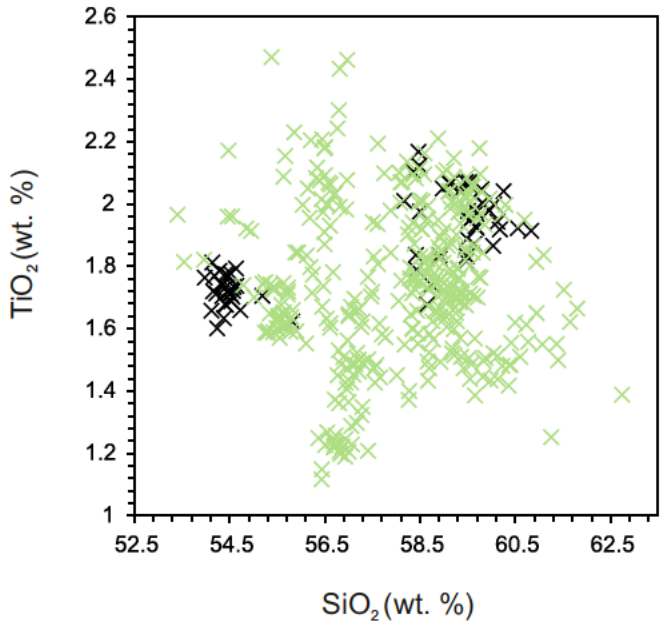
As mentioned in section 5, sub-sampling and mounting of tephras for analysis generally avoided mafic units, due to the assumption that felsic units would provide higher value results, such as extending polygenetic volcano histories and/or correlating caldera-forming eruption deposits. Despite this c.19% of the tephras analysed were chosen from mafic units deposits to understand if the assumed SCVF source was accurate. Microlites are generally abundant in mafic glasses (e.g., Nemeth et al., 2003; Genareau et al., 2010) also resulting in the study focusing of felsic deposits

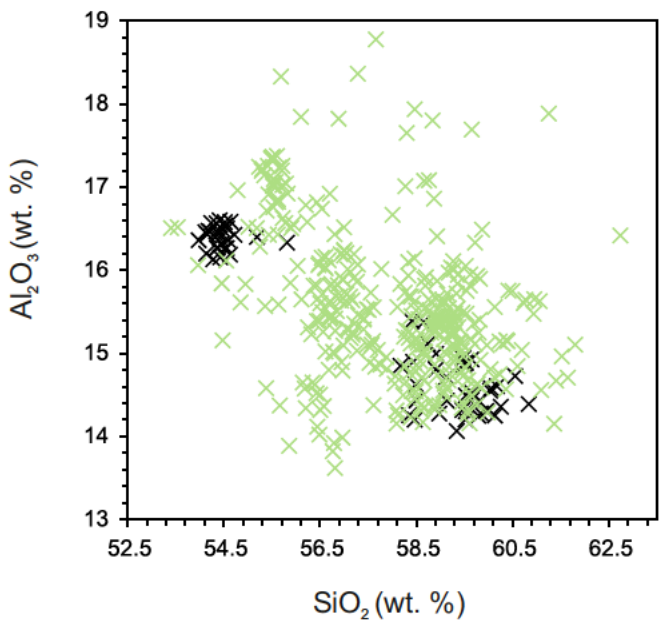
From the analysed deposits, 17 layers (12.4%), out of 137 analysed layers, have been assigned to the SCVF. In all analyses containing glass-shard characteristic data, all are noted to be microlite-rich (see Table 2) which is consistent with predictions made prior to analysis,

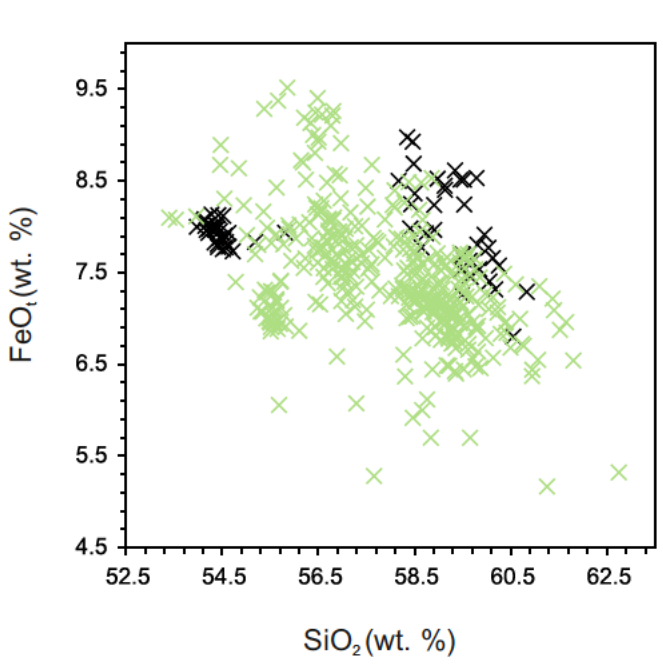
informing the sampling strategy undertaken. Fig. 18 displays all SCVF source (proximal) glass analyses (see section 4) with all assigned data points from the 17 layers within the core overlain. Unfortunately, only three cones were sampled (section 4) to give a general indication of a glass chemical field for the SCVF, and the true compositional spread of the SCVF may be far wider. Our analyses of core tephras that fall within the evolutionary trend of our defined SCVF field can be used to expand the range of the field. As seen in Fig. 18 data overlaps in all elements with the defined SCVF field, and due to using three contrasting cones, with a spread in SiO_2 contents, our assigned SCVF tephras fall almost entirely within the range of the source field. The tephra deposits assigned to the SCVF also exhibit a distinct evolutionary trend as a collective suite of deposits. This can be contrasted with the Popocatépetl and ITM fields (see Fig. 19). It can be seen that the SCVF field is compositionally distinct from Popocatépetl, displaying higher Mg and K and lower Na and Ca at given SiO_2 concentrations. All source fields show typical calc-alkaline differentiation trends from low to high SiO_2, consistent with fractional crystallisation of olivine, clinopyroxene and plagioclase. Given that the SCVF forms a distinct compositional field, our assignments are deemed to be robust.

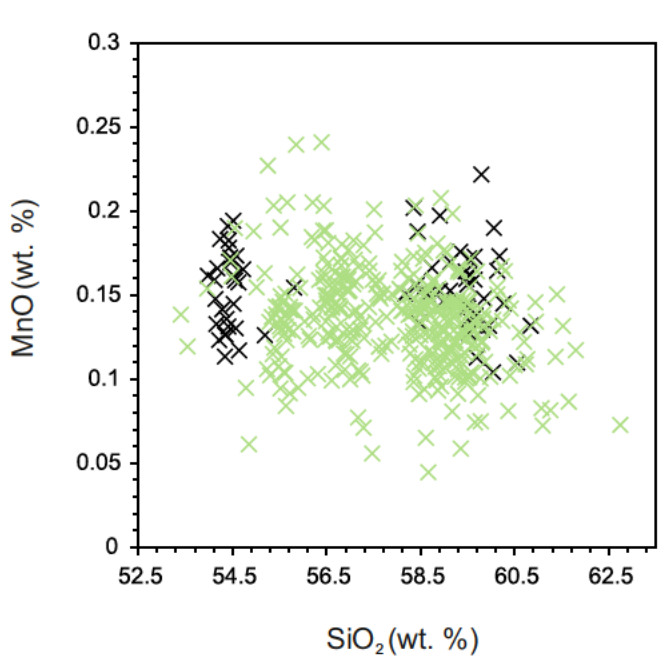
5.6.4. Tláloc-Telapón and caldera-forming eruption sources

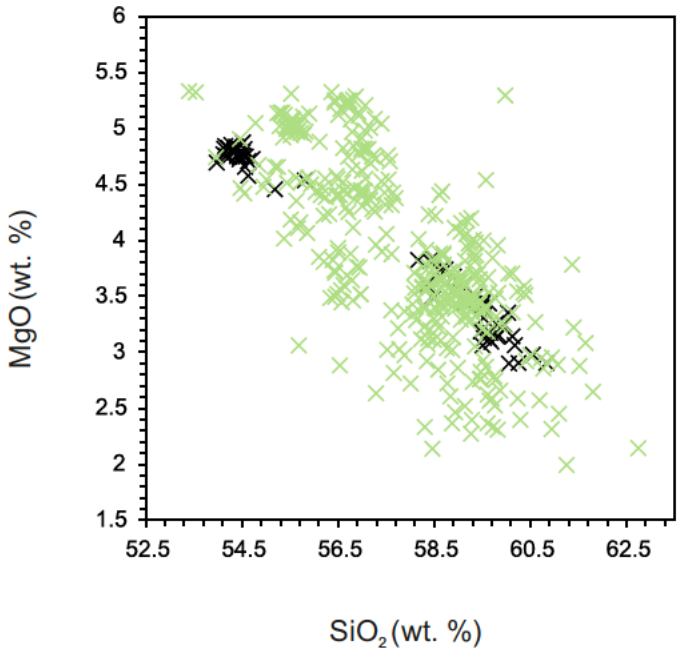
Due to a high SiO_2 content and similarity and/or overlap in most elements to the caldera source volcanoes descriped above, Tláloc-Telapón has been grouped with these more distal caldera sources when investigating potential source volcanoes for core tephras. As discussed in chapter 4 and Sunyé-Puchol et al. (2021), Tláloc-Telapón is a compound volcano, following the criteria of Macías et al. (2012), with two main craters, Tláloc and Telapón. This volcanic source (with a measurement taken from between the two craters) is the closest source to Lake Chalco,

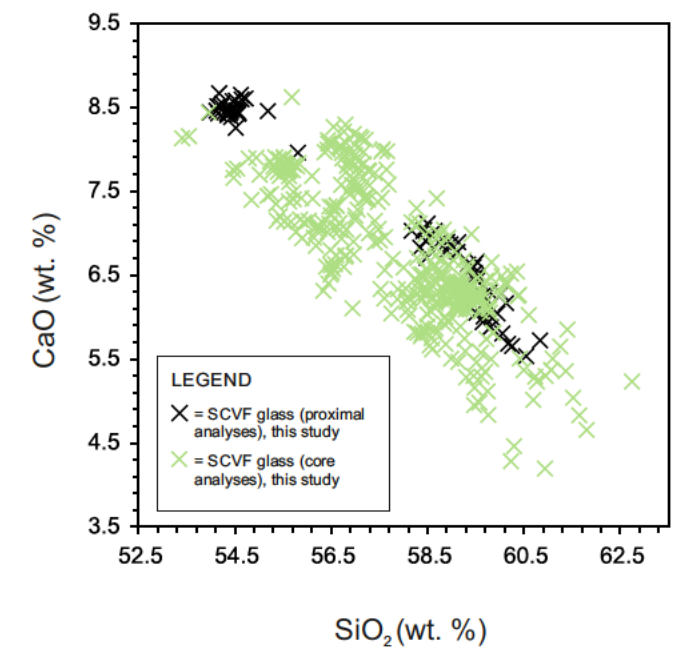

2.6
2.4
2.2
2
1.8
1.6
1.4
1.2
1
52.5
54.5
56.5
58.5
60.5
62.5
TiO2 (wt. %)
SiO2 (wt. %)

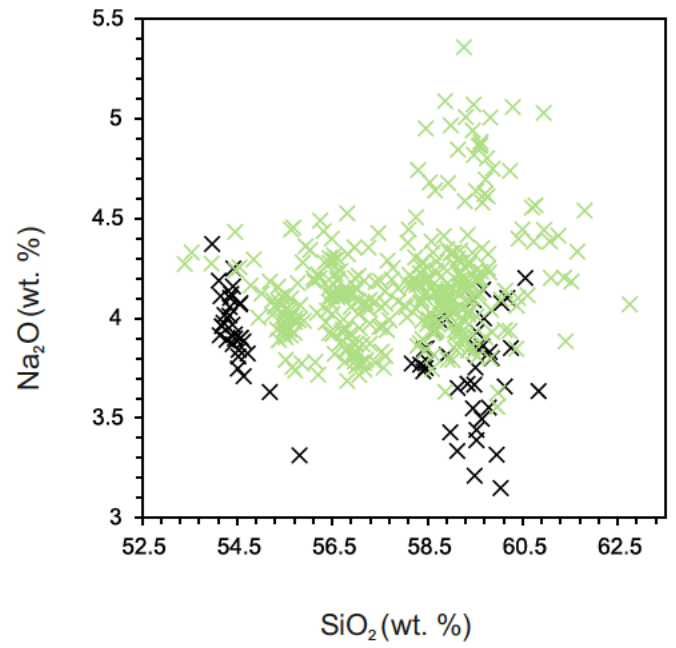

19
18
17
16
15
14
13
52.5
54.5
56.5
58.5
60.5
62.5
Al2O3 (wt. %)
SiO2 (wt. %)


9.5
8.5
7.5
6.5
5.5
4.5
52.5
54.5
56.5
58.5
60.5
62.5
FeOt (wt. %)
SiO2 (wt. %)


0.3
0.25
0.2
0.15
0.1
0.05
0
52.5
54.5
56.5
58.5
60.5
62.5
MnO (wt. %)
SiO2 (wt. %)


6
5.5
5
4.5
4
3.5
3
2.5
2
1.5
52.5
54.5
56.5
58.5
60.5
62.5
MgO (wt. %)
SiO2 (wt. %)


9.5
8.5
7.5
6.5
5.5
4.5
3.5
52.5
54.5
56.5
58.5
60.5
62.5
CaO (wt. %)
LEGEND
= SCVF glass (proximal analyses), this study
= SCVF glass (core analyses), this study
SiO2 (wt. %)


5.5
5
4.5
4
3.5
3
52.5
54.5
56.5
58.5
60.5
62.5
Na2O (wt. %)
SiO2 (wt. %)

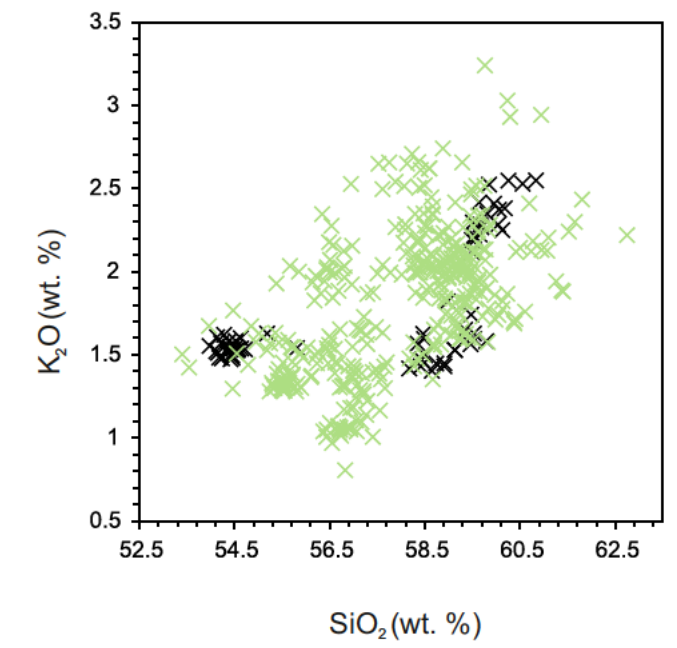

3.5
3
2.5
2
1.5
1
0.5
52.5
54.5
56.5
58.5
60.5
62.5
K2O (wt. %)
SiO2 (wt. %)

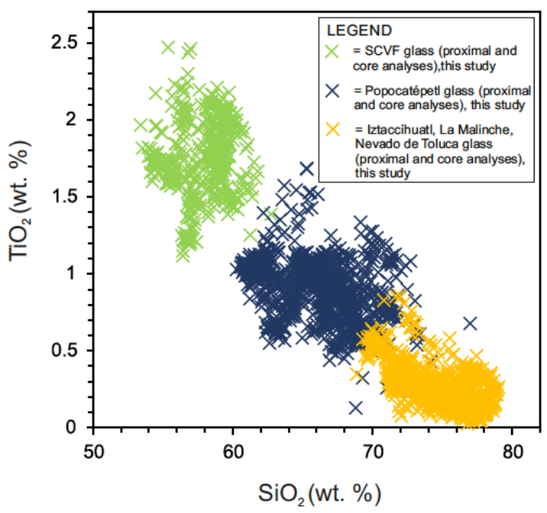
Fig. 18. Selected bivariate plots showing the overlap and positive correlation between proximal source glass data from the SCVF cones sampled in this study and tephras assigned to this source from the Chalco core.

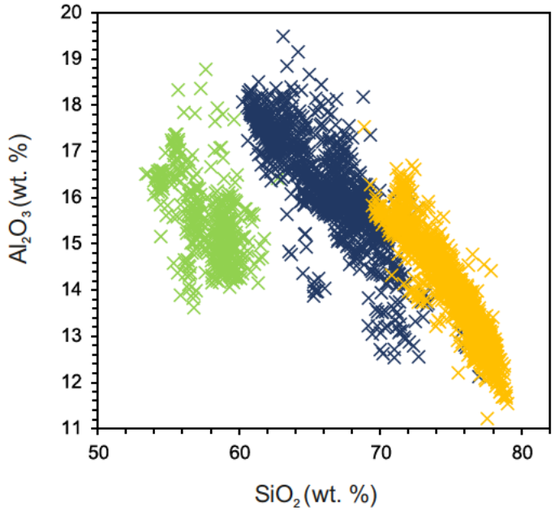
---

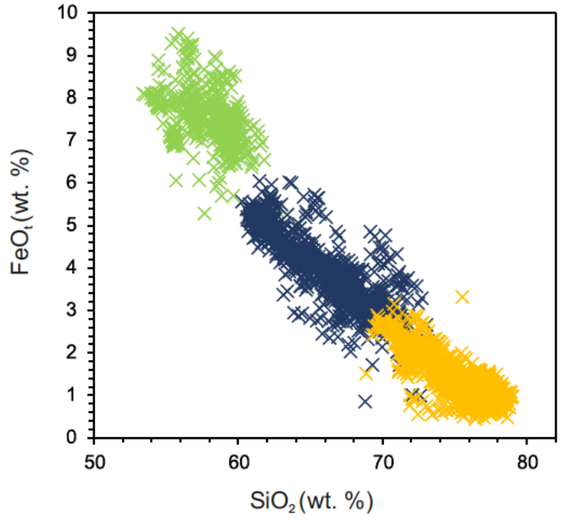
at c.35 km from the core site. Well known eruptions since c.45 ka are described by various authors (e.g., Macías et al. (2012); Rueda et al., 2013) and a new date presented in chapter 4 and Sunyé-Puchol et al. (2021) for the San Valentin Ignimbrite is 102 ± 2 ka (2 σ), demonstrating that this volcano has experienced explosive eruptions over a longer timescale.

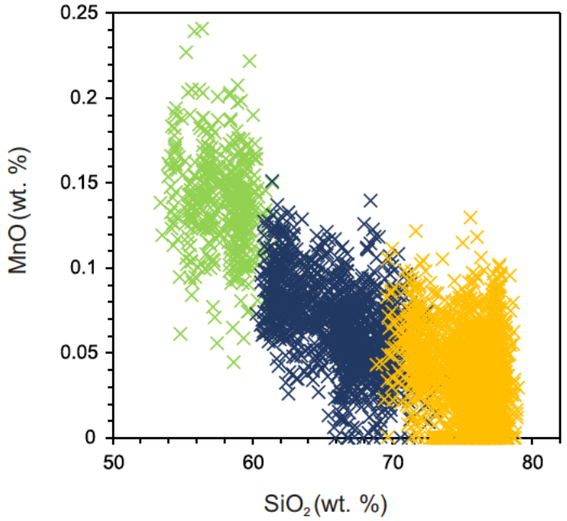
In Fig. 20, Tláloc-Telapón glass data is presented alongside data from Los Humeros and Atitlán, c.160 km and c.970 km from Lake Chalco, respectively. Core tephras that have been attributed to these volcanoes are also presented. As seen in section 4, all three volcanoes display unique glass fields, although these are similar (and sometimes overlapping) in all elements. To determine the source of high SiO_2 deposits in the core, also plotted in Fig. 20, individual tephras were plotted with data from all three sources. From the core, one deposit has been interpreted to have originated from Tláloc-Telapón (78.82 m_c), three layers from Los Humeros (110.31 m_c, 136.78 m_c and 144.65 m_c) and one deposit from Atitlán (75.34 m_c). The glass from all three volcanic sources is microlite-poor and glass-shard morphologies are cuspate and/or vesicular (see Table 2). This is consistent with these fine-ash deposits being sourced from very large explosive eruptions at distal source volcanoes.

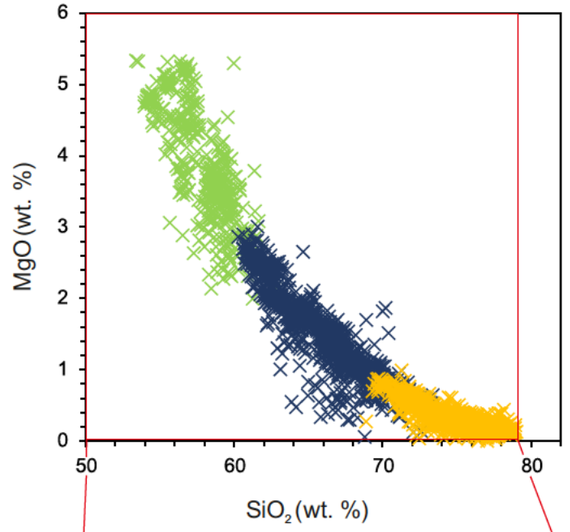
Direct overlap between the core tephras and their assigned sources is observable in all bivariates, best seen in TiO_2, Al_2O_3, FeO_t, MnO, CaO and K_2O. In these bivariate plots, distinct

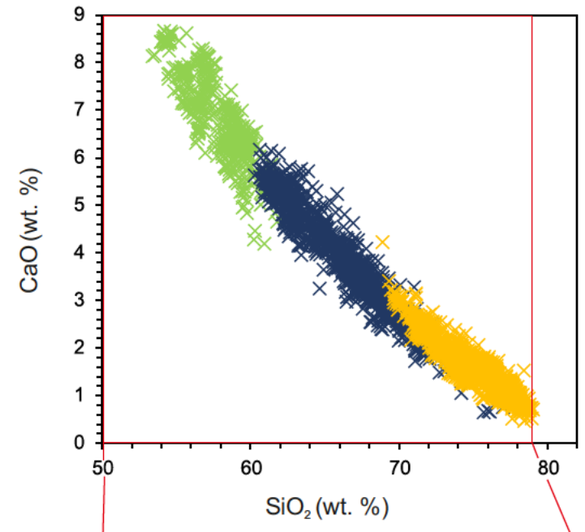

LEGEND
= SCVF glass (proximal and core analyses),this study
= Popocatépetl glass (proximal and core analyses), this study
= Iztaccíhuatl, La Malinche, Nevado de Toluca glass (proximal and core analyses), this study
TiO2 (wt. %)
SiO2 (wt. %)

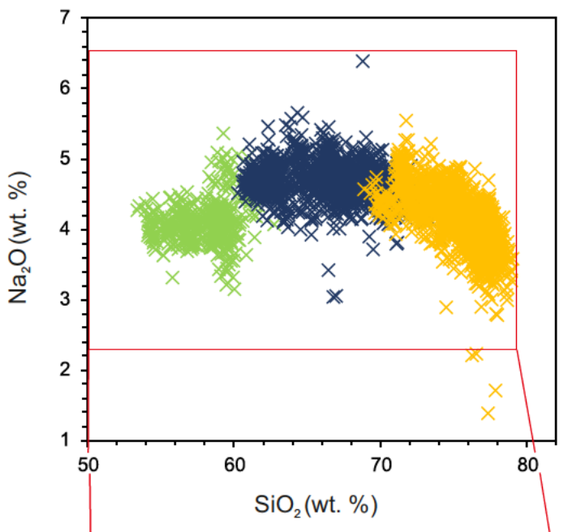

Al2O3 (wt. %)
SiO2 (wt. %)

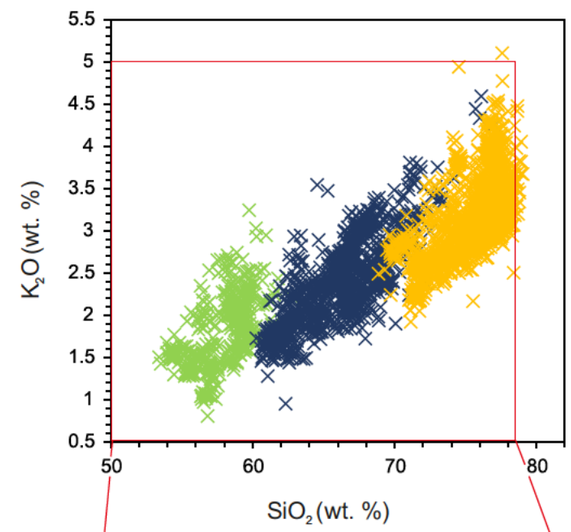

FeOt (wt. %)
SiO2 (wt. %)

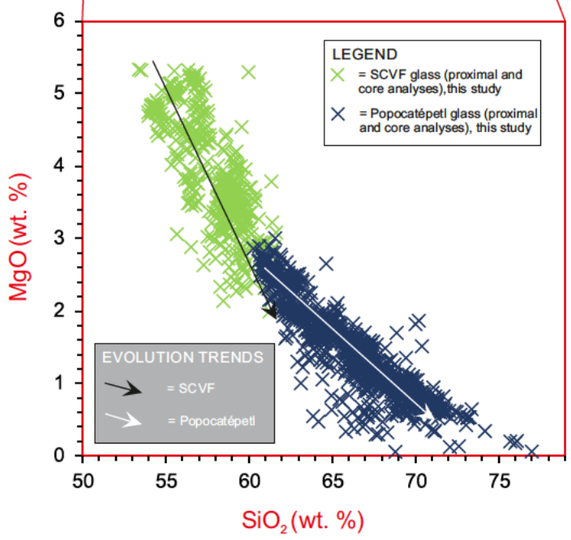

MnO (wt. %)
SiO2 (wt. %)

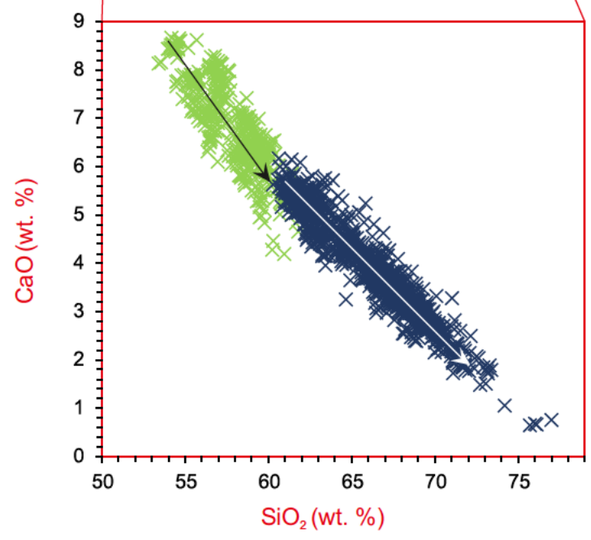

MgO (wt. %)
SiO2 (wt. %)

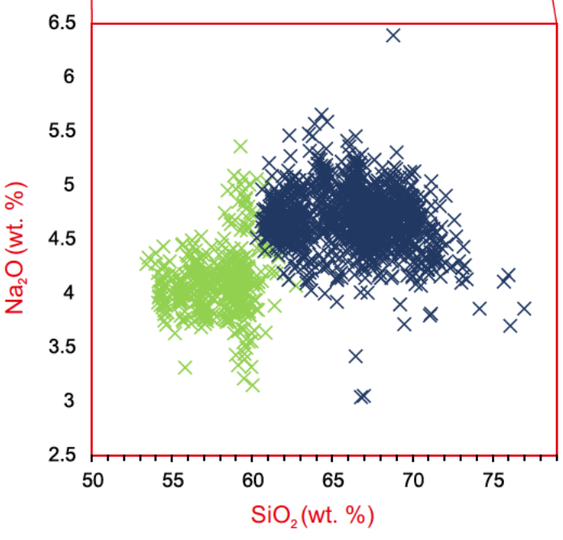

CaO (wt. %)
SiO2 (wt. %)


Na2O (wt. %)
SiO2 (wt. %)


K2O (wt. %)
SiO2 (wt. %)


LEGEND
= SCVF glass (proximal and core analyses),this study
= Popocatépetl glass (proximal and core analyses), this study
EVOLUTION TRENDS
= SCVF
= Popocatépetl
MgO (wt. %)
SiO2 (wt. %)


CaO (wt. %)
SiO2 (wt. %)


Na2O (wt. %)
SiO2 (wt. %)

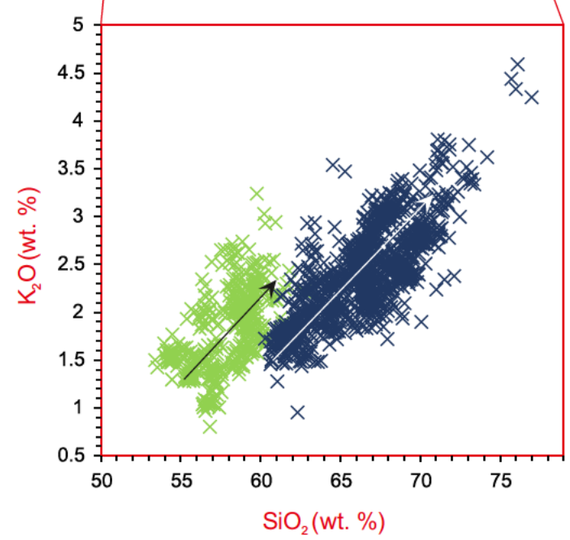

K2O (wt. %)
SiO2 (wt. %)

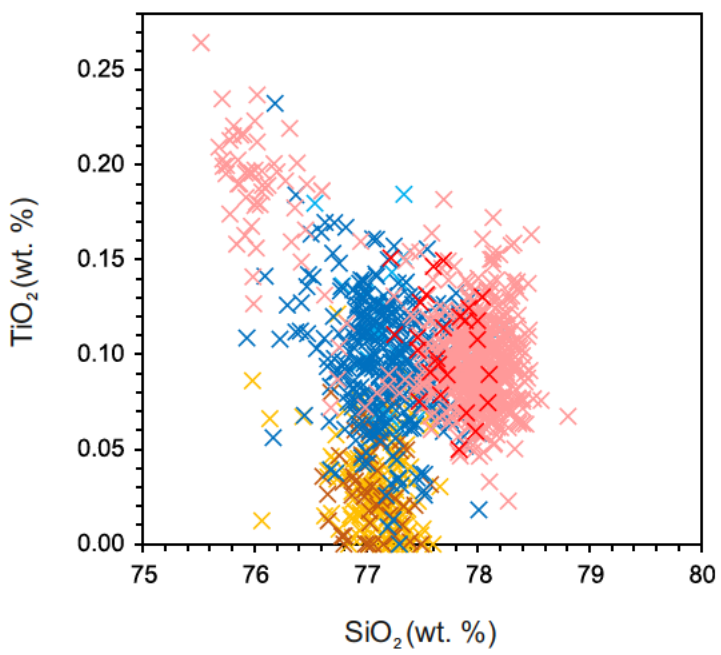
Fig. 19. Selected bivariate plots displaying the combined source and core data for Popocatépetl, Iztaccíhuatl, Tláloc-Telapón and Nevado de Toluca (combined as one group) and the SCVF. Different evolution trends can be noted in all bivariate plots, corroborating findings between Popocatépetl and Iztaccíhuatl in chapter 3 and Sunyé-Puchol et al. (2021). Higher resolution selected bivariate plots displaying Popocatépetl and the SCVF highlight the distinct evolution trends in these two sources, further supporting the assignation of tephras to the SCVF in the core.

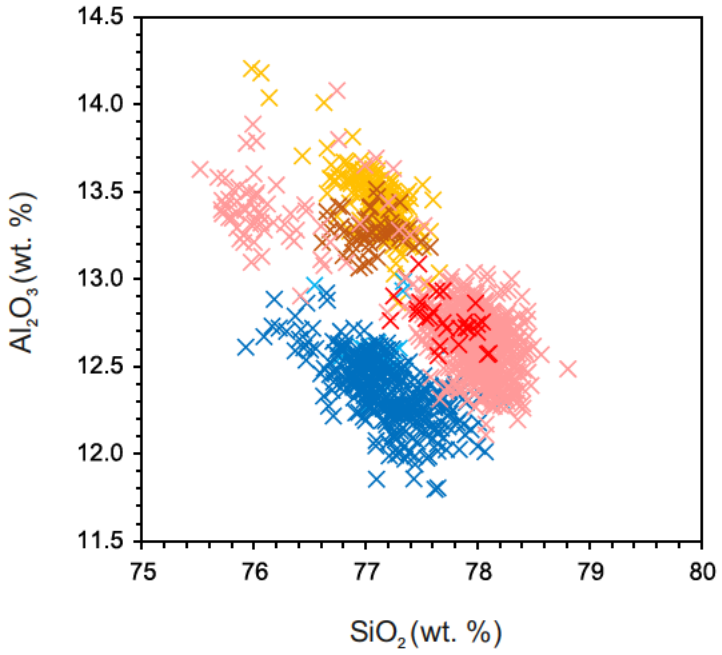
---

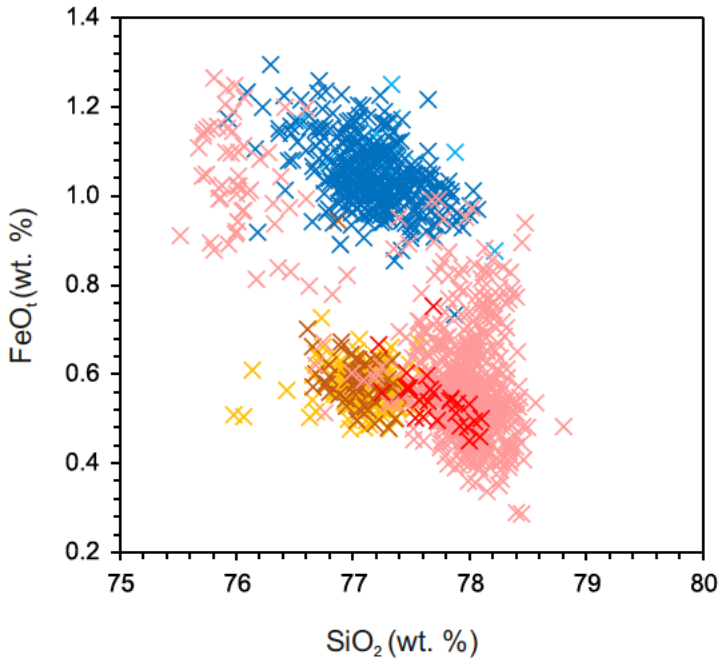
separation between glass compositions can be observed and there are sufficient and robust correlations between core and source glass analyses for all volcanic sources.

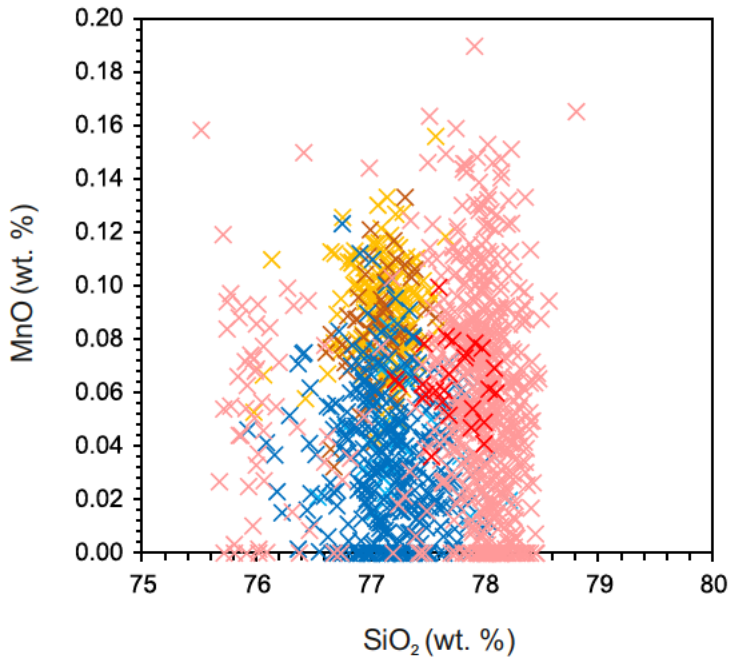
It can be concluded with confidence that within Lake Chalco that at least one tephra has been sourced from Tláloc-Telapón, three from Los Humeros and one from Atitlán. The deposits from Los Humeros and Atitlán are further explored below (section 5.9). Under closer investigation, the deposit from Tláloc-Telapón cannot be correlated to any known eruption (using source glass data presented in this study).

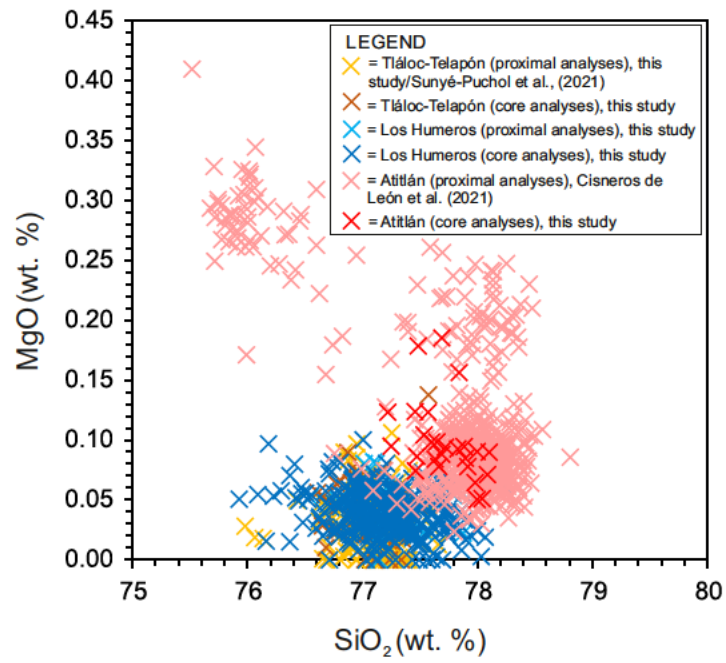
Furthermore, due to a sparsity in the longer-term explosive eruption record of Tláloc-Telapón, it is possible that the glass chemistry from this volcano is more variable than has currently been determined. However, since c.102 ka, the glass chemical field of known explosive eruptions is both narrow and distinctive. Silica and K_2O are higher than other volcanoes of the SNVR (e.g., Sunyé-Puchol et al, 2021). The deposit from Tláloc-Telapón is 1.5 cm in thickness and comprised of fine-grained ash (3 φ). A relatively thin and fine deposit from the closest stratovolcano to the core site is curious, as is the absence of any other tephras that can be compositionally assigned to this source. It is possible that the volcano has had very few explosive eruptions during the lifetime of the core, but those that have occurred have been large and are those that are known from proximal field mapping. From these small number of

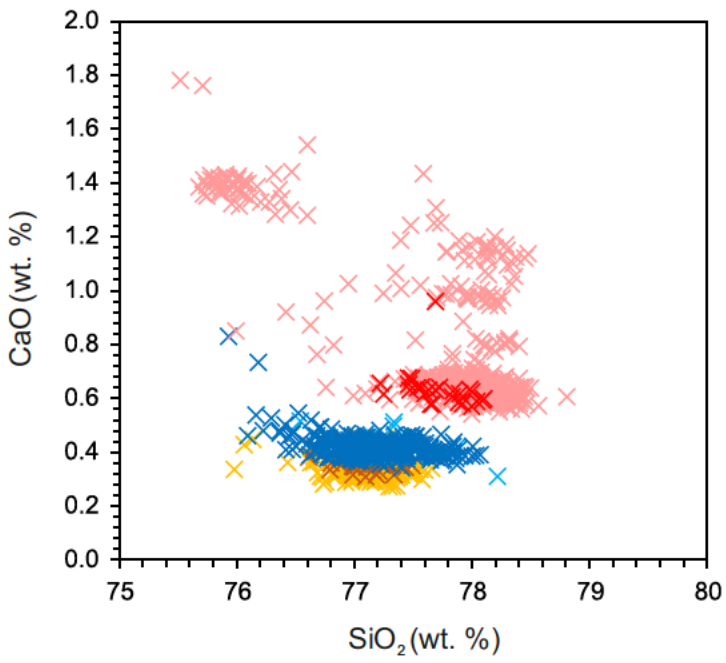

0.25
0.20
0.15
0.10
0.05
0.00
TiO_2 (wt. %)
75
76
77
78
79
80
SiO_2 (wt. %)

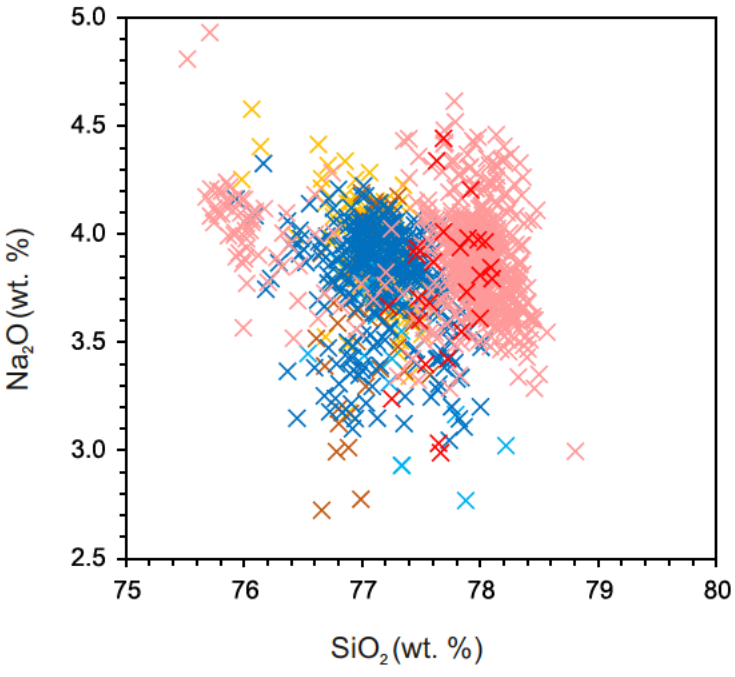

14.5
14.0
13.5
13.0
12.5
12.0
11.5
Al_2O_3 (wt. %)
75
76
77
78
79
80
SiO_2 (wt. %)


1.4
1.2
1.0
0.8
0.6
0.4
0.2
FeO_t (wt. %)
75
76
77
78
79
80
SiO_2 (wt. %)


0.20
0.18
0.16
0.14
0.12
0.10
0.08
0.06
0.04
0.02
0.00
MnO (wt. %)
75
76
77
78
79
80
SiO_2 (wt. %)


LEGEND
= Tláloc-Telapón (proximal analyses), this study/Sunyé-Puchol et al., (2021)
= Tláloc-Telapón (core analyses), this study
= Los Humeros (proximal analyses), this study
= Los Humeros (core analyses), this study
= Atitlán (proximal analyses), Cisneros de León et al. (2021)
= Atitlán (core analyses), this study
0.45
0.40
0.35
0.30
0.25
0.20
0.15
0.10
0.05
0.00
MgO (wt. %)
75
76
77
78
79
80
SiO_2 (wt. %)


2.0
1.8
1.6
1.4
1.2
1.0
0.8
0.6
0.4
0.2
0.0
CaO (wt. %)
75
76
77
78
79
80
SiO_2 (wt. %)


5.0
4.5
4.0
3.5
3.0
2.5
Na_2O (wt. %)
75
76
77
78
79
80
SiO_2 (wt. %)

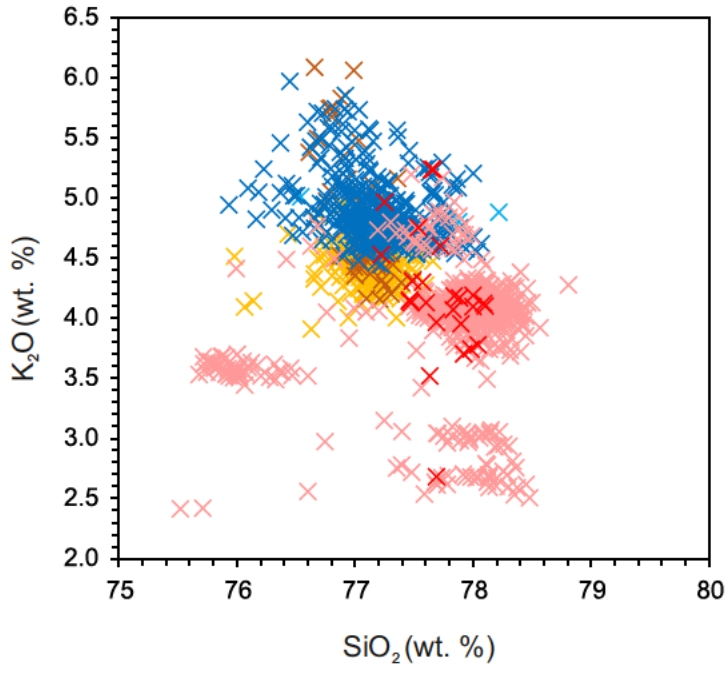

6.5
6.0
5.5
5.0
4.5
4.0
3.5
3.0
2.5
2.0
K_2O (wt. %)
75
76
77
78
79
80
SiO_2 (wt. %)

Fig. 20. Selected bivariate plots displaying source data used in this study with core analyses overlain for distal sources found within the core: Los Humeros and Atitlán. Tláloc-Telapón is also provided alongside these volcanoes, due to a similar glass chemistry to these sources.

---

events, dispersal may have generally been away from the core site, explaining the absence of deposits. Tephra 78.82 is consistent with this, and may be a cross- to up-wind deposit from a Plinian or larger event.

5.7. Other sources

As discussed above, out of the tephras analysed in the core (137 separate layers), 35 are likely sourced from Popocatépetl, 43 from Iztaccíhuatl, Nevado de Toluca and La Malinche, 17 from the SCVF, 1 from Tláloc-Telapón, 3 from Los Humeros and 1 from Atitlán, resulting in 100 of 137 layers assigned to a source volcano(es).

Of the 37 layers with no source identified, these layers are sub-divided into two categories: (1) Central TMVB arc signature – ambiguous source; (2) exotic sources, (c.f. chapter 2). The former category (ambiguous sources) includes deposits with glass chemistries that fall within the source fields identified (section 4) but are either varied in terms of chemistry, complicating source assignment; are bimodal in chemistry with two populations that sit within multiple source fields; lie on evolution trends identified however have few overlapping points to make a credible assignation and/or including analyses that comprise too few glass data points, defined here as ≤5. It is important to note that if all analyses (≤5 points) are tightly clustered, a source is still not assigned as it is possible the analyses are gathered from one or two glass shards, thus not representing any glass heterogeneity there may be within the samples. In

contrast, the latter category (exotic sources), comprise data that plot off the main trends from all analysed source volcanoes in at least 2 bivariate plots. In total, 23 layers are placed within category 1 (ambiguous sources) and 14 layers are within category 2 (exotic sources).

Fig. 21 displays four selected bivariate plots (CaO, MgO, Na_2O and K_2O) containing all core analyses. Layers assigned to exotic sources are presented in a different colour (yellow) highlighting different trends observed within the core. It can be noted there is some overlap with analyses from the core which are assigned to source volcanoes, as some of the layers overlap in many elements with clear contrasting trends in two major elements. In Fig. 21 major breakaways from the main trends are highlighted in all selected bivariates with examples of some of the tephras that account for these contrasting trends. In most cases tephras are thin (≤5 cm) and very thin (≤1 cm), although a couple of tephras are thicker, including tephra 184.224 which is 26.6 cm in thickness (see Table 2). Glass is also mixed with glass-shard morphologies and concentrations of microlites. The example 'exotic' tephras shown in Fig. 21 can be seen to sometimes display distinctive visual characteristics, i.e., pinkish colour.

It is possible that some of these tephras are sourced from the volcanoes analysed in this study, and represent geochemical variation (e.g., of that sometimes experienced at arc volcanoes following sector collapse, Watt et al., 2019) at specific points in the history of a given volcano. However, this is unlikely as analyses in this study from volcanoes with older and younger eruptions (e.g., Popocatépetl) spanning major edifice destruction and construction (Gisbert et al., 2022, section 5.6.1) show very little change in glass geochemistry. As a result, these tephras are likely sourced from volcanoes outside of the central TMVB and are good targets for further analysis with a wider study of glass analyses from other parts of the TMVB.

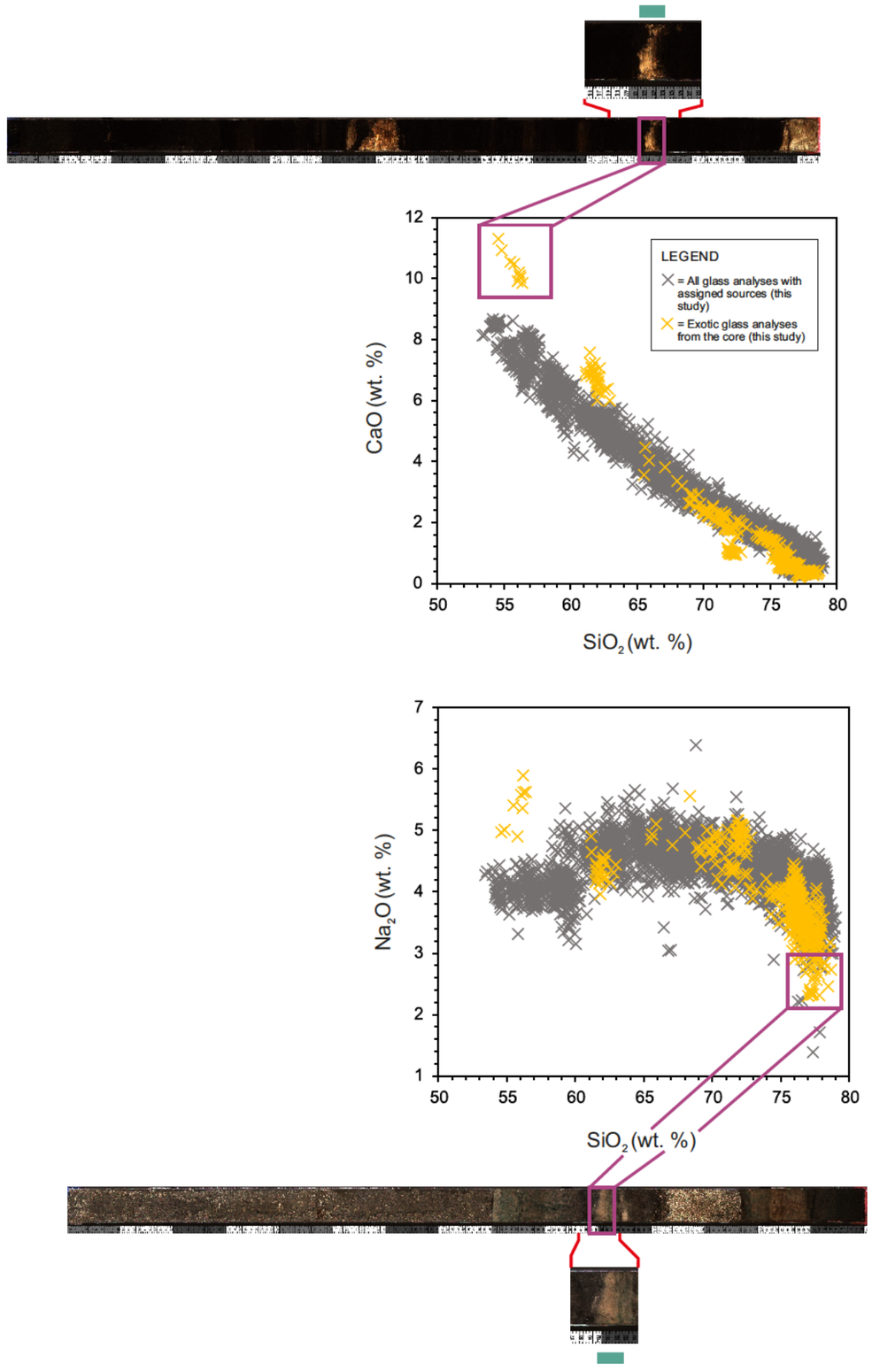

LEGEND
= All glass analyses with assigned sources (this study)
= Exotic glass analyses from the core (this study)
CaO (wt. %)
SiO2 (wt. %)
MgO (wt. %)
SiO2 (wt. %)
Na2O (wt. %)
SiO2 (wt. %)
K2O (wt. %)
SiO2 (wt. %)
LEGEND
= tephra
= bioturbation

Fig. 21. Selected bivariate plots displaying all glass analyses from known or assigned sources in this study (grey), with exotic analyses overlain (yellow). Examples are provided of tephras that display these exotic chemistries. Further information regarding their visual and physical characteristics are provided within Table 2.

5.8. Spread though the core

Considering all sources (outlined above) the spread of data throughout the core is important to visualise to understand if particular sources dominate in certain portions of core (i.e., time intervals). It is important to note that out of the minimum number of 450 eruptions in the core, glass has only been obtained from 137 layers (30.4%). Fig. 22 contains six TAS plots displaying the spread of glass data throughout the core at 50 m_c intervals. In all TAS diagrams, it is clear that tephra deposits at Lake Chalco are from a variety of source volcanoes and these source volcanoes are distributed throughout all depths within the core, at a 50 m_c resolution.

Considering the source fields presented in section 4, tephras from Popocatépetl are present in all six 50 m_c sections of core, with the highest number (14 eruptions) between 101 and 150.99 m_c. Generally, the fewest Popocatépetl eruptions occur within the upper 50 m and lowermost 100 m of the composite core. In contrast, eruptions from Iztaccíhuatl, Nevado de Toluca and La Malinche are sparse in the upper 150 m of composite core, with the densest clusters between 151 and 200.99 m_c and 251 and 300 m_c. Eruptions from the SCVF occur throughout all 50 m_c sections of core with the exception of between 151 and 200.99 m_c. The densest clusters of eruptions are within the lowermost 50 m and uppermost 150 m of composite core. It must be noted however that a diverse source of eruptions and range of compositions are throughout

the core, reinforcing the vulnerability of Mexico City to a range of explosive volcanic hazards from multiple sources.

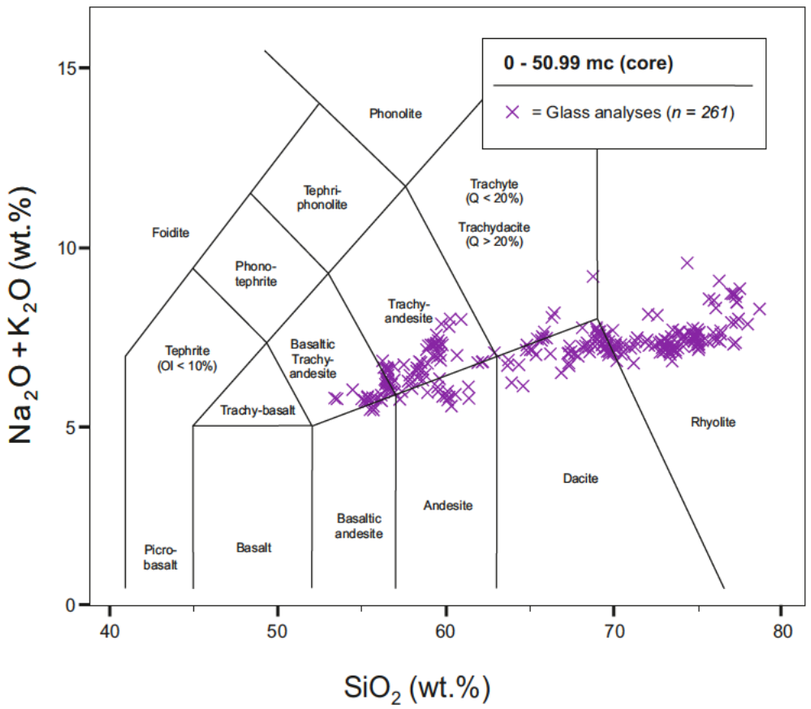
Additionally, due to a lack of data for many identified eruptions with the core (described above and presented in chapter 3), accurate frequency patterns for each volcanic source cannot be ascertained. While findings from the core surrounding volcanic output from Iztaccíhuatl, Nevado de Toluca and La Malinche compared with Popocatépetl (i.e., a period of coeval activity between Iztaccíhuatl and Popocatépetl, with more recent (<60 ka) activity continuing from Popocatépetl) are generally consistent with that presented in chapter 4 and Sunyé-Puchol et al, (2021), as sources cannot be discriminated between Iztaccíhuatl, Nevado de Toluca and La Malinche, this interpretation is difficult to support with meaningful data.

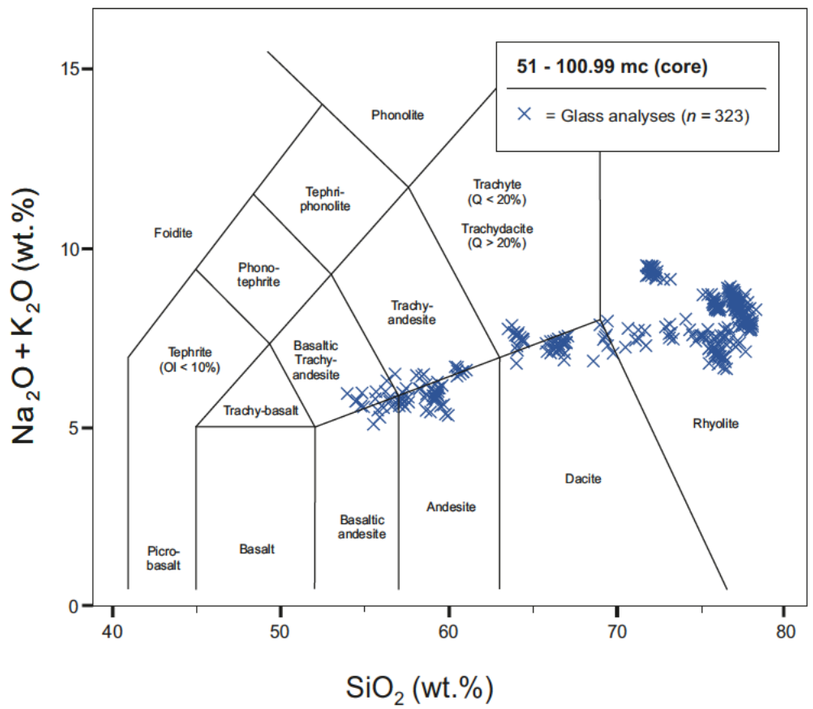
In summary, the tephra deposits at Lake Chalco are varied and have been throughout the entire history of the lacustrine-dominated stage of the lake. This is clear by the diversity of data in Fig. 22.

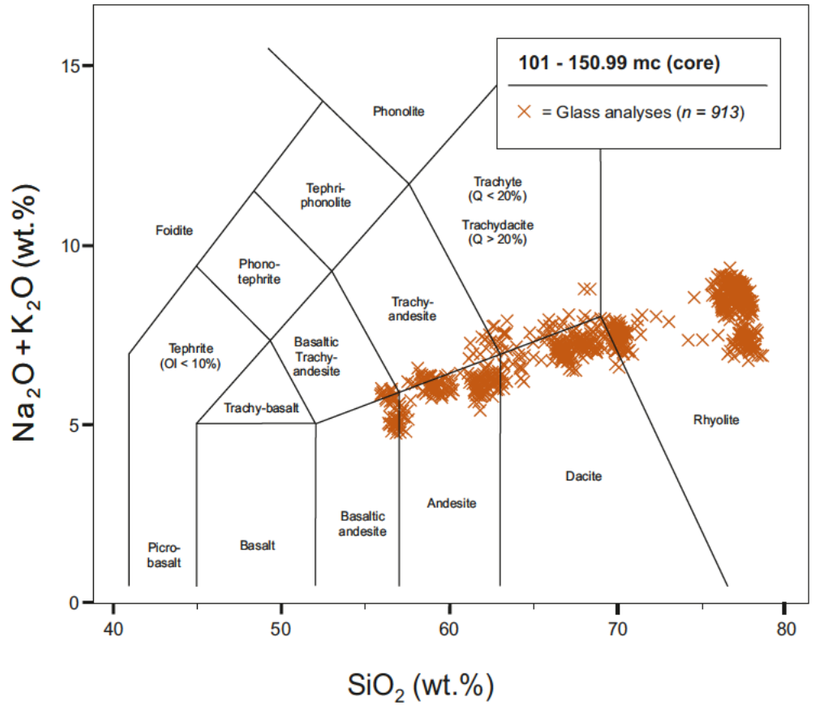
5.9. New glass geochemical fields using core analyses

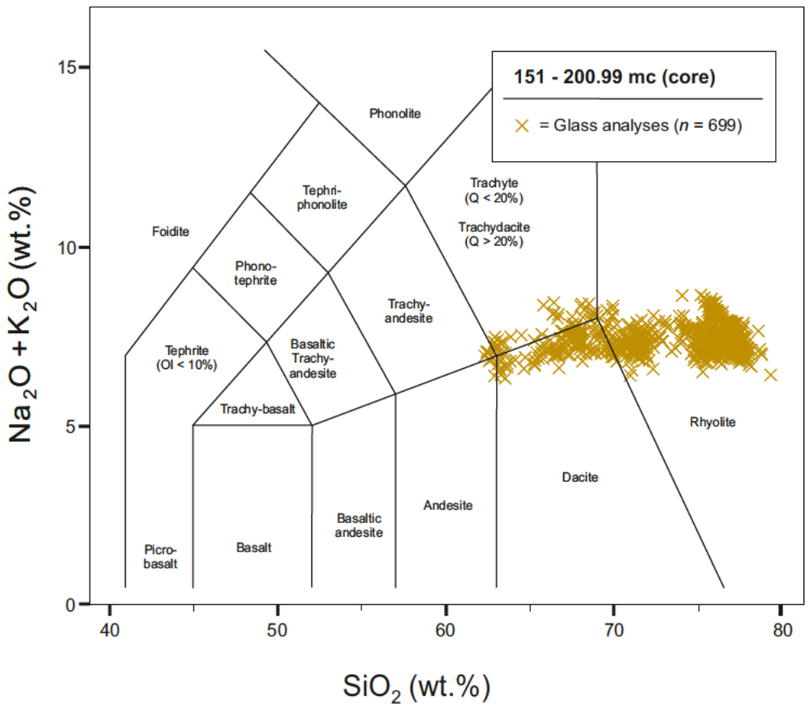
With all positively identified volcanic sources in the core, it is possible to expand the glass geochemical fields for these volcanoes. By expanding the glass fields, the new fields are likely to be more representative of the volcanic sources over a longer timescale, including eruptions that have not been described or identified at the surface.

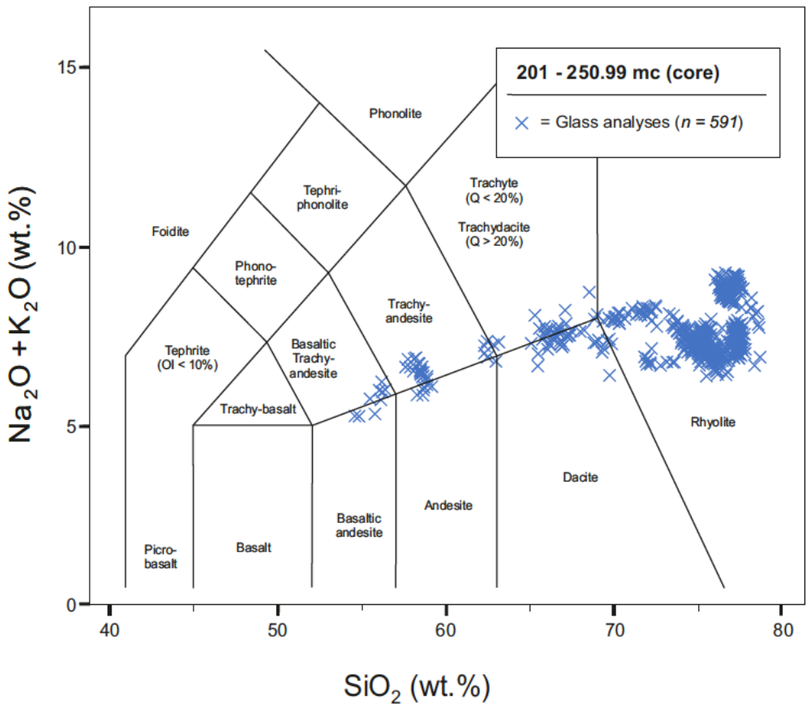
Fig. 23a presents a TAS diagram containing all source data and correlated core data for the SCVF, Popocatépetl, Iztaccíhuatl, Nevado de Toluca, La Malinche and Tláloc-Telapón. As per the core deposits, Iztaccíhuatl, Nevado de Toluca and La Malinche are grouped together due


0 - 50.99 mc (core)
= Glass analyses (n = 261)
Phonolite
Tephri-phonolite
Foidite
Phono-tephrite
Tephrite (Ol < 10%)
Basaltic Trachy-andesite
Trachy-basalt
Trachyte (Q < 20%)
Trachydacite (Q > 20%)
Trachy-andesite
Rhyolite
Dacite
Andesite
Basaltic andesite
Picro-basalt
Basalt
Na2O + K2O (wt.%)
SiO2 (wt.%)


51 - 100.99 mc (core)
= Glass analyses (n = 323)
Phonolite
Tephri-phonolite
Foidite
Phono-tephrite
Tephrite (Ol < 10%)
Basaltic Trachy-andesite
Trachy-basalt
Trachyte (Q < 20%)
Trachydacite (Q > 20%)
Trachy-andesite
Rhyolite
Dacite
Andesite
Basaltic andesite
Picro-basalt
Basalt
Na2O + K2O (wt.%)
SiO2 (wt.%)


101 - 150.99 mc (core)
= Glass analyses (n = 913)
Phonolite
Tephri-phonolite
Foidite
Phono-tephrite
Tephrite (Ol < 10%)
Basaltic Trachy-andesite
Trachy-basalt
Trachyte (Q < 20%)
Trachydacite (Q > 20%)
Trachy-andesite
Rhyolite
Dacite
Andesite
Basaltic andesite
Picro-basalt
Basalt
Na2O + K2O (wt.%)
SiO2 (wt.%)


151 - 200.99 mc (core)
= Glass analyses (n = 699)
Phonolite
Tephri-phonolite
Foidite
Phono-tephrite
Tephrite (Ol < 10%)
Basaltic Trachy-andesite
Trachy-basalt
Trachyte (Q < 20%)
Trachydacite (Q > 20%)
Trachy-andesite
Rhyolite
Dacite
Andesite
Basaltic andesite
Picro-basalt
Basalt
Na2O + K2O (wt.%)
SiO2 (wt.%)


201 - 250.99 mc (core)
= Glass analyses (n = 591)
Phonolite
Tephri-phonolite
Foidite
Phono-tephrite
Tephrite (Ol < 10%)
Basaltic Trachy-andesite
Trachy-basalt
Trachyte (Q < 20%)
Trachydacite (Q > 20%)
Trachy-andesite
Rhyolite
Dacite
Andesite
Basaltic andesite
Picro-basalt
Basalt
Na2O + K2O (wt.%)
SiO2 (wt.%)

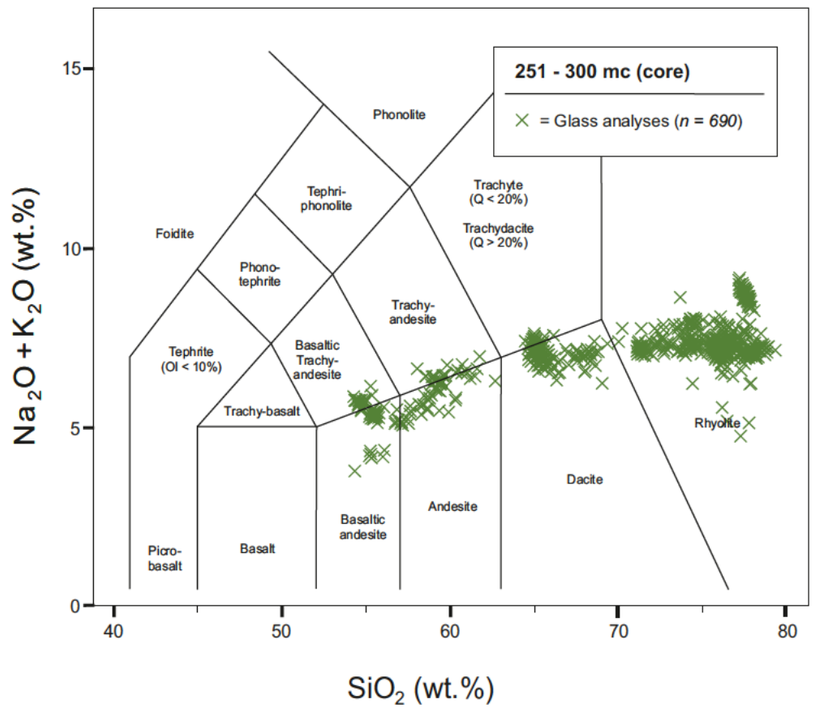

251 - 300 mc (core)
= Glass analyses (n = 690)
Phonolite
Tephri-phonolite
Foidite
Phono-tephrite
Tephrite (Ol < 10%)
Basaltic Trachy-andesite
Trachy-basalt
Trachyte (Q < 20%)
Trachydacite (Q > 20%)
Trachy-andesite
Rhyolite
Dacite
Andesite
Basaltic andesite
Picro-basalt
Basalt
Na2O + K2O (wt.%)
SiO2 (wt.%)

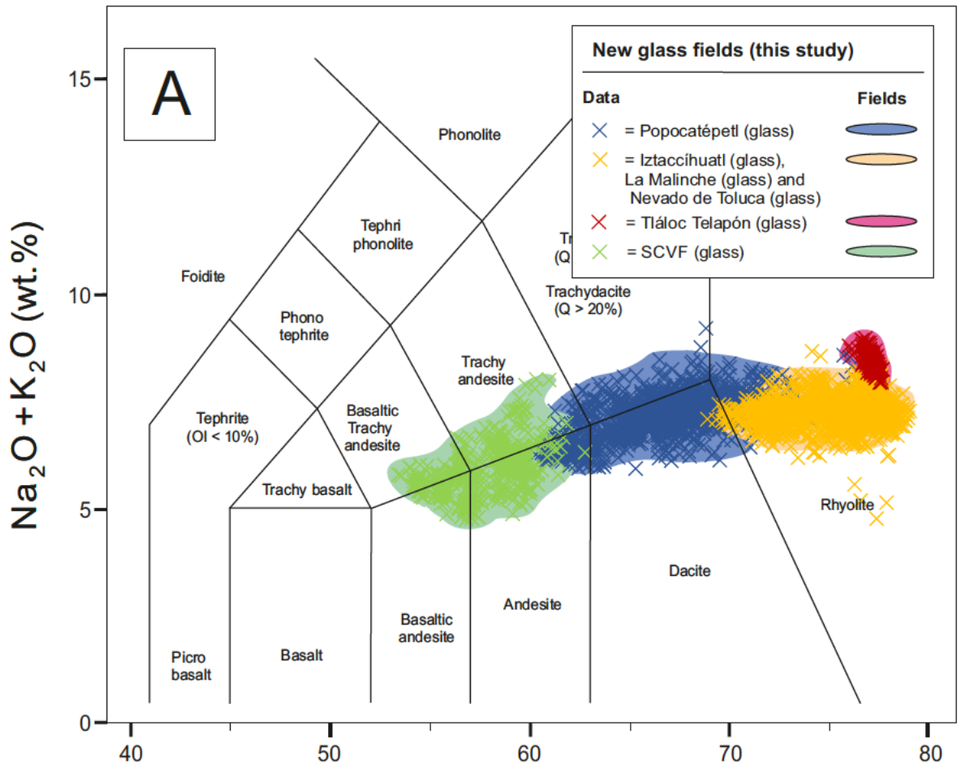
Fig. 22. Total alkali vs. silica (TAS) diagrams of all glass analyses at 50 m intervals in the composite core. The number of analyses comprising the data points are also provided. TAS diagrams show a variety of sources at all depths. Data can be compared with Table 2 and Fig. 26.

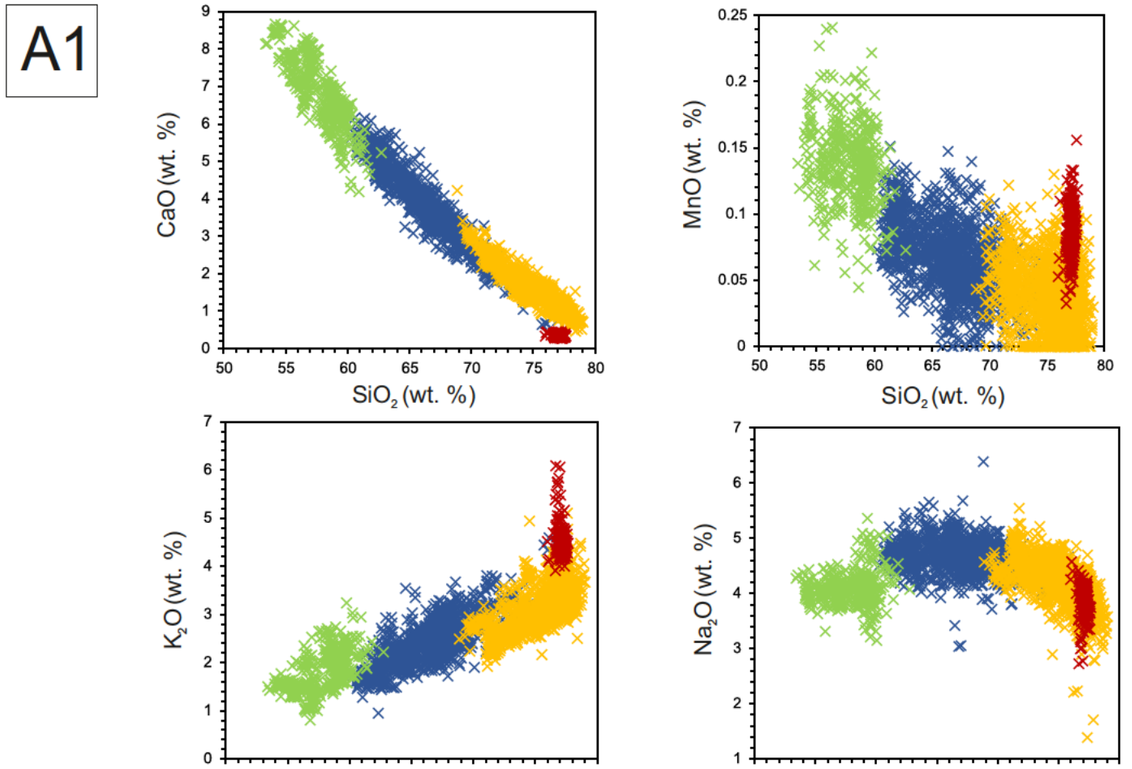
---

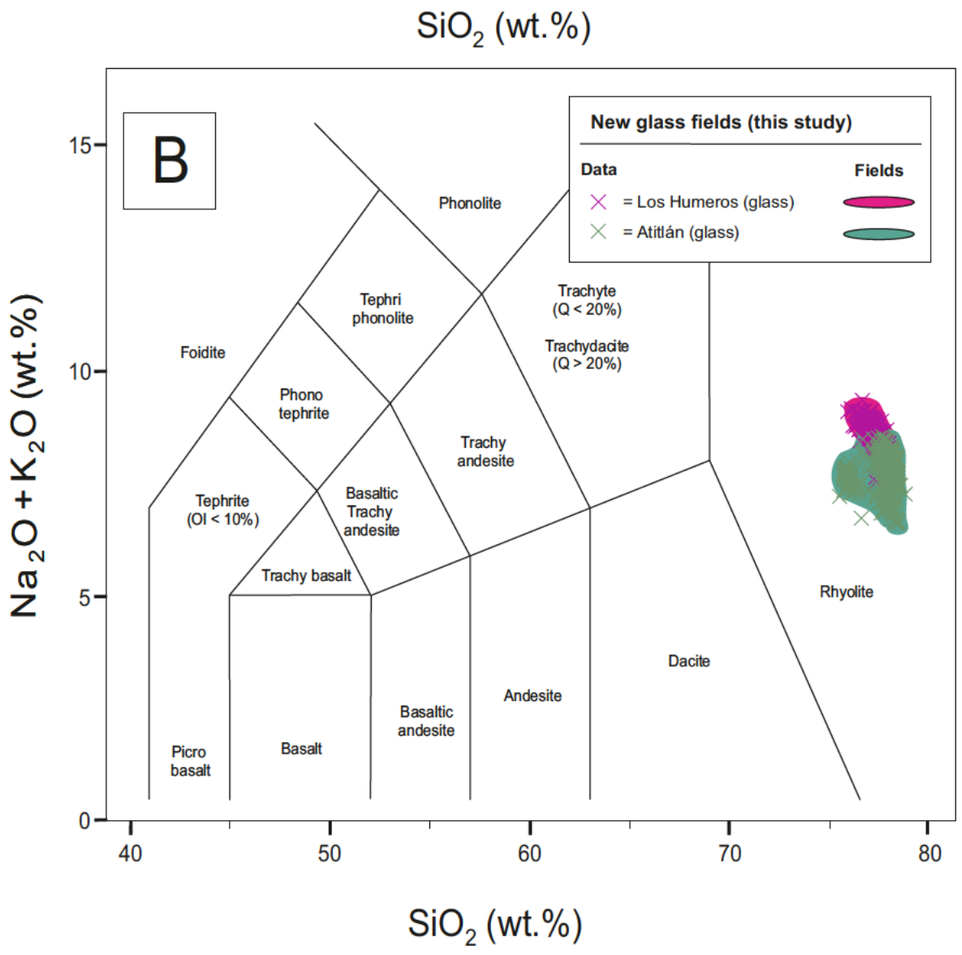
to similar glass chemistries. When compared with Fig.7a the SCVF glass field can be seen to be much larger, due to an increase in data from 3 to 20 samples now comprising the field. Nevertheless, the same rock types are represented: basaltic tracyandesite, basaltic andesite, andesite and trachyandesite. In Fig. 23a1 (selected bivariate plots) the unique evolution trend of SCVF glass compared with Popocatépetl can be seen in all plots (c.f. Fig. 19).

Furthermore, the fields of Popocatépetl and Iztaccíhuatl, Nevado de Toluca and La Malinche are further expanded with core analyses added, although similarly to SCVF data, the rock type compositions spanned by Popocatépetl remain unchanged with andesitic, trachyandesitic, trachydacitic, dacitic and rhyolitic glasses. It can be seen in Fig. 23a,a1 that the Popocatépetl glass field appears to now extend further into rhyolitic compositions, with more SiO_2 enriched samples within the deeper sections of the core, as discussed in section 5.6.1. Interestingly, the and Iztaccíhuatl, Nevado de Toluca and La Malinche field can be seen (Fig. 23a,a1) to now slightly extend into dacitic glass compositions, although ≥95% of analyses are rhyolitic in composition. Again, a separate evolution trend can be seen for these volcanoes in Fig. 23a1, and there is a slightly wider extension into lower $Na_2O + K_2O$ values.

Moreover, the glass field for Tláloc-Telapón is largely unchanged, with only one eruption identified in the core, the field has virtually no differences when compared with the field presented in Fig. 7a. In Fig. 23a1 unique compositions can be best seen in CaO and K_2O.


A
New glass fields (this study)
Data
Fields
= Popocatépetl (glass)
= Iztaccíhuatl (glass), La Malinche (glass) and Nevado de Toluca (glass)
= Tláloc Telapón (glass)
= SCVF (glass)
Phonolite
Tephri phonolite
Foidite
Phono tephrite
Trachydacite (Q > 20%)
Trachy andesite
Tephrite (Ol < 10%)
Basaltic Trachy andesite
Trachy basalt
Rhyolite
Dacite
Andesite
Basaltic andesite
Picro basalt
Basalt
$Na_2O + K_2O$ (wt.%)
SiO_2 (wt.%)


A1
CaO (wt. %)
MnO (wt. %)
K_2O (wt. %)
Na_2O (wt. %)
SiO_2 (wt. %)


B
New glass fields (this study)
Data
Fields
= Los Humeros (glass)
= Atitlán (glass)
Phonolite
Tephri phonolite
Foidite
Phono tephrite
Trachyte (Q < 20%)
Trachydacite (Q > 20%)
Trachy andesite
Tephrite (Ol < 10%)
Basaltic Trachy andesite
Trachy basalt
Rhyolite
Dacite
Andesite
Basaltic andesite
Picro basalt
Basalt
$Na_2O + K_2O$ (wt.%)
SiO_2 (wt.%)

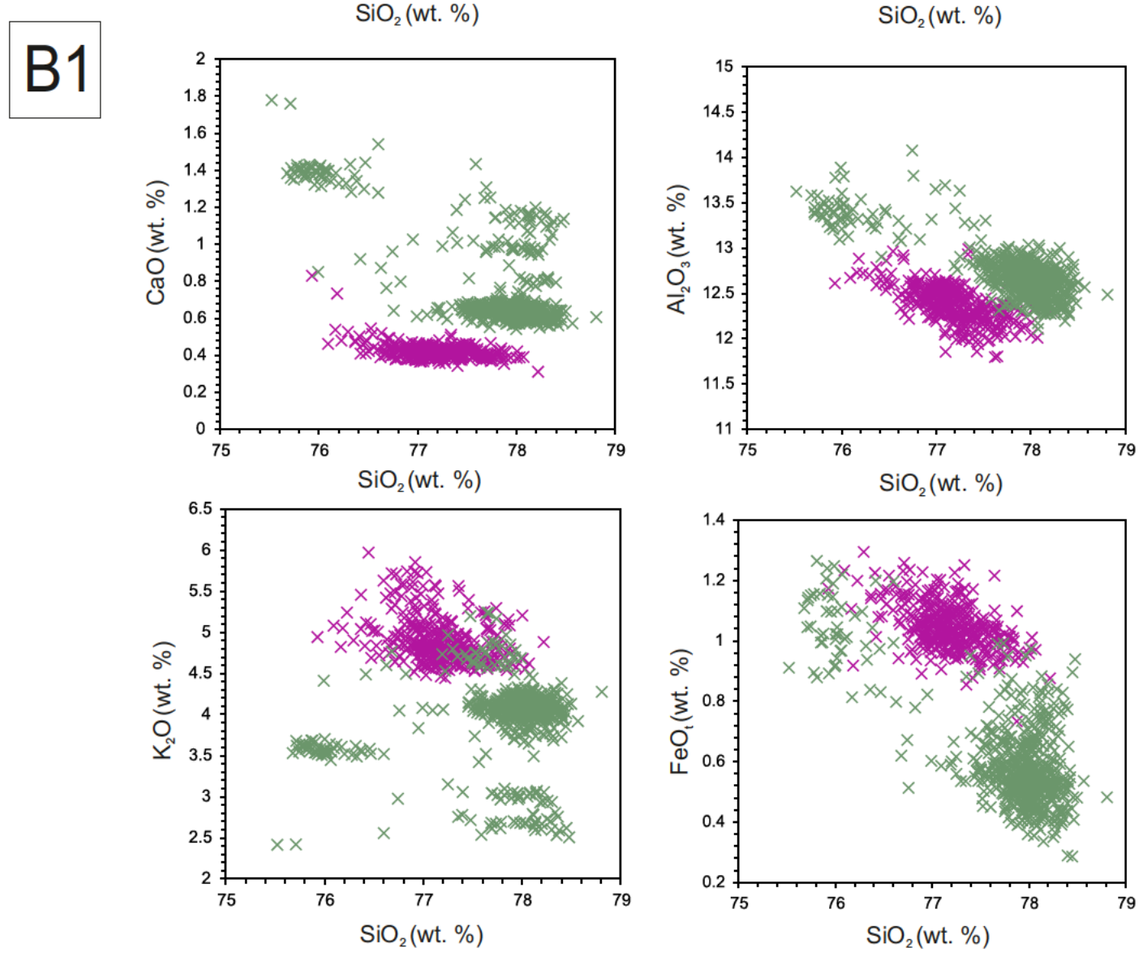

B1
CaO (wt. %)
Al_2O_3 (wt. %)
K_2O (wt. %)
FeO_t (wt. %)
SiO_2 (wt. %)

Fig. 23. (a) Total alkali vs. silica (TAS) diagram including all data (source and core) for the SCVF, Popocatépetl, Iztaccíhuatl, Tláloc-Telapón and Nevado de Toluca (combined as one group) and Tláloc-Telapón volcanoes. New inferred fields are drawn around the data, acting as an updated reference for future correlations. (a1) Selected bivariates of the data in a. (b) Total alkali vs. silica (TAS) diagram including all data (source and core) for Los Humeros and Atitlán volcanoes. (b1) Selected bivariates of the data in b.

Fig. 23b presents a TAS diagram of the caldera sources identified in the core: Los Humeros and Atitlán, combining the data shown in Fig. 8 (proximal source analyses) with data from assigned layers, to these volcanoes, in the core. The Los Humeros field has remained a tight and unique cluster (best seen in bivariate plots in Fig. 23b1) although has a slightly wider compositional range (e.g., the range in SiO_2 has increased from 76.54 – 78.22 wt.% to 75.93 – 78.22 wt.%). Altogether, there is minimal change to the glass geochemical field. Similarly, Atitlán shows a similar result, which has only increased by 26 data points. These analyses fall mostly within or extremely close (≤0.2 wt%) in all major elements, thus unaffecting the geochemical field for this volcano.

While expanding source geochemical fields using tephras attributed to the volcanoes is unconventional and fairly circular, the correlations and unique trends for all volcanoes discussed in this study are clear. With limited glass data in the study area, and with generally poor exposure of pyroclastic successions around Mexico City, particularly for older eruptions from proximal polygenetic and monogenetic centres, the glass geochemical fields presented in Fig. 23 may assist with correlations of untraceable fall deposits (by field methods) which are yet to be discovered. The wider glass fields (particularly for the SCVF, Popocatépetl and Iztaccíhuatl, Nevado de Toluca and La Malinche group) may provide glass geochemical

context for deposits that have a wider temporal spectrum than currently identified and mapped deposits.

6. GEOCHRONOLOGICAL MARKER ERUPTIONS

As discussed in section 5, 100 tephras in the core have been assigned volcanic sources. The majority of these sources (96) are attributed to local polygenetic volcanoes (e.g., Popocatépetl) or the SCVF. In the majority of cases (with the exception of up to 6 possibly reworked layers) , these deposits are representative of explosive eruptions from these volcanoes, with a visible deposit at Lake Chalco indicating that if these eruptions occurred in present day, there would be significant hazard implications for Mexico City and its c.25 million inhabitants. To better understand the frequency of these eruptions, and their temporal impact on the Mexico City region, a reliable chronology for the core is crucial, which would allow extrapolation of modelled eruption ages for each event, using Bayesian statistics (e.g., McNamara et al., 2018; McLean et al., 2020). Development of this chronology is underway: Chapter 6 outlines the detailed sub-sampling and methodology applied to various core deposits in this study to obtain direct $^{40}Ar/^{39}Ar$ ages. However, due to significant laboratory delays, the ages have unfortunately not been returned in time for this thesis, despite preparation being completed for analysis in early 2019. A further explanation is provided within chapter 6 accompanied by a supporting statement.

In addition to the direct dating of deposits from within the core, correlated eruption layers, using glass geochemistry through tephrochronological techniques, can also be used to better constrain the chronology of the core (e.g., Albert et al., 2019). At Lake Chalco (from earlier and shallower coring projects) some attempts at correlating well-known eruptions have previously

been conducted (see Ortega-Guerrero and Newton, 1998), including possibly correlating the Upper Toluca Pumice (UTP) from Nevado de Toluca volcano, with a reported eruption age of 12,520 ± 135 yr BP. Ortega-Guerrero and Newton, (1998) highlight the importance of tephrochronology at Lake Chalco although were unable to make reliable correlations due to a lack of a source glass geochemical data to compare with. The new work presented here provides the glass chemical framework over a long timescale to enable better characterisation of sources and correlation with specific volcanoes.

Unfortunately, correlating individual eruptions, particularly from proximal polygenetic and monogenetic sources which are well described and contain accurate and reliable dates, is largely unfeasible at Lake Chalco due to the similar chemistries with overlapping data points across many eruptions from the same volcanic source, coupled with a sparsity of well dated eruptions at each volcanic source. Additionally, with a potential 603 tephra layers within the core (chapter 3), target layers for chemical analysis require a reliable, highly precise and well-established chronology to enable specific tephra layers to be tied to known eruptions, based on chemical and chronological correlation. This chronology is currently lacking.

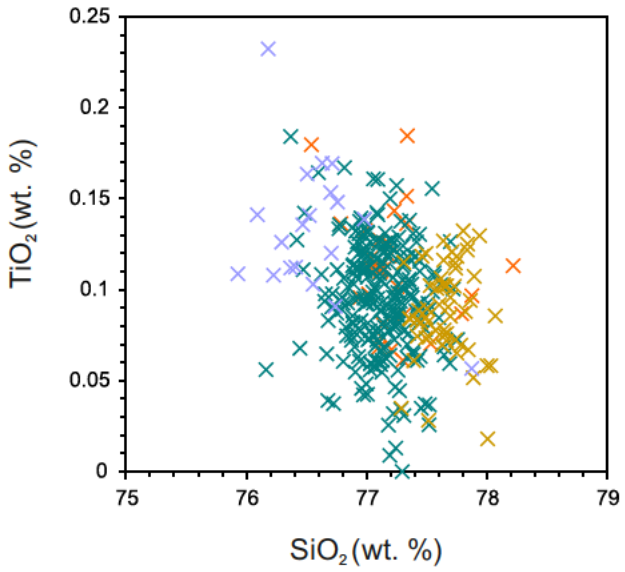
Despite this, distal (and silicic) calderas (e.g., Los Humeros and Atitlán) which typically erupt more explosively yet less frequently than composite volcanoes (e.g., Branney and Acocella, 2015), offer an alternative to develop direct correlative tie points for the Chalco core. Such eruptions often have multiple and accurate known ages, due to their widespread deposits, forming isochronous markers in other well dated successions (e.g., Smith et al., 2016; Abbott et al., 2020). The correlation of well dated eruptions from both Los Humeros and Atitlán into the Chalco core is explored below.

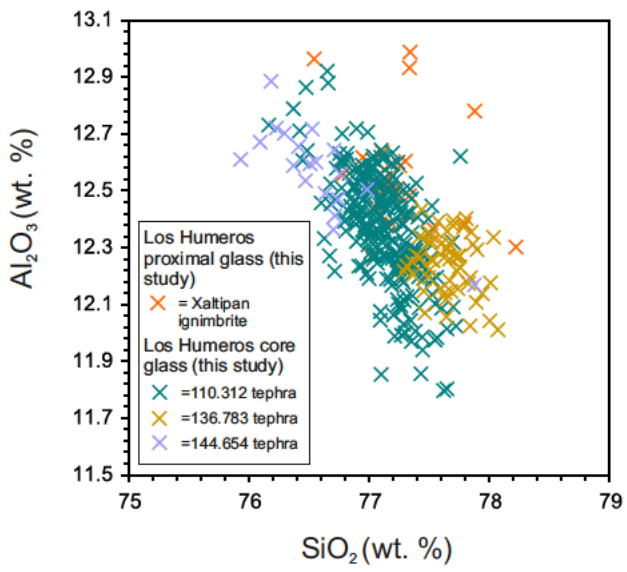
6.1. Los Humeros caldera, Mexico

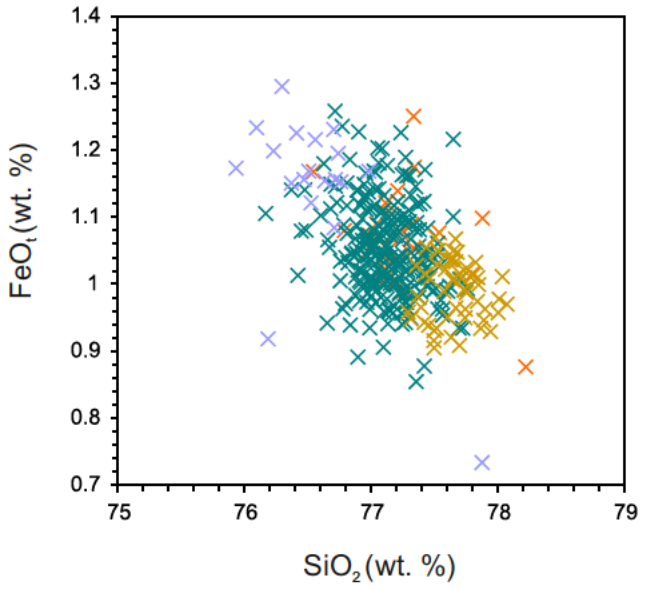
As outlined in chapter 2, section 2 and Table 1, Los Humeros is a large silicic volcanic complex with an effusive and also a highly explosive eruption history. Over the past c.693 ka, Los Humeros has undergone several stages of growth, during a pre-caldera stage, constructed upon an andesitic and basaltic volcanic basement (Cavazos-Álvarez and Carrasco-Núñez, 2019). Following this, the volcanic complex entered a caldera-forming stage, beginning with the eruption of the Xáltipan ignimbrite (164 ± 4.3 ka), the largest known eruption of the TMVB, erupting c.290 km^3 DRE of magma (Carrasco-Núñez et al., 2017; Cavazos-Álvarez and Carrasco-Núñez, 2019). Also within this caldera stage were younger eruptions including the Faby Tuff (70 ± 23 ka) and the Zaragoza ignimbrite (69 ± 16 ka), which were less widespread with c.10 and c.15 km^3 DRE magma volumes, respectively (e.g., Ferriz and Mahood, 1984; Carrasco-Núñez et al., 2012; Carrasco-Núñez et al., 2018). Since these events, the Los Humeros volcanic complex has undergone resurgent, post-caldera volcanism, with explosive eruptions such as the Llano tuff erupted at 28.3 ± 1.1 ka (Rojas-Ortega, 2016; Cavazos-Álvarez and Carrasco-Núñez, 2019).

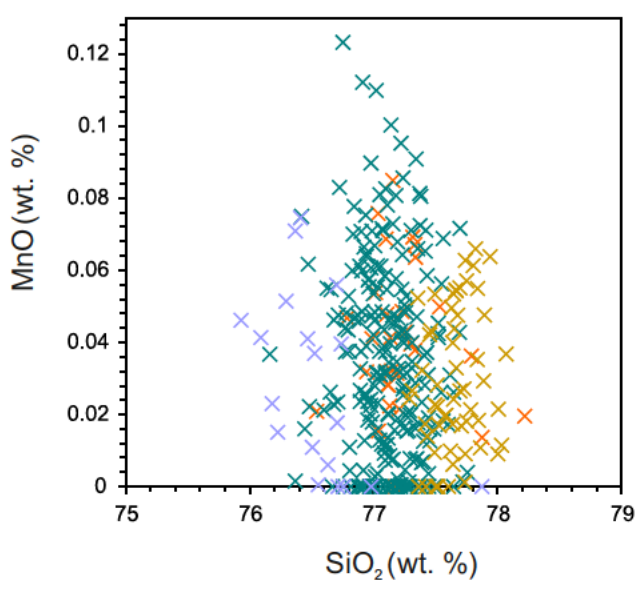
As noted above, three eruptions with the Los Humeros glass-geochemical fingerprint have been identified within the Chalco core, including tephras 110.312, 136.783 and 144.654. Our defined glass geochemical field is based on samples from the Xáltipan ignimbrite, and these three tephras thus display close similarity to this specific magma. The three tephras were plotted alongside the Xáltipan data in an attempt to positively identify whether one of these units can correlate with the Xáltipan ignimbrite specifically (Fig. 24a). From the bivariate plots the glass chemistry from all three eruptions can be seen to be similar. However, some variation

A

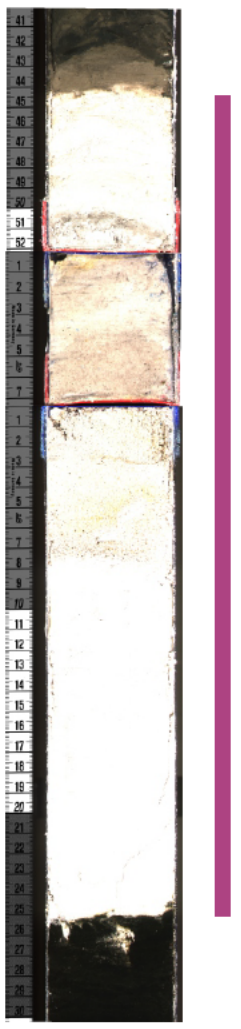






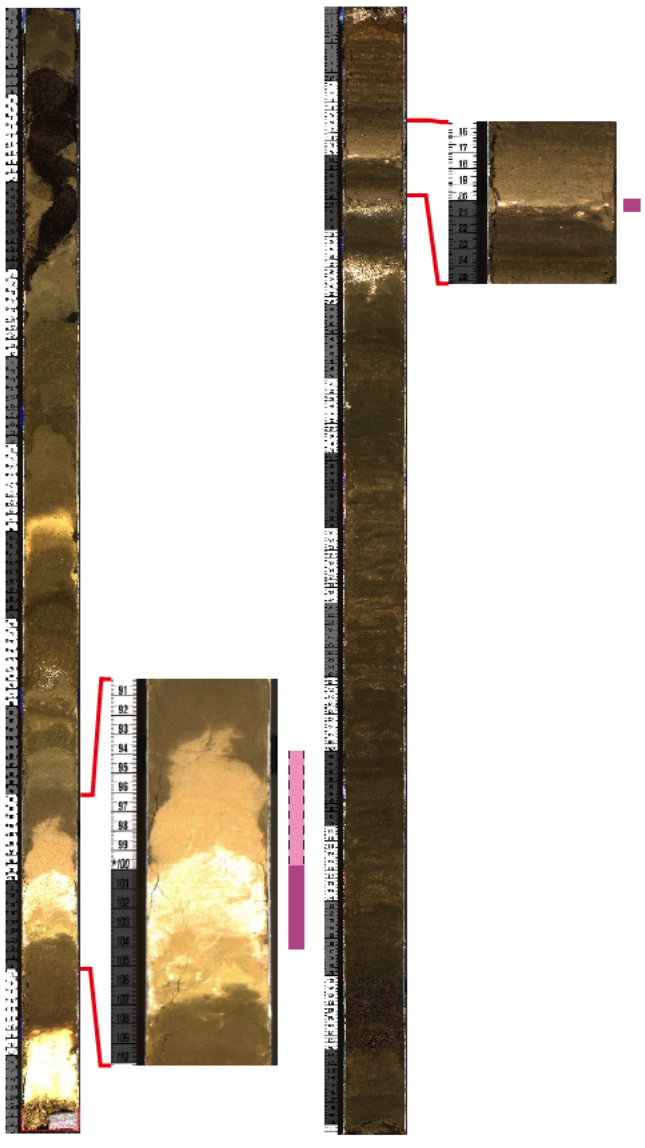


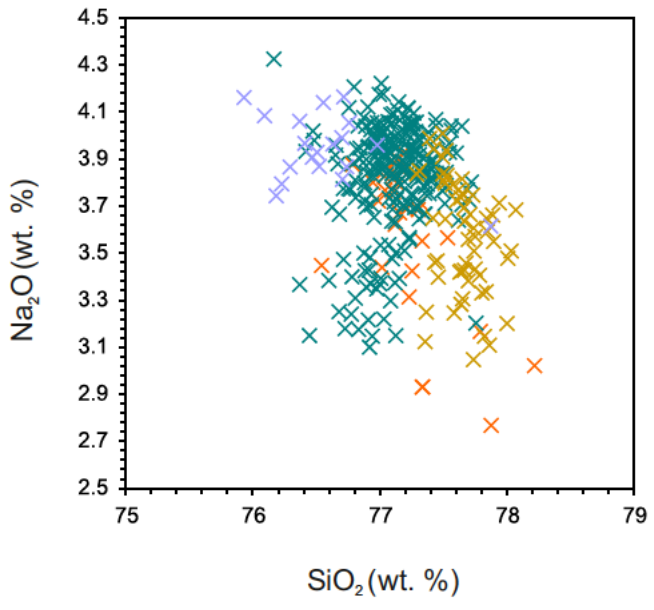
B



C

LEGEND (B+C)
= tephra
= reworking





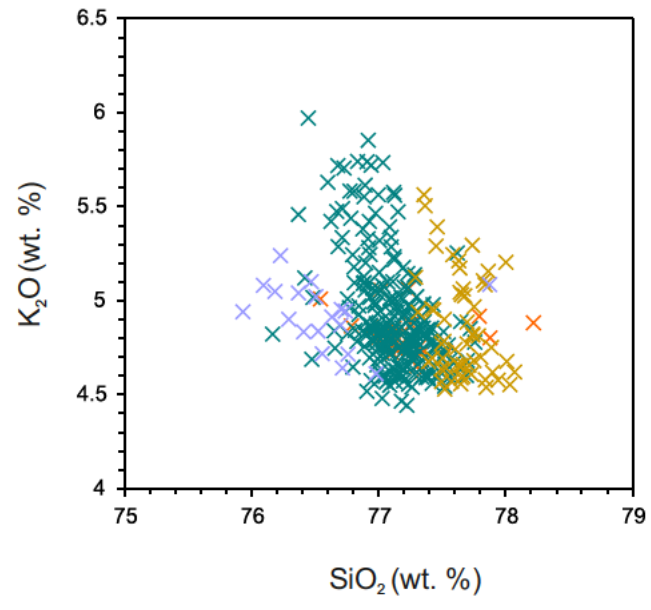


Fig. 24. (a) Selected bivariate plots displaying the data from the Xáltipan ignimbrite from Los Humeros with core data assigned to Los Humeros overlain. A positive correlation between the Xáltipan ignimbrite and tephra 110.312 can be seen in all elements. (b) Core section photographs displaying the physical characteristics of tephra 110.312. (c) Core section photographs displaying the physical characteristics of other tephras (136.783 and 144.654) in the core which are from Los Humeros.

---

exists between each, mostly due to their SiO_2 contents. The source data of the Xáltipan ignimbrite is fairly scattered. However, the majority of analyses overlap with tephra 110.312, in all major elements. As the Xáltipan ignimbrite is the largest known eruption from the TMVB, and with a known radial plume dispersal, with distal component towards the SW, it can be expected that the deposit will be represented by a fall deposit of substantial thickness at Chalco, which is SW from the caldera (Cavazos-Álvarez and Carrasco-Núñez, 2020). Fig. 24b displays the physical characteristics of tephra 110.312 in the core, which is 39.6 cm thick, comprised of mostly fine ash with up to medium ash in parts and sharp upper and lower contacts due to good preservation and core recovery. It can also be noted from the glass-shard characteristics (Table 2) that the deposit is comprised of microlite-free cuspate shards, as expected from a large, explosive eruption. It is therefore concluded that tephra 110.312 is the distal fall (c.160 km from the vent(s)) of the Xáltipan ignimbrite. It is also possible, due to dispersal directions noted by Cavazos-Álvarez and Carrasco-Núñez, (2020) that the deposit in Lake Chalco is on or near to the dispersal axis of this eruption.

The other two eruptions in the core, 136.783 and 144.654, correlated to Los Humeros lie stratigraphically below the Xáltipan ignimbrite at up to 26.47 m and 34.34 m below in the composite stratigraphy, respectively. These older eruptions therefore pre-date the caldera

stage of the volcano (Cavazos-Álvarez and Carrasco-Núñez, 2020). Without glass chemistry of older eruptions, it is not possible to corelate these deposits to any specific eruptions. It is however noted in Carrasco-Núñez et al. (2018) that this stage of the volcano is dominated by rhyolitic domes and lavas, with no mention of widespread explosive pyroclastic deposits. It is therefore possible that proximally to the caldera, surface deposits are dominated by the Xáltipan ignimbrite, burying any older and more widespread explosive deposits. The two events may therefore extend the known explosive history of Xáltipan. Fig. 24c displays the physical characteristics of tephras 136.783 and 144.654 in the core (left and right core images, respectively), where it can be seen that tephra 136.783 is a fine-grained white to yellow ash that is 3.5 cm in thickness and tephra 144.654 is a fine white ash 1 cm in thickness. Notwithstanding our absence of knowledge about dispersal directions, the thickness is consistent with these events being much smaller than that Xáltipan ignimbrite, but still likely large magnitude explosive eruptions. Similarly, to the Xáltipan ignimbrite, tephra 136.783 also comprises cuspate glass-shard morphologies and is microlite-free (see Table 2).

In summary, the Xáltipan ignimbrite is present within the Chalco core at a composite depth of 110.31 m. At 39.6 cm thick, this is the ninth thickest tephra deposit in the core, despite being mostly comprised of fine ash and from a distal (c.160 km) source. This eruption provides a reliable date of 164 ± 4.3 ka at 110.31 m_c in the core, which can be incorporated into the age-depth model. Furthermore, the thickness and grain size of the deposit makes it possible to reassess the eruptive volume of this eruption (see section 7). In addition, two possible newly identified explosive eruptions with far-reaching widespread visible fall deposits over the Mexico City region have been identified in Lake Chalco. With a more refined age-depth model,

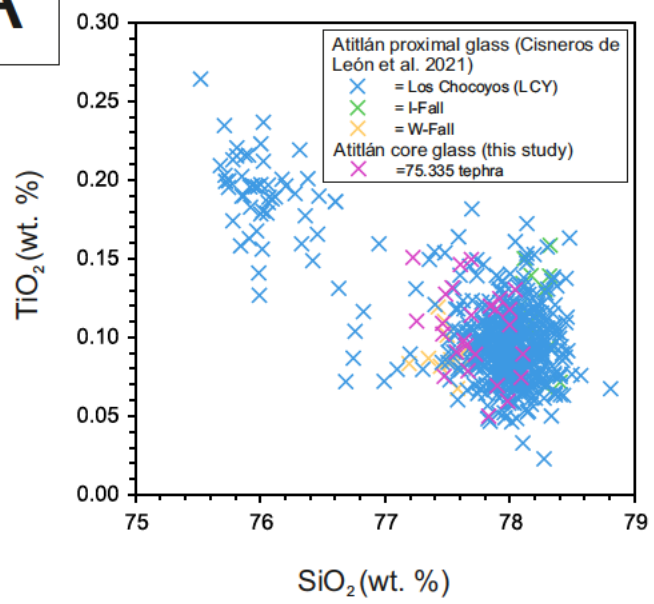
these eruption ages can be estimated and used to expand the tephrostratigraphic framework at Los Humeros.

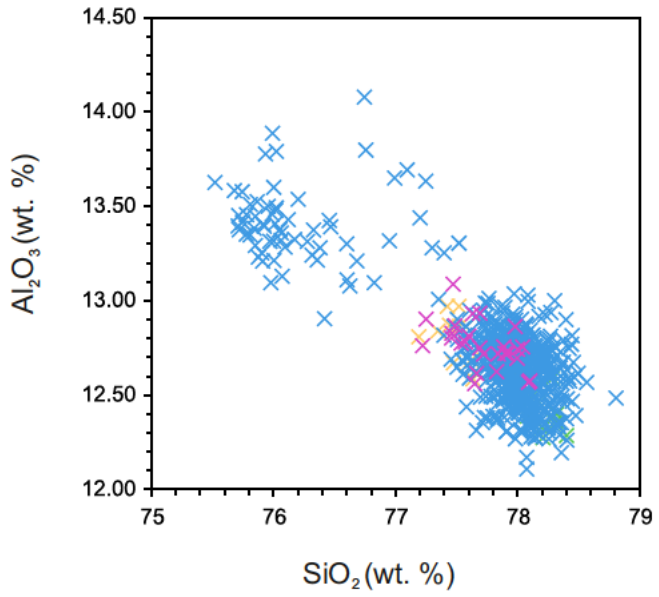
6.2. Atitlán caldera, Guatemala

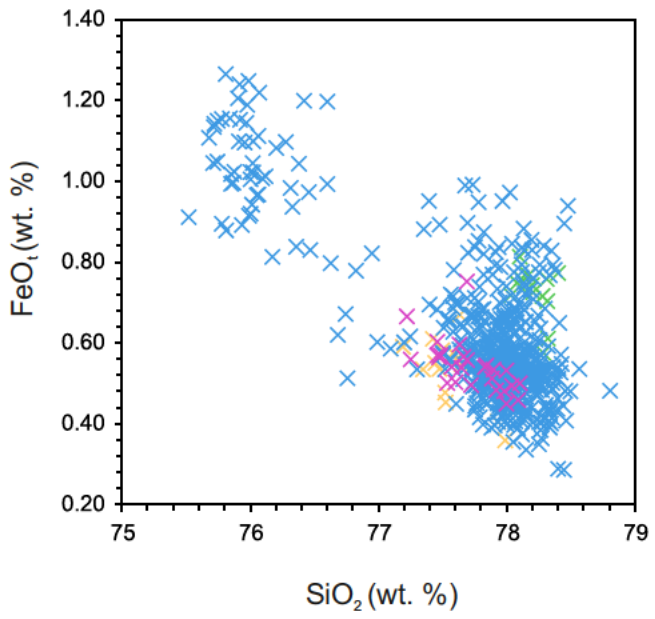
As discussed in section 2 and section 4, Atitlán caldera has been investigated in this study as it is responsible for the third largest eruption known from the Quaternary globally, and one of the largest explosive events in Central America: the Los Chocoyos (LCY) eruption, dated at 75 ± 2 ka (e.g., Drexler et al., 1980; Newhall, 1987; Rose et al., 1987; Cisneros de León et al., 2021; Paine et al., 2021). Kutterolf et al. (2016) estimate the fall deposit from the LCY to have a volume of 1220 km^3 (510 km^3 DRE) and to be between 6 and 9 cm at Lake Chalco and Mexico City, also noting a radial ash dispersal pattern (see Table 2). Atitlán has also had several other explosive eruptions including the large L-Fall (c.191 ka), W-Fall (158 ± 3 ka) and the I-Fall (>40 ka), and other explosive eruptions producing interspersed and more localised deposits, such as the F-Fall and D-Fall that lie stratigraphically between the I-Fall and LCY (Kutterolf et al., 2016; Cisneros de León et al., 2021).

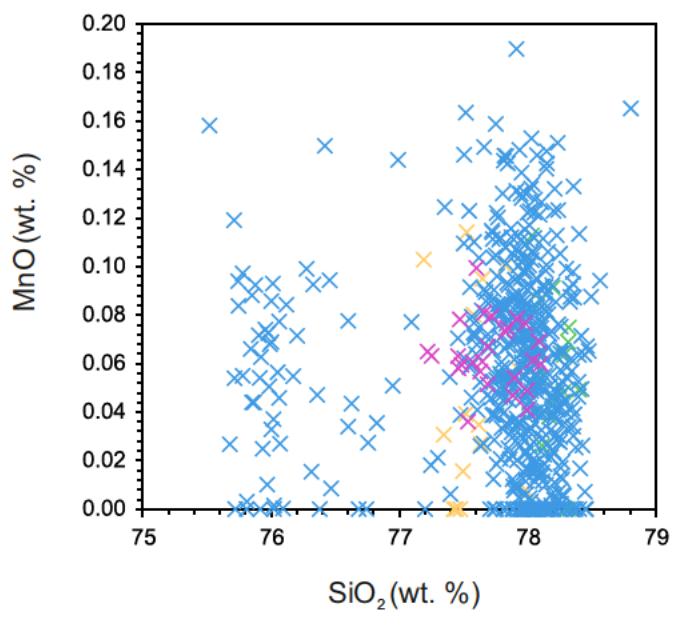
Using proximal data from the LCY, I-Fall and W-Fall eruption units, reported in Cisneros de León et al. (2021), a glass geochemical field for Atitlán was defined (see section 4). Within the core, only one eruption with an Atitlán glass geochemical signature has been identified: tephra 75.335. Fig. 25a displays glass data from tephra 75.335 alongside glass data from Cisneros de León et al. (2021). It can be seen that the LCY glass data is fairly widespread with higher and lower K/Ca clusters. The I-fall is fairly geochemically distinct with a clear population best observed in CaO. The W-Fall is more geochemically similar to the LCY data, although it is not

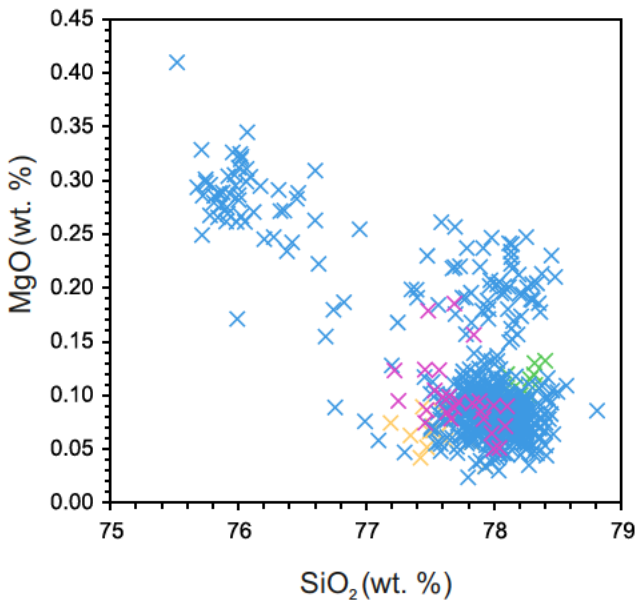
A

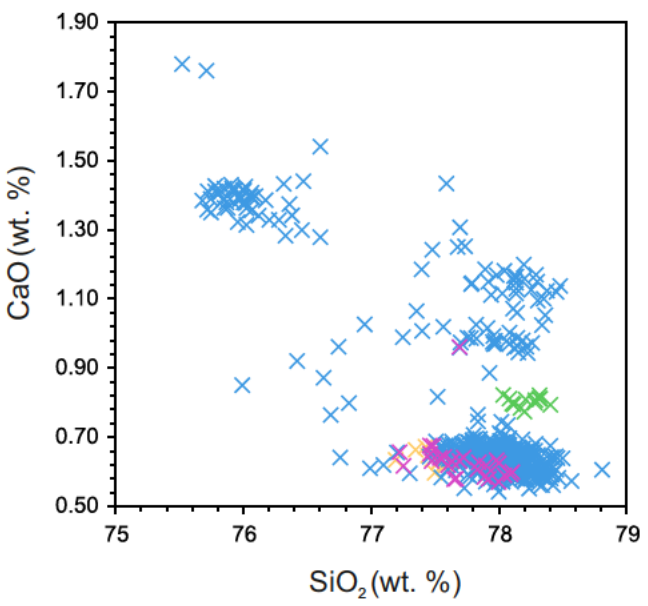


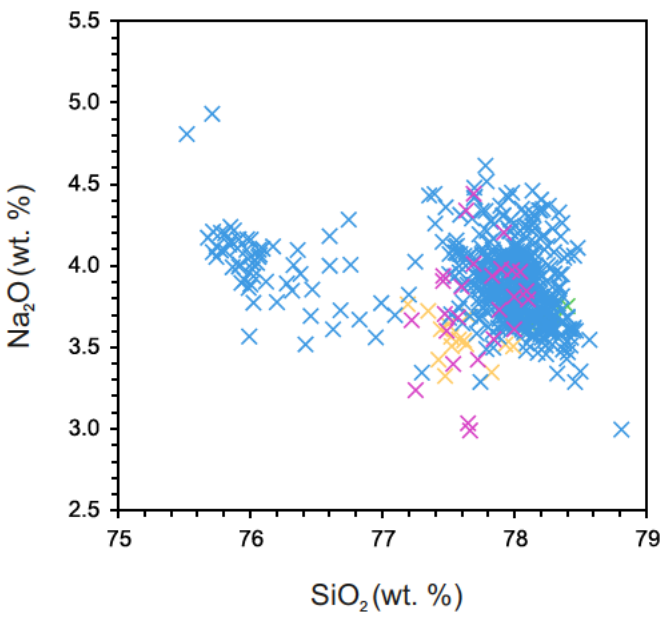


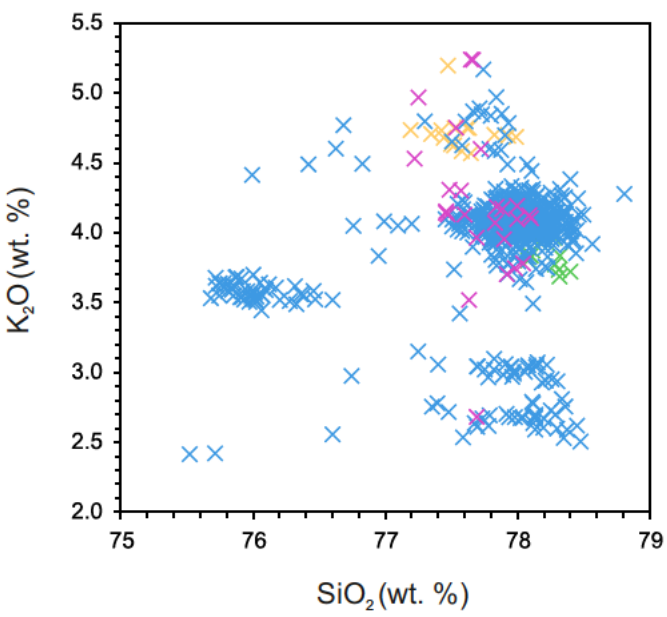






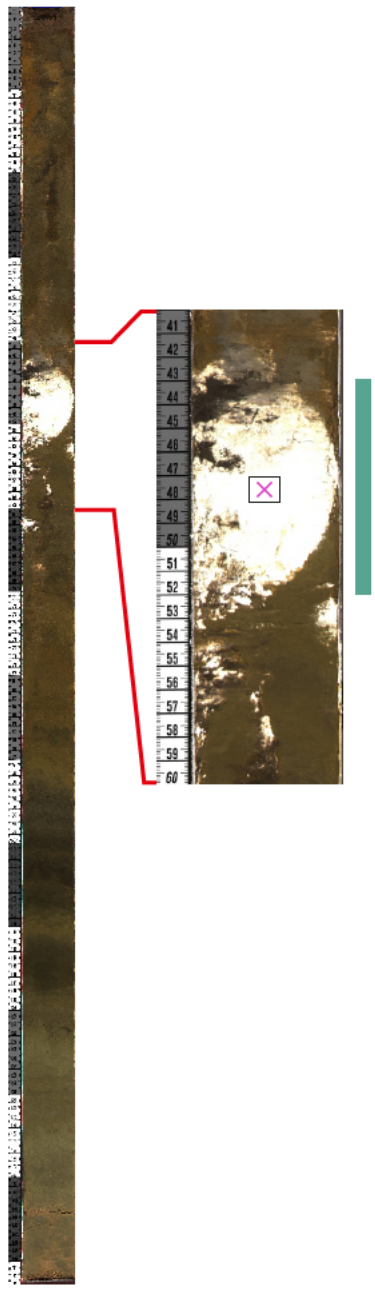






B

Sampled section:



LEGEND

= tephra

= bioturbation

Splice/composite section:

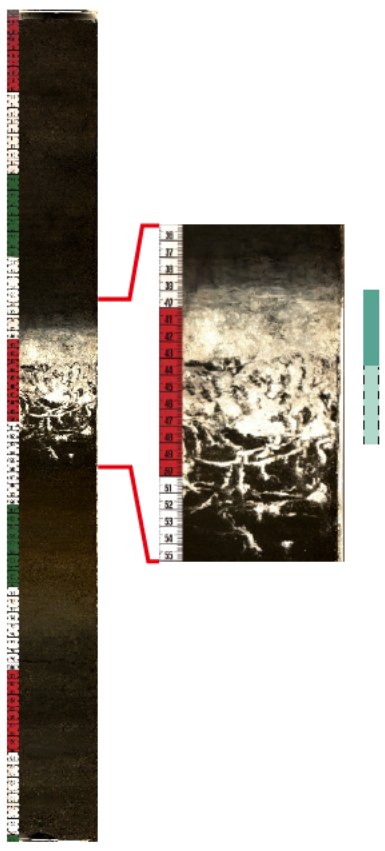


Fig. 25. (a) Selected bivariate plots displaying source data from the Los Chocoyos (LCY) eruption of Atitlán, Guatemala reported in Cisneros de León et al. (2021) overlain by core geochemical data from tephra 75.335. A positive correlation in all elements can be seen between the two datasets. (b) Core section photograph of the LCY eruption, sampled for this study. Below is the splice/composite core section correlated by visual characteristics to this eruption unit.

---

as widespread in all elements. Generally, all W-Fall analyses are towards the higher end of K_2O spectrum seen from LCY analyses. Tephra 75.335 can be seen to overlap with all data in all elements, however, overlaps clearly with LCY data. This correlation is best observed in TiO_2, Al_2O_3, FeO_t, MnO, MgO, CaO and Na_2O bivariate plots. In K_2O the correlation is also robust and it can also be seen that analyses from the core tephra are more spread in K, as source glass data shows for the LCY eruption (Cisneros de León et al., 2021). It is therefore highly likely from the glass geochemistry alone that tephra 75.335 is the LCY eruption layer at Lake Chalco.

Moreover, Fig. 25b displays the core section images of tephra 75.335 from the sampled section, and a correlated and better-preserved section, which is part of the composite core. The sampled tephra deposit can be seen to be c.8 cm thick, although the upper and lower contacts are irregular. The on-splice tephra deposit is measured at 4.25 cm in (minimum) thickness, although bioturbation of the deposit has also occurred, meaning the maximum thickness is c.8 cm. Remarkably, both of these deposits (present in parallel boreholes) are between and/or very close to the estimated deposit thickness of 6 to 9 cm in Kutterolf et al. (2016), based on the extrapolation of isopachs based on correlated marine LCY deposits. In both borehole examples provided in Fig. 25b, the ash is fine to medium in terms of grainsize (maximum of 2 φ) consistent with a distal volcanic source of VEI 8 at c.970 km from source (c.f. the Campanian Ignimbrite, Campi Flegrei, Italy, Engwell et al., 2014).

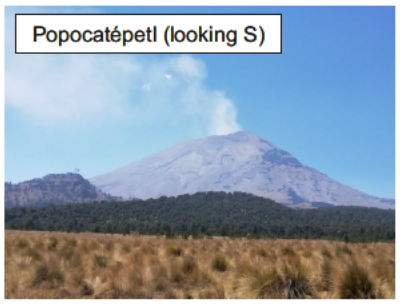
In summary, it can be concluded that the Los Chocoyos (LCY) eruption is present within Lake Chalco at 75.34 m in the composite core, thus providing a well-dated and reliable chronological marker of 75 ± 2 ka at this depth within the succession. Without glass data from the L-Fall (Kutterolf et al., 2015) it is not possible to test correlations between this deposit and Lake Chalco (and given that many tephras in the Chalco core remain unanalysed, we also can't conform the absence of any of the other known Atitlán tephras), although assuming the glass geochemistry is similar to LCY, as seen in the I-Fall and W-Fall (Cisneros de León et al., 2021), it can be concluded that there are no other Atitlán deposits within our geochemically analysed tephras.

7. DISCUSSION

7.1. Frequency of explosive eruptions recorded at Lake Chalco

This study has significantly improved upon our understanding of the glass geochemistry of major source volcanoes around Mexico City permitting the assignments of >70% of analysed tephra layers within Lake Chalco to eruptive sources. Although the number of possible tephra layers within Lake Chalco (see chapter 3) is higher than the number of analysed layers, this study is a comprehensive investigation into the tephrostratigraphy and tephrochronology of the core.

Sources vary consistently throughout the succession, with multiple volcanic sources contributing to tephra layers throughout all of the core. Fig. 26 graphically portrays the distribution from individual volcanic sources throughout the core (summarising the results discussed in section 5.8). With Popocatépetl and Iztaccíhuatl, Nevado de Toluca and La Malinche (ITM, as a combined source), these sources account for c.57% of the sources for











Popocatépetl

Iztaccíhuatl, La Malinche and Nevado de Toluca

Tláloc-Telapón

0
25
50
75
100
125
150
175
200
225
250
275
300

m_c depth

LEGEND

= deposit in the core assigned to the ascribed volcanic source (above)

= deposit in the core assigned to the ascribed volcanic source (above) which is likely reworked, from chemical and physical characteristics

= deposit in the core assigned to the ascribed volcanic source (above) which is likely reworked, from physical characteristics



SCVF



Los Humeros



Atitlán (Guatemala)

?

Ambiguous source volcano (central TMVB signature)

Unknown



Exotic glass chemistry

Exotic sources

Los Chocoyos (LCY) eruption

75 ± 2 ka[a]

Xáltipan ignimbrite eruption

164 ± 4.2 ka[b]

m_c depth

Fig. 26. Chronostratigraphic diagram (using composite core depth) for all analysed core tephras in this study. Deposits are marked in different colours depending upon the likelihood that they are reworked: green = likely primary, yellow = likely reworked from physical observations and characteristics and orange = likely reworked from physical observations and characteristics and glass geochemistry. Correlated eruptions are also marked on the schematic diagram. Caldera scarp locations for Los Humeros and Atitlán are taken from Carrasco-Núñez et al. (2017) and Mooser et al. (1958); Newhall, (1981) and Rose et al. (1987), respectively.

---

analysed deposits in Lake Chalco. Assuming that no bias is introduced through our selection of samples for geochemical analysis, this implies that these volcanoes represent the dominant sources responsible for explosive eruption deposits over Mexico City. The SCVF accounts for c.12% of the analysed deposits, although as the sampling and analytical strategy was to target felsic ascribed sources (see chapter 3) this number is not comparable to the proportion of felsic tephras analysed. Based on visual identification of mafic layers, the SCVF represents closer to 50% of the explosive eruptive record in Lake Chalco, as discussed in chapter 3. With this considered, the SCVF, Popocatépetl, and Iztaccíhuatl, Nevado de Toluca and La Malinche (as a combined source) are responsible for c.≥75% of fall deposits in Lake Chalco, which represent explosive eruptions that have deposited material over Mexico City previously.

Fig. 26 displays temporal patterns for all volcanoes investigated in this study, for example possibly indicating that activity at Popocatépetl has become more dominant over time, when compared with Iztaccíhuatl, Nevado de Toluca and La Malinche (as a combined source), corroborating the suggestion from field exposures between Popocatépetl and Iztaccíhuatl, (chapter 4 and Sunyé-Puchol et al., 2021). However, without all tephras analysed, the longer-term frequency pattern from these volcanic sources are difficult to ascertain. It can also be seen

in Fig. 26 that eruptions containing a central TMVB arc signature but from an ambiguous source are fairly well distributed throughout the core as well. One reason for ambiguity is due to too few analyses per tephra, which is often due to a high microlite contents within the glass, thus resulting in multiple mineral and/or partial mineral analyses. It is likely that many of these eruptions are from localised proximal source volcanoes, e.g., the SCVF, Popocatépetl Iztaccíhuatl, Nevado de Toluca and La Malinche, which appear from their glass-shard characteristics to often have high microlite contents.

Distal caldera sources (e.g., Los Humeros and Atitlán) and Tláloc-Telapón generally display microlite-free glass, and our analysis indicates that these infrequently disperse pyroclastic material over Mexico City (Fig. 26). Coupled with eruptions displaying exotic source chemistries, frequency patterns can be constructed using these more easily identifiable eruptions. It can be seen in Fig. 26 that Tláloc-Telapón, Los Humeros and Atitlán have together dispersed tephra over Mexico City between 75.34 and 136.78 m_c. Similarly, from all analysed tephra layers, no exotic sources were identified in the upper c.89 m of core with a fairly even distribution of deposits below this point. These observations could imply that more exotic sources and distal caldera sources, plus explosive eruptions from Tláloc-Telapón are the least likely to affect Mexico City in the near future, but we again note that not all tephras have been chemically analysed, so we cannot be sure that there aren't younger deposits from these sources. Nevertheless, the most likely source for an explosive eruption dispersing tephra over the Mexico City region, remains the SCVF, Popocatépetl Iztaccíhuatl, Nevado de Toluca or La Malinche.

7.2. Exotic source volcanoes and implications for further tephrostratigraphic investigations

As mentioned above, and in section 5.7, exotic sources (analyses from glasses that display anomalous data from all sources analysed in at least two bivariate plots) comprise c.10% of the tephras analysed from the core in this study. These all occur below 89 m_c thus suggesting these sources have not dispersed tephra over Mexico City in recent years, at least since c.75 ka (see correlated LCY eruption at 75.34m_c in section 6.2), although again we note that it is possible that such eruptions have not been sub-sampled and analysed from the shallower part of the core.

Regardless, the origin of these tephras is interesting. In most cases experiencing high K, lower Na and deviations from main liquid lines of decent in Ca and Mg from all analysed sources. It is possible these eruptions are sourced from a different region of the arc. Typically, higher K and lower Na is associated with increased distance from the arc front (e.g., Michelfelder et al., 2013), perhaps suggesting that these eruptions are from more distal sources towards the N/NE of the core site. More distal volcanic sources, further from the subduction zone also includes Los Humeros, at c.160 km NE of Lake Chalco. The glasses are higher in K than localised proximal sources to Lake Chalco, although the glass chemistries from these exotic sources are generally even more K-rich and Na-poor. It is possible that these are more distal sources than Los Humeros, indicating that the tephrostratographic and tephrochronological investigations of target volcanoes which pose a risk to Mexico City should be widened to include other sources in the TMVB and beyond.

7.3. Revised estimated eruption volumes/magnitude for correlated eruptions

As explored in section 6, robust correlations between core tephras and specific eruptions from two calderas have been made: (1) the Los Chocoyos (LCY) ultra-Plinian event, dated at 75 ± 2 ka from Atitlán (e.g., Cisneros de León et al., 2021), Guatemala at 75.34 m in the composite core and (2) the Xáltipan ignimbrite ultra-Plinian event, dated at 164 ± 4.3 ka (e.g., Cavazos-Álvarez and Carrasco-Núñez, 2020) from Los Humeros, Mexico at 110.31 m in the composite core. While the presence of these eruptions at Lake Chalco is extremely important for establishing an improved chronology for the succession, from a volcanological perspective, current estimations of eruptive volume or magnitudes can be reviewed, and general re-estimations attempted.

Firstly, the LCY eruption (Atitlán) has a calculated tephra volume of 1220 km^3, equivalent to c.510 km^3 DRE (Kutterolf et al., 2016). As discussed in section 6, the on-splice thickness of tephra 110.312 (LCY eruption in the core) is 4.25 cm omitting the thickness of bioturbation. With bioturbation also counted, the total thickness is closer to 8 cm, which is also the thickness in the sub-sampled off-splice core section. It is therefore concluded that the current volume and magnitude estimation of VEI 8 (e.g., Kutterolf et al., 2016) is accurate and requires no attempt at re-estimation, as due to the preservation and core recovery of sections containing the LCY, thicknesses are near identical the predicted values in Kutterolf et al. (2016).

Secondly, the Xáltipan ignimbrite (Los Humeros) is calculated to have a tephra volume of 340 km^3, equivalent to c.290 km^3 DRE and a VEI 7 (Carrasco-Núñez et al., 2018; Cavazos-Álvarez and Carrasco-Núñez, 2020). At Chalco, the Xáltipan ignimbrite is 39.6 cm in thickness. Although no isopach maps and/or estimations of thickness at Mexico City are published, the

Campanian ignimbrite (often referred to as the CI eruption or Y5 ash) can be used as a proxy eruption, as an eruption of comparable size, with a well-established chronology and widespread deposit identified in terrestrial, marine and lacustrine settings (e.g., Pyle et al., 2006; Engwell et al., 2014; Marti et al., 2016; Silleni et al., 2020). Engwell et al. (2014) note an exponential trend between distance from source and thickness for the CI eruption. Remarkably, the downwind thickness at c.160 km from source for the CI eruption deposit is c.30-40 cm, closely mimicking the thickness of the Xáltipan ignimbrite at c.160 km from source in Lake Chalco. Furthermore, Engwell et al. (2014) report grain sizes calculated to be between 2 and 3 φ at c.160 m form source, which again is concordant with the grain size of the Xáltipan ignimbrite at Chalco. These downwind deposits are directly comparable with the Xáltipan ignimbrite eruption (dispersed distally to the SW, Carrasco-Núñez et al., 2018; Cavazos-Álvarez and Carrasco-Núñez, 2020), thus suggesting these eruptions are of direct comparison and extremely similar in terms of magnitude and volume. Silleni et al. (2020) report that previously published magnitudes and volumes for the CI eruption are diverse due to a lack of reproducible methods for its calculation,. However, the same authors provide a best estimate between 7.7 and 7.8 and 181-265 km^3 DRE, respectively. This compares closely with magnitude and volume estimates calculated in Carrasco-Núñez et al. (2018) and Cavazos-Álvarez and Carrasco-Núñez, (2020) for the Xáltipan ignimbrite, at 7.8 and 290 km^3 DRE. We therefore conclude that a re-estimation of the volume and magnitude of the Xáltipan ignimbrite is not necessary, and the deposit at Lake Chalco is broadly as expected when considering the proximal eruption source parameters, calculated at Los Humeros, alongside previously inferred transport directions and comparative data from the Campanian Ignimbrite, of which it is deemed to be similar in magnitude.

7.4. Hazard implications

Volcanic hazards in the Mexico City region, as demonstrated in this study, are not limited to a particular volcanic source. While this study focuses on explosive eruptions and tephra deposits in the Chalco core, it can be seen from chapter 3 that the city is vulnerable to a wide range of volcanic hazards, including fall deposits, lahars and lavas. This study highlights that the major sources of explosive eruptions are from the SCVF, Popocatépetl and Iztaccíhuatl, Nevado de Toluca and La Malinche, grouped here as one source. Although deposits from caldera-forming eruptions, Tláloc-Telapón and exotic sources are present within the core, these are in the minority (approximately 14%) and have not been identified from analysed deposits in the core for at least c.75 ka.

It is also important to note that the frequency of eruptions in the core, with a better chronological constraint, will allow estimations of recurrence times of tephra layers over a long timescale.

8. CONCLUSIONS

1. This study significantly builds upon the glass geochemical fields defined in chapter 4 and Sunyé-Puchol et al. (2021) presenting more eruption sources (e.g., Nevado de Toluca and La Malinche). It also expands upon these fields by using correlated deposits from the Chalco core.
2. Using glass geochemistry, in conjunction with the physical characteristics of deposits, this study corroborates the correlations made between boreholes in chapter 3 and confirms that the volcanic stratigraphy presented in chapter 3 is accurate and reliable at a range of depths throughout the succession.

3. General compositional assignments (e.g., mafic, intermediate and felsic) ascribed to tephra layers in chapter 3 show some consistency when compared with their glass geochemical compositions, although there are outliers from some deposits due to differences between bulk and glass geochemistry. The visual characteristics and colours of these anomalous layers are assumed to be due to the presence and high abundance of crystals within the deposits.
4. Variation in glass chemistry is seen in some finer ash components (often interpreted as co-ignimbritic portions) of a given tephra. These finer ash tops are richer in SiO_2 and poorer in FeO_t although only two tephras contain analyses in these different portions of the deposit.
5. Glasses within volcaniclastic deposits form geochemically distinct compositions consistent with a rapid sedimentation and limited entrainment of glass sourced from other deposits.
6. The core (using glass geochemistry) contains very few reworked tephra deposits, with successive layers in the sequence displaying sufficiently unique chemistries from one another thus suggesting the lake sedimentation is stable with limited erosion and remobilisation of terrestrial fall deposits.
7. Some geochemically bimodal eruptions occur within the core, suggesting the eruptions were supplied by multistage events tapping compositionally distinct magmas.
8. Care should be taken when deciphering the temporal evolution of volcanoes in this study, as not all of the eruption layers have been analysed in this study.
9. Tephra geochemical analyses are distributed throughout the core and a range of volcanoes are responsible for different layers within any given section of core.

10. Popocatépetl, Tláloc-Telapón, Los Humeros, Atitlán, La Primavera and Ceboruco all comprise unique glass geochemical fields, although only Popocatépetl, Tláloc-Telapón, Los Humeros and Atitlán are present in Lake Chalco, based on analysed deposits in this study. The latter three volcanoes generally erupt microlite-free glasses, and Popocatépetl glass generally contains a high abundance of microlites.
11. Iztaccíhuatl, Nevado de Toluca and La Malinche are grouped based on their glass geochemistry due to overlapping data in all major elements. Deposits from all of these sources contain microlite-rich and microlite-poor glass and various glass-shard morphologies, so they are not limited to or diagnostic of a particular volcanic source.
12. Out of a total of 137 analysed tephra layers within Lake Chalco, 35 are assigned to Popocatépetl; 43 to either Iztaccíhuatl, Nevado de Toluca or La Malinche; 1 to Tláloc-Telapón; 17 to the SCVF; 3 to Los Humeros and 1 to Atitlán. A total of 23 layers have an ambiguous source (with a central TMVB arc signature) and 14 are from sources displaying exotic glass chemistries.
13. The SCVF has a unique evolution trend in its glass chemistry when compared with Popocatépetl. Core analyses also corroborate that a separate evolution rend from Popocatépetl occurs with other sources, which includes, but it not exclusive to Iztaccíhuatl, as noted in chapter 4 and Sunyé-Puchol et al. (2021). Other glass displaying this evolutionary trend include deposits from Nevado de Toluca and La Malinche.
14. Popocatépetl shows signs of having a denser frequency of eruptions with time, and the sparser (older) deposits from this volcano are slightly richer in SiO_2 (by up to c.5 wt.%) relative to younger deposits. More tephra analyses from within the core are needed to confirm this.

15. The Los Chocoyos (LCY) eruption from Atitlán caldera Guatemala is present within Lake Chalco. It is found at 75.34 m in the composite core, and is up to 8 cm in thickness, with a grain size of up to 2 φ.
16. The Xáltipan ignimbrite from Los Humeros caldera, Mexico is present within Lake Chalco. It is found at 110.31 m in the composite core, and is 39.6 cm in thickness, with a grain size of up to 2 φ.
17. The volumes of the Los Chocoyos and Xáltipan ignimbrite eruptions are not re-estimated due to their discovery within the core, because their thickness in the core corroborates eruptive volumes and magnitudes in the published literature. This study highlights the very similar magnitude between the Xáltipan ignimbrite and the Campanian Ignimbrite eruption from Camp Flegrei, Italy.
18. Exotic sources are likely to be sourced from greater distances from the arc front due to higher K and lower Na (e.g., Michelfelder et al., 2013). Future studies on volcanoes located further from the arc front should be carefully considered as to whether they are hazardous to Mexico City.
19. This study highlights that Mexico City, and its c.25 million inhabitants are vulnerable to explosive volcanic hazards from a range of sources. When considering future work on volcanic hazards to Mexico City, the SCVF, Popocatépetl, Iztaccíhuatl, Nevado de Toluca and La Malinche should be the focus of scientific efforts, although distal volcanoes should not be omitted from hazard assessments and preparedness planning.

CHAPTER 6

IMPROVING UPON THE CHRONOLOGY OF THE SUCCESSION AT LAKE CHALCO: AN $^{40}Ar/^{39}Ar$ GEOCHRONOLOGICAL APPROACH BY THE DATING OF VOLCANIC DEPOSITS IN THE MEXIDRILL CORE

"Please excuse the crudity of this model. I didn't have time to build it to scale"

Dr. Emmett Brown, Back to the Future Part I

COVID-19 Disruption Statement:

This chapter unfortunately does not present any new data due to laboratory delays at the Scottish Universities Environment Research Centre (SUERC).

Samples for this study were selected and sampled in 2018 with preparation taking place shortly after and submission to SUERC in early 2019. They have been sent to the United States three times for irradiation but unfortunately the laboratory has failed to analyse material in the required timeframe after irradiation.

This chapter therefore presents the samples submitted for dating and the methodology I have undertaken.

1. INTRODUCTION

During the investigation of any geological dataset, it is important to understand its stratigraphic context. This often includes the physical characteristics of strata or deposits, any structural features (e.g., processes that may have offset the law of superposition) and the understanding of what is a primary deposit compared with what is remobilised or reworked material. Geochronology, relative or absolute (the process of obtaining quantifiable age data from earth materials), is crucial to this stratigraphic context, allowing geological data to be considered in time as well as space.

Chapter 3 presents a detailed volcanic stratigraphy for the succession recovered from Lake Chalco and chapter 5 investigates the glass geochemistry of 137 tephra layers identified in the core. In chapter 5 is it noted that sub-samples of volcanic rocks and deposits were extracted from the core for $^{40}Ar/^{39}Ar$ dating, to improve upon the chronology of the core. This approach was also undertaken on proximal exposures of coarse-grained deposits collected during fieldwork, with those new $^{40}Ar/^{39}Ar$ dates presented in chapter 4 and Sunyé-Puchol et al. (2021).

As outlined in the statement provided alongside this chapter, this thesis does not contain new $^{40}Ar/^{39}Ar$ ages from deposits in the core, due to significant laboratory delays at the Scottish Universities Environment Research Centre (SUERC) where analyses are to be undertaken. This chapter therefore does, however, outline the methodologies and stratigraphic context of samples prepared and submitted for analysis in early 2019.

1.1. $^{40}Ar/^{39}Ar$ Dating

$^{40}Ar/^{39}Ar$ dating is a radiometric dating method using the ratio of naturally occurring radiogenic argon, ^{40}Ar, to the isotopic tracer, ^{39}Ar (e.g., Lanphere and Darlymple, 2000; Jourdan and Renne, 2007). ^{40}Ar is generated by the decay of its parent nuclide, ^{40}K, within a mineral (Aldrich and Nier, 1948) and ^{39}Ar is formed by the irradiation of the mineral within a fast-neutron reactor (a nuclear reactor containing mostly neutrons with high kinetic energies (c.5 MeV, Alameri and Alkaabi, 2020), converting ^{39}K to ^{39}Ar by its interaction with fast neutrons (e.g., McDougall and Harrison, 1999).

Following irradiation, the crystals are degassed in a mass spectrometer, where argon is released. Generally, the higher the abundance of ^{40}Ar, the older the sample (e.g., McDougall and Harrison, 1999). Age equations can then be used to calculate the age of the sample, factoring in parameters in the irradiation process (including fast neutron bombardment) and the radioactive decay constant of ^{40}K.

$^{40}Ar/^{39}Ar$ dating is typically reliable for material older than c.10 ka (Bradley, 2015), although reliable ages as young as c.0.5 ka have been achieved (Preece et al., 2018). As the technique is possible from both mineral and glass phases, it is a popular methodology for the dating of volcanic material (e.g., Chambers and Fitton, 2004; McGarvie, 2009; Carey et al., 2020). It is generally considered to be more accurate and reliable than K-Ar dating, which the $^{40}Ar/^{39}Ar$ utilises and builds upon (e.g., McDougall and Harrison, 1999).

Resultantly, higher K material is considered to yield better results than lower K samples. Therefore, when dating feldspars, sanidines are considered to yield more accurate ages than plagioclase (e.g., chapter 4, Sunyé-Puchol et al., (2021)). Additionally, crystals free of melt

inclusions are desired for the best ages, as samples containing melt and fluid inclusions may contain excess argon (Kelley, 2002).

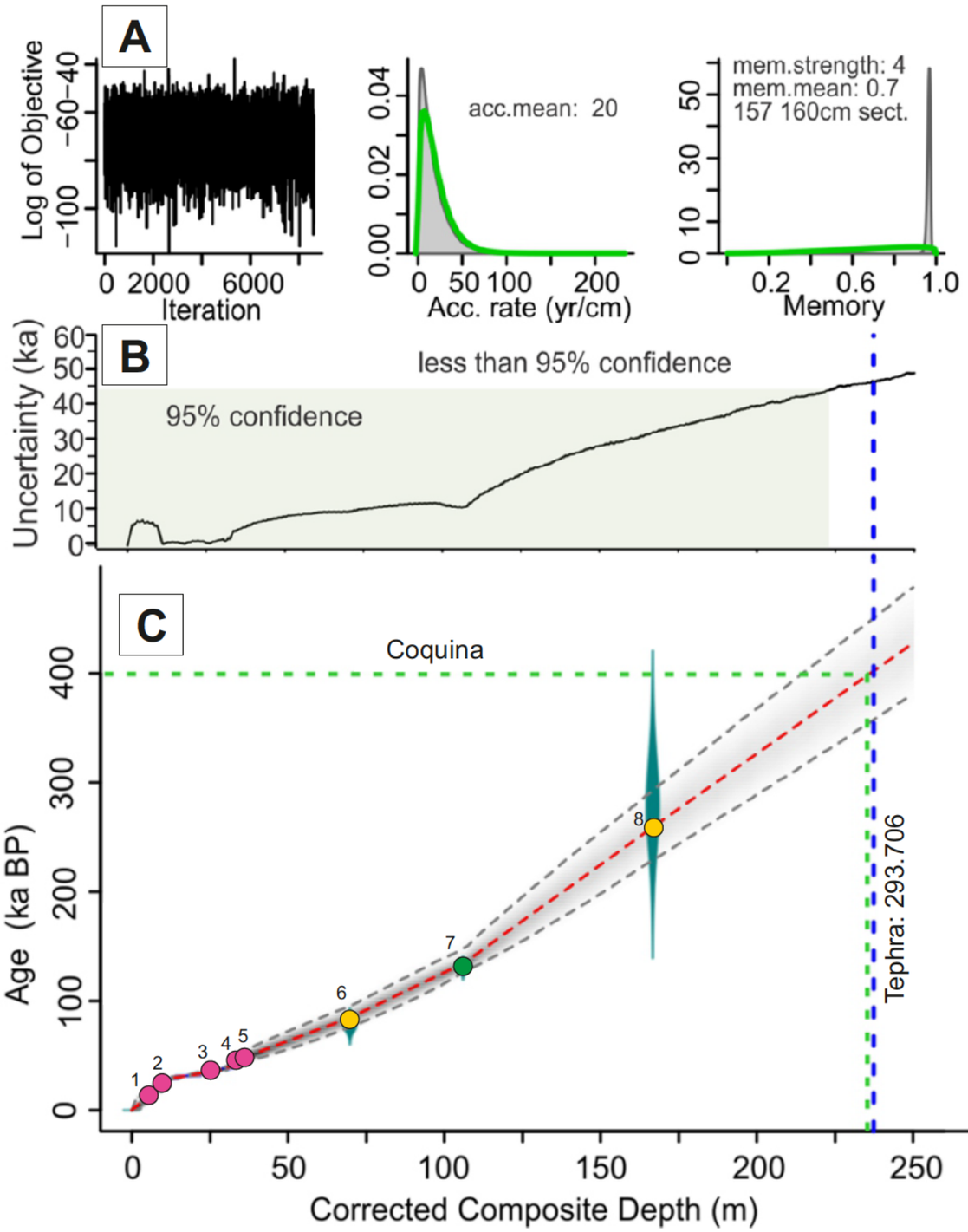
1.2. Current age-depth model for Lake Chalco

The current-age depth model at Lake Chalco (Martínez-Abarca et al., 2021) is derived from radiocarbon (^{14}C) ages from pollen and ostracods and $^{234}U/^{230}Th$ ages from zircons and lacustrine carbonates (Lisiecki and Raymo, 2005; Herrera-Hernandez, 2011; Ortega-Guerrero et al., 2017; Avendaño-Villeda et al., 2018; Martínez-Abarca et al., 2021). This age-depth model uses Bayesian statistics and has a high level of uncertainty in deeper parts of the core, due to the majority of dates being from ^{14}C methods, which are limited to ages less than c.50 ka (e.g., Brook et al., 2020). This age model is presented in Fig. 1 with the relative positions of dated material marked.

2. IMPROVING THE CHRONOLOGY OF LAKE CHALCO

As mentioned above (section 1.1), $^{40}Ar/^{39}Ar$ is an accurate and reliable technique that surpasses the upper timescales of other dating procedures such as ^{14}C or dendrochronology. It also allows the direct dating of volcanic material (e.g., tephra and/or lava) within sedimentary successions (e.g., Cullen et al., 2014; Mark et al., 2014; Albert et al., 2019).

Here, 12 dates were submitted for $^{40}Ar/^{39}Ar$ geochronological analysis: 8 plagioclase samples from tephras within the lacustrine section of core (Stage III, chapter 3); 1 plagioclase sample from pumice clasts and 1 from a lava clast in mixed volcaniclastic deposits deeper in the core (Stage II, chapter 3), and 2 lava samples in the deepest, lava-dominated sections of core (Stage I, chapter 3). All the lava-derived material (a total of 3 samples) was submitted for analysis



Ages from Lake Chalco used in the age-depth model (Martínez-Abarca et al., 2021):

- ^{14}C ages
- ^{234}U/^{230}Th ages
- MIS 6-5 transition

Ages (Martínez-Abarca et al., 2021):

- 1 = 24.6 ka (uncal.)
- 2 = 27.65 ka (uncal.)
- 3 = 31.74 ka (uncal.)
- 4 = 34.01 ka (uncal.)
- 5 = 40.46 ka (uncal.)
- 6 = 76.6 ka
- 7 = 130 ka
- 8 = 280 ka

Fig. 1. Current existing Bayesian age-depth model for Lake Chalco, comprising ^{14}C from pollen and ostracod samples and $^{234}U/^{230}Th$ ages zircons and lacustrine sediments. The model also includes a date obtained from an interpreted transition between marine isotope stages (MIS) 6 and 5. (a) Parameters obtained during model development. (b) Uncertainty along the sequence; 95% confidence range is marked in a green square. (c) Age-depth model; depth data corresponds to the corrected composite depth (m_c) which considers volcanic lithologies as geologically deposited instantaneous event layers. Stratigraphic markers are displayed: e.g., Coquina (dashed green line) and Tephra 293.706 (dashed blue line) Modified from Martínez-Abarca et al. (2021).

---

based on multigrain aliquot groundmass dating. The remaining 9 samples pumice- or tephra-derived samples were submitted for multigrain aliquot plagioclase crystal dating. Only plagioclase dating was attempted due to lack of higher-K feldspars (sanidines) within the samples. The relative positions of all samples submitted $^{40}Ar/^{39}Ar$ dating within the composite core is provided in Fig. 2, along with core section photographs of the physical characteristics of the deposits and a phase diagram of a subset of mineral analyses (filtered out of data provided in chapter 5) to demonstrate that all feldspars from the mineral separates are of plagioclase compositions. Additionally, depths and descriptions of the samples submitted for $^{40}Ar/^{39}Ar$ dating are provided in Table 1.

Multigrain aliquots were selected (rather than single crystal dating) in order to reduce the effects of anomalous data from the analysis of xenocrysts. The preparation methodology below (section 3) outlines the steps taken to "high grade" the samples as much as possible and reduce the probability of xenocrystic material within multigrain aliquots of plagioclase phenocrysts.

Table 1. Summary of the samples submitted for $^{40}Ar/^{39}Ar$ dating in this study, including their sample name, basalt composite core depth, lithology, maximum grain size, thickness, and description.

Sample Name	Basal core depth (m_c)	Lithology/deposit type (core stage)	Maximum grain size (φ)	Best preserved thickness (cm)	Brief description
AR17	115.78	Felsic tephra (Stage III)	-1	9	Yellow/white fine lapilli fall with grey fine to medium ash in lower 2.5 cm. Tephra is massive. Lithics are rare.
AR11	169.15	Felsic tephra (Stage III)	-2	103.5	White pumice lapilli fall. Deposit is massive. Pumices are vesicular and lithics are black, accounting for c.10 % of the deposit.
AR8	181.72	Felsic tephra (Stage III)	-1	40	Mostly light grey in colour. Structured deposit with variations in grain sizes. Deposit is generally normally graded.
AR6	231.05	Felsic tephra (Stage III)	-1	17.2	Ash to fine lapilli. Deposit is massive. The upper 7.3. cm is finer and possibly co-ignimbritic ash. Some laminations within the ash.
AR4	275.48	Felsic tephra (Stage III)	-1	14.8	Yellow to white fine to medium lapilli fall. Pumice is sub0angualr to sub-rounded. Red and black lithics comprise c.10-20 % of the deposit.
AR1	288.27	Felsic tephra (Stage III)	-4	21	Reverse graded (fine to coarse lapilli) pumice lapilli fall deposit. Very few lithics (<10 %). No laminations or sharp changes in grain size.
AR2	290.30	Felsic tephra (Stage III)	-3	41.25	Reverse graded (fine to medium/coarse lapilli). Pumice lapilli fall deposit with abundant black lithics (c.20 %).
AR15	293.71	Felsic tephra (Stage III)	-2	67	Pumice lapilli fall deposit with laminations in the lower 20 cm. Fall is generally massive. Sharp contact with fine ash in upper c.6 cm, interpreted to be a co-ignimbritic ash.
AR*1	381.37	Pumice horizon (Stage II)	-3	33.5	Medium to coarse pumice lapilli-dominated deposit. Pumices are sub-rounded. Some matrix between pyroclasts. Unsure if a fall deposit or a pumice lens in volcaniclastic deposits.
ARL3	402.84	Lava clast (Stage II)	N/A	N/A	Lava clast sample. Fine aphanitic black lava. Dense groundmass with very few vesicles.
ARL1	461.31	Lava (Stage I)	N/A	605 (entire lava)	Aphanitic black lava with small (c.4 mm) vesicles throughout.
ARL2	480.24	Lava (Stage I)	N/A	1,158 (entire lava)	Aphanitic black lava with small (c.4 mm) vesicles throughout.

3. METHODOLOGY

3.1. Sample selection

Samples were identified and selected by the analysis of core section photographs. As only working halves could be sampled, and given a core diameter of only c.3 cm, only the thickest deposits (≥ 5 cm) were initially targeted in order obtain enough material to take through the preparatory steps (outlined below and summarised in Fig. 3). Crystallinity was also noted during extraction of tephras, with crystal-rich layers expanding the number of deposits from the core that were potentially suitable for dating. In total, 25 samples were taken from pyroclastic deposits and lavas within the core, but after preparation procedures, only 12 samples yielded enough material to be submitted for $^{40}Ar/^{39}Ar$ dating.

Sub-samples were extracted in 2018 at the National Lacustrine Core Facility (LacCore), University of Minnesota, where the MexiDrill core are stored. All samples were from the MexiDrill cores, not being supplemented by earlier coring projects. Parallel holes were sampled if deposits were present in more than one hole, but only where a robust and reliable correlation could be made by visual characteristics alone. Where this was not possible, material from only one borehole was used. Samples were selected as evenly as possible throughout the core, focussing on the lower 200 m of lacustrine-dominated sediments (Stage III, chapter 3), thus to better constrain the areas of the core beyond the radiocarbon dating window and which has the lowest age-resolution based on previously existing age constraints and the current age-depth model (see Martínez-Abarca et al., 2021 and Fig. 1). Samples of lava material (Stage I) from the deepest parts of the whole core sequence were chosen to constrain the full timescale represented within the Chalco core.

A

COMPOSITE CORE

Background sediment types

COMPOSITE DEPTH (m)

STAGE III: LACUSTRINE-DOMINATED SECTION

STAGE II: PRE-LACUSTRINE SECTION

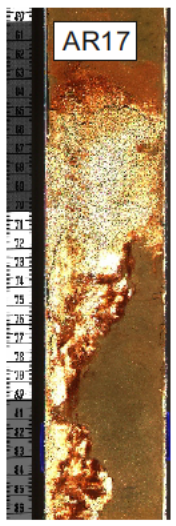
STAGE I: LAVA-DOMINATED SECTION

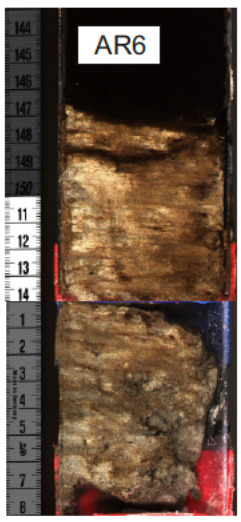
B

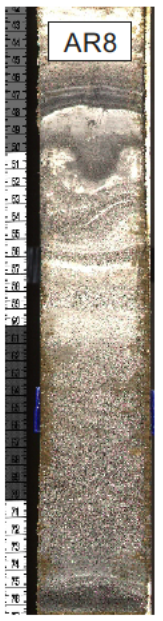
$^{40}Ar/^{39}Ar$ samples submitted for analysis:

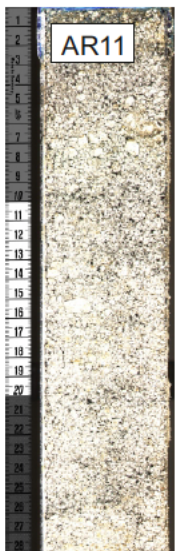
1 = AR17 (tephra)
2 = AR11 (tephra)
3 = AR8 (tephra)
4 = AR6 (tephra)
5 = AR4 (tephra)
6 = AR1 (tephra)
7 = AR2 (tephra)
8 = AR15 (tephra)
9 = AR*1 (pumice)
10 = ARL3 (lava clast)
11 = ARL1 (lava)
12 = ARL2 (lava)

= Plagioclase aliquots
= Groundmass aliquots
= Los Chocoyos (75 +/- 2 ka)
= Xaltipan ignimbrite (164 +/- 4.2 ka)



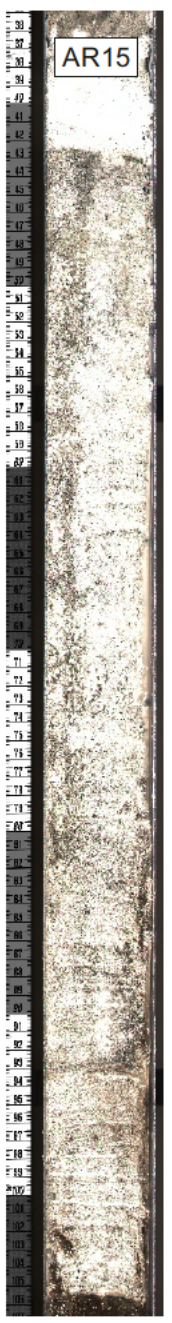


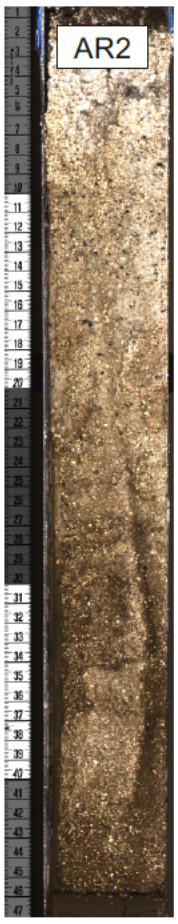


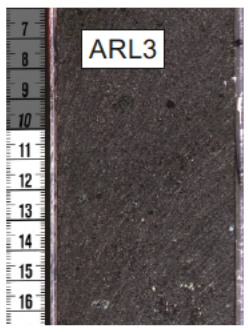


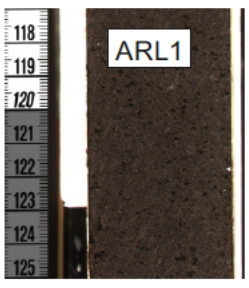


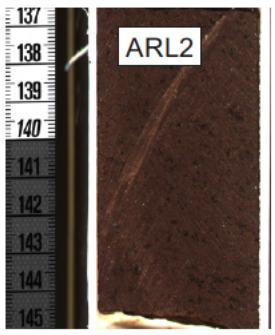


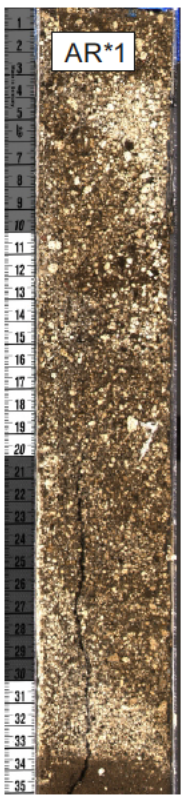




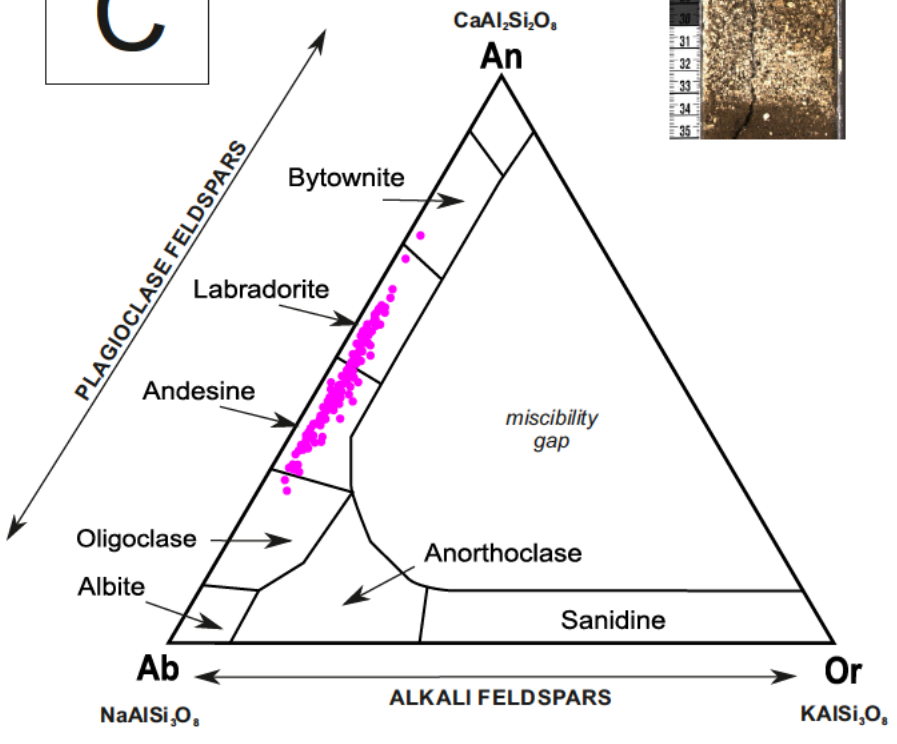








C



Background sediment types (minus tephras)
(Valero-Garcés et al., 2021)

= silty clay
= organic rich
= diatomaceous seds.
= calcareous seds.
= coquina

Volcanic deposits (minus tephras)
(this study)

= volcaniclastics
= lava
= scoriaceous

Fig. 2. (a) Schematic of the stratigraphic position of all samples submitted for $^{40}Ar/^{39}Ar$ dating in this study. Volcanic deposits (minus tephra) and major sediment types as interpreted by Valero-Garcés et al. (2021) are also noted, as well as correlated eruption deposits and their ages in chapter 5. (b) Core section images of all volcanic layers submitted for $^{40}Ar/^{39}Ar$ dating in this study. (c) Ternary phase diagram displaying compositional data for feldspars. Data points are comprised of plagioclase analyses rejected from chapter 5 due to being mineral analyses instead of glass. All analyses can be seen to be plagioclase in composition.

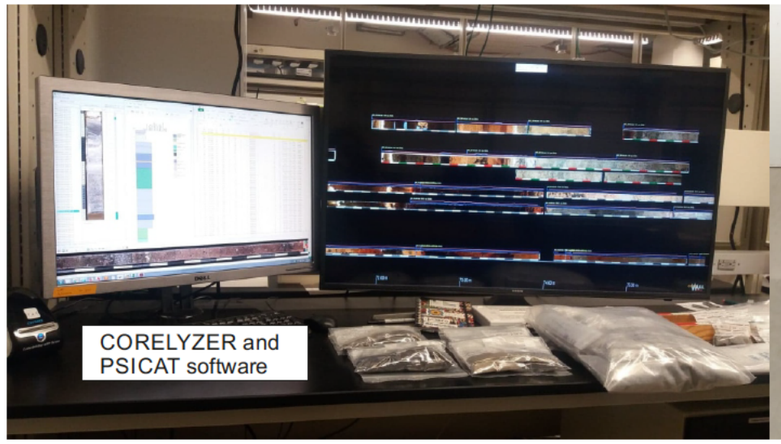
Furthermore, where thick deposits were found in close proximity to one another, these were both sampled, in an attempt to test the accuracy of age information within a portion of core, where the expectation was that ages should be close and in stratigraphic sequence (see Fig. 2).

3.2. Preparation of volcanic units for $^{40}Ar/^{39}Ar$ dating

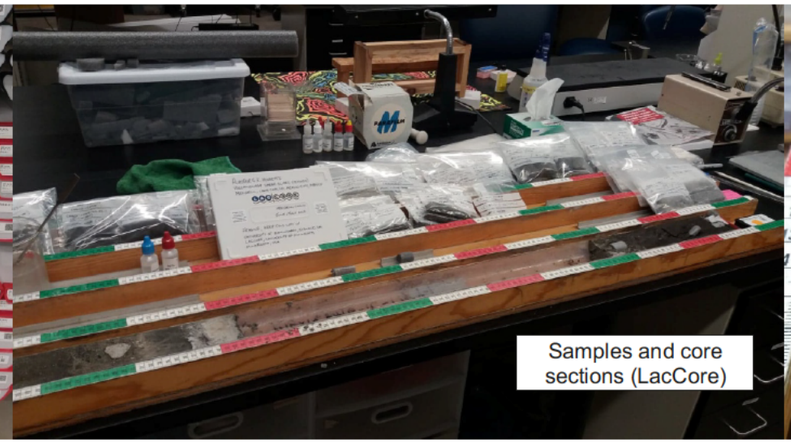
Following the removal of material for analysis, samples were taken to SUERC, where most preparation stages were completed. All samples were prepared separately thus to avoid contamination, and thorough cleaning and washing of equipment was carried out between samples. The methodology used for all plagioclase aliquots is as follows (see also Fig. 3).

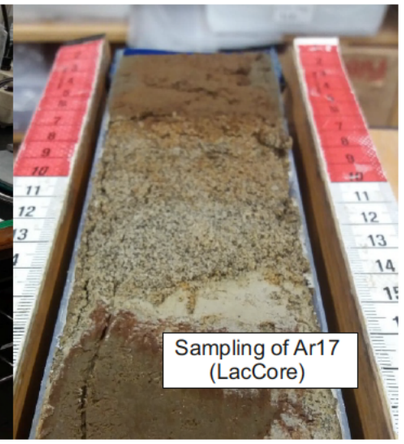
3.2.1. Sieving and drying

Firstly, all samples were cleaned in beakers of deionised (DI) water and placed within an ultrasonic bath, with repeated decantation of material and replacement of DI water at several points over a 24-hour period. The cleaning steps in the ultrasonic baths lasted for 1 hour thus to ensure the effective removal of altered and adhered clay or lacustrine sediment to the samples. Following cleaning, samples were lightly crushed in a pestle and mortar (if pyroclasts were flocculated together or of lapilli size). Samples were wet sieved using DI water at all times, with a focus on capturing 250 – 500 μm and 500 – 1000 μm size fractions. 125 – 250 μm







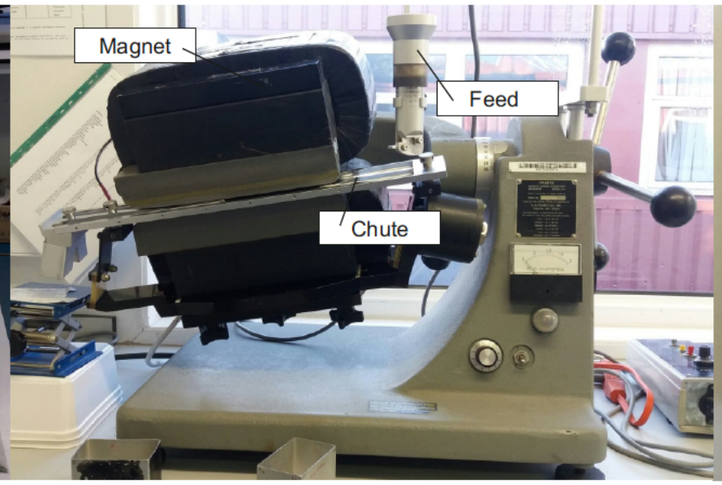


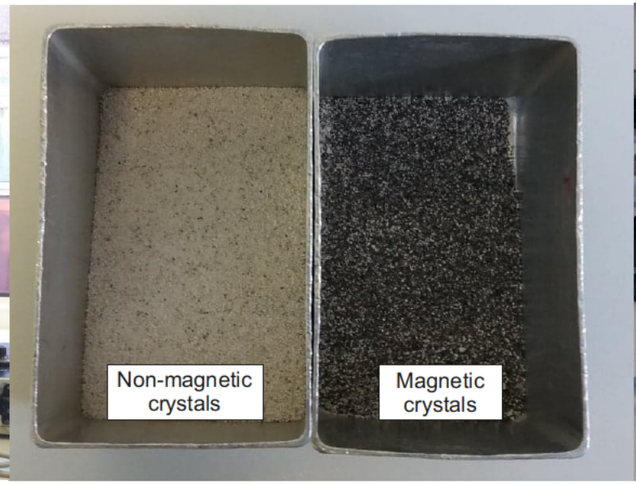
SAMPLE SELECTION AND EXTRACTION

IDENTIFICATION OF TARGET SAMPLES

CORE SECTION SAMPLING









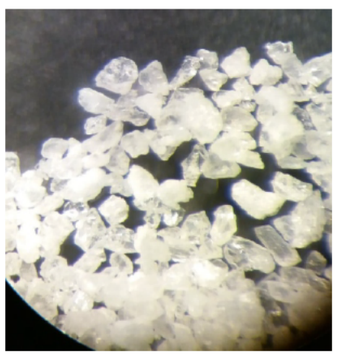
CLEANING/SIEVING

MAGNETIC SEPARATION

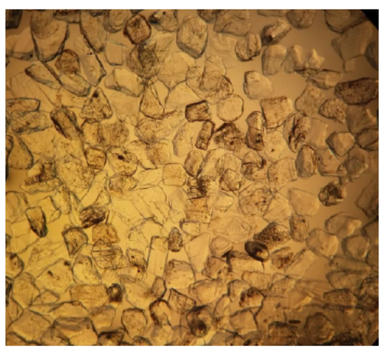
ACID LEACHING

SAMPLE PREPARATION

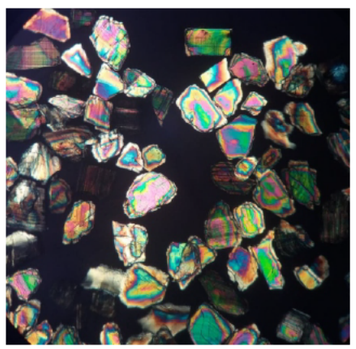




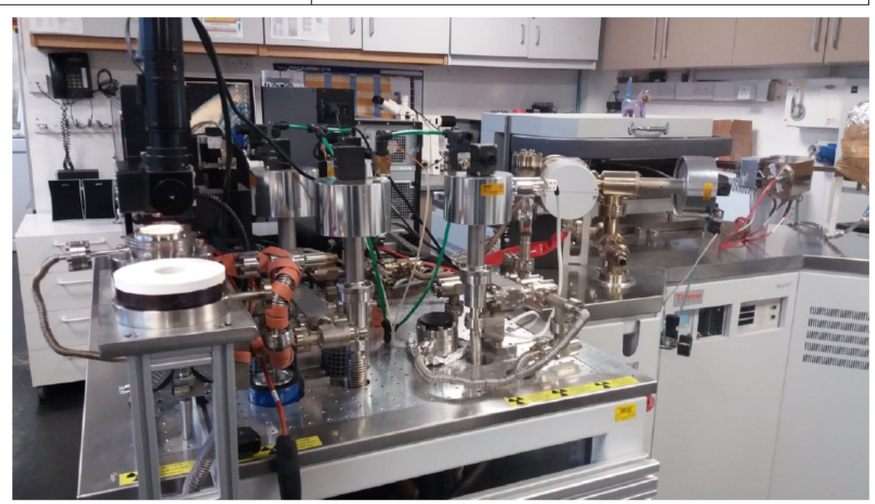
CRYSTAL SEPARATES



OPTICAL PROPERTIES (PPL)



OPTICAL PROPERTIES (XPL)



PICKING/ HIGH GRADING

ANALYSIS

PICKING AND ANALYSIS

Fig. 3. Photographs displaying the major stages involved in the $^{40}Ar/^{39}Ar$ dating of core samples in this study, from sample selection and extraction to picking and analysis.

---

size fractions were also separated for use if little material could be used from the coarser and more desirable size fractions. All finer material was collected in a base tray and kept. Following the sieving of material, sieves and samples were dried in an oven for 24 hours at 80˚C, with a paper towel placed above and below each sieve to ensure there was no contamination from other samples in the oven.

3.2.2. Magnetic separation

Following the cleaning, sieving, and drying stages, samples were loaded into a Frantz Isodynamic Magnetic Barrier (magnetic separator), following thorough cleaning with analytical grade ethanol. Thorough cleaning of all parts occurred between each sample, to avoid any cross contamination. Each size fraction was loaded into the feed component of the instrument with a medium tempo release of grains. As samples travelled down the chute, aided by gravity, a medium level electromagnetic charge was applied, separating the crystals into magnetic and non-magnetic separates. Non-magnetic separates were loaded back into the magnetic separator where a high pass (slower feed and high electromagnetic field) was applied, thus to further filter the grains, removing grains with large melt inclusions or small magnetic crystal components. This step was often repeated multiple times per sample until non-magnetic separates appeared to be clear of magnetic material when observed under a stereoscopic microscope.

3.2.3. Acid leaching

Following magnetic separation, sub-sets of non-magnetic grains were placed into clean plastic beakers for hydrofluoric acid (HF) leaching. This process is to digest the glass, leaving behind only mineral separates. Dilute HF was used, combining 1 part HF acid with 10 parts DI water. Acid digestion was left for 20 minutes per sample before neutralising the acid and cleaning thoroughly with DI water. Samples were checked under a stereoscopic microscope for remainder glass. If glass was visible, the HF leaching process was repeated until the sample could be seen to be clear.

For some samples, following leaching, another pass through the magnetic separator occurred, on a low feed and high magnetic charge.

3.2.4. Picking and high grading

Subsequent steps involved picking and high grading, ie., extracting the best material (e.g., free of melt inclusions) for analysis. Each size fraction was picked under a stereoscopic microscope separately, using tweezers. This was conducted at the University of Birmingham. Picking of separates were to obtain the cleanest, most euhedral plagioclase crystals, and avoiding altered or fractured crystals, which could potentially be xenocrystic and would not provide an accurate eruption age. Over 700 mg of fresh, clean plagioclase crystals of each size separate were picked for each sample. This included 9 separate mineral samples with sufficient material for analysis following all preparation stages, as for many samples, there was too little (<100 mg) or no material remaining. These 9 separates were placed in sample vials for a second round of clove oil picking (see below).

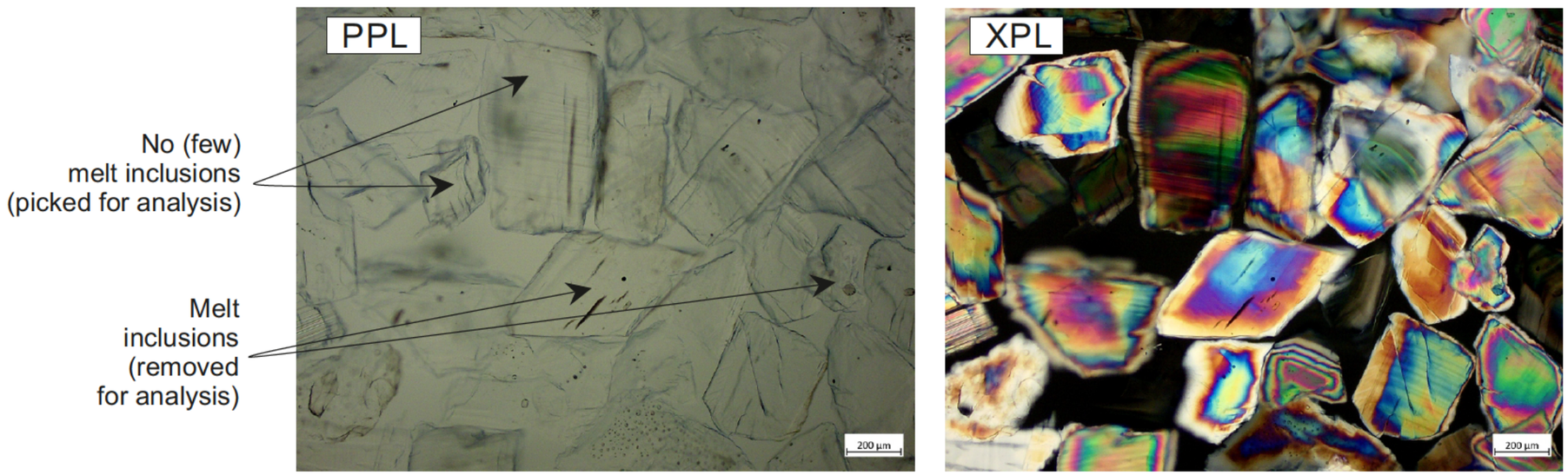
3.2.5. Picking under clove oil

All mineral separates were further high graded by a second picking stage under clove oil (e.g., Sprain et al., 2018). Clove oil has a refractive index (RI) of 1.53 thus resulting in the reflected light of a petrographic microscope highlighting melt inclusions within the sample, otherwise difficult/impossible to see with the naked eye. In order to pick under clove oil, all samples were processed in stages using clean microscope slides with a couple of drops of oil. The best grains, largely free of melt inclusions, were picked using tweezers and placed into a clean glass beaker. Following the picking of up to 400 mg of material, per size fraction, samples were cleaned thoroughly using ethanol. Ethanol cleaning was repeated 3 times and 2 cycles of rinsing with DI followed, with 24 hours of drying in an oven in between each step, again with each beaker covered above and below to avoid any cross-contamination. The petrography of these samples under clove oil is displayed in Fig. 4.

3.3. Groundmass preparation: Lavas

Lava sample preparation included all of the steps outlined above with the exception of HF leaching and picking under clove oil.

Samples of lava from the core were initially cleaned using DI water and scrubbing off adhering sediment with a cleaning brush. Following the drying of the samples, rocks were placed into a clean jaw crusher. Cleaning involved using a vacuum cleaner to remove dust and fragments and cleaning all working parts and areas the sample enters with ethanol. The jaw crusher was set to crush material to the same size fractions as mineral samples, with a focus on 250 – 500 μm and 500 – 1000 μm size fractions. Again, finer material was kept. To ensure fine dust was


No (few)
melt inclusions
(picked for analysis)
Melt
inclusions
(removed
for analysis)
PPL
200 µm
XPL
200 µm

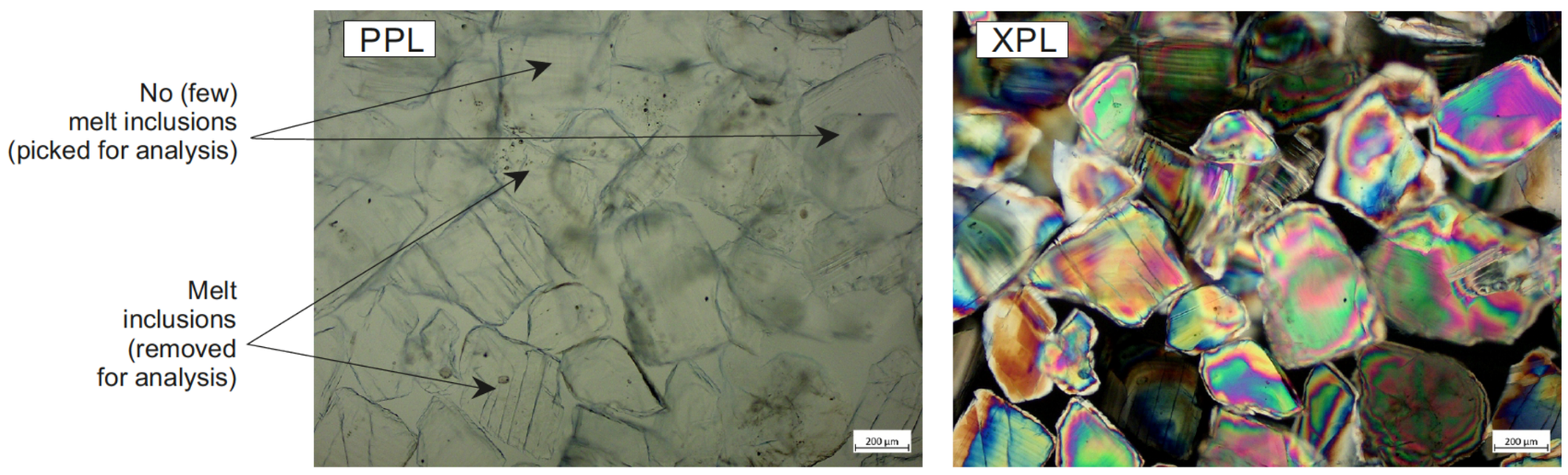

No (few)
melt inclusions
(picked for analysis)
Melt
inclusions
(removed
for analysis)
PPL
200 µm
XPL
200 µm

Fig. 4. Petrographic example images of crystals being picked under clove oil allowing melt inclusions to be seen more clearly. Images are presented in plane polarised light (PPL) and cross polarised light (XPL). Example photos are from sample AR4.

---

not adhering to the crushed separates, samples were cleaning using DI water in an ultrasonic bath, twice, each lasting 1 hour.

Picking of the material included pulling out representative samples of the groundmass and avoiding loose crystals freed by the crushing process. Additionally, altered groundmass grains were avoided and only fresh grains were selected. As with crystal separates, c. 400 mg of material from each size fraction was picked for analysis.

4. ANALYSIS

Samples were sent to SUERC for analysis in early 2019. The samples have been sent for irradiation at Oregon State University (OSU) on three separate occasions. Three irradiation steps have occurred due to the expiry of the samples following lack of analysis in the required timeframe (after which there is undetectable ^{37}Ar due to the surpassing of its half-life). Analysis is currently underway at the NEIF Argon Isotope Laboratory, SUERC. The results are not presented in this study due to the ongoing analysis and data filtering by colleagues at SUERC.

CHAPTER 7

CONCLUSIONS AND AVENUES FOR FUTURE RESEARCH

"If you need me, I'll be back at my lab, dismantling this thing"

Dr. Emmett Brown, Back to the Future Part III

This chapter summarises the main findings of this thesis and offers suggestions for future research

1. SYNTHESIS AND CONCLSUIONS

This thesis improves upon the explosive eruption record of the Mexico City region, providing insights that can be used to better understand volcanic hazards from diverse eruptions in a region that is home to one of the world's largest populations. The results presented in this study greatly extend the timescale of the record of volcanic activity that has impacted Mexico City in the past, offering unique insight into the frequency, magnitude and glass geochemistry of eruptions, significantly building upon current eruptive and geochemical knowledge in the region.

In chapter 3, the first detailed and comprehensive volcanic stratigraphy of Lake Chalco is presented. Through detailed logging of c.1,500 m of core (across multiple boreholes) correlations between volcanic deposits were made, and a vast quantity of metadata was collected from a volcanological perspective with the aim to assesses the volcanic record in terms of volcanic output of an arc segment over a long timescale. The core from Lake Chalco contains a unique record from a continental setting within a volcanic belt, allowing a novel approach to be undertaken to decipher the eruptive record.

In chapter 4, focused fieldwork at the Sierra Nevada Volcanic Range extends our knowledge of explosive volcanism from Popocatépetl, Iztaccíhuatl, and Tláloc-Telapón volcanoes. New $^{40}Ar/^{39}Ar$ dates improve the chronology of these volcanoes. Additionally, glass geochemical analyses of pyroclastic deposits are also presented, providing the most comprehensive glass geochemical record for the Sierra Nevada Volcanic Range.

In chapter 5, glass geochemistry is presented for a substantial number (137) of tephra layers within the Chalco core, providing the most comprehensive tephrochronological investigation of the lake, attributing 100 layers to their volcanic sources. Additionally, well documented and dated caldera-forming eruptions from Los Humeros, Mexico and Atitlán, Guatemala, are discovered within the core, providing two isochrons which can be used to improve the chronology of the core.

Chapter 6, unfortunately due to COVID-19 related external laboratory disruptions, did not present any new chronological data for the core. However, 12 samples submitted for $^{40}Ar/^{39}Ar$ dating will allow the most detailed and comprehensive age-depth model to be constructed for Lake Chalco. Data will be useful for all disciplines involved in the MexiDrill project, from palaeoclimatology through to our volcanological assessment.

A synthesis of the major findings of this thesis are outlined below:

1. The Chalco core is comprised of volcanic material (59.81%), including tephra layers (3.91%), other volcaniclastic (e.g. laharic) deposits (39.98%), lava (15.51%) and scoria/monogenetic cone flank deposits (0.41%). This is the first detailed volcanic study into the succession of the MexiDrill cores.
2. The core is sub-divided into three main stages:
    i. Lava-dominated section (448.86 - 553.93 m_c)
    ii. Pre-Lacustrine deposits (293.71 – 448.86 m_c)
    iii. Lacustrine-dominated deposits (0 – 293.71 m_c)

Stage I includes predominantly basaltic andesite and andesite lavas with minor deposits of volcaniclastics and scoria. Stage II is comprised of volcaniclastic material of varying grain sizes, interpreted to be representative of fluctuations in sediment:water ratios within the mass flows that transported the deposited material (i.e., coarser deposits transported by debris flow processes and finer deposits by dilute to hyperconcentrated streamflow processes). With stratigraphic height, these deposits generally become finer-grained, interpreted to be representative of reworking of a coarser primary deposit, likely sourced from a mass wasting event from a nearby volcano. Stage III is comprised of mostly lacustrine sediments with intercalated tephra layers from multiple volcanic sources. In the lower half of Stage III deposits, other volcaniclastic layers are also present, representing periods of laharic input into the lake.

3. The Chalco core has been approached using a detailed, novel and reproducible methodology which can be replicated at any core or sedimentary succession containing volcanic material. This methodology begins by detailed stratigraphic logging of the sequence and by the careful correlation of volcanic layers using their physical characteristics, supplemented by quantitative data, such as magnetic susceptibility. These geological tie points allow volcanic deposits that occur between boreholes to also be correlated, and layers which are only preserved in one or some of the boreholes to also be included in the final volcanic stratigraphy. This methodology mimics that used in the production of the composite stratigraphy (splice), but also allows for volcanic layers that are missing from the composite sequence to be given a stratigraphic position, called a ghost horizon, within the splice. While ghost layers are collapsed to zero thickness on-splice, so

as not to add sediment to a finite overall thickness, deposit characteristics are documented, providing context for volcanological assessment. This approach is necessary for cores that contain drilling artefacts, are poorly recovered in whole or in part, or have poor preservation, in order to reconstruct accurate volcanic records.

4. The maximum number of potential tephra layers identified in Lake Chalco is 603, with a minimum number (representing those with the greatest level of certainty in their identification) of 450. The difference in values comes from the methodology applied, which uses a confidence scale for determining if a deposit is volcanic in origin, and whether such layers are primary deposits or are reworked (based on visual analysis of photographs). The minimum number therefore excludes all layers which are ambiguous as to whether they are primary or volcanic in origin.
5. The colour of visible tephra is used at the description stage to infer its volcanic composition and general SiO_2 content. Mafic layers are black or dark grey in colour and are inferred to be sourced from local monogenetic volcanoes of the Sierra Chichinautzin Volcanic Field. Felsic tephras are generally white to light grey in colour and are inferred to be sourced from polygenetic or caldera sources. Intermediate tephras are generally brown and/or difficult to assign by eye to either the mafic or felsic category, and are inferred to be from either source. Glass geochemical compositions generally support the assignments of felsic and mafic units, with some outliers, thus implying that the overall visual assignment of composition is broadly accurate. As visual characteristics are from the bulk deposit and not the glass, it is to be expected that there will be some difference between bulk composition and glass chemistry.

6. Felsic eruptions, within Stage III, can be seen to be gradually decreasing in frequency over time. Mafic eruptions however are clustered, consistent with a volcanic field source, which is likely to be active in clusters and/or different regions in time and space leading to a clustered frequency pattern at Lake Chalco.
7. Thick tephra deposits within the core typically contain structures which are likely related to the plume/eruption dynamics of the volcano during the eruption (e.g., grain size changes are related to an unsteady eruption with waxing and waning of the mass flux). Due to shallow lake conditions (e.g., Valero-Garcés et al., 2021), induvial particle settling is assumed likely, rather than plumes of material through the water column, as occurs in deeper waters (e.g., McNamara et al., 2018).
8. The volcanic record at Lake Chalco is an accurate representation of eruptions which have impacted the city in the past. As Chalco is a stable lacustrine environment, it can be assumed that the deposit preserved is accurate in terms of its thickness and volume of material and has not been resuspended or eroded. It is therefore inferred that the succession at Chalco is an accurate archive for reliable hazard assessment to understand the volume and thickness of tephra hazards in the region in the past.
9. Using grain size measurements, it is shown that observational maximum ash grain sizes from visual descriptions are accurate when compared with quantitative grain size data. However, for samples finer than 3 φ, accurate visual assignments cannot be made.
10. Whole rock lava analyses within Stage I deposits, and clasts within Stage II are consistent with a source from within the Sierra Chichinautzin Volcanic Field, implying that the volcanic field has been active throughout the entire timeframe represented in the Chalco core, including a source very local to the core site.

11. Thickness, grain size and the stratigraphic position (i.e., to determine frequency of layers) are the most important data to obtain from a core record that shares similarities with Chalco. These data can be used as reliably as data obtained from terrestrial deposits, if cores demonstrate good recovery and if factors affecting these parameters (e.g., bioturbation) are considered.
12. Tephra hazards over a long timescale are principally from ash fall, presenting a major hazard for aviation and human health if inhaled. Lahars are also hazard in the region which the population is vulnerable to. Strong emphasis on relaying this to the public should be maintained to ensure the population is resilient if an eruption occurs. Numerous tephra falls have occurred over time that are ≥5 cm in thickness at Chalco, presenting major challenges for infrastructure of the city and relief efforts in the case of this eruption scenario.
13. Glass compositional fields have been defined for the Sierra Chichinautzin Volcanic Field, Popocatépetl, Tláloc-Telapón, Los Humeros, Atitlán, La Primavera and Ceboruco. All of these voclanoes are sufficiently distinct in major elements to define glass compositional fields. These fields have been constructed using known eruption deposits and/or using deposits attributed to the volcanic sources from field relationships (i.e., imbrication of deposits).
14. Glass compositional fields have been extended (for the above volcanoes in point 13) by using positive correlations of core tephras.
15. Out of 137 chemically analysed tephra layers in the Lake Chalco cores, 35 are assigned to Popocatépetl; 43 to either Iztaccíhuatl, Nevado de Toluca or La Malinche; 1 to Tláloc-Telapón; 17 to the SCVF; 3 to Los Humeros and 1 to Atitlán. A total of 23 layers have an

ambiguous source (with a central TMVB arc signature), and 14 are from sources displaying exotic glass chemistries.

16. A range of volcanic sources are evident throughout the core at different depths indicating that multiple volcanic sources pose a risk to Mexico City at all points in time.
17. Unique evolutionary trends can also be noted between the Sierra Chichinautzin Volcanic Field glass when compared with Popocatépetl.
18. Sierra Chichinautzin Volcanic Field glass is generally between 50 and 60 wt.% SiO_2, Popocatépetl is typically between 60 and 70 wt.% SiO_2, and Iztaccíhuatl, Nevado de Toluca and La Malinche volcanoes are generally above 70 wt.% SiO_2. Some overlap occurs for all volcanoes. Popocatépetl analyses in the core hint at older eruptions being more Si-rich, with analyses being attributed to Popocatépetl due to them aligning with the Popocatépetl evolution trend, although further analysis of all tephras would be required to confirm this.
19. Iztaccíhuatl, Nevado de Toluca and La Malinche have similar glass chemistries, resulting in them being grouped for correlative purposes. They display a different evolutionary trend to Popocatépetl, which is also observed in samples analysed from proximal deposits collected from Popocatépetl and Iztaccíhuatl.
20. Field and core data suggests that Popocatépetl and Iztaccíhuatl (and possibly Nevado de Toluca and La Malinche) had a period of coeval activity at c.600 ka, with volcanism becoming more dominant from Popocatépetl. With Iztaccíhuatl, Nevado de Toluca and La Malinche being presented as one geochemical field, a more detailed temporal analysis cannot be accurately developed.

21. Finer ash components of tephras within the core (interpreted to be of a co-PDC origin) are generally richer in SiO_2 and poorer in FeO_t than the coarser part (primary fallout) of the eruption.
22. The laharic volcaniclastic deposits within Chalco generally display homogenous glass compositions for groundmass material at given points within them. The glass is similar in composition to the fields defined, based on fall deposits.
23. Reworking is generally considered to be low within the core, with only one chemically analysed layer out of 77 compared with the nearest adjacent tephra both chemically and visually indicating reworking.
24. Isochronous eruption deposits: (1) the Los Chocoyos (LCY) eruption from Atitlán, Guatemala and (2) the Xáltipan ignimbrite from Los Humeros are present within the Chalco core, providing accurate chronological markers to be imported into the age-depth model.
25. Volumes of the Xáltipan and LCY eruptions are consistent with published estimates, when considering the physical characteristics (i.e., thickness and grain size) of these deposits at Lake Chalco.
26. Detailed tephrastratigraphy of the sequences logged and described at Xalitzintla and Nepopualco provide the first detailed assessments of pyroclastic deposits from these successions which are in close proximity to the Sierra Nevada Volcanic Range. The tephra deposits outlined here will aid other studies into the explosive eruption histories of these volcanoes.

2. SUGGESTIONS FOR FUTURE STUDY

While the findings of this thesis are a significant increase on current knowledge in Mexico, the data presented here is the first step in unravelling the eruptive history of the Mexico City region. Various avenues for future work could be undertaken to further our knowledge and understanding of volcanism in the region.

Some of these suggestions include:

1. Obtaining smear slides of all ambiguous volcanic layers in the core to resolve the uncertainty as to whether these deposits are volcanic in origin. A high concentration of glass shards on the slide will result in the positive identification of a tephra.
2. Sub-sampling of all 'possibly reworked' volcanic deposits, inferred by visual characteristics, with their surrounding tephras to test if they display the same glass chemistry.
3. Obtaining glass chemistry for all tephra layers within the core. This would allow:
    i. Frequencies from each volcanic source to be accurately assessed.
    ii. Chapter 3 plots to be reproduced using quantitative chemical assignments to compare with visual assignment data, presented in this thesis. These could also be subdivided and assessed per volcanic source.
    iii. Insight into the chemical evolution of the volcanic sources in the core over time.
4. Conduct trace element or mineral phase (e.g., Fe-Ti oxides) chemical investigations to better characterise (fingerprint) the geochemical fields for each volcano. This would also determine if Iztaccíhuatl, Nevado de Toluca and La Malinche can be chemcically distinguished and, if so, allow the tephras in the core to be further analysed and

assignments to be made. This would permit an even more detailed analysis of frequency patterns for an improved understanding of the most hazardous volcanoes to Mexico City.

5. Conduct focused fieldwork at other volcanic sources within the Trans Mexican Volcanic Belt, concentrating on other nearby major sources, such as Jocotitlan and the Sierra de las Cruces (to the west of Mexico City). Little study into the eruptive histories of these volcanoes has been published. It is possible that these are the source of exotic chemistries within the core, as microlite-rich glass for some of these deposits implies distal volcanic sources are unlikely.
6. Sample and analyse other calderas, such as Los Azufres, Las Cumbres and Citlaltépetl, extending the distal glass chemical field record for comparison to the unassigned layers within Chalco.
7. Conduct further investigation into the eruptive history of Nevado de Toluca based on deposits within the quarry at Zinacantepec, which display lithic lag breccias and surge deposits, which indicate the volcano has undergone caldera collapse and hydromagmatic activity previously.
8. Conduct a pilot study into cones of the Sierra Chichinautzin Volcanic Field, which in this study show promising signs of unique compositions (fingerprints) for individual cones. While this is largely irrelevant to the record at Chalco, due to the probability of a large number of sources being buried, short cores from lake or peat bogs could be extracted to determine the depository radii of tephras from cones, providing a more accurate assessment of the fallout extent of monogenetic cones, and further insight into distances of tephra dispersed from monogenetic cones in the geological record, such as the record at Chalco. Fingerprinting would also allow successions proximal to cones to be investigated

to better understand if 'monogenetic' volcanoes do usually erupt once, or if cones are often destroyed during a subsequent eruption, effectively overprinting the record.

9. Incorporate modelling (using grain size data) to further infer the depository radius of cones, allowing field deposits to be assessed for comparison. A field and modelling approach could narrow down available proxies for different eruptions from cones.
10. Construct a detailed age-depth model using dates directly from the core and marker layers to better understand the frequency of eruptions in Chalco, as well as further extending the impact and understanding of paleoenvironmental aspects of the MexiDrill project.

3. SUMMARY

This thesis provides a comprehensive investigation into the older explosive eruptive history of the Mexico City region combining volcanic stratigraphy, glass geochemistry and geochronology. The study concludes that explosive eruption hazards have been, and remain, high risk for Mexico City, from multiple volcanic sources. While gathering this data is important and necessary to better understand Mexico City's vulnerability, it must be combined with monitoring and geophysical approaches at nearby volcanoes. One day an explosive eruption, depositing tephra over Mexico City, will occur again, which would be devastating for the city, one of the largest populations in the world. It is important that volcanoes of direct threat to Mexico City are monitored and that plans and procedures are in place in the event of a likely eruption. It is also important that the residents of Mexico City are informed of these hazards and that the resilience of communities is strengthened to minimise the effect of a potential eruption as much as possible. Colleagues at Centro Nacional de

Prevención de Desastres (CENAPRED) and Universidad Nacional Autónoma de México (UNAM), as well as those working in civil protection are working tirelessly to protect the city. Funding and support must continue.

REFERENCES

REFERENCES

Abbott, P.M. and Davies, S.M., 2012. Volcanism and the Greenland ice-cores: the tephra record. Earth-Science Reviews, 115(3), pp.173-191.

Abbott, P.M., Jensen, B.J., Lowe, D.J., Suzuki, T. and Veres, D., 2020. Crossing new frontiers: extending tephrochronology as a global geoscientific research tool.

Agustín-Flores, J., Siebe, C. and Guilbaud, M.N., 2011. Geology and geochemistry of Pelagatos, Cerro del Agua, and Dos Cerros monogenetic volcanoes in the Sierra Chichinautzin volcanic field, south of Mexico City. Journal of Volcanology and Geothermal Research, 201(1-4), pp.143-162.

Alameri, S.A. and Alkaabi, A.K., 2020. Fundamentals of nuclear reactors. In Nuclear Reactor Technology Development and Utilization (pp. 27-60). Woodhead Publishing.

Albert, P.G., Smith, V.C., Suzuki, T., McLean, D., Tomlinson, E.L., Miyabuchi, Y., Kitaba, I., Mark, D.F., Moriwaki, H., Nakagawa, T., Members, S.P., 2019. Geochemical characterisation of the Late Quaternary widespread Japanese tephrostratigraphic markers and correlations to the Lake Suigetsu sedimentary archive (SG06 core). Quaternary Geochronology 1–75. https://doi.org/10.1016/j.quageo.2019.01.005

Albert, P.G., Smith, V.C., Suzuki, T., Tomlinson, E.L., Nakagawa, T., McLean, D., Yamada, M., Staff, R.A., Schlolaut, G., Takemura, K. and Nagahashi, Y., 2018. Constraints on the frequency and dispersal of explosive eruptions at Sambe and Daisen volcanoes (South-West Japan Arc) from the distal Lake Suigetsu record (SG06 core). Earth-Science Reviews, 185, pp.1004-1028.

Albert, P.G., Tomlinson, E.L., Smith, V.C., Di Traglia, F., Pistolesi, M., Morris, A., Donato, P., De Rosa, R., Sulpizio, R., Keller, J. and Rosi, M., 2017. Glass geochemistry of pyroclastic deposits from the Aeolian Islands in the last 50 ka: A proximal database for tephrochronology. Journal of Volcanology and Geothermal Research, 336, pp.81-107.

Alcalá-Reygosa, J., Palacios, D., Schimmelpfennig, I., Vázquez-Selem, L., García-Sancho, L., Franco-Ramos, O., Villanueva, J., Zamorano, J.J., Aumaitre, G., Bourles, D. and Keddadouche, K., 2018. Dating late Holocene lava flows in Pico de Orizaba (Mexico) by means of in situ-produced cosmogenic 36Cl, lichenometry and dendrochronology. Quaternary Geochronology, 47, pp.93-106.

Aldrich, L.T. and Nier, A.O., 1948. Argon 40 in potassium minerals. Physical Review, 74(8), p.876.

Alvarez, G.M., Miranda, C.C., Fucugauchi, J.U. and Uchiumi, S., 1991. Southward migration of volcanic activity in the Sierra de Las Cruces, basin of Mexico?-a preliminary K-Ar dating and palaeomagnetic study. Geofísica Internacional, 30(2), pp.61-70.

Andrews, B.J. and Manga, M., 2011. Effects of topography on pyroclastic density current runout and formation of coignimbrites. Geology, 39(12), pp.1099-1102.

Arana-Salinas, L., Siebe, C., Macías, J.L., (2010). Dynamics of the ca. 4,965 yr. B.P. "Ochre Pumice" Plinian eruption of Popocatépetl Volcano, México. J. Volcanol. Geotherm. Res. 192:212–231. http://dx.doi.org/10.1016/j.jvolgeores.2010.02.022.

Arce, J. L., Cruz-Fuentes, D., Ramírez-Luna, A., Herrera-Huerta, I. A., & Girón-García, P. (2017). Pómez Bosque de Tlalpan, producto de una erupción de gran magnitud en el margen suroeste de la cuenca de México. Revista Mexicana de Ciencias Geológicas, 34(3). DOI: http://dx.doi.org/10.22201/cgeo.20072902e.2017.3.485

Arce, J. L., Layer, P. W., Morales-Casique, E., Benowitz, J. A., Rangel, E., & Escolero, O. (2013). New constraints on the subsurface geology of the Mexico City Basin: The San Lorenzo Tezonco deep well, on the basis of 40Ar/39Ar geochronology and whole-rock chemistry. Journal of Volcanology and Geothermal Research, 266, 34–49. doi:10.1016/j.jvolgeores.2013.09.004

Arce, J.L., Ferrari, L., Morales-Casique, E., Vasquez-Serrano, A., Arroyo, S.M., Layer, P.W., Benowitz, J. and López-Martínez, M., 2020. Early Miocene arc volcanism in the Mexico City Basin: inception of the Trans-Mexican volcanic belt. Journal of Volcanology and Geothermal Research, 408, p.107104.

Arce, J.L., Layer, P., Martínez, I., Salinas, J.I., Macías-Romo, M.D.C., Morales-Casique, E., Benowitz, J., Escolero, O. and Lenhardt, N., 2015. Geología y estratigrafía del pozo profundo San Lorenzo Tezonco y de sus alrededores, sur de la Cuenca de México. Boletín de la Sociedad Geológica Mexicana, 67(2), pp.123-143.

Arce, J.L., Layer, P.W., Macías, J.L., Morales-Casique, E., García-Palomo, A., Jiménez-Domínguez, F.J., Benowitz, J. and Vásquez-Serrano, A., 2019. Geology and stratigraphy of the Mexico basin (Mexico city), central trans-Mexican volcanic belt. Journal of Maps, 15(2), pp.320-332.

Arce, J.L., Macías, J.L. and Vázquez-Selem, L., 2003. The 10.5 ka Plinian eruption of Nevado de Toluca volcano, Mexico: Stratigraphy and hazard implications. Geological Society of America Bulletin, 115(2), pp.230-248.

Ardid, A., Dempsey, D., Caudron, C. and Cronin, S., 2022. Seismic precursors to the Whakaari 2019 phreatic eruption are transferable to other eruptions and volcanoes. Nature communications, 13(1), pp.1-9.

Austin, W.E., Abbott, P.M., Davies, S., Pearce, N.J. and Wastegård, S., 2014. Marine tephrochronology: an introduction to tracing time in the ocean. Geological Society, London, Special Publications, 398(1), pp.1-5.

Avendaño-Villeda, D.A., Caballero, M., Ortega-Guerrero, B., Lozano-García, S. and Brown, E., 2018. Condiciones ambientales a finales del Estadio Isotópico 6 (EI 6:> 130000 años) en

el centro de México: caracterización de una sección de sedimentos laminados proveniente del Lago de Chalco. Revista mexicana de ciencias geológicas, 35(2), pp.168-178.

Bacon, C.R. and Lanphere, M.A., 2006. Eruptive history and geochronology of Mount Mazama and the Crater Lake region, Oregon. Geological Society of America Bulletin, 118(11-12), pp.1331-1359.

Barberi, F., Bertagnini, A., Landi, P. and Principe, C., 1992. A review on phreatic eruptions and their precursors. Journal of volcanology and geothermal research, 52(4), pp.231-246.

Barclay, J., Haynes, K., Mitchell, T., Solana, C., Teeuw, R., Darnell, A., Crosweller, H.S., Cole, P., Pyle, D., Lowe, C. and Fearnley, C., 2008. Framing volcanic risk communication within disaster risk reduction: finding ways for the social and physical sciences to work together. Geological Society, London, Special Publications, 305(1), pp.163-177.

Bertotto, G.W., Bjerg, E.A. and Cingolani, C.A., 2006. Hawaiian and Strombolian style monogenetic volcanism in the extra-Andean domain of central-west Argentina. Journal of Volcanology and Geothermal Research, 158(3-4), pp.430-444.

Bischoff, A., Nicol, A., Barrier, A. and Wang, H., 2019. Paleogeography and volcanic morphology reconstruction of a buried monogenetic volcanic field (part 2). Bulletin of Volcanology, 81(9), pp.1-23.

Blong, R., Enright, N. and Grasso, P., 2017. Preservation of thin tephra. Journal of Applied Volcanology, 6(1), pp.1-15.

Bloomfield, K. and Valastro Jr, S., 1974. Late Pleistocene eruptive history of Nevado de Toluca volcano, central Mexico. Geological Society of America Bulletin, 85(6), pp.901-906.

Bloomfield, K., Rubio, G.S. and Wilson, L., 1977. Plinian eruptions of Nevado de Toluca volcano, Mexico. Geologische Rundschau, 66(1), pp.120-146.

Blum, P., 1997. Magnetic susceptibility. Physical Properties Handbook.

Bonasia, R., Scaini, C., Capra, L., Nathenson, M., Siebe, C., Arana-Salinas, L. and Folch, A., 2014. Long-range hazard assessment of volcanic ash dispersal for a Plinian eruptive scenario at Popocatépetl volcano (Mexico): implications for civil aviation safety. Bulletin of Volcanology, 76(1), pp.1-16.

Brand, B.D., Bendaña, S., Self, S. and Pollock, N., 2016. Topographic controls on pyroclastic density current dynamics: Insight from 18 May 1980 deposits at Mount St. Helens, Washington (USA). Journal of Volcanology and Geothermal Research, 321, pp.1-17.

Branney, M. and Acocella, V., 2015. Calderas. In The encyclopedia of volcanoes (pp. 299-315). Academic Press.

Branney, M.J., Brown, R.J. and Calder, E., 2021. Pyroclastic rocks.

Branney, M.J., Kokelaar, B.P. and McConnell, B.J., 1992. The Bad Step Tuff: a lava-like rheomorphic ignimbrite in a calc-alkaline piecemeal caldera, English Lake District. Bulletin of Volcanology, 54(3), pp.187-199.

Branney, M.J., Kokelaar, P. and Kokelaar, B.P., 2002. Pyroclastic density currents and the sedimentation of ignimbrites. Geological Society of London.

Brenna, M., Cronin, S.J., Smith, I.E., Pontesilli, A., Tost, M., Barker, S., Tonga'onevai, S., Kula, T. and Vaiomounga, R., 2022. Post-caldera volcanism reveals shallow priming of an intra-ocean arc andesitic caldera: Hunga volcano, Tonga, SW Pacific. Lithos, 412, p.106614.

Bronk Ramsey, C. (2009). Bayesian analysis of radiocarbon dates. Radiocarbon, 51(1), 337–360.

Bronk Ramsey, C., Housley, R.A., Lane, C.S., Smith, V.C., Pollard, A.M., (2015). The RESET tephra database and associated analytical tools. Quat. Sci. Rev. 118, 33–47. doi:https://doi.org/10.1016/j.quascirev.2014.11.008

Brook, G.A., Cowart, J.B. and Brandt, S.A., 2020. Comparison of Quaternary environmental change in eastern and southern Africa using cave speleothem, tufa and rock shelter sediment data. In Quaternary deserts and climatic change (pp. 239-249). CRC Press.

Brown ET, Caballero M, Cabral Cano E, Fawcett PJ, Lozano-García S, Ortega B et al (2019). Scientific drilling of Lake Chalco, Basin of Mexico (MexiDrill). Scient Drill. https://doi.org/10.5194/ sd-7-1-2019

Brown, R.J. and Branney, M.J., 2004. Event-stratigraphy of a caldera-forming ignimbrite eruption on Tenerife: the 273 ka Poris Formation. Bulletin of Volcanology, 66(5), pp.392-416.

Büttner, R., Dellino, P., La Volpe, L., Lorenz, V. and Zimanowski, B., 2002. Thermohydraulic explosions in phreatomagmatic eruptions as evidenced by the comparison between pyroclasts and products from Molten Fuel Coolant Interaction experiments. Journal of Geophysical Research: Solid Earth, 107(B11), pp.ECV-5.

Caballero, M., Guerrero, B., (1998). Lake Levels since about 40,000 Years Ago at Lake Chalco, near Mexico City. Quatern Res 50(1):69–79. https ://doi.org/10.1006/qres.1998.1969

Cadoux, A., Missenard, Y., Martinez-Serrano, R.G. and Guillou, H., 2011. Trenchward Plio-Quaternary volcanism migration in the Trans-Mexican Volcanic Belt: the case of the Sierra Nevada range. Geological Magazine, 148(3), pp.492-506.

Capra, L. and Macıas, J.L., 2002. The cohesive Naranjo debris-flow deposit (10 km3):: A dam breakout flow derived from the Pleistocene debris-avalanche deposit of Nevado de Colima Volcano (México). Journal of Volcanology and Geothermal Research, 117(1-2), pp.213-235.

Capra, L., Carreras, L.M., Arce, J.L. and Macías, J.L., 2006. The Lower Toluca Pumice: A ca. 21,700 yrB. P. Plinian eruption ofNevado de Toluca volcano, México. Neogene-Quaternary continental margin volcanism: A perspective from Mexico, 402, p.155.

Capra, L., Norini, G., Groppelli, G., Macías, J.L. and Arce, J.L., 2008. Volcanic hazard zonation of the Nevado de Toluca volcano, México. Journal of Volcanology and Geothermal Research, 176(4), pp.469-484.

Carey, S., Gardner, J. and Sigurdsson, H., 1995. The intensity and magnitude of Holocene plinian eruptions from Mount St. Helens volcano. Journal of Volcanology and Geothermal Research, 66(1-4), pp.185-202.

Carey, S., Sparks, R.S.J., Tucker, M.E., Li, T., Robinson, L., Watt, S.F.L., Gee, M., Hastie, A., Barfod, D.N., Stinton, A. and Leng, M., 2020. The polygenetic Kahouanne Seamounts in the northern Lesser Antilles island arc: evidence for large-scale volcanic island subsidence. Marine Geology, 419, p.106046.

Carlino, S., Somma, R. and Mayberry, G.C., 2008. Volcanic risk perception of young people in the urban areas of Vesuvius: Comparisons with other volcanic areas and implications for emergency management. Journal of Volcanology and Geothermal Research, 172(3-4), pp.229-243.

Carrasco-Núñez, G., Bernal, J.P., Davila, P., Jicha, B., Giordano, G. and Hernández, J., 2018. Reappraisal of Los Humeros volcanic complex by new U/Th zircon and 40Ar/39Ar dating: Implications for greater geothermal potential. Geochemistry, Geophysics, Geosystems, 19(1), pp.132-149.

Carrasco-Núñez, G., McCurry, M., Branney, M.J., Norry, M. and Willcox, C., 2012. Complex magma mixing, mingling, and withdrawal associated with an intra-Plinian ignimbrite eruption at a large silicic caldera volcano: Los Humeros of central Mexico. Bulletin, 124(11-12), pp.1793-1809.

Cassidy, M., Manga, M., Cashman, K. and Bachmann, O., 2018. Controls on explosive-effusive volcanic eruption styles. Nature communications, 9(1), pp.1-16.

Cassidy, M., Watt, S.F., Palmer, M.R., Trofimovs, J., Symons, W., Maclachlan, S.E. and Stinton, A.J., 2014. Construction of volcanic records from marine sediment cores.

Castro-Govea, R. and Siebe, C., 2007. Late Pleistocene–Holocene stratigraphy and radiocarbon dating of La Malinche volcano, central Mexico. Journal of Volcanology and Geothermal Research, 162(1-2), pp.20-42.

Cavazos-Álvarez, J.A. and Carrasco-Núñez, G., 2020. Anatomy of the Xáltipan ignimbrite at Los Humeros Volcanic complex; the largest eruption of the Trans-Mexican Volcanic Belt. Journal of Volcanology and Geothermal Research, 392, p.106755.

Cembrano, J. and Lara, L., 2009. The link between volcanism and tectonics in the southern volcanic zone of the Chilean Andes: a review. Tectonophysics, 471(1-2), pp.96-113.

Chambers, L.M., Pringle, M.S. and Fitton, J.G., 2004. Phreatomagmatic eruptions on the Ontong Java Plateau: an Aptian 40Ar/39Ar age for volcaniclastic rocks at ODP Site 1184. Geological Society, London, Special Publications, 229(1), pp.325-331.

Chávez-Lara, C.M., Lozano-García, S., Ortega-Guerrero, B., Caballero-Miranda, M., Avendaño, D. and Brown, E.T., 2022. An ostracod-based record of paleoecological conditions during MIS6 and MIS5, from Lake Chalco, Basin of Mexico. Journal of Paleolimnology, 67(4), pp.359-373.

Chertkoff, D.G. and Gardner, J.E., 2004. Nature and timing of magma interactions before, during, and after the caldera-forming eruption of Volcán Ceboruco, Mexico. Contributions to mineralogy and Petrology, 146(6), pp.715-735.

Child, J.K., Begét, J.E. and Werner, A., 1998. Three Holocene tephras identified in lacustrine sediment cores from the Wonder Lake area, Denali National Park and Preserve, Alaska, USA. Arctic and Alpine Research, 30(1), pp.89-95.

Cisneros de León, A., Schindlbeck-Belo, J.C., Kutterolf, S., Danišík, M., Schmitt, A.K., Freundt, A., Pérez, W., Harvey, J.C., Wang, K.L. and Lee, H.Y., 2021. A history of violence: magma incubation, timing and tephra distribution of the Los Chocoyos supereruption (Atitlán Caldera, Guatemala). Journal of Quaternary Science, 36(2), pp.169-179.

Conte, G., Urrutia-Fucugauchi, J., Goguitchaichvili, A., Soler-Arechalde, A. M. & Morton-Bermea, O. (2004). Paleomagnetic study of lavas from the Popocatépetl volcanic region, Central Mexico. International Geology Review 46, 210–25.

Cornwall, I.W., (1971). Geology and Early Man in Central Mexico. The Henry Stopes Lecture, Proceedings Geologist's Association 82 (3), 379–391. 6/S0016-7878(71)80016-0

Costa, A., Smith, V.C., Macedonio, G. and Matthews, N.E., 2014. The magnitude and impact of the Youngest Toba Tuff super-eruption. Frontiers in Earth Science, 2, p.16.

Covaleda, S., Pajares, S., Gallardo, J.F. and Etchevers, J.D., 2006. Short-term changes in C and N distribution in soil particle size fractions induced by agricultural practices in a cultivated volcanic soil from Mexico. Organic Geochemistry, 37(12), pp.1943-1948.

Crandell, D.R. and Mullineaux, D.R., 1977. Potential hazards from future eruptions of Mount St. Helens volcano, Washington (No. 1383). US Government Printing Office.

Crosweller, H.S., Arora, B., Brown, S.K., Cottrell, E., Deligne, N.I., Guerrero, N.O., Hobbs, L., Kiyosugi, K., Loughlin, S.C., Lowndes, J. and Nayembil, M., 2012. Global database on large magnitude explosive volcanic eruptions (LaMEVE). Journal of Applied Volcanology, 1(1), pp.1-13.

Crummy, J.M., Savov, I.P., Navarro-Ochoa, C. and Morgan, D.J., 2019. Holocene eruption history and magmatic evolution of the Colima volcanic complex. In Volcán de Colima (pp. 1-25). Springer, Berlin, Heidelberg.

Cruz-Reyna, D., Yokoyama, I., Martínez-Bringas, A. and Ramos, E., 2008. Precursory seismicity of the 1994 eruption of Popocatépetl Volcano, Central Mexico. Bulletin of Volcanology, 70(6), pp.753-767.

Cullen, V.L., Smith, V.C. and Arz, H.W., 2014. The detailed tephrostratigraphy of a core from the south-east Black Sea spanning the last~ 60 ka. Journal of Quaternary Science, 29(7), pp.675-690.

Damby, D.E., Horwell, C.J., Baxter, P.J., Delmelle, P., Donaldson, K., Dunster, C., Fubini, B., Murphy, F.A., Nattrass, C., Sweeney, S. and Tetley, T.D., 2013. The respiratory health hazard of tephra from the 2010 Centennial eruption of Merapi with implications for occupational mining of deposits. Journal of Volcanology and Geothermal Research, 261, pp.376-387.

Davies, S.M., Abbott, P.M., Pearce, N.J., Wastegård, S. and Blockley, S.P., 2012. Integrating the INTIMATE records using tephrochronology: rising to the challenge. Quaternary Science Reviews, 36, pp.11-27.

Dávila-Harris, P. and Carrasco-Núñez, G., 2014. An unusual syn-eruptive bimodal eruption: the Holocene Cuicuiltic Member at Los Humeros caldera, Mexico. Journal of Volcanology and Geothermal Research, 271, pp.24-42.

De la Cruz-Reyna, S., Quezada, J.L., Peña, C., Zepeda, O., and Sánchez, T., (1995). Historia de la actividad del Popocatépetl (1354–1995), Volcán Popocatépetl: Estudios Realizados durante la crisis de 1994–1995: Centro Nacional de Prevención de Desastres, Universidad Nacional Autónoma de México, p. 3–22.

De Rosa, R., Donato, P., Gioncada, A., Masetti, M. and Santacroce, R., 2003. The Monte Guardia eruption (Lipari, Aeolian Islands): an example of a reversely zoned magma mixing sequence. Bulletin of Volcanology, 65(7), pp.530-543.

Del Pozzo, A.L., 1982. Monogenetic vulcanism in sierra Chichinautzin, Mexico. Bulletin Volcanologique, 45(1), pp.9-24.

Delgado Granados, H., Cassatta, W., Gisbert Pinto, G. and Renee, P., (2017). Los edificios volcánicos antiguos. In: Martin Del Pozzo, A.L., Alatorre Ibargüengoitia, M., Arana Salinas, L., Bonasia, R., Capra Pedol, L., Cassata, W., Cordoba, G., Cortés Ramos, J., Delgado Granados, H., Ferrés López, M.D., Fonseca Álvarez, R., García Reynoso, J.A., Gisbert, G., Guerrero López, D.A., Jaimes Viera, M.C., Macías Vázquez, J.L., Nieto Obregon, J., Nieto Torres, A., Paredes Ruiz, P.A., Portocarrero Martínez, J., Renne, P., Rodríguez Espinosa, D.M., Salinas Sánchez, S., Siebe Grabach, C., and Tellez Ugalde, E. Estudios geológicos y actualización del mapa de peligros del volcán Popocatépel.

Memoria técnica del mapa de peligros del volcán Popocatépetl. Monografías del Instituto de 846 Geofísica - UNAM, 22. Universidad Nacional Autónoma de México, México. 166 p. ISBN 978-607-02-9782-3.

Deligne, N.I., Jenkins, S.F., Meredith, E.S., Williams, G.T., Leonard, G.S., Stewart, C., Wilson, T.M., Biass, S., Blake, D.M., Blong, R.J. and Bonadonna, C., 2021. From anecdotes to quantification: advances in characterizing volcanic eruption impacts on the built environment. *Bulletin of Volcanology*, *84*(1), pp.1-9.

Donovan, A., Ayala, I.A., Eiser, J.R. and Sparks, R.S.J., 2018. Risk perception at a persistently active volcano: warnings and trust at Popocatépetl volcano in Mexico, 2012–2014. Bulletin of Volcanology, 80(5), pp.1-16.

Drexler, J.W., Rose, W.I., Sparks, R.S.J. and Ledbetter, M.T., 1980. The Los Chocoyos Ash, Guatemala: a major stratigraphic marker in Middle America and in three ocean basins. Quaternary Research, 13(3), pp.327-345.

Duncan, M., Loughlin, S., Mee, K., Crummy, J., Engwell, S.L., Dioguardi, F., Hicks, A., Jenkins, G. and Patton, A., 2019, March. Providing impact-based multi-hazard scientific advice: anticipating and responding to international volcanic activity. In Geoscience and Society Summit. AGU.

Eggertsson, G.H., Kendrick, J.E., Weaver, J., Wallace, P.A., Utley, J.E., Bedford, J.D., Allen, M.J., Markússon, S.H., Worden, R.H., Faulkner, D.R. and Lavallée, Y., 2020. Compaction of hyaloclastite from the active geothermal system at Krafla volcano, Iceland. Geofluids, 2020.

Engwell, S.L., Sparks, R.S.J. and Carey, S., 2014. Physical characteristics of tephra layers in the deep sea realm: the Campanian Ignimbrite eruption. Geological Society, London, Special Publications, 398(1), pp.47-64.

Erfurt-Cooper, P. ed., 2014. Volcanic tourist destinations. Springer Science & Business Media.

Erfurt-Cooper, P., Sigurdsson, H. and Lopes, R.M., 2015. Volcanoes and tourism. In The encyclopedia of volcanoes (pp. 1295-1311). Academic Press.

Espinasa-Pereña, R. and Granados, H.D., 2013. Hazards related to lava tubes and caves in the Sierra Chichinautzin monogenetic volcanic field (México). Geological Society of America Special Papers, 498, pp.163-176.

Espinasa-Pereña, R., and Martín-Del Pozzo, A.L., (2006). Morphostratigraphic evolution of Popocatépetl volcano, México, in Siebe, C., Macías, J.L., Aguirre-Díaz, G., eds., Neogene-Quaternary continental margin volcanism: A perspective from Mexico, Geological Society of America Special Paper 402, Penrose Conference Series, p. 115–137. doi:10.1130/2006.2402(05).

Ferrari, L., Orozco-Esquivel, T., Manea, V. and Manea, M., 2012. The dynamic history of the Trans-Mexican Volcanic Belt and the Mexico subduction zone. Tectonophysics, 522, pp.122-149

Ferriz, H. and Mahood, G.A., 1984. Eruption rates and compositional trends at Los Humeros volcanic center, Puebla, Mexico. Journal of Geophysical Research: Solid Earth, 89(B10), pp.8511-8524.

Flanagan, F.J., 1984. Three USGS mafic rock references samples, W-2, DNC-1, and BIR-1 (No. 1623). USGPO,

Fontijn, K., Rawson, H., Van Daele, M., Moernaut, J., Abarzúa, A.M., Heirman, K., Bertrand, S., Pyle, D.M., Mather, T.A., De Batist, M. and Naranjo, J.A., 2016. Synchronisation of sedimentary records using tephra: A postglacial tephrochronological model for the Chilean Lake District. Quaternary Science Reviews, 137, pp.234-254.

Foo, Z.H., Jensen, B.J. and Bolton, M.S., 2020. Glass geochemical compositions from widespread tephras erupted over the last 200 years from Mount St. Helens. Journal of Quaternary Science, 35(1-2), pp.102-113.

Francis, P. and Oppenheimer, C., 2004. Volcanoes: A planetary perspective. 2nd ed. Oxford: Oxford University Press. p.10-490.

Froggatt, P.C. and Gosson, G.J., 1982. Techniques for the preparation of tephra samples for mineral and chemical analysis and radiometric dating. Department of Geology, Victoria University of Wellington.

García Tenorio, F., 2008. Avalancha de escombros del Pleistoceno Tardío del cono de los Píes, Complejo Volcánico Iztaccíhuatl (tesis de maestría). México: ESIA TICOMAN–IPN.

García-Palomo, A., Macías, J.L., Tolson, G., Valdez, G., Mora, J.C., (2002). Volcanic stratigraphy and geologic evolution of the Apan region, east-central sector of the Trans-Mexican Volcanic Belt. Geofisica International 41, 133–150.

García-Palomo, A., Zamorano, J.J., López-Miguel, C., Galván-García, A., Carlos-Valerio, V., Ortega, R. and Macías, J.L., 2008. El arreglo morfoestructural de la Sierra de Las Cruces, México central. Revista mexicana de ciencias geológicas, 25(1), pp.158-178.

García-Tenorio F., Macías J.L. and Layer P.W., 2012, Euptive History of the Iztaccíhuatl Volcanic Complex during the past 450,000 years, Cities on Volcanoes 7, 19-23 November 2012, Colima Mexico.

García-Tenorio F., Sosa-Ceballos G., and Macías J.L., 2015. Las erupciones piroclásticas del volcán Iztaccíhuatl de los últimos 300,000 Años . Resumen de la Reunión Anual de la Unión Geofísica Mexicana, Puerto Vallarta, 2-7 Noviembre 2015.

García-Tenorio, F., (2008). Avalancha de Escombros del Pleistoceno Tardío Del Cono Los Pies, Complejo Volcánico Iztaccíhuatl [M.S. thesis]: Posgrado en Geología, ESIA- IPN, p 147.

García-Tenorio, F., Reyes-Agustín, G. and López-Pizaña, F., 2012. Geology and geochronology of T laloc, Telapón, Iztaccíhuatl, and Popocatépetl volcanoes, Sierra Nevada, central Mexico. The Southern Cordillera and Beyond, 25, p.163.

García-Tovar, G.P., and Martínez-Serrano, R.G., (2011). Geología y geoquímica de las lavas pleistocénicas del estratovolcán Telapón, Sierra Nevada: México Revista Mexicana de Ciencias Geológicas, v. 28, p. 301–322.

Genareau, K., Valentine, G.A., Moore, G. and Hervig, R.L., 2010. Mechanisms for transition in eruptive style at a monogenetic scoria cone revealed by microtextural analyses (Lathrop Wells volcano, Nevada, USA). Bulletin of Volcanology, 72(5), pp.593-607.

Giaccio, B., Leicher, N., Mannella, G., Monaco, L., Regattieri, E., Wagner, B., Zanchetta, G., Gaeta, M., Marra, F., Nomade, S. and Palladino, D.M., 2019. Extending the tephra and palaeoenvironmental record of the Central Mediterranean back to 430 ka: A new core from Fucino Basin, central Italy. Quaternary Science Reviews, 225, p.106003.

Gisbert, G., Delgado-Granados, H., Mangler, M., Prytulak, J., Espinasa-Pereña, R. and Petrone, C.M., 2022. Evolution of the Popocatépetl Volcanic Complex: constraints on periodic edifice construction and destruction by sector collapse. Journal of the Geological Society, 179(3).

Glicken, H., 1986. Rockslide-debris avalanche of May 18, 1980, Mount St. Helens volcano, Washington (Doctoral dissertation, University of California, Santa Barbara).

Goff, F., Janik, C.J., Delgado, H., Werner, C., Counce, D., Stimac, J.A., Siebe, C., Love, S.P., Williams, S.N., Fischer, T., Johnson, L., (1998). Geochemical surveillance of magmatic volatiles at Popocatépetl volcano, México. Geol. Soc. Am. Bull. 110-6:695–710. http://dx.doi.org/10.1130/0016-7606(1998)110b0695:GSOMVAN2.3.CO;2.

Gómez-Tuena, A., Orozco-Esquivel, T., Ferrari, L., (2007). Igneous petrogenesis of the Trans-Mexican Volcanic Belt. In: Alaniz-Álvarez, S.A., Nieto-Samaniego, Á.F. (Eds.), Geology of México: celebrating the Centenary of the Geological Society of México: Geological Society of America Special Paper, 422, pp. 1–53. doi:10.1130/2007.2422(05).

Gómez-Vázquez, A., De la Cruz-Reyna, S., Mendoza-Rosas, A.T., (2016). The ongoing dome emplacement and destruction cyclic process at Popocatépetl volcano, CentralMéxico. Bull. Volcanol. 78:58. http://dx.doi.org/10.1007/s00445-016-1054-z.

Guilbaud, M.N., Alcalá-Reygosa, J., Schimmelpfennig, I., Arce, J.L. and ASTER Team, 2022. Testing less-conventional methods to date a late-pleistocene to Holocene eruption: Radiocarbon dating of paleosols and 36Cl exposure ages at Pelado volcano, Sierra Chichinautzin, Central Mexico. Quaternary Geochronology, 68, p.101252.

Hampton, S.J., Cole, J.W., Wilson, G., Wilson, T.M. and Broom, S., 2015. Volcanic ashfall accumulation and loading on gutters and pitched roofs from laboratory empirical

experiments: Implications for risk assessment. Journal of Volcanology and Geothermal Research, 304, pp.237-252.

Harangi, S., Molnar, K., Schmitt, A.K., Dunkl, I., Seghedi, I., Novothny, A., Molnar, M., Kiss, B., Ntaflos, T., Mason, P.R. and Lukacs, R., 2020. Fingerprinting the Late Pleistocene tephras of Ciomadul volcano, eastern–central Europe. Journal of Quaternary Science, 35(1-2), pp.232-244.

Harning, D.J., Thordarson, T., Geirsdóttir, Á., Ólafsdóttir, S. and Miller, G.H., 2019. Marker tephra in Haukadalsvatn lake sediment: A key to the Holocne tephra stratigraphy of northwest Iceland. Quaternary Science Reviews, 219, pp.154-170.

Herrera-Hernández, M.G., Guevara-Lara, F., Reynoso-Camacho, R. and Guzmán-Maldonado, S.H., 2011. Effects of maturity stage and storage on cactus berry (Myrtillocactus geometrizans) phenolics, vitamin C, betalains and their antioxidant properties. Food chemistry, 129(4), pp.1744-1750.

Hicks, A., Barclay, J., Chilvers, J., Armijos, M.T., Oven, K., Simmons, P. and Haklay, M., 2019. Global mapping of citizen science projects for disaster risk reduction. Frontiers in Earth Science, 7, p.226.

Hodgetts, A.G.E., McGarvie, D., Tuffen, H. and Simmons, I.C., 2021. The Thórólfsfell tuya, South Iceland–A new type of basaltic glaciovolcano. Journal of Volcanology and Geothermal Research, 411, p.107175.

Hodgson, D.A., Dyson, C.L., Jones, V.J. and Smellie, J.L., 1998. Tephra analysis of sediments from Midge Lake (South Shetland Islands) and Sombre Lake (South Orkney Islands), Antarctica. Antarctic Science, 10(1), pp.13-20.

Howie, R.A., Zussman, J. and Deer, W., 1992. An introduction to the rock-forming minerals (p. 696). London, UK: Longman.

Huddart, D., González, S., (2004). Pyroclastic flows and associated sediments, Tláloc–Telapón, piedmont fringe of the eastern basin of Mexico. In: Aguirre-Diaz, G.J., Macías, J.L., Siebe, C. (Eds.), Penrose Conference, Metepec, Puebla, Mexico, p. 35.

Hunt, J.B. and Hill, P.G., 1993. Tephra geochemistry: a discussion of some persistent analytical problems. The Holocene, 3(3), pp.271-278.

Jaimes-Viera, M.D.C., Del Pozzo, A.M., Layer, P.W., Benowitz, J.A. and Nieto-Torres, A., 2018. Timing the evolution of a monogenetic volcanic field: Sierra Chichinautzin, Central Mexico. Journal of Volcanology and Geothermal Research, 356, pp.225-242.

Jenkins, S.F., Wilson, T.M., Magill, C., Miller, V., Stewart, C., Blong, R., Marzocchi, W., Boulton, M., Bonadonna, C. and Costa, A., 2015. Volcanic ash fall hazard and risk. *Global volcanic hazards and risk*, pp.173-222.

Jenner, G.A., Longerich, H.P., Jackson, S.E. and Fryer, B.J., 1990. ICP-MS—A powerful tool for high-precision trace-element analysis in Earth sciences: Evidence from analysis of selected USGS reference samples. Chemical Geology, 83(1-2), pp.133-148.

Jensen, B.J., Davies, L.J., Nolan, C., Pyne-O'Donnell, S., Monteath, A.J., Ponomareva, V., Portnyagin, M., Booth, R., Bursik, M., Cook, E. and Plunkett, G., 2021. A latest Pleistocene and Holocene composite tephrostratigraphic framework for northeastern North America. Quaternary Science Reviews, 272, p.107242.

Jochum, K.P., Stoll, B., Herwig, K., Willbold, M., Hofmann, A.W., Amini, M., Aarburg, S., Abouchami, W., Hellebrand, E., Mocek, B., Raczek, I., Stracke, A., Alard, O., Bouman, C., Becker, S., Dücking, M., Brätz, H., Klemd, R., de Bruin, D., Canil, D., Cornell, D., de Hoog, C., Dalpé, C., Danyushevsky, L., Eisenhauer, A., Gao, Y., Snow, J.E., Groschopf, N., Günther, D., Latkoczy, C., Guillong, M., Hauri, E., Höfer, H.E., Lahaye, Y., Horz, K., Jacob, D.E., Kasemann, S.A., Kent, A.J.R., Ludwig, T., Zack, T., Mason, P.R.D., Meixner, A., Rosner, M., Misawa, K., Nash, B.P., Pfänder, J., Premo, W.R., Sun, W.D., Tiepolo, M., Vannucci, R., Vennemann, T., Wayne, D., Woodhead, J.D., (2006). MPI-DING reference glasses for in situ microanalysis: New reference values for element concentrations and isotope ratios. Geochem. Geophys. Geosyst. 7 (Q02008).

Johnston, E.N., Phillips, J.C., Bonadonna, C. and Watson, I.M., 2012. Reconstructing the tephra dispersal pattern from the Bronze Age eruption of Santorini using an advection–diffusion model. Bulletin of Volcanology, 74(6), pp.1485-1507.

Jourdan, F. and Renne, P.R., 2007. Age calibration of the Fish Canyon sanidine 40Ar/39Ar dating standard using primary K–Ar standards. Geochimica et Cosmochimica Acta, 71(2), pp.387-402.

Kelley, S., 2002. Excess argon in K–Ar and Ar–Ar geochronology. Chemical Geology, 188(1-2), pp.1-22.

Kilgour, G., Gates, S., Kennedy, B., Farquhar, A., McSporran, A. and Asher, C., 2019. Phreatic eruption dynamics derived from deposit analysis: a case study from a small, phreatic eruption from Whakāri/White Island, New Zealand. Earth, Planets and Space, 71(1), pp.1-21.

Kokelaar, B.P. and Durant, G.P., 1983. The submarine eruption and erosion of Surtla (Surtsey), Iceland. Journal of Volcanology and Geothermal Research, 19(3-4), pp.239-246.

Kutterolf, S., Freundt, A. and Peréz, W., 2008. Pacific offshore record of plinian arc volcanism in Central America: 2. Tephra volumes and erupted masses. Geochemistry, Geophysics, Geosystems, 9(2).

Kutterolf, S., Schindlbeck, J.C., Anselmetti, F.S., Ariztegui, D., Brenner, M., Curtis, J., Schmid, D., Hodell, D.A., Mueller, A., Perez, L. and Peréz, W., 2016. A 400-ka

tephrochronological framework for Central America from Lake Petén Itzá (Guatemala) sediments. Quaternary Science Reviews, 150, pp.200-220.

Lane, C.S., Chorn, B.T. and Johnson, T.C., 2013. Ash from the Toba supereruption in Lake Malawi shows no volcanic winter in East Africa at 75 ka. Proceedings of the National Academy of Sciences, 110(20), pp.8025-8029.

Lane, C.S., Cullen, V.L., White, D., Bramham-Law, C.W.F. and Smith, V.C., 2014. Cryptotephra as a dating and correlation tool in archaeology. Journal of Archaeological Science, 42, pp.42-50.

Lane, C.S., Lowe, D.J., Blockley, S.P., Suzuki, T. and Smith, V.C., 2017. Advancing tephrochronology as a global dating tool: Applications in volcanology, archaeology, and palaeoclimatic research. Quaternary Geochronology, 40, pp.1-7.

Lanphere, M.A. and Dalrymple, G.B., 2000. First-principles calibration of 38Ar tracers: Implications for the ages of 40Ar/39Ar fluence monitors (No. 1621). US Geological Survey.

Larsen, G. and Eiríksson, J., 2008. Late Quaternary terrestrial tephrochronology of Iceland—frequency of explosive eruptions, type and volume of tephra deposits. Journal of Quaternary Science: Published for the Quaternary Research Association, 23(2), pp.109-120.

Lautze, N.C. and Houghton, B.F., 2005. Physical mingling of magma and complex eruption dynamics in the shallow conduit at Stromboli volcano, Italy. Geology, 33(5), pp.425-428.

Lisiecki, L.E. and Raymo, M.E., 2005. A Pliocene-Pleistocene stack of 57 globally distributed benthic δ18O records. Paleoceanography, 20(1).

Liu, E.J., Cashman, K.V., Rust, A.C. and Höskuldsson, A., 2017. Contrasting mechanisms of magma fragmentation during coeval magmatic and hydromagmatic activity: the Hverfjall Fires fissure eruption, Iceland. Bulletin of Volcanology, 79(10), pp.1-26.

Lockwood, J.P. and Lipman, P.W., 1987. Holocene eruptive history of Mauna Loa volcano. US Geol. Surv. Prof. Pap, 1350(1), pp.509-535.

Lorenzo-Merino, A., Guilbaud, M.N. and Roberge, J., 2018. The violent Strombolian eruption of 10 ka Pelado shield volcano, Sierra Chichinautzin, Central Mexico. Bulletin of Volcanology, 80(3), pp.1-17.

Loughlin, S.C., Sparks, R.S.J., Sparks, S., Brown, S.K., Jenkins, S.F. and Vye-Brown, C. eds., 2015. Global volcanic hazards and risk. Cambridge University Press.

Love, S.P., Goff, F., Counce, D., Siebe, C. and Delgado, H., 1998. Passive infrared spectroscopy of the eruption plume at Popocatépetl volcano, Mexico. Nature, 396(6711), pp.563-567.

Lowe, D.J., 2011. Tephrochronology and its application: a review. Quaternary Geochronology, 6(2), pp.107-153.

Lowe, D.J., 2014. Marine tephrochronology: a personal perspective. Geological Society, London, Special Publications, 398(1), pp.7-19.

Lowenstern, J.B. and Ramsey, D.W., 2017. The Volcano Disaster Assistance Program—Helping to save lives worldwide for more than 30 years (No. 2017-3071). US Geological Survey.

Lozano-García, M.S., Ortega-Guerrero, B., (1994). Palynological and magnetic susceptibility records of Lake Chalco, central Mexico. Palaeogeography, Palaeoclimatology, Palaeoecology109, 177–191.

Lozano-García, S., Ortega, B., Roy, P., Beramendi-Orosco, L., Caballero, M. (2015) Climatic variability in the northern sector of the American tropics since the latest MIS 3. Quatern Res 84(2):262–271. https://doi.org/10.1016/j.yqres .2015.07.002

Macedonio, G. and Costa, A., 2012. Brief Communication" Rain effect on the load of tephra deposits". Natural Hazards and Earth System Sciences, 12(4), pp.1229-1233.

Macías, J.L., Arce, J.L., García-Tenorio, F., Layer, P.W., Rueda, H., Reyes-Agustín, G., López-Pizaña, F., Avellán, D., (2012). Geology and geochronology of Tláloc, Telapón, Iztaccíhuatl, and Popocatépetl volcanoes, Sierra Nevada, central Mexico. Geol. Soc. Am. Field Guide 25:163–193. http://dx.doi.org/10.1130/2012.0025(08).

Macías, J.L., Arce, J.L., García-Tenorio, F., Sosa-Ceballos, G. and Gardner, J.E., 2020. Source and behavior of pyroclastic density currents generated by Vulcanian-style explosions of Popocatépetl volcano (Mexico) on 22 January 2001. Journal of Volcanology and Geothermal Research, 406, p.107071.

Macías, J.L., García, P.A., Arce, J.L., Siebe, C., Espíndola, J.M., Komorowski, J.C. and Scott, K., 1997. Late Pleistocene-Holocene cataclysmic eruptions at Nevado de Toluca and Jocotitlan volcanoes, central Mexico. Brigham Young University Geology Studies, 42(1), pp.493-528.

Macías, J.L., Siebe, C., (2005). Popocatépetl's crater filled to the brim: significance for hazard evaluation. J. Volcanol. Geotherm. Res. 141:327–330. http://dx.doi.org/10.1016/j. jvolgeores.2004.10.005.

Maeno, F., Nakada, S., Oikawa, T., Yoshimoto, M., Komori, J., Ishizuka, Y., Takeshita, Y., Shimano, T., Kaneko, T. and Nagai, M., 2016. Reconstruction of a phreatic eruption on 27 September 2014 at Ontake volcano, central Japan, based on proximal pyroclastic density current and fallout deposits. Earth, Planets and Space, 68(1), pp.1-20.

Mahony, S.H., Sparks, R.S.J. and Barnard, N.H., 2014. Quantifying uncertainties in marine volcanic ash layer records from ocean drilling cores. Marine Geology, 357, pp.218-224.

Mahony, S.H., Sparks, R.S.J., Wallace, L.M., Engwell, S.L., Scourse, E.M., Barnard, N.H., Kandlbauer, J. and Brown, S.K., 2016. Increased rates of large-magnitude explosive eruptions in Japan in the late Neogene and Quaternary. *Geochemistry, Geophysics, Geosystems*, *17*(7), pp.2467-2479.

Mahood, G.A., 1981. A summary of the geology and petrology of the Sierra La Primavera, Jalisco, Mexico. Journal of Geophysical Research: Solid Earth, 86(B11), pp.10137-10152.

Mangler, M., Prytulak, J., Gisbert, G., Delgado-Granados, H. and Petrone, C.M., 2019. Interplinian effusive activity at Popocatépetl volcano, Mexico: new insights into evolution and dynamics of the plumbing system.

Mangler, M.F., Petrone, C.M. and Prytulak, J., 2022. Magma recharge patterns control eruption styles and magnitudes at Popocatépetl volcano (Mexico). Geology, 50(3), pp.366-370.

Mark, D.F., Petraglia, M., Smith, V.C., Morgan, L.E., Barfod, D.N., Ellis, B.S., Pearce, N.J., Pal, J.N. and Korisettar, R., 2014. A high-precision 40Ar/39Ar age for the Young Toba Tuff and dating of ultra-distal tephra: Forcing of Quaternary climate and implications for hominin occupation of India. Quaternary Geochronology, 21, pp.90-103.

Marshall, A.A., Brand, B.D., Martínez, V., Bowers, J.M., Walker, M., Wanless, V.D., Andrews, B.J., Manga, M., Valdivia, P. and Giordano, G., 2022. The mafic Curacautín ignimbrite of Llaima volcano, Chile. Journal of Volcanology and Geothermal Research, 421, p.107418.

Marti, A., Folch, A., Costa, A. and Engwell, S., 2016. Reconstructing the plinian and co-ignimbrite sources of large volcanic eruptions: A novel approach for the Campanian Ignimbrite. Scientific reports, 6(1), pp.1-11.

Martinez-Abarca R, Lozano-Garcia S, Flores-Martinez A, Ortega-Guerrero B, Caballero M. (2022) PAGES Horizons, 25-27 p. Vol 2

Martínez-Abarca, R., Ortega-Guerrero, B., Lozano-García, S., Caballero, M., Valero-Garcés, B., McGee, D., Brown, E.T., Stockhecke, M., Hodgetts, A.G.E., (2021). Sedimentary stratigraphy of Lake Chalco (Central Mexico) during its formative stages. Int. J. Earth Sci. doi:10.1007/s00531-020-01964-z

Martínez-Serrano, G.P.G.R.G., (2011). Geología y geoquímica de las lavas pleistocénicas del estratovolcán Telapón , Sierra Nevada , México 301–322.

Mastin LG, Randall MJ, Schwaiger HF, Denlinger RP (2013) User's guide and reference to Ash3d—A three-dimensional model for Eulerian atmospheric tephra transport and deposition. In: Open-File Report. Reston, VA, p 25

Mastin, L.G. and Ghiorso, M.S., 2000. A numerical program for steady-state flow of magma-gas mixtures through vertical eruptive conduits. Department of the Interior Washington DC.

Mastin, L.G., Bonadonna, C., Folch, A., Webley, P., Stunder, B. and Pavolonis, M., 2014. Summary of data on well-documented eruptions for validation of volcanic ash transport and dispersal models.

Matthews, N.E., Smith, V.C., Costa, A., Durant, A.J., Pyle, D.M. and Pearce, N.J., 2012. Ultra-distal tephra deposits from super-eruptions: examples from Toba, Indonesia and Taupo Volcanic Zone, New Zealand. Quaternary International, 258, pp.54-79.

Mazzarini, F., Ferrari, L. and Isola, I., 2010. Self-similar clustering of cinder cones and crust thickness in the Michoacan–Guanajuato and Sierra de Chichinautzin volcanic fields, Trans-Mexican Volcanic Belt. Tectonophysics, 486(1-4), pp.55-64.

McDougall, I., Mac Dougall, I. and Harrison, T.M., 1999. Geochronology and Thermochronology by the 40Ar/39Ar Method. Oxford University Press on Demand

McGarvie, D., 2009. Rhyolitic volcano–ice interactions in Iceland. Journal of Volcanology and Geothermal Research, 185(4), pp.367-389.

McLean, D., Albert, P.G., Nakagawa, T., Suzuki, T., Staff, R.A., Yamada, K., Kitaba, I., Haraguchi, T., Kitagawa, J., Smith, V.C., (2018). Integrating the Holocene tephrostratigraphy for East Asia using a high-resolution cryptotephra study from Lake Suigetsu (SG14 core), central Japan. Quat. Sci. Rev. 183, 36–58. doi:https://doi.org/10.1016/j.quascirev.2017.12.013

McLean, D., Albert, P.G., Suzuki, T., Nakagawa, T., Kimura, J.I., Chang, Q., MacLeod, A., Blockley, S., Staff, R.A., Yamada, K. and Kitaba, I., 2020. Refining the eruptive history of Ulleungdo and Changbaishan volcanoes (East Asia) over the last 86 kyrs using distal sedimentary records. Journal of Volcanology and Geothermal Research, 389, p.106669.

McNamara, K., Cashman, K.V., Rust, A.C., Fontijn, K., Chalié, F., Tomlinson, E.L. and Yirgu, G., 2018. Using lake sediment cores to improve records of volcanism at Aluto volcano in the Main Ethiopian Rift. Geochemistry, Geophysics, Geosystems, 19(9), pp.3164-3188.

McNamara, K., Rust, A.C., Cashman, K.V., Castruccio, A. and Abarzúa, A.M., 2019. Comparison of lake and land tephra records from the 2015 eruption of Calbuco volcano, Chile. Bulletin of Volcanology, 81(2), pp.1-15.

Meier, M., Grobéty, B., Arce, J.L., Rueda, H., (2007). Origin and Age of the Volcanic Rocks of Tlaloc Volcano, Sierra Nevada, Central Mexico. AGU, Joint Assembly. (#V23A-01).

Michelfelder, G.S., Feeley, T.C., Wilder, A.D. and Klemetti, E.W., 2013. Modification of the continental crust by subduction zone magmatism and vice-versa: Across-strike geochemical variations of silicic lavas from individual eruptive centers in the Andean Central volcanic zone. Geosciences, 3(4), pp.633-667.

Mirwald, A., Cruz-Atienza, V. M., Díaz-Mojica, J., Iglesias, A., Singh, S. K., Villafuerte, C., & Tago, J. (2019). The 19 September 2017 (Mw7.1) intermediate-depth Mexican

earthquake: A slow and energetically inefficient deadly shock. Geophysical Research Letters, 46, 2054– 2064. https://doi.org/10.1029/2018GL080904

Mooser F (1963). Historia tectónica de la Cuenca de México. Boletín de la Asociación Mexicana de Geólogos Petroleros 15:239–245.

Mora-Alvarez, G., Caballero, C., Urrutia-Fucugauchi, J., Uchiumi, S., (1991). Southward migration of volcanic activity in the Sierra de Las Cruces, Basin of Mexico. A preliminary K-Ar dating and paleomagnetic study: Geofísica Internacional, 30, 61-70.

Morgan, G.B. and London, D., 1996. Optimizing the electron microprobe analysis of hydrous alkali aluminosilicate glasses. American Mineralogist, 81(9-10), pp.1176-1185.

Morgavi, D., Arienzo, I., Montagna, C., Perugini, D. and Dingwell, D.B., 2017. Magma mixing: History and dynamics of an eruption trigger. Volcanic Unrest, pp.123-137.

Mori, L., Gómez-Tuena, A., Cai, Y. and Goldstein, S.L., 2007. Effects of prolonged flat subduction on the Miocene magmatic record of the central Trans-Mexican Volcanic Belt. Chemical geology, 244(3-4), pp.452-473.

Nakagawa, T., Gotanda, K., Haraguchi, T., Danhara, T., Yonenobu, H., Brauer, A., Yokoyama, Y., Tada, R., Takemura, K., Staff, R.A. and Payne, R., 2012. SG06, a fully continuous and varved sediment core from Lake Suigetsu, Japan: stratigraphy and potential for improving the radiocarbon calibration model and understanding of late Quaternary climate changes. Quaternary Science Reviews, 36, pp.164-176.

Neall, V., McGee, L., Turner, M., O'Neill, T., Zernack, A. and Athens, J.S., 2021. Geochemical fingerprinting of Holocene tephras in the Willaumez Isthmus District of West New Britain, Papua New Guinea.

Németh, K. and Kereszturi, G., 2015. Monogenetic volcanism: personal views and discussion. International Journal of Earth Sciences, 104(8), pp.2131-2146.

Németh, K., 2010. Monogenetic volcanic fields: Origin, sedimentary record, and relationship with polygenetic volcanism. In What Is a Volcano? GSA Special Paper (Vol. 470, p. 43).

Nemeth, K., White, J.D., Reay, A. and Martin, U., 2003. Compositional variation during monogenetic volcano growth and its implications for magma supply to continental volcanic fields. Journal of the Geological Society, 160(4), pp.523-530.

Newhall, C.G., 1987. Geology of the Lake Atitlan region, western Guatemala. Journal of Volcanology and Geothermal research, 33(1-3), pp.23-55.

Niespolo EM, Rutte D, Deino AL, Renne PR (2017). Intercalibration and age of the Alder Creek sanidine Ar-40/Ar-39 standard. Quaternary Geochronology 39, 205-213. 10.1016/j.quageo.2016.09.004

Nieto-Torres, A. and Del Pozzo, A.L.M., 2019. Spatio-temporal hazard assessment of a monogenetic volcanic field, near México City. Journal of Volcanology and Geothermal Research, 371, pp.46-58.

Nixon, G. T. (1988). Petrology of the younger andesites and dacites of Iztaccíhuatl volcano, Mexico: II. Chemical stratigraphy, magma mixing, and the composition of basaltic magma influx. Journal of Petrology 29, 265–303.

Nixon, G. T. (1989). The Geology of Iztaccíhuatl Volcano and Adjacent Areas of the Sierra Nevada and Valley of Mexico. Geological Society of America, Special Paper no. 219, 58 pp.

Ortega, E.R., 2016. Litoestratigrafía, petrografía, y geoquímica de la Toba Llano, y su relación con el cráter El Xalapazco, Caldera de Los Humeros, Puebla.

Ortega-Guerrero, B. and Newton, A.J., 1998. Geochemical characterization of Late Pleistocene and Holocene tephra layers from the Basin of Mexico, Central Mexico. Quaternary Research, 50(1), pp.90-106.

Ortega-Guerrero, B., Avendaño, D., Caballero, M., Lozano-García, S., Brown, E.T., Rodríguez, A., García, B., Barceinas, H., Soler, A.M. and Albarrán, A., 2020. Climatic control on magnetic mineralogy during the late MIS 6-Early MIS 3 in Lake Chalco, central Mexico. Quaternary Science Reviews, 230, p.106163.

Ortega-Guerrero, B., García, L.C. and Linares-López, C., 2018. Tephrostratigraphy of the late Quaternary record from Lake Chalco, central México. Journal of South American Earth Sciences, 81, pp.122-140.

Ortega-Guerrero, B., Lozano-García, S., Herrera-Hern, D., (2017). Lithostratigraphy and physical properties of lacustrine sediments of the last ca. 150 kyr from Chalco basin, central México Journal of South American Earth Sciences doi:10.1016/j.jsames.2017.09.003

Paine, A.R., Wadsworth, F.B. and Baldini, J.U., 2021. Supereruption doublet at a climate transition. Communications Earth & Environment, 2(1), pp.1-3.

Pan, B., Liu, G., Cheng, T., Zhang, J., Sun, Z., Ma, B., Wu, H., Liang, G., Guo, M., Kong, Q. and Wei, F., 2021. Development and status of active volcano monitoring in China. Geological Society, London, Special Publications, 510(1), pp.227-252.

Panfil, M.S., Gardner, T.W., Hirth, K.G., (1999). Late Holocene stratigraphy of the Tetimpa archaeological sites, northeast flank of Popocatépetl volcano, central Mexico. Geological Society of America Bulletin, 111(2), 204–218.

Pinel, V. and Albino, F., 2013. Consequences of volcano sector collapse on magmatic storage zones: Insights from numerical modeling. Journal of Volcanology and Geothermal Research, 252, pp.29-37.

Pinti, D.L., Castro, M.C., López-Hernández, A., Hernández-Hernández, M.A., Shouakar-Stash, O., Hall, C.M., Bahena-Romero, J. and Ramírez-Montes, M., 2021. Origin of volatile species and aqueous fluids in the Los Humeros geothermal field, Mexico. Chemical Geology, 584, p.120539.

Pioli, L., Erlund, E., Johnson, E., Cashman, K., Wallace, P., Rosi, M. and Granados, H.D., 2008. Explosive dynamics of violent Strombolian eruptions: the eruption of Parícutin Volcano 1943–1952 (Mexico). Earth and planetary science letters, 271(1-4), pp.359-368.

Plunkett, G., Sigl, M., Schwaiger, H.F., Tomlinson, E.L., Toohey, M., McConnell, J.R., Pilcher, J.R., Hasegawa, T. and Siebe, C., 2022. No evidence for tephra in Greenland from the historic eruption of Vesuvius in 79 CE: implications for geochronology and paleoclimatology. Climate of the Past, 18(1), pp.45-65.

Pomonis, A., Spence, R. and Baxter, P., 1999. Risk assessment of residential buildings for an eruption of Furnas Volcano, Sao Miguel, the Azores. Journal of volcanology and geothermal research, 92(1-2), pp.107-131.

Ponomareva, V., Portnyagin, M. and Davies, S.M., 2015. Tephra without borders: far-reaching clues into past explosive eruptions. Frontiers in Earth Science, 3, p.83.

Preece, K., Mark, D.F., Barclay, J., Cohen, B.E., Chamberlain, K.J., Jowitt, C., Vye-Brown, C., Brown, R.J. and Hamilton, S., 2018. Bridging the gap: 40Ar/39Ar dating of volcanic eruptions from the 'Age of Discovery'. Geology, 46(12), pp.1035-1038.

Pyle, D.M., Ricketts, G.D., Margari, V., van Andel, T.H., Sinitsyn, A.A., Praslov, N.D. and Lisitsyn, S., 2006. Wide dispersal and deposition of distal tephra during the Pleistocene 'Campanian Ignimbrite/Y5'eruption, Italy. Quaternary Science Reviews, 25(21-22), pp.2713-2728.

Ramsey, C.B. and Lee, S., 2013. Recent and planned developments of the program OxCal. Radiocarbon, 55(2), pp.720-730.

Ramsey, C.B., Albert, P.G., Blockley, S.P., Hardiman, M., Housley, R.A., Lane, C.S., Lee, S., Matthews, I.P., Smith, V.C. and Lowe, J.J., 2015. Improved age estimates for key Late Quaternary European tephra horizons in the RESET lattice. Quaternary Science Reviews, 118, pp.18-32.

Rasmussen, T.L., Thomsen, E., Kuijpers, A. and Wastegård, S., 2003. Late warming and early cooling of the sea surface in the Nordic seas during MIS 5e (Eemian Interglacial). Quaternary Science Reviews, 22(8-9), pp.809-821.

Reimer, P.J., Austin, WEN,, Bard, E., Bayliss. A,, Blackwell, P.G., Bronk Ramsey, C., Butzin, M., Cheng, H., Edwards, R.L., Friedrich, M., Grootes, P.M., Guilderson, T.P., Hajdas, I., Heaton, T.J., Hogg, A.G., Hughen, K.A., Kromer, B., Manning, S.W., Muscheler, R., Palmer, J.G., Pearson, C., van der Plicht, J., Reimer, R.W., Richards, D.A., Scott, E.M., Southon, J.R., Turney, C.S.M., Wacker, L., Adolphi, F., Büntgen, U,, Capano, M., Fahrni,

S., Fogtmann-Schulz, A,, Friedrich, R., Köhler, P., Kudsk, S., Miyake, F., Olsen, J., Reinig, F., Sakamoto, M., Sookdeo, A., Talamo, S., 2020. The IntCal20 Northern Hemisphere radiocarbon age calibration curve (0-55 cal kBP). Radiocarbon 62 (4), 725–757. doi: 10.1017/RDC.2020.41.

Renne, P.R., Balco, G., Ludwig, K.R., Mundil, R., Min, K., (2011). Response to the comment by W.H. Schwarz et al. on "Joint determination of K-40 decay constants and Ar-40*/K-40 for the Fish Canyon sanidine standard, and improved accuracy for Ar-40/Ar-39 geochronology" by PR Renne, et al. (2010). Geochimica et Cosmochimica Acta 75 (17), 5097e5100. http://dx.doi.org/ 10.1016/j.gca.2011.06.021.

Riede, F. and Thastrup, M.B., 2013. Tephra, tephrochronology and archaeology–a (re-) view from northern Europe. Heritage Science, 1(1), pp.1-17.

Robidoux, P., Roberge, J. and Adams, C., 2020. Spatial Visualization of Geochemical Data: Application to the Chichinautzin Volcanic Field, Mexico. In Updates in Volcanology-Transdisciplinary Nature of Volcano Science. IntechOpen.

Robin, C., (1984). Le volcan Popocatépetl (Mexique): structure, evolution pétrologique et risques. Bull. Volcanol. 47, 1–23.

Robin, C., Boudal, C., (1987). A gigantic Bezymianny-type event at the begining of modern Popocatépetl. J. Volcanol. Geotherm. Res. 31, 115–130.

Rolandi, G., Paone, A., Di Lascio, M. and Stefani, G., 2008. The 79 AD eruption of Somma: The relationship between the date of the eruption and the southeast tephra dispersion. Journal of Volcanology and Geothermal Research, 169(1-2), pp.87-98.

Rose, W.I., Newhall, C.G., Bornhorst, T.J. and Self, S., 1987. Quaternary silicic pyroclastic deposits of Atitlán Caldera, Guatemala. Journal of volcanology and geothermal research, 33(1-3), pp.57-80.

Rueda, H., Arce, J.L., Macías, J.L., García-Palomo, A., (2006). ~31 ka Plinian–Subplinian eruption at Tláloc Volcano, Sierra Nevada, México. AGU Fall Meeting, San Francisco (CA, US).

Rueda, H., Macías, J.L., Arce, J.L., Gardner, J.E. and Layer, P.W., 2013. The~ 31 ka rhyolitic Plinian to sub-Plinian eruption of Tlaloc volcano, Sierra Nevada, central Mexico. Journal of volcanology and geothermal research, 252, pp.73-91.

Scandone, R., Cashman, K.V. and Malone, S.D., 2007. Magma supply, magma ascent and the style of volcanic eruptions. Earth and Planetary Science Letters, 253(3-4), pp.513-529.

Scarpati, C., Sparice, D. and Perrotta, A., 2020. Dynamics of large pyroclastic currents inferred by the internal architecture of the Campanian Ignimbrite. Scientific reports, 10(1), pp.1-13.

Schipper, C.I., Castro, J.M., Tuffen, H., James, M.R. and How, P., 2013. Shallow vent architecture during hybrid explosive–effusive activity at Cordón Caulle (Chile, 2011–12): evidence

from direct observations and pyroclast textures. Journal of Volcanology and Geothermal Research, 262, pp.25-37.

Schlolaut, G., Brauer, A., Marshall, M.H., Nakagawa, T., Staff, R.A., Ramsey, C.B., Lamb, H.F., Bryant, C.L., Naumann, R., Dulski, P. and Brock, F., 2014. Event layers in the Japanese Lake Suigetsu 'SG06'sediment core: description, interpretation and climatic implications. Quaternary Science Reviews, 83, pp.157-170.

Shane, P. and Smith, I., 2000. Geochemical fingerprinting of basaltic tephra deposits in the Auckland Volcanic Field. New Zealand Journal of Geology and Geophysics, 43(4), pp.569-577.

Shane, P., Sikes, E.L. and Guilderson, T.P., 2006. Tephra beds in deep-sea cores off northern New Zealand: implications for the history of Taupo Volcanic Zone, Mayor Island and White Island volcanoes. Journal of Volcanology and Geothermal Research, 154(3-4), pp.276-290.

Siebe, C., 2000. Age and archaeological implications of Xitle volcano, southwestern Basin of Mexico-City. Journal of Volcanology and Geothermal Research, 104(1-4), pp.45-64.

Siebe, C., Abrams, M. and Macías, J. L. (1995). Derrumbes Gigantes, Depósitos de Avalancha de Escombros y Edad del Actual Cono del Volcán Popocatépetl. Volcán Popocatépetl: Estudios Realizados Durante la Crisis de 1994–1995. pp. 195–220. México D.F.: SINAPROC –CENAPRED – UNAM.

Siebe, C., Abrams, M., Luis Macías, J. and Obenholzner, J., 1996. Repeated volcanic disasters in Prehispanic time at Popocatepetl, central Mexico: Past key to the future?. Geology, 24(5), pp.399-402.

Siebe, C., and Macías, J.L., (2006). Volcanic hazards in the Mexico City metropolitan area from eruptions at Popocatépetl, Nevado de Toluca, and Jocotitlán stratovolcanoes and monogenetic scoria cones in the Sierra Chichinautzin Volcanic Field, in Siebe, C., Macías, J.L., and Aguirre, G., eds., Neogene-Quaternary Continental Margin Volcanism: A perspective from Mexico: Geological Society of America Special Paper 402, p. 253–329

Siebe, C., Delgado, H., Abrams, M., (1993). Recurrent cone collapse of Volcán Popocatépetl, Central Mexico: implications for risk evaluation. Eos. Trans. AGU 74-43, 640.

Siebe, C., Macías, J.L., (2004). Volcanic hazards in the Mexico City metropolitan area from eruptions at Popocatépetl, Nevado de Toluca, and Jocotitlán stratovolcanoes and monogenetic scoria cones in the Sierra Chichinautzin volcanic field. Field Guide, Penrose Conference. Neogene-Quaternary Continental Margin Volcanism, January 2004. Geological Society of America, State of Puebla, México: Boulder, Colorado, p. 77.

Siebe, C., Salinas, S., Arana-Salinas, L., Macías, J.L., Gardner, J., Bonasia, R., (2017). The ~ 23, 500 y 14 C BP White Pumice Plinian eruption and associated debris avalanche and

Tochimilco lava flow of Popocatépetl volcano, México Journal of Volcanology and Geothermal Research, Volumes 333–334, 2017, Pages 66-95, ISSN 0377-0273, https://doi.org/10.1016/j.jvolgeores.2017.01.011.

Siebe, C., Schaaf, P. and Urrutia-Fucugauchi, J., 1999. Mammoth bones embedded in a late Pleistocene lahar from Popocatépetl volcano, near Tocuila, central Mexico. Geological Society of America Bulletin, 111(10), pp.1550-1562.

Siegburg, M., Gernon T.M., Bull J. M., Kier, D., Barfod D. N., Taylor R.N., Abebe, B., Ayele, A., (2018) Geological evolution of the Boset-Bericha Volcanic Complex, Main Ethiopian Rift: 40Ar/39Ar evidence for episodic Pleistocene to Holocene volcanism. Journal of Volcanology and Geothermal Research 351(1) 115-133. 10.1016/j.jvolgeores.2017.12.014

Sieron, K. and Siebe, C., 2008. Revised stratigraphy and eruption rates of Ceboruco stratovolcano and surrounding monogenetic vents (Nayarit, Mexico) from historical documents and new radiocarbon dates. Journal of Volcanology and Geothermal Research, 176(2), pp.241-264.

Silleni, A., Giordano, G., Isaia, R. and Ort, M.H., 2020. The magnitude of the 39.8 ka Campanian Ignimbrite eruption, Italy: method, uncertainties and errors. Frontiers in Earth Science, 8, p.543399.

Simmons, J.M., Cas, R.A.F., Druitt, T.H. and Folkes, C.B., 2016. Complex variations during a caldera-forming Plinian eruption, including precursor deposits, thick pumice fallout, co-ignimbrite breccias and climactic lag breccias: The 184 ka Lower Pumice 1 eruption sequence, Santorini, Greece. Journal of Volcanology and Geothermal Research, 324, pp.200-219.

Singer, B.S., Thompson, R.A., Dungan, M.A., Feeley, T.C., Nelson, S.T., Pickens, J.C., Brown, L.L., Wulff, A.W., Davidson, J.P. and Metzger, J., 1997. Volcanism and erosion during the past 930 ky at the Tatara–San Pedro complex, Chilean Andes. Geological Society of America Bulletin, 109(2), pp.127-142.

Sisson, T.W. and Vallance, J.W., 2009. Frequent eruptions of Mount Rainier over the last~ 2,600 years. Bulletin of Volcanology, 71(6), pp.595-618.

Smith, G.A. and Lowe, D.R., 1991. Lahars: volcano-hydrologic events and deposition in the debris flow—hyperconcentrated flow continuum.

Smith, I.E.M. and Németh, K., 2017. Source to surface model of monogenetic volcanism: a critical review. Geological Society, London, Special Publications, 446(1), pp.1-28.

Smith, R.E., Smith, V.C., Fontijn, K., Gebhardt, A.C., Wastegård, S., Zolitschka, B., Ohlendorf, C., Stern, C. and Mayr, C., 2019. Refining the Late Quaternary tephrochronology for southern South America using the Laguna Potrok Aike sedimentary record. Quaternary Science Reviews, 218, pp.137-156.

Smith, V.C., Isaia, R., Engwell, S.L. and Albert, P., 2016. Tephra dispersal during the Campanian Ignimbrite (Italy) eruption: implications for ultra-distal ash transport during the large caldera-forming eruption. Bulletin of Volcanology, 78(6), pp.1-15.

Smith, V.C., Pearce, N.J., Matthews, N.E., Westgate, J.A., Petraglia, M.D., Haslam, M., Lane, C.S., Korisettar, R. and Pal, J.N., 2011. Geochemical fingerprinting of the widespread Toba tephra using biotite compositions. Quaternary International, 246(1-2), pp.97-104.

Snyder, D., 1997. The mixing and mingling of magmas. Endeavour, 21(1), pp.19-22.

Sosa-Ceballos, G., Gardner, J.E., Siebe, C. and Macías, J.L., 2012. A caldera-forming eruption~ 14,100 14C yr BP at Popocatépetl volcano, México: Insights from eruption dynamics and magma mixing. Journal of Volcanology and Geothermal Research, 213, pp.27-40.

Sosa-Ceballos, G., Macías, J.L., García-Tenorio, F., Layer, P., Schaaf, P., Solís-Pichardo, G., Arce, J.L., (2015). El Ventorrillo, a paleostructure of Popocatépetl volcano: insights from geochronology and geochemistry. Bull. Volcanol. 77 (10):1–20. http://dx.doi. org/10.1007/s00445-015-0975-2.

Sourisseau, D., Macías, J.L., Tenorio, F.G., Avellán, D.R., Girón, R.S., Bernal, J.P., Saldaña, J.L.A. and Murillo, Z.T., 2020. New insights into the stratigraphy and 230Th/U geochronology of the post-caldera explosive volcanism of La Primavera caldera, Mexico. Journal of South American Earth Sciences, 103, p.102747.

Sparks, R.S.J., Bursik, M.I., Carey, S.N., Gilbert, J., Glaze, L.S., Sigurdsson, H. and Woods, A.W., 1997. Volcanic plumes. Wiley.

Sparks, S.R., Sigurdsson, H. and Wilson, L., 1977. Magma mixing: a mechanism for triggering acid explosive eruptions. Nature, 267(5609), pp.315-318.

Sprain, C.J., Renne, P.R., Clemens, W.A. and Wilson, G.P., 2018. Calibration of chron C29r: New high-precision geochronologic and paleomagnetic constraints from the Hell Creek region, Montana. GSA Bulletin, 130(9-10), pp.1615-1644.

Stevenson, J.A., Millington, S.C., Beckett, F.M., Swindles, G.T. and Thordarson, T., 2015. Big grains go far: understanding the discrepancy between tephrochronology and satellite infrared measurements of volcanic ash. Atmospheric Measurement Techniques, 8(5), pp.2069-2091.

Stormer, J.C., Pierson, M.L. and Tacker, R.C., 1993. Variation of F and Cl X-ray intensity due to anisotropic diffusion in apatite during electron microprobe analysis. American Mineralogist, 78(5-6), pp.641-648.

Stremme, W., Ortega, I., Siebe, C. and Grutter, M., 2011. Gas composition of Popocatépetl Volcano between 2007 and 2008: FTIR spectroscopic measurements of an explosive event and during quiescent degassing. Earth and Planetary Science Letters, 301(3-4), pp.502-510.

Sunyé-Puchol, I., Hodgetts, A.G.E., Watt, S.F.L., Arce, J.L., Barfod, D.N., Mark, D.F., Sosa-Ceballos, G., Siebe, C., Dymock, R.C., Blaauw, M. and Smith, V.C., 2022. Reconstructing the middle to late Pleistocene explosive eruption histories of Popocatépetl, Iztaccíhuatl and Tláloc-Telapón volcanoes in Central México. Journal of Volcanology and Geothermal Research, 421, p.107413.

Tamburrino, S., Insinga, D.D., Sprovieri, M., Petrosino, P. and Tiepolo, M., 2012. Major and trace element characterization of tephra layers offshore Pantelleria Island: insights into the last 200 ka of volcanic activity and contribution to the Mediterranean tephrochronology. Journal of Quaternary Science, 27(2), pp.129-140.

Thomas, J.E., Kaufman, D.S., Praet, N., McKay, N.P., Van Daele, M., Jensen, B.J. and De Batist, M., 2021. A 2300-year record of glacier fluctuations at Skilak and Eklutna Lakes, south-central Alaska. Quaternary Science Reviews, 272, p.107215.

Tomlinson, E.L., Albert, P.G. and Menzies, M.A., 2022. Tephrochronology and Geochemistry of Tephra from the Campi Flegrei Volcanic Field, Italy. In Campi Flegrei (pp. 151-174). Springer, Berlin, Heidelberg.

Tuffen, H., McGarvie, D.W., Pinkerton, H., Gilbert, J.S. and Brooker, R.A., 2008. An explosive–intrusive subglacial rhyolite eruption at Dalakvísl, Torfajökull, Iceland. Bulletin of Volcanology, 70(7), pp.841-860.

Turkey, C.S.M. and Lowe, J.J., 2002. Tephrochronology. In Tracking environmental change using lake sediments (pp. 451-471). Springer, Dordrecht.

Tyce, S., 2018. Conquest of the Mexica (Aztec) Empire, 1519–1521. 50 Events that Shaped Latino History: An Encyclopedia of the American Mosaic [2 volumes], p.36.

Valentine, G.A. and Connor, C.B., 2015. Basaltic volcanic fields. In The encyclopedia of volcanoes (pp. 423-439). Academic Press.

Valero-Garcés, B., Stockhecke, M., Lozano-García, S., Ortega, B., Caballero, M., Fawcett, P., Werne, J.P., Brown, E., Najera, S.S., Pearthree, K. and McGee, D., Hodgetts, A.G.E., 2021. Stratigraphy and Sedimentology of the Upper Pleistocene to Holocene Lake Chalco Drill Cores (Mexico Basin). In Limnogeology: Progress, Challenges and Opportunities (pp. 415-443). Springer, Cham.

Van Eaton, A.R. and Wilson, C.J., 2013. The nature, origins and distribution of ash aggregates in a large-scale wet eruption deposit: Oruanui, New Zealand. Journal of Volcanology and Geothermal Research, 250, pp.129-154.

Van Otterloo, J. and Cas, R.A., 2013. Reconstructing the eruption magnitude and energy budgets for the pre-historic eruption of the monogenetic~ 5 ka Mt. Gambier Volcanic Complex, south-eastern Australia. Bulletin of volcanology, 75(12), pp.1-18.

Varley, N., 2012. Volcanoes of Mexico. J Am Ceram Soc, 82, pp.561-565.

Walker, G.P., 1971. Grain-size characteristics of pyroclastic deposits. The Journal of Geology, 79(6), pp.696-714.

Walker, G.P., 1973. Explosive volcanic eruptions—a new classification scheme. Geologische Rundschau, 62(2), pp.431-446.

Walker, G.P., 1993. Basaltic-volcano systems. Geological Society, London, Special Publications, 76(1), pp.3-38.

Walker, G.P.L., Wright, J.V., Clough, B.J. and Booth, B., 1981. Pyroclastic geology of the rhyolitic volcano of La Primavera, Mexico. Geologische Rundschau, 70(3), pp.1100-1118.

Watt, S.F., 2019. The evolution of volcanic systems following sector collapse. Journal of Volcanology and Geothermal Research, 384, pp.280-303.

Watt, S.F., Karstens, J., Micallef, A., Berndt, C., Urlaub, M., Ray, M., Desai, A., Sammartini, M., Klaucke, I., Böttner, C. and Day, S., 2019. From catastrophic collapse to multi-phase deposition: flow transformation, seafloor interaction and triggered eruption following a volcanic-island landslide. Earth and Planetary Science Letters, 517, pp.135-147.

Watt, S.F., Pyle, D.M. and Mather, T.A., 2013. The volcanic response to deglaciation: Evidence from glaciated arcs and a reassessment of global eruption records. Earth-Science Reviews, 122, pp.77-102.

Watt, S.F., Pyle, D.M., Mather, T.A., Martin, R.S. and Matthews, N.E., 2009. Fallout and distribution of volcanic ash over Argentina following the May 2008 explosive eruption of Chaitén, Chile. Journal of Geophysical Research: Solid Earth, 114(B4).

Williams, R. and Krippner, J., 2018. The use of social media in volcano science communication: challenges and opportunities. Volcanica, 1(2), pp.i-viii.

Wilson, L., Sparks, R.S.J. and Walker, G.P., 1980. Explosive volcanic eruptions—IV. The control of magma properties and conduit geometry on eruption column behaviour. Geophysical Journal International, 63(1), pp.117-148.

Wilson, T.M., Stewart, C., Sword-Daniels, V., Leonard, G.S., Johnston, D.M., Cole, J.W., Wardman, J., Wilson, G. and Barnard, S.T., 2012. Volcanic ash impacts on critical infrastructure. Physics and Chemistry of the Earth, Parts A/B/C, 45, pp.5-23.

Witter, J.B., Kress, V.C. and Newhall, C.G., 2005. Volcán Popocatépetl, Mexico. Petrology, magma mixing, and immediate sources of volatiles for the 1994–present eruption. Journal of Petrology, 46(11), pp.2337-2366.

Wulf, S., Hardiman, M.J., Staff, R.A., Koutsodendris, A., Appelt, O., Blockley, S.P., Lowe, J.J., Manning, C.J., Ottolini, L., Schmitt, A.K. and Smith, V.C., 2018. The marine isotope stage 1–5 cryptotephra record of Tenaghi Philippon, Greece: Towards a detailed tephrostratigraphic framework for the Eastern Mediterranean region. Quaternary Science Reviews, 186, pp.236-262.

Xu, J., Liu, G., Wu, J., Ming, Y., Wang, Q., Cui, D., Shangguan, Z., Pan, B., Lin, X. and Liu, J., 2012. Recent unrest of Changbaishan volcano, northeast China: A precursor of a future eruption?. Geophysical Research Letters, 39(16).

Yamamoto, T., Takarada, S. and Suto, S., 1993. Pyroclastic flows from the 1991 eruption of Unzen volcano, Japan. Bulletin of Volcanology, 55(3), pp.166-175.

Zarazúa-Carbajal, M.C. and De la Cruz-Reyna, S., 2021. Digital Elevation Model resolution: Effects on the chronometry-oriented morphological analysis of monogenetic scoria cones in the Sierra Chichinautzin, central Mexico. Geomorphology, 389, p.107842.

APPENDIX C1

THIS DATA IS REDUCED IN SIZE FOR INCLUSION IN THE THESIS. SEE FILE ON LINK PROVIDED BELOW:

https://drive.google.com/drive/folders/1ka5gUXAGsUy5yu5aAfIlh3fZTd2PN_3n?usp=sharing

Volcanic stratigraphy data

Deposit Type	Splice Section	Composition	On-Splice Thickness (cm)	Ghost Section(s)	Combined Basal Depth (m)	Event Free Depth (m)	Thickness Reliability	Grain Size (φ)	Fine ash component	Structures	Possible Reworking	Top/Base	Confidence Volcanic
Tephra	MEXI-CHA16-1D-1C-1-A	F	3.5		0 585	0.55	1	3	Possibly all	1	1	Flat Top/Base	1
Tephra	CHALCO-CHA11-7A-2L-1	M	11.2		4.432	4.285	1	2	No	1	1	Flat Top/Base	1
Tephra	CHALCO-CHA11-7A-3L-1	F	5.2		4.746	4.547	1	1	No	1	1	Flat-Irregular Top/Flat Base	1
Tephra		M	0	MEXI-CHA16-1D-3C-1-A	4.887333333	4.688333333	3	1	No	1	1	Flat Top (as top of core section)/Irregular Base	1
Tephra		M	0	MEXI-CHA16-1D-3C-1-A	5.028666667	4.829666667	1	1	No	1	1	Flat Top/Base	1
Tephra	MEXI-CHA16-1D-3C-1-A	F	42 25		5.5925	4.971	1	0	Yes (upper 31 cm)	1	1	Flat Top/Base	1
Tephra	MEXI-CHA16-1D-3C-1-A	F	1.375		5.92625	5.291	1	1	No	1	1	Flat Top/Base	1
Tephra	MEXI-CHA16-1D-3C-2-A	M	5 25		7 045	6 35725	2	2	No	1	1	Flat Top/Base (at end of section)	1
Tephra	CHALCO-CHA11-7A-4L-1	F	17		7 248	6 39025	1	0	No	1	1	Flat Top (as top of section)/Flat Base	1
Tephra	CHALCO-CHA11-7A-4L-1	M	4.6		7 624	6.72025	1	2	No	1	1	Flat Top/Base	1
Tephra	CHALCO-CHA11-7A-4L-1	M	2.1		7 673	6.74825	1	2	No	1	1	Flat Top/Base	1
Tephra	CHALCO-CHA11-7A-4L-1	M	1.2		7.73	6.79325	3	1	No	1	2	Pod within the middle of the core	1
Tephra	CHALCO-CHA11-7A-4L-2	M	7.2		8 303	7 29425	1	1	No	1	1	Flat Top/Base	1
Tephra	CHALCO-CHA11-7A-4L-2	M	5.5		8.413	7 34925	1	1	No	3	1	Flat Top/Base	1
Tephra	CHALCO-CHA11-7A-4L-2	F	28.3		8 851	7 50425	1	-1	Possibly all	1	1	Flat Top/Base	1
Tephra	MEXI-CHA16-1D-4C-2-A	F	4.625		8 898	7.505	1	3	Possibly all	1	1	Flat Top/Base	1
Tephra		F	0	MEXI-CHA16-1D-5C-1-A	9 219875	7.826875	2	-1	No	1	2	Flat Top (top of core section)/Flat-Irregular Base	1
Tephra	MEXI-CHA16-1D-5C-1-A	M	21.875		9.7605	8.14875	1	1	No	3	1	Flat Top/Base	1
Tephra	MEXI-CHA16-1D-5C-1-A	M	0.875		9.85175	8 23125	1	1	No	1	1	Flat Top/Base	1
Tephra	MEXI-CHA16-1D-5C-2-A	M	4		10.3355	8.675	3	3	Unsure	3	2	Unsure	2
Tephra	MEXI-CHA16-1D-6C-1-A	M	1		11.5415	9.871	1	1	No	1	1	Flat Top/Base	1
Tephra	MEXI-CHA16-1D-6C-2-A	F	1.75		12 324	10 636	1	1	No	1	1	Flat Top/Base	1
Tephra		F	0	CHALCO-CHA11-7A-8L-2	13.16175	11.47375	1	2	No	1	1	Flat Top/Base	1
Tephra	MEXI-CHA16-1D-7C-1-A	M	1		14.0095	12.3115	1	1	No	1	1	Flat Top/Base	1
Tephra	MEXI-CHA16-1D-7C-2-A	M	0.6		14.479	12.775	2	2	No	1	1	Flat Top/Base	1
Tephra	MEXI-CHA16-1D-7C-2-A	F	1.625		15.11325	13 393	1	0	No	1	1	Flat Top/Base	1
Tephra	CHALCO-CHA11-7A-9L-2	M	4.5		15 672	13.90675	2	3	No	1	2	Flat-Irregualr Top/Base	2
Tephra	CHALCO-CHA11-7A-9L-2	F	1.9		16 013	14.22875	1	2	No	1	1	Flat Top/Base	1
Tephra	MEXI-CHA16-1D-8C-1-A	M	1		16 097	14.30275	2	2	No	1	2	Flat-Irregualr Top/Base	1
Tephra	MEXI-CHA16-1D-8C-2-A	F	1.75		16.67075	14 859	1	3	No	1	1	Flat Top/Base	1
Tephra	MEXI-CHA16-1D-8C-2-A	M	3		16.94575	15.104	1	1	No	1	1	Flat Top/Base	1
Tephra		M	0	MEXI-CHA16-1D-9C-1-A	17 201375	15.359625	2	2	No	1	1	Flat-Irregular Top/Base	1
Tephra	CHALCO-CHA11-7A-10L-2	M	2		17.477	15.61525	2	2	No	1	1	Flat-Irregualr Top/Base	1
Tephra	CHALCO-CHA11-7A-12L-1	M	2.5		19.73	17.84325	1	2	No	1	2	Flat Top/Base	1
Tephra	CHALCO-CHA11-7A-12L-1	M	59.5		20 357	17.87525	2	1	No	2	1	Flat Top/Base(base is base of core section)	1
Tephra	MEXI-CHA16-1D-10C-1-A	M	21		20.74325	18.0515	1	1	No	2	1	Flat Top/Base	1
Tephra	MEXI-CHA16-1D-10C-1-A + MEXI-	M	33.5		21.172	18.14525	2	2	No	2	1	Flat Top/Flat Base (as base of section)	1
Tephra	MEXI-CHA16-1D-10C-2-A	M	1		21.61325	18.5765	1	2	No	1	1	Flat Top/Base	1
Tephra	MEXI-CHA16-1D-10C-2-A	M	0.875		21.7245	18 679	1	1	No	1	1	Flat Top/Base	1
Tephra	MEXI-CHA16-1D-10C-2-A	M	0.75		21.797	18.744	1	3	No	1	1	Flat Top/Base	1
Tephra	MEXI-CHA16-1D-10C-3-A + MEXI-	M	21.5		22.142	18 874	2	2	No	2	1	Flat Top (as top of section)/Flat Base (as bottom of section)	1
Tephra	MEXI-CHA16-1C-8Y-1-A	I	6.2		25 344	22 014	2	1	No	1	1	Flat-Irregualar Top/Base	1
Tephra	MEXI-CHA16-1C-8Y-1-A + MEXI-C	M	36.6		25.71	22 014	2	1	No	1	1	Flat-IrregularTop/Flat Base (as bottom of section)	1
Tephra	MEXI-CHA16-1C-9Y-1-A	M	5.5		25.87	22.119	3	2	No	1	2	Pod in the middle of the core	1
Tephra	MEXI-CHA16-1C-9Y-1-A	M	1		26 094	22 333	1	3	No	1	2	Flat Top/ Base	1
Tephra	MEXI-CHA16-1C-9Y-1-A + MEXI-C	M	38.3		26.497	22 353	2	3	No	1	1	Flat-Irregular Top/Flat Base (as base of section)	1
Tephra	MEXI-CHA16-1C-10Y-1-A	M	1.6		26 653	22.493	3	3	No	1	2	Pod at the middle of the core	1
Tephra	MEXI-CHA16-1C-10Y-1-A	M	1.2		26.729	22 557	3	3	No	1	2	Pod at the edge of the core	1
Tephra	MEXI-CHA16-1C-10Y-1-A	M	6.1		27 032	22.799	1	3	No	1	1	Flat-Irregular Top/ Base	1
Tephra	MEXI-CHA16-1C-10Y-1-A	M	9.5		27 222	22 894	1	3	No	1	1	Flat-Irregular Top/ Base	1
Tephra	MEXI-CHA16-1C-10Y-1-A	M	10.5		27 337	22 904	1	3	No	1	2	Flat-Irregular Top/ Base	1
Tephra	MEXI-CHA16-1C-10Y-1-A	M	5		27 531	23 048	3	3	No	1	2	Irregular Top/ Base	1
Tephra	MEXI-CHA16-1C-11Y-1-A	M	2		28 694	24.191	2	3	No	1	1	Flat-Irregular Top/ Base	1
Tephra	MEXI-CHA16-1C-11Y-1-A	M	4		28 968	24.425	1	2	No	1	1	Flat Top/Flat-Irregular Base	1
Tephra	MEXI-CHA16-1C-11Y-1-A	I	0.75		29.3255	24.775	2	0	No	1	2	Irregular Top/Flat Base	1
Tephra		I	0	MEXI-CHA16-1A-10Y-1-A	29.72025	25.16975	2	0	No	1	2	Irregular Top/Flat Base	1
Tephra		M	0	MEXI-CHA16-1A-10Y-1-A	30.115	25.5645	2	2	No	1	2	Semi-Irregular Top/ Base	1
Tephra	MEXI-CHA16-1C-12Y-1-A	M	1.5		30.52475	25.95925	2	3	No	1	2	Irregular Top/ Base	1
Tephra		F	0	CHALCO-CHA08-3A-21S-1	30.9158	26.3503	1	3	Possibly all	1	1	Flat Top/Base	1
Tephra		F	0	CHALCO-CHA08-3A-21S-1	31.30685	26.74135	1	3	Possibly all	1	1	Flat Top/Base	1
Tephra		F	0	CHALCO-CHA08-3A-21S-1	31.6979	27.1324	2	3	Possibly all	1	1	Flat Top/Flat-Irregular Base	1

Deposit Type	Splice Section	Composition	On-Splice Thickness (cm)	Ghost Section(s)	Combined Basal Depth (m)	Event Free Depth (m)	Thickness Reliability	Grain Size (φ)	Fine ash component	Structures	Possible Reworking	Top/Base	Confidence Volcanic
Tephra		F	0	CHALCO-CHA08-3A-21S-1	32.08895	27.52345	2	4	Possibly all	1	1	Flat Top/Base	1
Tephra	MEXI-CHA16-1C-14Y-1-A	M	2		32.5	27.9145	2	2	No	1	1	Flat-Irregular Top/Base	1
Tephra	MEXI-CHA16-1C-14Y-1-A	M	4.2		33 582	28.9545	3	2	No	1	1	Flat Top/Base (as base of core section)	1
Tephra	MEXI-CHA16-1C-15Y-1-A	M	0.5		35.424	30.7915	1	1	No	1	1	Flat Top/Base	1
Tephra	MEXI-CHA16-1C-15Y-1-A	F	2.5		35 554	30.8965	1	1	No	1	1	Flat Top/Base	1
Tephra	MEXI-CHA16-1C-15Y-1-A	F	3.125		35 864	31.17525	1	2	No	1	1	Flat Top/Base	1
Tephra		M	0	MEXI-CHA16-1A-13Y-1-A	36.8065	32.11775	3	2	No	1	2	Pod in the middle of the core	1
Tephra	MEXI-CHA16-1A-14Y-1-A	M	5 25		37.8015	33.06025	3	2	No	1	2	Present within the middle of the core section - no Top/ Base defi	1
Tephra	MEXI-CHA16-1A-15Y-1-A	F	1		38 868	34.11675	2	3	Unsure	1	1	Top/ BaseIrregular but equall	2
Tephra		M	0	MEXI-CHA16-1A-16Y-1-A/MEXI-(	39 575	34.82375	1	2	No	1	1	Flat-Irregualr Top/Flat Base	1
Tephra	MEXI-CHA16-1C-17Y-1-A	F	3		40 312	35.53075	2	2	No	1	1	Irregular Top/Base	1
Tephra	MEXI-CHA16-1C-17Y-1-A	M	0.5		40 627	35.84075	3	3	No	1	1	Irregular Top/Base	2
Tephra	MEXI-CHA16-1C-17Y-1-A	F	1		40.729	35.93275	3	2	No	1	1	Pod in the middle of the core	1
Tephra	MEXI-CHA16-1C-17Y-1-A	M	1		40 812	36.00575	3	2	No	1	1	Irregular Top/Base	2
Tephra	MEXI-CHA16-1C-17Y-1-A	M	5.5		41 202	36.34075	3	2	No	1	1	Irregular Top/Base	1
Tephra	MEXI-CHA16-1C-18Y-1-A	M	2		41 521	36.63975	3	2	No	1	2	Irregular Top/Base	1
Tephra	MEXI-CHA16-1C-18Y-1-A	M	4.7		41 656	36.72775	3	2	No	1	1	Irregular Top/Base	1
Tephra	MEXI-CHA16-1C-18Y-1-A	F	1		41 691	36.75275	3	2	No	1	1	Pod in the middle of the core	1
Tephra	MEXI-CHA16-1C-18Y-1-A	M	1.7		42 321	37.36575	3	3	No	1	1	Irregular Top/Base	2
Tephra	MEXI-CHA16-1C-18Y-1-A	F	3.5		42 381	37.39075	2	0	No	1	1	Flat-Irregular Top/Base	1
Tephra	MEXI-CHA16-1C-18Y-1-A	F	1.7		42.455	37.44775	2	0	No	1	2	Flat-Irregular Top/Base	1
Tephra	MEXI-CHA16-1C-18Y-1-A	F	0.8		42 606	37.59075	2	0	No	1	2	Flat-Irregular Top/Base	1
Tephra	MEXI-CHA16-1A-17Y-1-A	F	11 25		43.4185	38.29075	2	3	No	1	1	Top/BaseIrregular	1
Tephra	MEXI-CHA16-1A-17Y-1-A	F	5		43 511	38.33325	2	3	No	1	1	Top/BaseIrregular	2
Tephra	MEXI-CHA16-1A-17Y-1-A	F	3		44.111	38.90325	2	2	No	1	1	Irregular Top/Base at Base of core section	2
Tephra	MEXI-CHA16-1A-19Y-1-A	M	6.2		45 961	40.69125	3	2	No	1	1	Irregular Top/Base	1
Tephra	MEXI-CHA16-1B-23Y-1-A	M	0.8		46 949	41.67125	3	3	No	1	1	Flat-Irregular Top/Base(not continuous across core section width	2
Tephra		M	0	CHALCO-CHA08-5A-8S-1	47.05508333	41.77733333	2	2	No	1	1	Flat-Irregular Top/Base	1
Tephra		F	0	CHALCO-CHA08-5A-8S-1	47.16116667	41 88341667	2	2	No	1	1	Flat-Irregular Top/Base	1
Tephra	MEXI-CHA16-1C-20Y-1-A	F	4.625		47.3135	41.9895	2	2	No	1	1	Flat-Irregular Top/Base	1
Tephra		F	0	CHALCO-CHA08-5A-8S-1	49 978875	44.654875	1	2	No	2	1	Flat Top/Base	1
Tephra		I	0	MEXI-CHA16-1C-24Y-1-A/CHAL	52.64425	47.32025	2	0	No	1	1	Flat-Irregular Top/Base	1
Tephra		I	0	MEXI-CHA16-1C-25Y-1-A	55 309625	49.985625	3	0	No	1	1	Flat-Irregular Top/Base	1
Tephra	MEXI-CHA16-1B-31Y-1-A	M	6		58 035	52 651	1	3	No	1	1	Flat Top/Base	1
Tephra	MEXI-CHA16-1C-26Y-1-A	F	0.875		58.3875	52.99475	1	2	No	1	1	Flat-Irregular Top/Base	1
Tephra	MEXI-CHA16-1C-27Y-1-A	M	3		59.413	53.99025	1	2	No	1	1	Flat Top/Base	1
Tephra	MEXI-CHA16-1C-27Y-1-A	M	3		59 663	54.21025	1	3	No	1	1	Flat Top/Base	1
Tephra	MEXI-CHA16-1C-27Y-1-A	F	1		59.723	54.26025	1	2	No	1	1	Flat Top/Base	1
Tephra	MEXI-CHA16-1C-27Y-1-A	M	1		59 933	54.46025	1	2	No	1	1	Flat Top/Base	2
Tephra	MEXI-CHA16-1C-28Y-1-A	M	2		60 599	55.10625	1	2	No	1	1	Flat Top/Base	1
Tephra	MEXI-CHA16-1C-28Y-1-A	F	3		60.799	55.27625	1	2	No	1	1	Flat Top/Base (base bioturbated but not affecting thickness)	1
Tephra	MEXI-CHA16-1C-28Y-1-A	M	1.5		61 069	55.53125	1	2	No	1	1	Flat Top/Base	1
Tephra	MEXI-CHA16-1B-34Y-1-A	M	2		62.489	56.93125	1	3	No	1	1	Flat Top/Base	1
Tephra	MEXI-CHA16-1B-35Y-1-A	F	3.5		63.784	58.19125	1	2	No	1	1	Flat Top/Base	1
Tephra		M	0	CHALCO-CHA08-3A-47S-1	65.06866667	59.47591667	1	1	No	1	1	Flat Top/Base	1
Tephra		F	0	CHALCO-CHA08-3A-48S-1	66.35333333	60.76058333	1	2	No	1	1	Flat Top/Base	1
Tephra	MEXI-CHA16-1C-32Y-1-A	M	1		67 648	62.04525	2	3	No	1	1	Flat-Irregular Top/Base	2
Tephra		M	0	CHALCO-CHA08-3A-51S-1	67.74572727	62.14297727	2	2	No	1	1	Flat-Irregular Top/Base	1
Tephra		I	0	CHALCO-CHA08-3A-51S-1	67.84345455	62 24070455	1	1	No	2	1	Flat Top/Base	1
Tephra		M	0	CHALCO-CHA08-3A-52S-1	67.94118182	62 33843182	1	2	No	1	1	Flat Top/Base	1
Tephra		I	0	CHALCO-CHA08-3A-52S-1	68.03890909	62.43615909	2	2	No	1	1	Flat-Irregular Top/Base	1
Tephra		M	0	CHALCO-CHA08-3A-52S-1	68.13663636	62 53388636	1	2	No	1	1	Flat-Irregular Top/Base	1
Tephra		M	0	CHALCO-CHA08-3A-54S-1	68.23436364	62 63161364	2	2	No	1	2	Flat-Irregular Top/Base	1
Tephra		M	0	CHALCO-CHA08-3A-54S-1	68.33209091	62.72934091	1	1	No	1	1	Flat Top/Base	1
Tephra		M	0	CHALCO-CHA08-3A-54S-1	68.42981818	62 82706818	1	3	No	1	1	Flat Top/Base	1
Tephra		M	0	CHALCO-CHA08-3A-54S-1	68.52754545	62 92479545	1	3	No	1	1	Flat Top/Base	1
Tephra		F	0	CHALCO-CHA08-3A-54S-1	68.62527273	63 02252273	2	1	No	1	1	Irregular Top/Base	1
Tephra	MEXI-CHA16-1C-33Y-1-A	F	1		68.733	63.12025	1	2	No	1	1	Flat Top/Base	1
Tephra	MEXI-CHA16-1C-33Y-1-A	F	1		68 833	63.21025	3	2	No	1	1	Pod in the middle of the core	1
Tephra	MEXI-CHA16-1C-33Y-1-A	I	2		69 253	63.61025	1	1	No	1	1	Flat Top/Base	1
Tephra		M	0	CHALCO-CHA08-5A-29S-1	69.9865	64.34375	1	1	No	1	1	Flat Top/Base	1

Deposit Type	Splice Section	Composition	On-Splice Thickness (cm)	Ghost Section(s)	Combined Basal Depth (m)	Event Free Depth (m)	Thickness Reliability	Grain Size (φ)	Fine ash component	Structures	Possible Reworking	Top/Base	Confidence Volcanic
Tephra		I	0	CHALCO-CHA08-3A-57S-1	70.72	65.07725	1	2	No	1	1	Flat Top/Base	1
Tephra		M	0	CHALCO-CHA08-3A-58S-1	71.4535	65.81075	2	3	No	1	1	Flat-Irregular (dispersed) Top/Base	2
Tephra	MEXI-CHA16-1A-29Y-1-A	F	8		72 267	66.54425	2	4	Possibly all	1	1	Flat-Irregular Top/Base	1
Tephra	MEXI-CHA16-1A-29Y-1-A	F	0.5		72 637	66.90925	3	2	No	1	1	Flat-Irregular Top/Base (disturbed as nodules in sediment)	1
Tephra	MEXI-CHA16-1A-30Y-1-A	I	2.5		73 616	67.86325	2	2	No	1	1	Flat-Irregular Top/Base	2
Tephra	MEXI-CHA16-1A-30Y-1-A	F	4		74 251	68.45825	3	3	Possibly all	1	1	Flat-Irregualr Top/Base (material throughout core section)	1
Tephra	CHALCO-CHA08-5A-32S-1	F	4 25		75 335	69.49975	1	2	Possibly	1	1	Flat Top/Base (biotubated)	1
Tephra	CHALCO-CHA08-5A-32S-1	M	1		75.705	69.85975	1	2	No	1	1	Flat Top/Base	1
Tephra	CHALCO-CHA08-5A-33S-1	F	1.75		76.0125	70.14975	3	1	No	1	1	Irregular Top/Base	1
Tephra	CHALCO-CHA08-5A-33S-1	M	1 25		76.795	70.91975	1	2	No	1	1	Flat Top/Base	1
Tephra	CHALCO-CHA08-5A-34S-1	M	2		77.0125	71.11725	1	3	No	1	1	Flat Top/Base	1
Tephra	MEXI-CHA16-1B-42Y-1-A	M	3		77 575	71.64975	1	2	No	1	1	Flat Top/Base	1
Tephra	MEXI-CHA16-1B-42Y-1-A	F	1		77 815	71.87975	1	0	No	1	1	Flat Top/Base	1
Tephra	MEXI-CHA16-1B-43Y-1-A	M	1		78.32	72.37475	1	3	No	1	1	Flat Top/Base	1
Tephra	MEXI-CHA16-1B-43Y-1-A	M	1		78 385	72.42975	1	3	Possibly all	1	1	Flat Top/Base	1
Tephra	MEXI-CHA16-1B-43Y-1-A	F	4		78 815	72.81975	1	4	Possibly all	1	1	Flat Top/Base	1
Tephra	MEXI-CHA16-1B-43Y-1-A	F	5		79.48	73.43475	2	2	No	1	1	Flat-Irregular Top/Base	1
Tephra		M	0	MEXI-CHA16-1C-39Y-1-A/CHAL	80.0065	73.96125	1	2	No	1	1	Flat Top/Base	1
Tephra	MEXI-CHA16-1B-44Y-1-A	M	13.8		80 671	74.48775	1	3	No	1	1	Irregular Top/Flat Base	1
Tephra		F	0	CHALCO-CHA08-5A-37S-1	80 968	74.78475	1	1	No	1	1	Flat Top/Base	1
Tephra	MEXI-CHA16-1B-44Y-1-A	F	4		81 305	75.08175	1	1	No	1	1	Flat Top/Base	1
Tephra	MEXI-CHA16-1B-45Y-1-A	I	2		81.775	75.53175	1	2	No	1	1	Flat-Irregular Top/base	1
Tephra	MEXI-CHA16-1B-45Y-1-A	I	2		81 925	75.66175	3	2	No	1	2	Pod in the middle of the core	1
Tephra		I	0	MEXI-CHA16-1A-35Y-1-A/MEXI-(	82.7395	76.47625	1	3	Possibly all	1	1	Flat Top/Base	2
Tephra		I	0	MEXI-CHA16-1C-41Y-1-A	83 554	77.29075	1	1	No	1	1	Flat Top/Base (angled due to drilling)	1
Tephra		F	0	CHALCO-CHA08-3A-66S-1	84.3685	78.10525	1	0	No	1	1	Flat Top/Flat-Irregular Base	1
Tephra	MEXI-CHA16-1B-47Y-1	M	3.1		85 214	78.91975	2	2	No	1	1	Irregular Top/Base	2
Tephra	MEXI-CHA16-1B-47Y-1	M	19.6		85.463	78.97275	1	3	No	1	1	Flat -Irregular Top/Base	2
Tephra	MEXI-CHA16-1B-48Y-1	M	6.3		86 236	79.68275	1	2	No	1	1	Irregular Top/Base (drilling artefacts)	1
Tephra		I	0	MEXI-CHA16-1C-43Y-1-A/CHAL	87 254	80.70075	1	1	No	1	1	Flat-Irregular Top/Base (not a continuous layer)	1
Tephra		M	0	CHALCO-CHA08-3A-69S-1	88 272	81.71875	1	2	No	1	1	Flat Top/Base	1
Tephra	MEXI-CHA16-1B-49Y-2-A	F	1		89.3	82.73675	1	3	No	1	1	Flat Top/Base	1
Tephra		F	0	CHALCO-CHA08-6A-7S-1	89.3865	82.82325	2	4	Possibly all	1	1	Irregular Top/Base as bioturbted	1
Tephra		M	0	MEXI-CHA16-1A-36Y-1-A	89.473	82.90975	3	3	No	3	2	Unsure	2
Tephra		F	0	MEXI-CHA16-1A-36Y-1-A	89.5595	82.99625	2	0	No	1	1	Irregular Top/Base is smeared down side of core section	1
Tephra	CHALCO-CHA08-6A-8S-1	F	1.2		89 658	83.08275	1	2	No	1	1	Irregular Top/ Base (flamed through section)	1
Tephra	CHALCO-CHA08-6A-8S-1	F	1		89.789	83.20375	1	1	No	1	1	Irregular Top/Flat-Irregualr Base	1
Tephra	CHALCO-CHA08-6A-8S-1	F	1.1		89 836	83.23975	2	3	Possibly all	1	1	Irregular Top/Flat-Irregualr Base	1
Tephra	CHALCO-CHA08-6A-8S-1	F	1.5		89 989	83.37775	3	3	Possibly all	1	1	Pod in the middle of the core	1
Tephra		M	0	MEXI-CHA16-1C-46Y-1-A	90.2165	83.60525	3	1	No	1	1	Flat-Irregular Top/Base (nodule)	1
Tephra	CHALCO-CHA08-6A-9S-1	F	2		90.464	83.83275	3	3	Possibly all	1	1	Pod at the edge of the core	1
Tephra		I	0	MEXI-CHA16-1B-51Y-1	90 809	84.17775	1	1	No	1	1	Flat Top/Base	1
Tephra		M	0	MEXI-CHA16-1B-51Y-1	91.154	84.52275	1	1	No	1	1	Flat -Irregular Top/Base	1
Tephra		M	0	MEXI-CHA16-1B-51Y-1	91.499	84.86775	1	2	No	1	1	Flat -Irregular Top/Base	1
Tephra		M	0	MEXI-CHA16-1B-51Y-1	91 844	85.21275	1	1	No	1	1	Flat -Irregular Top/Base	1
Tephra	CHALCO-CHA08-6A-10S-1	F	0.5		92.194	85.55775	1	3	Possibly all	1	1	Flat-Irregualr Top/Base	1
Tephra	MEXI-CHA16-1C-48Y-1-A	I	2.5		92 696	86.03475	3	2	Possibly all	1	1	Flat-Irregular Top/Base	2
Tephra	CHALCO-CHA08-6A-11S-1	F	2		93.2585	86.57725	1	2	No	1	1	Irregular Top/ Base (drilling mushroom and smearing down core s	1
Tephra	CHALCO-CHA08-3A-74S-1	F	2.5		93 861	87.15475	3	2	No	1	1	Pod at the edge of the core section	2
Tephra	CHALCO-CHA08-6A-13S-1	M	1.5		95 056	88.33475	2	2	No	1	1	Flat-Irregular Top/base	1
Tephra	CHALCO-CHA08-6A-13S-1	M	1		95.181	88.44975	2	2	No	1	1	Flat-Irregular Top/base	1
Tephra	CHALCO-CHA08-6A-13S-1	M	1		95 326	88.58475	2	3	No	1	1	Flat Top/Base (discontinuous across core width)	2
Tephra	CHALCO-CHA08-6A-13S-1	M	0.5		95.431	88.68475	2	3	No	1	1	Flat Top/Base (discontinuous across core width)	2
Tephra	CHALCO-CHA08-6A-13S-1	M	0.7		95 658	88.90475	3	3	No	1	1	Pod within the middle-side of the core	2
Tephra	MEXI-CHA16-1B-54Y-1-A	M	20.5		96 381	89.42275	2	2	No	1	1	Flat-irregular Top/Flat Base (as base of the core)	1
Tephra	MEXI-CHA16-1A-41Y-1-A	M	14.5		96 586	89.48275	3	2	No	1	1	Irregular Top/Base	1
Tephra	MEXI-CHA16-1C-50Y-1-A	F	12		96.706	89.48275	2	2	No	1	1	Flat-Irregualr Top/Flat Base	1
Tephra	MEXI-CHA16-1C-50Y-1-A	M	10		96 806	89.48275	1	0	No	1	1	Flat Top/ Base	1
Tephra		F	0	MEXI-CHA16-1B-55Y-1-A	96.81975	89.4965	2	2	No	1	1	Flat-Irregualr Top/Flat Base	1
Tephra	MEXI-CHA16-1C-50Y-1-A	F	5		96.8835	89.51025	2	4	Possibly all	1	1	Flat Top/Irregular Base (nodules of the tephra are included in the	1
Tephra	MEXI-CHA16-1C-51Y-1-A	I	3.75		97 931	90.52025	2	2	No	1	1	Flat Top (at section top)/Irregular Disturbed Base	1

Deposit Type	Splice Section	Composition	On-Splice Thickness (cm)	Ghost Section(s)	Combined Basal Depth (m)	Event Free Depth (m)	Thickness Reliability	Grain Size (φ)	Fine ash component	Structures	Possible Reworking	Top/Base	Confidence Volcanic
Tephra	MEXI-CHA16-1C-51Y-1-A	M	16.375		98.60225	91.02775	2	2	No	1	1	Flat-Irregular Top/Base	1
Tephra	MEXI-CHA16-1A-43Y-1-A	M	9 25		100.126	92.459	1	2	No	1	1	Flat-Irregular Top/Flat Base	1
Tephra	CHALCO-CHA08-4A-3S-1	M	5		100.176	92.459	1	1	No	1	1	Flat Top/Base	1
Tephra	CHALCO-CHA08-4A-3S-1	I	2		100 266	92 529	3	1	No	1	1	Pod at the edge of the core	1
Tephra	CHALCO-CHA08-4A-3S-1	I	2		100.766	93 009	3	3	No	1	1	Irregular Top/Base (dispersed in section)	1
Tephra	CHALCO-CHA08-4A-4S-1	I	3.5		101 081	93 289	2	0	No	1	1	Irregular-Flat Top/Base (concetrated at the one side of the sectio	1
Tephra	CHALCO-CHA08-4A-4S-1	F	2.3		101.141	93 326	3	3	No	1	1	Irregular Top/Base (dispersed in section)	1
Tephra	CHALCO-CHA08-4A-4S-1	F	1.1		101.408	93 582	1	3	Possibly all	1	1	Flat Top/base	1
Tephra	MEXI-CHA16-1B-58Y-1-A	M	0.8		102 326	94.492	3	1	No	1	1	Pod within the middle of the core	1
Tephra	MEXI-CHA16-1B-58Y-1-A	M	1.5		102 626	94.777	2	2	No	1	1	Flat-Irregular Top/base	1
Tephra	CHALCO-CHA08-4A-5S-1	M	4.2		103 209	95 318	1	2	No	1	1	Flat Top/Base	1
Tephra	CHALCO-CHA08-3A-82S-1	M	3.5		103.464	95 538	1	1	No	1	1	Flat Top/Base	1
Tephra	CHALCO-CHA08-4A-6S-1	M	5.2		103 806	95 828	1	1	No	1	1	Flat Top/Base	1
Tephra	CHALCO-CHA08-4A-6S-1	M	3.5		103 951	95 938	2	2	No	1	1	Flat-Irregular Top/Base	1
Tephra	CHALCO-CHA08-4A-6S-1	M	7.1		104 553	96.469	1	1	No	2	1	Flat Top/Base	1
Tephra	MEXI-CHA16-1B-59Y-1-A	M	3		104.756	96 642	2	2	No	1	1	Flat-Irregular Top/base	1
Tephra	CHALCO-CHA08-4A-7S-1	M	3.5		105.169	97.02	1	1	No	1	1	Flat Top/Base	1
Tephra	CHALCO-CHA08-4A-7S-1	M	0.7		105.721	97 565	1	1	No	1	1	Flat Top/Base	1
Tephra		F	0	CHALCO-CHA08-4A-8S-1	106.0885	97.9325	1	3	Possibly all	1	1	Flat Top/Base	1
Tephra	MEXI-CHA16-1C-56Y-1-A	M	1		106.466	98.3	2	2	No	1	1	Flat-Irregular Top/base	1
Tephra	MEXI-CHA16-1A-48Y-1-A	F	1.5		107.412	99 231	3	2	No	1	1	Pod within the middle of the core	1
Tephra	MEXI-CHA16-1A-48Y-1-A	F	6 25		107.5645	99 321	1	3	Potentially all	1	1	Flat Top/ Base	1
Tephra	MEXI-CHA16-1A-48Y-1-A	F	2		107 622	99.3585	3	2	No	1	2	Pod within the middle of the core	1
Tephra		F	0	MEXI-CHA16-1C-57Y-1-A	108.143	99.8795	2	2	No	1	1	Flat-Irregualr Top/Base	1
Tephra		F	0	CHALCO-CHA08-4A-9S-1	108 664	100.4005	1	4	Possibly all	1	1	Flat Top/Base	1
Tephra		F	0	CHALCO-CHA08-4A-9S-1	109.185	100.9215	1	3	Possibly all	1	1	Flat Top/Base	1
Tephra	CHALCO-CHA08-4A-10S-1	F	1.5		109.446	101.1675	1	3	Possibly all	1	1	Flat Top/Base	1
Tephra	CHALCO-CHA08-4A-10S-1	F	1.5		109.721	101.4275	1	-1	No	1	1	Flat Top/Base	1
Tephra	CHALCO-CHA08-4A-10S-1	F	0.4		109 875	101.5775	1	3	Possibly all	1	1	Flat Top/Base	1
Tephra		I	0	MEXI-CHA16-1A-50Y-1-A	109.8886667	101.5911667	2	2	No	1	1	Irregular Top/Base	2
Tephra		M	0	MEXI-CHA16-1A-50Y-1-A	109.9023333	101.6048333	2	1	No	1	1	Irregular Top/Base (some flaming into sediments below)	1
Tephra	MEXI-CHA16-1A-50Y-1-A + MEXI-(	F	39.6		110 312	101.6185	2	2	Maybe upper 6 cm?	2	1	Flat Top/Flat Base (at core section end)	1
Tephra		M	0	MEXI-CHA16-1A-54Y-1-A/MEXI-(	112.485375	103.791875	3	2	No	1	1	Irregualr Dispersed Top/Base	1
Tephra	MEXI-CHA16-1A-54Y-1-A	F	1.125		114.67	105.96525	3	2	No	1	1	Irregualr Dispersed Top/Base	1
Tephra	MEXI-CHA16-1A-54Y-1-A	M	0.875		114.82375	106.11025	3	2	No	1	1	Irregualr Dispersed Top/Base ('nodule' within sediment)	1
Tephra	CHALCO-CHA08-4A-16S-1	F	7		115.775	106.9915	1	-1	No	1	1	FlatTop/Base (some smearing down core section side)	1
Tephra		F	0	MEXI-CHA16-1B-67Y-1-A	116.0725	107 289	2	0	No	1	1	Flat-Irregular Top/Irregular Base	1
Tephra	MEXI-CHA16-1B-67Y-1-A	I	2.5		116 395	107.5865	3	2	No	1	1	Irrgular Top/Base (dispersed)	1
Tephra	CHALCO-CHA08-4A-17S-1	M	5		116.757	107.8985	1	1	No	1	1	Flat-Irregular Top/Base	1
Tephra	MEXI-CHA16-1B-68Y-1-A	F	1		117.777	108.9085	3	1	No	1	1	Pod within the middle to edge of the core	1
Tephra		M	0	MEXI-CHA16-1A-56Y-1-A/MEXI-(	118.2048333	109.3363333	3	1	No	1	1	Irregular Top/Base (flamed throughout)	1
Tephra		F	0	MEXI-CHA16-1A-56Y-1-A/MEXI-(	118.6326667	109.7641667	3	2	No	1	1	Irregular Top/Base (flamed throughout/concentrated in a 'nodule'	1
Tephra	MEXI-CHA16-1A-56Y-1-A	M	3		119.0905	110.192	2	2	No	1	1	Irregular Top/Flat-Irregular Base	1
Tephra		F	0	MEXI-CHA16-1A-57Y-1-A	119.431125	110.532625	3	1	No	1	1	Pod within the middle of the coe	1
Tephra	MEXI-CHA16-1A-57Y-1-A	F	3.5		119.80675	110.87325	2	0	No	1	1	Irregular Top/Base	1
Tephra	MEXI-CHA16-1A-57Y-1-A	F	1.5		120.108	111.1595	1	2	No	1	1	Flat Top/Base (some slight mushrooming)	1
Tephra		F	0	MEXI-CHA16-1C-64Y-1-A	120.77525	111.82675	3	1	No	1	1	Pod within the middle of the coe	1
Tephra		F	0	MEXI-CHA16-1C-65Y-1-A	121.4425	112.494	3	2	No	1	1	Pod in the middle of the sediment	1
Tephra		F	0	MEXI-CHA16-1C-65Y-1-A	122.10975	113.16125	3	1	No	1	1	Pod within the middle of the coe	1
Tephra	CHALCO-CHA08-6A-15S-1	M	2.3		122.8	113.8285	1	1	No	2	1	Flat Top/Base	1
Tephra	CHALCO-CHA08-6A-15S-1	F	1.3		123.113	114.1285	1	0	No	1	1	Flat Top/Base	1
Tephra	CHALCO-CHA08-4A-22S-1	F	1.4		123.422	114.4235	1	3	No	1	1	Flat Top/Base	1
Tephra	CHALCO-CHA08-4A-22S-1	M	0.6		123.445	114.4405	1	3	No	1	1	Flat Top/Base	1
Tephra	CHALCO-CHA08-4A-22S-1	F	1.8		123.478	114.4555	2	0	No	1	1	Flat-Irregular Top/Flat Base	1
Tephra	CHALCO-CHA08-4A-22S-1	F	2.5		123 508	114.4605	1	4	Possibly all	1	1	Flat Top/Base	1
Tephra	CHALCO-CHA08-6A-16S-1	M	5.7		123.67	114.5655	1	1	No	2	1	Flat Top/Base	1
Tephra	CHALCO-CHA08-6A-17S-1	I	0.8		124 916	115.8035	1	2	No	1	1	Flat Top/Base	1
Tephra	MEXI-CHA16-1C-67Y-1-A	M	1		125.428	116.3055	1	2	No	1	1	Flat Top/Base	1
Tephra		F	0	MEXI-CHA16-1A-61Y-1-A	126.2665	117.144	2	1	No	1	1	Flat-Irregular Top/ Base	1
Tephra	MEXI-CHA16-1C-68Y-1-A	M	13.375		127.23875	117.9825	1	1	No	2	1	Flat Top/Base	1
Tephra		M	0	MEXI-CHA16-1C-69Y-1-A	127 585625	118.329375	1	2	No	1	1	Flat-Irregular Top/Base	1

Deposit Type	Splice Section	Composition	On-Splice Thickness (cm)	Ghost Section(s)	Combined Basal Depth (m)	Event Free Depth (m)	Thickness Reliability	Grain Size (φ)	Fine ash component	Structures	Possible Reworking	Top/Base	Confidence Volcanic
Tephra		M	0	MEXI-CHA16-1C-69Y-1-A	127.9325	118.67625	2	2	No	1	1	Irregular Top/Base	1
Tephra		F	0	MEXI-CHA16-1C-69Y-1-A	128 279375	119.023125	3	3	Possibly all	1	1	Pod at the edge of core	2
Tephra	MEXI-CHA16-1C-70Y-1-A	M	11.375		128.74	119.37	1	2	No	2	1	Flat-Irregular Top/Flat Base	1
Tephra	MEXI-CHA16-1C-70Y-1-A	M	2		129.09	119.7	2	3	No	1	1	Irregular Top/Base	2
Tephra	MEXI-CHA16-1C-70Y-1-A	F	3.5		129.98	120 555	2	4	Possibly all	1	1	Irregular Top/Flat Base	1
Tephra	MEXI-CHA16-1C-70Y-1-A	F	4		130.06	120 595	2	4	Possibly all	1	1	Irregular Top/Flat Base	1
Tephra	MEXI-CHA16-1A-63Y-1-A	M	9		130.68	121.125	1	1		1	1	Flat-Irregualr Top/Flat Base	1
Tephra	MEXI-CHA16-1A-63Y-1-A	F	5		131	121 395	1	3	Possibly all	1	1	Flat-Irregular Top/Base	1
Tephra	MEXI-CHA16-1A-63Y-1-A	M	3.5		131 285	121 645	1	2	No	1	1	Mushroomed Top/Flat-Irregular Base	1
Tephra	MEXI-CHA16-1A-64Y-1-A	M	1.6		131 889	122 233	1	3	No	1	1	Mushroomed Top/Flat-Irregular Base	1
Tephra	MEXI-CHA16-1A-64Y-1-A	M	2.625		132.03125	122 349	1	2	No	1	1	Mushroomed Top/Flat-Irregular Base	1
Tephra	MEXI-CHA16-1A-64Y-1-A	F	5		132.89	123.15775	1	3	Possibly all	1	1	Flat-Irregular Top/Base	1
Tephra	MEXI-CHA16-1C-72Y-1-A	M	9		134.6225	124.80025	1	1	No	2	1	Mushroomed Top/Flat-Irregular Base	1
Tephra	MEXI-CHA16-1C-72Y-1-A	F	7.5		134.99	125.09275	1	4	Possibly all	1	1	Flat-Irregular Top/Base	1
Tephra		M	0	MEXI-CHA16-1A-67Y-1-A	135.2726667	125.3754167	1	1	No	1	1	Flat-Irregular Top/Flat Base	1
Tephra		F	0	CHALCO-CHA08-6A-25S-1	135.5553333	125.6580833	1	3	Possibly all	1	1	Flat Top/Base	1
Tephra	MEXI-CHA16-1C-73Y-1-A	M	7		135 908	125.94075	3	2	No	1	1	Irregular Top/ Base	1
Tephra		F	0	CHALCO-CHA08-6A-26S-1	136 058	126.09075	1	1	No	1	1	Flat Top/Base	1
Tephra		F	0	CHALCO-CHA08-6A-26S-1	136 208	126.24075	1	2	No	1	1	FlatTop/Flat-Irregular Base	1
Tephra		F	0	CHALCO-CHA08-6A-26S-1	136 358	126.39075	1	4	Possibly all	1	1	Flat Top/Base	1
Tephra	MEXI-CHA16-1C-73Y-1-A	I	2.5		136 533	126.54075	1	0	No	1	1	Flat Top/Base	1
Tephra		I	0	CHALCO-CHA08-6A-26S-1	136.6046667	126.6124167	1	1	No	1	1	Flat Top/Base	1
Tephra		M	0	CHALCO-CHA08-6A-26S-1	136.6763333	126.6840833	1	1	No	1	1	Flat Top/Base	1
Tephra	MEXI-CHA16-1C-73Y-1-A	F	3.5		136.783	126.75575	1	4	Possibly all	1	1	Flat Top/Base	1
Tephra	CHALCO-CHA08-6A-27S-1	I	11.3		137 244	127.10375	1	1	No	2	1	Flat Top/Base	1
Tephra	CHALCO-CHA08-6A-27S-1	F	4.9		137 544	127.35475	1	1	Upper 2 5 cm	1	1	Flat Top/Base	1
Tephra	CHALCO-CHA08-6A-27S-1	F	3.5		137 684	127.45975	1	4	Possibly all	1	1	Flat Top/Base	1
Tephra	CHALCO-CHA08-6A-28S-1	F	1.2		138.422	128.18575	1	1	No	1	1	Flat Top/Base (bioturbated)	1
Tephra		F	0	MEXI-CHA16-1A-70Y-1-A	139.7885	129.55225	1	1	No	1	1	Flat-Irregular Top/FlatBase	1
Tephra	MEXI-CHA16-1C-77Y-1-A	F	3 25		141.1875	130.91875	2	-1	No	1	1	Irregular Top/Base	1
Tephra	MEXI-CHA16-1A-72Y-1-A	M	1.5		142.5	132.21625	2	3	Unsure	1	1	Flat-Irregular Top/Base	2
Tephra	MEXI-CHA16-1A-72Y-1-A	M	3.75		142.8875	132.56625	2	2	No	1	1	Flat-Irregular Top/Base	1
Tephra		F	0	MEXI-CHA16-1C-78Y-1-A	143.66625	133 345	3	3	Possibly all (if tephra)	1	1	Irregular top/base	2
Tephra	MEXI-CHA16-1A-74Y-1-A	F	1.9		144.464	134.12375	2	-1	No	1	1	Flat Top (top of core section)/Flat-Irregular Base	1
Tephra	MEXI-CHA16-1A-74Y-1-A	F	1		144 654	134.30375	2	3	Potentially all	1	1	Irregular Top/Base (not continuous across the width of the core s	1
Tephra	MEXI-CHA16-1A-74Y-1-A	F	1 25		144.7215	134.35875	1	-1	No	1	1	Flat Top/Flat Base	1
Tephra	MEXI-CHA16-1A-74Y-1-A	F	2 25		144 809	134.42375	2	-2	No	1	1	Flat Top/Flat-Irregular Base	1
Tephra	MEXI-CHA16-1A-74Y-1-A	M	11 25		145.85275	135 355	1	0	No	1	1	Flat-Irregular Top/Flat Base	1
Tephra	MEXI-CHA16-1A-75Y-1-A	F	3 25		146.2805	135.75025	2	-1	No	1	1	Flat Top(top of score section)/Irregular Base	1
Tephra		F	0	MEXI-CHA16-1C-80Y-1-A	146.8063333	136.2760833	1	2	No	1	1	Flat-Irregular Top/Base	2
Tephra		F	0	MEXI-CHA16-1C-80Y-1-A	147.3321667	136.8019167	1	3	Possibly all	1	1	Flat-Irregular Top/Base	2
Tephra	MEXI-CHA16-1A-76Y-1-A	I	7		147 928	137.32775	2	1	No	1	1	Flat Top (as top of core section)/Irregular Base	1
Tephra	MEXI-CHA16-1A-76Y-1-A	F	0.625		147.95425	137.34775	2	3	Possibly all	1	1	Irregular Top/Base (concentrated to one side of the core section)	2
Tephra	MEXI-CHA16-1A-76Y-1-A	M	0.5		148.17425	137.56275	1	1	No	1	1	Flat Top/ Base	1
Tephra	MEXI-CHA16-1A-76Y-1-A	M	4.5		148 658	138.0015	2	1	No	1	1	Flat-Irregular Top/ Base	1
Tephra	MEXI-CHA16-1A-76Y-1-A	M	1		148.91925	138.25275	1	2	No	1	1	Flat Top/ Base (but difficult to see)	2
Tephra	MEXI-CHA16-1A-76Y-1-A	F	0.75		148.9555	138.2815	2	3	Possibly all	1	1	Irregular Top/Base (concentrated to one side of the core section)	2
Volcaniclastic	MEXI-CHA16-1A-77Y-1-A to MEXI-CHA16-1C-9		1502.5		164 523	138 824							
Tephra	MEXI-CHA16-1C-91Y-1-A	F	3 25		164.5745	138 843	1	0	No	1	1	Flat Top/Base	1
Tephra	MEXI-CHA16-1C-91Y-1-A	F	1		164 922	139.1805	2	1	No	1	1	Flat-Irregular Top/Base	1
Tephra	MEXI-CHA16-1C-91Y-1-A	F	1.5		165 047	139.2905	2	3	Possibly all	1	1	Flat-Irregular Top/Base	1
Tephra	MEXI-CHA16-1C-92Y-1-A	M	1 25		165.8475	140.0785	1	2	No	1	1	Flat Top/Base	1
Tephra	MEXI-CHA16-1C-92Y-1-A	F	0.5		165 857	140 083	1	1	No	1	1	Flat Top/Base	1
Tephra	MEXI-CHA16-1C-92Y-1-A	M	0.5		165.93	140.151	1	3	No	1	1	Flat Top/Base	1
Tephra	MEXI-CHA16-1C-92Y-1-A	M	0.5		165.99	140 206	1	3	No	1	1	Flat Top/Base	1
Tephra	MEXI-CHA16-1C-92Y-1-A	F	0.5		166	140 211	1	2	No	1	1	Flat-slightlyIrregular top/base	2
Tephra	MEXI-CHA16-1C-92Y-1-A	M	0.5		166.0475	140.2535	1	2	No	1	1	Flat Top/Base	1
Tephra	MEXI-CHA16-1C-92Y-1-A	F	1		166.1775	140.3735	2	0	No	1	1	Flat-Irregular Top/Base	2
Tephra	MEXI-CHA16-1C-92Y-1-A	M	1.5		166 271	140.452	1	0	No	2	1	Flat-Irregular Top/Flat Base	1
Tephra	MEXI-CHA16-1C-92Y-1-A	M	2		166.31	140.471	1	2	No	1	1	Flat Top/Base	1
Tephra	MEXI-CHA16-1C-92Y-1-A	M	0.5		166.40125	140.55725	1	3	No	1	1	Flat Top/Base	1

Deposit Type	Splice Section	Composition	On-Splice Thickness (cm)	Ghost Section(s)	Combined Basal Depth (m)	Event Free Depth (m)	Thickness Reliability	Grain Size (φ)	Fine ash component	Structures	Possible Reworking	Top/Base	Confidence Volcanic
Tephra	MEXI-CHA16-1C-92Y-1-A	M	0.75		166.4275	140 576	1	3	No	1	1	Flat Top/Base	1
Tephra	MEXI-CHA16-1C-92Y-1-A	I	1.625		166.46625	140.5985	2	0	No	1	1	Flat Top (top of core section)/Flat-Irregular Base	1
Tephra	MEXI-CHA16-1C-93Y-1-A	F	5		166 945	141.02725	1	2	No	1	2	Flat Top/Base	1
Tephra	MEXI-CHA16-1C-93Y-1-A	F	116		168.105	141.02725	1	-4	No	2	2	Flat Top/Base	1
Tephra	MEXI-CHA16-1A-92Y-1-A	F	103.5		169.145	141.03225	1	-2	No	1	1	Flat Top/Base	1
Tephra	MEXI-CHA16-1C-94Y-1-A	M	1.8		169.2	141.06925	2	2	No	1	1	Flat-Irregular Top/Base	2
Tephra	MEXI-CHA16-1C-95Y-1-A	M	2.5		170.1715	142.01575	2	3	No	1	1	Flat-Irregular Top/ Base	1
Tephra	MEXI-CHA16-1C-95Y-1-A	M	0.75		170.8965	142.73325	1	3	No	1	1	Flat Top/Base	1
Tephra	MEXI-CHA16-1B-99Y-1-A	M	2		171 079	142.89575	1	3	No	1	1	Flat Top/Flat-Irregular Base	1
Tephra	MEXI-CHA16-1B-99Y-1-A	I	2		171 379	143.17575	2	2	No	1	1	Irregular (dispersed/gradational) Top/Flat Base	1
Tephra	MEXI-CHA16-1A-94Y-1-A	M	4		171.63275	143.3895	1	2	No	1	1	Flat Top/Base	1
Tephra	MEXI-CHA16-1A-94Y-1-A	F	7 25		171.779	143.46325	2	0	No	1	1	Flat Top/Flat-Irregular Base	1
Tephra	MEXI-CHA16-1B-100Y-1-A	F	0.8		172 069	143.74525	2	3	No	1	1	Flat-Irregular Top/Base	1
Tephra	MEXI-CHA16-1B-100Y-1-A	M	1		172.159	143.82525	1	3	No	1	1	Flat Top/Flat-Irregular Base	1
Tephra	MEXI-CHA16-1B-100Y-1-A	M	2		172 339	143.98525	1	2	No	1	1	Flat Top/Base	1
Tephra	MEXI-CHA16-1B-100Y-1-A	M	1		172.414	144.05025	1	3	No	1	1	Flat Top/Flat-Irregular Base	1
Tephra		I	0	MEXI-CHA16-1A-95Y-1-A	172.6565	144.29275	2	2	No	1	1	Flat Top (top of core section)/Flat Base	1
Tephra	MEXI-CHA16-1A-95Y-1-A	F	0.75		172.9065	144.53525	2	3	Possibly all	1	1	Flat Top/Irregular Base	2
Tephra	MEXI-CHA16-1A-95Y-1-A	F	0.5		173 289	144.91275	2	3	Possibly all	1	1	Flat-Irregular Top/Irregular Base	2
Tephra	MEXI-CHA16-1B-101Y-1-A	M	0.5		173 569	145.18775	1	1	No	1	1	Flat Top/Base	1
Tephra	MEXI-CHA16-1B-101Y-1-A	F	0.8		173 874	145.48475	2	4	Possibly all	1	1	Flat Top/Flat-Irregular Base	1
Tephra	MEXI-CHA16-1B-101Y-1-A	F	1		173 914	145.51475	2	1	No	1	1	Flat-Irregualr Top/Base	1
Tephra	MEXI-CHA16-1B-101Y-1-A	F	0.4		173 933	145.52975	2	1	No	1	2	Flat-Irregualr Top/Base	1
Tephra	MEXI-CHA16-1B-101Y-1-A	F	1.2		174.133	145.71775	1	-1	No	1	1	Flat-Irregualr Top/Base	1
Tephra	MEXI-CHA16-1B-101Y-1-A	M	3.9		174 244	145.78975	1	1	No	1	1	Flat Top/Base	1
Tephra		F	0	MEXI-CHA16-1B-101Y-1-A	174.4172	145.96295	2	2	No	1	1	Flat Top/Base (not fully continuous)	1
Tephra		F	0	MEXI-CHA16-1A-96Y-2-A	174.5904	146.13615	3	-2	No	1	2	Flat Top (top of core catcher)/Irregular Base	1
Tephra		F	0	MEXI-CHA16-1A-97Y-1-A	174.7636	146.30935	3	2	No	1	1	Irregular Top/Base	1
Tephra		M	0	MEXI-CHA16-1A-97Y-1-A	174.9368	146.48255	2	1	No	1	1	Flat-Irregular Top/Base	1
Tephra	MEXI-CHA16-1C-99Y-1-A	M	0.5		175.115	146.65575	3	3	No	1	1	Present as a nodule	2
Tephra	MEXI-CHA16-1C-99Y-1-A	M	1.625		175.45875	146.98325	1	1	No	1	1	Flat Top/Base	1
Tephra	MEXI-CHA16-1C-99Y-1-A	M	2.375		175.60875	147.1095	1	3	No (but possible)	1	1	Flat Top/Base	1
Tephra	MEXI-CHA16-1C-99Y-1-A	F	0.5		175.705	147.20075	1	2	No	1	1	Flat top/Base (slightly bioturbated at the base)	1
Tephra	MEXI-CHA16-1B-103Y-1-A	F	1		177.769	149.25475	2	0	No	1	1	Flat Top (top of core section)/Flat Base	1
Tephra	MEXI-CHA16-1B-104Y-1-A	F	11		178 667	150.04275	1	2	Upper 1.1 cm	1	1	Flat Top/Flat-Irregular Base	1
Tephra	MEXI-CHA16-1B-104Y-1-A	F	2		178 817	150.17275	2	2	Possibly all	1	1	Irregular Top/Base	1
Tephra	MEXI-CHA16-1B-105Y-1-A	F	1		181.17	152.51575	3	1	No	1	1	Irregular Top/ Base ('nodule' within sediment)	1
Tephra	MEXI-CHA16-1C-100Y-1-A	F	1.9		181 389	152.71575	1	3	Potentially all (1C-100Y is pı	1	2	Irregular-Flat Top/Base	1
Tephra	MEXI-CHA16-1C-100Y-1-A	F	33.425		181.72325	152.71575	1	-1	No	2	1	Flat Top/ Base	1
Tephra	MEXI-CHA16-1C-100Y-1-A	F	0.75		182.1645	153.1495	1	2	No	1	1	Flat Top/Base	1
Tephra	MEXI-CHA16-1C-100Y-1-A	F	8 25		182.31075	153.21325	1	1	Potentially in upper 1.5 cm?	2	1	Flat Top/Base	1
Tephra	MEXI-CHA16-1C-101Y-1-A	F	0.5		183 555	154.4525	1	-1	No	1	2	Flat Top/Flat Base	1
Tephra	MEXI-CHA16-1C-101Y-1-A	F	1.75		183.5875	154.4675	1	-1	No	1	1	Flat-Dispersed Top/Flat Base	1
Tephra	MEXI-CHA16-1C-101Y-1-A	F	3		183 645	154.495	1	0	No	2	1	Flat Top/Base	1
Tephra	MEXI-CHA16-1C-101Y-1-A + MEX	F	26.6		184.2235	154.8075	2	-1	Upper 18.5 cm	2	1	Flat Top (as top of core section)/Base	1
Tephra	MEXI-CHA16-1A-102Y-1-A	F	1.375		184.3935	154.96375	1	1	No	1	1	Flat-Irregular Top/Base	1
Tephra	MEXI-CHA16-1C-102Y-1-A	M	1		185 204	155.76425	1	1	No	1	1	Flat Top/Base	1
Tephra	MEXI-CHA16-1C-102Y-1-A	M	2.375		185.2385	155.775	1	1	No	1	1	Flat Top/Base	1
Tephra		I	0	MEXI-CHA16-1A-103Y-1-A	185.4155833	155.9520833	2	2	No	1	2	Flat Top/Flat-Irregular Base	2
Tephra		I	0	MEXI-CHA16-1A-103Y-1-A	185.5926667	156.1291667	3	1	No	1	1	Flat-Irregular Top/Irregular Base	1
Tephra	MEXI-CHA16-1A-103Y-2-A	M	2.125		185.791	156.30625	2	2	No	1	1	Flat-Irregular Top/Flat-Irregular Base	1
Tephra	MEXI-CHA16-1A-103Y-3-A	F	1.875		186.1235	156.62	2	3	Possibly all	1	1	Flat-Irregular Top/Base	1
Tephra	MEXI-CHA16-1C-103Y-1-A	F	4.5		186.8065	157 258	1	2	No	1	1	Flat Top/Base	1
Tephra	MEXI-CHA16-1C-103Y-1-A	M	1		187 019	157.4605	1	2	No	1	1	Flat Top/Flat-Irregular Base	1
Tephra	MEXI-CHA16-1C-103Y-1-A	M	2		187 079	157.5005	2	2	No	1	1	Flat Top/Base (not continuous across core width)	2
Tephra	MEXI-CHA16-1C-103Y-1-A	F	6 25		187.2265	157.5855	1	-1	No	1	1	Flat Top/Base	1
Tephra	MEXI-CHA16-1C-103Y-1-A	I	1		187 279	157 628	1	2	No	1	1	Flat Top/Flat-Irregular Base	1
Tephra	MEXI-CHA16-1C-103Y-1-A	F	1		187.3015	157.6405	1	3	Possibly all	1	2	Flat Top/Base (not continuous across core width)	1
Tephra	MEXI-CHA16-1C-103Y-1-A + MEX	F	41.15		187.723	157.6505	2	-1	No	2	1	Flat Top/Base (bottom of core)	1
Tephra	MEXI-CHA16-1A-105Y-1-A	F	3		189.0895	158 987	1	2	Possibly all	1	1	Flat Top/Base	1
Tephra	MEXI-CHA16-1A-105Y-1-A	F	1.75		189 682	159 562	1	2	Possibly all	1	1	Flat Top/Base (base slightly bioturbated)	1

Deposit Type	Splice Section	Composition	On-Splice Thickness (cm)	Ghost Section(s)	Combined Basal Depth (m)	Event Free Depth (m)	Thickness Reliability	Grain Size (φ)	Fine ash component	Structures	Possible Reworking	Top/Base	Confidence Volcanic
Tephra	MEXI-CHA16-1C-105Y-1-A	F	2.125		190.19575	160.0545	1	2	No	1	1	Flat Top/Base	2
Tephra	MEXI-CHA16-1C-105Y-1-A	F	1		190.54	160.38875	1	2	No	1	1	Flat Top/Base	2
Tephra	MEXI-CHA16-1C-105Y-1-A	F	2		190 682	160.51075	1	1	No	1	1	Flat Top/Base	1
Tephra	MEXI-CHA16-1C-106Y-1-A	M	1.5		191 267	161.08075	1	3	No	1	1	Flat Top/Base	2
Tephra	MEXI-CHA16-1C-106Y-1-A	F	1 25		191 917	161.71825	1	3	No	1	1	Flat-Irregular Top/Flat Base	1
Tephra	MEXI-CHA16-1C-106Y-1-A	F	1 25		191.9995	161.78825	1	-1	No	1	2	Flat Top/Base	1
Tephra	MEXI-CHA16-1C-106Y-1-A	F	8.75		192.137	161.83825	1	-2	No	2	1	Flat Top/Base	1
Tephra	MEXI-CHA16-1C-106Y-1-A	F	1.5		192.1695	161.85575	1	2	No	1	1	Flat Top/Base	1
Tephra	MEXI-CHA16-1C-106Y-1-A	F	3 25		192.2145	161.86825	1	0	No	1	1	Flat Top/Flat-Irregular Base	1
Tephra	MEXI-CHA16-1C-106Y-1-A	F	0.75		192.2845	161.93075	1	2	No	1	1	Flat-Irregular Top/Base	1
Tephra	MEXI-CHA16-1C-107Y-1-A	F	1.5		192 397	162.02825	2	1	No	1	1	Flat Top (as top of section)/Flat Base	1
Tephra	MEXI-CHA16-1C-107Y-1-A	M	2.75		193 032	162.63575	1	2	No	1	1	Flat Top/ Base	1
Tephra	MEXI-CHA16-1C-107Y-1-A	F	2 25		193.172	162.75325	1	1	No	1	1	Flat Top/ Base	1
Tephra	MEXI-CHA16-1A-108Y-1-A	I	3 25		193 971	163.51975	1	2	No	1	1	Flat Top/Irregular Base	1
Tephra	MEXI-CHA16-1C-108Y-1-A	I	13.1		194 977	164.39475	1	0	No	1	1	Flat Top/Base	1
Tephra	MEXI-CHA16-1C-109Y-1-A	I	0.8		196.137	165.54675	2	2	No	1	1	Flat-Irregular Top/Base	2
Tephra	MEXI-CHA16-1C-109Y-1-A	F	1		196.2875	165.68725	3	2	No	1	1	Irregular Top/Base	1
Tephra	MEXI-CHA16-1C-109Y-1-A	F	0.5		196 565	165.95975	1	2	No	1	1	Flat Top/Flat-Irregular Base	1
Tephra	MEXI-CHA16-1A-112Y-1-A	M	3.75		199.5665	168.92375	1	3	No	1	2	Flat-Irregular Top/Base	1
Tephra	MEXI-CHA16-1A-112Y-1-A	M	3.75		199 604	168.92375	1	2	No	1	1	Flat-Irregular Top/Base	1
Tephra	MEXI-CHA16-1A-112Y-1-A	F	0.5		200.127	169.44175	2	3	Possibly all	1	1	Flat Top/Base (not continuous across core width)	2
Tephra	MEXI-CHA16-1C-111Y-1-A	I	1		200 829	170.13375	1	2	No	1	2	Flat-Irregular Top/Base	1
Tephra		F	0	MEXI-CHA16-1A-115Y-1-A	202.39775	171.7025	1	2	No	1	1	Flat-Irregular Top/Base	2
Tephra	MEXI-CHA16-1A-115Y-1-A	M	4.75		204 014	173.27125	1	2	Possibly all - likely just rewor	1	2	Flat-Irregular Top/Flat Base	1
Tephra	MEXI-CHA16-1A-115Y-1-A	M	10		204.114	173.27125	1	2	No	3	1	Flat-Irregular Top/Flat Base	1
Tephra	MEXI-CHA16-1A-115Y-1-A	I	1.75		204 389	173.52875	2	2	No	1	1	Irregular Top/Base (some drilling disturbance)	1
Tephra	MEXI-CHA16-1A-115Y-1-A	M	0.4		204 695	173.83075	1	2	Np	1	1	Flat Top/Base	1
Tephra	MEXI-CHA16-1A-115Y-1-A	F	2		204 869	173.98475	1	2	No	2	1	Flat Top/Flat-Irregular Base	1
Tephra	MEXI-CHA16-1A-115Y-1-A	F	0.9		204 989	174.09575	2	2	No	1	1	Irregular Top/Base	1
Tephra	MEXI-CHA16-1C-114Y-1-A	F	1 25		205 524	174.61825	1	2	Possibly	1	1	Flat top/base	1
Tephra	MEXI-CHA16-1C-116Y-1-A	F	0.75		208.2265	177.31325	1	3	No	1	1	Flat Top/Base	1
Tephra	MEXI-CHA16-1C-116Y-1-A	F	0.75		208 304	177.38325	1	2	No	1	1	Flat Top/Base	1
Tephra	MEXI-CHA16-1C-116Y-1-A	F	0.75		208.3965	177.46825	1	3	No	1	1	Flat Top/Base	1
Tephra	MEXI-CHA16-1C-116Y-1-A	F	1		208 659	177.72075	1	2	No	1	1	Flat Top/Base	1
Tephra	MEXI-CHA16-1C-116Y-1-A	M	0.5		208.719	177.77575	1	1	No	1	1	Flat Top/Base	1
Tephra	MEXI-CHA16-1C-116Y-2-A	F	0.5		208.8465	177.89825	1	1	No	1	1	Flat top/base	1
Tephra	MEXI-CHA16-1C-117Y-1-A	F	1.75		209.91625	178.9505	1	2	Upper 1 cm?	1	1	Flat Top/Base	1
Tephra		I	0	MEXI-CHA16-1A-118Y-1-A	210 081625	179.115875	1	2	No	1	1	Flat Top/Base	1
Tephra	MEXI-CHA16-1C-117Y-1-A	M	22.8		210.475	179.28125	1	1	No	2	1	Flat Top/Base	1
Volcaniclastic	MEXI-CHA16-1C-117Y-1-A to MEXI-CHA16-1A-		891.4		219 389	179.28125							
Tephra	MEXI-CHA16-1A-124Y-1-A	F	2		219.4505	179.32275	1	-1	No	1	1	Flat Top/Flat-Irregular Base	1
Volcaniclastic	MEXI-CHA16-1C-124Y-1-A to MEXI-CHA16-1C-		561.3		226.121	180.38025							
Tephra	MEXI-CHA16-1C-128Y-1-A	F	8.75		227.2585	181.43025	1	2	No	1	1	Flat top/base	1
Tephra	MEXI-CHA16-1C-129Y-1-A	F	4.5		228 011	182.13775	1	3	Possibly but likelyNot	1	1	Flat top/flat-irrgular base	1
Tephra	MEXI-CHA16-1C-129Y-1-A	F	4.5		228 071	182.15275	1	3	Possibly but likelyNot	1	1	Flat top/base	1
Fine clayey layer	MEXI-CHA16-1B-135Y-1-A	C	47.3		229 264	182.87275	1	3	No	2	C	Flat Top/Base	1
Tephra	MEXI-CHA16-1B-136Y-1-A	M	0.7		229.468	183.06975	1	2	No	1	1	Flat Top/Base	1
Tephra	MEXI-CHA16-1B-136Y-1-A	M	1		229 561	183.15275	2	2	No	1	1	Flat-Irregular Top/Base	2
Tephra	MEXI-CHA16-1B-136Y-1-A	F	1.1		230 208	183.78875	1	2	Possibly	1	1	Flat-irregular top/flat base	1
Tephra		F	0	MEXI-CHA16-1B-136Y-1-A	230.23	183.81075	1	2	Possibly	1	1	Flat-irregular top/flat base	1
Tephra	MEXI-CHA16-1C-130Y-1-A	M	1.6		230 268	183.83275	2	3	No	1	1	Unsure	1
Tephra	MEXI-CHA16-1C-130Y-1-A	M	2.2		230.407	183.94975	1	2	No	1	1	Flat Top/Base	1
Tephra	MEXI-CHA16-1C-130Y-1-A	F	2.1		230 638	184.15975	1	3	Possibly alll	1	1	Flat-Iregualr Top/Flat Base	1
Tephra	MEXI-CHA16-1B-137Y-1-A	F	17.2		231 048	184.39775	1	-1	Upper 7.3 cm?	1	1	Flat Top/Base	1
Tephra	MEXI-CHA16-1B-137Y-1-A	F	2.5		231.191	184.51575	1	-1	No	1	1	Flat Top/Base	1
Tephra	MEXI-CHA16-1B-137Y-1-A	F	0.8		231.735	185.05175	1	-1	No	1	1	Flat Top/Base	1
Fine clayey layer	MEXI-CHA16-1B-137Y-1-A	C	1.3		231.755	185.05875	1	3	No	2	C	Flat Top/Base	1
Tephra	MEXI-CHA16-1B-137Y-1-A	F	0.4		231.761	185.06075	1	-1	No	1	1	Flat Top/Base	1
Tephra	MEXI-CHA16-1C-131Y-1-A	M	0.7		232 079	185.37175	1	2	No	1	1	Flat Top/Base	2
Fine clayey layer		C	0	MEXI-CHA16-1B-138Y-1-A	232.115	185.40775	1	4	No	1	C	Flat Top/Base	1
Tephra	MEXI-CHA16-1B-138Y-1-A	F	0.8		232.159	185.44375	1	1	No	1	1	Flat Top/Base	1

Deposit Type	Splice Section	Composition	On-Splice Thickness (cm)	Ghost Section(s)	Combined Basal Depth (m)	Event Free Depth (m)	Thickness Reliability	Grain Size (φ)	Fine ash component	Structures	Possible Reworking	Top/Base	Confidence Volcanic
Tephra	MEXI-CHA16-1B-138Y-1-A	F	0.9		232.194	185.46975	2	3	Possibly all	1	1	Flat-Irregular Top/Base (bioturbated)	2
Tephra	MEXI-CHA16-1B-138Y-1-A	M	3.4		232.452	185.69375	1	3	No	1	1	Flat-Irregular Top/Base (bioturbated)	2
Fine clayey layer	MEXI-CHA16-1B-138Y-1-A	C	0.7		232 612	185.84675	1	3	No	1	C	Flat Top/Base	1
Fine clayey layer	MEXI-CHA16-1B-138Y-1-A	C	0.6		232 632	185.86075	1	3	No	1	C	Flat Top/Base	1
Fine clayey layer	MEXI-CHA16-1B-138Y-1-A	C	1.9		232.728	185.93775	1	4	No	1	C	Flat Top/Base	1
Tephra	MEXI-CHA16-1B-138Y-1-A	F	8		233 055	186.18475	1	-2	No	1	1	Flat top/ base	1
Tephra	MEXI-CHA16-1C-132Y-1-A	F	3.375		233 286	186 382	2	2	No	1	1	Flat top/Biotubated base	1
Tephra	MEXI-CHA16-1A-138Y-1-A	F	6		233 661	186 697	2	-1	No	1	1	Flat Top/Irregular Base	1
Tephra	MEXI-CHA16-1A-138Y-1-A	F	1.75		233.726	186.7445	2	-1	No	1	2	Scattered pumices in sediment	1
Fine clayey layer	MEXI-CHA16-1A-138Y-1-A	C	0.5		234 377	187.3905	1	3	No	1	C	Flat Top/Irregular Base (mushroomed artefact)	1
Fine clayey layer	MEXI-CHA16-1A-138Y-1-A	C	0.5		234.431	187.4395	1	3	No	1	C	Flat Top/Irregular Base (mushroomed artefact)	1
Fine clayey layer	MEXI-CHA16-1A-138Y-1-A	C	0.75		234.9235	187.9245	1	3	No	1	C	Flat Top/Irregular Base (mushroomed artefact)	1
Tephra	MEXI-CHA16-1C-133Y-1-A	M	1		235 271	188 262	1	3	No	1	1	Flat Top/Base	2
Tephra	MEXI-CHA16-1C-133Y-1-A	M	2.5		235.411	188 377	1	2	No	3	1	Flat Top/Base	1
Tephra	MEXI-CHA16-1C-133Y-1-A	M	0.8		235.499	188.457	1	2	No	1	1	Flat Top/Base	1
Tephra	MEXI-CHA16-1C-133Y-1-A	F	2.5		235 556	188.489	1	0	No	1	1	Flat-Irregular Top/Base	1
Tephra	MEXI-CHA16-1C-133Y-1-A	M	0.6		235 629	188 556	1	0	No	1	1	Flat Top/Base	1
Fine clayey layer		C	0	MEXI-CHA16-1A-139Y-1-A	235 651	188 578	1	3	No	1	C	Flat Top/Base	1
Tephra	MEXI-CHA16-1C-133Y-1-A	M	8.5		235.758	188.6	1	2	No	2	1	Flat Top/Base	1
Tephra	MEXI-CHA16-1C-133Y-1-A	F	1.4		235 822	188 643	1	2	No	1	1	Flat Top/Base	2
Tephra	MEXI-CHA16-1C-133Y-1-A	F	0.7		235 906	188.727	1	2	No	1	1	Flat Top/Base	2
Tephra	MEXI-CHA16-1C-133Y-1-A	I	2.8		236 045	188 838	2	2	No	1	1	Flat-irregular Top/Base	1
Tephra	MEXI-CHA16-1C-133Y-1-A	F	0.9		236 097	188 881	1	0	No	1	1	Flat Top/Base	1
Fine clayey layer	MEXI-CHA16-1C-133Y-1-A	C	0.3		236.142	188 923	3	3	No	1	C	Irregular Top/Base - not continuous layer across core width	1
Tephra	MEXI-CHA16-1C-133Y-1-A	M	1.2		236 215	188 984	1	3	No	1	1	Flat Top/Base	2
Fine clayey layer	MEXI-CHA16-1B-140Y-1-A	C	1.3		236 247	189 003	1	3	No	2	C	Flat Top/Base	1
Tephra	MEXI-CHA16-1B-140Y-1-A	M	0.8		236 551	189 299	1	2	No	1	1	Flat Top/Base	2
Tephra	MEXI-CHA16-1C-134Y-1-A	M	0.6		237.178	189.92	1	1	No	1	1	Flat Top/Base	1
Tephra	MEXI-CHA16-1C-134Y-1-A	F	0.6		237 208	189 944	1	2	No	1	2	Flat Top/base	1
Tephra	MEXI-CHA16-1B-141Y-1-A	F	4		237 291	189 987	1	0	Upper 1.5 cm	1	1	Flat Top/ Base	1
Tephra	MEXI-CHA16-1B-141Y-1-A	I	0.7		237 373	190 062	1	2	No	1	1	Flat Top/Base	1
Tephra	MEXI-CHA16-1C-135Y-1-A	M	0.5		238.111	190.795	1	2	No	1	1	Flat Top/Base	2
Tephra	MEXI-CHA16-1C-135Y-1-A	F	0.2		238 313	190 995	1	2	No	1	1	Flat Top/Base	2
Tephra	MEXI-CHA16-1C-135Y-1-A	M	1 25		238.7685	191.438	3	1	No	1	1	Irregular Top/ Base (disturbed by mushrooming in core section)	1
Fine clayey layer	MEXI-CHA16-1C-135Y-1-A	C	0.2		239 068	191.7355	3	3	No	1	C	Irregular Top/Base - not continuous layer across core width	1
Tephra	MEXI-CHA16-1B-142Y-1-A	M	5.8		239.729	192.3385	1	3	Possibly	1	1	Flat Top/Base	1
Tephra	MEXI-CHA16-1C-136Y-1-A	F	1.725		240.95725	193.5495	2	3	No	1	1	Flat-Irregular Top/Base (disturbed slightly by mushrooming in cor	1
Tephra	MEXI-CHA16-1C-137Y-1-A	F	2.875		241.4285	193 992	1	1	Upper 1.5 cm	1	1	Flat top/bioturbated base	1
Tephra	MEXI-CHA16-1B-144Y-1-A	F	0.8		242 269	194.8245	1	2	No	1	1	Flat top/ base	1
Tephra	MEXI-CHA16-1B-144Y-1-A	F	0.5		242 906	195.4565	2	3	Possibly all	1	1	Flat-Irregular Top/Base	2
Tephra	MEXI-CHA16-1B-145Y-1-A	M	0.6		243.414	195.9585	1	1	No	1	1	Flat Top/Base	1
Tephra	MEXI-CHA16-1B-145Y-1-A	F	0.8		243.444	195.9805	1	2	No	1	1	Flat Top/Base	2
Tephra	MEXI-CHA16-1B-145Y-1-A	M	0.5		243 697	196.2285	1	2	No	1	1	Flat Top/Base	2
Tephra	MEXI-CHA16-1B-145Y-1-A	M	0.5		244.07	196.5965	1	2	No	1	1	Flat Top/Base	2
Fine clayey layer	MEXI-CHA16-1B-145Y-1-A	C	0.4		244.118	196.6405	1	3	No	1	C	Flat Top/Base	1
Tephra	MEXI-CHA16-1B-145Y-1-A	F	10.7		244 238	196.6535	1	2	No	1	1	Flat Top/Base	1
Tephra	MEXI-CHA16-1B-145Y-1-A	M	4.7		244 333	196.7015	1	2	No	1	1	Flat Top/Base	2
Tephra		M	0	MEXI-CHA16-1C-139Y-1-A	244 530625	196.899125	1	2	No	1	1	Flat top/base	1
Tephra		M	0	MEXI-CHA16-1C-139Y-1-A	244.72825	197.09675	1	3	No	1	1	Flat Top/base	2
Tephra		M	0	MEXI-CHA16-1C-139Y-1-A	244 925875	197.294375	1	2	No	1	1	Flat Top/base	1
Fine clayey layer	MEXI-CHA16-1C-139Y-1-A	C	0 25		245.126	197.492	1	3	Possibly	1	C	Flat top/base	1
Fine clayey layer	MEXI-CHA16-1C-139Y-1-A	C	1.5		245 201	197 552	1	3	Possibly	1	C	Flat top/base	1
Fine clayey layer	MEXI-CHA16-1C-139Y-1-A	C	1.375		245 236	197.57325	1	3	Possibly	1	C	Flat top/base	1
Tephra	MEXI-CHA16-1C-140Y-1-A	I	6.625		245.52825	197.79925	1	1	No	2	1	Flat Top/Base	1
Fine clayey layer	MEXI-CHA16-1C-140Y-1-A	C	0 25		245.53075	197.79925	1	3	Possibly	1	C	Flat top/base	1
Fine clayey layer	MEXI-CHA16-1C-140Y-1-A	C	0.375		245 557	197.82175	1	3	Possibly	1	C	Flat top/base	1
Fine clayey layer	MEXI-CHA16-1C-140Y-1-A	C	0 25		245.59825	197.8605	1	3	Possibly	1	C	Flat top/base	1
Tephra	MEXI-CHA16-1C-140Y-1-A	M	0.4		245 675	197.93325	1	2	No	1	1	Flat Top/Base	2
Tephra	MEXI-CHA16-1C-140Y-1-A	F	0 25		245.7195	197.97525	1	2	Possibly	1	1	Flat top/base	1
Tephra	MEXI-CHA16-1C-140Y-1-A	I	0.5		245 962	198.21275	1	1	No	1	1	Flat Top/Base	1
Fine clayey layer	MEXI-CHA16-1C-140Y-1-A	C	0.625		245 987	198.2315	1	3	Possibly	1	C	Flat top/base	1

Deposit Type	Splice Section	Composition	On-Splice Thickness (cm)	Ghost Section(s)	Combined Basal Depth (m)	Event Free Depth (m)	Thickness Reliability	Grain Size (φ)	Fine ash component	Structures	Possible Reworking	Top/Base	Confidence Volcanic
Fine clayey layer	MEXI-CHA16-1C-140Y-1-A	C	2.375		246.1095	198.33025	1	3	Possibly	1	C	Flat top/base	1
Fine clayey layer	MEXI-CHA16-1C-140Y-1-A	C	0.375		246.36325	198.58025	1	3	Possibly	1	C	Flat top/base	1
Fine clayey layer	MEXI-CHA16-1C-140Y-1-A	C	0.875		246.4945	198.70275	1	3	Possibly	1	C	Flat top/base	1
Fine clayey layer	MEXI-CHA16-1B-147Y-1-A	C	0.3		246 806	199.01125	1	3	Possibly	1	C	Flat top/base	1
Fine clayey layer	MEXI-CHA16-1B-147Y-1-A	C	0.5		246 822	199.02225	1	3	Possibly	2	C	Flat top/base	1
Fine clayey layer		C	0	MEXI-CHA16-1C-140Y-1-A	246.8388	199.03905	1	3	Possibly	1	C	Flat top/base	1
Fine clayey layer		C	0	MEXI-CHA16-1C-140Y-1-A	246.8556	199.05585	1	3	Possibly	1	C	Flat top/base	1
Fine clayey layer		C	0	MEXI-CHA16-1C-140Y-1-A	246.8724	199.07265	1	3	Possibly	1	C	Flat top/base	1
Tephra		M	0	MEXI-CHA16-1C-140Y-1-A	246.8892	199.08945	1	3	Possibly	1	2	Flat top/base	1
Fine clayey layer	MEXI-CHA16-1B-147Y-1-A	C	1.6		246 922	199.10625	1	3	Possibly	2	C	Flat top/base	1
Volcaniclastic	MEXI-CHA16-1B-147Y-1-A to MEXI-CHA16-1B-		149.2		248.414	199.10625							
Fine clayey layer		C withF	0	MEXI-CHA16-1C-142Y-1-A	248.6465	199.33875	1	3	No	2	C	Flat top/base	1
Tephra	MEXI-CHA16-1B-148Y-1-A	M	0.5		248 884	199.57125	1	2	No	1	1	Flat Top/Base	2
Tephra	MEXI-CHA16-1B-148Y-1-A	F	0.4		248 932	199.61525	1	3	No	1	1	Flat top/base	2
Tephra	MEXI-CHA16-1B-148Y-1-A	F	0.5		249 274	199.95225	1	2	No	1	1	Flat top/base	1
Tephra	MEXI-CHA16-1C-143Y-1-A	M	0.625		249.9285	200.6005	1	2	No	1	1	Flat top/base	1
Fine clayey layer	MEXI-CHA16-1C-143Y-1-A	C	0.375		250.19975	200 868	1	3	Possibly	1	C	Flat top/base	2
Fine clayey layer	MEXI-CHA16-1C-144Y-1-A	C	0.2		251 552	202.21825	1	3	Possibly	1	C	Flat top/base	2
Tephra	MEXI-CHA16-1C-144Y-1-A	F	1 25		251 574	202.22775	1	3	Possibly	1	1	Flat top/base	1
Tephra	MEXI-CHA16-1C-144Y-1-A	M	0.5		251.779	202.42775	1	3	Possibly	1	1	Flat top/base	1
Tephra	MEXI-CHA16-1C-144Y-1-A	F	3		251 809	202.42775	1	1	Possibly upper 1 5cm	1	1	Flat top/base	1
Fine clayey layer	MEXI-CHA16-1C-144Y-1-A	C	0.4		251 985	202.59975	1	3	Possibly	1	C	Flat top/base	2
Fine clayey layer	MEXI-CHA16-1C-144Y-1-A	C	0.3		252 009	202.62075	1	3	Possibly	1	C	Flat top/base	2
Tephra	MEXI-CHA16-1C-144Y-1-A	M	2		252 029	202.62075	1	2	No	1	1	Flat Top/Base	1
Tephra	MEXI-CHA16-1C-144Y-1-A	F	0.7		252 336	202.92075	1	3	Possibly all	1	1	Flat Top/Base	1
Tephra	MEXI-CHA16-1C-144Y-1-A	F	1 25		252 639	203.21125	1	-1	No	1	1	Flat top/base	1
Fine clayey layer	MEXI-CHA16-1C-144Y-1-A	C	1		252 652	203.21425	1	3	Possibly	1	C	Flat top/base	1
Volcaniclastic	MEXI-CHA16-1C-144Y-1-A to MEXI-CHA16-1C-		23		252 882	203.21425							
Tephra	MEXI-CHA16-1C-145Y-1-A	F	1		253 047	203.36925	1	-1	No	1	1	Flat top/base	1
Volcaniclastic	MEXI-CHA16-1C-145Y-1-A to MEXI-CHA16-1C-		54.8		253 606	203.38025							
Fine clayey layer	MEXI-CHA16-1C-145Y-1-A	C	15.3		253.765	203.38625	1	3	Possibly	2	C	Flat top/base	1
Volcaniclastic	MEXI-CHA16-1C-145Y-1-A to MEXI-CHA16-1C-		105.3		254 837	203.40525							
Tephra	MEXI-CHA16-1C-146Y-1-A	F	16.925		255.00625	203.40525	1	-1	No	2	2	Flat Top/Base	1
Tephra	MEXI-CHA16-1C-146Y-1-A	F	16.875		255.175	203.40525	1	-1	Upper 4cm	2	1	Flat top/base	1
Tephra	MEXI-CHA16-1C-146Y-1-A	F	2		255.21	203.42025	1	-1	No	1	1	Flat top/base	1
Tephra	MEXI-CHA16-1C-147Y-1-A	F	2.75		256.12	204.30275	1	-1	No	1	2	Flat Top/Bioturbated Base	1
Tephra	MEXI-CHA16-1C-147Y-1-A	M	0.5		256.19	204.36775	1	2	No	1	1	Flat Top/Base	1
Volcaniclastic	MEXI-CHA16-1C-147Y-1-A to MEXI-CHA16-1C-		1486.5		271.13	204.44275							
Volcaniclastic	MEXI-CHA16-1C-161Y-1-A to MEXI-CHA16-1C-		165.7		273 618	205.27375							
Tephra	MEXI-CHA16-1C-162Y-1-A	M	1		273.784	205.42975	1	1	No	1	1	Flat top/base	1
Tephra	MEXI-CHA16-1C-163Y-1-A	M	2.875		274.07	205 687	1	0	No	1	1	Flat top/base	1
Tephra	MEXI-CHA16-1C-163Y-1-A	M	1		274.1	205.707	1	1	No	1	1	Flat top/base	1
Tephra	MEXI-CHA16-1C-163Y-1-A	M	2.5		274.43125	206.01325	1	1	No	1	1	Flat top/base	1
Tephra	MEXI-CHA16-1C-163Y-1-A	M	1		274 625	206.197	1	1	No	1	1	Flat Top/Base	1
Tephra	MEXI-CHA16-1C-163Y-1-A	M	1.5		275.21	206.767	2	3	No	1	1	Flat-Irregular Top/Base	1
Tephra		I	0	MEXI-CHA16-1B-169Y-1-A	275 225	206.782	1	3		1	1	Flat Top/Base	1
Tephra	MEXI-CHA16-1B-169Y-1-A	F	1		275.25	206.797	2	3		1	1	Flat Top/Base	1
Tephra	MEXI-CHA16-1C-163Y-1-A	F	14.7		275.48	206.88	1	-1	No	1	1	Flat Top/ Base	1
Tephra		M	0	MEXI-CHA16-1A-164Y-1-A	276.3975	207.7975	1	2	No	1	1	Flat Top/ Base	1
Tephra	MEXI-CHA16-1A-165Y-1-A	M	0.7		277 322	208.715	1	2	No	1	1	Flat Top/Base	1
Tephra	MEXI-CHA16-1A-165Y-1-A	M	0 25		277.3805	208.771	1	2	No	1	1	Flat Top/ Base	1
Tephra	MEXI-CHA16-1A-165Y-1-A	M	0 25		277.498	208 886	1	2	No	1	1	Flat Top/ Base	1
Tephra	MEXI-CHA16-1A-165Y-1-A	F	0.75		277.7205	209.101	3	3	No	1	1	Irregular Top/ Base (very disturbed core section)	2
Tephra	MEXI-CHA16-1A-165Y-1-A	F	0.5		278 003	209.3785	3	3	No	1	1	Irregular Top/ Base (very disturbed core section)	2
Tephra	MEXI-CHA16-1A-165Y-1-A	F	0.5		278.2355	209 606	3	3	No	1	1	Irregular Top/ Base (very disturbed core section)	2
Tephra	MEXI-CHA16-1A-166Y-1-A	F	1 25		279 011	210 369	3	2	No	1	1	Irregular Top/ Base (very disturbed core section)	2
Tephra	MEXI-CHA16-1B-172Y-1-A	M	4		279.161	210.479	1	1	No	1	1	Flat Top/ Base	1
Tephra	MEXI-CHA16-1B-172Y-1-A	F	1		279 231	210 539	3	3	No	1	1	Irregular Top/ Base (very disturbed core section)	2
Tephra	MEXI-CHA16-1B-172Y-1-A	F	5		279 811	211 069	1	2	No	1	1	Flat-Irregular Top/ Bioturbated Base	1
Tephra	MEXI-CHA16-1B-172Y-1-A	F	0.8		280.114	211 364	2	3	Possibly all	1	1	Flat Top/Irregular Base	1
Tephra	MEXI-CHA16-1B-172Y-1-A	I	1		280 231	211.471	1	2	No	1	1	Flat Top/Base	1

Deposit Type	Splice Section	Composition	On-Splice Thickness (cm)	Ghost Section(s)	Combined Basal Depth (m)	Event Free Depth (m)	Thickness Reliability	Grain Size (φ)	Fine ash component	Structures	Possible Reworking	Top/Base	Confidence Volcanic
Tephra	MEXI-CHA16-1A-167Y-1-A	F	0.5		280.426	211 661	1	3	Possibly all (if tephra)	1	1	Flat Top/Base	2
Tephra	MEXI-CHA16-1A-167Y-1-A	F	1		280.476	211.701	2	3	Possibly all (if tephra)	1	1	Flat-Irregular Top/Base	2
Tephra	MEXI-CHA16-1A-167Y-1-A	M	0.875		280.71725	211.9335	1	2	No	1	1	Flat Top/Base	1
Tephra	MEXI-CHA16-1A-167Y-1-A	F	1		280.766	211.97225	1	3	Possibly all (if tephra)	1	1	Flat Top/Base	2
Tephra	MEXI-CHA16-1A-167Y-1-A	M	1		280 866	212.06225	2	3	No	1	1	Flat-Irregualr Top/Base	2
Tephra	MEXI-CHA16-1A-167Y-1-A	M	0.4		280 903	212.09525	1	3	No	1	1	Flat Top/Base	2
Tephra	MEXI-CHA16-1A-167Y-1-A	I	0.375		280 956	212.1445	1	3	No	1	2	Flat top/base	2
Tephra	MEXI-CHA16-1A-167Y-1-A	M	0.6		280 978	212.1605	1	2	No	1	1	Flat top/base	2
Tephra	MEXI-CHA16-1A-167Y-1-A	M	0.7		281 022	212.1975	2	2	No	1	1	Flat Top/Flat-irregular base	2
Tephra	MEXI-CHA16-1A-167Y-1-A	I	1 25		281.17725	212.34025	1	2	No	1	1	Flat-Irregular Top/ Base	2
Tephra	MEXI-CHA16-1A-167Y-1-A	F	1 25		281.39475	212.54525	1	0	No	1	2	Flat Top/ Base	1
Tephra	MEXI-CHA16-1B-173Y-1-A	M	6.9		281 657	212.7385	1	2	3 cm fine black ash at top	1	1	Flat Top/Base	1
Tephra	MEXI-CHA16-1B-173Y-1-A	F	10		282 057	213.0385	1	2	Upper 6.5 cm?	1	1	Flat Top/ Bioturbated Base	1
Tephra	MEXI-CHA16-1C-168Y-1-A	F	1.625		282.24325	213.2085	1	-1	No	1	2	Flat Top/ Base	1
Tephra	MEXI-CHA16-1C-168Y-1-A	F	1 25		282.29575	213.2485	2	1	No	1	2	Flat-Irregular Top/ Bioturbated Base	1
Tephra	MEXI-CHA16-1C-168Y-1-A	F	1.875		282.37825	213.31225	1	1	No	1	2	Flat-Irregular Top/ Base	2
Tephra	MEXI-CHA16-1C-168Y-1-A	I	0.875		282.47075	213 396	1	3	No	1	1	Flat Top/ Base	1
Tephra	MEXI-CHA16-1C-168Y-1-A	I	2.75		282.54075	213.4385	1	2	No	1	1	Flat Top/ Base	1
Tephra	MEXI-CHA16-1C-168Y-1-A	M	6.125		282.79325	213.62975	1	0	No	1	1	Flat top/Base	1
Tephra	MEXI-CHA16-1C-168Y-1-A	M	4.6		283 017	213.8075	1	2	No	2	1	Flat top/Base	1
Tephra	MEXI-CHA16-1A-169Y-1-A	M	0.625		283.26575	214.05	1	2	No	1	1	Flat Top/Base	1
Tephra	MEXI-CHA16-1A-169Y-1-A	M	0.375		283.3545	214.135	1	2	No	1	1	Flat Top/Base	1
Tephra	MEXI-CHA16-1A-169Y-1-A	M	0.5		283 562	214.3375	1	2	No	1	1	Flat Top/Base	1
Tephra	MEXI-CHA16-1A-169Y-1-A	M	0.75		283.71075	214.47875	2	2	No	1	1	Flat Top/Base	1
Tephra	MEXI-CHA16-1A-169Y-1-A	M	0.625		283.78825	214.55	1	2	No	1	1	Flat Top/Base	1
Tephra	MEXI-CHA16-1A-169Y-1-A	F	1		283 802	214.55375	2	3	Possibly all	1	1	Flat top/flat tolrregular base	2
Tephra	MEXI-CHA16-1A-169Y-1-A	M	1 25		283.92575	214 665	1	2	No	1	2	Flat Top/Base	1
Tephra	MEXI-CHA16-1A-169Y-1-A	M	0.75		284 047	214.77875	1	2	No	1	2	Flat Top/Base	1
Tephra	MEXI-CHA16-1A-169Y-1-A	M	0.75		284.0895	214.81375	1	2	No	1	1	Flat Top/Base	1
Tephra	MEXI-CHA16-1A-169Y-1-A	I	2.5		284.25825	214.9575	1	0	No	1	2	Flat Top/Base	1
Tephra	MEXI-CHA16-1A-169Y-1-A	M	0.5		284 339	215.03325	2	2	No	1	1	Flat-irregualr Top/Base	1
Tephra	MEXI-CHA16-1B-175Y-1-A	M	1		284.477	215.16125	1	2	No	1	1	Flat Top/Base	1
Tephra	MEXI-CHA16-1B-175Y-1-A	M	1		284 512	215.18625	1	2	No	1	1	Flat Top/Base	1
Tephra	MEXI-CHA16-1B-175Y-1-A	M	1.3		284 569	215.23025	1	3	Possibly all	1	1	Flat top/flat tolrregular base	2
Tephra	MEXI-CHA16-1B-175Y-1-A	M	1.6		284 806	215.45125	1	3	Possibly all	1	1	Flat top/ base at base of core section	2
Tephra	MEXI-CHA16-1B-175Y-1-A	M	1		284 923	215.55825	1	2	No	1	2	Flat Top/Base	1
Tephra	MEXI-CHA16-1B-175Y-1-A	M	1		284 982	215.60725	1	1	No	1	2	Flat Top/Base	1
Tephra	MEXI-CHA16-1A-170Y-1-A	M	26.5		285.3145	215.67475	1	1	No	2	1	Flat Top/Base	1
Tephra	MEXI-CHA16-1A-170Y-1-A	M	1 25		285.4445	215.79225	1	2	No	1	2	Flat Top/Base	1
Tephra	MEXI-CHA16-1A-170Y-1-A	M	1		285 502	215.83975	1	2	No	1	1	Flat Top/Flat-Irregular Base	1
Tephra	MEXI-CHA16-1B-176Y-1-A	M	1.1		285 635	215.96175	1	2	No	1	1	Flat Top/Base	1
Tephra	MEXI-CHA16-1B-176Y-1-A	M	4.3		285.7	215.98375	1	1	No	1	1	Flat Top/Base	1
Tephra	MEXI-CHA16-1B-176Y-1-A	F	0.8		285.708	215.98375	1	3	No	1	1	Flat Top/Base	1
Tephra	MEXI-CHA16-1B-176Y-1-A	M	0.4		285.84	216.11175	1	2	No	1	1	Flat top/base	2
Tephra	MEXI-CHA16-1B-176Y-1-A	M	0.5		285 939	216.20575	1	2	No	1	1	Flat top/base	1
Tephra	MEXI-CHA16-1B-176Y-1-A	M	0.5		286 099	216.36075	1	2	No	1	1	Flat top/base	1
Tephra	MEXI-CHA16-1B-176Y-1-A	F	1.7		286 239	216.48375	2	3	Possibly all	1	1	Flat Top/Flat-Irregular Base	1
Tephra	MEXI-CHA16-1B-176Y-1-A	F	1.3		286 361	216.59275	2	3	Possibly all	1	1	Flat top/base	1
Tephra	MEXI-CHA16-1B-176Y-1-A	M	2.3		286 384	216.59275	1	2	No	2	1	Flat top/base	1
Tephra	MEXI-CHA16-1B-176Y-1-A	I	0.3		286 555	216.76075	1	2	No	1	1	Flat top/base	2
Tephra	MEXI-CHA16-1A-171Y-1-A	I	0.5		286.71	216.91075	1	3	No	1	1	Flat Top/Base	2
Tephra	MEXI-CHA16-1A-171Y-1-A	F	1 25		287.02	217.20825	1	0	No	1	1	Flat Top/Base	1
Tephra	MEXI-CHA16-1A-171Y-1-A	I	0.3		287 253	217.43825	1	2	No	1	1	Flat Top/Base	2
Tephra	MEXI-CHA16-1A-171Y-1-A	I	0.3		287 266	217.44825	1	2	No	1	1	Flat Top/Base	2
Tephra	MEXI-CHA16-1B-177Y-1-A	M	1.7		287 321	217.48625	1	1	No	1	1	Flat Top/Base	1
Tephra	MEXI-CHA16-1B-177Y-1-A	I	5		287 396	217.51125	1	1	No	2	1	Flat Top/Base	1
Tephra	MEXI-CHA16-1B-177Y-1-A	F	0.5		287.404	217.51425	1	2	No	1	1	Flat Top/Base	1
Tephra	MEXI-CHA16-1B-177Y-1-A	F	6		287.481	217.53125	2	3	Possibly all	1	1	Flat Top/Base	1
Tephra	MEXI-CHA16-1B-177Y-1-A	M	0.5		287 536	217.58125	1	2	No	1	1	Flat Top/Base	1
Tephra	MEXI-CHA16-1B-177Y-1-A	M	1		287 608	217.64325	1	2	No	1	1	Flat Top/Base	1
Tephra	MEXI-CHA16-1B-177Y-1-A	M	0.4		287 858	217.88925	1	2	No	1	1	Flat Top/Base	2

Deposit Type	Splice Section	Composition	On-Splice Thickness (cm)	Ghost Section(s)	Combined Basal Depth (m)	Event Free Depth (m)	Thickness Reliability	Grain Size (φ)	Fine ash component	Structures	Possible Reworking	Top/Base	Confidence Volcanic
Tephra	MEXI-CHA16-1B-177Y-1-A	F	0.5		287 991	218.01725	1	0	No	1	2	Flat Top/Base	1
Tephra	MEXI-CHA16-1A-172Y-1-A	F	21		288 271	218.08725	1	-4	No	1	1	Flat Top/Base	1
Tephra	MEXI-CHA16-1A-172Y-1-A	M	0.7		288 369	218.17825	1	2	No	1	1	Flat top/Base	1
Tephra	MEXI-CHA16-1A-172Y-1-A	M	0.5		288 586	218.39025	1	1	No	1	1	Flat Top/Base	1
Tephra	MEXI-CHA16-1A-172Y-1-A	M	8.5		288.7735	218.49275	1	1	No	2	1	Flat Top/Base	1
Tephra	MEXI-CHA16-1A-172Y-1-A	M	0.7		289.01	218.72225	1	2	No	1	1	Flat top/base	2
Tephra	MEXI-CHA16-1A-172Y-1-A	M	2		289.1885	218.88075	1	2	No	1	1	Flat Top/Base	1
Tephra	MEXI-CHA16-1B-178Y-1-A	M	1		289 216	218.89825	1	3	No	1	1	Flat Top/Base	2
Tephra	MEXI-CHA16-1B-178Y-1-A	F	1		289 381	219.05325	1	0	No	1	2	Flat Top/Base	1
Tephra	MEXI-CHA16-1B-178Y-1-A	I	0.5		289.492	219.15925	1	1	No	1	1	Flat Top/Flat Base	1
Tephra	MEXI-CHA16-1B-178Y-1-A	F	2.5		289 566	219.20825	1	-1	No	2	2	Flat Top/Base	1
Tephra	MEXI-CHA16-1A-173Y-1-A	M	1		289 628	219.26025	2	1	No	1	1	Gradaional Top/Flat Base	1
Tephra	MEXI-CHA16-1A-173Y-1-A	F	14 25		289.781	219.27075	1	-1	No	2	2	Flat Top/Base	1
Tephra	MEXI-CHA16-1A-173Y-1-A	M	1		289 831	219.31075	1	3	No	1	1	Flat Top/Flat Base	1
Tephra	MEXI-CHA16-1A-173Y-1-A	F	41 25		290 296	219.36325	1	-3	No	1	1	Flat Top/Base	1
Tephra	MEXI-CHA16-1B-179Y-1-A	F	1.5		290.428	219.48025	1	-1	No	1	1	Flat Top/Base	1
Tephra	MEXI-CHA16-1B-179Y-1-A	M	1		290 508	219.55025	2	3	No	1	1	Gradational Top/Base	2
Tephra	MEXI-CHA16-1B-179Y-1-A	M	1		290 638	219.67025	1	2	No	1	1	Flat Top/Flat Base	1
Tephra	MEXI-CHA16-1B-179Y-1-A	M	0.6		290 666	219.69225	1	2	No	1	1	Flat Top/Flat Base	1
Tephra	MEXI-CHA16-1B-179Y-1-A	M	0.5		290 868	219.88925	1	2	No	1	1	Flat Top/Flat Base	1
Tephra	MEXI-CHA16-1B-179Y-1-A	M	0.5		290 888	219.90425	1	2	No	1	1	Flat Top/Flat Base	1
Tephra	MEXI-CHA16-1B-179Y-1-A	M	0.5		290 933	219.94425	2	3	Unsure	1	1	Flat Top/Base (but unclear as dark)	2
Tephra	MEXI-CHA16-1B-179Y-1-A	F	1		290 968	219.96925	1	1	No	1	1	Flat Top/Bioturbated Base	1
Tephra	MEXI-CHA16-1B-179Y-1-A	F	0.6		291 015	220.01025	1	4	No	1	1	Flat Top/Flat Base	2
Tephra	MEXI-CHA16-1B-179Y-1-A	M	1		291.158	220.14325	2	2	Unsure	1	1	Hard to see - dark in image	2
Tephra	MEXI-CHA16-1B-179Y-1-A	M	1		291.191	220.16625	2	2	Unsure	1	1	Hard to see - dark in image	2
Tephra	MEXI-CHA16-1C-174Y-1-A	F	1.125		291.29925	220.26325	1	-1	No	1	1	Flat Top/Bioturbated Base	1
Tephra	MEXI-CHA16-1C-174Y-1-A	M	0.5		291 353	220 312	2	3	No	1	1	Gradational Top/Base	2
Tephra	MEXI-CHA16-1C-174Y-1-A	M	0.5		291.423	220 377	2	2	No	1	1	Gradational Top/Base	2
Tephra	MEXI-CHA16-1C-174Y-1-A	F	0.875		291.44175	220 387	1	1	No	1	1	Flat-Irregular Top/Base	1
Tephra	MEXI-CHA16-1C-174Y-1-A	F	3		291 513	220.42825	1	-2	Yes (upper 1 cm)	2	2	Flat Top/Flat Base	1
Tephra	MEXI-CHA16-1C-174Y-1-A	M	0.875		292.04675	220.95325	1	2	No	1	1	Flat Top/Flat Base	1
Tephra	MEXI-CHA16-1C-174Y-1-A	F	1 25		292.133	221 027	1	0	Unsure	1	1	Flat Top/Dispersed Base	1
Tephra	MEXI-CHA16-1C-174Y-1-A	M	1		292.30925	221.19325	1	2	No	1	1	Flat Top/Flat Base	1
Tephra	MEXI-CHA16-1C-174Y-1-A	M	0.75		292.34425	221.22075	1	2	No	1	1	Flat Top/Flat Base	2
Tephra	MEXI-CHA16-1C-174Y-1-A	M	0.8		292 363	221.2315	1	2	No	1	1	Flat Top/Flat Base	1
Tephra	MEXI-CHA16-1C-174Y-1-A	M	4.5		292.423	221.2465	1	2	No	1	1	Flat Top/Flat base	1
Tephra	MEXI-CHA16-1A-175Y-1-A	F	5.5		293.0355	221 804	2	-4	No	1	2	Flat Top/Flat Base	1
Tephra	MEXI-CHA16-1A-175Y-1-A	F	67		293.7055	221 804	1	-2	Yes (upper 6.4 cm)	2	1	Flat Top/Flat Base	1

APPENDIX C2

THIS DATA IS REDUCED IN SIZE FOR INCLUSION IN THE THESIS. SEE FILE ON LINK PROVIDED BELOW FOR FULL DATASET:

https://drive.google.com/drive/folders/1ka5gUXAGsUy5yu5aAfIlh3fZTd2PN_3n?usp=sharing

Modal grain size values for each analysed sample:

Core section name and depth of sample	Modal grain size value (μm)
CHA08-4A-17S-1_11-15cm	6.749121333
MEXI-CHA16-1A-76Y-1_76.5-79cm	5.402340333
MEXI-CHA16-1A-172Y-1_72-74cm	3.843745333
CHA08-4A-5S-1_91.5-95.5cm	4.622213
MEXI-CHA16-1C-96Y-1_14-18cm	6.934825333
MEXI-CHA16-1C-96Y-1_81.5-83cm	6.135879333
MEXI-CHA16-1C-163Y-1_123-124cm	3.618904
MEXI-CHA16-1C-105Y-1_127-128cm	3.870232667
MEXI-CHA16-1C-107Y-1_0-1.5cm	4.693599333
MEXI-CHA16-1C-107Y-1_76-78cm	4.950502333
MEXI-CHA16-1C-100Y-1_120-121cm	6.064417667
MEXI-CHA16-1A-115Y-1_94-95cm	4.860923667
MEXI-CHA16-1B-173Y-1_134-136cm	4.029361
MEXI-CHA16-1B-138Y-1_15.5-17cm	4.274202667
MEXI-CHA16-1C-163Y-1_126-127cm	3.921935333
MEXI-CHA16-1C-130Y-1_122-123cm	3.622803333
MEXI-CHA16-1C-70Y-1_134-137cm	5.312748333
MEXI-CHA16-1C-70Y-1_142-145cm	5.513501
MEXI-CHA16-1C-73Y-1_101-103cm_RE-RUN	5.240515

APPENDIX C3

Quality Analysis ... *Innovative Technologies*

Report No.: A22-02786
Report Date: 22-Apr-22
Date Submitted: 03-Mar-22
Your Reference:

Univerisity of Birmingham
Aston Webb – Block A, Earth Science
School if Geography, Earth & Enviro Scie
Edgbaston Birmingham B15 2TT
United Kingdom

ATTN: Alastair Hodgetts

CERTIFICATE OF ANALYSIS

3 Pulp samples were submitted for analysis.

The following analytical package(s) were requested:		Testing Date:
4LITHO (1-10)	QOP WRA/ QOP WRA 4B2 (/Major/Trace Elements Fusion ICPOES/ICPMS)	2022-03-10 12:54:00

REPORT **A22-02786**

This report may be reproduced without our consent. If only selected portions of the report are reproduced, permission must be obtained. If no instructions were given at time of sample submittal regarding excess material, it will be discarded within 90 days of this report. Our liability is limited solely to the analytical cost of these analyses. Test results are representative only of material submitted for analysis.

Notes:

We recommend using option 4B1 for accurate levels of the base metals Cu, Pb, Zn, Ni and Ag. Option 4B-INAA for As, Sb, high W >100ppm, Cr >1000ppm and Sn >50ppm by Code 5D. Values for these elements provided by Fusion ICP/MS, are order of magnitude only and are provided for general information. Mineralized samples should have the Quant option selected or request assays for values which exceed the range of option 4B1. Total includes all elements in % oxide to the left of total.

SCC Accredited LAB Accrédité CCN TM

Lab D: 266

CERTIFIED BY:



Emmanuel Eseme , Ph.D
Quality Control Coordinator

ACTIVATION LABORATORIES LTD.
41 Bittern Street, Ancaster, Ontario, Canada, L9G 4V5
TELEPHONE +905 648-9611 or +1.888.228.5227 FAX +1.905.648.9613
E-MAIL Ancaster@actlabs.com ACTLABS GROUP WEBSITE www.actlabs.com

Analyte Symbol	LO	SiO2	Al2O3	Fe2O3( )	MnO	MgO	CaO	Na2O	K2O	iO2	P2O5	otal	Sc	Be	V	Ba	Sr	Y	Zr	Cr	Co	Ni	Cu
Unit Symbol	%	%	%	%	%	%	%	%	%	%	%	%	ppm	ppm	ppm	ppm	ppm	ppm	ppm	ppm	ppm	ppm	ppm
Lower Limit		0 0	0 0	0 0	0 00	0 0	0 0	0 0	0 0	0 00	0 0	0 0			5	2	2		2	20		20	0
Method Code	GRAV	FUS CP	FUS CP	FUS CP	FUS CP	FUS CP	FUS CP	FUS CP	FUS CP	FUS CP	FUS CP	FUS CP	FUS CP	FUS CP	FUS CP	FUS CP	FUS CP	FUS CP	FUS CP	FUS MS	FUS MS	FUS MS	FUS MS
ARL	0 34	57 39	6 33	7 35	0 9	4 59	7 77	4 00	20	598	< 0 0	00 7	22	2	70	432	475		290	70	9	60	50
ARL 2	0 4	54 85	6 83	8 00	0 5	4 4	7 62	4	0	9 7	0 04	99 42	23	2	73	365	492		282	70	2	70	20
ARL 3	0 27	57 47	7 9	7 37	0 44	4 07	7 77	3 66	6	328	0 09	00 5	23		74	423	400	9	208	00	8	< 20	< 0

Analyte Symbol	Zn	Ga	Ge	As	Rb	Nb	Mo	Ag	n	Sn	Sb	Cs	La	Ce	Pr	Nd	Sm	Eu	Gd	b	Dy	Ho	Er
Unit Symbol	ppm	ppm	ppm	ppm	ppm	ppm	ppm	ppm	ppm	ppm	ppm	ppm	ppm	ppm	ppm	ppm	ppm	ppm	ppm	ppm	ppm	ppm	ppm
Lower Limit	30			5	2		2	0 5	0 2		0 5	0 5	0	0	0 05	0	0	0 05	0	0	0	0	0
Method Code	FUS MS	FUS MS	FUS MS	FUS MS	FUS MS	FUS MS	FUS MS	FUS MS	FUS MS	FUS MS	FUS MS	FUS MS	FUS MS	FUS MS	FUS MS	FUS MS	FUS MS	FUS MS	FUS MS	FUS MS	FUS MS	FUS MS	FUS MS
ARL	70	9		< 5	6	20	< 2	< 0 5	< 0 2	2	< 0 5	< 0 5	6 2	2 3	48	6 7	7	50	8	0 3	2 3	0 5	4
ARL 2	70	20		< 5	2	20	< 2	< 0 5	< 0 2		< 0 5	< 0 5	5 2	8	6	7 7	2 0	59	2	0 3	2 2	0 5	4
ARL 3	70	2		< 5	28	8	< 2	< 0 5	< 0 2	2	< 0 5	0 8	6 2	3 2	7	8 0	2 0	6	2 0	0 3	2 2	0 4	3

Analyte Symbol	m	Yb	Lu	Hf	a	W	I	Pb	Bi	h	U
Unit Symbol	ppm	ppm	ppm	ppm	ppm	ppm	ppm	ppm	ppm	ppm	ppm
Lower Limit	0 05	0	0 0	0 2	0		0	5	0 4	0	0
Method Code	FUS MS	FUS MS	FUS MS	FUS MS	FUS MS	FUS MS	FUS MS	FUS MS	FUS MS	FUS MS	FUS MS
ARL	0 23	6	0 26	5 3		<	< 0	6	< 0 4	8	0 7
ARL 2	0 20	5	0 25	5 3		<	< 0	< 5	< 0 4	2	0 5
ARL 3	0 20	3	0 22	5 0	0 5	<	< 0	5	< 0 4	6	0 6

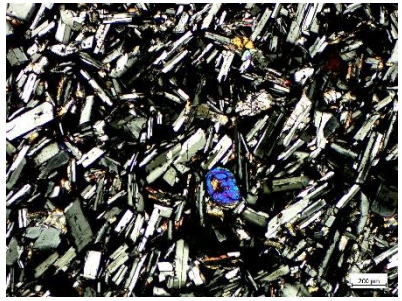
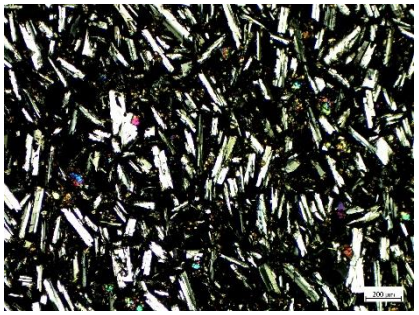
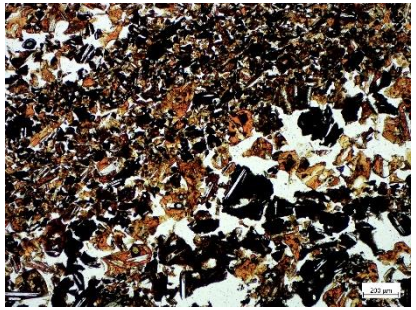
Analyte Symbol	SiO2	Al2O3	Fe2O3( )	MnO	MgO	CaO	Na2O	K2O	iO2	P2O5	otal	Sc	Be	V	Ba	Sr	Y	Zr	Cr	Co	Ni	Cu	Zn
Unit Symbol	%	%	%	%	%	%	%	%	%	%	%	ppm	ppm	ppm	ppm	ppm	ppm	ppm	ppm	ppm	ppm	ppm	ppm
Lower Limit	0 0	0 0	0 0	0 00	0 0	0 0	0 0	0 0	0 00	0 0	0 0			5	2	2		2	20		20	0	30
Method Code	FUS CP	FUS CP	FUS CP	FUS CP	FUS CP	FUS CP	FUS CP	FUS CP	FUS CP	FUS CP	FUS CP	FUS CP	FUS CP	FUS CP	FUS CP	FUS CP	FUS CP	FUS CP	FUS MS	FUS MS	FUS MS	FUS MS	FUS MS
DNC Meas	47 58	7 87	9 83	0 50	0 04	63	93	0 22	0 460	0 07		3		55	07	38	5	4					
DNC Cert	47 5	8 34	9 97	0 50	0 3	49	890	0 234	0 480	0 070		3		48	8	44 0	8 0	38					
DNC Meas	46 72	8 38	9 87	0 48	9 94	40	9	0 22	0 472	0 08		3		55	07	44	5	35					
DNC Cert	47 5	8 34	9 97	0 50	0 3	49	890	0 234	0 480	0 070		3		48	8	44 0	8 0	38					
GBW 07 3 Meas	70 66	2 83	3 5	0 30	0 4	0 60	2 50	5 45	0 280	0 04		5	4	< 5	496	39	4	422					
GBW 07 3 Cert	72 8	3 0	3 2	0 40	0 60	0 590	2 57	5 43	0 300	0 0500		5 00	4 00	5 00	506	43 0	43 0	403					
W 2a Meas	52 8	5 25	0 83	0 70	6 25	5	2 23	0 6	080	0		35	<	277	76	96	20	03					
W 2a Cert	52 4	5 4	0 7	0 63	6 37	0 9	2 4	0 626	06	0 40		36 0	30	262	82	90	24 0	94 0					
SY 4 Meas	49 26	2 40	6 46	0 0	0 49	8 3	6 92	65	0 3 0	0 2		<	3	8	339	232	6	492		2			90
SY 4 Cert	49 9	20 69	6 2	0 08	0 54	8 05	7 0	66	0 287	0 3			2 6	8 0	340	9	9	5 7		2 8			93
SY 4 Meas	49 90	20 70	6 8	0 0	0 50	8 4	6 95	70	0 284	0 3			3	7	352	99	4	532					
SY 4 Cert	49 9	20 69	6 2	0 08	0 54	8 05	7 0	66	0 287	0 3			2 6	8 0	340	9	9	5 7					
B R a Meas	48 62	5 65	57	0 70	9 62	3 67	82	0 0	0 970	0 03		44	<	34	7	05	4	9		52	90	30	70
B R a Cert	47 96	5 50	30	0 75	9 700	3 30	82	0 030	0 96	0 02		44	0 58	3 0	6	0	6	8		52	70	25	70
B R a Meas	48 04	5 73	48	0 73	9 58	3 66	83	0 0	0 972	0 04		44	<	344	8	09	3	5					
B R a Cert	47 96	5 50	30	0 75	9 700	3 30	82	0 030	0 96	0 02		44	0 58	3 0	6	0	6	8					
ZW C Meas																			60				960
ZW C Cert																			56 0				050
NCS DC863 6 Meas	69 94	4 03	0 40	0 024	0 07	0 68	4 0	3 9	0 7 3	0 04								> 0000					
NCS DC863 6 Cert	70 73	4 57	0 38	0 02	0 079	0 63	4 20	3 90	0 64	0 040								34700					
OREAS 0 b (Fusion) Meas																				46		420	
OREAS 0 b (Fusion) Cert																				47		420	
NCS DC863 8 Meas																							
NCS DC863 8 Cert																							
BCR 2 Meas	53 9	3 29	4 00	0 200	3 5	7 2	3 5	8	2 230	0 37		33		442	706	338	3	70					
BCR 2 Cert	54	3 5	3 8	0 96	3 59	7 2	3 6	79	2 26	0 35		33		4 6	683	346	37	88					
USZ 42 2006 Meas	82	2 83		63	2 77	32 95	0 22	60	0 87	0 2				30	30	50 7	48			5	< 20	20	480
USZ 42 2006 Cert	86	2 72		67	2 78	32 68	0 25	55	0 200	0 22				5 00	307	4900	67			7 89	3 8	27 37	469
REE Meas																			300			80	
REE Cert																			277	58		79 7	
W 2b Meas	52 46	5 70	02	0 67	6 28	07	2 24	0 63	086	0 3		36	<	276	82	97	8	87	90	4		20	80
W 2b Cert	52 4	5 4	0 7	0 63	6 37	0 9	2 4	0 626	06	0 40		36 0	30	262	82	90	24 0	94 0	92 0	43 0		0	80 0
ARL 3 Orig	57 38	7 20	7 37	0 44	4 04	7 76	3 65	6	3 7	0 09	00 4	23		74	422	399	9	207	00	7	20	< 0	70
ARL 3 Dup	57 56	7 7	7 37	0 43	4 09	7 78	3 66	6	338	0 08	00 6	23		74	423	402	9	2 0	0	9	< 20	< 0	70
ARL 3 Orig	48 85	22 48	6 3	0 088	7 48	8 60	3 05	53	0 99	0 05	98 72	9	<	50	67	609	3	7					
ARL 3 Dup	54 37	5 47	8 38	0 35	6 67	9 99	2 85	38	0 696	0 20	00 4	29		203	506	529		66					
Method Blank	0 0	< 0 0	< 0 0	0 003	< 0 0	< 0 0	< 0 0	< 0 0	< 0 00	0 03	0 06	<	<	< 5	< 2	< 2	<	< 2	< 20	<	< 20	< 0	< 30
Method Blank	< 0 0	< 0 0	< 0 0	0 003	< 0 0	< 0 0	< 0 0	< 0 0	< 0 00	< 0 0		<	<	< 5	< 2	< 2	<	< 2					
Method Blank	0 0	< 0 0	< 0 0	0 003	< 0 0	< 0 0	< 0 0	< 0 0	< 0 00	< 0 0		<	<	< 5	< 2	< 2	<	< 2					

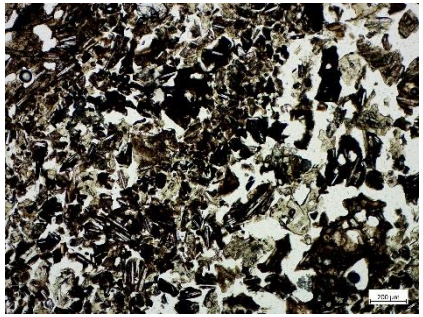
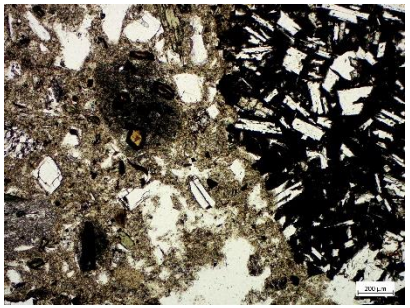
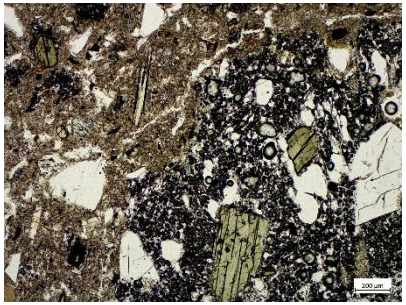
Analyte Symbol	Ga	Ge	As	Rb	Nb	Mo	Ag	n	Sn	Sb	Cs	La	Ce	Pr	Nd	Sm	Eu	Gd	b	Dy	Ho	Er	m
Unit Symbol	ppm	ppm	ppm	ppm	ppm	ppm	ppm	ppm	ppm	ppm	ppm	ppm	ppm	ppm	ppm	ppm	ppm	ppm	ppm	ppm	ppm	ppm	ppm
Lower Limit			5	2		2	0 5	0 2		0 5	0 5	0	0	0 05	0	0	0 05	0	0	0	0	0	0 05
Method Code	FUS MS	FUS MS	FUS MS	FUS MS	FUS MS	FUS MS	FUS MS	FUS MS	FUS MS	FUS MS	FUS MS	FUS MS	FUS MS	FUS MS	FUS MS	FUS MS	FUS MS	FUS MS	FUS MS	FUS MS	FUS MS	FUS MS	FUS MS
DNC Meas																							
DNC Cert																							
DNC Meas																							
DNC Cert																							
GBW 07 3 Meas																							
GBW 07 3 Cert																							
W 2a Meas																							
W 2a Cert																							
SY 4 Meas	34			55	4						5	62 9	32	5 8	6 5	3 3	99	4	2 8	9 0	4 4	5	2 30
SY 4 Cert	35			55 0	3						5	58	22	5 0	57	2 7	2 00	4 0	2 6	8 2	4 3	4 2	2 3
SY 4 Meas																							
SY 4 Cert																							
B R a Meas	7									0 5		0 7	2 2		2 7	2	0 57	2 0		2 9			
B R a Cert	6									0 58		0 63	9		2 5		0 55	2 0		4			
B R a Meas																							
B R a Cert																							
ZW C Meas	99			> 000	2 2				> 000	4	264	32	02	0 3	25 8	7 3		4 8					
ZW C Cert	99			8500	98				300	4 2	260	30 0	97	9 5	25 0	6 6		4 70					
NCS DC863 6 Meas																							
NCS DC863 6 Cert																							
OREAS 0 b (Fusion) Meas						20						8 7	360	33	4 3	52 0	8 05		5 7	33 7	6 6	20	
OREAS 0 b (Fusion) Cert						2						789	33	27	378	48	7 77		5 37	32	6 34	8 7	
NCS DC863 8 Meas				388							3	970	425	727	> 2000	> 000	9 3	> 000	469	> 000	568	> 000	269
NCS DC863 8 Cert				369 42							88	960	432	737	3429	725	8 9	2 68	468	3224	560	750	27
BCR 2 Meas																							
BCR 2 Cert																							
USZ 42 2006 Meas				62	36	37						> 2000	> 3000	> 000	> 2000	547	92 0			58 0	8 3		
USZ 42 2006 Cert				67 2	3 00	34 40						2 00	27600	2300	6500	539	87 22			57 63	7 86		
REE Meas			2	> 000					5 0			750	> 3000	468			25 4	45	6	9 7	2 6	752	6
REE Cert			24	050					498		07	66	3960	435			23 5	433	06	847	208	70	06
W 2b Meas	8	2	< 5	9	7	< 2				0 8	0 9	0	25 0		3 3	3 5	00		0 7		0 8	2 3	0 36
W 2b Cert	7 0	00	20	2 0	7 90	0 600				0 790	0 990	0 0	23 0		3 0	3 30	00		0 630		0 760	2 50	0 380
ARL 3 Orig	2		< 5	28	8	< 2	< 0 5	< 0 2	2	< 0 5	0 8	6 3	3 3	68	7 7	2 0	6	2 0	0 3	2 2	0 4	3	0 20
ARL 3 Dup	2		< 5	28	8	2	< 0 5	< 0 2	2	< 0 5	0 8	6 2	3 2	75	8 2	2 0	6	2	0 3	2 2	0 4	2	0 9
ARL 3 Orig																							
ARL 3 Dup																							
Method Blank	<	<	< 5	< 2	<	< 2	< 0 5	< 0 2	<	< 0 5	< 0 5	< 0	< 0	< 0 05	< 0	< 0	< 0 05	< 0	< 0	< 0	< 0	< 0	< 0 05
Method Blank																							
Method Blank																							

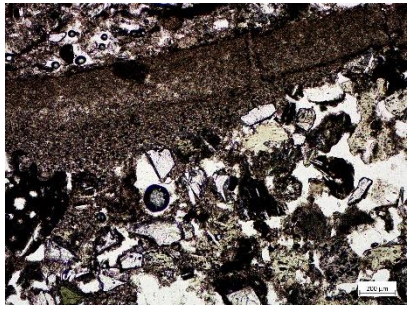
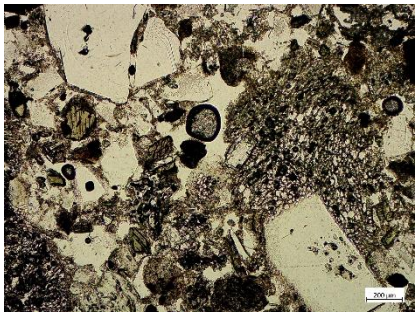
Analyte Symbol	Yb	Lu	Hf	a	W	I	Pb	Bi	h	U
Unit Symbol	ppm	ppm	ppm	ppm	ppm	ppm	ppm	ppm	ppm	ppm
Lower Limit	0	0 0	0 2	0		0	5	0 4	0	0
Method Code	FUS MS	FUS MS	FUS MS	FUS MS	FUS MS	FUS MS	FUS MS	FUS MS	FUS MS	FUS MS
DNC Meas										
DNC Cert										
DNC Meas										
DNC Cert										
GBW 07 3 Meas										
GBW 07 3 Cert										
W 2a Meas										
W 2a Cert										
SY 4 Meas	5 4	2 24	0 5	0 8			0		3	0 8
SY 4 Cert	4 8	2	0 6	0 9			0		4	0 8
SY 4 Meas										
SY 4 Cert										
B R a Meas	8	0 28	0 6				< 5			
B R a Cert	7	0 3	0 60				3			
B R a Meas										
B R a Cert										
ZW C Meas				84 8	327	33 4				20 5
ZW C Cert				82	320	34				20 0
NCS DC863 6 Meas										
NCS DC863 6 Cert										
OREAS 0 b (Fusion) Meas	8 8	2 77							40 6	4
OREAS 0 b (Fusion) Cert	7 6	2 58							37	396
NCS DC863 8 Meas	> 000	260							73 5	
NCS DC863 8 Cert	844	264							67 0	
BCR 2 Meas										
BCR 2 Cert										
USZ 42 2006 Meas	9						6 0		963	
USZ 42 2006 Cert	7 85						600		946	
REE Meas	738		498						77	42
REE Cert	678		479						7 9	37
W 2b Meas	2		2 5	0 5	<	< 0		< 0 4	2 5	0 6
W 2b Cert	2 0		2 60	0 500	0 300	0 200		0 0300	2 40	0 530
ARL 3 Orig	3	0 23	5 0	0 5		< 0	5	< 0 4	6	0 6
ARL 3 Dup	4	0 22	5 0	0 5	<	< 0	5	< 0 4	6	0 6
ARL 3 Orig										
ARL 3 Dup										
Method Blank	< 0	< 0 0	< 0 2	< 0	<	< 0	< 5	< 0 4	< 0	< 0
Method Blank										
Method Blank										

APPENDIX C4

THIN SECTION DESCRIPTIONS

Sample ID	Lithology	Composite basal depth (mc)	Description	Photograph (PPL, XPL as stated)
AH1	Lava	419.18	Groundmass is dominated by euhedral feldspar (plagioclase) laths (c.90 vol. %). These are typically 200 – 400 μm in length and display simple and albite twinning. Occasional zoning (in c.5% of plagioclase crystals). Higher birefringence minerals occur, accounting for c.10 vol. %. These are typically olivine and pyroxene. These are generally rounded and exhibit pervasive fracturing.	 XPL
AH2	Lava	453.07	Groundmass is generally finer than in AH1, with euhedral plagioclase laths still dominating (c.95 vol. %) but displaying typical lengths of c.200 μm. Similarly, plagioclase laths display simple and albite twinning with occasional zoned crystals. Olivine and pyroxene are present in smaller quantities and are generally smaller than plagioclase laths. The groundmass is dark, perhaps due to a high glass content.	 XPL
AH3	Scoria	517.87	Despite being an indurated lithology, AH3 is composed of grains which are held together by silica (quartz, but perhaps a secondary siliceous phase). Grains are dominated by glass shards, which are blocky in shape and contain plagioclase microlite laths within. The sample is red in colour due to oxidation, seen in hand sample. Glass is typically well sorted in grain size, and is layered, as also observable in hand sample. Some grains appear to be sintered together, strengthening the cohesion of the deposit. Very few minerals (apart from plagioclase laths in the glass are present).	 PPL

AH4	Volcaniclastics	448.35	AH4 is composed of grains which are loosely held together (i.e., a friable deposit). Grains are dominated by glass shards, which are blocky in shape and contain plagioclase microlite laths within. Very few minerals are present, however some sections of the deposit are comprised of a finer matrix with more variable mineralogy, similar to that of AH5-11.	 PPL
AH5	Volcaniclastics with pumice and lava clasts	409.66	A poorly sorted deposit with lava clasts that are rounded in shape and contain a dark, fine groundmass with euhedral plagioclase laths. Pumice clasts are also present exhibiting dark vesicular glass in both XPL and PPL. These clasts are also rounded and lack a more complex mineralogy. The matrix of the overall deposit is fine grained and glassy with suspended loose, free crystals throughout. These contain large euhedral plagioclase crystals often with zoned and simple twins and often they are partial fragments assumed to be broken during transportation. Other minerals of hornblende, pyroxene and biotite also are present and are less fragmented than the plagioclase.	 PPL
AH6	Volcaniclastics with pumice and lava clasts	401.37	Similarly, to AH5, this sample is a poorly sorted deposit with rounded lava clasts exhibiting a dark, fine groundmass with euhedral plagioclase laths. Pumice clasts are also present and larger, allowing more detail to be seen. These typically display dark vesicular glass in both XPL and PPL and occasionally contain large phenocrysts of pyroxene. These clasts are also rounded. The matrix of the overall deposit is fine grained and glassy with suspended loose, free crystals throughout, comprising a similar mineralogy to AH5.	 PPL

AH7	Volcaniclastics with finer beds	539.80	As in AH5, the groundmass of AH7 is dominated by partial or whole, mostly euhedral crystals of plagioclase, pyroxene hornblende and (some) olivine. Abundances of these minerals are fairly equal with plagioclase dominating (c.60 vol. %) and olivine comprising (c.5 vol. %) of the deposit. Sharp contacts occur within the sample alternating between coarse- and fine-grained components. Under high magnification, mineralogy of the finer deposits is similar to that of the coarser beds.	 PPL
AH8, 9, 10, 11	Volcaniclastics with pumice clasts	Between 363.36 and 543.73	AH8, 9, 10 and 11 are all similar in terms of microscopic features. Similarly, to AH6, the samples are poorly sorted with rounded lava clasts exhibiting a dark, fine groundmasses with euhedral plagioclase laths. Pumice clasts are also present and large. These typically display dark vesicular glass in both XPL and PPL and often contain large phenocrysts of pyroxene. These clasts are also rounded. The matrix of the overall deposit is fine grained and glassy with suspended loose, free crystals throughout, comprising a similar mineralogy to AH5.	 XPL (AH9)  PPL (AH10)

APEPENDIX C5

NON-VOLCANIC EVENT LAYERS

Description

Very fine-grained clay-rich deposits (all ≤3 φ), often grey to purple in colour, but sometimes white to light grey. Layers are generally very thin (<1 cm) with very few displaying greater thicknesses. Some layers preserve internal structures, such as cross laminations and diffuse laminations, however details of these are often difficult to see as the deposits are so fine grained. Most layers do not correspond with MS spikes and many of subjected to the same drilling artefacts as other sedimentological layers in the core. Clustering is common with many often occurring within a core section. The deposits are only present between c.229 mc and c.254 mc which spans background sediment types. The part of core these deposits occur is typically well preserved.

Interpretation

We interpret these deposits to resemble event layers that are non-volcanic in origin (see Fig. S1). Their abrupt difference to the background sediments suggests that there was sudden and short-lived (based on their thicknesses) change in sediment input into the lake and ultimately a sharp difference in depositional processes. As the sediment types above and below the layers possess similar characteristics, it is interpreted that these layers are formed on instantaneous geological timescales and are 'events'. While it is possible these are very fine distal ashes, the high frequency over short-timescales is not consistent with large explosive eruptions that typically have long repose times between eruptions. While they could be sourced from different volcanoes and resemble a change in wind direction, allowing ashes from a particular region of volcanoes to be represented in the core, we would expect to see a change in the thicker and higher confidence volcanic material, which we do not. We therefore interpret these to be formed from another type of event, such as a flood or turbidity currents from the edge of the lake transporting material across the lakebed (e.g., Schlolaut et al., 2014). Moreover, these deposits could be liquefaction features from seismic activity. A more detailed investigation is needed for these deposits, but due to the above interpretation, they have been omitted from our volcanological investigation into the core.

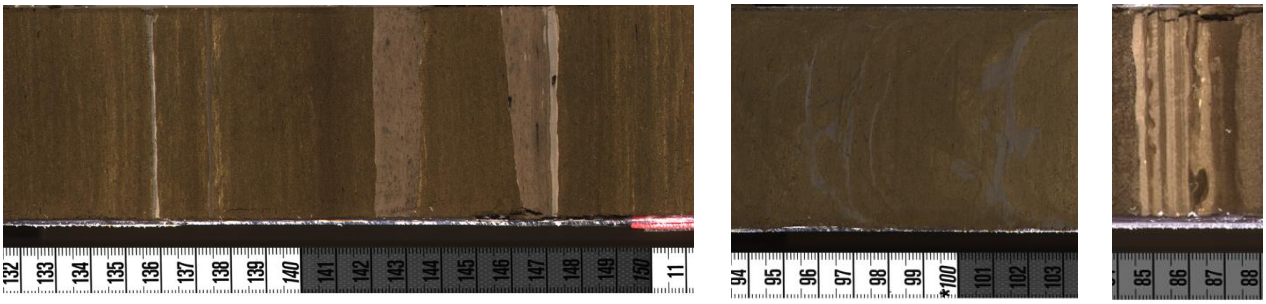


Fig. S1. Example photographs of interpreted event layers that are non-volcanic in origin.

SMEAR SLIDE METHODS

1. Clean a glass slide with alcohol. This is very important for tephra (glass shard identification) as industrial glass shards can also be present within some sediments and obscure the tephra.

2. Place 1-2 drops of deionised water on the slide so it forms a small sphere of water in the centre of the slide.

3. Place a toothpick or thin, clean wooden stick at an angle within the layer of interest, to avoid splitting apart sediment.

4. Remove the toothpick and rub it gently within the deionised water droplet(s) to disperse sediment within the water.

5. Dry the slide on a hot plate to evaporate the water and leave behind the dry grains.

6. Add a cover slide with ultraviolet (UV) curing glue and place under a UV light for 5 – 10 minutes.

7. Label the slide with the core section name and depth of the sample.

8. Observe under a petrological microscope to determine the componentry of the layer of interest.

APPENDIX E1

Filtered core analyses, normalised to 100% (0-50.99 mc)

Date Analysed	Core Section Identifier	sample_no	SiO2	Na2O	Cl	K2O	FeOt	Al2O3	MgO	P2O5	CaO	MnO	TiO2	total	Analytical Total
Mar 12 01:19 2020	CHA16-1D-1CY-1(64-67cm)_3	0.585-S	69 00437408	5.024165683	0.144364556	2.719271111	3.124622196	15.41471916	0.966999336	0.174207427	2.697163215	0 074171988	0 655941251	100	90.46541885
Mar 12 01:27 2020	CHA16-1D-1CY-1(64-67cm)_5	0.585-S	69 04457296	4.868913545	0.1218144	2.743866588	3.04870861	15.51593622	0.948625489	0.203379017	2.810250457	0 060077402	0 63385531	100	90 38340314
Mar 12 01:39 2020	CHA16-1D-1CY-1(64-67cm)_8	0.585-S	69 20512033	4.861663927	0.165965253	2 657215521	2.915752246	15.84323742	0.870127366	0.174345372	2.64614379	0 056355113	0 604073662	100	90 32011068
Mar 12 01:51 2020	CHA16-1D-1CY-1(64-67cm)_11	0.585-S	69.17283452	5.003646014	0 077130413	2 628523284	2.86874652	15.76267977	0.810173798	0.214733939	2.7909031	0 048105021	0 622523622	100	98 53441345
Mar 12 02:03 2020	CHA16-1D-1CY-1(64-67cm)_14	0.585-S	69.40643613	4.483911933	0.146747909	2 65926314	2.946739921	15.91695308	0.870284566	0.147897179	2.691825546	0 071528751	0 658411845	100	92.13078476
Mar 12 02:07 2020	CHA16-1D-1CY-1(64-67cm)_15	0.585-S	69 3438107	4.580518008	0.11171619	2 694453573	2.95046661	15.91206651	0.877562802	0.164654886	2.68409029	0 06518505	0 615475376	100	96.49451843
Mar 12 02:11 2020	CHA16-1D-1CY-1(64-67cm)_16	0.585-S	69 07085515	4.861044056	0 078109989	2 544806819	2.872717733	16.12245111	0.745368724	0.144202001	2.866802783	0 075720987	0 617920643	100	96 2744984
Mar 12 02:15 2020	CHA16-1D-1CY-1(64-67cm)_17	0.585-S	69 63360986	4.790256251	0 090718536	2.745293566	2.938329551	15.29736985	0.919570138	0.208553985	2.724652261	0 057382828	0 594263171	100	96 89309854
Mar 12 02:19 2020	CHA16-1D-1CY-1(64-67cm)_18	0.585-S	69.19962431	4.926895987	0 067375051	2.705133637	2.987519696	15.57628328	0.930788866	0.232864761	2.705133637	0 045693456	0 622687316	100	98.70122361
Mar 12 02:27 2020	CHA16-1D-1CY-1(64-67cm)_20	0.585-S	68 99955447	4.980185001	0.134055406	2.715730991	3.179407436	15.67444372	0.855076575	0.069262979	2.759009573	0 066865408	0 566408436	100	92.42447091
Mar 12 02:43 2020	CHA16-1D-1CY-1(64-67cm)_24	0.585-S	69 97228888	4.988831903	0 075163631	2 675315693	2.137346835	16.15412978	0.437711373	0.099349268	2.866409671	0 0581775	0 535275465	100	94.194491
Mar 12 02:47 2020	CHA16-1D-1CY-1(64-67cm)_25	0.585-S	69.49155316	4.826100145	0.10932819	2 684494181	2.872675757	15.5535699	0.891187121	0.220128392	2.652020461	0 037236532	0 661706166	100	92 38239433
Mar 12 03:07 2020	CHA16-1D-1CY-1(64-67cm)_30	0.585-S	69.12249135	4.823155013	0 091076911	2.729240762	2.930994556	15.68487187	0.943887985	0.226136285	2.719018886	0 063988941	0 66513744	100	97 82940506
Mar 14 13:57 2020	CHA16-1D-3CY-1(52-54cm)_3	5.593-S	73.47175277	4.429021445	0 093391061	2.747422312	1.970978809	14.69433034	0.396443288	0.073264595	1.916806264	0	0 20658912	100	93 90620396
Mar 14 14:09 2020	CHA16-1D-3CY-1(52-54cm)_6	5.593-S	74 87601776	4.327810591	0 064495839	2 888657282	1.815297021	13.8339149	0.294855833	0.069117691	1.491597578	0 048949611	0 289285897	100	95.19994002
Mar 14 14:17 2020	CHA16-1D-3CY-1(52-54cm)_8	5.593-S	73 36612232	4.363332927	0 06293725	2 685596018	2.117329399	14.74882579	0.406925885	0.050739314	1.875817066	0 05760706	0 264766966	100	97 55748751
Mar 14 14:21 2020	CHA16-1D-3CY-1(52-54cm)_9	5.593-S	73.15775895	4.403877789	0 057716303	2.726915933	2.138542795	14.78077489	0.482042289	0.04746474	1.906790841	0 019990549	0 278124922	100	97 54609475
Mar 14 14:25 2020	CHA16-1D-3CY-1(52-54cm)_10	5.593-S	72 91527298	4.467383787	0 059972209	2.718463439	2.206902798	14.86814217	0.391847626	0.061736097	2.012908042	0 046691166	0 250679682	100	96 37797451
Mar 14 14:29 2020	CHA16-1D-3CY-1(52-54cm)_11	5.593-S	73.13815558	4.445647833	0 068985613	2.786766397	2.2259874	14.60406742	0.439036813	0.086968144	1.924446229	0 013670929	0 266267642	100	95 09229059
Mar 14 14:33 2020	CHA16-1D-3CY-1(52-54cm)_12	5.593-S	73 5569127	4.381640885	0 060725062	2.743794405	1.892251132	14.61221346	0.419386322	0.056364769	1.967449477	0 01542055	0 293841238	100	94 03036887
Mar 14 14:37 2020	CHA16-1D-3CY-1(52-54cm)_13	5.593-S	73 08621664	4.508699097	0 081181586	2 685156711	2.104749452	14.70471148	0.420793493	0.088704204	1.995583392	0 067912524	0 256291417	100	95.71135978
Mar 14 14:45 2020	CHA16-1D-3CY-1(52-54cm)_15	5.593-S	73 50660827	4.404755755	0 055141622	2.402002482	1.751407193	14.9959094	0.332204296	0.06213876	2.234906657	0	0 254925568	100	95.75343979
Mar 14 14:49 2020	CHA16-1D-3CY-1(52-54cm)_16	5.593-S	73 50066748	4.546932716	0 078253843	2 629582593	1.900630972	14.63469103	0.439140668	0.044248799	1.94314537	0 050585143	0 232121387	100	94 6918346
Mar 14 14:53 2020	CHA16-1D-3CY-1(52-54cm)_17	5.593-S	74.18004658	4.331304608	0 07892707	2 887318711	2.036590117	14.01260679	0.382218347	0.117705657	1.591186589	0 071656085	0 31043945	100	94 89773294
Mar 14 14:57 2020	CHA16-1D-3CY-1(52-54cm)_18	5.593-S	73.4464895	4.828861215	0 069139578	2 665622283	1.842054236	14.54218613	0.356840641	0.075803634	1.93674119	0 010308461	0 225953139	100	96 03761255
Mar 14 15:01 2020	CHA16-1D-3CY-1(52-54cm)_19	5.593-S	72 8531675	4.741541414	0 069482711	2 609484834	1.874239851	15.13359757	0.356488146	0.054882022	2.029599315	0 042870108	0 234646533	100	96 57078544
Mar 14 15:05 2020	CHA16-1D-3CY-1(52-54cm)_20	5.593-S	72 88009527	4.882087877	0 056113231	2.453659749	1.799751645	15.0084205	0.285759285	0.093073423	2.236246859	0 043689638	0 261102527	100	96 59040955
Mar 14 15:09 2020	CHA16-1D-3CY-1(52-54cm)_21	5.593-S	73.49665445	4.473445187	0 081272467	2 695260396	1.939885678	14.6610526	0.415985079	0.039081276	1.907415049	0 041154553	0 248793267	100	96.46563293
Mar 14 15:13 2020	CHA16-1D-3CY-1(52-54cm)_22	5.593-S	73 52330628	4.501569763	0 058273329	2 617188114	1.934035171	14.64972506	0.385991459	0.072381609	1.932220912	0 049890148	0 275418155	100	97 81490242
Mar 14 15:17 2020	CHA16-1D-3CY-1(52-54cm)_23	5.593-S	73.40723604	4.291447525	0 075723956	2 697731049	2.034369887	14.73115016	0.403024556	0.114262971	1.916534799	0 02916466	0 299354403	100	96 0066053
Mar 14 15:21 2020	CHA16-1D-3CY-1(52-54cm)_24	5.593-S	73 85373165	4.481633074	0 079259683	2 692993099	2.273973883	14.25633481	0.312032807	0.058756213	1.683120687	0 030704202	0 277459895	100	98 03218585
Mar 14 15:25 2020	CHA16-1D-3CY-1(52-54cm)_25	5.593-S	73 08316388	4.691184619	0 068281054	2.718597536	1.885649311	14.78871354	0.43179015	0.063223199	1.970456353	0 049419467	0 24952089	100	94 90187371
Mar 14 15:33 2020	CHA16-1D-3CY-1(52-54cm)_27	5.593-S	73 25327318	4.648026829	0 087842315	2.717424134	1.863294451	14.7202198	0.388206879	0.072675297	1.916942606	0 084893173	0 247201335	100	94 94285295
Mar 14 15:41 2020	CHA16-1D-3CY-1(52-54cm)_29	5.593-S	73.71539308	4.404023297	0.132126718	2.713119593	1.917257375	14.53582161	0.353088682	0	1.930064751	0 066504517	0 232600375	100	90 67053316
Mar 14 15:45 2020	CHA16-1D-3CY-1(52-54cm)_30	5.593-S	72.78207623	4.445137858	0 093404757	2 601685021	2.006228421	14.68182359	0.357081672	0.358797955	2.377769507	0 046595752	0 249399232	100	93.78537295
Mar 14 15:49 2020	CHA16-1D-3CY-1(52-54cm)_31	5.593-S	73.74535905	4.317605829	0 084963497	2.723053695	1.888740153	14.54325064	0.355623136	0.036940651	1.931468319	0 054249984	0 318745045	100	94.7465709
Mar 14 15:53 2020	CHA16-1D-3CY-1(52-54cm)_32	5.593-S	73.44878909	4.618670514	0 066502386	2 695759187	1.90926248	14.55658979	0.417436764	0.059579425	1.930037706	0 040803515	0 256569143	100	95 33492502
Mar 14 15:57 2020	CHA16-1D-3CY-1(52-54cm)_33	5.593-S	73 25743691	4.529493588	0 083009006	2 673347683	2.052944911	14.76272367	0.393247725	0	1.903589984	0 040256247	0 30395027	100	96.13414732
Mar 14 16:01 2020	CHA16-1D-3CY-1(52-54cm)_34	5.593-S	73 32625485	4.408018567	0 084575435	2 681401624	1.918281235	14.89547512	0.423123364	0.072175277	1.897118145	0 027555906	0 266020477	100	94 35363868
Mar 14 16:05 2020	CHA16-1D-3CY-1(52-54cm)_35	5.593-S	72 96879919	4.337135961	0 061493329	2.725038827	2.239773435	14.85665819	0.399493124	0.071467999	1.994934085	0 058202716	0 287003146	100	97 2463208
Mar 14 11:51 2020	CHA16-1D-4CY-2(64-66cm)_16	8.851-OS	74.19037698	3.858612524	0.117566791	3 61914766	1.577978813	14.70806603	0.343819441	0.068941432	1.052661292	0 034526225	0.428302812	100	90 0764574
Mar 14 11:55 2020	CHA16-1D-4CY-2(64-66cm)_17	8.851-OS	72 08006074	4.903026774	0.11238129	3 215268507	1.002957549	16.06108945	0.121184986	0.044707543	2.143512338	0 055527177	0 260283641	100	97 9700449
Mar 14 12:07 2020	CHA16-1D-4CY-2(64-66cm)_20	8.851-OS	68 80063094	6.389561286	0 059983111	2.781678822	0.851071874	18.18297627	0.055009543	0.019926936	2.720987648	0 008395612	0.129777961	100	98 86116176
Mar 14 12:23 2020	CHA16-1D-4CY-2(64-66cm)_24	8.851-OS	76.10980877	3.700002087	0.126434539	4 591627905	1.428026008	12.76100437	0.205491782	0.02339753	0.663589095	0 046685212	0 343932703	100	91 03525125
Mar 14 12:31 2020	CHA16-1D-4CY-2(64-66cm)_26	8.851-OS	66 90117462	4.329768786	0.113991109	2.152806598	2.377532358	18.13271409	0.591266532	0.175130817	4.628534185	0 056080612	0 541000298	100	92 90198211
Mar 14 12:35 2020	CHA16-1D-4CY-2(64-66cm)_27	8.851-OS	68 89155706	4.658869911	0.12255016	2.71128672	3.426822288	14.90114311	1.697267973	0.132527695	2.624525545	0.106065536	0.727384001	100	92 20714214
Mar 14 12:55 2020	CHA16-1D-4CY-2(64-66cm)_32	8.851-OS	72 61880619	4.679782575	0 097958827	3.411813858	0.996357226	15.74780019	0.134983006	0.025954903	2.040808903	0 009314461	0 236419862	100	95 55034757
Mar 14 12:59 2020	CHA16-1D-4CY-2(64-66cm)_33	8.851-OS	75.709346	4.108928311	0.118787309	4.440057094	1.296895418	13.09142088	0.200831307	0.042506708	0.643913493	0 035983401	0 31133007	100	95 04382288
Mar 14 13:03 2020	CHA16-1D-4CY-2(64-66cm)_34	8.851-OS	76 00016578	4.169637924	0.135119131	4 333418805	1.372412736	12.80778794	0.178923851	0.019004391	0.679772444	0	0 303756995	100	95.76734184
Mar 14 05:52 2020	CHA16-1D-4CY-2(74-76cm)_3	8.898-S	70.48476849	4.222249987	0 023695285	2.7733046	3.085837624	14.54739252	1.048235712	0.156197615	2.762678912	0 056847431	0 83879182	100	94.11155197
Mar 14 06:00 2020	CHA16-1D-4CY-2(74-76cm)_5	8.898-S	70.12011231	4.43705776	0 056362338	2.760390126	2.822722145	14.82342161	0.944831115	0.155757374	3.001793065	0 000524789	0 877027372	100	95 27638776
Mar 14 06:08 2020	CHA16-1D-4CY-2(74-76cm)_7	8.898-S	69.74643538	4.45319208	0 037837214	2 90258077	3.413342115	14.53875545	1.044210995	0.137043278	2.715986292	0 026952536	0 98366389	100	96.46587716
Mar 14 06:12 2020	CHA16-1D-4CY-2(74-76cm)_8	8.898-S	69 65754579	4.245173589	0 051272193	2 832078016	3.595812724	14.32075778	1.091039729	0.219301803	2.842606187	0 069275366	1 075136829	100	94 9832591
Mar 14 06:44 2020	CHA16-1D-4CY-2(74-76cm)_16	8.898-S	70.14245165	4.575222227	0 086225863	2 547081105	2.356539618	15.57272228	0.781153922	0.161535663	2.933002485	0 058770313	0.785294876	100	90 69204728
Mar 14 06:48 2020	CHA16-1D-4CY-2(74-76cm)_17	8.898-S	65 0633802	4.759428412	0 075029589	2 370440316	4.068048845	16.49045222	1.86157898	0.350206791	4.081279849	0 085232789	0.794922007	100	97 02838685
Mar 14 06:52 2020	CHA16-1D-4CY-2(74-76cm)_18	8.898-S	67 35151053	4.436749231	0 051217573	2 320295071	3.750379955	15.61634047	1.470758529	0.184019715	3.817259632	0 064048698	0 937420594	100	93 52258803
Mar 14 06:56 2020	CHA16-1D-4CY-2(74-76cm)_19	8.898-S	67 37209153	4.413689409	0 064230811	2 26571246	3.519025946	15.76618435	1.612360613	0.180829504	3.826061607	0 078231204	0 901582562	100	93 56880176
Mar 14 07:00 2020	CHA16-1D-4CY-2(74-76cm)_20	8.898-S	70.13483136	4.283202515	0 051216677	2 979137413	3.046408937	14.69001654	0.91414895	0.19884722	2.744479329	0 05846047	0 899250588	100	98 01494847
Mar 14 07:12 2020	CHA16-1D-4CY-2(74-76cm)_23	8.898-S	71 29851285	4.55294635	0 060924699	2 654038921	2.77989582	14.59470608	0.793647798	0.132916848	2.439136984	0 045129407	0 648144242	100	93 06570376
Mar 14 07:20 2020	CHA16-1D-4CY-2(74-76cm)_25	8.898-S	63.7631428	4.738523158	0 060362232	2.100442543	4.014227486	17.45696384	2.001005084	0.334439395	4.680112267	0.105022127	0.745759066	100	98 0745704
Mar 14 07:24 2020	CHA16-1D-4CY-2(74-76cm)_26	8.898-S	63 94069714	4.152424804	0.145711347	2 054761984	4.891410815	15.98208235	3.440707943	0.197853694	4.308371903	0.106273174	0.779704843	100	90 52143334

Date Analysed	Core Section Identifier	sample_no	SiO2	Na2O	Cl	K2O	FeOt	Al2O3	MgO	P2O5	CaO	MnO	TiO2	total	Analytical Total
Mar 14 07:36 2020	CHA16-1D-4CY-2(74-76cm)_29	8.898-S	65.47703123	5.106021796	0 071437248	2 323245755	3.495533165	17.20055188	1.048521927	0.265996287	4.165467058	0 063863672	0.78232998	100	97.70813077
Mar 14 07:40 2020	CHA16-1D-4CY-2(74-76cm)_30	8.898-S	65.73445985	4.746430959	0 066391203	2 644939846	3.733970567	16.38643331	1.350378241	0.231512548	4.133387776	0 058252926	0 913842779	100	93 38586674
Mar 14 07:44 2020	CHA16-1D-4CY-2(74-76cm)_31	8.898-S	65.78150263	4.777885616	0 093199765	2.722222777	3.71867378	16.11411086	1.444171934	0.250402935	4.135284982	0 026287113	0 936257612	100	96 24487834
Mar 14 07:52 2020	CHA16-1D-4CY-2(74-76cm)_33	8.898-S	62 91580312	4.872625603	0 074547524	2.170370943	6.261438703	17.05448445	1.20540527	0.222594083	4.110074443	0 054102	1 058553867	100	95 37540145
Mar 14 07:56 2020	CHA16-1D-4CY-2(74-76cm)_34	8.898-S	66 0455494	5.074734607	0 08663026	2 37468829	3.27248755	16.90830636	1.177581038	0.264477086	3.964608347	0 041378689	0.789558377	100	98.11814079
Mar 14 08:00 2020	CHA16-1D-4CY-2(74-76cm)_35	8.898-S	62 22535538	4.722352134	0 081571222	2 070023472	4.778442983	15.6412815	3.5719113	0.334483001	5.257039807	0 097557542	1 219981655	100	97 58343457
Mar 14 08:04 2020	CHA16-1D-6C-1(95-96cm)_1	11.542-S	59.13913076	4.846599109	0 085976978	2.41554367	7.075338976	15.72312418	2.51832618	0.627529586	5.465679321	0.117092456	1 985658779	100	97.70057273
Mar 14 08:08 2020	CHA16-1D-6C-1(95-96cm)_2	11.542-S	59.46999966	5.071865552	0 081997567	2.465020034	7.509966802	14.72633705	2.824437548	0.742154379	4.950412134	0.140974699	2 016834573	100	98.1736443
Mar 14 08:12 2020	CHA16-1D-6C-1(95-96cm)_3	11.542-S	59 30464494	5.008131421	0.100062553	2 26633083	7.087017826	15.48249246	2.736299346	0.595013018	5.281360238	0.165725442	1 972921928	100	98 83817359
Mar 14 08:28 2020	CHA16-1D-6C-1(95-96cm)_7	11.542-S	59.71983556	4.697209139	0 05424017	2.134876747	6.559697764	16.33394354	2.333731711	0.568347092	5.740673359	0 090298136	1.767146781	100	97 89792327
Mar 14 08:32 2020	CHA16-1D-6C-1(95-96cm)_8	11.542-S	59 69747908	4.622868776	0 078848327	2 341928264	7.236721598	15.35813342	2.586106577	0.611969377	5.348595991	0.164037246	1 953311347	100	97.7826706
Mar 14 08:40 2020	CHA16-1D-6C-1(95-96cm)_10	11.542-S	59 26769117	5.360268162	0 078388917	1 596246435	6.851463806	16.10802525	2.273234924	0.673575327	5.744453733	0.145390599	1 901261678	100	98 35574039
Mar 14 08:44 2020	CHA16-1D-6C-1(95-96cm)_11	11.542-S	58 99238413	4.967635131	0 096979539	2 269300868	7.388278032	15.35226903	2.861463781	0.523363873	5.505344259	0.129848785	1 913132571	100	98 26815082
Mar 14 08:48 2020	CHA16-1D-6C-1(95-96cm)_12	11.542-S	59.45299517	4.941191895	0.108494635	2 335861827	7.616305896	14.78139198	2.760768134	0.595439866	5.296669142	0.123349896	1 987531554	100	97 60851323
Mar 14 08:56 2020	CHA16-1D-6C-1(95-96cm)_14	11.542-S	59.75933571	4.611295808	0 082194846	3 240766942	7.537398341	14.62941261	2.525326919	0.540911605	4.835592313	0.142000798	2 09576411	100	97 81635203
Mar 14 09:00 2020	CHA16-1D-6C-1(95-96cm)_15	11.542-S	59 61747788	4.884503872	0 052182628	2 337453683	6.657015338	15.95019725	2.62251516	0.594615411	5.290026757	0.128149873	1 865862151	100	97 54203971
Mar 14 09:04 2020	CHA16-1D-6C-1(95-96cm)_16	11.542-S	59 61070413	4.868304927	0 070133626	2.168872259	7.047365215	15.81785808	2.364975525	0.498941969	5.574204404	0.134084953	1 844554912	100	98 66878933
Mar 14 09:12 2020	CHA16-1D-6C-1(95-96cm)_18	11.542-S	58 8718074	5.089731792	0 074023033	2 036397068	6.44496824	16.86201024	2.366017614	0.49983366	6.00737135	0 093165166	1 654674437	100	98 21267334
Mar 14 09:20 2020	CHA16-1D-6C-1(95-96cm)_20	11.542-S	58.46429145	4.951672639	0 078317074	1 843353756	5.915290997	17.93680533	2.137849469	0.42753586	6.568857307	0 091047418	1 584978702	100	98.19059387
Mar 14 09:24 2020	CHA16-1D-6C-1(95-96cm)_21	11.542-S	60 29214419	5.058644101	0 085882399	2 930343954	6.832880672	15.11761613	2.395767514	0.663636719	4.461423321	0.164160099	1 997500896	100	98 62323487
Mar 14 09:28 2020	CHA16-1D-6C-1(95-96cm)_22	11.542-S	60 23361452	4.738906883	0 061284864	3 02855317	7.121920512	15.14328841	2.588574391	0.698504687	4.282802462	0.134500392	1 968049703	100	98 06662896
Mar 14 09:36 2020	CHA16-1D-6C-1(95-96cm)_24	11.542-S	60 93853443	5.029353414	0 079840632	2 943619267	6.370667307	15.47593123	2.312997678	0.695278838	4.193649366	0.145568021	1 814559822	100	99.19761135
Mar 14 09:40 2020	CHA16-1D-6C-1(95-96cm)_25	11.542-S	60 69244067	4.55565175	0 088830294	2.409649363	6.995428408	15.04251514	2.571994902	0.55789509	5.013295921	0.122116129	1 950182324	100	97 93956067
Mar 14 09:44 2020	CHA16-1D-6C-1(95-96cm)_26	11.542-S	59 57660881	4.863964138	0 094565411	2 51633283	7.657207746	14.67915949	2.872916145	0.593468981	4.981933143	0.104103124	2 059740179	100	98 55611986
Mar 14 09:48 2020	CHA16-1D-6C-1(95-96cm)_27	11.542-S	59.74939377	4.803537062	0 07751865	2 51604555	7.656081542	14.37649316	2.784762272	0.626974104	5.113582454	0.115717722	2.179893716	100	98.16992382
Mar 14 09:56 2020	CHA16-1D-6C-1(95-96cm)_29	11.542-S	59 82014706	5.007376015	0 065825017	2 25217789	6.636925349	15.89695968	2.308875624	0.541034552	5.497361485	0.130626318	1 842691001	100	97 6832252
Mar 14 10:00 2020	CHA16-1D-6C-1(95-96cm)_30	11.542-S	58 93295173	4.678531121	0 076528998	2 06393293	6.906266542	16.40866465	2.464051118	0.673332575	5.936361547	0.122405527	1.736973258	100	97 87139738
Mar 14 10:04 2020	CHA16-1D-6C-1(95-96cm)_31	11.542-S	58 54729259	4.682365629	0 065408325	2 08163779	7.554595706	15.41437214	3.387368637	0.541838072	5.663279282	0.143469742	1 918372081	100	97 99975815
Mar 14 10:20 2020	CHA16-1D-6C-1(95-96cm)_35	11.542-S	59.47506753	4.819496674	0 086921127	2.493638885	7.431275362	14.96497676	2.762617905	0.573333381	5.160305774	0.145852429	2 086514169	100	98 2499918
Mar 14 10:24 2020	CHA16-1D-6C-1(95-96cm)_36	11.542-S	58 30114344	4.744387865	0 071474509	1 872915605	6.36677146	17.65131525	2.332743736	0.465799173	6.408408531	0.138798232	1 646242198	100	98.77647421
Mar 14 10:28 2020	CHA16-1D-6C-1(95-96cm)_37	11.542-S	59 51962329	4.637359464	0 075426524	2 272988501	7.358592303	14.99654283	2.925824385	0.637150274	5.463326622	0.145960517	1 967205295	100	98.10872333
Mar 14 10:31 2020	CHA16-1D-6C-1(95-96cm)_38	11.542-S	59 28343048	4.587702259	0 095689964	2 656377553	6.914373142	16.01067713	2.397089504	0.5228234	5.594492119	0.146302006	1.791042441	100	99 38346292
Mar 11 20:54 2020	CHA16-1D-7CY-2(92-93cm)_1	15.113-S	71 22026628	4.307816741	0.118161327	2.443984276	2.009642615	16.14792488	0.450543188	0.128944066	2.784016871	0 036553504	0 352146256	100	94.10862512
Mar 11 20:58 2020	CHA16-1D-7CY-2(92-93cm)_2	15.113-S	75 09256676	4.258087118	0 080237961	3 332003305	1.346114863	13.99420603	0.252443366	0.056708494	1.425287769	0 011521881	0.150822455	100	96 33843987
Mar 11 21:02 2020	CHA16-1D-7CY-2(92-93cm)_3	15.113-S	75 02993461	4.228162323	0 091943023	3.121195835	1.240405336	14.24332806	0.209067219	0.127029525	1.469183911	0 034703466	0 205046696	100	94 51505627
Mar 11 21:06 2020	CHA16-1D-7CY-2(92-93cm)_4	15.113-S	74 81300063	4.246275359	0 095595948	3.111428154	1.326789709	14.1052044	0.393649307	0	1.684462828	0 033260094	0.190333571	100	93 20478753
Mar 11 21:18 2020	CHA16-1D-7CY-2(92-93cm)_7	15.113-S	74 63391398	4.544577625	0 05865119	3 027158217	1.432131004	14.13959789	0.292940623	0.063773966	1.58715587	0 071684788	0.14841484	100	95.13873389
Mar 11 21:26 2020	CHA16-1D-7CY-2(92-93cm)_9	15.113-S	64 81262202	4.473665435	0 063853938	2 640114746	4.494921997	15.49016656	2.138697604	0.258215431	4.205764188	0 085650234	1 336327847	100	97.72302526
Mar 11 21:30 2020	CHA16-1D-7CY-2(92-93cm)_10	15.113-S	65.18917461	4.364538711	0 056551771	2.754819713	4.598030851	15.27519372	2.01673594	0.352784935	4.054262973	0 07443211	1 263474671	100	96.19504274
Mar 11 21:34 2020	CHA16-1D-7CY-2(92-93cm)_11	15.113-S	63.7052299	4.269889158	0 062893817	2.415856522	5.87680346	14.61664033	3.425011778	0.388120553	3.9754601	0 079509202	1.184585175	100	98.10185242
Mar 11 21:38 2020	CHA16-1D-7CY-2(92-93cm)_12	15.113-S	65 39733463	4.336445216	0 064830873	2 646576777	4.4120505	15.46742424	1.94902941	0.290362751	4.062187612	0 088014065	1 285743927	100	97.4844192
Mar 11 21:46 2020	CHA16-1D-7CY-2(92-93cm)_14	15.113-S	75 66703727	4.18269741	0 089315037	3.164789661	1.231030333	13.87822379	0.167266568	0.005597205	1.384436175	0 053100498	0.176506054	100	94.16107608
Mar 11 21:54 2020	CHA16-1D-7CY-2(92-93cm)_16	15.113-S	75 31766233	4.152096896	0.144864721	3 222882564	1.129958594	14.24406677	0.205582509	0.019512582	1.338761218	0 026839022	0.197772794	100	90 91240348
Mar 11 22:02 2020	CHA16-1D-7CY-2(92-93cm)_18	15.113-S	74.79097077	4.359416417	0 088789668	3.18652817	1.363132119	14.1163788	0.28214696	0.079537022	1.536545946	0 037330848	0.159223285	100	96 97074167
Mar 11 22:06 2020	CHA16-1D-7CY-2(92-93cm)_19	15.113-S	75 05061388	4.02634465	0 093871189	3 239435724	1.316700745	14.25916112	0.23897307	0.018359587	1.479997791	0 025563598	0 250978646	100	96 62176584
Mar 11 22:10 2020	CHA16-1D-7CY-2(92-93cm)_20	15.113-S	74.72996748	4.435907396	0 06803084	3 050710322	1.234683746	14.3109907	0.237650334	0.069803913	1.616876471	0 045862345	0.199516455	100	98 3377536
Mar 11 22:14 2020	CHA16-1D-7CY-2(92-93cm)_21	15.113-S	74 89531072	4.000346203	0 080431253	3.41934895	1.380338411	14.21354974	0.282938367	0.022961246	1.459602686	0 044502571	0 200669852	100	97 97186682
Mar 11 22:18 2020	CHA16-1D-7CY-2(92-93cm)_22	15.113-S	74 90597399	4.077127727	0 064439253	3.480132737	1.407038634	14.05469294	0.289460299	0.097038054	1.427164226	0 022099359	0.174832781	100	96 83538689
Mar 11 22:34 2020	CHA16-1D-7CY-2(92-93cm)_26	15.113-S	74 83378098	4.364531877	0 072725236	3.100608523	1.283179157	14.29370685	0.279775839	0.056673888	1.473046574	0 047590735	0.194380342	100	97 07771807
Mar 11 22:38 2020	CHA16-1D-7CY-2(92-93cm)_27	15.113-S	75.11497438	4.10850956	0 084073612	3 082000257	1.407001587	14.14329381	0.268050158	0.081796143	1.509551146	0 039730548	0.161018789	100	95 39259424
Mar 11 22:42 2020	CHA16-1D-7CY-2(92-93cm)_28	15.113-S	75 07747841	3.890101096	0 098725861	3 240454949	1.427786928	14.21110257	0.398683974	0.028741794	1.401820811	0 030460277	0.194643327	100	92 5795929
Mar 11 22:46 2020	CHA16-1D-7CY-2(92-93cm)_29	15.113-S	74 84369522	4.274460707	0.109058644	3 207607191	1.367723008	14.11293528	0.270473716	0.054932369	1.479638156	0 055770977	0 223704734	100	96 64525035
Mar 11 22:54 2020	CHA16-1D-7CY-2(92-93cm)_31	15.113-S	66.49215996	4.73392743	0 092986724	3.420321563	3.275708277	15.96733285	0.756968414	0.410223173	3.702733435	0 064954731	1 08268344	100	95 6050459
Mar 11 22:58 2020	CHA16-1D-7CY-2(92-93cm)_32	15.113-S	74 91110013	4.401933721	0 099061625	3 074677351	1.469996383	14.04696229	0.299017463	0.014526948	1.413231666	0 036957215	0 232535201	100	98 22168817
Mar 11 23:02 2020	CHA16-1D-7CY-2(92-93cm)_33	15.113-S	75.10915996	4.30366689	0 07346703	2 979496211	1.231844162	14.30957256	0.257236642	0	1.49995186	0 049284133	0.186320551	100	98 00314527
23.07.13	CHA08-III-10-72-74.5cm	15.11325-OS	75 0340616	4.519961913	0 082265897	3.171692243	1.014440048	14.31136502	0.102780567	0.056156318	1.480371709	0 034916382	0.191988296	100	96 5163
23.07.13	CHA08-III-10-72-74.5cm	15.11325-OS	75.11150474	4.305173244	0 091446229	3 07574093	1.293825271	14.13178543	0.232164385	0.037031094	1.557466086	0	0.16386259	100	97 2156
23.07.13	CHA08-III-10-72-74.5cm	15.11325-OS	73 87542898	4.246431837	0 0981988	3 380375821	1.389953791	14.56007347	0.416678625	0.080465614	1.663536879	0 024395944	0 264460235	100	97 5572
23.07.13	CHA08-III-10-72-74.5cm	15.11325-OS	74 20818595	4.491349347	0 088197931	3 036543377	1.188985785	14.82062503	0.220852525	0.061523934	1.683119039	0 017578267	0.183038812	100	97 8481
23.07.13	CHA08-III-10-72-74.5cm	15.11325-OS	68.16470194	4.427043423	0 067473815	3 309611213	3.391382072	15.28035062	0.823159976	0.250249684	2.997030535	0 095965045	1.193031683	100	97 2229
23.07.13	CHA08-III-10-72-74.5cm	15.11325-OS	64 38724631	4.012747595	0 097080963	2 694377945	5.134515586	15.51150486	2.180509599	0.278129336	4.334182156	0 056012158	1 313693499	100	98 3715

Date Analysed	Core Section Identifier	sample_no	SiO2	Na2O	Cl	K2O	FeOt	Al2O3	MgO	P2O5	CaO	MnO	TiO2	total	Analytical Total
23.07.13	CHA08-III-10-72-74.5cm	15.11325-OS	75 99732133	4.043916037	0 03451997	3 372176075	0.771671648	14.00754049	0.115792213	0.077125699	1.296934979	0 021976678	0 26102488	100	96.4659
23.07.13	CHA08-III-10-72-74.5cm	15.11325-OS	75 95238563	3.997771436	0 087447374	3 609323172	1.087096964	13.48157352	0.178719278	0.037004917	1.2526888	0 056747764	0 259241151	100	96.7439
23.07.13	CHA08-III-10-72-74.5cm	15.11325-OS	64 85481126	4.66682098	0 036810854	2 594298498	4.549148609	15.64675448	1.824023722	0.363723872	4.156975351	0 030794676	1 275837702	100	98 0689
Mar 11 23:22 2020	CHA16-1D-8CY-2(57-60cm)_5	16.946-S	60 22880069	3.937154468	0 090533969	1 867002354	7.063197979	14.75045818	3.546261454	0.349133571	6.518862967	0.167195797	1.481398571	100	95 87561561
Mar 11 23:38 2020	CHA16-1D-8CY-2(57-60cm)_9	16.946-S	59 83131169	4.043157792	0.11974106	1.777232806	7.149297417	14.92045165	3.532250201	0.340542655	6.653515317	0.13595831	1.496541099	100	90 02759767
Mar 11 23:51 2020	CHA16-1D-8CY-2(57-60cm)_12	16.946-S	61 3678742	4.203766166	0 044674977	1 8869568	7.218297618	14.1532005	3.784113366	0.322147067	5.354877404	0.113217408	1 550874494	100	98 04146022
Mar 12 00:22 2020	CHA16-1D-8CY-2(57-60cm)_20	16.946-S	60 60298021	4.116091909	0.118385576	1.760068741	7.371599951	14.84707866	3.26869909	0.253453774	6.024044798	0.12770975	1 509887541	100	95.4508174
Mar 12 00:30 2020	CHA16-1D-8CY-2(57-60cm)_22	16.946-S	60.12651207	3.941872482	0 08084466	1.774889115	7.229257151	14.71126068	3.703670349	0.356871372	6.412171657	0.150403898	1 512246564	100	97.4708778
Mar 12 00:34 2020	CHA16-1D-8CY-2(57-60cm)_23	16.946-S	60.1302246	4.139551862	0 060390585	1 823111987	6.572348508	15.55777266	3.356183432	0.386683897	6.380891956	0.154653761	1.438186752	100	96 53822761
Mar 12 00:42 2020	CHA16-1D-8CY-2(57-60cm)_25	16.946-S	60 36143146	3.846875222	0.16155112	1.701115735	7.487899377	14.56906009	3.533930753	0.298663271	6.541064376	0 080995059	1.41741353	100	91.11666936
Mar 12 00:46 2020	CHA16-1D-8CY-2(57-60cm)_26	16.946-S	60 04115795	4.09329293	0 086744315	1.738954031	7.103690707	14.81249444	3.701633141	0.276609091	6.488027319	0.135455367	1 521940703	100	98 33497435
Mar 12 00:50 2020	CHA16-1D-8CY-2(57-60cm)_27	16.946-S	61.40171131	3.885083655	0 048983787	1 880083092	7.088669804	14.67252017	3.221547785	0.298242837	5.853664115	0.150305021	1.499188421	100	98 39990623
23.07.13	CH08-III-15_61-63cm	20.357-OS	56 33963969	4.279963654	0 063655792	2 346533196	9.132626385	14.65149215	3.485738361	1.111184434	6.313091062	0.158987193	2.117088077	100	98.4985
23.07.13	CH08-III-15_61-63cm	20.357-OS	56 20581372	3.718481523	0 088257367	1 974733001	9.190540694	14.34131028	3.807660371	1.182259655	7.080759587	0 205183021	2 205000773	100	97 6689
23.07.13	CH08-III-15_61-63cm	20.357-OS	55 85482802	3.774598484	0 087281642	2 000417478	9.516461748	13.88842275	4.063456721	1.179888181	7.164871237	0 239436159	2 230337585	100	97.7296
23.07.13	CH08-III-15_61-63cm	20.357-OS	56 57704178	4.119131782	0.110927416	2.160496646	9.222503347	14.36626751	3.446666037	1.173922619	6.629054864	0.125237357	2 068750641	100	98 5329
23.07.13	CH08-III-15_61-63cm	20.357-OS	55 01250036	4.125221897	0 067959126	1 627518092	7.908382861	16.52127533	4.540287405	0.643758263	7.69719473	0.154658495	1.701243446	100	97.1172
23.07.13	CH08-III-15_61-63cm	20.357-OS	55 62565196	3.913831295	0 081871491	1 58890953	7.917845907	16.43154588	4.561114782	0.702557133	7.379966836	0.150651855	1 646053337	100	96 2484
23.07.13	CH08-III-15_61-63cm	20.357-OS	55.71450936	3.982531339	0 07305895	1.45698373	7.40126042	17.25398627	4.161290422	0.665614099	7.489053948	0 091374849	1.710336613	100	97.7293
23.07.13	CH08-III-15_61-63cm	20.357-OS	55 66195616	3.756595596	0 061030842	2 034835308	9.372042391	14.37220487	4.109782401	1.13937779	7.132890851	0 205128622	2.154155175	100	98.4748
23.07.13	CH08-III-15_61-63cm	20.357-OS	56.48592383	4.119365795	0.140438661	2.177758393	9.403231604	14.02125056	3.521163733	1.257183473	6.506419188	0.188496751	2.178768017	100	99 0468
17.10.12	CH08-III-15_61-63cm	20.357-OS	56.44198775	4.302665083	0 082151605	2 025430665	9.247909121	14.11937819	3.709740415	1.259119686	6.400659635	0 203057776	2 207900078	100	99 0851
17.10.12	CH08-III-15_61-63cm	20.357-OS	55 35954303	4.158814166	0 093257513	1 632160022	8.166123262	15.57021697	4.91900109	0.892856229	7.350350355	0.114857222	1.742820144	100	97 6865
17.10.12	CH08-III-15_61-63cm	20.357-OS	56 50764548	4.132378232	0 084870856	2 071823485	8.971742878	14.31708402	3.891064804	1.140680551	6.530792081	0.16821891	2.183698704	100	98 5026
17.10.12	CH08-III-15_61-63cm	20.357-OS	56.49605803	4.02273527	0 081370247	1 997049698	8.928040268	14.50286006	3.929668681	1.18304474	6.616096789	0.150136676	2 092939543	100	99.1763
17.10.12	CH08-III-15_61-63cm	20.357-OS	56.14237777	3.781194373	0 084649827	1 935402866	8.726425124	14.6505967	4.404119895	1.152796988	6.949386289	0.123329533	2 049720635	100	98.7598
17.10.12	CH08-III-15_61-63cm	20.357-OS	56.76309617	4.1245962	0 091947649	2 019994026	9.10189981	13.8219131	3.878926761	1.234055697	6.597498657	0.123344407	2 242727522	100	98 0993
17.10.12	CH08-III-15_61-63cm	20.357-OS	55.43384949	4.110211701	0 090705886	1 573483916	7.990216722	16.42809129	4.513832648	0.796106126	7.204031553	0.13322427	1.726246396	100	98.7808
17.10.12	CH08-III-15_61-63cm	20.357-OS	55.72253752	4.000979865	0 077915769	1 546375836	7.409202912	16.62652512	4.521378975	0.818167034	7.402409728	0.142965657	1.731541579	100	97.1562
17.10.12	CH08-III-15_61-63cm	20.357-OS	56.18216265	4.027633138	0 081225793	1 827375752	8.701185242	14.57808622	4.463122058	1.149743944	6.849564511	0.184445977	1 955454711	100	97.7522
17.10.12	CH08-III-15_61-63cm	20.357-OS	56 80833592	4.127959888	0.101411171	2 033576794	9.263668034	13.62000507	3.462625842	1.239862671	6.7359643	0.172015163	2.434575149	100	99 0029
17.10.12	CH08-III-15_61-63cm	20.357-OS	56 39274038	4.039198943	0 084885959	1 943797622	9.003059326	14.62905038	3.823703672	1.167308106	6.599807619	0 240930778	2 075517214	100	99 0741
17.10.12	CH08-III-15_61-63cm	20.357-OS	55.18269117	4.184372073	0 097439379	1 528049863	7.700880533	16.50580137	4.657050194	0.792500133	7.444143617	0.162876108	1.744195558	100	97 8044
17.10.12	CH08-III-15_61-63cm	20.357-OS	55 52006101	3.99645895	0 099668691	1.452198385	7.297077101	17.01451892	4.186391697	0.750837473	7.89396478	0.190137195	1 598685804	100	97 8241
17.10.12	CH08-III-15_61-63cm	20.357-OS	56 96866853	3.785078409	0 064365905	2.154240079	8.910844142	13.98535928	3.517727863	1.243734917	6.748432216	0.159401458	2.462147198	100	99.1208
17.10.12	CH08-III-15_61-63cm	20.357-OS	56.78933005	3.838586275	0 093708248	2.124933501	9.214475132	13.92070028	3.642641618	1.214653818	6.719175774	0.141222289	2 300573011	100	98.4972
17.10.12	CH08-III-15_61-63cm	20.357-OS	55 25068192	4.089789521	0.104628913	1 567194561	7.802283923	16.28394333	4.656902658	0.80171396	7.46610756	0 227069169	1.749684485	100	98 252
17.10.12	CH08-III-15_61-63cm	20.357-OS	54.47475176	4.24064834	0.106739347	1.767513961	8.893689443	15.15912616	4.466552798	0.898627157	7.659159265	0.161127526	2.172064235	100	98.1831
17.10.12	CH08-III-15_61-63cm	20.357-OS	56.42607741	4.150763118	0 071812161	2 010437509	8.804716372	14.52413586	3.731707342	1.063648199	7.013553409	0.188368046	2 014780579	100	99 0083
Mar 11 16:09 2020	CHA16-1D-10CY-1(42-44cm)_1	21.172-S	58.77435527	4.206334009	0.106024476	2 220571612	7.64285747	15.51400412	2.720982116	0.876171035	6.213430425	0.159401596	1 565867869	100	95 92124788
Mar 11 16:13 2020	CHA16-1D-10CY-1(42-44cm)_2	21.172-S	58 38216343	4.094075761	0 099824424	2 503368981	8.488253697	14.23169717	3.124038976	1.258204517	5.803264456	0.142754099	1 872354486	100	96 6697286
Mar 11 16:17 2020	CHA16-1D-10CY-1(42-44cm)_3	21.172-S	58 63584054	4.131510454	0.141522843	2.447230912	8.481544	14.17302461	3.103297071	1.167567414	5.842112943	0.143501455	1.732847761	100	96 0269008
Mar 11 16:25 2020	CHA16-1D-10CY-1(42-44cm)_5	21.172-S	57.4073657	4.084038728	0.11264621	1 875700072	7.703012752	15.40436939	3.897287928	0.961240622	6.887987488	0.164436373	1 50191473	100	95 96416967
Mar 11 16:29 2020	CHA16-1D-10CY-1(42-44cm)_6	21.172-S	56 56344236	4.225841189	0 050271153	1 843962358	8.201553048	15.25877876	3.554005662	0.880734003	7.272834775	0.150092355	1 998484343	100	97 0735651
Mar 11 16:33 2020	CHA16-1D-10CY-1(42-44cm)_7	21.172-S	56 61232685	4.19055295	0 028564991	1 990268357	8.283554547	15.02071266	3.598982676	1.006264418	7.063905826	0.142412466	2 062454256	100	96 97184772
Mar 11 16:37 2020	CHA16-1D-10CY-1(42-44cm)_8	21.172-S	56 68128238	4.123925394	0 035858986	1 885158144	8.479879606	14.80218102	3.688352891	1.080737631	7.038606766	0.155423093	2 02859409	100	97 60454346
Mar 11 16:41 2020	CHA16-1D-10CY-1(42-44cm)_9	21.172-S	56 96322395	4.356185263	0 027656766	1 922607885	8.310966985	14.793255	3.516213351	0.97297957	6.898769469	0.161313998	2 076827769	100	97 26372261
Mar 11 16:45 2020	CHA16-1D-10CY-1(42-44cm)_10	21.172-S	58 66706694	3.934337745	0 096029759	2 340660078	8.074938768	14.35538613	3.646831997	1.195471238	5.86209957	0.154337274	1 6728405	100	95 69950037
Mar 11 16:49 2020	CHA16-1D-10CY-1(42-44cm)_11	21.172-S	57 28834765	3.873750699	0.106960059	1 864729722	7.797264879	15.46569636	3.959931657	0.97389717	6.997974462	0.179558806	1.491888538	100	95.45619287
Mar 11 16:53 2020	CHA16-1D-10CY-1(42-44cm)_12	21.172-S	58 00725958	4.066801317	0 086863711	1 981285133	7.241847905	16.66886406	2.721660104	1.039790791	6.590380022	0.144008146	1.451239221	100	95 89735309
Mar 11 16:57 2020	CHA16-1D-10CY-1(42-44cm)_13	21.172-S	58 28934357	4.17818432	0 087090086	2 345930815	8.264257464	14.65935042	3.228249926	1.188894343	5.812925912	0.149994249	1.795778898	100	96 33702691
Mar 11 17:05 2020	CHA16-1D-10CY-1(42-44cm)_15	21.172-S	58 34991669	4.261011734	0 077019143	2 087239653	7.48112229	15.69490278	2.922135514	1.042773016	6.386953337	0 098204626	1 598721212	100	95 82033368
Mar 11 17:09 2020	CHA16-1D-10CY-1(42-44cm)_16	21.172-S	57 5266946	4.057459797	0.110153143	2 650301175	8.221321152	14.88580518	3.022999777	1.169776613	6.335876246	0.18717752	1 832434796	100	96 59279574
Mar 11 17:37 2020	CHA16-1D-10CY-1(42-44cm)_23	21.172-S	58 04867453	4.055516149	0 083917412	2.173701332	8.235188699	14.63498864	3.427759793	1.154491345	6.343445714	0.153622161	1 688694222	100	95 68931892
Mar 11 17:45 2020	CHA16-1D-10CY-1(42-44cm)_25	21.172-S	57.77296924	4.253631924	0 098370729	1 994565736	7.305311534	16.01350334	3.028398238	1.130279561	6.693804382	0.137113341	1 572051968	100	95.76019307
Mar 11 17:53 2020	CHA16-1D-10CY-1(42-44cm)_27	21.172-S	56 53704538	4.314697887	0 042025873	2 276401465	7.153401513	16.73936632	2.884128552	0.925799193	7.313325972	0.180979067	1 632828779	100	97 08305123
Mar 11 18:01 2020	CHA16-1D-10CY-1(42-44cm)_29	21.172-S	57 88429733	4.150262887	0.110234961	2 268933872	8.079944981	14.81517928	2.973443019	1.392788451	6.330221898	0.150537028	1 844156298	100	96 52110303
17.10.12	CHA08-III-17_44-49	22.142-OS	59 5451137	4.198491797	0 062252279	1 882626157	6.930517967	15.47868567	3.392850285	0.459817973	6.470093641	0.140168688	1.439381843	100	98 9522
17.10.12	CHA08-III-17_44-51	22.142-OS	58 93342995	4.103861556	0 091331482	1 825216774	7.350620045	15.41705689	3.506018795	0.647999386	6.389166976	0 095670989	1 639627166	100	99 0896
17.10.12	CHA08-III-17_44-52	22.142-OS	59 57672188	4.12726771	0 080717284	1 832635098	7.239759384	14.32026294	4.538635359	0.459507521	6.206308398	0.131450898	1.486733523	100	96 3858
17.10.12	CHA08-III-17_44-53	22.142-OS	56 94517077	4.127495693	0 073983987	2 527718658	8.560251343	14.89621972	3.756055539	0.873213743	6.104084321	0.152427283	1 98337894	100	98 67

Date Analysed	Core Section Identifier	sample_no	SiO2	Na2O	Cl	K2O	FeOt	Al2O3	MgO	P2O5	CaO	MnO	TiO2	total	Analytical Total
17.10.12	CHA08-III-17_44-54	22.142-OS	53.40310682	4.273584073	0 044145451	1 501757192	8.099726095	16.50725254	5.330639277	0.603219675	8.132099426	0.138423896	1 966045552	100	98 5379
17.10.12	CHA08-III-17_44-56	22.142-OS	59 6493714	4.351430217	0.109818147	1 962860211	7.484739326	14.49457842	3.537966208	0.484110782	6.223804323	0.132996355	1 5683246	100	98.7997
17.10.12	CHA08-III-17_44-58	22.142-OS	53 54262973	4.331357765	0 081981216	1.424309907	8.075705761	16.51997319	5.3200856	0.614707491	8.154755467	0.119383251	1 815110624	100	98 9251
17.10.12	CHA08-III-17_44-60	22.142-OS	55 37417028	3.89173461	0 074359208	1 929601229	9.287626668	14.58087069	4.015296174	1.022136009	7.149900484	0 203275442	2.471029208	100	98 979
23.07.13	CH08-III-21_25-27cm	31.307-G	76 36476511	3.948211406	0 069188023	3.40505407	0.769742886	13.57747021	0.28992081	0.032712766	1.30391205	0 035221093	0 203801579	100	95 6813
23.07.13	CH08-III-21_25-27cm	31.307-G	78 0094583	3.428737196	0 07001895	4.412967802	0.86829759	12.12444381	0.136489995	0	0.787321874	0 007617561	0.154646921	100	95 8312
23.07.13	CH08-III-21_33 5-35.5cm	31.307-G	77 04051543	3.365366863	0.119215792	4 520810541	0.999619142	12.44380769	0.164581094	0.007068547	1.036016884	0 063405921	0 239592092	100	94.7861
23.07.13	CH08-III-21_33 5-35.5cm	31.307-G	77 29512068	3.41376035	0 049004837	4.479146357	0.948608523	12.48810069	0.178294194	0	0.875831127	0 001355453	0 27077779	100	95 9089
23.07.13	CH08-III-21_33 5-35.5cm	31.307-G	69.72376087	4.740891187	0.108423601	2 239044806	2.541235844	15.63310356	0.871902183	0.46200558	3.115768095	0.105243722	0.458620548	100	97.488
23.07.13	CH08-III-21_33 5-35.5cm	31.307-G	76 39319718	4.289402879	0.10555671	3 368313567	0.938316668	13.22987871	0.203909253	0.034245896	1.193699173	0 048967455	0.194512513	100	95.7779
23.07.13	CH08-III-21_33 5-35.5cm	31.307-G	75.11684824	4.651622278	0 053643966	2 966139504	1.190258681	13.89081275	0.32759998	0.053112837	1.461665279	0 052581709	0 235714771	100	94.1392
23.07.13	CH08-III-21_33 5-35.5cm	31.307-G	72.73051779	4.664164086	0.103167912	2 653872716	1.581201832	15.29427217	0.549522716	0.121492397	1.915703131	0 091410583	0 294674672	100	94.4092
Mar 14 00:43 2020	CHA08-3A-21S-1(84-87cm)_1	31.698-G	67 2897538	4.603410888	0 062396304	2.413060951	4.057519414	15.06326577	1.589664938	0.24615241	3.523674778	0 046039991	1.105060758	100	99 04
Mar 14 00:47 2020	CHA08-3A-21S-1(84-87cm)_2	31.698-G	67 68463131	4.401574452	0 047913629	2 607957023	3.917577526	14.97169437	1.536956433	0.219957926	3.477276031	0 049530967	1 084930338	100	98 93
Mar 14 00:51 2020	CHA08-3A-21S-1(84-87cm)_3	31.698-G	67 34774401	4.543679627	0 050341977	2.492077975	3.909518819	15.11865384	1.532009608	0.191259478	3.572979266	0 08957469	1.152160709	100	99 92
Mar 14 00:55 2020	CHA08-3A-21S-1(84-87cm)_4	31.698-G	67.40264435	4.689574211	0 031445422	2 544127976	3.860739685	15.04262945	1.562023854	0.257771047	3.449837536	0 058616709	1.100589763	100	98 27
Mar 14 00:59 2020	CHA08-3A-21S-1(84-87cm)_5	31.698-G	67.48410953	4.589837359	0 051406138	2.483437698	3.939907368	15.08668785	1.575769464	0.187739714	3.433889163	0 04895336	1.118262358	100	97 85
Mar 14 01:07 2020	CHA08-3A-21S-1(84-87cm)_7	31.698-G	68.44372602	4.710631048	0 056155129	2 605030375	3.638182244	14.80387652	1.18126416	0.203942456	3.203072368	0 082914975	1 071204708	100	98 66
Mar 14 01:11 2020	CHA08-3A-21S-1(84-87cm)_8	31.698-G	69 57720374	4.620710828	0 015205315	2 567784919	3.295081091	15.1322297	0.565713926	0.160209639	3.051132668	0 028698773	0 986029409	100	99 31
Mar 14 01:19 2020	CHA08-3A-21S-1(84-87cm)_10	31.698-G	68.16284291	4.54653505	0 078923777	2 661031562	3.947685423	14.82022061	1.221409865	0.272654938	3.114616487	0 049289562	1.124789818	100	99 21
Mar 14 01:23 2020	CHA08-3A-21S-1(84-87cm)_11	31.698-G	68 35575662	4.588621755	0 060917323	2 642440185	3.919089087	14.67042061	1.277968628	0.243568437	3.086208766	0 045385423	1.109623165	100	99.15
Mar 14 01:27 2020	CHA08-3A-21S-1(84-87cm)_12	31.698-G	66 25443478	5.117179385	0 024359518	1 896847734	2.746178826	17.84795837	0.601900051	0.168519946	4.552434561	0 011181418	0.779005414	100	100.17
Mar 14 01:31 2020	CHA08-3A-21S-1(84-87cm)_13	31.698-G	67 90932359	4.429131944	0 050607788	2 52030815	3.999843747	14.96123893	1.425642719	0.243360955	3.266319363	0 061596331	1.132626483	100	99.19
Mar 14 01:35 2020	CHA08-3A-21S-1(84-87cm)_14	31.698-G	69.75423841	4.352612934	0 038067563	2.717657546	3.507607861	14.35530241	1.075274331	0.260162273	2.778728502	0 051503173	1.108844993	100	98 25
Mar 14 01:39 2020	CHA08-3A-21S-1(84-87cm)_15	31.698-G	69.48205359	4.600934353	0 036618963	2.774472957	3.504681327	14.33588821	1.062636087	0.297235816	2.743872152	0 053143397	1.108463148	100	98 04
Mar 14 01:43 2020	CHA08-3A-21S-1(84-87cm)_16	31.698-G	69.49500917	4.77620611	0 051259699	2 59349667	3.130470929	14.93389481	0.551220411	0.270333888	3.18339003	0 022476971	0 992241314	100	98 32
Mar 14 01:51 2020	CHA08-3A-21S-1(84-87cm)_18	31.698-G	71.42750676	4.400025956	0 034610948	3 063748556	3.528556731	13.25721152	0.659313683	0.294977293	2.154034821	0 062111489	1.117902246	100	95 63
Mar 14 01:55 2020	CHA08-3A-21S-1(84-87cm)_19	31.698-G	69 99969944	4.163853414	0 029742989	2 873475215	3.464172726	14.33864468	1.045136372	0.199328439	2.742404416	0 064123868	1 079418444	100	99.18
Mar 14 01:59 2020	CHA08-3A-21S-1(84-87cm)_20	31.698-G	72.48845403	4.250525955	0 021460045	2 998245553	3.160446969	13.32095171	0.60241406	0.111510091	2.074128773	0 074340061	0 897522753	100	97 39
Mar 14 02:03 2020	CHA08-3A-21S-1(84-87cm)_21	31.698-G	68 90169015	4.825574719	0 043664799	2 395499378	3.121420832	15.56659724	0.601886911	0.137766483	3.416366201	0 050436886	0 939096402	100	98 94
Mar 14 02:15 2020	CHA08-3A-21S-1(84-87cm)_24	31.698-G	69 34071312	4.532734172	0 028672311	2.724379763	3.558020356	14.44095293	1.152452975	0.168666657	2.969267831	0 052242788	1 031897099	100	98 00
Mar 14 02:19 2020	CHA08-3A-21S-1(84-87cm)_25	31.698-G	69 623929	4.491374593	0 025201681	2.710180823	3.466780463	14.47800426	1.124056929	0.197913205	2.780185494	0 072304824	1 030068726	100	99 99
Mar 14 02:23 2020	CHA08-3A-21S-1(84-87cm)_26	31.698-G	71 04586533	4.286391991	0 032979664	2 881819222	3.829897321	13.34364418	0.871530924	0.269663373	2.247194772	0 033083701	1.157929528	100	96.12
Mar 14 02:27 2020	CHA08-3A-21S-1(84-87cm)_27	31.698-G	70 20897963	4.085757966	0 05052822	2.727903925	4.765399894	12.62331003	1.866402989	0.239208242	2.221588424	0 078323908	1.132596777	100	96.78
Mar 14 02:31 2020	CHA08-3A-21S-1(84-87cm)_28	31.698-G	71 33908202	4.474327766	0 042319079	2 879761751	3.725844509	13.07622092	0.794928023	0.248031093	2.260458149	0 079374078	1 079652613	100	96 88
Mar 14 02:35 2020	CHA08-3A-21S-1(84-87cm)_29	31.698-G	68 58908271	4.789699669	0 016182193	2 273700589	2.618291367	16.45792326	0.553885778	0.117372112	3.830468561	0 049980445	0.703413317	100	97 64
Mar 14 02:39 2020	CHA08-3A-21S-1(84-87cm)_30	31.698-G	68 55402252	4.455849502	0 064807667	2.738352136	3.920261126	14.45341622	1.324624572	0.189351979	3.133891889	0 053549997	1.111872388	100	98 60
Mar 14 02:43 2020	CHA08-3A-21S-1(84-87cm)_31	31.698-G	70 01340749	4.14923344	0 038606471	2 924413843	4.485674491	12.70641086	1.817924533	0.244262192	2.356362233	0 066903856	1.196800586	100	95 06
Mar 11 05:10 2020	CHA08-3A-21S-1(94-99cm)_2	32.089-G	77.46198146	3.189489114	0 025954618	4.799975292	1.232078575	11.51571158	0.592177947	0.091017127	0.728684032	0 016398106	0 346532153	100	92 08380734
Mar 11 05:22 2020	CHA08-3A-21S-1(94-99cm)_5	32.089-G	77 28923424	3.700475566	0 090643403	3 625736122	0.866141195	12.75227757	0.275295413	0.117076703	1.042344857	0 052323497	0.188451434	100	92.11922457
Mar 11 05:30 2020	CHA08-3A-21S-1(94-99cm)_7	32.089-G	76 20486913	3.668000376	0 062586131	3.733586456	1.060772058	13.26106312	0.439181991	0	1.284742207	0 0802829	0 204915627	100	92 67228817
17.10.12	CHA08-III-24_92-95cm	35.864-OS	77 25219162	3.834010488	0.125727498	4 854855168	0.976396619	12.39454019	0.014607344	0.004277865	0.456375167	0 029006012	0 058012024	100	95 8422
17.10.12	CHA08-III-24_92-95cm	35.864-OS	77.12700134	3.915183602	0.159469286	4.771002105	0.826795093	12.43222555	0.012863856	0.021475197	0.631817312	0 02604665	0 076120006	100	94 062
17.10.12	CHA08-III-24_92-95cm	35.864-OS	77 00662388	4.206887617	0.143663179	4.496320474	1.02460074	12.51417937	0.020433033	0.025172654	0.462165712	0 046658936	0 053294405	100	94 9443
17.10.12	CHA08-III-24_92-95cm	35.864-OS	76 32127415	4.386817342	0.138627911	4 662910002	0.858414482	13.01273029	0.039230324	0.014063701	0.488740051	0 03151115	0 045680593	100	94 5697
17.10.12	CHA08-III-24_92-95cm	35.864-OS	78.71796721	2.822406986	0.181286637	5.442523968	0.974535009	11.39559948	0.015063021	0	0.428341392	0	0 022276298	100	94 2706
17.10.12	CHA08-III-24_92-95cm	35.864-OS	66 35338619	5.721274385	0 01783459	2 307401977	3.69217497	15.3834748	1.544143722	0.373904261	3.447053041	0 050393087	1.108958978	100	96.4418
17.10.12	CHA08-III-24_92-95cm	35.864-OS	65 90327496	5.308927447	0 029422143	2 317474023	3.746318441	15.04300587	2.130021607	0.39775502	3.82336199	0.123047244	1.177391257	100	98 9051
17.10.12	CHA08-III-24_92-95cm	35.864-OS	62.19955711	4.506336316	0.10775421	2 271024862	4.915863712	16.30199422	2.409375947	0.363069266	5.437443206	0.100795723	1 386785425	100	97.7224
17.10.12	CHA08-III-24_92-95cm	35.864-OS	74.40630914	4.90313971	0.117444206	4 647568645	0.795190816	14.39252764	0.007067439	0.013719146	0.642825146	0 012991616	0 061216493	100	96 2159
17.10.12	CHA08-III-24_92-95cm	35.864-OS	77 53970803	3.999754863	0.135459548	4 833327698	0.861467781	12.15754727	0.019019281	0	0.44336058	0	0 010354942	100	94 6408
17.10.12	CHA08-III-24_92-95cm	35.864-OS	64 6322023	4.111657822	0.151127188	1 99715163	3.625884275	17.90012861	1.205512797	0.340912349	5.132164602	0.102804721	0 8004537	100	94.1591
17.10.12	CHA08-III-24_92-95cm	35.864-OS	77 36217638	3.926125607	0.120596992	4 517781439	0.929517993	12.43017233	0.034093267	0	0.493611218	0 098256373	0 087668402	100	94.4468
17.10.12	CHA08-III-24_92-95cm	35.864-OS	77 35639644	3.73672863	0.161571318	4.720892342	1.002139305	12.42134372	0.042326251	0.027903973	0.453152156	0 006897611	0 07064826	100	95 6853
17.10.12	CHA08-III-24_92-95cm	35.864-OS	77 29606167	4.045008237	0.146478376	4 566660262	0.875720185	12.41296612	0.008085186	0	0.529422203	0 091037098	0 028560658	100	95 2359
17.10.12	CHA08-III-24_92-95cm	35.864-OS	65 82739939	5.068948674	0 087798282	2 39390531	3.904015369	15.99907001	0.995455088	0.357005559	4.313638714	0	1 052763606	100	98 0657
17.10.12	CHA08-III-24_92-95cm	35.864-OS	61 93493245	4.366153049	0.130130933	2 399093872	6.134996788	15.43602711	2.496119496	0.46326612	5.023262206	0 080368864	1 535649109	100	96 0571
01/10/2021	1A-17Y-1-76-83cm	43.419-S	77.16	4.22	0 06	3 06	0.92	12.94	0.22	0.01	1.16	0 08	0.18	100	
01/10/2021	1A-17Y-1-76-83cm	43.419-S	56 53	4.50	0 06	1.74	8.04	15.30	4.13	0.56	6.83	0.15	2.18	100	
01/10/2021	1A-17Y-1-76-83cm	43.419-S	74.18	4.62	0 20	2.74	1.35	14.53	0.45	0.07	1.57	0 05	0 23	100	
01/10/2021	1A-17Y-1-76-83cm	43.419-S	72.14	4.63	0 09	2 62	1.83	15.30	0.64	0.09	2.25	0 04	0 38	100	

Date Analysed	Core Section Identifier	sample_no	SiO2	Na2O	Cl	K2O	FeOt	Al2O3	MgO	P2O5	CaO	MnO	TiO2	total	Analytical Total
01/10/2021	1A-17Y-1-76-83cm	43.419-S	56 58	4.63	0 06	1.78	7.98	15.44	4.00	0.61	6.64	0.13	2.14	100	
01/10/2021	1A-17Y-1-76-83cm	43.419-S	70 61	4.68	0 08	2 39	2.44	15.49	0.80	0.21	2.75	0 08	0.47	100	
01/10/2021	1A-17Y-1-76-83cm	43.419-S	74.10	4.69	0.12	2.76	1.29	14.33	0.63	0.12	1.65	0 03	0 28	100	
01/10/2021	1A-17Y-1-76-83cm	43.419-S	71 91	4.71	0 08	2 63	1.87	15.33	0.62	0.12	2.27	0 05	0.41	100	
01/10/2021	1A-17Y-1-76-83cm	43.419-S	56 60	4.74	0 06	1 83	7.87	15.34	4.00	0.49	6.78	0.17	2.13	100	
01/10/2021	1A-17Y-1-76-83cm	43.419-S	76.40	4.74	0 07	2 81	0.96	13.23	0.28	0.07	1.20	0 04	0 20	100	
01/10/2021	1A-17Y-1-76-83cm	43.419-S	56 58	4.76	0 05	1 80	7.89	15.39	3.99	0.58	6.74	0.16	2 07	100	
01/10/2021	1A-17Y-1-76-83cm	43.419-S	72 02	4.83	0 08	2 57	1.89	15.24	0.61	0.06	2.31	0 07	0 32	100	
01/10/2021	1A-17Y-1-76-83cm	43.419-S	56 53	4.83	0 06	1 80	7.89	15.51	3.91	0.48	6.76	0.13	2.10	100	
01/10/2021	1A-17Y-1-76-83cm	43.419-S	73 55	4.85	0.12	2 83	1.34	14.70	0.61	0.06	1.58	0 06	0 30	100	
01/10/2021	1A-17Y-1-76-83cm	43.419-S	70.71	4.88	0 07	2 37	2.42	15.36	0.82	0.15	2.70	0 06	0.46	100	
01/10/2021	1A-17Y-1-76-83cm	43.419-S	70.46	4.92	0.12	2 35	2.40	15.56	0.83	0.08	2.74	0 09	0.45	100	
01/10/2021	1A-17Y-1-76-83cm	43.419-S	74.74	4.98	0 04	2.75	1.20	14.07	0.36	0.07	1.54	0 01	0 24	100	
01/10/2021	1A-17Y-1-76-83cm	43.419-S	56 26	4.98	0 04	1 83	8.24	15.29	3.89	0.50	6.68	0.15	2.13	100	
01/10/2021	1A-17Y-1-76-83cm	43.419-S	73 97	5.01	0 08	2 62	1.41	14.30	0.53	0.05	1.66	0 07	0 30	100	
01/10/2021	1A-17Y-1-76-83cm	43.419-S	74 54	5.06	0 07	2 55	1.14	14.36	0.41	0.05	1.53	0 01	0 27	100	
01/10/2021	1A-17Y-1-76-83cm	43.419-S	70.16	5.08	0 09	2 25	2.32	15.84	0.80	0.13	2.78	0 07	0.49	100	

Filtered core analyses, normalised to 100% (51-100.99 mc)

Date Analysed	Core Section Identifier	sample_no	SiO2	Na2O	Cl	K2O	FeOt	Al2O3	MgO	P2O5	CaO	MnO	TiO2	total	Analytical Total
01/10/2021	1C-28Y-1-50-51.5cm	60.799-S	77.86	3.11	0.08	5.18	0.94	12 24	0 00	0 06	0.42	0.01	0.11	100	
01/10/2021	1C-28Y-1-50-51.5cm	60.799-S	77.77	3 20	0.09	5.13	0.52	12 58	0 06	0 07	0.42	0.10	0.07	100	
01/10/2021	1C-28Y-1-50-51.5cm	60.799-S	78.32	3 30	0.06	4.99	0.87	11 94	0 03	0 03	0.41	0.00	0.06	100	
01/10/2021	1C-28Y-1-50-51.5cm	60.799-S	77.96	3.40	0.08	4.93	0.77	12 23	0 06	0 00	0.42	0.02	0.11	100	
01/10/2021	1C-28Y-1-50-51.5cm	60.799-S	77.57	3.42	0.05	5.17	0.84	12 34	0 04	0 00	0.41	0.06	0.11	100	
01/10/2021	1C-28Y-1-50-51.5cm	60.799-S	77.83	3.46	0.08	5.03	0.79	12 28	0 03	0 00	0.38	0.05	0.07	100	
01/10/2021	1C-28Y-1-50-51.5cm	60.799-S	78.09	3 63	0.13	4.20	0.85	12 07	0.16	0 00	0.66	0.04	0.18	100	
01/10/2021	1C-28Y-1-50-51.5cm	60.799-S	77.67	3 63	0.09	5.08	0.77	12.19	0 03	0 00	0.39	0.04	0.09	100	
01/10/2021	1C-28Y-1-50-51.5cm	60.799-S	76.59	3.78	0.11	3.53	1.01	13 35	0 22	0 03	1.13	0.08	0.17	100	
01/10/2021	1C-28Y-1-50-51.5cm	60.799-S	77.30	3 95	0.08	3.85	0.78	12 88	0.10	0 08	0.78	0.04	0.16	100	
01/10/2021	1C-28Y-1-50-51.5cm	60.799-S	76.45	3 95	0.08	3.81	0.83	13 32	0.15	0.14	1.01	0.04	0.22	100	
01/10/2021	1C-28Y-1-50-51.5cm	60.799-S	77.36	3 97	0.10	3.40	0.80	12 82	0 24	0 05	1.05	0.06	0.16	100	
01/10/2021	1C-28Y-1-50-51.5cm	60.799-S	75.97	4 00	0.09	3.51	1.00	13 67	0 27	0 07	1.20	0.05	0.15	100	
01/10/2021	1C-28Y-1-50-51.5cm	60.799-S	77.11	4 02	0.09	3.24	0.87	13.15	0 20	0 05	1.09	0.04	0.14	100	
01/10/2021	1C-28Y-1-50-51.5cm	60.799-S	76.70	4.15	0.09	3.29	0.98	13 31	0 21	0 00	1.08	0.03	0.16	100	
01/10/2021	1C-28Y-1-50-51.5cm	60.799-S	75.90	4.17	0.08	2.84	1.16	13.78	0 33	0 02	1.45	0.03	0.24	100	
01/10/2021	1C-28Y-1-50-51.5cm	60.799-S	77.14	4.19	0.06	3.19	0.79	13.19	0.19	0 03	1.05	0.05	0.12	100	
01/10/2021	1C-28Y-1-50-51.5cm	60.799-S	77.23	4.19	0.03	4.18	0.59	13 28	0 02	0 00	0.34	0.12	0.01	100	
01/10/2021	1C-28Y-1-50-51.5cm	60.799-S	76.21	4 20	0.06	3.37	0.97	13 57	0 21	0 06	1.15	0.04	0.16	100	
01/10/2021	1C-28Y-1-50-51.5cm	60.799-S	76.49	4 20	0.08	3.32	0.94	13.40	0 24	0 05	0.99	0.05	0.22	100	
01/10/2021	1C-28Y-1-50-51.5cm	60.799-S	76.39	4 20	0.06	3.36	0.89	13 58	0 21	0 06	0.99	0.06	0.20	100	
01/10/2021	1C-28Y-1-50-51.5cm	60.799-S	69.81	4 23	0.02	2.85	3.62	14.10	0 65	0 50	3.05	0.04	1.14	100	
01/10/2021	1C-28Y-1-50-51.5cm	60.799-S	74.92	4 25	0.09	3.30	1.17	14 24	0 29	0 07	1.37	0.08	0.23	100	
01/10/2021	1C-28Y-1-50-51.5cm	60.799-S	75.81	4 25	0.10	3.24	1.01	13.77	0 28	0 05	1.23	0.05	0.21	100	
01/10/2021	1C-28Y-1-50-51.5cm	60.799-S	58.39	4 26	0.05	2.18	8.12	14.48	3 38	0.79	6.08	0.14	2.12	100	
01/10/2021	1C-28Y-1-50-51.5cm	60.799-S	58.51	4 33	0.06	2.16	7.92	14.46	3 38	0 93	6.16	0.12	1.98	100	
01/10/2021	1C-28Y-1-50-51.5cm	60.799-S	75.44	4 38	0.09	3.36	0.85	14 01	0.19	0 03	1.38	0.05	0.21	100	
01/10/2021	1C-28Y-1-50-51.5cm	60.799-S	68.62	4.40	0.03	2.46	3.55	15 05	0 97	0 27	3.57	0.07	1.00	100	
01/10/2021	1C-28Y-1-50-51.5cm	60.799-S	75.50	4.41	0.06	2.79	1.26	13 87	0 29	0 02	1.49	0.06	0.24	100	
01/10/2021	1C-28Y-1-50-51.5cm	60.799-S	74.13	4.45	0.11	3.58	1.23	14.49	0 33	0.11	1.23	0.06	0.28	100	
01/10/2021	1C-28Y-1-50-51.5cm	60.799-S	65.86	4 56	0.08	2.56	4.52	15.10	1.75	0 34	4.00	0.08	1.14	100	
01/10/2021	1C-28Y-1-50-51.5cm	60.799-S	74.36	4 61	0.09	3.12	1.23	14.41	0 31	0.16	1.42	0.03	0.25	100	
01/10/2021	1C-28Y-1-50-51.5cm	60.799-S	60.50	4 64	0.05	1.80	5.52	16 62	3.18	0.48	5.89	0.12	1.20	100	
01/10/2021	1C-28Y-1-50-51.5cm	60.799-S	73.22	4.72	0.13	4.43	1.88	14.16	0 24	0 02	0.89	0.04	0.28	100	
01/10/2021	1C-28Y-1-50-51.5cm	60.799-S	61.07	4.72	0.07	1.89	5.33	16 58	3 03	0 31	5.70	0.11	1.21	100	
01/10/2021	1C-28Y-1-50-51.5cm	60.799-S	64.03	4.74	0.02	2.05	3.88	17.47	1 31	0 28	5.20	0.08	0.94	100	
01/10/2021	1C-28Y-1-50-51.5cm	60.799-S	60.69	4.76	0.06	1.73	5.60	16.46	3.18	0 33	5.83	0.11	1.24	100	
01/10/2021	1C-28Y-1-50-51.5cm	60.799-S	60.86	4.76	0.06	1.79	5.62	16.45	3.11	0 28	5.75	0.12	1.19	100	
01/10/2021	1C-28Y-1-50-51.5cm	60.799-S	60.83	4.77	0.06	1.79	5.36	16.41	3.16	0 36	5.87	0.12	1.26	100	
01/10/2021	1C-28Y-1-50-51.5cm	60.799-S	60.52	4.78	0.07	1.80	5.62	16 64	3 24	0 33	5.76	0.05	1.20	100	
01/10/2021	1C-28Y-1-50-51.5cm	60.799-S	60.39	4 83	0.08	1.87	5.65	16.47	3 08	0.43	5.90	0.12	1.18	100	
01/10/2021	1C-28Y-1-50-51.5cm	60.799-S	60.53	4 85	0.06	1.84	5.61	16 53	3 09	0.41	5.76	0.11	1.21	100	
Feb 16 11:28 2020	CHA16-1B-41Y-1(47-48cm)_1	75.335-OS	77.66526142	2 989958069	0.110726597	5.236489939	0.565885461	12 61469355	0 077851292	0	0.579333549	0.081063863	0.078736255	100	93.38316424
Feb 16 11:32 2020	CHA16-1B-41Y-1(47-48cm)_2	75.335-OS	77.64814197	3 033694732	0.149327797	5.23745289	0.538419965	12 56110295	0 098600266	0	0.577766816	0.060829117	0.094663493	100	91.07480487
Feb 16 11:36 2020	CHA16-1B-41Y-1(47-48cm)_3	75.335-OS	77.48597042	3 601536274	0.129304692	4.306620597	0.569410059	12 86682459	0.178735362	0	0.674633177	0.059507738	0.127457086	100	94.2734543
Feb 16 11:40 2020	CHA16-1B-41Y-1(47-48cm)_4	75.335-OS	77.46001603	3 905736476	0.10674207	4.141128678	0.603215742	12 80272607	0.123917744	0 009062012	0.675436001	0.063117966	0.108901214	100	94.90166343
Feb 16 11:44 2020	CHA16-1B-41Y-1(47-48cm)_5	75.335-OS	77.98088387	3 973821092	0.100143633	3.743388194	0.481072658	12 8618979	0 064522788	0 02516922	0.632856568	0.076680801	0.059563283	100	93.76532217
Feb 16 11:47 2020	CHA16-1B-41Y-1(47-48cm)_6	75.335-OS	77.53663867	3 397877237	0.103509643	4.752129844	0.501295052	12.7746564	0.104462186	0 022120159	0.639685363	0.036090786	0.131534665	100	94.4839503
Feb 16 11:51 2020	CHA16-1B-41Y-1(47-48cm)_7	75.335-OS	77.69123795	4.442497066	0.134437808	2.682369557	0.751953085	12 93285322	0.185424118	0 017669577	0.960437322	0.051518526	0.149601765	100	93.94678646
Feb 16 11:55 2020	CHA16-1B-41Y-1(47-48cm)_8	75.335-OS	77.84095478	3 550426857	0.126966294	4.184861511	0.544934217	12.7184825	0.156358664	0 055288249	0.626964369	0.07484674	0.119915818	100	91.52035234
Feb 16 11:59 2020	CHA16-1B-41Y-1(47-48cm)_9	75.335-OS	77.46208861	3 937105612	0.093723851	4.152590007	0.569547947	12 82759356	0 074387363	0 071006119	0.651734737	0.058009463	0.102212734	100	94.63973071
Feb 16 12:03 2020	CHA16-1B-41Y-1(47-48cm)_10	75.335-OS	77.91879138	4 203905123	0.110902875	3.703858012	0.483312279	12.71870783	0 077908737	0	0.57952606	0.078547334	0.124540377	100	93.95608548
Feb 16 12:07 2020	CHA16-1B-41Y-1(47-48cm)_11	75.335-OS	77.99791337	3 8096003	0.105983717	4.096760131	0.450084977	12 69463594	0 090447951	0 025644654	0.570247728	0.040861192	0.117820048	100	93.97670054
Feb 16 12:15 2020	CHA16-1B-41Y-1(47-48cm)_13	75.335-OS	77.22246995	3 666018602	0.09784855	4.528266244	0.666032231	12.7614776	0.123181508	0 063015733	0.656018058	0.064915705	0.150755819	100	94.7382457
Feb 16 12:19 2020	CHA16-1B-41Y-1(47-48cm)_14	75.335-OS	77.63336305	4 338903968	0.090161218	3.518747424	0.59642675	12 93059464	0 083957955	0 022780948	0.630486811	0.056684989	0.097892245	100	93.49918034
Feb 16 12:23 2020	CHA16-1B-41Y-1(47-48cm)_15	75.335-OS	77.60085173	3 871419097	0.107646704	4.128768518	0.503164294	12 81305165	0 098364976	0 012482323	0.618461785	0.099431841	0.146357082	100	93.73254963
Feb 16 12:26 2020	CHA16-1B-41Y-1(47-48cm)_16	75.335-OS	77.72319242	3.423430361	0.129740215	4.599199716	0.496149186	12.717322	0 093909241	0 007487069	0.640679216	0.079576851	0.089313721	100	93.49452656
Feb 16 12:30 2020	CHA16-1B-41Y-1(47-48cm)_17	75.335-OS	77.47367517	3.705313123	0.17039361	4.129747673	0.564219641	13 08676072	0 086137901	0	0.630312426	0.078276987	0.075162751	100	90.3202882
Feb 16 12:34 2020	CHA16-1B-41Y-1(47-48cm)_18	75.335-OS	77.99812261	3 609988321	0.095752716	4.190514199	0.532322593	12.74214877	0 050328822	0	0.623992089	0.048942647	0.107887233	100	93.78324028
Feb 16 12:38 2020	CHA16-1B-41Y-1(47-48cm)_19	75.335-OS	77.25171315	3 238256174	0.167621811	4.965769057	0.559299784	12 90232572	0 094978465	0 030249991	0.61616737	0.063210554	0.110407933	100	92.23143379
Feb 16 12:46 2020	CHA16-1B-41Y-1(47-48cm)_21	75.335-OS	77.69086296	4 011143099	0.125704683	3.96404312	0.557748963	12.75065207	0 08807807	0	0.630537233	0.06709196	0.114137844	100	94.34811596

Date Analysed	Core Section Identifier	sample_no	SiO2	Na2O	Cl	K2O	FeOt	Al2O3	MgO	P2O5	CaO	MnO	TiO2	total	Analytical Total
Feb 16 12:50 2020	CHA16-1B-41Y-1(47-48cm)_22	75.335-OS	77.57217293	3 682317958	0.148506194	4.299710014	0.54102167	12.78118288	0.123308392	0 057901332	0.642490334	0.060689174	0.090699114	100	93.26210342
Feb 16 13:02 2020	CHA16-1B-41Y-1(47-48cm)_25	75.335-OS	78.04174599	3 964461945	0.104257659	3.778678593	0.494079235	12.75436332	0 051017453	0 030589303	0.589241001	0.061284451	0.130281049	100	94.47747174
Feb 16 13:06 2020	CHA16-1B-41Y-1(47-48cm)_26	75.335-OS	77.8978929	3 980993729	0.085551167	3.954223692	0.534472444	12.72136308	0 084809087	0	0.617304144	0.054065793	0.06932396	100	94.32951422
Feb 16 13:09 2020	CHA16-1B-41Y-1(47-48cm)_27	75.335-OS	77.83114891	3 938370794	0.112604619	4.069533068	0.540210804	12 62407509	0 092576551	0 062108319	0.606381734	0.073081144	0.049908971	100	93.86826293
Feb 16 13:13 2020	CHA16-1B-41Y-1(47-48cm)_28	75.335-OS	78.10195395	3.794469993	0.0878103	4.102787089	0.500448458	12 57477601	0 089728486	0	0.598687217	0.059890035	0.089448458	100	93.83864959
Feb 16 13:17 2020	CHA16-1B-41Y-1(47-48cm)_29	75.335-OS	78.08986591	3 845717443	0.105699483	4.124857892	0.458572022	12 56792639	0 071325668	0	0.592303813	0.069177304	0.074554075	100	93.09411622
Feb 16 13:21 2020	CHA16-1B-41Y-1(47-48cm)_30	75.335-OS	77.8863259	3.731870223	0.090902723	4.169061056	0.512285271	12.75431823	0 094663474	0 011282253	0.584635598	0.046848212	0.117807064	100	93.06651901
Jan 17 19:07 2020	CHA16-1C-38Y-1_72-73cm_1	78.815-OS	77.13264484	3 985931367	0.026114723	4.541634387	0.520113144	13 26555779	0	0 014801867	0.38865474	0.10139279	0.023154349	100	94.58266218
Jan 17 19:11 2020	CHA16-1C-38Y-1_72-73cm_2	78.815-OS	77.10454594	4.146494027	0.029151747	4.469474104	0.525958942	13.12323885	0 057356326	0 017890964	0.385708137	0.085876628	0.054304338	100	95.02003318
Jan 17 19:15 2020	CHA16-1C-38Y-1_72-73cm_3	78.815-OS	77.3043909	4.174943739	0	4.200818603	0.480004836	13 23373333	0 04323292	0 009536674	0.396195803	0.107976337	0.04916685	100	94.37252923
Jan 17 19:19 2020	CHA16-1C-38Y-1_72-73cm_4	78.815-OS	77.23490062	3.715696173	0.025894087	4.685617182	0.563731506	13 2983829	0	0	0.350728035	0.056630157	0.068419335	100	95.00238545
Jan 17 19:23 2020	CHA16-1C-38Y-1_72-73cm_5	78.815-OS	77.30539906	3.478470201	0.046019513	4.535182827	0.588982952	13.4393737	0 024414108	0	0.394730749	0.133089295	0.054337594	100	92.56942892
Jan 17 19:26 2020	CHA16-1C-38Y-1_72-73cm_6	78.815-OS	76.98894439	2.774955047	0.030587573	6.061203227	0.595747857	13 07671444	0 070950555	0	0.316071584	0.056339996	0.028485334	100	95.13667628
Jan 17 19:30 2020	CHA16-1C-38Y-1_72-73cm_7	78.815-OS	76.88435556	3 013056931	0.018078342	5.828596921	0.554589323	13.15252368	0 073899186	0	0.35162903	0.087537233	0.035733798	100	94.58832228
Jan 17 19:34 2020	CHA16-1C-38Y-1_72-73cm_8	78.815-OS	76.94671349	3.794934295	0.007906113	4.80543522	0.528006984	13 30770612	0 074001219	0 015495982	0.38276129	0.067676328	0.069362966	100	94.8633025
Jan 17 19:38 2020	CHA16-1C-38Y-1_72-73cm_9	78.815-OS	77.0259778	4 018925793	0.022770415	4.507491501	0.580861817	13 25697866	0 065897791	0	0.388566115	0.074187481	0.05834263	100	95.29909726
Jan 17 19:42 2020	CHA16-1C-38Y-1_72-73cm_10	78.815-OS	77.13588475	3.795179118	0.040048575	4.595378995	0.554012959	13 3159849	0 0315566	0	0.387171174	0.091210106	0.053572832	100	95.38416732
Jan 17 19:46 2020	CHA16-1C-38Y-1_72-73cm_11	78.815-OS	76.75913698	3 682343535	0.041174331	4.971930141	0.578474386	13.41713596	0 023770748	0	0.40123749	0.078103886	0.046692541	100	94.23346755
Jan 17 19:50 2020	CHA16-1C-38Y-1_72-73cm_12	78.815-OS	77.21200152	3.703270899	0.015543306	4.704605741	0.593684807	13 26985682	0 030669342	0 010744701	0.368345058	0.075838815	0.015438989	100	95.86120207
Jan 17 19:54 2020	CHA16-1C-38Y-1_72-73cm_13	78.815-OS	76.65383875	3 909961461	0.016546198	4.824824701	0.661727263	13 3859178	0 028244466	0 038678055	0.41513041	0.038783445	0.026347449	100	94.88584573
Jan 17 19:58 2020	CHA16-1C-38Y-1_72-73cm_14	78.815-OS	76.90199329	3.171142641	0.018120815	5.346531366	0.671998136	13 28980372	0 064160328	0 000948182	0.450491891	0.051728606	0.033081023	100	94.91846759
Jan 17 20:02 2020	CHA16-1C-38Y-1_72-73cm_15	78.815-OS	77.36052105	3 367257949	0.06658481	5.163208092	0.499446242	13 01008613	0 016184562	0	0.36377248	0.103190163	0.049748521	100	92.06303904
Jan 17 20:10 2020	CHA16-1C-38Y-1_72-73cm_17	78.815-OS	76.95828993	3 503222735	0.006350253	5.041197705	0.586731092	13 23849012	0 060962426	0 039265729	0.414248151	0.104249982	0.04699187	100	94.48442905
Jan 17 20:14 2020	CHA16-1C-38Y-1_72-73cm_18	78.815-OS	76.68260355	3 390683863	0.020302243	5.494348063	0.600582666	13 28194689	0 010151121	0	0.407196016	0.032232427	0.079953163	100	95.55594478
Jan 17 20:18 2020	CHA16-1C-38Y-1_72-73cm_19	78.815-OS	76.61189939	3 516766297	0.030732102	5.380047101	0.701115297	13 20985267	0 056078165	0	0.382619949	0.075087713	0.035801315	100	94.68926049
Jan 17 20:22 2020	CHA16-1C-38Y-1_72-73cm_20	78.815-OS	77.04889477	3 82417954	0.034004477	4.46790656	0.632823272	13.41400933	0 04343251	0	0.402121483	0.071398809	0.061229246	100	94.39933357
Jan 17 20:30 2020	CHA16-1C-38Y-1_72-73cm_22	78.815-OS	77.18827667	3 602843537	0.024264048	4.97247565	0.488636472	13 26028088	0 022373343	0 030566399	0.316377981	0.066699873	0.027205145	100	95.20258
Jan 17 20:34 2020	CHA16-1C-38Y-1_72-73cm_23	78.815-OS	77.57565338	3 350516789	0.028521804	4.668187211	0.545530117	13.18057256	0.137625658	0 00106029	0.392731462	0.088110109	0.031490617	100	94.31380885
Jan 17 20:38 2020	CHA16-1C-38Y-1_72-73cm_24	78.815-OS	77.00026465	4 078407354	0.027844964	4.355752956	0.572580796	13 33734368	0 050307258	0 039024355	0.344490855	0.121006553	0.072976578	100	96.60633815
Jan 17 20:42 2020	CHA16-1C-38Y-1_72-73cm_25	78.815-OS	77.02600577	3 909543379	0.006271995	4.78561113	0.634559374	13.16614528	0 041395165	0	0.355622101	0.057179685	0.017666118	100	95.66334576
Jan 17 20:53 2020	CHA16-1C-38Y-1_72-73cm_28	78.815-OS	77.20860937	4.11352612	0.012465231	4.158589083	0.572270782	13 39427554	0 016828061	0	0.329913105	0.116861538	0.076661169	100	96.26777329
Jan 17 20:57 2020	CHA16-1C-38Y-1_72-73cm_29	78.815-OS	77.09776292	4.128314636	0.025428771	4.161612383	0.586637799	13 51328768	0 043959859	0	0.309263271	0.094920351	0.038812335	100	97.13406932
Jan 17 21:13 2020	CHA16-1B-43Y-1_53-56cm_1	78.815-S	77.43592844	3 588499324	0.02954011	4.741598103	0.561077252	13.18111646	0 019450706	0	0.343143747	0.079051	0.020594866	100	96.14046678
Jan 17 21:17 2020	CHA16-1B-43Y-1_53-56cm_2	78.815-S	76.89811486	3 829439599	0.036091157	4.731604806	0.660246855	13 23462513	0 039238641	0 026963451	0.387770103	0.095683532	0.060221872	100	95.31420735
Jan 17 21:21 2020	CHA16-1B-43Y-1_53-56cm_3	78.815-S	77.32232814	3 84901063	0.018824396	4.445727799	0.572946715	13 27606794	0 061310743	0 021768995	0.350196869	0.071616837	0.01020093	100	95.08937106
Jan 17 21:25 2020	CHA16-1B-43Y-1_53-56cm_4	78.815-S	77.15428757	3 378371403	0.02186005	5.10420031	0.610783344	13 21411901	0 044556849	0 031378063	0.333548805	0.1068946	0	100	95.60819741
Jan 17 21:29 2020	CHA16-1B-43Y-1_53-56cm_5	78.815-S	77.25330141	4.134900173	0.011783939	4.273597803	0.550750013	13 28231941	0 044294987	0	0.363513488	0.081330225	0.00420855	100	95.04461621
Jan 17 21:33 2020	CHA16-1B-43Y-1_53-56cm_6	78.815-S	77.22790464	3 854809641	0.051746629	4.315991681	0.633533489	13 32490819	0 034881837	0 007018268	0.361178903	0.109987775	0.078038945	100	95.46515504
Jan 17 21:37 2020	CHA16-1B-43Y-1_53-56cm_7	78.815-S	76.99523434	4.190481733	0.016698112	4.423649599	0.610701542	13 23166036	0 05328506	0 025844849	0.369485623	0.082958775	0	100	94.02260291
Jan 17 21:41 2020	CHA16-1B-43Y-1_53-56cm_8	78.815-S	77.06241908	3 981380742	0.03075564	4.616783819	0.607786818	13 26618718	0 021381489	0	0.352952563	0.060352676	0	100	94.9419371
Jan 17 21:45 2020	CHA16-1B-43Y-1_53-56cm_9	78.815-S	77.25878189	3 992412144	0.014919014	4.421001191	0.549536104	13 28362981	0 01481395	0	0.358161395	0.082579893	0.0241646	100	95.18055409
Jan 17 21:49 2020	CHA16-1B-43Y-1_53-56cm_10	78.815-S	77.39163527	3 945500737	0.015020405	4.296496534	0.55413126	13 29223401	0 045590102	0	0.351921741	0.106094832	0.001375107	100	94.5380637
Jan 17 21:53 2020	CHA16-1B-43Y-1_53-56cm_11	78.815-S	77.03505585	4 048131282	0.040902993	4.425738483	0.496089704	13.41011405	0 021189437	0	0.388789275	0.087287831	0.046701098	100	94.8585837
Jan 17 21:57 2020	CHA16-1B-43Y-1_53-56cm_12	78.815-S	76.78246003	2 994894173	0.05478205	5.7409717	0.577949968	13 3004821	0 06277554	0	0.410119316	0.071301929	0.004263195	100	93.82635372
Jan 17 22:00 2020	CHA16-1B-43Y-1_53-56cm_13	78.815-S	76.65887581	2.723121851	0.051750164	6.08696705	0.570772811	13 34001995	0 052943564	0 011934	0.409553187	0.081802146	0.012259473	100	92.17362047
Jan 17 22:04 2020	CHA16-1B-43Y-1_53-56cm_14	78.815-S	76.98310624	3 857889413	0.010962309	4.722931366	0.6440423	13 25582622	0 039949183	0	0.34910737	0.111098783	0.025086822	100	94.87052656
Jan 17 22:08 2020	CHA16-1B-43Y-1_53-56cm_15	78.815-S	76.94018946	3 634945658	0.046599158	5.156586648	0.544097432	13 06418456	0 033813448	0 045331154	0.386846978	0.081046608	0.066358892	100	94.63690309
Jan 17 22:12 2020	CHA16-1B-43Y-1_53-56cm_16	78.815-S	76.79978043	3.192356065	0.055551196	5.748561354	0.594325607	13.13519246	0 025097799	0	0.380982494	0.068152602	0	100	95.2274727
Jan 17 22:16 2020	CHA16-1B-43Y-1_53-56cm_17	78.815-S	77.33815285	3 65436909	0.004752792	4.732376134	0.630402476	13 22117286	0	0	0.316324723	0.082487349	0.019961727	100	94.68118614
Jan 17 22:20 2020	CHA16-1B-43Y-1_53-56cm_18	78.815-S	77.10431131	3 678391261	0.023541704	4.62714838	0.623340512	13.47043592	0	0 018181763	0.344297422	0.090278231	0.020073507	100	95.15029131
Jan 17 22:24 2020	CHA16-1B-43Y-1_53-56cm_19	78.815-S	76.80328813	3.123728654	0.037296693	5.678340429	0.559511388	13 26941264	0 066549002	0 008880165	0.359803394	0.088697178	0.004492319	100	95.71894139
Jan 17 22:28 2020	CHA16-1B-43Y-1_53-56cm_20	78.815-S	76.79401827	3 588529605	0.019403096	5.050095529	0.62105275	13.41084099	0 044752302	0 02701829	0.335590109	0.076047619	0.032651447	100	95.86098983
Jan 17 22:32 2020	CHA16-1B-43Y-1_53-56cm_21	78.815-S	77.03456747	3 937057913	0.02182613	4.689391502	0.569271916	13 20369385	0 056810597	0 026107811	0.3549618	0.041354773	0.064956234	100	95.75678295
Jan 17 22:36 2020	CHA16-1B-43Y-1_53-56cm_22	78.815-S	77.02208072	3 942854579	0.044054829	4.598444474	0.553051366	13 34439664	0 000210286	0	0.374834042	0.07727995	0.042793115	100	95.10875749
Jan 17 22:40 2020	CHA16-1B-43Y-1_53-56cm_23	78.815-S	77.12769375	4 044710777	0.044638518	4.368466909	0.581856437	13 26867937	0 059413239	0	0.356793787	0.092630164	0.055117043	100	95.43327603
Jan 17 22:44 2020	CHA16-1B-43Y-1_53-56cm_24	78.815-S	77.1709803	3.788481177	0.019624542	4.569309426	0.630330616	13 26853349	0 075979512	0 018260269	0.366989437	0.066219713	0.025291523	100	95.28884615
Jan 17 22:48 2020	CHA16-1B-43Y-1_53-56cm_25	78.815-S	77.05352019	3 613938867	0.032147247	4.952823307	0.520336136	13 26245125	0 069652368	0	0.37746751	0.087196781	0.030466345	100	95.18700029
Jan 17 22:52 2020	CHA16-1B-43Y-1_53-56cm_26	78.815-S	77.01916951	4 049506269	0.018827575	4.610403898	0.581706483	13 25800628	0 021457124	0 019563848	0.366138476	0.05522054	0	100	95.07331867
Jan 17 22:56 2020	CHA16-1B-43Y-1_53-56cm_27	78.815-S	77.03257317	3 296708301	0.019097436	5.476685109	0.565743866	13 0979356	0 021657987	0	0.416089397	0.06241341	0.011095717	100	93.72985773
Jan 17 23:00 2020	CHA16-1B-43Y-1_53-56cm_28	78.815-S	77.18753541	3 979860853	0	4.42895929	0.538576321	13 25653795	0 074451751	0	0.38370479	0.079072169	0.071301465	100	95.22946004
Jan 17 23:04 2020	CHA16-1B-43Y-1_53-56cm_29	78.815-S	76.87247833	3 853831255	0.009320407	4.51891025	0.944841274	13 20023765	0 089643466	0 025447853	0.372187942	0.087339545	0.025762024	100	95.48939112

Date Analysed	Core Section Identifier	sample_no	SiO2	Na2O	Cl	K2O	FeOt	Al2O3	MgO	P2O5	CaO	MnO	TiO2	total	Analytical Total
Jan 17 23:08 2020	CHA16-1B-43Y-1_53-56cm_30	78.815-S	77.49096483	3 88861454	0.026065373	4.324421005	0.543542492	13 21250128	0 045879294	0 026065373	0.350717006	0.091228804	0	100	94.37808666
Jan 17 11:44 2020	CHA16-1C-38Y-1_128-134cm_1	79.480-OS	66.9151597	4.765912901	0.075111604	2.753557206	3.320646904	16.71493763	0 877458654	0	3.56167795	0.072662312	0.942875146	100	97.98752299
Jan 17 11:48 2020	CHA16-1C-38Y-1_128-134cm_2	79.480-OS	67.00864101	4 520872596	0.079264638	2.841967777	3.705876992	15 92511661	1 380957294	0	3.495212073	0.049092295	0.992998712	100	100.423091
Jan 17 11:52 2020	CHA16-1C-38Y-1_128-134cm_3	79.480-OS	67.11469633	4.778586074	0.074171966	2.782655155	3.232261632	16 5331625	0 898685829	0 035423866	3.542386633	0.044669392	0.963300623	100	96.26278419
Jan 17 11:56 2020	CHA16-1C-38Y-1_128-134cm_4	79.480-OS	67.01853386	4 688668659	0.123008601	2.697239109	3.264352884	16 69553608	0 945456245	0 024050112	3.530291696	0.033427449	0.979435302	100	90.64406784
Jan 17 12:00 2020	CHA16-1C-38Y-1_128-134cm_5	79.480-OS	66.85257485	4 642311534	0.105610014	2.737193503	3.537675053	16 20337183	1 324757194	0 030880121	3.468866934	0.045702579	1.051056388	100	97.14987817
Jan 17 12:04 2020	CHA16-1C-38Y-1_128-134cm_6	79.480-OS	66.29983998	4.45997947	0.087041535	2.732693293	3.845337363	16.18665021	1 543009026	0	3.771457293	0.0269243	1.04706753	100	97.30986498
Jan 17 12:08 2020	CHA16-1C-38Y-1_128-134cm_7	79.480-OS	66.07858294	4.432784483	0.081958677	2.650730902	3.847991101	16.14875283	1.443365653	0	4.283961982	0.052831988	0.979039451	100	94.07179654
Jan 17 12:16 2020	CHA16-1C-38Y-1_128-134cm_9	79.480-OS	66.22548212	4.49458752	0.090699766	2.67598607	4.077217094	15 89928114	1 532300837	0 00565611	3.908776112	0.04979397	1.040219255	100	99.00797305
Jan 17 12:20 2020	CHA16-1C-38Y-1_128-134cm_10	79.480-OS	66.57229655	4 582564499	0.076031262	2.750759496	3.670910415	16.16387213	1.456386582	0 013240818	3.589503118	0.055756259	1.068678868	100	96.67076156
Jan 17 12:31 2020	CHA16-1C-38Y-1_128-134cm_13	79.480-OS	66.91577745	4 359034397	0.057158907	2.716162532	3.84571321	15 90040564	1 296919572	0 028526034	3.760735558	0.0533127	1.066254002	100	93.59871083
Jan 17 12:39 2020	CHA16-1C-38Y-1_128-134cm_15	79.480-OS	66.42619678	4 639908544	0.067283818	2.785882455	3.943825837	15 89710006	1.485696658	0 020061689	3.559663761	0.056069848	1.118310552	100	97.20019171
Jan 17 12:43 2020	CHA16-1C-38Y-1_128-134cm_16	79.480-OS	66.62953447	4 534966003	0.060500569	2.710629978	3.982432788	15 85635548	1.438821032	0 031332492	3.679506507	0.06245885	1.013461834	100	97.0238806
Jan 17 12:51 2020	CHA16-1C-38Y-1_128-134cm_18	79.480-OS	66.81203973	4 525909255	0.049622637	2.817091525	3.797189761	15 90562377	1.427488015	0 015018712	3.561870288	0.079355629	1.00879067	100	98.5437345
Jan 17 13:03 2020	CHA16-1C-38Y-1_128-134cm_21	79.480-OS	66.06992026	4 652712163	0.059530335	2.750873488	4.069868985	15.78557047	1 533464849	0	3.92128143	0.052419203	1.104358819	100	98.43720908
Jan 17 13:07 2020	CHA16-1C-38Y-1_128-134cm_22	79.480-OS	66.52424043	4 549316978	0.102687465	2.623409163	3.979650018	15 87878668	1.483521171	0	3.792778678	0.07050937	0.995100044	100	99.13576085
Jan 17 13:19 2020	CHA16-1C-38Y-1_128-134cm_25	79.480-OS	66.34876297	4 569596958	0.051054125	2.717901152	3.998826507	16 01185838	1.436794513	0 04195537	3.700160369	0.076227347	1.046862312	100	98.91463167
Jan 17 13:22 2020	CHA16-1C-38Y-1_128-134cm_26	79.480-OS	66.58741027	4 391595575	0.106289342	2.769120824	3.947722184	15 89963486	1 38207968	0	3.818778761	0.072450719	1.024917788	100	94.27097576
Jan 17 13:26 2020	CHA16-1C-38Y-1_128-134cm_27	79.480-OS	66.8739016	4 222296719	0.06572539	2.66586435	3.786389068	16.10416451	1 388474297	0	3.744108898	0.082614577	1.066460583	100	98.28773949
Jan 17 13:30 2020	CHA16-1C-38Y-1_128-134cm_28	79.480-OS	65.8017782	4 653584293	0.068547397	2.702096095	3.914252764	16 03515436	1.447737109	0 030554852	4.201292083	0.096086967	1.048915889	100	99.49320155
Jan 17 13:58 2020	CHA16-1C-38Y-1_128-134cm_35	79.480-OS	66.26257268	4 685932147	0.068140847	2.724998692	3.799603283	16 00755263	1.469124654	0 030673372	3.856652044	0.042263311	1.052486338	100	100 0868099
Jan 17 14:02 2020	CHA16-1C-38Y-1_128-134cm_36	79.480-OS	66.5407648	4.719868967	0.076886565	2.754536509	3.632695127	16 0166414	1.412035852	0 030090423	3.753755063	0.05585346	1.006871834	100	99.36716534
Jan 17 14:06 2020	CHA16-1C-38Y-1_128-134cm_37	79.480-OS	66.80685569	4 560328419	0.059253935	2.807046145	3.67055126	15 94649819	1 390647378	0	3.700843019	0.097981336	0.959994634	100	98.89638608
30/09/2021	CHA08-6A-6S-1-73-74cm	89.3-OS	72.08507409	4 687377005	0.236484294	4.754180478	1.881631149	14.73016574	0 264972169	0 035962536	0.976329117	0.046205735	0.30161768	100	
30/09/2021	CHA08-6A-6S-1-73-74cm	89.3-OS	72.37422705	4.738613271	0.107124606	4.525641888	1.906093877	14.71632256	0 264487158	0 028538165	0.964867185	0.04696019	0.327124044	100	
30/09/2021	CHA08-6A-6S-1-73-74cm	89.3-OS	72.08149409	4.798310386	0.138511226	4.446434291	1.823357947	14 85343637	0 211288112	0	1.291132948	0.069735444	0.286299186	100	
30/09/2021	CHA08-6A-6S-1-73-74cm	89.3-OS	72.35892808	4 846340514	0.109857393	4.320707052	1.976381815	14.71773692	0 220199203	0	1.01882959	0.06927849	0.361740948	100	
30/09/2021	CHA08-6A-6S-1-73-74cm	89.3-OS	72.80930038	4 884197568	0.110475897	4.249886195	1.543491006	14.7265957	0 292631126	0 007611736	1.028842076	0.074531586	0.272436734	100	
30/09/2021	CHA08-6A-6S-1-73-74cm	89.3-OS	72.1997502	4 912275901	0.127807089	4.417751482	1.78028791	14 90166918	0 273961055	0 020660131	0.998680147	0.057694516	0.309462392	100	
30/09/2021	CHA08-6A-6S-1-73-74cm	89.3-OS	72.42858695	4 943693622	0.131274401	4.421104444	1.891772824	14 63249698	0 226696963	0 009824677	0.944974075	0.049227901	0.320347166	100	
30/09/2021	CHA08-6A-6S-1-73-74cm	89.3-OS	72.04323056	4 956215429	0.121642994	4.409032409	1.967754321	14 84760079	0 265650234	0 0746063	0.994059675	0.036934854	0.28327244	100	
30/09/2021	CHA08-6A-6S-1-73-74cm	89.3-OS	72.0908506	4 956604273	0.122538272	4.554144952	1.948750398	14.70035626	0 298988547	0	0.993195907	0.036221339	0.29834945	100	
30/09/2021	CHA08-6A-6S-1-73-74cm	89.3-OS	71.91041906	4 958318213	0.134357818	4.338528436	1.922398799	14 93798411	0 292276387	0 028153163	1.110837559	0.057671964	0.309054495	100	
30/09/2021	CHA08-6A-6S-1-73-74cm	89.3-OS	71.82052045	4 960781402	0.129865042	4.550016063	1.990632028	14 84021443	0 277054401	0 019379698	1.041321058	0.075622952	0.294592475	100	
30/09/2021	CHA08-6A-6S-1-73-74cm	89.3-OS	72.2687138	4 97312023	0.100721422	4.500988563	1.86754304	14 68854076	0 280368063	0 034937743	0.940829934	0.056760718	0.287475726	100	
30/09/2021	CHA08-6A-6S-1-73-74cm	89.3-OS	71.93426698	4 989400385	0.129975976	4.517713374	1.865784178	14 93675536	0 256076789	0 04108918	0.970141193	0.034590381	0.324206206	100	
30/09/2021	CHA08-6A-6S-1-73-74cm	89.3-OS	72.31978521	4 997284609	0.137056329	4.196032225	1.887160222	14 86534029	0 22083021	0	1.006458816	0.050183702	0.319868386	100	
30/09/2021	CHA08-6A-6S-1-73-74cm	89.3-OS	71.76594036	5 016528168	0.117925067	4.220586329	1.979381678	14 96580115	0 321901266	0 034455903	1.161391007	0.037178862	0.378910207	100	
30/09/2021	CHA08-6A-6S-1-73-74cm	89.3-OS	71.91889042	5 057189357	0.101979686	4.200392813	1.995709023	14 8790034	0 317219408	0 008358991	1.068095126	0.070215522	0.38294626	100	
30/09/2021	CHA08-6A-6S-1-73-74cm	89.3-OS	72.2918756	5 057747951	0.119989251	4.253587189	1.904591279	14 69709603	0 233812901	0 043382357	0.993826655	0.064967725	0.339123058	100	
30/09/2021	CHA08-6A-6S-1-73-74cm	89.3-OS	72.13974694	5 06748067	0.109202114	4.439280587	1.821780241	14 61612193	0 313491636	0 086586911	1.012008716	0.082608311	0.311691941	100	
30/09/2021	CHA08-6A-6S-1-73-74cm	89.3-OS	72.07342562	5 069553388	0.098981982	4.283982098	1.92726823	14 82111166	0 255036226	0 047553249	1.076493494	0.027547367	0.319046686	100	
30/09/2021	CHA08-6A-6S-1-73-74cm	89.3-OS	71.90612093	5 084761395	0.115743847	4.371846396	2.023420514	14 6881458	0 282723829	0 043928145	1.071600731	0.040992612	0.3707158	100	
30/09/2021	CHA08-6A-6S-1-73-74cm	89.3-OS	72.16696975	5 092639821	0.099227724	4.315618488	1.932053046	14.72140419	0 271287701	0 046726283	1.016593732	0.040741119	0.296738147	100	
30/09/2021	CHA08-6A-6S-1-73-74cm	89.3-OS	72.09452311	5 097394102	0.117850909	4.402294906	1.906256885	14 60761492	0 324998799	0 010215852	1.016735731	0.05918875	0.362926035	100	
30/09/2021	CHA08-6A-6S-1-73-74cm	89.3-OS	71.7868413	5.159487534	0.119754977	4.36815509	1.899197865	14 81374335	0 256154143	0 032180853	1.144973187	0.056764914	0.362746792	100	
30/09/2021	CHA08-6A-6S-1-73-74cm	89.3-OS	71.89246051	5.163825077	0.128205312	4.304933279	1.895846529	14 82112066	0 27018917	0.115636164	1.03112783	0.061274598	0.315380878	100	
01/10/2021	1C-46Y-1-11-12cm	89.56-G	76.16	3 61	0.18	3.67	1.09	13.47	0 25	0 08	1.38	0.02	0.11	100	
01/10/2021	1C-46Y-1-11-12cm	89.56-G	76.56	3 64	0.12	3.00	1.26	13.48	0 25	0 04	1.38	0.10	0.17	100	
01/10/2021	1C-46Y-1-11-12cm	89.56-G	75.78	3.76	0.13	3.41	1.22	13 65	0 28	0 07	1.50	0.06	0.13	100	
01/10/2021	1C-46Y-1-11-12cm	89.56-G	76.07	3.77	0.11	3.33	1.35	13.47	0 26	0 01	1.42	0.08	0.13	100	
01/10/2021	1C-46Y-1-11-12cm	89.56-G	76.40	3.77	0.11	2.89	1.25	13 57	0 23	0 08	1.50	0.03	0.18	100	
01/10/2021	1C-46Y-1-11-12cm	89.56-G	75.51	3.78	0.13	3.42	1.46	13 36	0 39	0 09	1.63	0.03	0.21	100	
01/10/2021	1C-46Y-1-11-12cm	89.56-G	75.88	3 86	0.17	3.38	1.11	13 69	0 29	0 03	1.42	0.04	0.12	100	
01/10/2021	1C-46Y-1-11-12cm	89.56-G	76.44	3 88	0.09	3.08	1.19	13.41	0 29	0 06	1.40	0.01	0.16	100	
01/10/2021	1C-46Y-1-11-12cm	89.56-G	75.52	3 91	0.13	2.88	1.21	14.18	0 21	0 02	1.78	0.00	0.17	100	
01/10/2021	1C-46Y-1-11-12cm	89.56-G	76.04	3 92	0.12	2.84	1.27	13 85	0 25	0 00	1.55	0.01	0.14	100	
01/10/2021	1C-46Y-1-11-12cm	89.56-G	76.49	3 94	0.08	2.90	1.09	13 58	0 24	0 06	1.45	0.05	0.12	100	
01/10/2021	1C-46Y-1-11-12cm	89.56-G	76.38	3 94	0.09	3.02	1.16	13 58	0 29	0 00	1.40	0.01	0.14	100	
01/10/2021	1C-46Y-1-11-12cm	89.56-G	76.39	3 97	0.09	3.02	1.16	13 51	0 25	0 03	1.38	0.02	0.18	100	
01/10/2021	1C-46Y-1-11-12cm	89.56-G	76.10	3 97	0.12	2.94	1.17	13 84	0 24	0 04	1.37	0.05	0.15	100	

Date Analysed	Core Section Identifier	sample_no	SiO2	Na2O	Cl	K2O	FeOt	Al2O3	MgO	P2O5	CaO	MnO	TiO2	total	Analytical Total
01/10/2021	1C-46Y-1-11-12cm	89.56-G	75.75	3 98	0.13	3.24	1.24	13.75	0 23	0 02	1.48	0.04	0.13	100	
01/10/2021	1C-46Y-1-11-12cm	89.56-G	76.09	3 99	0.14	3.00	1.25	13 67	0 27	0 00	1.48	0.01	0.10	100	
01/10/2021	1C-46Y-1-11-12cm	89.56-G	76.20	4 01	0.09	2.99	1.28	13 52	0 24	0 04	1.45	0.03	0.14	100	
01/10/2021	1C-46Y-1-11-12cm	89.56-G	75.66	4 03	0.15	3.09	1.22	13.74	0 26	0 05	1.56	0.04	0.19	100	
01/10/2021	1C-46Y-1-11-12cm	89.56-G	76.05	4 08	0.11	2.98	1.15	13 67	0 23	0 07	1.47	0.05	0.15	100	
01/10/2021	1C-46Y-1-11-12cm	89.56-G	75.99	4 08	0.10	2.92	1.31	13 61	0 27	0 00	1.49	0.04	0.18	100	
01/10/2021	1C-46Y-1-11-12cm	89.56-G	76.05	4.12	0.15	2.94	1.23	13 60	0 27	0 05	1.45	0.05	0.09	100	
01/10/2021	1C-46Y-1-11-12cm	89.56-G	76.13	4.13	0.10	2.96	1.21	13 53	0 27	0 02	1.47	0.02	0.13	100	
01/10/2021	1C-46Y-1-11-12cm	89.56-G	75.86	4.14	0.11	2.94	1.38	13.70	0 20	0 07	1.33	0.01	0.24	100	
01/10/2021	1C-46Y-1-11-12cm	89.56-G	76.04	4.16	0.12	2.97	1.27	13 53	0 23	0 00	1.45	0.03	0.21	100	
Jan 25 10:46 2020	CHA16-1C-46Y-1(71-74cm)_2	89.658-OS	64.46538677	5 095166364	0.103371071	2.295970028	4.259837874	16 82620452	1 647017769	0 237669591	4.24597197	0.045814562	0.777589484	100	95.38452041
Jan 25 10:50 2020	CHA16-1C-46Y-1(71-74cm)_3	89.658-OS	63.78264678	5.453971303	0.123488156	2.401455075	4.347577181	17 02504808	1 587735364	0 276327431	4.247907199	0.051444504	0.702398926	100	93.69319559
Jan 25 10:58 2020	CHA16-1C-46Y-1(71-74cm)_5	89.658-OS	64.15642223	5 249255572	0.103128793	2.402900881	4.117024634	16 98759228	1 634178856	0 235649292	4.248906278	0.092712785	0.772228403	100	96.96613034
Jan 25 11:41 2020	CHA16-1C-46Y-1(71-74cm)_16	89.658-OS	64.39082825	5.106015346	0.074806692	2.374653843	4.203213043	17 02829597	1 563602544	0 280270303	4.137808843	0.098349397	0.742155763	100	98.1195641
Jan 25 11:56 2020	CHA16-1C-46Y-1(71-74cm)_20	89.658-OS	63.90676243	5 569756604	0.108594094	2.090005379	3.950607242	17 27999878	1.483365158	0 226345428	4.578620032	0.065070271	0.740874587	100	92.82272759
Jan 25 12:00 2020	CHA16-1C-46Y-1(71-74cm)_21	89.658-OS	63.54526867	5.478564199	0.086077256	2.27851561	3.919272366	17 33786112	1 616935944	0 280004252	4.627918372	0.101166093	0.728416124	100	98.74850058
Jan 25 12:04 2020	CHA16-1C-46Y-1(71-74cm)_22	89.658-OS	64.1162247	5 242270947	0.099867293	2.356990038	4.386010548	16 99445325	1 61392861	0 205322279	4.206008085	0.082088274	0.696835977	100	98.43062391
Jan 25 12:08 2020	CHA16-1C-46Y-1(71-74cm)_23	89.658-OS	64.3760563	5.155813185	0.079485453	2.271012951	4.218942919	17 08196762	1 66479571	0 244901126	4.040766286	0.094830135	0.771428318	100	97.75373581
Jan 25 12:12 2020	CHA16-1C-46Y-1(71-74cm)_24	89.658-OS	64.26804201	5 236734764	0.105485866	2.285705952	4.164041972	16 94862659	1.774051211	0 241447812	4.152902364	0.10076422	0.722197233	100	93.18783975
Jan 25 12:16 2020	CHA16-1C-46Y-1(71-74cm)_25	89.658-OS	64.09572698	4 964663503	0.070172637	2.194158819	4.498766123	16 97360422	1.77959425	0 243379736	4.277092998	0.084834067	0.818006675	100	98.89894848
Jan 25 12:23 2020	CHA16-1C-46Y-1(71-74cm)_27	89.658-OS	64.08658854	5 296993751	0.075484674	2.271576068	4.257610027	17 07027283	1 688605219	0 21007053	4.251666711	0.071966746	0.719164901	100	99.49039488
Jan 25 12:35 2020	CHA16-1C-46Y-1(71-74cm)_30	89.658-OS	63.97786617	5 058216555	0.112202388	2.518391717	4.223749227	17 27337283	1 602875954	0 23822914	4.222324836	0.042223248	0.730547929	100	93.31352165
Jan 25 12:39 2020	CHA16-1C-46Y-1(71-74cm)_31	89.658-OS	64.07117731	5 200198058	0.103142645	2.077925932	4.002808552	17.70298796	1.428170336	0 246444169	4.285049331	0.066429031	0.815666677	100	92.88107773
Jan 25 12:43 2020	CHA16-1C-46Y-1(71-74cm)_32	89.658-OS	64.4350535	5.121922801	0.124570221	2.339643748	4.239385642	17 08029211	1 573990062	0 282548869	3.983717734	0.06723841	0.751636902	100	94.88624076
01/10/2021	CHA08-6A-10S-1-95.5-96.2cm	92.194-S	75.67	3 30	0.27	5.42	1.06	13 02	0.16	0 02	0.80	0.08	0.22	100	
01/10/2021	CHA08-6A-10S-1-95.5-96.2cm	92.194-S	76.13	3.44	0.29	4.82	0.97	13.11	0.18	0 04	0.80	0.04	0.18	100	
01/10/2021	CHA08-6A-10S-1-95.5-96.2cm	92.194-S	75.82	3 51	0.28	5.08	1.02	13 07	0.15	0 00	0.78	0.11	0.18	100	
01/10/2021	CHA08-6A-10S-1-95.5-96.2cm	92.194-S	75.78	3.74	0.23	4.87	0.97	13 09	0.15	0 09	0.82	0.05	0.20	100	
01/10/2021	CHA08-6A-10S-1-95.5-96.2cm	92.194-S	76.06	3 83	0.27	4.52	1.06	13 03	0.14	0 04	0.80	0.05	0.19	100	
01/10/2021	CHA08-6A-10S-1-95.5-96.2cm	92.194-S	76.07	3 86	0.28	4.45	1.06	13.11	0.13	0 02	0.75	0.08	0.19	100	
01/10/2021	CHA08-6A-10S-1-95.5-96.2cm	92.194-S	75.45	3 89	0.30	4.82	1.11	13.18	0.15	0 09	0.81	0.04	0.16	100	
01/10/2021	CHA08-6A-10S-1-95.5-96.2cm	92.194-S	75.15	3 95	0.18	4.76	1.16	13.41	0 20	0 06	0.82	0.08	0.23	100	
01/10/2021	CHA08-6A-10S-1-95.5-96.2cm	92.194-S	75.86	3 98	0.27	4.45	1.05	13 22	0.11	0 04	0.80	0.09	0.13	100	
01/10/2021	CHA08-6A-10S-1-95.5-96.2cm	92.194-S	76.10	3 98	0.26	4.37	0.93	13 21	0.11	0 01	0.78	0.08	0.17	100	
01/10/2021	CHA08-6A-10S-1-95.5-96.2cm	92.194-S	76.16	4 01	0.22	4.30	1.01	13.11	0.18	0 00	0.76	0.09	0.17	100	
01/10/2021	CHA08-6A-10S-1-95.5-96.2cm	92.194-S	75.75	4 03	0.26	4.41	1.01	13 31	0.14	0 01	0.81	0.07	0.20	100	
01/10/2021	CHA08-6A-10S-1-95.5-96.2cm	92.194-S	76.06	4 04	0.27	4.28	0.97	13 20	0.15	0 02	0.76	0.07	0.18	100	
01/10/2021	CHA08-6A-10S-1-95.5-96.2cm	92.194-S	75.87	4 06	0.29	4.47	1.00	13 08	0.17	0 01	0.80	0.07	0.19	100	
01/10/2021	CHA08-6A-10S-1-95.5-96.2cm	92.194-S	75.89	4 07	0.26	4.26	1.04	13 24	0.14	0 05	0.79	0.08	0.18	100	
01/10/2021	CHA08-6A-10S-1-95.5-96.2cm	92.194-S	75.79	4 09	0.27	4.39	0.98	13 30	0.13	0 00	0.86	0.07	0.12	100	
01/10/2021	CHA08-6A-10S-1-95.5-96.2cm	92.194-S	75.84	4.10	0.27	4.32	0.95	13 29	0.17	0 04	0.80	0.05	0.18	100	
01/10/2021	CHA08-6A-10S-1-95.5-96.2cm	92.194-S	75.93	4.12	0.28	4.23	0.95	13 28	0.15	0 07	0.80	0.00	0.19	100	
01/10/2021	CHA08-6A-10S-1-95.5-96.2cm	92.194-S	75.71	4.14	0.25	4.36	1.05	13.15	0.16	0 05	0.81	0.10	0.21	100	
01/10/2021	CHA08-6A-10S-1-95.5-96.2cm	92.194-S	76.01	4.14	0.27	4.17	1.05	13 20	0.12	0 00	0.78	0.08	0.18	100	
01/10/2021	CHA08-6A-10S-1-95.5-96.2cm	92.194-S	76.02	4.15	0.28	4.18	1.06	13 07	0.12	0 06	0.88	0.03	0.15	100	
01/10/2021	CHA08-6A-10S-1-95.5-96.2cm	92.194-S	75.93	4.18	0.28	4.18	1.10	13.16	0.13	0 00	0.78	0.10	0.16	100	
01/10/2021	CHA08-6A-10S-1-95.5-96.2cm	92.194-S	75.88	4.18	0.27	4.12	0.98	13 36	0.14	0 00	0.82	0.09	0.16	100	
01/10/2021	CHA08-6A-10S-1-95.5-96.2cm	92.194-S	75.90	4 28	0.29	4.09	1.06	13.18	0.17	0 07	0.77	0.02	0.17	100	
01/10/2021	CHA08-6A-10S-1-95.5-96.2cm	92.194-S	76.01	4 29	0.27	3.99	1.05	13.16	0.16	0 03	0.79	0.12	0.14	100	
01/10/2021	CHA08-6A-10S-1-95.5-96.2cm	92.194-S	76.16	4 29	0.23	4.09	1.08	13 01	0.14	0 01	0.76	0.02	0.21	100	
01/10/2021	CHA08-6A-10S-1-95.5-96.2cm	92.194-S	75.91	4 37	0.26	4.15	1.00	13.15	0.13	0 04	0.78	0.08	0.14	100	
01/10/2021	CHA08-6A-10S-1-95.5-96.2cm	92.194-S	76.04	4.41	0.25	3.98	1.04	13.18	0 08	0 02	0.80	0.07	0.13	100	
Jan 21 05:49 2020	CHA08-6A-11S-1_33-36cm_2	93.259-S	73.15357342	4.158270461	0.077940916	3.347940833	2.282415938	13 89514693	0 523515589	0.107510575	1.828771919	0.015460236	0.609453178	100	93.7889932
Jan 21 05:53 2020	CHA08-6A-11S-1_33-36cm_3	93.259-S	73.18700632	4.431449137	0.046095452	3.457158902	2.135810748	13.79402907	0 53324057	0.126839288	1.722444074	0.028704895	0.537221541	100	95.45410246
Jan 21 05:57 2020	CHA08-6A-11S-1_33-36cm_4	93.259-S	72.91520414	4 296313033	0.058061285	3.519202148	2.285934024	13.75128051	0 542201366	0 092603011	1.847793834	0.026199738	0.665206917	100	90.0772353
Jan 21 06:01 2020	CHA08-6A-11S-1_33-36cm_5	93.259-S	69.46757293	4 629067407	0.101839483	3.345553262	3.045695901	14 90632967	0.773685493	0 255656327	2.647995379	0.025144253	0.801459898	100	95.05154307
Jan 21 06:09 2020	CHA08-6A-11S-1_33-36cm_7	93.259-S	70.69020366	4 357045504	0.077574128	3.410765931	2.999797084	14 35296031	0.745273153	0 245167386	2.205713353	0.035563474	0.879936016	100	96.1660831
Jan 21 06:17 2020	CHA08-6A-11S-1_33-36cm_9	93.259-S	71.13192404	4 381542035	0.10083836	3.06079013	2.938398983	14 39751193	0 806602056	0.130254095	2.244697742	0.038888806	0.768551823	100	95.40020309
Jan 21 06:21 2020	CHA08-6A-11S-1_33-36cm_10	93.259-S	69.48183076	4.407987113	0.081862618	2.881734916	3.209516782	14 98873596	1 047777469	0 225321366	2.729703766	0.058168353	0.887360892	100	93.69355886
Jan 21 06:28 2020	CHA08-6A-11S-1_33-36cm_12	93.259-S	71.69537147	4.495268574	0.052028571	3.215365716	2.704826721	14.11210415	0 640575772	0.181255621	2.091037403	0.064203257	0.747962743	100	96.10104332
Jan 21 06:44 2020	CHA08-6A-11S-1_33-36cm_16	93.259-S	73.27284682	4 26139175	0.081449261	3.39022053	2.17194506	13 66845224	0 533303731	0 088453171	1.885486413	0.042928799	0.603522231	100	95.27403811

Date Analysed	Core Section Identifier	sample_no	SiO2	Na2O	Cl	K2O	FeOt	Al2O3	MgO	P2O5	CaO	MnO	TiO2	total	Analytical Total
Jan 21 06:48 2020	CHA08-6A-11S-1_33-36cm_17	93.259-S	73.38323269	4.131467633	0.103861958	3.336552342	2.185689624	13.7114254	0 644404357	0 048242116	1.793984463	0.050623553	0.610515863	100	95.60767143
Jan 21 06:52 2020	CHA08-6A-11S-1_33-36cm_18	93.259-S	71.75110577	4.156220422	0.071761343	3.132520811	2.692276217	14 3467243	0 695603886	0.132858531	2.244145459	0.069611574	0.707171692	100	97.68490569
Jan 21 06:56 2020	CHA08-6A-11S-1_33-36cm_19	93.259-S	71.35256412	4 346611127	0.062359932	3.138645564	2.788957755	14 34006674	0.732832441	0.163756466	2.326196402	0.028495598	0.719513847	100	96.85706582
Jan 21 07:04 2020	CHA08-6A-11S-1_33-36cm_21	93.259-S	73.13117234	4 238247365	0.077594175	3.382035776	2.25833742	13 93750471	0 529780921	0 060785969	1.770530583	0.032643067	0.581367669	100	93.43484838
Jan 21 07:08 2020	CHA08-6A-11S-1_33-36cm_22	93.259-S	69.4011428	4.410912005	0.072502402	3.174599376	3.07585711	15.1778884	0 959713871	0 202679224	2.658343026	0.034574845	0.831786945	100	95.4451142
Jan 21 07:12 2020	CHA08-6A-11S-1_33-36cm_23	93.259-S	71.31122041	4 596974049	0.073974295	3.128055904	2.736175073	14.12828614	0.770389444	0 088150128	2.348830208	0.055269366	0.762674982	100	94.6274648
Jan 21 07:16 2020	CHA08-6A-11S-1_33-36cm_24	93.259-S	69.22846727	4 340640739	0.07466747	3.126106226	3.197391676	15.13673376	0 960221548	0 232027172	2.829701734	0.039604386	0.834438017	100	94.68648171
Jan 21 07:27 2020	CHA08-6A-11S-1_33-36cm_27	93.259-S	69.02032203	4 625297519	0.11492504	3.243149789	3.294841772	14.78043027	0 986548753	0.192507319	2.827583395	0.0349346	0.879459512	100	91.88598102
Jan 21 07:31 2020	CHA08-6A-11S-1_33-36cm_28	93.259-S	70.53028408	4 07238741	0.098452132	3.173429551	2.903650628	14 95986289	0 812094702	0.141096746	2.473252592	0.083830528	0.75165874	100	92.3291333
Jan 21 07:39 2020	CHA08-6A-11S-1_33-36cm_30	93.259-S	69.32035974	4.405771142	0.088006906	3.125276081	3.141532889	15.10361714	0 942900134	0 202334868	2.753344936	0.026695067	0.8901611	100	92.15185876
Mar 11 12:24 2020	CHA16-1C-50Y-1(41 5-42.5cm)_5	96.706-S	55.89828352	3 987720379	0.040172178	1.301206781	7.980400385	16 50776956	5.132537858	0 524495297	6.939769499	0.094698938	1.592945603	100	96.83318734
Mar 11 12:32 2020	CHA16-1C-50Y-1(41 5-42.5cm)_7	96.706-S	55.52515834	3.793297694	0.062800963	1.299330272	7.822096239	16.75835718	5 310754682	0 512736545	7.13600435	0.149216738	1.630247005	100	96.97303506
Mar 11 12:44 2020	CHA16-1C-50Y-1(41 5-42.5cm)_10	96.706-S	55.77100078	4.177018113	0.055933795	1.307543269	7.808229326	16 56770351	5.105645147	0.461018182	7.015073413	0.140820335	1.590014125	100	96.36392383
Mar 11 13:00 2020	CHA16-1C-50Y-1(41 5-42.5cm)_14	96.706-S	59.81747794	3.798603657	0.048944114	1.57581263	6.918477636	15.40640174	3 955185344	0.440678436	6.470224045	0.122412465	1.445781999	100	95.82357515
Mar 11 13:04 2020	CHA16-1C-50Y-1(41 5-42.5cm)_15	96.706-S	58.92637417	3.793055483	0.048574047	1.642945716	7.149108299	15.44721991	4.112466606	0 317447199	6.94935424	0.12000647	1.493447861	100	97.9947167
Mar 11 13:08 2020	CHA16-1C-50Y-1(41 5-42.5cm)_16	96.706-S	56.11630424	4.185881961	0.047877719	1.373793214	8.026803095	15 65055566	4 880041566	0 345679523	7.412332042	0.125589305	1.835141681	100	97.5401528
Mar 11 13:12 2020	CHA16-1C-50Y-1(41 5-42.5cm)_17	96.706-S	59.98017336	3 628494037	0.114589873	1.712770524	6.786404418	14 28772532	5 293013427	0.406817186	6.254374947	0.101329714	1.434307187	100	90.49665312
Mar 11 13:24 2020	CHA16-1C-50Y-1(41 5-42.5cm)_20	96.706-S	57.61156	3 810709136	0.050030376	2.040173116	8.673064702	14 37740873	3 875303708	0 656958449	6.561360776	0.149476	2.193955009	100	97.54074221
Mar 11 13:28 2020	CHA16-1C-50Y-1(41 5-42.5cm)_21	96.706-S	57.28881695	4 093972573	0.05364216	1.564125591	6.073414689	18 36307829	2 634869284	0.496718078	7.736648056	0.071067988	1.623646343	100	95.26089266
Mar 11 13:32 2020	CHA16-1C-50Y-1(41 5-42.5cm)_22	96.706-S	57.40552133	4.182160212	0.034190069	1.396351174	7.600154856	15 28910227	4 527874027	0.48384583	7.146032478	0.168794215	1.765973543	100	97.39670259
Mar 11 13:52 2020	CHA16-1C-50Y-1(41 5-42.5cm)_27	96.706-S	56.48928334	4.110472007	0.052608373	1.612358789	8.134172298	15 39087569	4 547678634	0.430866605	7.214272015	0.146662636	1.87074962	100	96.75265897
Mar 11 13:56 2020	CHA16-1C-50Y-1(41 5-42.5cm)_28	96.706-S	58.08851422	4.173687774	0.042113066	2.284966832	8.397410717	14.15744314	3 524791885	1 010514215	6.086413894	0.164353668	2.069790583	100	97.59441444
Mar 11 14:09 2020	CHA16-1C-50Y-1(47-48cm)_1	96.806-S	59.25410208	4 047277982	0.060974429	1.739168777	6.863021509	15.10947179	3 985595115	0.470015239	6.677165842	0.143377902	1.649829334	100	96.59787031
Mar 11 14:13 2020	CHA16-1C-50Y-1(47-48cm)_2	96.806-S	59.3193508	4.144654379	0.036207594	1.815479376	6.740932679	14 9366052	4 008333679	0.459665622	6.609160875	0.165127029	1.764482764	100	98.0457296
Mar 11 14:17 2020	CHA16-1C-50Y-1(47-48cm)_3	96.806-S	59.71178093	3 905947541	0.024377801	1.729711176	6.963081296	15.1125746	3 843802613	0.455877532	6.433311743	0.120169408	1.699365366	100	98.86043541
Mar 11 14:21 2020	CHA16-1C-50Y-1(47-48cm)_4	96.806-S	59.32938803	4 098725979	0.032000063	1.815388173	7.01853735	15 07077736	3 856417813	0.404492419	6.564115426	0.125333579	1.684823814	100	97.49980895
Mar 11 14:25 2020	CHA16-1C-50Y-1(47-48cm)_5	96.806-S	58.26622403	4 048063022	0.033253991	2.039159848	7.751388493	14 85054581	3.764602796	0 902519912	6.274337993	0.145773786	1.924130318	100	95.6276185
Mar 11 14:29 2020	CHA16-1C-50Y-1(47-48cm)_6	96.806-S	58.60618426	3 924840125	0.025397211	1.904790825	7.945005463	14 31107812	4.403548682	0 560134995	6.441470049	0.064926741	1.812623527	100	97.64851738
Mar 11 14:33 2020	CHA16-1C-50Y-1(47-48cm)_7	96.806-S	59.44610196	4.103692795	0.038168003	1.996321032	7.71977156	14 34263499	3 651302199	0 607908325	6.144117581	0.098471379	1.85151018	100	96.67783732
Mar 11 14:37 2020	CHA16-1C-50Y-1(47-48cm)_8	96.806-S	57.61522321	4 074258128	0.061719336	1.632840999	7.403350711	15 55544411	4 313164903	0.464937868	6.952411045	0.119228201	1.807421483	100	97.37629084
Mar 11 14:41 2020	CHA16-1C-50Y-1(47-48cm)_9	96.806-S	58.66306801	4.124608895	0.047956535	1.352620207	6.782944199	15 89528954	4.437004163	0 322457252	6.82458377	0.116509786	1.432957649	100	97.58836911
Mar 11 14:45 2020	CHA16-1C-50Y-1(47-48cm)_10	96.806-S	58.66040324	4 640816779	0.05789365	1.562209601	6.000825887	17 07621008	3 318419086	0.415150781	6.728732855	0.044517868	1.494820167	100	97.93820237
Mar 11 14:49 2020	CHA16-1C-50Y-1(47-48cm)_11	96.806-S	59.37489482	4 042538012	0.051503138	1.965924938	6.798517194	15 3179007	3 686109259	0 524772096	6.389256048	0.128399473	1.720184321	100	97.66395263
Mar 11 14:53 2020	CHA16-1C-50Y-1(47-48cm)_12	96.806-S	59.62344113	4 235003856	0.037110819	1.937553796	6.723369752	15.17482437	3 670075445	0.45925463	6.304738544	0.129067737	1.705559921	100	97.54567865
Mar 11 14:57 2020	CHA16-1C-50Y-1(47-48cm)_13	96.806-S	59.33862378	4.418601232	0.041816294	1.851719086	6.424371268	15.722136	3 81535526	0.415115962	6.257182627	0.144678271	1.570400225	100	98.28704653
Mar 11 15:01 2020	CHA16-1C-50Y-1(47-48cm)_14	96.806-S	59.04656776	4 043580553	0.029876604	1.735101732	6.764700299	15.40990344	4 07594904	0.468912966	6.673468201	0.113448959	1.638490446	100	97.40062894
Mar 11 15:05 2020	CHA16-1C-50Y-1(47-48cm)_15	96.806-S	59.37457013	4 283156685	0.03325757	1.815904155	6.804748451	15.14117808	3 866447612	0.436430439	6.396471379	0.133948436	1.713887068	100	98.02279457
Mar 11 15:09 2020	CHA16-1C-50Y-1(47-48cm)_16	96.806-S	59.14259711	4.186474752	0.036212479	1.810623948	6.94811139	15 39415327	3 81560866	0.403430887	6.383216631	0.109864979	1.769705893	100	97.7563564
Mar 11 15:13 2020	CHA16-1C-50Y-1(47-48cm)_17	96.806-S	59.20739777	4 227312221	0.043591813	1.753929425	6.778985052	15.44547017	3 928391636	0.408070737	6.472102146	0.136109026	1.598640001	100	97.49537101
Mar 11 15:17 2020	CHA16-1C-50Y-1(47-48cm)_18	96.806-S	59.35997471	4 266750884	0.060988942	1.627053984	6.399046558	15 94404397	3 980654087	0.403043939	6.33425419	0.113893779	1.510294953	100	97.72263339
Mar 11 15:21 2020	CHA16-1C-50Y-1(47-48cm)_19	96.806-S	59.16982398	4 221665901	0.046504116	1.659397967	6.488718024	15 96995872	4 056306142	0 3827713	6.40199833	0.080716395	1.522139123	100	97.62576742
Mar 11 15:25 2020	CHA16-1C-50Y-1(47-48cm)_20	96.806-S	59.52605962	4 009245633	0.063676992	1.591924797	6.443544992	16 05064951	4 000221284	0.421077249	6.286062018	0.10092395	1.506613955	100	97.99457884
Mar 11 15:29 2020	CHA16-1C-50Y-1(47-48cm)_21	96.806-S	59.22126847	4.199699567	0.05303149	1.597087352	6.485260634	16 03207531	3 972242901	0.444683545	6.378111668	0.101558375	1.514980682	100	97.67781318
Mar 11 15:33 2020	CHA16-1C-50Y-1(47-48cm)_22	96.806-S	56.61001162	4.198619261	0.037020185	1.38825694	7.455228011	16 02247969	4 822907444	0.430803518	7.33205332	0.099131829	1.603488183	100	97.24424644
Mar 11 15:37 2020	CHA16-1C-50Y-1(47-48cm)_23	96.806-S	59.1797305	4 339290571	0.043724918	1.687267409	6.485852609	15 54332757	4.177015658	0 5181593	6.368405646	0.121195183	1.536030635	100	97.19858225
Mar 11 15:41 2020	CHA16-1C-50Y-1(47-48cm)_24	96.806-S	59.27283005	4.192432728	0.072288357	1.6429172	6.723832357	15 25003081	4.199707091	0 559522951	6.335499451	0.126607307	1.624331699	100	97.38774422
060418	MEX5-1C-50Y-1_41.5-42.5cm-3	96.806-S	59.0615	4 2714	0.0365	1.6194	7.3894	14 5145	4.1542	0 3894	6.7823	0.1755	1.6061	100	97.7783
060418	MEX5-1C-50Y-1_41.5-42.5cm-5	96.806-S	56.4385	4 2777	0.046	1.5392	7.1788	16 819	3.4946	0 2938	8.07	0.1722	1.6702	100	97.53
060418	MEX5-1C-50Y-1_41.5-42.5cm-10	96.806-S	58.2568	4 5068	0.033	1.5753	7.3252	15.7318	3 5864	0 3965	7.0955	0.1206	1.3721	100	99.5343
060418	MEX5-1C-50Y-1_41.5-42.5cm-15	96.806-S	55.6344	4.4468	0.0252	1.3569	8.4282	15 5888	4 3533	0 387	7.6076	0.084	2.0877	100	98.466
060418	MEX5-1C-50Y-1_41.5-42.5cm-22	96.806-S	55.6855	4.4556	0.1099	1.5455	6.0571	18 332	3 0601	0 3853	8.6205	0.1292	1.6193	100	95.1094
060418	MEX5-1C-50Y-1_41.5-42.5cm-23	96.806-S	58.6897	4 2844	0.0508	1.6522	7.0731	15 02	3 8681	0 344	7.4154	0.1293	1.473	100	98.2087
060418	MEX5-1C-50Y-1_41.5-42.5cm-24	96.806-S	54.4593	4.4339	0.0498	1.2969	8.6755	15 8451	4 9046	0.4509	7.754	0.1707	1.9593	100	98.1655
060418	MEX5-1C-50Y-1_41.5-42.5cm-25	96.806-S	53.9618	4 2745	0.0795	1.6742	8.1144	16 0609	4.74	0 6837	8.4358	0.1538	1.8213	100	97.9667
060418	MEX5-1C-50Y-1_41.5-42.5cm-26	96.806-S	56.2458	4.49	0.0432	1.519	8.5149	15 3131	4 3837	0.4791	7.0548	0.1824	1.774	100	98.5216
060418	MEX5-1C-50Y-1_41.5-42.5cm-30	96.806-S	54.7848	4.1648	0.0448	1.4399	7.397	16 9622	5 0459	0.4372	7.8887	0.0948	1.74	100	96.7032
060418	MEX4-1B-55Y-1_8-9cm-3	96.884-OS	75.0115	3 951	0.0385	3.6245	1.6528	13.7337	0 2171	0 0347	1.5192	0.0384	0.1786	100	98.7353
060418	MEX4-1B-55Y-1_8-9cm-7	96.884-OS	75.4669	4 0554	0.0308	3.4651	1.0699	14.1605	0.124	0 0464	1.4534	0	0.1276	100	99.3814
060418	MEX4-1B-55Y-1_8-9cm-11	96.884-OS	76.716	3 6619	0.165	4.0172	0.8865	13 2368	0 0702	0 0395	1.0537	0.0675	0.0856	100	98.1645
060418	MEX5-1B-55Y-1_17-19cm-2	96.884-OS	74.5397	4 8437	0.0244	2.7468	1.1177	14 5968	0.1591	0 0407	1.7387	0.0064	0.186	100	96.859
060418	MEX5-1B-55Y-1_17-19cm-3	96.884-OS	75.2555	4 2624	0.0852	3.2645	1.2594	13 8736	0.1894	0 0843	1.5683	0	0.1575	100	96.0546

Date Analysed	Core Section Identifier	sample_no	SiO2	Na2O	Cl	K2O	FeOt	Al2O3	MgO	P2O5	CaO	MnO	TiO2	total	Analytical Total
060418	MEX5-1B-55Y-1_17-19cm-22	96.884-OS	76.6384	3 9367	0.0408	3.859	1.2405	12.705	0 2356	0 078	1.0946	0	0.1714	100	97.2629
060418	MEX5-1B-55Y-1_17-19cm-24	96.884-OS	75.1444	4.4168	0.0863	3.1331	1.3549	13 9142	0 2216	0 0488	1.4366	0.0628	0.1804	100	96.3322
060418	MEX5-1B-55Y-1_17-19cm-25	96.884-OS	74.7319	4 5827	0.0498	2.8349	0.9651	14 6491	0.1388	0 0403	1.8407	0.0218	0.145	100	97.6499
060418	MEX5-1B-55Y-1_17-19cm-26	96.884-OS	75.0901	4 3773	0.0744	3.1716	1.0928	14 2077	0.1963	0 0285	1.591	0.0029	0.1676	100	98.0329
060418	MEX5-1B-55Y-1_17-19cm-30	96.884-OS	76.0392	3 9132	0.0748	3.4349	1.2372	13 5915	0 2024	0	1.3028	0.0476	0.1563	100	97.4363
050319	CHA16-1A-43Y-1_63-64cm_2	100.176-OS	57.0706	3 9503	0.0572	1.661	7.0506	16 0104	4 5493	0 2871	7.7164	0.1564	1.4905	100	98.5619
050319	CHA16-1A-43Y-1_63-64cm_3	100.176-OS	56.9748	4 202	0.0487	1.5484	7.19	15 8884	4.4489	0 319	7.64	0.1769	1.5629	100	99.0303
050319	CHA16-1A-43Y-1_63-64cm_4	100.176-OS	57.2617	4 3555	0.0555	1.6199	7.1293	15 8622	4 2553	0 357	7.3957	0.1021	1.6059	100	98.97
050319	CHA16-1A-43Y-1_63-64cm_5	100.176-OS	57.1259	4 0735	0.0451	1.6499	7.2976	15 6842	4 3816	0 3632	7.5243	0.1583	1.6964	100	98.623
050319	CHA16-1A-43Y-1_63-64cm_6	100.176-OS	57.4698	4.428	0.0473	1.6664	6.9683	15 5328	4.4268	0 3309	7.3705	0.0557	1.7033	100	99.0189
050319	CHA16-1A-43Y-1_63-64cm_7	100.176-OS	57.2203	4 0542	0.0325	1.729	7.2016	15 9205	4 2794	0 3521	7.4417	0.1044	1.6643	100	98.2096
050319	CHA16-1A-43Y-1_63-64cm_8	100.176-OS	57.17	4.1875	0.0458	1.6449	7.4591	15 6393	4 3602	0 3439	7.4156	0.0771	1.6566	100	98.6831
050319	CHA16-1A-43Y-1_63-64cm_11	100.176-OS	56.3142	4.4367	0.035	1.8687	8.0497	15 2312	4 2345	0 5121	7.1316	0.1029	2.0833	100	99.3733
050319	CHA16-1A-43Y-1_63-64cm_12	100.176-OS	56.8122	4 527	0.0194	1.9659	7.6143	15 2718	4.1138	0.4774	7.0392	0.1677	1.9913	100	99.4001
050319	CHA16-1A-43Y-1_63-64cm_13	100.176-OS	54.5498	4 2555	0.0649	1.5069	8.3053	16.1153	4.4173	0 8655	7.7688	0.1897	1.961	100	99.0446
050319	CHA16-1A-43Y-1_63-64cm_14	100.176-OS	54.8457	4 296	0.0675	1.6714	8.6367	15 6124	4 6727	0 816	7.3983	0.0612	1.9221	100	98.4717
050319	CHA16-1A-43Y-1_63-64cm_15	100.176-OS	54.9473	4 0038	0.0498	1.5766	8.2342	15 8321	4.4786	0 8764	7.899	0.188	1.9142	100	99.4775

Filtered core analyses, normalised to 100% (101-150.99 mc)

Date Analysed	Core Section Identifier	sample_no	SiO2	Na2O	Cl	K2O	FeOt	Al2O3	MgO	P2O5	CaO	MnO	TiO2	total	Analytical Total
Mar 12 07:44 2020	CHA08-4A-4S-1(36-38cm)_1	101.141-S	76.18788798	4.205509143	0 045915485	4.196461774	0.526801289	14.04862312	0.05926301	0 074121342	0.472822716	0.138066796	0.044527342	100	93.65032287
Mar 12 07 52 2020	CHA08-4A-4S-1(36-38cm)_3	101.141-S	76.49523566	2.980555595	0 055841746	5 254442387	0.448723109	13.94161552	0.083922167	0	0 556715616	0.145082174	0.037866022	100	94.01568495
Mar 12 07 56 2020	CHA08-4A-4S-1(36-38cm)_4	101.141-S	76.1852451	4.0356932	0 031565506	4 308264966	0.440015929	14.13530227	0.078807124	0 050034861	0 502915287	0.180648536	0.051507227	100	93.7732482
Mar 12 08 00 2020	CHA08-4A-4S-1(36-38cm)_5	101.141-S	77.0460905	3.150776403	0 084275475	5 316996778	0.492040744	13.29083585	0.031858928	0 023243821	0 343129266	0.182650679	0.038101556	100	92.90959176
Mar 12 08 04 2020	CHA08-4A-4S-1(36-38cm)_6	101.141-S	76.42226059	3.669295171	0 037575429	4 519636124	0.557386984	13.98833902	0.06827085	0 06966335	0 541509565	0.120982297	0.005080621	100	94.47663225
Mar 12 08 08 2020	CHA08-4A-4S-1(36-38cm)_7	101.141-S	76.65108716	3.893402987	0 039800212	4.148487661	0.507894579	13.96691262	0.034640925	0 048319295	0 511927589	0.149935189	0.047591787	100	94.9743695
Mar 12 08:12 2020	CHA08-4A-4S-1(36-38cm)_8	101.141-S	76.35770185	4.152665301	0 043545057	4.144143083	0.588750324	13.96265126	0.054904637	0 07896055	0 527484202	0.089193739	0	100	95.07393738
Mar 12 08:16 2020	CHA08-4A-4S-1(36-38cm)_9	101.141-S	76.36662361	4.050814486	0 032025606	4.174955257	0.438910307	14.09335208	0.05316462	0 036548184	0 503108532	0.135183994	0.115313321	100	94.61179238
Mar 12 08 20 2020	CHA08-4A-4S-1(36-38cm)_10	101.141-S	76.28412725	3.957387219	0 03268298	4 293011885	0.514932059	14.0105829	0.074210859	0 022462228	0 605228384	0.151118333	0.054255904	100	92.7088046
Mar 12 08 24 2020	CHA08-4A-4S-1(36-38cm)_11	101.141-S	76.14968201	4.16360992	0 030899605	4 248695649	0.574154961	14.09458719	0.065125209	0 005792533	0 50319148	0.146665832	0.017595608	100	93.20507581
Mar 12 08 32 2020	CHA08-4A-4S-1(36-38cm)_13	101.141-S	75.57485902	4.065442504	0 025014488	4 834023504	0.345354115	14.32316501	0	0 082762178	0 604252938	0.120745041	0.02438121	100	94.74509167
Mar 12 08 36 2020	CHA08-4A-4S-1(36-38cm)_14	101.141-S	76.9907701	3.170610682	0 033247706	5.137306816	0.400004276	13.42349133	0.000750755	0.151515296	0.477479957	0.149185674	0.065637407	100	93.23951579
Mar 12 08:40 2020	CHA08-4A-4S-1(36-38cm)_15	101.141-S	76.41087887	3.992966302	0 02828187	4 221015942	0.534490836	13.96749132	0.058264905	0 0599998	0 53544172	0.120251109	0.070917321	100	94.0531866
Mar 12 08:44 2020	CHA08-4A-4S-1(36-38cm)_16	101.141-S	76.23287982	3.919371642	0 040486854	4 542689478	0.558539173	13.88571649	0.023626281	0 032165285	0 530732184	0.192017229	0.04177556	100	93.11664424
Mar 12 08:48 2020	CHA08-4A-4S-1(36-38cm)_17	101.141-S	76.01030824	3.068705816	0 042381872	5 625624383	0.513819945	13.8870021	0.06135074	0 085273402	0 512376232	0.141236774	0.051920502	100	92.25642607
Mar 12 08 52 2020	CHA08-4A-4S-1(36-38cm)_18	101.141-S	76.29770723	3.83208362	0 04075026	4.743584925	0.487183115	13.8154091	0.059958064	0 043515967	0 54641429	0.087973868	0.04541956	100	94.23252816
Mar 12 08 56 2020	CHA08-4A-4S-1(36-38cm)_19	101.141-S	76.66654948	3.798689348	0 015568963	4.102632025	0.551393884	14.13043689	0.010624765	0 088301877	0.488949581	0.143907708	0.002945479	100	95.06092616
Mar 12 09 00 2020	CHA08-4A-4S-1(36-38cm)_20	101.141-S	76.59008364	3.781758546	0 034036221	4 251909482	0.565441674	14.03649452	0.033826768	0 041329024	0 504888069	0.124939114	0.035292943	100	95.48651063
Mar 12 09 04 2020	CHA08-4A-4S-1(36-38cm)_21	101.141-S	75.82069045	3.036834868	0 024709189	5 873850954	0.563974195	13.85241159	0.029911123	0 0624109	0 518676212	0.145437417	0.071093104	100	92.27336619
Mar 12 09 08 2020	CHA08-4A-4S-1(36-38cm)_22	101.141-S	76.27385158	3.929776448	0 029088891	4 208832232	0.547672576	14.24971381	0.043047297	0 056431362	0.496535651	0.126051862	0.038998294	100	93.85026016
Mar 12 09:12 2020	CHA08-4A-4S-1(36-38cm)_23	101.141-S	76.03055329	3.688380145	0 022960254	4 935381612	0.571649081	13.86204722	0.08068276	0 074475849	0 528300414	0.120702268	0.084867106	100	93.2045455
Mar 12 09:16 2020	CHA08-4A-4S-1(36-38cm)_24	101.141-S	76.41332468	3.929481214	0 032537913	4 295434086	0.507296177	14.01189351	0.060243463	0 049418424	0 515774248	0.151521437	0.033074842	100	93.12213666
Mar 12 09 20 2020	CHA08-4A-4S-1(36-38cm)_25	101.141-S	76.11554328	3.819319963	0 041163376	4 695197625	0.535611921	13.98715948	0.027335055	0 023149832	0 526869779	0.154041073	0.07460862	100	93.28680813
Mar 12 09 24 2020	CHA08-4A-4S-1(36-38cm)_26	101.141-S	76.56185503	3.919263827	0 033203055	4.155737199	0.469275802	14.04934835	0.048626409	0 080956639	0 568200666	0.101215764	0.012317262	100	93.36490289
Mar 12 09 28 2020	CHA08-4A-4S-1(36-38cm)_27	101.141-S	76.02236699	3.38889834	0 038333095	5.121907941	0.481928367	14.0545899	0.078615331	0 098133783	0 538720761	0.132108408	0.044397088	100	92.34839936
Mar 12 09 36 2020	CHA08-4A-4S-1(36-38cm)_29	101.141-S	76.41408667	3.171347256	0 01487324	5 375613916	0.43349294	13.85157545	0.024434609	0 037418546	0 51737628	0.113567812	0.046213282	100	94.12878378
Mar 12 09:40 2020	CHA08-4A-4S-1(36-38cm)_30	101.141-S	76.30825477	4.131589359	0 044821837	4 35442545	0.488116066	13.92323809	0.032791272	0 030382207	0.498789321	0.13797886	0.049612769	100	93.92743191
060418	MEX4-1A-44Y-1_86-88cm-1	101.141-OS	76.1958	3.9066	0 0102	4.4372	0.4765	14.1846	0.0439	0 0523	0.4761	0.176	0.0408	100	96.1768
060418	MEX4-1A-44Y-1_86-88cm-2	101.141-OS	76.2111	3.935	0 0423	4 3612	0.4497	14.1551	0.0153	0 0577	0 5342	0.1438	0.0946	100	95.7304
060418	MEX4-1A-44Y-1_86-88cm-3	101.141-OS	76.3228	3.8842	0 0357	4 3872	0.4524	14.0338	0.0524	0 0415	0 5339	0.1506	0.1053	100	96.5213
060418	MEX4-1A-44Y-1_86-88cm-4	101.141-OS	76.4517	3.9609	0 0427	4.1938	0.4854	14.0673	0.0347	0 0472	0 5048	0.1307	0.0809	100	97.0341
060418	MEX4-1A-44Y-1_86-88cm-5	101.141-OS	76.2499	3.3858	0 0275	5.132	0.4694	13.9972	0.0219	0 0289	0 5249	0.1264	0.0362	100	98.3356
060418	MEX4-1A-44Y-1_86-88cm-6	101.141-OS	75.9478	4.1701	0 0436	4 2426	0.5013	14.249	0.0352	0 0755	0 531	0.1254	0.0786	100	98.3846
060418	MEX4-1A-44Y-1_86-88cm-7	101.141-OS	76.6894	3.2943	0 0399	5 0735	0.5524	13.6173	0.035	0 0471	0.4688	0.1593	0.023	100	95.7831
060418	MEX4-1A-44Y-1_86-88cm-9	101.141-OS	76.3261	4.1061	0 042	4 3689	0.4871	13.9229	0.0444	0 0267	0.4942	0.1283	0.0533	100	96.3721
060418	MEX4-1A-44Y-1_86-88cm-10	101.141-OS	76.2043	4.3323	0 0236	4.1774	0.5847	13.933	0.0348	0 0204	0 5384	0.1512	0	100	95.5174
060418	MEX4-1A-44Y-1_86-88cm-11	101.141-OS	76.262	3.9318	0 0265	4 3244	0.5288	14.0877	0.0292	0 0539	0 6126	0.1228	0.0204	100	96.2974
060418	MEX4-1A-44Y-1_86-88cm-12	101.141-OS	76.1781	4.0963	0 0106	4.1615	0.5089	14.1911	0.0697	0 027	0 5373	0.1924	0.0271	100	99.3861
060418	MEX4-1A-44Y-1_86-88cm-13	101.141-OS	75.8115	4.1387	0 0326	4.4435	0.4322	14.3318	0.0312	0 0644	0 5678	0.1351	0.0114	100	96.762
060418	MEX4-1A-44Y-1_86-88cm-14	101.141-OS	75.6514	4.0189	0 0668	4 841	0.4339	14.218	0.0366	0 0508	0 5102	0.1222	0.0502	100	97.44
060418	MEX4-1A-44Y-1_86-88cm-15	101.141-OS	77.3993	3.302	0 0394	4.7365	0.5858	13.2943	0.0562	0 0397	0 38	0.1289	0.0378	100	96.7181
060418	MEX4-1A-44Y-1_86-88cm-16	101.141-OS	75.6398	4.0677	0 0637	4 5131	0.5695	14.2542	0.0576	0 0485	0 5417	0.1606	0.0835	100	94.9585
060418	MEX4-1A-44Y-1_86-88cm-18	101.141-OS	76.4051	3.9599	0 0487	4 284	0.4798	14.0615	0.0636	0 0251	0 5273	0.0885	0.0564	100	95.2203
060418	MEX4-1A-44Y-1_86-88cm-19	101.141-OS	76.5251	3.4349	0 0434	5 0919	0.509	13.6734	0.0655	0 0212	0.4218	0.1556	0.0582	100	96.5281
060418	MEX4-1A-44Y-1_86-88cm-21	101.141-OS	76.1995	4.1222	0 0201	4 0546	0.5373	14.3661	0.0305	0 0322	0.4926	0.1084	0.0365	100	96.7021
060418	MEX4-1A-44Y-1_86-88cm-22	101.141-OS	76.1568	4.0764	0 041	4.4722	0.4106	14.1075	0.0275	0 0247	0 5139	0.1025	0.0669	100	96.6125
060418	MEX4-1A-44Y-1_86-88cm-24	101.141-OS	76.2307	3.6698	0 0527	4 5531	0.4991	13.9984	0.0522	0 068	0 6206	0.1794	0.076	100	96.1506
060418	MEX4-1A-44Y-1_86-88cm-26	101.141-OS	75.8693	3.5615	0 0381	5.1324	0.3729	14.0884	0.0351	0 041	0 6548	0.1774	0.0292	100	95.8777
060418	MEX4-1A-44Y-1_86-88cm-27	101.141-OS	76.2034	4.1194	0 035	4.1515	0.5224	14.1892	0.0315	0 0731	0 5093	0.1272	0.0379	100	96.3789
060418	MEX4-1A-44Y-1_86-88cm-29	101.141-OS	75.9217	4.4585	0 0263	4.1771	0.4755	14.1725	0.0746	0 0552	0.4889	0.1284	0.0214	100	96.5577
Mar 13 22 39 2020	CHA08-4A-4S-1(63-64cm)_1	101.408-S	77.3358202	3.876961532	0 092093221	4 657466795	1.031256589	12.40383725	0.03279041	0 039076252	0.428465823	0.023234528	0.078997396	100	94.69
Mar 13 22:43 2020	CHA08-4A-4S-1(63-64cm)_2	101.408-S	77.3658248	3.681466208	0 106045891	4.73192821	1.061939239	12.50904504	0.052284943	0 012780431	0 385102907	0.021969667	0.071612664	100	94.68
Mar 13 22:47 2020	CHA08-4A-4S-1(63-64cm)_3	101.408-S	68.18534252	4.455617098	0 051652585	2.499653198	3.94551157	15.0869485	1.240530236	0 205365698	3 204949536	0.075508196	1.048920863	100	96.41
Mar 13 22 51 2020	CHA08-4A-4S-1(63-64cm)_4	101.408-S	67.58726413	4.594731001	0 097695049	2 531667404	4.296821021	14.82589853	1.22308473	0 334579281	3 319530705	0.051578784	1.137149363	100	95.19
Mar 13 22 55 2020	CHA08-4A-4S-1(63-64cm)_5	101.408-S	67.3835646	4.687123538	0 054292349	2.493121136	4.287657525	15.05622025	1.279249878	0 207691414	3 399710639	0.0899378	1.06143087	100	97.07
Mar 13 22 59 2020	CHA08-4A-4S-1(63-64cm)_6	101.408-S	68.2352866	4.400713229	0 055976199	2.746397755	4.083991081	14.629432	1.205533033	0 20472194	3 228589728	0.082706406	1.126652026	100	95.40
Mar 13 23 03 2020	CHA08-4A-4S-1(63-64cm)_7	101.408-S	67.77381317	4.88676613	0 07861128	2.48246147	4.02447915	14.92659968	1.23168801	0 213027486	3 239309479	0.079620411	1.063623736	100	99.10
Mar 13 23 07 2020	CHA08-4A-4S-1(63-64cm)_8	101.408-S	67.995089	4.608870387	0 040664042	2 516339249	3.983252279	15.00692596	1.251909888	0 186813026	3 261175667	0.080824817	1.068135685	100	99.35
Mar 13 23:11 2020	CHA08-4A-4S-1(63-64cm)_9	101.408-S	77.4279987	3.670945104	0 104026086	4.731306926	0.997106227	12.33855678	0.073421621	0 047104182	0.488797272	0.035719801	0.085017303	100	95.75
Mar 13 23:15 2020	CHA08-4A-4S-1(63-64cm)_10	101.408-S	77.47447423	3.78677774	0.12058601	4.449317296	1.039426345	12.50589405	0.07914349	0 010674134	0.443135093	0.029168921	0.061402692	100	94.62
Mar 13 23:19 2020	CHA08-4A-4S-1(63-64cm)_11	101.408-S	77.10865875	3.827630462	0 111848548	4 800996717	1.059810286	12.48663816	0.056495461	0	0 453369231	0.014256235	0.080296146	100	95.40
Mar 13 23 23 2020	CHA08-4A-4S-1(63-64cm)_12	101.408-S	67.77123488	4.944444694	0 076476005	2.481130751	4.353886446	14.72144592	0.981648178	0 243007868	3 29796392	0.046763699	1.081997637	100	97.94
Mar 13 23 27 2020	CHA08-4A-4S-1(63-64cm)_13	101.408-S	67.96504041	4.673900912	0 069727485	2.424851355	4.139772418	14.82089948	1.259459714	0 201168999	3 340675042	0.062546595	1.041957586	100	96.09
Mar 13 23 35 2020	CHA08-4A-4S-1(63-64cm)_15	101.408-S	67.52968692	4.775433714	0 070121526	2 506514764	4.078153133	15.01021075	1.251467564	0 247505648	3 348784907	0.085038841	1.097082231	100	98.54
Mar 13 23 39 2020	CHA08-4A-4S-1(63-64cm)_16	101.408-S	67.66369702	4.807276153	0 088629665	2 523483512	4.132941436	14.90104665	1.159497847	0 245475449	3 395418871	0.032210318	1.050323076	100	97.48
Mar 13 23:43 2020	CHA08-4A-4S-1(63-64cm)_17	101.408-S	67.74157807	4.796849059	0 074684647	2.47217608	4.216873907	14.802921	1.242967417	0 200890275	3 365483403	0.057545611	1.028030532	100	96.27

Date Analysed	Core Section Identifier	sample_no	SiO2	Na2O	Cl	K2O	FeOt	Al2O3	MgO	P2O5	CaO	MnO	TiO2	total	Analytical Total
Mar 13 23:47 2020	CHA08-4A-4S-1(63-64cm)_18	101.408-S	67.5570035	4.568531175	0 066383622	2.456397034	4.172601565	14.88431997	1.329085469	0 218538133	3 67444515	0.033699331	1.038995043	100	98.52
Mar 13 23 51 2020	CHA08-4A-4S-1(63-64cm)_19	101.408-S	68.72925138	4.426670336	0 082521473	2 561367365	3.854878734	14.66780117	1.162170037	0 211932493	3 253349678	0.050607662	0.999449677	100	96.82
Mar 13 23 55 2020	CHA08-4A-4S-1(63-64cm)_20	101.408-S	68.16665433	4.645596405	0 071475278	2 53099425	4.172091852	14.6764205	1.18249633	0 26403332	3.158680824	0.086053805	1.045503105	100	98.78
Mar 13 23 59 2020	CHA08-4A-4S-1(63-64cm)_21	101.408-S	68.53966263	4.704954986	0 022586126	2 518821424	3.735827324	14.78178345	1.157177238	0 244908546	3.13291425	0.070048216	1.091315811	100	96.08
Mar 14 00 03 2020	CHA08-4A-4S-1(63-64cm)_22	101.408-S	67.67814542	4.715265677	0 067983938	2.471211031	4.099842886	14.96567195	1.206191599	0.198824821	3.435085873	0.071162675	1.09061413	100	97.52
Mar 14 00:11 2020	CHA08-4A-4S-1(63-64cm)_24	101.408-S	67.92482752	4.481437209	0 056805437	2 357373702	4.215904351	14.96282249	1.264481284	0 258272617	3 323169977	0.052443776	1.10246164	100	96.29
Mar 14 00:15 2020	CHA08-4A-4S-1(63-64cm)_25	101.408-S	77.08313873	3.840746401	0.114364798	4 518244298	1.058393998	12.67585492	0.04278974	0 042991147	0 503267719	0.022747743	0.097460512	100	95.83
Mar 14 00:19 2020	CHA08-4A-4S-1(63-64cm)_26	101.408-S	77.45528559	3.839240206	0.106205407	4.409326281	1.077798779	12.49036315	0.047190252	0	0.411148477	0.062748105	0.100693749	100	94.35
Mar 14 00 23 2020	CHA08-4A-4S-1(63-64cm)_27	101.408-S	77.18975422	3.991084648	0.131826308	4 373084266	1.086849683	12.6240311	0.034446295	0	0.407203861	0.05809653	0.103623084	100	94.67
Mar 14 00 27 2020	CHA08-4A-4S-1(63-64cm)_28	101.408-S	68.05022626	4.586176758	0 076968358	2.409709503	4.117268556	14.81953141	1.186890899	0 239445818	3 334956612	0.080730352	1.09809547	100	98.35
Mar 14 00 35 2020	CHA08-4A-4S-1(63-64cm)_30	101.408-S	67.91043438	4.794976695	0 067158319	2.46076284	3.973702901	14.84356577	1.287483896	0 260635797	3 332283013	0.028503836	1.040492554	100	97.53
Mar 14 00 39 2020	CHA08-4A-4S-1(63-64cm)_31	101.408-S	68.20779057	4.625240081	0 048408562	2 627302323	3.892439017	14.71031053	1.155847876	0 287658573	3 289299759	0.052132298	1.103570413	100	96.68
050319	CHA16-1A-44Y-1_125-125cm_5	101.408-OS	67.588	4.7804	0 0317	2 5714	4.1185	15.1509	1.2025	0 3041	3.1517	0.0595	1.0413	100	99.7312
050319	CHA16-1A-44Y-1_125-125cm_6	101.408-OS	67.6049	4.7933	0 0849	2 507	4.1021	14.9466	1.3106	0 2579	3 3308	0.0727	0.9891	100	99.1684
050319	CHA16-1A-44Y-1_125-125cm_7	101.408-OS	68.4494	4.5978	0 0495	2.4659	3.9626	14.8765	1.2219	0	3 2736	0	1.1027	100	98.7989
050319	CHA16-1A-44Y-1_125-125cm_9	101.408-OS	67.789	4.8743	0 0651	2.493	3.5992	15.4244	0.9984	0.1922	3 3795	0.1171	1.0676	100	99.4903
050319	CHA16-1A-44Y-1_125-125cm_10	101.408-OS	68.0082	4.6033	0 0523	2 6259	3.8493	15.2424	0.8775	0 2495	3 3765	0.0416	1.0736	100	99.266
050319	CHA16-1A-44Y-1_125-125cm_14	101.408-OS	67.3549	4.7257	0 0943	2.4599	4.2459	15.0192	1.2509	0 305	3.4321	0.0377	1.0743	100	98.9824
050319	CHA16-1A-44Y-1_125-125cm_17	101.408-OS	67.4311	4.9428	0 0318	2.4607	3.7564	15.4314	1.0641	0 2742	3.4778	0.1195	1.0104	100	99.4952
050319	CHA16-1A-44Y-1_125-125cm_18	101.408-OS	68.0975	4.6067	0 0599	2.7826	4.1638	14.5549	1.2058	0 2861	3 0416	0.1119	1.0891	100	99.2166
050319	CHA16-1A-44Y-1_125-125cm_19	101.408-OS	66.9723	4.8221	0 0399	2.4367	3.735	15.7167	1.1604	0 2697	3.7132	0.095	1.0391	100	98.3105
050319	CHA16-1A-44Y-1_125-125cm_24	101.408-OS	67.5208	4.8082	0 0651	2 8523	4.3302	14.4291	1.3426	0 3328	3 0684	0.0864	1.164	100	99.6097
050319	CHA16-1A-44Y-1_125-125cm_25	101.408-OS	67.0053	5.0986	0 0372	2 2699	3.7771	15.6955	1.1115	0 2323	3.7475	0.0607	0.9645	100	97.3823
050319	CHA16-1A-44Y-1_125-125cm_27	101.408-OS	67.795	4.4512	0 0441	2 9368	4.2592	14.7105	1.1965	0 3208	3 0792	0.0794	1.1272	100	99.0794
050319	CHA16-1A-44Y-1_125-125cm_30	101.408-OS	67.4024	4.972	0 0901	2 6472	4.302	14.6412	1.1871	0 2859	3 3614	0.0469	1.0638	100	99.3695
Mar 12 23 57 2020	CHA08-4A-7S-1(39-42 5cm)_1	105.169-S	56.99889055	4.156090631	0 045219359	1.407966412	7.55274095	16.23330433	4.393285342	0 295039252	7.163157583	0.113562254	1.64074334	100	97.30345757
Mar 13 00 01 2020	CHA08-4A-7S-1(39-42 5cm)_2	105.169-S	56.61305093	4.299930334	0 040609694	1.45405555	7.548259787	16.15921504	4.439874015	0 361831221	7 322208304	0.143224472	1.61774066	100	96.28242884
Mar 13 00 05 2020	CHA08-4A-7S-1(39-42 5cm)_3	105.169-S	57.00421431	4.14949845	0 041136117	1.433062717	7.450825809	16.24418115	4.306860978	0 389350444	7 2065528	0.127326076	1.646991144	100	96.99505705
Mar 13 00:12 2020	CHA08-4A-7S-1(39-42 5cm)_5	105.169-S	57.04742662	4.085762404	0 032235633	1 390354792	7.401031201	16.20669224	4.442718127	0 302403483	7 281339543	0.139653415	1.670382547	100	97.09751837
Mar 13 00:16 2020	CHA08-4A-7S-1(39-42 5cm)_6	105.169-S	56.84600967	3.859990596	0 043172229	1 308561607	8.579054388	15.51179868	4.464816639	0 239029303	7 501046062	0.160942774	1.485578051	100	97.05313019
Mar 13 00 24 2020	CHA08-4A-7S-1(39-42 5cm)_8	105.169-S	56.69914413	3.93099833	0 063487675	1 029341375	7.380977055	16.92006347	4.424413076	0.184014537	8 020575478	0.12297532	1.224009562	100	97.49923832
Mar 13 00 28 2020	CHA08-4A-7S-1(39-42 5cm)_9	105.169-S	56.48659452	4.398338116	0 056157775	1 560508558	7.607633997	16.08468238	4.398741162	0 566959848	6.796425431	0.134388533	1.909569683	100	97.40414379
Mar 13 00:44 2020	CHA08-4A-7S-1(39-42 5cm)_13	105.169-S	56.92923687	3.812412421	0 030180075	1.179503484	7.669387081	16.19300267	4.770555695	0 28283822	7 576025705	0.129608953	1.427248826	100	96.75257563
Mar 13 00:48 2020	CHA08-4A-7S-1(39-42 5cm)_14	105.169-S	56.9961637	3.868130809	0 085716779	1.183441155	7.519999819	16.51726774	4.621090724	0.186471832	7 557028008	0.099879601	1.364809828	100	94.61391426
Mar 13 00 52 2020	CHA08-4A-7S-1(39-42 5cm)_15	105.169-S	56.80011576	3.947868447	0 067299648	1.170808385	7.540539577	16.43255456	4.632395698	0.178091348	7.72661611	0.142305363	1.361405099	100	97.32591723
Mar 13 00 56 2020	CHA08-4A-7S-1(39-42 5cm)_16	105.169-S	56.7145326	4.115429011	0 037192592	1 654145658	7.958444543	15.62986884	4.251967802	0 538254771	6 935082727	0.130790523	2.034290933	100	97.33121097
Mar 13 01 00 2020	CHA08-4A-7S-1(39-42 5cm)_17	105.169-S	57.48438115	3.954504507	0 046005359	1.410007635	8.422724784	15.10798156	4.319478644	0 326892108	7 050038174	0.15921765	1.718768431	100	97.16259446
Mar 13 01 04 2020	CHA08-4A-7S-1(39-42 5cm)_18	105.169-S	57.20637666	4.078783663	0 068290316	1 281089135	7.518987605	16.19650573	4.406410335	0.188322643	7.417919346	0.137303827	1.500010738	100	96.79264043
Mar 13 01 07 2020	CHA08-4A-7S-1(39-42 5cm)_19	105.169-S	56.20214113	4.21996556	0 079179174	1.491633472	7.549906088	16.78372107	4.218210856	0.489503824	7 02906732	0.138538013	1.7981335	100	97.87927312
Mar 13 01:11 2020	CHA08-4A-7S-1(39-42 5cm)_20	105.169-S	56.46469409	4.077271487	0 043062815	1.449130525	7.730872213	16.06133389	4.573595542	0 39579955	7 317595273	0.149743488	1.736901125	100	97.29972394
Mar 13 01:15 2020	CHA08-4A-7S-1(39-42 5cm)_21	105.169-S	56.03041864	4.342665437	0 040986774	1 544727665	7.872202676	16.0529334	4.432370939	0.404515391	7.146939997	0.134391307	1.99784778	100	97.10449512
Mar 13 01:19 2020	CHA08-4A-7S-1(39-42 5cm)_22	105.169-S	55.93991963	4.360361964	0 051507875	1.482017333	7.626955408	16.55442136	4.50096119	0 354628472	7.130265212	0.154212713	1.844748848	100	96.49009954
Mar 13 01 23 2020	CHA08-4A-7S-1(39-42 5cm)_23	105.169-S	56.23127519	4.203584575	0 075914274	1.448432019	7.653952269	16.58127018	4.551384904	0 304931229	7 098344151	0.13539244	1.715518774	100	97.34664667
Mar 13 01 27 2020	CHA08-4A-7S-1(39-42 5cm)_24	105.169-S	57.55257949	3.959780163	0 052502961	1.164499268	7.74485704	15.7315687	4.54337304	0 242479728	7.42424683	0.156278345	1.427834432	100	97.51830947
Mar 13 01 31 2020	CHA08-4A-7S-1(39-42 5cm)_25	105.169-S	56.67394683	4.237453561	0 089677204	1.449746944	7.705080979	16.12156204	4.295630617	0 357906265	7.124470694	0.163407191	1.781117674	100	96.56857745
Mar 13 01 35 2020	CHA08-4A-7S-1(39-42 5cm)_26	105.169-S	56.46212048	4.110989618	0 040316188	1 519610155	8.207390919	15.66487564	4.398954331	0 385768001	7.112189025	0.123326185	1.974459453	100	96.7353367
Mar 13 01 39 2020	CHA08-4A-7S-1(39-42 5cm)_27	105.169-S	55.87998547	4.280113556	0 086628726	1 512894016	8.016132849	15.8457699	4.560865322	0 391451454	7.419398052	0.162273427	1.844487225	100	96.50378575
Mar 13 01:43 2020	CHA08-4A-7S-1(39-42 5cm)_28	105.169-S	56.53741119	4.294815721	0 064284787	1 59681762	7.749322246	16.1505488	4.403939075	0 504119306	6 572707366	0.127436348	1.998597538	100	97.06806715
Mar 13 01:47 2020	CHA08-4A-7S-1(39-42 5cm)_29	105.169-S	56.60759456	4.107709047	0 051585502	1 536147744	7.775794074	16.03595247	4.517851576	0 561398093	6.736215445	0.139187441	1.930564057	100	96.34489949
Mar 13 01 51 2020	CHA08-4A-7S-1(39-42 5cm)_30	105.169-S	57.29025077	3.973278697	0 032263572	1 223844141	7.346981358	16.06842511	4.732698876	0 288323303	7 569530304	0.124400887	1.35000298	100	96.70349026
Mar 13 01 55 2020	CHA08-4A-7S-1(39-42 5cm)_31	105.169-S	57.04889312	4.024006708	0 067047182	1 242375038	7.754734191	15.7110606	4.819117868	0 239606781	7 536390724	0.129268609	1.427499186	100	97.39410109
Mar 13 01 59 2020	CHA08-4A-7S-1(39-42 5cm)_32	105.169-S	56.70960937	4.125337662	0 032287529	1 30391945	7.931783637	15.81456577	4.746290211	0 235676492	7 575151091	0.15202045	1.373358335	100	96.63173595
Mar 11 09 55 2020	CHA08-4A-7S-1(97-97 5cm)_2	105.721-S	56.82613556	4.322008032	0 044259537	0 80477553	8.102666242	15.68620227	4.841536241	0.1908483	7 802561624	0.180051122	1.198955541	100	96.25044135
Mar 11 09 59 2020	CHA08-4A-7S-1(97-97 5cm)_3	105.721-S	56.72303623	3.945398883	0 049647103	1 062657034	8.076983692	15.43028283	5.184202705	0.164452512	7 953988425	0.150822671	1.258527919	100	95.67527124
Mar 11 10 03 2020	CHA08-4A-7S-1(97-97 5cm)_4	105.721-S	56.55052461	3.822980545	0 071774583	0 96953148	8.158502947	15.49573619	5.171531065	0 072252855	8 264002166	0.155668309	1.26749525	100	95.71633503
Mar 11 10:15 2020	CHA08-4A-7S-1(97-97 5cm)_7	105.721-S	57.40421805	3.779016916	0 074835143	1 005316736	8.012512244	15.41877414	5.041195842	0.199371944	7.713134011	0.142781696	1.208843276	100	95.81060033
Mar 11 10:19 2020	CHA08-4A-7S-1(97-97 5cm)_8	105.721-S	56.9246248	3.877926099	0 040271238	1 065032286	7.879506279	15.6885878	5.141680203	0 233019496	7 843953847	0.114820343	1.190577606	100	95.10509809
Mar 11 10 23 2020	CHA08-4A-7S-1(97-97 5cm)_9	105.721-S	57.06924501	3.71632402	0 001472214	1 038857408	7.976586865	15.61773261	5.205328646	0.181001564	7.781703431	0.182554556	1.229193668	100	95.09486021
Mar 11 10 27 2020	CHA08-4A-7S-1(97-97 5cm)_10	105.721-S	56.43401582	3.924065004	0 058709952	1 049427258	8.244276165	15.39120628	5.251337359	0 226272995	8.108064883	0.163316592	1.149307694	100	95.21384093
Mar 11 10 31 2020	CHA08-4A-7S-1(97-97 5cm)_11	105.721-S	56.71345421	3.885443696	0 047109399	1 048765072	8.087289629	15.4582716	5.21794688	0.158182132	8 027610584	0.122421061	1.233505742	100	94.67325203
Mar 11 10 35 2020	CHA08-4A-7S-1(97-97 5cm)_12	105.721-S	56.93204494	3.804147643	0 054908901	1 052385666	7.9485078	15.63504414	5.11365334	0.116516214	7 942928753	0.153619176	1.246243426	100	95.43079431
Mar 11 10 39 2020	CHA08-4A-7S-1(97-97 5cm)_13	105.721-S	56.99773131	3.758435556	0 014202422	1 39920158	7.327478171	16.1739099	4.912985999	0.154708247	7 932315724	0.123718877	1.205312218	100	95.05420941
Mar 11 10:43 2020	CHA08-4A-7S-1(97-97 5cm)_14	105.721-S	56.50345817	3.922012382	0 034132839	1 090052093	8.13361256	15.60157248	5.119925785	0.140646812	8 08299122	0.144907511	1.226688149	100	95.50919691
Mar 11 10:47 2020	CHA08-4A-7S-1(97-97 5cm)_15	105.721-S	56.69165051	4.112449043	0 046283119	1 069876376	7.839876732	15.41497013	5.248926474	0 201742576	8 046951408	0.108239386	1.219034247	100	95.06705846
Mar 11 10 51 2020	CHA08-4A-7S-1(97-97 5cm)_16	105.721-S	56.67356152	3.876782503	0 027540347	1 069343305	7.855806278	15.61144624	5.213745005	0 266325978	8 020337579	0.144429146	1.240682103	100	95.13315275
Mar 11 10 55 2020	CHA08-4A-7S-1(97-97 5cm)_17	105.721-S	56.81126152	3.686449293	0 052469344	1 052307635	8.071562623	15.42022399	5.257365663	0.195637334	8 073811554	0.171385948	1.207525097	100	95.86550229

Date Analysed	Core Section Identifier	sample_no	SiO2	Na2O	Cl	K2O	FeOt	Al2O3	MgO	P2O5	CaO	MnO	TiO2	total	Analytical Total
Mar 11 10 59 2020	CHA08-4A-7S-1(97-97 5cm)_18	105.721-S	57.26588266	4.048158193	0 040047178	1.139143014	8.005414126	15.03257291	5.084523851	0.180850562	7.747346652	0.133036304	1.323024557	100	95.38749629
Mar 11 11 03 2020	CHA08-4A-7S-1(97-97 5cm)_19	105.721-S	57.17110436	3.77704552	0 039433371	1 094590684	8.15779552	15.25542099	5.002584616	0 274616033	7 823748687	0.105190616	1.298469605	100	95.350711
Mar 11 11 07 2020	CHA08-4A-7S-1(97-97 5cm)_20	105.721-S	56.73471421	3.996545477	0 060738748	1 014159363	7.621565241	15.83526526	5.247995055	0 215014861	7 89290093	0.156812601	1.224288249	100	95.65557793
Mar 11 11:11 2020	CHA08-4A-7S-1(97-97 5cm)_21	105.721-S	56.86882364	3.920144756	0 012558252	1 063788603	7.69345758	15.82104206	5.284931084	0.138427419	7 859372761	0.115117311	1.222336536	100	95.55469919
Mar 11 11:15 2020	CHA08-4A-7S-1(97-97 5cm)_22	105.721-S	57.05435617	4.214144549	0 03615639	1.104072353	7.871902658	15.30042974	4.980620847	0.170507224	7 856460499	0.122744171	1.288605398	100	95.9719711
Mar 11 11 23 2020	CHA08-4A-7S-1(97-97 5cm)_24	105.721-S	56.42950273	4.194542162	0 052395806	1 006644026	7.790562077	15.81885554	5.229184603	0 206334609	7 994518807	0.160306216	1.117153434	100	96.19090512
Mar 11 11 27 2020	CHA08-4A-7S-1(97-97 5cm)_25	105.721-S	56.36371926	3.981219623	0 034766473	1 038400414	7.876905202	15.81437527	5.324594923	0 207886655	7 96601162	0.142615621	1.249504942	100	95.7819341
060418	MEX4-1A-48Y-1_80-81cm-1	107.565-S	75.9688	4.3659	0.1077	3.1015	0.7179	13.9646	0.174	0 0403	1.4148	0	0.1445	100	97.6703
060418	MEX4-1A-48Y-1_80-81cm-4	107.565-S	59.8666	4.2473	0 0389	1 817	5.0521	18.919	1.4323	0 3622	6 6306	0.0939	1.54	100	101.603
060418	MEX4-1A-48Y-1_80-81cm-9	107.565-S	75.0499	3.9552	0 0758	3 3827	1.1979	13.6208	0.5788	0 0516	1.7895	0.0125	0.2852	100	96.2822
060418	MEX4-1A-48Y-1_80-81cm-13	107.565-S	71.175	4.0797	0 0765	3 6506	3.0572	14.11	0.3548	0.1484	2.4704	0.0698	0.8077	100	93.7145
060418	MEX4-1A-48Y-1_80-81cm-14	107.565-S	74.1875	3.8093	0 0188	3 5199	2.2594	13.9381	0.1472	0 0606	1.7296	0.0092	0.3204	100	99.1247
060418	MEX4-1A-48Y-1_80-81cm-15	107.565-S	64.7604	5.5938	0 0443	1 9495	3.034	18.435	0.5609	0.1938	4.4478	0.1017	0.8788	100	99.9201
060418	MEX4-1A-48Y-1_80-81cm-17	107.565-S	77.0764	3.6788	0.1493	5 0738	0.9374	12.4863	0.0269	0 0122	0.4484	0.0197	0.0907	100	95.0142
060418	MEX4-1A-48Y-1_80-81cm-24	107.565-S	69.9583	3.8524	0 0317	3 2066	2.8783	15.259	0.4778	0.1702	3 0307	0.0653	1.0696	100	97.8578
060418	MEX4-1A-48Y-1_80-81cm-28	107.565-S	59.8943	4.4026	0 0566	1 9634	6.0636	17.1004	2.1119	0.4218	6.1504	0.1025	1.7325	100	101.554
Jan 17 16 52 2020	CHA16-1B-62Y-1_94-95cm_9	108.14-G (Hole B)	77.72493911	4.212733482	0 068945237	2 9927414	0.838144245	12.80914269	0.166503276	0	1 043997711	0.051735323	0.091117519	100	94.71285135
Jan 17 17:12 2020	CHA16-1B-62Y-1_94-95cm_14	108.14-G (Hole B)	77.28479029	3.993347999	0 081842835	3.160426114	0.835259736	13.11822933	0.214226481	0 042429322	1 061357023	0.036189716	0.171901152	100	96.15991397
Jan 17 17:15 2020	CHA16-1B-62Y-1_94-95cm_15	108.14-G (Hole B)	76.91884312	4.020471215	0 09898967	2 85277487	0.920193852	13.43431121	0.242697897	0	1 322346629	0.022044359	0.167327183	100	95.26246539
Jan 17 17 23 2020	CHA16-1B-62Y-1_94-95cm_17	108.14-G (Hole B)	77.82374833	3.956231178	0 072949554	3 027829559	0.791889647	12.9197498	0.169448103	0	1 08063722	0.017687912	0.1398287	100	95.54547825
Jan 17 17:43 2020	CHA16-1B-62Y-1_94-95cm_22	108.14-G (Hole B)	76.55493822	3.97948409	0.111661535	2 967264884	1.08293371	13.5100536	0.29422439	0	1 325672342	0	0.17376723	100	93.22816515
Jan 17 18 03 2020	CHA16-1B-62Y-1_94-95cm_27	108.14-G (Hole B)	78.13438823	3.951079104	0 061896801	3.135137975	0.62927331	12.80417545	0.17547743	0 003301163	0 936601754	0.042915115	0.125753667	100	96.93554342
Jan 17 18:11 2020	CHA16-1B-62Y-1_94-95cm_29	108.14-G (Hole B)	76.70887821	4.15225591	0 0924915	2 871624	0.977414115	13.42525725	0.253183804	0	1 301939841	0.034982756	0.181972615	100	96.33317615
Jan 17 18:15 2020	CHA16-1B-62Y-1_94-95cm_30	108.14-G (Hole B)	78.01652294	3.477693948	0 080758607	3 55221849	0.83492637	12.75261275	0.142384612	0	0 952507604	0.046721603	0.143653072	100	94.60291931
Jan 17 18 22 2020	CHA16-1B-62Y-1_94-95cm_32	108.14-G (Hole B)	77.32392369	4.116481721	0.111718187	2 882919724	0.795709786	13.21655167	0.20988846	0	1.18763103	0.03835102	0.116824709	100	95.95572792
Jan 17 18 30 2020	CHA16-1B-62Y-1_94-95cm_34	108.14-G (Hole B)	77.42525646	3.421221981	0 073679608	3 969714568	0.890737628	12.82494686	0.156046332	0	1 070338413	0.011368324	0.156689822	100	93.24153819
Jan 25 15 55 2020	CHA16-1C-57Y-1(60-61cm)_1	108.14-G (Hole C)	77.70915492	3.621947913	0.136479197	3 842414307	0.61618571	12.72225397	0.130600093	0 042938455	0 984224976	0.035484591	0.158315868	100	95.25261222
Jan 25 15 59 2020	CHA16-1C-57Y-1(60-61cm)_2	108.14-G (Hole C)	77.3913146	3.688793871	0.101337036	3 982220657	0.669368448	12.78178137	0.129946148	0 073356696	0 999327794	0.026303615	0.156249763	100	95.42414466
Jan 25 16:11 2020	CHA16-1C-57Y-1(60-61cm)_5	108.14-G (Hole C)	76.82799561	4.283386473	0 090182083	2 939578952	1.009069364	13.19700925	0.223303015	0	1 260029521	0.037059692	0.132386038	100	95.25173658
Jan 25 16:15 2020	CHA16-1C-57Y-1(60-61cm)_6	108.14-G (Hole C)	77.68442506	3.977911538	0 060192082	3.475438502	0.789442435	12.68564284	0.158593052	0 022925332	1 022323265	0.021564468	0.101541426	100	95.52751397
Jan 25 16 23 2020	CHA16-1C-57Y-1(60-61cm)_8	108.14-G (Hole C)	77.3482533	4.192826028	0.108784019	3 254133634	0.720974491	13.00829241	0.159056211	0 050063594	1 008677127	0	0.148939193	100	95.87805392
Jan 25 16 26 2020	CHA16-1C-57Y-1(60-61cm)_9	108.14-G (Hole C)	77.20827002	4.13035416	0 087429324	3 396534893	0.68503948	13.13648378	0.165738323	0 014571554	1 016654179	0.050319035	0.108605252	100	95.39133565
Jan 25 16 30 2020	CHA16-1C-57Y-1(60-61cm)_10	108.14-G (Hole C)	77.38320736	3.724607608	0 078185106	3 893428349	0.741369262	12.77598542	0.144130708	0 041783134	1 052386297	0.073964587	0.090952174	100	94.77508429
Jan 25 16 34 2020	CHA16-1C-57Y-1(60-61cm)_11	108.14-G (Hole C)	77.45154686	4.175539413	0.102138508	3 275548462	0.731267009	12.95949611	0.159696069	0 017895169	0 992815599	0.003558104	0.130498688	100	95.55651629
Jan 25 16 38 2020	CHA16-1C-57Y-1(60-61cm)_12	108.14-G (Hole C)	77.33338978	3.918563985	0.110249327	3.420800452	0.790398738	13.00066405	0.176123565	0 020863706	1 08300636	0.012285228	0.133654804	100	94.42234487
Jan 25 16:42 2020	CHA16-1C-57Y-1(60-61cm)_13	108.14-G (Hole C)	77.33284651	3.857483496	0.118310527	3 588106157	0.886578201	12.77162731	0.18199133	0 034372548	1 038611269	0.064973814	0.125098836	100	92.80661871
Jan 25 16:46 2020	CHA16-1C-57Y-1(60-61cm)_14	108.14-G (Hole C)	77.52165949	3.713932879	0 081021533	3 510576324	0.865314657	12.70718606	0.164076631	0 073957568	1.173260294	0.07331539	0.115699177	100	93.43195241
Jan 25 16 54 2020	CHA16-1C-57Y-1(60-61cm)_16	108.14-G (Hole C)	77.19730039	4.027593795	0 036805687	3 333543689	0.743476265	13.11554646	0.191074097	0 041432688	1.107115078	0.039119188	0.166992662	100	95.09399892
Jan 25 16 58 2020	CHA16-1C-57Y-1(60-61cm)_17	108.14-G (Hole C)	77.70606051	3.935409029	0 085284594	3.434348994	0.782874911	12.74230518	0.149378523	0 039980415	0 92090659	0.030063602	0.17338765	100	95.79690376
Jan 25 17 01 2020	CHA16-1C-57Y-1(60-61cm)_18	108.14-G (Hole C)	77.44033536	3.61792547	0 087102079	3 900249134	0.745750357	12.79471887	0.198881337	0	1 077326189	0	0.137711209	100	95.63491642
Jan 25 17 05 2020	CHA16-1C-57Y-1(60-61cm)_19	108.14-G (Hole C)	77.57647482	4.035831276	0.116754597	3 340361657	0.769830097	12.79025091	0.188303668	0	0 973025222	0.025500553	0.183667204	100	94.89990383
Jan 25 17 09 2020	CHA16-1C-57Y-1(60-61cm)_20	108.14-G (Hole C)	77.29362176	4.164142738	0 097862599	3 304042727	0.752656421	13.04077811	0.169607527	0 030313281	0 97484994	0.022866073	0.149258819	100	95.33775015
Jan 25 17:13 2020	CHA16-1C-57Y-1(60-61cm)_21	108.14-G (Hole C)	76.9727524	3.909463042	0 084011865	3 21283	0.983203185	13.21312887	0.268359684	0 042525808	1.155163149	0.01881949	0.139742509	100	96.17689078
Jan 25 17 21 2020	CHA16-1C-57Y-1(60-61cm)_23	108.14-G (Hole C)	76.85931273	3.734012854	0 087162226	3 596499632	0.963946519	13.15132492	0.251331857	0 042840657	1.150245206	0.060188479	0.103134916	100	94.53636445
Jan 25 17 25 2020	CHA16-1C-57Y-1(60-61cm)_24	108.14-G (Hole C)	76.91051289	3.786295582	0.13650592	3.443093351	0.985602411	13.15505259	0.236588119	0 013617379	1 204971962	0.030002518	0.097757281	100	90.32575312
Jan 25 17 29 2020	CHA16-1C-57Y-1(60-61cm)_25	108.14-G (Hole C)	77.72868333	3.927865072	0.117513114	3 551220476	0.756450946	12.66005888	0.178744764	0	0 939028784	0.0168952	0.123539427	100	92.92579895
Jan 25 17 33 2020	CHA16-1C-57Y-1(60-61cm)_26	108.14-G (Hole C)	77.43284937	3.858890388	0.125524825	3.792357795	0.827118446	12.62029879	0.185182384	0 044576837	0 937444234	0.061875311	0.113881622	100	90.18136433
Jan 25 17 37 2020	CHA16-1C-57Y-1(60-61cm)_27	108.14-G (Hole C)	77.59082028	3.550730741	0.122279603	4.128512371	0.744740922	12.53422844	0.168922338	0 021430446	1 002713755	0.005672765	0.129948341	100	95.19167311
Jan 25 17:41 2020	CHA16-1C-57Y-1(60-61cm)_28	108.14-G (Hole C)	78.31346989	3.836319489	0.102266818	3.710193916	0.834162587	12.09641499	0.118663143	0 01608101	0.789546082	0.006411383	0.176470696	100	95.14327498
Jan 25 17 52 2020	CHA16-1C-57Y-1(60-61cm)_31	108.14-G (Hole C)	77.50457806	3.622795077	0.124843842	4.150899316	0.776138332	12.52953051	0.150404087	0	0 972134282	0.020384824	0.14829167	100	94.67827815
Jan 25 17 56 2020	CHA16-1C-57Y-1(60-61cm)_32	108.14-G (Hole C)	77.2273977	3.887949702	0.10590233	3 606516345	0.844092567	13.02072707	0.119244355	0 00500326	0 980221957	0.010840396	0.192104324	100	95.93745511
Jan 22 23 52 2020	CHA16-1C-57Y-2(6-13cm)_1	110.312-OS	77.11826144	3.373032316	0 07374151	5 575321043	1.059790109	12.27652178	0.029454526	0 003787011	0.41087863	0.020302584	0.058909053	100	95.06179033
Jan 22 23 56 2020	CHA16-1C-57Y-2(6-13cm)_2	110.312-OS	77.1204376	3.633305101	0.107809515	5 233471607	1.005123061	12.36639569	0	0 004291447	0.420100432	0.019991862	0.089073687	100	95.53887698
Jan 23 00 00 2020	CHA16-1C-57Y-2(6-13cm)_3	110.312-OS	76.9985859	3.370287068	0.109098533	5 563302654	0.982572919	12.37348343	0.031171009	0	0.436183273	0.042111827	0.093203382	100	96.88489617
Jan 23 00 08 2020	CHA16-1C-57Y-2(6-13cm)_5	110.312-OS	76.95436217	3.653876367	0.10327703	5 065245311	1.132883987	12.52305939	0.019721242	0	0 389700774	0.01847569	0.139398042	100	96.34281659
Jan 23 00:12 2020	CHA16-1C-57Y-2(6-13cm)_6	110.312-OS	76.71530954	3.473837654	0.119259273	5.489543714	1.146480301	12.46682411	0	0	0.443315055	0.047554768	0.097875586	100	93.99688333
Jan 23 00:16 2020	CHA16-1C-57Y-2(6-13cm)_7	110.312-OS	77.12454423	3.500728789	0.125373323	5 218638323	0.977752758	12.43611215	0.04074108	0 022155587	0.414930078	0.03433591	0.104687775	100	95.2355709
Jan 23 00 28 2020	CHA16-1C-57Y-2(6-13cm)_10	110.312-OS	76.91910597	3.100765943	0 088688378	5 853223555	1.002845825	12.43154448	0.068270157	0 00806258	0.447495566	0.00450248	0.075495066	100	95.50293009
Jan 23 00 35 2020	CHA16-1C-57Y-2(6-13cm)_12	110.312-OS	76.91695269	3.428294546	0 095093111	5 328584072	1.117657896	12.52295935	0.066238723	0	0.411855985	0	0.112363621	100	94.9595602
Jan 23 00 39 2020	CHA16-1C-57Y-2(6-13cm)_13	110.312-OS	77.09325279	3.636075786	0.105361129	5 01069377	1.046462909	12.5322629	0.021114244	0 015336715	0.412859338	0.031198659	0.09538176	100	95.19639831
Jan 23 00:47 2020	CHA16-1C-57Y-2(6-13cm)_15	110.312-OS	76.6793828	3.2522656	0.124142621	5.718462446	1.112444618	12.52427519	0.057288597	0 008941596	0.460933169	0.022769878	0.039093489	100	96.17969956
Jan 23 00 51 2020	CHA16-1C-57Y-2(6-13cm)_16	110.312-OS	76.92813556	3.370125421	0.125776039	5.421741221	1.097585277	12.48308468	0.041159269	0	0.424375576	0.012744748	0.095272216	100	95.72570487
Jan 23 01:14 2020	CHA16-1C-57Y-2(6-13cm)_22	110.312-OS	77.33819446	3.847176196	0.124293527	4 917336498	1.042579267	12.23008471	0.024691307	0	0 384411753	0.028667026	0.06256526	100	95.58019879
Jan 23 01:18 2020	CHA16-1C-57Y-2(6-13cm)_23	110.312-OS	76.87462719	3.499907055	0.102087248	5 381006927	1.010756677	12.51461232	0.037428375	0 026471082	0.433332321	0.047517763	0.072253037	100	92.17605677
Jan 23 01 22 2020	CHA16-1C-57Y-2(6-13cm)_24	110.312-OS	76.94147099	3.1470672	0.101578842	5.719767942	1.054648703	12.36135211	0.027645545	0	0.4697914	0.038979159	0.137698117	100	94.40942455
Jan 23 01 26 2020	CHA16-1C-57Y-2(6-13cm)_25	110.312-OS	76.89443492	3.355598304	0.124145164	5 613520449	1.020659183	12.40084037	0.016516704	0 012738373	0.434702564	0.023641557	0.103202414	100	92.63349171

Date Analysed	Core Section Identifier	sample_no	SiO2	Na2O	Cl	K2O	FeOt	Al2O3	MgO	P2O5	CaO	MnO	TiO2	total	Analytical Total
Jan 23 01 30 2020	CHA16-1C-57Y-2(6-13cm)_26	110.312-OS	76.59893041	3.383454108	0.134058553	5 629208278	1.102247608	12.45672989	0.026269639	0 052122299	0.431423832	0.021265898	0.164289486	100	95.92823242
Jan 23 01:45 2020	CHA16-1C-57Y-2(6-13cm)_30	110.312-OS	76.8870812	3.784450424	0.11130994	5 097371098	1.140586896	12.38076131	0.058879838	0	0.411500853	0.04587634	0.082182105	100	96.12798256
Jan 23 01:49 2020	CHA16-1C-57Y-2(6-13cm)_31	110.312-OS	77.29656339	3.990269767	0.102930256	4.745823738	1.110379678	12.26611091	0.043191159	0 028516572	0.408408898	0.007805631	0	100	96.08447872
Jan 23 01 53 2020	CHA16-1C-57Y-2(6-13cm)_32	110.312-OS	76.97643274	3.347897746	0 091289157	5.464858308	0.987017186	12.50872071	0.045176162	0	0.417785019	0.022483988	0.138338985	100	96.06836453
Jan 23 01 57 2020	CHA16-1C-57Y-2(6-13cm)_33	110.312-OS	77.05571518	3.836238139	0.109856036	4.799029107	1.071471338	12.52681644	0.027750907	0 011371612	0.438124079	0.030985036	0.092642127	100	95.85272141
Jan 23 02 01 2020	CHA16-1B-63Y-1(4-52cm)_1	110.312-OS	77.39069674	3.812382507	0.101926647	4 591953086	1.030269239	12.5260851	0.026479913	0 010192665	0.421957884	0.023432621	0.064623596	100	95.1664775
Jan 23 02 05 2020	CHA16-1B-63Y-1(4-52cm)_2	110.312-OS	77.15458232	4.06426656	0.107214947	4.74748629	1.022538905	12.25808344	0.0610089	0 015965934	0.400417395	0.047474863	0.120960452	100	94.57636579
Jan 23 02 09 2020	CHA16-1B-63Y-1(4-52cm)_3	110.312-OS	77.25368672	4.054105464	0.110075401	4 694858596	1.04404481	12.2688908	0.045785445	0	0.43782779	0.004546823	0.086178148	100	94.5715384
Jan 23 02:13 2020	CHA16-1B-63Y-1(4-52cm)_4	110.312-OS	77.2094246	3.881473455	0 099483186	4.754249121	1.041188447	12.39243566	0.080424302	0	0 371885655	0.042201815	0.12723376	100	95.49352347
Jan 23 02:17 2020	CHA16-1B-63Y-1(4-52cm)_5	110.312-OS	76.81675914	3.943785235	0.11528831	4 843161897	1.031552238	12.6318775	0.027269107	0	0.423217486	0	0.167089085	100	94.97927382
Jan 23 02 21 2020	CHA16-1B-63Y-1(4-52cm)_6	110.312-OS	77.00756925	4.055622575	0.134128568	4 622569748	0.998078153	12.5484895	0.100173308	0	0.442398419	0.04844707	0.04252341	100	94.53616145
Jan 23 02 25 2020	CHA16-1B-63Y-1(4-52cm)_7	110.312-OS	77.13608242	3.949188486	0 09665857	4 599760892	1.098504372	12.46062708	0.067194664	0	0.431627796	0.039638492	0.120717227	100	94.35273055
Jan 23 02 28 2020	CHA16-1B-63Y-1(4-52cm)_8	110.312-OS	77.04995217	3.989557634	0.125334307	4 597000301	1.087709703	12.53645341	0.019127748	0 061081981	0 386995773	0.03751575	0.109271226	100	94.62692441
Jan 23 02 32 2020	CHA16-1B-63Y-1(4-52cm)_9	110.312-OS	77.03268803	4.016774883	0.110181742	4 600534137	1.167078596	12.62197862	0	0	0 368311493	0.023212741	0.059239755	100	95.20633626
Jan 23 02 36 2020	CHA16-1B-63Y-1(4-52cm)_10	110.312-OS	77.22162549	4.118771461	0.112713812	4.443119357	0.987868811	12.54006396	0.018891173	0 005593476	0.401278445	0.043270284	0.106803724	100	94.75325018
Jan 23 02:40 2020	CHA16-1B-63Y-1(4-52cm)_11	110.312-OS	77.26311096	4.047554231	0.114942108	4 540530768	0.985332782	12.42315044	0.058000253	0 016299341	0.41232304	0.052814099	0.085941981	100	94.48234622
Jan 23 02:44 2020	CHA16-1B-63Y-1(4-52cm)_12	110.312-OS	76.88429405	3.425911981	0 077674557	5 552639034	1.045990096	12.46540072	0.03940918	0 008422542	0 387229404	0	0.113028439	100	96.17048699
Jan 23 02:48 2020	CHA16-1B-63Y-1(4-52cm)_13	110.312-OS	77.09673398	3.893674697	0.125812507	4 618698349	1.07140203	12.61750757	0.020272115	0 031871109	0.407828715	0.037304871	0.078894056	100	95.69795787
Jan 23 02 56 2020	CHA16-1B-63Y-1(4-52cm)_15	110.312-OS	76.97189044	3.859354665	0.111636242	4 974303227	1.041583631	12.47929455	0.008203966	0 028350413	0 374699902	0.020146447	0.130536517	100	96.2948936
Jan 23 03 04 2020	CHA16-1B-63Y-1(4-52cm)_17	110.312-OS	77.00754498	3.393653013	0.12779492	5 320483722	1.007583106	12.50425655	0.029443454	0	0.431546433	0.045973112	0.131720714	100	96.79571011
Jan 23 03 07 2020	CHA16-1B-63Y-1(4-52cm)_18	110.312-OS	77.1936602	3.702524937	0 092379977	4 924173446	1.002323941	12.55092233	0.029896767	0 036207158	0.412048769	0.046862407	0.009000065	100	96.66596947
Jan 23 03:11 2020	CHA16-1B-63Y-1(4-52cm)_19	110.312-OS	77.17917403	3.891620901	0.126133907	4.464823662	1.117028854	12.59255795	0.064280795	0	0.406158375	0.080746811	0.077474718	100	94.74058374
Jan 23 03:15 2020	CHA16-1B-63Y-1(4-52cm)_20	110.312-OS	77.17179603	4.027003191	0.105316057	4 646607935	0.956928649	12.50531916	0.069646196	0 002116906	0 381477443	0.015665102	0.118123336	100	94.47752126
Jan 23 03:19 2020	CHA16-1B-63Y-1(4-52cm)_21	110.312-OS	77.02788077	4.176652905	0 074856002	4.480817045	1.056180768	12.5883461	0.066737816	0	0.419407519	0.031629297	0.077491777	100	94.84877329
Jan 23 03 23 2020	CHA16-1B-63Y-1(4-52cm)_22	110.312-OS	77.08643163	4.089511448	0 087634212	4 550644026	1.040355703	12.55570952	0.011930923	0	0.421730297	0.038854687	0.117197561	100	94.71186882
Jan 23 03 27 2020	CHA16-1B-63Y-1(4-52cm)_23	110.312-OS	76.8447913	3.946945948	0.100209549	4 926620094	1.046355313	12.44494554	0.060062836	0 034905627	0.415918673	0.077672883	0.101572231	100	95.40008992
Jan 23 03 31 2020	CHA16-1B-63Y-1(4-52cm)_24	110.312-OS	77.12893578	3.983803618	0.118093158	4 567952802	1.088665787	12.61769246	0.050836894	0	0 389393522	0	0.054625979	100	95.00973825
Jan 23 03 35 2020	CHA16-1B-63Y-1(4-52cm)_25	110.312-OS	77.08783054	3.893844954	0.142556808	4.727381268	1.016691892	12.46228078	0.029414817	0 03529778	0.418757491	0.043491908	0.142451756	100	95.19012208
Jan 23 03 39 2020	CHA16-1B-63Y-1(4-52cm)_26	110.312-OS	77.4876179	3.839986825	0.10576569	4 697178854	0.990279472	12.349008	0.012877659	0	0.46398054	0.015938742	0.037366322	100	94.7377168
Jan 23 03:42 2020	CHA16-1B-63Y-1(4-52cm)_27	110.312-OS	76.93323278	3.705675477	0.106617131	5 24640734	1.038212614	12.40064163	0.04528589	0 021006742	0.41467097	0.025018079	0.063231348	100	94.73149296
Jan 23 03:46 2020	CHA16-1B-63Y-1(4-52cm)_28	110.312-OS	77.19476615	3.804688715	0.100652546	4 641490466	1.035147827	12.5942902	0.040365322	0	0.428910641	0.032542585	0.127145548	100	95.87437554
Jan 23 03 50 2020	CHA16-1B-63Y-1(4-52cm)_29	110.312-OS	77.07159082	3.535868718	0.112115436	5 098040156	1.105825902	12.52162182	0.054503437	0	0 38303372	0.048493553	0.068906437	100	96.5076745
030418	MEX1-1A-50Y-1_47-50cm-1	110.312-S	76.45	3.15	0.16	5 97	1.08	12.61	0.05	0 00	0.46	0.02	0.07	100	94.6082
030418	MEX1-1A-50Y-1_47-50cm-4	110.312-S	76.42	3.93	0.10	5.12	1.01	12.71	0.05	0 04	0.41	0.08	0.13	100	95.7229
030418	MEX1-1A-50Y-1_47-50cm-5	110.312-S	77.10	3.69	0.15	4 99	1.02	12.41	0.07	0 00	0.44	0.00	0.13	100	96.0544
030418	MEX1-1A-50Y-1_47-50cm-7	110.312-S	76.83	3.17	0.12	5.74	0.94	12.56	0.05	0 00	0.44	0.07	0.07	100	95.5843
030418	MEX1-1A-50Y-1_47-50cm-10	110.312-S	76.93	3.75	0.14	5 02	1.02	12.56	0.05	0 04	0 38	0.03	0.08	100	95.6795
030418	MEX1-1A-50Y-1_47-50cm-12	110.312-S	76.62	3.70	0.15	5.42	1.18	12.33	0.03	0 01	0 39	0.06	0.11	100	95.0695
030418	MEX1-1A-50Y-1_47-50cm-13	110.312-S	76.78	3.24	0.12	5 58	0.96	12.70	0.02	0 04	0 38	0.04	0.14	100	95.0815
030418	MEX1-1A-50Y-1_47-50cm-15	110.312-S	77.23	3.71	0.12	5.14	0.99	12.21	0.01	0 00	0.41	0.05	0.12	100	95.7524
030418	MEX1-1A-50Y-1_47-50cm-17	110.312-S	77.10	3.84	0.13	5 29	1.13	11.85	0.06	0 00	0.44	0.08	0.08	100	96.0519
030418	MEX1-1A-50Y-1_47-50cm-18	110.312-S	77.23	3.57	0.14	5 07	1.23	12.12	0.02	0 06	0.41	0.06	0.09	100	95.3832
030418	MEX1-1A-50Y-1_47-50cm-19	110.312-S	76.98	4.06	0.11	4 99	1.07	12.21	0.03	0 00	0 38	0.09	0.10	100	96.4009
030418	MEX1-1A-50Y-1_47-50cm-20	110.312-S	77.30	3.81	0.17	5 02	1.09	12.00	0.06	0 01	0.43	0.00	0.11	100	95.3323
030418	MEX1-1A-50Y-1_47-50cm-22	110.312-S	77.43	3.94	0.13	4 98	1.05	11.86	0.04	0 02	0.43	0.04	0.09	100	95.061
030418	MEX1-1A-50Y-1_47-50cm-25	110.312-S	77.62	3.64	0.12	5 25	1.00	11.80	0.01	0 04	0.40	0.03	0.10	100	95.2398
030418	MEX1-1A-51Y-1_6.5-7 5cm-1	110.312-S	77.65	4.04	0.13	4 64	1.22	11.80	0.05	0 00	0.41	0.00	0.06	100	95.3216
030418	MEX1-1A-51Y-1_6.5-7 5cm-2	110.312-S	77.27	4.10	0.13	4.79	1.09	12.08	0.03	0 03	0.40	0.02	0.08	100	94.011
030418	MEX1-1A-51Y-1_6.5-7 5cm-3	110.312-S	77.44	4.04	0.14	4.75	1.08	11.94	0.02	0 03	0.43	0.02	0.12	100	93.8528
030418	MEX1-1A-51Y-1_6.5-7 5cm-4	110.312-S	77.38	4.01	0.14	4 81	1.12	12.01	0.04	0 00	0.42	0.00	0.07	100	92.7316
030418	MEX1-1A-51Y-1_6.5-7 5cm-6	110.312-S	77.24	4.06	0.14	4.79	1.16	12.10	0.04	0 01	0 39	0.04	0.01	100	94.3856
030418	MEX1-1A-51Y-1_6.5-7 5cm-7	110.312-S	76.98	3.93	0.13	4.73	1.06	12.55	0.05	0 00	0.43	0.02	0.12	100	93.7819
030418	MEX1-1A-51Y-1_6.5-7 5cm-8	110.312-S	77.31	3.99	0.11	4 86	1.07	12.13	0.05	0 00	0.42	0.03	0.03	100	94.9101
030418	MEX1-1A-51Y-1_6.5-7 5cm-9	110.312-S	77.38	3.92	0.14	4 60	1.08	12.29	0.04	0 00	0 38	0.08	0.10	100	94.1318
030418	MEX1-1A-51Y-1_6.5-7 5cm-10	110.312-S	77.26	3.75	0.13	4.76	1.10	12.44	0.05	0 00	0.40	0.00	0.11	100	93.1924
030418	MEX1-1A-51Y-1_6.5-7 5cm-11	110.312-S	77.55	3.93	0.13	4.76	1.03	11.97	0.05	0 00	0 39	0.03	0.16	100	93.9142
030418	MEX1-1A-51Y-1_6.5-7 5cm-12	110.312-S	77.41	3.82	0.13	4 84	1.02	12.20	0.02	0 00	0.44	0.04	0.09	100	93.7581
030418	MEX1-1A-51Y-1_6.5-7 5cm-13	110.312-S	77.36	3.78	0.13	4 89	1.09	12.13	0.04	0 03	0.43	0.02	0.10	100	94.2747
030418	MEX1-1A-51Y-1_6.5-7 5cm-14	110.312-S	77.60	3.93	0.14	4 67	0.99	12.09	0.04	0 02	0.42	0.02	0.08	100	93.6548
030418	MEX1-1A-51Y-1_6.5-7 5cm-15	110.312-S	77.34	3.87	0.12	4 81	1.08	12.04	0.03	0 05	0.46	0.09	0.10	100	94.7369
030418	MEX1-1A-51Y-1_6.5-7 5cm-16	110.312-S	77.30	3.70	0.11	4.78	1.16	12.28	0.03	0 01	0.44	0.07	0.12	100	93.9593
030418	MEX1-1A-51Y-1_6.5-7 5cm-17	110.312-S	77.56	4.04	0.14	4 69	0.96	11.98	0.06	0 00	0 39	0.07	0.11	100	94.5449
030418	MEX1-1A-51Y-1_6.5-7 5cm-18	110.312-S	77.46	3.99	0.14	4 60	1.05	12.19	0.05	0 01	0.46	0.01	0.03	100	93.929
030418	MEX1-1A-51Y-1_6.5-7 5cm-19	110.312-S	77.43	3.87	0.13	4 65	1.02	12.24	0.07	0 02	0.42	0.06	0.09	100	93.6372
030418	MEX1-1A-51Y-1_6.5-7 5cm-20	110.312-S	77.55	3.97	0.12	4 65	0.98	12.10	0.05	0 00	0.43	0.06	0.10	100	93.3969
030418	MEX1-1A-51Y-1_6.5-7 5cm-21	110.312-S	77.06	3.93	0.13	4 57	1.18	12.50	0.03	0 01	0 37	0.06	0.16	100	93.4454

Date Analysed	Core Section Identifier	sample_no	SiO2	Na2O	Cl	K2O	FeOt	Al2O3	MgO	P2O5	CaO	MnO	TiO2	total	Analytical Total
030418	MEX1-1A-51Y-1_6.5-7 5cm-22	110.312-S	77.41	3.81	0.10	4 86	1.12	12.09	0.05	0 03	0 38	0.03	0.13	100	93.3207
030418	MEX1-1A-51Y-1_6.5-7 5cm-24	110.312-S	77.70	3.73	0.12	4 68	1.01	12.09	0.06	0 02	0.40	0.07	0.13	100	93.1401
030418	MEX1-1A-51Y-1_6.5-7 5cm-25	110.312-S	77.52	3.94	0.11	4.73	0.96	12.13	0.05	0 00	0.42	0.04	0.09	100	93.7568
030418	MEX1-1A-51Y-1_8-17cm-1	110.312-S	76.99	3.89	0.14	4 93	1.04	12.38	0.07	0 05	0 39	0.02	0.11	100	96.0388
030418	MEX1-1A-51Y-1_8-17cm-2	110.312-S	77.24	4.04	0.12	4.74	1.01	12.26	0.05	0 02	0 39	0.09	0.05	100	93.6722
030418	MEX1-1A-51Y-1_8-17cm-3	110.312-S	76.89	3.90	0.14	4 83	0.89	12.72	0.05	0 00	0.44	0.03	0.11	100	94.174
030418	MEX1-1A-51Y-1_8-17cm-4	110.312-S	77.29	4.06	0.13	4 83	1.02	12.11	0.03	0 00	0.42	0.02	0.10	100	95.5399
030418	MEX1-1A-51Y-1_8-17cm-5	110.312-S	77.12	3.83	0.14	4 85	1.06	12.49	0.02	0 02	0 38	0.01	0.09	100	96.1503
030418	MEX1-1A-51Y-1_8-17cm-6	110.312-S	77.09	3.96	0.13	5 01	1.11	12.04	0.04	0 02	0.47	0.00	0.12	100	96.1056
030418	MEX1-1A-51Y-1_8-17cm-7	110.312-S	77.16	3.75	0.14	4 85	1.10	12.31	0.04	0 03	0.41	0.07	0.13	100	96.0212
030418	MEX1-1A-51Y-1_8-17cm-8	110.312-S	77.24	4.03	0.12	4 66	0.94	12.49	0.04	0 00	0 39	0.02	0.08	100	94.3477
030418	MEX1-1A-51Y-1_8-17cm-9	110.312-S	77.20	3.86	0.15	5 07	1.10	12.06	0.05	0 00	0.42	0.00	0.09	100	95.9478
030418	MEX1-1A-51Y-1_8-17cm-10	110.312-S	77.21	4.01	0.11	4 93	1.12	11.99	0.05	0 02	0.41	0.03	0.13	100	95.2591
030418	MEX1-1A-51Y-1_8-17cm-11	110.312-S	77.19	3.85	0.14	5 01	1.07	12.17	0.05	0 01	0.40	0.03	0.09	100	96.0051
030418	MEX1-1A-51Y-1_8-17cm-12	110.312-S	77.26	4.06	0.13	4 80	1.17	12.10	0.04	0 00	0 38	0.02	0.06	100	95.2882
030418	MEX1-1A-51Y-1_8-17cm-13	110.312-S	77.27	3.95	0.10	4 96	0.94	12.19	0.04	0 00	0 37	0.04	0.13	100	95.5291
030418	MEX1-1A-51Y-1_8-17cm-14	110.312-S	77.03	3.95	0.13	4 86	1.14	12.31	0.06	0 00	0 39	0.06	0.06	100	95.0749
030418	MEX1-1A-51Y-1_8-17cm-15	110.312-S	77.09	4.05	0.12	4 89	1.11	12.08	0.04	0 00	0.40	0.06	0.16	100	96.2236
030418	MEX1-1A-51Y-1_8-17cm-16	110.312-S	77.00	3.53	0.13	5.15	1.00	12.57	0.05	0 03	0.42	0.00	0.11	100	96.0559
030418	MEX1-1A-51Y-1_8-17cm-17	110.312-S	77.15	4.01	0.10	4 94	1.04	12.19	0.03	0 01	0.42	0.00	0.11	100	95.7855
030418	MEX1-1A-51Y-1_8-17cm-18	110.312-S	77.18	3.87	0.16	5 02	0.97	12.19	0.02	0 03	0.43	0.05	0.09	100	94.9095
030418	MEX1-1A-51Y-1_8-17cm-19	110.312-S	76.99	3.99	0.12	4 86	1.11	12.33	0.05	0 01	0.43	0.00	0.11	100	95.4715
030418	MEX1-1A-51Y-1_8-17cm-21	110.312-S	77.09	3.93	0.16	4.72	1.11	12.45	0.03	0 03	0.41	0.01	0.07	100	94.8955
030418	MEX1-1A-51Y-1_8-17cm-22	110.312-S	76.89	4.04	0.14	4.76	1.09	12.42	0.03	0 04	0.46	0.06	0.08	100	94.8399
030418	MEX1-1A-51Y-1_8-17cm-23	110.312-S	77.35	3.84	0.14	4 98	1.15	11.97	0.03	0 01	0.42	0.05	0.08	100	95.3195
030418	MEX1-1A-51Y-1_8-17cm-24	110.312-S	77.25	3.83	0.14	4 86	1.04	12.23	0.02	0 01	0.42	0.05	0.16	100	95.1096
030418	MEX1-1A-51Y-1_8-17cm-25	110.312-S	77.11	3.72	0.13	5.10	1.00	12.32	0.02	0 02	0.40	0.08	0.11	100	95.3975
030418	MEX1-1A-51Y-1_6.5-7 5cm_HoleE-1	110.312-S	77.22	3.90	0.14	4 94	0.99	12.28	0.04	0 00	0.42	0.00	0.08	100	94.6217
030418	MEX1-1A-51Y-1_6.5-7 5cm_HoleE-2	110.312-S	77.51	3.71	0.12	4 83	0.99	12.26	0.04	0 00	0.44	0.00	0.09	100	94.8787
030418	MEX1-1A-51Y-1_6.5-7 5cm_HoleE-3	110.312-S	76.96	3.95	0.14	4 99	0.97	12.38	0.03	0 00	0 39	0.06	0.12	100	96.8999
030418	MEX1-1A-51Y-1_6.5-7 5cm_HoleE-4	110.312-S	77.52	3.78	0.12	4 55	1.04	12.45	0.02	0 00	0.46	0.04	0.03	100	93.138
030418	MEX1-1A-51Y-1_6.5-7 5cm_HoleE-5	110.312-S	77.40	3.82	0.14	4 62	1.04	12.41	0.03	0 00	0.41	0.01	0.12	100	93.9883
030418	MEX1-1A-51Y-1_6.5-7 5cm_HoleE-6	110.312-S	76.65	3.92	0.12	4 84	0.94	12.92	0.03	0 00	0.46	0.03	0.09	100	92.4456
030418	MEX1-1A-51Y-1_6.5-7 5cm_HoleE-7	110.312-S	77.07	3.73	0.13	4 88	0.98	12.60	0.05	0 02	0.42	0.07	0.06	100	94.5943
030418	MEX1-1A-51Y-1_6.5-7 5cm_HoleE-8	110.312-S	77.27	3.94	0.12	4 92	1.19	11.99	0.02	0 00	0.41	0.05	0.08	100	93.8276
030418	MEX1-1A-51Y-1_6.5-7 5cm_HoleE-9	110.312-S	77.07	3.98	0.13	4.76	1.04	12.40	0.03	0 02	0.45	0.07	0.06	100	94.0056
030418	MEX1-1A-51Y-1_6.5-7 5cm_HoleE-10	110.312-S	77.46	3.83	0.16	4.73	1.04	12.28	0.02	0 00	0 39	0.02	0.08	100	95.3286
030418	MEX1-1A-51Y-1_6.5-7 5cm_HoleE-11	110.312-S	76.76	4.12	0.12	4 83	1.03	12.61	0.03	0 00	0.40	0.00	0.11	100	95.3232
030418	MEX1-1A-51Y-1_6.5-7 5cm_HoleE-12	110.312-S	77.11	4.09	0.14	4 64	1.02	12.35	0.03	0 00	0.46	0.05	0.11	100	94.9953
030418	MEX1-1A-51Y-1_6.5-7 5cm_HoleE-13	110.312-S	76.83	4.04	0.14	4.78	1.19	12.43	0.05	0 02	0 39	0.06	0.08	100	95.3184
030418	MEX1-1A-51Y-1_6.5-7 5cm_HoleE-14	110.312-S	77.16	3.98	0.12	4 61	1.07	12.53	0.01	0 01	0.44	0.01	0.06	100	94.0149
030418	MEX1-1A-51Y-1_6.5-7 5cm_HoleE-15	110.312-S	77.34	3.85	0.12	4 69	1.00	12.42	0.05	0 02	0.43	0.01	0.07	100	94.3927
030418	MEX1-1A-51Y-1_6.5-7 5cm_HoleE-16	110.312-S	77.22	4.00	0.12	4 65	1.03	12.44	0.03	0 03	0 36	0.10	0.03	100	93.9129
030418	MEX1-1A-51Y-1_6.5-7 5cm_HoleE-17	110.312-S	77.24	3.95	0.12	4 56	0.96	12.60	0.03	0 00	0.43	0.03	0.09	100	93.4973
030418	MEX1-1A-51Y-1_6.5-7 5cm_HoleE-18	110.312-S	77.56	4.02	0.11	4 60	0.95	12.20	0.00	0 04	0.40	0.02	0.11	100	93.9852
030418	MEX1-1A-51Y-1_6.5-7 5cm_HoleE-19	110.312-S	76.91	3.95	0.12	4 82	1.01	12.57	0.04	0 01	0.41	0.06	0.12	100	93.4375
030418	MEX1-1A-51Y-1_6.5-7 5cm_HoleE-20	110.312-S	76.94	4.01	0.14	4 57	1.13	12.59	0.04	0 02	0.43	0.06	0.06	100	94.9289
030418	MEX1-1A-51Y-1_6.5-7 5cm_HoleE-21	110.312-S	77.15	4.14	0.14	4 65	1.00	12.35	0.04	0 00	0.45	0.00	0.07	100	94.2044
030418	MEX1-1A-51Y-1_6.5-7 5cm_HoleE-22	110.312-S	76.99	3.99	0.13	4 66	0.93	12.71	0.04	0 02	0 37	0.05	0.12	100	94.0796
030418	MEX1-1A-51Y-1_6.5-7 5cm_HoleE-23	110.312-S	77.20	3.96	0.13	4 57	1.04	12.49	0.00	0 00	0.44	0.02	0.15	100	93.45
030418	MEX1-1A-51Y-1_6.5-7 5cm_HoleE-24	110.312-S	77.45	3.84	0.13	4.76	1.03	12.33	0.03	0 00	0 37	0.00	0.06	100	92.7105
030418	MEX1-1A-51Y-1_6.5-7 5cm_HoleE-25	110.312-S	77.27	3.94	0.12	4.77	0.97	12.38	0.06	0 00	0 38	0.03	0.09	100	96.3687
030418	MEX1-1A-50Y-1_3-5.5cm-1	110.312-S	76.98	3.95	0.12	4 88	1.01	12.36	0.06	0 03	0.42	0.06	0.13	100	95.865
030418	MEX1-1A-50Y-1_3-5.5cm-2	110.312-S	77.28	3.87	0.13	4 83	1.16	12.18	0.01	0 00	0.42	0.02	0.09	100	94.4476
030418	MEX1-1A-50Y-1_3-5.5cm-3	110.312-S	77.34	3.83	0.12	4 59	1.03	12.51	0.03	0 00	0.41	0.02	0.12	100	94.189
030418	MEX1-1A-50Y-1_3-5.5cm-4	110.312-S	77.05	4.03	0.13	4.77	1.20	12.27	0.06	0 00	0 38	0.01	0.08	100	95.2341
030418	MEX1-1A-50Y-1_3-5.5cm-5	110.312-S	77.02	3.87	0.14	4 84	1.08	12.51	0.06	0 00	0 37	0.03	0.07	100	94.7953
030418	MEX1-1A-50Y-1_3-5.5cm-6	110.312-S	77.14	4.11	0.13	4 63	0.96	12.38	0.04	0 00	0.43	0.10	0.08	100	94.6951
030418	MEX1-1A-50Y-1_3-5.5cm-7	110.312-S	77.24	4.03	0.14	4.73	1.03	12.24	0.05	0 00	0.43	0.03	0.08	100	94.3381
030418	MEX1-1A-50Y-1_3-5.5cm-8	110.312-S	76.93	4.03	0.13	4.70	1.07	12.55	0.04	0 03	0.41	0.00	0.12	100	95.9846
030418	MEX1-1A-50Y-1_3-5.5cm-9	110.312-S	77.19	3.85	0.15	4 60	1.03	12.63	0.03	0 01	0.44	0.00	0.06	100	93.3925
030418	MEX1-1A-50Y-1_3-5.5cm-10	110.312-S	77.15	3.80	0.11	4 96	0.96	12.46	0.03	0 00	0.42	0.01	0.11	100	96.1733
030418	MEX1-1A-50Y-1_3-5.5cm-11	110.312-S	77.19	4.08	0.12	4.73	1.00	12.26	0.01	0 00	0.41	0.07	0.12	100	95.0177
030418	MEX1-1A-50Y-1_3-5.5cm-12	110.312-S	77.28	4.02	0.15	4 61	0.99	12.38	0.05	0 05	0.44	0.00	0.03	100	94.3605
030418	MEX1-1A-50Y-1_3-5.5cm-13	110.312-S	77.01	4.22	0.13	4 82	1.00	12.28	0.05	0 01	0 38	0.02	0.07	100	95.645
030418	MEX1-1A-50Y-1_3-5.5cm-14	110.312-S	77.09	3.98	0.13	4 85	0.91	12.47	0.00	0 01	0.42	0.01	0.14	100	96.4009

Date Analysed	Core Section Identifier	sample_no	SiO2	Na2O	Cl	K2O	FeOt	Al2O3	MgO	P2O5	CaO	MnO	TiO2	total	Analytical Total
030418	MEX1-1A-50Y-1_3-5.5cm-15	110.312-S	77.38	3.79	0.14	4.70	1.06	12.23	0.06	0 02	0.44	0.07	0.10	100	93.7956
030418	MEX1-1A-50Y-1_3-5.5cm-16	110.312-S	77.22	4.12	0.12	4.72	1.03	12.23	0.03	0 00	0.43	0.00	0.10	100	94.5971
030418	MEX1-1A-50Y-1_3-5.5cm-17	110.312-S	76.80	4.21	0.12	4 65	1.04	12.60	0.02	0 00	0.43	0.05	0.09	100	95.2022
030418	MEX1-1A-50Y-1_3-5.5cm-18	110.312-S	77.05	3.91	0.13	4.76	1.07	12.42	0.04	0 03	0.40	0.08	0.10	100	95.4375
030418	MEX1-1A-50Y-1_3-5.5cm-19	110.312-S	77.37	3.98	0.12	4 59	0.98	12.30	0.03	0 00	0.45	0.08	0.10	100	94.3781
030418	MEX1-1A-50Y-1_3-5.5cm-20	110.312-S	77.00	4.18	0.13	4 69	1.05	12.42	0.03	0 00	0.41	0.00	0.09	100	95.9229
030418	MEX1-1A-50Y-1_3-5.5cm-21	110.312-S	77.06	3.97	0.14	4.74	1.14	12.36	0.04	0 05	0 38	0.00	0.12	100	95.9183
030418	MEX1-1A-50Y-1_3-5.5cm-22	110.312-S	77.28	3.91	0.14	4.70	0.97	12.50	0.04	0 00	0 36	0.00	0.10	100	95.1399
030418	MEX1-1A-50Y-1_3-5.5cm-23	110.312-S	76.47	4.02	0.15	4 69	1.14	12.86	0.06	0 03	0.41	0.06	0.11	100	95.5618
030418	MEX1-1A-50Y-1_3-5.5cm-24	110.312-S	77.26	3.84	0.12	4.72	1.10	12.34	0.06	0 02	0.40	0.05	0.10	100	94.4149
030418	MEX1-1A-50Y-1_3-5.5cm-25	110.312-S	77.01	4.00	0.15	4 59	1.00	12.58	0.06	0 03	0.46	0.00	0.12	100	95.5884
030418	MEX1-1A-50Y-1_51-52cm-1	110.312-S	77.15	3.39	0.13	5.47	1.01	12.27	0.04	0 02	0.40	0.00	0.13	100	94.9547
030418	MEX1-1A-50Y-1_51-52cm-2	110.312-S	76.87	4.08	0.13	4 84	1.07	12.51	0.01	0 00	0.41	0.00	0.07	100	95.709
030418	MEX1-1A-50Y-1_51-52cm-3	110.312-S	76.89	3.87	0.14	5 06	1.14	12.32	0.05	0 01	0 38	0.03	0.11	100	96.4121
030418	MEX1-1A-50Y-1_51-52cm-4	110.312-S	77.03	3.91	0.12	5 08	0.97	12.26	0.06	0 05	0.44	0.03	0.06	100	96.0325
030418	MEX1-1A-50Y-1_51-52cm-5	110.312-S	77.00	4.03	0.14	5 04	1.01	12.19	0.05	0 00	0.43	0.05	0.05	100	96.0852
030418	MEX1-1A-50Y-1_51-52cm-6	110.312-S	77.09	3.77	0.13	4 94	1.00	12.41	0.03	0 00	0.45	0.06	0.13	100	96.9054
030418	MEX1-1A-50Y-1_51-52cm-7	110.312-S	77.13	3.73	0.14	5 01	0.94	12.54	0.05	0 00	0 39	0.01	0.06	100	95.5579
030418	MEX1-1A-50Y-1_51-52cm-8	110.312-S	77.01	3.93	0.12	4 84	1.06	12.34	0.04	0 02	0.45	0.07	0.13	100	96.9476
030418	MEX1-1A-50Y-1_51-52cm-9	110.312-S	76.97	3.99	0.13	4 84	1.07	12.37	0.07	0 02	0.41	0.00	0.12	100	96.2917
030418	MEX1-1A-50Y-1_51-52cm-10	110.312-S	76.81	3.81	0.12	5.18	1.12	12.40	0.05	0 02	0.43	0.01	0.06	100	96.201
030418	MEX1-1A-50Y-1_51-52cm-11	110.312-S	77.22	3.92	0.13	4.79	1.04	12.27	0.05	0 00	0.48	0.00	0.10	100	95.354
030418	MEX1-1A-50Y-1_51-52cm-12	110.312-S	77.65	3.71	0.13	4 89	1.10	12.02	0.00	0 00	0.42	0.03	0.07	100	93.6839
030418	MEX1-1A-50Y-1_51-52cm-13	110.312-S	77.31	3.65	0.14	4 87	1.13	12.29	0.02	0 02	0.43	0.03	0.11	100	96.0325
030418	MEX1-1A-50Y-1_51-52cm-14	110.312-S	76.99	3.90	0.14	5 07	0.96	12.31	0.04	0 00	0.41	0.07	0.11	100	96.3804
030418	MEX1-1A-50Y-1_51-52cm-15	110.312-S	76.79	3.88	0.14	5 24	0.97	12.39	0.06	0 00	0 38	0.04	0.10	100	96.8068
030418	MEX1-1A-50Y-1_51-52cm-16	110.312-S	77.39	3.75	0.15	4 85	0.99	12.29	0.02	0 00	0.43	0.01	0.13	100	95.6226
030418	MEX1-1A-50Y-1_51-52cm-17	110.312-S	77.28	3.94	0.12	4 80	1.00	12.23	0.06	0 00	0.43	0.00	0.14	100	95.1199
030418	MEX1-1A-50Y-1_51-52cm-18	110.312-S	77.27	3.69	0.12	5.12	1.00	12.30	0.03	0 02	0.41	0.00	0.04	100	96.1632
030418	MEX1-1A-50Y-1_51-52cm-19	110.312-S	77.72	3.80	0.12	4 85	0.93	12.02	0.03	0 03	0.40	0.00	0.10	100	95.7896
030418	MEX1-1A-50Y-1_51-52cm-21	110.312-S	77.03	3.86	0.12	4.72	1.02	12.61	0.05	0 01	0.40	0.06	0.13	100	95.0634
030418	MEX1-1A-50Y-1_51-52cm-22	110.312-S	76.90	3.70	0.12	5 20	1.05	12.43	0.01	0 01	0.45	0.04	0.10	100	96.1668
030418	MEX1-1A-50Y-1_51-52cm-23	110.312-S	76.84	3.90	0.15	4 97	1.04	12.47	0.05	0 00	0.42	0.05	0.09	100	96.086
030418	MEX1-1A-50Y-1_51-52cm-24	110.312-S	77.28	3.82	0.17	5.14	0.96	12.03	0.04	0 01	0.42	0.00	0.12	100	96.0503
030418	MEX1-1A-50Y-1_51-52cm-25	110.312-S	77.44	4.07	0.12	4.78	1.00	11.99	0.02	0 02	0.41	0.03	0.13	100	95.6824
060418	MEX4-1A-50Y-1_50.5-51cm-1	110.312-S	76.6804	3.6661	0.1563	5 288	1.1494	12.4529	0.0474	0 0205	0.4097	0.0462	0.0831	100	95.9472
060418	MEX4-1A-50Y-1_50.5-51cm-2	110.312-S	77.1498	3.8012	0.137	4.7994	1.0839	12.4385	0.0134	0 0491	0.4481	0	0.0795	100	97.0766
060418	MEX4-1A-50Y-1_50.5-51cm-3	110.312-S	76.7127	3.7745	0.1328	5 3361	1.2584	12.2165	0.0254	0 0218	0.4078	0.0235	0.0905	100	93.2991
060418	MEX4-1A-50Y-1_50.5-51cm-5	110.312-S	77.0991	3.4765	0.132	5 3365	1.0797	12.3228	0.043	0 0426	0 3956	0.0115	0.0609	100	95.1076
060418	MEX4-1A-50Y-1_50.5-51cm-8	110.312-S	77.012	3.9765	0.1455	4.7535	1.114	12.4256	0.0219	0 0304	0.4111	0.0279	0.0816	100	97.3
060418	MEX4-1A-50Y-1_50.5-51cm-9	110.312-S	76.8097	3.7359	0 0855	5 0949	1.0757	12.6112	0.0442	0	0.4324	0.0044	0.1063	100	97.5906
060418	MEX4-1A-50Y-1_50.5-51cm-10	110.312-S	77.7577	3.2021	0.1569	4.7793	0.9934	12.6212	0.0395	0	0 3734	0.0039	0.0727	100	97.8276
060418	MEX4-1A-50Y-1_50.5-51cm-11	110.312-S	76.9545	3.9934	0.1107	4.7805	1.1659	12.3554	0.0365	0 0516	0.4448	0.0236	0.083	100	98.5513
060418	MEX4-1A-50Y-1_50.5-51cm-12	110.312-S	76.7693	3.7731	0 0766	4 9631	1.2357	12.51	0.0447	0	0.4499	0.0439	0.1336	100	97.2776
060418	MEX4-1A-50Y-1_50.5-51cm-13	110.312-S	77.3509	3.6665	0 0933	4 8546	1.0219	12.4722	0.0204	0	0 3948	0.0078	0.1177	100	97.2351
060418	MEX4-1A-50Y-1_50.5-51cm-14	110.312-S	77.2449	3.7491	0.1296	4 9732	1.0663	12.2617	0.0428	0 0028	0.4057	0.028	0.0959	100	96.6876
060418	MEX4-1A-50Y-1_50.5-51cm-16	110.312-S	76.4829	3.9797	0.1245	5 0173	1.0806	12.6413	0.0312	0	0.4783	0.0222	0.1421	100	98.2703
060418	MEX4-1A-50Y-1_50.5-51cm-17	110.312-S	76.8058	3.3088	0 0964	5 5813	1.1512	12.3589	0.0811	0	0.4866	0.0375	0.0925	100	96.3153
060418	MEX4-1A-50Y-1_50.5-51cm-18	110.312-S	76.9434	3.8293	0.1177	4 8438	1.149	12.4273	0.073	0 0276	0.4127	0.0646	0.1116	100	97.0708
060418	MEX4-1A-50Y-1_50.5-51cm-19	110.312-S	76.6691	3.8801	0.1074	5.4732	1.055	12.2708	0.0394	0 0372	0.4032	0	0.0647	100	91.1881
060418	MEX4-1A-50Y-1_50.5-51cm-20	110.312-S	76.3691	3.3659	0.1188	5.4579	1.1406	12.7879	0.0704	0 0328	0.4709	0.0015	0.1842	100	94.7531
060418	MEX4-1A-50Y-1_50.5-51cm-21	110.312-S	76.6569	3.9584	0 0908	4.7477	1.066	12.8786	0.0196	0	0.4296	0.0546	0.0976	100	97.4195
060418	MEX4-1A-50Y-1_50.5-51cm-22	110.312-S	76.9075	4.1215	0.1349	4 5179	1.1191	12.5834	0.0575	0 0141	0.4407	0.0485	0.0547	100	96.8471
060418	MEX4-1A-50Y-1_50.5-51cm-23	110.312-S	76.9375	4.0556	0.1138	4 8701	1.0751	12.2355	0.0526	0 0454	0.4084	0.0753	0.1307	100	93.9518
060418	MEX4-1A-50Y-1_50.5-51cm-24	110.312-S	76.9105	3.2164	0.1209	5.7393	0.9751	12.4808	0.0664	0 0005	0 3828	0	0.1072	100	94.3666
060418	MEX4-1A-50Y-1_50.5-51cm-25	110.312-S	76.9236	3.4825	0.1112	5 282	0.9965	12.4811	0.0566	0 0478	0.4263	0.0664	0.1261	100	97.356
060418	MEX4-1A-50Y-1_50.5-51cm-26	110.312-S	77.0859	3.2969	0.1293	5 392	1.2023	12.3564	0.0102	0 0175	0.4007	0.0093	0.0994	100	96.6969
060418	MEX4-1A-50Y-1_50.5-51cm-28	110.312-S	76.1649	4.3258	0.1234	4 8221	1.1054	12.731	0.0155	0 0812	0 538	0.0367	0.0561	100	94.2631
060418	MEX4-1A-50Y-1_50.5-51cm-30	110.312-S	77.1948	3.5107	0.1256	5.1767	1.0815	12.3221	0.0328	0 0218	0.4108	0	0.1233	100	95.5532
260318	MEX1-1A-50Y-1_44-46cm-1	110.312-S	76.78	3.40	0.13	5.44	1.09	12.61	0.03	0 00	0 39	0.05	0.09	100	96.0848
260318	MEX1-1A-50Y-1_44-46cm-2	110.312-S	76.96	3.86	0.13	4 81	1.06	12.55	0.04	0 00	0 39	0.06	0.13	100	96.8824
260318	MEX1-1A-50Y-1_44-46cm-3	110.312-S	77.40	3.89	0.13	4.78	1.01	12.27	0.03	0 01	0 34	0.01	0.12	100	96.698
260318	MEX1-1A-50Y-1_44-46cm-4	110.312-S	77.11	3.96	0.14	4 80	1.05	12.37	0.06	0 00	0.41	0.01	0.09	100	96.591
260318	MEX1-1A-50Y-1_44-46cm-5	110.312-S	77.01	3.86	0.10	4 94	1.03	12.49	0.06	0 01	0 39	0.00	0.11	100	96.927
260318	MEX1-1A-50Y-1_44-46cm-6	110.312-S	76.73	3.18	0.13	5.71	1.12	12.58	0.04	0 00	0 39	0.08	0.04	100	95.4018
260318	MEX1-1A-50Y-1_44-46cm-7	110.312-S	77.10	3.84	0.15	4.79	0.96	12.64	0.03	0 00	0 39	0.03	0.07	100	95.9345

Date Analysed	Core Section Identifier	sample_no	SiO2	Na2O	Cl	K2O	FeOt	Al2O3	MgO	P2O5	CaO	MnO	TiO2	total	Analytical Total
260318	MEX1-1A-50Y-1_44-46cm-8	110.312-S	77.44	3.83	0.14	4.75	1.01	12.24	0.04	0 03	0.40	0.00	0.11	100	97.5348
260318	MEX1-1A-50Y-1_44-46cm-9	110.312-S	77.42	3.87	0.13	4 56	1.17	12.28	0.03	0 00	0.41	0.07	0.06	100	96.9102
260318	MEX1-1A-50Y-1_44-46cm-10	110.312-S	76.98	3.98	0.12	4.77	1.14	12.55	0.03	0 02	0 38	0.00	0.04	100	96.5535
260318	MEX1-1A-50Y-1_44-46cm-11	110.312-S	77.36	3.67	0.15	4 81	1.12	12.24	0.05	0 00	0.41	0.07	0.14	100	96.5117
260318	MEX1-1A-50Y-1_44-46cm-12	110.312-S	76.75	3.78	0.14	5 01	1.01	12.63	0.05	0 01	0.41	0.12	0.09	100	96.3838
260318	MEX1-1A-50Y-1_44-46cm-13	110.312-S	76.96	3.98	0.10	4.79	1.11	12.47	0.06	0 00	0.42	0.06	0.05	100	97.195
260318	MEX1-1A-50Y-1_44-46cm-14	110.312-S	76.90	3.84	0.13	4 88	1.23	12.45	0.02	0 03	0 38	0.07	0.07	100	97.5297
260318	MEX1-1A-50Y-1_44-46cm-15	110.312-S	77.03	3.22	0.13	5.73	1.04	12.27	0.05	0 00	0.42	0.00	0.09	100	96.4931
260318	MEX1-1A-50Y-1_44-46cm-16	110.312-S	77.30	3.94	0.12	4.71	1.01	12.31	0.04	0 01	0.43	0.02	0.11	100	96.5957
260318	MEX1-1A-50Y-1_44-46cm-17	110.312-S	77.18	3.70	0.13	4 86	1.10	12.48	0.05	0 01	0.40	0.06	0.03	100	97.0459
260318	MEX1-1A-50Y-1_44-46cm-18	110.312-S	76.88	3.72	0.14	5.13	1.04	12.51	0.03	0 02	0.44	0.00	0.09	100	96.9472
260318	MEX1-1A-50Y-1_44-46cm-19	110.312-S	77.13	3.15	0.14	5 56	1.18	12.27	0.06	0 00	0.40	0.05	0.07	100	97.0026
260318	MEX1-1A-50Y-1_44-46cm-20	110.312-S	76.88	3.80	0.14	5 09	0.98	12.52	0.02	0 00	0.43	0.00	0.13	100	97.1168
260318	MEX1-1A-50Y-1_44-46cm-21	110.312-S	77.52	3.84	0.13	4 63	1.06	12.19	0.07	0 01	0.46	0.05	0.04	100	94.6696
260318	MEX1-1A-50Y-1_44-46cm-22	110.312-S	77.42	3.89	0.14	4.78	0.88	12.25	0.04	0 00	0.46	0.07	0.08	100	96.6911
260318	MEX1-1A-50Y-1_44-46cm-23	110.312-S	77.06	4.06	0.13	4 85	1.09	12.25	0.03	0 00	0.42	0.01	0.10	100	96.6549
260318	MEX1-1A-50Y-1_44-46cm-24	110.312-S	77.35	3.75	0.13	4 98	0.85	12.35	0.02	0 00	0.44	0.00	0.11	100	96.1994
260318	MEX1-1A-50Y-1_44-46cm-25	110.312-S	77.31	3.92	0.12	4 66	0.95	12.42	0.06	0 02	0.42	0.04	0.08	100	96.2026
260318	MEX1-1A-50Y-1_44-46cm-26	110.312-S	77.02	3.86	0.14	4 83	1.17	12.35	0.05	0 00	0 38	0.11	0.10	100	96.3403
260318	MEX1-1A-50Y-1_44-46cm-27	110.312-S	77.69	3.77	0.15	4 60	0.93	12.32	0.05	0 00	0 38	0.04	0.06	100	96.1634
260318	MEX1-1A-50Y-1_44-46cm-28	110.312-S	77.23	3.56	0.12	4 97	1.10	12.45	0.04	0 01	0.41	0.04	0.07	100	97.489
260318	MEX1-1A-50Y-1_44-46cm-29	110.312-S	77.49	3.77	0.16	4 62	0.99	12.40	0.04	0 00	0.45	0.00	0.08	100	94.9987
260318	MEX1-1A-50Y-1_44-46cm-30	110.312-S	76.91	3.95	0.12	5 09	1.02	12.23	0.04	0 00	0 39	0.11	0.13	100	97.5943
Mar 12 21 59 2020	CHA08-4A-16S-1(36-44cm)_3	115.775-S	70.62159035	4.341835282	0 087969458	2 696551228	2.756008785	15.22929489	0.802806426	0 082203107	2 685499789	0.045752959	0.650487727	100	90.48595015
Mar 12 22:14 2020	CHA08-4A-16S-1(36-44cm)_7	115.775-S	70.70899571	4.429462006	0 059893402	2 628949346	2.783850493	15.26774159	0.751888839	0.124480278	2 565345732	0	0.679392595	100	94.33426338
Mar 12 22:18 2020	CHA08-4A-16S-1(36-44cm)_8	115.775-S	70.62705207	4.411268461	0 062565117	2 601613433	2.991201574	15.04529978	0.738877907	0 099262075	2.706941912	0.067726212	0.64819146	100	94.9410842
Mar 12 22 22 2020	CHA08-4A-16S-1(36-44cm)_9	115.775-S	69.95435174	4.741483054	0 068362184	2 68565724	2.982186568	15.21542947	0.829626055	0.171564369	2 653811502	0.034924159	0.662603656	100	94.20412859
Mar 12 22 38 2020	CHA08-4A-16S-1(36-44cm)_13	115.775-S	70.09224473	4.553196003	0 084583994	2 591240678	3.173657244	14.94217523	0.769592375	0 237832601	2.791377153	0.085110669	0.678989326	100	94.93521851
Mar 12 22:42 2020	CHA08-4A-16S-1(36-44cm)_14	115.775-S	69.98222149	4.460531411	0 08186584	2 589098914	3.200874218	15.25250499	0.845969286	0.141859973	2.756813823	0.018867927	0.669392132	100	95.39998594
Mar 12 22:46 2020	CHA08-4A-16S-1(36-44cm)_15	115.775-S	69.7409871	4.650646746	0 093868383	2 553546867	3.2438001	15.38722866	0.712247055	0.146792049	2.778258991	0.067617921	0.625006131	100	97.9030396
Mar 12 22 54 2020	CHA08-4A-16S-1(36-44cm)_17	115.775-S	70.16672678	4.482536635	0 071077936	2 657321011	2.86975675	15.2912097	0.871895062	0.199879535	2 635716775	0.023116532	0.730763278	100	92.57443831
Mar 12 23 06 2020	CHA08-4A-16S-1(36-44cm)_20	115.775-S	70.89453777	4.426866864	0 066439199	2 50992529	2.833892871	15.05353248	0.785081044	0.175891086	2 573200717	0.029106697	0.651525985	100	94.82353956
Mar 12 23 09 2020	CHA08-4A-16S-1(36-44cm)_21	115.775-S	70.41015745	4.737508514	0 099798254	2 539744371	2.842591822	15.10522212	0.786776883	0.148184723	2 581897805	0.065337822	0.68278024	100	94.89143975
Mar 12 23:13 2020	CHA08-4A-16S-1(36-44cm)_22	115.775-S	69.69126896	4.594366323	0 093639229	2 529640913	3.061709766	15.36076996	0.923312304	0.169464426	2 869760699	0.041026949	0.66504047	100	94.08449982
Mar 12 23:17 2020	CHA08-4A-16S-1(36-44cm)_23	115.775-S	70.0687785	4.510803807	0 071340162	2 586478376	2.913254689	15.50817966	0.842497809	0.166456018	2 660680625	0.028514864	0.643015485	100	94.33676393
Mar 12 23 21 2020	CHA08-4A-16S-1(36-44cm)_24	115.775-S	70.30135417	4.644464347	0 074004305	2 586455753	2.944321268	15.16317387	0.857761261	0.124452548	2 649797526	0.014779747	0.639435204	100	94.72421855
Mar 12 23 33 2020	CHA08-4A-16S-1(36-44cm)_27	115.775-S	70.34932209	4.343193912	0 066536076	2 592871227	2.85734406	15.32571989	0.806279949	0.188785373	2.732157698	0.044143097	0.693646625	100	93.33282636
Mar 12 23 37 2020	CHA08-4A-16S-1(36-44cm)_28	115.775-S	69.82115472	4.492902442	0 066561665	2 518549493	3.242169326	15.4711283	0.826317423	0 078105009	2 698445885	0.077672913	0.706992822	100	94.49883779
Mar 12 23 53 2020	CHA08-4A-16S-1(36-44cm)_32	115.775-S	70.51365194	4.490233156	0 076482541	2 620730441	2.928897769	15.11050733	0.793610502	0.195107761	2 567246146	0.062362688	0.641169725	100	93.48538719
030418	MEX2-1B-67Y-1_66-70cm-6	115.775-OS	77.25	4.16	0 07	3 34	0.84	12.89	0.14	0 05	1.12	0.00	0.15	100	95.328
030418	MEX2-1B-67Y-1_66-70cm-13	115.775-OS	77.26	4.22	0 08	3 31	0.95	12.71	0.14	0 00	1.17	0.02	0.15	100	95.0607
030418	MEX2-1B-67Y-1_72-72.5cm-15	115.775-OS	69.92	4.88	0 07	2 80	3.02	14.61	0.90	0.18	2 80	0.06	0.76	100	94.2796
030418	MEX2-1B-67Y-1_72-72.5cm-17	115.775-OS	70.08	4.68	0.10	2 66	2.93	15.05	0.87	0 20	2.74	0.03	0.67	100	93.483
030418	MEX2-1B-67Y-1_72-72.5cm-18	115.775-OS	70.20	4.39	0 07	2.79	3.08	14.78	0.96	0 20	2.78	0.07	0.68	100	93.8316
060418	MEX5-1B-69Y-1_7-8cm-4	118.20-G	57.6861	3.9278	0 0388	1.7234	7.1151	16.2876	3.8886	0.4075	6 9911	0.2101	1.7239	100	100.0023
060418	MEX5-1B-69Y-1_7-8cm-5	118.20-G	57.7433	4.26	0 0437	1 8655	7.3404	15.417	3.965	0.4859	6 9485	0.1051	1.8258	100	98.5074
060418	MEX5-1B-69Y-1_7-8cm-6	118.20-G	57.941	4.2821	0 0313	1 8304	7.2483	15.2701	4.1726	0.4499	6 9539	0.1153	1.705	100	98.2503
060418	MEX5-1B-69Y-1_7-8cm-8	118.20-G	67.9302	5.2466	0 0486	2 6038	1.5562	18.0652	0.2082	0.1562	3 8366	0.0126	0.3358	100	97.8915
060418	MEX5-1B-69Y-1_7-8cm-12	118.20-G	56.5715	4.2116	0 0547	1.758	7.7597	15.2672	4.5181	0.4847	7 3446	0.1786	1.8512	100	99.919
060418	MEX5-1B-69Y-1_7-8cm-13	118.20-G	64.1224	4.4476	0 06	2.4775	4.5839	16.3053	1.2325	0 3475	5 0918	0.0643	1.2671	100	96.9265
060418	MEX5-1B-69Y-1_7-8cm-16	118.20-G	69.7921	4.883	0 0499	2 9625	2.2798	15.7817	0.6872	0.1083	2 8561	0.0861	0.5133	100	98.3432
060418	MEX5-1B-69Y-1_7-8cm-22	118.20-G	58.9237	4.2546	0 035	1.463	5.8027	18.0563	2.517	0 2816	7 3532	0.0772	1.2357	100	99.275
060418	MEX5-1B-69Y-1_7-8cm-25	118.20-G	65.7483	4.5492	0 0359	2 8775	4.1725	15.8772	0.9059	0 3007	4.4113	0.0474	1.074	100	96.9706
060418	MEX5-1B-69Y-1_7-8cm-26	118.20-G	56.0665	4.0407	0 0303	1.7924	8.0784	14.7377	5.2136	0.4295	7 6282	0.1127	1.8698	100	98.8544
060418	MEX5-1B-69Y-1_7-8cm-30	118.20-G	55.9419	4.3751	0 0292	1 6131	6.3705	18.1365	2.9591	0.4372	8 3582	0.1624	1.6168	100	97.9854
060418	MEX5-1B-69Y-1_7-8cm-2	118.63-G	77.2901	3.9256	0 0502	3 5953	0.6305	13.1429	0.1397	0 0501	1 0657	0	0.1099	100	98.3727
060418	MEX5-1B-69Y-1_7-8cm-11	118.63-G	78.1219	3.9025	0 0935	3 569	0.7526	12.3658	0.134	0 0443	0 8554	0	0.1611	100	94.3508
060418	MEX5-1B-69Y-1_7-8cm-15	118.63-G	78.192	3.8526	0 0757	3 3599	0.724	12.5131	0.1467	0 036	0 9448	0	0.155	100	94.9539
060418	MEX5-1B-69Y-1_7-8cm-19	118.63-G	78.1383	3.8658	0 073	3 3812	0.7196	12.5703	0.1557	0 0214	0 9082	0.0414	0.1252	100	95.4852
060418	MEX5-1B-69Y-1_7-8cm-21	118.63-G	77.7457	4.066	0 0606	3 3349	0.8236	12.6502	0.1799	0 041	0 987	0.0011	0.1101	100	95.2083
060418	MEX5-1B-69Y-1_7-8cm-28	118.63-G	77.8526	3.7716	0 0924	3 6071	0.8852	12.5016	0.1287	0 0138	0 992	0.002	0.153	100	94.7416
060418	MEX5-1B-69Y-1_7-8cm-29	118.63-G	77.7696	4.1087	0 0752	3.1702	0.7808	12.669	0.1088	0 0541	1 0369	0.097	0.1298	100	95.0928
01/10/2021	1B-69Y-1-7-8cm	118.633-G	77.80	3.26	0 09	3.78	0.85	12.81	0.11	0 08	1 04	0.04	0.14	100	
01/10/2021	1B-69Y-1-7-8cm	118.633-G	78.16	3.28	0 07	3 93	0.76	12.40	0.14	0 07	1 05	0.03	0.11	100	
01/10/2021	1B-69Y-1-7-8cm	118.633-G	77.77	3.29	0.14	3.48	1.08	12.74	0.18	0 06	1 06	0.06	0.15	100	
01/10/2021	1B-69Y-1-7-8cm	118.633-G	78.51	3.35	0 09	3 56	0.77	12.49	0.14	0 06	0 88	0.01	0.13	100	

Date Analysed	Core Section Identifier	sample_no	SiO2	Na2O	Cl	K2O	FeOt	Al2O3	MgO	P2O5	CaO	MnO	TiO2	total	Analytical Total
01/10/2021	1B-69Y-1-7-8cm	118.633-G	77.97	3.37	0.10	4.10	0.73	12.45	0.13	0 05	0 92	0.03	0.15	100	
01/10/2021	1B-69Y-1-7-8cm	118.633-G	77.84	3.56	0 06	3 57	0.83	12.66	0.22	0 04	1 02	0.03	0.16	100	
01/10/2021	1B-69Y-1-7-8cm	118.633-G	77.90	3.60	0 09	3 52	0.72	12.70	0.16	0 05	1 01	0.03	0.19	100	
01/10/2021	1B-69Y-1-7-8cm	118.633-G	78.62	3.61	0 09	3 29	0.75	12.41	0.13	0 00	0 98	0.02	0.11	100	
01/10/2021	1B-69Y-1-7-8cm	118.633-G	78.33	3.70	0 08	3 20	0.80	12.55	0.13	0 02	1 02	0.03	0.13	100	
01/10/2021	1B-69Y-1-7-8cm	118.633-G	77.49	3.79	0 09	3 58	0.78	12.79	0.18	0 03	1 08	0.01	0.19	100	
01/10/2021	1B-69Y-1-7-8cm	118.633-G	77.55	3.79	0.19	3.71	0.73	12.68	0.13	0 07	1 03	0.02	0.11	100	
01/10/2021	1B-69Y-1-7-8cm	118.633-G	78.05	3.84	0 06	3 38	0.71	12.65	0.14	0 03	0 99	0.07	0.11	100	
01/10/2021	1B-69Y-1-7-8cm	118.633-G	78.02	3.87	0 06	3 29	0.64	12.74	0.19	0 04	0 94	0.03	0.18	100	
01/10/2021	1B-69Y-1-7-8cm	118.633-G	77.91	3.87	0 09	3 27	0.79	12.63	0.18	0 06	0 99	0.05	0.16	100	
01/10/2021	1B-69Y-1-7-8cm	118.633-G	77.93	3.87	0 08	3.40	0.74	12.70	0.16	0 01	0 98	0.01	0.11	100	
01/10/2021	1B-69Y-1-7-8cm	118.633-G	77.81	3.88	0 07	3 24	0.76	12.77	0.20	0 03	1 06	0.03	0.14	100	
01/10/2021	1B-69Y-1-7-8cm	118.633-G	78.18	3.90	0 05	3.17	0.79	12.57	0.13	0 00	0 99	0.06	0.15	100	
01/10/2021	1B-69Y-1-7-8cm	118.633-G	77.74	3.91	0 06	3 33	0.79	12.76	0.17	0 09	1 01	0.00	0.13	100	
01/10/2021	1B-69Y-1-7-8cm	118.633-G	77.36	3.94	0 09	3 33	0.86	12.95	0.20	0 01	1 07	0.05	0.15	100	
01/10/2021	1B-69Y-1-7-8cm	118.633-G	77.59	3.94	0 07	3 24	0.76	12.92	0.19	0 04	1 03	0.08	0.15	100	
01/10/2021	1B-69Y-1-7-8cm	118.633-G	77.82	3.95	0 07	3 39	0.77	12.64	0.12	0 07	1 00	0.01	0.15	100	
01/10/2021	1B-69Y-1-7-8cm	118.633-G	77.67	3.96	0 07	3 50	0.80	12.65	0.17	0 07	0 92	0.02	0.16	100	
01/10/2021	1B-69Y-1-7-8cm	118.633-G	77.67	3.97	0 07	3 36	0.80	12.84	0.12	0 03	1 02	0.01	0.13	100	
01/10/2021	1B-69Y-1-7-8cm	118.633-G	77.66	3.97	0 07	3.14	0.77	12.95	0.20	0 06	1 06	0.00	0.13	100	
01/10/2021	1B-69Y-1-7-8cm	118.633-G	78.19	3.99	0 07	3.46	0.72	12.50	0.10	0 00	0 86	0.03	0.09	100	
01/10/2021	1B-69Y-1-7-8cm	118.633-G	77.58	4.07	0 08	3 27	0.75	12.82	0.18	0 02	1 04	0.02	0.17	100	
060418	MEX4-1A-57Y-1_45-46cm-13	119.807-S	70.0779	4.6778	0	1 8995	3.6897	13.9424	0.9579	0 2096	3 3195	0.0523	1.1734	100	99.0171
060418	MEX4-1A-57Y-1_45-46cm-15	119.807-S	71.1862	5.0391	0 0271	2 8634	1.7155	15.2364	0.3494	0 2166	2 8232	0	0.543	100	98.5612
060418	MEX4-1A-57Y-1_45-46cm-16	119.807-S	76.9905	3.8584	0 0484	4 2471	1.1629	12.1267	0.0619	0 068	0.7578	0	0.6782	100	98.1871
060418	MEX4-1A-57Y-1_45-46cm-17	119.807-S	71.3759	4.3026	0 0237	3.1821	3.2822	13.7461	0.5216	0 2475	2.1929	0.0675	1.0579	100	99.5176
060418	MEX4-1A-57Y-1_45-46cm-18	119.807-S	69.8675	4.2629	0 0549	2.4023	3.4426	14.6737	1.0985	0.1734	2 9855	0.0895	0.9492	100	96.9018
060418	MEX4-1A-57Y-1_45-46cm-29	119.807-S	65.4434	4.8442	0 0116	1 9248	2.7591	18.1561	0.7832	0.1883	5 0565	0.0132	0.8196	100	100.612
Mar 9 21:44 2020	MEXI-CHA16-1A-57Y-1(76 5-77.5cm)_2	120.108-S	62.14308131	4.495520967	0.172587812	1 584343442	4.731905746	16.65027122	2.598323244	0.142802156	6.78098993	0.083442088	0.61673209	100	94.67644203
Mar 9 21:48 2020	MEXI-CHA16-1A-57Y-1(76 5-77.5cm)_3	120.108-S	62.2031321	4.601555833	0.158883444	1 566767292	4.512731145	16.92310971	2.063278054	0.188563754	7 061486388	0.051416448	0.669075835	100	90.63247662
Mar 9 22 00 2020	MEXI-CHA16-1A-57Y-1(76 5-77.5cm)_6	120.108-S	61.18808565	4.649156849	0.119661901	1 50473049	4.544900254	18.08363741	2.251977603	0.159788047	6 817350381	0.03674818	0.643963232	100	97.69191295
Mar 9 22 08 2020	MEXI-CHA16-1A-57Y-1(76 5-77.5cm)_8	120.108-S	61.62219447	4.247258316	0.129559958	1.767210598	4.992902232	15.98033625	3.321504256	0.154790615	7 058196545	0.064300916	0.661745848	100	93.93334342
Mar 9 22:12 2020	MEXI-CHA16-1A-57Y-1(76 5-77.5cm)_9	120.108-S	61.88156216	4.16319662	0.137533245	1 642187994	5.039464408	16.10835264	3.356221714	0.17335347	6.732970777	0.067329708	0.697827261	100	97.43098875
Mar 9 22:16 2020	MEXI-CHA16-1A-57Y-1(76 5-77.5cm)_10	120.108-S	62.56403152	4.146487412	0.118851277	1 613646576	4.985754163	16.14200367	3.010071497	0.154951447	6 35114742	0.11109336	0.80196166	100	96.67544452
Mar 9 22 20 2020	MEXI-CHA16-1A-57Y-1(76 5-77.5cm)_11	120.108-S	61.9305513	4.370416099	0.104531843	1 622399927	5.185518754	16.38022143	2.926480881	0 229292344	6.469063	0.098986932	0.682537488	100	97.38659216
Mar 9 22 28 2020	MEXI-CHA16-1A-57Y-1(76 5-77.5cm)_13	120.108-S	61.93824321	4.34777951	0.100455972	1 552501382	4.941622046	16.67938417	2.891914339	0.157482493	6 595594107	0.089395668	0.705627099	100	98.55063691
Mar 9 22 32 2020	MEXI-CHA16-1A-57Y-1(76 5-77.5cm)_14	120.108-S	61.56191605	4.424589633	0 090907789	1 521893792	4.738162672	17.22041092	2.719116908	0.163349934	6.79779227	0.102068344	0.659791689	100	98.56141132
Mar 9 22 36 2020	MEXI-CHA16-1A-57Y-1(76 5-77.5cm)_15	120.108-S	62.17032611	4.240110847	0.127098992	1 659605657	5.411757577	16.10659672	3.051200462	0.153384672	6 25702257	0.117821694	0.705074701	100	97.01099736
Mar 9 22:40 2020	MEXI-CHA16-1A-57Y-1(76 5-77.5cm)_16	120.108-S	62.02357499	4.22797438	0.104636197	1.706248392	5.272924248	16.4576789	2.888287941	0.166616183	6 290506121	0.141330816	0.720221836	100	97.28946897
Mar 9 22:44 2020	MEXI-CHA16-1A-57Y-1(76 5-77.5cm)_17	120.108-S	62.00932253	4.480761342	0.104664426	1 835684218	5.070950877	16.57040472	2.535475439	0 205677768	6 3589724	0.088640221	0.739446057	100	98.60083682
Mar 9 22:48 2020	MEXI-CHA16-1A-57Y-1(76 5-77.5cm)_18	120.108-S	62.95283067	4.440613573	0.112072084	1 869580132	4.879398695	16.27474607	2.414018302	0 223116926	5 999092291	0.085671969	0.748859295	100	97.34806062
Mar 9 22 56 2020	MEXI-CHA16-1A-57Y-1(76 5-77.5cm)_20	120.108-S	61.73643829	4.133665632	0.104316397	1.478336162	4.986781842	16.06077617	3.622964678	0.116288838	6 985658906	0.0852646	0.689508479	100	96.05393121
Mar 9 23 00 2020	MEXI-CHA16-1A-57Y-1(76 5-77.5cm)_21	120.108-S	62.01783815	4.554714874	0.131991404	1 831760167	4.940518852	16.80113563	2.721472249	0 228708341	6 008173349	0.077352615	0.686334367	100	95.53652444
Mar 9 23 04 2020	MEXI-CHA16-1A-57Y-1(76 5-77.5cm)_22	120.108-S	61.69852935	4.306864017	0.1098642	1.493904136	4.907060112	16.10728322	3.444278979	0.183314487	6 971552633	0.093680239	0.683668629	100	96.39172726
Mar 9 23 08 2020	MEXI-CHA16-1A-57Y-1(76 5-77.5cm)_23	120.108-S	61.14993474	4.903183538	0.13977171	1 923174655	4.813191213	15.96257141	3.215800243	0 206189545	6 936039739	0.077977901	0.672165306	100	95.15516416
Mar 9 23:12 2020	MEXI-CHA16-1A-57Y-1(76 5-77.5cm)_24	120.108-S	62.80406007	4.311842817	0.131679483	1 638167896	4.549307024	16.61375096	2.681586939	0.134079347	6 385724538	0.053631739	0.696169185	100	95.8387723
Mar 9 23 20 2020	MEXI-CHA16-1A-57Y-1(76 5-77.5cm)_26	120.108-S	61.81840252	3.962298668	0.122863443	1.414854213	5.014409786	15.92554593	3.526732194	0.132434516	7 230321164	0.089988889	0.762148674	100	96.1229777
Mar 9 23 24 2020	MEXI-CHA16-1A-57Y-1(76 5-77.5cm)_27	120.108-S	61.48685457	4.355070454	0.110164444	1 507404758	5.193319132	15.8869871	3.36584898	0.149914501	7 216958396	0.09694884	0.630528826	100	96.85520709
Mar 9 23 28 2020	MEXI-CHA16-1A-57Y-1(76 5-77.5cm)_28	120.108-S	61.57908055	4.326475598	0 098912794	1.473388492	4.914729446	16.17072436	3.389823874	0 201431783	7 078446813	0.106125185	0.660861104	100	97.05518996
Mar 9 23 32 2020	MEXI-CHA16-1A-57Y-1(76 5-77.5cm)_29	120.108-S	61.71654359	4.409568123	0.141201311	1 516186471	4.930184579	16.0445668	3.403683914	0.122120053	6 931138153	0.107267614	0.677539383	100	96.95377371
Mar 9 23:40 2020	MEXI-CHA16-1A-57Y-1(76 5-77.5cm)_31	120.108-S	62.02662327	4.507022151	0.109401617	1 588256515	4.754320489	16.7616577	2.789897957	0.187978518	6 572456236	0.033854942	0.668530604	100	95.702425
Mar 9 23:44 2020	MEXI-CHA16-1A-57Y-1(76 5-77.5cm)_32	120.108-S	62.09775027	4.221373818	0 085407132	1 600109761	5.004164922	16.57111626	2.884274283	0.167450977	6 512548646	0.095700832	0.760103096	100	98.11826901
Mar 9 23:48 2020	MEXI-CHA16-1A-57Y-1(76 5-77.5cm)_33	120.108-S	61.85553563	4.252217819	0.125042918	1 509138671	5.14339098	16.53961574	2.823218602	0.167647854	6.796257143	0.109027569	0.678907077	100	97.4065557
Mar 9 23 52 2020	MEXI-CHA16-1A-57Y-1(76 5-77.5cm)_34	120.108-S	61.45871109	4.155961213	0.118915475	1.461820573	4.955675416	15.9734384	3.400547147	0.151780519	7 578658429	0.06417496	0.68031678	100	96.45506614
Mar 10 00 00 2020	MEXI-CHA16-1A-57Y-1(76 5-77.5cm)_36	120.108-S	62.08531784	4.212315743	0.105438273	1 593834364	5.088009699	16.27787441	3.003764762	0 236010088	6 630759628	0.111568405	0.655106791	100	97.8771719
Mar 10 00 04 2020	MEXI-CHA16-1A-57Y-1(76 5-77.5cm)_37	120.108-S	61.47283925	4.467988625	0 097614719	1.475926405	5.038507383	16.66095166	2.992568021	0.1589929	6 891049491	0.093543198	0.650018346	100	98.2433809
Mar 11 03 01 2020	CHA08-4A-22S-1(33-36cm)_1	123.113-OS	70.52451139	4.6646607	0 056600885	2 809386999	2.909093964	14.8613169	0.85727618	0 095860272	2 540842653	0.049164272	0.631285784	100	96.81827393
Mar 11 03 05 2020	CHA08-4A-22S-1(33-36cm)_2	123.113-OS	70.22633055	4.603615052	0 064807775	2 833408303	2.797196948	15.19042193	0.845695104	0 208335839	2 565522427	0.076141409	0.588524663	100	97.05625544
Mar 11 03 09 2020	CHA08-4A-22S-1(33-36cm)_3	123.113-OS	70.15866631	4.674817035	0 075242292	2 813855591	2.913528497	15.08437732	0.830345079	0 257039391	2 535562181	0.072253215	0.58431309	100	97.01990423
Mar 11 03:13 2020	CHA08-4A-22S-1(33-36cm)_4	123.113-OS	69.9609888	4.775040867	0 09002685	2 838028866	2.822284162	15.20371911	0.858373786	0.15848846	2 619718953	0.06382966	0.609500485	100	96.19352477
Mar 11 03:17 2020	CHA08-4A-22S-1(33-36cm)_5	123.113-OS	70.22628272	4.688559518	0 067051151	2 836779476	2.936880188	15.09666824	0.797805544	0.102634327	2 568574871	0.078810892	0.59995307	100	96.94091568
Mar 11 03 21 2020	CHA08-4A-22S-1(33-36cm)_6	123.113-OS	70.08808123	4.792089837	0 07469861	2 865860795	2.829846758	15.16170583	0.798302595	0.159061582	2 586516963	0.082561621	0.561274181	100	96.65507846
Mar 11 03 25 2020	CHA08-4A-22S-1(33-36cm)_7	123.113-OS	70.24457742	4.578615326	0 089445132	2 835805125	2.88344518	15.2238644	0.793598998	0 092777403	2 601264852	0.041577594	0.615028563	100	93.80052163
Mar 11 03 29 2020	CHA08-4A-22S-1(33-36cm)_8	123.113-OS	70.20171184	4.80448925	0 073402769	2 87451405	2.734909826	15.16595672	0.821597712	0.170897208	2 504933672	0.029874414	0.617712537	100	97.40776881
Mar 11 03 33 2020	CHA08-4A-22S-1(33-36cm)_9	123.113-OS	70.27863427	4.667311325	0 075281319	2 815315085	2.810182146	15.17350609	0.862332042	0.11612541	2 547189839	0.046096917	0.608025558	100	96.96960792
Mar 11 03 53 2020	CHA08-4A-22S-1(33-36cm)_14	123.113-OS	70.61418599	4.575264159	0 057272897	2 938721686	2.824509079	15.14662456	0.713122646	0.110708824	2 391733343	0.021772281	0.606084535	100	93.23781878

Date Analysed	Core Section Identifier	sample_no	SiO2	Na2O	Cl	K2O	FeOt	Al2O3	MgO	P2O5	CaO	MnO	TiO2	total	Analytical Total
Mar 11 04 01 2020	CHA08-4A-22S-1(33-36cm)_16	123.113-OS	70.1230034	4.44499823	0 079486021	2.760979844	2.818329134	15.40115996	0.847922794	0.135449258	2 674699224	0.059533628	0.654438504	100	92.72070585
Mar 11 04 09 2020	CHA08-4A-22S-1(33-36cm)_18	123.113-OS	70.58387177	4.699147171	0 054485772	2 863863173	2.722748802	15.16132656	0.778309096	0 075222493	2.481325493	0.031533511	0.548166157	100	96.722498
Mar 11 04:13 2020	CHA08-4A-22S-1(33-36cm)_19	123.113-OS	70.33027661	4.770800879	0 084649806	2 814735885	2.735290386	15.25163498	0.74201008	0.135650333	2 503141507	0.059826121	0.571983414	100	96.27901553
Mar 11 04:17 2020	CHA08-4A-22S-1(33-36cm)_20	123.113-OS	70.51165241	4.636143454	0 029250031	2 903652736	2.811323684	15.04435539	0.718760804	0.139421026	2 583396919	0.03469438	0.587349167	100	93.67511364
Mar 11 04 21 2020	CHA08-4A-22S-1(33-36cm)_21	123.113-OS	70.23008953	4.699847702	0 080122548	2.712645736	2.747567291	15.21432098	0.714190397	0.175427037	2.765013415	0.046083557	0.614691808	100	95.47874112
Mar 11 04 25 2020	CHA08-4A-22S-1(33-36cm)_22	123.113-OS	70.29364064	4.601818146	0 065969136	2 836153389	2.926052763	15.15271862	0.789344082	0.125398244	2 524488181	0.032724847	0.651691949	100	96.25713514
Mar 11 04 29 2020	CHA08-4A-22S-1(33-36cm)_23	123.113-OS	70.11942708	4.739255653	0 089568799	2 836171508	2.91562453	14.97217562	0.916542189	0.108033245	2 679764991	0.07528367	0.548152706	100	95.9039322
Mar 11 04 37 2020	CHA08-4A-22S-1(33-36cm)_25	123.113-OS	70.35136363	4.694472763	0 05393712	2 883561439	2.847629566	15.077808	0.807293478	0.109734463	2 530895652	0.066695324	0.576608563	100	96.40855791
Jan 20 22 00 2020	CHA16-1B-71Y-1_137 5-140cm_4	123.113-OS	69.92070482	4.705395153	0 065707857	2.777126315	2.87362048	15.36319819	0.777490571	0.152077774	2 680248208	0.042233279	0.642197361	100	95.42237907
Jan 20 22 04 2020	CHA16-1B-71Y-1_137 5-140cm_5	123.113-OS	69.71508701	4.928821072	0 060903904	2.731257537	2.858803531	15.45188691	0.848992046	0.104490737	2 633895498	0.048764981	0.61709677	100	95.56037704
Jan 20 22:12 2020	CHA16-1B-71Y-1_137 5-140cm_7	123.113-OS	69.80704467	5.074661578	0 052269014	2 31404568	2.503685748	15.95417884	0.650470121	0 096736271	2 94596666	0.018776248	0.582165176	100	98.52873779
Jan 20 22:16 2020	CHA16-1B-71Y-1_137 5-140cm_8	123.113-OS	69.91240069	4.650515149	0 053001437	2 392282737	2.995689188	15.33518566	0.924637901	0.126236895	3 003524176	0.012889454	0.593636712	100	96.97850357
Jan 20 22 20 2020	CHA16-1B-71Y-1_137 5-140cm_9	123.113-OS	70.34153968	4.892078563	0 062532636	2 507446126	2.733343343	15.36840731	0.710477184	0.114872973	2 669459666	0.050046578	0.549795942	100	97.70897867
Jan 20 22 24 2020	CHA16-1B-71Y-1_137 5-140cm_10	123.113-OS	70.01337176	4.824149882	0 064357109	2.73860037	2.813092263	15.27909063	0.821790772	0.130886846	2.704584466	0.056667961	0.553407936	100	94.93900712
Jan 20 22 28 2020	CHA16-1B-71Y-1_137 5-140cm_11	123.113-OS	69.74749866	4.80759925	0 070674907	2.782224843	2.825221062	15.44247027	0.855134394	0.120693716	2.737139624	0.036350141	0.574993134	100	93.80981578
Jan 20 22:43 2020	CHA16-1B-71Y-1_137 5-140cm_15	123.113-OS	70.38764777	4.77697226	0 079027737	2.762336133	2.911085438	15.18391906	0.724542075	0.130062432	2.49785916	0.037696542	0.508851393	100	96.29530485
Jan 20 22:47 2020	CHA16-1B-71Y-1_137 5-140cm_16	123.113-OS	70.05139384	4.586190523	0.10505576	2.741048754	2.804986099	15.61508834	0.730377505	0 081377672	2 565409488	0.062606833	0.656465178	100	93.75973324
Jan 20 22 51 2020	CHA16-1B-71Y-1_137 5-140cm_17	123.113-OS	70.01477421	4.826434308	0 098627136	2 811922597	2.738015507	15.37145587	0.705498789	0.145824239	2 587614374	0.101145275	0.598687699	100	95.30845562
Jan 20 22 55 2020	CHA16-1B-71Y-1_137 5-140cm_18	123.113-OS	69.91089757	5.001108805	0 061624542	2 814431524	2.911577966	15.23727896	0.77820601	0.129240646	2 559058199	0.016530862	0.580044921	100	95.57880434
Jan 20 23 07 2020	CHA16-1B-71Y-1_137 5-140cm_21	123.113-OS	69.94851068	4.900921373	0 070643912	2.792642134	2.936720688	15.13986404	0.736683542	0 072711029	2 699830636	0.061151136	0.640320831	100	90.59520979
Jan 20 23:11 2020	CHA16-1B-71Y-1_137 5-140cm_22	123.113-OS	69.95548029	4.735048736	0 074052703	2 864812591	2.854154493	15.32764289	0.811444653	0.128102826	2 60029968	0.055782766	0.593178366	100	92.50168783
Jan 20 23:15 2020	CHA16-1B-71Y-1_137 5-140cm_23	123.113-OS	69.99950315	4.714614129	0 069258933	2.764098992	2.955832942	15.42173795	0.804404959	0.148293596	2.498299121	0.023781682	0.600174551	100	95.87210906
Jan 20 23:19 2020	CHA16-1B-71Y-1_137 5-140cm_24	123.113-OS	70.32301103	4.761896757	0 071322159	2.784859264	2.838772719	15.14214344	0.847575106	0 076276203	2 535096742	0.053039877	0.566006702	100	94.08015816
Jan 20 23 26 2020	CHA16-1B-71Y-1_137 5-140cm_26	123.113-OS	69.72957294	4.881832892	0.101559559	2.724237105	3.15464581	15.1456685	0.810623993	0.122442337	2 676362739	0.04217119	0.610882928	100	91.76881099
Jan 20 23 30 2020	CHA16-1B-71Y-1_137 5-140cm_27	123.113-OS	70.0842088	4.650137077	0.105324533	2 828654812	2.817883941	15.22247491	0.76855837	0 208716972	2 664199999	0.044894181	0.604946404	100	93.33058205
Jan 20 23 34 2020	CHA16-1B-71Y-1_137 5-140cm_28	123.113-OS	70.02259537	4.629679844	0 055640143	2.719018321	2.867969539	15.56210031	0.80772691	0.111908581	2 631685798	0.044512115	0.547163069	100	95.25496684
Jan 20 23 38 2020	CHA16-1B-71Y-1_137 5-140cm_29	123.113-OS	70.0480688	4.892947573	0 069027389	2 809498929	2.745901443	15.2434288	0.76866628	0 074993735	2 691180727	0.059451944	0.596834379	100	95.03473991
Jan 20 23:46 2020	CHA16-1B-71Y-1_137 5-140cm_31	123.113-OS	69.9285936	4.858022574	0 069503905	2 693146843	3.030372059	15.36471919	0.752423795	0.10431844	2 607132361	0.030764024	0.561003204	100	96.54133813
Jan 20 23 50 2020	CHA16-1B-71Y-1_137 5-140cm_32	123.113-OS	69.81120748	4.908105757	0 099217622	2.744317197	2.980355695	15.42281896	0.760386965	0.101509868	2 570969441	0.023748899	0.577362118	100	94.74123481
Jan 21 00 02 2020	CHA16-1B-71Y-1_137 5-140cm_35	123.113-OS	69.83660684	4.622158094	0 064290017	2.752285047	2.987608546	15.27869591	1.057528762	0.104120135	2.708011782	0.044435747	0.544259116	100	95.1936284
Jan 21 00 06 2020	CHA16-1B-71Y-1_137 5-140cm_36	123.113-OS	70.00246308	4.714005615	0 071490549	2.747235061	2.864066042	15.38570829	0.775677657	0 094589154	2 67200415	0.070241806	0.602518599	100	96.09661867
Jan 21 00:10 2020	CHA16-1B-71Y-1_137 5-140cm_37	123.113-OS	69.8517074	5.123420688	0.105354848	2.762729868	3.089429788	15.22169461	0.675013253	0.074102436	2.4795718	0.065563291	0.551412017	100	97.00550283
Jan 21 07:47 2020	CHA08-6A-15S-1_87-88cm_2	123.113-S	69.72036452	4.776365271	0 086057823	2.715972409	2.927664448	15.40550484	0.863179737	0.148582981	2.724766342	0.059730581	0.571811049	100	96.098178
Jan 21 07 51 2020	CHA08-6A-15S-1_87-88cm_3	123.113-S	69.35306134	4.831194007	0 093869252	2.786412333	2.851155686	15.34810255	0.841327009	0 066931122	3.129012786	0.07056086	0.628373063	100	94.38660492
Jan 21 07 59 2020	CHA08-6A-15S-1_87-88cm_5	123.113-S	70.05330988	4.528677691	0 070910935	3.13765198	2.707974706	15.27214147	0.857624875	0.115595133	2 589989816	0.085971664	0.580151851	100	95.6128984
Jan 21 08:19 2020	CHA08-6A-15S-1_87-88cm_10	123.113-S	70.32000153	4.261169399	0.136614376	2.730146223	2.761173006	15.644026	0.751379066	0.170208784	2 65130852	0.039506822	0.534466272	100	93.40159068
Jan 21 08:42 2020	CHA08-6A-15S-1_87-88cm_16	123.113-S	70.0374835	4.592802425	0 058263609	2.775506502	2.963964553	15.44615199	0.776591125	0 068228265	2.705090429	0.041081902	0.534835697	100	90.79423877
Jan 21 08:46 2020	CHA08-6A-15S-1_87-88cm_17	123.113-S	69.65716587	4.665478449	0 082825348	2.715413299	2.896228601	15.53136882	0.840834543	0.149056478	2.745241758	0.077163868	0.639222969	100	95.3814287
Jan 21 08 54 2020	CHA08-6A-15S-1_87-88cm_19	123.113-S	70.19628383	4.459124107	0 091331458	2 858137379	2.86965789	15.28618739	0.809304163	0.121392634	2 628108067	0.065651201	0.614821883	100	93.06760477
Jan 21 08 58 2020	CHA08-6A-15S-1_87-88cm_20	123.113-S	69.48513178	4.779226606	0.119261435	2.773266815	3.005735662	15.47826667	0.84370888	0.135673035	2.714473922	0.060617255	0.604637935	100	91.22814964
Jan 21 09 02 2020	CHA08-6A-15S-1_87-88cm_21	123.113-S	69.93208235	4.908402307	0 055055069	2 833716796	2.878259764	15.21663196	0.813175516	0.11371693	2 639710196	0.026313085	0.582936027	100	98.81015649
Jan 21 09 06 2020	CHA08-6A-15S-1_87-88cm_22	123.113-S	69.44459357	4.918202184	0 077722339	2.780311299	2.887813539	15.47965411	0.843677038	0.118335817	2.789682119	0.060977282	0.599030707	100	94.95339609
Jan 21 09:14 2020	CHA08-6A-15S-1_87-88cm_24	123.113-S	70.07560085	4.825658341	0 094131404	2 909892691	2.755107389	15.21099831	0.767652474	0 099844568	2 564396608	0.042871729	0.653845639	100	96.5671349
Jan 21 09:41 2020	CHA08-6A-15S-1_87-88cm_31	123.113-S	69.81544168	4.758519208	0 057898721	2 838773261	2.883321361	15.35345194	0.839071938	0.153445176	2 653081486	0.073011614	0.573983615	100	97.92962467
Jan 21 09:45 2020	CHA08-6A-15S-1_87-88cm_32	123.113-S	68.5600093	5.078902318	0 06165022	2.482559178	2.530620257	16.53916869	0.733182477	0 086918091	3 317417752	0.064753419	0.5448183	100	96.67443263
Jan 21 09 53 2020	CHA08-6A-15S-1_87-88cm_34	123.113-S	69.01355303	4.939745588	0 072259088	2 520903224	2.621724977	16.27933925	0.681358296	0 087261614	3 221397543	0.029393527	0.533063868	100	97.98075455
Jan 21 09 57 2020	CHA08-6A-15S-1_87-88cm_35	123.113-S	70.08240403	4.815865123	0 082332367	2 839047125	2.904728183	15.28323524	0.781789458	0 059075248	2 518520869	0.038590011	0.594412348	100	95.10233121
060418	MEX5-1B-71Y-1_138-139.5cm-5	123.113-OS	69.5804	4.9362	0 0878	2 8716	2.9655	15.1992	0.8861	0.1026	2 6733	0.0783	0.6189	100	97.3455
060418	MEX5-1B-71Y-1_138-139.5cm-6	123.113-OS	69.8736	4.7258	0 0889	2 8313	2.9958	15.2155	0.7928	0.1379	2 6727	0.0268	0.6388	100	96.0235
060418	MEX5-1B-71Y-1_138-139.5cm-8	123.113-OS	70.1279	4.5396	0 0812	2 9142	3.0292	15.0035	0.77	0.1516	2 6058	0.0886	0.6884	100	99.1979
060418	MEX5-1B-71Y-1_138-139.5cm-9	123.113-OS	69.2352	4.8811	0 0552	2 5762	2.7054	15.904	0.6798	0.1432	3 2319	0.0535	0.5346	100	98.6235
060418	MEX5-1B-71Y-1_138-139.5cm-24	123.113-OS	68.382	5.0269	0 0661	2.4858	2.9334	16.144	0.9601	0.1709	3 229	0.033	0.5688	100	97.4714
060418	MEX5-1B-71Y-1_138-139.5cm-25	123.113-OS	70.1285	5.1288	0 0876	2.7226	2.5217	15.3825	0.6596	0.1247	2 63	0.0297	0.5843	100	95.9727
060418	MEX5-1B-71Y-1_138-139.5cm-29	123.113-OS	68.9847	5.1525	0 049	2.7938	2.3201	16.0821	0.6213	0.1356	3 3054	0.0195	0.5362	100	96.053
060418	MEX5-1B-71Y-1_138-139.5cm-30	123.113-OS	69.2089	5.0708	0 087	2 8489	3.1518	15.2015	0.8549	0.1724	2.7441	0.0417	0.6181	100	97.2883
Mar 13 02 03 2020	CHA08-6A-16S-1(15 5-16.5cm)_1	123.478-OS	62.27328951	4.12557873	0 064984687	1 887310366	5.108958373	17.82732448	2.40403135	0 215468505	5 039628762	0.068861324	0.984563911	100	98.02309323
Mar 13 02 07 2020	CHA08-6A-16S-1(15 5-16.5cm)_2	123.478-OS	62.32170166	5.461750173	0 05183296	0 951527497	4.860280363	17.13997022	2.385996687	0 282584166	5 392722143	0.082095032	1.069539106	100	95.49907939
Mar 13 02:14 2020	CHA08-6A-16S-1(15 5-16.5cm)_4	123.478-OS	61.80309267	4.408480113	0 084310084	1 813230234	4.869588133	17.88145996	2.443987238	0 25058641	5 378225269	0.078061098	0.988978795	100	97.61584421
Mar 13 02:18 2020	CHA08-6A-16S-1(15 5-16.5cm)_5	123.478-OS	61.76935286	4.671132952	0 050899915	1 631275156	4.781643524	17.97060832	2.302283395	0 267245906	5.441025361	0.065457497	1.049075117	100	96.85674392
Mar 13 02 22 2020	CHA08-6A-16S-1(15 5-16.5cm)_6	123.478-OS	61.9519738	4.519334364	0 057195887	1 660525757	4.851535562	17.49689878	2.734855147	0 221904786	5 39158363	0.103936612	1.01025567	100	97.55946232
Mar 13 02 26 2020	CHA08-6A-16S-1(15 5-16.5cm)_7	123.478-OS	61.5997826	4.420443653	0 038469594	1 664947477	4.894668444	18.14280206	2.426860807	0 256165407	5 522248153	0.072802672	0.960809131	100	96.69974714
Mar 13 02 30 2020	CHA08-6A-16S-1(15 5-16.5cm)_8	123.478-OS	62.06252757	4.486844349	0 070838336	1 691046163	4.702028896	17.96788402	2.490098118	0.161325066	5 289674889	0.092285751	0.98544684	100	96.98138559
Mar 13 02 34 2020	CHA08-6A-16S-1(15 5-16.5cm)_9	123.478-OS	61.29367408	4.651325256	0 053014083	1 690606589	5.141248179	17.90663992	2.601481081	0 257429514	5 353587531	0.065954529	0.985039234	100	95.82359437
Mar 13 02:42 2020	CHA08-6A-16S-1(15 5-16.5cm)_11	123.478-OS	61.60732817	4.831898719	0 069371627	1.463710399	4.585048304	18.22663869	2.258408481	0 23782486	5 576530465	0.090811892	1.052428393	100	97.01372626
Mar 13 02:46 2020	CHA08-6A-16S-1(15 5-16.5cm)_12	123.478-OS	61.851888	4.598540841	0 072189148	1 693459717	5.204354167	17.2648531	2.663814488	0 243109495	5 210645283	0.089883631	1.107262123	100	92.11910885
Mar 13 02 50 2020	CHA08-6A-16S-1(15 5-16.5cm)_13	123.478-OS	61.97674687	4.186020177	0 066129285	1.797985169	5.107818443	17.70101454	2.443222143	0 221194614	5 353323073	0.102495313	1.044050371	100	98.44352617

Date Analysed	Core Section Identifier	sample_no	SiO2	Na2O	Cl	K2O	FeOt	Al2O3	MgO	P2O5	CaO	MnO	TiO2	total	Analytical Total
Mar 13 02 58 2020	CHA08-6A-16S-1(15 5-16.5cm)_15	123.478-OS	61.60673697	4.500280516	0 058943439	1 697164523	5.027353307	17.86957466	2.464109395	0 208928381	5.416698746	0.099492459	1.050717605	100	98.39941725
Mar 13 03 02 2020	CHA08-6A-16S-1(15 5-16.5cm)_16	123.478-OS	62.02459378	4.512105058	0 056199803	1 593725753	4.930689362	18.14641521	2.154297223	0 24817215	5.169123659	0.102229119	1.062448885	100	95.37400003
Mar 13 03 06 2020	CHA08-6A-16S-1(15 5-16.5cm)_17	123.478-OS	62.16437594	4.954650072	0 054836637	1 596775633	4.405479545	18.24340582	2.004977688	0 225374092	5 30507694	0.065866995	0.979180637	100	95.19183336
Mar 13 03 21 2020	CHA08-6A-16S-1(15 5-16.5cm)_21	123.478-OS	61.54887443	4.532068558	0 045240462	1.715665391	5.218223669	17.72481904	2.515920964	0 229290752	5 351242053	0.099876235	1.018778449	100	97.92119191
Mar 13 03 25 2020	CHA08-6A-16S-1(15 5-16.5cm)_22	123.478-OS	62.10065148	4.746112819	0 058879168	1.770492456	4.578705755	17.98788929	2.365542748	0 26880752	5 012964105	0.0693786	1.04057606	100	97.14811234
060418	MEX5-1C-66Y-1_151-151 5cm-15	124.916-OS	78.1351	4.1706	0 0901	3.4647	0.6301	12.3436	0.0991	0	0 882	0.0648	0.1198	100	93.9155
060418	MEX5-1C-66Y-1_151-151 5cm-19	124.916-OS	77.5919	3.0037	0 0803	5.1001	0.7979	11.2155	0.3732	0 398	1 0344	0.0883	0.3166	100	95.5212
060418	MEX5-1C-66Y-1_151-151 5cm-20	124.916-OS	74.5415	3.5876	0 0466	4 9398	0.9694	13.8397	0.3659	0 048	1.446	0.0344	0.1811	100	96.9707
060418	MEX5-1C-66Y-1_151-151 5cm-27	124.916-OS	78.2257	4.0858	0 0846	3 5232	0.6409	12.306	0.129	0 0435	0 8492	0	0.112	100	92.8596
01/10/2021	1C-70Y-1-142-143cm	130.06-S	66.71	4.43	0 06	2 64	3.46	16.46	1.21	0 20	3 88	0.07	0.87	100	
01/10/2021	1C-70Y-1-142-143cm	130.06-S	68.49	4.53	0 05	2 88	3.60	14.89	1.31	0 20	2 96	0.05	1.03	100	
01/10/2021	1C-70Y-1-142-143cm	130.06-S	63.76	4.59	0.11	2 09	4.31	17.53	1.62	0 27	4 86	0.04	0.82	100	
01/10/2021	1C-70Y-1-142-143cm	130.06-S	64.13	4.60	0.12	2 23	4.52	16.53	1.97	0 24	4 60	0.08	0.99	100	
01/10/2021	1C-70Y-1-142-143cm	130.06-S	63.24	4.76	0 06	1 86	4.37	17.34	2.11	0 26	5.15	0.03	0.82	100	
01/10/2021	1C-70Y-1-142-143cm	130.06-S	67.25	4.84	0 08	2 69	3.54	15.32	1.44	0.19	3 64	0.05	0.97	100	
060418	MEX4-1A-63Y-1_76.5-80cm-6	131.00-S	68.3652	5.5598	0 0007	3.1988	1.0587	17.9086	0.1796	0.1176	3.1899	0	0.421	100	100.742
060418	MEX4-1A-63Y-1_76.5-80cm-7	131.00-S	65.5266	4.8558	0 0346	2 6135	3.5609	17.4981	1.0788	0 2557	3 5638	0.0946	0.9175	100	101.6692
060418	MEX4-1A-63Y-1_76.5-80cm-9	131.00-S	65.8988	5.1054	0 0571	2 8004	2.6769	18.0304	0.3022	0 249	4 0312	0.0483	0.8003	100	100.2976
060418	MEX4-1A-63Y-1_76.5-80cm-10	131.00-S	65.6039	4.9357	0 0162	2 807	2.0169	19.0108	0.2519	0 2653	4.4645	0	0.6278	100	99.4874
060418	MEX4-1A-63Y-1_76.5-80cm-29	131.00-S	68.0024	4.9622	0 072	3.7996	2.3061	16.0667	0.1506	0 3516	3 3615	0.0346	0.8927	100	94.5984
060418	MEX4-1A-63Y-1_76.5-80cm-30	131.00-S	67.0872	4.7572	0 0764	3 2908	2.0214	17.6773	0.1516	0 2211	3 8128	0	0.9041	100	97.8541
Mar 10 00 20 2020	MEXI-CHA16-1C-72Y-1(29.5-31cm)_4	134.623-S	64.20087592	4.503619918	0 039310303	2 039090561	4.761381568	16.05876783	1.870918144	0 221041621	5.160791059	0.084086209	1.060116876	100	95.14045315
Mar 10 00 24 2020	MEXI-CHA16-1C-72Y-1(29.5-31cm)_5	134.623-S	64.24377272	4.250257127	0 033887714	2 016882084	5.129228041	15.56082801	2.50830513	0 204759602	4 903992478	0.109648767	1.038438324	100	97.67551686
Mar 10 00 36 2020	MEXI-CHA16-1C-72Y-1(29.5-31cm)_8	134.623-S	64.45774714	4.358476056	0 031329859	2 553180031	5.767542143	14.31163077	2.207330943	0 304143757	4.414661887	0.112706115	1.481251299	100	98.30877452
Mar 10 00:40 2020	MEXI-CHA16-1C-72Y-1(29.5-31cm)_9	134.623-S	63.21413463	4.51356542	0 040892668	2.156528752	5.238737298	15.62227042	2.482042526	0 292250335	5.106497327	0.115150498	1.21793013	100	98.30613194
Mar 10 00 52 2020	MEXI-CHA16-1C-72Y-1(29.5-31cm)_12	134.623-S	64.33585768	4.20642671	0 044884917	2 325119575	5.549959334	14.43359445	3.002437017	0 343713329	4 3570719	0.115750518	1.285184572	100	98.91964373
Mar 10 01:12 2020	MEXI-CHA16-1C-72Y-1(29.5-31cm)_17	134.623-S	59.46431303	4.144545583	0 055731313	1 993309744	7.383382011	14.59084156	3.53914179	0.403848622	6.437576878	0.136378998	1.850930477	100	98.32892283
Mar 10 01:16 2020	MEXI-CHA16-1C-72Y-1(29.5-31cm)_18	134.623-S	60.0298465	3.816980557	0 024810992	2 019737753	7.310015321	14.52639522	3.588366567	0 280302691	6.459059821	0.170806249	1.773678332	100	97.53741527
Mar 10 01 20 2020	MEXI-CHA16-1C-72Y-1(29.5-31cm)_19	134.623-S	58.57526169	4.107191316	0 027729687	1.725402772	6.264855301	17.03451309	2.916752304	0 322794102	7 394583307	0.103421464	1.527494966	100	97.36856969
Mar 10 01 24 2020	MEXI-CHA16-1C-72Y-1(29.5-31cm)_20	134.623-S	59.9520312	3.912125534	0 037823979	2 049223655	7.207965791	14.57648115	3.537714469	0 359378775	6 392354386	0.149970547	1.824930518	100	98.08592611
Mar 10 01 28 2020	MEXI-CHA16-1C-72Y-1(29.5-31cm)_21	134.623-S	60.0967166	4.07429127	0 048582901	2 022593564	7.124814514	14.58200247	3.425196136	0 351158832	6 32187536	0.143614307	1.809154042	100	98.38852628
Mar 10 01 32 2020	MEXI-CHA16-1C-72Y-1(29.5-31cm)_22	134.623-S	60.01354938	4.143205991	0 038610399	2 073521447	7.139859564	14.66472558	3.380963542	0 304082431	6 322708254	0.100611755	1.818161663	100	97.90108528
Mar 10 01 36 2020	MEXI-CHA16-1C-72Y-1(29.5-31cm)_23	134.623-S	60.08962947	3.819080063	0 031150824	2 015641532	7.258345517	14.71622642	3.369582561	0 36851628	6 352324829	0.147101112	1.832401393	100	98.23175244
Mar 10 01:40 2020	MEXI-CHA16-1C-72Y-1(29.5-31cm)_24	134.623-S	60.13539602	3.999339537	0 029768673	1 957392213	7.238273287	14.51531472	3.40504687	0 315629494	6.473666953	0.11550653	1.814665697	100	98.08969237
Mar 10 01 52 2020	MEXI-CHA16-1C-72Y-1(29.5-31cm)_27	134.623-S	59.55439575	3.89799679	0 056620771	1 904331703	7.118330805	14.98374957	3.604991567	0 304489401	6 568416837	0.143079468	1.863597335	100	98.1971784
Mar 10 01 56 2020	MEXI-CHA16-1C-72Y-1(29.5-31cm)_28	134.623-S	60.22516027	4.026133788	0 044326471	1 909919376	7.047296095	14.53185077	3.462367212	0 327546066	6.414060794	0.152487146	1.858852013	100	97.90989206
Mar 10 02 00 2020	MEXI-CHA16-1C-72Y-1(29.5-31cm)_29	134.623-S	59.58259402	3.992708769	0 034808242	1 913435529	7.13467184	15.08622703	3.491002056	0 279789057	6 50364523	0.169461179	1.811657044	100	98.25259181
Jan 21 03 20 2020	CHA08-6A-26S-1_34-36cm_1	136.533-OS	64.21366443	4.640614062	0.117569624	1 96504471	4.221194583	17.09876936	1.865127183	0.184394972	4.799914293	0.069609211	0.824097564	100	90.07428638
Jan 21 03 27 2020	CHA08-6A-26S-1_34-36cm_3	136.533-OS	64.40623054	4.2345445	0 098661638	1 938576638	4.040530594	17.47277868	1.830276267	0 238996944	4 847225753	0.071586545	0.82059191	100	92.33578725
Jan 21 04 03 2020	CHA08-6A-26S-1_34-36cm_12	136.533-OS	63.40351933	4.69808333	0 071810616	1.483605262	3.45524734	18.84508317	1.384080076	0.149131409	5.76145515	0.072325757	0.675658563	100	97.06085822
Jan 21 04:46 2020	CHA08-6A-26S-1_34-36cm_23	136.533-OS	66.89118443	4.25882355	0.100220627	2 842902993	3.743642522	16.1527079	1.308952184	0.181694063	3 615009998	0.040154622	0.864707109	100	90.40055205
Jan 21 04 50 2020	CHA08-6A-26S-1_34-36cm_24	136.533-OS	66.63264489	4.843899905	0 071233822	2 859906044	3.668294749	15.79613039	1.268173097	0.156379799	3 823625986	0.060997258	0.818714062	100	94.75835772
Jan 21 05 06 2020	CHA08-6A-26S-1_34-36cm_28	136.533-OS	63.98275527	5.051000536	0 072947513	2.100314625	4.396832909	16.69737015	1.93638763	0 279006751	4 564778715	0.080016864	0.838589034	100	97.6044244
Mar 14 16:10 2020	CHA16-1C-73Y-1(101-103cm)_1	136.783-S (101 - 103 cm)	77.86239544	3.108541219	0.111385521	5.156930411	0.933836321	12.31182813	0.007950006	0 024740739	0 377478955	0.010752304	0.094160956	100	95.79341985
Mar 14 16:14 2020	CHA16-1C-73Y-1(101-103cm)_2	136.783-S (101 - 103 cm)	77.64649747	3.751465487	0 084823947	4 5570863	1.049238952	12.3574892	0.050358463	0	0 371713244	0.053442194	0.077884748	100	96.55292243
Mar 14 16:18 2020	CHA16-1C-73Y-1(101-103cm)_3	136.783-S (101 - 103 cm)	77.70906352	3.664886891	0.104213888	4 655923939	1.00851737	12.27052088	0.040295	0 011717581	0 397360814	0.016798657	0.120701458	100	96.4362833
Mar 14 16 22 2020	CHA16-1C-73Y-1(101-103cm)_4	136.783-S (101 - 103 cm)	77.3648368	3.249561916	0.165565357	5 504621408	0.981133945	12.20415485	0.051244989	0	0 39513794	0	0.083742787	100	93.73941671
Mar 14 16 26 2020	CHA16-1C-73Y-1(101-103cm)_5	136.783-S (101 - 103 cm)	77.6421319	3.424741344	0.176261699	5 043829842	1.039899629	12.0557658	0.075730004	0	0.419193461	0.006209467	0.116236856	100	91.79532509
Mar 14 16 30 2020	CHA16-1C-73Y-1(101-103cm)_6	136.783-S (101 - 103 cm)	77.63876739	3.282963392	0.114996175	5.173211261	1.036404434	12.1177497	0.047562641	0	0.421508943	0.039876837	0.126959226	100	92.78569457
Mar 14 16:42 2020	CHA16-1C-73Y-1(101-103cm)_9	136.783-S (101 - 103 cm)	77.58464239	3.246070233	0.112854389	5 244163036	1.022215155	12.15337677	0.024474433	0 034506593	0.457186134	0.019822936	0.10068793	100	95.34409906
Mar 14 16:46 2020	CHA16-1C-73Y-1(101-103cm)_10	136.783-S (101 - 103 cm)	77.35651841	3.123791744	0.117421584	5 562625335	1.027838272	12.24958593	0.021744846	0	0.403917701	0.052280313	0.084275865	100	95.63829451
Mar 14 16 50 2020	CHA16-1C-73Y-1(101-103cm)_11	136.783-S (101 - 103 cm)	77.63102999	3.419399836	0.129082986	5 211555167	0.920874934	12.14040618	0.018735729	0	0.409689055	0.049598905	0.069627216	100	95.36500797
Mar 14 16 54 2020	CHA16-1C-73Y-1(101-103cm)_12	136.783-S (101 - 103 cm)	77.9399545	3.713233835	0 090638269	4 578421132	0.928963288	12.13827277	0.020282273	0 009921635	0 386840413	0.063767175	0.129704707	100	96.75824639
Mar 14 16 58 2020	CHA16-1C-73Y-1(101-103cm)_13	136.783-S (101 - 103 cm)	77.66621883	3.636082305	0.106630654	4 660539825	1.033259158	12.25898091	0.031689935	0 058360778	0 391880659	0.054303611	0.102053339	100	96.12620358
Mar 14 17 02 2020	CHA16-1C-73Y-1(101-103cm)_14	136.783-S (101 - 103 cm)	77.46123241	3.398005442	0 092915705	5 393082564	1.008706933	12.06985937	0.013163932	0	0.401345679	0.043270081	0.118417879	100	95.67811987
Mar 14 17:10 2020	CHA16-1C-73Y-1(101-103cm)_16	136.783-S (101 - 103 cm)	77.66522662	3.693611987	0 095102432	4 598359355	1.067611848	12.31533955	0.035100817	0	0.403192509	0.054553263	0.071901619	100	95.68630157
Mar 14 17:14 2020	CHA16-1C-73Y-1(101-103cm)_17	136.783-S (101 - 103 cm)	77.43416014	3.461469342	0.141712014	4 951004473	1.054822025	12.43299056	0	0 031153566	0 389996496	0.013950924	0.088740462	100	95.33418977
Mar 14 17:18 2020	CHA16-1C-73Y-1(101-103cm)_18	136.783-S (101 - 103 cm)	77.89610162	3.550248493	0 098850342	4 618588906	0.962527356	12.29300803	0.01693572	0 024137874	0 384638592	0.047544298	0.107418765	100	95.70022554
Mar 14 17 22 2020	CHA16-1C-73Y-1(101-103cm)_19	136.783-S (101 - 103 cm)	77.66729903	3.427466251	0.133235931	5 062757041	0.964470553	12.18357538	0.067941609	0	0 384394516	0.032918338	0.075941356	100	95.99512598
Mar 14 17 26 2020	CHA16-1C-73Y-1(101-103cm)_20	136.783-S (101 - 103 cm)	77.73758482	3.04768269	0.133905884	5 295956193	0.990538131	12.1555968	0.040357017	0 016361491	0.466194843	0.001184055	0.114638076	100	92.90107056
Mar 14 17 34 2020	CHA16-1C-73Y-1(101-103cm)_22	136.783-S (101 - 103 cm)	77.83701873	3.336816218	0 086387206	5 084683874	0.974289903	12.02458372	0.067864757	0 009645174	0.421661826	0.035225851	0.121822735	100	95.38449431
Mar 14 17 38 2020	CHA16-1C-73Y-1(101-103cm)_23	136.783-S (101 - 103 cm)	77.65174062	3.306316997	0.117007498	5 032580559	1.008123177	12.29325578	0.053537703	0 003879281	0 387823239	0.043720544	0.102014602	100	95.37850301
Mar 14 17:42 2020	CHA16-1C-73Y-1(101-103cm)_24	136.783-S (101 - 103 cm)	78.00192894	3.20150826	0.114614331	5 205010477	0.957419243	12.04217801	0.02408843	0	0 385899477	0.009056718	0.058296117	100	96.06128599
Mar 14 17 50 2020	CHA16-1C-73Y-1(101-103cm)_26	136.783-S (101 - 103 cm)	77.73055976	3.747369791	0.105162008	4 607989092	0.992081516	12.2166631	0.069059778	0 015810707	0 386322156	0.027044631	0.101937456	100	96.13738034
Mar 14 17 54 2020	CHA16-1C-73Y-1(101-103cm)_27	136.783-S (101 - 103 cm)	77.64732006	3.816355718	0.107311806	4 590094825	1.00593989	12.29784033	0.032742066	0	0.402838459	0.024208034	0.075348817	100	95.42286525
Mar 14 17 58 2020	CHA16-1C-73Y-1(101-103cm)_28	136.783-S (101 - 103 cm)	77.78409829	3.40608979	0.104555918	4 812724678	1.010498854	12.37255331	0.028521928	0 003888009	0 386068787	0.021331509	0.069668918	100	95.16438829

Date Analysed	Core Section Identifier	sample_no	SiO2	Na2O	Cl	K2O	FeOt	Al2O3	MgO	P2O5	CaO	MnO	TiO2	total	Analytical Total
Mar 14 18 02 2020	CHA16-1C-73Y-1(101-103cm)_29	136.783-S (101 - 103 cm)	77.80400288	3.330016552	0.113411131	4 699064558	1.013837626	12.40213008	0.032888997	0	0.410983354	0.061246235	0.132418583	100	94.69969916
Mar 14 18 06 2020	CHA16-1C-73Y-1(101-103cm)_30	136.783-S (101 - 103 cm)	78.03284419	3.508655908	0 09758991	4 552790621	1.011083504	12.33623599	0.002675321	0	0 388462644	0.011487365	0.058174547	100	94.88685862
Mar 14 18:10 2020	CHA16-1C-73Y-1(101-103cm)_31	136.783-S (101 - 103 cm)	77.75027256	3.570241354	0.112839413	4 680746019	1.02384972	12.27105617	0.019484038	0 00449268	0 391699036	0.057046592	0.118272422	100	95.7112388
Mar 14 18:14 2020	CHA16-1C-73Y-1(101-103cm)_32	136.783-S (101 - 103 cm)	77.84657485	3.592660509	0.105151998	4 539463107	0.999363212	12.35414669	0.039919928	0	0.437381988	0.01834656	0.066991153	100	95.38572949
Mar 14 18:18 2020	CHA16-1C-73Y-1(101-103cm)_33	136.783-S (101 - 103 cm)	77.69708069	3.382712955	0.109959328	4 885928619	1.015905621	12.37718475	0	0 008298817	0.4006254	0.026556215	0.095747603	100	96.3992798
Mar 14 18 26 2020	CHA16-1C-73Y-1(101-103cm)_35	136.783-S (101 - 103 cm)	77.6971559	3.558646648	0.100809094	4.769686467	0.908493786	12.3949698	0.049009463	0	0 380637643	0.05509092	0.085500275	100	96.02308311
Mar 14 18 30 2020	CHA16-1C-73Y-1(101-103cm)_36	136.783-S (101 - 103 cm)	77.74151154	3.508641813	0.117318872	4 8160285	0.962842295	12.26967345	0.034475722	0 006477088	0 368567214	0.062681499	0.111782006	100	95.7220249
Mar 14 18 34 2020	CHA16-1C-73Y-1(101-103cm)_37	136.783-S (101 - 103 cm)	78.0079243	3.47797024	0.118744127	4 676206758	0.97763624	12.17655614	0.054992952	0 048863734	0.421594191	0.021436993	0.018074327	100	95.16260145
Mar 14 18 38 2020	CHA16-1C-73Y-1(101-103cm)_38	136.783-S (101 - 103 cm)	78.06967003	3.684604207	0.10558751	4 620760318	0.96982166	12.0110966	0.018780949	0 006481609	0 390778327	0.036798815	0.085619971	100	95.65525359
Mar 14 18:42 2020	CHA16-1C-73Y-1(101-103cm)_39	136.783-S (101 - 103 cm)	77.75153092	3.4325259	0.107547523	4 967720682	0.987239108	12.23150445	0.027440972	0 01265265	0 398558467	0.018149293	0.065130033	100	96.42249044
Mar 14 18:46 2020	CHA16-1C-73Y-1(101-103cm)_40	136.783-S (101 - 103 cm)	77.82270441	3.146017295	0.10702705	5.10549367	1.032601849	12.17437286	0.031869927	0	0.426015783	0.065911086	0.087986069	100	95.58331309
Mar 14 18 50 2020	CHA16-1C-73Y-1(101-103cm)_41	136.783-S (101 - 103 cm)	77.67820777	3.457420689	0 067086927	5 026327008	1.047398811	12.14588922	0.031939233	0	0.407921746	0.047459327	0.090349266	100	96.29297879
Jan 17 14 26 2020	CHA16-1C-73Y-1_97-101cm_4	136.783-S (97 -101 cm)	77.61985423	3.769747791	0.100043307	4 660558902	1.036319434	12.26448092	0.026823205	0	0.406076404	0.009838627	0.106257177	100	96.55818377
Jan 17 14:45 2020	CHA16-1C-73Y-1_97-101cm_9	136.783-S (97 -101 cm)	77.51972144	3.936556933	0.112323091	4 529748701	1.050005175	12.32005201	0.043879488	0	0.41370589	0	0.07400727	100	95.2609111
Jan 17 14:49 2020	CHA16-1C-73Y-1_97-101cm_10	136.783-S (97 -101 cm)	77.49329275	3.909569098	0.111716988	4 637343531	0.915499728	12.35455022	0.016710255	0 049184902	0.429211833	0.009458635	0.073462065	100	95.15115109
Jan 17 14 53 2020	CHA16-1C-73Y-1_97-101cm_11	136.783-S (97 -101 cm)	77.418269	3.649501348	0.106878254	4 956446467	0.942987874	12.3381388	0.049841761	0 009384432	0.428034372	0.017413335	0.083104359	100	95.90351301
Jan 17 14 57 2020	CHA16-1C-73Y-1_97-101cm_12	136.783-S (97 -101 cm)	77.88772775	3.661478233	0 097258016	4.751948767	0.946312833	12.10750894	0.033702243	0 01986768	0.413268552	0.029333434	0.051593557	100	96.13603513
Jan 17 15 01 2020	CHA16-1C-73Y-1_97-101cm_13	136.783-S (97 -101 cm)	77.31110471	3.850085917	0 099851822	4 939300377	0.947942753	12.23528332	0.048517343	0 003443166	0.422883421	0.026606285	0.114980886	100	95.84201703
Jan 17 15 05 2020	CHA16-1C-73Y-1_97-101cm_14	136.783-S (97 -101 cm)	77.52946628	3.830909887	0.110359274	4 641660472	1.050158485	12.25450362	0.056165915	0 03187234	0 375719861	0.016922447	0.102261416	100	96.32176451
Jan 17 15 09 2020	CHA16-1C-73Y-1_97-101cm_15	136.783-S (97 -101 cm)	77.49584769	3.837171404	0.115535654	4.771878368	0.930958077	12.19597428	0.029540963	0 035112747	0.445322139	0.022707644	0.119951029	100	95.1221516
Jan 17 15:13 2020	CHA16-1C-73Y-1_97-101cm_16	136.783-S (97 -101 cm)	77.45263206	3.466817554	0.105790463	5 290451092	0.938430927	12.14695891	0.023637392	0 011556059	0.439655499	0.042127086	0.08194296	100	95.18816461
Jan 17 15:17 2020	CHA16-1C-73Y-1_97-101cm_17	136.783-S (97 -101 cm)	77.60357912	3.723260034	0.103377667	4.741014775	0.950594334	12.31625301	0.000208003	0 036088582	0.433790994	0	0.091833481	100	96.15229577
Jan 17 15 21 2020	CHA16-1C-73Y-1_97-101cm_18	136.783-S (97 -101 cm)	77.4227504	3.943818814	0.11466288	4 695179972	1.01463122	12.26496012	0.037873181	0 028900471	0.402832922	0	0.074390022	100	95.84618813
Jan 17 15 25 2020	CHA16-1C-73Y-1_97-101cm_19	136.783-S (97 -101 cm)	77.83901397	3.648651879	0.123949917	4 579584115	1.009654692	12.19440744	0.023872608	0	0.400934718	0.054938273	0.124992389	100	95.92584099
Jan 17 15 29 2020	CHA16-1C-73Y-1_97-101cm_20	136.783-S (97 -101 cm)	77.740079	3.605979135	0 092725178	4 823198218	0.949688411	12.26730287	0.022813337	0 010513059	0.406119458	0.00904123	0.072540105	100	95.11979607
Jan 17 15 33 2020	CHA16-1C-73Y-1_97-101cm_21	136.783-S (97 -101 cm)	77.51517123	3.644886657	0.131930191	4 900892543	1.028867887	12.25672808	0.030041429	0 006617518	0.43444528	0.022163432	0.02825575	100	95.20186295
Jan 17 15 37 2020	CHA16-1C-73Y-1_97-101cm_22	136.783-S (97 -101 cm)	77.28914261	3.836632405	0 092993168	5.124285298	0.958323575	12.21654636	0	0 036134488	0 3867453	0.02433764	0.034859153	100	94.09293409
Jan 17 15:40 2020	CHA16-1C-73Y-1_97-101cm_23	136.783-S (97 -101 cm)	77.51378992	3.797789605	0 098846579	4.783713367	0.933993515	12.3419453	0.013526374	0	0.405999316	0.028197287	0.082198734	100	96.10853626
Jan 17 15:44 2020	CHA16-1C-73Y-1_97-101cm_24	136.783-S (97 -101 cm)	77.57309566	3.790874067	0.125245453	4 569765501	0.988787495	12.3912453	0.034767132	0	0.429038979	0.019582692	0.077597726	100	95.49248896
Jan 17 15 52 2020	CHA16-1C-73Y-1_97-101cm_26	136.783-S (97 -101 cm)	77.39259364	3.98860543	0.121557499	4 676552205	0.965640083	12.2718495	0.048010991	0 010551866	0.43146581	0.032183192	0.060989787	100	94.76996575
Jan 17 15 56 2020	CHA16-1C-73Y-1_97-101cm_27	136.783-S (97 -101 cm)	77.50369387	3.807538528	0.121528285	4 694383131	1.070252146	12.22260639	0.029625779	0 018463954	0.44219605	0	0.089711867	100	95.8624574
Jan 17 16 00 2020	CHA16-1C-73Y-1_97-101cm_28	136.783-S (97 -101 cm)	77.63862789	3.735586889	0.10906672	4 656705037	1.006421982	12.29428824	0.025766236	0 015832266	0 397462306	0.01728097	0.102961467	100	96.63809483
Jan 17 16 08 2020	CHA16-1C-73Y-1_97-101cm_30	136.783-S (97 -101 cm)	77.49523735	4.00986109	0.145278737	4 57044621	0.904904768	12.31950441	0	0	0.416521696	0.053324854	0.08492088	100	95.26514546
Mar 12 05 36 2020	CHA16-1C-74Y-1(30-35cm)_1	137.244-OS	58.81516271	4.044706139	0 066283105	1 926000583	7.187584636	15.44727119	3.718820275	0 504377999	6 525863678	0.107364288	1.656565395	100	97.61160077
Mar 12 05:44 2020	CHA16-1C-74Y-1(30-35cm)_3	137.244-OS	58.38492243	3.987968999	0.173632046	2.1985212	7.226238952	15.1162906	4.23343152	0 631997634	6 206987761	0.111868939	1.72813992	100	97.7930074
Mar 12 05:48 2020	CHA16-1C-74Y-1(30-35cm)_4	137.244-OS	59.02335969	3.792116776	0 076509968	2 066178272	6.96829518	15.59439425	3.631154884	0 671755327	6 351963895	0.129084999	1.695186757	100	97.76503932
Mar 12 05 52 2020	CHA16-1C-74Y-1(30-35cm)_5	137.244-OS	59.35716339	3.839234842	0 060523453	2 003747583	6.676434217	15.83824016	3.483438106	0 568908035	6 370889752	0.110051983	1.691368473	100	97.317647
Mar 12 05 56 2020	CHA16-1C-74Y-1(30-35cm)_6	137.244-OS	58.9294049	4.176377762	0 075263698	2 000937729	6.90921617	15.65546137	3.565122553	0 53414064	6 368466783	0.122087673	1.663520717	100	98.45383848
Mar 12 06 00 2020	CHA16-1C-74Y-1(30-35cm)_7	137.244-OS	58.75858611	4.082629488	0 046913903	2 001796729	6.899571813	15.65083284	3.634030985	0 666532803	6.477608903	0.157679989	1.623816444	100	97.41248807
Mar 12 06 04 2020	CHA16-1C-74Y-1(30-35cm)_8	137.244-OS	59.29209159	3.896380516	0 076817857	2.115571993	7.466240005	14.96892243	3.450641698	0 6822474	6 089971806	0.163905481	1.797209218	100	97.37319299
Mar 12 06 08 2020	CHA16-1C-74Y-1(30-35cm)_9	137.244-OS	59.19806369	4.228585644	0 069034919	2 032240956	7.040234624	15.37826188	3.461958211	0 607670424	6.106935133	0.140929272	1.736085238	100	97.92145929
Mar 12 06:12 2020	CHA16-1C-74Y-1(30-35cm)_10	137.244-OS	59.11918851	3.869725588	0 076486478	2 034867534	7.558798934	14.99504498	3.619814609	0 604906814	6.186406323	0.145303858	1.789456374	100	97.79506363
Mar 12 06:16 2020	CHA16-1C-74Y-1(30-35cm)_11	137.244-OS	58.92473389	4.122880982	0 063349816	2 032943837	7.067798754	15.43091963	3.511448445	0 553669948	6.406853304	0.129677175	1.755724223	100	97.39570588
Mar 12 06 20 2020	CHA16-1C-74Y-1(30-35cm)_12	137.244-OS	58.99005883	4.081791091	0 039263875	1 957986356	7.222233118	15.23166881	3.530624333	0 615037503	6 342626014	0.176531217	1.812178861	100	96.0170123
Mar 12 06 24 2020	CHA16-1C-74Y-1(30-35cm)_13	137.244-OS	59.00489374	3.967184897	0 071890801	1 967212455	7.184182063	15.31683074	3.666636827	0 629016046	6 36511674	0.107012238	1.720023456	100	97.09169922
Mar 12 06:40 2020	CHA16-1C-74Y-1(30-35cm)_17	137.244-OS	59.46280527	3.833621073	0 06155415	1 970141109	7.016524339	15.49253622	3.593210728	0.498765826	6 267702804	0.127191493	1.675946981	100	97.96252618
Mar 12 06:44 2020	CHA16-1C-74Y-1(30-35cm)_18	137.244-OS	59.110819	3.839889385	0 057302869	1 978435377	6.983524783	15.61837424	3.587836175	0 612081247	6.427352234	0.135620207	1.648764487	100	97.55183428
Mar 12 06:48 2020	CHA16-1C-74Y-1(30-35cm)_19	137.244-OS	58.87456637	4.058364701	0 047349397	1 969489986	7.200974188	15.35667807	3.663455465	0.715435353	6 306449798	0.103066574	1.704170091	100	97.9949131
Mar 12 06 52 2020	CHA16-1C-74Y-1(30-35cm)_20	137.244-OS	59.07099629	3.940621729	0 07310494	2 025551779	7.19284791	15.16913089	3.670669975	0 620278136	6 36455102	0.134591232	1.737656094	100	97.25744958
Mar 12 06 56 2020	CHA16-1C-74Y-1(30-35cm)_21	137.244-OS	58.79952948	4.082583966	0 038085041	1 837526252	7.129130113	15.62030799	3.449211289	0.494714634	6 682846873	0.110662196	1.755402174	100	97.41357425
Mar 12 07 00 2020	CHA16-1C-74Y-1(30-35cm)_22	137.244-OS	59.07910598	3.920199965	0 05732248	1 979112448	7.319570351	15.01736533	3.640336367	0 593704497	6.4090429	0.117926389	1.866313293	100	97.51846098
Mar 12 07 04 2020	CHA16-1C-74Y-1(30-35cm)_23	137.244-OS	59.29635789	4.165883891	0 080563175	2 003803471	7.042319516	15.26144095	3.483535264	0 641839156	6 206652801	0.091250127	1.726353759	100	97.31493276
Mar 12 07 08 2020	CHA16-1C-74Y-1(30-35cm)_24	137.244-OS	59.29603133	3.984454349	0 042297005	2 053550263	7.012104318	15.37482184	3.402150435	0.718775927	6 252600799	0.105946847	1.757266891	100	97.8792697
Mar 12 07:12 2020	CHA16-1C-74Y-1(30-35cm)_25	137.244-OS	59.85519063	3.930879698	0 07059296	2 281482635	7.44835972	14.58957399	3.243183836	0 696628236	5 811130659	0.139344365	1.933633265	100	97.74345706
Mar 12 07:16 2020	CHA16-1C-74Y-1(30-35cm)_26	137.244-OS	59.31092545	4.142748205	0 064891385	2 03298958	6.796514799	15.44138571	3.696344691	0.482145847	6 232447854	0.101033422	1.698573062	100	97.39351444
Mar 12 07 20 2020	CHA16-1C-74Y-1(30-35cm)_27	137.244-OS	58.93010227	4.025677168	0 057137718	2 064726127	7.597378736	14.73727492	3.741038429	0 594812894	6.194178382	0.207596969	1.850076382	100	97.83379854
Mar 12 07 24 2020	CHA16-1C-74Y-1(30-35cm)_28	137.244-OS	59.54401452	3.808572495	0 059224592	1 926583129	6.757854863	15.75193033	3.394455989	0.725143401	6 218072533	0.101629808	1.712518337	100	98.10113935
Mar 12 07 28 2020	CHA16-1C-74Y-1(30-35cm)_29	137.244-OS	59.24206541	3.998392702	0 072740455	2 071011556	7.136910303	15.39300641	3.478891334	0 676435852	6.151822505	0.110998058	1.667725414	100	98.01973309
Mar 12 07 32 2020	CHA16-1C-74Y-1(30-35cm)_30	137.244-OS	59.21966544	3.934526724	0 054003194	2 058234928	7.086552225	15.45410894	3.443977256	0 631843714	6 296976166	0.122373275	1.697738137	100	98.14234383
Mar 12 07 36 2020	CHA16-1C-74Y-1(30-35cm)_31	137.244-OS	59.35332429	4.026971178	0 067981677	2.111552074	7.048526151	15.54121259	3.326982049	0 648390786	6.108050634	0.058608445	1.708400132	100	97.08498431
Mar 12 07:40 2020	CHA16-1C-74Y-1(30-35cm)_32	137.244-OS	59.24269418	3.907692551	0 068996824	2 064793846	7.192282513	15.20114644	3.475395583	0.745544301	6 276155553	0.122865456	1.702432748	100	97.83058989
10.05.12	CH08-VI-27-40	137.244-S	58.10434343	4.445959596	0 06040404	2.11010101	7.328686869	15.55868687	3.575656566	0 655858586	6 236464646	0.16969697	1.754141414	100	99
10.05.12	CH08-VI-27-40_8	137.244-S	58.35365983	4.073136895	0 077725432	2.17418401	7.552946017	15.26833515	3.570607018	0.703886373	6 31035248	0.162240438	1.752926357	100	98.6807
10.05.12	CH08-VI-27-40_7	137.244-S	58.81162866	4.132016421	0 064626265	2 21934317	7.263341869	15.24946145	3.439417957	0 669430557	6 238974922	0.101105556	1.810653172	100	98.412
10.05.12	CH08-VI-27-40_6	137.244-S	58.39223125	3.895819809	0 066029128	2 02016724	7.297028791	15.68232293	3.600106538	0 647024689	6.472474867	0.156667271	1.770127491	100	98.7443
10.05.12	CH08-VI-27-40_5	137.244-S	58.33295369	4.228663065	0.100733074	1 992085114	7.001707906	15.93394745	3.399412205	0 667369267	6 504420613	0.125536695	1.713170925	100	98.7759

Date Analysed	Core Section Identifier	sample_no	SiO2	Na2O	Cl	K2O	FeOt	Al2O3	MgO	P2O5	CaO	MnO	TiO2	total	Analytical Total
10.05.12	CH08-VI-27-40_4	137.244-S	58.49658457	4.182988418	0 067175474	2.139599537	7.707171589	15.05894041	3.755250613	0 672766416	6 031831462	0.138903502	1.748788009	100	98.8456
10.05.12	CH08-VI-27-40_3	137.244-S	59.76764527	4.249913255	0 082639198	2 069470308	6.478399859	15.93160554	2.752860548	0 690986887	6.113042211	0.100193612	1.763243316	100	97.4114
10.05.12	CH08-VI-27-40_20	137.244-S	58.84700244	4.412970532	0 045701129	1 927728828	7.454907197	15.31294538	3.47287684	0.723856807	5 918449556	0.141704172	1.741857122	100	97.8094
10.05.12	CH08-VI-27-40_2	137.244-S	58.88832837	4.099530305	0 065017676	2 231000669	7.322678608	15.45139552	3.131801984	0 650980692	6.190446522	0.10762586	1.861193793	100	99.5114
10.05.12	CH08-VI-27-40_19	137.244-S	61.0936343	4.203109254	0 075757043	2 204389287	7.351447371	14.5584138	2.449243284	0 649059015	5 505246225	0.072240469	1.837459949	100	99.5287
10.05.12	CH08-VI-27-40_18	137.244-S	58.68123273	4.238793996	0 0686375	2 095509938	7.083571448	15.54473079	3.471283622	0 682645799	6 268286955	0.139089208	1.726218013	100	99.2169
10.05.12	CH08-VI-27-40_17	137.244-S	59.17901915	4.117529075	0 074221816	2.169028224	7.669078621	14.8361164	3.318295525	0 678177666	5 889282227	0.198433909	1.870817387	100	98.2191
10.05.12	CH08-VI-27-40_15	137.244-S	59.05364769	4.030415871	0 055417209	2.19872066	7.12005144	15.63663673	3.290510333	0 651783092	6.115677619	0.144750961	1.702388391	100	99.0667
10.05.12	CH08-VI-27-40_14	137.244-S	58.39572733	4.284634213	0 090045394	1 995438938	7.017455191	15.45015993	3.760039855	0 536662297	6 50895142	0.203195219	1.757690217	100	96.9511
10.05.12	CH08-VI-27-40_13	137.244-S	58.43954399	3.838731471	0 071396184	2 049585508	7.281905864	15.60708468	3.593540615	0 539258308	6.73477075	0.18641776	1.657764865	100	99.0249
10.05.12	CH08-VI-27-40_12	137.244-S	58.2437687	4.306408472	0 065448479	2 091408695	7.359757607	15.20078985	3.573994326	0 663820081	6.453220065	0.138101365	1.903282368	100	98.5508
10.05.12	CH08-VI-27-40_11	137.244-S	57.50684669	4.187803562	0 067987754	1 990003581	7.097760136	15.52097886	4.057779504	0 516363966	6 911752097	0.200836229	1.941887618	100	99.1355
10.05.12	CH08-VI-27-40_10	137.244-S	58.49361277	4.192829059	0 076185427	2 059637102	7.29508346	15.51977078	3.505946106	0 664421911	6 293847091	0.143568554	1.755097746	100	98.8378
10.05.12	CH08-VI-27-40_1	137.244-S	58.34889593	4.172468811	0 070133202	2.1884401	7.330086839	15.18662942	3.637791951	0.708538185	6 242362484	0.173150858	1.941502211	100	98.5268
Mar 11 06 02 2020	CHA08-6A-27S-1(70-72cm)_3	137.544-S (70 - 72 cm)	66.53622982	4.908405645	0 071382427	2 386391977	3.927069753	15.78193096	1.377827368	0 319408481	3.757520701	0.081849058	0.851983802	100	95.54172248
Mar 11 06 06 2020	CHA08-6A-27S-1(70-72cm)_4	137.544-S (70 - 72 cm)	67.00524624	4.610237037	0 060746011	2 295993283	3.559426119	15.96085852	1.371933206	0 339610569	3 902158987	0.05776019	0.836029841	100	97.1257197
Mar 11 06:14 2020	CHA08-6A-27S-1(70-72cm)_6	137.544-S (70 - 72 cm)	67.03436786	4.567888593	0 089833208	2 289651266	3.698251602	16.04366699	1.380254369	0 296297226	3.724791534	0.053133056	0.821864297	100	91.2802762
Mar 11 06:18 2020	CHA08-6A-27S-1(70-72cm)_7	137.544-S (70 - 72 cm)	66.33153105	4.681111813	0 056593201	2 394327753	3.920575985	16.23144902	1.420219865	0 319506424	3.76251504	0.040527366	0.841642483	100	96.47801965
Mar 11 06 22 2020	CHA08-6A-27S-1(70-72cm)_8	137.544-S (70 - 72 cm)	66.77541348	4.70239259	0 064761499	2.431176002	3.857201275	15.78023784	1.480083183	0 282478658	3.762035279	0.053548747	0.810671446	100	95.42706897
Mar 11 06 26 2020	CHA08-6A-27S-1(70-72cm)_9	137.544-S (70 - 72 cm)	67.20208803	4.590197241	0 047155426	2 368022487	3.61691775	15.99250637	1.369967641	0 240093836	3 680173475	0.076268776	0.816608967	100	97.54974934
Mar 11 06 30 2020	CHA08-6A-27S-1(70-72cm)_10	137.544-S (70 - 72 cm)	66.90839384	4.699648461	0 059901234	2.445367683	3.70877836	15.99875079	1.442150454	0 236813413	3 616678254	0.088978505	0.794539004	100	97.32687713
Mar 11 06 58 2020	CHA08-6A-27S-1(70-72cm)_17	137.544-S (70 - 72 cm)	66.61994511	4.724797794	0 080900745	2 279930076	3.760449607	16.12174997	1.445391615	0 331432542	3.782372476	0.030469112	0.822560948	100	95.17835757
Mar 11 07:10 2020	CHA08-6A-27S-1(70-72cm)_20	137.544-S (70 - 72 cm)	66.69505502	4.812057569	0 093644907	2 362119296	3.693437241	15.97454071	1.402258997	0 219026481	3 810885797	0.065194493	0.871779495	100	95.25344482
Mar 11 07:42 2020	CHA08-6A-27S-1(70-72cm)_28	137.544-S (70 - 72 cm)	66.60130067	4.905023759	0 072989532	2 339806264	3.789738789	16.01890729	1.454924665	0 225180415	3.727125023	0.034372375	0.830631224	100	96.5891935
Mar 11 07:46 2020	CHA08-6A-27S-1(70-72cm)_29	137.544-S (70 - 72 cm)	66.75178534	4.760706623	0 075183719	2 359107136	3.848411559	15.94091687	1.436593676	0 271346356	3.702772505	0.047900132	0.805276092	100	97.49451242
Mar 11 07 50 2020	CHA08-6A-27S-1(70-72cm)_30	137.544-S (70 - 72 cm)	66.29356256	4.872017306	0 07217014	2 21149157	3.674612517	16.41498531	1.312115706	0 317421263	3 905170479	0.084360313	0.842092839	100	92.69761766
10.05.12	CH08-VI-27-67	137.544-S (67 cm)	68.6784856	4.718103977	0 089370247	2 362329245	3.223883392	15.55333604	1.145687027	0.18956064	3 279232602	0	0.760011236	100	96.117
10.05.12	CH08-VI-27-67_11	137.544-S (67 cm)	69.20447259	4.600619696	0 08244645	2.477919978	3.102249764	15.34689479	1.066522969	0.175670214	3 24569581	0.006035296	0.69147245	100	92.7875
10.05.12	CH08-VI-27-67_4	137.544-S (67 cm)	68.11134724	4.682659728	0 057155669	2.422537227	3.452181336	15.72833479	1.123114152	0 214833738	3.45618118	0.045366654	0.706288281	100	95.0037
10.05.12	CH08-VI-27-67_21	137.544-S (67 cm)	68.03425873	4.581477041	0 085123314	2.416329437	3.480527911	15.96842166	1.19706623	0 228147233	3 249658407	0.042509305	0.716480732	100	95.5085
10.05.12	CH08-VI-27-67_25	137.544-S (67 cm)	68.2018993	4.753242318	0 069794552	2.486192241	3.394582118	15.43976401	1.118728169	0 244387001	3.402855637	0.11222285	0.776331798	100	94.2767
10.05.12	CH08-VI-27-67_20	137.544-S (67 cm)	68.72769454	4.50018637	0 087936523	2 535163898	3.249902531	15.48561097	1.169416513	0 214218083	3 239084518	0.040594327	0.750191725	100	93.3628
10.05.12	CH08-VI-27-67_5	137.544-S (67 cm)	68.2816483	4.74848143	0 083754449	2.480860962	3.346844468	15.57093137	1.110684005	0 233658246	3 380387916	0.069691202	0.693057652	100	95.9949
10.05.12	CH08-VI-27-67_19	137.544-S (67 cm)	68.4575327	4.769608581	0 084835961	2.482152777	3.633201286	15.23558334	1.166105074	0.161261013	3 232177439	0.049842425	0.727699409	100	96.3035
10.05.12	CH08-VI-27-67_8	137.544-S (67 cm)	68.81002109	4.606682466	0.101044298	2.498919243	3.134144118	15.4393604	1.098257767	0 219068205	3 24800125	0.055626449	0.78887471	100	95.9975
10.05.12	CH08-VI-27-67_10	137.544-S (67 cm)	68.98490612	4.714148349	0.109650973	2 533570067	3.175660858	15.25687849	1.070573053	0.145814707	3.122944044	0.065790584	0.820062754	100	94.8464
10.05.12	CH08-VI-27-67_24	137.544-S (67 cm)	67.87620327	4.846568803	0 07313095	2.468580397	3.317289718	15.64899609	1.186118267	0.177383638	3 537812399	0.062243477	0.80567299	100	97.3596
10.05.12	CH08-VI-27-67_9	137.544-S (67 cm)	68.80272281	4.667276878	0 076486865	2 572567833	3.29377479	15.39479637	1.030941935	0.183799935	3.192879462	0.07501394	0.709739187	100	95.049
10.05.12	CH08-VI-27-67_17	137.544-S (67 cm)	68.17919613	4.65851123	0 079998273	2 51912298	3.225637287	15.75523819	1.147635887	0.18087013	3.435401395	0.111462889	0.706925609	100	97.2521
10.05.12	CH08-VI-27-67_1	137.544-S (67 cm)	68.75091781	4.48774816	0 039327391	2 510918129	3.196482059	15.71305287	1.117863487	0.192814855	3 291229891	0.005632568	0.694012782	100	99.4218
Mar 11 08:14 2020	CHA08-6A-28S-1(17-18cm)_3	138.422-S	66.54032342	5.00980184	0 044456189	2 249461833	2.644973442	17.80851274	0.524199234	0 303548925	4 275043578	0.018443455	0.581235351	100	93.80021343
Mar 11 08 34 2020	CHA08-6A-28S-1(17-18cm)_8	138.422-S	67.78674277	4.792404073	0 079650057	2 504515975	2.032900606	17.55303298	0.297102238	0 273861089	4 084618328	0.041921083	0.553250804	100	93.03194802
Mar 11 08 38 2020	CHA08-6A-28S-1(17-18cm)_9	138.422-S	70.14596425	4.440238401	0.106731765	3.117040476	3.475416669	14.31072275	1.048722894	0 239304644	2 224921995	0.070187153	0.820749003	100	93.0369696
Mar 11 08:42 2020	CHA08-6A-28S-1(17-18cm)_10	138.422-S	68.04245215	4.782020696	0 091456308	2.466842692	2.234454198	17.29373633	0.47042367	0 228064857	3.78105583	0.034471164	0.575022109	100	92.83121324
Mar 11 08 54 2020	CHA08-6A-28S-1(17-18cm)_13	138.422-S	67.17379102	4.869895659	0 060347111	2 305514643	3.003227713	17.09842513	0.673592758	0 208957699	3 952310817	0.041860496	0.612076952	100	94.12215214
Mar 11 08 58 2020	CHA08-6A-28S-1(17-18cm)_14	138.422-S	67.51366076	4.928492106	0 086663775	2 548302065	2.809771476	17.00745663	0.565034909	0 224740787	3 602030345	0.039353526	0.674493622	100	93.00310323
Mar 11 09 02 2020	CHA08-6A-28S-1(17-18cm)_15	138.422-S	68.25344382	4.60903924	0 088553114	2 623399397	3.451381033	15.63897585	1.069918644	0 266478686	3 20161804	0.08223554	0.714956644	100	93.39027838
Mar 11 09 06 2020	CHA08-6A-28S-1(17-18cm)_16	138.422-S	67.17983071	4.972940906	0 06977031	2 360808088	3.107749318	16.90942508	0.557951697	0 227198011	3 889009752	0.051115711	0.674200417	100	94.88276542
Mar 11 09:14 2020	CHA08-6A-28S-1(17-18cm)_18	138.422-S	64.96726478	5.082009728	0 061816519	2.18670681	4.436195072	17.40597195	0.63824505	0.196359371	4.173666363	0.051513766	0.800250588	100	95.12020498
Mar 11 09:18 2020	CHA08-6A-28S-1(17-18cm)_19	138.422-S	70.39965306	4.251329651	0.100406679	3.118286412	3.69366945	13.52801008	1.512529646	0 390236945	2.164583695	0.072652859	0.768641527	100	93.3204849
Mar 11 09 26 2020	CHA08-6A-28S-1(17-18cm)_21	138.422-S	64.97805241	4.961603186	0 063448064	1 894925395	2.825191799	18.66421965	0.83025411	0.154909245	5 003454693	0.040666376	0.583275069	100	93.93509661
Mar 11 09 34 2020	CHA08-6A-28S-1(17-18cm)_23	138.422-S	70.19175638	4.457233928	0 095904407	3 085813084	2.562040516	15.28209874	0.519815204	0 302495889	2.708411484	0.056943241	0.737487127	100	90.08970811
Mar 11 09 38 2020	CHA08-6A-28S-1(17-18cm)_24	138.422-S	69.03261542	4.703261746	0 079825684	2 807884573	2.942566859	15.72322647	0.752319418	0 248234415	3 001531785	0.032920026	0.675613606	100	92.95253889
Mar 11 09:46 2020	CHA08-6A-28S-1(17-18cm)_26	138.422-S	73.05035959	4.09797476	0 05929811	3.74798617	2.657780966	13.41222484	0.427616059	0.176887331	1 512155803	0.033267428	0.824448946	100	92.58305241
010319	CHA16_1B_80Y-1_146.5-148.5cm_3	138.422?	65.939	5.4125	0 0877	2 3184	3.137	17.206	0.8576	0.1892	4.1753	0	0.6773	100	92.9805
010319	CHA16_1B_80Y-1_146.5-148.5cm_17	138.422?	66.1774	5.0272	0.1212	2.7657	3.8207	16.0921	1.1141	0 3147	3.7814	0.0155	0.7701	100	92.8501
010319	CHA16_1B_80Y-1_146.5-148.5cm_18	138.422?	68.3686	4.8351	0 0949	3 0638	3.534	14.9207	1.0792	0 2481	3 0177	0.0484	0.7896	100	95.4906
010319	CHA16_1B_80Y-1_146.5-148.5cm_22	138.422?	69.0636	4.7894	0 0966	3 0428	3.0807	15.0351	0.9459	0 267	2 8157	0.0433	0.82	100	93.0964
010319	CHA16_1B_80Y-1_146.5-148.5cm_26	138.422?	66.7376	5.2128	0 0523	2 6254	2.8506	16.9272	0.6796	0 2179	3 966	0.0251	0.7055	100	93.0862
010319	CHA16_1B_80Y-1_146.5-148.5cm_30	138.422?	65.6381	4.9417	0 0856	2 3349	3.056	17.894	0.7481	0 2136	4.4185	0.0607	0.6089	100	95.1233
Mar 14 02 51 2020	CHA16-1C-77Y-1(31-32cm)_2	141.188-S	62.18186869	4.931248973	0 099749002	2.1767261	5.089265836	17.29130528	1.949875658	0 365288453	4 96631683	0.10323599	0.845119192	100	94.64
Mar 14 02 55 2020	CHA16-1C-77Y-1(31-32cm)_3	141.188-S	63.41686592	5.052598858	0.127972851	2 82185863	4.791551283	16.53804976	1.962148261	0 279166162	3 956849739	0.07059853	0.982340012	100	96.04
Mar 14 03 07 2020	CHA16-1C-77Y-1(31-32cm)_6	141.188-S	62.44942591	4.855883647	0 079661057	2.445553176	5.117621572	17.0987086	2.035113725	0 272725614	4 622817818	0.086058707	0.936430172	100	96.91
Mar 14 03:15 2020	CHA16-1C-77Y-1(31-32cm)_8	141.188-S	63.21077621	4.803095308	0 064063968	2.71123962	5.064214458	16.71871099	1.793221975	0 229799423	4 37296713	0.058051139	0.97385978	100	91.47
Mar 14 03:19 2020	CHA16-1C-77Y-1(31-32cm)_9	141.188-S	61.39780302	4.783526444	0 067381577	2.177575351	5.430321458	17.61609884	2.166205385	0 261719905	5 002260358	0.151197685	0.945909972	100	97.36
Mar 14 03 23 2020	CHA16-1C-77Y-1(31-32cm)_10	141.188-S	63.13366538	4.712259564	0 095921314	2 316743604	4.935536871	17.25694202	1.904815444	0 257890143	4.440425242	0.106184082	0.839616334	100	98.41

Date Analysed	Core Section Identifier	sample_no	SiO2	Na2O	Cl	K2O	FeOt	Al2O3	MgO	P2O5	CaO	MnO	TiO2	total	Analytical Total
Mar 14 03 27 2020	CHA16-1C-77Y-1(31-32cm)_11	141.188-S	63.09604068	4.9175497	0 097600998	2 356583687	4.674800114	17.38576206	1.876243048	0 309187825	4 399630488	0.077271671	0.809329728	100	98.87
Mar 14 03 35 2020	CHA16-1C-77Y-1(31-32cm)_13	141.188-S	61.91581987	5.08458317	0 087240019	2 344065929	5.148332652	17.15838173	2.029928321	0 230431872	4 932730041	0.127598719	0.940887681	100	98.12
Mar 14 03:43 2020	CHA16-1C-77Y-1(31-32cm)_15	141.188-S	62.35768236	5.021382231	0 079061997	2.462926098	4.888932761	17.33089496	1.939921701	0 347086308	4 532611894	0.113418782	0.92608091	100	96.63
Mar 14 03 51 2020	CHA16-1C-77Y-1(31-32cm)_17	141.188-S	63.24318774	4.927180261	0 083193796	2 589610813	4.462129984	17.30493996	1.861448129	0 356428323	4.180080446	0.077586371	0.914214179	100	98.08
Mar 14 03 55 2020	CHA16-1C-77Y-1(31-32cm)_18	141.188-S	62.97981131	4.762360948	0.115782307	2.476454895	4.702982902	17.27982209	1.957350486	0 232636672	4.43832176	0.089945699	0.964530939	100	93.28
Mar 14 03 59 2020	CHA16-1C-77Y-1(31-32cm)_19	141.188-S	62.73058147	5.019672806	0 060725413	2 236719387	4.822839511	17.37757251	1.956559086	0 264256756	4 524043284	0.129749966	0.877279803	100	98.81
Mar 14 04 03 2020	CHA16-1C-77Y-1(31-32cm)_20	141.188-S	63.23173413	4.886051911	0 059850412	2 665692407	4.752023607	17.06457298	1.854774092	0 295064573	4.146632633	0.051169038	0.992434219	100	97.91
Mar 14 04:10 2020	CHA16-1C-77Y-1(31-32cm)_22	141.188-S	62.65239911	5.08492138	0 072915492	2 645790701	4.953046294	17.03538947	1.861150134	0 233121244	4.427011999	0.093748489	0.940505679	100	96.00
Mar 14 04:14 2020	CHA16-1C-77Y-1(31-32cm)_23	141.188-S	62.57372044	5.004998555	0 078428454	2.716457233	4.993549847	17.00573489	1.898873881	0 383157878	4 344217598	0.026107585	0.974753642	100	94.61
Mar 14 04:18 2020	CHA16-1C-77Y-1(31-32cm)_24	141.188-S	63.37140772	4.882979257	0 069337722	2 635040102	4.681105618	17.07228838	1.81605126	0 262263991	4.15406322	0.093828095	0.961634635	100	96.77
Mar 14 04 22 2020	CHA16-1C-77Y-1(31-32cm)_25	141.188-S	62.46442341	4.454878423	0 099914179	1 848679457	5.190471215	17.95926665	1.940604372	0 318870491	4.798017781	0.058986766	0.865887262	100	93.58
Mar 14 04:42 2020	CHA16-1C-77Y-1(31-32cm)_30	141.188-S	63.43975209	4.523302586	0 065479865	2 532711749	4.621818039	17.51558722	1.728970781	0.406984128	4.159412791	0.080614362	0.92536639	100	97.12909497
Mar 14 04 50 2020	CHA16-1C-77Y-1(31-32cm)_32	141.188-S	62.77453586	4.776113493	0.104061255	2 242144574	4.761071692	17.54476779	1.895852084	0 302528598	4 602296757	0.100306468	0.896321431	100	93.21432812
Mar 14 04 54 2020	CHA16-1C-77Y-1(31-32cm)_33	141.188-S	61.23828776	5.087173013	0 078363475	2.164226856	5.317725938	17.70197872	2.153115541	0 254373583	5 077214662	0.089748744	0.837791704	100	97.49440055
Mar 14 04 58 2020	CHA16-1C-77Y-1(31-32cm)_34	141.188-S	62.13630196	5.078151273	0 063136756	2 286518719	5.076524542	17.2694215	2.071560189	0 267069506	4 809929016	0.106395218	0.834991318	100	97.09082991
Mar 14 05 02 2020	CHA16-1C-77Y-1(31-32cm)_35	141.188-S	61.81599341	4.822430778	0 078257864	2.11397866	5.2276068	17.48043713	2.153304991	0 313031455	5 051189395	0.083034643	0.860734869	100	98.39266778
01/10/2021	1A-74Y-1-0-1cm	144.464-S	77.41	3.57	0.13	4 31	1.61	11.80	0.19	0 00	0 60	0.00	0.38	100	
01/10/2021	1A-74Y-1-0-1cm	144.464-S	76.86	3.58	0.11	4 53	1.67	11.85	0.17	0.11	0 66	0.03	0.43	100	
01/10/2021	1A-74Y-1-0-1cm	144.464-S	77.44	3.59	0.10	4.45	1.49	11.67	0.18	0 06	0 54	0.00	0.49	100	
01/10/2021	1A-74Y-1-0-1cm	144.464-S	76.33	3.65	0 05	4 34	1.83	12.10	0.25	0 03	0 83	0.02	0.57	100	
01/10/2021	1A-74Y-1-0-1cm	144.464-S	76.99	3.69	0.11	4 57	1.54	11.86	0.13	0 03	0 55	0.04	0.50	100	
01/10/2021	1A-74Y-1-0-1cm	144.464-S	66.11	4.51	0 09	2 24	3.86	16.66	1.45	0 30	4 05	0.04	0.70	100	
01/10/2021	1A-74Y-1-0-1cm	144.464-S	67.60	4.60	0 07	2 56	3.81	15.38	1.61	0 25	3 31	0.09	0.73	100	
01/10/2021	1A-74Y-1-0-1cm	144.464-S	71.45	4.63	0 09	3.41	2.33	14.59	0.26	0 24	2.14	0.05	0.81	100	
01/10/2021	1A-74Y-1-0-1cm	144.464-S	70.10	4.64	0 09	2 88	2.70	15.33	0.65	0.16	2.70	0.04	0.70	100	
01/10/2021	1A-74Y-1-0-1cm	144.464-S	72.29	4.74	0 06	3 25	2.00	14.33	0.48	0 09	2.14	0.05	0.57	100	
01/10/2021	1A-74Y-1-0-1cm	144.464-S	66.31	4.75	0.11	2 20	3.62	16.64	1.37	0 29	3 93	0.08	0.70	100	
01/10/2021	1A-74Y-1-0-1cm	144.464-S	68.36	4.77	0 09	2 51	2.76	16.48	0.78	0.16	3 37	0.08	0.64	100	
01/10/2021	1A-74Y-1-0-1cm	144.464-S	68.86	4.96	0 08	2.73	2.88	15.76	0.64	0.19	3 09	0.04	0.76	100	
01/10/2021	1A-74Y-1-0-1cm	144.464-S	68.39	5.05	0.10	2 57	2.78	16.09	0.81	0.18	3 34	0.05	0.65	100	
01/10/2021	1A-74Y-1-0-1cm	144.464-S	68.05	5.40	0 04	2 61	1.27	18.22	0.09	0 07	3 89	0.00	0.35	100	
290419	MEXI-CHA16-1A-74Y-1_20-20 5cm_1	144.654-S	76.369	4.0609	0.1058	5 0417	1.1507	12.5886	0.0149	0 0073	0.4782	0.0709	0.1119	100	95.3561
290419	MEXI-CHA16-1A-74Y-1_20-20 5cm_2	144.654-S	76.2269	3.7946	0.1066	5 2394	1.1991	12.72	0.053	0 0581	0.4792	0.0151	0.108	100	95.206
290419	MEXI-CHA16-1A-74Y-1_20-20 5cm_3	144.654-S	76.0923	4.085	0.1381	5 0813	1.2335	12.6711	0.0546	0	0.4616	0.0413	0.1413	100	92.7086
290419	MEXI-CHA16-1A-74Y-1_20-20 5cm_4	144.654-S	77.8749	3.6147	0 0576	5 0854	0.7339	12.1686	0.0548	0	0 3534	0	0.0567	100	95.0127
290419	MEXI-CHA16-1A-74Y-1_20-20 5cm_5	144.654-S	75.93	4.162	0.1483	4 9414	1.1731	12.6101	0.0507	0	0 8295	0.0461	0.1087	100	93.4666
290419	MEXI-CHA16-1A-74Y-1_20-20 5cm_6	144.654-S	76.1834	3.7443	0.1213	5 0487	0.9182	12.8846	0.0969	0 014	0.7332	0.023	0.2324	100	91.8856
290419	MEXI-CHA16-1A-74Y-1_20-20 5cm_9	144.654-S	76.4098	3.9677	0.1313	4 8351	1.2255	12.6549	0.0797	0 0073	0 5017	0.0745	0.1124	100	95.626
290419	MEXI-CHA16-1A-74Y-1_20-20 5cm_10	144.654-S	76.7391	3.8677	0.1143	4 9449	1.1953	12.4695	0.0818	0 0102	0.4467	0.0396	0.0909	100	95.5592
290419	MEXI-CHA16-1A-74Y-1_20-20 5cm_13	144.654-S	76.5251	3.8687	0.1016	4 838	1.1214	12.7175	0.0502	0 0544	0 5452	0.0369	0.1408	100	94.7889
290419	MEXI-CHA16-1A-74Y-1_20-20 5cm_14	144.654-S	76.7145	4.1645	0.1297	4 6421	1.1563	12.4116	0.0718	0 0474	0.4929	0	0.1694	100	95.8689
290419	MEXI-CHA16-1A-74Y-1_20-20 5cm_15	144.654-S	76.2935	3.8664	0.1415	4 9013	1.295	12.7014	0.0576	0 0391	0 5265	0.0514	0.1261	100	92.9869
290419	MEXI-CHA16-1A-74Y-1_20-20 5cm_16	144.654-S	76.9809	3.9599	0.1298	4 6114	1.1685	12.5047	0.0407	0 0046	0.4606	0	0.1388	100	93.5208
290419	MEXI-CHA16-1A-74Y-1_20-20 5cm_18	144.654-S	76.469	3.9081	0.1272	5.1012	1.1562	12.5353	0.0603	0	0.4659	0.041	0.1357	100	91.1359
290419	MEXI-CHA16-1A-74Y-1_20-20 5cm_19	144.654-S	76.5554	4.1414	0.135	4.7171	1.2157	12.6013	0.0541	0 0334	0.4428	0.0005	0.1031	100	94.8177
290419	MEXI-CHA16-1A-74Y-1_20-20 5cm_21	144.654-S	76.6317	3.9643	0.1162	4 9135	1.1539	12.4896	0.0359	0	0 5193	0.006	0.1696	100	94.3854
290419	MEXI-CHA16-1A-74Y-1_20-20 5cm_23	144.654-S	76.5054	3.9292	0.129	5 0209	1.1689	12.594	0.0555	0	0.4227	0.0109	0.1635	100	92.846
290419	MEXI-CHA16-1A-74Y-1_20-20 5cm_26	144.654-S	76.7011	3.9908	0 0966	4 8701	1.231	12.3627	0.0464	0	0.4921	0.0559	0.1534	100	94.0215
290419	MEXI-CHA16-1A-74Y-1_20-20 5cm_27	144.654-S	76.7072	3.813	0.1159	4 9541	1.0842	12.643	0.0756	0 0176	0.4519	0.0177	0.1201	100	95.0292
290419	MEXI-CHA16-1A-74Y-1_20-20 5cm_29	144.654-S	76.759	4.0554	0 0925	4.7165	1.153	12.5591	0.0553	0	0.4611	0	0.1481	100	95.7703
Mar 13 04 26 2020	CHA16-1A-74Y-1(26 5-27.5cm)_1	144.722-S	66.64118154	4.647422141	0 09581676	2 208728826	3.907613788	16.26013646	1.336759667	0 216470028	3.723285736	0.068891304	0.893693754	100	95.07731211
Mar 13 04 30 2020	CHA16-1A-74Y-1(26 5-27.5cm)_2	144.722-S	67.27162309	4.366946161	0.133711184	2 246347889	3.876175064	15.82910186	1.40796286	0 204071859	3 583459728	0.078943083	1.001657221	100	93.4850746
Mar 13 04:42 2020	CHA16-1A-74Y-1(26 5-27.5cm)_5	144.722-S	67.48774929	4.915382709	0 073463697	2 391369995	3.795580928	15.33487632	1.461410821	0 200640338	3 293200205	0.080860731	0.965464971	100	98.68819987
Mar 13 04:45 2020	CHA16-1A-74Y-1(26 5-27.5cm)_6	144.722-S	66.92805704	4.645075541	0.127517406	2 307457816	3.820868275	15.9885174	1.352772745	0.191743562	3 643354447	0.014904632	0.979731132	100	90.57587034
Mar 13 04:49 2020	CHA16-1A-74Y-1(26 5-27.5cm)_7	144.722-S	66.10659873	5.139264529	0.111316962	2.197585778	3.951113694	15.89599797	1.423751567	0 321095002	3 820102381	0.075272447	0.957900941	100	97.37958905
Mar 13 04 53 2020	CHA16-1A-74Y-1(26 5-27.5cm)_8	144.722-S	66.67569758	4.822626024	0 090288328	2 259764493	3.819729734	16.04013962	1.31958773	0 273594624	3 650388796	0.081085667	0.967097402	100	97.7978018
Mar 13 04 57 2020	CHA16-1A-74Y-1(26 5-27.5cm)_9	144.722-S	66.20159563	5.115669033	0.10712247	2 296933411	3.775969647	16.29465708	1.357637822	0 217927089	3 608014871	0.037909565	0.98656339	100	98.39205567
Mar 13 05 01 2020	CHA16-1A-74Y-1(26 5-27.5cm)_10	144.722-S	66.06084807	5.294499799	0 092164588	2 339253706	3.934393547	16.03681668	1.340819697	0 246390231	3.704655011	0.029918352	0.920240321	100	99.6044163
Mar 13 05 05 2020	CHA16-1A-74Y-1(26 5-27.5cm)_11	144.722-S	66.31847996	4.979926822	0 096937575	2 341635522	3.830251561	16.12142554	1.310864621	0 327126075	3 650497298	0.054604077	0.96825095	100	97.79489501
Mar 13 05 09 2020	CHA16-1A-74Y-1(26 5-27.5cm)_12	144.722-S	66.76428131	4.901866058	0.10196025	2 218719588	4.13695167	15.42188402	1.414444338	0.171215189	3.781908389	0.090765801	0.996003393	100	99.15628869
Mar 13 05:13 2020	CHA16-1A-74Y-1(26 5-27.5cm)_13	144.722-S	67.29499439	4.922858557	0 082850965	2 307768422	3.629351543	16.09144288	0.966202927	0 219559106	3.45125728	0.056342815	0.977371113	100	96.19682715
Mar 13 05 25 2020	CHA16-1A-74Y-1(26 5-27.5cm)_16	144.722-S	66.81062593	4.752783208	0.110539311	2 27580934	3.83669637	15.83731649	1.399703576	0 240708779	3.748989494	0.078129347	0.908698158	100	98.42652283
Mar 13 05 37 2020	CHA16-1A-74Y-1(26 5-27.5cm)_19	144.722-S	66.98586921	4.723528374	0 074951495	2 287884026	3.73027336	16.19883005	1.354960009	0 30314232	3 343830499	0.064184982	0.93254567	100	96.59580534
Mar 13 05:41 2020	CHA16-1A-74Y-1(26 5-27.5cm)_20	144.722-S	66.74751416	4.669383932	0 094503275	2 284583966	3.995227723	16.01634987	1.339097763	0 28950543	3 58287177	0.059278412	0.921683699	100	99.36163581
Mar 13 05:48 2020	CHA16-1A-74Y-1(26 5-27.5cm)_22	144.722-S	66.67048871	4.590707082	0 073116529	2 215961838	4.001832777	15.978811	1.398506743	0 294922264	3.778368111	0.077813959	0.919470986	100	97.92587411
Mar 13 05 52 2020	CHA16-1A-74Y-1(26 5-27.5cm)_23	144.722-S	67.15268853	4.604149452	0 08403387	2 231988965	3.643403051	16.12486085	1.324388714	0 239674995	3 569125212	0.026434155	0.999252203	100	97.22270288

Date Analysed	Core Section Identifier	sample_no	SiO2	Na2O	Cl	K2O	FeOt	Al2O3	MgO	P2O5	CaO	MnO	TiO2	total	Analytical Total
Mar 13 06 20 2020	CHA16-1A-74Y-1(26 5-27.5cm)_30	144.722-S	67.24797567	4.711330567	0.111706606	2.161392933	2.898121704	16.86532424	0.71053321	0 291756959	4 270829304	0.021094364	0.709934448	100	96.23423712
Mar 13 06 28 2020	CHA16-1A-74Y-1(26 5-27.5cm)_32	144.722-S	66.763647	4.722728251	0 082111701	2 209919862	3.745607974	16.80346043	1.188698784	0.166980713	3.456801252	0.053828782	0.80621526	100	98.64611101
Mar 13 06 32 2020	CHA16-1A-74Y-1(26 5-27.5cm)_33	144.722-S	66.4633591	4.94130694	0 080008062	2 225321258	4.330038351	15.73546626	1.331002017	0 211836103	3 664017326	0.051234141	0.966410446	100	96.61526365
01/10/2021	1A-74Y-1-34.5-36cm	144.809-S	67.51	4.39	0.12	2.10	3.36	16.53	1.26	0 31	3 53	0.07	0.83	100	
01/10/2021	1A-74Y-1-34.5-36cm	144.809-S	67.13	4.54	0 08	1 99	3.73	16.20	1.32	0 29	3 80	0.06	0.86	100	
01/10/2021	1A-74Y-1-34.5-36cm	144.809-S	67.33	4.56	0.17	1 92	3.62	16.40	1.24	0 21	3 63	0.06	0.86	100	
01/10/2021	1A-74Y-1-34.5-36cm	144.809-S	67.40	4.67	0.14	2.14	3.63	15.97	1.22	0 28	3 56	0.07	0.92	100	
01/10/2021	1A-74Y-1-34.5-36cm	144.809-S	67.06	4.69	0.13	2 06	3.60	16.07	1.31	0 32	3 81	0.07	0.88	100	
01/10/2021	1A-74Y-1-34.5-36cm	144.809-S	66.99	4.69	0 06	2 04	3.57	16.39	1.35	0 20	3.78	0.08	0.86	100	
01/10/2021	1A-74Y-1-34.5-36cm	144.809-S	67.07	4.74	0.10	2 04	3.49	16.36	1.32	0 20	3.76	0.08	0.84	100	
01/10/2021	1A-74Y-1-34.5-36cm	144.809-S	66.67	4.75	0 08	1 98	3.69	16.25	1.42	0 20	4 03	0.09	0.85	100	
01/10/2021	1A-74Y-1-34.5-36cm	144.809-S	66.78	4.76	0.11	2 06	3.68	16.25	1.30	0 25	3.78	0.07	0.96	100	
01/10/2021	1A-74Y-1-34.5-36cm	144.809-S	66.83	4.79	0.16	2 08	3.59	16.20	1.37	0 25	3 80	0.06	0.87	100	
01/10/2021	1A-74Y-1-34.5-36cm	144.809-S	66.99	4.80	0 06	2 06	3.35	16.67	1.12	0 26	3 82	0.05	0.82	100	
01/10/2021	1A-74Y-1-34.5-36cm	144.809-S	67.09	4.82	0 09	2 03	3.49	16.25	1.25	0 32	3.78	0.05	0.84	100	
01/10/2021	1A-74Y-1-34.5-36cm	144.809-S	66.73	4.82	0 09	2.11	3.62	16.16	1.37	0 28	3 88	0.08	0.85	100	
01/10/2021	1A-74Y-1-34.5-36cm	144.809-S	66.86	4.86	0 06	2.12	3.59	16.29	1.27	0 22	3.73	0.08	0.93	100	
01/10/2021	1A-74Y-1-34.5-36cm	144.809-S	66.75	4.87	0 06	2 02	3.70	16.22	1.32	0 28	3.77	0.10	0.92	100	
01/10/2021	1A-74Y-1-34.5-36cm	144.809-S	66.40	4.90	0 06	2 07	3.77	16.20	1.43	0 23	4 06	0.02	0.86	100	
01/10/2021	1A-74Y-1-34.5-36cm	144.809-S	66.48	4.92	0 27	2.15	3.70	15.99	1.38	0 35	3.78	0.06	0.91	100	
01/10/2021	1A-74Y-1-34.5-36cm	144.809-S	66.57	4.96	0.10	2 05	3.84	16.18	1.25	0 29	3 89	0.06	0.81	100	
01/10/2021	1A-74Y-1-34.5-36cm	144.809-S	66.73	4.98	0.13	2.12	3.58	16.00	1.39	0 25	3 89	0.06	0.87	100	
01/10/2021	1A-74Y-1-34.5-36cm	144.809-S	66.69	4.98	0.10	2 09	3.60	16.20	1.38	0 21	3 81	0.08	0.87	100	
01/10/2021	1A-74Y-1-34.5-36cm	144.809-S	66.78	4.98	0 05	2 09	3.61	16.34	1.31	0 30	3 65	0.06	0.83	100	
01/10/2021	1A-74Y-1-34.5-36cm	144.809-S	66.46	5.00	0 09	2 07	3.76	16.01	1.43	0 22	4 02	0.05	0.89	100	
01/10/2021	1A-74Y-1-34.5-36cm	144.809-S	66.61	5.01	0 07	2.11	3.74	16.19	1.27	0 33	3.72	0.07	0.89	100	
01/10/2021	1A-74Y-1-34.5-36cm	144.809-S	66.45	5.05	0 05	2 05	3.65	16.28	1.38	0 29	3 81	0.07	0.91	100	
01/10/2021	1A-74Y-1-34.5-36cm	144.809-S	66.57	5.10	0 08	2.15	3.52	16.05	1.32	0 27	4 03	0.05	0.86	100	
01/10/2021	1A-74Y-1-34.5-36cm	144.809-S	66.41	5.11	0 09	2 07	3.87	16.25	1.26	0.19	3 85	0.06	0.85	100	
01/10/2021	1A-74Y-1-34.5-36cm	144.809-S	66.58	5.15	0 07	2 07	3.60	16.25	1.30	0 27	3.79	0.05	0.87	100	
01/10/2021	1A-74Y-1-34.5-36cm	144.809-S	66.31	5.18	0 07	2 02	3.68	16.20	1.38	0 29	3 96	0.07	0.86	100	
01/10/2021	1A-74Y-1-34.5-36cm	144.809-S	66.43	5.23	0.15	2 09	3.58	16.08	1.37	0 32	3 86	0.06	0.83	100	
30/09/2021	1A-75Y-1-0-1.5cm	146.2805-S	63.22185704	4.345400985	0 067662654	1 630791512	4.65940432	17.24992512	2.404407756	0.155887462	5.186618802	0.081742158	0.996302193	100	
30/09/2021	1A-75Y-1-0-1.5cm	146.2805-S	62.90040572	4.444238468	0 065000767	1 521723376	4.857421636	17.13198502	2.402449431	0.172831496	5 52812637	0.037589591	0.938228121	100	
30/09/2021	1A-75Y-1-0-1.5cm	146.2805-S	62.6360953	4.532860968	0 073835269	1 551245753	4.704102382	17.45655124	2.380825156	0.14867784	5 545471653	0.038781144	0.931553294	100	
30/09/2021	1A-75Y-1-0-1.5cm	146.2805-S	63.21784126	4.543533948	0.10403126	1.754744146	4.929995457	16.60739995	2.436798596	0.199915494	5.162816058	0.055775796	0.987148031	100	
30/09/2021	1A-75Y-1-0-1.5cm	146.2805-S	63.14327876	4.55253387	0 091368296	1 588093211	4.626644887	17.25727956	2.35136937	0.157856465	5 233194326	0.034832178	0.963549087	100	
30/09/2021	1A-75Y-1-0-1.5cm	146.2805-S	62.79936109	4.556840351	0 065651123	1 569918152	4.811697194	16.81035736	2.471797452	0 263521976	5 51164522	0.114787522	1.024422566	100	
30/09/2021	1A-75Y-1-0-1.5cm	146.2805-S	61.53792231	4.575660241	0 055272356	1 569087029	5.456373606	16.95626306	2.805200265	0.193959403	5 642975803	0.083617154	1.123668776	100	
30/09/2021	1A-75Y-1-0-1.5cm	146.2805-S	62.98547569	4.599328364	0 06175954	1 546499057	4.569201759	17.18220705	2.465616991	0 225648271	5 28081014	0.085358714	0.998094424	100	
30/09/2021	1A-75Y-1-0-1.5cm	146.2805-S	62.66772612	4.644282806	0 050582298	1 585113914	4.836111878	17.04249864	2.468605547	0 259474061	5 388929436	0.059668938	0.997006363	100	
30/09/2021	1A-75Y-1-0-1.5cm	146.2805-S	61.39290495	4.65421444	0 051388181	1.474002838	5.34073631	16.93084082	2.807939485	0 203230665	6.145752038	0.075517406	0.923472874	100	
30/09/2021	1A-75Y-1-0-1.5cm	146.2805-S	61.23710069	4.691061659	0 028628535	1 587125786	5.263632354	17.05657965	2.896145184	0 242990967	5.777862753	0.093419429	1.125452994	100	
30/09/2021	1A-75Y-1-0-1.5cm	146.2805-S	62.54521778	4.697671248	0 067007908	1.484545459	4.707839367	17.16378586	2.486173997	0 253287859	5 577760247	0.076667622	0.940042656	100	
30/09/2021	1A-75Y-1-0-1.5cm	146.2805-S	62.73387295	4.698180669	0 051427397	1.495334923	4.617351754	17.30749137	2.316001902	0 216722528	5 522439051	0.076888505	0.964288953	100	
30/09/2021	1A-75Y-1-0-1.5cm	146.2805-S	63.12155803	4.703188521	0 037199789	1 69274242	4.956593075	16.44088746	2.003345106	0 307937214	5 500238251	0.078352688	1.15795745	100	
30/09/2021	1A-75Y-1-0-1.5cm	146.2805-S	61.90452001	4.729570749	0 046991881	1 519134073	5.16505585	16.51805116	2.775471415	0.160116731	6 085083533	0.094186313	1.001818284	100	
30/09/2021	1A-75Y-1-0-1.5cm	146.2805-S	61.58445699	4.7571232	0 022870785	1 534883767	5.163714926	16.71091996	3.003144136	0 200348073	5 856738033	0.080911754	1.084888374	100	
30/09/2021	1A-75Y-1-0-1.5cm	146.2805-S	62.54773552	4.768582146	0 048087386	1 676533091	4.718386545	17.0564654	2.444405165	0 209616832	5.447569181	0.090352083	0.992266651	100	
30/09/2021	1A-75Y-1-0-1.5cm	146.2805-S	62.38370572	4.771189039	0 04993575	1 556701508	4.791405941	17.29556026	2.523076059	0 243815847	5.435325202	0.032448129	0.916836538	100	
30/09/2021	1A-75Y-1-0-1.5cm	146.2805-S	62.45216032	4.798244334	0 044844351	1.488063116	4.757752821	17.02668137	2.598867818	0.18474253	5 552942993	0.090296075	1.005404277	100	
30/09/2021	1A-75Y-1-0-1.5cm	146.2805-S	62.88464492	4.805644505	0 065707751	1 663099903	4.805644505	16.9779033	2.349193583	0.182124744	5 21440668	0.069482886	0.982147219	100	
30/09/2021	1A-75Y-1-0-1.5cm	146.2805-S	62.85742113	4.810915492	0 048513434	1 586793555	4.770487631	16.95948781	2.38884732	0 239636148	5 255037223	0.110974479	0.971885785	100	
30/09/2021	1A-75Y-1-0-1.5cm	146.2805-S	62.28087557	4.888777042	0 018193162	1.758333531	5.518931255	16.36368199	2.454048456	0.193213413	5 314659317	0.060067926	1.149218337	100	
30/09/2021	1A-75Y-1-0-1.5cm	146.2805-S	60.62670832	4.961458042	0 071346587	1.455634384	5.197229809	17.23184084	2.892833002	0 232388954	6.169332853	0.095846349	1.065380856	100	

Filtered core analyses, normalised to 100% (151-200.99 mc)

Date Analysed	Core Section Identifier	sample_no	SiO2	Na2O	Cl	K2O	FeOt	Al2O3	MgO	P2O5	CaO	MnO	TiO2	total	Analytical Total
Mar 11 00 52 2020	CHA16-1C-91Y-1(92-93cm)_1	164 575-S	76 5824359	3.674603658	0.047220073	3.901252046	1 085448427	13 09939242	0.155090758	0.036995209	1.245202907	0 007141636	0.165216958	100	93.8160354
Mar 11 00 56 2020	CHA16-1C-91Y-1(92-93cm)_2	164 575-S	76 61965894	3.473437757	0.04330616	3.915642997	1.125942314	13.11820324	0.188865933	0.065516333	1.245344719	0 017450148	0.186631462	100	93.98201017
Mar 11 01 00 2020	CHA16-1C-91Y-1(92-93cm)_3	164 575-S	76 57202756	3.644873453	0.053568855	3.859951449	1.176134347	13 01377737	0.176958993	0	1.332592103	0 01272394	0.157391926	100	93.52449242
Mar 11 01 04 2020	CHA16-1C-91Y-1(92-93cm)_4	164 575-S	76 24443218	3.849926588	0.039448815	3.817284242	1.148638659	13 26647466	0.147800142	0.06041449	1.310423705	0 0061672	0.108989313	100	94.04591778
Mar 11 01 08 2020	CHA16-1C-91Y-1(92-93cm)_5	164 575-S	76 30604071	3.784513522	0.051123477	3.908815817	1.197001318	13 07853082	0.166683835	0	1.250288525	0 054638216	0 202363762	100	93.89032823
Mar 11 01:12 2020	CHA16-1C-91Y-1(92-93cm)_6	164 575-S	76 53587565	3.553518695	0.057959026	3.902928917	1 225259653	13 09027562	0.186319658	0.019412064	1.226923458	0 020099552	0.181427704	100	94.03194571
Mar 11 01:16 2020	CHA16-1C-91Y-1(92-93cm)_7	164 575-S	76.71912663	3.653856365	0.056174571	3.847428139	1 026943463	13 05676778	0.182620349	0.019755621	1.225029599	0 007313293	0 204984188	100	94.34874075
Mar 11 01 20 2020	CHA16-1C-91Y-1(92-93cm)_8	164 575-S	76 079495	3.722899201	0.075416063	3.80257956	1 230159239	13 30931858	0.230061359	0.06875971	1.256969684	0 066306819	0.158034783	100	94.409596
Mar 11 01 32 2020	CHA16-1C-91Y-1(92-93cm)_11	164 575-S	77.11805571	3.381654135	0.074054604	4.148330967	1 05612336	12.78747723	0.140152051	0	1.093949887	0 02896405	0.17123801	100	94.25477454
Mar 11 01 36 2020	CHA16-1C-91Y-1(92-93cm)_12	164 575-S	76.7060203	3.612133062	0.072136629	3.857973793	1 095337406	13 09136631	0.142563353	0.020881152	1.178445347	0 04648805	0.176654589	100	93.57243448
Mar 11 01:40 2020	CHA16-1C-91Y-1(92-93cm)_13	164 575-S	77 01781351	3.497781081	0.046307193	3.993464341	1 05790351	12 90585608	0.138496742	0	1.175098124	0 022516341	0.144763082	100	94.15383935
Mar 11 01:44 2020	CHA16-1C-91Y-1(92-93cm)_14	164 575-S	76 62361173	3.602437884	0.045878614	4.009019087	1.115442661	13 05710113	0.139565317	0.054703589	1.128849733	0 041162121	0.18222814	100	93.28965313
Mar 11 01:48 2020	CHA16-1C-91Y-1(92-93cm)_15	164 575-S	76 93679985	3.554472413	0.052301331	3.960265424	1.167114247	12 90710458	0.11783942	0.011205217	1.151490218	0 025612586	0.115794717	100	92.92306464
Mar 11 01 52 2020	CHA16-1C-91Y-1(92-93cm)_16	164 575-S	75 89794674	3.73977517	0.039804802	3.958964051	1 006586924	13 57080107	0.109194253	0.0395511	1.485364583	0 012264182	0.139747128	100	92.9536099
Mar 11 01 56 2020	CHA16-1C-91Y-1(92-93cm)_17	164 575-S	76.72634409	3.632260489	0.036130737	4.068681184	0 999782955	12 90632753	0.174826145	0.058838959	1.178540125	0 031574661	0.186693131	100	94.37947646
Mar 11 02 04 2020	CHA16-1C-91Y-1(92-93cm)_19	164 575-S	77 00075254	3.5871244	0.058919023	3.863892447	1 027132583	12 86484894	0.201626874	0.049531611	1.183290378	0 021774422	0.14110679	100	93.68790797
Mar 11 02:12 2020	CHA16-1C-91Y-1(92-93cm)_21	164 575-S	76 90162601	3.627210057	0.043200714	4.107260014	1 046877987	12 84584733	0.133964776	0.009164283	1.109598638	0 043945554	0.131304634	100	93.97992791
Mar 11 02 20 2020	CHA16-1C-91Y-1(92-93cm)_23	164 575-S	76 83925872	3.521267002	0.067729235	3.974720339	1 035376768	12 97354553	0.170436008	0.071667103	1.185738572	0 039429226	0.120831498	100	94.34626037
Mar 11 02 24 2020	CHA16-1C-91Y-1(92-93cm)_24	164 575-S	77 0306778	3.426355199	0.054019631	3.924779606	1 007874521	13 00639932	0.182329734	0.045323187	1.141744265	0 019839545	0.160657187	100	92.74406121
Mar 11 02 28 2020	CHA16-1C-91Y-1(92-93cm)_25	164 575-S	77.15274205	3.369088363	0.04904535	4.154056564	1 041021349	12 67745883	0.134769011	0.068209108	1.153622731	0 050947971	0.149038671	100	94.6063189
Mar 11 02 32 2020	CHA16-1C-91Y-1(92-93cm)_26	164 575-S	76 56226817	3.728097787	0.056526486	3.924857889	1 062440315	13 04396649	0.158700776	0.051686398	1.158473	0 046501034	0 206481654	100	93.76135656
Mar 11 02 36 2020	CHA16-1C-91Y-1(92-93cm)_27	164 575-S	76.75005485	3.543452365	0.072296886	3.971999577	1 096178767	12 98062139	0.181066902	0.089456705	1.14203105	0 044049151	0.128792357	100	92.39678727
Mar 11 02:40 2020	CHA16-1C-91Y-1(92-93cm)_28	164 575-S	76 37946167	3.5246297	0.052917764	3.917846617	1 078208786	13 31809383	0.134924197	0.049534503	1.301369107	0 029410684	0 213603144	100	93.16342258
Mar 11 02:44 2020	CHA16-1C-91Y-1(92-93cm)_29	164 575-S	75 30416592	3.773207395	0.064426131	3.791636222	1 088084721	13 93716903	0.162332726	0.086347174	1.647619082	0	0.145011603	100	94.68207892
Mar 11 02:48 2020	CHA16-1C-91Y-1(92-93cm)_30	164 575-S	76 88085246	3.336316208	0.05778047	4.303945591	1 204125089	12 69295402	0.136112279	0.082849978	1.030579772	0 045729422	0 228754708	100	92.93797785
Mar 11 02 52 2020	CHA16-1C-91Y-1(92-93cm)_31	164 575-S	76.79856418	3.561202085	0.057645517	3.973725903	1 235741148	12 94941353	0.13086804	0.032691638	1.092085844	0 015365073	0.152697041	100	94.36987079
29/09/2021	1C-91Y-1-140 5-141cm	165 047-S	71 01950205	4.171505971	0.180523432	2.236894506	2 019250717	16 03309252	0.63267172	0.143161248	3.280581823	0 023336251	0 259479763	100	
29/09/2021	1C-91Y-1-140 5-141cm	165 047-S	72.14144262	4.453789738	0.06300483	2.378975494	1 86841911	15 60998989	0.524459788	0.097766116	2.497158912	0 068979426	0 296014074	100	
29/09/2021	1C-91Y-1-140 5-141cm	165 047-S	71 51812781	4.563806527	0.097997176	2.341525439	2 005473177	15 81613711	0.633702333	0.041301907	2.59893734	0 071438207	0 311552968	100	
29/09/2021	1C-91Y-1-140 5-141cm	165 047-S	69 29732556	4.725808068	0.107503948	2.291962343	1.713514704	17 35342917	0.61632913	0.087094569	3.467276377	0 015061467	0 324694665	100	
29/09/2021	1C-91Y-1-140 5-141cm	165 047-S	68 06573985	4.74676397	0.101226171	2.276159108	3 271263844	15 9788657	1.197322115	0.213661569	3.464434238	0 05535985	0 629203581	100	
29/09/2021	1C-91Y-1-140 5-141cm	165 047-S	68.170504	4.756923993	0.100939607	2.053598894	3 271835527	16 08072355	1.020431201	0.230304735	3.61721101	0 074254423	0 623273066	100	
29/09/2021	1C-91Y-1-140 5-141cm	165 047-S	68 01009932	4.914692395	0.072822001	2.230107732	3 244753904	16 05466182	1.150959649	0.138562618	3.461990547	0 089944155	0 631405857	100	
29/09/2021	1C-91Y-1-140 5-141cm	165 047-S	67 8011957	5.000757054	0.07705569	2.243526225	3 302386734	16.10306674	1.143895841	0.166062876	3.537430281	0 022959451	0 601663412	100	
29/09/2021	1C-91Y-1-140 5-141cm	165 047-S	68 90199546	5.094418168	0.056846252	1.936293084	2.733590236	16 23586928	0.741590992	0.115038589	3.493815762	0 027853628	0 662688542	100	
29/09/2021	1C-91Y-1-140 5-141cm	165 047-S	69 02490957	5.305774465	0.088463983	2.095471238	2 849015082	15 9792585	0.624461248	0.148850716	3.167309192	0 061625435	0 654860568	100	
01/10/2021	1C-93Y-1-122-123cm	168.105-S (122 - 123 cm)	77 60	3.72	0.08	3.66	0 69	12 92	0.12	0.02	1.06	0 03	0 09	100	
01/10/2021	1C-93Y-1-122-123cm	168.105-S (122 - 123 cm)	77 23	3.93	0.06	3.34	0 86	13.12	0.16	0.04	1.10	0 02	0.13	100	
01/10/2021	1C-93Y-1-122-123cm	168.105-S (122 - 123 cm)	77.49	3.96	0.08	3.41	0 86	12 97	0.07	0.00	0.99	0 03	0.14	100	
01/10/2021	1C-93Y-1-122-123cm	168.105-S (122 - 123 cm)	77.79	3.99	0.05	3.39	0 65	12 87	0.07	0.03	1.08	0 03	0 05	100	
01/10/2021	1C-93Y-1-122-123cm	168.105-S (122 - 123 cm)	77 56	4.01	0.04	3.55	1 04	12.44	0.16	0.06	0.99	0 06	0 09	100	
01/10/2021	1C-93Y-1-122-123cm	168.105-S (122 - 123 cm)	76.78	4.03	0.07	3.24	0 90	13.47	0.17	0.04	1.13	0 06	0.12	100	
01/10/2021	1C-93Y-1-122-123cm	168.105-S (122 - 123 cm)	77 26	4.04	0.09	3.28	0 81	13.19	0.11	0.00	1.09	0 05	0 08	100	
01/10/2021	1C-93Y-1-122-123cm	168.105-S (122 - 123 cm)	77.46	4.06	0.08	3.68	0 60	12 97	0.05	0.00	0.96	0 05	0.10	100	
01/10/2021	1C-93Y-1-122-123cm	168.105-S (122 - 123 cm)	77 24	4.11	0.09	3.31	0 83	13.10	0.08	0.01	1.06	0 06	0.11	100	
01/10/2021	1C-93Y-1-122-123cm	168.105-S (122 - 123 cm)	77 38	4.14	0.06	3.31	0 92	12 94	0.10	0.00	1.06	0 00	0.10	100	
01/10/2021	1C-93Y-1-122-123cm	168.105-S (122 - 123 cm)	76 97	4.16	0.10	3.21	0 93	13.18	0.18	0.04	1.12	0 00	0.12	100	
01/10/2021	1C-93Y-1-122-123cm	168.105-S (122 - 123 cm)	77.19	4.22	0.07	3.20	0 87	13 00	0.14	0.08	1.11	0 01	0.10	100	
30/09/2021	1C-93Y-1-59-60cm	168.105-S (59 - 60 cm)	76.72268071	3.542234108	0.162820623	3.578877909	0 946020799	13 52156261	0.137132531	0	1.233300993	0 068646054	0 086723663	100	
30/09/2021	1C-93Y-1-59-60cm	168.105-S (59 - 60 cm)	77 37140745	3.543153411	0.094593448	3.543153411	0 878461461	13 21027568	0.183046801	0	1.071691505	0 003718124	0.100498703	100	
30/09/2021	1C-93Y-1-59-60cm	168.105-S (59 - 60 cm)	76 63278929	3.609503835	0.110613827	3.557754676	1.180657061	13.14428637	0.127057402	0.032343224	1.449099972	0 037906259	0.117988082	100	
30/09/2021	1C-93Y-1-59-60cm	168.105-S (59 - 60 cm)	77 2411776	3.698339887	0.105310499	3.372972741	0 91981292	13 28582511	0.127729117	0.036007297	1.145148464	0 026246283	0 041430083	100	
30/09/2021	1C-93Y-1-59-60cm	168.105-S (59 - 60 cm)	77 01903069	3.741210289	0.150131148	3.608457666	0.742690585	13.17871496	0.164015876	0.025343683	1.224256537	0 044291102	0.101857467	100	
30/09/2021	1C-93Y-1-59-60cm	168.105-S (59 - 60 cm)	76.49044552	3.820315245	0.114271376	3.673813481	0 974011347	13 39927677	0.13444233	0.0089028	1.330766244	0	0 053754878	100	
30/09/2021	1C-93Y-1-59-60cm	168.105-S (59 - 60 cm)	76 35897133	3.932155881	0.088939013	3.012097123	1 061901149	13.70230364	0.179098087	0.07765734	1.436709704	0 026287393	0.12387934	100	
30/09/2021	1C-93Y-1-59-60cm	168.105-S (59 - 60 cm)	76 99031437	3.947220514	0.057813909	3.507448663	0 687867531	13 35404766	0.096708907	0.007079254	1.200689619	0 045264322	0.105545244	100	
30/09/2021	1C-93Y-1-59-60cm	168.105-S (59 - 60 cm)	76.45839861	3.965610001	0.097869929	3.358065293	0 904357913	13 56481638	0.171281256	0	1.272924957	0 060091695	0.146583969	100	
30/09/2021	1C-93Y-1-59-60cm	168.105-S (59 - 60 cm)	76 33107942	3.993742739	0.060816243	3.308489293	0 918774972	13 68365475	0.184893051	0.021307099	1.319933102	0 02890913	0.148400199	100	
30/09/2021	1C-93Y-1-59-60cm	168.105-S (59 - 60 cm)	76 81513591	4.032248196	0.102658287	3.503081766	1 011660381	13 09157748	0.104262561	0.039475816	1.103049695	0 021484157	0.175365755	100	
30/09/2021	1C-93Y-1-59-60cm	168.105-S (59 - 60 cm)	75 91114746	4.035284456	0.132980965	3.037927218	1.185594086	13.7337238	0.283803272	0.01203707	1.480411209	0 052733831	0.13435663	100	
30/09/2021	1C-93Y-1-59-60cm	168.105-S (59 - 60 cm)	76 27659972	4.050797678	0.072320524	3.255483998	1 032529241	13 55214511	0.221899979	0.05291487	1.3294274	0 056732376	0 099149105	100	
30/09/2021	1C-93Y-1-59-60cm	168.105-S (59 - 60 cm)	76 51153436	4.074486941	0.082340807	3.500016197	0 694258532	13 68091438	0.101661527	0.039361884	1.168190652	0 041276787	0.105957937	100	
30/09/2021	1C-93Y-1-59-60cm	168.105-S (59 - 60 cm)	76 85163744	4.099305985	0.074183151	3.044256724	0 921959193	13.4079177	0.087780328	0	1.396024848	0 03308019	0 083854436	100	
30/09/2021	1C-93Y-1-59-60cm	168.105-S (59 - 60 cm)	75 8604414	4.16340103	0.068548926	3.027928022	1 216743437	13 95159891	0.246568738	0.034800145	1.292766413	0 003048955	0.134154033	100	
30/09/2021	1C-93Y-1-59-60cm	168.105-S (59 - 60 cm)	76.41365802	4.166442629	0.121185825	3.383194929	0 86255153	13.45663063	0.138755624	0.000435138	1.299843426	0 057546949	0 099755297	100	
30/09/2021	1C-93Y-1-59-60cm	168.105-S (59 - 60 cm)	76.71507918	4.206642724	0.080759106	3.025830731	0 832367025	13 62150977	0.134584001	0.025408544	1.25892591	0 036267797	0 062625207	100	

Date Analysed	Core Section Identifier	sample_no	SiO2	Na2O	Cl	K2O	FeOt	Al2O3	MgO	P2O5	CaO	MnO	TiO2	total	Analytical Total
30/09/2021	1C-93Y-1-59-60cm	168.105-S (59 - 60 cm)	76 80273209	4.219166573	0.060319241	2.947056049	0 889841312	13.49497248	0.171503794	0.052898596	1.301720673	0 033710929	0 026078266	100	
30/09/2021	1C-93Y-1-59-60cm	168.105-S (59 - 60 cm)	76 26110953	4.261413389	0.088408427	3.158958184	1 0404421	13 68528529	0.115447611	0	1.292364636	0 017914897	0 078655939	100	
30/09/2021	1C-93Y-1-59-60cm	168.105-S (59 - 60 cm)	76.17096741	4.268303932	0.078654249	2.84204021	1 035404539	13 86412235	0.16902348	0	1.400437055	0 062923399	0.108123375	100	
30/09/2021	1C-93Y-1-59-60cm	168.105-S (59 - 60 cm)	76 60286308	4.271626748	0.070629868	3.267160062	0.745208548	13 58673359	0.131632391	0.006555467	1.21164544	0 023895734	0 082049068	100	
30/09/2021	1C-93Y-1-59-60cm	168.105-S (59 - 60 cm)	75.74013728	4.288504792	0.076428798	2.972231044	1 318821375	13.78902902	0.22980692	0.013693493	1.353419049	0 052863252	0.165064974	100	
30/09/2021	1C-93Y-1-59-60cm	168.105-S (59 - 60 cm)	76 07898946	4.324838369	0.0862858	2.9957417	1.122242815	13 61796667	0.217078607	0.053269351	1.350635624	0 029535482	0.123416119	100	
30/09/2021	1C-93Y-1-59-60cm	168.105-S (59 - 60 cm)	76 64408569	4.392641428	0.078263259	3.062475362	0 819444165	13 50788796	0.104839835	0	1.21702826	0 052175506	0.121158537	100	
30/09/2021	1C-93Y-1-59-60cm	168.105-S (59 - 60 cm)	75 92133231	4.501430695	0.056849054	2.884719671	1.197317165	13 588826	0.240601389	0.024937503	1.367685073	0 051037348	0.165263794	100	
030418	MEX2-1A-92Y-1_3-4cm~_HOLED-6	169.145-S	77.49	4.08	0.09	3.31	0 81	12 91	0.14	0.01	1.08	0 01	0 08	100	95 2974
030418	MEX2-1A-92Y-1_3-4cm~_HOLED-7	169.145-S	77 87	3.98	0.09	3.29	0 84	12 61	0.13	0.00	1.09	0 01	0 08	100	95 8419
030418	MEX2-1A-92Y-1_3-4cm~_HOLED-9	169.145-S	77.16	4.06	0.06	3.30	1.11	12 93	0.12	0.00	1.16	0 02	0 09	100	95 6997
060418	MEX2_1A-92Y-1_3-4cm-SAMPLE_C-5	169.145-S	77.4642	4.0179	0.092	3.3854	0 8313	12 8691	0.1058	0	1.1458	0 0129	0 0756	100	94 8701
060418	MEX2_1A-92Y-1_3-4cm-SAMPLE_C-7	169.145-S	76 8901	4.1022	0.1339	3.806	0 9387	12 822	0.1006	0.0264	1.0477	0 039	0 0935	100	93 9336
060418	MEX2_1A-92Y-1_3-4cm-SAMPLE_C-14	169.145-S	76 8413	4.3116	0.1389	3.476	0 9617	12 8443	0.155	0.0427	1.1192	0 0264	0 083	100	92.1839
060418	MEX2_1A-92Y-1_3-4cm-SAMPLE_C-15	169.145-S	77.1157	4.0722	0.0775	3.444	1 079	12.7889	0.174	0.0285	1.0683	0 0084	0.1436	100	92.7809
060418	MEX2_1A-92Y-1_3-4cm-SAMPLE_C-19	169.145-S	76 3543	4.5675	0.0786	3.5817	0.7615	13 2059	0.0621	0.0345	1.1836	0.1062	0 0641	100	94.422
060418	MEX2_1A-92Y-1_3-4cm-SAMPLE_C-20	169.145-S	76 644	3.9769	0.0736	3.7931	1 0006	12 9395	0.1505	0	1.2301	0 0595	0.1321	100	92 3967
060418	MEX2_1A-92Y-1_3-4cm-SAMPLE_C-22	169.145-S	76 2759	4.5162	0.0762	3.4473	1 0722	13.1348	0.2016	0.0398	1.091	0 0381	0.1069	100	93 2318
060418	MEX2_1A-92Y-1_3-4cm-SAMPLE_C-25	169.145-S	77.7642	4.2277	0.1377	3.5516	0 8079	12 3286	0.069	0	0.9735	0 0096	0.1302	100	91.753
060418	MEX2_1A-92Y-1_3-4cm-SAMPLE_C-28	169.145-S	77 0481	4.161	0.0664	3.3043	0 9279	12 9903	0.1821	0.0547	1.1454	0 0578	0 062	100	93 3983
Mar 10 22:48 2020	CHA16-1A-94Y-1(41-42cm)_1	171 633-S	65.73476947	4.956443991	0.047647183	2.098129768	2 816478353	18 02898798	0.543756685	0.138706113	4.847403258	0 05229821	0.73537898	100	96.75283343
Mar 10 22 52 2020	CHA16-1A-94Y-1(41-42cm)_2	171 633-S	67.77507121	4.727515623	0.056998966	2.537910181	3.426626331	15 98064529	0.684091609	0.210450492	3.692451288	0 050654191	0 857584813	100	96.14209431
Mar 10 23 08 2020	CHA16-1A-94Y-1(41-42cm)_6	171 633-S	67 62995143	5.235438088	0.054778197	2.621162343	2.196704936	17 29523819	0.296211823	0.125562839	3.82935436	0 060307212	0 655290586	100	97.66659464
Mar 10 23:12 2020	CHA16-1A-94Y-1(41-42cm)_7	171 633-S	70 95621473	4.232351905	0.067128369	3.539116187	3 577340992	13 60154844	0.545796443	0.155404102	2.077534281	0 051886158	1.195678398	100	95.78662641
Mar 10 23 28 2020	CHA16-1A-94Y-1(41-42cm)_11	171 633-S	67 84877206	4.720446903	0.087393703	2.519553082	4.105439925	14 83595797	0.994959916	0.329299204	3.426170509	0 095616512	1 036390224	100	94.85809277
Mar 10 23:44 2020	CHA16-1A-94Y-1(41-42cm)_15	171 633-S	67 00703944	5.18830899	0.062062057	2.454851924	2 863482351	16 97688907	0.581725517	0.263377788	3.708845547	0 039638951	0 85377837	100	94.09936206
Mar 10 23 52 2020	CHA16-1A-94Y-1(41-42cm)_17	171 633-S	63 87426614	4.961536065	0.062095947	1.847482733	2 943013859	18 29819389	0.550036665	0.896907879	5.71693268	0 037360206	0 812173937	100	97.42986863
Mar 11 00:12 2020	CHA16-1A-94Y-1(41-42cm)_22	171 633-S	71.70310801	4.808531343	0.089297346	3.15105523	3 24656928	12 97872218	0.818646242	0.308030775	1.842477477	0 077363117	0 976199004	100	95.52355578
Mar 11 00:16 2020	CHA16-1A-94Y-1(41-42cm)_23	171 633-S	64.18191212	5.018621798	0.060047918	1.823067151	2 86955979	19.1541584	0.475748428	0.238849715	5.386802936	0 050778085	0.740453658	100	97.08912804
Mar 11 00 24 2020	CHA16-1A-94Y-1(41-42cm)_25	171 633-S	69 69137897	4.765020934	0.080542265	2.842668171	4.100119291	13 58200307	0.760150526	0.248075379	2.66368536	0 058748476	1 207607553	100	94.98118801
Mar 11 00 28 2020	CHA16-1A-94Y-1(41-42cm)_26	171 633-S	70.13870246	4.698395128	0.051808556	2.663251054	4 061988435	13 5129238	0.875439751	0.233359975	2.55921781	0 098623516	1.10628952	100	96.12311974
Mar 11 00:40 2020	CHA16-1A-94Y-1(41-42cm)_29	171 633-S	69 91837366	5.106871148	0.076835947	2.964865357	2.781142506	14.79473862	0.518538247	0.156877241	2.756072022	0 071929304	0 853755947	100	95.7849824
Mar 11 00:44 2020	CHA16-1A-94Y-1(41-42cm)_30	171 633-S	68 90162125	4.693098399	0.080950535	3.179828455	2.757770287	15 6175852	0.568316399	0.090433581	3.252569629	0 038760654	0 819065617	100	96.2316063
Mar 11 00:48 2020	CHA16-1A-94Y-1(41-42cm)_31	171 633-S	72.72500371	4.525962995	0.077772838	3.393340647	3 289616558	12 5562416	0.566540351	0.227989318	1.485903824	0 069447562	1 082180593	100	94.89174047
29/09/2021	1C-96Y-1-31 2-33.5cm	171.779-OS	78 65895555	3.174247097	0.149866092	4.475168038	0.480300012	12 0205095	0.087579119	0.019565851	0.739295043	0 055263122	0.139250578	100	
29/09/2021	1C-96Y-1-31 2-33.5cm	171.779-OS	77 04414984	3.756980136	0.096548093	4.103293947	0.475919132	13 20190226	0.043834834	0	1.097918232	0 045125739	0.134327781	100	
29/09/2021	1C-96Y-1-31 2-33.5cm	171.779-OS	77 04306533	3.828997867	0.117575206	4.089120005	0.789522712	12 9228678	0	0.027781044	0.964960565	0 013526351	0 202583121	100	
29/09/2021	1C-96Y-1-31 2-33.5cm	171.779-OS	76 51628412	4.086970771	0.098690465	4.086970771	0 50385174	13.4360464	0.028393793	0.031406238	1.029707889	0 055116909	0.126560901	100	
29/09/2021	1C-96Y-1-31 2-33.5cm	171.779-OS	74.11461745	4.533272933	0.099752895	4.10501443	0 584729536	14 87414898	0.041288917	0.080951302	1.473677936	0 010236423	0 082309195	100	
29/09/2021	1C-96Y-1-31 2-33.5cm	171.779-OS	76.44834773	4.86083107	0.080568532	3.216575317	0.445490543	13 64732275	0	0.010071066	1.116604651	0 017881281	0.156307063	100	
01/10/2021	1C-96Y-1-61-61 6cm	172 069-OS	77 50	3.71	0.17	3.13	0.79	12 93	0.21	0.02	1.35	0 02	0.17	100	
01/10/2021	1C-96Y-1-61-61 6cm	172 069-OS	77.75	3.73	0.06	3.26	0 65	12 99	0.22	0.03	1.18	0 00	0.12	100	
01/10/2021	1C-96Y-1-61-61 6cm	172 069-OS	77 52	3.74	0.08	3.03	0.78	13 24	0.22	0.01	1.25	0 01	0.11	100	
01/10/2021	1C-96Y-1-61-61 6cm	172 069-OS	77.11	3.76	0.08	3.16	0 84	13 22	0.24	0.04	1.36	0 04	0.16	100	
01/10/2021	1C-96Y-1-61-61 6cm	172 069-OS	77 05	3.82	0.07	3.25	0 85	13 23	0.24	0.01	1.21	0 03	0 23	100	
01/10/2021	1C-96Y-1-61-61 6cm	172 069-OS	77 60	3.83	0.09	3.11	0.75	12 98	0.21	0.07	1.26	0 02	0.10	100	
01/10/2021	1C-96Y-1-61-61 6cm	172 069-OS	77 61	3.85	0.07	3.25	0.74	12 98	0.17	0.00	1.15	0 05	0.14	100	
01/10/2021	1C-96Y-1-61-61 6cm	172 069-OS	77.75	3.92	0.08	3.02	0 80	12 87	0.18	0.00	1.21	0 03	0.16	100	
01/10/2021	1C-96Y-1-61-61 6cm	172 069-OS	77.18	3.94	0.05	2.94	0 83	13 27	0.25	0.02	1.30	0 03	0 20	100	
01/10/2021	1C-96Y-1-61-61 6cm	172 069-OS	77 36	3.95	0.08	2.93	0 89	13 06	0.21	0.03	1.30	0 01	0.17	100	
01/10/2021	1C-96Y-1-61-61 6cm	172 069-OS	77 50	3.96	0.08	3.00	0.73	13 08	0.16	0.04	1.27	0 06	0.12	100	
01/10/2021	1C-96Y-1-61-61 6cm	172 069-OS	77 84	3.96	0.05	3.10	0 80	12 65	0.18	0.04	1.16	0 06	0.17	100	
01/10/2021	1C-96Y-1-61-61 6cm	172 069-OS	77 87	3.98	0.09	3.03	0.77	12 80	0.17	0.01	1.10	0 03	0.15	100	
01/10/2021	1C-96Y-1-61-61 6cm	172 069-OS	77 37	4.00	0.09	3.16	0.77	13 06	0.20	0.01	1.13	0 04	0.18	100	
01/10/2021	1C-96Y-1-61-61 6cm	172 069-OS	77 26	4.02	0.08	3.02	0 89	13 06	0.17	0.00	1.31	0 02	0.16	100	
01/10/2021	1C-96Y-1-61-61 6cm	172 069-OS	77 26	4.03	0.08	2.97	0.78	13 06	0.22	0.05	1.27	0 08	0 20	100	
01/10/2021	1C-96Y-1-61-61 6cm	172 069-OS	77 53	4.04	0.05	2.93	0.75	13 04	0.18	0.06	1.21	0 02	0 20	100	
01/10/2021	1C-96Y-1-61-61 6cm	172 069-OS	77 07	4.04	0.07	2.93	0 95	13.12	0.22	0.01	1.36	0 04	0.17	100	
01/10/2021	1C-96Y-1-61-61 6cm	172 069-OS	77.14	4.05	0.09	3.00	0 87	13.19	0.22	0.02	1.30	0 00	0.12	100	
01/10/2021	1C-96Y-1-61-61 6cm	172 069-OS	77.43	4.07	0.07	3.02	0 69	13 07	0.19	0.03	1.25	0 00	0.17	100	
01/10/2021	1C-96Y-1-61-61 6cm	172 069-OS	77 61	4.07	0.09	3.04	0 83	12 87	0.19	0.00	1.15	0 04	0.11	100	
01/10/2021	1C-96Y-1-61-61 6cm	172 069-OS	77 62	4.07	0.08	3.00	0.70	13 03	0.16	0.00	1.22	0 00	0.12	100	
01/10/2021	1C-96Y-1-61-61 6cm	172 069-OS	77.16	4.07	0.08	3.01	0 88	13.15	0.22	0.00	1.28	0 04	0.13	100	
01/10/2021	1C-96Y-1-61-61 6cm	172 069-OS	77 62	4.10	0.08	3.07	0 65	12 90	0.15	0.00	1.25	0 07	0.10	100	
01/10/2021	1C-96Y-1-61-61 6cm	172 069-OS	77.15	4.12	0.09	2.91	0.79	13 25	0.21	0.00	1.28	0 04	0.16	100	
01/10/2021	1C-96Y-1-61-61 6cm	172 069-OS	77 31	4.14	0.08	3.06	0.77	13 08	0.17	0.09	1.16	0 04	0.10	100	

Date Analysed	Core Section Identifier	sample_no	SiO2	Na2O	Cl	K2O	FeOt	Al2O3	MgO	P2O5	CaO	MnO	TiO2	total	Analytical Total
01/10/2021	1C-96Y-1-61-61 6cm	172 069-OS	77 00	4.15	0.06	2.97	0 96	13 05	0.27	0.02	1.32	0 04	0.17	100	
01/10/2021	1C-96Y-1-61-61 6cm	172 069-OS	77 07	4.17	0.07	3.07	0 81	13.10	0.26	0.01	1.29	0 00	0.14	100	
Mar 10 06:46 2020	MEXI-CHA16-1B-100Y-1(66-67cm)_2	172 339-S	66 33142295	4.946104615	0.045517213	2.218834512	2 353623524	18 09104093	0.376165028	0.144016876	4.810930905	0 012027327	0 670316127	100	96.44703056
Mar 10 06 50 2020	MEXI-CHA16-1B-100Y-1(66-67cm)_3	172 339-S	68 93154386	4.623687202	0.030011008	2.886475431	3 021941787	15 51815687	0.586569321	0.157766202	3.240772054	0 083572321	0 919503942	100	95.96478704
Mar 10 06 54 2020	MEXI-CHA16-1B-100Y-1(66-67cm)_4	172 339-S	71.1923885	4.251748738	0.061679321	2.859093543	3 651501492	13 51697755	0.824639677	0.213307653	2.302266336	0 04026289	1 0861343	100	93.38624146
Mar 10 06 58 2020	MEXI-CHA16-1B-100Y-1(66-67cm)_5	172 339-S	66 83857446	5.284866989	0.004494626	2.163692066	2 654965144	17 57518927	0.401903188	0.159193382	4.201952709	0 038465637	0 676702533	100	95.66980589
Mar 10 07 06 2020	MEXI-CHA16-1B-100Y-1(66-67cm)_7	172 339-S	72 05423671	4.285119306	0.053224549	3.520197877	3 583434965	12 87587487	0.623412289	0.178960958	1.770638453	0 03583435	1 019065667	100	94.88102988
Mar 10 07:10 2020	MEXI-CHA16-1B-100Y-1(66-67cm)_8	172 339-S	68 32420959	4.940732914	0.048763341	2.698654991	2 521523196	16.48714961	0.323630209	0.202242832	3.657250586	0 047304609	0.748538126	100	95.9737354
Mar 10 07:14 2020	MEXI-CHA16-1B-100Y-1(66-67cm)_9	172 339-S	69 54013242	4.488277398	0.047346395	3.208685053	3 334105967	14 91228753	0.564812183	0.118731799	2.83242231	0 04389732	0 909301627	100	95.67782284
Mar 10 07:18 2020	MEXI-CHA16-1B-100Y-1(66-67cm)_10	172 339-S	71 6285285	4.295497276	0.062728163	3.254560529	3 694946607	13.12217612	0.672394354	0.22201903	1.858214427	0 061009584	1.127925416	100	93.10012744
Mar 10 07 30 2020	MEXI-CHA16-1B-100Y-1(66-67cm)_13	172 339-S	69 37851154	4.816806585	0.034772485	2.827882812	3 382985735	14 67371618	0.752321564	0.248748951	2.848830092	0.101803781	0 933620274	100	95.47778954
Mar 10 07 34 2020	MEXI-CHA16-1B-100Y-1(66-67cm)_14	172 339-S	71.40793778	4.333943387	0.043005239	3.557611014	3.70410088	13.11484405	0.605421686	0.190018282	1.925295372	0 029193337	1 08862897	100	95.56975134
Mar 10 07 38 2020	MEXI-CHA16-1B-100Y-1(66-67cm)_15	172 339-S	67.13770649	4.740424534	0.036159989	2.400184776	2 850874494	17 03123352	0.531709055	0.194425448	4.161019022	0 04024764	0 876015038	100	95.4093211
Mar 10 07:42 2020	MEXI-CHA16-1B-100Y-1(66-67cm)_16	172 339-S	71.16421065	4.34751126	0.050592258	3.232866284	3 904630707	13.18710123	0.759723577	0.145793872	2.067774864	0 035792448	1.104002844	100	95.27149375
Mar 10 07:46 2020	MEXI-CHA16-1B-100Y-1(66-67cm)_17	172 339-S	71.76175044	4.484914217	0.050781886	3.122612853	3.76395758	12 9278569	0.584990502	0.27598851	1.903006486	0 03459056	1 089550067	100	95.11265533
Mar 10 07 50 2020	MEXI-CHA16-1B-100Y-1(66-67cm)_18	172 339-S	67 00450002	5.076163806	0.029041304	2.188469667	2.738180057	17 20309513	0.434167489	0.209615981	4.314707969	0 035057002	0.767001573	100	96.41440464
Mar 10 07 58 2020	MEXI-CHA16-1B-100Y-1(66-67cm)_20	172 339-S	65 8303216	4.821851901	0.047155279	2.050229513	2.450024269	18.44511599	0.334289922	0.124551443	5.238336407	0 0062532	0 651870474	100	97.55005412
Mar 10 08 02 2020	MEXI-CHA16-1B-100Y-1(66-67cm)_21	172 339-S	71 3416392	4.374846816	0.056096952	3.045263116	3 526094134	13.42431941	0.70468457	0.230692037	2.137026748	0 090930488	1 068406523	100	93.58797226
Mar 10 08:14 2020	MEXI-CHA16-1B-100Y-1(66-67cm)_24	172 339-S	68 85733034	5.16706207	0.016497749	1.981805019	3.133534638	15 56490567	0.583335488	0.166845156	3.579700165	0 050323321	0 898660381	100	96.3767869
Mar 10 08:18 2020	MEXI-CHA16-1B-100Y-1(66-67cm)_25	172 339-S	68 63246091	4.369290797	0.074743834	2.733736745	2 929003656	15 92932651	0.620840293	0.210454337	3.579893357	0 052071176	0 86817838	100	92.1815169
Mar 10 08 30 2020	MEXI-CHA16-1B-100Y-1(66-67cm)_28	172 339-S	69 99554708	4.680893492	0.050522929	2.840604525	3 259881946	14 68533825	0.585520918	0.167082052	2.798676783	0 035428942	0 90050308	100	95.40222781
Mar 10 08 34 2020	MEXI-CHA16-1B-100Y-1(66-67cm)_29	172 339-S	70 99835223	4.21823143	0.03359688	3.200712246	3.741229877	12 53825437	0.693982245	0.758950344	2.69198977	0 063484326	1 061216282	100	94.35399899
Mar 10 08:42 2020	MEXI-CHA16-1B-100Y-1(66-67cm)_31	172 339-S	72 36355278	4.236051831	0.06880307	3.259651606	3 567566578	12.79261841	0.615723768	0.196109984	1.82625432	0 019111964	1 054555692	100	94.18184429
Mar 10 08 50 2020	MEXI-CHA16-1B-100Y-1(66-67cm)_33	172 339-S	70 39783329	4.429303405	0.055612526	3.188312086	3 397381732	14.13795838	0.594280466	0.130563993	2.582010116	0 077251234	1 009492781	100	95.66190251
Mar 10 04 04 2020	MEXI-CHA16-1B-101Y-1(71-72cm)_1	173 914-S	71 6264362	4.814041776	0.094982558	2.538509347	1 988498988	15.45797521	0.612626922	0.103232713	2.337544024	0 086943945	0 339208311	100	94.54367395
Mar 10 04 08 2020	MEXI-CHA16-1B-101Y-1(71-72cm)_2	173 914-S	71 95414997	4.525039772	0.083982683	2.497352067	2 033708645	15.44161289	0.62233592	0.119915049	2.297142407	0 076079671	0 348680928	100	94.9005161
Mar 10 04:12 2020	MEXI-CHA16-1B-101Y-1(71-72cm)_3	173 914-S	71 65617885	4.623345037	0.083103239	2.612117015	2.148676899	15 3826618	0.711591232	0.087316331	2.201340549	0 072570509	0.421098541	100	94.94214792
Mar 10 04:16 2020	MEXI-CHA16-1B-101Y-1(71-72cm)_4	173 914-S	71.78343552	4.634312673	0.058173015	2.174889486	1 942619735	15 64928962	0.610552714	0.160371705	2.618313556	0 054477814	0 313564164	100	94.71745637
Mar 10 04 20 2020	MEXI-CHA16-1B-101Y-1(71-72cm)_5	173 914-S	72 02221929	4.631490343	0.061403267	2.531446439	2 207170242	15 08028091	0.674599094	0.100421016	2.259472855	0 023954596	0.407541956	100	95.59751938
Mar 10 04 24 2020	MEXI-CHA16-1B-101Y-1(71-72cm)_6	173 914-S	71 68179368	4.667972245	0.085978303	2.594172943	2 23416527	15 36963404	0.729121424	0.09508438	2.160046043	0 055695305	0 326336368	100	94.44243131
Mar 10 04 28 2020	MEXI-CHA16-1B-101Y-1(71-72cm)_7	173 914-S	71.14389895	5.061465376	0.075715023	1.921595079	1 556074276	16.18355264	0.41147199	0.134824959	3.059931294	0 068404607	0 383065802	100	95.75378393
Mar 10 04 32 2020	MEXI-CHA16-1B-101Y-1(71-72cm)_8	173 914-S	72 03079191	4.385993766	0.09159925	2.550865183	2 287346052	15.15418601	0.692633682	0.14546256	2.213560696	0 067987936	0 379572955	100	94.86977268
Mar 10 04 36 2020	MEXI-CHA16-1B-101Y-1(71-72cm)_9	173 914-S	71 80446788	4.675447258	0.057077084	2.507614526	2.182359086	15.18819461	0.760468205	0.122338014	2.234819641	0 065365851	0.401847851	100	95.30970469
Mar 10 04:40 2020	MEXI-CHA16-1B-101Y-1(71-72cm)_10	173 914-S	71.48643657	4.618574967	0.059553744	2.472637783	2 293766114	15 38764143	0.841328158	0.11132131	2.283244251	0 050189286	0 395306389	100	95.04020427
Mar 10 04:48 2020	MEXI-CHA16-1B-101Y-1(71-72cm)_12	173 914-S	72.40744561	4.811053728	0.056803942	2.374676751	1.47501948	15 59941113	0.242907463	0.151895623	2.500210324	0 030651114	0 349924834	100	95.59195789
Mar 10 04 52 2020	MEXI-CHA16-1B-101Y-1(71-72cm)_13	173 914-S	72 9127861	4.487229798	0.098070824	2.879944099	1.723602908	14 90518801	0.398610445	0.116288652	1.996324887	0 032617549	0.449336733	100	91.66844596
Mar 10 05 04 2020	MEXI-CHA16-1B-101Y-1(71-72cm)_16	173 914-S	71.49033639	4.617157068	0.078011728	2.270013409	2 06752395	15 69136373	0.715427231	0.103802491	2.504474887	0 04294908	0.418940033	100	93.83204486
Mar 10 05 08 2020	MEXI-CHA16-1B-101Y-1(71-72cm)_17	173 914-S	71 38953989	4.659677777	0.091757743	2.362498222	2 056639077	15.75860881	0.695460414	0.106945232	2.436326292	0 022042952	0.42050359	100	94.81488616
Mar 10 05:16 2020	MEXI-CHA16-1B-101Y-1(71-72cm)_19	173 914-S	71.49734739	4.419682894	0.059333895	2.772415606	1 900784942	15.7117448	0.595754308	0.089158366	2.541380973	0 051667745	0 360729076	100	95.22381832
Mar 10 05 20 2020	MEXI-CHA16-1B-101Y-1(71-72cm)_20	173 914-S	71.76708288	4.043111073	0.080077367	2.929145799	2 212664092	15 36728213	0.658004155	0.154991851	2.318029049	0 087347549	0 382264063	100	94.90821527
Mar 10 05 24 2020	MEXI-CHA16-1B-101Y-1(71-72cm)_21	173 914-S	71 27559363	4.286544473	0.052730231	2.688616503	2 365565682	15.18850008	0.988743929	0.204668326	2.511459601	0 07200907	0 365568476	100	95.96013405
Mar 10 05 28 2020	MEXI-CHA16-1B-101Y-1(71-72cm)_22	173 914-S	72 08824131	4.735125157	0.054985835	2.587568717	1 970999609	15 34276924	0.642141565	0.027897225	2.142830344	0 037701685	0 369739311	100	98.93457061
Mar 10 05 32 2020	MEXI-CHA16-1B-101Y-1(71-72cm)_23	173 914-S	71 57724375	4.675003017	0.096382102	2.701925034	2 076852825	15.48329044	0.630012296	0.121889081	2.228079972	0 05776877	0 351552709	100	99.18854024
Mar 10 05 36 2020	MEXI-CHA16-1B-101Y-1(71-72cm)_24	173 914-S	72 02852471	4.623046829	0.07916882	2.742045072	2.102921784	15 29001157	0.597889527	0.10236281	1.999837383	0 053810057	0 38038144	100	97.00788756
Mar 10 05:40 2020	MEXI-CHA16-1B-101Y-1(71-72cm)_25	173 914-S	71 82449854	4.805287614	0.044812759	2.408162291	2 041702812	15.43668023	0.623085817	0.115905898	2.324400124	0 045964489	0 329499423	100	95.50851321
Mar 10 05:44 2020	MEXI-CHA16-1B-101Y-1(71-72cm)_26	173 914-S	71 62183599	4.820154558	0.07588186	2.400130648	2.106664892	15.45238046	0.629169619	0.062885519	2.389649728	0 059950862	0 381295865	100	95.41147278
Mar 10 05:48 2020	MEXI-CHA16-1B-101Y-1(71-72cm)_27	173 914-S	71 56594044	4.903620347	0.079140958	2.207118343	1 975896421	15 60993229	0.589090396	0.104365167	2.606501662	0 008302969	0 350091009	100	95.14668785
Mar 10 05 53 2020	MEXI-CHA16-1B-101Y-1(71-72cm)_28	173 914-S	71 01800031	4.874251751	0.047003587	2.177449037	1 947141927	15 93195023	0.594611083	0.115153555	2.847433356	0 059461108	0 387544055	100	95.52462376
Mar 10 05 56 2020	MEXI-CHA16-1B-101Y-1(71-72cm)_29	173 914-S	71 57263649	4.660351881	0.080946744	2.33218655	2 081188894	15 54328261	0.674347035	0.100503645	2.49951832	0 04036879	0.414669044	100	95.61842298
Mar 10 06 00 2020	MEXI-CHA16-1B-101Y-1(71-72cm)_30	173 914-S	72 38083762	4.100142269	0.102448016	2.487240611	1 994175291	15.45948397	0.66432334	0.109350931	2.311928497	0 032323171	0 357746282	100	91.26579834
290419	MEXI-CHA16-1B-101Y-1_71-72cm_6	173 914-S	71 938	4.8278	0.0874	2.6898	1 8207	15 3731	0.4849	0.1061	2.1806	0 0689	0.4228	100	95 5645
290419	MEXI-CHA16-1B-101Y-1_71-72cm_7	173 914-S	71 9245	5.0412	0.0678	2.4025	1 9249	15 2716	0.5479	0.0796	2.307	0 0382	0 3948	100	96 2226
290419	MEXI-CHA16-1B-101Y-1_71-72cm_8	173 914-S	71.1136	4.9767	0.07	2.0562	1 5413	16.123	0.399	0.1708	3.1244	0 076	0 349	100	97 5941
290419	MEXI-CHA16-1B-101Y-1_71-72cm_9	173 914-S	71.1301	4.5048	0.0463	2.0567	1 6017	16 6229	0.3738	0.1469	3.1484	0 008	0 3603	100	97 9605
290419	MEXI-CHA16-1B-101Y-1_71-72cm_11	173 914-S	71 8305	4.7385	0.0733	2.5586	1 9623	15 39	0.643	0.0961	2.3375	0 067	0 3032	100	98 36
290419	MEXI-CHA16-1B-101Y-1_71-72cm_12	173 914-S	71.4363	4.8688	0.0561	2.5211	2.1737	15 2958	0.6961	0.143	2.3707	0 0941	0 3443	100	99 8567
290419	MEXI-CHA16-1B-101Y-1_71-72cm_16	173 914-S	71 848	5.0979	0.0765	2.4814	1 5623	15 6454	0.4638	0.1207	2.3085	0 0762	0 3194	100	97 635
290419	MEXI-CHA16-1B-101Y-1_71-72cm_17	173 914-S	71 9441	4.8946	0.0461	2.3996	1 5776	15.4838	0.4586	0.1366	2.5845	0 0889	0 3856	100	98 2506
Mar 10 02 04 2020	MEXI-CHA16-1B-101Y-1(101-102cm)_1	174 244-S	65 32057687	4.153010397	0.044531303	2.531574079	5.490160653	14 07280793	2.002891942	0.32066605	4.524299056	0.121393552	1.418088163	100	98.35777751
Mar 10 02 08 2020	MEXI-CHA16-1B-101Y-1(101-102cm)_2	174 244-S	65 34245676	4.247638699	0.063523129	2.590263507	5 334709366	13 98321402	2.107158806	0.340331844	4.399336433	0.109161105	1.48220634	100	97.28739925
Mar 10 02:12 2020	MEXI-CHA16-1B-101Y-1(101-102cm)_3	174 244-S	63 31567603	4.3326068	0.058693056	2.096180584	4.734300539	16.73701237	1.799647721	0.312177528	5.388717892	0 086301288	1.138686194	100	97.79691766
Mar 10 02 20 2020	MEXI-CHA16-1B-101Y-1(101-102cm)_5	174 244-S	65 31199817	4.122088817	0.114562821	2.610710451	5 573921892	14.17792171	1.690793026	0.358449443	4.252043182	0.107512802	1 679997683	100	90.7798871
Mar 10 02 32 2020	MEXI-CHA16-1B-101Y-1(101-102cm)_8	174 244-S	65.47226831	4.329178199	0.076564267	2.709512945	5 63455533	13 96210507	1.796078657	0.353365647	4.064269418	0 074922138	1 527180024	100	97.43448558
Mar 10 02:40 2020	MEXI-CHA16-1B-101Y-1(101-102cm)_10	174 244-S	64.76804074	4.355147534	0.075920827	2.561809327	5 258450723	14 93167486	1.856533884	0.232326028	4.501316793	0 070008959	1 388770319	100	96.41623107
Mar 10 02:44 2020	MEXI-CHA16-1B-101Y-1(101-102cm)_11	174 244-S	63 38958743	4.095245378	0.053892819	2.940559652	5 253241798	15 63572691	1.737127766	0.275638225	5.200918672	0 066450369	1 351610977	100	95.5600407
Mar 10 02:48 2020	MEXI-CHA16-1B-101Y-1(101-102cm)_12	174 244-S	62 91880034	4.40553592	0.041811336	2.928915932	4.128073541	17 3910735	1.300183985	0.22380738	5.443963308	0 047860184	1.169974571	100	94.23281734

Date Analysed	Core Section Identifier	sample_no	SiO2	Na2O	Cl	K2O	FeOt	Al2O3	MgO	P2O5	CaO	MnO	TiO2	total	Analytical Total
Mar 10 02 52 2020	MEXI-CHA16-1B-101Y-1(101-102cm)_13	174 244-S	66 08664272	4.395777928	0.067457024	2.698280941	5.196298844	14 03587624	1.634778805	0.309248292	3.952559972	0.105717804	1 517361423	100	94.87522077
Mar 10 02 56 2020	MEXI-CHA16-1B-101Y-1(101-102cm)_14	174 244-S	63 24563326	4.51922673	0.052125737	2.041504989	3 84466168	17 84543146	1.223141289	0.229021626	5.730722127	0.101660731	1.166870364	100	96.49743745
Mar 10 03 00 2020	MEXI-CHA16-1B-101Y-1(101-102cm)_15	174 244-S	63 54706331	4.469528164	0.054781052	2.187115455	6 0145675	14 83188406	2.249014949	0.341685207	4.694044962	0.128647782	1.481667555	100	96.93132548
Mar 10 03 04 2020	MEXI-CHA16-1B-101Y-1(101-102cm)_16	174 244-S	63 69652106	4.316278434	0.037965985	2.333974466	5 995721072	14.76941901	2.147256508	0.302379359	4.719815031	0.107155361	1 573513719	100	96.40208293
Mar 10 03 08 2020	MEXI-CHA16-1B-101Y-1(101-102cm)_17	174 244-S	63 57065727	4.190790397	0.054812554	2.13952347	4 58469315	16 58549298	1.701430569	0.247471548	5.593325643	0 075494614	1 256307805	100	98.15269753
Mar 10 03:12 2020	MEXI-CHA16-1B-101Y-1(101-102cm)_18	174 244-S	63 25677211	4.576079923	0.097304306	2.015050412	4 525781675	16 93325909	1.50342157	0.263141877	5.624900082	0 062283376	1.142005576	100	92.80164846
Mar 10 03:16 2020	MEXI-CHA16-1B-101Y-1(101-102cm)_19	174 244-S	64 69492546	4.247005342	0.049320128	2.348089246	5 321652047	15 21892552	1.876420664	0.254701034	4.562880849	0.100896062	1 325183643	100	97.5261057
Mar 10 03 20 2020	MEXI-CHA16-1B-101Y-1(101-102cm)_20	174 244-S	64 53784301	3.997893719	0.067433972	3.541343812	5 672511795	14 36095103	1.70832729	0.323386186	4.135102056	0.109739247	1 545467886	100	94.31447996
Mar 10 03 28 2020	MEXI-CHA16-1B-101Y-1(101-102cm)_22	174 244-S	65 55794378	4.19092071	0.140544832	2.701129616	5 649773101	13 96805897	1.671902379	0.353083915	4.153928413	0 082110036	1 530604244	100	92.92408573
Mar 10 03 32 2020	MEXI-CHA16-1B-101Y-1(101-102cm)_23	174 244-S	63.70175079	4.526487765	0.072809753	2.2060423	4 898863887	16 08037935	1.791762056	0.299421046	5.085289997	0 065041998	1 27215106	100	96.552999
Mar 10 03:48 2020	MEXI-CHA16-1B-101Y-1(101-102cm)_27	174 244-S	65 29381037	3.923430344	0.060811674	3.470459311	5.724685148	13 86862132	1.59012042	0.418866615	3.900334936	0 063013476	1 685846383	100	95.37642436
Mar 10 04 00 2020	MEXI-CHA16-1B-101Y-1(101-102cm)_30	174 244-S	65 64778532	4.658706171	0.057099264	2.556370708	5 269895354	14 25271512	1.749647165	0.336623733	3.970756141	0 071138349	1.429262672	100	95.44781561
010319	CHA16_1B_104Y-1_54-55cm_1	178 667-S	71 6813	5.2654	0.0726	2.378	1 5015	15 9197	0.4007	0.0997	2.3758	0 0574	0 2479	100	96.1901
010319	CHA16_1B_104Y-1_54-55cm_17	178 667-S	75 3667	4.1009	0.0713	3.4886	1.7681	13.1385	0.3773	0.1624	1.0891	0 0773	0 3597	100	93.7365
010319	CHA16_1B_104Y-1_54-55cm_18	178 667-S	75.7283	4.045	0.0626	3.5955	0 92	13 6324	0.2032	0.0593	1.5539	0	0.1999	100	94.7884
010319	CHA16_1B_104Y-1_54-55cm_24	178 667-S	73.7051	4.6115	0.0831	2.562	1 9349	14.4235	0.43	0.1147	1.7912	0 018	0 3259	100	93.1765
Jan 21 00:18 2020	CHA16-1C-100Y-1_41-77cm_1	181.723-S (44 -77 cm)	76.72369789	3.713624757	0.075640119	3.787266042	1 0768889	13 03111275	0.252484403	0.056394401	1.09300143	0 010835789	0.179053522	100	95.05537664
Jan 21 00 25 2020	CHA16-1C-100Y-1_41-77cm_3	181.723-S (44 -77 cm)	76 80369816	3.69570685	0.092549713	3.748053972	1.10082786	13 00857546	0.191695163	0.028253791	1.074870995	0 049310989	0 206457051	100	95.51623393
Jan 21 00 29 2020	CHA16-1C-100Y-1_41-77cm_4	181.723-S (44 -77 cm)	76 39872455	3.431698217	0.081231338	4.300482576	1 293202629	12 90786418	0.170390332	0.071136829	1.098968986	0 057339768	0.188960598	100	92.0826891
Jan 21 00:41 2020	CHA16-1C-100Y-1_41-77cm_7	181.723-S (44 -77 cm)	75 87456367	3.594679512	0.071464375	3.94878227	1 240711112	13 38450636	0.251412958	0.059495627	1.287560879	0 027899005	0 258924229	100	93.19328716
Jan 21 00:45 2020	CHA16-1C-100Y-1_41-77cm_8	181.723-S (44 -77 cm)	75 65894657	3.673273866	0.098233838	3.809709752	1 320591654	13 54588186	0.276649997	0	1.354335751	0 05698822	0 205388484	100	95.28284924
Jan 21 00:49 2020	CHA16-1C-100Y-1_41-77cm_9	181.723-S (44 -77 cm)	75 55687545	4.011213867	0.091866323	3.545532046	1 348247887	13 51753033	0.285970973	0.01986366	1.318830404	0 031645196	0 272423865	100	94.48511413
Jan 21 00 53 2020	CHA16-1C-100Y-1_41-77cm_10	181.723-S (44 -77 cm)	77 64095744	3.435068744	0.092862409	4.033842194	0 94092645	12 59720661	0.153685186	0.018040433	0.898219136	0 030463912	0.158727488	100	95.19460145
Jan 21 00 57 2020	CHA16-1C-100Y-1_41-77cm_11	181.723-S (44 -77 cm)	77 98470831	3.717580895	0.058615267	3.759826132	0 863845459	12 3801402	0.196123515	0	0.879684442	0 020911393	0.138564379	100	94.68522945
Jan 21 01 01 2020	CHA16-1C-100Y-1_41-77cm_12	181.723-S (44 -77 cm)	77.72677883	3.510037612	0.057762781	3.868419831	0 935757244	12.7011214	0.145988051	0	0.887591921	0 014756915	0.15178541	100	94.87077826
Jan 21 01 05 2020	CHA16-1C-100Y-1_41-77cm_13	181.723-S (44 -77 cm)	77 20043041	3.473911817	0.074102949	4.033179354	1 05829305	12 80418555	0.165844335	0.059105177	0.940473736	0 027855825	0.162617792	100	92.97875623
Jan 21 01:17 2020	CHA16-1C-100Y-1_41-77cm_16	181.723-S (44 -77 cm)	77 29427574	3.336829505	0.065127187	4.538517301	0 841935662	12 6598027	0.146992168	0.01710993	0.962610527	0 028969259	0.107830021	100	93.20224468
Jan 21 01 21 2020	CHA16-1C-100Y-1_41-77cm_17	181.723-S (44 -77 cm)	77 68822884	3.206584027	0.087202153	4.233114226	0 932161951	12 52763525	0.16286907	0.007918831	0.916702119	0 055136313	0.182447223	100	94.4930797
Jan 21 01 24 2020	CHA16-1C-100Y-1_41-77cm_18	181.723-S (44 -77 cm)	77.43947389	3.471987656	0.101112117	3.863810714	1 024261044	12.78982319	0.131369564	0.029506045	0.968308333	0 037767389	0.142580057	100	91.87820685
Jan 21 01 28 2020	CHA16-1C-100Y-1_41-77cm_19	181.723-S (44 -77 cm)	77 63156768	3.420834709	0.091400427	4.243973061	0 969838653	12.43845006	0.147951101	0	0.911026434	0 029397798	0.115560073	100	93.54442035
Jan 21 01 36 2020	CHA16-1C-100Y-1_41-77cm_21	181.723-S (44 -77 cm)	77 39912481	3.496138369	0.102409961	4.087792554	0 968372632	12 60994089	0.122311056	0.060964704	0.979751711	0 02807668	0.145116636	100	92.95970746
Jan 21 01:40 2020	CHA16-1C-100Y-1_41-77cm_22	181.723-S (44 -77 cm)	77.13305841	3.471097473	0.110284236	4.097213157	1.121393542	12 66458893	0.190580826	0.052011368	0.959524887	0 039104769	0.161142405	100	91.03748957
Jan 21 01:48 2020	CHA16-1C-100Y-1_41-77cm_24	181.723-S (44 -77 cm)	77 22043855	3.594078049	0.090896741	4.0015462	1 031149202	12 59942168	0.200599705	0.03729523	0.958884517	0 055164919	0 210525211	100	95.71300214
Jan 21 01 52 2020	CHA16-1C-100Y-1_41-77cm_25	181.723-S (44 -77 cm)	77 56464625	3.74233738	0.072128849	3.669163185	0 992697118	12 6665334	0.147707338	0.021414484	0.942631735	0 015366581	0.16537368	100	95.66213938
Jan 21 01 56 2020	CHA16-1C-100Y-1_41-77cm_26	181.723-S (44 -77 cm)	78 00634898	3.484311744	0.083095556	3.843301439	0 839938902	12 50908078	0.200083962	0	0.859306292	0 010664106	0.163868237	100	94.71023957
Jan 21 02 00 2020	CHA16-1C-100Y-1_41-77cm_27	181.723-S (44 -77 cm)	77 88933677	3.797421619	0.084703599	3.734131259	0 83848813	12.47676242	0.148732347	0.022514733	0.841139029	0 022151626	0.144618473	100	94.80116671
Jan 21 02:16 2020	CHA16-1C-100Y-1_41-77cm_31	181.723-S (44 -77 cm)	76 05695739	3.812273821	0.075302881	3.560915108	1.162620438	13.42696879	0.255129094	0.082480061	1.249907308	0 078654331	0 238790778	100	95.4810743
030418	MEX2-1C-100Y-1_53-54cm-7	181.723-S (53 - 54 cm)	77 20	3.56	0.10	4.20	0 94	12.49	0.22	0.00	1.09	0 02	0 20	100	96.1649
030418	MEX2-1C-100Y-1_53-54cm-14	181.723-S (53 - 54 cm)	77.41	3.56	0.08	4.32	0 92	12.47	0.13	0.03	0.93	0 00	0.16	100	95.117
030418	MEX2-1C-100Y-1_53-54cm-20	181.723-S (53 - 54 cm)	77.76	3.77	0.07	3.97	0 87	12 28	0.15	0.02	0.91	0 00	0 20	100	95 8185
030418	MEX2-1C-100Y-1_53-54cm-24	181.723-S (53 - 54 cm)	76 96	3.86	0.06	4.00	1 04	12 62	0.21	0.02	1.07	0 00	0.16	100	94.7299
Jan 23 07 38 2020	CHA16-1C-100Y-1(120-121cm)_2	182.165-S	62 94491759	4.502069257	0.067282298	1.893637016	3 283961065	19 02826904	1.263341522	0.190633179	5.783119196	0 026659024	1 016110812	100	94.52709175
Jan 23 07 50 2020	CHA16-1C-100Y-1(120-121cm)_5	182.165-S	66 82218199	4.063176268	0.064771266	2.992662707	4.129278827	16.1310181	1.064697309	0.22392651	3.614987668	0 088628857	0 804670497	100	95.56706785
Jan 23 08 02 2020	CHA16-1C-100Y-1(120-121cm)_8	182.165-S	76 21451171	3.646805584	0.052467275	4.572449278	0 917234849	13.73588162	0.017699804	0.070693859	0.751184829	0 021071195	0	100	94.91630712
Jan 23 08 05 2020	CHA16-1C-100Y-1(120-121cm)_9	182.165-S	76.43325488	3.48525707	0.072734705	4.512436398	0 806212425	13 65996641	0	0	0.982129093	0 048009027	0	100	97.06508001
Jan 23 08 09 2020	CHA16-1C-100Y-1(120-121cm)_10	182.165-S	76.15675595	3.772376957	0.070309534	3.806307111	0 668330661	14.1198626	0	0	1.356973171	0 049084014	0	100	97.99524555
Jan 23 08:13 2020	CHA16-1C-100Y-1(120-121cm)_11	182.165-S	76 66500668	2.750448605	0.07558371	4.55001087	0 821174797	13 91669088	0.051709535	0	1.133188955	0 026229474	0 009956494	100	93.40637026
Jan 23 08 25 2020	CHA16-1C-100Y-1(120-121cm)_14	182.165-S	66 65774391	4.282810836	0.080518967	2.755158271	4.430808943	16 06151781	1.122460023	0.191259243	3.56992349	0 031182411	0 816616097	100	93.64253324
Jan 23 08 37 2020	CHA16-1C-100Y-1(120-121cm)_17	182.165-S	66 50544475	4.189507745	0.07388336	2.792770165	4.143996106	16 33554058	1.104498917	0.276150781	3.65305038	0 057418521	0 8677387	100	95.96206783
Jan 23 08:41 2020	CHA16-1C-100Y-1(120-121cm)_18	182.165-S	66 81680842	4.374260086	0.08543824	2.775932713	4.1747806	15 82957198	1.124522781	0.201120106	3.65473767	0.115249813	0 847577588	100	92.58149477
Jan 23 08:44 2020	CHA16-1C-100Y-1(120-121cm)_19	182.165-S	66 63301725	4.183929687	0.069594945	2.785869077	4 254968167	16 28445826	1.066190414	0.233536608	3.567338208	0 060895577	0 860201805	100	96.55873718
Jan 23 08 48 2020	CHA16-1C-100Y-1(120-121cm)_20	182.165-S	65 85850373	5.281581739	0.060983811	3.089311475	4 070088399	16 27382323	1.059994924	0.193984688	3.230772725	0 026981324	0 853973958	100	99.69859059
Jan 23 08 52 2020	CHA16-1C-100Y-1(120-121cm)_21	182.165-S	65.75612259	4.710982637	0.061884575	2.848495854	4 314157315	16 33125527	1.121645392	0.273616081	3.638326186	0.100900945	0 842613157	100	99.70174246
Jan 23 08 56 2020	CHA16-1C-100Y-1(120-121cm)_22	182.165-S	66 25411313	4.621907769	0.068559846	2.775041388	4.191683212	16.42538439	1.062473567	0.173950205	3.56611355	0 051930002	0 808842946	100	98.01655615
Jan 23 09 00 2020	CHA16-1C-100Y-1(120-121cm)_22	182.165-S	66 09421768	4.455177295	0.038436587	2.705183688	4 333643415	16 29261212	1.114556569	0.22456158	3.831248857	0 043972291	0 866389911	100	95.74211212
Jan 23 09 04 2020	CHA16-1C-100Y-1(120-121cm)_23	182.165-S	66 60890776	4.316505672	0.085470186	2.849006185	4 367879794	16.12973425	1.058309403	0.142021887	3.580501152	0 059764867	0 801898846	100	93.36589068
Jan 23 09 27 2020	CHA16-1C-100Y-1(120-121cm)_29	182.165-S	66 93144565	4.329713988	0.037907701	2.816605686	4 210787757	16.14001886	1.054532933	0.228610965	3.378393459	0 076344838	0.795638163	100	94.43991443
Jan 23 09 31 2020	CHA16-1C-100Y-1(120-121cm)_30	182.165-S	66 5961762	4.26592386	0.054821922	2.876074339	4.466003552	16 08626023	1.116242622	0.166542355	3.439332017	0 070603991	0 860018908	100	96.31183599
Jan 23 09 35 2020	CHA16-1C-100Y-1(120-121cm)_31	182.165-S	67 28851786	4.096595955	0.036066307	2.887419895	4.452749501	15.79566096	1.072999078	0.204446251	3.267059512	0 062930946	0 835553743	100	94.54807748
Jan 23 09:43 2020	CHA16-1C-100Y-1(120-121cm)_33	182.165-S	66.78170875	3.911986723	0.07724354	2.705645969	4 079461774	16.44884365	1.083107218	0.314597659	3.611700756	0 059099796	0 926604167	100	94.24736381
Jan 23 09:47 2020	CHA16-1C-100Y-1(120-121cm)_34	182.165-S	67.43453096	4.167884121	0.049484632	2.812810653	3 878606025	16 36098336	0.682158672	0.256278304	3.524983854	0 021877416	0 810402003	100	95.98939754
Jan 23 09 51 2020	CHA16-1C-100Y-1(120-121cm)_35	182.165-S	66 57091857	4.364540081	0.05320762	2.762703353	4.193577998	16 32569606	1.084923839	0.185510414	3.566159595	0 055458712	0 837303761	100	97.73036245
Jan 23 09 55 2020	CHA16-1C-100Y-1(120-121cm)_36	182.165-S	66 58503516	4.319239607	0.04404824	2.688930552	4 065164326	16.42149811	1.055483713	0.16949679	3.710291691	0.121995838	0 818815973	100	95.57703146
Jan 23 09 59 2020	CHA16-1C-100Y-1(120-121cm)_37	182.165-S	76.72992659	2.807202577	0.047370509	4.459006605	1 298014327	13.45577681	0.067451486	0.033159356	0.968836446	0 025847821	0.10740748	100	97.10683082
Jan 23 10 03 2020	CHA16-1C-100Y-1(128-135cm)_1	182 311-S	76 00139205	3.681990508	0.090865592	4.481042905	1.124879313	13 5236128	0.07074239	0.027591607	0.885130671	0 040350132	0 072402036	100	96.40612892
Jan 23 10 07 2020	CHA16-1C-100Y-1(128-135cm)_2	182 311-S	75 82046599	3.749197696	0.076366678	4.328475699	1 258452486	13 67456811	0.090691872	0.076572796	0.842143162	0 022879086	0 060186424	100	97.03184891

Date Analysed	Core Section Identifier	sample_no	SiO2	Na2O	Cl	K2O	FeOt	Al2O3	MgO	P2O5	CaO	MnO	TiO2	total	Analytical Total
Jan 23 10:10 2020	CHA16-1C-100Y-1(128-135cm)_3	182 311-S	75 95850862	3.275329807	0.065747554	4.70380411	1 21954302	13 62851389	0.017123961	0.03234526	0.94602516	0 046720931	0.106337684	100	94.60427976
Jan 23 10:14 2020	CHA16-1C-100Y-1(128-135cm)_4	182 311-S	75.79723042	3.820226454	0.072982925	4.38947663	1.171822989	13 61006587	0.069727571	0	0.933002425	0 066682241	0 068782469	100	95.22775383
Jan 23 10:18 2020	CHA16-1C-100Y-1(128-135cm)_5	182 311-S	75 96073892	3.565763865	0.0374002	4.52739265	1 215893159	13 62687059	0.03802181	0	0.920898283	0 077701247	0 02931927	100	96.52354761
Jan 23 10 22 2020	CHA16-1C-100Y-1(128-135cm)_6	182 311-S	75.77498826	3.779499961	0.038858968	4.400515604	1 253684236	13 55105315	0.094941912	0	0.969506306	0 051881974	0 085069633	100	95.21611505
Jan 23 10 26 2020	CHA16-1C-100Y-1(128-135cm)_7	182 311-S	76 03896428	3.80165801	0.067743047	4.335554981	1 227485743	13 39711672	0.071286529	0.02980694	0.911781305	0 024700157	0 093902285	100	95.95080718
Jan 23 10 30 2020	CHA16-1C-100Y-1(128-135cm)_8	182 311-S	75 81020822	3.74049697	0.064240611	4.68442951	1 226201947	13.4208349	0.05313212	0.025360894	0.916722851	0 042442818	0 015929156	100	95.42250536
Jan 23 10 34 2020	CHA16-1C-100Y-1(128-135cm)_9	182 311-S	76.10878718	3.431498533	0.052285318	4.607320133	1.145372939	13 52841553	0.05642673	0.071335811	0.853504901	0 020499986	0.124552947	100	96.58543084
Jan 23 10:42 2020	CHA16-1C-100Y-1(128-135cm)_11	182 311-S	75 89968058	3.38436035	0.056927391	4.81936139	1 29238952	13.42513316	0.095229739	0.027148368	0.877601846	0 029252892	0 092914762	100	95.03333802
Jan 23 10 53 2020	CHA16-1C-100Y-1(128-135cm)_14	182 311-S	75 88879465	3.478346208	0.069911182	4.405645479	1.119535674	13.74224674	0.124619784	0.026682078	0.978541118	0 084906923	0 080770167	100	96.69411715
Jan 23 10 57 2020	CHA16-1C-100Y-1(128-135cm)_15	182 311-S	75 87062742	3.620887305	0.070316074	4.545580502	1 232279594	13 56142382	0.081445985	0.012898215	0.849450447	0 056689734	0 098400896	100	96.13733598
Jan 23 11 05 2020	CHA16-1C-100Y-1(128-135cm)_17	182 311-S	76 00149245	3.524264927	0.064315422	4.708057054	1 215669993	13.47865744	0.060532162	0.089957519	0.85148323	0	0 0055698	100	95.15602611
Jan 23 11:17 2020	CHA16-1C-100Y-1(128-135cm)_20	182 311-S	76.15798755	3.35400912	0.074718956	4.726665797	1.194592755	13.44066682	0.060439333	0.001771116	0.858085969	0 037636215	0 093426368	100	90.33852156
Jan 23 11 25 2020	CHA16-1C-100Y-1(128-135cm)_22	182 311-S	75.76464124	3.628791039	0.069820466	4.528895118	1 233032949	13 58727246	0.060175597	0.03920849	0.917804898	0 049587208	0.120770536	100	95.38750375
Jan 23 11 32 2020	CHA16-1C-100Y-1(128-135cm)_24	182 311-S	76 20480421	3.240850563	0.074259417	4.936682348	1.1152445	13.45483421	0.023219142	0.031900172	0.805561227	0 043614333	0 06902988	100	95.61076989
Jan 23 11 36 2020	CHA16-1C-100Y-1(128-135cm)_25	182 311-S	75 86189148	3.685009338	0.067728224	4.501257532	1.194253036	13.49660975	0.105517851	0.075893296	0.911660346	0 037789627	0 062389523	100	95.52885986
Jan 23 11:40 2020	CHA16-1C-100Y-1(128-135cm)_26	182 311-S	76.19865341	3.122321685	0.081879159	4.926063208	1 089157335	13.47134022	0.093861475	0.013868421	0.917425611	0 049371579	0 036057895	100	90.13282641
Jan 23 11:44 2020	CHA16-1C-100Y-1(128-135cm)_27	182 311-S	76 02052258	2.901173722	0.110045108	5.044620986	1.160408036	13 66026291	0.083225604	0.018624656	0.911079499	0 031821554	0 058215352	100	93.96146932
Jan 23 11:48 2020	CHA16-1C-100Y-1(128-135cm)_28	182 311-S	75 66365053	3.49811388	0.070066847	4.838457607	1.155586521	13 53453487	0.109906686	0.036528753	0.948107382	0 04240326	0.102643659	100	93.62487734
Jan 23 11 52 2020	CHA16-1C-100Y-1(128-135cm)_29	182 311-S	75 94579038	3.372003531	0.050644421	4.689298253	1 218764655	13 62617054	0.032825088	0	0.903087063	0 040744791	0.120671275	100	95.96318589
Jan 23 11 56 2020	CHA16-1C-100Y-1(128-135cm)_30	182 311-S	75 85512749	3.713468649	0.057895173	4.554835312	1 203901957	13 56708783	0.085390193	0	0.875450638	0 029362606	0 057480154	100	96.38109172
Jan 23 12 00 2020	CHA16-1C-100Y-1(128-135cm)_31	182 311-S	75 84131117	3.595465013	0.06675289	4.58599664	1 227398652	13 57943462	0.067797536	0.001253575	0.88833944	0 06132073	0 084929733	100	95.72619312
290419	MEXI-CHA16-1C-100Y-1_132-133cm_1	182 311-S	75.728	3.8104	0.0754	4.3514	1 0312	13.7666	0.0717	0.0545	0.9756	0 0553	0 0798	100	94 804
290419	MEXI-CHA16-1C-100Y-1_132-133cm_3	182 311-S	75.7214	3.6549	0.0744	4.6246	1 302	13.401	0.0714	0.0149	0.9429	0 0527	0.1397	100	95 0999
290419	MEXI-CHA16-1C-100Y-1_132-133cm_4	182 311-S	75 9339	3.5398	0.087	4.8409	1 0581	13 3254	0.1028	0.0357	0.9702	0 0172	0 089	100	96.1617
290419	MEXI-CHA16-1C-100Y-1_132-133cm_5	182 311-S	76 2585	3.757	0.0522	4.4138	1 3809	13 0736	0.0689	0	0.87	0 08	0 0453	100	95 6556
290419	MEXI-CHA16-1C-100Y-1_132-133cm_6	182 311-S	75.7906	3.9543	0.0291	4.4975	1 2606	13 2265	0.0889	0.0464	0.9498	0 0164	0.1399	100	94.7422
290419	MEXI-CHA16-1C-100Y-1_132-133cm_7	182 311-S	75.414	3.7914	0.0871	4.6075	1 2612	13 5628	0.0662	0.0415	0.9714	0 0942	0.1026	100	94 6011
290419	MEXI-CHA16-1C-100Y-1_132-133cm_9	182 311-S	76.1312	3.7295	0.1075	4.7328	1 0816	13 2017	0.0734	0	0.8882	0 0068	0 0472	100	92 0365
290419	MEXI-CHA16-1C-100Y-1_132-133cm_11	182 311-S	75.4539	3.8728	0.0903	4.7094	1 2202	13.4876	0.0937	0.0305	0.9215	0 0089	0.1111	100	92 3138
290419	MEXI-CHA16-1C-100Y-1_132-133cm_12	182 311-S	75 531	3.8244	0.1223	4.6644	1 3688	13 332	0.0827	0.0083	0.9185	0 0382	0.1096	100	91.1809
290419	MEXI-CHA16-1C-100Y-1_132-133cm_13	182 311-S	75 9938	3.5363	0.0733	4.7026	1.1173	13 3742	0.0943	0.0537	0.9393	0 0239	0 0913	100	94 8927
290419	MEXI-CHA16-1C-100Y-1_132-133cm_15	182 311-S	76 276	3.6164	0.0735	4.4943	1 2959	13.1254	0.0619	0.0391	0.86	0 0661	0 0915	100	95 6977
290419	MEXI-CHA16-1C-100Y-1_132-133cm_16	182 311-S	75 2345	3.8361	0.1297	4.8199	1.1959	13 5663	0.0911	0.0137	0.9455	0 0593	0.1081	100	91.4478
290419	MEXI-CHA16-1C-100Y-1_132-133cm_17	182 311-S	75.7862	3.5754	0.09	4.5044	1 3324	13 6156	0.0964	0.0438	0.8466	0 0183	0 0908	100	95.1078
290419	MEXI-CHA16-1C-100Y-1_132-133cm_18	182 311-S	76 5335	3.4826	0.0617	4.5517	1 2136	13 0863	0.0537	0.0193	0.9237	0 0157	0 0582	100	95.4547
290419	MEXI-CHA16-1C-100Y-1_132-133cm_19	182 311-S	75.7634	3.8206	0.0694	4.4514	1.4397	13 2986	0.0699	0.0096	0.9117	0 0796	0 0862	100	96 0215
290419	MEXI-CHA16-1C-100Y-1_132-133cm_20	182 311-S	76 0342	3.8558	0.0851	4.4247	1.1648	13.1698	0.137	0.025	1.0186	0 0254	0 0597	100	95 0487
290419	MEXI-CHA16-1C-100Y-1_132-133cm_21	182 311-S	75 612	3.5718	0.0483	4.6304	1 356	13 657	0.0689	0.0451	0.9279	0 0254	0 0573	100	94 8182
290419	MEXI-CHA16-1C-100Y-1_132-133cm_22	182 311-S	76.1348	3.5927	0.045	4.5072	1 2388	13 275	0.0769	0.0455	0.9446	0 0239	0.1156	100	95 0745
290419	MEXI-CHA16-1C-100Y-1_132-133cm_23	182 311-S	76.1228	3.7775	0.0825	4.4586	1 0746	13 3003	0.0485	0.0278	0.9254	0 0941	0 0879	100	95 3291
290419	MEXI-CHA16-1C-100Y-1_132-133cm_24	182 311-S	75 8164	3.9228	0.057	4.4468	1.1774	13.4856	0.0898	0.0228	0.9024	0 0415	0 0376	100	95 3208
290419	MEXI-CHA16-1C-100Y-1_132-133cm_25	182 311-S	75 8808	3.9465	0.0654	4.2719	1.1993	13 51	0.0924	0.0509	0.8835	0 0196	0 0798	100	95 8926
290419	MEXI-CHA16-1C-100Y-1_132-133cm_26	182 311-S	76.1475	3.7959	0.0775	4.5489	1 2446	13.1042	0.1009	0.0261	0.8398	0 0474	0 0671	100	95.4982
290419	MEXI-CHA16-1C-100Y-1_132-133cm_27	182 311-S	76 3772	3.5813	0.0666	4.5527	1 251	13.1275	0.1036	0.0364	0.8466	0 0208	0 0363	100	95.147
290419	MEXI-CHA16-1C-100Y-1_132-133cm_28	182 311-S	75 8175	3.8949	0.0608	4.4187	1 3122	13.4396	0.1055	0.0385	0.8426	0 0141	0 0555	100	95.4634
290419	MEXI-CHA16-1C-100Y-1_132-133cm_29	182 311-S	75 9831	3.9133	0.0704	4.524	1.1725	13 2593	0.0939	0	0.8943	0 0409	0 0483	100	94 3458
290419	MEXI-CHA16-1C-100Y-1_132-133cm_30	182 311-S	75 8583	4.0351	0.0653	4.5127	1.1993	13 3475	0.0679	0	0.8924	0 0214	0	100	94 6832
29/09/2021	1C-101Y-1-109-110cm	183 588-S	77 6075882	3.433232242	0.092433176	3.612816698	0 932043325	13 0779739	0.182849103	0.064122214	0.876725203	0 058312129	0 061903818	100	
29/09/2021	1C-101Y-1-109-110cm	183 588-S	77 58508317	3.460116281	0.09065715	3.554769918	0 803504206	13.19892381	0.212469768	0.060052474	0.854896826	0 079614226	0 099912172	100	
29/09/2021	1C-101Y-1-109-110cm	183 588-S	77 65487548	3.518453522	0.099463975	3.292911629	0 951674015	13.16036942	0.211280097	0.054355596	0.942266526	0 025599005	0 088750735	100	
29/09/2021	1C-101Y-1-109-110cm	183 588-S	78 09094786	3.524533583	0.082344959	3.185839665	0 895739571	12 84920051	0.20250355	0.068479677	0.945458162	0 06869136	0 086261107	100	
29/09/2021	1C-101Y-1-109-110cm	183 588-S	77.49871961	3.563897758	0.119257938	3.575431408	0 965020471	12 87155307	0.208096584	0.080850884	0.898955625	0 086963719	0.131252934	100	
29/09/2021	1C-101Y-1-109-110cm	183 588-S	77 61624847	3.573432252	0.092613215	3.309125133	0 881622827	13 03562712	0.242666417	0.077812016	0.936676437	0 089124361	0.145051747	100	
29/09/2021	1C-101Y-1-109-110cm	183 588-S	77.74061406	3.574864958	0.105909551	3.329858637	0 965881738	12 88510516	0.253010826	0.075395127	0.925697144	0 089093208	0 05456959	100	
29/09/2021	1C-101Y-1-109-110cm	183 588-S	78 0408794	3.581790237	0.079137489	3.328212167	0 87959893	12 68946925	0.248329136	0.129113501	0.905450434	0 03719145	0 08082801	100	
29/09/2021	1C-101Y-1-109-110cm	183 588-S	77 54685421	3.605001148	0.073997392	3.383641428	0 828728626	13.17617378	0.239906549	0.107939216	0.900620025	0 055866977	0 08127064	100	
29/09/2021	1C-101Y-1-109-110cm	183 588-S	77.42987792	3.619546935	0.090541746	3.428485807	0 897031999	13.14075984	0.241148369	0.070161892	0.932144069	0 043625624	0.106675797	100	
29/09/2021	1C-101Y-1-109-110cm	183 588-S	77 61161135	3.638167308	0.071172311	3.277532648	0 884721677	13 08891679	0.207584798	0.073293691	0.939952708	0 075202934	0.131843789	100	
29/09/2021	1C-101Y-1-109-110cm	183 588-S	77 61317024	3.654162693	0.085543006	3.476166229	0 930293281	13 00421222	0.168751858	0.097583944	0.799554034	0 093291088	0 077271406	100	
29/09/2021	1C-101Y-1-109-110cm	183 588-S	77 54366444	3.702143915	0.099706708	3.363599781	0 882508111	13 08309265	0.197706369	0	0.9407235	0 057115672	0.129738849	100	
29/09/2021	1C-101Y-1-109-110cm	183 588-S	77 66621198	3.711847334	0.088636354	3.221200847	0 887750154	13 07679549	0.209723841	0.0664506	0.914376519	0 068903833	0 088103043	100	
29/09/2021	1C-101Y-1-109-110cm	183 588-S	77 80725233	3.721105958	0.035840681	3.425947412	0 876093814	12 87102089	0.273101021	0.04142761	0.806639598	0 03889768	0.102673009	100	
29/09/2021	1C-101Y-1-109-110cm	183 588-S	77 88121735	3.735709198	0.097297285	3.218619507	0 910394442	12 82171377	0.190615481	0.032397252	0.911320488	0 054874824	0.145840399	100	
29/09/2021	1C-101Y-1-109-110cm	183 588-S	77 51801788	3.740960184	0.072705667	3.318252818	0 933549216	13.1250637	0.224366065	0.066893441	0.88267839	0 061926629	0 055586019	100	
29/09/2021	1C-101Y-1-109-110cm	183 588-S	77 53565515	3.761387752	0.096676118	3.243668652	0 943622304	12 995806	0.242622824	0.096676118	0.968824655	0 035183767	0 079876661	100	
29/09/2021	1C-101Y-1-109-110cm	183 588-S	77 5856533	3.7729817	0.084519053	3.250732821	0 833892905	13 08819641	0.227589566	0.051159074	0.916732667	0 066933122	0.121609382	100	

Date Analysed	Core Section Identifier	sample_no	SiO2	Na2O	Cl	K2O	FeOt	Al2O3	MgO	P2O5	CaO	MnO	TiO2	total	Analytical Total
29/09/2021	1C-101Y-1-109-110cm	183 588-S	77 51882891	3.783551129	0.077163127	3.303946056	0 856361502	13 08788954	0.205108116	0.054568399	0.918183295	0 089099965	0.105299958	100	
29/09/2021	1C-101Y-1-109-110cm	183 588-S	77 68504945	3.819453446	0.07164113	3.344659509	0 869400453	12 92494605	0.205092913	0.090210848	0.779476259	0.101922432	0.108147508	100	
29/09/2021	1C-101Y-1-109-110cm	183 588-S	77 67355961	3.822072377	0.101637232	3.149473048	0 91847175	12 90750141	0.281596702	0.094590953	0.92607885	0 080071349	0 044946717	100	
29/09/2021	1C-101Y-1-109-110cm	183 588-S	77.4330419	3.886693232	0.069769329	3.207052886	0 969868013	13 07245729	0.203176933	0.071043655	0.96201285	0 050123476	0 074760438	100	
29/09/2021	1C-101Y-1-109-110cm	183 588-S	77 50839317	3.90339128	0.077439934	3.275499921	0 910337822	12 99735113	0.203951948	0.078591068	0.915698107	0 057556708	0 071788912	100	
29/09/2021	1C-101Y-1-109-110cm	183 588-S	77 35652752	4.013494318	0.088000364	3.251036295	0 904254037	12 98296579	0.202501082	0.119557654	0.910427577	0 069680192	0.101555173	100	
Feb 15 10:09 2020	CHA16-1A-102Y-1(5-10cm)_1	184 224-S	75 34461458	4.072241731	0.071953917	3.825532269	1 321521241	13 51122893	0.275311159	0	1.32537208	0 034334417	0 217889673	100	94.36595344
Feb 15 10:13 2020	CHA16-1A-102Y-1(5-10cm)_2	184 224-S	75 30528422	4.037527021	0.099582448	3.812223083	1 317349114	13 58038472	0.259780299	0.010454573	1.271550641	0 054490502	0 251373375	100	94.6954027
Feb 15 10:21 2020	CHA16-1A-102Y-1(5-10cm)_4	184 224-S	75.70365394	3.456704278	0.109343835	4.103143915	1 385339598	13 38746956	0.299760514	0.051261798	1.235123321	0 02937103	0 238828218	100	90.90590233
Feb 15 10:28 2020	CHA16-1A-102Y-1(5-10cm)_6	184 224-S	74.73754238	3.927018533	0.142653217	3.804085785	1.468911812	13.71584264	0.327468385	0.016378703	1.563901934	0 027473953	0 268722663	100	94.63508983
Feb 15 10:32 2020	CHA16-1A-102Y-1(5-10cm)_7	184 224-S	74.42327943	3.954514077	0.108430126	3.781958992	1 540746908	14 01734385	0.365100473	0.025771798	1.448249338	0 015924038	0 318680967	100	95.45317671
Feb 15 10:36 2020	CHA16-1A-102Y-1(5-10cm)_8	184 224-S	74 82697996	3.490897306	0.117424882	3.619473783	1.456296572	14 38428805	0.360699284	0.063340791	1.398801808	0 026209983	0 255587578	100	96.14657291
Feb 15 10:40 2020	CHA16-1A-102Y-1(5-10cm)_9	184 224-S	74 29737387	4.008964206	0.081783437	3.804616057	1.475663279	14 06970204	0.369817112	0.013595442	1.507091679	0 046688225	0 324704655	100	94.88473859
Feb 15 10:44 2020	CHA16-1A-102Y-1(5-10cm)_10	184 224-S	74 23656652	3.887477867	0.125967452	3.792913108	1 53903825	14.11391047	0.377154458	0.089427275	1.517165243	0 052032357	0 268346999	100	93.59560578
Feb 15 10:48 2020	CHA16-1A-102Y-1(5-10cm)_11	184 224-S	75 31817587	4.007278916	0.10398236	3.716681105	1 397295674	13.44782052	0.283039561	0.008471068	1.41297415	0 013871374	0 290409393	100	94.439095
Feb 15 10:52 2020	CHA16-1A-102Y-1(5-10cm)_12	184 224-S	75.15387594	3.890639534	0.111976591	3.809729867	1 547773132	13.41824746	0.329299579	0.00726164	1.420334649	0 03546627	0 275395336	100	95.01986036
Feb 15 10:56 2020	CHA16-1A-102Y-1(5-10cm)_13	184 224-S	74 54958388	3.976800871	0.094144839	3.695899735	1.461450656	13 99994112	0.337608262	0.022133039	1.535545735	0 023933334	0 302958535	100	94.4289686
Feb 15 11:04 2020	CHA16-1A-102Y-1(5-10cm)_15	184 224-S	74.40271798	4.072592556	0.129582637	3.628734547	1 599859657	13 90489006	0.354248636	0.024927829	1.493566103	0 050907464	0 33797253	100	95.07446619
Feb 15 11:07 2020	CHA16-1A-102Y-1(5-10cm)_16	184 224-S	74 31374484	3.998451088	0.11962047	3.742081498	1 66238546	13 92769097	0.30977287	0.036579898	1.566208267	0 01944621	0 304018426	100	95.13421881
Feb 15 11:11 2020	CHA16-1A-102Y-1(5-10cm)_17	184 224-S	71.48064528	4.409212467	0.112140227	3.430919128	2 2506956	14 95203027	0.594692649	0.099539012	2.202565366	0 042780597	0.424779402	100	94.43533581
Feb 15 11:23 2020	CHA16-1A-102Y-1(5-10cm)_20	184 224-S	72.44508623	4.258317067	0.078938316	3.495225178	1 960826689	14 62617305	0.520627233	0.107007663	2.054116951	0 046997335	0.406684287	100	92.98399486
Feb 15 11:31 2020	CHA16-1A-102Y-1(5-10cm)_22	184 224-S	74.78305752	3.973377743	0.112897723	3.798526949	1 673359491	13.48000929	0.271293123	0.104009805	1.451270074	0 049730019	0 302468265	100	94.51032065
Feb 15 11:35 2020	CHA16-1A-102Y-1(5-10cm)_23	184 224-S	74 29606661	3.634408821	0.097745992	3.937433548	1 892262704	13.42548097	0.661085541	0	1.719310606	0 010719159	0 32548605	100	94.22381241
Feb 15 11:39 2020	CHA16-1A-102Y-1(5-10cm)_24	184 224-S	73 22751063	4.037137771	0.129626167	3.711244209	1 82073021	14 36369156	0.428771701	0.063208799	1.828884034	0 041818343	0 347376577	100	93.49964069
Feb 15 11:43 2020	CHA16-1A-102Y-1(5-10cm)_25	184 224-S	75.15805446	3.884766316	0.140669404	3.843250828	1 386045936	13.74577734	0.263353678	0	1.336680497	0 03254452	0 208857027	100	93.41050482
Feb 15 11:46 2020	CHA16-1A-102Y-1(5-10cm)_26	184 224-S	75 55992947	3.780120782	0.123167006	3.811044782	1 363364772	13.46640126	0.286679989	0.033852297	1.341317437	0	0 234122214	100	93.93749496
Feb 15 11:54 2020	CHA16-1A-102Y-1(5-10cm)_28	184 224-S	69.76681211	4.660997932	0.100347978	3.211556495	2 651701114	15.49970873	0.816367131	0.118774942	2.621893663	0 057281532	0.494558371	100	94.96952659
Feb 15 11:58 2020	CHA16-1A-102Y-1(5-10cm)_29	184 224-S	74 82195829	4.031508452	0.104233336	3.678823609	1 671853462	13 59473322	0.324751325	0.039536782	1.459689551	0 039959636	0 232952337	100	94.59545687
Feb 15 12:02 2020	CHA16-1A-102Y-1(5-10cm)_30	184 224-S	74 69454451	3.923017852	0.116457864	3.76991642	1 671333798	13.76702069	0.293402409	0.010081114	1.452730467	0 042529698	0 258965184	100	95.22757537
Feb 15 12:06 2020	CHA16-1A-102Y-1(5-10cm)_31	184 224-S	73 94030366	4.211180831	0.081856484	3.574015498	1.710353586	14 04451838	0.395133092	0.01959944	1.635033483	0 069069684	0 31893587	100	95.41089014
Feb 15 12:10 2020	CHA16-1A-102Y-1(5-10cm)_32	184 224-S	74 0399079	3.994770722	0.115769035	3.837469394	1 624189891	14.11371797	0.348919486	0.046974065	1.569385242	0 033322563	0 275573738	100	93.03005792
Feb 15 12:14 2020	CHA16-1A-102Y-1(16 5-18cm)_1	184 224-S	75 08827541	4.003055568	0.099702726	3.661041904	1 337191913	13.76847171	0.315883558	0.079129148	1.357012132	0 028908515	0 261327414	100	94.78176135
Feb 15 12:18 2020	CHA16-1A-102Y-1(16 5-18cm)_2	184 224-S	76 22272418	3.643902389	0.1184253	3.84469115	1.18926352	13 25261735	0.265492999	0.03624365	1.176211101	0 02941354	0 221014825	100	90.77452164
Feb 15 12:22 2020	CHA16-1A-102Y-1(16 5-18cm)_3	184 224-S	75.74062016	3.791509197	0.11850231	3.696596136	1 297644769	13 61403548	0.26657739	0	1.258955027	0	0 215559529	100	94.68169827
Feb 15 12:30 2020	CHA16-1A-102Y-1(16 5-18cm)_5	184 224-S	71.4582804	4.304399845	0.095094556	3.355044986	2 29180118	15 0033418	0.604851704	0.132943658	2.180779241	0 082617983	0.490844653	100	95.37875091
Feb 15 12:33 2020	CHA16-1A-102Y-1(16 5-18cm)_6	184 224-S	71 55572854	4.386293101	0.06967903	3.279013192	2 265537101	14 98677183	0.664735847	0.071465672	2.20702811	0 032895228	0.480852349	100	95.15057785
Feb 15 12:37 2020	CHA16-1A-102Y-1(16 5-18cm)_7	184 224-S	70.71294638	4.35122297	0.069632577	3.179569743	2.402140771	15.45270895	0.736282367	0.058398098	2.543655794	0 043348134	0.450094214	100	94.35238862
Feb 15 12:45 2020	CHA16-1A-102Y-1(16 5-18cm)_9	184 224-S	69.18246175	4.410719456	0.091102729	3.068836061	2 875887472	15 98574882	0.821849267	0.115696189	2.790823038	0 049828488	0 607046731	100	93.52079887
Feb 15 12:57 2020	CHA16-1A-102Y-1(16 5-18cm)_12	184 224-S	70 66799946	4.119658063	0.133056335	3.11520784	2.4572301	15 68163946	0.724734624	0.076771393	2.492166272	0 042768108	0.488768342	100	94.69673139
Feb 15 13:01 2020	CHA16-1A-102Y-1(16 5-18cm)_13	184 224-S	71 5833128	4.324002174	0.095876688	3.164142359	2 227921826	15 0270306	0.649125392	0.125719101	2.275219422	0 042435488	0.485214144	100	94.49638039
Feb 15 13:16 2020	CHA16-1A-102Y-1(16 5-18cm)_17	184 224-S	72.78298113	4.064754487	0.073799732	3.40129633	1 829424112	14 81243556	0.515338385	0.108862478	1.96309387	0 050809488	0 397204423	100	95.25779837
Feb 15 13:20 2020	CHA16-1A-102Y-1(16 5-18cm)_18	184 224-S	71.15915724	4.475412243	0.080530421	3.118989105	2.164605339	15.48020011	0.612949163	0.102644993	2.28447697	0 057789965	0.463244447	100	95.86439385
Feb 15 13:28 2020	CHA16-1A-102Y-1(16 5-18cm)_20	184 224-S	70 95063489	4.567747169	0.104588706	3.248833906	2.185374677	15 33751821	0.645233525	0.080303403	2.299008711	0 047707129	0 533049679	100	92.64862676
Feb 15 13:32 2020	CHA16-1A-102Y-1(16 5-18cm)_21	184 224-S	69 6166506	5.004447838	0.058403046	2.826624281	2.428600061	15.73348956	0.583095178	0.175624817	2.909760289	0 063079446	0 600224875	100	96.22785802
Feb 15 13:36 2020	CHA16-1A-102Y-1(16 5-18cm)_22	184 224-S	69 06636125	4.669472712	0.073652745	2.896936695	2 853543014	15 88504771	0.844173767	0.179054205	2.950385711	0 068628537	0 512743661	100	93.54709079
Feb 15 13:44 2020	CHA16-1A-102Y-1(16 5-18cm)_24	184 224-S	72 68482179	4.050450035	0.10888138	3.433196676	1 9103204	14.71370004	0.515851424	0.08523047	2.059918006	0 03836461	0 399265166	100	91.75122479
Feb 15 13:56 2020	CHA16-1A-102Y-1(16 5-18cm)_27	184 224-S	70 22929024	4.454765932	0.104603436	3.381757684	2 665974494	15.1443931	0.809311326	0.12938899	2.415541203	0 084228871	0 580744723	100	95.21675712
Feb 15 13:59 2020	CHA16-1A-102Y-1(16 5-18cm)_28	184 224-S	74 98655706	3.923070128	0.158289033	3.720652552	1 26031249	14 03309705	0.233024684	0.06333712	1.355134782	0 055917322	0 21060778	100	92.99443987
Feb 15 14:03 2020	CHA16-1A-102Y-1(16 5-18cm)_29	184 224-S	71 3310329	4.370153489	0.104275962	3.210148425	2 278751561	15.13509576	0.653556057	0.088332943	2.229868201	0 083485404	0 515299301	100	92.83059864
Feb 15 14:07 2020	CHA16-1A-102Y-1(16 5-18cm)_30	184 224-S	71 35522731	4.432715549	0.094713234	3.206327746	2 273615066	15.12458549	0.652761922	0.038602499	2.341463025	0 000738299	0.479249865	100	94.81251577
Feb 15 16:45 2020	CHA16-1A-102Y-1(11-15cm)_1	184 224-S	75.18007181	3.535649325	0.135233732	3.871523903	1.444800798	13.78219373	0.329349137	0.011754766	1.368082235	0 053058211	0 288282359	100	92.72834392
Feb 15 16:49 2020	CHA16-1A-102Y-1(11-15cm)_2	184 224-S	75 07900685	3.708296798	0.111323548	3.916166091	1 399105009	13.75357531	0.314442029	0.016395682	1.367316337	0 065060573	0 269311768	100	95.75691921
Feb 15 16:53 2020	CHA16-1A-102Y-1(11-15cm)_3	184 224-S	75 08001251	3.989786527	0.142226592	3.61859693	1 346255689	13.79262308	0.320324493	0.012166877	1.404854704	0 046779543	0 246373058	100	95.3408204
Feb 15 16:57 2020	CHA16-1A-102Y-1(11-15cm)_4	184 224-S	75 04251027	4.063816772	0.117002896	3.619514056	1 388455471	13 67839614	0.306816947	0.023674147	1.444122977	0 062604967	0 253085354	100	95.04038241
Feb 15 17:12 2020	CHA16-1A-102Y-1(11-15cm)_8	184 224-S	71 66017522	4.077127411	0.104875592	3.336002919	2.121273412	15.44986352	0.566182245	0.059214052	2.157976888	0 050248544	0.417060198	100	95.92317746
Feb 15 17:16 2020	CHA16-1A-102Y-1(11-15cm)_9	184 224-S	71 25905304	4.358030523	0.133430134	3.245310273	2 261557718	15 39660316	0.598520337	0.108850899	2.159993395	0 040858988	0.437791533	100	93.98176889
Feb 15 17:32 2020	CHA16-1A-102Y-1(11-15cm)_13	184 224-S	69.10850515	4.628830114	0.060329504	2.995743407	3 03856544	15 9323793	0.41712358	0.130921243	2.871352677	0 063750249	0.752499341	100	96.47021148
Feb 15 17:51 2020	CHA16-1A-102Y-1(11-15cm)_18	184 224-S	70 37561125	4.213255943	0.111633195	3.269107698	2 911859182	15.48358727	0.630485787	0.094289055	2.396644872	0 067694706	0.44583104	100	95.13299306
Feb 15 17:55 2020	CHA16-1A-102Y-1(11-15cm)_19	184 224-S	72 95869021	3.891447969	0.154459638	3.468139652	1 841641187	14 82546599	0.501273603	0.033240955	1.927975398	0 049196614	0 348468787	100	90.2501143
Feb 15 18:15 2020	CHA16-1A-102Y-1(11-15cm)_24	184 224-S	72 29975507	4.291036094	0.096339608	3.41884262	2 338436684	14 63560097	0.550708013	0.041996894	1.920460978	0 051282639	0 355540435	100	94.76891335
Feb 15 18:19 2020	CHA16-1A-102Y-1(11-15cm)_25	184 224-S	71 56409168	4.373254279	0.094515316	3.311179568	2.121585526	15 20418213	0.597164948	0.024624278	2.252859516	0 071777152	0 384765613	100	95.43426853
Feb 15 18:23 2020	CHA16-1A-102Y-1(11-15cm)_26	184 224-S	71 69692545	4.382356588	0.126691786	3.242892619	2.184763088	15 05703197	0.600717183	0.054326272	2.168879951	0 052657903	0.432757186	100	95.90203454
Feb 15 14:11 2020	CHA16-1A-102Y-1(34-35cm)_1	184 394-S	62 94889321	5.047747094	0.11004171	2.437504792	4 625440769	17 30527261	2.002597298	0.289769761	4.521015112	0 067764656	0 643952988	100	98.87160049
Feb 15 14:15 2020	CHA16-1A-102Y-1(34-35cm)_2	184 394-S	63 35890104	4.94756592	0.098179792	2.361158403	4.492627085	17 36561373	1.886908638	0.292924908	4.459965872	0 081126981	0 655027639	100	99.10389735
Feb 15 14:19 2020	CHA16-1A-102Y-1(34-35cm)_3	184 394-S	62 9350052	5.044939517	0.069378481	2.288983464	4 54007537	17.49147984	2.015520838	0.250268944	4.628608156	0 078696467	0 657043724	100	98.73378446
Feb 15 14:23 2020	CHA16-1A-102Y-1(34-35cm)_4	184 394-S	63.16346361	4.794316169	0.173892777	2.246929141	4.417425481	17.70406488	1.910432507	0.332154743	4.515567743	0.111152437	0 63060052	100	92.12573561

Date Analysed	Core Section Identifier	sample_no	SiO2	Na2O	Cl	K2O	FeOt	Al2O3	MgO	P2O5	CaO	MnO	TiO2	total	Analytical Total
Feb 15 14:27 2020	CHA16-1A-102Y-1(34-35cm)_5	184 394-S	62 57985395	4.878550877	0.120310311	2.185603276	4.711854522	17.49503931	1.981341288	0.310682484	4.994205617	0.105705579	0 636852783	100	97.91346963
Feb 15 14:31 2020	CHA16-1A-102Y-1(34-35cm)_6	184 394-S	63 22022795	4.628812229	0.110215272	2.238434024	4 691656972	17 50595936	1.937299402	0.25475989	4.637473179	0 091544925	0 683616798	100	99.62321768
Feb 15 14:35 2020	CHA16-1A-102Y-1(34-35cm)_7	184 394-S	63 0608585	4.952293568	0.096839881	2.241006681	4 616981644	17.48188017	2.038200646	0.27358534	4.552995474	0 075038233	0 610319867	100	98.61639499
Feb 15 14:39 2020	CHA16-1A-102Y-1(34-35cm)_8	184 394-S	63 08400896	4.953308258	0.102029941	2.204969254	4 512905254	17 55957333	1.914314216	0.306089823	4.620412845	0 076873246	0 665514869	100	99.77463388
Feb 15 14:54 2020	CHA16-1A-102Y-1(34-35cm)_12	184 394-S	62 63051678	4.938762341	0.106585914	1.874732487	4 26495243	18 36816549	1.665457574	0.276786347	5.245038081	0 078359605	0 550642947	100	94.94687975
Feb 15 15:10 2020	CHA16-1A-102Y-1(34-35cm)_16	184 394-S	62 86479822	4.677332177	0.079719083	2.218984789	4 811963922	17 32040905	2.177892479	0.325964756	4.715342678	0.106840008	0.700752839	100	97.34181191
Feb 15 15:14 2020	CHA16-1A-102Y-1(34-35cm)_17	184 394-S	62 67633499	4.734621328	0.086218477	2.122917197	4 932588531	17 60419072	2.20302728	0.321241432	4.616343527	0 058981049	0 643535468	100	99.86258546
Feb 15 15:18 2020	CHA16-1A-102Y-1(34-35cm)_18	184 394-S	63.13968278	4.774651392	0.160226351	1.94314702	4 686519956	17 3994936	2.054183992	0.250277336	4.819004609	0 091383428	0 681429534	100	90.06009232
Feb 15 15:29 2020	CHA16-1A-102Y-1(34-35cm)_21	184 394-S	63 58379598	4.709837339	0.081240943	2.327106308	4 384812867	17 57796372	1.755718598	0.281434419	4.581490543	0 073968736	0 642630551	100	96.25688318
Feb 15 15:33 2020	CHA16-1A-102Y-1(34-35cm)_22	184 394-S	62.46929735	4.917911476	0.226459893	2.160643447	4 547993188	17.45840672	2.181026875	0.238384199	5.075473757	0 069099823	0 655303278	100	98.11891931
Feb 15 15:37 2020	CHA16-1A-102Y-1(34-35cm)_23	184 394-S	62 51790539	4.898229605	0.107976504	2.133243665	4.796757376	17 61189794	2.123133506	0.315335876	4.74166483	0.105550066	0 648305245	100	98.91040739
Feb 15 15:41 2020	CHA16-1A-102Y-1(34-35cm)_24	184 394-S	62 93995616	4.918684779	0.090720521	2.293496311	4 53844036	17 3897987	1.99789012	0.302435714	4.76027901	0.120077274	0 648221059	100	98.1034933
Feb 15 15:45 2020	CHA16-1A-102Y-1(34-35cm)_25	184 394-S	63 89404559	5.166657403	0.136663936	2.316509348	4 045366903	17 08552091	1.719679428	0.366392876	4.450934991	0 065347818	0.752880797	100	98.8556339
Feb 15 15:49 2020	CHA16-1A-102Y-1(34-35cm)_26	184 394-S	63.43972246	5.04542636	0.080324737	2.3094628	4.41807268	17.43239245	1.884035442	0.263258501	4.416341143	0 091973343	0 618990083	100	98.72425744
Feb 15 15:53 2020	CHA16-1A-102Y-1(34-35cm)_27	184 394-S	63 27545928	4.99356616	0.087350381	2.316417801	4.49201615	17 36803126	1.949056387	0.270316773	4.571608699	0 092758757	0 58341835	100	97.99613866
Feb 15 15:57 2020	CHA16-1A-102Y-1(34-35cm)_28	184 394-S	63.1244288	4.98025427	0.107360415	2.42754391	4 368837626	17.48034757	1.929846623	0.337926301	4.540218108	0 066021069	0 637215312	100	98.45341994
Feb 15 16:01 2020	CHA16-1A-102Y-1(34-35cm)_29	184 394-S	62 36774563	4.689156491	0.089469769	2.262219667	4 886046406	17 55767787	2.252029488	0.258626735	4.921856302	0 09466676	0 620504887	100	98.13370613
Jan 25 00:40 2020	CHA16-1C-103Y-1(35-36cm)_6	186.124-OS	67 5514601	4.97659187	0.114125641	3.076247717	3 295513865	15 89103865	1.296013714	0.226046462	2.824268382	0 045881237	0.702812362	100	95.24590571
Jan 25 00:48 2020	CHA16-1C-103Y-1(35-36cm)_8	186.124-OS	68 80765365	4.762244089	0.145785109	3.303350933	2.752198659	16 24338407	0.794992564	0.179860685	2.396753043	0 059710413	0 554066779	100	95.96316179
Jan 25 00 52 2020	CHA16-1C-103Y-1(35-36cm)_9	186.124-OS	68.75540299	4.914100274	0.130097655	3.265566635	2 890536326	16 05778478	0.794236207	0.081061654	2.457050137	0 052291067	0 601872281	100	95.23615186
Jan 25 00 56 2020	CHA16-1C-103Y-1(35-36cm)_10	186.124-OS	66.46989956	5.453833319	0.10824083	2.988115573	3 258222309	16 61451828	1.113438729	0.159958215	2.977667616	0 070732666	0.785372894	100	95.71249606
Jan 25 00 59 2020	CHA16-1C-103Y-1(35-36cm)_11	186.124-OS	66.74666927	5.155775473	0.122191879	2.959415121	3 226158408	16 52935213	1.182219316	0.225204273	3.072842182	0 037740276	0.742431668	100	96.97862187
Jan 25 01 03 2020	CHA16-1C-103Y-1(35-36cm)_11	186.124-OS	68.1478851	5.162877887	0.138167445	3.238628084	2 830526431	16 29746036	0.881054049	0.131122377	2.544636352	0 034594436	0 59304748	100	95.10199752
Jan 25 01 23 2020	CHA16-1C-103Y-1(35-36cm)_16	186.124-OS	66.40812498	5.203700825	0.122832775	2.914496389	3 369660483	16 5513188	1.203951963	0.174127912	3.179450606	0 056382257	0 815953007	100	94.35592409
Jan 25 01 34 2020	CHA16-1C-103Y-1(35-36cm)_18	186.124-OS	68 56187409	5.081373614	0.11723829	3.331704762	2.703236768	16.15623688	0.804009508	0.130858467	2.472585924	0 063176666	0 577705033	100	95.4466325
Jan 25 01 38 2020	CHA16-1C-103Y-1(35-36cm)_19	186.124-OS	67.10296515	4.673940806	0.098008627	2.882606665	3 34648061	16 92782556	1.069241172	0.193031696	2.975261879	0 043650901	0 686986938	100	97.13430675
Jan 25 01:42 2020	CHA16-1C-103Y-1(35-36cm)_20	186.124-OS	66 69651695	5.034093513	0.13953421	2.976590562	3 288871564	16 55718444	1.186458554	0.25254021	3.081032337	0 051176469	0.736001182	100	95.74712881
Jan 25 01 50 2020	CHA16-1C-103Y-1(35-36cm)_22	186.124-OS	66.4932446	5.162381963	0.122551418	3.000358748	3 227065267	16 82572853	1.056192464	0.221938301	3.066543132	0 063867931	0.760127652	100	90.65582581
Jan 25 01 54 2020	CHA16-1C-103Y-1(35-36cm)_23	186.124-OS	69 03529091	4.83048809	0.097653064	3.244669106	2.776657389	16 02680237	0.756185263	0.173605447	2.451759614	0 030986068	0 575902684	100	95.84952729
Jan 25 01 58 2020	CHA16-1C-103Y-1(35-36cm)_24	186.124-OS	68 60286851	4.605066116	0.114285545	3.374945715	2 830209686	16 27496999	0.84783683	0.100827817	2.575893147	0 071914731	0 601181919	100	95.11264095
Jan 25 02:10 2020	CHA16-1C-103Y-1(35-36cm)_27	186.124-OS	69 97935677	4.777405957	0.087942832	3.481293579	2 350293064	15 80213833	0.687582261	0.146107214	2.153046183	0 041132823	0.493700988	100	93.35610245
Jan 25 02:13 2020	CHA16-1C-103Y-1(35-36cm)_28	186.124-OS	68 28306447	5.004220912	0.120456508	3.238639839	2.769825741	16.13076722	0.90243132	0.154305517	2.653595223	0 0941295	0 648563746	100	95.71919553
Jan 25 02:17 2020	CHA16-1C-103Y-1(35-36cm)_29	186.124-OS	68 07506436	5.105629827	0.121428374	3.247138806	2 842406833	16 27501985	0.896565303	0.153586533	2.547594433	0 060661982	0 674903706	100	95.77662631
Jan 25 02 37 2020	CHA16-1C-103Y-1(35-36cm)_34	186.124-OS	68 88774123	4.767428445	0.116999307	3.391593391	2.730160511	16.12170146	0.835846459	0.112519844	2.389046917	0 087882797	0 55907964	100	93.76123944
Jan 25 02:48 2020	CHA16-1C-103Y-1(35-36cm)_37	186.124-OS	68 21148137	4.809985907	0.116678916	3.224160859	2 933742548	16.42201273	0.897724007	0.128441327	2.636040311	0 031191393	0 588540634	100	95.2185742
01/10/2021	1C-103Y-1-57-61cm	186 807-S	78.73	3.17	0.11	3.97	1.15	11 92	0.14	0.03	0.64	0 03	0.11	100	
01/10/2021	1C-103Y-1-57-61cm	186 807-S	78 24	3.23	0.11	3.43	1 53	12 28	0.11	0.02	0.87	0 00	0.17	100	
01/10/2021	1C-103Y-1-57-61cm	186 807-S	77.77	3.33	0.13	4.53	1 02	11 98	0.23	0.00	0.83	0 07	0.10	100	
01/10/2021	1C-103Y-1-57-61cm	186 807-S	78 86	3.48	0.08	3.50	0 96	12.13	0.15	0.04	0.63	0 04	0.12	100	
01/10/2021	1C-103Y-1-57-61cm	186 807-S	79 39	3.50	0.08	2.92	0.70	11.79	0.15	0.05	1.24	0 05	0.13	100	
01/10/2021	1C-103Y-1-57-61cm	186 807-S	76 87	3.60	0.11	3.91	1 28	12.75	0.16	0.08	1.06	0 07	0.11	100	
01/10/2021	1C-103Y-1-57-61cm	186 807-S	76 37	3.90	0.11	2.99	1.17	13 57	0.12	0.12	1.44	0 06	0.14	100	
01/10/2021	1C-103Y-1-57-61cm	186 807-S	76 21	3.93	0.14	4.24	0 65	13 26	0.11	0.08	1.27	0 01	0.10	100	
01/10/2021	1C-103Y-1-57-61cm	186 807-S	75.10	3.94	0.25	3.47	0 93	14 25	0.19	0.03	1.73	0 00	0.12	100	
01/10/2021	1C-103Y-1-57-61cm	186 807-S	77 21	4.02	0.06	3.16	0 95	13 04	0.14	0.08	1.16	0 01	0.17	100	
01/10/2021	1C-103Y-1-57-61cm	186 807-S	76 28	4.04	0.15	3.49	0 68	13.72	0.08	0.01	1.38	0 07	0.10	100	
01/10/2021	1C-103Y-1-57-61cm	186 807-S	76 67	4.05	0.09	3.20	0 91	13 54	0.10	0.00	1.27	0 04	0.12	100	
01/10/2021	1C-103Y-1-57-61cm	186 807-S	76 90	4.12	0.12	3.53	0 84	13 27	0.07	0.07	0.95	0 03	0 09	100	
01/10/2021	1C-103Y-1-57-61cm	186 807-S	75 83	4.21	0.12	3.15	1.14	13.73	0.12	0.08	1.39	0 03	0 20	100	
01/10/2021	1C-103Y-1-57-61cm	186 807-S	75 35	4.29	0.08	2.98	0 96	14.44	0.10	0.05	1.63	0 05	0 07	100	
01/10/2021	1C-103Y-1-57-61cm	186 807-S	76.46	4.32	0.22	3.12	0 91	13 54	0.06	0.01	1.24	0 04	0 08	100	
01/10/2021	1C-103Y-1-57-61cm	186 807-S	75 09	4.42	0.14	3.30	0.71	14 32	0.07	0.10	1.71	0 05	0 07	100	
01/10/2021	1C-103Y-1-57-61cm	186 807-S	73.48	4.42	0.07	2.67	0.70	15 86	0.13	0.06	2.45	0 05	0.10	100	
01/10/2021	1C-103Y-1-57-61cm	186 807-S	75.40	4.48	0.04	2.63	0 93	14 59	0.08	0.01	1.73	0 00	0.12	100	
01/10/2021	1C-103Y-1-57-61cm	186 807-S	74 32	4.70	0.19	2.94	0.76	14 87	0.09	0.05	1.89	0 06	0.13	100	
Jan 16 20 35 2020	CHA16-1B-107Y-1_73-74cm_2	187 227-OS	69.70760876	4.508056345	0.046128949	2.695938127	2 633063497	15 95681723	0.686587465	0.009749982	3.187090998	0 048959589	0 519999058	100	95.38478827
Jan 16 20 39 2020	CHA16-1B-107Y-1_73-74cm_3	187 227-OS	70.18954212	4.321038882	0.050021879	2.809419195	2 608090651	15 61346974	0.751498905	0	3.075813392	0 053214765	0 527890464	100	93.95888606
Jan 16 20:43 2020	CHA16-1B-107Y-1_73-74cm_4	187 227-OS	71 28071254	4.305775495	0.075191991	3.00610019	2 631229161	14.78040175	0.699847598	0	2.513469932	0 086009456	0 621261893	100	94.2919575
Jan 16 20:47 2020	CHA16-1B-107Y-1_73-74cm_5	187 227-OS	70 63468788	4.487839458	0.072544605	2.797708101	2.491035212	15 52179643	0.624812849	0	2.819419142	0 020802456	0 529353864	100	94.70035726
Jan 16 20 51 2020	CHA16-1B-107Y-1_73-74cm_6	187 227-OS	70.41830162	4.479418405	0.071331023	2.832988788	2.460863502	15 65403248	0.651957058	0	2.897822807	0 039592964	0.493691351	100	94.20865878
Jan 16 20 55 2020	CHA16-1B-107Y-1_73-74cm_7	187 227-OS	70 63058903	4.38574574	0.038201873	2.899952907	2 397934969	15 50000455	0.679843944	0	2.934501407	0 061998012	0.471227571	100	93.71268294
Jan 16 20 58 2020	CHA16-1B-107Y-1_73-74cm_8	187 227-OS	71.77081387	4.423262306	0.047578826	2.964015223	2.403002736	14 83588161	0.584539865	0	2.436454178	0 028861002	0 505590384	100	95.63077447
Jan 16 21 02 2020	CHA16-1B-107Y-1_73-74cm_9	187 227-OS	71 8499144	4.332245622	0.06535261	2.844042831	2 304375285	14 99555108	0.576578675	0.001686519	2.529778466	0 035733121	0.464741386	100	94.86996718
Jan 16 21 30 2020	CHA16-1B-107Y-1_73-74cm_16	187 227-OS	71.19578995	4.303527537	0.088833309	2.877394921	2 355426494	15 3732218	0.679532311	0	2.667124474	0 046329333	0.412819864	100	94.10884362
Jan 16 21 34 2020	CHA16-1B-107Y-1_73-74cm_17	187 227-OS	70 92851807	4.391534821	0.059125054	3.004761981	2.406956529	15 38257717	0.642877854	0.02999097	2.624209832	0 087080922	0.4423668	100	93.36143665
Jan 16 21 38 2020	CHA16-1B-107Y-1_73-74cm_18	187 227-OS	70 93730658	4.402996862	0.052305481	2.914301645	2.416527806	15.46218709	0.638805882	0.001803637	2.663017379	0 052729866	0.45801777	100	94.25398495

Date Analysed	Core Section Identifier	sample_no	SiO2	Na2O	Cl	K2O	FeOt	Al2O3	MgO	P2O5	CaO	MnO	TiO2	total	Analytical Total
Jan 16 22:13 2020	CHA16-1B-107Y-1_73-74cm_27	187 227-OS	70 9402441	4.649998578	0.055523956	2.854124446	2 299332681	15 2671747	0.68146897	0	2.664725212	0 061362995	0 52604436	100	94.1935772
Jan 16 22 25 2020	CHA16-1B-107Y-1_73-74cm_30	187 227-OS	71 27742465	4.277988755	0.072746987	2.898342514	2.433381555	15 20739764	0.669759378	0	2.615503026	0 058451728	0.489003764	100	94.43690088
Jan 16 22 29 2020	CHA16-1B-107Y-1_73-74cm_31	187 227-OS	71.17724369	4.542977918	0.042429699	2.953563542	2 38595574	15.10840724	0.724626407	0.004285828	2.635784358	0 051965667	0 37275991	100	93.33085206
Jan 20 19:46 2020	CHA16-1C-103Y-1_97-104cm_1	187 227-S	70 52864602	4.246515689	0.058985015	2.817497283	2 62409647	15.40433411	0.75525143	0.129419787	2.818343907	0 063647061	0 553263226	100	98.66912797
Jan 20 19 50 2020	CHA16-1C-103Y-1_97-104cm_2	187 227-S	70 50845911	4.223215663	0.029471361	2.805349493	2 684157052	15 5688779	0.787624657	0.054538472	2.754651816	0 053777638	0 529876843	100	98.73992551
Jan 20 19 54 2020	CHA16-1C-103Y-1_97-104cm_3	187 227-S	70 60007501	4.386545054	0.044675898	2.84669552	2 633311579	15 28071502	0.798493028	0.112091447	2.745179032	0 037483179	0 514735229	100	98.71094328
Jan 20 19 58 2020	CHA16-1C-103Y-1_97-104cm_4	187 227-S	69 99676139	4.374166212	0.029396821	2.717438132	2 646475507	15 81167836	0.779066278	0.092319809	2.911725561	0 048893682	0 592078249	100	98.99029415
Jan 20 20 06 2020	CHA16-1C-103Y-1_97-104cm_6	187 227-S	70 51900269	4.347545438	0.024108199	2.794130131	2 550033646	15 57462514	0.76470399	0.147246528	2.753872652	0 033085729	0.491645858	100	99.13639918
Jan 20 20 22 2020	CHA16-1C-103Y-1_97-104cm_10	187 227-S	70.79671506	4.13527272	0.04738113	2.813254587	2 55507184	15 62679732	0.694429685	0.097042112	2.683441435	0 056476615	0.494117497	100	94.55240959
Jan 20 20 29 2020	CHA16-1C-103Y-1_97-104cm_12	187 227-S	70 31804299	4.394877687	0.092854183	2.907888996	2 604889184	15 5003439	0.778851632	0.154977466	2.671754267	0 068621774	0 506897923	100	90.78750956
Jan 20 20 33 2020	CHA16-1C-103Y-1_97-104cm_13	187 227-S	71 01429683	4.082647027	0.055623366	2.840571873	2 510222693	15.47997254	0.630542152	0.15223037	2.674635311	0 069880228	0.489377611	100	92.58699013
Jan 20 20:41 2020	CHA16-1C-103Y-1_97-104cm_15	187 227-S	71 00389405	4.441008826	0.042111213	2.873593946	2 524459587	15.17788537	0.666987278	0.047811545	2.651291189	0 072519062	0.498437932	100	95.69897667
Jan 20 20:49 2020	CHA16-1C-103Y-1_97-104cm_17	187 227-S	71.11128861	4.299263421	0.042361935	2.82763291	2.410907989	15 35937519	0.627124831	0.109731559	2.688413095	0 056342425	0.467558037	100	95.13257504
Jan 20 20 53 2020	CHA16-1C-103Y-1_97-104cm_18	187 227-S	71 33379767	4.474304055	0.028588784	2.858878363	2 36171377	15.16057513	0.59430661	0.030245629	2.610258252	0 052076223	0.495255508	100	94.09284546
Jan 20 20 57 2020	CHA16-1C-103Y-1_97-104cm_19	187 227-S	70 05619762	4.282533846	0.05234208	2.660361935	2.755960554	15 6143702	0.764367405	0.142210494	3.073182582	0 035255203	0 563218088	100	92.4686212
Jan 20 21 01 2020	CHA16-1C-103Y-1_97-104cm_20	187 227-S	71.18169405	4.249493615	0.043137177	2.836563748	2 389561209	15 36208499	0.714707024	0.10963883	2.628976802	0 018410904	0.465731655	100	93.422896
Jan 20 21 05 2020	CHA16-1C-103Y-1_97-104cm_21	187 227-S	70 21454579	4.160861973	0.07909972	2.643881045	2.739246631	15 65527009	0.808117411	0.10287842	2.98020466	0 061871151	0 554023106	100	92.28856966
Jan 20 21 09 2020	CHA16-1C-103Y-1_97-104cm_22	187 227-S	70 87657903	4.265720034	0.049749092	2.900266227	2 524820631	15 28291354	0.745177892	0.078944544	2.674923482	0 052924566	0 547980958	100	94.47408567
Jan 20 21:13 2020	CHA16-1C-103Y-1_97-104cm_23	187 227-S	70.79907769	4.594181664	0.058213251	2.829529104	2 212336099	15.71749124	0.494914051	0.035082482	2.737891998	0 041175226	0.480107196	100	98.60297942
Jan 20 21 24 2020	CHA16-1C-103Y-1_97-104cm_26	187 227-S	69 80941019	4.308029161	0.040824216	2.78249265	2.71589711	15 82191212	0.811972179	0.117156736	2.932994546	0 064781586	0 594529511	100	93.08200689
Jan 20 21 32 2020	CHA16-1C-103Y-1_97-104cm_28	187 227-S	69 92759077	4.202086079	0.047121018	2.727475397	2.712466273	15.77333223	0.825449363	0.161710727	2.981922296	0 0865918	0 554254045	100	90.19329753
Jan 20 21 36 2020	CHA16-1C-103Y-1_97-104cm_29	187 227-S	70 90135027	4.081851859	0.059769974	2.707350723	2.717305749	15 22510037	0.807519417	0.109211539	2.737131418	0 046441478	0 606967206	100	96.03484241
Jan 20 21:40 2020	CHA16-1C-103Y-1_97-104cm_30	187 227-S	72 21670861	4.078324187	0.067248963	3.243135457	2.487733123	14 67869495	0.640058272	0.048830504	2.058544313	0 052714509	0.428007108	100	92.19473066
050319	CHA16-1C-103Y-1_100-102cm_2	187 227-S	69.4487	4.6328	0.0696	2.7711	2 6277	15 832	0.8011	0.1026	3.2239	0 0227	0.4677	100	95 579
050319	CHA16-1C-103Y-1_100-102cm_3	187 227-S	70 0661	4.3664	0.0395	2.8515	2.7125	15 5271	0.7724	0.1307	2.9384	0 0222	0 5732	100	95 6139
050319	CHA16-1C-103Y-1_100-102cm_5	187 227-S	69 317	4.5127	0.0845	2.5355	2.4169	16 2799	0.6998	0.1325	3.4026	0 0437	0 5749	100	94.7424
050319	CHA16-1C-103Y-1_100-102cm_6	187 227-S	70 0757	4.2513	0.0598	2.6868	2 6555	15.7954	0.7842	0.1234	2.9642	0 0686	0 5352	100	96.1933
050319	CHA16-1C-103Y-1_100-102cm_7	187 227-S	69 6204	4.2323	0.0863	2.7944	2 8844	15.7004	0.8626	0.1157	3.0357	0 0828	0 5848	100	94 5208
050319	CHA16-1C-103Y-1_100-102cm_16	187 227-S	70.1418	4.285	0.0641	2.8942	2 586	15.4198	0.771	0.1613	3.0557	0 0673	0 5538	100	96.7826
050319	CHA16-1C-103Y-1_100-102cm_17	187 227-S	69 9243	4.4335	0.0627	2.8703	2 6291	15 6788	0.8635	0.1214	2.8052	0 0853	0 5259	100	93 969
050319	CHA16-1C-103Y-1_100-102cm_18	187 227-S	69 6997	4.6598	0.0411	2.7339	2 6475	15.755	0.7242	0.1414	3.1278	0 0005	0.4689	100	95 5911
050319	CHA16-1C-103Y-1_100-102cm_19	187 227-S	69 655	4.3515	0.0644	2.9471	2 6138	16 0394	0.776	0.1186	2.9575	0 0337	0.443	100	95 0594
050319	CHA16-1C-103Y-1_100-102cm_20	187 227-S	70 0077	4.3987	0.0383	2.8582	2 5789	15 6923	0.818	0.1218	2.8378	0.1114	0 5369	100	94.7256
Jan 16 22 33 2020	CHA16-1B-109Y-1_0-40cm_1	187.723-OS	69.72050104	4.518849033	0.073111567	2.761396222	2 817596654	15 60419087	0.814032286	0	3.048091564	0 071726071	0 57050469	100	93.82920229
Jan 16 22:41 2020	CHA16-1B-109Y-1_0-40cm_3	187.723-OS	70 00610603	4.448342477	0.07185784	2.728923056	2 67475182	15 57355721	0.820056213	0	2.972690405	0 07431726	0 629397688	100	93.51797938
Jan 16 22:45 2020	CHA16-1B-109Y-1_0-40cm_4	187.723-OS	69 98354723	4.468542654	0.035148249	2.818244907	2 647766149	15 63778873	0.802623129	0	3.032608084	0 030111762	0 54361911	100	93.31901524
Jan 16 22:49 2020	CHA16-1B-109Y-1_0-40cm_5	187.723-OS	69 93844298	4.375996219	0.043974472	2.674495393	2 66103202	15.713837	0.800871661	0	3.099663988	0 048264664	0 643421601	100	93.23591237
Jan 16 22 53 2020	CHA16-1B-109Y-1_0-40cm_6	187.723-OS	69 96699292	4.354384013	0.044502018	2.758482094	2 608939214	15 82405694	0.773142707	0.039604666	3.002289222	0 053445007	0 574161198	100	93.92832574
Jan 16 22 57 2020	CHA16-1B-109Y-1_0-40cm_7	187.723-OS	70.16823816	4.452261888	0.06789435	2.729792235	2 666820508	15 59608732	0.767459965	0	2.950548852	0 088516466	0 512380258	100	94.55867839
Jan 16 23 05 2020	CHA16-1B-109Y-1_0-40cm_9	187.723-OS	72 23363926	4.422796488	0.107831991	3.313105777	2.473450051	14 68619228	0.459233702	0.025273123	1.874423273	0 042332481	0 36172157	100	94.96254262
Jan 16 23 09 2020	CHA16-1B-109Y-1_0-40cm_10	187.723-OS	72.40476646	4.60417899	0.106550839	3.476702449	2.426708703	14 25860773	0.414904111	0	1.848007622	0 053645021	0.405928074	100	94.69657913
Jan 16 23:13 2020	CHA16-1B-109Y-1_0-40cm_11	187.723-OS	76.72987583	3.827853434	0.097251066	3.937436369	1 010999273	12 94607419	0.174665917	0	1.03941768	0 03463296	0 201793282	100	93.26375895
Jan 16 23:17 2020	CHA16-1B-109Y-1_0-40cm_12	187.723-OS	76 86796473	4.00637389	0.11009558	3.747173577	1.107586085	12 69768265	0.182571627	0.012752384	0.98012696	0 024016989	0 263655534	100	94.10005416
Jan 16 23 21 2020	CHA16-1B-109Y-1_0-40cm_13	187.723-OS	76 84800421	3.937224398	0.070148392	3.928122007	1 061182211	12.77251463	0.187628376	0	0.968069029	0 024833167	0 202273577	100	94.22881769
Jan 16 23 24 2020	CHA16-1B-109Y-1_0-40cm_14	187.723-OS	76 52491614	3.92291685	0.097057452	4.039800123	0 99211535	12 9886037	0.192725316	0	1.010765715	0 020523162	0 210576191	100	93.55283684
Jan 16 23 28 2020	CHA16-1B-109Y-1_0-40cm_15	187.723-OS	76 68660902	3.927357559	0.097060308	3.908865796	1 058961029	12 87936731	0.222585933	0	1.004204996	0 009203072	0 205784975	100	93.44705554
Jan 16 23 32 2020	CHA16-1B-109Y-1_0-40cm_16	187.723-OS	76 95456398	3.873654328	0.087050803	3.970117563	0 951264432	12.75659515	0.191128659	0	1.015237975	0 023305777	0.177081341	100	93.9681162
Jan 16 23 36 2020	CHA16-1B-109Y-1_0-40cm_17	187.723-OS	77 04995291	3.804924801	0.095815893	3.996903888	0 976332953	12.76566198	0.172553873	0	0.941425792	0 040074278	0 156353633	100	93.82577021
Jan 16 23:40 2020	CHA16-1B-109Y-1_0-40cm_18	187.723-OS	76.76765032	3.905503239	0.054314239	4.043250342	1.130920701	12.75000218	0.191647099	0	0.945537273	0 039801987	0.171372628	100	93.71391537
Jan 16 23:44 2020	CHA16-1B-109Y-1_0-40cm_19	187.723-OS	76 53589281	4.042030414	0.093783593	3.823503034	1.153931679	12 880981	0.22926057	0	1.037984923	0 006365402	0.196266569	100	94.25955794
Jan 16 23:48 2020	CHA16-1B-109Y-1_0-40cm_20	187.723-OS	76 58433019	3.905806368	0.091982269	4.000379401	1 054330132	12 93337131	0.161101282	0	1.091402966	0 018311775	0.158984313	100	94.47472948
Jan 16 23 52 2020	CHA16-1B-109Y-1_0-40cm_21	187.723-OS	76 84035708	3.709888666	0.111191564	3.982179996	1 016058804	12 90229537	0.169940226	0.020703911	1.057896298	0 003573264	0.185914817	100	95.15110337
Jan 16 23 56 2020	CHA16-1B-109Y-1_0-40cm_22	187.723-OS	72 28741607	4.409035717	0.066496932	3.097787138	0 90199257	16.13452885	0.165313025	0	2.756938024	0 045845711	0.134645962	100	96.84657314
Jan 17 00 00 2020	CHA16-1B-109Y-1_0-40cm_23	187.723-OS	75 81402546	3.955967261	0.106309956	3.801412324	1 004324234	13 584586	0.13062156	0	1.39951672	0 039559673	0.163676813	100	93.7823737
Jan 17 00 04 2020	CHA16-1B-109Y-1_0-40cm_24	187.723-OS	76 30305712	4.092263217	0.110308512	3.912868928	1.132777441	12 83373083	0.214172516	0	1.093418361	0 045970831	0 261432249	100	93.10251561
Jan 17 00 08 2020	CHA16-1B-109Y-1_0-40cm_25	187.723-OS	76 94415457	3.419381115	0.095870499	4.503159395	0 966380581	12.76902595	0.165962485	0.003302206	0.905124029	0 04452652	0.183112652	100	93.87663709
Jan 17 00:12 2020	CHA16-1B-109Y-1_0-40cm_26	187.723-OS	76 98301155	3.791219679	0.077109553	3.953666307	0 979971485	12 8481475	0.204126122	0.036519941	0.907750791	0 031914787	0.186562279	100	93.3736449
Jan 17 00:16 2020	CHA16-1B-109Y-1_0-40cm_27	187.723-OS	76 87296697	3.931672346	0.082178397	3.986633592	0 934567141	12 91837752	0.19239413	0	0.938230226	0	0.142979669	100	93.09015803
Jan 17 00 20 2020	CHA16-1B-109Y-1_0-40cm_28	187.723-OS	76 84618078	3.862467481	0.110539125	3.918165078	0 975564667	12 96509469	0.151724551	0.026461103	0.931580209	0 055482958	0.156739357	100	93.72247192
Jan 17 00 24 2020	CHA16-1B-109Y-1_0-40cm_29	187.723-OS	76 9258734	3.705083818	0.093585307	3.982310615	0 990241154	12 91658685	0.215916954	0.035666755	0.937343619	0 000851743	0.196539791	100	93.92500064
Jan 22 21:48 2020	CHA16-1C-103Y-2(0-7 5cm)_3	187.723-S	77 01937577	3.643649313	0.086667911	4.180327961	1.101418418	12 64486676	0.162251618	0	0.87462531	0 047609291	0 239207656	100	94.72940967
Jan 22 21 51 2020	CHA16-1C-103Y-2(0-7 5cm)_4	187.723-S	76 80771168	3.643623867	0.116647226	4.021954116	1 077851138	13.11235064	0.180407338	0	0.88448736	0 04085292	0.114113711	100	94.73007125
Jan 22 21 55 2020	CHA16-1C-103Y-2(0-7 5cm)_5	187.723-S	76.76845831	3.755098791	0.083409764	4.070816158	0 991224976	13 04231587	0.206793264	0	0.885371556	0 016681953	0.179829353	100	95.31258229
Jan 22 21 59 2020	CHA16-1C-103Y-2(0-7 5cm)_6	187.723-S	76.77216485	3.985983797	0.088336832	3.91791182	1 029013153	12 91562511	0.151674656	0.045691465	0.864930919	0 033402036	0.195265364	100	95.20377619
Jan 22 22 03 2020	CHA16-1C-103Y-2(0-7 5cm)_7	187.723-S	77 02459397	3.780544555	0.095488526	3.971646644	0 884463859	12 87642111	0.17766781	0.025667823	0.933551595	0 047849892	0.182104224	100	94.67106056
Jan 22 22 07 2020	CHA16-1C-103Y-2(0-7 5cm)_8	187.723-S	76 61578992	3.229727681	0.077517893	4.258763788	1.425920087	12 94864285	0.207378719	0	1.003705384	0 047517734	0.185035944	100	95.33282901

Date Analysed	Core Section Identifier	sample_no	SiO2	Na2O	Cl	K2O	FeOt	Al2O3	MgO	P2O5	CaO	MnO	TiO2	total	Analytical Total
Jan 22 22:11 2020	CHA16-1C-103Y-2(0-7 5cm)_9	187.723-S	76.49430383	3.23364311	0.085040798	4.199021946	1 379245579	13 03834786	0.177398074	0.025872761	1.171489798	0 034673742	0.160962508	100	94.30767572
Jan 22 22:15 2020	CHA16-1C-103Y-2(0-7 5cm)_10	187.723-S	77 0495474	3.877915849	0.107313393	3.933775395	0 86942719	12 81795144	0.198786783	0.050037623	0.846000922	0 011329273	0 237914736	100	95.32826925
Jan 22 22 23 2020	CHA16-1C-103Y-2(0-7 5cm)_12	187.723-S	77 27191016	3.262257238	0.115604469	4.498635441	0 969831683	12 66270037	0.176283738	0	0.820983718	0 017052967	0 204740222	100	95.58454016
Jan 22 22 27 2020	CHA16-1C-103Y-2(0-7 5cm)_13	187.723-S	77.10032822	3.462466522	0.086558191	4.364366053	0 946777711	12 8479839	0.124577131	0	0.881951478	0	0.18499079	100	96.00477937
Jan 22 22 30 2020	CHA16-1C-103Y-2(0-7 5cm)_14	187.723-S	77 25163187	3.121212536	0.094296747	4.182516983	0 862371111	13 05480163	0.161217018	0.038891976	0.989387785	0 044106543	0.19956581	100	92.04983543
Jan 22 22 38 2020	CHA16-1C-103Y-2(0-7 5cm)_16	187.723-S	74 02497562	4.215711147	0.085458015	3.667002351	1.731728596	13 941111	0.382400906	0.038250628	1.595344125	0 021074726	0 296942892	100	94.90040276
Jan 22 22:46 2020	CHA16-1C-103Y-2(0-7 5cm)_18	187.723-S	76 8304289	3.576830882	0.080852257	4.250459275	0 924264829	12 97870124	0.139672794	0.084905262	0.910345733	0 065367699	0.158171125	100	96.2248956
Jan 22 22 50 2020	CHA16-1C-103Y-2(0-7 5cm)_19	187.723-S	76 63884392	3.600363069	0.104845164	4.287190937	0 944328187	13 09960481	0.180932192	0.009975147	0.93345856	0 017085093	0.183372919	100	94.23419809
Jan 22 23 02 2020	CHA16-1C-103Y-2(0-7 5cm)_22	187.723-S	77 60894425	3.246302919	0.108394685	4.352288967	0 961195784	12.7014857	0.124174311	0	0.725287654	0 016398435	0.155527293	100	96.96047373
Jan 22 23 09 2020	CHA16-1C-103Y-2(0-7 5cm)_24	187.723-S	76 84571185	3.672718225	0.069228475	4.271544224	0.793120187	12 94697875	0.184433917	0.028406821	0.951554876	0 042715442	0.193587226	100	95.04759373
Jan 22 23 29 2020	CHA16-1C-103Y-2(0-7 5cm)_29	187.723-S	73 34475606	4.252820336	0.082571495	3.544735901	1 977786657	14 22504094	0.410459566	0.055360434	1.694966479	0 057237059	0 354265076	100	95.91687774
Jan 22 23 33 2020	CHA16-1C-103Y-2(0-7 5cm)_30	187.723-S	73.10999782	4.341396647	0.090537077	3.495882501	2 240400625	14.17014809	0.371987018	0.054322246	1.701635383	0 045006871	0 378685715	100	95.54096851
Jan 22 23 37 2020	CHA16-1C-103Y-2(0-7 5cm)_31	187.723-S	73.11039497	4.447237699	0.122967914	3.487931451	2 072006857	14.16020443	0.392156617	0.093535219	1.756078057	0 085260547	0 272226241	100	95.47205979
Jan 17 07:46 2020	CHA16-1B-109Y-1_117-118cm_2	189 090-OS	68 01153287	5.046845711	0.110806754	2.378672803	2 938327438	17 01886571	0.885640022	0.002645524	3.15427857	0 046601922	0.405782675	100	98.27920812
Jan 17 07 50 2020	CHA16-1B-109Y-1_117-118cm_3	189 090-OS	67.46742637	5.398261383	0.086801589	2.429936512	3 056404399	16 87367944	0.988045417	0	3.210329686	0 087210548	0.40190465	100	97.80926905
Jan 17 07 54 2020	CHA16-1B-109Y-1_117-118cm_4	189 090-OS	67.79015416	5.341660197	0.127101954	2.447303388	2 93043361	16.78081452	0.968360652	0	3.14587893	0 082130665	0 386161917	100	94.7271038
Jan 17 08:10 2020	CHA16-1B-109Y-1_117-118cm_8	189 090-OS	67 92801577	5.190611557	0.138909645	2.337480563	2 977558517	16.79424813	0.986110481	0	3.139738559	0 080660624	0.426666156	100	94.5938633
01/10/2021	1A-105Y-1-96-97cm	189 682-S	68.40	4.66	0.11	2.34	2 80	16 96	0.92	0.19	3.17	0 02	0.44	100	
01/10/2021	1A-105Y-1-96-97cm	189 682-S	68 39	4.80	0.12	2.37	2 67	17.12	0.89	0.20	3.01	0 05	0 39	100	
01/10/2021	1A-105Y-1-96-97cm	189 682-S	68.45	4.80	0.12	2.45	2 88	16 57	0.97	0.22	3.09	0 07	0 39	100	
01/10/2021	1A-105Y-1-96-97cm	189 682-S	67 82	4.83	0.12	2.47	3 05	16 82	0.92	0.23	3.20	0 06	0.47	100	
01/10/2021	1A-105Y-1-96-97cm	189 682-S	68 02	4.89	0.14	2.36	2 96	16 94	0.93	0.15	3.16	0 06	0 38	100	
01/10/2021	1A-105Y-1-96-97cm	189 682-S	67 97	4.92	0.14	2.46	2 84	16.43	0.97	0.28	3.51	0 09	0.40	100	
01/10/2021	1A-105Y-1-96-97cm	189 682-S	67 89	4.95	0.12	2.41	2 94	16 84	0.91	0.23	3.15	0.10	0.45	100	
01/10/2021	1A-105Y-1-96-97cm	189 682-S	67 83	4.97	0.12	2.31	2 83	17 07	0.88	0.22	3.22	0 07	0.48	100	
01/10/2021	1A-105Y-1-96-97cm	189 682-S	68.19	5.01	0.11	2.36	2.74	16.77	0.96	0.19	3.13	0 06	0.48	100	
01/10/2021	1A-105Y-1-96-97cm	189 682-S	68.16	5.05	0.09	2.53	3 08	16.41	0.93	0.19	3.03	0.10	0.44	100	
01/10/2021	1A-105Y-1-96-97cm	189 682-S	67 66	5.07	0.11	2.37	3 07	16.78	1.04	0.31	3.10	0 09	0 39	100	
01/10/2021	1A-105Y-1-96-97cm	189 682-S	68 04	5.09	0.13	2.42	3.19	16.44	0.88	0.15	3.16	0 05	0.44	100	
01/10/2021	1A-105Y-1-96-97cm	189 682-S	67 53	5.10	0.10	2.40	3 04	16 80	0.91	0.22	3.38	0 08	0.44	100	
01/10/2021	1A-105Y-1-96-97cm	189 682-S	67 80	5.10	0.20	2.36	2 94	16.76	0.94	0.21	3.20	0 07	0.42	100	
01/10/2021	1A-105Y-1-96-97cm	189 682-S	68.10	5.14	0.10	2.44	2 99	16 61	0.91	0.27	2.99	0 07	0 39	100	
01/10/2021	1A-105Y-1-96-97cm	189 682-S	67 62	5.15	0.09	2.27	2 88	17 02	1.01	0.17	3.31	0 05	0.43	100	
01/10/2021	1A-105Y-1-96-97cm	189 682-S	68 03	5.18	0.13	2.39	3 01	16 61	1.00	0.21	2.96	0 08	0.40	100	
01/10/2021	1A-105Y-1-96-97cm	189 682-S	68 02	5.19	0.10	2.47	2 95	16 52	1.01	0.17	3.07	0 07	0.42	100	
01/10/2021	1A-105Y-1-96-97cm	189 682-S	68 05	5.22	0.12	2.42	2 94	16 52	0.89	0.27	3.05	0.10	0.42	100	
01/10/2021	1A-105Y-1-96-97cm	189 682-S	67 96	5.24	0.12	2.34	2.75	16.79	0.95	0.18	3.23	0 06	0.40	100	
01/10/2021	1A-105Y-1-96-97cm	189 682-S	68 04	5.27	0.11	2.40	3 01	16 56	0.96	0.19	3.00	0 08	0 38	100	
01/10/2021	1A-105Y-1-96-97cm	189 682-S	67.41	5.27	0.09	2.31	2 94	16 94	1.02	0.25	3.21	0 06	0.49	100	
01/10/2021	1A-105Y-1-96-97cm	189 682-S	67 94	5.30	0.11	2.24	2 87	16 66	0.88	0.21	3.34	0 07	0 37	100	
01/10/2021	1A-105Y-1-96-97cm	189 682-S	67 80	5.34	0.14	2.32	2 94	16 61	0.95	0.20	3.23	0 04	0.42	100	
01/10/2021	1A-105Y-1-96-97cm	189 682-S	67 67	5.40	0.12	2.36	3 01	16 59	0.98	0.18	3.25	0 07	0 38	100	
01/10/2021	1A-105Y-1-96-97cm	189 682-S	67.76	5.44	0.15	2.32	2 91	16 60	0.98	0.22	3.14	0 07	0.42	100	
050319	CHA16-1C-105Y-1_127-128cm_1	190 682-S	75.7616	4.0029	0.0729	3.0416	1 0364	13 8434	0.327	0.0525	1.6339	0 0334	0.1944	100	94.7035
050319	CHA16-1C-105Y-1_127-128cm_4	190 682-S	75.456	3.9442	0.1002	3.1689	1 2829	13 8462	0.323	0.0485	1.5487	0 0299	0 2514	100	92 35
050319	CHA16-1C-105Y-1_127-128cm_5	190 682-S	75 8377	4.2295	0.062	2.9375	1 0526	13 622	0.3366	0.0815	1.6155	0 0361	0.189	100	95.4716
050319	CHA16-1C-105Y-1_127-128cm_7	190 682-S	76 0774	4.0661	0.0783	2.9594	0 8668	13 6391	0.3527	0.0852	1.5695	0.1183	0.1872	100	95 0764
050319	CHA16-1C-105Y-1_127-128cm_8	190 682-S	74.7429	4.3848	0.1166	2.8855	1 2057	14 2022	0.3866	0.0462	1.7509	0 0577	0 2209	100	95 6058
050319	CHA16-1C-105Y-1_127-128cm_11	190 682-S	76 3188	3.9499	0.0901	3.0766	1 0232	13.4322	0.2853	0.0911	1.4643	0 0795	0.1891	100	95 9382
050319	CHA16-1C-105Y-1_127-128cm_13	190 682-S	76 0884	4.1156	0.0986	3.0514	0 9751	13 6417	0.2825	0.0438	1.4471	0 0425	0 2133	100	96 206
050319	CHA16-1C-105Y-1_127-128cm_14	190 682-S	75.768	4.0921	0.0767	3.0651	1 0822	13.7381	0.3124	0.0443	1.4922	0 0971	0 2317	100	94.7525
050319	CHA16-1C-105Y-1_127-128cm_15	190 682-S	75 8037	4.0288	0.1019	2.9857	1.1184	13.7206	0.3399	0.0606	1.5894	0 0357	0 2152	100	95.1479
050319	CHA16-1C-105Y-1_127-128cm_19	190 682-S	76 3415	3.7854	0.0578	3.0255	0 9602	13.7931	0.2876	0.0554	1.4685	0 0788	0.1463	100	94.4731
050319	CHA16-1C-105Y-1_127-128cm_20	190 682-S	75.7956	4.3863	0.0677	2.9835	1 0614	13 5197	0.2913	0.0612	1.4992	0 0761	0 2579	100	95.1352
050319	CHA16-1C-105Y-1_127-128cm_22	190 682-S	75 0531	4.5655	0.0686	2.5248	1.1698	14.1047	0.3225	0.0266	1.858	0.1149	0.1915	100	97 2381
050319	CHA16-1C-105Y-1_127-128cm_23	190 682-S	75.4926	4.2785	0.0785	3.009	1.1623	13.7743	0.3339	0.0807	1.5455	0 0474	0.1974	100	95 5761
050319	CHA16-1C-105Y-1_127-128cm_25	190 682-S	75 6105	4.0219	0.0816	3.2569	0 9808	13 8692	0.2738	0.0496	1.567	0.1298	0.1588	100	95 6981
050319	CHA16-1C-105Y-1_127-128cm_27	190 682-S	74.1502	4.2414	0.0847	3.1169	1 0231	14.7365	0.3619	0.0205	2.0494	0 0275	0.1878	100	94.7652
050319	CHA16-1C-105Y-1_127-128cm_28	190 682-S	75.7376	4.2151	0.0696	2.9073	1.1292	13.7546	0.3305	0.0506	1.5718	0 0626	0.1711	100	96 0195
050319	CHA16-1C-105Y-1_127-128cm_29	190 682-S	75 3558	4.1877	0.0658	2.9559	1 2108	13 8977	0.3383	0.0406	1.6792	0 0747	0.1935	100	95.7501
050319	CHA16-1C-105Y-1_127-128cm_30	190 682-S	75 8721	3.9458	0.1031	2.9746	1 2014	13 8455	0.3136	0.0114	1.4876	0 056	0.1887	100	94 9158
01/10/2021	1C-106Y-1-86-87cm	191 917-S	66.44	4.42	0.33	2.51	3 35	16.79	1.29	0.22	4.06	0.10	0.49	100	
01/10/2021	1C-106Y-1-86-87cm	191 917-S	68.14	4.52	0.15	2.78	2 86	16.15	1.07	0.30	3.50	0.10	0.44	100	
01/10/2021	1C-106Y-1-86-87cm	191 917-S	66.74	4.53	0.15	2.44	3 34	16 89	1.21	0.23	3.81	0.10	0 54	100	
01/10/2021	1C-106Y-1-86-87cm	191 917-S	67 91	4.55	0.11	2.69	3.17	16 29	1.16	0.25	3.32	0 07	0.48	100	
01/10/2021	1C-106Y-1-86-87cm	191 917-S	67 67	4.63	0.17	2.62	3 27	16 26	1.10	0.15	3.53	0.10	0 51	100	

Date Analysed	Core Section Identifier	sample_no	SiO2	Na2O	Cl	K2O	FeOt	Al2O3	MgO	P2O5	CaO	MnO	TiO2	total	Analytical Total
01/10/2021	1C-106Y-1-86-87cm	191 917-S	69 22	4.67	0.15	2.96	2.77	15.72	0.92	0.19	2.83	0.12	0.45	100	
01/10/2021	1C-106Y-1-86-87cm	191 917-S	68 09	4.67	0.21	2.69	3.10	16 21	1.03	0.24	3.24	0 09	0.43	100	
01/10/2021	1C-106Y-1-86-87cm	191 917-S	70 00	4.71	0.13	3.36	2 54	15 55	0.70	0.13	2.37	0 04	0.48	100	
01/10/2021	1C-106Y-1-86-87cm	191 917-S	68 23	4.73	0.17	2.91	2 91	16 09	1.03	0.27	3.15	0 08	0.43	100	
01/10/2021	1C-106Y-1-86-87cm	191 917-S	66 58	4.76	0.10	2.26	3 04	17 28	1.05	0.21	4.15	0 07	0.49	100	
01/10/2021	1C-106Y-1-86-87cm	191 917-S	68 81	4.82	0.13	2.86	2.71	16.15	0.86	0.19	2.91	0.10	0.46	100	
01/10/2021	1C-106Y-1-86-87cm	191 917-S	67 88	4.82	0.15	2.72	3 21	16 05	1.11	0.18	3.33	0.11	0.44	100	
01/10/2021	1C-106Y-1-86-87cm	191 917-S	67 81	4.83	0.12	2.71	3 07	16.41	1.00	0.17	3.33	0 09	0.45	100	
01/10/2021	1C-106Y-1-86-87cm	191 917-S	69 24	4.83	0.13	3.18	2 67	15 86	0.79	0.15	2.63	0 05	0.47	100	
01/10/2021	1C-106Y-1-86-87cm	191 917-S	67 69	4.86	0.11	2.68	3.16	16 21	1.04	0.18	3.54	0.12	0.41	100	
01/10/2021	1C-106Y-1-86-87cm	191 917-S	67 09	4.86	0.08	2.48	3.17	16.75	1.14	0.19	3.68	0.13	0.44	100	
01/10/2021	1C-106Y-1-86-87cm	191 917-S	66 94	4.89	0.11	2.55	3 23	16 58	1.20	0.24	3.69	0.10	0.47	100	
01/10/2021	1C-106Y-1-86-87cm	191 917-S	65 92	4.91	0.15	2.35	3 59	16 80	1.24	0.23	4.20	0.11	0 50	100	
01/10/2021	1C-106Y-1-86-87cm	191 917-S	67 97	4.92	0.11	2.68	3 08	16.14	1.10	0.19	3.26	0 07	0.48	100	
01/10/2021	1C-106Y-1-86-87cm	191 917-S	67 64	4.93	0.10	2.70	3.17	16 30	1.06	0.23	3.32	0 05	0 51	100	
01/10/2021	1C-106Y-1-86-87cm	191 917-S	69 63	4.94	0.13	3.28	2 56	15 65	0.68	0.12	2.45	0 06	0.49	100	
01/10/2021	1C-106Y-1-86-87cm	191 917-S	66 91	4.97	0.11	2.69	3 22	16 63	1.13	0.35	3.54	0 06	0.40	100	
01/10/2021	1C-106Y-1-86-87cm	191 917-S	67 25	5.00	0.11	2.56	3 25	16.46	1.12	0.27	3.46	0 07	0.45	100	
01/10/2021	1C-106Y-1-86-87cm	191 917-S	69 97	5.12	0.11	3.23	2.41	15.44	0.70	0.18	2.32	0 02	0 50	100	
01/10/2021	1C-106Y-1-86-87cm	191 917-S	67 20	5.14	0.09	2.21	2.79	16 86	0.94	0.23	4.00	0.10	0.44	100	
29/09/2021	1C-106Y-1-106-107cm	192.137-S	75 34349724	3.688089997	0.073983974	2.821611022	1 318381087	14 09694641	0.291533803	0.027549588	2.060467087	0 049322649	0 228617145	100	
29/09/2021	1C-106Y-1-106-107cm	192.137-S	75.45826235	3.92318708	0.18995178	2.855484267	1 289437374	13 96704261	0.400824083	0.022968026	1.58929204	0 054254201	0 249296192	100	
29/09/2021	1C-106Y-1-106-107cm	192.137-S	75 56075015	3.94630013	0.096657324	2.811063107	1 265951458	14.14180978	0.369326469	0.027894395	1.546712714	0 02324533	0 210289144	100	
29/09/2021	1C-106Y-1-106-107cm	192.137-S	75 66031349	3.949723986	0.094814611	2.824265001	1 347259346	13 93020933	0.326238174	0.049159199	1.581776652	0 047354218	0.188885994	100	
29/09/2021	1C-106Y-1-106-107cm	192.137-S	74 80717127	3.977820609	0.076472006	2.861052791	1 808100277	14.12445393	0.301554928	0.061369051	1.636977068	0 082428101	0 262599975	100	
29/09/2021	1C-106Y-1-106-107cm	192.137-S	75 62336227	4.003578919	0.124350291	2.937408446	1 246875489	13.75142324	0.321756437	0.04232044	1.674439959	0 082029851	0.19245465	100	
29/09/2021	1C-106Y-1-106-107cm	192.137-S	74 98696554	4.022665067	0.089156693	2.759611919	1.783133855	14.15893192	0.315096692	0.062409685	1.560290048	0 02557948	0 236159097	100	
29/09/2021	1C-106Y-1-106-107cm	192.137-S	75 25085546	4.03494461	0.142955517	2.838991499	1.18991746	14 03847765	0.373152581	0.175704513	1.720280948	0 053985547	0.180734223	100	
29/09/2021	1C-106Y-1-106-107cm	192.137-S	74 93168372	4.03973416	0.080067739	2.866238118	1.713511919	14.10272234	0.321841488	0.027416191	1.649580322	0 038320357	0 228883653	100	
29/09/2021	1C-106Y-1-106-107cm	192.137-S	75 03016344	4.093026609	0.128061271	2.960435684	1 648424415	13 9050767	0.306515195	0.076477922	1.637411457	0 021194028	0.193213283	100	
29/09/2021	1C-106Y-1-106-107cm	192.137-S	74 82532381	4.102511966	0.082050239	2.821122838	1 932417475	14 08494662	0.322467521	0.022217634	1.539503579	0 037614971	0 22982334	100	
29/09/2021	1C-106Y-1-106-107cm	192.137-S	75.72097146	4.115918895	0.091312031	2.846226691	1 31328497	13.74441811	0.380514793	0.047930881	1.524103529	0 022113806	0.19320483	100	
29/09/2021	1C-106Y-1-106-107cm	192.137-S	75 30378906	4.153321516	0.086261293	2.822128722	1 218094654	14 09999407	0.382445627	0.037486389	1.639079238	0 053886684	0 203512754	100	
29/09/2021	1C-106Y-1-106-107cm	192.137-S	75 35116149	4.202569702	0.111075513	2.893921415	1 285667146	13 88443914	0.396172972	0.056920881	1.637520833	0	0.180550906	100	
29/09/2021	1C-106Y-1-106-107cm	192.137-S	75 94639415	4.28536879	0.066801337	3.161509818	1 053591528	13 62285128	0.264411547	0.0485255	1.397512176	0 032770467	0.120263413	100	
29/09/2021	1C-106Y-1-106-107cm	192.137-S	74.7257937	4.288908135	0.11185021	2.990949094	1 279449016	14 28883605	0.328398363	0.024040459	1.659181214	0 085326699	0 217267057	100	
29/09/2021	1C-106Y-1-106-107cm	192.137-S	75.18557134	4.304549983	0.065734507	2.852029422	1 34236225	13 99508861	0.339272994	0.034351581	1.642274614	0 018023978	0 220740716	100	
29/09/2021	1C-106Y-1-106-107cm	192.137-S	75 38363697	4.304921314	0.089694675	2.792381393	1.130491376	14 04652458	0.359373691	0.092444748	1.607074224	0 006663637	0.186793392	100	
29/09/2021	1C-106Y-1-106-107cm	192.137-S	75.43852374	4.307527822	0.066494847	2.812439282	1.182165463	14 03083091	0.309212857	0.043702588	1.567901837	0 017878331	0 223322316	100	
29/09/2021	1C-106Y-1-106-107cm	192.137-S	75.18130109	4.35912542	0.101923512	2.800790729	1 307632333	13 93024863	0.342835217	0.030429644	1.651735693	0 050961756	0 243015978	100	
29/09/2021	1C-106Y-1-106-107cm	192.137-S	74 88959047	4.380025122	0.033481923	2.842804767	1 315271005	14.15085039	0.425310491	0.07665044	1.630899987	0 048011814	0 207103592	100	
29/09/2021	1C-106Y-1-106-107cm	192.137-S	74 80453102	4.423267343	0.081986824	2.960014763	1 395898283	14.15222153	0.280507553	0.075284904	1.619980339	0 03440319	0.171904254	100	
29/09/2021	1C-106Y-1-106-107cm	192.137-S	75 08392748	4.448725829	0.223875585	2.839333838	1 361964328	13.79105007	0.345518539	0.06921694	1.649802602	0 020804335	0.16578046	100	
29/09/2021	1C-106Y-1-106-107cm	192.137-S	75.1979543	4.484567161	0.082039949	2.699241846	1 297230126	13 90003281	0.375246174	0.059723383	1.656569169	0 052922143	0.194472936	100	
Jan 24 21:45 2020	CHA16-1C-107Y-1(0-1 5cm)_1	192 397-S	76.70679301	3.876726323	0.061084634	3.321411472	0 910530321	13.47972228	0.215001146	0.011839732	1.220749686	0 016135564	0.180005833	100	95.44135158
Jan 24 21 52 2020	CHA16-1C-107Y-1(0-1 5cm)_3	192 397-S	76.77363601	3.982703859	0.060520461	3.358781584	0 956063604	13 26575012	0.218164822	0.011750536	1.241709315	0 063640072	0 067279619	100	96.16582441
Jan 24 21 56 2020	CHA16-1C-107Y-1(0-1 5cm)_4	192 397-S	76.77941114	3.677993233	0.071267631	3.469608347	1 004944712	13.44555785	0.199945298	0.028965499	1.1622667	0 039280551	0.120759041	100	95.97625054
Jan 24 22 00 2020	CHA16-1C-107Y-1(0-1 5cm)_5	192 397-S	76.44343988	3.720836367	0.077222945	3.388247641	1 04689962	13 52456821	0.238424543	0.017149106	1.362158699	0 001662944	0.179390044	100	96.21492716
Jan 24 22 04 2020	CHA16-1C-107Y-1(0-1 5cm)_6	192 397-S	74 6442514	4.176548023	0.0476147	2.832253696	1 375966882	14 59383663	0.349926997	0.00389948	1.785551243	0 01313509	0.177015856	100	97.44889745
Jan 24 22 08 2020	CHA16-1C-107Y-1(0-1 5cm)_7	192 397-S	76.44290845	4.020591048	0.034934699	2.914670117	0 924444068	13 90662126	0.165061283	0	1.441831494	0 021084848	0.127852728	100	96.75194403
Jan 24 22:12 2020	CHA16-1C-107Y-1(0-1 5cm)_8	192 397-S	75 90070246	4.04473564	0.063663314	3.219279387	0 999601357	13 95405362	0.219984091	0.077489706	1.343533234	0 03250234	0.144454844	100	96.91609908
Jan 24 22:16 2020	CHA16-1C-107Y-1(0-1 5cm)_9	192 397-S	77.180013	3.99687743	0.034081901	3.211960932	1 000850521	13 06370278	0.279471585	0.01704095	1.062735627	0 001962291	0.151302983	100	96.82558618
Jan 24 22 20 2020	CHA16-1C-107Y-1(0-1 5cm)_10	192 397-S	73 98961103	4.897657467	0.045992708	2.520853108	0 891750336	15 0979903	0.254348934	0.066262425	2.098996057	0	0.136537636	100	97.18932023
Jan 24 22 23 2020	CHA16-1C-107Y-1(0-1 5cm)_11	192 397-S	75.77237926	4.549205177	0.03363345	2.985096431	0 678628486	14 22710858	0.043243007	0.041096191	1.523217014	0 029339818	0.117052583	100	97.8192855
Jan 24 22 27 2020	CHA16-1C-107Y-1(0-1 5cm)_12	192 397-S	77 99567384	3.759570213	0.090394038	3.369232322	0 849257015	12 62967873	0.10528851	0.093167491	0.930134106	0 019516895	0.158086846	100	97.35155332
Jan 24 22 31 2020	CHA16-1C-107Y-1(0-1 5cm)_13	192 397-S	77 85407405	3.536491843	0.045000577	3.587745348	0.796781986	12 89559586	0.083748227	0.018656276	0.975251693	0 063451839	0.143202293	100	97.5543039
Jan 24 22 35 2020	CHA16-1C-107Y-1(0-1 5cm)_14	192 397-S	76 38582932	4.027878006	0.047779675	3.308614076	1 062549079	13 36066161	0.298597283	0.053431035	1.295086081	0 033805405	0.125768436	100	97.32171616
Jan 24 22:47 2020	CHA16-1C-107Y-1(0-1 5cm)_17	192 397-S	76.47586797	4.054836762	0.071319845	3.231519653	1 02230993	13 53353174	0.205932192	0.005454476	1.277067751	0 046826161	0 075333515	100	97.16790665
Jan 24 22 51 2020	CHA16-1C-107Y-1(0-1 5cm)_18	192 397-S	76 32202004	4.380059348	0.048633053	3.146239813	0.773926261	13.7330731	0.109090211	0.012749469	1.360902947	0 022825661	0 090480099	100	97.25895614
Jan 24 22 55 2020	CHA16-1C-107Y-1(0-1 5cm)_19	192 397-S	75 54770097	4.654646604	0.021673521	2.807236976	0.727579781	14 36320318	0.089996715	0.043863078	1.599712247	0 026008225	0.118378706	100	96.89242566
Jan 24 22 59 2020	CHA16-1C-107Y-1(0-1 5cm)_20	192 397-S	75 06932932	4.597720357	0.051699257	2.951375076	0 823845289	14.4442844	0.284898043	0.029011816	1.586113136	0 019776221	0.141947087	100	99.61458385
Jan 24 23:10 2020	CHA16-1C-107Y-1(0-1 5cm)_23	192 397-S	72 05750615	5.023950012	0.038622253	2.557832562	0 907011135	16 39551069	0.230408742	0.001019057	2.700500513	0 011107719	0 076531165	100	98.12995727
Jan 24 23:14 2020	CHA16-1C-107Y-1(0-1 5cm)_24	192 397-S	76 91716873	3.791238893	0.066935715	3.427108604	1 232372813	12 93622769	0.26324478	0.084606744	1.07729017	0 076574458	0.127231407	100	93.37317167
Jan 24 23:18 2020	CHA16-1C-107Y-1(0-1 5cm)_25	192 397-S	76 58075226	3.757996044	0.036550372	4.015393033	0 8313558	13 36731403	0.13333164	0.032637938	1.145725479	0 005868651	0 093074751	100	97.12623316
Jan 24 23 22 2020	CHA16-1C-107Y-1(0-1 5cm)_26	192 397-S	76.43171976	3.994941615	0.060234612	3.053128954	1.123858971	13 66082801	0.241766415	0.051851444	1.208625082	0 043571773	0.129473367	100	96.62218806
Jan 24 23 26 2020	CHA16-1C-107Y-1(0-1 5cm)_27	192 397-S	76 99217222	4.264150078	0.048836392	2.901274024	0.712451039	13 54695145	0.091684389	0.015590476	1.252297247	0 013422264	0.161170418	100	96.85400197

Date Analysed	Core Section Identifier	sample_no	SiO2	Na2O	Cl	K2O	FeOt	Al2O3	MgO	P2O5	CaO	MnO	TiO2	total	Analytical Total
Jan 24 23 30 2020	CHA16-1C-107Y-1(0-1 5cm)_28	192 397-S	78.79210658	3.574903371	0.03399764	3.451275589	0 804979995	12.17074545	0.123318713	0.060165521	0.811822437	0 025137649	0.151547056	100	97.06556065
Jan 24 23 34 2020	CHA16-1C-107Y-1(0-1 5cm)_29	192 397-S	75.72488672	4.629737427	0.057871718	2.734822772	0 821761963	14 21446445	0.159480114	0	1.49544616	0 047628936	0.113899735	100	97.62972677
Jan 24 23:49 2020	CHA16-1C-107Y-1(0-1 5cm)_33	192 397-S	78 01826244	3.539640119	0.08729024	3.644054281	0 823273296	12 65319981	0.128220592	0.062335255	0.92354327	0 029653622	0 090527079	100	95.77244823
Jan 24 23 53 2020	CHA16-1C-107Y-1(0-1 5cm)_34	192 397-S	74 94257864	4.19986153	0.074537146	3.44097566	0.732970728	14.7638401	0.031810832	0.059983171	1.6529158	0 027132769	0 07339362	100	96.19364759
Jan 24 23 57 2020	CHA16-1C-107Y-1(0-1 5cm)_35	192 397-S	77 86161004	3.40999752	0.079987596	4.041478542	0 8824386	12 53688239	0.099563508	0.047466324	0.900491938	0 024522513	0.115561027	100	95.01473186
Jan 25 00 09 2020	CHA16-1C-107Y-1(0-1 5cm)_38	192 397-S	76.73876636	3.638295735	0.109253421	3.711479844	0.78843827	13.41960736	0.119081001	0.01808693	1.359133464	0	0 097857609	100	95.649179
Jan 25 00:13 2020	CHA16-1C-107Y-1(0-1 5cm)_39	192 397-S	77.41924602	3.549125886	0.07077251	3.822135569	0.765630344	13 01360645	0.097758467	0.005145182	1.137505347	0 021525764	0 09754846	100	95.2347172
Jan 25 00:16 2020	CHA16-1C-107Y-1(0-1 5cm)_40	192 397-S	75 89358666	4.119377102	0.064320099	3.644461446	0.732862552	13.75929631	0.119658097	0.01466044	1.466043981	0 025500906	0.160232413	100	96.85930424
Jan 23 16:45 2020	CHA16-1C-107Y-1(63-64cm)_1	193 032-S	76.14874367	3.997016328	0.061929142	3.122653862	1.10032951	13 61125718	0.314780275	0.083829634	1.409929282	0 023262723	0.126268386	100	95.43164666
Jan 23 16:49 2020	CHA16-1C-107Y-1(63-64cm)_2	193 032-S	75 29082801	3.848014837	0.098370989	3.20499029	1 577372604	13.77017594	0.309604178	0.044214057	1.459983431	0 072879152	0 323566512	100	94.540068
Jan 23 16 53 2020	CHA16-1C-107Y-1(63-64cm)_3	193 032-S	76 88433841	4.185566229	0.06166754	2.975638348	1 051739914	13.18991882	0.125695068	0.067824033	1.279688987	0 040222422	0.13770023	100	97.45807996
Jan 23 16 57 2020	CHA16-1C-107Y-1(63-64cm)_4	193 032-S	75.73293548	4.33936888	0.070682707	2.694137973	1 000848487	13.73036327	0.355154994	0.054497392	1.82153826	0 018951161	0.181521387	100	97.61935085
Jan 23 17 01 2020	CHA16-1C-107Y-1(63-64cm)_5	193 032-S	75.19540964	4.553976603	0.03745991	2.643628491	0 671289031	14 68351276	0.131058648	0.060936147	1.835735432	0 033172944	0.153820391	100	97.9140591
Jan 23 17 05 2020	CHA16-1C-107Y-1(63-64cm)_6	193 032-S	76.49664312	4.179550191	0.046937387	3.019604334	0.774357092	13 63784291	0.132287428	0.029682505	1.408249416	0 055770243	0 219075376	100	97.36374952
Jan 23 17 20 2020	CHA16-1C-107Y-1(63-64cm)_10	193 032-S	77 94988062	3.469276313	0.075917841	3.372980146	1.144241484	12 51455137	0.384643516	0.064777723	0.805673497	0 040537651	0.177519842	100	96.94690922
Jan 23 17 24 2020	CHA16-1C-107Y-1(63-64cm)_11	193 032-S	76 99433658	3.967238461	0.044257881	3.203818753	0 966601332	13.16043088	0.237411185	0.028033414	1.069377403	0 0692107	0 259283409	100	97.38378604
Jan 23 17 28 2020	CHA16-1C-107Y-1(63-64cm)_12	193 032-S	75 632363	4.318419057	0.055661505	3.22143506	0 664045499	14 21377931	0.087977799	0.064530645	1.574497773	0 011213856	0.15607649	100	98.09292881
Jan 23 17 32 2020	CHA16-1C-107Y-1(63-64cm)_13	193 032-S	76.46017423	4.050490363	0.063923349	2.674660336	0 866691958	13 80184187	0.247431898	0.041410764	1.584462573	0 015696848	0.19321581	100	96.83472572
Jan 23 17 36 2020	CHA16-1C-107Y-1(63-64cm)_14	193 032-S	76 57841041	3.856027015	0.060651017	3.245817694	0 857061347	13 63346861	0.252591197	0.040884819	1.228426552	0 050975983	0.195685355	100	96.12369806
Jan 23 17:40 2020	CHA16-1C-107Y-1(63-64cm)_15	193 032-S	76 94675165	4.051029155	0.054386721	3.106318505	0 91873475	13 29358674	0.223613096	0.043195607	1.161571268	0 017048145	0.183764364	100	95.61157349
Jan 23 17:48 2020	CHA16-1C-107Y-1(63-64cm)_17	193 032-S	78 08857227	3.433107545	0.132178869	3.656246999	0 84185302	12.47138844	0.195443021	0.054068137	0.889374847	0 078110731	0.159656119	100	90.25648434
Jan 23 17 55 2020	CHA16-1C-107Y-1(63-64cm)_19	193 032-S	77 39731866	3.664592713	0.046250499	3.344902127	0.751123855	13 21119471	0.104683048	0.082590176	1.252398449	0 011975576	0.132970183	100	96.86382073
Jan 23 17 59 2020	CHA16-1C-107Y-1(63-64cm)_20	193 032-S	77.11987418	3.958815685	0.053555468	3.378114147	0.718509261	13.17965875	0.204334709	0.039960619	1.147271104	0 056542215	0.143363869	100	97.0955941
Jan 23 18 03 2020	CHA16-1C-107Y-1(63-64cm)_21	193 032-S	74 03623438	4.450125744	0.046105039	2.857068393	0 691632188	15 35426618	0.113251303	0.050127626	2.253281712	0 045383036	0.102524404	100	96.95252683
Jan 23 18 07 2020	CHA16-1C-107Y-1(63-64cm)_22	193 032-S	76 52913448	4.264792332	0.051615781	2.848121759	0 962749614	13.48449225	0.288719347	0.052643983	1.40822685	0	0.109503598	100	97.25707798
Jan 23 18:11 2020	CHA16-1C-107Y-1(63-64cm)_23	193 032-S	76 2383148	3.827186243	0.063152325	3.281850325	0 922959035	13.76676486	0.181381759	0.053420655	1.386892715	0 06863933	0 209437956	100	96.59185174
Jan 23 18:15 2020	CHA16-1C-107Y-1(63-64cm)_24	193 032-S	75 89300903	4.169218958	0.041759052	3.037021942	0.780133635	14 08901255	0.127337991	0.021693014	1.653169262	0 048158491	0.139486079	100	92.19558019
Jan 23 18:19 2020	CHA16-1C-107Y-1(63-64cm)_25	193 032-S	75 00797285	4.524005463	0.055549967	2.555091614	0 836689188	14 86130866	0.136961186	0.112961945	1.786876796	0	0.12258233	100	96.66972356
Jan 23 18 23 2020	CHA16-1C-107Y-1(63-64cm)_26	193 032-S	77 99781228	3.462037033	0.067479023	3.572418883	1 032220983	12 33120303	0.379700077	0.060584882	0.821404885	0 035619732	0 239519196	100	95.73345434
Jan 23 18 31 2020	CHA16-1C-107Y-1(63-64cm)_28	193 032-S	78 2482974	3.709027408	0.077313059	3.408425172	0 897524754	12 35735678	0.207830803	0.039176106	0.786738943	0 048424577	0 21988499	100	96.23212581
Jan 23 18 34 2020	CHA16-1C-107Y-1(63-64cm)_29	193 032-S	76.70069451	3.183965304	0.072729635	4.080757775	0 937007005	13.41467964	0.174419486	0.027643843	1.185306585	0 051557961	0.17123825	100	91.15953961
Jan 23 18 38 2020	CHA16-1C-107Y-1(63-64cm)_30	193 032-S	75 36888278	4.706062196	0.035243323	2.539592392	0 954704168	14.16312331	0.327866561	0.056078346	1.664145076	0 032755559	0.151546289	100	96.47217435
040319	CHA16-1C-107Y-1_77-78cm_3	193.172-S	73 9428	4.6024	0.0714	3.4644	2 2583	13 2174	0.3549	0.0795	1.3868	0 0671	0 5548	100	95 0582
040319	CHA16-1C-107Y-1_77-78cm_5	193.172-S	74.1921	4.668	0.0919	3.4087	2 0579	13 3066	0.3586	0.0832	1.2506	0 0449	0 5375	100	92 9201
040319	CHA16-1C-107Y-1_77-78cm_27	193.172-S	68 8746	4.5694	0.0556	2.4905	1 5109	17 534	0.2743	0.0762	4.2224	0 043	0 3491	100	95 9846
040319	CHA16-1C-107Y-1_77-78cm_28	193.172-S	70 8191	4.3731	0.0888	3.1767	3.1539	14 3218	0.8457	0.1639	2.1709	0 0578	0 8281	100	94 0535
060418	MEX3_1C-108Y-1_50-52cm-SAMPLE_A-9	194 977-S	75 8868	3.6544	0.0951	4.1313	0 998	13.4462	0.1738	0.0525	1.364	0	0.1978	100	92 9732
060418	MEX3_1C-108Y-1_50-52cm-SAMPLE_A-10	194 977-S	75 3115	4.3425	0.0872	3.1655	0 8836	14 2385	0.2208	0.0783	1.4929	0 0178	0.1614	100	95 5426
060418	MEX3_1C-108Y-1_50-52cm-SAMPLE_A-11	194 977-S	72.7684	4.5875	0.0706	2.9011	0 8576	15.7939	0.2817	0.0524	2.541	0	0.1458	100	97 3252

Filtered core analyses, normalised to 100% (201-250.99 mc)

Date Analysed	Core Section Identifier	sample_no	SiO2	Na2O	Cl	K2O	FeOt	Al2O3	MgO	P2O5	CaO	MnO	TiO2	total	Analytical Total
Feb 13 19:16 2020	CHA16-1A-115Y-1(13-14cm)_1	204.114-S	58 59314884	3.746109092	0.108333988	2 619509738	8.183429647	14.37684414	3.218544911	1 201532367	5.614685601	0.175243171	2.162618505	100	98.49171249
Feb 13 19 20 2020	CHA16-1A-115Y-1(13-14cm)_2	204.114-S	58.49141858	3.971518536	0.088698819	2 519737351	7.894499685	14.53929093	3.109030764	1 334736489	5.811652278	0.12608847	2.113328101	100	98.42295662
Feb 13 19 24 2020	CHA16-1A-115Y-1(13-14cm)_3	204.114-S	58 87831401	3.631654325	0.083242222	2.740142965	7.888290354	14.38575057	3.020384859	1 330108683	5.677493189	0.153821662	2.210797165	100	96 34533795
Feb 13 19 28 2020	CHA16-1A-115Y-1(13-14cm)_4	204.114-S	58 58143792	4.023113038	0.104027976	2 620938317	7.660425893	14.90595421	2.843566282	1 275276031	5.747849283	0.142684287	2.094726763	100	98 81957095
Feb 13 19 32 2020	CHA16-1A-115Y-1(13-14cm)_5	204.114-S	59.16544274	3.961383162	0.085330824	2.128203461	7.580458042	14.67446958	3.344319724	0 818063149	6.090715619	0.145021864	2.006591835	100	98 67477609
Feb 13 19:40 2020	CHA16-1A-115Y-1(13-14cm)_7	204.114-S	58 62885805	3.816329848	0.075307433	2 031784446	7.318467358	15.10192021	3.649125299	0.793766445	6.610880735	0.143943336	1.829616839	100	98 92781707
Feb 13 19:44 2020	CHA16-1A-115Y-1(13-14cm)_8	204.114-S	58 28256901	3.862163091	0.110490827	1 995113925	7.524719016	15.28237012	3.645893467	0.71495625	6.704392986	0.115149469	1.762181842	100	98.74122853
Feb 13 19 52 2020	CHA16-1A-115Y-1(13-14cm)_10	204.114-S	58 8793031	4.067726381	0.074360856	2 072351715	7.070376441	15.25819743	3.474236699	0.728098872	6.410068296	0.126575992	1.838704218	100	98.43888877
Feb 13 19 56 2020	CHA16-1A-115Y-1(13-14cm)_11	204.114-S	58 65450101	3.996449009	0.086990941	1 994178306	7.315378581	15.02755795	3.581381447	0.764933263	6.613346422	0.144069208	1.821213861	100	98 2860958
Feb 13 20 00 2020	CHA16-1A-115Y-1(13-14cm)_12	204.114-S	58.70093524	4.045458641	0.077003397	2 02587471	7.216548719	14.96728331	3.52764253	0 939751541	6.551336127	0.154107584	1.794058201	100	99 21640218
Feb 13 20 04 2020	CHA16-1A-115Y-1(13-14cm)_13	204.114-S	58 3615252	4.081367207	0.086021194	2 659203192	7.866809443	14.76663591	3.072185506	1.137607511	5.771679655	0.101835395	2.095129788	100	99 27785918
Feb 13 20 08 2020	CHA16-1A-115Y-1(13-14cm)_14	204.114-S	58.41201918	4.115531553	0.08481142	2 61036348	7.759991045	14.54490468	3.199472748	1 217852362	5.840307396	0.132549585	2.08219655	100	98.45372187
Feb 13 20:15 2020	CHA16-1A-115Y-1(13-14cm)_16	204.114-S	58 5502962	4.2005455	0.089036288	2 274351918	7.496182331	14.82918246	3.273842896	1 027299303	6.078536965	0.171545288	2.009180843	100	98 04990961
Feb 13 20:19 2020	CHA16-1A-115Y-1(13-14cm)_17	204.114-S	58.49142214	4.25401751	0.090960163	2 276533564	7.740214118	14.78229128	3.298444186	1 012854268	5.888633486	0.151161829	2.013467463	100	98 83447517
Feb 13 20 23 2020	CHA16-1A-115Y-1(13-14cm)_18	204.114-S	58 50367461	4.196832445	0.095308956	2 231724209	7.196798712	15.16139245	3.398772649	0 91604123	6.326631015	0.140352931	1.832470796	100	97 68232073
Feb 13 20 31 2020	CHA16-1A-115Y-1(13-14cm)_20	204.114-S	57 60517354	4.136278966	0.124149747	2.495420261	7.589805193	15.14854706	3.375547739	1 207044464	6.223018992	0.158733579	1.936280452	100	96 57691882
Feb 13 20 35 2020	CHA16-1A-115Y-1(13-14cm)_21	204.114-S	57 88024471	4.084942477	0.088957792	2 540193836	7.661387835	14.95551873	3.366521952	1.108045625	6.212763238	0.122316964	1.979106844	100	98 02401551
Feb 13 20 39 2020	CHA16-1A-115Y-1(13-14cm)_22	204.114-S	58 22699736	4.188746678	0.10207326	2.707649036	7.867508519	14.49869427	3.116350777	1.17301783	5.823999813	0.159495855	2.135466598	100	97 87088227
Feb 13 20:43 2020	CHA16-1A-115Y-1(13-14cm)_23	204.114-S	58 66316462	3.997039308	0.110917113	2 391332252	7.418217924	14.67362174	3.398744563	1 033979264	6.166584447	0.151925917	1.994472857	100	98 27158052
Feb 13 20:47 2020	CHA16-1A-115Y-1(13-14cm)_24	204.114-S	58.46933436	4.200044571	0.123310335	2 350221736	7.630590052	14.45742462	3.489723184	0 888042137	6.277432083	0.109575273	2.004301654	100	98 28859824
Feb 13 20 51 2020	CHA16-1A-115Y-1(13-14cm)_25	204.114-S	58 66270766	4.133547967	0.083557877	2 35101943	7.592469674	14.50304194	3.429842198	1 058194611	6.106543973	0.1249806	1.954094071	100	98 25524922
Feb 13 20 55 2020	CHA16-1A-115Y-1(13-14cm)_26	204.114-S	57.75075264	4.195347938	0.129986167	2 65650356	7.827560107	14.86425274	3.214166521	1 09960286	6.043038632	0.119948233	2.098840599	100	98 62587951
Feb 13 20 59 2020	CHA16-1A-115Y-1(13-14cm)_27	204.114-S	58.12231883	4.218769412	0.100882663	2 648931101	7.885898337	14.25957164	3.288328264	1 245649328	6.018452656	0.140768867	2.070428907	100	98 53030902
Feb 13 21 03 2020	CHA16-1A-115Y-1(13-14cm)_28	204.114-S	58 06660475	4.005954912	0.086763437	2 515028606	7.787498215	14.72655304	3.343270959	1 032879733	6.181516093	0.153022825	2.10090743	100	99 0048381
Feb 13 21 07 2020	CHA16-1A-115Y-1(13-14cm)_29	204.114-S	58 88405161	4.132280088	0.079479384	2.162082864	7.328750366	14.87066383	3.410609589	0 838312101	6.212181751	0.132668653	1.948919765	100	98 5161131
Jan 23 14:37 2020	CHA16-1C-114Y-1(76-77cm)_1	204 869-OS	76 89983253	3.138416724	0.103912926	5.462363243	1.011940777	12.59446704	0.043741581	0	0.613460317	0 05206315	0.079801713	100	93.73232376
Jan 23 14:40 2020	CHA16-1C-114Y-1(76-77cm)_2	204 869-OS	76 69932881	3.485299037	0.078985759	5 258788669	0.995057194	12.799248	0.030658946	0 011951792	0.561696033	0 027437158	0.0515486	100	96 21987721
Jan 23 14:44 2020	CHA16-1C-114Y-1(76-77cm)_3	204 869-OS	76 9579881	3.337873129	0.076170022	5.12703047	1.018805797	12.79721039	0.072177663	0	0.571665148	0 019331426	0.021747855	100	95.18180219
Jan 23 14:48 2020	CHA16-1C-114Y-1(76-77cm)_4	204 869-OS	76 84302403	2.78221776	0.054400253	5 834693801	1.141497343	12.56133819	0.01280006	0 009813379	0.646187986	0 058986941	0.055040256	100	93.74956401
Jan 23 14:52 2020	CHA16-1C-114Y-1(76-77cm)_5	204 869-OS	76 97711981	3.513633525	0.086228623	4 997697856	0.985609196	12.64099899	0.093562771	0 009639166	0.590003113	0	0.105506955	100	95.44394514
Jan 23 15:04 2020	CHA16-1C-114Y-1(76-77cm)_8	204 869-OS	77.16574449	3.118996218	0.0730328	5 252502201	0.99042954	12.67423849	0.05723344	0	0.565388569	0 004185261	0.098248995	100	95 57349636
Jan 23 15:08 2020	CHA16-1C-114Y-1(76-77cm)_9	204 869-OS	76.79159749	3.454108276	0.064878017	5 289083053	0.929742091	12.69663533	0.063300755	0	0.567019055	0 021450754	0.122185179	100	95.10155067
Jan 23 15:12 2020	CHA16-1C-114Y-1(76-77cm)_10	204 869-OS	76.78712765	3.565854283	0.092173982	4 992319413	1.009271766	12.74128389	0.070943486	0 021335597	0.607441566	0 017551944	0.094696417	100	95.14615566
Jan 23 15:16 2020	CHA16-1C-114Y-1(76-77cm)_11	204 869-OS	76 97526089	3.528332847	0.077717922	5 083567984	0.982492673	12.57979352	0.009623215	0 02552244	0.603800294	0 051986282	0.081901929	100	95 60214431
Jan 23 15:19 2020	CHA16-1C-114Y-1(76-77cm)_12	204 869-OS	77.12746305	3.328286062	0.073837666	5.117462003	0.941027218	12.73124748	0.047832604	0	0.570285558	0 002715388	0.059842974	100	95.75058881
Jan 23 15:23 2020	CHA16-1C-114Y-1(76-77cm)_13	204 869-OS	76 57926353	3.2666279	0.084226714	5 321787397	1.069859498	12.86123581	0.082236282	0 040541963	0.600356306	0 024723264	0.069141332	100	95.45665057
Jan 23 15:27 2020	CHA16-1C-114Y-1(76-77cm)_14	204 869-OS	76.49432918	2.89990208	0.087675877	5 862475228	1.027352832	12.7791094	0.077225832	0 019123582	0.57943974	0 017033573	0.156332673	100	95 69336811
Jan 23 15:31 2020	CHA16-1C-114Y-1(76-77cm)_15	204 869-OS	76 81515223	2.684499095	0.071371727	6 071923003	0.99430426	12.69845115	0.03110529	0	0.578758988	0	0.054434257	100	93 87470819
Jan 23 15:47 2020	CHA16-1C-114Y-1(76-77cm)_19	204 869-OS	76.71724118	3.491227146	0.067731959	5.161533458	1.072875305	12.72931696	0.030231839	0 036446746	0.582475106	0 012324478	0.098595823	100	94 93302794
Jan 23 15:51 2020	CHA16-1C-114Y-1(76-77cm)_20	204 869-OS	76 67992948	3.131191223	0.071794915	5 593447696	0.96827835	12.79787591	0.002749143	0	0.646565098	0 015754701	0.092413484	100	94 57494353
Jan 23 15:55 2020	CHA16-1C-114Y-1(76-77cm)_21	204 869-OS	76 89642779	3.420355444	0.046963661	5 200673829	0.98557152	12.75698992	0.037087634	0 031834428	0.591105644	0	0.032990133	100	95.17997404
Jan 23 15:58 2020	CHA16-1C-114Y-1(76-77cm)_22	204 869-OS	76 97471298	3.621602374	0.071146941	4 948897545	1.091015844	12.56297465	0.056708297	0 007114694	0.566325586	0 001360162	0.098140928	100	95 57684226
Jan 23 16:02 2020	CHA16-1C-114Y-1(76-77cm)_23	204 869-OS	77 01328015	3.665771259	0.055971686	4 845310101	1.001926298	12.6693067	0.052525668	0 007100885	0.594511669	0	0.094295582	100	95.76270463
Jan 23 16:06 2020	CHA16-1C-114Y-1(76-77cm)_24	204 869-OS	76 88513362	3.451009258	0.041961957	5 008362577	1.118612106	12.74309568	0.013848487	0 02707223	0.594597619	0 040920717	0.075385749	100	96 03937266
Jan 23 16:10 2020	CHA16-1C-114Y-1(76-77cm)_25	204 869-OS	77.14847423	3.462757436	0.046564094	4 979337116	1.095120733	12.58827053	0.037605454	0 006146044	0.563742738	0 016458897	0.055522734	100	95 99671379
Jan 23 16:14 2020	CHA16-1C-114Y-1(76-77cm)_26	204 869-OS	77 22940542	3.486029385	0.065455738	5 008514107	1.007908908	12.36375705	0.085322495	0 004705285	0.608997815	0 025722223	0.114181574	100	95 63714702
Jan 23 16:18 2020	CHA16-1C-114Y-1(76-77cm)_27	204 869-OS	77 05092905	3.245334889	0.083106422	5 314217193	1.022284322	12.47590351	0.081018321	0 051576096	0.581456841	0	0.094173358	100	95.78080487
Jan 23 16:22 2020	CHA16-1C-114Y-1(76-77cm)_28	204 869-OS	76 56997908	3.599203499	0.055892018	5.182524799	1.047256499	12.75168069	0.038686453	0 013451624	0.600552537	0 014702938	0.126069869	100	95 89920343
Jan 23 16:26 2020	CHA16-1C-114Y-1(76-77cm)_29	204 869-OS	76 81413737	3.597972712	0.08697518	4 892353877	1.023793043	12.8440324	0.04432389	0	0.586124494	0 005540486	0.104746551	100	95 65947431
Jan 23 16:30 2020	CHA16-1C-114Y-1(76-77cm)_30	204 869-OS	76 88803735	3.564903149	0.06239796	4 948085319	1.107167638	12.63842114	0.043959832	0	0.593168201	0 037605448	0.116253962	100	95 9967279
Jan 23 16:34 2020	CHA16-1C-114Y-1(76-77cm)_31	204 869-OS	76.78134124	3.148676615	0.066642793	5 537773961	0.926940886	12.80358353	0.030847296	0 00126337	0.622706278	0 011159773	0.069064253	100	94 98401411
Jan 23 16:37 2020	CHA16-1C-114Y-1(76-77cm)_32	204 869-OS	76 93391255	3.307651625	0.063587806	5.154069305	1.0614427	12.67941267	0.031846282	0 039179307	0.574904215	0 043369608	0.110623927	100	95.4585534
Jan 23 16:41 2020	CHA16-1C-114Y-1(76-77cm)_33	204 869-OS	76.76784185	3.470037298	0.063468654	5.14638918	1.01386936	12.75545738	0.050524389	0 038206459	0.626978762	0 004593126	0.06263354	100	95.79532032
Jan 25 20:41 2020	CHA16-1A-115Y-1(94-95cm)_1	204 869-S	76 82721352	3.53373631	0.058369752	5 016643511	1.120251914	12.79656436	0.023873754	0	0.556037615	0	0.067309263	100	95 08349535
Jan 25 20:49 2020	CHA16-1A-115Y-1(94-95cm)_3	204 869-S	76.7095289	3.528074672	0.063985496	5 020721649	1.074092028	12.71072297	0.038934078	0 05406931	0.675031329	0 064820544	0.060019022	100	95 80296093
Jan 25 20:57 2020	CHA16-1A-115Y-1(94-95cm)_5	204 869-S	77 03811151	3.201665119	0.075922222	5 308298194	0.961274194	12.74050189	0.018250534	0	0.560030674	0	0.095945665	100	95 88760492
Jan 25 21:01 2020	CHA16-1A-115Y-1(94-95cm)_6	204 869-S	76.76976187	3.017975897	0.067694876	5.74253747	0.948125247	12.8224351	0	0	0.571738767	0 019281513	0.04044926	100	95.42819753
Jan 25 21:05 2020	CHA16-1A-115Y-1(94-95cm)_7	204 869-S	76 51445911	3.643047171	0.054645708	5 098172334	1.033943521	12.86096163	0.073698426	0	0.614921238	0 030044671	0.076106187	100	95 52442878
Jan 25 21:09 2020	CHA16-1A-115Y-1(94-95cm)_8	204 869-S	76 6957866	3.433049495	0.075130566	5.123487241	1.063683747	12.79901745	0.061774021	0 02880005	0.617427169	0 020869602	0.080974055	100	95 83316536
Jan 25 21:13 2020	CHA16-1A-115Y-1(94-95cm)_9	204 869-S	76 91945951	3.576917454	0.079825049	4 888104205	0.998081576	12.78362737	0.06986003	0 003566428	0.625383632	0 005664327	0.049510412	100	95 33348318
Jan 25 21:17 2020	CHA16-1A-115Y-1(94-95cm)_10	204 869-S	76.46061869	3.396851838	0.062485299	5 325928191	1.035908722	12.88010746	0.077582419	0 00188714	0.659240875	0 031347491	0.068041878	100	95 3824351
Jan 25 21:20 2020	CHA16-1A-115Y-1(94-95cm)_11	204 869-S	76 36237472	3.520065565	0.054581969	5 374385819	1.10261559	12.80883805	0.046410388	0	0.636230898	0 022943284	0.071553714	100	95 4527675
Jan 25 21:24 2020	CHA16-1A-115Y-1(94-95cm)_12	204 869-S	76.40261414	3.604486568	0.065526649	5.198378028	0.969440537	12.92125051	0.090424692	0	0.649328462	0	0.098550413	100	95 99147991

Date Analysed	Core Section Identifier	sample_no	SiO2	Na2O	Cl	K2O	FeOt	Al2O3	MgO	P2O5	CaO	MnO	TiO2	total	Analytical Total
Jan 25 21:28 2020	CHA16-1A-115Y-1(94-95cm)_13	204 869-S	76.48724865	3.345926249	0.058579768	5 576543749	0.960667774	12.7543568	0.080885943	0 027622133	0.589654355	0 019491845	0.099022739	100	95 93755991
Jan 25 21:32 2020	CHA16-1A-115Y-1(94-95cm)_14	204 869-S	76 5264648	3.465587126	0.052088825	5.187878909	1.039361352	12.90181391	0.026674519	0 057759785	0.603117178	0 049043309	0.090210283	100	95 22196039
Jan 25 21:36 2020	CHA16-1A-115Y-1(94-95cm)_15	204 869-S	76 6055364	3.346329763	0.066503009	5 580746155	1.000511944	12.55182398	0.081540314	0 061737666	0.613352594	0 011119134	0.080799038	100	94.43181707
Jan 25 21:40 2020	CHA16-1A-115Y-1(94-95cm)_16	204 869-S	76.49269463	3.331200637	0.062876412	5 558941063	1.009234813	12.7583686	0.067769113	0 039141607	0.550064505	0 037996507	0.091712118	100	96 06146098
Jan 25 21:44 2020	CHA16-1A-115Y-1(94-95cm)_17	204 869-S	76 35758491	3.438495132	0.056228279	5.424252199	1.073864245	12.81931975	0.052570306	0	0.611613177	0 065843524	0.100228475	100	95 68139181
Jan 25 21:48 2020	CHA16-1A-115Y-1(94-95cm)_18	204 869-S	76 61682759	3.323895113	0.069195552	5 362132682	1.071752415	12.75908897	0.056861602	0	0.594224645	0 039614976	0.106406454	100	95 67088889
Jan 25 21:55 2020	CHA16-1A-115Y-1(94-95cm)_20	204 869-S	76 92876589	3.498190307	0.058966501	5.184443719	0.942524497	12.71281719	0.007645745	0	0.586313453	0 014034656	0.066298038	100	95.47793878
Jan 25 21:59 2020	CHA16-1A-115Y-1(94-95cm)_21	204 869-S	76 67490859	3.680732136	0.054895491	4 974246573	1.001280516	12.84739794	0.041960346	0	0.578821419	0 032811098	0.112945895	100	95 08977753
Jan 25 22:07 2020	CHA16-1A-115Y-1(94-95cm)_23	204 869-S	76 93929873	2.980673722	0.075728071	5 634842549	0.985047393	12.67031173	0.052451432	0 015061355	0.602454194	0 034019704	0.010111119	100	94 94497767
Jan 25 22:11 2020	CHA16-1A-115Y-1(94-95cm)_24	204 869-S	77 02251477	3.449241623	0.063710763	5 042010691	0.945908591	12.75142897	0.038606191	0 012024879	0.59048485	0 010970065	0.073098607	100	94 80344833
Jan 25 22:15 2020	CHA16-1A-115Y-1(94-95cm)_25	204 869-S	76 83141427	3.668621418	0.074525424	4 936916251	1.016619048	12.74331538	0.025261079	0 022326182	0.565701423	0 019705738	0.095593792	100	95.40368442
Jan 25 22:19 2020	CHA16-1A-115Y-1(94-95cm)_26	204 869-S	76 64703398	3.674643895	0.070474049	5 069551209	0.999588361	12.79899124	0.097435317	0 014677756	0.585236487	0 005308976	0.037058732	100	96 06373029
Jan 25 22:27 2020	CHA16-1A-115Y-1(94-95cm)_28	204 869-S	76 56332922	3.435399724	0.082323908	5 257837383	1.026802052	12.79535797	0.06462322	0 045979893	0.632825766	0	0.09552087	100	95.47651695
Jan 25 22:31 2020	CHA16-1A-115Y-1(94-95cm)_29	204 869-S	76 65075201	3.525014114	0.072801478	5.125391441	0.979123059	12.86074561	0.055124108	0 035459341	0.582725627	0 012970378	0.099892833	100	95 6024541
Jan 25 22:34 2020	CHA16-1A-115Y-1(94-95cm)_30	204 869-S	76.42689154	3.476805699	0.061577161	5.100013179	1.111015659	13.0405777	0.055189054	0	0.577338248	0 030788581	0.119803184	100	95.48994932
010319	CHA16_1A_115Y-1_94-95cm_4	204 869-S	76 6635	3.8891	0.0772	5 3754	0.9872	12.2132	0.0479	0 0189	0.5908	0 0486	0.0881	100	92 6326
010319	CHA16_1A_115Y-1_94-95cm_20	204 869-S	76.4403	3.8624	0.0725	5 2853	1.0378	12.5209	0.048	0 0433	0.5892	0 0255	0.0749	100	91 9956
010319	CHA16_1A_115Y-1_94-95cm_29	204 869-S	76.1936	3.8401	0.0581	5 3847	1.0412	12.6497	0.0576	0	0.5987	0 0379	0.1385	100	92 2894
050319	CHA16-1C-114Y-1_76-77cm_1	204 869-OS	76 0301	4.0148	0.0632	5 055	0.9087	13.0925	0.0196	0 0405	0.72	0	0.0556	100	95.7258
050319	CHA16-1C-114Y-1_76-77cm_2	204 869-OS	76 5111	3.7829	0.0738	5.1109	1.0528	12.6912	0.0715	0 0028	0.5922	0 0072	0.1036	100	95 2245
050319	CHA16-1C-114Y-1_76-77cm_3	204 869-OS	76 3596	3.4783	0.0714	5 3172	1.0202	12.8726	0.0581	0	0.6499	0 0601	0.1127	100	94.1719
050319	CHA16-1C-114Y-1_76-77cm_4	204 869-OS	76 2768	3.2286	0.0915	5 9565	1.0828	12.5547	0.033	0 0222	0.6195	0 0136	0.1209	100	93 9914
050319	CHA16-1C-114Y-1_76-77cm_5	204 869-OS	76 8501	3.5744	0.0718	5 081	1.0691	12.6652	0.0195	0 0017	0.6111	0	0.0561	100	94.7929
050319	CHA16-1C-114Y-1_76-77cm_6	204 869-OS	76 3597	3.7886	0.0767	5.1655	1.2196	12.6443	0.0493	0 032	0.5648	0	0.0995	100	95 5227
050319	CHA16-1C-114Y-1_76-77cm_7	204 869-OS	76 6971	3.2582	0.0632	5 6055	1.114	12.4373	0.0554	0 0176	0.5692	0 0282	0.1543	100	94 3732
050319	CHA16-1C-114Y-1_76-77cm_8	204 869-OS	76.7931	3.6196	0.0565	5 0582	0.9896	12.643	0.0492	0 0781	0.5803	0	0.1325	100	95 0517
050319	CHA16-1C-114Y-1_76-77cm_10	204 869-OS	76 3411	3.5064	0.0832	5.1329	0.9548	13.1039	0.0629	0	0.6355	0 0658	0.1135	100	93 6338
050319	CHA16-1C-114Y-1_76-77cm_11	204 869-OS	76 2447	3.7682	0.0745	5 0795	1.0308	12.944	0.0187	0 0529	0.6504	0	0.1361	100	94.466
050319	CHA16-1C-114Y-1_76-77cm_12	204 869-OS	76 8448	3.6783	0.0544	5 2516	0.9597	12.5125	0.0577	0	0.5626	0	0.0784	100	94 6963
050319	CHA16-1C-114Y-1_76-77cm_13	204 869-OS	76.7979	3.0539	0.093	5.7174	0.9582	12.6756	0.0368	0	0.6159	0 015	0.0363	100	95.1879
050319	CHA16-1C-114Y-1_76-77cm_14	204 869-OS	76 5428	3.4499	0.083	5 3694	1.0844	12.717	0.0467	0 0091	0.6298	0	0.0678	100	94 8137
050319	CHA16-1C-114Y-1_76-77cm_15	204 869-OS	76 6453	3.6105	0.0746	5 2816	0.9431	12.6343	0.0282	0 0057	0.6445	0 0078	0.1245	100	95.465
050319	CHA16-1C-114Y-1_76-77cm_16	204 869-OS	76.4798	4.0814	0.0629	4 9508	1.0057	12.5885	0.0614	0 0102	0.6561	0 029	0.0741	100	95 2151
050319	CHA16-1C-114Y-1_76-77cm_17	204 869-OS	76 8225	3.5459	0.0689	5 083	1.0652	12.6204	0.039	0 0308	0.654	0 0114	0.0589	100	94.4714
050319	CHA16-1C-114Y-1_76-77cm_18	204 869-OS	76.7691	3.3195	0.0727	5 6193	0.906	12.6373	0.0187	0 0148	0.5656	0	0.0771	100	94 6933
050319	CHA16-1C-114Y-1_76-77cm_19	204 869-OS	76 8453	3.6312	0.0815	5 021	1.0257	12.5631	0.0227	0 0165	0.653	0 0656	0.0744	100	94.7273
050319	CHA16-1C-114Y-1_76-77cm_20	204 869-OS	76 3669	3.6821	0.0792	5 2607	0.9884	12.7631	0.0649	0 0343	0.6425	0 0144	0.1035	100	95 5782
050319	CHA16-1C-114Y-1_76-77cm_21	204 869-OS	76 8051	3.7383	0.0551	4 9064	1.0908	12.5635	0.0625	0	0.6399	0 0146	0.1239	100	94.7375
050319	CHA16-1C-114Y-1_76-77cm_22	204 869-OS	76 6293	3.9059	0.0929	4 8572	1.0398	12.6177	0.0801	0 0005	0.6328	0	0.1439	100	95 3746
050319	CHA16-1C-114Y-1_76-77cm_23	204 869-OS	76 8014	3.7588	0.0796	5 0837	1.0358	12.5172	0.0601	0	0.5859	0 0203	0.0573	100	95.1763
050319	CHA16-1C-114Y-1_76-77cm_24	204 869-OS	76.4684	3.4378	0.1012	5 2058	1.1956	12.7163	0.0661	0	0.6975	0	0.1114	100	94.4065
050319	CHA16-1C-114Y-1_76-77cm_25	204 869-OS	76.4433	3.7019	0.0679	4 86	1.1096	12.9548	0.0729	0 0268	0.6589	0 014	0.09	100	94 9356
050319	CHA16-1C-114Y-1_76-77cm_26	204 869-OS	76 2864	3.5176	0.0694	5.413	1.0963	12.7551	0.0104	0 0187	0.6487	0 0593	0.1251	100	95 0114
050319	CHA16-1C-114Y-1_76-77cm_27	204 869-OS	76.7599	3.6194	0.0738	5.168	1.1058	12.5161	0.0563	0	0.5678	0 0331	0.0998	100	95 5224
050319	CHA16-1C-114Y-1_76-77cm_28	204 869-OS	76 3704	3.848	0.0617	5 0254	1.1053	12.6921	0.039	0	0.6963	0 0401	0.1216	100	94 6594
050319	CHA16-1C-114Y-1_76-77cm_29	204 869-OS	76 8658	3.724	0.0749	4.7639	1.0488	12.7671	0.0413	0 0079	0.6209	0 0373	0.0481	100	95 054
Jan 23 12:55 2020	CHA16-1C-114Y-1(142.5-143.cm)_5	205 524-S	65.76113182	5.114547556	0.080283808	2 290901015	3.496399719	17.50929948	1.095337048	0 310498905	3.720296019	0 097567838	0.52373679	100	97.77812245
Jan 23 13:14 2020	CHA16-1C-114Y-1(142.5-143.cm)_10	205 524-S	68 54921852	5.053392775	0.043978139	3 673591561	1.501325311	16.49383656	0.135922888	0 567727336	3.530099792	0 04786165	0.403045474	100	95 27460912
Jan 23 13:22 2020	CHA16-1C-114Y-1(142.5-143.cm)_12	205 524-S	67.11390076	5.679991227	0.023659664	2 539334644	1.603559792	18.46108185	0.461465432	0.147566957	3.554273758	0 068633422	0.346532495	100	98 05718227
Jan 23 13:30 2020	CHA16-1C-114Y-1(142.5-143.cm)_14	205 524-S	67 38229443	4.240587551	0.039162359	3 277491555	3.632923219	14.94253065	2.481678909	0 32366538	3.170659989	0 097801186	0.411204771	100	95.49986468
Jan 23 13:34 2020	CHA16-1C-114Y-1(142.5-143.cm)_15	205 524-S	66.196511	4.604069885	0.09144016	2 650737209	4.992468706	15.49235479	1.993189995	0 244833596	2.933522698	0.130995734	0.669876225	100	97 33141373
Jan 23 13:38 2020	CHA16-1C-114Y-1(142.5-143.cm)_16	205 524-S	65 98915605	5.217822426	0.070064326	2.451230065	2.569551837	18.49866282	0.45409037	0 230109222	3.97473127	0 072311287	0.472270326	100	97 91002624
Jan 23 13:50 2020	CHA16-1C-114Y-1(142.5-143.cm)_19	205 524-S	65.49513594	4.651246886	0.100067909	2 355787456	3.940007833	17.3397839	1.365507792	0 249798364	3.806220993	0.110573447	0.585869484	100	94 23600565
Jan 23 13:53 2020	CHA16-1C-114Y-1(142.5-143.cm)_20	205 524-S	65 09499759	4.948079213	0.087019891	2 347992319	4.210171049	17.27383168	1.476866572	0 29689745	3.63101016	0 073529233	0.559604836	100	97.10423587
Jan 23 13:57 2020	CHA16-1C-114Y-1(142.5-143.cm)_21	205 524-S	65 57430663	5.257819582	0.049314011	2.450321965	3.827418398	17.07851333	1.41780345	0 261846121	3.458593335	0 081301478	0.542761694	100	97 53820251
Jan 23 14:05 2020	CHA16-1C-114Y-1(142.5-143.cm)_23	205 524-S	65.47400852	4.972468249	0.058158306	1 693733117	3.239769394	18.10676789	1.115619151	0 267936335	4.509852237	0 086217138	0.475469658	100	98 00835698
Jan 23 14:09 2020	CHA16-1C-114Y-1(142.5-143.cm)_24	205 524-S	66 07008848	4.881094988	0.057141138	2 250385999	4.355424541	16.36646721	1.706145182	0 218090403	3.382505256	0 069793077	0.642863724	100	96.42790174
Jan 23 14:32 2020	CHA16-1C-114Y-1(142.5-143.cm)_30	205 524-S	66.4215336	4.730126221	0.109992147	2 827775417	3.954942263	16.53730596	1.180076425	0 274148668	3.137390841	0.147314624	0.679393836	100	96.18868542
Mar 15 00 39 2020	CHA16-1A-118Y-1(94-95cm)_3	209.196-OS	66 82248595	4.738603396	0.09809893	2 529595038	3.501529521	17.20094968	1.083493672	0 219334399	3.249398504	0 087610365	0.468900544	100	97 24876762
Mar 15 00 51 2020	CHA16-1A-118Y-1(94-95cm)_6	209.196-OS	66 33444876	4.936151082	0.098106735	2.491599615	3.280372467	17.59062422	1.071701392	0 202961552	3.467476131	0 08679072	0.439767332	100	96 32366233
Mar 15 00 55 2020	CHA16-1A-118Y-1(94-95cm)_7	209.196-OS	66 91835541	4.742692723	0.092379727	2.459999459	3.311608013	17.1589075	1.098663152	0 217663243	3.46683468	0 065392391	0.467503695	100	96 34148461
Mar 15 00 59 2020	CHA16-1A-118Y-1(94-95cm)_8	209.196-OS	66 56858643	4.988641627	0.104472852	2 539270704	3.486875821	16.93995075	1.192562239	0 207080117	3.326962841	0.12737811	0.518218511	100	96.48439592
Mar 15 01 03 2020	CHA16-1A-118Y-1(94-95cm)_9	209.196-OS	66 25936529	5.103094962	0.124059297	2 602936174	3.348606357	17.23714219	1.126616532	0 240036896	3.369123032	0 089633367	0.4993859	100	95 27701927

Date Analysed	Core Section Identifier	sample_no	SiO2	Na2O	Cl	K2O	FeOt	Al2O3	MgO	P2O5	CaO	MnO	TiO2	total	Analytical Total
Mar 15 01 07 2020	CHA16-1A-118Y-1(94-95cm)_10	209.196-OS	65 89302449	5.209131777	0.162992174	2 559291623	3.792551993	17.04249644	1.207038639	0 280979856	3.27502572	0.107902337	0.469564946	100	92 21301626
Mar 15 01:11 2020	CHA16-1A-118Y-1(94-95cm)_11	209.196-OS	67 01137564	4.714458788	0.114895831	2 541474599	3.389350907	17.0789076	1.094084431	0 228309135	3.250969592	0.123155623	0.453017847	100	94.4333656
Mar 15 01:15 2020	CHA16-1A-118Y-1(94-95cm)_12	209.196-OS	65 91473188	5.05473713	0.141491646	2.455914411	3.959368855	16.97227782	1.164576788	0 254330956	3.48474342	0 097240935	0.500586158	100	90 39402963
Mar 15 01:18 2020	CHA16-1A-118Y-1(94-95cm)_13	209.196-OS	66 82485493	4.934512335	0.105338917	2 625689272	3.385409097	17.10538476	1.062530025	0 238802807	3.165356633	0.115198225	0.436922997	100	96 35565132
Mar 15 01 34 2020	CHA16-1A-118Y-1(94-95cm)_17	209.196-OS	66 64206169	5.012741669	0.072460148	2 618916787	3.249654719	17.24439082	1.00066518	0.196367002	3.384924068	0.124734969	0.453082956	100	96 60482581
Mar 15 01 50 2020	CHA16-1A-118Y-1(94-95cm)_21	209.196-OS	67.48117834	4.755815448	0.1163093	2 879351789	3.830847076	16.06655181	1.290364992	0 290102433	2.662626386	0.116928515	0.509923914	100	96 89680887
Mar 15 02 06 2020	CHA16-1A-118Y-1(94-95cm)_25	209.196-OS	66.71272269	4.940273278	0.122418184	2 832379135	3.417026477	16.97350379	1.150701643	0.196250989	3.129407658	0 0853957	0.43992046	100	94 267041
Mar 15 02:14 2020	CHA16-1A-118Y-1(94-95cm)_27	209.196-OS	67 31907659	4.982065703	0.125641933	2 546231865	3.532106431	16.20474441	1.274600197	0 217160185	3.182789831	0 094335804	0.521247056	100	95 82787938
Mar 15 02 34 2020	CHA16-1A-118Y-1(94-95cm)_32	209.196-OS	67 29398101	4.945490441	0.116944121	2 623746313	2.770600723	17.4193013	0.668031889	0 218681223	3.459061465	0 055580585	0.428580928	100	93 37793018
Mar 15 02 38 2020	CHA16-1A-118Y-1(94-95cm)_33	209.196-OS	66 57688445	4.826232373	0.103777658	2 664985184	3.676298155	16.76300016	1.186297148	0 256361124	3.250236833	0.130845547	0.565081368	100	95 68533494
Mar 15 02 54 2020	CHA16-1A-118Y-1(94-95cm)_37	209.196-OS	67.17027643	5.059051102	0.1960195	2.791006126	3.915993939	15.99064184	1.335786812	0 255409514	2.715281153	0.1179146	0.452618978	100	92.43978278
Jan 25 08:37 2020	CHA16-1B-135Y-1(10-14cm)_1	228 011-OS	75 20385761	4.205375387	0.112527875	2 810575072	1.321609502	14.07955648	0.328879232	0 065230511	1.667468046	0 050233786	0.154686501	100	95 35415108
Jan 25 08:41 2020	CHA16-1B-135Y-1(10-14cm)_2	228 011-OS	75.18620044	4.024050165	0.10017767	2.753297481	1.060746794	14.4355764	0.329972113	0 073915448	1.789643363	0 053159821	0.193260304	100	94.43222238
Jan 25 08:45 2020	CHA16-1B-135Y-1(10-14cm)_3	228 011-OS	75.4910519	4.416678117	0.090866819	3 07295061	1.158096276	13.68284256	0.319520778	0 005396938	1.534272473	0 031390356	0.196933179	100	90.79221746
Jan 25 08:49 2020	CHA16-1B-135Y-1(10-14cm)_4	228 011-OS	75 62879595	4.084556916	0.086420625	2 837692173	1.108688376	13.96595665	0.375026818	0 039018267	1.601576264	0 074059466	0.198208499	100	93 03334678
Jan 25 08:57 2020	CHA16-1B-135Y-1(10-14cm)_6	228 011-OS	75.74830297	4.082638178	0.107553371	2 974179963	1.103236493	13.73106539	0.357011344	0 072982645	1.569401235	0 041814117	0.211814293	100	91.11755286
Jan 25 09:01 2020	CHA16-1B-135Y-1(10-14cm)_7	228 011-OS	75 38461644	4.217247655	0.07845553	2.776442347	1.055486437	14.21233088	0.303620798	0 021138822	1.766826948	0 021664664	0.162169473	100	95 08571295
Jan 25 09:12 2020	CHA16-1B-135Y-1(10-14cm)_10	228 011-OS	75 80802569	3.947092169	0.059965439	2 819351549	1.197667464	13.93995934	0.366407265	0 067339127	1.626548971	0 049447089	0.118195892	100	92 21978723
Jan 25 09:16 2020	CHA16-1B-135Y-1(10-14cm)_11	228 011-OS	75 50934784	4.230215565	0.090315102	2.791942273	1.182341669	14.01103696	0.311449621	0 073499995	1.565179759	0 050974098	0.183697111	100	94 55782898
Jan 25 09:20 2020	CHA16-1B-135Y-1(10-14cm)_12	228 011-OS	75 68097234	4.282631521	0.079625223	2.791641288	1.14171859	13.82245567	0.356251496	0 057630474	1.649606215	0	0.137467185	100	94 56802389
Jan 25 09:36 2020	CHA16-1B-135Y-1(10-14cm)_16	228 011-OS	75.19221557	4.282016832	0.082321774	2 997411782	1.338402829	13.82488804	0.368574599	0 034791387	1.584346228	0 071509681	0.223521279	100	93.41392519
Jan 25 09:40 2020	CHA16-1B-135Y-1(10-14cm)_17	228 011-OS	75 52443587	4.018828222	0.065292773	3 006210087	1.131700768	14.05762766	0.359057514	0 025631897	1.561119624	0 061179012	0.188916571	100	94 80375348
Jan 25 09:44 2020	CHA16-1B-135Y-1(10-14cm)_18	228 011-OS	75 51974071	4.270903102	0.057651893	2.78721468	1.178368422	14.04049578	0.328742963	0 029355835	1.610861716	0 025646614	0.151018286	100	94 35943414
Jan 25 09:48 2020	CHA16-1B-135Y-1(10-14cm)_19	228 011-OS	75.71249633	4.162036375	0.081842627	2 882237076	1.069628428	13.99460905	0.360494727	0 030650655	1.559419314	0 010324431	0.136260984	100	92 98332958
Jan 25 09:59 2020	CHA16-1B-135Y-1(10-14cm)_22	228 011-OS	75.42138204	4.185859593	0.117008873	2.732737351	1.163027514	14.06854429	0.367184471	0	1.659161963	0 05259435	0.232499559	100	92 21522879
Jan 25 10:11 2020	CHA16-1B-135Y-1(10-14cm)_25	228 011-OS	75.40345804	4.212238564	0.142163052	2 884944641	1.229157682	13.9075082	0.401369294	0 036857087	1.557650719	0 046948909	0.177703814	100	91.16292779
Jan 25 10:15 2020	CHA16-1B-135Y-1(10-14cm)_26	228 011-OS	75.77369623	4.26028334	0.100254429	2.755407136	1.143913596	13.78002971	0.350678547	0 052988599	1.589657963	0 016320488	0.176769965	100	94 35992113
Jan 25 10:19 2020	CHA16-1B-135Y-1(10-14cm)_27	228 011-OS	75 60357702	4.191986044	0.076025943	2 861532035	1.158092909	13.95820218	0.35109203	0 018584119	1.573314661	0 057336232	0.15025683	100	94.70451376
Jan 25 10:23 2020	CHA16-1B-135Y-1(10-14cm)_28	228 011-OS	75.75687873	3.856208858	0.092933565	2 916191186	1.16679342	14.0156257	0.377502551	0 034716562	1.559574774	0 037921167	0.18565349	100	93 61526133
Jan 25 10:26 2020	CHA16-1B-135Y-1(10-14cm)_29	228 011-OS	75 55287754	4.145263278	0.08781413	2 96713582	1.192095482	13.83044366	0.386600344	0 046906927	1.614470961	0 027925984	0.148465877	100	91 67089627
Jan 25 10:30 2020	CHA16-1B-135Y-1(10-14cm)_30	228 011-OS	75.14441007	3.924658374	0.098116459	3 050142106	1.248550044	14.04548427	0.503166799	0 0158906	1.685043541	0 046072077	0.238465656	100	93.76612303
Jan 25 10:38 2020	CHA16-1B-135Y-1(10-14cm)_32	228 011-OS	75 30666725	4.249811921	0.065765839	2 847373987	1.157707853	14.23257411	0.324048159	0 067040783	1.583054941	0 008924605	0.15703055	100	94.1218123
01/10/2021	1B-135Y-1-17-19cm	228 071-OS	77 82	3.73	0.07	3 28	1.05	12.39	0.39	0 04	1.02	0 01	0.20	100	
01/10/2021	1B-135Y-1-17-19cm	228 071-OS	77.46	3.85	0.06	3 02	0.85	13.15	0.19	0 07	1.22	0 05	0.09	100	
01/10/2021	1B-135Y-1-17-19cm	228 071-OS	77.17	3.85	0.09	3 04	0.98	12.98	0.37	0 03	1.31	0 04	0.13	100	
01/10/2021	1B-135Y-1-17-19cm	228 071-OS	77 25	3.86	0.07	3.15	0.95	13.03	0.18	0 02	1.32	0 03	0.14	100	
01/10/2021	1B-135Y-1-17-19cm	228 071-OS	77 09	3.86	0.11	3.10	0.83	13.32	0.22	0 04	1.30	0 01	0.12	100	
01/10/2021	1B-135Y-1-17-19cm	228 071-OS	77.13	3.87	0.11	3 04	1.01	12.90	0.26	0 09	1.39	0 06	0.14	100	
01/10/2021	1B-135Y-1-17-19cm	228 071-OS	77.14	3.94	0.06	3.18	0.75	13.21	0.20	0 06	1.28	0 06	0.12	100	
01/10/2021	1B-135Y-1-17-19cm	228 071-OS	77 39	3.96	0.06	3 04	0.80	13.23	0.15	0 03	1.19	0 05	0.09	100	
01/10/2021	1B-135Y-1-17-19cm	228 071-OS	77 28	4.00	0.08	3.11	0.84	13.12	0.23	0 00	1.22	0 00	0.12	100	
01/10/2021	1B-135Y-1-17-19cm	228 071-OS	77 53	4.01	0.08	2 99	0.69	13.10	0.14	0 01	1.32	0 04	0.08	100	
01/10/2021	1B-135Y-1-17-19cm	228 071-OS	77 58	4.02	0.03	2 94	0.82	13.05	0.23	0 01	1.20	0 01	0.10	100	
01/10/2021	1B-135Y-1-17-19cm	228 071-OS	77 22	4.02	0.06	3 04	0.85	13.21	0.15	0 02	1.25	0 03	0.15	100	
01/10/2021	1B-135Y-1-17-19cm	228 071-OS	77.44	4.03	0.09	2 87	0.83	13.09	0.20	0 03	1.26	0 06	0.11	100	
01/10/2021	1B-135Y-1-17-19cm	228 071-OS	77 60	4.04	0.06	3.12	0.85	12.74	0.19	0 02	1.21	0 06	0.11	100	
01/10/2021	1B-135Y-1-17-19cm	228 071-OS	76.41	4.05	0.07	2 97	1.05	13.65	0.20	0 07	1.40	0 00	0.13	100	
01/10/2021	1B-135Y-1-17-19cm	228 071-OS	77 38	4.06	0.08	2 97	0.80	13.15	0.20	0 05	1.20	0 03	0.08	100	
01/10/2021	1B-135Y-1-17-19cm	228 071-OS	77.16	4.06	0.09	3 01	0.88	13.01	0.24	0 03	1.31	0 03	0.18	100	
01/10/2021	1B-135Y-1-17-19cm	228 071-OS	77 22	4.06	0.06	3 22	0.82	13.00	0.22	0 00	1.31	0 05	0.05	100	
01/10/2021	1B-135Y-1-17-19cm	228 071-OS	76 21	4.08	0.08	2.76	1.10	13.68	0.29	0 07	1.51	0 04	0.19	100	
01/10/2021	1B-135Y-1-17-19cm	228 071-OS	77 27	4.09	0.05	3 03	0.83	13.16	0.13	0 05	1.27	0 01	0.12	100	
01/10/2021	1B-135Y-1-17-19cm	228 071-OS	77.49	4.09	0.06	2 91	0.75	13.22	0.20	0 00	1.17	0 01	0.10	100	
01/10/2021	1B-135Y-1-17-19cm	228 071-OS	76 96	4.11	0.07	3 04	0.97	13.12	0.25	0 00	1.25	0 03	0.19	100	
01/10/2021	1B-135Y-1-17-19cm	228 071-OS	77 25	4.11	0.06	3 01	0.81	13.17	0.17	0 07	1.20	0 00	0.15	100	
01/10/2021	1B-135Y-1-17-19cm	228 071-OS	77 35	4.12	0.05	2 96	0.77	13.22	0.17	0 01	1.23	0 00	0.12	100	
01/10/2021	1B-135Y-1-17-19cm	228 071-OS	77 20	4.13	0.07	2 98	0.81	13.10	0.21	0.11	1.23	0 03	0.13	100	
01/10/2021	1B-135Y-1-17-19cm	228 071-OS	76 38	4.21	0.06	2 86	1.07	13.44	0.34	0 08	1.41	0 02	0.14	100	
01/10/2021	1B-135Y-1-17-19cm	228 071-OS	76 93	4.24	0.09	3.10	0.86	13.12	0.15	0 03	1.31	0 02	0.14	100	
040319	CHA16-1A-135Y-1_95-96cm_1	230 208-S	77 0651	3.9114	0.1062	5 2174	0.8807	12.3184	0.041	0	0.366	0 0629	0.0311	100	95.1766
040319	CHA16-1A-135Y-1_95-96cm_2	230 208-S	77 3056	3.6881	0.1131	5 0996	0.8586	12.4507	0.0199	0 0068	0.3752	0 0213	0.0611	100	94 9465
040319	CHA16-1A-135Y-1_95-96cm_3	230 208-S	77 5485	3.7097	0.1014	5.1313	0.8011	12.1762	0.0254	0 0134	0.4304	0 0133	0.0494	100	92 5394
040319	CHA16-1A-135Y-1_95-96cm_5	230 208-S	77 2376	3.7433	0.0951	5 2821	0.7767	12.183	0.065	0	0.4744	0 0283	0.1145	100	93 8364

Date Analysed	Core Section Identifier	sample_no	SiO2	Na2O	Cl	K2O	FeOt	Al2O3	MgO	P2O5	CaO	MnO	TiO2	total	Analytical Total
040319	CHA16-1A-135Y-1_95-96cm_7	230 208-S	77 3771	3.9762	0.0966	5 0136	0.7997	12.2017	0.0086	0 0188	0.3744	0 0982	0.0352	100	94 6942
040319	CHA16-1A-135Y-1_95-96cm_10	230 208-S	77 3244	4.1397	0.0811	4 8432	0.7288	12.3336	0.0333	0 0101	0.3619	0 0809	0.0629	100	96.1656
040319	CHA16-1A-135Y-1_95-96cm_11	230 208-S	77 3638	3.7415	0.0854	5 2359	0.8224	12.1884	0.0503	0	0.3688	0 0725	0.071	100	95 6698
040319	CHA16-1A-135Y-1_95-96cm_12	230 208-S	77 5091	4.1501	0.1037	4 814	0.7281	12.1007	0.0335	0	0.3896	0 0747	0.0963	100	94 8892
040319	CHA16-1A-135Y-1_95-96cm_13	230 208-S	77.449	3.5427	0.068	5 3916	0.6992	12.295	0.0449	0 0284	0.3868	0 0578	0.0366	100	94 6065
040319	CHA16-1A-135Y-1_95-96cm_14	230 208-S	77 397	4.3641	0.074	4.7071	0.8361	12.0883	0.0305	0	0.3865	0 0347	0.0818	100	95.1421
040319	CHA16-1A-135Y-1_95-96cm_15	230 208-S	77 5189	4.0994	0.083	4.7753	0.6982	12.2774	0.0272	0	0.3692	0 0903	0.0611	100	94 9156
040319	CHA16-1A-135Y-1_95-96cm_16	230 208-S	77.4367	3.9303	0.0557	5 2369	0.7359	11.9976	0.0396	0	0.4068	0 0735	0.087	100	93.707
040319	CHA16-1A-135Y-1_95-96cm_17	230 208-S	77.1638	3.8172	0.0814	5.4172	0.8162	12.0986	0.0474	0 0602	0.3691	0 0494	0.0795	100	94 6878
040319	CHA16-1A-135Y-1_95-96cm_18	230 208-S	77 2962	3.4594	0.0867	5.4691	0.9434	12.128	0.0284	0	0.4228	0 0899	0.0761	100	94.1267
040319	CHA16-1A-135Y-1_95-96cm_19	230 208-S	76 9325	3.3057	0.1047	5.7073	0.9189	12.4054	0.0587	0	0.4295	0 0421	0.095	100	92 3301
040319	CHA16-1A-135Y-1_95-96cm_20	230 208-S	77 3825	3.6341	0.1001	5 347	0.7768	12.237	0.0393	0 0074	0.3853	0 0631	0.0274	100	94.4175
040319	CHA16-1A-135Y-1_95-96cm_21	230 208-S	77 2137	3.4954	0.1212	5.4984	0.823	12.2089	0.0382	0	0.3859	0 0868	0.1285	100	94.1601
040319	CHA16-1A-135Y-1_95-96cm_22	230 208-S	77 5234	3.8519	0.0977	4 9005	0.8722	12.2078	0.0173	0	0.3705	0 09	0.0686	100	95 2744
040319	CHA16-1A-135Y-1_95-96cm_23	230 208-S	76 8217	4.1757	0.0796	4 8058	0.8992	12.3405	0.0245	0 0179	0.6354	0 0872	0.1126	100	93.1405
040319	CHA16-1A-135Y-1_95-96cm_25	230 208-S	77.7189	3.9232	0.0976	4 8979	0.8199	12.103	0.0265	0	0.3288	0 0583	0.0259	100	95 3564
040319	CHA16-1A-135Y-1_95-96cm_26	230 208-S	77 6175	3.8791	0.0798	4.7425	0.817	12.268	0.0625	0	0.4425	0 0572	0.0338	100	94 8335
040319	CHA16-1A-135Y-1_95-96cm_27	230 208-S	77 6637	3.8854	0.1144	4 9144	0.7582	12.0195	0.0568	0 0176	0.4243	0 053	0.0927	100	94 6572
040319	CHA16-1A-135Y-1_95-96cm_28	230 208-S	77 5396	3.9768	0.1316	4 8943	0.8494	12.1011	0.0204	0	0.3676	0 0776	0.0416	100	92 0232
01/10/2021	1B-136Y-1-124-127cm	230 23-G	77 56	3.31	0.35	4.11	0.71	12.72	0.17	0 00	0.88	0 07	0.12	100	
01/10/2021	1B-136Y-1-124-127cm	230 23-G	77.43	3.56	0.17	3 83	0.69	13.08	0.15	0 00	0.88	0 08	0.14	100	
01/10/2021	1B-136Y-1-124-127cm	230 23-G	77 34	3.59	0.14	3 94	0.69	13.08	0.13	0 04	0.89	0 07	0.10	100	
01/10/2021	1B-136Y-1-124-127cm	230 23-G	77.75	3.77	0.14	3 68	0.73	12.73	0.13	0 00	0.90	0 07	0.10	100	
01/10/2021	1B-136Y-1-124-127cm	230 23-G	77.17	3.87	0.14	3.75	0.72	13.15	0.13	0 00	0.88	0 04	0.16	100	
01/10/2021	1B-136Y-1-124-127cm	230 23-G	77 54	3.88	0.20	3 54	0.72	12.80	0.15	0 02	0.94	0 08	0.12	100	
01/10/2021	1B-136Y-1-124-127cm	230 23-G	77 06	3.91	0.11	3 87	0.84	12.97	0.17	0 00	0.87	0 05	0.15	100	
01/10/2021	1B-136Y-1-124-127cm	230 23-G	77.47	3.93	0.39	3.41	0.64	12.91	0.09	0 05	0.94	0 06	0.12	100	
01/10/2021	1B-136Y-1-124-127cm	230 23-G	77.17	3.95	0.10	3 54	0.73	13.25	0.13	0 00	0.90	0 06	0.18	100	
01/10/2021	1B-136Y-1-124-127cm	230 23-G	77 24	3.99	0.14	3 57	0.64	13.12	0.09	0 06	0.95	0 09	0.11	100	
01/10/2021	1B-136Y-1-124-127cm	230 23-G	77.43	4.05	0.14	3 38	0.66	13.08	0.17	0 03	0.90	0 06	0.12	100	
01/10/2021	1B-136Y-1-124-127cm	230 23-G	77 35	4.05	0.12	3.42	0.67	13.19	0.14	0 03	0.86	0 06	0.11	100	
01/10/2021	1B-136Y-1-124-127cm	230 23-G	77 55	4.06	0.09	3 55	0.72	12.82	0.14	0 00	0.93	0 05	0.09	100	
01/10/2021	1B-136Y-1-124-127cm	230 23-G	77.78	4.09	0.12	3.46	0.65	12.74	0.12	0 03	0.80	0.10	0.12	100	
01/10/2021	1B-136Y-1-124-127cm	230 23-G	77.15	4.09	0.12	3 63	0.74	13.04	0.12	0 02	0.89	0 08	0.11	100	
01/10/2021	1B-136Y-1-124-127cm	230 23-G	77.44	4.11	0.10	3 30	0.71	13.11	0.17	0 00	0.88	0 07	0.12	100	
01/10/2021	1B-136Y-1-124-127cm	230 23-G	77 65	4.18	0.12	3.42	0.67	12.78	0.13	0 04	0.89	0 01	0.11	100	
01/10/2021	1B-136Y-1-124-127cm	230 23-G	77.47	4.22	0.12	3 20	0.65	13.09	0.14	0 07	0.88	0 03	0.14	100	
01/10/2021	1B-136Y-1-124-127cm	230 23-G	77 65	4.23	0.12	3 64	0.60	12.69	0.08	0 00	0.80	0 08	0.11	100	
01/10/2021	1B-136Y-1-124-127cm	230 23-G	77.45	4.23	0.10	3 32	0.67	12.98	0.13	0 00	0.89	0 09	0.14	100	
01/10/2021	1B-136Y-1-124-127cm	230 23-G	77.12	4.25	0.12	3 28	0.76	13.15	0.19	0 04	0.96	0 03	0.10	100	
01/10/2021	1B-136Y-1-124-127cm	230 23-G	77 32	4.29	0.11	3 25	0.70	13.12	0.13	0 00	0.90	0 07	0.11	100	
01/10/2021	1B-136Y-1-124-127cm	230 23-G	77 39	4.33	0.13	3.17	0.71	13.08	0.12	0 00	0.89	0 08	0.09	100	
01/10/2021	1B-136Y-1-124-127cm	230 23-G	77.43	4.35	0.07	3 32	0.69	12.90	0.13	0 00	0.91	0 08	0.11	100	
01/10/2021	1B-136Y-1-124-127cm	230 23-G	77 38	4.36	0.09	3 34	0.63	12.98	0.12	0 03	0.87	0 05	0.15	100	
01/10/2021	1B-136Y-1-124-127cm	230 23-G	77 34	4.40	0.11	3 22	0.62	13.12	0.13	0 02	0.90	0 04	0.09	100	
01/10/2021	1B-136Y-1-124-127cm	230 23-G	77.42	4.42	0.12	3.18	0.66	12.95	0.16	0 02	0.89	0 07	0.13	100	
01/10/2021	1B-136Y-1-124-127cm	230 23-G	77.41	4.43	0.11	3.13	0.67	13.05	0.14	0 00	0.88	0 06	0.12	100	
01/10/2021	1B-136Y-1-124-127cm	230 23-G	77 35	4.47	0.13	3 33	0.67	12.85	0.15	0 00	0.87	0 04	0.14	100	
01/10/2021	1B-136Y-1-124-127cm	230 23-G	77.45	4.49	0.10	3.16	0.69	12.92	0.16	0 03	0.88	0 07	0.06	100	
01/10/2021	1C-130Y-1-70-71cm	230 23-G	77.42	3.67	0.11	4.11	0.67	12.87	0.12	0 01	0.84	0 05	0.14	100	
01/10/2021	1C-130Y-1-70-71cm	230 23-G	77 61	3.70	0.16	3.42	0.68	13.18	0.14	0 00	0.94	0 05	0.12	100	
01/10/2021	1C-130Y-1-70-71cm	230 23-G	77.47	3.78	0.18	3 58	0.75	13.04	0.16	0 00	0.92	0 00	0.12	100	
01/10/2021	1C-130Y-1-70-71cm	230 23-G	77 56	3.79	0.18	3.40	0.71	13.13	0.17	0 00	0.90	0 01	0.15	100	
01/10/2021	1C-130Y-1-70-71cm	230 23-G	77.45	3.79	0.12	3.73	0.64	13.04	0.16	0 04	0.87	0 05	0.11	100	
01/10/2021	1C-130Y-1-70-71cm	230 23-G	77 50	3.85	0.13	3 62	0.66	13.01	0.17	0 04	0.85	0 05	0.11	100	
01/10/2021	1C-130Y-1-70-71cm	230 23-G	77.45	3.88	0.14	3 62	0.69	13.05	0.12	0 02	0.91	0 02	0.11	100	
01/10/2021	1C-130Y-1-70-71cm	230 23-G	77 34	3.89	0.14	3 81	0.78	12.76	0.12	0 08	0.90	0 07	0.11	100	
01/10/2021	1C-130Y-1-70-71cm	230 23-G	77 27	3.93	0.09	3 50	0.64	13.28	0.07	0 08	0.93	0.10	0.13	100	
01/10/2021	1C-130Y-1-70-71cm	230 23-G	77 57	3.95	0.15	3.75	0.56	12.87	0.14	0 00	0.86	0 04	0.11	100	
01/10/2021	1C-130Y-1-70-71cm	230 23-G	77 22	3.95	0.11	3 88	0.64	12.96	0.15	0 05	0.90	0 07	0.07	100	
01/10/2021	1C-130Y-1-70-71cm	230 23-G	77 06	3.95	0.13	3.76	0.71	13.23	0.07	0 02	0.92	0 06	0.09	100	
01/10/2021	1C-130Y-1-70-71cm	230 23-G	77 09	4.02	0.12	3 58	0.83	13.13	0.15	0 02	0.91	0 04	0.11	100	
01/10/2021	1C-130Y-1-70-71cm	230 23-G	77 67	4.03	0.12	3.40	0.68	12.89	0.09	0 06	0.85	0.10	0.11	100	

Date Analysed	Core Section Identifier	sample_no	SiO2	Na2O	Cl	K2O	FeOt	Al2O3	MgO	P2O5	CaO	MnO	TiO2	total	Analytical Total
01/10/2021	1C-130Y-1-70-71cm	230 23-G	77.11	4.05	0.13	3.48	0.75	13.19	0.13	0 02	0.89	0 09	0.14	100	
01/10/2021	1C-130Y-1-70-71cm	230 23-G	77 39	4.05	0.09	3 59	0.66	12.93	0.11	0 03	0.93	0 06	0.15	100	
01/10/2021	1C-130Y-1-70-71cm	230 23-G	77 32	4.05	0.12	3 65	0.67	12.96	0.14	0 01	0.92	0 05	0.11	100	
01/10/2021	1C-130Y-1-70-71cm	230 23-G	77 25	4.08	0.12	3 52	0.68	13.24	0.10	0 03	0.88	0 02	0.09	100	
01/10/2021	1C-130Y-1-70-71cm	230 23-G	77.45	4.14	0.09	3 37	0.68	13.04	0.18	0 00	0.87	0 08	0.11	100	
01/10/2021	1C-130Y-1-70-71cm	230 23-G	77 39	4.15	0.11	3 32	0.75	13.04	0.13	0 04	0.93	0 06	0.07	100	
01/10/2021	1C-130Y-1-70-71cm	230 23-G	77 32	4.18	0.10	3.48	0.71	13.05	0.14	0 01	0.84	0 06	0.13	100	
01/10/2021	1C-130Y-1-70-71cm	230 23-G	77 36	4.20	0.11	3 20	0.77	13.18	0.09	0 00	0.91	0 09	0.10	100	
01/10/2021	1C-130Y-1-70-71cm	230 23-G	77 52	4.24	0.10	3 30	0.70	12.93	0.13	0 07	0.83	0 09	0.10	100	
01/10/2021	1C-130Y-1-70-71cm	230 23-G	77 30	4.25	0.11	3 30	0.68	13.14	0.09	0 05	0.88	0 08	0.12	100	
01/10/2021	1C-130Y-1-70-71cm	230 23-G	77 28	4.28	0.13	3.12	0.75	13.09	0.12	0 05	0.96	0 08	0.14	100	
01/10/2021	1C-130Y-1-70-71cm	230 23-G	77 23	4.29	0.12	3 23	0.75	13.16	0.11	0 02	0.93	0 08	0.08	100	
01/10/2021	1C-130Y-1-70-71cm	230 23-G	77 63	4.32	0.13	3 38	0.64	12.84	0.11	0 01	0.78	0 07	0.08	100	
01/10/2021	1C-130Y-1-70-71cm	230 23-G	77.40	4.34	0.12	3.18	0.68	13.08	0.16	0 00	0.89	0 05	0.11	100	
01/10/2021	1C-130Y-1-70-71cm	230 23-G	77 08	4.44	0.10	3.19	0.69	13.23	0.14	0 02	0.91	0 07	0.13	100	
290419	MEXI-CHA16-1C-130Y-1-70-71cm_9	230 23-G	77 2152	4.3901	0.1597	3.4866	0.6186	12.9931	0.124	0	0.9423	0 0257	0.0447	100	93 3564
290419	MEXI-CHA16-1C-130Y-1-70-71cm_10	230 23-G	77 369	4.6989	0.1099	3 2456	0.6511	12.8679	0.0909	0 0034	0.8424	0 0171	0.1038	100	95.4597
290419	MEXI-CHA16-1C-130Y-1-70-71cm_13	230 23-G	77 5301	4.2595	0.1124	3 5678	0.6601	12.7083	0.1393	0 0364	0.8731	0	0.113	100	93 0395
290419	MEXI-CHA16-1C-130Y-1-70-71cm_14	230 23-G	77 3263	4.2353	0.1267	3 5117	0.8486	12.7802	0.1277	0 0121	0.8626	0 0471	0.1217	100	93 351
290419	MEXI-CHA16-1C-130Y-1-70-71cm_18	230 23-G	77.4618	4.2128	0.1785	3.4105	0.8056	12.7069	0.1517	0	0.8839	0 0604	0.1279	100	92 6073
01/10/2021	1C-130Y-1-122-123cm	230.407-S	55.77	4.90	0.00	0.42	0.89	27.30	0.06	0 03	10.49	0 05	0.09	100	
01/10/2021	1C-130Y-1-122-123cm	230.407-S	54 58	4.97	0.01	0 30	0.59	28.06	0.10	0 01	11.31	0 01	0.07	100	
01/10/2021	1C-130Y-1-122-123cm	230.407-S	54 83	5.01	0.01	0 25	0.71	28.03	0.14	0 01	10.92	0 00	0.09	100	
01/10/2021	1C-130Y-1-122-123cm	230.407-S	56.13	5.36	0.01	0 35	0.56	27.23	0.05	0 02	10.20	0 00	0.08	100	
01/10/2021	1C-130Y-1-122-123cm	230.407-S	55.48	5.41	0.01	0 34	0.63	27.44	0.05	0 00	10.55	0 00	0.09	100	
01/10/2021	1C-130Y-1-122-123cm	230.407-S	56 03	5.58	0.01	0.40	0.93	26.78	0.16	0 02	9.92	0 00	0.17	100	
01/10/2021	1C-130Y-1-122-123cm	230.407-S	56 23	5.62	0.02	0 32	0.78	26.78	0.08	0 02	10.03	0 02	0.11	100	
01/10/2021	1C-130Y-1-122-123cm	230.407-S	56 39	5.63	0.01	0 38	0.67	26.87	0.08	0 01	9.86	0 01	0.09	100	
01/10/2021	1C-130Y-1-122-123cm	230.407-S	56.18	5.89	0.00	0 32	0.72	26.61	0.02	0 05	10.09	0 02	0.09	100	
Mar 14 18 54 2020	CHA16-1C-130Y-1(122-123cm)_1	230 638-S	75 57742278	4.282512293	0.110083279	2 881872163	1.164369235	13.9848817	0.258822282	0 017164092	1.434261157	0 066537343	0.222073678	100	94 38309009
Mar 14 18 58 2020	CHA16-1C-130Y-1(122-123cm)_2	230 638-S	76 09798526	3.971947745	0.057311532	2 980617973	1.276170678	13.79402306	0.259054101	0 035558249	1.324126461	0 015478297	0.187726641	100	95 61775532
Mar 14 19 02 2020	CHA16-1C-130Y-1(122-123cm)_3	230 638-S	75 39597455	4.185955394	0.054009763	3.132358104	1.156623907	14.06321399	0.112781129	0 025808133	1.665040853	0 007596749	0.200637423	100	96 09373834
Mar 14 19 06 2020	CHA16-1C-130Y-1(122-123cm)_4	230 638-S	76 86054153	3.826563811	0.078073891	2 989174414	1.050276974	13.49763141	0.221336646	0	1.274893339	0 003240014	0.198267967	100	95 67859228
Mar 14 19:10 2020	CHA16-1C-130Y-1(122-123cm)_5	230 638-S	75 9779014	4.227126215	0.065723457	2 948730156	1.204002562	13.68429554	0.276648791	0 003322513	1.3903678	0 037689755	0.184191806	100	96 31264476
Mar 14 19:14 2020	CHA16-1C-130Y-1(122-123cm)_6	230 638-S	76 21560887	4.003529879	0.063344773	2 915537579	1.201128676	13.60582106	0.269198715	0 039747796	1.436374197	0 065756909	0.183951544	100	95 35119768
Mar 14 19:18 2020	CHA16-1C-130Y-1(122-123cm)_7	230 638-S	75.71284966	3.972803887	0.10402608	2 876851645	1.521241945	13.83621306	0.214133514	0 053708523	1.423658713	0 020236409	0.264276562	100	91.41938217
Mar 14 19 26 2020	CHA16-1C-130Y-1(122-123cm)_9	230 638-S	75 92837474	3.856661728	0.088136182	2 941412327	1.444193697	13.76568764	0.319741536	0 005521785	1.417612078	0 026865607	0.205792675	100	94.17244819
Mar 14 19 30 2020	CHA16-1C-130Y-1(122-123cm)_10	230 638-S	75 99758782	4.02780374	0.059601969	3 047474568	1.377951009	13.61056625	0.233378375	0 059498313	1.333943885	0 037937949	0.21425612	100	96.47332354
Mar 14 19 34 2020	CHA16-1C-130Y-1(122-123cm)_11	230 638-S	75.40658811	4.294045087	0.11443838	2 89298516	1.319668826	13.85979188	0.199909792	0.119882743	1.526556745	0 066613385	0.199519899	100	93 67486696
Mar 14 19 38 2020	CHA16-1C-130Y-1(122-123cm)_12	230 638-S	74.19669981	4.291726527	0.093827578	2 805154401	1.604599987	14.6616452	0.296864154	0 067603146	1.655148574	0 043850689	0.282879938	100	93 04300679
Mar 14 19:42 2020	CHA16-1C-130Y-1(122-123cm)_13	230 638-S	75 04956026	4.051679963	0.084885302	2 819030395	1.768190643	14.10028539	0.270838231	0 041709074	1.5195517	0 027666321	0.266602726	100	95.4228803
Mar 14 19:46 2020	CHA16-1C-130Y-1(122-123cm)_14	230 638-S	76 81786624	3.940342192	0.054124994	3 034754009	1.00552716	13.4782415	0.244269533	0 030973263	1.17938258	0 054124994	0.160393528	100	95 8891558
Mar 14 19:49 2020	CHA16-1C-130Y-1(122-123cm)_15	230 638-S	76 0329481	4.221319919	0.079023008	2 906955281	1.249456511	13.4394029	0.306466878	0 040088697	1.479713699	0 045545798	0.199079212	100	95 28870353
Mar 14 19 53 2020	CHA16-1C-130Y-1(122-123cm)_16	230 638-S	75 92538098	4.21358973	0.081078092	2 922582402	1.381815109	13.54863138	0.267859226	0	1.418342857	0 006075619	0.234644609	100	95.46351878
Mar 14 20 01 2020	CHA16-1C-130Y-1(122-123cm)_18	230 638-S	74 64091739	4.230864615	0.066971942	2 819871262	1.632596133	14.36668158	0.308722844	0 045822908	1.606911932	0 038980573	0.24165882	100	96.4583042
Mar 14 20 05 2020	CHA16-1C-130Y-1(122-123cm)_19	230 638-S	76.40104477	3.881490029	0.070806083	3 094488063	1.189264646	13.48501755	0.302951784	0	1.332622927	0 030315493	0.211998657	100	95 33079269
Mar 14 20 09 2020	CHA16-1C-130Y-1(122-123cm)_20	230 638-S	74.40131324	4.307070269	0.054151039	2.738913574	1.656938543	14.52791943	0.300383344	0 009199404	1.72488832	0 049446799	0.229776032	100	95 65836704
Mar 14 20:13 2020	CHA16-1C-130Y-1(122-123cm)_21	230 638-S	75 05851503	4.11506585	0.140136387	2 975203285	1.477100436	14.12260097	0.286802292	0 037190041	1.541500253	0 066942074	0.178943386	100	92.7667704
Mar 14 20 21 2020	CHA16-1C-130Y-1(122-123cm)_23	230 638-S	76.1488337	3.941612175	0.071146712	3 067028326	1.254407125	13.63637933	0.254024412	0 048404801	1.365349208	0 054559722	0.158254489	100	95 85826043
Mar 14 20 29 2020	CHA16-1C-130Y-1(122-123cm)_25	230 638-S	75 87188519	4.295366328	0.06389815	2 880654299	1.403225311	13.7029313	0.215696738	0 032682332	1.30467452	0 041795675	0.187190154	100	95.46442283
Mar 14 20 33 2020	CHA16-1C-130Y-1(122-123cm)_26	230 638-S	76 3328565	4.008960683	0.082951299	2 999485861	1.196954942	13.50985781	0.228731289	0 057610815	1.334874639	0 01127393	0.23644223	100	96 68323621
Mar 14 20 37 2020	CHA16-1C-130Y-1(122-123cm)_27	230 638-S	74 6687936	4.512739913	0.07554099	2 806702547	1.504391554	14.28473544	0.296446036	0 030571147	1.56507577	0 024206505	0.230796507	100	95 84200516
Mar 14 20:41 2020	CHA16-1C-130Y-1(122-123cm)_28	230 638-S	75 01032083	4.185660484	0.08312943	2 833720181	1.475585652	14.17192726	0.286166847	0 098709662	1.599849401	0 047158959	0.207771291	100	95 63400149
Mar 14 20:45 2020	CHA16-1C-130Y-1(122-123cm)_29	230 638-S	76 38912782	4.042656506	0.06158777	2 917315438	1.16568989	13.70919623	0.21561633	0 010560891	1.346670449	0 001568449	0.140010228	100	95 63587
Mar 14 20 57 2020	CHA16-1C-130Y-1(122-123cm)_32	230 638-S	76 52013055	3.842341607	0.135025729	3.131031391	1.169633018	13.45233396	0.249761452	0	1.273612248	0 069904624	0.15622542	100	91 98246969
Mar 14 21 01 2020	CHA16-1C-130Y-1(122-123cm)_33	230 638-S	74 83636163	4.25677692	0.084153628	2 82613306	1.697442523	14.04288081	0.309371435	0 027630966	1.607428841	0 044965983	0.2668542	100	95.18306262
Mar 14 21 05 2020	CHA16-1C-130Y-1(122-123cm)_34	230 638-S	76.43325428	3.993918633	0.056392163	2 992237211	1.166149283	13.62457114	0.204402227	0 001360108	1.298275229	0 029085383	0.200354345	100	95 58065748
Mar 14 21 09 2020	CHA16-1C-130Y-1(122-123cm)_35	230 638-S	75 68730474	4.227841926	0.063242279	3 021921691	1.303601231	13.64578739	0.263109257	0 047353824	1.474614709	0 030738447	0.234484508	100	96 29634045
Mar 14 21:13 2020	CHA16-1C-130Y-1(122-123cm)_36	230 638-S	76 9375149	4.137944783	0.089603871	3.102481438	1.011125557	13.16841728	0.213271204	0	1.154754108	0 003786079	0.181100781	100	95 08517808
29/09/2021	1B-137Y-1-44-46cm	231 048-S	76.18593094	3.478836788	0.131211433	2 953096181	1.138619925	14.06076477	0.292194017	0 047764094	1.589207343	0 023154959	0.099219557	100	
29/09/2021	1B-137Y-1-44-46cm	231 048-S	76 69008856	3.527043884	0.101591847	2 888713856	0.889550761	13.6321328	0.313364472	0 036135971	1.72922969	0 056800553	0.135347604	100	
29/09/2021	1B-137Y-1-44-46cm	231 048-S	76 00637508	3.590795011	0.350374543	3.124457996	1.170039569	13.52377342	0.269378283	0 092334729	1.662464275	0 095909979	0.114097123	100	
29/09/2021	1B-137Y-1-44-46cm	231 048-S	76.12096147	3.628408223	0.079738073	3.12868733	1.175539083	13.73146106	0.316751688	0 014231182	1.607701218	0	0.196520673	100	

Date Analysed	Core Section Identifier	sample_no	SiO2	Na2O	Cl	K2O	FeOt	Al2O3	MgO	P2O5	CaO	MnO	TiO2	total	Analytical Total
29/09/2021	1B-137Y-1-44-46cm	231 048-S	76 03848565	3.643043676	0.078357774	2 920901882	0.989226475	13.9685935	0.289778861	0 061220379	1.807760967	0	0.202630832	100	
29/09/2021	1B-137Y-1-44-46cm	231 048-S	76 69915576	3.694676231	0.100099949	3.114697986	0.972107982	13.67245012	0.23558173	0 053916496	1.284931317	0 005799782	0.166582641	100	
29/09/2021	1B-137Y-1-44-46cm	231 048-S	76.77892933	3.696795134	0.079672309	2 804465274	0.960316897	13.73550606	0.267531078	0 044722723	1.467298865	0 046847318	0.117915017	100	
29/09/2021	1B-137Y-1-44-46cm	231 048-S	76 34298977	3.747530152	0.083829367	2 940369811	0.969976112	13.67560234	0.269602613	0 028596538	1.69508878	0 052119496	0.194295025	100	
29/09/2021	1B-137Y-1-44-46cm	231 048-S	75 63045954	3.747642178	0.052926312	3.444907852	0.500137985	14.22851334	0.31628913	0 041025721	1.740583171	0 04645406	0.251060709	100	
29/09/2021	1B-137Y-1-44-46cm	231 048-S	76.19395852	3.749414839	0.146078119	2.786262404	0.937812354	13.86251542	0.33782646	0 042768555	1.708193616	0 062375586	0.172794133	100	
29/09/2021	1B-137Y-1-44-46cm	231 048-S	76.10795222	3.820930028	0.090341441	2 690353472	0.966852322	13.99611903	0.357486679	0 094842811	1.662824835	0 053807069	0.158490084	100	
29/09/2021	1B-137Y-1-44-46cm	231 048-S	76 32878769	3.831211523	0.21215008	2 945080966	0.972267659	13.65683563	0.317430029	0 02358671	1.549888374	0 052125327	0.110636006	100	
29/09/2021	1B-137Y-1-44-46cm	231 048-S	75 91188798	3.833340346	0.0829855	2 906598724	1.090501079	14.02749819	0.307705158	0	1.652028467	0 051813282	0.135641274	100	
29/09/2021	1B-137Y-1-44-46cm	231 048-S	75 84491968	3.835612282	0.091424183	2 973913084	1.070503625	13.93430654	0.294625206	0 04129851	1.679582174	0 044661239	0.189153482	100	
29/09/2021	1B-137Y-1-44-46cm	231 048-S	76 59564922	3.842455467	0.122312396	2 988576474	0.988538018	13.54667483	0.259798426	0 024116312	1.475642084	0 040732336	0.115504442	100	
29/09/2021	1B-137Y-1-44-46cm	231 048-S	76.47540938	3.907814555	0.114778706	2 904168194	0.994784377	13.58125714	0.291301732	0 030856787	1.537977998	0 044203148	0.117447978	100	
29/09/2021	1B-137Y-1-44-46cm	231 048-S	75 89546707	3.912910205	0.150459272	3.113368182	1.009482376	13.64067149	0.277072445	0 020594264	1.72109268	0 039734816	0.2191472	100	
29/09/2021	1B-137Y-1-44-46cm	231 048-S	75 56390894	4.018914891	0.070357381	2.763663259	1.092912787	14.22970128	0.384614068	0 092403398	1.561059651	0 042509782	0.179954562	100	
29/09/2021	1B-137Y-1-44-46cm	231 048-S	75 92337266	4.067361532	0.091779065	2 834508425	0.958464262	13.79320271	0.317436184	0 086615834	1.684165989	0 033508315	0.209585028	100	
29/09/2021	1B-137Y-1-44-46cm	231 048-S	75 898659	4.124064393	0.094654099	2 885795695	1.061867878	13.80984413	0.303941064	0 057506038	1.594402674	0 039036945	0.130228089	100	
29/09/2021	1B-137Y-1-44-46cm	231 048-S	75 61007686	4.138120674	0.081589235	2 879620056	0.978430904	14.01415094	0.343024895	0 055566002	1.630975847	0 052686382	0.215758199	100	
29/09/2021	1B-137Y-1-44-46cm	231 048-S	75 60041126	4.142880214	0.093267919	2 836279531	1.046449051	13.96894226	0.27098904	0.11164531	1.687361172	0 08583198	0.15594226	100	
29/09/2021	1B-137Y-1-44-46cm	231 048-S	75 53222332	4.187562639	0.104478636	2 882894882	1.051625341	14.01465687	0.32275177	0 06712726	1.608993718	0 035667933	0.192017634	100	
Jan 17 05:21 2020	CHA16-1B-138Y-1_12-13 5cm_1	232.159-S	77 85245302	4.093306957	0.093424959	3 036822813	0.654837873	12.85494864	0.114209627	0 032131399	1.121629733	0 001590663	0.144644318	100	94 3002819
Jan 17 05:25 2020	CHA16-1B-138Y-1_12-13 5cm_2	232.159-S	77 64389881	4.282226024	0.092588671	2 838834406	0.645862177	13.02853341	0.075964796	0 032511249	1.227220746	0 034299894	0.09805982	100	95 04402563
Jan 17 05:28 2020	CHA16-1B-138Y-1_12-13 5cm_3	232.159-S	77.44698073	4.339159579	0.072143794	2 882702601	0.538880586	13.14318523	0.129437552	0 033912849	1.247719018	0	0.165878066	100	94 94926206
Jan 17 05:32 2020	CHA16-1B-138Y-1_12-13 5cm_4	232.159-S	77 20992115	4.161852627	0.055386271	2 958519718	0.647387455	13.24733094	0.153021652	0	1.383500706	0 031213895	0.151865582	100	95.14993334
Jan 17 05:36 2020	CHA16-1B-138Y-1_12-13 5cm_5	232.159-S	77.70521368	3.805760934	0.056719467	3.48236566	0.650291703	12.68896246	0.172989133	0	1.185552194	0 090164033	0.161980734	100	95 38171375
Jan 17 05:52 2020	CHA16-1B-138Y-1_12-13 5cm_9	232.159-S	78 3916842	4.174079421	0	2 500515132	0.570563011	12.42721414	0.226592883	0	1.526116205	0 0587201	0.124514912	100	98 94397262
Jan 17 05:56 2020	CHA16-1B-138Y-1_12-13 5cm_10	232.159-S	75 52822967	4.215793546	0.01819767	2.166461992	3.320391558	12.20658801	0.293487978	0	1.637790298	0 028509683	0.584549599	100	98 91376214
Jan 17 06:00 2020	CHA16-1B-138Y-1_12-13 5cm_11	232.159-S	76 52431708	3.965807469	0.062722376	3.151336919	0.655070143	13.77932122	0.112816786	0	1.565450317	0 054268944	0.128888743	100	95 81907417
Jan 17 06:04 2020	CHA16-1B-138Y-1_12-13 5cm_12	232.159-S	76.76239069	4.096043552	0.064290993	3 26997983	0.732620379	13.25573563	0.188122413	0 007706474	1.446283419	0 047927932	0.12889869	100	94.72555531
Jan 17 06:08 2020	CHA16-1B-138Y-1_12-13 5cm_13	232.159-S	78.71029546	3.713715187	0.041857976	3.198414775	0.741901015	12.30198822	0.111516363	0 025387544	0.939234239	0 062419789	0.153269432	100	95 32233415
Jan 17 06:16 2020	CHA16-1B-138Y-1_12-13 5cm_15	232.159-S	77 21165548	4.032467308	0.054643617	3 250996165	0.680776264	13.06792842	0.078859478	0 041693396	1.413785144	0 017688107	0.149506621	100	94 97907131
Jan 17 06:20 2020	CHA16-1B-138Y-1_12-13 5cm_16	232.159-S	75 99358619	4.369154747	0.056548151	2.799876998	0.678618267	14.01254719	0.132851571	0 028744439	1.756023917	0 024981531	0.147067003	100	95 67067871
Jan 17 06:28 2020	CHA16-1B-138Y-1_12-13 5cm_18	232.159-S	76.18099917	4.0538409	0.037265777	3 095188372	0.845336336	13.69394067	0.26254954	0 017735554	1.646872866	0 006545264	0.159725554	100	94.72498044
Jan 17 06:39 2020	CHA16-1B-138Y-1_12-13 5cm_20	232.159-S	76 39641023	4.332368199	0.047195605	2 986604756	0.53235216	13.85711518	0.084763726	0 029719627	1.62202191	0	0.111448602	100	95 55974492
Jan 17 06:43 2020	CHA16-1B-138Y-1_12-13 5cm_21	232.159-S	76 56136522	4.413921626	0.041832654	2.787984035	0.515231985	13.85286708	0.056825309	0	1.625078033	0 029251405	0.11564265	100	95 38003518
Jan 17 03:38 2020	CHA16-1B-138Y-1_15.5-17cm_2	232.194-S	76.75119551	4.180784017	0.046775108	2 953446451	0.910934779	13.34370778	0.279615802	0 005174238	1.361962833	0 02504331	0.141360172	100	96 63259293
Jan 17 03:46 2020	CHA16-1B-138Y-1_15.5-17cm_4	232.194-S	75.4713274	4.883425599	0.060373152	2 538936673	0.592514706	14.40815316	0.059651971	0	1.792649903	0 030289602	0.162677827	100	97 06301252
Jan 17 03:58 2020	CHA16-1B-138Y-1_15.5-17cm_7	232.194-S	73 57114064	4.742264891	0.070976248	2 990730173	1.379248361	15.06041243	0.365396242	0 00452145	1.493129966	0 064351799	0.257827794	100	95.10223708
Jan 17 04:06 2020	CHA16-1B-138Y-1_15.5-17cm_9	232.194-S	73.79786567	4.761567779	0.134838942	3.162304331	1.352691232	14.75819191	0.383414424	0	1.397736578	0 072938561	0.178450574	100	92.40653927
Jan 17 04:10 2020	CHA16-1B-138Y-1_15.5-17cm_10	232.194-S	73 31222532	5.088652219	0.104540931	3 038278691	1.321378747	15.01131668	0.371109658	0	1.471131486	0 038431035	0.242935238	100	93 93449964
Jan 17 04:25 2020	CHA16-1B-138Y-1_15.5-17cm_13	232.194-S	73 57252689	4.998027318	0.134724838	3 077469709	1.25354573	14.85903939	0.380399542	0	1.4674969	0 059490262	0.197279429	100	94 63733788
29/09/2021	1B-138Y-1-16-17cm	232.194-S	77 61574251	3.528460418	0.115666691	4.770729026	0.893911437	12.41224685	0.02967238	0 034345073	0.514250262	0 019103795	0.065871554	100	
29/09/2021	1B-138Y-1-16-17cm	232.194-S	74 35250561	3.882503377	0.108249459	3 345094717	1.209388834	15.00357237	0.352634832	0 093114276	1.355826309	0 058347226	0.23876299	100	
29/09/2021	1B-138Y-1-16-17cm	232.194-S	74.11964627	4.129449918	0.134097297	3 294773871	1.341302443	14.90336048	0.325482552	0 074901193	1.43602818	0 054253943	0.186703853	100	
29/09/2021	1B-138Y-1-16-17cm	232.194-S	74 56125888	4.142918972	0.113211385	3 216353547	1.252567353	14.76114575	0.297186107	0 047925798	1.357259542	0 066031099	0.184141566	100	
29/09/2021	1B-138Y-1-16-17cm	232.194-S	74 01569079	4.194418093	0.120254859	3.112347468	1.212030654	15.14898875	0.347196006	0 027107542	1.539735041	0 048525848	0.233704944	100	
29/09/2021	1B-138Y-1-16-17cm	232.194-S	74 0512431	4.222231287	0.218776925	3 254636617	1.34256902	14.67728019	0.360764141	0.102414241	1.489356363	0 033551659	0.247176457	100	
29/09/2021	1B-138Y-1-16-17cm	232.194-S	74.46693771	4.322465557	0.070132004	2 97169507	1.191811816	14.86928151	0.312327711	0 047222936	1.400167201	0 092392701	0.255565776	100	
29/09/2021	1B-138Y-1-16-17cm	232.194-S	74 29737691	4.340710757	0.119662837	3 263531921	1.165059565	14.83520556	0.304448755	0 037008025	1.311815638	0 080095179	0.245084848	100	
29/09/2021	1B-138Y-1-16-17cm	232.194-S	75 68747888	4.353148425	0.106305146	3 322693001	1.01026691	14.0899007	0.231599947	0 025971683	0.920384027	0 042164554	0.210086728	100	
29/09/2021	1B-138Y-1-16-17cm	232.194-S	75.75969172	4.374577438	0.124670161	3 315357719	0.979884162	13.89696271	0.232116547	0 073086161	0.973658273	0 065459779	0.204535328	100	
29/09/2021	1B-138Y-1-16-17cm	232.194-S	75 61970095	4.390832018	0.125877606	3 380834338	0.996920868	13.9804942	0.26233156	0 040612538	0.950109133	0 046459893	0.205826896	100	
29/09/2021	1B-138Y-1-16-17cm	232.194-S	73.77514053	4.419699882	0.112829838	3 240404962	1.259720709	15.10772412	0.370714572	0 037503703	1.395886975	0 081275731	0.19909898	100	
29/09/2021	1B-138Y-1-16-17cm	232.194-S	74 22430025	4.427028379	0.272624241	3 2401575	1.301047858	14.45608731	0.356338907	0.108598685	1.318167338	0 070381443	0.225268093	100	
29/09/2021	1B-138Y-1-16-17cm	232.194-S	75 59412358	4.437566599	0.116419613	3.18185231	1.085980027	13.95119859	0.258460817	0 048313075	1.040463596	0 053633898	0.231987894	100	
29/09/2021	1B-138Y-1-16-17cm	232.194-S	73 91214688	4.445447935	0.235347244	3.124888402	1.294932834	14.78765181	0.395748152	0 029810651	1.490694161	0 043931485	0.239400446	100	
29/09/2021	1B-138Y-1-16-17cm	232.194-S	74 38770104	4.454031251	0.232071715	3.183284583	1.228003371	14.60716877	0.306783096	0	1.337436692	0 040689565	0.222829921	100	
29/09/2021	1B-138Y-1-16-17cm	232.194-S	75.75737297	4.460261603	0.108441431	3 27649549	0.99795711	13.83526644	0.242491154	0 053903635	0.971974328	0 091213407	0.204622428	100	
29/09/2021	1B-138Y-1-16-17cm	232.194-S	73.79501553	4.476978575	0.291073342	3.152016069	1.184237542	15.0906256	0.321688873	0 006834017	1.401475219	0 072105854	0.207949379	100	
29/09/2021	1B-138Y-1-16-17cm	232.194-S	74 21272234	4.483388378	0.216976817	2 972942026	1.078410745	14.8766978	0.359177743	0 072645277	1.397138207	0 071206757	0.258693907	100	
29/09/2021	1B-138Y-1-16-17cm	232.194-S	74.12847875	4.515691927	0.09382841	3 227015693	1.217106777	14.77185071	0.327459291	0 062303768	1.377228985	0 073273492	0.205762189	100	
29/09/2021	1B-138Y-1-16-17cm	232.194-S	75.47773353	4.549539561	0.103552165	3 293402188	0.982320537	14.06029395	0.215294969	0 044439818	1.012801163	0 073995991	0.186626124	100	
29/09/2021	1B-138Y-1-16-17cm	232.194-S	74 09017137	4.55593411	0.097369848	3 093797117	1.295368615	14.80148826	0.398736051	0 057637864	1.359556105	0 02871298	0.221227684	100	
29/09/2021	1B-138Y-1-16-17cm	232.194-S	74 37912308	4.560935934	0.151565064	3 07648037	1.231560271	14.48957713	0.321753885	0.108860075	1.38529689	0 075513609	0.219333688	100	

Date Analysed	Core Section Identifier	sample_no	SiO2	Na2O	Cl	K2O	FeOt	Al2O3	MgO	P2O5	CaO	MnO	TiO2	total	Analytical Total
29/09/2021	1B-138Y-1-16-17cm	232.194-S	74.12224923	4.598968662	0.110205701	3.157817192	1.206646455	14.79299597	0.377741148	0 019815833	1.342708101	0 055420751	0.215430951	100	
29/09/2021	1B-138Y-1-16-17cm	232.194-S	73 61944403	4.64019179	0.093661146	3.172047967	1.342655033	14.93863131	0.401877309	0 052831745	1.426384409	0 074264501	0.238010761	100	
29/09/2021	1B-138Y-1-16-17cm	232.194-S	73.46954809	4.720055114	0.11332433	3 075024516	1.318819955	15.03106389	0.441873621	0.100852203	1.456986807	0 048813326	0.223638147	100	
Jan 17 01:32 2020	CHA16-1B-138Y-1_96-98cm_1	233 055-S	74 90444675	4.366215971	0.090192636	2 866343766	1.447477059	14.1083272	0.322632552	0 033463699	1.604132875	0 055241662	0.201525832	100	94.13185301
Jan 17 01:36 2020	CHA16-1B-138Y-1_96-98cm_2	233 055-S	74 85227273	4.565580003	0.051455036	2 824397826	1.4259464	14.11491345	0.325811598	0 00168705	1.623785959	0 035638939	0.178511015	100	94 84008598
Jan 17 01:40 2020	CHA16-1B-138Y-1_96-98cm_3	233 055-S	74 88569707	4.66111494	0.063288533	2.738698257	1.392828512	14.0428464	0.324246826	0	1.646357112	0 045969712	0.198952635	100	93 53985165
Jan 17 01:44 2020	CHA16-1B-138Y-1_96-98cm_4	233 055-S	74 83887427	4.485748331	0.055192818	2 833352242	1.505951924	14.01658973	0.444739039	0	1.619557592	0 025358862	0.17463519	100	93 85279086
Jan 17 01:52 2020	CHA16-1B-138Y-1_96-98cm_6	233 055-S	74 97183375	4.422627431	0.062150112	2 820278919	1.332711024	14.2487653	0.298659924	0	1.580267355	0 026302437	0.236403754	100	94 28784281
Jan 17 01:56 2020	CHA16-1B-138Y-1_96-98cm_7	233 055-S	75 01951752	4.411093843	0.063030811	2 847187105	1.377468066	14.14673323	0.296234182	0 010735433	1.615629552	0 01275497	0.199615283	100	94 08097283
Jan 17 02:00 2020	CHA16-1B-138Y-1_96-98cm_8	233 055-S	75 0037616	4.473416542	0.064991146	2.785017237	1.40536223	14.0726285	0.326854822	0	1.593127118	0 064569126	0.210271678	100	94.78214158
Jan 17 02:03 2020	CHA16-1B-138Y-1_96-98cm_9	233 055-S	75 21674506	4.418299357	0.071225115	2.789616061	1.382099782	14.01571018	0.304702958	0 006068508	1.607622176	0 027787377	0.160123427	100	93 92754236
Jan 17 02:07 2020	CHA16-1B-138Y-1_96-98cm_10	233 055-S	74 96520859	4.471165163	0.076755002	2 882712505	1.373110199	14.10703218	0.34044729	0	1.58619907	0 003406602	0.193963403	100	93 93524612
Jan 17 02:11 2020	CHA16-1B-138Y-1_96-98cm_11	233 055-S	75 01133083	4.603251747	0.06973347	2 811376215	1.392419642	13.9994485	0.265239998	0	1.590597285	0 010744432	0.245857885	100	94 9328918
Jan 17 02:15 2020	CHA16-1B-138Y-1_96-98cm_12	233 055-S	74 96790723	4.452193692	0.088197851	2 863662707	1.516193274	14.05463566	0.306154412	0 022631103	1.554566443	0 018400991	0.155456644	100	94 56012679
Jan 17 02:19 2020	CHA16-1B-138Y-1_96-98cm_13	233 055-S	75 3248453	4.342535804	0.057585801	2.799488858	1.471857117	13.89975999	0.315410753	0	1.552404104	0 030313837	0.205798436	100	95 33600152
Jan 17 02:23 2020	CHA16-1B-138Y-1_96-98cm_14	233 055-S	75.19745372	4.56387561	0.064531078	2 905071175	1.435358824	13.75735846	0.307796262	0 032902359	1.53898131	0 038103055	0.158568143	100	94 21816823
Jan 17 02:27 2020	CHA16-1B-138Y-1_96-98cm_15	233 055-S	74 84386543	4.510442676	0.078405826	2 833150168	1.425182689	14.22940729	0.310356394	0	1.58076262	0	0.188426904	100	94 89090778
Jan 17 02:31 2020	CHA16-1B-138Y-1_96-98cm_16	233 055-S	74.75978739	4.516517226	0.055636723	2 823003864	1.408933809	14.30235747	0.306742388	0	1.618330528	0 020202688	0.188487909	100	94 54187344
Jan 17 02:35 2020	CHA16-1B-138Y-1_96-98cm_17	233 055-S	75 05169469	4.456153347	0.083805462	2 859172121	1.360195063	13.97004893	0.30565596	0	1.605916839	0 067533589	0.239824005	100	94 02728482
Jan 17 02:39 2020	CHA16-1B-138Y-1_96-98cm_18	233 055-S	75 02472785	4.290542764	0.067179466	2 903690569	1.504753937	13.99516405	0.329828821	0 015756832	1.586329707	0 071970395	0.210055605	100	93 92751038
Jan 17 02:43 2020	CHA16-1B-138Y-1_96-98cm_19	233 055-S	74 85543543	4.759811607	0.068223966	2.79210441	1.441204294	14.02677013	0.310233943	0 004548264	1.57602651	0	0.165641444	100	94 54155693
Jan 17 02:47 2020	CHA16-1B-138Y-1_96-98cm_20	233 055-S	75 05626653	4.404496427	0.053407179	2 880884391	1.471222399	14.05701364	0.331933064	0 009894159	1.542637637	0 040534134	0.151710432	100	93 99485432
Jan 17 02:51 2020	CHA16-1B-138Y-1_96-98cm_21	233 055-S	75.17860242	4.237843847	0.068048929	3 082459102	1.337739435	13.88299687	0.329069128	0	1.637600233	0 030317734	0.215322301	100	90 37614735
Jan 17 02:55 2020	CHA16-1B-138Y-1_96-98cm_22	233 055-S	74 86183084	4.464026911	0.065162099	2 936596838	1.351083119	14.14027396	0.340302715	0	1.555004635	0 064421621	0.221297258	100	94 53348029
Jan 17 02:59 2020	CHA16-1B-138Y-1_96-98cm_23	233 055-S	75 06602598	4.579495117	0.042840438	2 867590862	1.38407964	13.9827343	0.289225717	0 017305005	1.53001565	0 028700983	0.211986306	100	94.77027246
Jan 17 03:03 2020	CHA16-1B-138Y-1_96-98cm_24	233 055-S	74 93062491	4.745776214	0.061800552	2.783871252	1.293795293	14.01594482	0.314803156	0 064331633	1.550286897	0 037122516	0.201642758	100	94 8211588
Jan 17 03:06 2020	CHA16-1B-138Y-1_96-98cm_25	233 055-S	75.18256842	4.402553326	0.064500058	2 810674452	1.382028367	14.13982076	0.303086623	0	1.538241523	0 008805107	0.167721369	100	94 2634806
Jan 17 03:22 2020	CHA16-1B-138Y-1_96-98cm_29	233 055-S	74 67103243	4.269157304	0.067923251	2 851777199	1.504721353	14.24146649	0.360802347	0 034600402	1.692758133	0 064942293	0.240818799	100	93 92954428
Jan 17 03:26 2020	CHA16-1B-138Y-1_96-98cm_30	233 055-S	75 03823328	4.609934867	0.035631836	2 811616355	1.381727865	14.04172396	0.324069963	0	1.575413521	0 015436938	0.166211413	100	94 57834277
Jan 17 00:52 2020	CHA16-1B-138Y-1_123.5-124 5cm_1	233 286-OS	74 8052597	4.521828863	0.075505011	3 042939911	0.630674062	14.72800506	0.148150786	0 014931566	1.842618787	0 079635019	0.11045123	100	94.43081835
Jan 17 00:56 2020	CHA16-1B-138Y-1_123.5-124 5cm_2	233 286-OS	75.7806355	3.924978178	0.059858506	3 621409186	0.630660816	14.08324475	0.224935425	0	1.532709157	0 039560466	0.102008008	100	96 56104641
Jan 17 01:12 2020	CHA16-1B-138Y-1_123.5-124 5cm_6	233 286-OS	76.13514312	3.815487101	0.055135885	3 032425703	0.937299891	13.9712731	0.28008191	0 016456909	1.62472665	0	0.131969732	100	95.40066324
Jan 17 01:20 2020	CHA16-1B-138Y-1_123.5-124 5cm_8	233 286-OS	74 96788848	4.359604373	0.063626658	3 004901717	0.691079159	14.65961614	0.113542522	0	1.928080558	0 041239501	0.170420898	100	93 35709509
Jan 17 01:28 2020	CHA16-1B-138Y-1_123.5-124 5cm_10	233 286-OS	74 65615385	4.466805024	0.096987572	2 628686957	1.315687955	14.28060413	0.383607561	0	1.892188239	0 058213223	0.221065489	100	96.71342216
060418	MEX3_1C-132Y-1_65-66cm-SAMPLE_B-2	233 286-S	75 5029	3.3832	0.1222	3.7047	1.0604	14.1973	0.2219	0 0229	1.5983	0 0917	0.0944	100	92 8148
060418	MEX3_1C-132Y-1_65-66cm-SAMPLE_B-5	233 286-S	76 0164	4.1385	0.0543	3.1231	0.7529	13.9215	0.1069	0 0777	1.6324	0 021	0.1554	100	97 6807
060418	MEX3_1C-132Y-1_65-66cm-SAMPLE_B-6	233 286-S	74 2196	3.9627	0.0518	3.7384	1.0864	14.5508	0.3143	0 0791	1.7806	0 0194	0.1969	100	97.7291
060418	MEX3_1C-132Y-1_65-66cm-SAMPLE_B-10	233 286-S	75 9008	3.9462	0.0478	3.1371	1.2616	13.5047	0.4104	0 0768	1.4186	0 0536	0.2424	100	97 9626
060418	MEX3_1C-132Y-1_65-66cm-SAMPLE_B-11	233 286-S	74.4578	4.2471	0.0937	3.4712	1.383	13.9276	0.6116	0 0707	1.5246	0 0548	0.1578	100	97.4397
060418	MEX3_1C-132Y-1_65-66cm-SAMPLE_B-15	233 286-S	76.1286	3.8825	0.0489	3 6056	0.7901	13.4451	0.296	0.1165	1.4573	0 061	0.1685	100	97 0771
060418	MEX3_1C-132Y-1_65-66cm-SAMPLE_B-20	233 286-S	74 8648	4.3765	0.0883	2.7868	1.4906	13.942	0.4947	0 05	1.6954	0 0154	0.1955	100	97.1654
060418	MEX3_1C-132Y-1_65-66cm-SAMPLE_B-25	233 286-S	74 5447	4.4108	0.0652	2 9594	1.299	14.2873	0.3937	0 0536	1.7612	0 08	0.1452	100	98 0008
Jan 25 03:01 2020	CHA16-1C-132Y-1(100-104cm)_1	233 661-OS	75 66061887	4.20453857	0.029189403	2 961091073	1.179715885	13.96089357	0.317605996	0 015068898	1.472853022	0 014331259	0.184093456	100	94 89745269
Jan 25 03:05 2020	CHA16-1C-132Y-1(100-104cm)_2	233 661-OS	75 00076908	4.533707079	0.084888669	2 934812703	1.331176043	14.0705862	0.287169845	0 034818029	1.470562064	0 016725277	0.234785016	100	95 06569183
Jan 25 03:09 2020	CHA16-1C-132Y-1(100-104cm)_3	233 661-OS	75 34622056	4.378523592	0.056459909	2 943457247	1.217274197	13.97040958	0.280937806	0 079714269	1.448264765	0 022206866	0.256531203	100	95.46596958
Jan 25 03:12 2020	CHA16-1C-132Y-1(100-104cm)_4	233 661-OS	75 20407662	4.388039006	0.055505028	2 911395808	1.213710241	14.12174766	0.30716273	0 029113958	1.462400398	0 041890587	0.264957964	100	95.4868449
Jan 25 03:16 2020	CHA16-1C-132Y-1(100-104cm)_5	233 661-OS	75 36487367	4.366995612	0.083235989	2 883269392	1.25448577	14.02401047	0.315265515	0 008313076	1.438898747	0 033883677	0.226768085	100	95 03100916
Jan 25 03:20 2020	CHA16-1C-132Y-1(100-104cm)_6	233 661-OS	75 54156594	4.210236739	0.0674271	2 975656041	1.272852907	13.94870162	0.274773345	0 048328031	1.441293825	0 024375055	0.194789399	100	94.7690177
Jan 25 03:24 2020	CHA16-1C-132Y-1(100-104cm)_7	233 661-OS	75 28403109	4.487197274	0.069777494	2 889881149	1.150632773	14.08768192	0.312632597	0 019230845	1.492229539	0 00830184	0.198403477	100	95.15962279
Jan 25 03:32 2020	CHA16-1C-132Y-1(100-104cm)_9	233 661-OS	74 96054419	4.593506292	0.089552302	2 88674478	1.327059793	14.09268778	0.349359332	0 038244101	1.449377662	0 002844603	0.210079164	100	94 91660015
Jan 25 03:40 2020	CHA16-1C-132Y-1(100-104cm)_11	233 661-OS	75 2453644	4.52266002	0.029872535	2 924583847	1.209650672	14.11518656	0.301649934	0 009400448	1.444326623	0 036870646	0.160434314	100	95.74011712
Jan 25 03:44 2020	CHA16-1C-132Y-1(100-104cm)_12	233 661-OS	75.41520286	4.425725695	0.059846693	2 898170254	1.189389228	14.01579899	0.234887806	0 041327699	1.475241898	0 053882949	0.190525922	100	95 57754572
Jan 25 03:48 2020	CHA16-1C-132Y-1(100-104cm)_13	233 661-OS	75 29605164	4.586242611	0.091620143	2 963257212	1.178511038	13.93411716	0.285226595	0 003978932	1.497334916	0 005444854	0.158214899	100	95 50301568
Jan 25 03:51 2020	CHA16-1C-132Y-1(100-104cm)_14	233 661-OS	75 3085075	4.357645094	0.048616619	2 940097895	1.210414358	14.0043026	0.287394569	0.129259304	1.462803706	0 0450465	0.205911856	100	95 23492416
Jan 25 03:55 2020	CHA16-1C-132Y-1(100-104cm)_15	233 661-OS	75.14749355	4.568584638	0.066603512	2 820242453	1.272043758	14.10455212	0.29628156	0 012175955	1.467358619	0 032677348	0.21198649	100	96 09102924
Jan 25 03:59 2020	CHA16-1C-132Y-1(100-104cm)_16	233 661-OS	75.125588	4.642416294	0.084274494	2 875370452	1.24458793	13.99639203	0.32110046	0 041196217	1.442704055	0 040987099	0.185382975	100	95 63985044
Jan 25 04:07 2020	CHA16-1C-132Y-1(100-104cm)_18	233 661-OS	75.47185412	4.440758845	0.05124762	2 830720686	1.241366852	13.91056923	0.323480869	0 064296295	1.454506369	0 034410619	0.176788504	100	95 02880357
Jan 25 04:11 2020	CHA16-1C-132Y-1(100-104cm)_19	233 661-OS	75 21262436	4.182017217	0.060713549	2 982606188	1.324572503	14.0831966	0.313757434	0 0735568	1.48079498	0 048188726	0.23797164	100	94 21290721
Jan 25 04:15 2020	CHA16-1C-132Y-1(100-104cm)_20	233 661-OS	75.11156761	4.478398239	0.052762127	2 978507142	1.277878222	14.0931601	0.330827043	0 021168676	1.396494349	0 006914392	0.252322105	100	94 00682511
Jan 25 04:19 2020	CHA16-1C-132Y-1(100-104cm)_21	233 661-OS	75.42762466	4.477823786	0.046147925	2 844735111	1.166689766	14.00014841	0.342211098	0 06016088	1.412990466	0 039931652	0.181536244	100	94 91217617
Jan 25 04:26 2020	CHA16-1C-132Y-1(100-104cm)_22	233 661-OS	75.13637355	4.494256547	0.090412626	2 943421542	1.342475343	14.01854149	0.293076166	0	1.450927472	0 035975152	0.194540119	100	94.7876463
Jan 25 04:30 2020	CHA16-1C-132Y-1(100-104cm)_23	233 661-OS	75 24801716	4.486877821	0.061522202	2 821535462	1.295686522	14.11563499	0.282259619	0 010501203	1.454787927	0 018987024	0.204190066	100	94 27490939
Jan 25 04:38 2020	CHA16-1C-132Y-1(100-104cm)_25	233 661-OS	75 3019108	4.421511946	0.064331951	2.797496895	1.224279144	14.11801651	0.318411725	0 067579981	1.439715537	0 056264263	0.190481249	100	95.44246519

Date Analysed	Core Section Identifier	sample_no	SiO2	Na2O	Cl	K2O	FeOt	Al2O3	MgO	P2O5	CaO	MnO	TiO2	total	Analytical Total
Jan 25 04:42 2020	CHA16-1C-132Y-1(100-104cm)_26	233 661-OS	75.17394758	4.438702376	0.074153677	2 892519321	1.243035734	14.12121785	0.292722955	0 059954037	1.422067681	0 015356648	0.266322143	100	95 07283082
Jan 25 04:46 2020	CHA16-1C-132Y-1(100-104cm)_27	233 661-OS	75 04702806	4.673411689	0.041390081	2 829195417	1.12359434	14.27382247	0.224973428	0 079427042	1.498425721	0 005763176	0.202968575	100	95.43349264
Jan 25 04:50 2020	CHA16-1C-132Y-1(100-104cm)_28	233 661-OS	75 55086855	4.388189006	0.066721621	3 024149532	1.120939771	13.97775396	0.251765735	0 055090276	1.347861331	0 034894033	0.18176619	100	94 57204315
Jan 25 04:54 2020	CHA16-1C-132Y-1(100-104cm)_29	233 661-OS	75 37817182	4.386365845	0.080469301	3 018913663	1.266401507	13.91527313	0.321666829	0 028506119	1.369871521	0 010518863	0.223841403	100	95 06730964
Jan 25 04:58 2020	CHA16-1C-132Y-1(100-104cm)_30	233 661-OS	75 32510341	4.361481512	0.026548148	3 023539116	1.306439176	13.86411496	0.29287243	0 047302058	1.456671615	0 063631276	0.232296298	100	94 92187433
Jan 25 05:02 2020	CHA16-1C-132Y-1(100-104cm)_31	233 661-OS	75.43109719	4.420947648	0.0639874	2 961400338	1.256249841	13.77313637	0.3095721	0 088313189	1.462402946	0	0.232892984	100	94 54986426
Jan 25 05:06 2020	CHA16-1C-132Y-1(100-104cm)_32	233 661-OS	75 33144513	4.294528213	0.075362716	2 866493346	1.240851409	14.12733974	0.30801774	0 060561187	1.459305703	0 018658266	0.21743655	100	95 93603292
Jan 25 05:09 2020	CHA16-1C-132Y-1(100-104cm)_33	233 661-OS	75 33275537	4.398454073	0.076260966	2 879563458	1.266891456	13.943255	0.328987488	0 067611728	1.447798096	0 032170947	0.226251415	100	94 80603709
Jan 25 05:13 2020	CHA16-1C-132Y-1(100-104cm)_34	233 661-OS	75.44461776	4.527314716	0.053562597	3 007582311	1.23921346	13.79786155	0.335297604	0 035920948	1.400916962	0	0.15771209	100	94 09551285
Jan 25 05:17 2020	CHA16-1C-132Y-1(100-104cm)_35	233 661-OS	75 33922407	4.320643691	0.075211205	2 891097383	1.294790855	14.10241832	0.302231693	0 034351784	1.43338688	0 051741042	0.154903078	100	93.73603309
Jan 25 05:21 2020	CHA16-1C-132Y-1(100-104cm)_36	233 661-OS	75.44345914	4.289181928	0.062607374	2 925872269	1.229115438	14.07925704	0.308212853	0 028734373	1.428119303	0 009752908	0.195687371	100	95 35617907
040319	CHA16-1A-138Y-1_22-23cm_1	233 661-S	75.4878	4.5895	0.0675	2 8853	1.2036	13.7039	0.3361	0 0181	1.4396	0 0284	0.2402	100	95.4464
040319	CHA16-1A-138Y-1_22-23cm_3	233 661-S	75.1623	4.6676	0.0564	2 965	1.2819	13.7754	0.2999	0 0599	1.4521	0 0532	0.2262	100	95 3524
040319	CHA16-1A-138Y-1_22-23cm_4	233 661-S	75 5268	4.7176	0.069	2 8457	1.1542	13.6366	0.3204	0 0508	1.4518	0 0448	0.1821	100	95.4723
040319	CHA16-1A-138Y-1_22-23cm_5	233 661-S	75 3981	4.8877	0.0672	2 8798	1.1202	13.6388	0.3185	0 0558	1.4525	0 0326	0.1488	100	93 5006
040319	CHA16-1A-138Y-1_22-23cm_6	233 661-S	75 3165	4.6701	0.0775	2 965	1.2446	13.5725	0.2853	0 0471	1.5751	0 0503	0.1959	100	93.7897
040319	CHA16-1A-138Y-1_22-23cm_7	233 661-S	75.1195	4.5708	0.0764	3.1092	1.1609	13.8545	0.3143	0 0429	1.4831	0 0455	0.2228	100	94 0879
040319	CHA16-1A-138Y-1_22-23cm_8	233 661-S	75 6018	4.5253	0.0622	2 8402	1.257	13.7185	0.2993	0 0552	1.4706	0 0818	0.088	100	93 8415
040319	CHA16-1A-138Y-1_22-23cm_9	233 661-S	75 2878	4.742	0.0964	2 9025	1.2848	13.5359	0.3151	0 0918	1.3894	0 0844	0.2699	100	92.7052
040319	CHA16-1A-138Y-1_22-23cm_11	233 661-S	75 217	4.7455	0.076	2 8477	1.2539	13.7878	0.3495	0 0387	1.4735	0 0389	0.1717	100	94 6568
040319	CHA16-1A-138Y-1_22-23cm_12	233 661-S	75 3366	4.6268	0.0801	2 9551	1.3086	13.6162	0.2913	0 0627	1.4492	0 0567	0.2165	100	94 3602
040319	CHA16-1A-138Y-1_22-23cm_13	233 661-S	75 3216	4.6374	0.0696	2 9322	1.2731	13.6701	0.2919	0 0822	1.4668	0 0298	0.2252	100	92 3494
040319	CHA16-1A-138Y-1_22-23cm_17	233 661-S	75 254	4.5967	0.0679	2 9355	1.3235	13.7631	0.3429	0 0295	1.4718	0 0405	0.1743	100	94.7763
040319	CHA16-1A-138Y-1_22-23cm_18	233 661-S	75.4666	4.5387	0.0522	2 9622	1.1857	13.7748	0.3248	0 0348	1.4251	0 0395	0.1957	100	94 3385
040319	CHA16-1A-138Y-1_22-23cm_19	233 661-S	75 3851	4.8564	0.0661	2.7839	1.2717	13.5653	0.3051	0 0172	1.5097	0 0849	0.1548	100	93 8069
040319	CHA16-1A-138Y-1_22-23cm_21	233 661-S	75 2878	4.5514	0.072	2 9673	1.2761	13.7759	0.2926	0 0585	1.4505	0 0519	0.2159	100	94 6218
040319	CHA16-1A-138Y-1_22-23cm_22	233 661-S	75 6108	4.6202	0.0718	2 8671	1.1762	13.6104	0.2717	0 0592	1.5041	0 0175	0.1911	100	92.784
040319	CHA16-1A-138Y-1_22-23cm_26	233 661-S	75 362	4.7142	0.0544	2 9081	1.3214	13.492	0.3014	0 0271	1.5991	0 0338	0.1865	100	93 2033
040319	CHA16-1A-138Y-1_22-23cm_28	233 661-S	75 3877	4.5077	0.0479	3.1329	1.3112	13.4631	0.3995	0 0659	1.451	0 0083	0.2248	100	94.702
040319	CHA16-1A-138Y-1_22-23cm_29	233 661-S	75 2107	4.7891	0.07	2 9049	1.2737	13.6249	0.2799	0 0887	1.506	0 064	0.1882	100	92 8331
040319	CHA16-1A-138Y-1_22-23cm_30	233 661-S	75.1644	4.8747	0.0936	2 8781	1.2293	13.737	0.3029	0 0609	1.3908	0 0551	0.2133	100	94.7929
040319	CHA16-1A-138Y-1_22-23cm_31	233 661-S	75.108	4.6237	0.073	2 9652	1.275	13.8373	0.3803	0 0836	1.4585	0	0.1953	100	93.4222
040319	CHA16-1A-138Y-1_22-23cm_32	233 661-S	75 5271	4.3855	0.059	2 8014	1.238	13.9198	0.3188	0 0834	1.4595	0	0.2077	100	93 6369
Jan 25 06:13 2020	CHA16-1C-132Y-1(110-112cm)_2	233.726-OS	75.10312791	4.107528095	0.052438747	2 575023958	1.440237812	14.53933674	0.298056417	0 048060164	1.647181317	0 043994336	0.145014507	100	95 92143764
Jan 25 06:21 2020	CHA16-1C-132Y-1(110-112cm)_4	233.726-OS	74 02930698	4.541275362	0.070074704	2 813852437	1.534006976	14.5537627	0.482048775	0 084524216	1.651372859	0 057580764	0.182194229	100	92 0446277
Jan 25 06:29 2020	CHA16-1C-132Y-1(110-112cm)_6	233.726-OS	74 36842767	4.479106649	0.086639654	2 94247882	1.410027912	14.28838981	0.370098447	0 042611453	1.678302735	0 060702248	0.273214608	100	91.75936905
Jan 25 06:37 2020	CHA16-1C-132Y-1(110-112cm)_6	233.726-OS	74 6935227	4.427381238	0.05687808	2 679730749	1.409460515	14.44900641	0.394439419	0 014722631	1.652324098	0 024043434	0.198490728	100	94.41247038
Jan 25 06:44 2020	CHA16-1C-132Y-1(110-112cm)_8	233.726-OS	76 58183058	3.794692054	0.096533526	3 257200262	1.154545477	13.058647	0.230368982	0 029347052	1.537226526	0 017199737	0.242408798	100	93 02467629
Jan 25 06:48 2020	CHA16-1C-132Y-1(110-112cm)_9	233.726-OS	74.19121046	4.370031138	0.119293022	2 913354092	1.111794264	14.84809278	0.245759074	0 061136294	1.876023468	0 020856967	0.242448445	100	90 61720329
Jan 25 06:52 2020	CHA16-1C-132Y-1(110-112cm)_10	233.726-OS	74 59098118	4.620587318	0.07308929	2 635835038	1.367017567	14.38749408	0.334572527	0 086005932	1.68021357	0 028458617	0.195744881	100	95 22598963
Jan 25 06:56 2020	CHA16-1C-132Y-1(110-112cm)_11	233.726-OS	74.16939533	4.523430553	0.098857132	2 590885105	1.252495963	14.7774487	0.395003795	0 056383606	1.900690303	0 006371029	0.229038491	100	94.17631045
Jan 25 07:08 2020	CHA16-1C-132Y-1(110-112cm)_14	233.726-OS	75 31044001	3.756451025	0.069686435	3.190849024	1.4092544	14.09652985	0.268714309	0.113013683	1.504714757	0 044501139	0.235845363	100	93.70546764
Jan 25 07:12 2020	CHA16-1C-132Y-1(110-112cm)_15	233.726-OS	74 94223893	4.527479032	0.046936251	2.782945827	1.278449442	14.27793998	0.288471026	0 067185297	1.505698302	0 05098606	0.231669856	100	96 30083252
Jan 25 07:15 2020	CHA16-1C-132Y-1(110-112cm)_16	233.726-OS	74.71138691	4.558377371	0.061370815	2.73920842	1.299493868	14.46786076	0.314590769	0	1.641434053	0 032305931	0.1739711	100	95 64807047
Jan 25 07:19 2020	CHA16-1C-132Y-1(110-112cm)_17	233.726-OS	74.70380723	4.555365028	0.053494195	2 831431015	1.369106978	14.45829987	0.292964301	0 064464684	1.48362806	0 047225344	0.1402133	100	95.71132002
Jan 25 07:23 2020	CHA16-1C-132Y-1(110-112cm)_18	233.726-OS	74 90538707	4.641640296	0.05878014	2 849946186	1.290081616	14.13891787	0.314856187	0 064542899	1.519272783	0 041177531	0.175397423	100	95.44039861
Jan 25 07:27 2020	CHA16-1C-132Y-1(110-112cm)_19	233.726-OS	74 9715336	4.361634508	0.064526845	3 062648928	1.358352566	14.07462353	0.360019662	0 030837706	1.474823872	0 047946297	0.193052491	100	94 68927284
Jan 25 07:31 2020	CHA16-1C-132Y-1(110-112cm)_20	233.726-OS	75 07572128	4.351603428	0.062739137	2 957400388	1.384053201	14.22166814	0.327215229	0 014153273	1.43444481	0 005386694	0.165614422	100	94 67774507
Jan 25 07:35 2020	CHA16-1C-132Y-1(110-112cm)_21	233.726-OS	75 2793704	4.166910921	0.062820941	2 982408324	1.322151356	14.00114229	0.342025125	0 094231412	1.52293191	0 023795811	0.202211515	100	94 55445712
Jan 25 07:39 2020	CHA16-1C-132Y-1(110-112cm)_22	233.726-OS	75.12068513	4.538192838	0.054270094	2 938323012	1.304269071	13.97687251	0.3038707	0 051551361	1.484846505	0 025095997	0.202022778	100	95 63278061
Jan 25 07:47 2020	CHA16-1C-132Y-1(110-112cm)_24	233.726-OS	74 98018528	4.398131009	0.088810453	3 031001129	1.221444741	14.18649311	0.344431947	0 078848421	1.475122543	0 022891477	0.172639889	100	94 35826244
Jan 25 07:51 2020	CHA16-1C-132Y-1(110-112cm)_25	233.726-OS	75 20859208	4.258482299	0.039738808	2 983045769	1.299237214	14.09968744	0.307896703	0 055655412	1.496793283	0 028776378	0.222094609	100	94 8694797
Jan 25 07:54 2020	CHA16-1C-132Y-1(110-112cm)_26	233.726-OS	74 64609749	4.279276068	0.059784004	2 884315977	1.672710465	14.07086098	0.608643113	0 037653434	1.51033273	0 073209184	0.157116558	100	95 34322944
Jan 25 07:58 2020	CHA16-1C-132Y-1(110-112cm)_27	233.726-OS	75.16226859	4.447970459	0.071462653	2 972340449	1.360515371	14.00567402	0.30682564	0 038471782	1.473311163	0 003583673	0.157576205	100	94 87473082
Jan 25 08:02 2020	CHA16-1C-132Y-1(110-112cm)_28	233.726-OS	74 60677113	4.307195034	0.104053921	2 670021412	1.730020098	14.47075357	0.234148791	0 088451327	1.560259426	0 030545924	0.197779364	100	91 01050611
Jan 25 08:14 2020	CHA16-1C-132Y-1(110-112cm)_31	233.726-OS	74 82136722	4.464105325	0.086849063	2 686925954	1.407681027	14.19163759	0.325922003	0.129268642	1.639659539	0 031523777	0.215059861	100	94 53181976
Jan 25 13:23 2020	CHA16-1A-140Y-1(65.5-71cm)_1	237 208-OS	72 52369402	4.659225692	0.084119052	3 64726717	1.552638892	15.13629466	0.447159172	0 016338914	1.539020251	0.117113116	0.277129058	100	94 86554832
Jan 25 13:31 2020	CHA16-1A-140Y-1(65.5-71cm)_3	237 208-OS	72.48906679	4.588979022	0.097765205	3.759392425	1.600062232	15.04769702	0.432645162	0 060381303	1.575164424	0 077603101	0.271243314	100	95 22815378
Jan 25 13:35 2020	CHA16-1A-140Y-1(65.5-71cm)_4	237 208-OS	71 59149603	4.748740039	0.093384821	3.423756769	1.755088278	15.52260224	0.556068979	0 09582279	1.844376711	0 064341188	0.304322157	100	94 34081385
Jan 25 13:39 2020	CHA16-1A-140Y-1(65.5-71cm)_5	237 208-OS	71 56241564	4.785716606	0.11039053	3 392541327	1.836514513	15.60530102	0.510689136	0 061788919	1.786667533	0 060512728	0.287462044	100	94 02980516
Jan 25 13:43 2020	CHA16-1A-140Y-1(65.5-71cm)_6	237 208-OS	69 01370255	4.731335331	0.092500264	3 37041191	2.451661773	16.14470379	0.800286765	0.1925494	2.6155247	0 073893889	0.513429625	100	94 05378584
Jan 25 13:54 2020	CHA16-1A-140Y-1(65.5-71cm)_9	237 208-OS	70 04013187	4.902702185	0.077287139	3.125740258	2.229127325	16.05470934	0.701364732	0.124601427	2.301486834	0 06187253	0.380976355	100	93.41787094
Jan 25 13:58 2020	CHA16-1A-140Y-1(65.5-71cm)_10	237 208-OS	70.12417726	4.8776528	0.085939597	3.167307013	2.123464855	15.9900354	0.735765419	0.115289975	2.343807189	0 091324019	0.345236464	100	94.71768881

Date Analysed	Core Section Identifier	sample_no	SiO2	Na2O	Cl	K2O	FeOt	Al2O3	MgO	P2O5	CaO	MnO	TiO2	total	Analytical Total
Jan 25 14:02 2020	CHA16-1A-140Y-1(65.5-71cm)_11	237 208-OS	69.71523755	4.805375537	0.088329408	3.196480401	2.381137374	16.01165248	0.747550217	0.124449637	2.41867017	0 069043977	0.44207324	100	93 85322678
Jan 25 14:06 2020	CHA16-1A-140Y-1(65.5-71cm)_12	237 208-OS	70 33723539	4.712994534	0.136340199	3.134982971	2.212077036	16.01578458	0.642145505	0.104674767	2.230256342	0 079531783	0.393976887	100	95 0563377
Jan 25 14:10 2020	CHA16-1A-140Y-1(65.5-71cm)_13	237 208-OS	70 36920452	4.90333547	0.087710527	3 244232736	2.082506359	15.78683586	0.758220517	0.125119595	2.187479402	0 078411097	0.376943914	100	94 6294625
Jan 25 14:18 2020	CHA16-1A-140Y-1(65.5-71cm)_15	237 208-OS	69 89905744	4.701925101	0.068302792	3 225107979	2.294362971	15.94469759	0.792703308	0.168965253	2.334674126	0 093712734	0.476490701	100	92 08993991
Jan 25 14:26 2020	CHA16-1A-140Y-1(65.5-71cm)_17	237 208-OS	70 04487567	4.735574804	0.087946389	3.16398844	2.304776291	15.87562751	0.722825649	0.149144587	2.4042149	0 080140497	0.430885268	100	96 08126127
Jan 25 14:29 2020	CHA16-1A-140Y-1(65.5-71cm)_18	237 208-OS	68 86679357	4.715889748	0.098124343	3 2567131	2.481142707	16.33650708	0.854675714	0.168439739	2.632862214	0 063759675	0.525092119	100	94 57388188
Jan 25 14:33 2020	CHA16-1A-140Y-1(65.5-71cm)_19	237 208-OS	69 94112512	4.659904594	0.112773947	3 276827888	2.464045603	15.74728782	0.714305923	0 204908134	2.340591349	0.107667202	0.430562418	100	93 99334067
Jan 25 14:37 2020	CHA16-1A-140Y-1(65.5-71cm)_20	237 208-OS	71 62621689	4.929184098	0.104283381	3 293159397	1.65116266	15.55026054	0.565853446	0 083173385	1.85767966	0 059635739	0.279390799	100	94.74184586
Jan 25 14:41 2020	CHA16-1A-140Y-1(65.5-71cm)_21	237 208-OS	71.73439892	4.995637616	0.096744272	3 326904543	1.652195697	15.36276477	0.545612345	0 091780319	1.890526709	0 022390596	0.281044222	100	94 68260838
Jan 25 14:49 2020	CHA16-1A-140Y-1(65.5-71cm)_23	237 208-OS	71 809302	4.965034329	0.085444777	3 296027018	1.706051265	15.43371895	0.462913349	0 056683267	1.784473226	0 097306275	0.303045541	100	95 26620938
Jan 25 14:53 2020	CHA16-1A-140Y-1(65.5-71cm)_24	237 208-OS	71 8445699	4.834987807	0.079117982	3 265186571	1.637137318	15.58274341	0.544616375	0.104967376	1.758177384	0 030349491	0.318146384	100	95 55349846
Jan 25 14:57 2020	CHA16-1A-140Y-1(65.5-71cm)_25	237 208-OS	72.17670822	4.841378495	0.082557131	3 350910443	1.556978232	15.43832741	0.490057439	0 06976659	1.775876828	0 001479897	0.215959307	100	94 60115553
Jan 25 15:01 2020	CHA16-1A-140Y-1(65.5-71cm)_26	237 208-OS	72 55987268	4.293989226	0.112690513	3.471508703	1.595009271	15.25381204	0.474475128	0.107563362	1.741095134	0 082461684	0.307522263	100	93 61923815
Jan 25 15:05 2020	CHA16-1A-140Y-1(65.5-71cm)_27	237 208-OS	71 61372123	4.684617141	0.088125421	3.403174784	1.845849666	15.53651553	0.507010021	0.12520322	1.796120025	0 057664906	0.341998059	100	95 20521882
Jan 25 15:08 2020	CHA16-1A-140Y-1(65.5-71cm)_28	237 208-OS	72 04384474	4.635444343	0.07599606	3.426655002	1.825828036	15.25847589	0.506745514	0 065800185	1.765883559	0 049087358	0.346239312	100	95.13651062
Jan 25 15:12 2020	CHA16-1A-140Y-1(65.5-71cm)_29	237 208-OS	72.12822456	4.901612467	0.093309068	3 369202574	1.663250526	15.17443896	0.465810624	0 08281311	1.773816931	0 049960761	0.297560414	100	95 27476992
Jan 25 15:16 2020	CHA16-1A-140Y-1(65.5-71cm)_30	237 208-OS	71 9949655	4.779086267	0.078658012	3 501824904	1.675873396	15.31501705	0.492703571	0 070249375	1.777522064	0 040340171	0.273759685	100	93 95101384
Jan 25 15:20 2020	CHA16-1A-140Y-1(65.5-71cm)_31	237 208-OS	72 24685272	4.737846833	0.108566804	3.431220913	1.694169231	15.23278557	0.461143343	0 070536554	1.731544919	0 053752253	0.231580854	100	94.13558853
Jan 25 15:24 2020	CHA16-1A-140Y-1(65.5-71cm)_32	237 208-OS	70 05587829	4.562219176	0.090822931	3.424298458	2.204786034	16.03013148	0.673480484	0.110420455	2.349595557	0 05773894	0.440628189	100	94 90995134
Jan 25 15:28 2020	CHA16-1A-140Y-1(65.5-71cm)_33	237 208-OS	70 30361986	4.702268035	0.084096241	3 257027525	2.127658952	15.7275934	0.734349743	0.126406181	2.398261425	0 062731816	0.47598682	100	95.48583719
Jan 25 15:32 2020	CHA16-1A-140Y-1(65.5-71cm)_34	237 208-OS	71 0985823	5.015121264	0.095445676	3 262468359	1.855431442	15.59641162	0.571934987	0.112338716	1.984932206	0 065038204	0.342295224	100	94.71356224
Jan 25 15:36 2020	CHA16-1A-140Y-1(65.5-71cm)_35	237 208-OS	70 86656386	4.89611971	0.102797319	3 232286822	1.948496396	15.76935051	0.649636663	0 059346906	2.055946372	0 053200262	0.366255189	100	94 36043793
Jan 25 15:40 2020	CHA16-1A-140Y-1(65.5-71cm)_36	237 208-OS	70 27206532	4.968306596	0.110839552	3.178874135	2.224030324	15.76628002	0.665037311	0.112418463	2.221001465	0 068314216	0.412832595	100	95 00218856
Jan 25 15:44 2020	CHA16-1A-140Y-1(65.5-71cm)_37	237 208-OS	70 66629521	4.810963066	0.091999118	3.16510728	2.079121597	15.85449979	0.648846992	0.192016508	2.099521163	0 072797467	0.318831807	100	94.78351709
Jan 25 15:47 2020	CHA16-1A-140Y-1(65.5-71cm)_38	237 208-OS	71 35785508	4.724149413	0.077821926	3 374392438	1.917386306	15.421493	0.565421633	0 07602928	1.982455557	0.106187912	0.396807461	100	94 83188631
Jan 25 15:51 2020	CHA16-1A-140Y-1(65.5-71cm)_39	237 208-OS	69 36495725	4.795497198	0.115961912	3.11919508	2.446425774	16.11022365	0.771947735	0.167418022	2.514453177	0 071083697	0.522836509	100	94 25508584
Mar 15 05 06 2020	CHA16-1C-136Y-1(131-132cm)_1	240 957-S	66 84388972	4.54379427	0.166894532	2 824868541	3.464174317	16.53048993	1.324512235	0.176635458	3.560849617	0 067320622	0.496570761	100	92 39368
Mar 15 05:18 2020	CHA16-1C-136Y-1(131-132cm)_4	240 957-S	68 25183589	4.133740008	0.157562076	3 528331995	3.371229497	16.04913016	0.980830722	0 296931189	2.591118809	0 095264964	0.54402469	100	90 69441323
Mar 15 05 22 2020	CHA16-1C-136Y-1(131-132cm)_5	240 957-S	66.17237955	4.191144847	0.112240897	3 099188955	3.811570945	16.67048884	1.401836519	0.193385203	3.769283864	0 050152416	0.528327955	100	95 5088587
Mar 15 05 34 2020	CHA16-1C-136Y-1(131-132cm)_8	240 957-S	65 30839162	4.729850778	0.145652961	3 349070259	4.264714764	16.4888319	1.297980805	0 288883639	3.085778572	0 073089772	0.967754925	100	94 95172553
Mar 15 05 54 2020	CHA16-1C-136Y-1(131-132cm)_13	240 957-S	67 2047228	4.386897647	0.105535383	3.102761005	3.162212606	16.69562924	1.17447576	0 215429159	3.445206199	0 040574567	0.466555635	100	96 36578504
Mar 15 05 58 2020	CHA16-1C-136Y-1(131-132cm)_14	240 957-S	67 22025645	4.212462618	0.114568096	3 288334757	3.426841505	16.41663107	1.138122755	0 206411077	3.455893216	0 066290315	0.454188148	100	95.48906156
Mar 15 06 06 2020	CHA16-1C-136Y-1(131-132cm)_16	240 957-S	69 09620425	4.420546212	0.167806108	2 972013542	2.83066442	16.09172213	0.964280439	0.104503292	2.843262053	0 073388349	0.435609205	100	93 20280546
Mar 15 06:14 2020	CHA16-1C-136Y-1(131-132cm)_18	240 957-S	68 00864563	4.655457226	0.210356332	2 970639185	3.08255599	16.33265514	1.007756513	0.186459677	3.025448027	0 048012545	0.472013739	100	91 2261581
050319	CHA16-1C-137Y-1_10-11cm_1	241.429-S	62 823	5.124	0.1502	2.134	5.0449	17.0426	1.9168	0 3512	4.4998	0.1351	0.7783	100	97 8921
050319	CHA16-1C-137Y-1_10-11cm_2	241.429-S	70 353	4.9155	0.181	2 9475	2.5012	15.1974	0.7468	0.1643	2.5363	0 0765	0.3806	100	92 812
050319	CHA16-1C-137Y-1_10-11cm_4	241.429-S	72 2627	4.5679	0.204	3 3588	2.1383	14.4256	0.5158	0 0886	1.9614	0 0344	0.4424	100	94.7039
050319	CHA16-1C-137Y-1_10-11cm_5	241.429-S	65 9757	5.0987	0.1202	2.4948	3.8587	16.3434	1.3334	0 2446	3.8562	0 066	0.6083	100	98 3229
050319	CHA16-1C-137Y-1_10-11cm_6	241.429-S	66 6529	5.2869	0.1517	2.41	3.6406	15.7911	1.3747	0 258	3.7001	0 075	0.659	100	94 3534
050319	CHA16-1C-137Y-1_10-11cm_7	241.429-S	63.1609	5.3206	0.1379	2 0143	4.6271	17.1815	1.8923	0 3991	4.3798	0 0813	0.8053	100	95 3095
050319	CHA16-1C-137Y-1_10-11cm_8	241.429-S	62 31	5.31	0.1285	1 9219	5.4183	16.7875	2.0107	0 3579	4.8182	0.1104	0.8267	100	98 014
050319	CHA16-1C-137Y-1_10-11cm_10	241.429-S	62.4712	4.9686	0.1246	1 9407	5.2009	17.2461	1.8681	0.4054	4.8123	0.1028	0.8594	100	98 6159
050319	CHA16-1C-137Y-1_10-11cm_12	241.429-S	62.4637	5.3658	0.128	1 9918	5.1372	16.8963	2.0007	0 3911	4.6723	0.1054	0.8476	100	99 2993
050319	CHA16-1C-137Y-1_10-11cm_13	241.429-S	62 301	5.0355	0.1383	1 9926	4.9069	17.795	1.9093	0.4033	4.5305	0.1139	0.8737	100	98.1685
050319	CHA16-1C-137Y-1_10-11cm_14	241.429-S	62 9789	4.6897	0.122	2.1039	5.1317	17.2024	1.8906	0 3777	4.5916	0 0559	0.8557	100	96.4985
050319	CHA16-1C-137Y-1_10-11cm_15	241.429-S	75 8094	4.661	0.1568	3 3104	1.0346	13.2683	0.2555	0 0169	1.2959	0 0149	0.1762	100	95 6794
050319	CHA16-1C-137Y-1_10-11cm_17	241.429-S	76.4513	3.9562	0.1302	3.7671	1.0286	13.2435	0.2281	0 0566	1.0431	0 0037	0.0917	100	94 5287
Feb 14 23:46 2020	CHA16-1C-138Y-1(57 5cm)_1	243.414-OS	78 20493641	2.748468356	0.163044597	5 817064276	0.966319466	11.49860555	0.069742222	0 0169925	0.279698628	0 013656549	0.221471449	100	95 92467498
Feb 15 00 06 2020	CHA16-1C-138Y-1(57 5cm)_6	243.414-OS	78 58397383	3.044287824	0.177461588	5.145335996	0.921519145	11.42474605	0.071614677	0	0.34011721	0 033812208	0.257131477	100	95 2318761
Feb 15 00:10 2020	CHA16-1C-138Y-1(57 5cm)_7	243.414-OS	78.45214984	2.46116521	0.174147933	5 678965146	0.98846086	11.55737639	0.068756417	0 013856255	0.300533775	0 005878411	0.298709762	100	95 26383523
Feb 15 00:17 2020	CHA16-1C-138Y-1(57 5cm)_9	243.414-OS	78 31808715	3.095903069	0.126250419	4 939781634	0.964078503	11.69948282	0.078932511	0 070924865	0.415669625	0 010295545	0.28059386	100	96.15809668
Feb 15 00 37 2020	CHA16-1C-138Y-1(57 5cm)_14	243.414-OS	78 60925927	3.174676589	0.167526337	4 655818788	0.896946104	11.66033188	0.104859847	0 035853962	0.411748974	0 024214415	0.258763838	100	96 2236763
Feb 15 00:49 2020	CHA16-1C-138Y-1(57 5cm)_17	243.414-OS	78.16682761	2.839765698	0.196138477	5.449457679	0.911086537	11.80190834	0.07087445	0 001994985	0.341562347	0 002099984	0.218283891	100	95 23883487
Feb 15 00 56 2020	CHA16-1C-138Y-1(57 5cm)_19	243.414-OS	78 20824486	2.847339156	0.162794629	5.447318674	0.908904479	11.70704816	0.072387887	0	0.371730026	0 006874245	0.267357886	100	96 01053864
Feb 15 01 00 2020	CHA16-1C-138Y-1(57 5cm)_20	243.414-OS	78 67686215	2.731190911	0.15277582	5 004906438	0.959378899	11.60801829	0.150567774	0 035328751	0.416269424	0 012932846	0.251768693	100	95.106673
Feb 15 01:16 2020	CHA16-1C-138Y-1(57 5cm)_24	243.414-OS	77 25073434	2.355299866	0.031038435	6 84914803	0.350072022	12.75679686	0	0	0.283277452	0 043971117	0.079661881	100	96 65435717
Feb 15 01 20 2020	CHA16-1C-138Y-1(57 5cm)_25	243.414-OS	77.11848374	2.407652695	0.034981507	6.78745657	0.49616762	12.78130283	0	0 024121576	0.267112522	0 031535567	0.051185363	100	95.76488531
Feb 15 01 24 2020	CHA16-1C-138Y-1(57 5cm)_26	243.414-OS	77 24324825	2.320674552	0.029999876	6 854138321	0.527583343	12.69786415	0	0	0.237811517	0 03874984	0.049930152	100	96 00039701
Feb 15 01 28 2020	CHA16-1C-138Y-1(57 5cm)_27	243.414-OS	77.19613919	2.387542828	0.038609069	6.787392161	0.573343901	12.78411988	0	0	0.206496908	0 017558912	0.008797155	100	97 38644598
Feb 15 01 31 2020	CHA16-1C-138Y-1(57 5cm)_28	243.414-OS	77 35928379	2.332487346	0.043093878	6 830948076	0.405987785	12.71114392	0	0	0.284605613	0 032449587	0	100	96.76548448
Feb 15 01 35 2020	CHA16-1C-138Y-1(57 5cm)_29	243.414-OS	76 99705111	2.301617075	0.024384525	6.72390305	0.748599597	12.83559888	0	0	0.306726195	0 02926143	0.032858137	100	96 37259716
Feb 15 01 39 2020	CHA16-1C-138Y-1(57 5cm)_30	243.414-OS	77 20828574	2.342684932	0.020669795	6 852037087	0.434225378	12.80493809	0	0 034208511	0.212175447	0 016019091	0.074755931	100	96.75954634
Feb 15 01:43 2020	CHA16-1C-138Y-1(57 5cm)_31	243.414-OS	77.13002438	2.365762283	0.039868212	6.731674536	0.596094741	12.82671008	0	0 003444113	0.269475716	0 036945935	0	100	95 81568399

Date Analysed	Core Section Identifier	sample_no	SiO2	Na2O	Cl	K2O	FeOt	Al2O3	MgO	P2O5	CaO	MnO	TiO2	total	Analytical Total
Feb 14 12:10 2020	CHA16-1C-138Y-1(60-61cm)_6	243.444-OS	75 9811888	4.06368617	0.069691284	3 048993688	1.266991697	13.80343741	0.253460564	0.11934694	1.08882261	0 062431776	0.241949057	100	96.425257
Feb 14 12:14 2020	CHA16-1C-138Y-1(60-61cm)_7	243.444-OS	72 26094724	4.672212422	0.058020347	2.476225524	0.915996228	16.70157132	0.07780943	0 078868029	2.559111734	0 010567992	0.188669736	100	96 51786466
Feb 14 12 30 2020	CHA16-1C-138Y-1(60-61cm)_11	243.444-OS	72 80222419	4.237447251	0.115328549	2.443490724	1.864214906	15.41926905	0.550522673	0.101999448	2.138054384	0 039812047	0.287636775	100	94 94613492
Feb 14 12 34 2020	CHA16-1C-138Y-1(60-61cm)_12	243.444-OS	76 06698418	3.612917326	0.090487574	3.432649259	1.134138917	13.9510424	0.161764908	0.193751569	1.034833529	0 047763162	0.273667175	100	95 26169886
Feb 14 12:46 2020	CHA16-1C-138Y-1(60-61cm)_15	243.444-OS	73 51432175	4.300577574	0.089261608	2.462389194	1.719426937	15.17765753	0.515297394	0 08621903	1.846791895	0 050627571	0.23742951	100	94 21743751
Feb 14 12 50 2020	CHA16-1C-138Y-1(60-61cm)_16	243.444-OS	73 61307743	4.265187463	0.104530232	2 505714408	1.65613742	15.15258198	0.478451648	0.13683348	1.763678811	0.105283022	0.218524106	100	92 98745269
Feb 14 12 54 2020	CHA16-1C-138Y-1(60-61cm)_17	243.444-OS	73.16135635	4.098718853	0.104711099	2 681625711	1.81967459	15.30229275	0.583147178	0.116581033	1.830315962	0 068211194	0.233365285	100	93 97284601
Feb 14 13 02 2020	CHA16-1C-138Y-1(60-61cm)_19	243.444-OS	72.17944655	4.388737465	0.106497687	2 370126571	1.885567361	15.84297939	0.522902591	0.152222131	2.264787612	0 047823887	0.238908758	100	94 931639
Feb 14 13 06 2020	CHA16-1C-138Y-1(60-61cm)_20	243.444-OS	71 91871907	4.435251987	0.090410745	2 357625955	1.883995741	16.0508017	0.517309445	0.15354932	2.252374796	0 044836994	0.295124249	100	95 0108305
Feb 14 13 09 2020	CHA16-1C-138Y-1(60-61cm)_21	243.444-OS	71 97542849	4.366306144	0.105335043	2 343145537	1.799961799	16.13575222	0.527207746	0.164503628	2.300542891	0 025029055	0.256787449	100	93 89088153
Feb 14 13:13 2020	CHA16-1C-138Y-1(60-61cm)_22	243.444-OS	72 03698105	4.541566225	0.113202127	2 334064467	1.729329582	15.91407591	0.572906733	0.110514333	2.334064467	0 075008344	0.238286763	100	94 25617978
Feb 14 13:17 2020	CHA16-1C-138Y-1(60-61cm)_23	243.444-OS	72.18480575	4.418391779	0.074129211	2 295752704	1.8344566	15.87716824	0.533601587	0.141685797	2.317208337	0 078527616	0.244272379	100	93 2156149
Feb 14 13 21 2020	CHA16-1C-138Y-1(60-61cm)_24	243.444-OS	71 84278266	4.552860686	0.081607306	2 366505764	1.931408291	15.92881234	0.505562038	0.185606637	2.239160162	0 080970578	0.284723541	100	94 23175867
Mar 15 02 58 2020	CHA16-1B-145Y-1(103-104cm)_1	244 238-S	69 3158774	4.299243237	0.148992739	2.746853231	2.907245008	16.01950718	0.841096687	0.149313384	3.088873867	0 019238661	0.463758606	100	93 5616061
Mar 15 03 02 2020	CHA16-1B-145Y-1(103-104cm)_2	244 238-S	69 88598864	4.333839664	0.136001909	2 948806828	2.639810645	15.76973753	0.781247068	0 203478165	2.759915287	0 048167343	0.493006921	100	95 29277991
Mar 15 03 06 2020	CHA16-1B-145Y-1(103-104cm)_3	244 238-S	69.74781105	4.395934228	0.119753184	3 02269211	2.844100664	15.60692447	0.799597782	0.130353597	2.812782935	0 039777789	0.480272191	100	95 27930387
Mar 15 03:10 2020	CHA16-1B-145Y-1(103-104cm)_4	244 238-S	69 60248583	4.402071886	0.104377016	2 974796768	3.169160671	14.47592947	1.584399753	0 086134359	2.974796768	0 057422906	0.568424581	100	96.4771789
Mar 15 03 26 2020	CHA16-1B-145Y-1(103-104cm)_8	244 238-S	69.75494768	3.750602861	0.163048402	2 651992073	2.879276145	16.14282074	0.777000247	0.156609408	3.175842359	0 055659093	0.492200998	100	91 62923316
Mar 15 03 30 2020	CHA16-1B-145Y-1(103-104cm)_9	244 238-S	68 81810582	4.591427677	0.112762374	2.717165633	3.035000523	15.95112053	0.973520744	0.189783569	3.041135381	0 051521641	0.518456104	100	95 68794661
Mar 15 03 58 2020	CHA16-1B-145Y-1(103-104cm)_16	244 238-S	74.1158685	4.286440375	0.118551391	3 516533262	1.647241817	14.05222222	0.35084323	0 068961955	1.537167234	0 057696414	0.248473608	100	94 97990637
Mar 15 04 02 2020	CHA16-1B-145Y-1(103-104cm)_17	244 238-S	73.76645243	4.345867442	0.129254034	3 542208373	1.634795762	14.32602124	0.354415552	0 015673488	1.546450853	0 05402129	0.284839529	100	95.70300906
Mar 15 04:10 2020	CHA16-1B-145Y-1(103-104cm)_19	244 238-S	73 94706123	4.10409098	0.124847819	3 615122031	1.644196106	14.29478361	0.384464957	0.100782036	1.513306897	0 030371229	0.240973105	100	95.15584731
Mar 15 04:14 2020	CHA16-1B-145Y-1(103-104cm)_20	244 238-S	68 95801015	4.505299567	0.124520133	2 81478284	3.060245818	15.91990777	0.896802356	0 2054059	2.982204868	0 052947216	0.479873387	100	95 56687505
Mar 15 04 54 2020	CHA16-1B-145Y-1(103-104cm)_30	244 238-S	69 37977222	4.415588457	0.121448263	2.741019821	2.802914442	15.82176178	0.84938893	0 049022085	3.320850937	0 03046749	0.467765575	100	94 85520609

Filtered core analyses, normalised to 100% (251-300 mc)

Date Analysed	Core Section Identifier	sample_no	SiO2	Na2O	Cl	K2O	FeOt	Al2O3	MgO	P2O5	CaO	MnO	TiO2	total	Analytical Total
Mar 13 08 30 2020	CHA16-1C-144Y-1(56-58.5cm)_1	251.779-S	65.21128996	4.755781985	0.053075269	2 546797942	4.178834698	16 30257608	1.686384365	0 291872677	3.830384105	0 080580687	1.06242223	100	98.16247918
Mar 13 08 34 2020	CHA16-1C-144Y-1(56-58.5cm)_2	251.779-S	65.4393313	4 379389957	0.151385247	2.493791797	4.126257868	16 52802563	1.643048712	0 323582753	3.724208896	0 074813754	1.116164082	100	91.02604325
Mar 13 08 54 2020	CHA16-1C-144Y-1(56-58.5cm)_7	251.779-S	64.85489748	4 608914383	0.07502634	2 514233809	4.486217049	16 25759287	1.784991672	0 269055688	4.03679771	0 047479953	1.064793044	100	99.83160638
Mar 13 08 58 2020	CHA16-1C-144Y-1(56-58.5cm)_8	251.779-S	64.52040663	4.786980542	0.079898326	2 619116037	4.553882295	16 00683545	1.716804661	0 325792585	4.270076341	0 076127614	1.044079525	100	98.12470938
Mar 13 09 02 2020	CHA16-1C-144Y-1(56-58.5cm)_9	251.779-S	65.39062945	4 623300232	0.05694758	2.51025763	4.096663758	16 26172439	1.707036465	0 277429878	3.941726857	0 028525655	1.105758113	100	96.40444753
Mar 13 09 06 2020	CHA16-1C-144Y-1(56-58.5cm)_10	251.779-S	65.45742475	4 387077268	0.101809109	2 600731138	4.175300526	16 33367231	1.610605143	0 30593388	3.753087617	0.105720778	1.16863748	100	94.5887856
Mar 13 09 09 2020	CHA16-1C-144Y-1(56-58.5cm)_11	251.779-S	65.23962436	4 677482671	0.075424862	2 590139479	4.176129842	16 07851989	1.715083339	0 294461257	3.968093682	0 055947013	1.129093602	100	96.51989865
Mar 13 09:13 2020	CHA16-1C-144Y-1(56-58.5cm)_12	251.779-S	64.93934188	4.742369064	0.06803443	2.458471307	4.412436524	15 99887074	1.807689985	0 271719858	4.134245627	0 057297433	1.109523153	100	99.6554238
Mar 13 09 29 2020	CHA16-1C-144Y-1(56-58.5cm)_16	251.779-S	64.98812799	4 653980053	0.096476756	2 538861996	4.220943942	16 22878655	1.771778649	0 278922293	4.062179194	0 075108001	1.084834574	100	94.53054178
Mar 13 09 33 2020	CHA16-1C-144Y-1(56-58.5cm)_17	251.779-S	65.32315028	4 619177985	0.072182086	2 551176121	4.235233769	15 98098026	1.754741174	0 306439263	3.938125044	0 076231572	1.142562449	100	98.77797064
Mar 13 09 37 2020	CHA16-1C-144Y-1(56-58.5cm)_18	251.779-S	65.01007399	4.498887973	0.089948731	2 853545964	4.262127899	16 26965357	1.64878225	0 383923286	3.846083691	0 072165764	1.06480688	100	96.72176424
Mar 13 09:41 2020	CHA16-1C-144Y-1(56-58.5cm)_19	251.779-S	65.09512495	4 621370314	0.053366234	2 900778232	4.259205911	16.18461547	1.62708856	0 310349319	3.739679254	0 047301889	1.161119872	100	98.93896638
Mar 13 09:45 2020	CHA16-1C-144Y-1(56-58.5cm)_20	251.779-S	65.05688093	4 587401395	0.058964044	3 028974867	4.398593706	16 02791503	1.750038412	0 204788396	3.644866423	0 094604982	1.146971816	100	99.04341012
Mar 13 09:49 2020	CHA16-1C-144Y-1(56-58.5cm)_21	251.779-S	65.20264304	4 881783671	0.056434903	2 566134112	4.244517999	16.12057486	1.639841338	0 327813031	3.809105322	0 071370605	1.079781119	100	99.76095903
Mar 13 09 53 2020	CHA16-1C-144Y-1(56-58.5cm)_22	251.779-S	65.36761999	4 619571359	0.050099746	2 640527706	4.281980326	16 08690768	1.622916711	0 271406516	3.86541128	0 074999019	1.118559664	100	99.60130296
Mar 13 09 57 2020	CHA16-1C-144Y-1(56-58.5cm)_23	251.779-S	65.27153178	4.702870356	0.051673274	2 583663693	4.215952794	16.15761112	1.634829606	0 273954194	3.880522123	0 080726924	1.146664128	100	99.47115047
Mar 13 10 01 2020	CHA16-1C-144Y-1(56-58.5cm)_24	251.779-S	64.99231658	4.745149815	0.106315382	2 598820455	4.21933375	16 26259344	1.698871471	0 333813541	3.898230683	0 041237482	1.103317411	100	93.11916855
Mar 13 10 05 2020	CHA16-1C-144Y-1(56-58.5cm)_25	251.779-S	65.87220463	4 543231786	0.044588373	2 583625341	3.99774298	16 29091618	1.694132952	0 218957879	3.625409753	0 03875438	1.090435744	100	95.98914985
Mar 13 10 09 2020	CHA16-1C-144Y-1(56-58.5cm)_26	251.779-S	65.28887909	4 612897937	0.069084665	2 590674937	4.29850913	15.9792272	1.634321722	0 332312697	3.970261997	0 049180699	1.174649929	100	94.95595008
Mar 13 10:16 2020	CHA16-1C-144Y-1(56-58.5cm)_28	251.779-S	66.21651972	4 963294714	0.051981941	2 599097055	3.904851469	16 23682455	1.07279956	0 318153725	3.493186443	0 051046266	1.092244547	100	96.18725067
Mar 13 10 20 2020	CHA16-1C-144Y-1(56-58.5cm)_29	251.779-S	65.1146567	4 831993205	0.066933136	2 561638536	4.237082085	16 00942929	1.74006485	0 338269092	3.976737244	0 054021651	1.069174213	100	96.8130345
Mar 13 10 24 2020	CHA16-1C-144Y-1(56-58.5cm)_30	251.779-S	65.37754551	4 609166278	0.039710416	2.58531352	4.294662462	16 07920885	1.691747932	0 250466729	3.898652789	0 08179932	1.091726193	100	96.70007062
Mar 13 10 28 2020	CHA16-1C-144Y-1(56-58.5cm)_31	251.779-S	65.51726176	4 644825059	0.025509123	2 571401529	4.014695121	16.18196955	1.665964763	0 331971984	3.85197998	0 062799567	1.131621565	100	97.61213763
29/09/2021	1C-146Y-1-64 5-77cm	255.175-S	55.450661	3 693098248	0.095896417	1 810342278	7.882747521	16 05514981	4.384253011	0 679447319	7.971096835	0.135930843	1.841376717	100	
29/09/2021	1C-146Y-1-64 5-77cm	255.175-S	54.95008434	3.97981755	0.061953861	1.743734494	7.221112256	16.79113745	4.671093853	0 594203172	8.267951106	0.14657627	1.57233565	100	
29/09/2021	1C-146Y-1-64 5-77cm	255.175-S	54.75583463	3 997170293	0.087201695	1.461880695	7.452524664	16.7758477	4.655464827	0 62850647	8.371405749	0.126560021	1.687603253	100	
29/09/2021	1C-146Y-1-64 5-77cm	255.175-S	54.79045861	4 002684316	0.086979451	1 537927053	7.39427179	16.6625739	4.710795754	0 608245057	8.491020786	0.136885693	1.578157595	100	
29/09/2021	1C-146Y-1-64 5-77cm	255.175-S	54.91892277	4 017804029	0.06949161	1 639920012	7.410388553	16.73743362	4.730211045	0 599903239	8.221245827	0.111412066	1.543267226	100	
29/09/2021	1C-146Y-1-64 5-77cm	255.175-S	54.56585182	4 068339301	0.081974001	1 528157299	7.519343533	16 62756585	4.742731925	0 576246865	8.526943583	0.166984076	1.595861752	100	
29/09/2021	1C-146Y-1-64 5-77cm	255.175-S	54.74809244	4 079151265	0.077493651	1.410834272	7.411991648	16 65397847	4.739013483	0 660025077	8.45250311	0.14864877	1.618267804	100	
29/09/2021	1C-146Y-1-64 5-77cm	255.175-S	54.64881319	4.12428995	0.094284141	1 620989583	8.022872491	15 89185357	4.807957295	0 663374598	8.168476755	0.151429153	1.805659282	100	
29/09/2021	1C-146Y-1-64 5-77cm	255.175-S	54 6372149	4.133675785	0.081142525	1 500371211	7.450823021	16 68780224	4.710415556	0 595351379	8.529217786	0.128603247	1.545382347	100	
29/09/2021	1C-146Y-1-64 5-77cm	255.175-S	55.39797991	4.135839699	0.073457451	1.759275096	7.911593853	15 60713638	4.486018358	0 693113235	7.957893325	0.115536019	1.862156681	100	
29/09/2021	1C-146Y-1-64 5-77cm	255.175-S	67.13112416	4.143264463	0.151355988	2.59708997	4.09494651	15 66709624	1.229278203	0 36467975	3.432301489	0 072839314	1.116023918	100	
29/09/2021	1C-146Y-1-64 5-77cm	255.175-S	54.43889393	4.145566291	0.100604562	1 625308868	8.147117872	15 65645631	4.70548932	0.788892007	8.322179454	0.156153093	1.913338288	100	
29/09/2021	1C-146Y-1-64 5-77cm	255.175-S	66.49333297	4.153434126	0.116013461	2 359411532	3.990341163	16.0374747	1.486981415	0 241051399	4.119263695	0 074805306	0.927890231	100	
29/09/2021	1C-146Y-1-64 5-77cm	255.175-S	66.07620696	4.15884729	0.143532362	2 397998298	3.822895838	16 38052944	1.646860741	0 270614687	4.011714771	0 039850793	1.050948819	100	
29/09/2021	1C-146Y-1-64 5-77cm	255.175-S	54.64221663	4.160790271	0.069210197	1.54368386	7.432173285	16 69427644	4.75967445	0 606637088	8.401770676	0.107751178	1.581815918	100	
29/09/2021	1C-146Y-1-64 5-77cm	255.175-S	54.99597151	4.164756994	0.074392588	1 627018089	8.370445261	15 32876161	4.691237322	0 628397364	8.127098872	0.170478751	1.821441634	100	
29/09/2021	1C-146Y-1-64 5-77cm	255.175-S	54 6271373	4 210971009	0.074681317	1.440862369	7.447837882	16 68153335	4.734556088	0 571981773	8.439294363	0.154436093	1.61670846	100	
29/09/2021	1C-146Y-1-64 5-77cm	255.175-S	54.60634124	4 221105059	0.086654416	1 522033074	7.427521402	16 64089494	4.703529372	0 554121508	8.529367589	0 086045603	1.622385788	100	
29/09/2021	1C-146Y-1-64 5-77cm	255.175-S	54 5709495	4 225224568	0.070522468	1.418614046	7.440069347	16 86007484	4.658081707	0 536521873	8.488313983	0.121755867	1.609871795	100	
29/09/2021	1C-146Y-1-64 5-77cm	255.175-S	65.73081889	4 244243316	0.098148127	2 376776257	4.180579666	16 24484129	1.433062631	0 336356283	4.135059695	0 084460442	1.135653405	100	
29/09/2021	1C-146Y-1-64 5-77cm	255.175-S	54.39866061	4 267556788	0.081973933	1.473688675	7.562888408	16.4561902	4.670903564	0 670221329	8.612647864	0.145015059	1.660253568	100	
29/09/2021	1C-146Y-1-64 5-77cm	255.175-S	54.36784195	4 272915754	0.042933603	1.482231541	7.400935421	16 89743957	4.738480285	0 584510342	8.52214979	0.108254014	1.582307726	100	
29/09/2021	1C-146Y-1-64 5-77cm	255.175-S	54.47054725	4 273260635	0.094542067	1.478813346	7.434861581	16.76668373	4.654821226	0 533392676	8.623242254	0.114531544	1.555303692	100	
29/09/2021	1C-146Y-1-64 5-77cm	255.175-S	65.28601205	4 310442436	0.065396173	2.408776655	4.035757379	16.49166824	1.763549951	0 31229578	4.221444809	0 037716371	1.066940151	100	
29/09/2021	1C-146Y-1-64 5-77cm	255.175-S	54.77648403	4 338632282	0.103861127	1.42233464	7.357256158	16.597315	4.670298441	0 505082286	8.510576255	0.155535874	1.562623905	100	
29/09/2021	1C-146Y-1-64 5-77cm	255.175-S	65.38195641	4 369678744	0.109718084	2 359414915	4.094590009	16.46300273	1.639596025	0 247791468	4.133700899	0 086229738	1.114320981	100	
29/09/2021	1C-146Y-1-64 5-77cm	255.175-S	55.31425848	4 392717647	0.10012509	1.752962441	8.39359663	15.18890398	4.296616883	0 624570206	7.843727072	0.153951349	1.938570229	100	
29/09/2021	1C-146Y-1-64 5-77cm	255.175-S	54.30029735	4.408953383	0.073414674	1.445892334	7.453473156	16.7194029	4.719963501	0 600961729	8.589307112	0.115060446	1.573273412	100	
29/09/2021	1C-146Y-1-64 5-77cm	255.175-S	65 9266358	4.44565763	0.086902022	2.413356999	4.286884143	15.6656507	1.574091465	0 32739093	4.145926857	0 054300532	1.073202922	100	
29/09/2021	1C-146Y-1-64 5-77cm	255.175-S	65.51481902	4.450867573	0.231317946	2 390751725	4.132948461	16 08670709	1 6409515	0 280023154	4.140330161	0 051375729	1.079907641	100	
29/09/2021	1C-146Y-1-64 5-77cm	255.175-S	65.63895861	4.454940887	0.085983474	2.419583279	4.143406559	16 23093848	1.548306772	0 278927068	4.026443505	0.100002519	1.072508846	100	
29/09/2021	1C-146Y-1-64 5-77cm	255.175-S	64.86035686	4 532975678	0.078183434	2 308074772	4.325041014	16.2189038	1.800634031	0 309614715	4.410722765	0 090139677	1.065353252	100	
29/09/2021	1C-146Y-1-64 5-77cm	255.175-S	65.14451778	4 536850916	0.072569316	2.405444445	3.998924521	16 23928739	1.830205619	0 281548645	4.295845794	0 077238111	1.117567459	100	
29/09/2021	1C-146Y-1-64 5-77cm	255.175-S	66.07858085	4 568911434	0.109304101	2.404690228	3.913086826	15.8600251	1.632822308	0 328021608	3.925384899	0.102964463	1.076208181	100	
29/09/2021	1C-146Y-1-64 5-77cm	255.175-S	65.79163964	4 616882729	0.08504784	2 387678482	4.247109513	15 63612458	1.622573431	0 265180221	4.148536204	0 063495344	1.135732022	100	
29/09/2021	1C-146Y-1-64 5-77cm	255.175-S	64.73490216	4 632513453	0.057749206	2.400103124	4.244723865	16 25572028	1.815193694	0 309078782	4.446387222	0 071793478	1.031834727	100	
29/09/2021	1C-146Y-1-64 5-77cm	255.175-S	65.90820228	4 634126269	0.090465745	2 396233857	4.042984877	16.10860293	1.456672714	0 272136162	4.051327483	0 062703212	0.976544467	100	
29/09/2021	1C-146Y-1-64 5-77cm	255.175-S	64.87860623	4 640897811	0.072514028	2.455117815	4.205813641	16 37781125	1.794124373	0 304040962	4.118825983	0 075310998	1.076936912	100	
29/09/2021	1C-146Y-1-64 5-77cm	255.175-S	65.41597196	4 643286966	0.072116995	2.41732944	3.857654898	16.47812902	1.672496402	0 327447417	4.014674787	0 072419161	1.028472955	100	
29/09/2021	1C-146Y-1-64 5-77cm	255.175-S	64.73422369	4 658579686	0.079487645	2 374567615	4.125308145	16 59178813	1.80411758	0.185236397	4.308307302	0 076368509	1.062015304	100	

Date Analysed	Core Section Identifier	sample_no	SiO2	Na2O	Cl	K2O	FeOt	Al2O3	MgO	P2O5	CaO	MnO	TiO2	total	Analytical Total
29/09/2021	1C-146Y-1-64 5-77cm	255.175-S	65.88744584	4.710401509	0.071807454	2.438941226	4.050945297	16 00489757	1.474954516	0 203489345	4.151603531	0 046475962	0.959037747	100	
29/09/2021	1C-146Y-1-64 5-77cm	255.175-S	65.09595339	4.721778838	0.062260624	2 350443006	4.32481513	16 09792298	1.595109582	0 31767543	4.21536243	0.117731079	1.100947504	100	
29/09/2021	1C-146Y-1-64 5-77cm	255.175-S	65.43100542	4.728291286	0.080497308	2.454057222	4.284022306	15 91963845	1.666041529	0 243290156	4.03879743	0 07150615	1.082852749	100	
29/09/2021	1C-146Y-1-64 5-77cm	255.175-S	64.68869527	4.775752673	0.048675941	2.428694735	4.061430692	16 26613197	1.798546665	0 247155405	4.50036671	0.117761081	1.066788856	100	
29/09/2021	1C-146Y-1-64 5-77cm	255.175-S	65.34082582	4 813496079	0.09104921	2.432851597	4.145244996	15.72478329	1.708062419	0.406589018	4.079428154	0 079876887	1.177792533	100	
29/09/2021	1C-146Y-1-64 5-77cm	255.175-S	65.08624556	4 816819737	0.085825114	2 500256008	4.163691637	16 06286921	1.575732979	0 278702006	4.269024602	0 061741016	1.099092131	100	
29/09/2021	1C-146Y-1-64 5-77cm	255.175-S	65.40080494	4 818971892	0.077812836	2.440777971	4.172270036	16 09453166	1.685263635	0 297900081	3.962028115	0 039949486	1.009689349	100	
29/09/2021	1C-146Y-1-64 5-77cm	255.175-S	65.25011847	4 842658943	0.091857594	2.497792508	4.210564513	16 00626219	1.555588547	0 242234898	4.134057397	0 077686445	1.091178498	100	
29/09/2021	1C-146Y-1-64 5-77cm	255.175-S	65.57074067	4 891860739	0.076304665	2 508646533	4.546921841	15.41772348	1.591170055	0 25201445	3.887890172	0 087279994	1.169447392	100	
29/09/2021	1C-146Y-1-64 5-77cm	255.175-S	65.50953984	4 921541856	0.089061375	2.409290365	4.169925631	15 81482906	1.500831205	0 30249979	4.144554505	0 036757122	1.10116925	100	
29/09/2021	1C-146Y-1-64 5-77cm	255.175-S	65.02290917	5 023727215	0.064708914	2.470516059	4.341492655	15 88779574	1.706547766	0 320650243	4.079380142	0 035662261	1.046609837	100	
30/09/2021	1C-146Y-1-72-73cm	255.175-S	65.71508538	4 339420705	0.246993009	2.425355983	3.933009702	16.13844981	1.62264654	0 321326893	4.022615827	0.10553576	1.129560386	100	
30/09/2021	1C-146Y-1-72-73cm	255.175-S	65 5611246	4 393707975	0.096258288	2 281756557	4.096548981	16 04658565	1.748318287	0 287819711	4.292982419	0 080020672	1.114876867	100	
30/09/2021	1C-146Y-1-72-73cm	255.175-S	65.45770571	4.402259955	0.085380393	2 377007191	4.34896383	16 09542986	1.708072804	0 270104763	4.038324956	0 089644083	1.127106459	100	
30/09/2021	1C-146Y-1-72-73cm	255.175-S	65.84399155	4.424068019	0.070885635	2.32263571	4.092262918	16 00708247	1.672969885	0 255489928	4.087057437	0.102960128	1.12059632	100	
30/09/2021	1C-146Y-1-72-73cm	255.175-S	65.68354252	4.491289358	0.1172666	2.411790228	4.126841056	15 89637737	1.65377814	0 269906124	4.156176375	0 091219266	1.101812967	100	
30/09/2021	1C-146Y-1-72-73cm	255.175-S	65.72360092	4 503101808	0.09292283	2.405186142	4.026302793	15 93568263	1.696787213	0 345732263	4.024648636	0 067917371	1.178117388	100	
30/09/2021	1C-146Y-1-72-73cm	255.175-S	65.31462171	4 531113813	0.083643073	2.448089928	4.466690394	15 86963558	1.740919925	0 271866829	4.110253914	0 083320955	1.079843877	100	
30/09/2021	1C-146Y-1-72-73cm	255.175-S	65.56559059	4 591696522	0.068210726	2.444132447	4.448525583	15.5442733	1.729476067	0 201052903	4.197247433	0 075880597	1.133913831	100	
30/09/2021	1C-146Y-1-72-73cm	255.175-S	65.31301971	4 626930909	0.093171001	2.455751485	4.215882377	15.9676545	1.749910322	0 305546075	4.149022556	0 077572236	1.04553883	100	
30/09/2021	1C-146Y-1-72-73cm	255.175-S	65.23335929	4 648099524	0.110137416	2 372355646	4.36899886	15 87653394	1.716548763	0 274592115	4.289305223	0 032740655	1.077328564	100	
30/09/2021	1C-146Y-1-72-73cm	255.175-S	64.92664877	4 650674159	0.088775967	2.404790511	4.301079063	15 91187377	1.791591995	0 385825861	4.31664019	0 062397428	1.159702278	100	
30/09/2021	1C-146Y-1-72-73cm	255.175-S	64.94727113	4 677355106	0.077720707	2.43948262	4.405181426	16 20945477	1.647892144	0 238807204	4.1472749	0 070765157	1.138794841	100	
30/09/2021	1C-146Y-1-72-73cm	255.175-S	65.60788976	4 687093849	0.071311541	2.444060224	4.147496137	15.8176192	1.617931939	0 318785864	4.102389383	0 054700395	1.130721715	100	
30/09/2021	1C-146Y-1-72-73cm	255.175-S	65.07487306	4 699759075	0.084405987	2.423642572	4.288793595	15.79582703	1.814291534	0 251110446	4.449681349	0 029505214	1.088110139	100	
30/09/2021	1C-146Y-1-72-73cm	255.175-S	65.32237078	4.701344788	0.162738858	2.418480252	4.215388476	15 85573735	1.680053942	0 267275972	4.203533649	0 052664103	1.120411832	100	
30/09/2021	1C-146Y-1-72-73cm	255.175-S	65 0140118	4.71388151	0.100966246	2.463109257	4.448460254	15.73417207	1.698037644	0 298545829	4.388884183	0 051491724	1.088439487	100	
30/09/2021	1C-146Y-1-72-73cm	255.175-S	65.38849968	4.722891202	0.125838108	2 504083255	4.226300852	15 80636519	1.693094361	0 210258467	4.190548554	0 047968515	1.084151826	100	
30/09/2021	1C-146Y-1-72-73cm	255.175-S	65.22974982	4.732255834	0.071297925	2.41847588	4.208776207	15 90331109	1.702857617	0 30089609	4.286692027	0 059257894	1.086429619	100	
30/09/2021	1C-146Y-1-72-73cm	255.175-S	65.44519089	4.757929115	0.062593201	2.452976788	4.091819039	15 97606865	1.706348287	0 240222554	4.110040312	0 064919299	1.091891866	100	
30/09/2021	1C-146Y-1-72-73cm	255.175-S	65.46450529	4.758187988	0.079760313	2.416020065	4.125169631	16 03646506	1.599687566	0 297729634	4.059514223	0 074801669	1.088158557	100	
30/09/2021	1C-146Y-1-72-73cm	255.175-S	65.33475036	4 804148145	0.129031767	2 391445426	4.12391478	15 87919763	1.725478917	0 297283238	4.110630397	0.100546994	1.103572349	100	
30/09/2021	1C-146Y-1-72-73cm	255.175-S	64.76958963	4 825054382	0.090933717	2.474386862	4.412656571	15 85669581	1.743588839	0 333629829	4.312872525	0 051652826	1.128939006	100	
30/09/2021	1C-146Y-1-72-73cm	255.175-S	65 2909592	4 855138642	0.085567886	2.495730014	4.142072923	15 89717102	1.690184865	0 277990768	4.107291796	0 068580144	1.089312747	100	
30/09/2021	1C-146Y-1-72-73cm	255.175-S	64.899351	4.88552991	0.084461704	2.49451845	4.316241467	15 66060753	1.75048099	0 239825695	4.452465603	0 093052784	1.123464865	100	
30/09/2021	1C-146Y-1-72-73cm	255.175-S	64.84903182	4 922946715	0.10429278	2 394947051	4.247448829	15 90490477	1.711697574	0 289747654	4.382421991	0 078193998	1.114366816	100	
30/09/2021	1C-146Y-1-72-73cm	255.175-S	65.10400373	4 940897478	0.078638284	2.434042126	4.18155955	15 96690027	1.707317781	0 279290731	4.146083114	0.0809267	1.080340236	100	
30/09/2021	1C-146Y-1-72-73cm	255.175-S	64.93276442	4.95356254	0.080339292	2.497594558	4.204284172	15 97419853	1.690922834	0 253193648	4.291720053	0 047870562	1.073549394	100	
30/09/2021	1C-146Y-1-72-73cm	255.175-S	65.05481247	4 966109593	0.09452301	2.472621793	4.194067345	15 97292812	1.609111611	0.18737674	4.271710865	0.108503235	1.068235213	100	
30/09/2021	1C-146Y-1-72-73cm	255.175-S	65.68724805	5 018685991	0.067158765	2 519755207	3.821281657	16 08686692	1.524861754	0 263845442	3.893378276	0 044668388	1.072249551	100	
30/09/2021	1C-146Y-1-72-73cm	255.175-S	65 0566465	5 050074217	0.083059105	2.489757149	4.092475314	16 03726164	1.633841215	0 267422094	4.107281721	0.107150277	1.075030769	100	
Jan 25 18:00 2020	CHA16-1C-147Y-1(16-19cm)_1	256.120-S	74.86492038	4 542365955	0.07528551	2.66022821	1.267720411	14.41618875	0.352033362	0 039955997	1.535151457	0 004626484	0.241523486	100	95.10462262
Jan 25 18:12 2020	CHA16-1C-147Y-1(16-19cm)_4	256.120-S	74.70824861	4.761231939	0.074413956	2.69067412	1.377278685	14 22436721	0.344111995	0 057387034	1.524014638	0 014294206	0 2239776	100	95.14344309
Jan 25 18:16 2020	CHA16-1C-147Y-1(16-19cm)_5	256.120-S	74.56423767	4 667591268	0.038150632	2.706776671	1.389069702	14.3907464	0.367333039	0	1.59849016	0 041560744	0.236043714	100	93.83855074
Jan 25 18:20 2020	CHA16-1C-147Y-1(16-19cm)_6	256.120-S	74.65962449	4 832098625	0.088817568	2 622232952	1.322174029	14 22659332	0.301345319	0 05572245	1.607175035	0 041236728	0.242979489	100	94.5758842
Jan 25 18:23 2020	CHA16-1C-147Y-1(16-19cm)_7	256.120-S	74.49185689	4 830240115	0.068897271	2.707057647	1.294476856	14 25233107	0.413914422	0 08110557	1.603002763	0 053716516	0.20340088	100	94.19821566
Jan 25 18:27 2020	CHA16-1C-147Y-1(16-19cm)_8	256.120-S	74 6954182	4 546861527	0.070317742	2 675246433	1.407101895	14.4456122	0.334247193	0 034471555	1 5438181	0 041344718	0.205560437	100	94.57072696
Jan 25 18:51 2020	CHA16-1C-147Y-1(16-19cm)_14	256.120-S	74.83676984	4.60453286	0.072371929	2 674614759	1.333727123	14.41139782	0.324624811	0 012796196	1.499882002	0 015733028	0.213549633	100	95.34083333
Jan 25 18:59 2020	CHA16-1C-147Y-1(16-19cm)_16	256.120-S	75.11501325	4 521316587	0.094467122	2 806711021	1.315821148	14.0394534	0.298144789	0 07415396	1.471830523	0 042264481	0.220823723	100	91.56624891
Jan 25 19:02 2020	CHA16-1C-147Y-1(16-19cm)_17	256.120-S	74.71061248	4 633216278	0.064135725	2 670534382	1.416293163	14 24072351	0.396611893	0 058773206	1.630205727	0 040755143	0.138138485	100	93.23976566
Jan 25 19:18 2020	CHA16-1C-147Y-1(16-19cm)_21	256.120-S	74.18701245	4.796119731	0.049120699	2 540362319	1.488347696	14 60749046	0.400765873	0 029303765	1.65492483	0 03267686	0.213875317	100	94.86835724
Jan 25 19:22 2020	CHA16-1C-147Y-1(16-19cm)_22	256.120-S	74.09440346	4.72693271	0.089416921	2 614217864	1.528290051	14.5665203	0.389785219	0 050150302	1.675233488	0	0.265049681	100	93.71827932
Jan 25 19:26 2020	CHA16-1C-147Y-1(16-19cm)_23	256.120-S	74.41259149	4 338864303	0.071922554	2 821330483	1.443818675	14 53663893	0.411871503	0 080685777	1.624402399	0 028320173	0.229553707	100	93.57287336
Jan 25 19:30 2020	CHA16-1C-147Y-1(16-19cm)_24	256.120-S	74 2179629	4 683657853	0.080003658	2.723303322	1.420848599	14.47623323	0.372255431	0 040584637	1.684845246	0 055101857	0.245203264	100	94.37068503
Jan 25 19:34 2020	CHA16-1C-147Y-1(16-19cm)_25	256.120-S	75.09658574	4.60184278	0.067549986	2 839210339	1.312742629	14.11826379	0.302708374	0 040318898	1.416122123	0 010660232	0.193995115	100	94.74465357
Jan 25 19:38 2020	CHA16-1C-147Y-1(16-19cm)_26	256.120-S	75.1977475	4.744830829	0.056207996	2 680047304	1.292773719	14.0720624	0 2716546	0.106263354	1.378503708	0	0.199908587	100	95.8938298
Jan 25 19:45 2020	CHA16-1C-147Y-1(16-19cm)_28	256.120-S	74.10344574	4 535421146	0.076195075	2 593193738	1 5176363	14.79904134	0.399330492	0 031908022	1.718124246	0 052184022	0.173519877	100	93.70684359
Feb 15 01:47 2020	CHA16-1B-169Y-1(100-101.5cm)_1	275.230-G	77.819675	3.453728402	0.099865351	5.109145056	0.669158958	12 32515405	0.017381628	0 000210686	0.362064568	0 060677681	0.082938612	100	94.92781956
Feb 15 01 51 2020	CHA16-1B-169Y-1(100-101.5cm)_2	275.230-G	77 6372222	3 535956465	0.10946025	5 050386048	0.72606789	12.43578322	0.053990529	0	0.363987028	0 064344877	0.022801499	100	94.6462301
Feb 15 01 55 2020	CHA16-1B-169Y-1(100-101.5cm)_3	275.230-G	77.4833277	3 064175364	0.111505946	5.496027655	0.830015556	12 37663151	0.045342228	0 038049422	0.38746995	0 063838475	0.103616196	100	94.61378884
Feb 15 01 59 2020	CHA16-1B-169Y-1(100-101.5cm)_4	275.230-G	77.61417962	2 558300515	0.115769224	6.157255109	0.744712227	12 30382054	0.02063108	0	0.356287001	0 07525534	0.053789349	100	93.5481785
Feb 15 02 03 2020	CHA16-1B-169Y-1(100-101.5cm)_5	275.230-G	77.33493037	2.731551001	0.119460574	6.172830713	0.790442614	12.3982409	0	0	0.347970985	0 010831372	0.093741464	100	95.09413547
Feb 15 02 07 2020	CHA16-1B-169Y-1(100-101.5cm)_6	275.230-G	77.83059498	3 063128288	0.10477506	5 509998086	0.730545922	12 26453242	0.009254244	0	0.378998517	0 063184148	0.044988337	100	94.01092195

Date Analysed	Core Section Identifier	sample_no	SiO2	Na2O	Cl	K2O	FeOt	Al2O3	MgO	P2O5	CaO	MnO	TiO2	total	Analytical Total
Feb 15 02:11 2020	CHA16-1B-169Y-1(100-101.5cm)_7	275.230-G	77.60038952	2 835449264	0.121316433	5 955342673	0.650981988	12 34207943	0.02830366	0	0.356373598	0 081123131	0.028640309	100	95.04071068
Feb 15 02:14 2020	CHA16-1B-169Y-1(100-101.5cm)_8	275.230-G	77.77872015	2 653451861	0.105531973	5 958465295	0.707360203	12 33654082	0.022868758	0 011329476	0.342716657	0 047520859	0.035493949	100	95.32656009
Feb 15 02:18 2020	CHA16-1B-169Y-1(100-101.5cm)_9	275.230-G	77.92249039	3 695451211	0.089364891	4 677530029	0.734806483	12.42109205	0.005022851	0	0.343542082	0 071889555	0.038810462	100	95.56325608
Feb 15 02 22 2020	CHA16-1B-169Y-1(100-101.5cm)_10	275.230-G	78.15786647	3 574131302	0.099280804	4.67975598	0.79202258	12 20235438	0	0 006997766	0.384877127	0 069868319	0.032845271	100	91.45776015
Feb 15 02 26 2020	CHA16-1B-169Y-1(100-101.5cm)_11	275.230-G	77.84459417	3 365585252	0.108681352	5.07457513	0.724984993	12 31652526	0.037720661	0 006773047	0.338443943	0 074086713	0.108029475	100	95.96862546
Feb 15 02 30 2020	CHA16-1B-169Y-1(100-101.5cm)_12	275.230-G	77 6414807	2 942173197	0.097892691	5 816659334	0.755122216	12 24448939	0.019810361	0 006743953	0.334563286	0 069757762	0.071307102	100	94.89983311
Feb 15 02 34 2020	CHA16-1B-169Y-1(100-101.5cm)_13	275.230-G	77 8468973	3.19931539	0.094033796	5.463416055	0.726028856	12 22964671	0.00147092	0 011662292	0.319399708	0 041816146	0.06631283	100	95.17854668
Feb 15 02 38 2020	CHA16-1B-169Y-1(100-101.5cm)_14	275.230-G	77.94238892	3.471800008	0.094600672	5 046776933	0.719699539	12 21573412	0.026078534	0 007496259	0.354435777	0 03431386	0.086675377	100	94.71391471
Feb 15 02:42 2020	CHA16-1B-169Y-1(100-101.5cm)_15	275.230-G	78.00470512	3.429733615	0.101552615	4 925038721	0.700067145	12 29154963	0.008734577	0 008734577	0.369588376	0 072191807	0.088103821	100	95.02463361
Feb 15 02:46 2020	CHA16-1B-169Y-1(100-101.5cm)_16	275.230-G	77.25192683	2 960433379	0.076390066	6.14898061	0.729857417	12 32944064	0.019307379	0	0.338718591	0 060965149	0.083979931	100	95.3003493
Feb 15 02:49 2020	CHA16-1B-169Y-1(100-101.5cm)_17	275.230-G	77.80566089	2 310762701	0.115672074	6 326815124	0.728727589	12.19562848	0.013420517	0 017680998	0.33689758	0 072960747	0.075773297	100	93.88610041
Feb 15 02 57 2020	CHA16-1B-169Y-1(100-101.5cm)_19	275.230-G	77 5778857	3.152361772	0.117368263	5 688983253	0.714151042	12.1590143	0.046018492	0	0.36086519	0 057100927	0.126251065	100	94.74452218
Feb 15 03 01 2020	CHA16-1B-169Y-1(100-101.5cm)_20	275.230-G	77.46997956	2 636358252	0 0898378	6.22116224	0.71026379	12 32633671	0.024357432	0 006010275	0.380650774	0 062317066	0.072726096	100	94.83758456
Feb 15 03 05 2020	CHA16-1B-169Y-1(100-101.5cm)_21	275.230-G	77.70214999	2 898296857	0.111586205	5.716161272	0.667951743	12.42186059	0.045055562	0	0.342022246	0 038634092	0.056281441	100	94.99382088
Feb 15 03 09 2020	CHA16-1B-169Y-1(100-101.5cm)_22	275.230-G	77.44553501	2.758585984	0.102774903	6 261363303	0.621908537	12 31190629	0.002951484	0 008538223	0.311381603	0 061770352	0.113284309	100	94.86751866
Feb 15 03:13 2020	CHA16-1B-169Y-1(100-101.5cm)_23	275.230-G	77.71360648	3 307426349	0.098317987	5 340859673	0.703095731	12.3081108	0	0	0.352979409	0 052254383	0.123349193	100	95.30300947
Feb 15 03:17 2020	CHA16-1B-169Y-1(100-101.5cm)_24	275.230-G	77.76427329	2 946151637	0.122412807	5 832735672	0.714291447	12.14531249	0.027617524	0	0.328744499	0 065151764	0.053308878	100	93.78103703
Feb 15 03 21 2020	CHA16-1B-169Y-1(100-101.5cm)_25	275.230-G	77.96475662	3.36318537	0.119203163	4 995782432	0.751457751	12.2470447	0.03404299	0	0.339375937	0 070510094	0.114640944	100	94.8800326
Feb 15 03 25 2020	CHA16-1B-169Y-1(100-101.5cm)_26	275.230-G	77 5902027	3 210447321	0.098580912	5.49999774	0.693431411	12 36189968	0.008695235	0 014457137	0.356818901	0 058561881	0.106907082	100	95.45458468
Feb 15 03 29 2020	CHA16-1B-169Y-1(100-101.5cm)_27	275.230-G	77.80482565	3 215837982	0.101894572	5.33083858	0.68391942	12 29870633	0.05498739	0 027913446	0.335171229	0 055092328	0.09081307	100	95.2945756
Feb 15 03 32 2020	CHA16-1B-169Y-1(100-101.5cm)_28	275.230-G	77.54456722	3.166709307	0.086939743	5.60532553	0.658813522	12 38579352	0.030782493	0 006447684	0.36637406	0 046069744	0.102177181	100	96.15855441
Feb 15 03 36 2020	CHA16-1B-169Y-1(100-101.5cm)_29	275.230-G	77.77852467	3 094941127	0.11699541	5 556758761	0.714492084	12.18091751	0.035789294	0	0.383636113	0 05975347	0.078191562	100	95.55930406
Feb 15 03:48 2020	CHA16-1B-169Y-1(100-101.5cm)_32	275.230-G	77 5175916	3 335967832	0.084631142	5 284235067	0.695760831	12 56960057	0.028349348	0	0.349989376	0 070352242	0.063521995	100	95.94576955
01/10/2021	1B-169Y-1-104.5-105 5cm	275.25-S	77.33	2.57	0.10	6.41	0 80	12.25	0 00	0.05	0 37	0.04	0 08	100	
01/10/2021	1B-169Y-1-104.5-105 5cm	275.25-S	77.50	2.94	0.08	6.02	0.73	12.29	0 04	0.00	0 35	0.01	0 04	100	
01/10/2021	1B-169Y-1-104.5-105 5cm	275.25-S	77.57	3.11	0.09	5.79	0.76	12.05	0 04	0.03	0 39	0.10	0 08	100	
01/10/2021	1B-169Y-1-104.5-105 5cm	275.25-S	77.53	3.16	0.11	5.40	0.71	12.48	0 09	0.03	0.41	0.07	0 00	100	
01/10/2021	1B-169Y-1-104.5-105 5cm	275.25-S	77.74	3.17	0.09	5.48	0 69	12.33	0 00	0.00	0 39	0.05	0 05	100	
01/10/2021	1B-169Y-1-104.5-105 5cm	275.25-S	77.63	3.20	0.09	5.66	0.73	12.12	0 03	0.04	0.40	0.05	0 07	100	
01/10/2021	1B-169Y-1-104.5-105 5cm	275.25-S	77.69	3.22	0.09	5.51	0 68	12.30	0 01	0.00	0 37	0.08	0 06	100	
01/10/2021	1B-169Y-1-104.5-105 5cm	275.25-S	77.79	3.24	0.09	5.40	0 59	12.43	0 02	0.01	0 35	0.04	0 03	100	
01/10/2021	1B-169Y-1-104.5-105 5cm	275.25-S	77.59	3.30	0.08	5.49	0.71	12.34	0 05	0.01	0 36	0.04	0 04	100	
01/10/2021	1B-169Y-1-104.5-105 5cm	275.25-S	77.29	3.30	0.10	5.87	0.73	12.22	0 03	0.01	0 38	0.05	0 03	100	
01/10/2021	1B-169Y-1-104.5-105 5cm	275.25-S	77.91	3.31	0.14	5.27	0 82	11.85	0 06	0.05	0.44	0.04	0.10	100	
01/10/2021	1B-169Y-1-104.5-105 5cm	275.25-S	77.95	3.31	0.16	5.04	0.72	12.22	0 05	0.00	0.40	0.05	0 09	100	
01/10/2021	1B-169Y-1-104.5-105 5cm	275.25-S	77.25	3.32	0.07	5.67	0.71	12.43	0 00	0.01	0.40	0.07	0 07	100	
01/10/2021	1B-169Y-1-104.5-105 5cm	275.25-S	77.44	3.40	0.11	5.38	0 63	12.53	0 00	0.00	0.42	0.03	0 07	100	
01/10/2021	1B-169Y-1-104.5-105 5cm	275.25-S	77.84	3.47	0.09	4.96	0.75	12.33	0 02	0.00	0 38	0.02	0.12	100	
01/10/2021	1B-169Y-1-104.5-105 5cm	275.25-S	77.51	3.50	0.12	5.24	0 62	12.48	0 02	0.00	0 36	0.04	0.11	100	
01/10/2021	1B-169Y-1-104.5-105 5cm	275.25-S	77.79	3.52	0.09	4.84	0 61	12.53	0 04	0.00	0 37	0.10	0.10	100	
01/10/2021	1B-169Y-1-104.5-105 5cm	275.25-S	77.41	3.54	0.11	5.24	0.78	12.29	0 02	0.03	0 39	0.04	0.15	100	
01/10/2021	1B-169Y-1-104.5-105 5cm	275.25-S	77.26	3.55	0.08	5.32	0.71	12.51	0 03	0.00	0 36	0.08	0 08	100	
01/10/2021	1B-169Y-1-104.5-105 5cm	275.25-S	77.36	3.67	0.10	5.11	0.73	12.49	0 04	0.00	0 38	0.04	0.10	100	
01/10/2021	1B-169Y-1-104.5-105 5cm	275.25-S	77.67	3.70	0.10	5.12	0.73	12.21	0 02	0.00	0 36	0.03	0 06	100	
01/10/2021	1B-169Y-1-104.5-105 5cm	275.25-S	77.64	3.72	0.08	4.92	0.75	12.30	0 04	0.00	0.40	0.03	0.11	100	
01/10/2021	1B-169Y-1-104.5-105 5cm	275.25-S	77.77	3.77	0.11	4.81	0.72	12.22	0 02	0.02	0.41	0.08	0 08	100	
01/10/2021	1B-169Y-1-104.5-105 5cm	275.25-S	77.81	3.83	0.08	4.67	0.71	12.34	0 02	0.00	0 34	0.11	0 09	100	
01/10/2021	1B-169Y-1-104.5-105 5cm	275.25-S	77.28	3.83	0.11	4.99	0.71	12.56	0 02	0.00	0 39	0.07	0 04	100	
01/10/2021	1B-169Y-1-104.5-105 5cm	275.25-S	77.72	3.86	0.08	4.65	0.73	12.43	0 06	0.00	0 38	0.04	0 06	100	
01/10/2021	1B-169Y-1-104.5-105 5cm	275.25-S	77.54	3.99	0.10	4.62	0.79	12.50	0 00	0.00	0 36	0.05	0 04	100	
01/10/2021	1B-169Y-1-104.5-105 5cm	275.25-S	77.61	4.05	0.08	4.53	0 66	12.52	0 02	0.00	0 36	0.09	0 07	100	
290419	MEXI-CHA16-1C-163Y-1_137 5-138.5cm_4	275.480-S	71.4037	4.819	0.1028	2.2659	2.2059	15.4328	0 64	0.1294	2.5762	0 0979	0.3264	100	91.8274
01/10/2021	1A-164Y-1-5-18.5cm	275.48-OS	72.15	4.63	0.10	2.35	2 28	15.15	0 66	0.12	2.13	0.05	0 38	100	
01/10/2021	1A-164Y-1-5-18.5cm	275.48-OS	71.65	4.76	0.14	2.24	2.16	15.66	0 61	0.10	2 33	0.04	0 31	100	
01/10/2021	1A-164Y-1-5-18.5cm	275.48-OS	71.45	4.76	0.12	2.27	2 23	15.63	0 64	0.12	2 38	0.06	0 34	100	
01/10/2021	1A-164Y-1-5-18.5cm	275.48-OS	71.70	4.77	0.13	2.37	2 22	15.35	0 67	0.12	2 30	0.04	0 33	100	
01/10/2021	1A-164Y-1-5-18.5cm	275.48-OS	72.02	4.79	0.16	2.27	2 04	15.37	0 59	0.14	2 34	0.01	0 27	100	
01/10/2021	1A-164Y-1-5-18.5cm	275.48-OS	71.57	4.81	0.10	2.24	2.15	15.68	0 65	0.15	2 25	0.04	0 37	100	
01/10/2021	1A-164Y-1-5-18.5cm	275.48-OS	71.22	4.82	0.10	2.22	2 24	15.74	0 68	0.15	2.43	0.09	0 30	100	
01/10/2021	1A-164Y-1-5-18.5cm	275.48-OS	71.44	4.83	0.09	2.28	2.12	15.65	0 62	0.16	2.43	0.03	0 34	100	
01/10/2021	1A-164Y-1-5-18.5cm	275.48-OS	71.16	4.83	0.08	2.30	2 24	15.83	0 69	0.13	2 37	0.06	0 30	100	
01/10/2021	1A-164Y-1-5-18.5cm	275.48-OS	71.58	4.84	0.11	2.30	2 26	15.36	0 61	0.12	2.43	0.07	0 32	100	
01/10/2021	1A-164Y-1-5-18.5cm	275.48-OS	71.63	4.91	0.07	2.30	1 97	15.62	0 63	0.11	2 39	0.05	0 32	100	

Date Analysed	Core Section Identifier	sample_no	SiO2	Na2O	Cl	K2O	FeOt	Al2O3	MgO	P2O5	CaO	MnO	TiO2	total	Analytical Total
01/10/2021	1A-164Y-1-5-18.5cm	275.48-OS	71.31	4.92	0.08	2.24	2 21	15.69	0 63	0.16	2 37	0.08	0 31	100	
01/10/2021	1A-164Y-1-5-18.5cm	275.48-OS	71.45	4.93	0.13	2.25	2.16	15.56	0 61	0.14	2.42	0.03	0 33	100	
01/10/2021	1A-164Y-1-5-18.5cm	275.48-OS	71.45	4.93	0.11	2.28	2.15	15.62	0 63	0.13	2 36	0.04	0 29	100	
01/10/2021	1A-164Y-1-5-18.5cm	275.48-OS	71.34	4.96	0.10	2.25	2.14	15.68	0 65	0.11	2.40	0.03	0 34	100	
01/10/2021	1A-164Y-1-5-18.5cm	275.48-OS	71.53	4.96	0.10	2.29	2 07	15.66	0 59	0.12	2 29	0.06	0 31	100	
01/10/2021	1A-164Y-1-5-18.5cm	275.48-OS	71.75	4.97	0.08	2.24	1 88	15.82	0 52	0.09	2 32	0.03	0 29	100	
01/10/2021	1A-164Y-1-5-18.5cm	275.48-OS	71.40	4.97	0.10	2.23	2 31	15.50	0 60	0.21	2 34	0.03	0 31	100	
01/10/2021	1A-164Y-1-5-18.5cm	275.48-OS	71.36	4.97	0.10	2.26	2.15	15.61	0 65	0.15	2 34	0.06	0 34	100	
01/10/2021	1A-164Y-1-5-18.5cm	275.48-OS	71.21	4.99	0.10	2.24	2.16	15.76	0 60	0.13	2 36	0.09	0 35	100	
01/10/2021	1A-164Y-1-5-18.5cm	275.48-OS	71.33	5.00	0.11	2.25	2.18	15.58	0.70	0.11	2 37	0.04	0 34	100	
01/10/2021	1A-164Y-1-5-18.5cm	275.48-OS	71.35	5.02	0.10	2.18	2.17	15.76	0 55	0.10	2 36	0.05	0 34	100	
01/10/2021	1A-164Y-1-5-18.5cm	275.48-OS	71.20	5.03	0.11	2.23	2.19	15.73	0 69	0.10	2.40	0.04	0 28	100	
01/10/2021	1A-164Y-1-5-18.5cm	275.48-OS	71.49	5.04	0.07	2.24	2.10	15.58	0 60	0.06	2.44	0.07	0 31	100	
01/10/2021	1A-164Y-1-5-18.5cm	275.48-OS	71.39	5.07	0.10	2.21	2 09	15.65	0 61	0.12	2 38	0.02	0 36	100	
01/10/2021	1A-164Y-1-5-18.5cm	275.48-OS	71.29	5.08	0.09	2.33	2.17	15.54	0 59	0.12	2.47	0.07	0 27	100	
01/10/2021	1A-164Y-1-5-18.5cm	275.48-OS	71.25	5.13	0.10	2.22	2.11	15.62	0 67	0.14	2 35	0.04	0 36	100	
Feb 15 03 52 2020	CHA16-1A-166Y-1(127-131cm)_1	279.811-OS	74.66449344	4.166357282	0.124090149	3 854315242	1.420441886	13 90269265	0.269697614	0 058911485	1.261165372	0 044601426	0.233233462	100	95.73684996
Feb 15 04 04 2020	CHA16-1A-166Y-1(127-131cm)_4	279.811-OS	73.44520982	4 219033201	0.12527129	3.53867767	1.745275067	14 50122808	0.404270298	0 07507877	1.61708119	0 010710538	0.318164084	100	95.23331353
Feb 15 04 08 2020	CHA16-1A-166Y-1(127-131cm)_5	279.811-OS	73.91907143	4.27113339	0.135375427	3 604423129	1.678198332	14 22908898	0.318216077	0 039397183	1.477394364	0 039082844	0.288618848	100	95.43829559
Feb 15 04:12 2020	CHA16-1A-166Y-1(127-131cm)_6	279.811-OS	73.38544527	4 237981923	0.12468819	3 630162508	1.600489226	14 67848318	0.370907908	0 037774735	1.588853735	0 044193283	0.30102004	100	95.03706769
Feb 15 04:16 2020	CHA16-1A-166Y-1(127-131cm)_7	279.811-OS	74.64078341	4 028133006	0.107610232	3 885038067	1.383123499	14.11386432	0.272271983	0 018520455	1.25236597	0 04076629	0.257522767	100	93.95017338
Feb 15 04:19 2020	CHA16-1A-166Y-1(127-131cm)_8	279.811-OS	74.72119736	4.17362759	0.145338374	3 683161096	1.444000867	13 89556232	0.291932371	0 042272644	1.289211019	0 036936246	0.276760112	100	95.57007984
Feb 15 04 23 2020	CHA16-1A-166Y-1(127-131cm)_9	279.811-OS	74.77580003	4 058520722	0.137131108	3 803943386	1.524252099	13 81819214	0.286871974	0	1.303008232	0 025850002	0.266430308	100	95.16440263
Feb 15 04 31 2020	CHA16-1A-166Y-1(127-131cm)_11	279.811-OS	74.57450415	4 069280944	0.131053695	3.783426633	1.376242622	14 20886891	0.273037289	0 072936058	1.282791819	0 014503135	0.213354745	100	95.15183852
Feb 15 04 35 2020	CHA16-1A-166Y-1(127-131cm)_12	279.811-OS	74.71266459	4.133891987	0.138751571	3 821149366	1.482862482	13 92735862	0.257248963	0 029963658	1.207942573	0 031947314	0.256218881	100	95.7826991
Feb 15 04 39 2020	CHA16-1A-166Y-1(127-131cm)_13	279.811-OS	74.65092673	4.15768411	0.111367722	3 852607402	1.463260305	13 98938589	0.247682656	0 026841937	1.237044869	0 036947137	0.226251239	100	95.00059617
Feb 15 04:43 2020	CHA16-1A-166Y-1(127-131cm)_14	279.811-OS	74.4364286	3.9307388	0.125547987	3.775958844	1.555538367	14.14133606	0.310326702	0 078480713	1.322537518	0 035432667	0.287673737	100	94.54552201
Feb 15 04:47 2020	CHA16-1A-166Y-1(127-131cm)_15	279.811-OS	74.44450235	4 211181637	0.133937126	3.722218334	1.558771285	14 00014143	0.304782765	0 058551749	1.266704357	0 028439421	0.270769545	100	95.64189094
Feb 15 04 51 2020	CHA16-1A-166Y-1(127-131cm)_16	279.811-OS	74.36807702	3 955697066	0.157077398	4 066036178	1.573654301	13 94222405	0.287404557	0 066661593	1.298456553	0 036273323	0.248437961	100	93.45711238
Feb 15 04 54 2020	CHA16-1A-166Y-1(127-131cm)_17	279.811-OS	74.36731545	4.126746456	0.137440359	3 884868825	1.49129164	14 05902529	0.324859031	0 049348334	1.264472304	0 030238979	0.264393331	100	95.24131101
Feb 15 04 58 2020	CHA16-1A-166Y-1(127-131cm)_18	279.811-OS	74.53009176	4 065993996	0.127054055	3.792814302	1.505080843	14 04281659	0.24136091	0 006687056	1.348173084	0 069796142	0.270131265	100	95.70729572
Feb 15 05 02 2020	CHA16-1A-166Y-1(127-131cm)_19	279.811-OS	74.55465197	4 249779732	0.123384092	3 801280118	1.375097497	13 97652994	0.29895703	0 039167886	1.27899425	0 02646195	0.275695539	100	95.2310771
Feb 15 05 06 2020	CHA16-1A-166Y-1(127-131cm)_20	279.811-OS	74.47843872	4.135846065	0.142689135	3 830298302	1.452180554	13 96375233	0.307476144	0 045668941	1.314718324	0 03588274	0.293048755	100	95.03176289
Feb 15 05:10 2020	CHA16-1A-166Y-1(127-131cm)_21	279.811-OS	74.30385354	3 969500677	0.114309391	3 911968129	1.483027619	14 28078688	0.313798734	0 053000859	1.267814187	0 008623156	0.293316827	100	95.09279926
Feb 15 05:14 2020	CHA16-1A-166Y-1(127-131cm)_22	279.811-OS	74.50009731	4 052478643	0.131626119	3 827201223	1.512271982	14.10355368	0.296978128	0 042183792	1.283169648	0.0239993	0.22644017	100	94.58609018
Feb 15 05:18 2020	CHA16-1A-166Y-1(127-131cm)_23	279.811-OS	74.34582165	4 095499357	0.119573358	3 842304577	1.459347185	14.13044251	0.315257941	0 057424607	1.306488537	0 039577837	0.288262435	100	95.2553325
Feb 15 05 22 2020	CHA16-1A-166Y-1(127-131cm)_24	279.811-OS	74.31919031	4 006165421	0.131984368	3 885619795	1.563502768	14 09593051	0.316551308	0 021117499	1.310763156	0 03875061	0.310424256	100	94.70818542
Feb 15 05 26 2020	CHA16-1A-166Y-1(127-131cm)_25	279.811-OS	74.26713299	4.11721363	0.149079029	3.764192327	1.510276592	14 20610437	0.320275347	0 054442556	1.325761297	0 029985939	0.255535914	100	94.04407885
Feb 15 05 30 2020	CHA16-1A-166Y-1(127-131cm)_26	279.811-OS	74.42613251	4 086643147	0.113881532	3 905112783	1.456536123	14 06896038	0.291300305	0 018681215	1.349163695	0 045172656	0.238415658	100	94.74758363
Feb 15 05 37 2020	CHA16-1A-166Y-1(127-131cm)_28	279.811-OS	74 3764208	4 233607732	0.139085773	3 687880345	1.539024789	14 01394531	0.315577189	0 043727724	1.321420211	0 042041836	0.287268295	100	94.90546528
Feb 15 05:41 2020	CHA16-1A-166Y-1(127-131cm)_29	279.811-OS	74.27713738	4.108633286	0.129095533	3.785272899	1.491584117	14 23387743	0.288848648	0.0523473	1.328390949	0 044943598	0.25986886	100	95.89797346
Feb 15 05:45 2020	CHA16-1A-166Y-1(127-131cm)_30	279.811-OS	72.76618471	4 232886191	0.114526396	3.493316549	1 8858769	14 85182485	0.479860369	0 048634497	1.778035369	0 036711201	0.312142964	100	95.61114639
Feb 15 08 27 2020	CHA16-1B-172Y-1(100-100.5cm)_1	280.114-S	78.79090081	3 352167245	0.042914274	3 821563118	1.073561434	11 86146367	0.110052665	0	0.727036721	0 002819186	0.217520886	100	95.77232895
Feb 15 08 31 2020	CHA16-1B-172Y-1(100-100.5cm)_2	280.114-S	78.58382082	3 515148396	0.059239657	3.71823382	1.048306475	11 85843498	0.172887369	0 004726568	0.748163263	0 025523469	0.265515179	100	95.20649243
Feb 15 08 35 2020	CHA16-1B-172Y-1(100-100.5cm)_3	280.114-S	78 9125392	3.405144539	0.02981981	3 817358718	0.979223588	11 66356417	0.179236095	0 018928178	0.735978301	0 014063953	0.244143451	100	94.56800544
Feb 15 08 39 2020	CHA16-1B-172Y-1(100-100.5cm)_4	280.114-S	78.91789507	3.412986489	0.043773801	3 675742602	1.081894276	11.78122629	0.118859483	0	0.737871293	0 012043031	0.217707672	100	95.49090838
Feb 15 08 59 2020	CHA16-1B-172Y-1(100-100.5cm)_9	280.114-S	78.76524741	3 561007358	0.083426487	3.702050348	1.004142306	11.70056476	0.162994498	0	0.735195914	0 034309143	0.251061771	100	95.89280712
Feb 15 09 02 2020	CHA16-1B-172Y-1(100-100.5cm)_10	280.114-S	77.44177093	3 693781403	0.048695989	3.765262236	1.462042926	12 08459863	0.147455242	0 021876384	0.835509587	0 031026602	0.467980078	100	95 079699
Feb 15 09 06 2020	CHA16-1B-172Y-1(100-100.5cm)_11	280.114-S	78.50667133	3 603711861	0.083137135	3 568965867	1.069097421	11 89308451	0.146192334	0	0.74584103	0 025596665	0.357701847	100	96.10627076
Feb 15 09:10 2020	CHA16-1B-172Y-1(100-100.5cm)_12	280.114-S	78.48976674	3 677860306	0.068773109	3 604373785	1.035499586	11.79707397	0.170172015	0 03480085	0.755157738	0 02641136	0.340110544	100	96.54936495
Feb 15 09:14 2020	CHA16-1B-172Y-1(100-100.5cm)_13	280.114-S	78.63865062	3 630060579	0.06751906	3 574538474	1.051998525	11 85241705	0.152701775	0	0.779918307	0	0.252195615	100	95.67668735
Feb 15 09 30 2020	CHA16-1B-172Y-1(100-100.5cm)_17	280.114-S	79.01929638	3 580941204	0.042856088	3 670399708	0.978098293	11 54298999	0.128985353	0 03680827	0.705404944	0 029613452	0.264606313	100	95.90236158
Feb 15 09 34 2020	CHA16-1B-172Y-1(100-100.5cm)_18	280.114-S	77.88895633	3.733250029	0.055663156	3.405151422	1.24035381	12.15523093	0.183646247	0 053976394	0.91443602	0 026355661	0.342980009	100	94.85628097
Feb 15 09 38 2020	CHA16-1B-172Y-1(100-100.5cm)_19	280.114-S	77.96533659	3 699070234	0.063616611	3.433611768	1.184677248	12.16509691	0.205490079	0	0.926443224	0 045289971	0.311367362	100	94.9437566
Feb 15 09:42 2020	CHA16-1B-172Y-1(100-100.5cm)_20	280.114-S	78.1442246	3 662996571	0.048303877	3 396036747	1.17479457	12 08651588	0.186887488	0 043768797	0.917457257	0 035120504	0.303893709	100	94.81640628
Feb 15 09:45 2020	CHA16-1B-172Y-1(100-100.5cm)_21	280.114-S	78.67444974	3 821425661	0.063203504	3.489251314	1.038656091	11 69003659	0.146047106	0 014103261	0.722922727	0 031862924	0.30804108	100	95.72254043
Feb 15 10 01 2020	CHA16-1B-172Y-1(100-100.5cm)_25	280.114-S	77.37307284	3.80539237	0.05652331	3 617911338	1.42607192	12 23797835	0.214662739	0 026111882	0.86693545	0 00209734	0.373242464	100	95.35888744
Feb 15 10 05 2020	CHA16-1B-172Y-1(100-100.5cm)_26	280.114-S	77.49108615	3 884695508	0.024956588	3.791277451	1.316767076	12 04288131	0.244680763	0 017841306	0.816770725	0 015823539	0.353219584	100	94.16351207
Jan 17 09:10 2020	CHA16-1B-173Y-1_70-71cm_1	281.395-OS	55.23482854	3 213120385	0.046580141	0 987451567	8.250094475	15 61294777	5.375408947	0	10.26581859	0.16803205	0.845717535	100	98.9692143
Jan 17 09:30 2020	CHA16-1B-173Y-1_70-71cm_6	281.395-OS	55.36423188	3.146933328	0.07228898	0 988729882	8.106994731	16.1566434	5.157753346	0 004423804	9.893234488	0.15674342	0.952022738	100	99.46191017
Jan 17 09:34 2020	CHA16-1B-173Y-1_70-71cm_7	281.395-OS	54.37091331	2 928938443	0.067971571	0 846443086	8.071946812	16.11308868	5.746779222	0 019593588	10.85727182	0.14846688	0.828586586	100	99.01198185
Jan 17 09:42 2020	CHA16-1B-173Y-1_70-71cm_9	281.395-OS	56.12723114	3 349221471	0.076971566	1 007001259	7.221408971	16 94137784	4.378199151	0	9.906432181	0.143754235	0.848402186	100	99.12751453
Jan 17 09:46 2020	CHA16-1B-173Y-1_70-71cm_10	281.395-OS	55.32862694	3 249525389	0.045674444	0 997193926	7.917751587	16 31249499	5.040285511	0	10.10069192	0.154830327	0.852924961	100	99.39913105

Date Analysed	Core Section Identifier	sample_no	SiO2	Na2O	Cl	K2O	FeOt	Al2O3	MgO	P2O5	CaO	MnO	TiO2	total	Analytical Total
Jan 17 09:49 2020	CHA16-1B-173Y-1_70-71cm_11	281.395-OS	55.30182605	3 398460792	0.046179085	0 935841333	7.277125558	17 21043685	4.757845109	0	10.12541407	0.151631324	0.795239825	100	100.0452913
Jan 17 09:53 2020	CHA16-1B-173Y-1_70-71cm_12	281.395-OS	56.03507192	3.188101562	0.07175727	0 985842164	7.743546942	16.15660003	4.84711366	0 019488395	9.894108295	0.163102876	0.89526689	100	100.0595476
Jan 17 10:13 2020	CHA16-1B-173Y-1_70-71cm_17	281.395-OS	74.41091192	3 601448871	0.154080335	3 937138376	2.060586371	13.18089448	0.286463869	0 034472584	1.607986346	0 03986925	0.686147598	100	90.79679088
Jan 17 10:21 2020	CHA16-1B-173Y-1_70-71cm_19	281.395-OS	73.93348902	4.407718751	0.055304396	3 240284256	1.648982763	14.11678542	0.217579136	0 022246505	1.840014667	0 04282972	0.474765366	100	96.19488537
Jan 17 10:25 2020	CHA16-1B-173Y-1_70-71cm_20	281.395-OS	73.61684363	4.5655104	0.045655104	3 008315416	1.59644571	14.40550911	0.208546731	0 022104507	2.055512601	0 038837826	0.436718959	100	96.81283389
Jan 17 10:29 2020	CHA16-1B-173Y-1_70-71cm_21	281.395-OS	75.50379594	4.101071091	0.059558269	3 352322611	1.864995237	13 06782435	0.211236074	0	1.28647921	0 033282562	0.519434658	100	97.04781778
Jan 17 11:04 2020	CHA16-1B-173Y-1_70-71cm_30	281.395-OS	73.62114269	4 052787938	0.024963557	3.701540163	1.00845101	14 83653272	0.05447513	0	2.213367976	0	0.486738821	100	98.94423447
Jan 17 11:08 2020	CHA16-1B-173Y-1_70-71cm_31	281.395-OS	72.74985603	4 248295926	0.025753393	3 614655706	1.701093485	14 63949275	0.30397115	0 014904523	2.088661004	0	0.61331604	100	98.62778095
Jan 17 11:12 2020	CHA16-1B-173Y-1_70-71cm_32	281.395-OS	76.81490379	3.751862699	0.074307725	3 674837338	1.907481964	12.11057101	0.259086963	0 001250621	0.855737351	0 011568243	0.538392297	100	95.95233857
Jan 17 11:16 2020	CHA16-1B-173Y-1_70-71cm_33	281.395-OS	75.87069756	4 016135407	0.066726416	3.494269169	1.765341414	12 82969613	0.217959015	0 002510085	1.164679268	0 046750326	0.525235209	100	95.61430607
Jan 17 11:20 2020	CHA16-1B-173Y-1_70-71cm_34	281.395-OS	75.97939156	4 245272399	0.041616217	3 595334877	1.786209148	12.43322903	0.281902817	0	1.048979623	0 049981286	0.538083048	100	95.63579481
Jan 17 11:24 2020	CHA16-1B-173Y-1_70-71cm_35	281.395-OS	76.03529679	3 963134427	0.072988597	3.493645439	1.82882243	12.49435771	0.184771993	0 050715572	1.308984611	0 037330844	0.52995159	100	95.63137638
Jan 17 11:28 2020	CHA16-1B-173Y-1_70-71cm_36	281.395-OS	75.18452732	4 302960274	0.066367692	3 277969596	1.663261123	13.18298245	0.239215419	0 012502548	1.541980922	0 025421848	0.502810806	100	95.98043525
Jan 17 11:32 2020	CHA16-1B-173Y-1_70-71cm_37	281.395-OS	75.92225238	4 031998234	0.05953987	3 550941923	1.752509867	12.75314364	0.23690601	0	1.167712649	0	0.524995418	100	95.73416892
Jan 17 11:36 2020	CHA16-1B-173Y-1_70-71cm_38	281.395-OS	74.88464741	4 232757549	0.075144511	3.440885204	1.806594943	13 25431941	0.251666177	0 014631754	1.473626702	0 04044635	0.525279986	100	95.68230529
040319	CHA16-1A-167Y-1_154-155cm_1	281.657-OS	59.4482	4.1701	0.0639	2.0539	7.1785	15 0387	3.3641	0.4823	6.2199	0.1236	1.8566	100	98.3876
040319	CHA16-1A-167Y-1_154-155cm_2	281.657-OS	59.6092	4.1989	0.0597	2.239	7.7019	14.1604	3.1829	0 6084	6.0627	0.1207	2.0562	100	97.8299
040319	CHA16-1A-167Y-1_154-155cm_3	281.657-OS	58.9757	4.3258	0.0571	2.0823	7.7124	14 3773	3.5133	0 5475	6.1976	0.1115	2.0997	100	98.5095
040319	CHA16-1A-167Y-1_154-155cm_4	281.657-OS	59.3512	4.0173	0.0482	2.0136	7 057	15 5388	3.0527	0 5134	6.3066	0.1636	1.9377	100	98.4284
040319	CHA16-1A-167Y-1_154-155cm_5	281.657-OS	59.5086	4.1935	0.1576	2.123	7.1299	14 8372	3.2048	0 5669	6.2115	0.102	1.9649	100	92.5493
040319	CHA16-1A-167Y-1_154-155cm_7	281.657-OS	59.7769	4.3228	0.0521	2.1332	6.9061	14 6312	3.4792	0 5546	6.0982	0 0749	1.9709	100	98.1146
040319	CHA16-1A-167Y-1_154-155cm_9	281.657-OS	59.0563	4.3314	0.0496	2.0827	7.5198	14 5502	3.4603	0 5916	6.1036	0.1458	2.1087	100	98.347
040319	CHA16-1A-167Y-1_154-155cm_10	281.657-OS	59.2067	4.1567	0.0453	2.1182	7.2629	14.751	3.4041	0 5933	6.1855	0.129	2.1474	100	97.9976
040319	CHA16-1A-167Y-1_154-155cm_11	281.657-OS	58.0879	4.3796	0.0621	2.2526	8.2097	14 3151	3.7101	0 6001	6.2375	0.1406	2.0046	100	96.2875
040319	CHA16-1A-167Y-1_154-155cm_12	281.657-OS	59.0918	4.1335	0.0413	2.1581	7.6181	14 6332	3.4406	0 5848	6.0912	0.1677	2.0396	100	98.5024
040319	CHA16-1A-167Y-1_154-155cm_13	281.657-OS	59.5319	4.2428	0.0454	2.0344	7 298	14 5707	3.3622	0.54	6.1864	0.1544	2.0337	100	97.8072
040319	CHA16-1A-167Y-1_154-155cm_15	281.657-OS	58.6156	4.3304	0.0544	2.1019	7.4045	14.7137	3 882	0 5836	6.2318	0.1359	1.9461	100	97.9873
040319	CHA16-1A-167Y-1_154-155cm_16	281.657-OS	59.4497	3.9155	0.0554	2.0906	7.6883	14.4135	3.4662	0 5505	6.2255	0.1152	2.0295	100	97.2968
040319	CHA16-1A-167Y-1_154-155cm_17	281.657-OS	59.5665	4.1085	0.0641	2.1163	7.6818	14 2754	3 388	0 5737	6.2506	0.1715	1.8036	100	98.9934
040319	CHA16-1A-167Y-1_154-155cm_18	281.657-OS	58.5856	4.3861	0.0402	2.0353	7.2651	15 2383	3.6473	0 5378	6.3824	0 0939	1.7881	100	99.2586
040319	CHA16-1A-167Y-1_154-155cm_19	281.657-OS	58.8555	4.0499	0.0404	1.8882	8.5314	14 3434	3.4593	0 3871	6.4967	0.1806	1.7674	100	98.7016
040319	CHA16-1A-167Y-1_154-155cm_20	281.657-OS	59.14	4.301	0.0557	2.104	7.5732	14 5681	3.4286	0 5655	6.1032	0.1181	2.0427	100	98.2105
01/10/2021	1A-168Y-1-25-35 5cm	282.057-OS	76.28	3.51	0.12	3.32	1 23	13.56	0 28	0.03	1.43	0.03	0.19	100	
01/10/2021	1A-168Y-1-25-35 5cm	282.057-OS	76.29	3.53	0.11	3.43	1 23	13.48	0 22	0.02	1.41	0.06	0.19	100	
01/10/2021	1A-168Y-1-25-35 5cm	282.057-OS	76.39	3.54	0.07	3.37	1.10	13.57	0 23	0.07	1 38	0.05	0 21	100	
01/10/2021	1A-168Y-1-25-35 5cm	282.057-OS	76.07	3.73	0.13	3.60	1.18	13.39	0 27	0.06	1 33	0.05	0 20	100	
01/10/2021	1A-168Y-1-25-35 5cm	282.057-OS	75.76	3.76	0.22	3.25	1 52	13.41	0 27	0.12	1.45	0.02	0 20	100	
01/10/2021	1A-168Y-1-25-35 5cm	282.057-OS	76.65	3.83	0.07	3.26	1.10	13.28	0 25	0.05	1 27	0.06	0.18	100	
01/10/2021	1A-168Y-1-25-35 5cm	282.057-OS	76.49	3.84	0.07	3.24	1.16	13.39	0 25	0.06	1 31	0.05	0.13	100	
01/10/2021	1A-168Y-1-25-35 5cm	282.057-OS	75.86	3.86	0.08	3.10	1 23	13.71	0 32	0.09	1 50	0.05	0 21	100	
01/10/2021	1A-168Y-1-25-35 5cm	282.057-OS	76.34	3.86	0.08	3.20	1.10	13.55	0 25	0.09	1 33	0.04	0.15	100	
01/10/2021	1A-168Y-1-25-35 5cm	282.057-OS	76.01	3.90	0.07	3.12	1.40	13.33	0 39	0.01	1.46	0.06	0 24	100	
01/10/2021	1A-168Y-1-25-35 5cm	282.057-OS	76.06	3.94	0.04	2.94	1 26	13.75	0 27	0.11	1.42	0.03	0.18	100	
01/10/2021	1A-168Y-1-25-35 5cm	282.057-OS	76.09	3.94	0.07	2.97	1.19	13.68	0 36	0.00	1.47	0.04	0.17	100	
01/10/2021	1A-168Y-1-25-35 5cm	282.057-OS	76.59	3.94	0.06	3.09	1 07	13.41	0 26	0.00	1 34	0.05	0.18	100	
01/10/2021	1A-168Y-1-25-35 5cm	282.057-OS	76.35	3.95	0.06	3.06	1 21	13.39	0 27	0.11	1 33	0.05	0 21	100	
01/10/2021	1A-168Y-1-25-35 5cm	282.057-OS	76.56	4.00	0.09	3.09	1.19	13.28	0 26	0.03	1 36	0.00	0.15	100	
01/10/2021	1A-168Y-1-25-35 5cm	282.057-OS	76.23	4.02	0.06	2.97	1 23	13.62	0 29	0.01	1 39	0.00	0.17	100	
01/10/2021	1A-168Y-1-25-35 5cm	282.057-OS	76.14	4.03	0.04	3.08	1.15	13.62	0 27	0.10	1.43	0.00	0.15	100	
01/10/2021	1A-168Y-1-25-35 5cm	282.057-OS	76.20	4.05	0.08	2.91	1 22	13.59	0 26	0.02	1 50	0.03	0.15	100	
01/10/2021	1A-168Y-1-25-35 5cm	282.057-OS	75.95	4.05	0.08	3.00	1 28	13.65	0 24	0.06	1.48	0.02	0.17	100	
01/10/2021	1A-168Y-1-25-35 5cm	282.057-OS	76.02	4.06	0.08	3.25	1 23	13.46	0 25	0.06	1.40	0.04	0.16	100	
01/10/2021	1A-168Y-1-25-35 5cm	282.057-OS	76.38	4.06	0.07	3.03	1.16	13.41	0 27	0.03	1 37	0.05	0.17	100	
01/10/2021	1A-168Y-1-25-35 5cm	282.057-OS	76.54	4.08	0.06	3.02	1 09	13.35	0 27	0.01	1 35	0.03	0 20	100	
01/10/2021	1A-168Y-1-25-35 5cm	282.057-OS	75.97	4.11	0.08	3.09	1 28	13.53	0 32	0.03	1 39	0.03	0.17	100	
01/10/2021	1A-168Y-1-25-35 5cm	282.057-OS	75.86	4.11	0.07	3.13	1 21	13.64	0 27	0.07	1 38	0.06	0 21	100	
01/10/2021	1A-168Y-1-25-35 5cm	282.057-OS	75.93	4.14	0.07	3.01	1.12	13.71	0 28	0.04	1.49	0.02	0.18	100	
01/10/2021	1A-168Y-1-25-35 5cm	282.057-OS	76.20	4.14	0.04	3.13	1.18	13.45	0 26	0.02	1.41	0.02	0.16	100	
01/10/2021	1A-168Y-1-25-35 5cm	282.057-OS	76.23	4.15	0.08	3.11	1 20	13.32	0 27	0.09	1 38	0.05	0.13	100	
01/10/2021	1A-168Y-1-25-35 5cm	282.057-OS	75.65	4.19	0.07	2.94	1 27	13.78	0 28	0.04	1 52	0.06	0 21	100	
01/10/2021	1A-168Y-1-25-35 5cm	282.057-OS	75.61	4.20	0.07	3.03	1 22	13.81	0 28	0.05	1 50	0.05	0.18	100	
01/10/2021	1A-168Y-1-25-35 5cm	282.057-OS	76.04	4.23	0.06	3.13	1.16	13.57	0 22	0.03	1 38	0.04	0.13	100	
01/10/2021	1A-168Y-1-25-35 5cm	282.057-OS	75.76	4.27	0.04	2.94	1 24	13.72	0 28	0.00	1.49	0.06	0 21	100	

Date Analysed	Core Section Identifier	sample_no	SiO2	Na2O	Cl	K2O	FeOt	Al2O3	MgO	P2O5	CaO	MnO	TiO2	total	Analytical Total
01/10/2021	1A-168Y-1-25-35 5cm	282.057-OS	76.15	4.36	0.05	2.99	1.16	13.42	0 26	0.03	1.41	0.01	0.17	100	
29/09/2021	1C-168Y-1-13 5-20 5cm	282.057-OS	76.39488297	3 328308211	0.109140283	3.151896115	1.144208854	13 96007719	0.297863891	0 066918988	1.348651515	0 053158845	0.144893135	100	
29/09/2021	1C-168Y-1-13 5-20 5cm	282.057-OS	76.32847575	3.410309699	0.151384479	3 517253209	1.085238972	13 62935619	0.223714186	0 049431667	1.394038309	0 014496787	0.196300753	100	
29/09/2021	1C-168Y-1-13 5-20 5cm	282.057-OS	76 5573046	3.484693283	0.106522062	3 204985461	1.143072633	13.5192114	0.317611917	0 023075895	1.399011498	0 050813588	0.193697667	100	
29/09/2021	1C-168Y-1-13 5-20 5cm	282.057-OS	76.20530468	3.64766585	0.09749216	2 862865016	1.275577694	13 96061203	0.244365828	0 077927407	1.432873418	0 027854903	0.167461023	100	
29/09/2021	1C-168Y-1-13 5-20 5cm	282.057-OS	75 8141397	3.735416633	0.083673333	3.45792854	1.238343977	13 53288083	0.313578222	0 059233035	1.495215375	0 09242488	0.177165475	100	
29/09/2021	1C-168Y-1-13 5-20 5cm	282.057-OS	76.24588959	3.751346104	0.077659446	3 674564166	1.131327009	13 32715063	0.229195624	0 04628854	1.347548939	0	0.169029952	100	
29/09/2021	1C-168Y-1-13 5-20 5cm	282.057-OS	76.22271269	3.754367452	0.065096735	3 060282713	1.196980682	13.76601399	0.261205246	0 070460117	1.420315052	0	0.182565319	100	
29/09/2021	1C-168Y-1-13 5-20 5cm	282.057-OS	76 3043869	3.762134409	0.067082566	3 285244132	1.212043133	13.49069606	0.263436176	0 033488295	1.365192094	0 023632563	0.192663672	100	
29/09/2021	1C-168Y-1-13 5-20 5cm	282.057-OS	76 5381566	3.791708367	0.053393444	3.183708483	1.117503787	13.46443379	0.278850277	0 032831994	1.395704192	0	0.143709063	100	
29/09/2021	1C-168Y-1-13 5-20 5cm	282.057-OS	76.17965282	3.794283931	0.092628364	2 924534033	1.309082316	13.70943277	0.270033555	0 050880369	1.450621025	0 032506902	0.186343916	100	
29/09/2021	1C-168Y-1-13 5-20 5cm	282.057-OS	76.13900008	3.799651517	0.071323068	2 939953827	1.258661099	13 82945789	0.295082809	0 016026463	1.461285206	0 020484155	0.169073879	100	
29/09/2021	1C-168Y-1-13 5-20 5cm	282.057-OS	76.00045923	3 819407063	0.064123003	3 227667941	1.282244884	13 60999982	0.285422501	0 010543715	1.457518806	0 04131415	0.201298891	100	
29/09/2021	1C-168Y-1-13 5-20 5cm	282.057-OS	76.34695521	3 834061523	0.042336679	3.121250085	1.215343502	13 58661802	0.257469752	0 009396151	1.382661809	0 014472232	0.18943504	100	
29/09/2021	1C-168Y-1-13 5-20 5cm	282.057-OS	76.29563086	3 855096814	0.137337824	3 088458243	1.120606551	13 68997448	0.21132566	0 052459982	1.358983214	0 022122999	0.168003367	100	
29/09/2021	1C-168Y-1-13 5-20 5cm	282.057-OS	76.18506399	3 873302041	0.057883145	3.105133201	1.220090143	13 59983426	0.277104287	0 061237122	1.414569114	0 036352779	0.169429916	100	
29/09/2021	1C-168Y-1-13 5-20 5cm	282.057-OS	76.22664486	3 887363607	0.097238232	3 086068601	1.106978221	13 66532833	0.30017111	0 020790357	1.387652871	0	0.221763807	100	
29/09/2021	1C-168Y-1-13 5-20 5cm	282.057-OS	76 0993648	3 907340072	0.073196802	3 054255043	1.27762648	13.74414769	0 2445295	0	1.376789629	0 033175529	0.189574451	100	
29/09/2021	1C-168Y-1-13 5-20 5cm	282.057-OS	76.10084731	3.91008639	0.058228584	3 022391101	1.157491249	13 83325158	0.280568347	0 02388323	1.387841015	0 046921037	0.17849016	100	
29/09/2021	1C-168Y-1-13 5-20 5cm	282.057-OS	75.86875196	3 912690454	0.129915381	3.174668003	1.185404632	13 64755802	0.319370476	0	1.493492915	0 021672088	0.246476069	100	
29/09/2021	1C-168Y-1-13 5-20 5cm	282.057-OS	75.98706359	3 954480582	0.055469606	3 270462319	1.174373855	13 54142405	0.281358387	0 024154395	1.441453522	0 054828339	0.214931364	100	
29/09/2021	1C-168Y-1-13 5-20 5cm	282.057-OS	75.95329052	3 956917139	0.07164658	3 387121071	1.222212566	13.43241472	0.231553324	0 081987323	1.422381721	0 017938024	0.22253702	100	
29/09/2021	1C-168Y-1-13 5-20 5cm	282.057-OS	76.07602818	3 960990006	0.074902645	3 388966926	1.219596378	13 25366683	0.277967733	0 042955695	1.457012962	0 039286113	0.208626531	100	
29/09/2021	1C-168Y-1-13 5-20 5cm	282.057-OS	76.33782195	3.96738487	0.04368344	3 292085318	1.116038026	13 52709416	0.263367515	0 003587529	1.212793384	0 072067124	0.164076688	100	
29/09/2021	1C-168Y-1-13 5-20 5cm	282.057-OS	75 8272462	3 992846688	0.072760893	2 901962845	1.328230512	13 89553012	0.248385499	0 064711653	1.450148821	0 021817677	0.196359092	100	
29/09/2021	1C-168Y-1-13 5-20 5cm	282.057-OS	76.53485504	4 001551595	0.074345181	3.143309966	1.170641582	13 33492931	0.200118651	0	1.294147886	0 040659197	0.20544159	100	
29/09/2021	1C-168Y-1-13 5-20 5cm	282.057-OS	76.00985165	4 026307074	0.062839521	2 975513755	1.085646365	13 87879493	0.289677787	0 030691488	1.411479637	0 022888567	0.206309223	100	
29/09/2021	1C-168Y-1-13 5-20 5cm	282.057-OS	75 5670407	4 048117621	0.084291043	3 210576044	1.260285319	13.76574745	0.320851053	0 050682003	1.444797111	0 022978705	0.224632946	100	
29/09/2021	1C-168Y-1-13 5-20 5cm	282.057-OS	75.76703118	4 051114488	0.076960197	3.161845454	1.547986837	13.4817577	0.260717424	0 049513622	1.417314674	0 027666148	0.158092273	100	
29/09/2021	1C-168Y-1-13 5-20 5cm	282.057-OS	75.90934487	4 053970127	0.05139285	3.181462121	1.175544933	13 63027751	0.315123095	0.102253682	1.355481179	0 044263821	0.180885806	100	
29/09/2021	1C-168Y-1-13 5-20 5cm	282.057-OS	76.04764048	4 073757007	0.057053927	3 039321327	1.134466676	13.6929424	0.262161379	0 039457856	1.396829528	0 05716057	0.19920885	100	
29/09/2021	1C-168Y-1-13 5-20 5cm	282.057-OS	75.92098559	4.08052725	0.077775062	3 206889562	1.19485935	13 58400064	0.275804791	0 060195768	1.436912851	0 010121412	0.151927725	100	
29/09/2021	1C-168Y-1-13 5-20 5cm	282.057-OS	75.85948659	4.109179922	0.042389435	3.07107131	1.239458428	13.70087095	0.276629127	0 01232754	1.45501226	0 066395697	0.167178741	100	
29/09/2021	1C-168Y-1-13 5-20 5cm	282.057-OS	75.91322012	4.118991109	0.058632578	3.110258593	1.173071856	13.7649958	0.247391268	0 036041172	1.370712415	0 015446217	0.191238873	100	
29/09/2021	1C-168Y-1-13 5-20 5cm	282.057-OS	76.02331542	4.161250293	0.067130603	3.112996402	1.233551295	13 51082792	0.26374837	0 040447776	1.314080018	0 08131909	0.191332806	100	
29/09/2021	1C-168Y-1-13 5-20 5cm	282.057-OS	75.78658917	4.163619656	0.055091151	2 977041027	1.223023545	13.77278767	0.261739866	0 01758679	1.494716894	0 060176488	0.187627746	100	
29/09/2021	1C-168Y-1-13 5-20 5cm	282.057-OS	75.98154752	4 217352292	0.049114801	3 028921347	1.223768361	13.5985948	0.276971886	0 079614356	1.356174274	0 003365468	0.184574895	100	
29/09/2021	1C-168Y-1-13 5-20 5cm	282.057-OS	75.94397998	4 250553821	0.055119401	3.02096718	1.257888334	13.43005409	0.319432389	0 067097271	1.464109601	0 036251606	0.154546321	100	
29/09/2021	1C-168Y-1-13 5-20 5cm	282.057-OS	75.78039416	4 312378064	0.059717981	3 054601128	1.202075385	13 53959877	0.251756565	0 060880631	1.455227563	0 075255225	0.20811452	100	
29/09/2021	1C-168Y-1-13 5-20 5cm	282.057-OS	75.71311443	4 366302839	0.064490187	3.150504228	1.143907911	13.70152174	0.255803834	0 012052264	1.391960101	0 043980193	0.156362274	100	
29/09/2021	1C-168Y-1-13 5-20 5cm	282.057-OS	75.88536703	4 369414118	0.065382516	3 089270999	1.131815793	13 51027077	0.247363421	0 050994131	1.40245055	0 031527492	0.216143173	100	
Feb 16 02 57 2020	CHA16-1C-169Y-1(28-30cm)_1	283.562-OS	71.42751532	4 385427751	0.023912463	3 368095842	2.306257528	14.71379634	0.287254821	0.135741385	2.45229939	0 03764941	0.862049747	100	98.27511314
Feb 16 03 01 2020	CHA16-1C-169Y-1(28-30cm)_2	283.562-OS	70.07985926	4 236971976	0.048517068	3.155161169	2.730183489	15.41373817	0.328964345	0.19820619	2.844817447	0 052861881	0.910719011	100	96.66701119
Feb 16 03 09 2020	CHA16-1C-169Y-1(28-30cm)_4	283.562-OS	70.29720481	4 627843588	0.034258161	3.136891834	1.361651884	16.72665021	0.123618303	0 029924297	3.18848545	0 013104778	0.460366691	100	96.91121533
Feb 16 03 21 2020	CHA16-1C-169Y-1(28-30cm)_7	283.562-OS	71.79201414	3 628563052	0.016317775	3.475474189	2.220099272	15.3005632	0.281322682	0 087204733	2.394686484	0 015364139	0.788390332	100	94.37561096
Feb 16 03 25 2020	CHA16-1C-169Y-1(28-30cm)_8	283.562-OS	68.65044961	4 658004691	0.040385181	2.737449094	2.138894216	16.71613401	0.47223599	0.169659392	3.684627297	0 075670171	0.656490351	100	96.07484596
Feb 16 03 29 2020	CHA16-1C-169Y-1(28-30cm)_9	283.562-OS	77.09113477	2 977896802	0.051784758	4.769648796	1.879593104	11 60439828	0.105875721	0.101682623	0.623094339	0 019812387	0.775078426	100	95.39486437
Feb 16 03 52 2020	CHA16-1C-169Y-1(28-30cm)_15	283.562-OS	75.47107728	3.189314963	0.039711618	4 695071542	1.823027608	12 82354342	0.135060869	0 066392862	0.935601591	0 024819761	0.796378489	100	96.69714209
Feb 16 04 00 2020	CHA16-1C-169Y-1(28-30cm)_17	283.562-OS	68.87146622	4 504607649	0.028369195	2 603886839	2.35759824	16 86953925	0.224015323	0.132322032	3.617072379	0 041439289	0.749683584	100	98.69860555
Feb 16 04 04 2020	CHA16-1C-169Y-1(28-30cm)_18	283.562-OS	73.72173465	3.405622493	0.036950968	4.452540411	1.056020186	14 65755832	0.037565111	0 041454687	1.985730666	0 020062021	0.584760496	100	97.69703582
Feb 16 04 31 2020	CHA16-1C-169Y-1(28-30cm)_25	283.562-OS	78.56188689	2.63704188	0.030152785	4 979937315	1.337179212	11.14707488	0.084259699	0 070811767	0.659579039	0 019016216	0.473060325	100	95.18192098
Feb 16 04:47 2020	CHA16-1C-169Y-1(28-30cm)_29	283.562-OS	69.4240594	4 373463482	0.040624072	2 959164616	1.422907378	17 37349261	0.135791631	0 037221548	3.825261577	0	0.408013693	100	96.9868315
Feb 13 21:14 2020	CHA16-1C-169Y-1(52-52.5cm)_1	283.788-OS	66.93794623	4.415172697	0.047823814	2.764498945	4.409073136	15.0433136	1.373572578	0 347492341	3.369863678	0 053877461	1.237365513	100	99.1138016
Feb 13 21 22 2020	CHA16-1C-169Y-1(52-52.5cm)_3	283.788-OS	73.81155524	4.164596794	0.075863411	3 017654456	2.310721419	13 57944505	0.474911283	0.122007359	1.888671845	0 015088272	0.539484868	100	94.77559613
Feb 13 21 26 2020	CHA16-1C-169Y-1(52-52.5cm)_4	283.788-OS	67.44251858	4 527318985	0.044094789	2.459132456	3.741697229	15 62397087	1.167133943	0 306199913	3.572101887	0 074409956	1.041421396	100	94.34221381
Feb 13 21 30 2020	CHA16-1C-169Y-1(52-52.5cm)_5	283.788-OS	68.08278049	4.424863025	0.065679428	2 586726257	4.119601076	14 82843488	1.259086344	0 291918623	3.225424098	0 090482194	1.025003586	100	93.94113479
Feb 13 21 34 2020	CHA16-1C-169Y-1(52-52.5cm)_6	283.788-OS	68.44638239	4 379734959	0.073214801	2 639266565	3.942335413	14 84173332	1.197166897	0 259658177	3.191414382	0 063828288	0.965264814	100	90.55546081
Feb 13 21 38 2020	CHA16-1C-169Y-1(52-52.5cm)_7	283.788-OS	68.38660879	4.199555756	0.037710854	2 640816113	3.982350698	15 07377837	1.148649376	0 321491683	3.105599749	0 005704163	1.097734442	100	94.66770472
Feb 13 21:42 2020	CHA16-1C-169Y-1(52-52.5cm)_8	283.788-OS	67.85897601	4.428257167	0.058875812	2 580424668	4.139211814	15.18764233	1.271148788	0 205018564	3.201833057	0 045289086	1.023322697	100	94.94561226
Feb 13 21:46 2020	CHA16-1C-169Y-1(52-52.5cm)_9	283.788-OS	68.49054317	4 293497238	0.043874027	2.60502036	3.933897143	14 86021736	1.209699738	0 331622141	3.174538981	0 077623279	0.979466562	100	94.81691729
Feb 13 21 50 2020	CHA16-1C-169Y-1(52-52.5cm)_10	283.788-OS	74.17111887	4 292384298	0.060912773	3.146277124	2.245827442	13.19953299	0.400647141	0 099226417	1.779712313	0 057310974	0.547049666	100	94.39727916
Feb 13 21 54 2020	CHA16-1C-169Y-1(52-52.5cm)_11	283.788-OS	67.62858819	4.23267241	0.079023013	2 616009084	4.037989125	15.17502365	1.322549987	0 309070312	3.451829414	0 079457205	1.067787608	100	92.12506236
Feb 13 21 58 2020	CHA16-1C-169Y-1(52-52.5cm)_12	283.788-OS	67.56951647	4.481685518	0.03625733	2 508501314	4.078949615	15 31450592	1.109010539	0 23923903	3.488714012	0 081789791	1.091830467	100	94.8773671

Date Analysed	Core Section Identifier	sample_no	SiO2	Na2O	Cl	K2O	FeOt	Al2O3	MgO	P2O5	CaO	MnO	TiO2	total	Analytical Total
Feb 13 22 02 2020	CHA16-1C-169Y-1(52-52.5cm)_13	283.788-OS	68.18643553	4 313105539	0.055574334	2.762898561	4.186529499	14 82685258	1.116548472	0 297929875	3.110897235	0 065065207	1.078163164	100	94.82794761
Feb 13 22 09 2020	CHA16-1C-169Y-1(52-52.5cm)_15	283.788-OS	74.41500479	3 978698877	0.037389565	3 209359249	2.203124501	13.41999396	0.424101466	0 061751178	1.652343376	0 052430126	0.545802911	100	94.41136889
Feb 13 22:13 2020	CHA16-1C-169Y-1(52-52.5cm)_16	283.788-OS	74.40224534	4.109857737	0.058783605	3.135125617	2.319569291	13 28191731	0.455440546	0 061749405	1.631112652	0 029232928	0.514965566	100	94.41407974
Feb 13 22:17 2020	CHA16-1C-169Y-1(52-52.5cm)_17	283.788-OS	74.28490946	4 077972172	0.043512828	3.147287048	2.312939139	13 37068927	0.434705822	0 080103138	1.63701172	0 042562305	0.568307101	100	94.68472226
Feb 13 22 21 2020	CHA16-1C-169Y-1(52-52.5cm)_18	283.788-OS	74.71981345	4.0036958	0.027714223	3.173384355	2.231946996	13 22243481	0.425021945	0 077013902	1.586692177	0 029406695	0.502875641	100	94.53629516
Feb 13 22 25 2020	CHA16-1C-169Y-1(52-52.5cm)_19	283.788-OS	74.7290631	4.13541533	0.042742822	3 208350084	2.237402032	13.11835248	0.426267302	0 092438847	1.540852343	0 012770078	0.456345584	100	94.75275205
Feb 13 22 29 2020	CHA16-1C-169Y-1(52-52.5cm)_20	283.788-OS	73.60856062	4 033695307	0.028489555	3 082824995	2.370586117	13.75577774	0.512067862	0.18181454	1.764651549	0 054534111	0.606997611	100	94.06956297
Feb 13 22 33 2020	CHA16-1C-169Y-1(52-52.5cm)_21	283.788-OS	73 9332074	3 977732761	0.034803919	3.10787285	2.384121639	13 53840502	0.4829975	0.149393325	1.734874228	0 066840553	0.589750804	100	93.95493769
Feb 13 22 37 2020	CHA16-1C-169Y-1(52-52.5cm)_22	283.788-OS	73.65554067	3 957431563	0.059815809	3.193014691	2.479908077	13 51709553	0.490659924	0 212179336	1.788088227	0 050236764	0.596029409	100	93.95509542
Feb 13 22:41 2020	CHA16-1C-169Y-1(52-52.5cm)_23	283.788-OS	74.06233818	3.93897372	0.023059863	3 063972555	2.380717351	13.47293855	0.504648023	0 063420334	1.804220773	0 048681933	0.637028719	100	93.66924634
Feb 13 22:45 2020	CHA16-1C-169Y-1(52-52.5cm)_24	283.788-OS	73.91272076	4.103768468	0.069508262	3 018401603	2.433851997	13 26396197	0.530558479	0.165037291	1.806789692	0 069508262	0.625893206	100	94.08953391
Feb 13 22:49 2020	CHA16-1C-169Y-1(52-52.5cm)_25	283.788-OS	73.03668895	4.165263053	0.038254619	2 994303053	2.578723625	13 85264757	0.559646962	0 098780006	2.01396184	0 009483736	0.652246583	100	93.84487644
Feb 13 22 53 2020	CHA16-1C-169Y-1(52-52.5cm)_26	283.788-OS	72.35779503	4 385021073	0.056437768	2 890457673	2.573984206	14 04087286	0.569230278	0.19776662	2.20476516	0 072894389	0.650774941	100	94.79467647
Feb 13 23 01 2020	CHA16-1C-169Y-1(52-52.5cm)_28	283.788-OS	68.45559754	4 337544395	0.068192192	2 821386881	4.237285833	14 21104462	1.213196359	0 332679529	3.071251402	0 079331985	1.172489264	100	96.05205221
Feb 13 23 04 2020	CHA16-1C-169Y-1(52-52.5cm)_29	283.788-OS	68 2070967	4.34982768	0.053212082	2 840028292	4.162640746	14.47696732	1.192504299	0 368275933	3.116854155	0 09104495	1.141547834	100	97.53423962
Feb 13 23 08 2020	CHA16-1C-169Y-1(52-52.5cm)_30	283.788-OS	68.72689743	4 396811281	0.044997952	2 697841016	4.011129662	14.49707776	1.166994399	0 346129955	3.064340173	0 089181462	0.958598906	100	98.22669253
Feb 13 23:12 2020	CHA16-1C-169Y-1(52-52.5cm)_31	283.788-OS	67.97340072	4 312997521	0.070277786	2 598594782	4.113565019	14 97085172	1.262896023	0 333565704	3.261394261	0 037874256	1.06458221	100	95.05137227
Feb 13 23:16 2020	CHA16-1C-169Y-1(52-52.5cm)_32	283.788-OS	68.38036084	4.49418923	0.041219894	2 582969879	3.971316189	14.75521543	1.16276694	0 342420006	3.131850978	0 076197611	1.061492996	100	92.91629839
Feb 13 23 20 2020	CHA16-1C-169Y-1(52-52.5cm)_33	283.788-OS	68.13495676	4.450974147	0.056835034	2 542619935	3.920762673	15.0741039	1.162874706	0 326620168	3.301132605	0 063138167	0.96598191	100	93.6042374
Feb 13 23 24 2020	CHA16-1C-169Y-1(52-52.5cm)_34	283.788-OS	73.710571	4.10481105	0.04348452	3 049284836	2.448017404	13 54999107	0.440321025	0.167170893	1.78232846	0 058945682	0.64507406	100	93.13659277
Feb 14 05 52 2020	CHA16-1C-169Y-1(53 5-54cm)_1	283.802-OS	78.00170266	3 668392469	0.01918632	3 512249763	1.328049783	12 23521037	0.188298525	0 024478476	0.688715483	0 015307118	0.318409031	100	95.38046057
Feb 14 05 55 2020	CHA16-1C-169Y-1(53 5-54cm)_2	283.802-OS	78.27095646	3 505238468	0.026126106	3.708221449	1.275227859	11 99904611	0.169819687	0 045408242	0.648412018	0 036555478	0.314988129	100	94.92421228
Feb 14 06 07 2020	CHA16-1C-169Y-1(53 5-54cm)_5	283.802-OS	77.42940242	3.69422842	0.029587829	3.401020929	1.516244625	12 38266444	0.174368132	0 051349779	0.942493447	0 029482534	0.349157443	100	94.97148259
Feb 14 06:11 2020	CHA16-1C-169Y-1(53 5-54cm)_6	283.802-OS	77 5865036	3.786844456	0.018592301	3.401546009	1.320898487	12.2857081	0.206522436	0 057062964	0.920318908	0 039719916	0.376282822	100	94.66283836
Feb 14 06:15 2020	CHA16-1C-169Y-1(53 5-54cm)_7	283.802-OS	76.82603972	3.702302871	0.03999394	3.440111991	1.572321125	12 59967398	0.275208959	0 062250085	1.08004743	0 046747534	0.355302364	100	94.76435674
Feb 14 06 31 2020	CHA16-1C-169Y-1(53 5-54cm)_11	283.802-OS	77.16954425	3.759544165	0.051802807	3.467616484	1.469508205	12 35866973	0.220214791	0 092160255	1.069463669	0 019241043	0.322234605	100	94.58946844
Feb 14 06 35 2020	CHA16-1C-169Y-1(53 5-54cm)_12	283.802-OS	77.31495532	3 638648911	0.024707696	3 374966111	1.514003489	12.49052878	0.255803506	0 076983446	0.954453033	0	0.354949707	100	95.11206615
Feb 14 06 39 2020	CHA16-1C-169Y-1(53 5-54cm)_13	283.802-OS	77.28460402	3 653219472	0.040634277	3.442333859	1.47378208	12.42187754	0.238752697	0 081442361	1.032279077	0 018843357	0.312231261	100	94.9936913
Feb 14 06:43 2020	CHA16-1C-169Y-1(53 5-54cm)_14	283.802-OS	77.12356291	3.718254729	0.02953945	3 279825055	1.482228631	12 65676079	0.243569059	0 071597869	1.004656668	0 003889536	0.386115302	100	95.127025
Feb 14 06:47 2020	CHA16-1C-169Y-1(53 5-54cm)_15	283.802-OS	78.41097026	3.46309215	0.036429086	3 663905232	1.152607895	12.14652823	0.139417368	0	0.698976534	0 005459114	0.282614123	100	95.2535554
Feb 14 06 51 2020	CHA16-1C-169Y-1(53 5-54cm)_16	283.802-OS	78.05163476	3.784844756	0.044635053	3 549799524	1.138561439	12.14073447	0.180535662	0 096196163	0.708804645	0 009347105	0.294906422	100	95.21664468
Feb 14 06 54 2020	CHA16-1C-169Y-1(53 5-54cm)_17	283.802-OS	78.1472845	3.489337516	0.06376054	3.775295145	1.167824631	12.0599706	0.185199201	0 091998178	0.659418219	0 023385856	0.336525614	100	95.35678304
Feb 14 06 58 2020	CHA16-1C-169Y-1(53 5-54cm)_18	283.802-OS	78 2853384	3.74596342	0.035182932	3.455090281	1.111106472	12 08228217	0.153056286	0 064904903	0.710189594	0 036657665	0.32022788	100	94.93239636
Feb 14 07 02 2020	CHA16-1C-169Y-1(53 5-54cm)_19	283.802-OS	77.67052713	3 672621236	0.037787089	3.453320054	1.317614791	12 25981101	0.207304167	0 064239441	0.93837937	0 039466515	0.338929193	100	95.27063663
Feb 14 07 06 2020	CHA16-1C-169Y-1(53 5-54cm)_20	283.802-OS	77.45810879	3 696182031	0.055399368	3.46378458	1.360938969	12 38276506	0.20221299	0 054730803	0.941047774	0 000317778	0.384511866	100	94.40540902
Feb 14 07:10 2020	CHA16-1C-169Y-1(53 5-54cm)_21	283.802-OS	77.05836118	3 830703763	0.047960156	3.495762487	1.47077812	12 54424527	0.23244689	0 050503245	0.92008895	0 010870969	0.338278968	100	93.82788481
Feb 14 07:14 2020	CHA16-1C-169Y-1(53 5-54cm)_22	283.802-OS	78.20853346	3 668722811	0.031560668	3 585962947	1.154009011	12.1838858	0.143228812	0	0.683744572	0 010275566	0.330076355	100	95.37187224
Feb 14 07:18 2020	CHA16-1C-169Y-1(53 5-54cm)_23	283.802-OS	78.28125092	3 680438777	0.030376788	3 501768663	1.147145662	12.16126286	0.124565927	0 080143656	0.70836983	0 024470191	0.260206726	100	94.80923269
Feb 14 07 26 2020	CHA16-1C-169Y-1(53 5-54cm)_25	283.802-OS	77.26859084	3 825134813	0.030222788	3.485624664	1.474282335	12 32078809	0.222827244	0 03040577	0.932799495	0 027379529	0.381944431	100	94.96145796
Feb 14 07 30 2020	CHA16-1C-169Y-1(53 5-54cm)_26	283.802-OS	77.33600675	3 820117648	0.050901195	3.460019259	1.39873119	12 33617809	0.228634707	0 040826865	0.977744652	0 000105168	0.350734475	100	95.08617594
Feb 14 07 34 2020	CHA16-1C-169Y-1(53 5-54cm)_27	283.802-OS	75.47955972	3 945846708	0.050995532	3 336353662	1.995477349	12 91253332	0.330784684	0 074389608	1.31173601	0 050573209	0.511750196	100	94.7141796
Feb 14 07 38 2020	CHA16-1C-169Y-1(53 5-54cm)_28	283.802-OS	75.67909531	3 979939622	0.050157423	3 343828174	1.892732929	12.78646245	0.295371489	0.108806726	1.328172757	0 06550959	0.469923525	100	95.10058037
Feb 14 07:42 2020	CHA16-1C-169Y-1(53 5-54cm)_29	283.802-OS	78.03301979	3.707348606	0.047892406	3.485973768	1.161920618	12.19561035	0.196337671	0 076410988	0.764265313	0	0.331220486	100	94.37822024
Feb 14 07:46 2020	CHA16-1C-169Y-1(53 5-54cm)_30	283.802-OS	78.18844269	3 814628286	0.031693192	3 537844672	1.23982503	11 91916717	0.175312839	0 047421379	0.729575171	0	0.316089575	100	94.97307856
Feb 14 07 50 2020	CHA16-1C-169Y-1(53 5-54cm)_31	283.802-OS	78.27961447	3 650194938	0.054529414	3 543884561	1.161149558	12.0027995	0.164853916	0 062510745	0.740629684	0 00537911	0.334454105	100	94.8112147
Feb 16 01:12 2020	CHA16-1A-170Y-1(47-48 5cm)_4	285.315-S	55 5074162	3 949074144	0.03138057	1 285591077	6.954282655	17 36054092	5.041136662	0 283842313	7.835019632	0.131292254	1.620423583	100	98.7872445
Feb 16 01:16 2020	CHA16-1A-170Y-1(47-48 5cm)_5	285.315-S	55.48567192	3 941293506	0.038284132	1 326778103	6.968134724	17 34939611	5.003270098	0 347291764	7.80874746	0.10766146	1.62347073	100	98.73542511
Feb 16 01 20 2020	CHA16-1A-170Y-1(47-48 5cm)_6	285.315-S	55.48516318	3.92320928	0.056172573	1 300196977	7.009040821	17 33934562	5.038263286	0 302600531	7.801181862	0.14292009	1.601905783	100	98.44662175
Feb 16 01 27 2020	CHA16-1A-170Y-1(47-48 5cm)_8	285.315-S	55.79397606	3 989655498	0.024666556	1 279006613	7.034925757	17 04327065	4.943462066	0 329394957	7.795849829	0.128103678	1.63768833	100	98.5139551
Feb 16 01 31 2020	CHA16-1A-170Y-1(47-48 5cm)_9	285.315-S	55 5221364	4.115272132	0.045851036	1.30858045	7.101733282	17 05212199	5.021297077	0 357780097	7.739898322	0 094339521	1.640989695	100	98.58010639
Feb 16 01 35 2020	CHA16-1A-170Y-1(47-48 5cm)_10	285.315-S	55.33645874	3 944012529	0.029871768	1 300539578	7.072296932	17.14070522	5.141195518	0 343626942	7.904842121	0.136963074	1.649487582	100	98.42068799
Feb 16 01 39 2020	CHA16-1A-170Y-1(47-48 5cm)_11	285.315-S	55.55141659	4 044910776	0.044328828	1 284007444	7.124022827	17.0181939	5.034124423	0 375928846	7.816140552	0.135330308	1.57159551	100	98.13027221
Feb 16 01:43 2020	CHA16-1A-170Y-1(47-48 5cm)_12	285.315-S	55.58406746	4 030944536	0.059611901	1 360816828	7.283559995	16 81725871	5.006587284	0 297754846	7.778997686	0.103990778	1.676409977	100	98.47026968
Feb 16 01:47 2020	CHA16-1A-170Y-1(47-48 5cm)_13	285.315-S	55.63142009	4.09908141	0.036144037	1 350324978	7.189700854	16 82322172	5.005339957	0 334129286	7.746601191	0.131275955	1.652760526	100	98.4948084
Feb 16 01 51 2020	CHA16-1A-170Y-1(47-48 5cm)_14	285.315-S	55.70346402	3 927425676	0 0366262	1 365894201	6.940635545	17.2001492	4.998161001	0 333177008	7.750184873	0.136184711	1.608097569	100	98.83635198
Feb 16 01 55 2020	CHA16-1A-170Y-1(47-48 5cm)_15	285.315-S	55.57423948	4 005841462	0.035147575	1 318034065	6.95748784	17 06292161	5.078007211	0 368845192	7.816248524	0.146005479	1.637221554	100	97.87303943
Feb 16 01 59 2020	CHA16-1A-170Y-1(47-48 5cm)_16	285.315-S	55.41452312	3 998332311	0.02756862	1 342825766	6.998988402	17 25327651	5.015250778	0 333671857	7.884014914	0.14303129	1.588516437	100	98.3001692
Feb 16 02 06 2020	CHA16-1A-170Y-1(47-48 5cm)_18	285.315-S	55.38728184	4 080771167	0.048869115	1 384624933	7.312259654	16.71730985	5.121076037	0 372423383	7.727428851	0.118609415	1.729345761	100	98.22154492
Feb 16 02:10 2020	CHA16-1A-170Y-1(47-48 5cm)_19	285.315-S	55.60103527	3 943953927	0.033224228	1 331001197	6.949375203	17 37413777	5.029355669	0 273515666	7.731999322	0.126902328	1.605499428	100	98.42215039
Feb 16 02:14 2020	CHA16-1A-170Y-1(47-48 5cm)_20	285.315-S	55.71825785	3.738078363	0.048283464	1 382431825	7.116368932	17 02627432	4.960490667	0 331783638	7.816838777	0.141089366	1.720102801	100	98.37736481
Feb 16 02:18 2020	CHA16-1A-170Y-1(47-48 5cm)_21	285.315-S	55.54247712	4 052338785	0.041755083	1 307380033	7.044173819	17 09728772	5.087633927	0 289042469	7.783471824	0.11330627	1.641132951	100	98.6706212
Feb 16 02 22 2020	CHA16-1A-170Y-1(47-48 5cm)_22	285.315-S	55.23352259	4 018571963	0.038261933	1 278780777	7.115470609	17 24324238	5.135421214	0 387084911	7.855367628	0.105854631	1.588421368	100	98.53135292
Feb 16 02 26 2020	CHA16-1A-170Y-1(47-48 5cm)_23	285.315-S	55.62258855	4 007432039	0.036196066	1 396862252	7.210061379	16.8541117	5.016468817	0 328007727	7.677644348	0.103694081	1.746933044	100	98.0769577

Date Analysed	Core Section Identifier	sample_no	SiO2	Na2O	Cl	K2O	FeOt	Al2O3	MgO	P2O5	CaO	MnO	TiO2	total	Analytical Total
Feb 16 02 30 2020	CHA16-1A-170Y-1(47-48 5cm)_24	285.315-S	55.42898231	4 068671698	0.040091773	1.414405185	7.287817282	16 91180875	4.996208242	0 297025089	7.682560535	0.138387845	1.734041291	100	98.27452664
Feb 16 02 34 2020	CHA16-1A-170Y-1(47-48 5cm)_25	285.315-S	55 2878221	4 060225587	0.046069578	1 330674906	7.230142636	17.19796508	5.020273511	0 363919425	7.742108547	0.133974769	1.586823862	100	99.19778254
Feb 16 02 38 2020	CHA16-1A-170Y-1(47-48 5cm)_26	285.315-S	55.29908543	4 063018218	0.051494812	1 317780629	7.076228315	17 22237914	5.139344452	0 339784667	7.795179258	0.10228005	1.593425023	100	98.65071405
Feb 16 02:42 2020	CHA16-1A-170Y-1(47-48 5cm)_27	285.315-S	55.82402452	4 066607755	0.023987158	1 325872435	6.912401814	16 92258559	4.969491342	0 320334829	7.833780648	0.140684174	1.660229738	100	98.80286859
Feb 16 02:46 2020	CHA16-1A-170Y-1(47-48 5cm)_28	285.315-S	55.51785782	3 904474709	0.041967377	1.34458585	6.905553675	17 35738098	4.940334375	0 320459628	7 904535	0.129059869	1.633790724	100	98.1714927
Feb 16 02:49 2020	CHA16-1A-170Y-1(47-48 5cm)_29	285.315-S	55.50992221	3.97034809	0 0350099	1 323048538	6.858472128	17 36246773	4.986875257	0 347758219	7.836518261	0.143296334	1.626283334	100	98.25792199
Feb 16 02 53 2020	CHA16-1A-170Y-1(47-48 5cm)_30	285.315-S	55.64899664	4 012188315	0.057899971	1 330683537	6.886322983	17 23793865	4.967208014	0 355018241	7.770785543	0.123215201	1.609742904	100	98.44564565
Feb 15 22:45 2020	CHA16-1A-170Y-1(82.5-88.5cm)_1	285.7-OS	58.52765986	3 995961888	0.061713031	1 891041805	7.179183253	15.12833444	4.219259941	0.430567852	6.537311186	0.11051411	1.918452631	100	98.35848129
Feb 15 22:49 2020	CHA16-1A-170Y-1(82.5-88.5cm)_2	285.7-OS	58.91846892	4 348465272	0.053637122	1 838696789	7.111892491	15 38003833	3.525015391	0.411217934	6.37956676	0.138156223	1.894844765	100	98.4392865
Feb 15 23 09 2020	CHA16-1A-170Y-1(82.5-88.5cm)_7	285.7-OS	59.21960324	4 047203111	0.066851273	1 986910886	7.213600561	15 24333195	3.270124166	0.435568121	6.291884472	0.137531488	2.087390733	100	96.63241637
Feb 15 23:12 2020	CHA16-1A-170Y-1(82.5-88.5cm)_8	285.7-OS	59.19124046	4 280110682	0.071263772	1 834814056	6.800745899	15 33742357	3.466886227	0.432853924	6.426917743	0.145974157	2.011769501	100	98.64759832
Feb 15 23:16 2020	CHA16-1A-170Y-1(82.5-88.5cm)_9	285.7-OS	58.93403498	4.146876131	0.056326526	1.74561487	6.808681994	15 87291661	3.389740503	0 383629314	6.627247151	0.141881953	1.893049975	100	98.5326162
Feb 15 23 20 2020	CHA16-1A-170Y-1(82.5-88.5cm)_10	285.7-OS	58.76029461	4 066443628	0.043114417	1 680045354	6.11692286	17 08383468	3.036226542	0 344611713	6.983321048	0.115376609	1.769808545	100	98.80685641
Feb 15 23 24 2020	CHA16-1A-170Y-1(82.5-88.5cm)_11	285.7-OS	59.44495005	4 328391961	0.063283244	1 869039619	6.947671794	15.11484214	3.433344518	0 344959704	6.358797835	0.100867192	1.993851943	100	98.44628123
Feb 15 23 36 2020	CHA16-1A-170Y-1(82.5-88.5cm)_14	285.7-OS	57.66203606	4 289844625	0.041555006	1.30049898	5.281029379	18.77595403	2.814361075	0 299927577	7.975716403	0.114911277	1.444165588	100	98.42376037
Feb 15 23:40 2020	CHA16-1A-170Y-1(82.5-88.5cm)_15	285.7-OS	59.96597151	3 557330717	0.107330729	1 860542701	7.269171152	15 09943325	3.237129208	0.433194566	6.323694266	0.128517256	2.017684642	100	92.98362243
Feb 15 23:44 2020	CHA16-1A-170Y-1(82.5-88.5cm)_16	285.7-OS	58 8382976	4 254489766	0.051225552	1 560377522	5.697791223	17 80062252	2.607472964	0 305402837	7.042230132	0 099268754	1.742821127	100	97.41232353
Feb 15 23:48 2020	CHA16-1A-170Y-1(82.5-88.5cm)_17	285.7-OS	59.79498411	4 229786632	0.042055543	1.89961028	6.876398123	15 24767396	3.321778403	0 373725466	6.05437287	0.121595375	2.038019239	100	98.4412445
Feb 15 23 59 2020	CHA16-1A-170Y-1(82.5-88.5cm)_20	285.7-OS	56.1026283	4 201878278	0.059387409	1 364993623	6.86468759	17.8467823	3 8505044	0 37486392	7.68063576	0.100337218	1.553301204	100	98.16895678
Feb 16 00 03 2020	CHA16-1A-170Y-1(82.5-88.5cm)_21	285.7-OS	56.88561994	4 058814861	0.051160664	1.431280472	6.585069093	17 82502488	3.765993298	0 320972259	7.460930119	0.105569623	1.509564784	100	98.51318646
Feb 15 05 54 2020	CHA16-1A-171Y-1(55.5-56.5cm)_1	287.020-S	71.67823583	4 283150073	0.041686673	3 073328663	2.828029439	14.13305811	0.674643496	0.136226091	2.25448331	0 044557948	0.852600369	100	94.03485005
Feb 15 05 57 2020	CHA16-1A-171Y-1(55.5-56.5cm)_2	287.020-S	72.4557917	4 221324015	0.059622463	3.150866792	2.864027761	13 89776262	0.590707956	0 099724404	1.888398279	0 059728552	0.712045462	100	94.25977664
Feb 15 06 01 2020	CHA16-1A-171Y-1(55.5-56.5cm)_3	287.020-S	72.32965524	4 262355801	0.045188242	3.111321587	2.792979182	14 00094714	0.625333308	0 098736838	1.978969853	0 067411968	0.687100835	100	94.49360722
Feb 15 06 05 2020	CHA16-1A-171Y-1(55.5-56.5cm)_4	287.020-S	72.25514191	4.162929661	0.070818265	3 091613091	2.877182378	13 94970059	0.618108666	0.116604092	2.011153152	0 035944014	0.810804185	100	93.47870886
Feb 15 06 09 2020	CHA16-1A-171Y-1(55.5-56.5cm)_5	287.020-S	72.02426922	4 295169156	0.050305271	3.120200379	2.768877578	13 97722415	0.671585986	0 056142381	2.111972365	0 072910805	0.851342707	100	94.22471773
Feb 15 06:17 2020	CHA16-1A-171Y-1(55.5-56.5cm)_7	287.020-S	72.80275286	3 892063384	0.067345656	3.166723627	2.711427045	13 85969374	0.617194435	0.128780094	1.942257158	0 051089808	0.760672191	100	94.73513807
Feb 15 06 21 2020	CHA16-1A-171Y-1(55.5-56.5cm)_8	287.020-S	73.31761963	4.127391444	0.079257023	3.187166579	2.22184082	13.75125183	0.450846875	0 217613824	2.005171027	0 031027383	0.610813559	100	94.75500966
Feb 15 06 25 2020	CHA16-1A-171Y-1(55.5-56.5cm)_9	287.020-S	72.88504785	4 002770369	0.078057682	3 215384188	2.301345769	14.18365196	0.436509557	0.105134601	2.125961256	0 061769223	0.604367543	100	94.54546712
Feb 15 06 29 2020	CHA16-1A-171Y-1(55.5-56.5cm)_10	287.020-S	74.09974667	4 266827211	0.041533423	3 339583105	2.224950197	13 34776412	0.476104958	0 026103703	1.564108543	0 051467626	0.561813442	100	94.62258913
Feb 15 06 37 2020	CHA16-1A-171Y-1(55.5-56.5cm)_12	287.020-S	76.20731463	4 002016394	0.037963996	3.426277115	1.746988953	12 59474088	0.342416213	0 06281508	1.15129256	0 042616965	0.385557212	100	94.56327937
Feb 15 06:44 2020	CHA16-1A-171Y-1(55.5-56.5cm)_14	287.020-S	75.80463112	3 930072969	0.045118697	3 557032194	1.849673105	12 87456785	0.267354514	0 050050276	1.118419061	0 025392383	0.477687832	100	95.30416975
Feb 15 06:48 2020	CHA16-1A-171Y-1(55.5-56.5cm)_15	287.020-S	72.7705749	4 074934897	0.060819318	3 067409087	2.557135722	14 08892726	0.604596908	0.153476227	1.903909089	0 071502364	0.646714234	100	94.54232929
Feb 15 06 52 2020	CHA16-1A-171Y-1(55.5-56.5cm)_16	287.020-S	72.68704493	4.3010087	0.041994033	3.102071772	2.582733647	13 88546412	0.616932437	0.128092351	1.941432674	0 058031955	0.655193381	100	94.77537002
Feb 15 06 56 2020	CHA16-1A-171Y-1(55.5-56.5cm)_17	287.020-S	72.67613962	4 313574011	0.048889255	3.185209042	2.536981129	13 93661232	0.563390463	0 095132988	1.904776171	0 022857314	0.716437691	100	94.49929222
Feb 15 07 00 2020	CHA16-1A-171Y-1(55.5-56.5cm)_18	287.020-S	73.18600796	4 050001467	0.061113693	3 236683397	2.509639431	13.79849238	0.580580084	0 082514133	1.788693456	0 034283291	0.671990708	100	93.92330442
Feb 15 07 04 2020	CHA16-1A-171Y-1(55.5-56.5cm)_19	287.020-S	76.41867141	3 830961293	0.071999838	3 610549068	1.520729667	12 85862212	0.280187053	0	1.037452213	0	0.370827335	100	94.72243515
Feb 15 07 08 2020	CHA16-1A-171Y-1(55.5-56.5cm)_20	287.020-S	76.74084431	3 868389872	0.055943068	3 553283697	1.523335205	12 51051968	0.247037819	0 034158055	1.05752491	0 043464274	0.364599103	100	94.56042034
Feb 15 07:12 2020	CHA16-1A-171Y-1(55.5-56.5cm)_21	287.020-S	76.71937403	3.797183915	0.051478744	3 554987047	1.487664477	12 61651189	0.210134546	0 08629019	1.06016676	0 034916935	0.381291463	100	94.79640729
Feb 15 07:16 2020	CHA16-1A-171Y-1(55.5-56.5cm)_22	287.020-S	76.72928444	3.88300471	0.068211382	3.53727755	1.44654542	12.73419918	0.19175212	0 03663986	1.041121094	0 021646027	0.310318215	100	94.70560205
Feb 15 07 20 2020	CHA16-1A-171Y-1(55.5-56.5cm)_23	287.020-S	76.40441465	3 890229327	0.068973015	3.6813818	1.523829897	12 69442	0.262139773	0 014175436	1.069822245	0 038189047	0.35242481	100	94.52972251
Feb 15 07 23 2020	CHA16-1A-171Y-1(55.5-56.5cm)_24	287.020-S	72.69666313	4 338070547	0.05008535	3.1805254	2.68226541	13.73648844	0.591725656	0 076079013	1.912541852	0 03930749	0.696247717	100	94.63845187
Feb 15 07 27 2020	CHA16-1A-171Y-1(55.5-56.5cm)_25	287.020-S	72.64985514	4 323110292	0.049925632	3.155975486	2.679364563	13 83773867	0.594041138	0 06417502	1.910473455	0.031032	0.704308605	100	94.74091333
Feb 15 07 31 2020	CHA16-1A-171Y-1(55.5-56.5cm)_26	287.020-S	73.00976167	4.181741825	0.060515363	3.12609903	2.606429248	13.72948898	0.599239388	0.138562227	1.858761585	0 007709636	0.681691046	100	94.68669967
Feb 15 07 35 2020	CHA16-1A-171Y-1(55.5-56.5cm)_27	287.020-S	72.99652085	4.129478975	0.078738545	3 236557452	2.447866896	13 86944456	0.545333401	0.116409952	1.867652825	0 024512943	0.687483606	100	94.23592955
Feb 14 03 53 2020	CHA16-1A-171Y-1(80.5-81.5cm)_1	287.253-S	65.07303167	4 623724846	0.104828402	2.457083328	4.130904285	16 30902471	1.689808093	0 367170265	4.141633906	0 057510771	1.045279728	100	93.19993238
Feb 14 03 57 2020	CHA16-1A-171Y-1(80.5-81.5cm)_2	287.253-S	65.23370348	4 539545855	0.08030423	2 554179029	3.857546105	16.523331	1.682604852	0.478763575	3.941634304	0 066114346	1.04227322	100	95.13820185
Feb 14 04 01 2020	CHA16-1A-171Y-1(80.5-81.5cm)_3	287.253-S	65.02786493	4 322990857	0.106260618	2 394307043	4.227117301	16.47410377	1.700381771	0 395909357	4.248305859	0 059433905	1.043324591	100	94.39056728
Feb 14 04 05 2020	CHA16-1A-171Y-1(80.5-81.5cm)_4	287.253-S	64.72421792	4.45201794	0.087714389	2.429499261	4.217442441	16 50166381	1.695811519	0 352058876	4.427788697	0 043962368	1.067822771	100	95.08132135
Feb 14 04 09 2020	CHA16-1A-171Y-1(80.5-81.5cm)_5	287.253-S	65.32137164	4.148394156	0.113899537	2.410233651	4.223241265	16.19975627	1.781013362	0 330326494	4.372547775	0 053643696	1.045572156	100	93.76684284
Feb 14 04:13 2020	CHA16-1A-171Y-1(80.5-81.5cm)_6	287.253-S	65.22559933	4 381190632	0.111664865	2.455972098	3.984132515	16.48230164	1.682504619	0.447269362	4.115117693	0 034165301	1.080081952	100	91.61341865
Feb 14 04:17 2020	CHA16-1A-171Y-1(80.5-81.5cm)_7	287.253-S	77.49842	3 587259974	0.108570291	4 098975175	1.744691997	11 63478338	0.194964076	0 029185278	0.594141196	0 034158126	0.474850509	100	95.1457336
Feb 14 04 21 2020	CHA16-1A-171Y-1(80.5-81.5cm)_8	287.253-S	77.56935223	3 556584886	0.095521155	4.15080926	1.754899105	11 50667377	0.186944042	0 001016227	0.654882109	0 04087759	0.482439628	100	95.16216603
Feb 14 04 25 2020	CHA16-1A-171Y-1(80.5-81.5cm)_9	287.253-S	77.91334974	3 677915614	0.118593618	4.186280535	1.589726786	11.1280875	0.129615724	0 039971548	0.653059764	0 025753574	0.537645599	100	94.35583608
Feb 14 04 29 2020	CHA16-1A-171Y-1(80.5-81.5cm)_10	287.253-S	77.69252183	3.449401311	0.090822607	4 212216721	1.729449183	11 55441816	0.12445668	0 067134038	0.610293969	0	0.469285505	100	94.24966148
Feb 14 04 33 2020	CHA16-1A-171Y-1(80.5-81.5cm)_11	287.253-S	77.64157268	3 583938439	0.092460801	4 062830219	1.738221176	11 52880431	0.129005331	0 096778784	0.605026624	0 03853406	0.482827581	100	95.49992962
Feb 14 04 37 2020	CHA16-1A-171Y-1(80.5-81.5cm)_12	287.253-S	72.28396584	3 970485916	0.056467542	3 350477088	2.619843455	14 20560535	0.452679724	0 084499926	2.035336549	0 059076948	0.881561666	100	95.80725119
Feb 14 04:41 2020	CHA16-1A-171Y-1(80.5-81.5cm)_13	287.253-S	75.78836771	3 306394029	0.099445315	4.70067141	2.517470689	11.7725704	0.191682934	0 095679303	0.812902776	0 031964566	0.682850867	100	95.73100536
Feb 14 04:44 2020	CHA16-1A-171Y-1(80.5-81.5cm)_14	287.253-S	76.15281623	3 534123988	0.094443033	4 331676055	2.384504367	11.77674427	0.13099155	0 043731394	0.805837524	0	0.745131583	100	96.03672914
Feb 14 04:48 2020	CHA16-1A-171Y-1(80.5-81.5cm)_15	287.253-S	73.75836359	4 680938225	0.08011279	3.94255856	2.954290547	12.19564781	0.339585711	0.181412169	0.924451131	0 033432897	0.909206571	100	95.11589855
Feb 14 04 52 2020	CHA16-1A-171Y-1(80.5-81.5cm)_16	287.253-S	78.04907458	3.416495661	0.105279612	4.166655357	1.749359119	11 24890925	0.175253977	0 01889478	0.604112016	0 008057654	0.457908002	100	94.32025602
Feb 14 04 56 2020	CHA16-1A-171Y-1(80.5-81.5cm)_17	287.253-S	77.76356448	3.424332498	0.1205728	4.174488865	1.663438456	11.46395165	0.137525039	0.102022734	0.601592583	0 00709875	0.541412135	100	94.38281254
Feb 14 05 00 2020	CHA16-1A-171Y-1(80.5-81.5cm)_18	287.253-S	77.52091266	3 507093823	0.154434361	4.146546268	1.610731884	11 56897292	0.190131662	0 018794408	0.720149519	0 037656299	0.524576195	100	91.88369678
Feb 14 05 04 2020	CHA16-1A-171Y-1(80.5-81.5cm)_19	287.253-S	72.24221264	4 505065072	0.071605293	3 253844015	1.273973195	15.76145461	0.104972738	0 011882348	2.466289413	0	0.308700679	100	96.50124546

Date Analysed	Core Section Identifier	sample_no	SiO2	Na2O	Cl	K2O	FeOt	Al2O3	MgO	P2O5	CaO	MnO	TiO2	total	Analytical Total
Feb 14 05:16 2020	CHA16-1A-171Y-1(80.5-81.5cm)_22	287.253-S	76.1023304	3.784812588	0.118675721	4.137896821	1.785386953	12.43469502	0.173497603	0 055714951	0.900570184	0 011552504	0.494867254	100	95.21745394
Feb 14 05 20 2020	CHA16-1A-171Y-1(80.5-81.5cm)_23	287.253-S	72.36166487	4 564056914	0.087058866	3.132878446	1.314464808	15.74710849	0.101741003	0 001714112	2.398771615	0 007858045	0.282682827	100	96.71616862
Feb 14 05 24 2020	CHA16-1A-171Y-1(80.5-81.5cm)_24	287.253-S	77.46951377	3.411383923	0.137849417	4 612572368	1.66770351	11 61059406	0.128033187	0 042579612	0.47898978	0 019632459	0.421147912	100	94.74106099
Feb 14 05 28 2020	CHA16-1A-171Y-1(80.5-81.5cm)_25	287.253-S	74.02664107	3 657057298	0.082079131	3.763678735	1.322237053	14.642257	0.079810612	0 09430501	2.031355372	0 019179294	0.281399432	100	96.97958453
Feb 14 05 32 2020	CHA16-1A-171Y-1(80.5-81.5cm)_26	287.253-S	79.40868249	3 251690685	0.105866455	3.90089205	1.647970438	10 51363419	0.173871311	0 006628378	0.497415887	0 027327105	0.466021008	100	95.87550621
Feb 14 01:11 2020	CHA16-1A-171Y-1(85-87cm)_1	287.321-OS	67.56594659	4 576277016	0.122771786	2 562102855	4.026161629	15 25758394	0.817258523	0.472138719	3.409165432	0 046013276	1.144580235	100	95.62457632
Feb 14 01:15 2020	CHA16-1A-171Y-1(85-87cm)_2	287.321-OS	67.02760537	4 636027426	0.100370971	2.431346503	4.062634541	15.6894582	0.788732962	0.417859517	3.719752342	0 054445537	1.071766632	100	96.24296648
Feb 14 01:18 2020	CHA16-1A-171Y-1(85-87cm)_3	287.321-OS	66.01930077	4 662919328	0.116016691	2.17143539	4.167087916	16.43052779	0.902179704	0 394984311	4.011985388	0 056250517	1.067312195	100	96.71022262
Feb 14 01 22 2020	CHA16-1A-171Y-1(85-87cm)_4	287.321-OS	68.70357089	3.88875545	0.096554862	2 836099907	4.386926074	14 33983099	0.977339148	0.437744412	3.016675557	0 037283561	1.279219145	100	94.14336897
Feb 14 01 26 2020	CHA16-1A-171Y-1(85-87cm)_5	287.321-OS	66.62893445	4.785828462	0.119923558	2 075403429	4.447293061	15 23325669	1.534980644	0 377539628	3.660071071	0 066351568	1.070417433	100	97.8123083
Feb 14 01 30 2020	CHA16-1A-171Y-1(85-87cm)_6	287.321-OS	66.58527522	4.45051912	0.152867935	2 082697368	4.575778454	15.2765339	1.422697754	0 397292458	3.919164506	0 034574828	1.102598454	100	97.46975393
Feb 14 01 34 2020	CHA16-1A-171Y-1(85-87cm)_7	287.321-OS	65 6234544	4 617168197	0.182072872	2.02990129	4.441053077	15.5488378	1.673586637	0 296236022	4.502877481	0 092942689	0.991869534	100	97.04905403
Feb 14 01 50 2020	CHA16-1A-171Y-1(85-87cm)_11	287.321-OS	66.4504373	4 597598811	0.129785071	2.20152383	4.099027702	15.70420332	1.41998287	0 324710848	4.015160128	0 071916445	0.985653669	100	95.38847463
Feb 14 01 58 2020	CHA16-1A-171Y-1(85-87cm)_13	287.321-OS	68.12142921	4 288773561	0.142257218	2 296861333	4.159753474	14.78670637	1.194262047	0 298744902	3.630522752	0 063084302	1.017604832	100	94.47675264
Feb 14 02 02 2020	CHA16-1A-171Y-1(85-87cm)_14	287.321-OS	66.40092577	4 283791677	0.148958216	2.03366828	4.408055854	15 61985009	1.556554795	0 314640501	4.12057395	0 094869028	1.018111838	100	93.91895514
Feb 14 02:17 2020	CHA16-1A-171Y-1(85-87cm)_18	287.321-OS	68.04737418	4.27652931	0.121494352	2 264067972	3.986035163	15 22133961	0.954841436	0 330407174	3.752187767	0 053040841	0.992682197	100	94.07844755
Feb 14 02 29 2020	CHA16-1A-171Y-1(85-87cm)_21	287.321-OS	66.28440465	4 596264847	0.084857618	2.33306834	4.449347143	15 53658341	1.389311226	0.44953377	3.747361979	0 053371519	1.075895497	100	96.86814405
Feb 14 02 57 2020	CHA16-1A-171Y-1(85-87cm)_28	287.321-OS	67.60874031	4 628421311	0.194293454	2 537453635	4.582096026	14.17618725	1.204556502	0 522644484	3.135118334	0 091851627	1.318637062	100	95.37120075
Feb 14 03 01 2020	CHA16-1A-171Y-1(85-87cm)_29	287.321-OS	67.78619189	4 590455313	0.221400965	2.428472119	4.436429585	14 37108825	1.148635774	0.489014066	3.090782697	0 061290011	1.376239329	100	95.12153678
Feb 14 03 05 2020	CHA16-1A-171Y-1(85-87cm)_30	287.321-OS	69.10215667	3 908539537	0.125955244	2 319949413	3.760648592	15.18030826	0.862724567	0 29240647	3.42166055	0 061759384	0.963891311	100	94.39861006
Feb 14 03 09 2020	CHA16-1A-171Y-1(85-87cm)_31	287.321-OS	66.16565687	4 547552489	0.141441276	2.131448635	4.097347862	15 64441911	1.62134952	0 375655805	4.211163081	0 078532501	0.985432855	100	96.64788378
Feb 13 23 28 2020	CHA16-1A-171Y-1 (91-93cm)_1	287.396-OS	76.41355215	3.792336526	0.082298321	3 365790325	1.075681265	13.42095703	0.24467924	0 057285673	1 3588719	0 005064512	0.183483053	100	94.77714569
Feb 13 23 32 2020	CHA16-1A-171Y-1 (91-93cm)_2	287.396-OS	76.17938858	4 306853667	0.084675459	2 868039731	1.104142768	13 58379257	0.237532521	0 064876458	1.355122509	0	0.215575734	100	95.18696586
Feb 13 23 36 2020	CHA16-1A-171Y-1 (91-93cm)_3	287.396-OS	76.38158362	4.199684978	0.084000201	2 922660322	1.15213793	13.48839278	0.224035581	0 040231888	1.310045693	0 006097637	0.191129369	100	95.11881963
Feb 13 23:44 2020	CHA16-1A-171Y-1 (91-93cm)_5	287.396-OS	74.36934562	4 227351307	0.125084256	3 090067918	1.873089114	13.77831654	0.393348714	0 090935331	1.619110929	0 012593085	0.420757193	100	94.49630487
Feb 13 23:48 2020	CHA16-1A-171Y-1 (91-93cm)_6	287.396-OS	74.62076454	4.20317194	0.104866524	3 092492384	1.894017827	13 54704276	0.39624565	0 078203027	1.615800519	0 002675166	0.444719666	100	93.45212992
Feb 13 23 52 2020	CHA16-1A-171Y-1 (91-93cm)_7	287.396-OS	75.40066702	4 004634806	0.086934277	3 082405255	1.157208075	14.14771768	0.129878974	0 016456204	1.724057177	0 026749008	0.223291526	100	95.70448256
Feb 13 23 56 2020	CHA16-1A-171Y-1 (91-93cm)_8	287.396-OS	76.27928495	4 048642381	0.074677828	3 034757801	1.191737995	13.40265049	0.192753729	0.11103892	1.419293042	0 03231551	0.212847347	100	96.54806718
Feb 14 00:19 2020	CHA16-1A-171Y-1 (91-93cm)_14	287.396-OS	75.69790649	4.410074366	0.055213278	2 655295071	1.114907823	14 02459421	0.226016188	0 050221356	1.527848355	0 013487213	0.224435655	100	94.90470672
Feb 14 00 23 2020	CHA16-1A-171Y-1 (91-93cm)_15	287.396-OS	76.51808066	3 839411319	0.081071066	3 255526521	1.126433316	13.42376195	0.21488589	0 051108797	1.266590075	0 042173866	0.180956539	100	94.6083523
Feb 14 00 27 2020	CHA16-1A-171Y-1 (91-93cm)_16	287.396-OS	76.55042697	3 972697551	0.09150066	3.125198606	1.144724809	13 37069507	0.233799222	0 04866487	1.216572158	0 033614679	0.212105404	100	93.11408224
Feb 14 00 31 2020	CHA16-1A-171Y-1 (91-93cm)_17	287.396-OS	76.62922937	4.106068472	0.071919766	3 292838121	0.975829964	13 26543357	0.291651376	0 075818681	1.055380751	0 055925981	0.179903949	100	95.66215782
Feb 14 00 35 2020	CHA16-1A-171Y-1 (91-93cm)_18	287.396-OS	74.02447575	4.142217026	0.115076874	3 095760068	1.804080867	14 02699562	0.416860106	0 097335289	1.729355624	0 057965439	0.489877343	100	93.67651034
Feb 14 00 39 2020	CHA16-1A-171Y-1 (91-93cm)_19	287.396-OS	74.12567431	4 243284334	0.076176261	3.156179358	1.797417397	13 80159787	0.440260273	0.19673191	1.733223919	0 030598891	0.39885548	100	93.46743849
Feb 14 00:43 2020	CHA16-1A-171Y-1 (91-93cm)_20	287.396-OS	73.58296487	4 051658951	0.110194613	3 053842947	1.740476924	14 21211525	0.43565312	0.2193556	2.199621143	0 018152213	0.375964371	100	93.6524913
Feb 14 00:47 2020	CHA16-1A-171Y-1 (91-93cm)_21	287.396-OS	76.29364448	4 041513767	0.080947872	3 024894181	1.285260496	13 23923756	0.36533053	0 041053779	1.357368008	0 037491646	0.233257685	100	93.88758186
Feb 14 00 51 2020	CHA16-1A-171Y-1 (91-93cm)_22	287.396-OS	76.43227097	4.137634362	0.079997262	2 958063383	1.124711837	13 37606034	0.216024994	0.120958073	1.239255824	0 041564029	0.273458925	100	92.62817069
Feb 14 00 55 2020	CHA16-1A-171Y-1 (91-93cm)_23	287.396-OS	76.60181144	3.768481489	0.080754716	3.421449813	1.082006939	13 27140005	0.221650444	0.065177	1.224283998	0 02996425	0.233019858	100	94.11215059
Feb 14 00 59 2020	CHA16-1A-171Y-1 (91-93cm)_24	287.396-OS	76.25675768	4.186712657	0.066083299	2 980643189	1.131477612	13.4500198	0.299018973	0 061107824	1.310528349	0 03914083	0.218509785	100	94.27495416
Feb 15 18:47 2020	CHA16-1A-171Y-1(97-98cm)_1	287.481-OS	77 9111488	3 979339836	0.090133157	3.07035582	0.778347422	12 89549445	0.132909979	0 046731856	0.975540512	0 017173177	0.102824999	100	96.0800693
Feb 15 18 51 2020	CHA16-1A-171Y-1(97-98cm)_2	287.481-OS	77.72385669	3 987835403	0.092981458	3 082086276	0.83501684	13 05476274	0.111038125	0 031235959	0.920267377	0 044103928	0.116815196	100	96.36329857
Feb 15 18 55 2020	CHA16-1A-171Y-1(97-98cm)_3	287.481-OS	77 3804764	3 686995844	0.09307093	3 329196358	0.85800944	13.15974787	0.193993737	0 035490489	1.070996187	0 03182628	0.160196473	100	95.51854737
Feb 15 18 58 2020	CHA16-1A-171Y-1(97-98cm)_4	287.481-OS	77.81188281	3 946966467	0.074327054	3 218392892	0.737731117	12 97840521	0.174128684	0 00345951	0.911318873	0 00775769	0.135629692	100	95.38922383
Feb 15 19 02 2020	CHA16-1A-171Y-1(97-98cm)_5	287.481-OS	77.84189354	3.792494196	0.074067338	3.150232461	0.823572754	13 01182973	0.177529823	0	0.961400375	0 045409705	0.121570076	100	94.91363056
Feb 15 19 06 2020	CHA16-1A-171Y-1(97-98cm)_6	287.481-OS	77.99484085	3.744863662	0.068432388	3 244279388	0.813751942	12 81020929	0.140620213	0 064363999	0.929470397	0 025244875	0.163922999	100	95.86104119
Feb 15 19:10 2020	CHA16-1A-171Y-1(97-98cm)_7	287.481-OS	75.51135203	4 304214598	0.062042742	3.107281625	0.811840356	14.4046168	0.132522475	0 033850849	1.450750692	0 029220794	0.152307038	100	97.19106167
Feb 15 19:14 2020	CHA16-1A-171Y-1(97-98cm)_8	287.481-OS	77.59891637	3 900898917	0.095752698	3 080375791	0.739129395	13 22995297	0.126660876	0 031847953	1.060380209	0 027149075	0.108935744	100	95.76753617
Feb 15 19:18 2020	CHA16-1A-171Y-1(97-98cm)_9	287.481-OS	77.82205395	3 953434696	0.078871506	3 071287779	0.789755599	12 96417733	0.179785247	0 018281475	0.975917362	0 028728032	0.117707023	100	95.72531821
Feb 15 19 22 2020	CHA16-1A-171Y-1(97-98cm)_10	287.481-OS	76.66719701	4 273584066	0.061103504	2.99792319	0.697088407	13 69884346	0.13917442	0 039035458	1.272972315	0 029354665	0.123723505	100	96.06650397
Feb 15 19 26 2020	CHA16-1A-171Y-1(97-98cm)_11	287.481-OS	78 3051447	3 838560998	0.079651142	3 259894437	0.799262582	12 56483584	0.132400243	0 029750493	0.835018268	0	0.155481299	100	94.78834545
Feb 15 19 30 2020	CHA16-1A-171Y-1(97-98cm)_12	287.481-OS	76.16248658	3 964075177	0.05997046	3.32240528	0.653771179	14.10455072	0.124224524	0 034582269	1.454753809	0 01358216	0.105597843	100	95.71378962
Feb 15 19 34 2020	CHA16-1A-171Y-1(97-98cm)_13	287.481-OS	77.04473174	3 841743191	0.040318203	3.451404025	0.679570745	13.46358507	0.124063983	0	1.218459631	0 001243749	0.134879659	100	96.48247425
Feb 15 19:41 2020	CHA16-1A-171Y-1(97-98cm)_15	287.481-OS	78.16335553	3 847939117	0.073887412	3 297799728	0.726624037	12 67983123	0.120536667	0 035900098	0.924427531	0	0.129698651	100	95.82146464
Feb 15 19:49 2020	CHA16-1A-171Y-1(97-98cm)_17	287.481-OS	77 0273574	3 611453384	0.06014163	3 629236286	0.928785635	12.76454248	0.38822459	0.18083966	1.237258496	0 009332322	0.16282812	100	96.43902253
Feb 15 19 53 2020	CHA16-1A-171Y-1(97-98cm)_18	287.481-OS	77.35209687	3 873646402	0.076804836	2 996750761	0.895792927	13 31772803	0.167126485	0 058572856	1.052110993	0 042331724	0.167038112	100	95.43669887
Feb 15 19 57 2020	CHA16-1A-171Y-1(97-98cm)_19	287.481-OS	77.62786186	3 909224349	0.063308636	3 003236135	0.769272626	13 23726032	0.143150768	0 021660971	1.053644064	0 026579163	0.144801115	100	95.56358111
Feb 15 20 01 2020	CHA16-1A-171Y-1(97-98cm)_20	287.481-OS	76.55536623	4 328614075	0.047716216	2 682087966	0.764338104	13 97180708	0.146579226	0 051354708	1.356637518	0 006549285	0.088949592	100	96.193713
Feb 15 20:13 2020	CHA16-1A-171Y-1(97-98cm)_23	287.481-OS	78.17598279	3 615977012	0.067863653	3.455826018	0.796874627	12 64352057	0.171747245	0 026832244	0.883897978	0 005115875	0.156361994	100	95.78028475
Feb 15 20:17 2020	CHA16-1A-171Y-1(97-98cm)_24	287.481-OS	78.03239062	3.56869771	0.076918122	3 584635315	0.748495675	12.72911316	0.156030919	0 030202904	0.865119858	0 043266444	0.165129269	100	95.68616326
Feb 15 20 20 2020	CHA16-1A-171Y-1(97-98cm)_25	287.481-OS	78.17363469	3.744391736	0.069675419	3 389896872	0.689878863	12 69385998	0.175544506	0 011890715	0.891282116	0 006675489	0.153269615	100	95.87312307
Feb 15 20 24 2020	CHA16-1A-171Y-1(97-98cm)_26	287.481-OS	78.01202886	3.770062575	0.080525481	3 260604845	0.747875707	12 83407402	0.134278583	0 044169216	0.939637562	0 012709067	0.164034083	100	95.99445957
Feb 15 20 28 2020	CHA16-1A-171Y-1(97-98cm)_27	287.481-OS	77.89078587	4 033083105	0.065768237	3 054638485	0.788718838	12.8627294	0.185044597	0 014649797	0.934989515	0 017143379	0.152448772	100	96.24706866
Feb 15 20 32 2020	CHA16-1A-171Y-1(97-98cm)_28	287.481-OS	77.54853935	4 231098479	0.068448613	3.127575083	0.753781256	12 85780868	0.180599033	0 023167223	1.027571639	0 016848889	0.16456176	100	94.96174898

Date Analysed	Core Section Identifier	sample_no	SiO2	Na2O	Cl	K2O	FeOt	Al2O3	MgO	P2O5	CaO	MnO	TiO2	total	Analytical Total
Feb 15 20 36 2020	CHA16-1A-171Y-1(97-98cm)_29	287.481-OS	77.24729414	4 038186788	0.070012693	3.152131664	0.743189018	13 31593574	0.109024224	0 022054519	1.210605814	0 007178122	0.084387275	100	96.12542631
Feb 15 20:40 2020	CHA16-1A-171Y-1(97-98cm)_30	287.481-OS	77.68517075	3 600573105	0.059216104	3 534200562	0.647325863	13 09426521	0.111655717	0 029712306	1.118329482	0 012823206	0.106727696	100	95.91985347
Feb 15 20:48 2020	CHA16-1A-171Y-1(103-104cm)_1	287.536-OS	56.76724167	3.783288795	0.053837413	1 313107646	7.895643567	15 01993131	5.080716508	0 279994954	8.211973203	0.143633775	1.450631165	100	99.00178433
Feb 15 20 52 2020	CHA16-1A-171Y-1(103-104cm)_2	287.536-OS	60.37215384	4 063380655	0.043789861	1 688893023	6.947665174	15.15958468	3.590161815	0 25383961	6.249915497	0.146741543	1.483874301	100	98.88133693
Feb 15 20 56 2020	CHA16-1A-171Y-1(103-104cm)_3	287.536-OS	57.21346011	3.794442431	0.041832057	1 263045191	7.613411611	15 35862953	4.749049919	0 260591484	8.113802309	0.129638958	1.462096405	100	98.96716353
Feb 15 21 00 2020	CHA16-1A-171Y-1(103-104cm)_4	287.536-OS	56.79298381	3 838277148	0.041274336	1 315113661	7.754850485	15 00241199	4.967083133	0 30004824	8.29533232	0.161556655	1.531068227	100	98.85077153
Feb 15 21:11 2020	CHA16-1A-171Y-1(103-104cm)_7	287.536-OS	59.41240815	3 859640113	0.037759833	1.60101694	7.323266451	15.14421055	3.705498327	0 308019548	6.988086518	0.146910926	1.473182637	100	99.31187861
Feb 15 21:15 2020	CHA16-1A-171Y-1(103-104cm)_8	287.536-OS	60.39838108	4.103311764	0.043085816	1.715360354	6.962510351	15.14562289	3.511443547	0 267798022	6.266110468	0.102013489	1.484362218	100	99.10454071
Feb 15 21:19 2020	CHA16-1A-171Y-1(103-104cm)_9	287.536-OS	58.33337506	3 875998254	0.046009441	1.476346912	7.150583985	16 09824852	3.913330513	0 257147274	7.118823466	0.128219718	1.601916855	100	98.89274588
Feb 15 21 27 2020	CHA16-1A-171Y-1(103-104cm)_11	287.536-OS	58.17298488	4.167263853	0.047189433	1.478467222	7.24245873	15 83782696	4.010089179	0 239491437	7.129047429	0.125872244	1.549308639	100	98.75092108
Feb 15 21 31 2020	CHA16-1A-171Y-1(103-104cm)_12	287.536-OS	58.69660326	3 944971808	0.043576246	1 543325368	7.132996515	15 91743419	3.782660217	0 218486454	7.010530269	0.125987803	1.583427864	100	99.13658074
Feb 15 21 35 2020	CHA16-1A-171Y-1(103-104cm)_13	287.536-OS	58.45682291	4.130660268	0.061002855	1.499737956	7.022810364	16.14244976	3.820278443	0 226582032	6.981888188	0.106197661	1.551569566	100	98.68390633
Feb 15 21 39 2020	CHA16-1A-171Y-1(103-104cm)_14	287.536-OS	58.26914025	4.167199186	0.03572915	1.431196068	6.605130087	17 01194759	3.400359453	0 238938691	7.298084916	0.142104574	1.400170037	100	98.51899619
Feb 15 21:46 2020	CHA16-1A-171Y-1(103-104cm)_16	287.536-OS	58.68967374	3 974906541	0.039235668	1 561315998	7.128437516	15.8159283	3.883013165	0 301212327	6.934676253	0.147513947	1.524086549	100	98.63474156
Feb 15 21 50 2020	CHA16-1A-171Y-1(103-104cm)_17	287.536-OS	57.17400167	3.744178878	0.046487254	1 387528054	7.774008524	15 22229683	4.689237147	0 301812672	7.970690355	0.166807205	1.522951412	100	98.73674236
Feb 15 21 54 2020	CHA16-1A-171Y-1(103-104cm)_18	287.536-OS	56.96607319	3 817319516	0.052452854	1 372313039	7.454519174	15 89850069	4.432062852	0 265110549	8.183051825	0.152174268	1.406422047	100	98.37405619
Feb 15 21 58 2020	CHA16-1A-171Y-1(103-104cm)_19	287.536-OS	57.64613428	3 942215581	0.044270052	1.428392972	7.877977352	14 84110428	4.427005169	0 268254226	7.759922104	0.147904521	1.616819463	100	98.7123311
Feb 15 22 02 2020	CHA16-1A-171Y-1(103-104cm)_20	287.536-OS	57.69597325	3 992121424	0.046391521	1.455420253	7.849629083	15 03934262	4.376367844	0 231149036	7.580313818	0.150999851	1.582291306	100	98.94049481
Feb 15 22 06 2020	CHA16-1A-171Y-1(103-104cm)_21	287.536-OS	57.09471596	3.775704221	0.062850157	1 324233454	7.582885128	15 28980319	4.807986081	0 288784757	8.149128951	0.17092798	1.452980112	100	98.17000134
Feb 15 22:10 2020	CHA16-1A-171Y-1(103-104cm)_22	287.536-OS	57.13512865	3 870044439	0.06052594	1 289071597	7.649045618	15.18687475	4.813876744	0 241902342	8.127193582	0.14069008	1.485646261	100	99.29626899
Feb 15 22 29 2020	CHA16-1A-171Y-1(103-104cm)_27	287.536-OS	57.57372954	3.752798919	0.054933724	1 353146889	7.568013816	15.10677423	4.70571978	0 25265474	7.997704003	0.150663818	1.483860543	100	99.02842112
Feb 15 22 33 2020	CHA16-1A-171Y-1(103-104cm)_28	287.536-OS	57 5394926	3 833480509	0.02643823	1 387753843	7.540586832	15 07283006	4.760907344	0 259621394	7.971987403	0.134014477	1.472887306	100	98.72067782
Feb 15 22 37 2020	CHA16-1A-171Y-1(103-104cm)_29	287.536-OS	56.98401146	3 835247683	0.069491808	1 367711413	7.901672047	15 09510905	4.817160049	0 250311302	8.055417952	0.152962431	1.470904804	100	99.43618131
Feb 16 04 55 2020	CHA16-1A-171Y-1(108-109.5cm)_1	287.608-OS	61.06627457	4 385038073	0.072544983	2.126493902	6.549189385	15 62820399	2 8895898	0 277258176	5.372195121	0 082719595	1.550492405	100	98.28384638
Feb 16 04 58 2020	CHA16-1A-171Y-1(108-109.5cm)_2	287.608-OS	60 9511193	4.443696381	0.07582295	2.131568884	6.441536355	15 65180581	2.953745454	0 267562647	5.298471226	0.134187336	1.650483664	100	98.51898362
Feb 16 05 02 2020	CHA16-1A-171Y-1(108-109.5cm)_3	287.608-OS	61.79962521	4 540352162	0.06716421	2.43495625	6.540767778	15.1068744	2.648014922	0.422972192	4.656853829	0.11718227	1.665236772	100	98.56439925
Feb 16 05 26 2020	CHA16-1A-171Y-1(108-109.5cm)_9	287.608-OS	61.64728367	4 334711094	0.066732608	2 299019735	6.957814883	14.70965724	3.082314069	0 361434386	4.832010504	0 086569283	1.62245253	100	98.30276643
Feb 16 05 30 2020	CHA16-1A-171Y-1(108-109.5cm)_10	287.608-OS	61 5226012	4.184532234	0.081077636	2 241498777	6.875448974	14 96351886	2.877599781	0 358841741	5.038323828	0.131662811	1.724894158	100	99.04087491
Feb 16 05 53 2020	CHA16-1A-171Y-1(108-109.5cm)_16	287.608-OS	60.4128945	4 399162588	0.067118363	2.118993644	6.842692219	15.75557953	2.919952964	0 281755184	5.505327983	0.142043545	1.554479474	100	98.63172578
Feb 16 05 57 2020	CHA16-1A-171Y-1(108-109.5cm)_17	287.608-OS	59.86791717	4.750776317	0.054191411	1 981626205	6.456895515	16.48996092	2.659018836	0 309477439	5.813444224	0.110202682	1.506489276	100	98.90866376
Feb 16 06:13 2020	CHA16-1A-171Y-1(108-109.5cm)_21	287.608-OS	61.25396477	4.413560407	0.059485412	1 941321471	5.165967097	17 88714917	1.993228462	0 303759712	5.647480642	0 081493976	1.252588884	100	96.32613805
Feb 16 06:17 2020	CHA16-1A-171Y-1(108-109.5cm)_22	287.608-OS	59.65103951	4 580606089	0.051771756	1 875197463	5.697587485	17 69208041	2.568205221	0 298095249	6.124965626	0 074192595	1.386258597	100	98.12299965
Feb 16 06 21 2020	CHA16-1A-171Y-1(108-109.5cm)_23	287.608-OS	60.49824168	4.445902484	0.079973517	2.143411577	6.681014065	15.752053	2.972466998	0 329802291	5.368639374	0.108181622	1.620313386	100	98.90774235
Feb 16 06 28 2020	CHA16-1A-171Y-1(108-109.5cm)_25	287.608-OS	60.73321027	4 385398908	0.131048218	2.123127547	6.721551979	15 60446453	2.949369301	0 337294893	5.292130732	0.108875654	1.61352797	100	95.61366218
Feb 16 06 32 2020	CHA16-1A-171Y-1(108-109.5cm)_26	287.608-OS	60.76920616	4 566149671	0.061869082	2.18421226	6.702958276	15 64505526	2.854714628	0 314323383	5.231950297	0.111953577	1.557607409	100	98.43365682
Feb 16 06 36 2020	CHA16-1A-171Y-1(108-109.5cm)_27	287.608-OS	62.74311403	4 071057243	0.095844572	2.21911358	5.322296638	16.42144049	2.145143127	0 290281191	5.230767725	0 072596716	1.388344683	100	94.63238019
060418	MEX3_1A-173Y-1_47-49cm_SAMPLE_D-1	290.296-S	76.6033	4.0892	0 048	3.4806	1.5542	12 5845	0.2472	0 0678	0.9595	0 0207	0.3449	100	95.1301
060418	MEX3_1A-173Y-1_47-49cm_SAMPLE_D-2	290.296-S	76.4089	4.1949	0 047	3.2686	1.5891	12 6997	0.2559	0 0698	0.9947	0 0483	0.4231	100	95.6708
060418	MEX3_1A-173Y-1_47-49cm_SAMPLE_D-3	290.296-S	76.8642	3.9728	0.0695	3.4921	1.2947	12 6613	0.2812	0 0469	0.9364	0	0.3809	100	93.8735
060418	MEX3_1A-173Y-1_47-49cm_SAMPLE_D-4	290.296-S	77.3823	3.0775	0.0556	3.5035	1.5607	12 6814	0.2888	0 0349	0.9663	0.061	0.3879	100	95.6096
Feb 14 09 52 2020	CHA16-1C-173Y-1(104-105.5cm)_1	290.428-OS	78.08688404	3 909386567	0.043829592	3 211380609	0.746672143	12 81414086	0.147911797	0 020521015	0.834331327	0 038494725	0.146447324	100	95.59751316
Feb 14 09 56 2020	CHA16-1C-173Y-1(104-105.5cm)_2	290.428-OS	78.29312558	3 982087888	0.095039903	2 943438667	0.823333689	12 65471342	0.15173219	0	0.826339313	0 04933369	0.18085565	100	96.48578826
Feb 14 10 00 2020	CHA16-1C-173Y-1(104-105.5cm)_3	290.428-OS	78.11509947	3.90136418	0.068375825	3.131717188	0.763095088	12 84004047	0.118170129	0 080761876	0.782929297	0 036327919	0.16211856	100	95.7940906
Feb 14 10 04 2020	CHA16-1C-173Y-1(104-105.5cm)_4	290.428-OS	78.48102342	3 936396643	0.089961214	3.182442959	0.762954299	12.49056861	0.12812973	0 032759038	0.682457212	0 074777009	0.13852987	100	96.15254818
Feb 14 10 08 2020	CHA16-1C-173Y-1(104-105.5cm)_5	290.428-OS	78.79237698	3 684705756	0.062255569	3 342580867	0.713849926	12 35710364	0.110200713	0 082688223	0.692227606	0	0.162010716	100	95.73440786
Feb 14 10:12 2020	CHA16-1C-173Y-1(104-105.5cm)_6	290.428-OS	77.97573223	3 840560649	0.047307103	3.171021978	0.776022414	12 90099821	0.163405758	0 032963244	0.83376187	0 056396678	0.201829868	100	96.81421388
Feb 14 10:47 2020	CHA16-1C-173Y-1(104-105.5cm)_15	290.428-OS	77.98947923	3 923736521	0.076817186	3 068540763	0.788075908	12 89616456	0.203601826	0 077767316	0.806735953	0	0.169080743	100	96.46278894
Feb 14 10 51 2020	CHA16-1C-173Y-1(104-105.5cm)_16	290.428-OS	78.21697068	3 837274531	0.084958318	3.174266808	0.814521012	12 65557355	0.169086761	0 032101632	0.822404812	0 050622294	0.142219601	100	96.40021413
Feb 14 10 55 2020	CHA16-1C-173Y-1(104-105.5cm)_17	290.428-OS	78.22545023	3 659985812	0.072201025	3 308346671	0.74625065	12 69239918	0.175300759	0 068989377	0.872550425	0 013836796	0.164689081	100	96.1205193
Feb 14 10 59 2020	CHA16-1C-173Y-1(104-105.5cm)_18	290.428-OS	78.06671326	4 009969205	0.081406944	3 057978781	0.839326463	12 81637523	0.163544462	0 008362804	0.764703431	0 041747151	0.149872271	100	95.81492254
Feb 14 11 03 2020	CHA16-1C-173Y-1(104-105.5cm)_19	290.428-OS	78.25880485	3 869927086	0.090029562	3 059964314	0.789762218	12 80189152	0.146337069	0 062692071	0.749691257	0 023209933	0.147690114	100	96.07955185
Feb 14 11 23 2020	CHA16-1C-173Y-1(104-105.5cm)_24	290.428-OS	77.91978667	3 926270334	0.072724036	3.101774456	0.842509008	12.74242479	0.194489642	0 09627139	0.917643207	0 056691216	0.129415252	100	95.42924676
Feb 14 11 27 2020	CHA16-1C-173Y-1(104-105.5cm)_25	290.428-OS	78.40270214	3 897965005	0.064248566	3 066408817	0.813432734	12.48466447	0.153737639	0 024927913	0.860367562	0 04933372	0.182211436	100	95.87762674
Feb 14 11 35 2020	CHA16-1C-173Y-1(104-105.5cm)_27	290.428-OS	77.72211152	3 948489244	0.067313124	3.145473091	0.752711711	13.0222586	0.207496375	0 020858559	0.931269733	0 026002578	0.156015465	100	95.37516021
Feb 14 11 39 2020	CHA16-1C-173Y-1(104-105.5cm)_28	290.428-OS	77.71884183	3 999071226	0.064011804	3 039259623	0.852762126	12 93767024	0.22544645	0 04486386	0.863482802	0 068071089	0.186518947	100	96.07603043
010319	CHA16_1C_174Y-1_35-36cm_1	291.513-S	76.7739	4.414	0.0914	3.1156	0.9854	13 0719	0.2043	0 0449	1.0919	0 0315	0.175	100	94.8521
010319	CHA16_1C_174Y-1_35-36cm_2	291.513-S	76.6311	4.4618	0.1219	3.3308	0.9982	12 9864	0.2162	0 0373	0.9986	0 0446	0.1731	100	93.899
010319	CHA16_1C_174Y-1_35-36cm_6	291.513-S	76.5719	4.4904	0.0931	3.3577	0.8152	13 0817	0.1433	0 0346	1.1786	0 0384	0.1952	100	94.8385
010319	CHA16_1C_174Y-1_35-36cm_17	291.513-S	75.1014	4.8166	0.0692	3.1759	1.2245	13.4135	0.4176	0 0405	1.4904	0.03	0.2203	100	93.013
010319	CHA16_1C_174Y-1_35-36cm_25	291.513-S	76.1594	4.7116	0.0691	3.3807	0.7845	13 3764	0.2516	0 0737	1.0742	0	0.1189	100	95.543
010319	CHA16_1C_174Y-1_35-36cm_26	291.513-S	76.3905	4.6038	0.0766	3.0512	1.1224	12 9301	0.3582	0 0278	1.2191	0 0254	0.1948	100	94.1274
Jan 23 04:35 2020	CHA16-1B-181Y-1(42-46cm)_2	293.706-OS	76.54376339	2 230915123	0.047268475	2 939995255	1.41220538	14.77472469	0.216188344	0	1.572833051	0 075733447	0.186372844	100	96.25865876
Jan 23 04:42 2020	CHA16-1B-181Y-1(42-46cm)_4	293.706-OS	77.34787732	1 385389067	0.033580548	3 368292739	1.370947209	14 55053616	0.145686339	0 052520796	1.518808263	0 027642524	0.198719034	100	97.67559578

Date Analysed	Core Section Identifier	sample_no	SiO2	Na2O	Cl	K2O	FeOt	Al2O3	MgO	P2O5	CaO	MnO	TiO2	total	Analytical Total
Jan 23 04:46 2020	CHA16-1B-181Y-1(42-46cm)_5	293.706-OS	76.25086482	2 209828358	0.052194583	3 337902071	1.488181491	14 53486476	0.237373736	0 076537882	1.577004611	0 038587849	0.196659835	100	94.0710642
Jan 23 04:50 2020	CHA16-1B-181Y-1(42-46cm)_6	293.706-OS	75.35309001	4 026071268	0.072716704	3 273872422	1.193986719	14 06612662	0.245162262	0 060615262	1.527701476	0 034467502	0.146189749	100	92.55094912
Jan 23 05:10 2020	CHA16-1B-181Y-1(42-46cm)_11	293.706-OS	77.97412546	2.781667318	0.021409699	3.446961614	0.938051418	13.41024091	0.118502687	0	1.17886992	0 045067417	0.085103555	100	93.41560366
Jan 23 05:13 2020	CHA16-1B-181Y-1(42-46cm)_12	293.706-OS	76.90312504	3 829678411	0.053115647	3.40565031	0.907883203	13.47814973	0.142683209	0	1.139947392	0 060614327	0.079152729	100	96.01690434
Jan 23 05:17 2020	CHA16-1B-181Y-1(42-46cm)_13	293.706-OS	76.58974417	3 518425455	0.026270325	3.769684843	1.027327605	13 24417495	0.152496033	0 015270961	1.501333087	0 047414733	0.107857838	100	93.64178034
Jan 23 05:21 2020	CHA16-1B-181Y-1(42-46cm)_14	293.706-OS	74.99013214	3.441929962	0.046694399	3 606739822	1.377196548	14 00533627	0.339312636	0 018248386	1.941474561	0 039609732	0.193325548	100	93.15892373
Jan 23 05:37 2020	CHA16-1B-181Y-1(42-46cm)_18	293.706-OS	75.97204847	4.186667432	0.056228967	3 304500866	1.056124071	13.5558433	0.193759146	0 041752106	1.477921457	0 028534103	0.126620081	100	95.32453245
Jan 23 05:52 2020	CHA16-1B-181Y-1(42-46cm)_22	293.706-OS	75.64249732	4 076782003	0.048487438	3 372128498	1.217490919	13.77455733	0.261706494	0 009320479	1.340559245	0 028066163	0.228404107	100	95.48865064
Jan 23 06:08 2020	CHA16-1B-181Y-1(42-46cm)_26	293.706-OS	77.84811327	1.710016383	0.073584066	3.41336489	1.042479384	14.41647381	0.130792486	0 056570409	1.130174577	0 028497875	0.14993285	100	94.04209932
Jan 23 06:16 2020	CHA16-1B-181Y-1(42-46cm)_28	293.706-OS	74.49183186	2 893265797	0.045648697	3 324764596	0.985060027	15 58493859	0.162924156	0 061150011	2.30288652	0 033247646	0.114282101	100	93.54045707
Jan 23 06:24 2020	CHA16-1B-181Y-1(42-46cm)_30	293.706-OS	76.88884651	2 897725303	0.082258826	3 528528737	1.099811913	13 98325132	0.11258212	0 017091311	1.224504177	0 037380351	0.128019433	100	90.68935635
Jan 23 07:03 2020	CHA16-1B-181Y-1(42-46cm)_40	293.706-OS	76.98405596	3 370205989	0.07724929	3 547499564	1.08961173	13.40807935	0.161792503	0 020113549	1.225904934	0 006962382	0.108524753	100	90.48626905
Jan 23 07:10 2020	CHA16-1B-181Y-1(42-46cm)_42	293.706-OS	74.20569312	4 303355614	0.029365863	3 261669631	1.516999474	14 31549249	0.33754488	0 078345088	1.706637707	0 043452808	0.201443317	100	92.28402447
Jan 23 07:14 2020	CHA16-1B-181Y-1(42-46cm)_43	293.706-OS	76.58301909	3 357645573	0.062776565	3 566850273	1.123265731	13 68516363	0.222242209	0 006584954	1.223108895	0 026778814	0.142564262	100	91.11680478
Jan 23 07:22 2020	CHA16-1B-181Y-1(42-46cm)_45	293.706-OS	76.52111854	3.59832024	0.070210645	3.457503069	1.105609952	13.6436365	0.182314349	0 052498896	1.224866594	0	0.143921217	100	94.28769649
060418	MEX3_1A-175Y-1_85-87cm_SAMPLE_F-2	293.706-S	77.1673	3.2927	0.0622	4.2494	0.7551	13 0811	0.0829	0	1.153	0 0733	0.0831	100	93.0394
060418	MEX3_1A-175Y-1_65-67cm_SAMPLE_E-1	293.706-S	76.6774	4.4574	0.0387	3.3228	1.4439	12 6627	0.2128	0 0597	0.8565	0	0.2681	100	95.4252
060418	MEX3_1A-175Y-1_65-67cm_SAMPLE_E-4	293.706-S	77.1973	4.0706	0.0319	3.2664	1.3544	12 5767	0.1859	0 0646	0.8965	0	0.3557	100	94.3283
060418	MEX3_1A-175Y-1_65-67cm_SAMPLE_E-5	293.706-S	76.7818	4.2689	0.0576	3.1576	1.4323	12 5734	0 259	0 0548	1.0081	0 0309	0.3756	100	93.8507
060418	MEX3_1A-175Y-1_65-67cm_SAMPLE_E-7	293.706-S	76.7388	4.3156	0.0438	3.1745	1.4939	12 5725	0.2709	0 0793	0.9411	0 0133	0.3562	100	94.4914
060418	MEX3_1A-175Y-1_65-67cm_SAMPLE_E-8	293.706-S	76 803	4.1685	0.0397	3.1929	1.4149	12.7005	0 268	0 0212	1.0033	0 0285	0.3597	100	94.8138
060418	MEX3_1A-175Y-1_65-67cm_SAMPLE_E-10	293.706-S	76.7969	4.3401	0.0396	3.2582	1.4452	12.4774	0 263	0.069	0.9342	0 0663	0 31	100	94.6032
060418	MEX3_1A-175Y-1_65-67cm_SAMPLE_E-11	293.706-S	76.7419	4.2356	0.0434	3.3024	1.5947	12 5477	0.2149	0 0621	0.9247	0	0.3325	100	93.3343
060418	MEX3_1A-175Y-1_65-67cm_SAMPLE_E-12	293.706-S	77.1417	4.2862	0 064	3.1957	1.3098	12.4027	0.2421	0 0575	0.9238	0 0345	0 342	100	95.0868
060418	MEX3_1A-175Y-1_65-67cm_SAMPLE_E-13	293.706-S	77.0635	4.0491	0.0361	3.2595	1.3886	12 6164	0.2345	0 0426	0.9566	0 0318	0.3213	100	95.4887
060418	MEX3_1A-175Y-1_65-67cm_SAMPLE_E-15	293.706-S	77.0309	4.1085	0 052	3.2908	1.427	12 5231	0.2582	0 0229	0.9241	0 0228	0.3398	100	95.3345
060418	MEX3_1A-175Y-1_65-67cm_SAMPLE_E-16	293.706-S	76 911	4.3235	0.0341	3.3733	1.2461	12 5124	0.2204	0 0826	0.9502	0	0.3464	100	94.5927
060418	MEX3_1A-175Y-1_65-67cm_SAMPLE_E-20	293.706-S	76 546	4.3385	0.0742	3.5216	1.3969	12.4592	0.2553	0 0388	0.9976	0	0.3719	100	92.0185
060418	MEX3_1A-175Y-1_65-67cm_SAMPLE_E-21	293.706-S	77.8884	2.799	0.0387	3.4043	1.4965	12 6012	0 252	0 0905	0.9925	0 0524	0.3846	100	92.9792
060418	MEX3_1A-175Y-1_65-67cm_SAMPLE_E-22	293.706-S	76 655	4.1185	0.0518	3.3438	1.4351	12 5344	0 269	0 0951	1 003	0 0827	0.4115	100	95.6089
060418	MEX3_1A-175Y-1_65-67cm_SAMPLE_E-29	293.706-S	76.2862	4.3665	0.0484	3.4612	1.4158	12.7663	0.2631	0 0491	0.9625	0 0498	0.3311	100	92.8499
060418	MEX3_1A-175Y-1_65-67cm_SAMPLE_E-30	293.706-S	77.5802	3.53	0.0481	3.2434	1.3286	12 6285	0.2905	0 0533	0.9407	0 0355	0.3211	100	95.0418

Filtered source volcano data, normalised to 100%

sample_no	SiO2	Na2O	Cl	K2O	FeOt	Al2O3	MgO	P2O3	CaO	MnO	TiO2	total
Los Humeros (Xaltipan Ignimbrite)	77.17670677	3.850072562	0.131734915	4.755359895	1.002189087	12.51793863	0.015296234	0	0.424841144	0	0.125860767	100.00
Los Humeros (Xaltipan Ignimbrite)	77.87708009	2.767940571	0.120363476	4.801957506	1.098382645	12.78075589	0.022122555	0	0.421100912	0.01363118	0.096665172	100.00
Los Humeros (Xaltipan Ignimbrite)	77.30105713	3.685660669	0.132164677	4.651199943	1.048384933	12.60392127	0.037479535	0	0.439378351	0.039586407	0.06116708	100.00
Los Humeros (Xaltipan Ignimbrite)	77.12080606	3.622933637	0.131781563	4.85176493	1.007361776	12.574334	0.08061557	0.019385873	0.452216164	0.02823955	0.110560878	100.00
Los Humeros (Xaltipan Ignimbrite)	77.10764303	3.761949103	0.113378079	4.759593065	1.042031017	12.52251014	0.062976275	0.025252863	0.429602511	0.047799143	0.127264782	100.00
Los Humeros (Xaltipan Ignimbrite)	77.13224782	3.834381403	0.106926246	4.81116149	1.037182897	12.51109813	0.03855164	0	0.432329302	0.022364997	0.073756073	100.00
Los Humeros (Xaltipan Ignimbrite)	76.7869886	3.877750227	0.144505974	4.865380982	1.080120932	12.55850476	0.050109266	0	0.453572515	0.046795262	0.136271491	100.00
Los Humeros (Xaltipan Ignimbrite)	77.53354335	3.565559658	0.181331062	4.721367988	1.076757836	12.36496836	0.02289809	0	0.41319386	0.049914606	0.070465191	100.00
Los Humeros (Xaltipan Ignimbrite)	77.0165211	3.438898159	0.471620319	5.05492173	1.062515312	12.26885095	0.080284051	0.032061908	0.422901256	0.05381413	0.097611081	100.00
Los Humeros (Xaltipan Ignimbrite)	77.15569446	3.672177269	0.127954052	4.75406519	1.104654637	12.49372493	0.022574008	0	0.458541876	0.084899123	0.125714455	100.00
Los Humeros (Xaltipan Ignimbrite)	77.11283313	3.887435364	0.090325704	4.760549189	1.12074676	12.44187201	0.034716669	0	0.413644545	0.028162871	0.109713756	100.00
Los Humeros (Xaltipan Ignimbrite)	78.21898239	3.021757652	0.184462519	4.882168147	0.87627259	12.3012597	0.062802948	0.009245676	0.310278163	0.019586445	0.113183776	100.00
Los Humeros (Xaltipan Ignimbrite)	77.20810896	3.686986489	0.132230167	4.835905791	1.139358938	12.49188623	0.034780921	0	0.382128877	0.021453016	0.067160605	100.00
Los Humeros (Xaltipan Ignimbrite)	76.98858805	3.722719308	0.115655268	4.799798209	1.072510561	12.60077743	0.030534664	0.055317936	0.440518576	0.041014593	0.132565399	100.00
Los Humeros (Xaltipan Ignimbrite)	77.33830848	2.931271448	0.114642965	4.621185948	1.174438913	12.98730588	0.056434799	0.016794829	0.511422948	0.063594211	0.18459958	100.00
Los Humeros (Xaltipan Ignimbrite)	77.33277029	2.930669844	0.095012108	4.714102382	1.250688604	12.93249326	0.058404808	0	0.496605332	0.03782965	0.151423715	100.00
Los Humeros (Xaltipan Ignimbrite)	77.10025204	3.773149971	0.196845566	4.813255828	1.008518033	12.48127028	0.081880674	0	0.407874664	0.06866441	0.068288526	100.00
Los Humeros (Xaltipan Ignimbrite)	77.13672064	3.797091332	0.135967079	4.743763417	1.051248711	12.53560289	0.05191092	0.026215535	0.399212164	0.041257078	0.081010237	100.00
Los Humeros (Xaltipan Ignimbrite)	77.18900495	3.929837233	0.134052273	4.732483034	1.006021639	12.38367807	0.053579213	0.008860376	0.412378008	0.031432286	0.11867292	100.00
Los Humeros (Xaltipan Ignimbrite)	77.31841994	3.714672969	0.117995494	4.75519761	1.089091415	12.41345897	0.045574979	0	0.389725796	0.069231434	0.086631392	100.00
Los Humeros (Xaltipan Ignimbrite)	77.23038314	3.313155606	0.143210342	5.06146573	1.07707149	12.50797181	0.058384925	0	0.416458502	0.048577408	0.143321044	100.00
Los Humeros (Xaltipan Ignimbrite)	77.25362652	3.424726299	0.219998974	4.876265922	0.989534995	12.58757017	0.06509248	0.039803938	0.398891624	0.042867553	0.101621518	100.00
Los Humeros (Xaltipan Ignimbrite)	76.54226457	3.447811759	0.085094929	5.009282737	1.16773583	12.96335303	0.052083965	0.016453083	0.515388026	0.02083784	0.179694233	100.00
Los Humeros (Xaltipan Ignimbrite)	77.33332843	3.552037947	0.215699465	4.728580484	1.053632666	12.48255606	0.034063708	0.006274894	0.390363532	0.067086102	0.136376709	100.00
Los Humeros (Xaltipan Ignimbrite)	77.04125155	3.767583706	0.124755802	4.815864571	1.090238753	12.50671726	0.057292182	0.051583722	0.417389923	0.01542158	0.111900954	100.00
Los Humeros (Xaltipan Ignimbrite)	76.94539572	3.800589942	0.116821412	4.859770746	1.04425797	12.61671251	0.060954817	0	0.428104182	0.031765934	0.095626767	100.00
Los Humeros (Xaltipan Ignimbrite)	77.10822944	3.847684577	0.110542938	4.721212967	1.023126374	12.63496422	0.024437997	0	0.38609564	0.031811887	0.111893963	100.00
Los Humeros (Xaltipan Ignimbrite)	77.03766732	3.826639771	0.139369148	4.809437964	1.069169616	12.44180691	0.044016813	0.024988167	0.413831136	0.075732744	0.117340421	100.00
Los Humeros (Xaltipan Ignimbrite)	77.14675391	3.898533471	0.129184648	4.839198384	1.07142826	12.37496952	0	0	0.396171728	0.032087244	0.111672833	100.00
Los Humeros (Xaltipan Ignimbrite)	77.791531	3.166190731	0.146314753	4.916780829	1.014758201	12.38380402	0.054030559	0	0.403635462	0.036244448	0.086709993	100.00
Ceboruco	71.23544643	5.511522411	0.089536628	3.298717874	1.952409747	15.80721019	0.361732075	0.056959228	1.373753912	0.066486581	0.24622493	100.00
Ceboruco	71.39500289	5.38839862	0.08415472	3.266326576	1.798326814	15.93634495	0.335162555	0.068343203	1.391084357	0.117858217	0.2189971	100.00
Ceboruco	71.05698691	5.54994785	0.077901086	3.299696267	1.996688833	15.89303248	0.359737529	0.051463153	1.386438302	0.103027214	0.225080376	100.00
Ceboruco	71.21827032	5.323945944	0.125885895	3.289845739	1.913022658	16.07561845	0.322965298	0.029369916	1.335849008	0.164803629	0.200423142	100.00
Ceboruco	71.21317139	5.475271296	0.084069931	3.279033743	1.968081854	15.79248027	0.390828134	0.075795733	1.380799132	0.082946274	0.257522249	100.00
Ceboruco	71.5929366	5.164063827	0.081975709	3.195835178	1.996945437	15.8675753	0.388877341	0.010957149	1.294793337	0.162531046	0.243509082	100.00
Ceboruco	71.13763632	5.468108564	0.08507076	3.293061663	1.926445895	15.89613716	0.394354298	0.045127141	1.378968686	0.109057258	0.266032247	100.00
Ceboruco	71.50067174	5.247495224	0.105052395	3.289933529	1.825192925	15.84497581	0.401863843	0.049297758	1.324068184	0.105462355	0.305986233	100.00
Ceboruco	71.40533706	5.242338593	0.068717141	3.390315499	1.781199596	16.01038543	0.314034298	0.0469584	1.392050925	0.110918979	0.237744078	100.00
Ceboruco	71.2587159	5.406839061	0.104318975	3.260612869	1.869786326	15.91096533	0.366406212	0.088738198	1.401850184	0.049218745	0.282548205	100.00
Ceboruco	71.64357111	5.122849444	0.120512934	3.317254968	1.869469811	15.86193752	0.337814129	0.039786064	1.334356038	0.059521632	0.292926343	100.00
Ceboruco	71.15558472	5.555042128	0.10668556	3.296060117	1.871365919	15.91555508	0.321391532	0.088613703	1.352307153	0.101756872	0.235637215	100.00
Ceboruco	71.48800127	5.237252123	0.101190819	3.345151057	1.83985262	15.87901392	0.403299774	0.084987744	1.316334144	0.081015377	0.223901148	100.00
Ceboruco	71.10696496	5.354296281	0.090808046	3.317001902	1.887141877	16.06288884	0.388212074	0.064497259	1.342739316	0.107495432	0.277954007	100.00
Ceboruco	71.32891906	5.351577274	0.116873527	3.249904207	1.975211482	15.87019468	0.342418929	0.044493957	1.373092299	0.067151018	0.280163571	100.00
Ceboruco	71.17896274	5.546675364	0.096809074	3.340376985	1.857492851	15.82555146	0.345172288	0.060827853	1.35917287	0.099902015	0.289056504	100.00
Ceboruco	71.28178531	5.360953561	0.113025907	3.30782241	1.814225886	16.04138329	0.34115159	0.057238808	1.351831199	0.133660912	0.196921125	100.00
Ceboruco	71.32417642	5.411958917	0.110289163	3.238975412	1.846703818	15.98987862	0.338247432	0.101064233	1.344452572	0.066419496	0.227833923	100.00
Ceboruco	71.08966845	5.440563084	0.100681685	3.36647869	1.888657341	15.95690054	0.377295754	0.042628167	1.334419223	0.141225344	0.261481727	100.00
Ceboruco	71.19956385	5.502395885	0.113228493	3.350206358	1.865957534	15.87107252	0.3187997	0.057780458	1.322085651	0.134220293	0.264689251	100.00

sample_no	SiO2	Na2O	Cl	K2O	FeOt	Al2O3	MgO	P2O3	CaO	MnO	TiO2	total
Ceboruco	71.37048627	5.286938962	0.074984018	3.312051257	1.90674122	15.99453324	0.354965493	0.034251959	1.319556679	0.070561092	0.274929809	100.00
Ceboruco	71.27116332	5.295271031	0.095355848	3.338991017	1.994664381	15.87557079	0.344653521	0.064526514	1.364020089	0.077022124	0.27876137	100.00
Ceboruco	71.17947178	5.267384255	0.14733868	3.363510428	1.916661777	15.90792353	0.380563224	0.084933927	1.365150193	0.12533836	0.261723845	100.00
Ceboruco	71.47680745	5.341716549	0.111048703	3.445249135	1.84337094	15.77228732	0.347791052	0.056683304	1.323031664	0.027498777	0.2545151	100.00
Ceboruco	71.38198732	5.456138714	0.093694367	3.249161256	1.872782701	15.76558434	0.35996211	0.0219676	1.394631102	0.136199118	0.267891377	100.00
La Malinche	74.61514475	4.819264178	0.096761887	2.644551574	1.177235458	14.58603446	0.336309059	0.137660185	1.329655931	0.038028242	0.219354278	100.00
La Malinche	73.94607704	4.670112189	0.081526171	2.487936099	1.449582603	14.96873951	0.436828119	0.067647188	1.624354974	0.017066008	0.250130105	100.00
La Malinche	73.40658678	3.795107308	0.292469426	2.368911242	1.503347519	15.91042791	0.5322078	0.058767221	1.817610714	0.039064258	0.275499822	100.00
La Malinche	74.50612604	4.453956081	0.35501484	2.725597803	1.394864758	14.41818334	0.334057512	0.088295626	1.467033585	0.057260458	0.199609957	100.00
La Malinche	74.81187676	3.982017241	0.169279103	2.67742932	1.247463497	14.96081934	0.327739205	0.014097485	1.519241413	0.045898788	0.244137841	100.00
La Malinche	74.82242256	4.260205004	0.053868312	2.621454098	1.377548428	14.54650019	0.360013029	0.064765337	1.52570546	0.053354301	0.314163283	100.00
La Malinche	73.14841478	4.455315585	0.054756715	2.727619942	1.797981685	14.71075924	0.66229064	0.107981059	1.952298463	0.029012886	0.353569012	100.00
La Malinche	72.6692999	4.50814851	0.117441422	2.435275455	1.686770878	15.73968075	0.489479824	0.081175848	1.843233377	0.059247827	0.370246208	100.00
La Malinche	74.37872623	4.498602962	0.085572847	2.631416836	1.408947597	14.79394977	0.344466968	0.070550979	1.495409187	0.049209567	0.24314706	100.00
La Malinche	73.42594537	4.263634323	0.118853524	2.523384359	1.611573204	15.39476508	0.444879024	0.116839057	1.767527036	0.057147234	0.275451788	100.00
La Malinche	73.39604082	4.552027048	0.171583841	2.55415106	1.716898223	14.99636411	0.454448122	0.051083021	1.712941094	0.066662283	0.327800383	100.00
La Malinche	75.79952349	4.30298416	0.059278742	2.861732391	1.160228075	13.93050446	0.294656232	0.057745671	1.331390231	0.016046142	0.185910401	100.00
La Malinche	75.88373017	4.129416891	0.076961945	2.861798761	1.144719505	13.93082754	0.300284456	0.026880467	1.323836736	0.062959573	0.25858396	100.00
La Malinche	76.06126814	4.111384604	0.072486394	2.780017957	1.114993128	13.94127524	0.292519667	0.01616529	1.34012488	0.030889088	0.238875617	100.00
La Malinche	75.70825328	4.317662633	0.087597977	2.746370151	1.108247137	14.10960427	0.307409685	0.014191281	1.345016337	0.043696893	0.211950351	100.00
La Malinche	75.67	3.98	0.18	3.06	1.04	14.01	0.33	0.07	1.41	0.05	0.20	100.00
La Malinche	75.31	4.00	0.13	2.84	1.25	14.16	0.45	0.03	1.58	0.02	0.23	100.00
La Malinche	75.43	4.17	0.13	2.88	1.08	14.20	0.36	0.06	1.50	0.04	0.15	100.00
La Malinche	75.94	4.02	0.11	2.95	1.06	13.95	0.29	0.04	1.43	0.04	0.15	100.00
La Malinche	75.67	4.20	0.10	2.88	1.12	14.08	0.28	0.02	1.44	0.04	0.18	100.00
La Malinche	75.63	4.10	0.17	3.11	1.17	13.70	0.31	0.02	1.55	0.05	0.19	100.00
La Malinche	75.85	3.96	0.17	2.89	1.09	14.08	0.30	0.02	1.46	0.03	0.15	100.00
La Malinche	75.34	4.27	0.11	2.90	1.11	14.31	0.30	0.03	1.44	0.04	0.17	100.00
La Malinche	76.17	3.99	0.12	2.88	1.02	13.90	0.28	0.00	1.44	0.05	0.15	100.00
La Malinche	75.75	4.15	0.12	2.79	1.07	14.11	0.31	0.02	1.45	0.06	0.17	100.00
La Malinche	76.22	3.91	0.10	2.90	1.05	13.85	0.31	0.06	1.47	0.00	0.13	100.00
La Malinche	75.83	4.13	0.13	2.95	0.99	13.99	0.28	0.06	1.42	0.05	0.16	100.00
La Malinche	75.57	4.10	0.13	2.89	1.10	14.14	0.31	0.05	1.52	0.03	0.16	100.00
La Malinche	75.39	4.22	0.12	2.97	1.13	14.19	0.30	0.05	1.46	0.01	0.16	100.00
La Malinche	75.63	4.07	0.20	3.01	1.17	13.95	0.31	0.03	1.46	0.04	0.14	100.00
La Malinche	75.52	4.12	0.11	2.86	1.34	13.97	0.32	0.07	1.44	0.03	0.22	100.00
La Malinche	75.77	3.97	0.14	3.05	1.08	13.97	0.29	0.09	1.45	0.02	0.18	100.00
La Malinche	75.64	4.09	0.12	2.90	1.08	14.14	0.34	0.02	1.46	0.05	0.15	100.00
La Malinche	75.42	4.20	0.12	2.84	1.15	14.15	0.33	0.06	1.53	0.04	0.17	100.00
La Malinche	77.69451937	3.923680623	0.076988919	3.040392369	0.742886379	13.19221096	0.189122712	0	1.004669316	0.077195047	0.058334308	100.00
La Malinche	77.78247387	3.912526808	0.108968811	3.055684335	0.605854158	13.11354701	0.194735137	0	1.071457585	0.058627706	0.096124578	100.00
La Malinche	78.04307494	3.751195019	0.122756701	3.119842793	0.667817895	12.83316778	0.21592314	0.033878705	1.070181126	0.035058027	0.107103881	100.00
La Malinche	77.2313037	4.040270692	0.090383616	2.967508311	0.794748881	13.27019562	0.23928148	0.018494682	1.149491512	0.028839165	0.169482341	100.00
La Malinche	78.14982151	3.599560368	0.124992596	3.154018772	0.693034563	12.93466284	0.189028735	0	1.030949975	0.038973902	0.084956735	100.00
La Malinche	76.53347185	4.272739274	0.113790553	2.938892041	0.621350805	13.84730627	0.131988675	0	1.358897662	0.047691629	0.133871239	100.00
La Malinche	76.99115818	4.083352492	0.09554428	3.006350205	0.855471365	13.45650588	0.184705215	0.033049261	1.108437202	0.051272685	0.13415323	100.00
La Malinche	77.48246005	3.911984452	0.123173334	3.020831339	0.772226603	13.21081874	0.199757791	0.037547657	1.066757658	0.044461532	0.129980841	100.00
La Malinche	77.79979157	3.699746361	0.095858932	3.378975386	0.723620575	12.86090016	0.205753609	0.070074751	0.993314795	0.048969151	0.122994704	100.00
La Malinche	77.70900373	3.872603722	0.085052509	3.180404413	0.739987906	13.04276598	0.194450133	0.054906005	1.033804767	0.021755209	0.065265628	100.00
La Malinche	77.65832647	3.709525885	0.094792493	3.260778165	0.741408984	13.03266145	0.186240599	0.029472418	1.070035398	0.043686066	0.173072072	100.00

sample_no	SiO2	Na2O	Cl	K2O	FeOt	Al2O3	MgO	P2O3	CaO	MnO	TiO2	total
La Malinche	77.83683277	3.550543552	0.441450696	3.179731748	0.645720622	12.96637693	0.137458442	0	1.069412624	0.056047412	0.116425197	100.00
La Malinche	77.50987724	3.802036636	0.25717669	3.114872957	0.734562348	13.1326695	0.193395958	0.043927696	1.05950256	0.02236319	0.129615226	100.00
La Malinche	77.38180637	3.842503578	0.077897856	2.944414975	0.833631033	13.41000224	0.229870994	0.017356551	1.146392807	0.028101083	0.088022511	100.00
La Malinche	77.03427756	3.789106268	0.183791309	3.195896355	0.895069129	13.29623774	0.210732825	0.050392632	1.143361957	0.046356858	0.15477737	100.00
La Malinche	77.06425648	3.675475581	0.281886434	3.312962529	0.906795414	13.18354161	0.209137875	0.06079457	1.156009267	0.023907977	0.125232261	100.00
La Malinche	77.70119199	3.544918035	0.13758751	3.16122421	0.872200854	13.20712799	0.1336625	0	1.088905444	0	0.153181468	100.00
La Malinche	77.02774949	3.798411356	0.091269364	3.007383185	0.89100276	13.61181449	0.216489675	0.029969045	1.143895839	0.028187668	0.153827126	100.00
La Malinche	77.77571559	3.772167071	0.095841902	3.080260917	0.725214133	13.10151518	0.223943294	0.018731316	1.043856267	0.004890955	0.157863372	100.00
La Malinche	77.33129394	3.66652663	0.325424999	3.114282252	0.891244595	13.19195965	0.202486666	0.002682715	1.079193468	0.017845887	0.177059193	100.00
La Malinche	78.12091378	3.486493581	0.100530096	3.256300928	0.852429649	12.82851439	0.130142765	0.02076165	1.059674323	0.052013397	0.092225436	100.00
La Malinche	77.53171962	3.537983295	0.075371666	3.045841279	0.77312744	13.44300117	0.190700639	0.029012929	1.240876927	0.042538529	0.089826506	100.00
La Malinche	77.92996129	3.642831362	0.063204219	3.12892171	0.672926763	13.07889275	0.206717428	0.006153546	1.081195469	0.014184445	0.175011021	100.00
La Malinche	74.12	3.79	0.12	2.78	1.42	15.05	0.39	0.08	1.90	0.07	0.29	100.00
La Malinche	74.82	4.13	0.39	3.01	1.23	14.37	0.31	0.05	1.39	0.04	0.25	100.00
La Malinche	76.39	3.66	0.09	3.29	1.11	13.95	0.18	0.04	1.02	0.04	0.22	100.00
La Malinche	75.45	4.24	0.07	2.94	1.34	13.93	0.28	0.07	1.35	0.08	0.25	100.00
La Malinche	75.10	4.32	0.08	3.05	1.14	14.26	0.35	0.04	1.40	0.03	0.24	100.00
La Malinche	74.27	3.84	0.34	2.69	1.44	15.22	0.36	0.10	1.42	0.03	0.30	100.00
La Malinche	75.21	4.13	0.08	3.08	1.15	14.33	0.31	0.05	1.40	0.04	0.23	100.00
La Malinche	74.57	3.92	0.13	2.84	1.54	14.86	0.36	0.08	1.46	0.01	0.23	100.00
La Malinche	74.16	4.33	0.09	2.95	1.40	14.66	0.45	0.03	1.62	0.06	0.25	100.00
La Malinche	74.74	4.27	0.08	2.97	1.40	14.36	0.38	0.10	1.47	0.00	0.23	100.00
La Malinche	74.92	3.88	0.08	3.52	1.13	14.57	0.28	0.07	1.27	0.03	0.24	100.00
La Malinche	75.20	3.93	0.12	2.93	1.25	14.47	0.31	0.13	1.41	0.03	0.21	100.00
La Malinche	72.95	4.24	0.07	2.61	1.87	15.21	0.52	0.09	2.08	0.05	0.31	100.00
La Malinche	72.13	3.96	0.26	2.47	1.99	15.85	0.53	0.14	2.31	0.06	0.30	100.00
La Malinche	75.02	3.92	0.11	3.04	1.27	14.58	0.31	0.05	1.45	0.05	0.21	100.00
La Malinche	74.32	4.25	0.11	2.92	1.36	14.65	0.40	0.07	1.60	0.05	0.27	100.00
La Malinche	75.06	4.27	0.08	3.06	1.19	14.47	0.28	0.02	1.34	0.06	0.18	100.00
Toluca	72.51	4.26	0.18	2.64	1.80	15.55	0.47	0.07	2.21	0.07	0.24	100.00
Toluca	72.89	4.34	0.13	2.52	1.87	15.11	0.51	0.11	2.17	0.06	0.30	100.00
Toluca	73.76	4.17	0.20	2.75	1.63	14.88	0.43	0.05	1.87	0.02	0.24	100.00
Toluca	72.41298901	4.199268927	0.533064224	2.477586476	1.922631117	15.09005107	0.568567783	0.103828753	2.31156264	0.055298708	0.325151297	100.00
Toluca	73.04863252	4.088410353	0.158320914	2.55455996	1.956612736	15.20617346	0.464662096	0.118457418	2.08073029	0.057683612	0.265756641	100.00
Toluca	73.43264638	4.309076658	0.129661541	2.703448326	1.764967096	14.78425087	0.492859426	0.049077985	2.048382001	0.075280638	0.210349076	100.00
Toluca	72.93981592	4.232374877	0.36767265	2.644513261	1.785404497	15.09846508	0.48673668	0.037169426	2.047365106	0.035707022	0.324775477	100.00
Toluca	73.69941174	4.316134415	0.14698104	2.742917547	1.843903163	14.5978902	0.411109793	0.021309519	1.999816379	0.029942606	0.190583594	100.00
Toluca	73.05880003	3.88893808	0.444520243	2.538363869	1.883257591	15.16828759	0.515643482	0.074924653	2.096909283	0.070142229	0.260212953	100.00
Toluca	73.125894	4.100206014	0.135163906	2.667981856	1.908990394	14.99669907	0.521969369	0.084711019	2.148919238	0.030001819	0.279463313	100.00
Toluca	72.34269071	4.522748655	0.173304969	2.615140844	1.992189976	15.03238465	0.592869033	0.056453834	2.29343701	0.051265063	0.327515258	100.00
Toluca	72.24165287	4.472206467	0.098363185	2.629920955	1.96675125	15.12116271	0.709768037	0.047317869	2.340008409	0.062124117	0.310724125	100.00
Toluca	73.34796408	4.306948149	0.12432133	2.664777868	1.664215472	15.11410936	0.432973947	0.072389635	1.982846524	0.035670255	0.253783373	100.00
Toluca	72.39670204	4.229759736	0.205129128	2.518374393	1.989931532	15.13211894	0.599566827	0.087927858	2.453800691	0.09825965	0.288429204	100.00
Toluca	73.36477475	4.276174198	0.15688193	2.703392829	1.763607332	14.76484269	0.415300741	0.111009398	2.075439376	0.065881896	0.302694851	100.00
Toluca	74.17061657	3.698776357	0.124499442	2.593307878	1.544986468	15.19102362	0.384036868	0.149192692	1.911402221	0.032338859	0.199819021	100.00
Toluca	72.70354849	4.115818741	0.389191556	2.718199355	2.068418988	15.10271856	0.480177309	0.075745639	2.069925869	0.032527407	0.243728084	100.00
Toluca	72.87692793	4.352796021	0.124846186	2.607480901	1.823097256	15.07732209	0.57072542	0.0819792	2.200713881	0.03546174	0.248649379	100.00
Toluca	72.85879263	4.390209361	0.132598595	2.643710303	1.857276259	14.91831684	0.547433919	0.071875874	2.209976581	0.079311309	0.290498324	100.00
Toluca	76.80467719	3.741266356	0.096322106	3.224516859	1.152137325	13.37822043	0.188096817	0.024390576	1.233073796	0.078545923	0.078752623	100.00
Toluca	76.84546098	3.913500517	0.059220167	3.333722663	1.12209284	13.24830622	0.139146685	0	1.232326341	0.001449445	0.104774141	100.00

sample_no	SiO2	Na2O	Cl	K2O	FeOt	Al2O3	MgO	P2O3	CaO	MnO	TiO2	total
Toluca	76.29325638	3.979046629	0.08774573	3.121226187	1.267901688	13.55208808	0.208357351	0.027905002	1.255562528	0.042684318	0.164226106	100.00
Toluca	76.38097583	4.032365611	0.075450965	3.003488818	1.275274472	13.49399472	0.25784276	0.04531215	1.298630737	0.023279637	0.113384301	100.00
Toluca	75.86194721	4.200888722	0.086585555	3.132692079	1.220060966	13.65076995	0.289132072	0.018796152	1.289744459	0.080833727	0.168549105	100.00
Toluca	76.03189845	4.203544721	0.065790123	3.139748391	1.16852624	13.65508381	0.207491925	0.004957497	1.342113466	0.033979514	0.146865862	100.00
Toluca	76.77465716	3.723747028	0.084117701	3.385224571	1.089435392	13.40053056	0.144743996	0	1.249004035	0.047290561	0.101248989	100.00
Toluca	76.26668175	3.835546197	0.073760504	3.286157617	1.378841592	13.51145535	0.15179403	0.027672906	1.294015271	0.040288496	0.133786293	100.00
Toluca	76.6545045	3.929423031	0.074608006	3.163951012	1.196759921	13.43350296	0.132273565	0.008573287	1.277906484	0.017758951	0.110738285	100.00
Toluca	76.23626374	4.107135427	0.080083994	3.170420329	1.214860901	13.50769346	0.196401363	0.01636678	1.280754658	0.05465887	0.135360478	100.00
Toluca	76.66126851	4.094756548	0.06239629	3.017189036	0.946308291	13.52782616	0.088463162	0.053365248	1.388741505	0.028324632	0.131360611	100.00
Toluca	75.80097234	4.224989799	0.098069106	2.950297013	1.134983702	13.94669726	0.19860536	0.046773001	1.356831979	0.042455494	0.199324945	100.00
Toluca	76.66396812	3.785992494	0.079020988	3.197977311	1.597843127	13.17022492	0.14586903	0	1.207664312	0.054056133	0.097383567	100.00
Toluca	76.46551632	4.073806905	0.078208925	3.073222753	1.112510139	13.4989706	0.209305869	0.017969675	1.288239555	0.035020445	0.147228811	100.00
Toluca	76.98210391	3.924940011	0.057372474	3.075744547	1.211997376	13.18034172	0.196971924	0.008181273	1.219640503	0.034174939	0.108531323	100.00
Toluca	76.04766225	4.267335124	0.066896147	3.020118819	1.189834387	13.73995634	0.163684255	0.027830446	1.330211624	0	0.146470609	100.00
Toluca	76.05039098	4.243554485	0.090756311	3.025210375	1.252547565	13.6712981	0.172839664	0.002787737	1.329648815	0.036343824	0.124622148	100.00
Toluca	76.63936218	3.875200813	0.078537403	3.296504158	1.161700201	13.31550157	0.169682126	0.061073165	1.236579789	0.021081092	0.144777502	100.00
Toluca	76.12156021	4.055407193	0.094455054	3.049255535	1.129894758	13.71611308	0.257184684	0.024743117	1.332189043	0.048151544	0.171045782	100.00
Toluca	76.46606647	4.050721647	0.09026735	3.145991939	1.177026179	13.36931211	0.200479878	0.040404406	1.246912912	0.038348202	0.174468899	100.00
Toluca	76.46265622	4.004591062	0.100783924	3.078078991	1.127386131	13.52935857	0.206097463	0	1.322422444	0.047046224	0.121578973	100.00
Toluca	76.435935	4.013482568	0.072757235	3.169622131	1.203124676	13.46361713	0.145205741	0.037253351	1.251124355	0.035503884	0.172373931	100.00
Toluca	76.60220281	3.842170732	0.075298306	3.265330086	1.196706472	13.35422399	0.162030417	0.04058486	1.274803175	0.063246457	0.123402695	100.00
Toluca	76.6340829	3.984246014	0.074833636	3.075920498	1.1649805	13.47344499	0.188787201	0.00433519	1.268384404	0	0.130984668	100.00
Toluca	76.48680688	3.800417498	0.097121781	3.264857309	1.195378757	13.50494624	0.164787751	0.051290187	1.263632295	0.030485734	0.140275573	100.00
Toluca	75.72	3.91	0.11	2.89	1.26	14.17	0.23	0.01	1.52	0.02	0.15	100.00
Toluca	75.92	3.96	0.14	3.12	1.31	13.58	0.28	0.11	1.48	0.01	0.08	100.00
Toluca	75.79	3.91	0.10	3.08	1.21	13.99	0.25	0.01	1.42	0.05	0.19	100.00
Toluca	75.88	3.97	0.12	2.94	1.28	14.00	0.27	0.00	1.40	0.00	0.13	100.00
Toluca	75.82	3.86	0.11	3.11	1.27	13.90	0.27	0.06	1.34	0.05	0.20	100.00
Toluca	75.78	3.72	0.51	3.02	1.30	13.76	0.25	0.03	1.44	0.02	0.17	100.00
Toluca	75.96	3.98	0.10	3.01	1.18	13.98	0.23	0.02	1.37	0.04	0.12	100.00
Toluca	75.87	4.09	0.12	2.90	1.28	13.79	0.28	0.03	1.41	0.04	0.20	100.00
Toluca	75.97	4.22	0.11	2.81	1.26	13.72	0.24	0.04	1.44	0.05	0.14	100.00
Toluca	75.70	3.99	0.49	3.09	1.25	13.66	0.25	0.07	1.34	0.02	0.13	100.00
Toluca	76.17	3.81	0.11	2.96	1.24	13.95	0.20	0.05	1.36	0.04	0.11	100.00
Toluca	75.75	4.16	0.25	3.03	1.38	13.57	0.23	0.05	1.42	0.02	0.14	100.00
Toluca	75.92	3.79	0.13	3.09	1.20	13.94	0.27	0.00	1.46	0.03	0.16	100.00
Toluca	75.99	3.89	0.12	2.96	1.31	13.90	0.24	0.02	1.38	0.03	0.15	100.00
Toluca	75.67	4.06	0.13	2.99	1.25	14.01	0.27	0.03	1.40	0.02	0.16	100.00
Toluca	75.82	4.10	0.12	3.02	1.21	13.83	0.26	0.04	1.42	0.02	0.16	100.00
Toluca	75.79	3.94	0.10	2.93	1.38	13.98	0.26	0.00	1.43	0.03	0.15	100.00
Toluca	75.3783022	4.269192732	0.119641523	2.801006939	1.368763708	13.84917676	0.314462489	0.06934835	1.634659576	0.050917933	0.144527793	100.00
Toluca	75.28402744	3.618477532	0.364761963	2.804927215	1.562874906	14.03823383	0.387347092	0.004128464	1.747376432	0.046263085	0.14158204	100.00
Toluca	76.04303835	4.169725651	0.119608011	3.000546995	1.255082344	13.49563613	0.300778969	0.039524447	1.372642708	0.07915236	0.124264032	100.00
Toluca	75.68990297	4.116754257	0.151306884	3.017516209	1.168889111	14.00342685	0.248406245	0.058949335	1.454107122	0.025648888	0.065092135	100.00
Toluca	76.10609369	3.81114914	0.329008383	3.186370593	1.27610782	13.47093837	0.19892949	0.035737333	1.406603649	0.02474123	0.154320301	100.00
Toluca	75.82407715	4.018232204	0.10757472	3.016310788	1.185285735	13.75627912	0.307009815	0.065494021	1.528316727	0.047670366	0.143749357	100.00
Toluca	75.11992879	3.902732555	0.289414847	2.904359111	1.502901672	13.91230608	0.342510162	0	1.75821463	0.033127846	0.234504308	100.00
Toluca	76.14500317	4.142436707	0.089389424	3.031557691	1.152834071	13.64431134	0.224875136	0.050768209	1.342225638	0.035091318	0.141507299	100.00
Toluca	76.38513661	3.992005986	0.17055764	3.306729754	1.31823672	13.12374482	0.219288394	0.011312497	1.309282702	0.037962128	0.12574275	100.00
Toluca	76.00766293	4.069793789	0.099762125	2.911467864	1.371748123	13.70407644	0.241891846	0.049359294	1.378628288	0.036732498	0.128876803	100.00

sample_no	SiO2	Na2O	Cl	K2O	FeOt	Al2O3	MgO	P2O3	CaO	MnO	TiO2	total
Toluca	76.08662692	4.127407879	0.118043865	2.930459594	1.165547458	13.61180306	0.266320993	0.028169559	1.444185232	0.067070378	0.154365055	100.00
Toluca	75.82087578	4.281950085	0.088749377	3.037799939	1.215183261	13.63598761	0.315806779	0.022498382	1.440352463	0.054742606	0.086053718	100.00
Toluca	75.82248265	4.159926097	0.105550364	2.959549412	1.360273192	13.65079113	0.256321814	0.118692419	1.418538927	0.02493886	0.122935129	100.00
Toluca	76.21270418	3.840713416	0.158055872	3.076998068	1.284306306	13.55098073	0.243060711	0.063532262	1.415023761	0.000221367	0.15440332	100.00
Toluca	76.12642276	4.06929983	0.070025007	3.005498098	1.265146832	13.67556445	0.236411861	0.054945876	1.334532984	0.006919875	0.155232428	100.00
Toluca	75.99365381	3.808635215	0.098570369	2.941628825	1.493510305	13.6871341	0.234298156	0.060071157	1.474932607	0.031274159	0.176291299	100.00
Toluca	75.01587254	4.265418787	0.115760495	2.822391535	1.236586816	14.2695653	0.226958477	0.026632341	1.879269702	0.037348941	0.104195056	100.00
Toluca	76.10672297	4.150969369	0.083019387	3.04130429	1.206767611	13.54381419	0.242893356	0.022604289	1.368669383	0.058565657	0.174669503	100.00
Toluca	75.8678222	3.888298927	0.183069485	3.040143071	1.288781666	13.6924945	0.270859124	0.082392283	1.482030588	0.042517943	0.161590213	100.00
Toluca	76.12569862	4.088142086	0.08904452	2.912671207	1.180322047	13.66077713	0.222715323	0	1.54930159	0.025693921	0.14563356	100.00
Toluca	76.24880725	4.031334283	0.086694255	3.064636777	1.188267904	13.59677316	0.237869291	0.058721732	1.312889793	0.033423052	0.140582499	100.00
Toluca	76.07165273	4.094261385	0.154883686	3.02573322	1.247850239	13.50653996	0.225977838	0.026871896	1.472725468	0.005712923	0.16779066	100.00
Toluca	76.1443813	4.143295731	0.14899124	2.99238025	1.169165131	13.54375335	0.212396221	0.02615717	1.369626325	0.093747297	0.156105991	100.00
Toluca	75.79261696	4.19646814	0.205027443	3.030176995	1.310747016	13.50634164	0.256257054	0.075536427	1.423217867	0.031391762	0.172218692	100.00
Toluca	75.8738786	4.1074052	0.112542902	2.998405796	1.464915113	13.69803651	0.205472945	0.001745647	1.385828663	0.052574787	0.099193836	100.00
Toluca	75.44325418	4.249334722	0.158279888	3.017340872	1.404356377	13.71098032	0.257883459	0.067864068	1.502461632	0.008978938	0.179265546	100.00
Toluca	76.06040338	4.192432052	0.115369138	2.997537413	1.264524943	13.53755575	0.24557145	0.021631713	1.387182077	0.012154963	0.165637119	100.00
Toluca	75.89977667	4.102015015	0.135387213	3.024718142	1.260749258	13.5623495	0.278957738	0	1.521933707	0.013673383	0.20043937	100.00
Toluca	75.83577737	4.182097644	0.158940569	2.961884616	1.222149974	13.62379954	0.267716824	0.056838983	1.511308441	0.003233043	0.176252993	100.00
Toluca	75.66986697	4.008266272	0.280910816	2.934228072	1.545771969	13.68744217	0.216579249	0.076843558	1.361075715	0.044511686	0.174503526	100.00
Toluca	75.77626953	4.074762208	0.11784338	3.090115299	1.473019924	13.36275188	0.326504725	0.007018228	1.528486089	0.041899868	0.201328868	100.00
Toluca	75.57299001	4.266468034	0.106249482	3.009199676	1.449185927	13.75753093	0.243621508	0	1.405855017	0.042767735	0.146131683	100.00
Toluca	75.78129644	4.0645768	0.182412948	3.045693667	1.346261996	13.66210985	0.276741806	0.029032691	1.455973724	0.018186516	0.137713559	100.00
Toluca	75.63799718	4.082857145	0.133394111	3.012795348	1.386819043	13.73550848	0.276034388	0.027842385	1.495025126	0.037919666	0.173807125	100.00
Toluca	75.5388194	4.184167026	0.127082393	3.010939051	1.417704218	13.70652676	0.267039146	0.036235094	1.473207425	0.039038382	0.199241105	100.00
Toluca	75.74058721	4.043851037	0.212540053	3.175612432	1.549750424	13.29216828	0.235256981	0.088726849	1.44932349	0.041271068	0.170912175	100.00
Toluca	75.80826755	4.309131428	0.119305832	2.990433376	1.211924845	13.63589405	0.248683609	0.012356305	1.49423361	0.02564712	0.144122275	100.00
Toluca	75.86830115	4.117163349	0.107108945	3.093097339	1.258305162	13.61957845	0.258628916	0.032289428	1.398497461	0.041694116	0.205335685	100.00
Toluca	75.80808401	4.109799073	0.117408079	3.097838497	1.339815888	13.60143283	0.268995643	0.033250133	1.445250139	0.020652257	0.157473457	100.00
Toluca	75.78972685	4.184020916	0.108743118	2.993024863	1.248352916	13.63118778	0.309762539	0.055614337	1.490353663	0.021852188	0.167360837	100.00
Toluca	75.9862464	4.023364212	0.129225884	3.118886986	1.160030397	13.52948147	0.259491397	0.024847133	1.506543568	0.052189376	0.209693168	100.00
Toluca	76.21068002	3.987870482	0.113628413	2.972776178	1.305439227	13.46955347	0.254912968	0.004764728	1.511433826	0.004661147	0.164279548	100.00
Toluca	75.97057275	4.25170796	0.122461913	3.053595742	1.149467586	13.55721001	0.23665367	0.020993471	1.408105161	0.059375473	0.169856263	100.00
Toluca	75.6933575	4.342483481	0.137581568	3.027212042	1.372181063	13.49179029	0.264933247	0.024530856	1.470664808	0.017432566	0.157832573	100.00
Toluca	75.52918957	4.187272563	0.124898007	3.024712859	1.520133364	13.49039726	0.236935841	0	1.459811413	0.030864417	0.395784706	100.00
Toluca	75.90478955	3.933334861	0.127370032	2.924259425	1.238731564	13.80684342	0.312710418	0.036862143	1.502471977	0.053439811	0.159186798	100.00
Toluca	75.8328996	4.141037313	0.126291337	2.91520786	1.296783734	13.68041756	0.277717328	0.052020494	1.472015066	0.053153613	0.1524561	100.00
Toluca	75.7811063	4.064473195	0.146835525	2.953174195	1.384069715	13.54342125	0.255495872	0.055873644	1.491112738	0.056285236	0.268152333	100.00
Toluca	75.75492834	4.094600735	0.119728199	3.02689472	1.255846785	13.77697095	0.249718814	0.016482064	1.43738459	0.054421908	0.213022899	100.00
Toluca	75.7164165	4.051584525	0.120928973	3.000028236	1.277026505	13.77292044	0.268662322	0.043093189	1.51469792	0.027422939	0.207218445	100.00
Toluca	75.839371	4.044990721	0.126616637	3.002141551	1.304293088	13.73969937	0.234799071	0.005793607	1.494673167	0.015590068	0.192031721	100.00
Toluca	76.1674259	3.916703128	0.087894519	3.094298272	1.303669325	13.70328287	0.210330042	0.026111354	1.33742009	0.033615799	0.119248704	100.00
Toluca	75.34720334	4.171428916	0.085170944	3.208003073	1.27855578	14.00649956	0.230504758	0.043559147	1.443973735	0.081173752	0.103927001	100.00
Toluca	75.27574786	4.157233452	0.07669379	3.153763309	1.377301998	14.13486873	0.206120959	0.048330399	1.419316587	0.027339442	0.123283475	100.00
Toluca	75.56056647	4.152939238	0.125917936	2.997071913	1.355032658	13.72607309	0.268918159	0.019230359	1.544050934	0.054520114	0.195679132	100.00
Toluca	75.98820825	3.951758787	0.095192106	3.025565321	1.333794853	13.67724043	0.286811243	0.041987437	1.391768418	0.0346808	0.172992357	100.00
Toluca	76.03322477	4.069407276	0.116164968	2.958625188	1.314689521	13.71492671	0.238143375	0.005605816	1.391626655	0.007682044	0.149903676	100.00
Toluca	75.92209265	4.12152689	0.113085676	2.911725465	1.339149978	13.66661714	0.264105803	0.025733912	1.444444768	0.035986466	0.155531251	100.00
Toluca	75.83693422	3.909184005	0.127808599	3.181641426	1.42741478	13.45544739	0.256377318	0.006080953	1.573573106	0.043761143	0.181777056	100.00
Toluca	75.77533486	4.093498575	0.132961758	2.893149369	1.379979217	13.76697462	0.260588631	0.106287331	1.434051716	0.020826572	0.136347359	100.00

sample_no	SiO2	Na2O	Cl	K2O	FeOt	Al2O3	MgO	P2O3	CaO	MnO	TiO2	total
Toluca	76.00126788	4.112896324	0.104165816	2.914162722	1.301020999	13.72400769	0.270438434	0	1.403494062	0.001653426	0.166892652	100.00
Toluca	76.10252125	4.131674844	0.116409939	2.923159952	1.220221989	13.58504852	0.243045773	0.018282661	1.517608745	0.045035256	0.096991067	100.00
Toluca	73.65	4.45	0.11	2.74	1.89	14.73	0.25	0.00	1.91	0.00	0.25	100.00
Toluca	73.53	4.41	0.13	2.67	1.98	14.79	0.24	0.00	2.03	0.00	0.21	100.00
Toluca	73.04	4.60	0.09	2.69	2.20	14.83	0.21	0.00	2.09	0.00	0.26	100.00
Toluca	73.65	4.24	0.10	2.71	1.93	14.82	0.22	0.00	2.08	0.00	0.24	100.00
Toluca	73.76	4.23	0.08	2.71	1.92	14.74	0.22	0.00	2.05	0.00	0.28	100.00
Toluca	73.41	4.54	0.10	2.81	1.99	14.64	0.24	0.00	2.04	0.00	0.23	100.00
Toluca	73.52	4.46	0.08	2.71	2.01	14.70	0.24	0.00	2.00	0.00	0.27	100.00
Toluca	73.67	4.48	0.10	2.72	2.06	14.60	0.21	0.00	1.88	0.00	0.29	100.00
Toluca	73.50	4.44	0.09	2.74	1.93	14.72	0.26	0.00	2.03	0.00	0.29	100.00
Toluca	73.67	3.95	0.11	2.83	1.99	14.91	0.24	0.00	2.03	0.00	0.28	100.00
Toluca	73.04	4.63	0.11	2.85	1.97	14.84	0.25	0.00	2.02	0.00	0.26	100.00
Toluca	72.99	4.66	0.10	2.86	2.09	14.80	0.24	0.00	1.99	0.00	0.26	100.00
Toluca	72.96	4.52	0.11	2.92	1.96	14.87	0.26	0.00	2.09	0.00	0.30	100.00
Toluca	73.35	4.40	0.09	2.85	1.90	14.95	0.23	0.00	1.98	0.00	0.26	100.00
Toluca	73.27	4.51	0.12	2.75	2.04	14.82	0.23	0.00	2.00	0.00	0.27	100.00
Toluca	74.25	3.54	0.11	2.75	2.14	14.59	0.23	0.00	2.11	0.00	0.25	100.00
Toluca	73.89	3.85	0.09	2.81	2.14	14.51	0.24	0.00	2.17	0.00	0.28	100.00
Toluca	74.01	3.83	0.11	2.83	1.99	14.72	0.24	0.00	1.97	0.00	0.27	100.00
Toluca	74.09	3.82	0.10	2.70	2.09	14.70	0.21	0.00	1.99	0.00	0.27	100.00
Toluca	74.14	3.84	0.20	3.00	1.56	14.67	0.25	0.00	2.14	0.00	0.17	100.00
Toluca	74.64	3.96	0.19	2.69	1.50	14.63	0.22	0.00	1.95	0.00	0.20	100.00
Toluca	75.69	3.62	0.14	2.94	1.40	13.97	0.23	0.00	1.79	0.00	0.21	100.00
Toluca	75.67	3.69	0.14	2.92	1.46	13.97	0.21	0.00	1.73	0.00	0.20	100.00
Toluca	75.07	4.03	0.17	2.76	1.66	14.04	0.30	0.00	1.79	0.00	0.16	100.00
Toluca	76.30	3.55	0.13	3.02	1.23	13.83	0.16	0.00	1.62	0.00	0.15	100.00
Toluca	75.95	3.84	0.15	2.98	1.29	13.87	0.18	0.00	1.60	0.00	0.15	100.00
Toluca	75.72	4.13	0.09	2.93	1.28	13.93	0.15	0.00	1.63	0.00	0.13	100.00
Toluca	75.26	4.14	0.14	2.93	1.38	13.94	0.22	0.00	1.79	0.00	0.19	100.00
Toluca	75.39	4.02	0.13	3.02	1.45	13.90	0.22	0.00	1.68	0.00	0.16	100.00
Toluca	75.39	3.96	0.13	3.04	1.36	13.96	0.22	0.00	1.71	0.00	0.21	100.00
Toluca	73.78	3.83	0.18	2.82	1.81	14.51	0.39	0.00	2.38	0.00	0.28	100.00
Toluca	74.75	4.05	0.20	2.88	1.41	14.30	0.24	0.00	1.92	0.00	0.24	100.00
Toluca	74.27	3.85	0.17	2.82	1.77	14.54	0.27	0.00	2.01	0.00	0.28	100.00
Toluca	74.72	3.57	0.17	2.97	1.52	14.45	0.26	0.00	2.11	0.00	0.22	100.00
Toluca	73.13	3.89	0.17	2.80	2.24	15.12	0.30	0.00	1.98	0.00	0.34	100.00
Toluca	72.34	4.50	0.18	2.58	2.15	15.38	0.27	0.00	2.27	0.00	0.32	100.00
Toluca	73.70	4.29	0.15	2.80	2.34	14.21	0.38	0.00	1.74	0.00	0.37	100.00
Toluca	73.80	4.27	0.14	2.98	2.22	14.48	0.28	0.00	1.50	0.00	0.30	100.00
Toluca	73.47	4.32	0.13	3.11	2.31	14.53	0.29	0.00	1.51	0.00	0.32	100.00
Toluca	73.66	4.18	0.15	2.85	2.32	14.40	0.31	0.00	1.79	0.00	0.33	100.00
Toluca	73.42	4.20	0.13	2.85	2.00	15.00	0.20	0.00	1.81	0.00	0.36	100.00
SCVF (SSC, Volcan Yuhalizqui)	59.66619032	4.144607618	0.092511735	2.28209259	7.452142254	14.52147706	3.172415707	0.597437513	6.004704069	0.137520416	1.928900716	100
SCVF (SSC, Volcan Yuhalizqui)	59.53095867	3.932342511	0.065062394	2.216411234	7.639951757	14.49349097	3.125446256	0.625906361	6.295920562	0.127323896	1.947185393	100
SCVF (SSC, Volcan Yuhalizqui)	59.68822417	4.000813183	0.078281217	2.26576665	7.612911672	14.48253548	3.092465292	0.566033416	6.176397394	0.112843458	1.92372807	100
SCVF (SSC, Volcan Yuhalizqui)	60.12849683	3.659515483	0.065283323	2.250449965	7.656494181	14.25284978	3.142520221	0.570823592	6.165732395	0.164355392	1.943478843	100
SCVF (SSC, Volcan Yuhalizqui)	60.03629854	3.149149523	0.071849528	2.282878619	7.771796967	14.5533512	3.352977971	0.529444394	6.282079573	0.104107036	1.866066651	100
SCVF (SSC, Volcan Yuhalizqui)	59.80849766	3.83209973	0.108559218	2.348050498	7.804381735	14.42373877	3.140898718	0.519620526	5.881162817	0.129487448	2.003502877	100
SCVF (SSC, Volcan Yuhalizqui)	59.48308607	3.668189475	0.111837616	2.118695645	7.258544424	14.95735881	3.425751665	0.470329352	6.529748577	0.143721178	1.832737184	100

sample_no	SiO2	Na2O	Cl	K2O	FeOt	Al2O3	MgO	P2O3	CaO	MnO	TiO2	total
SCVF (SSC, Volcan Yuhalizqui)	60.83569988	3.635950673	0.089070635	2.549227986	7.290037145	14.39145839	2.904698024	0.537267572	5.720551158	0.13171018	1.914328357	100
SCVF (SSC, Volcan Yuhalizqui)	59.95254032	3.31707666	0.081038734	2.408707975	7.910804396	14.30935839	3.245631932	0.623508348	6.040905333	0.131690884	1.978737027	100
SCVF (SSC, Volcan Yuhalizqui)	59.84311621	3.800535867	0.088071084	2.523555815	7.538541719	14.2798801	3.151911079	0.640821021	5.988150747	0.147818401	1.997597958	100
SCVF (SSC, Volcan Yuhalizqui)	59.48972097	3.21186614	0.061382331	2.192226096	7.701236366	14.86635185	3.405597749	0.574465201	6.451918177	0.15629253	1.888942587	100
SCVF (SSC, Volcan Yuhalizqui)	60.17607936	4.102215192	0.048860131	2.381931402	7.317084094	14.60714342	3.063937401	0.529521673	5.681425994	0.173155253	1.918646073	100
SCVF (SSC, Volcan Yuhalizqui)	59.46937493	4.091297417	0.077347911	1.740328006	7.527814531	14.94035972	3.185512666	0.519655836	6.471079004	0.159558729	1.817671247	100
SCVF (SSC, Volcan Yuhalizqui)	59.64288864	3.496486169	0.085766749	2.41668897	7.627960833	14.43843112	3.434783472	0.557381031	6.254911685	0.172799667	1.871901663	100
SCVF (SSC, Volcan Yuhalizqui)	60.05379907	4.076205179	0.056884356	2.372716448	7.404974452	14.58105236	2.899986769	0.561238698	5.804560326	0.189988702	1.99859364	100
SCVF (SSC, Volcan Yuhalizqui)	59.51030082	3.754848849	0.086524778	2.295763562	7.695888552	14.88675128	3.061018083	0.538943251	6.04956229	0.142242371	1.978156163	100
SCVF (SSC, Volcan Yuhalizqui)	60.25630865	3.85157413	0.054411127	2.547337387	7.579145353	14.35679352	2.903964622	0.608507955	5.655846439	0.144829631	2.041281188	100
SCVF (SSC, Volcan Yuhalizqui)	59.52961471	3.389777901	0.08372343	2.184977321	7.552088526	14.88643427	3.308096505	0.543181278	6.43975942	0.135867041	1.946479591	100
SCVF (SSC, Volcan Yuhalizqui)	59.64682204	3.859301708	0.094552892	2.22417651	7.469738515	14.92940397	3.117909537	0.580621786	5.9384415	0.159113839	1.979917698	100
SCVF (SSC, Volcan Yuhalizqui)	60.5517585	4.202400207	0.078234004	2.529600125	6.80073309	14.72880073	2.978400147	0.561102028	5.536636775	0.109766569	1.922567824	100
SCVF(Maar, Xicotencatl)	54.1779864	3.962018746	0.07553563	1.481897921	7.965630802	16.47582341	4.754422496	0.503742383	8.668307857	0.165949452	1.768684906	100
SCVF(Maar, Xicotencatl)	54.28274675	3.893054915	0.072284839	1.621245681	8.13292071	16.12984556	4.853410636	0.642405693	8.444821716	0.141475222	1.785788274	100
SCVF(Maar, Xicotencatl)	54.63692903	3.709881213	0.072742769	1.537989971	7.783881963	16.58535131	4.707496329	0.517305005	8.593926368	0.11693989	1.737556158	100
SCVF(Maar, Xicotencatl)	54.41031264	3.871151678	0.063967159	1.531899594	7.806973679	16.60247939	4.771660223	0.570218572	8.464667271	0.13117777	1.775492022	100
SCVF(Maar, Xicotencatl)	54.21542347	3.977483256	0.063743043	1.570331052	7.932145676	16.46781379	4.824635534	0.599515203	8.512046572	0.123141956	1.71372045	100
SCVF(Maar, Xicotencatl)	54.13490907	3.915631726	0.085149452	1.605616184	8.082903979	16.20118523	4.816848551	0.68368173	8.513681642	0.14757789	1.812814545	100
SCVF(Maar, Xicotencatl)	54.62831119	3.884745313	0.0636437	1.601424265	7.932640217	16.18988273	4.576973866	0.521754357	8.649876901	0.15757735	1.79317012	100
SCVF(Maar, Xicotencatl)	54.42193875	4.250104522	0.06771353	1.502458257	8.126327629	16.15657167	4.764645021	0.471113281	8.38415308	0.178089537	1.676884729	100
SCVF(Maar, Xicotencatl)	54.33986367	4.014645045	0.064565425	1.53135945	7.976689929	16.46211409	4.81136584	0.51507482	8.429951339	0.113383544	1.740986842	100
SCVF(Maar, Xicotencatl)	53.97570035	4.373791486	0.066996194	1.553982387	7.998039329	16.36312579	4.692820982	0.612536633	8.437131768	0.161569574	1.764305504	100
SCVF(Maar, Xicotencatl)	54.37342661	4.1224562	0.063748258	1.580791475	8.018903556	16.27285342	4.835362159	0.502547041	8.459934278	0.135794584	1.634182416	100
SCVF(Maar, Xicotencatl)	54.11561655	4.189852408	0.06445131	1.520761244	8.061592889	16.45939551	4.769190024	0.541473765	8.460285272	0.158914194	1.658466833	100
SCVF(Maar, Xicotencatl)	55.18475475	3.630718214	0.061450949	1.627563337	7.836535907	16.40083055	4.454932981	0.514038754	8.457418201	0.126067196	1.705689158	100
SCVF(Maar, Xicotencatl)	55.80868314	3.313031814	0.295972326	1.540376415	7.934506591	16.33288009	4.535552779	0.501355848	7.960623174	0.154400185	1.622617635	100
SCVF(Maar, Xicotencatl)	54.51980099	3.809531459	0.079399745	1.583854112	8.120715299	16.26297262	4.875786188	0.572464918	8.254098878	0.144766269	1.776609526	100
SCVF(Maar, Xicotencatl)	54.40149339	3.968653127	0.06349845	1.546228491	7.978969211	16.44156296	4.752075563	0.547983377	8.429925142	0.191003765	1.678606526	100
SCVF(Maar, Xicotencatl)	54.52688659	3.842734996	0.08628221	1.547341292	7.857104788	16.53913142	4.754744101	0.532961726	8.463925797	0.161103001	1.687784076	100
SCVF(Maar, Xicotencatl)	54.55508893	4.071364883	0.070060543	1.529345184	7.901607038	16.2647927	4.815370648	0.479780385	8.450552618	0.158844276	1.703192793	100
SCVF(Maar, Xicotencatl)	54.45030787	3.919891012	0.084793432	1.495747886	7.952390145	16.31912521	4.72450022	0.630380368	8.478084934	0.172431058	1.772347857	100
SCVF(Maar, Xicotencatl)	54.57965434	3.903474484	0.0536599	1.534611341	7.832683141	16.3657545	4.748025692	0.640828977	8.433269317	0.17339974	1.734638571	100
SCVF(Maar, Xicotencatl)	54.15537573	4.111569701	0.068252057	1.511001865	8.009858179	16.43599988	4.841373322	0.586926575	8.427006961	0.132739082	1.719896652	100
SCVF(Maar, Xicotencatl)	54.34764186	4.102449754	0.085347447	1.535841742	7.967822798	16.26549174	4.81367848	0.584856782	8.429493969	0.12612811	1.741247316	100
SCVF(Maar, Xicotencatl)	54.51871409	3.748301924	0.059931641	1.524034848	7.756165058	16.57902774	4.788352733	0.540929396	8.5791075	0.194181406	1.711253657	100
SCVF(Maar, Xicotencatl)	54.72194795	3.824691858	0.064470416	1.53402275	7.731409392	16.42855446	4.726448474	0.539291917	8.603544971	0.165331882	1.660285939	100
SCVF(Maar, Xicotencatl)	54.23705743	4.016811143	0.038729867	1.479337096	7.983972757	16.57063011	4.746206517	0.593789473	8.548312287	0.183396218	1.601757101	100
SCVF(Maar, Xicotencatl)	54.56795262	4.077303913	0.085468548	1.527698681	7.774811149	16.50533913	4.655352063	0.533765532	8.420351061	0.130141397	1.721815902	100
SCVF(Maar, Xicotencatl)	54.34730359	4.05661955	0.061261133	1.51351034	7.830085075	16.56624583	4.787634748	0.596137746	8.409422172	0.126660184	1.705119636	100
SCVF(Maar, Xicotencatl)	54.41560152	4.160121056	0.083820261	1.472518096	7.777466927	16.38305099	4.829447463	0.510026722	8.452622379	0.182477415	1.73284717	100
SCVF(Maar, Xicotencatl)	54.45577173	3.898988875	0.079522913	1.481410021	7.877269216	16.50126163	4.742569582	0.505222543	8.570806959	0.169379055	1.717797479	100
SCVF (Teuthli)	58.4821216	3.849984222	0.049064443	1.594848345	8.688373053	14.62790839	3.484286512	0.240954158	6.70816253	0.151712695	2.122584055	100
SCVF (Teuthli)	58.46369296	3.751094107	0.041475512	1.62649067	8.927600163	14.20129666	3.49695494	0.279349773	6.910421816	0.133718578	2.167904824	100
SCVF (Teuthli)	58.43276267	3.846072859	0.039272565	1.471452677	8.246097454	14.89718986	3.82577696	0.220311984	7.043676316	0.18770201	1.789684642	100
SCVF (Teuthli)	58.73772158	3.993259732	0.030968137	1.446537964	7.927525665	15.11734042	3.738587556	0.205978857	6.893674922	0.166274541	1.742130633	100
SCVF (Teuthli)	58.90656241	3.818222603	0.038794775	1.449699491	7.966123276	14.99724333	3.675294484	0.216229825	6.898305445	0.197199391	1.836324976	100
SCVF (Teuthli)	59.52600879	3.441523803	0.043121474	1.628578228	8.515103964	14.20652832	3.462009064	0.283311156	6.659167435	0.171660561	2.062987207	100
SCVF (Teuthli)	58.17128685	3.774312193	0.033866801	1.417917283	8.501619155	14.85242852	3.825316411	0.233701331	7.02825178	0.150676823	2.010622849	100
SCVF (Teuthli)	59.34018336	3.672949608	0.041141139	1.65180136	8.614747412	14.06596065	3.4985358	0.266340145	6.62827228	0.175756611	2.044311631	100

sample_no	SiO2	Na2O	Cl	K2O	FeOt	Al2O3	MgO	P2O3	CaO	MnO	TiO2	total
SCVF (Teuthli)	58.34956538	3.767549005	0.061808169	1.568114991	8.974352252	14.25559083	3.604627967	0.282566175	6.828296077	0.201803241	2.105725917	100
SCVF (Teuthli)	59.45703285	3.548864122	0.055840917	1.564772941	8.512992273	14.31818378	3.446591381	0.2637614	6.596910237	0.164140352	2.070909755	100
SCVF (Teuthli)	58.9797294	3.430031159	0.026666711	1.821885986	8.525105776	14.27992201	3.623415705	0.250076752	6.866942623	0.146227005	2.049996874	100
SCVF (Teuthli)	59.12280765	3.334613139	0.034467867	1.529639055	8.445792284	14.7151277	3.599750575	0.224551013	6.775828103	0.152522818	2.064899797	100
SCVF (Teuthli)	59.13384866	3.651420308	0.040084027	1.52992471	8.404867022	14.43228977	3.447430347	0.233466511	6.891782743	0.169600497	2.065285411	100
SCVF (Teuthli)	58.50148645	3.782848438	0.050130431	1.49673678	8.362380033	14.43428347	3.834106547	0.306933556	7.115635092	0.138994631	1.976464572	100
SCVF (Teuthli)	59.53310937	3.854702644	0.029651559	1.59504937	8.2445329	14.30432095	3.455940302	0.269624692	6.480261625	0.162423029	2.070383552	100
SCVF (Teuthli)	59.79048252	3.553427434	0.188491103	1.583097479	8.530948308	14.24787731	3.257308481	0.279490735	6.298562465	0.221734987	2.048579186	100
SCVF (Teuthli)	58.41218668	3.735058671	0.028723413	1.431095849	7.983110198	15.38681778	3.816255598	0.190102307	7.024082388	0.156018958	1.83654815	100
SCVF (Teuthli)	58.64777823	3.935612192	0.022474685	1.403396596	7.776299079	15.37634531	3.742390922	0.240407939	7.02747561	0.150103338	1.677716101	100
SCVF (Teuthli)	58.90744414	3.99843267	0.036330936	1.430911184	8.23581507	14.80637885	3.5620555	0.2498513	6.79494873	0.152450878	1.825380742	100

Secondary standard raw analyses, StHs6/80-G

Date	SiO2	Na2O	Cl	K2O	FeO	Al2O3	MgO	P2O5	CaO	MnO	TiO2	Total
Mar 13 21:50 2020	63.43	4.49	0.00	1.25	4.26	17.84	1.94	0.17	5.20	0.07	0.73	99.39
Mar 13 21:54 2020	63.65	4.44	0.01	1.23	4.26	17.45	1.96	0.15	5.26	0.05	0.67	99.14
Mar 13 21:58 2020	63.59	4.57	0.03	1.25	4.40	17.76	1.91	0.15	5.30	0.09	0.66	99.71
Mar 14 05:19 2020	63.25	4.66	0.04	1.22	4.29	17.73	1.97	0.17	5.24	0.07	0.70	99.34
Mar 14 05:23 2020	62.66	4.52	0.01	1.22	4.39	17.45	2.00	0.20	5.24	0.06	0.70	98.44
Mar 14 05:27 2020	62.81	4.78	0.02	1.20	4.26	17.51	1.98	0.18	5.32	0.05	0.74	98.85
Mar 14 21:26 2020	63.55	4.53	0.00	1.29	4.34	17.81	1.92	0.14	5.31	0.07	0.71	99.68
Mar 14 21:30 2020	63.63	4.51	0.01	1.28	4.25	17.60	1.94	0.17	5.35	0.09	0.67	99.52
Mar 14 21:34 2020	63.18	4.61	0.02	1.29	4.34	17.72	1.96	0.14	5.25	0.11	0.69	99.29
Mar 15 07:07 2020	63.11	4.57	0.00	1.25	4.20	17.62	1.89	0.17	5.30	0.08	0.70	98.90
Mar 15 07:11 2020	63.03	4.64	0.03	1.27	4.31	17.45	1.93	0.13	5.35	0.11	0.68	98.91
Mar 15 07:15 2020	62.80	4.40	0.00	1.24	4.35	17.58	1.95	0.14	5.28	0.08	0.71	98.53
Mar 9 21:03 2020	63.80	4.51	0.02	1.33	4.33	18.05	1.98	0.17	5.29	0.09	0.70	100.28
Mar 9 21:07 2020	63.56	4.50	0.03	1.31	4.29	17.79	1.94	0.19	5.33	0.10	0.71	99.74
Mar 9 21:11 2020	64.09	4.60	0.01	1.29	4.27	17.92	1.98	0.19	5.31	0.09	0.68	100.42
Mar 10 06:05 2020	63.30	4.68	0.01	1.29	4.27	17.78	1.97	0.14	5.31	0.11	0.71	99.57
Mar 10 06:09 2020	63.38	4.49	0.02	1.26	4.19	17.60	1.97	0.13	5.38	0.07	0.69	99.17
Mar 10 06:13 2020	63.28	4.68	0.03	1.29	4.27	17.71	1.93	0.13	5.34	0.04	0.70	99.40
Mar 10 22:11 2020	63.50907612	4.660686746	0.018	1.3	4.280725815	17.69978975	2	0.139858122	5.27	0.1036	0.6871	99.66883655
Mar 10 22:15 2020	62.89110617	4.670316264	0.018	1.32	4.382405763	17.85747162	2	0.162225137	5.31	0.0873	0.6632	99.36202495
Mar 10 22:19 2020	63.00254337	4.651057228	0.0065	1.25	4.27055782	17.8476165	2.04	0.160682585	5.31	0.0746	0.7155	99.3290575
Mar 11 04:50 2020	63.54959874	4.525873493	0.0265	1.31	4.199381857	17.6702244	2.02	0.221484875	5.18	0.0288	0.6482	99.38006336
Mar 11 04:54 2020	63.49894547	4.496984938	0.0273	1.3	4.351901779	17.71949998	1.98	0.223670158	5.29	0.0986	0.672	99.65890232
Mar 11 18:09 2020	62.63783979	4.545132529	0.0184	1.3	4.250221831	17.70964487	2	0.099494656	5.27	0.035	0.7266	98.59233367
Mar 11 18:13 2020	63.30646302	4.699204818	0.0258	1.29	4.453581727	17.69978975	2.05	0.124304047	5.29	0.0785	0.6739	99.69154336
Mar 12 09:45 2020	63.80286511	4.631798191	0.0249	1.27	4.372237769	17.74906533	2	0.197318214	5.3	0.0593	0.674	100.0814846
Mar 12 09:49 2020	63.56986005	4.516243975	0.019	1.3	4.301061805	17.59138346	2.02	0.119933481	5.21	0.0855	0.7241	99.45708278
Mar 12 09:53 2020	63.62051333	4.525873493	0.0212	1.29	4.27055782	17.73921022	1.99	0.17816485	5.2	0.0958	0.7078	99.6391197
Mar 12 21:14 2020	63.18	4.69	0.02	1.26	4.46	17.96	1.98	0.18	5.26	0.08	0.70	99.76
Mar 12 21:18 2020	63.39	4.30	0.04	1.25	4.25	17.78	1.94	0.15	5.25	0.08	0.71	99.14
Mar 12 21:22 2020	63.54	4.50	0.01	1.30	4.29	17.62	1.92	0.15	5.20	0.04	0.69	99.25
Mar 13 10:33 2020	63.62	4.66	0.02	1.26	4.38	17.98	1.98	0.15	5.16	0.09	0.66	99.96
Mar 13 10:37 2020	63.50	4.41	0.01	1.26	4.42	17.85	1.96	0.10	5.17	0.07	0.69	99.44
Mar 13 10:41 2020	63.31	4.40	0.01	1.28	4.35	17.91	1.96	0.13	5.18	0.06	0.76	99.34
Feb 14 22:47 2020	63.69	4.66	0.02	1.32	4.27	17.86	2.00	0.12	5.23	0.09	0.72	99.97
Feb 14 22:51 2020	63.48	4.85	0.00	1.27	4.32	17.77	1.87	0.14	5.24	0.08	0.72	99.76
Feb 14 22:55 2020	63.91	4.68	0.03	1.29	4.44	17.85	1.99	0.14	5.25	0.08	0.75	100.41

Date	SiO2	Na2O	Cl	K2O	FeO	Al2O3	MgO	P2O5	CaO	MnO	TiO2	Total
Feb 14 22:59 2020	63.88	4.72	0.00	1.28	4.44	17.60	1.98	0.12	5.23	0.09	0.70	100.03
Feb 14 23:02 2020	63.87	4.63	0.00	1.29	4.33	17.71	1.94	0.12	5.18	0.05	0.73	99.85
Feb 15 08:15 2020	63.07	4.82	0.02	1.26	4.17	17.69	2.04	0.10	5.23	0.10	0.78	99.28
Feb 15 08:19 2020	63.03	4.74	0.02	1.30	4.43	17.70	2.01	0.17	5.28	0.04	0.65	99.36
Feb 15 08:23 2020	63.39	4.61	0.01	1.29	4.31	17.60	1.98	0.13	5.22	0.07	0.73	99.35
Feb 16 00:24 2020	63.59	4.72	0.00	1.23	4.29	17.66	2.03	0.15	5.32	0.08	0.73	99.80
Feb 16 00:28 2020	63.46	4.61	0.01	1.29	4.22	17.60	1.96	0.07	5.20	0.08	0.76	99.27
Feb 16 00:32 2020	63.78	4.54	0.00	1.32	4.14	17.82	2.00	0.11	5.21	0.06	0.69	99.66
Feb 16 13:26 2020	63.50	4.63	0.01	1.27	4.32	17.51	1.96	0.15	5.24	0.05	0.71	99.36
Feb 16 13:30 2020	63.22	4.67	0.01	1.27	4.33	17.24	2.00	0.11	5.27	0.09	0.70	98.91
Feb 16 13:34 2020	63.36	4.70	0.01	1.25	4.36	17.84	2.07	0.15	5.21	0.08	0.67	99.71
Feb 16 13:38 2020	63.16	4.65	0.02	1.25	4.24	17.88	1.99	0.14	5.22	0.05	0.71	99.32
Feb 16 13:42 2020	63.43	4.73	0.00	1.27	4.33	17.54	2.03	0.11	5.31	0.06	0.68	99.50
Feb 13 18:17 2020	63.48	4.55	0.00	1.24	4.32	17.61	2.01	0.22	5.34	0.07	0.70	99.53
Feb 13 18:21 2020	63.85	4.56	0.00	1.27	4.45	17.79	2.01	0.12	5.36	0.08	0.72	100.21
Feb 13 18:25 2020	63.56	4.45	0.01	1.25	4.24	17.80	1.95	0.15	5.30	0.06	0.63	99.41
Feb 13 18:29 2020	63.61	4.52	0.01	1.36	4.39	17.67	1.96	0.22	5.29	0.08	0.67	99.78
Feb 13 18:33 2020	63.47	4.59	0.00	1.31	4.25	17.73	1.95	0.12	5.31	0.10	0.72	99.54
Feb 14 13:42 2020	63.60	4.66	0.00	1.34	4.25	17.58	1.96	0.09	5.20	0.09	0.67	99.44
Feb 14 13:46 2020	63.38	4.51	0.01	1.31	4.32	17.55	1.96	0.18	5.29	0.07	0.71	99.28
Feb 14 13:49 2020	63.86	4.67	0.00	1.30	4.36	17.45	1.99	0.03	5.20	0.05	0.65	99.57
Feb 12 16:52 2020	63.40	4.60	0.00	1.32	4.36	17.50	2.05	0.16	5.25	0.08	0.70	99.42
Feb 12 16:56 2020	63.39	4.58	0.01	1.32	4.34	17.45	2.03	0.15	5.35	0.05	0.71	99.38
Feb 12 17:00 2020	63.68	4.70	0.01	1.34	4.21	17.06	2.02	0.18	5.23	0.07	0.65	99.16
Feb 13 00:34 2020	63.77	4.56	0.00	1.28	4.41	17.81	2.05	0.19	5.32	0.03	0.70	100.14
Feb 13 00:38 2020	63.67	4.67	0.02	1.31	4.33	17.74	2.07	0.13	5.28	0.06	0.74	100.03
Feb 13 00:42 2020	63.61	4.51	0.02	1.25	4.42	17.79	2.04	0.08	5.24	0.04	0.74	99.76
Feb 13 07:59 2020	63.55	4.59	0.02	1.25	4.33	17.54	2.08	0.19	5.31	0.06	0.73	99.66
Feb 13 08:03 2020	63.56	4.67	0.00	1.32	4.37	17.58	2.06	0.18	5.28	0.07	0.74	99.84
Feb 13 08:07 2020	63.48	4.47	0.01	1.26	4.30	17.63	1.99	0.13	5.30	0.08	0.70	99.36
Feb 13 08:11 2020	63.36	4.74	0.01	1.25	4.36	17.84	2.03	0.20	5.24	0.05	0.72	99.82
Feb 13 08:15 2020	63.46	4.62	0.01	1.33	4.35	17.89	2.03	0.13	5.29	0.09	0.70	99.89
Feb 13 08:19 2020	63.55	4.75	0.01	1.30	4.29	17.43	2.01	0.14	5.20	0.08	0.71	99.47
Jan 20 18:51 2020	63.65	4.50	0.01	1.30	4.29	17.77	1.87	0.09	5.23	0.08	0.69	99.47
Jan 20 19:10 2020	63.59	4.77	0.02	1.30	4.39	17.90	1.85	0.16	5.20	0.05	0.72	99.95
Jan 20 19:14 2020	63.24	4.68	0.01	1.30	4.27	17.79	1.88	0.20	5.14	0.06	0.70	99.27
Jan 20 19:18 2020	63.56	4.50	0.04	1.24	4.32	17.98	1.91	0.10	5.20	0.10	0.68	99.63

Date	SiO2	Na2O	Cl	K2O	FeO	Al2O3	MgO	P2O5	CaO	MnO	TiO2	Total
Jan 20 19:22 2020	63.38	4.62	0.02	1.26	4.23	17.95	1.78	0.13	5.24	0.05	0.70	99.36
Jan 21 03:07 2020	63.66	4.59	0.03	1.32	4.23	17.75	1.96	0.15	5.26	0.04	0.68	99.68
Jan 21 03:11 2020	63.89	4.81	0.02	1.28	4.25	17.86	1.92	0.21	5.33	0.09	0.73	100.39
Jan 21 03:15 2020	63.61	4.77	0.04	1.32	4.28	17.84	1.94	0.10	5.30	0.12	0.71	100.02
Jan 21 12:39 2020	63.38	4.69	0.03	1.32	4.20	17.80	1.99	0.14	5.36	0.08	0.68	99.67
Jan 21 12:43 2020	63.29	4.69	0.02	1.31	4.32	17.67	1.99	0.18	5.37	0.05	0.66	99.56
Jan 21 12:47 2020	63.59	4.75	0.03	1.30	4.19	17.76	2.01	0.21	5.33	0.06	0.72	99.95
Jan 21 12:51 2020	63.60	4.67	0.03	1.29	4.31	18.01	2.01	0.14	5.36	0.08	0.74	100.24
Jan 21 12:55 2020	63.46	4.81	0.01	1.28	4.30	17.85	1.94	0.22	5.37	0.08	0.70	100.02
Jan 21 12:59 2020	63.73	3.34	0.03	1.35	4.33	17.85	2.03	0.16	5.40	0.09	0.77	99.07
Jan 21 13:03 2020	64.07	3.58	0.02	1.30	4.43	17.98	1.93	0.13	5.36	0.07	0.66	99.53
Jan 16 19:51 2020	63.60	4.37	0.03	1.29	4.31	17.76	1.90	0.00	5.26	0.08	0.73	99.33
Jan 16 19:55 2020	63.06	4.63	0.02	1.31	4.27	17.76	1.93	0.00	5.36	0.05	0.73	99.12
Jan 16 19:59 2020	63.23	4.76	0.00	1.29	4.42	17.77	1.93	0.00	5.30	0.07	0.68	99.45
Jan 16 20:03 2020	63.25	4.80	0.03	1.29	4.20	17.75	1.94	0.00	5.22	0.04	0.69	99.21
Jan 16 20:07 2020	62.89	4.71	0.02	1.31	4.28	17.81	1.92	0.00	5.33	0.06	0.71	99.05
Jan 17 00:28 2020	63.75	4.76	0.04	1.23	4.33	17.71	1.95	0.00	5.39	0.05	0.67	99.88
Jan 17 00:32 2020	63.46	4.77	0.04	1.28	4.25	17.75	1.94	0.00	5.29	0.06	0.66	99.50
Jan 17 00:36 2020	63.30	4.42	0.03	1.31	4.37	17.77	1.97	0.01	5.31	0.05	0.61	99.16
Jan 17 08:58 2020	63.19	4.52	0.00	1.30	4.23	17.85	1.91	0.02	5.26	0.09	0.67	99.04
Jan 17 09:02 2020	63.10	4.54	0.03	1.30	4.39	17.89	1.95	0.02	5.29	0.05	0.67	99.24
Jan 17 09:06 2020	63.20	4.75	0.01	1.27	4.21	17.60	1.95	0.00	5.30	0.08	0.77	99.15
Jan 17 23:16 2020	63.27	4.68	0.01	1.20	4.32	17.83	1.93	0.00	5.29	0.09	0.66	99.28
Jan 17 23:20 2020	63.34	4.63	0.00	1.30	4.42	17.86	1.87	0.00	5.24	0.09	0.71	99.45
Jan 17 23:24 2020	63.16	4.65	0.02	1.28	4.28	17.77	1.88	0.00	5.29	0.07	0.63	99.04
Jan 17 23:28 2020	63.00	4.62	0.03	1.30	4.37	17.78	1.92	0.04	5.32	0.06	0.69	99.13
Jan 17 23:32 2020	63.71	4.67	0.03	1.29	4.34	17.95	1.85	0.01	5.29	0.08	0.66	99.89
Jan 22 20:41 2020	63.16	4.72	0.02	1.27	4.41	17.35	1.93	0.19	5.24	0.07	0.74	99.11
Jan 22 20:45 2020	63.44	4.65	0.00	1.27	4.41	17.78	1.98	0.14	5.39	0.10	0.70	99.85
Jan 22 20:48 2020	63.51	4.64	0.01	1.28	4.27	17.61	1.99	0.15	5.29	0.08	0.67	99.49
Jan 22 20:52 2020	63.34	4.60	0.03	1.33	4.37	17.61	1.94	0.16	5.27	0.03	0.70	99.39
Jan 22 20:56 2020	63.43	4.81	0.00	1.28	4.37	17.78	1.92	0.14	5.32	0.07	0.68	99.81
Jan 23 04:06 2020	63.64	4.67	0.01	1.28	4.38	17.83	1.93	0.22	5.24	0.10	0.69	100.00
Jan 23 04:10 2020	63.16	4.68	0.01	1.31	4.36	17.76	1.94	0.14	5.20	0.06	0.77	99.39
Jan 23 04:14 2020	63.26	4.68	0.04	1.31	4.08	17.75	1.95	0.12	5.37	0.05	0.65	99.25
Jan 23 12:16 2020	63.58	4.69	0.01	1.31	4.30	17.93	1.97	0.12	5.24	0.07	0.72	99.94
Jan 23 12:20 2020	63.82	4.53	0.04	1.32	4.29	17.99	1.87	0.16	5.34	0.04	0.70	100.10

Date	SiO2	Na2O	Cl	K2O	FeO	Al2O3	MgO	P2O5	CaO	MnO	TiO2	Total
Jan 23 12:24 2020	62.92	4.55	0.02	1.35	4.24	17.75	1.95	0.16	5.30	0.06	0.70	98.99
Jan 24 20:45 2020	63.53	4.81	0.03	1.30	4.28	18.01	2.01	0.17	5.24	0.08	0.76	100.21
Jan 24 20:49 2020	63.76	4.79	0.03	1.31	4.27	17.80	1.97	0.17	5.28	0.08	0.68	100.13
Jan 24 20:53 2020	63.81	4.70	0.03	1.31	4.30	17.91	1.96	0.17	5.26	0.07	0.72	100.24
Jan 24 20:57 2020	63.61	4.62	0.03	1.36	4.31	17.87	1.96	0.14	5.25	0.08	0.76	99.98
Jan 24 21:01 2020	63.28	4.66	0.03	1.33	4.38	17.45	1.91	0.14	5.38	0.08	0.61	99.25
Jan 25 05:53 2020	63.12	4.64	0.01	1.35	4.38	17.58	1.95	0.16	5.27	0.06	0.65	99.16
Jan 25 05:57 2020	63.14	4.75	0.01	1.31	4.25	17.83	1.98	0.19	5.32	0.10	0.63	99.51
Jan 25 06:01 2020	63.17	4.67	0.00	1.33	4.49	17.62	1.94	0.14	5.27	0.05	0.69	99.37
Jan 25 06:05 2020	63.71	3.24	0.03	1.30	4.35	17.90	2.00	0.20	5.26	0.08	0.70	98.77
Jan 25 23:03 2020	62.90	4.79	0.02	1.28	4.29	17.72	1.97	0.09	5.27	0.05	0.68	99.06
Jan 25 23:07 2020	63.06	4.71	0.03	1.32	4.31	17.78	1.98	0.22	5.29	0.07	0.74	99.50
Jan 25 23:11 2020	63.51	3.98	0.03	1.30	4.25	17.55	2.05	0.17	5.35	0.09	0.75	99.04

Secondary standard raw analyses, AtHo-G

Date	SiO2	Na2O	Cl	K2O	FeO	Al2O3	MgO	P2O5	CaO	MnO	TiO2	Total
Mar 13 22:14 2020	75.64	4.22	0.02	2.66	3.24	12.23	0.11	0.04	1.75	0.09	0.26	100.25
Mar 13 22:18 2020	75.14	4.23	0.03	2.58	3.21	12.24	0.12	0.00	1.69	0.11	0.26	99.61
Mar 13 22:22 2020	75.65	4.25	0.05	2.62	3.26	12.23	0.09	0.00	1.73	0.13	0.25	100.24
Mar 14 13:12 2020	75.67	3.91	0.02	2.64	3.21	12.37	0.07	0.02	1.64	0.11	0.22	99.88
Mar 14 13:16 2020	76.13	3.88	0.04	2.67	3.20	12.23	0.09	0.01	1.69	0.11	0.21	100.26
Mar 14 13:20 2020	75.79	4.10	0.04	2.61	3.05	12.27	0.11	0.00	1.69	0.10	0.23	99.98
Mar 14 21:50 2020	74.92	4.18	0.03	2.67	3.27	12.09	0.11	0.03	1.71	0.12	0.25	99.36
Mar 14 21:54 2020	75.11	4.07	0.04	2.73	3.22	12.08	0.09	0.04	1.78	0.13	0.26	99.55
Mar 14 21:58 2020	75.28	4.13	0.04	2.65	3.30	12.21	0.12	0.01	1.69	0.13	0.25	99.81
Mar 15 07:43 2020	75.89	4.04	0.05	2.64	3.32	12.23	0.11	0.04	1.71	0.07	0.34	100.43
Mar 15 07:47 2020	75.65	4.02	0.06	2.59	3.34	12.33	0.10	0.00	1.68	0.11	0.23	100.12
Mar 15 07:51 2020	75.35	3.96	0.04	2.62	3.26	12.07	0.07	0.02	1.72	0.07	0.21	99.40
Mar 9 21:27 2020	75.77	4.04	0.04	2.67	3.34	12.43	0.09	0.00	1.71	0.14	0.24	100.46
Mar 9 21:31 2020	75.22	4.03	0.03	2.70	3.22	12.31	0.09	0.03	1.67	0.09	0.25	99.62
Mar 9 21:35 2020	76.27	4.00	0.04	2.74	3.26	12.52	0.09	0.00	1.68	0.11	0.28	100.99
Mar 10 08:54 2020	75.37	4.08	0.03	2.71	3.11	12.24	0.06	0.00	1.68	0.11	0.24	99.62
Mar 10 08:58 2020	75.52	4.06	0.02	2.71	3.07	12.33	0.11	0.00	1.69	0.08	0.28	99.86
Mar 10 09:02 2020	75.15	4.08	0.03	2.73	3.02	12.24	0.12	0.04	1.67	0.09	0.25	99.43
Mar 10 22:35 2020	75.51390228	4.236987951	0.0313	2.79	3.162246386	12.11193853	0.1011	0	1.72	0.1071	0.2272	100.0017751
Mar 10 22:39 2020	75.31128918	4.179210842	0.0494	2.72	3.162246386	11.89512596	0.1174	0.011697692	1.71	0.0827	0.2414	99.48047006
Mar 10 22:43 2020	75.28089722	4.150322288	0.0399	2.77	3.111406412	12.2696204	0.0741	0.027765951	1.73	0.1292	0.285	99.86821227
Mar 11 04:58 2020	75.94952045	3.8903253	0.0529	2.69	3.21308636	12.31889598	0.0761	0	1.72	0.1028	0.2845	100.2981281
Mar 11 05:02 2020	75.68612342	4.054027107	0.05	2.71	3.202918365	12.14150388	0.0705	0	1.7	0.1148	0.2683	99.99817277
Mar 11 11:56 2020	75.28089722	3.996249999	0.0362	2.7	3.284262324	12.07251806	0.0642	0	1.72	0.088	0.2843	99.5266276
Mar 11 12:00 2020	74.81488709	4.082915661	0.0441	2.69	3.253758339	12.14150388	0.0783	0	1.74	0.0999	0.2408	99.18616497
Mar 11 12:04 2020	75.06815346	4.121433734	0.0563	2.64	3.284262324	12.08237318	0.0985	0.00848404	1.67	0.1119	0.2554	99.39680674
Mar 11 18:25 2020	75.69625407	3.919213854	0.0409	2.74	3.243590345	12.16121411	0.0763	0.054503533	1.74	0.0769	0.251	99.99987592
Mar 11 18:29 2020	75.11880674	4.150322288	0.0542	2.74	3.21308636	12.2696204	0.1217	0	1.73	0.1017	0.2809	99.78033578
Mar 12 03:11 2020	75.23024394	3.948102408	0.0518	2.71	3.172414381	11.95425666	0.119	0.002442375	1.72	0.1122	0.2475	99.26795977
Mar 12 03:15 2020	74.96684691	4.333283131	0.0185	2.64	3.192750371	12.07251806	0.0936	0	1.67	0.0964	0.2758	99.35969848
Mar 12 21:38 2020	75.04	3.97	0.04	2.73	3.15	12.09	0.10	0.05	1.67	0.11	0.25	99.20
Mar 12 21:42 2020	75.24	4.10	0.02	2.66	3.12	12.11	0.14	0.03	1.66	0.11	0.28	99.48
Mar 12 21:46 2020	75.65	4.08	0.04	2.69	3.18	12.26	0.09	0.03	1.67	0.12	0.25	100.06
Mar 13 04:13 2020	75.12	3.96	0.05	2.66	3.25	12.28	0.07	0.00	1.68	0.09	0.31	99.46
Mar 13 04:17 2020	75.22	4.03	0.05	2.63	3.25	11.97	0.12	0.05	1.73	0.11	0.26	99.42
Mar 13 04:21 2020	74.97	3.97	0.05	2.65	3.29	12.13	0.09	0.03	1.70	0.09	0.22	99.19
Mar 13 10:57 2020	75.73	3.97	0.03	2.65	3.25	12.42	0.11	0.00	1.75	0.09	0.19	100.18
Mar 13 11:01 2020	75.82	3.99	0.04	2.65	3.22	12.37	0.11	0.08	1.65	0.07	0.27	100.26

Date	SiO2	Na2O	Cl	K2O	FeO	Al2O3	MgO	P2O5	CaO	MnO	TiO2	Total
Mar 13 11:05 2020	75.56	4.08	0.06	2.65	3.22	12.26	0.08	0.00	1.71	0.11	0.29	100.02
Feb 14 23:07 2020	76.33	4.10	0.04	2.70	3.12	12.25	0.07	0.04	1.67	0.10	0.23	100.65
Feb 14 23:10 2020	75.92	4.06	0.04	2.72	3.17	12.32	0.08	0.01	1.67	0.08	0.26	100.32
Feb 14 23:14 2020	75.70	4.10	0.04	2.71	3.15	12.36	0.09	0.05	1.67	0.11	0.27	100.25
Feb 14 23:18 2020	76.27	4.02	0.02	2.66	3.16	12.28	0.09	0.03	1.68	0.10	0.24	100.55
Feb 14 23:22 2020	75.91	4.10	0.03	2.70	3.25	12.29	0.11	0.00	1.67	0.13	0.24	100.43
Feb 15 16:09 2020	75.45	4.20	0.03	2.62	3.24	12.15	0.13	0.02	1.67	0.11	0.24	99.87
Feb 15 16:13 2020	75.37	4.07	0.02	2.73	3.18	12.30	0.06	0.05	1.70	0.12	0.28	99.88
Feb 15 16:17 2020	75.75	4.10	0.03	2.68	3.10	12.39	0.12	0.01	1.67	0.07	0.24	100.16
Feb 16 00:36 2020	75.64	4.16	0.02	2.63	3.23	12.37	0.11	0.00	1.68	0.13	0.28	100.26
Feb 16 00:40 2020	75.04	4.04	0.03	2.68	3.11	12.18	0.09	0.09	1.61	0.09	0.23	99.19
Feb 16 00:44 2020	75.37	4.11	0.04	2.66	3.19	12.28	0.12	0.02	1.68	0.11	0.31	99.89
Feb 16 10:52 2020	75.54	4.02	0.04	2.62	3.17	12.16	0.12	0.07	1.65	0.12	0.25	99.75
Feb 16 10:55 2020	75.65	4.02	0.02	2.65	3.10	12.32	0.12	0.04	1.65	0.11	0.22	99.91
Feb 16 10:59 2020	75.56	4.06	0.03	2.63	3.29	12.28	0.07	0.02	1.65	0.14	0.25	99.97
Feb 16 13:46 2020	75.54	3.99	0.04	2.57	3.16	12.27	0.09	0.00	1.71	0.09	0.22	99.69
Feb 16 13:50 2020	75.48	4.05	0.03	2.59	3.17	12.34	0.11	0.00	1.71	0.09	0.20	99.76
Feb 16 13:53 2020	75.67	4.04	0.03	2.59	3.18	12.18	0.12	0.00	1.68	0.09	0.23	99.82
Feb 16 13:57 2020	75.44	4.08	0.04	2.62	3.18	12.16	0.08	0.05	1.64	0.08	0.25	99.61
Feb 16 14:01 2020	75.27	4.13	0.02	2.65	3.13	12.34	0.09	0.01	1.69	0.09	0.27	99.69
Feb 13 18:56 2020	75.26	4.16	0.03	2.69	3.07	12.26	0.09	0.01	1.68	0.12	0.27	99.64
Feb 13 19:00 2020	75.44	4.01	0.01	2.70	3.15	12.22	0.10	0.00	1.66	0.09	0.26	99.65
Feb 13 19:04 2020	75.45	4.10	0.02	2.63	3.19	12.33	0.12	0.04	1.67	0.10	0.24	99.90
Feb 13 19:08 2020	75.62	4.09	0.02	2.69	3.24	12.41	0.10	0.04	1.70	0.10	0.25	100.27
Feb 13 19:12 2020	75.94	4.19	0.02	2.66	3.12	12.32	0.07	0.02	1.72	0.12	0.25	100.45
Feb 14 03:25 2020	75.58	3.98	0.03	2.71	3.08	12.11	0.08	0.01	1.64	0.09	0.26	99.57
Feb 14 03:29 2020	75.74	3.94	0.03	2.68	3.16	12.35	0.12	0.04	1.71	0.11	0.23	100.10
Feb 14 03:33 2020	75.57	4.12	0.05	2.64	3.11	12.20	0.09	0.03	1.66	0.10	0.26	99.83
Feb 14 13:30 2020	75.80	4.06	0.02	2.68	3.16	12.15	0.09	0.02	1.72	0.09	0.28	100.08
Feb 14 13:34 2020	75.52	4.11	0.03	2.72	3.19	12.34	0.14	0.00	1.72	0.11	0.23	100.11
Feb 14 13:37 2020	75.72	4.12	0.03	2.63	3.19	12.17	0.07	0.05	1.68	0.09	0.27	100.02
Feb 12 17:04 2020	75.59	4.03	0.03	2.68	3.13	12.36	0.09	0.04	1.69	0.12	0.24	99.99
Feb 12 17:08 2020	75.86	3.89	0.04	2.74	3.19	12.20	0.11	0.07	1.69	0.12	0.25	100.16
Feb 12 17:12 2020	75.74	4.13	0.03	2.67	3.18	12.29	0.07	0.00	1.72	0.12	0.28	100.23
Feb 12 17:16 2020	75.78	4.24	0.03	2.76	3.27	12.21	0.11	0.00	1.68	0.09	0.27	100.44
Feb 12 17:20 2020	75.45	4.03	0.03	2.73	3.18	12.19	0.05	0.04	1.69	0.10	0.28	99.78
Feb 13 08:23 2020	75.82	4.08	0.03	2.68	3.17	12.38	0.10	0.03	1.64	0.10	0.24	100.28
Feb 13 08:27 2020	75.24	4.10	0.04	2.72	3.33	12.19	0.07	0.00	1.71	0.10	0.28	99.78

Date	SiO2	Na2O	Cl	K2O	FeO	Al2O3	MgO	P2O5	CaO	MnO	TiO2	Total
Feb 13 08:31 2020	75.59	4.17	0.02	2.69	3.14	12.30	0.09	0.04	1.64	0.12	0.28	100.07
Feb 13 08:35 2020	75.33	3.97	0.01	2.65	3.20	12.19	0.10	0.04	1.66	0.11	0.19	99.45
Feb 13 08:39 2020	75.65	4.16	0.03	2.71	3.23	12.37	0.13	0.00	1.70	0.08	0.26	100.32
Feb 13 08:43 2020	74.70	4.07	0.05	2.73	3.22	12.10	0.08	0.01	1.69	0.12	0.26	99.03
Jan 20 18:55 2020	75.36	4.03	0.04	2.67	3.21	12.04	0.08	0.03	1.74	0.10	0.29	99.60
Jan 20 18:59 2020	75.07	4.05	0.05	2.66	3.22	12.17	0.09	0.07	1.68	0.10	0.25	99.42
Jan 20 19:03 2020	75.37	4.06	0.04	2.60	3.27	12.25	0.08	0.01	1.68	0.10	0.22	99.70
Jan 20 19:06 2020	75.19	4.03	0.02	2.62	3.37	12.12	0.11	0.03	1.68	0.11	0.33	99.62
Jan 21 02:44 2020	76.09	4.24	0.04	2.74	3.28	12.31	0.12	0.00	1.67	0.15	0.23	100.87
Jan 21 02:47 2020	76.07	3.99	0.01	2.70	3.15	12.40	0.10	0.00	1.73	0.11	0.30	100.55
Jan 21 02:51 2020	76.10	4.09	0.02	2.72	3.24	12.11	0.08	0.05	1.63	0.14	0.29	100.48
Jan 16 19:31 2020	75.26	3.91	0.03	2.66	3.24	12.22	0.08	0.03	1.68	0.13	0.26	99.50
Jan 16 19:35 2020	75.38	4.03	0.03	2.66	3.27	12.05	0.09	0.01	1.73	0.12	0.23	99.60
Jan 16 19:39 2020	75.23	4.02	0.04	2.67	3.22	12.26	0.08	0.00	1.73	0.11	0.26	99.62
Jan 16 19:43 2020	75.03	4.14	0.04	2.70	3.16	12.28	0.13	0.00	1.69	0.12	0.22	99.50
Jan 16 19:47 2020	75.44	4.21	0.05	2.67	3.18	12.34	0.10	0.01	1.72	0.08	0.24	100.04
Jan 17 08:46 2020	75.22	4.04	0.07	2.68	3.27	12.15	0.08	0.00	1.73	0.11	0.26	99.60
Jan 17 08:50 2020	75.19	4.24	0.04	2.64	3.22	12.05	0.09	0.00	1.70	0.09	0.25	99.51
Jan 17 08:54 2020	74.87	4.19	0.05	2.62	3.28	12.23	0.09	0.00	1.71	0.11	0.23	99.38
Jan 22 21:20 2020	75.36	4.25	0.04	2.72	3.30	12.33	0.11	0.01	1.71	0.10	0.25	100.18
Jan 22 21:24 2020	74.97	4.19	0.06	2.68	3.24	12.08	0.13	0.02	1.71	0.09	0.20	99.36
Jan 22 21:28 2020	75.21	4.17	0.04	2.68	3.11	12.02	0.15	0.00	1.73	0.11	0.20	99.41
Jan 22 21:32 2020	75.61	4.04	0.02	2.70	3.28	12.29	0.12	0.02	1.72	0.13	0.21	100.13
Jan 22 21:35 2020	75.66	4.07	0.06	2.68	3.29	12.13	0.09	0.02	1.74	0.09	0.26	100.09
Jan 23 04:18 2020	75.87	4.09	0.02	2.67	3.15	12.27	0.06	0.00	1.69	0.14	0.23	100.19
Jan 23 04:22 2020	76.32	4.03	0.00	2.74	3.11	12.37	0.15	0.03	1.69	0.12	0.29	100.85
Jan 23 04:26 2020	76.15	4.18	0.03	2.74	3.22	12.39	0.12	0.06	1.65	0.12	0.21	100.86
Jan 23 19:06 2020	75.58	4.05	0.03	2.72	3.26	12.07	0.11	0.05	1.73	0.12	0.22	99.94
Jan 23 19:10 2020	75.81	4.16	0.03	2.79	3.18	12.21	0.14	0.00	1.63	0.10	0.28	100.31
Jan 23 19:14 2020	75.64	4.17	0.03	2.74	3.28	12.32	0.10	0.05	1.70	0.11	0.23	100.35
Jan 25 05:29 2020	75.38	4.24	0.04	2.75	3.13	12.22	0.08	0.00	1.71	0.11	0.23	99.87
Jan 25 05:33 2020	75.34	4.17	0.03	2.66	2.95	11.46	0.07	0.00	1.69	0.08	0.27	98.72
Jan 25 05:37 2020	75.37	4.04	0.04	2.70	3.29	12.27	0.07	0.00	1.72	0.10	0.25	99.84
Jan 25 12:47 2020	75.50	4.05	0.03	2.67	3.27	12.23	0.11	0.02	1.76	0.12	0.22	99.97
Jan 25 12:51 2020	75.52	4.23	0.02	2.73	3.21	12.22	0.10	0.00	1.71	0.13	0.18	100.05
Jan 25 12:55 2020	75.61	4.20	0.04	2.72	3.33	12.19	0.08	0.03	1.69	0.09	0.21	100.19
Jan 25 20:05 2020	75.59	4.32	0.04	2.70	3.19	12.23	0.13	0.00	1.65	0.09	0.23	100.18
Jan 25 20:09 2020	75.56	4.34	0.03	2.67	3.21	12.41	0.11	0.04	1.69	0.09	0.25	100.41

Date	SiO2	Na2O	Cl	K2O	FeO	Al2O3	MgO	P2O5	CaO	MnO	TiO2	Total
Jan 25 20:13 2020	75.10	4.22	0.05	2.73	3.23	12.11	0.11	0.00	1.72	0.12	0.22	99.60
Jan 25 22:51 2020	75.45	4.32	0.03	2.74	3.24	12.40	0.16	0.00	1.68	0.08	0.25	100.35
Jan 25 22:55 2020	75.21	4.31	0.01	2.78	3.23	12.17	0.15	0.00	1.67	0.12	0.23	99.88
Jan 25 22:59 2020	75.01	4.09	0.03	2.77	3.29	12.23	0.12	0.00	1.69	0.09	0.25	99.56

Secondary standard raw analyses, GOR132-G

Date	SiO2	Na2O	Cl	K2O	FeO	Al2O3	MgO	P2O5	CaO	MnO	TiO2	Total
Mar 14 05:07 2020	45.63	0.81	0.00	0.02	9.97	11.13	23.07	0.03	8.56	0.19	0.26	99.67
Mar 14 05:11 2020	45.85	0.93	0.02	0.06	10.15	11.39	22.70	0.02	8.61	0.17	0.32	100.22
Mar 14 05:15 2020	45.64	0.88	0.02	0.03	10.58	11.64	21.40	0.04	9.06	0.17	0.34	99.80
Mar 14 13:36 2020	45.16	0.81	0.01	0.03	10.37	10.97	22.46	0.06	8.39	0.16	0.32	98.74
Mar 14 13:40 2020	44.99	0.82	0.01	0.05	10.13	11.08	22.28	0.03	8.53	0.18	0.28	98.38
Mar 14 13:44 2020	45.32	0.84	0.00	0.03	10.08	11.03	22.43	0.07	8.49	0.09	0.28	98.67
Mar 15 07:31 2020	45.32	0.75	0.02	0.04	10.12	10.86	22.40	0.06	8.49	0.17	0.28	98.51
Mar 15 07:35 2020	45.40	0.78	0.00	0.01	10.16	10.90	22.40	0.04	8.41	0.15	0.29	98.54
Mar 15 07:39 2020	45.21	0.80	0.02	0.02	10.32	10.70	22.57	0.09	8.46	0.17	0.36	98.74
Mar 9 21:15 2020	45.79	0.74	0.00	0.05	10.11	10.88	22.67	0.04	8.46	0.14	0.32	99.20
Mar 9 21:19 2020	45.31	0.84	0.02	0.06	10.12	10.94	22.52	0.01	8.49	0.13	0.31	98.73
Mar 9 21:23 2020	45.76	0.88	0.00	0.04	10.02	10.98	22.43	0.02	8.56	0.12	0.28	99.10
Mar 10 06:17 2020	45.32	0.74	0.01	0.04	10.09	10.69	22.81	0.00	8.58	0.17	0.30	98.74
Mar 10 06:21 2020	45.29	0.80	0.02	0.03	9.98	10.68	22.86	0.04	8.53	0.14	0.27	98.64
Mar 10 06:25 2020	45.34	0.80	0.01	0.04	10.14	10.77	22.27	0.03	8.42	0.15	0.34	98.30
Mar 11 04:42 2020	45.689254	0.71672503	0.0007	0.0201	10.46286666	10.82091823	22.84	0.089468063	8.49	0.1854	0.3111	99.62653198
Mar 11 04:45 2020	45.71964596	0.816968313	0.0014	0.0265	10.34085072	10.83077335	22.85	0.077898917	8.5	0.1523	0.3622	99.67853726
Mar 11 11:44 2020	45.689254	0.73030265	0.0113	0.0365	10.23917077	10.82091823	23.34	0.042677294	8.41	0.1424	0.3018	99.76432295
Mar 11 11:48 2020	45.61833941	0.854234548	0.005	0.0351	10.34085072	11.2742536	22.48	0.073785443	8.68	0.1338	0.3242	99.81956373
Mar 11 11:52 2020	46.03369627	0.78625015	0	0.035	10.5747146	11.75715433	21.55	0.089339517	8.86	0.1214	0.3337	100.1412549
Mar 11 18:17 2020	45.67912334	0.813694277	0	0.0683	10.04597887	11.26439849	23.14	0	8.59	0.1652	0.3487	100.115395
Mar 11 18:21 2020	45.76016858	0.816005361	0.0131	0.0265	10.34085072	10.93917963	23.26	0.054632079	8.54	0.1881	0.3225	100.2610364
Mar 12 03:27 2020	45.64873138	0.805220301	0.0094	0.0525	10.78824249	11.05744103	22.25	0.045248216	8.77	0.1578	0.3701	99.95468342
Mar 12 03:31 2020	45.55755548	0.79645744	0	0.0317	10.34085072	11.25454337	22.62	0.024680845	8.68	0.1305	0.2928	99.72908786
Mar 12 09:57 2020	45.79056055	0.874649126	0	0.0069	10.46286666	10.78149776	23.17	0.033293432	8.23	0.149	0.3006	99.79936753
Mar 12 10:01 2020	45.14219863	0.752835723	0.0065	0.0477	10.02564288	11.02787568	22.7	0.016582443	8.33	0.1864	0.3051	98.54083536
Mar 12 10:05 2020	45.13206797	0.897278494	0.0166	0.0336	10.27984275	11.32352919	22.75	0.006298757	8.35	0.1693	0.3387	99.29721716
Mar 13 03:49 2020	45.42	0.84	0.00	0.04	10.26	10.92	22.36	0.00	8.37	0.15	0.35	98.69
Mar 13 03:53 2020	45.10	0.84	0.00	0.05	10.28	11.11	22.45	0.05	8.32	0.16	0.31	98.68
Mar 13 03:57 2020	45.62	0.87	0.01	0.03	10.34	10.76	22.39	0.00	8.38	0.16	0.34	98.88
Feb 14 23:26 2020	45.49	0.80	0.01	0.03	10.10	10.76	22.98	0.02	8.54	0.18	0.26	99.17
Feb 14 23:30 2020	45.48	0.84	0.00	0.02	10.16	10.97	22.82	0.04	8.39	0.15	0.34	99.21
Feb 14 23:34 2020	45.49	0.88	0.00	0.05	10.14	10.91	23.00	0.07	8.49	0.13	0.28	99.45
Feb 14 23:38 2020	45.60	0.73	0.01	0.03	10.28	10.69	23.03	0.01	8.44	0.20	0.28	99.31
Feb 14 23:42 2020	45.62	0.78	0.01	0.04	10.06	10.83	22.90	0.02	8.42	0.16	0.30	99.15
Feb 15 08:03 2020	45.60	0.83	0.00	0.04	10.15	10.90	23.08	0.03	8.36	0.15	0.29	99.43
Feb 15 08:07 2020	45.54	0.77	0.00	0.03	10.07	11.06	23.05	0.03	8.35	0.17	0.31	99.38
Feb 15 08:11 2020	45.26	0.79	0.00	0.04	10.19	10.97	23.07	0.02	8.43	0.14	0.33	99.24

Date	SiO2	Na2O	Cl	K2O	FeO	Al2O3	MgO	P2O5	CaO	MnO	TiO2	Total
Feb 15 16:33 2020	45.38	0.87	0.00	0.05	10.29	11.07	23.08	0.01	8.48	0.15	0.25	99.63
Feb 15 16:37 2020	45.68	0.87	0.00	0.03	10.22	10.97	23.01	0.06	8.55	0.14	0.29	99.84
Feb 15 16:41 2020	45.28	0.83	0.00	0.02	10.16	11.01	23.02	0.05	8.42	0.16	0.31	99.27
Feb 16 11:03 2020	45.48	0.89	0.00	0.02	10.13	10.81	23.11	0.04	8.43	0.16	0.31	99.39
Feb 16 11:07 2020	45.44	0.88	0.00	0.02	10.23	10.95	23.00	0.04	8.46	0.16	0.34	99.51
Feb 16 11:11 2020	44.61	0.80	0.00	0.05	10.27	11.14	22.08	0.00	8.09	0.14	0.32	97.51
Feb 13 18:37 2020	45.55	0.88	0.00	0.03	10.13	10.87	22.58	0.01	8.47	0.16	0.29	98.98
Feb 13 18:40 2020	45.53	0.78	0.01	0.05	10.14	10.98	22.65	0.00	8.52	0.15	0.35	99.16
Feb 13 18:44 2020	45.62	0.92	0.00	0.02	10.14	11.13	22.77	0.05	8.54	0.16	0.27	99.63
Feb 13 18:48 2020	45.18	0.89	0.01	0.04	10.01	10.75	22.55	0.03	8.49	0.16	0.27	98.38
Feb 13 18:52 2020	45.50	0.97	0.00	0.04	10.09	10.89	22.61	0.00	8.57	0.16	0.31	99.14
Feb 14 03:37 2020	45.41	0.80	0.01	0.04	10.06	11.12	22.77	0.06	8.51	0.13	0.33	99.24
Feb 14 03:41 2020	45.68	0.86	0.00	0.02	10.34	10.87	22.57	0.07	8.48	0.16	0.32	99.38
Feb 14 03:45 2020	45.46	0.83	0.00	0.03	9.98	10.79	22.81	0.00	8.40	0.17	0.28	98.75
Feb 14 03:49 2020	45.35	0.76	0.02	0.05	10.13	10.77	22.82	0.08	8.48	0.14	0.32	98.91
Feb 14 13:54 2020	45.21	0.91	0.00	0.05	9.98	11.17	22.68	0.01	8.46	0.16	0.31	98.94
Feb 14 13:58 2020	45.53	0.82	0.00	0.03	10.08	11.04	22.89	0.08	8.36	0.11	0.32	99.26
Feb 14 14:01 2020	45.42	0.75	0.01	0.00	10.17	10.89	22.86	0.05	8.48	0.16	0.34	99.13
Feb 12 17:24 2020	45.70	0.82	0.00	0.02	10.42	10.94	23.73	0.06	8.66	0.16	0.27	100.78
Feb 12 17:28 2020	45.50	0.81	0.02	0.04	10.16	11.07	23.76	0.00	8.42	0.13	0.26	100.18
Feb 12 17:32 2020	45.62	0.81	0.01	0.04	10.41	10.88	23.67	0.02	8.62	0.18	0.31	100.57
Feb 12 17:35 2020	45.33	0.79	0.00	0.01	10.23	10.92	23.47	0.06	8.48	0.18	0.34	99.82
Feb 12 17:39 2020	45.70	0.84	0.01	0.02	10.27	10.83	23.64	0.01	8.61	0.16	0.30	100.38
Feb 13 00:22 2020	45.62	0.78	0.01	0.04	10.33	10.89	23.75	0.03	8.46	0.12	0.30	100.34
Feb 13 00:26 2020	45.39	0.85	0.00	0.04	10.14	10.99	23.45	0.08	8.58	0.14	0.30	99.96
Feb 13 00:30 2020	45.90	0.80	0.01	0.01	10.18	10.85	23.32	0.01	8.47	0.16	0.32	100.03
Jan 20 19:26 2020	45.74	0.72	0.01	0.04	10.83	10.96	20.41	0.04	8.94	0.14	0.30	98.13
Jan 20 19:30 2020	45.52	0.82	0.00	0.04	10.23	10.67	21.52	0.00	8.17	0.20	0.27	97.44
Jan 20 19:34 2020	45.90	0.83	0.00	0.03	10.08	10.98	20.98	0.05	8.26	0.13	0.31	97.55
Jan 20 19:38 2020	45.60	0.76	0.00	0.03	10.02	10.89	20.55	0.07	8.14	0.16	0.31	96.53
Jan 20 19:42 2020	45.65	0.87	0.00	0.03	10.36	10.80	21.18	0.05	8.30	0.15	0.31	97.69
Jan 21 12:19 2020	45.68	0.82	0.01	0.03	10.47	10.98	22.29	0.00	8.50	0.18	0.38	99.34
Jan 21 12:23 2020	46.01	0.90	0.01	0.06	10.30	10.74	22.16	0.06	8.50	0.14	0.32	99.20
Jan 21 12:27 2020	45.78	0.80	0.00	0.03	9.96	10.87	22.22	0.00	8.46	0.15	0.30	98.58
Jan 21 12:31 2020	45.64	0.60	0.03	0.05	9.97	10.86	22.32	0.06	8.59	0.17	0.36	98.64
Jan 21 12:35 2020	45.75	0.86	0.00	0.02	10.10	10.92	22.21	0.08	8.66	0.18	0.24	99.02
Jan 16 20:11 2020	45.39	0.89	0.00	0.03	10.28	10.89	21.64	0.01	8.50	0.14	0.27	98.03
Jan 16 20:15 2020	45.83	0.85	0.02	0.05	10.27	10.98	22.10	0.00	8.51	0.14	0.32	99.07

Date	SiO2	Na2O	Cl	K2O	FeO	Al2O3	MgO	P2O5	CaO	MnO	TiO2	Total
Jan 16 20:19 2020	45.62	0.90	0.01	0.03	10.15	10.94	21.92	0.01	8.44	0.15	0.37	98.53
Jan 16 20:23 2020	45.37	0.79	0.02	0.02	10.38	10.63	22.23	0.00	8.46	0.13	0.26	98.26
Jan 16 20:26 2020	45.71	0.86	0.00	0.03	10.14	10.75	22.02	0.00	8.54	0.15	0.30	98.49
Jan 17 00:40 2020	45.13	0.74	0.02	0.02	10.36	10.89	22.27	0.01	8.46	0.12	0.25	98.27
Jan 17 00:44 2020	45.60	0.99	0.00	0.02	10.14	10.93	21.99	0.00	8.43	0.15	0.27	98.51
Jan 17 00:48 2020	45.60	0.80	0.01	0.04	10.02	10.83	22.14	0.00	8.51	0.17	0.30	98.41
Jan 17 18:39 2020	46.05	0.86	0.01	0.02	10.43	10.94	21.91	0.00	8.52	0.12	0.32	99.18
Jan 17 18:43 2020	45.55	0.93	0.00	0.02	10.25	10.97	21.66	0.00	8.42	0.16	0.33	98.29
Jan 17 18:46 2020	45.76	0.81	0.00	0.03	10.02	10.83	21.54	0.00	8.46	0.15	0.30	97.90
Jan 17 23:36 2020	45.41	0.82	0.01	0.03	10.31	10.88	21.79	0.02	8.39	0.16	0.34	98.15
Jan 17 23:40 2020	45.66	0.79	0.00	0.05	10.21	10.96	21.96	0.01	8.48	0.15	0.27	98.54
Jan 17 23:44 2020	45.70	0.84	0.00	0.04	10.11	10.84	21.59	0.03	8.41	0.17	0.30	98.02
Jan 17 23:47 2020	46.18	0.72	0.00	0.02	10.29	11.05	21.74	0.00	8.44	0.15	0.29	98.88
Jan 17 23:51 2020	45.84	0.78	0.00	0.05	10.20	10.94	21.44	0.00	8.51	0.16	0.29	98.19
Jan 17 23:55 2020	45.74	0.92	0.00	0.04	10.24	10.89	21.37	0.00	8.37	0.15	0.31	98.02
Jan 22 21:00 2020	45.47	0.79	0.00	0.06	10.40	10.94	22.14	0.06	8.46	0.15	0.29	98.76
Jan 22 21:04 2020	45.67	0.81	0.01	0.02	10.14	11.04	22.22	0.01	8.42	0.14	0.34	98.83
Jan 22 21:08 2020	45.53	0.84	0.02	0.05	10.20	10.85	21.93	0.00	8.43	0.15	0.36	98.36
Jan 22 21:12 2020	45.58	0.88	0.00	0.03	10.13	10.88	22.26	0.03	8.57	0.17	0.29	98.82
Jan 22 21:16 2020	45.53	0.85	0.00	0.05	10.17	10.68	21.90	0.00	8.55	0.17	0.27	98.17
Jan 23 12:27 2020	45.24	0.85	0.01	0.03	10.21	11.14	21.88	0.00	8.44	0.12	0.31	98.24
Jan 23 12:31 2020	45.49	0.81	0.00	0.03	10.06	11.03	21.92	0.00	8.35	0.19	0.27	98.15
Jan 23 12:35 2020	45.82	0.71	0.00	0.04	10.23	10.94	22.02	0.03	8.42	0.21	0.30	98.72
Jan 23 18:54 2020	45.72	0.85	0.02	0.05	10.25	11.15	22.56	0.03	8.50	0.17	0.30	99.60
Jan 23 18:58 2020	45.44	0.76	0.00	0.04	10.30	11.03	22.54	0.01	8.57	0.19	0.30	99.18
Jan 23 19:02 2020	44.89	0.78	0.02	0.04	10.23	10.59	22.60	0.02	8.49	0.13	0.30	98.10
Jan 24 21:05 2020	45.28	0.73	0.01	0.04	10.20	10.73	22.40	0.00	8.40	0.14	0.28	98.21
Jan 24 21:09 2020	45.47	0.93	0.00	0.01	10.36	10.88	22.52	0.00	8.32	0.15	0.33	98.97
Jan 24 21:13 2020	45.58	0.79	0.01	0.03	10.16	11.09	21.97	0.03	8.47	0.17	0.31	98.60
Jan 24 21:17 2020	45.35	0.79	0.02	0.03	10.07	10.84	21.72	0.01	8.44	0.12	0.26	97.65
Jan 24 21:21 2020	45.73	0.82	0.00	0.02	10.17	10.80	21.89	0.00	8.46	0.17	0.33	98.39
Jan 25 13:11 2020	45.66	0.91	0.00	0.04	10.26	11.01	22.03	0.04	8.32	0.16	0.30	98.73
Jan 25 13:15 2020	45.64	0.84	0.00	0.03	10.36	10.92	22.03	0.02	8.41	0.16	0.34	98.75
Jan 25 13:19 2020	45.20	0.95	0.01	0.02	10.07	11.01	22.25	0.00	8.50	0.15	0.31	98.46
Jan 25 20:29 2020	45.34	0.81	0.01	0.06	10.15	10.82	22.57	0.01	8.45	0.15	0.31	98.68
Jan 25 20:33 2020	45.51	0.83	0.00	0.03	10.33	10.84	22.52	0.02	8.60	0.17	0.35	99.21
Jan 25 20:37 2020	45.47	0.80	0.00	0.04	10.08	11.09	22.59	0.01	8.44	0.17	0.28	98.96
Jan 25 22:39 2020	45.43	0.75	0.00	0.03	10.35	11.02	22.44	0.01	8.55	0.10	0.27	98.96

Date	SiO2	Na2O	Cl	K2O	FeO	Al2O3	MgO	P2O5	CaO	MnO	TiO2	Total
Jan 25 22:43 2020	45.46	0.91	0.00	0.03	10.27	10.94	22.55	0.00	8.39	0.17	0.31	99.04
Jan 25 22:47 2020	45.20	0.83	0.00	0.05	10.29	10.84	22.57	0.04	8.39	0.16	0.35	98.73

Secondary standard raw analyses, ML3B-G

Date	SiO2	Na2O	Cl	K2O	FeO	Al2O3	MgO	P2O5	CaO	MnO	TiO2	Total
Mar 13 22:02 2020	51.77	2.28	0.01	0.38	10.97	13.63	6.50	0.21	10.36	0.19	2.06	98.38
Mar 13 22:06 2020	52.15	2.36	0.01	0.36	10.95	13.80	6.57	0.14	10.45	0.19	2.08	99.06
Mar 13 22:10 2020	51.93	2.46	0.02	0.41	11.12	13.80	6.61	0.17	10.41	0.19	2.12	99.23
Mar 14 13:24 2020	52.06	2.34	0.01	0.38	11.00	13.86	6.64	0.16	10.47	0.16	2.15	99.23
Mar 14 13:28 2020	51.65	2.24	0.00	0.39	10.87	13.71	6.67	0.22	10.45	0.17	2.01	98.37
Mar 14 13:32 2020	51.59	2.41	0.02	0.37	11.12	13.55	6.69	0.23	10.45	0.20	2.07	98.70
Mar 15 07:19 2020	51.70	2.34	0.00	0.37	11.15	13.31	6.64	0.13	10.41	0.20	2.01	98.26
Mar 15 07:23 2020	51.63	2.35	0.00	0.35	10.96	13.45	6.74	0.20	10.44	0.17	2.06	98.36
Mar 15 07:27 2020	51.59	2.43	0.00	0.40	11.06	13.72	6.65	0.16	10.42	0.16	2.03	98.62
Mar 10 06:29 2020	51.44	2.35	0.01	0.36	10.72	13.76	6.63	0.18	10.55	0.16	2.15	98.32
Mar 10 06:33 2020	51.21	2.38	0.00	0.39	10.83	13.70	6.75	0.15	10.46	0.16	2.11	98.14
Mar 10 06:37 2020	51.59	2.41	0.00	0.40	10.79	13.60	6.61	0.17	10.57	0.15	2.13	98.42
Mar 10 22:23 2020	51.56503389	2.397749999	0	0.4132	11.08311434	13.6789021	6.72	0.306453825	10.6	0.146	2.1	99.01045416
Mar 10 22:27 2020	51.87908419	2.320713855	0.0028	0.3966	10.82891447	13.70846745	6.76	0.314937866	10.46	0.1778	2.03	98.87931784
Mar 10 22:31 2020	52.06143598	2.282195782	0	0.3731	10.87975445	13.84643909	6.69	0.208373176	10.51	0.1618	2.11	99.12309847
Mar 11 11:31 2020	51.80816961	2.407379517	0.0014	0.3866	10.80857848	13.62962652	6.77	0.162610776	10.35	0.176	2.11	98.6103649
Mar 11 11:36 2020	51.48398865	2.349602409	0	0.3648	11.06277835	13.59020605	6.81	0.210044275	10.33	0.1483	2.1	98.44971974
Mar 11 11:40 2020	51.93986812	2.426638553	0.0155	0.3853	10.93059442	13.34382813	6.71	0.179707403	10.34	0.1543	2.11	98.53573663
Mar 12 03:19 2020	51.60555651	2.359231927	0	0.408	11.15429031	13.60006117	6.8	0.207473353	10.41	0.2023	2.14	98.88691326
Mar 12 03:23 2020	51.61568716	2.436268072	0.0086	0.4017	11.15429031	13.58035093	6.77	0.265061991	10.28	0.1554	2.04	98.70735847
Mar 12 21:26 2020	51.83	2.31	0.01	0.41	10.96	13.78	6.58	0.23	10.29	0.15	2.09	98.64
Mar 12 21:30 2020	51.78	2.44	0.00	0.35	10.96	13.48	6.58	0.15	10.34	0.16	2.12	98.37
Mar 12 21:34 2020	51.69	2.40	0.00	0.38	10.99	13.85	6.62	0.21	10.27	0.17	2.09	98.69
Mar 13 10:45 2020	51.83	2.30	0.00	0.35	11.02	13.76	6.63	0.26	10.18	0.17	2.09	98.59
Mar 13 10:49 2020	51.95	2.31	0.02	0.37	10.94	13.67	6.58	0.22	10.25	0.17	2.11	98.60
Mar 13 10:53 2020	51.69	2.52	0.02	0.38	10.93	13.64	6.65	0.23	10.10	0.17	2.13	98.45
Feb 15 07:51 2020	51.81	2.43	0.00	0.36	10.95	13.82	6.76	0.23	10.27	0.15	2.20	98.98
Feb 15 07:55 2020	51.93	2.33	0.01	0.39	11.05	13.58	6.81	0.16	10.31	0.16	2.19	98.92
Feb 15 07:59 2020	52.03	2.35	0.01	0.38	11.00	13.71	6.82	0.20	10.40	0.17	2.19	99.27
Feb 15 16:21 2020	51.72	2.41	0.00	0.38	10.93	13.66	6.82	0.21	10.39	0.16	2.19	98.88
Feb 15 16:25 2020	51.81	2.41	0.01	0.38	10.86	13.96	6.77	0.23	10.39	0.14	2.21	99.17
Feb 15 16:29 2020	51.84	2.40	0.00	0.37	10.98	13.67	6.79	0.19	10.47	0.17	2.13	99.01
Feb 16 00:48 2020	51.19	2.36	0.01	0.39	10.92	13.58	6.78	0.25	10.35	0.17	2.20	98.20
Feb 16 00:51 2020	51.02	2.34	0.01	0.40	10.98	13.67	6.80	0.22	10.33	0.18	2.17	98.11
Feb 16 00:55 2020	51.76	2.37	0.01	0.36	11.15	13.83	6.80	0.24	10.36	0.18	2.19	99.25
Feb 16 11:15 2020	51.31	2.33	0.00	0.38	10.73	13.71	6.70	0.16	10.36	0.19	2.11	97.98
Feb 16 11:19 2020	51.51	2.49	0.00	0.37	10.97	13.73	6.79	0.18	10.38	0.18	2.11	98.71
Feb 16 11:23 2020	51.72	2.36	0.01	0.40	10.79	13.64	6.73	0.20	10.33	0.17	2.18	98.54

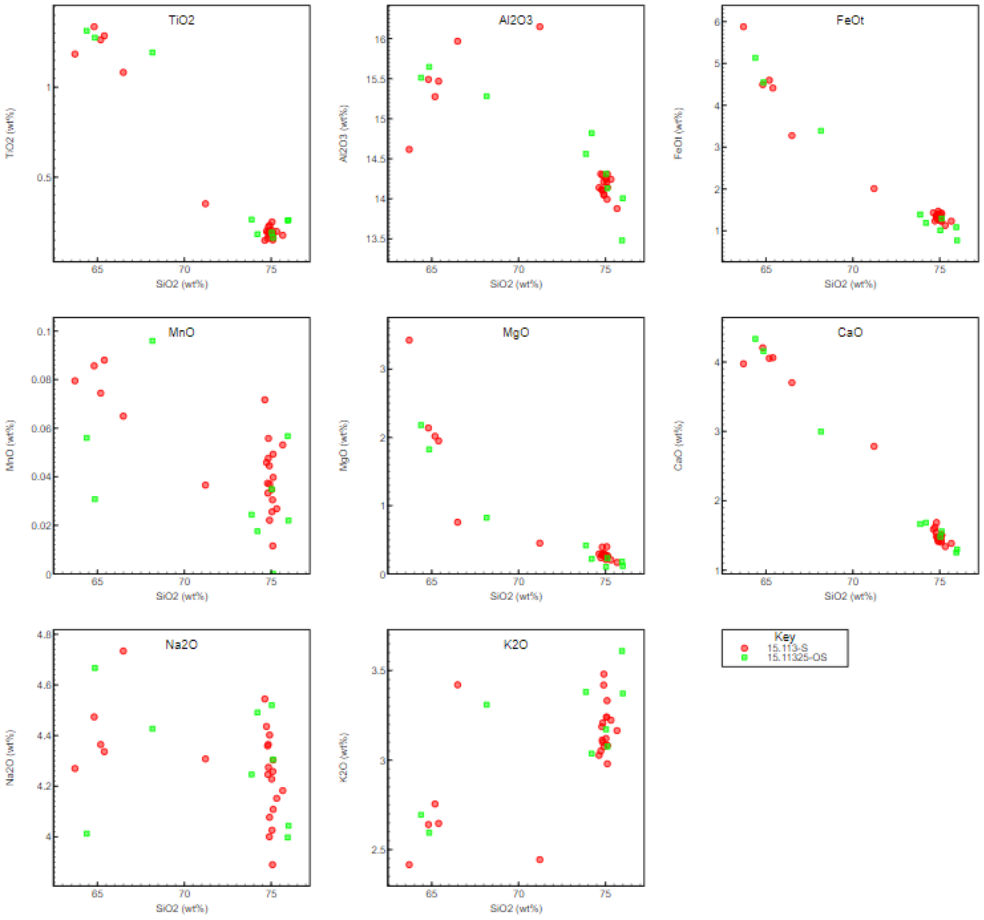
Date	SiO2	Na2O	Cl	K2O	FeO	Al2O3	MgO	P2O5	CaO	MnO	TiO2	Total
Feb 14 03:13 2020	51.03	2.26	0.00	0.40	10.86	13.61	6.70	0.30	10.50	0.17	2.11	97.95
Feb 14 03:17 2020	51.79	2.36	0.00	0.35	11.02	13.78	6.83	0.27	10.48	0.18	2.12	99.19
Feb 14 03:21 2020	51.60	2.31	0.00	0.35	10.85	13.81	6.80	0.30	10.40	0.18	2.13	98.73
Feb 14 14:06 2020	51.43	2.26	0.01	0.33	10.95	13.62	6.72	0.28	10.53	0.21	2.13	98.47
Feb 14 14:10 2020	51.43	2.38	0.00	0.41	10.94	13.85	6.68	0.25	10.41	0.19	2.19	98.74
Feb 14 14:14 2020	51.88	2.43	0.01	0.38	10.93	13.54	6.72	0.26	10.52	0.14	2.08	98.90
Feb 13 00:10 2020	52.14	2.27	0.00	0.39	11.05	13.82	7.00	0.31	10.55	0.22	2.13	99.86
Feb 13 00:14 2020	51.80	2.40	0.00	0.39	11.12	13.76	6.93	0.24	10.41	0.16	2.11	99.32
Feb 13 00:18 2020	51.27	2.28	0.01	0.40	11.05	13.81	6.90	0.33	10.56	0.15	2.17	98.92
Feb 13 08:47 2020	51.50	2.46	0.00	0.39	10.90	13.83	6.97	0.27	10.49	0.16	2.12	99.08
Feb 13 08:51 2020	51.38	2.47	0.00	0.39	10.94	13.75	6.91	0.27	10.46	0.14	2.09	98.80
Feb 13 08:55 2020	51.23	2.31	0.00	0.37	11.15	13.78	6.92	0.23	10.42	0.16	2.08	98.66
Feb 13 08:59 2020	51.70	2.28	0.01	0.39	11.09	13.61	7.00	0.24	10.55	0.16	2.09	99.13
Feb 13 09:03 2020	50.80	2.45	0.01	0.38	11.00	13.93	6.97	0.30	10.43	0.20	2.11	98.57
Feb 13 09:06 2020	51.45	2.34	0.01	0.39	10.87	13.88	6.87	0.23	10.53	0.15	2.10	98.82
Jan 21 12:00 2020	52.09	2.44	0.03	0.38	10.93	13.91	6.58	0.26	10.45	0.20	2.07	99.33
Jan 21 12:04 2020	52.05	2.55	0.00	0.41	11.11	13.74	6.70	0.24	10.43	0.19	2.26	99.69
Jan 21 12:08 2020	51.93	2.34	0.00	0.37	11.04	13.61	6.56	0.22	10.58	0.11	2.13	98.90
Jan 21 12:11 2020	52.06	2.56	0.00	0.36	10.89	13.68	6.60	0.30	10.42	0.17	2.13	99.17
Jan 21 12:15 2020	52.04	2.40	0.00	0.37	11.16	13.85	6.74	0.25	10.48	0.17	2.07	99.54
Jan 17 18:51 2020	51.74	2.48	0.01	0.39	11.08	13.70	6.65	0.02	10.47	0.18	2.18	98.90
Jan 17 18:54 2020	51.92	2.39	0.01	0.37	11.09	13.71	6.61	0.00	10.44	0.15	2.06	98.76
Jan 17 18:58 2020	51.90	2.49	0.00	0.36	10.98	13.79	6.53	0.00	10.42	0.18	2.13	98.79
Jan 17 19:02 2020	51.81	2.45	0.00	0.36	10.99	13.81	6.48	0.01	10.44	0.19	2.13	98.67
Jan 23 03:55 2020	51.83	2.32	0.00	0.39	11.04	13.62	6.53	0.21	10.54	0.16	2.14	98.78
Jan 23 03:59 2020	51.81	2.37	0.00	0.39	11.10	13.49	6.59	0.22	10.28	0.17	2.18	98.60
Jan 23 04:02 2020	51.69	2.50	0.00	0.38	10.95	13.74	6.62	0.21	10.39	0.15	2.20	98.82
Jan 23 18:43 2020	51.62	2.52	0.00	0.38	10.96	13.77	6.74	0.17	10.39	0.19	2.15	98.89
Jan 23 18:47 2020	51.76	2.31	0.02	0.37	11.17	13.52	6.61	0.16	10.45	0.14	2.13	98.64
Jan 23 18:50 2020	51.54	2.41	0.03	0.39	10.95	13.62	6.69	0.22	10.38	0.17	2.12	98.52
Jan 25 05:41 2020	51.75	2.44	0.01	0.39	10.91	13.74	6.65	0.13	10.36	0.15	2.11	98.65
Jan 25 05:45 2020	51.58	2.47	0.01	0.38	10.99	13.65	6.65	0.19	10.44	0.19	2.03	98.58
Jan 25 05:49 2020	51.80	2.46	0.00	0.38	11.09	13.81	6.70	0.17	10.54	0.14	2.17	99.27
Jan 25 20:17 2020	51.60	2.45	0.00	0.38	10.75	13.74	6.51	0.19	10.42	0.12	2.01	98.17
Jan 25 20:21 2020	51.53	2.48	0.00	0.38	11.05	13.84	6.43	0.25	10.43	0.16	2.02	98.58
Jan 25 20:25 2020	51.52	2.45	0.01	0.39	10.82	13.60	6.72	0.26	10.49	0.19	2.14	98.58

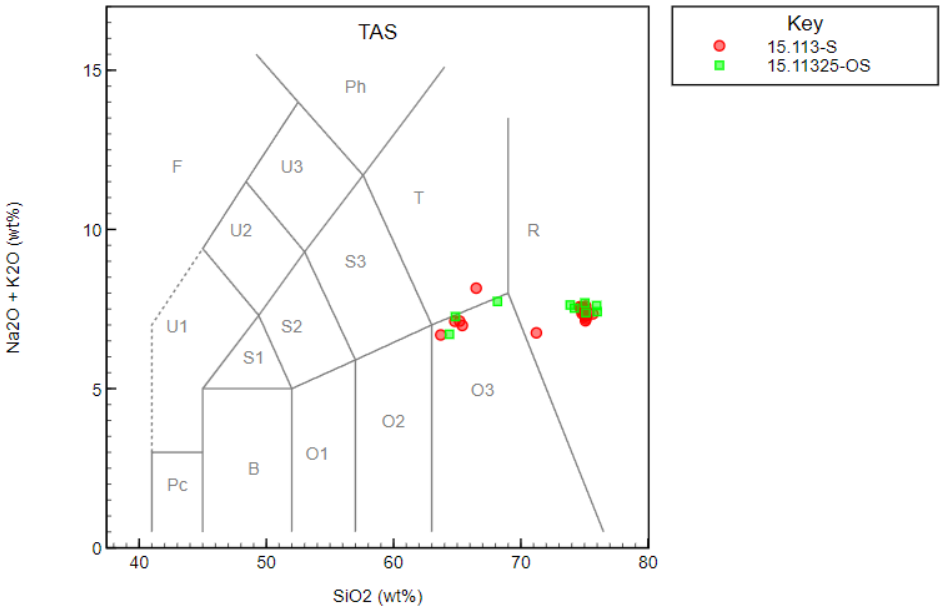
Secondary standard raw analyses, KL2-G

Date	SiO2	Na2O	Cl	K2O	FeO	Al2O3	MgO	P2O5	CaO	MnO	TiO2	Total
Mar 13 22:30 2020	50.43	2.25	0.00	0.47	10.72	13.23	7.40	0.21	11.02	0.15	2.55	98.43
Mar 13 22:34 2020	49.97	2.20	0.00	0.47	10.67	13.13	7.33	0.16	11.00	0.21	2.53	97.67
Mar 14 05:31 2020	50.48	2.41	0.00	0.48	10.73	13.35	7.42	0.32	10.88	0.16	2.46	98.68
Mar 14 05:35 2020	50.47	2.19	0.01	0.49	10.76	13.39	7.38	0.24	11.03	0.18	2.61	98.74
Mar 14 05:39 2020	50.36	2.39	0.00	0.47	10.66	13.40	7.28	0.18	11.04	0.15	2.54	98.47
Mar 14 21:38 2020	50.56	2.41	0.00	0.48	10.76	13.26	7.39	0.24	11.16	0.16	2.58	99.00
Mar 14 21:42 2020	50.62	2.52	0.01	0.49	10.73	13.21	7.35	0.25	11.02	0.17	2.57	98.94
Mar 14 21:46 2020	50.99	2.16	0.00	0.47	10.80	13.29	7.30	0.23	11.02	0.15	2.60	99.01
Mar 10 09:06 2020	50.72	2.40	0.00	0.51	10.55	13.20	7.43	0.24	11.11	0.18	2.60	98.94
Mar 10 09:10 2020	50.20	2.41	0.00	0.52	10.62	13.15	7.51	0.26	10.98	0.16	2.62	98.43
Mar 10 09:14 2020	50.47	2.35	0.00	0.50	10.39	13.47	7.45	0.19	11.17	0.14	2.67	98.80
Mar 13 04:01 2020	50.35	2.31	0.00	0.48	10.67	13.33	7.20	0.30	10.81	0.19	2.58	98.22
Mar 13 04:05 2020	50.40	2.30	0.01	0.50	10.71	13.23	7.38	0.27	10.97	0.17	2.54	98.47
Mar 13 04:09 2020	50.51	2.32	0.00	0.45	10.60	13.18	7.39	0.30	10.89	0.18	2.56	98.38
Jan 21 02:55 2020	50.19	2.34	0.01	0.47	10.82	13.29	7.32	0.21	10.90	0.20	2.58	98.32
Jan 21 02:59 2020	50.26	2.21	0.00	0.49	10.65	13.18	7.17	0.25	10.98	0.15	2.65	98.00
Jan 21 03:03 2020	50.78	2.37	0.00	0.45	10.64	13.34	7.36	0.24	11.01	0.17	2.64	99.00
Jan 23 12:04 2020	50.95	2.17	0.00	0.48	10.92	13.45	7.29	0.22	10.87	0.15	2.50	98.99
Jan 23 12:08 2020	50.44	2.39	0.00	0.46	10.52	13.35	7.37	0.24	10.99	0.16	2.68	98.61
Jan 23 12:12 2020	50.72	2.47	0.03	0.50	10.85	13.32	7.33	0.26	11.01	0.17	2.54	99.21
Jan 24 21:25 2020	50.29	2.39	0.02	0.50	10.83	13.39	7.36	0.19	11.00	0.17	2.62	98.74
Jan 24 21:28 2020	50.12	2.43	0.01	0.49	10.94	13.43	7.41	0.22	11.02	0.16	2.48	98.70
Jan 24 21:32 2020	50.60	2.33	0.02	0.46	10.81	13.17	7.35	0.18	10.95	0.17	2.61	98.64
Jan 24 21:36 2020	50.49	2.24	0.02	0.49	10.97	13.42	7.50	0.21	10.89	0.16	2.59	98.97
Jan 24 21:40 2020	50.26	2.38	0.00	0.50	10.90	13.20	7.40	0.21	11.00	0.16	2.63	98.64
Jan 25 12:59 2020	50.72	2.43	0.00	0.50	10.82	13.40	7.43	0.20	10.98	0.16	2.64	99.28
Jan 25 13:03 2020	50.47	2.33	0.00	0.52	10.83	13.45	7.21	0.22	11.02	0.16	2.62	98.84
Jan 25 13:07 2020	50.34	2.17	0.00	0.50	10.73	13.27	7.29	0.25	10.93	0.13	2.47	98.08

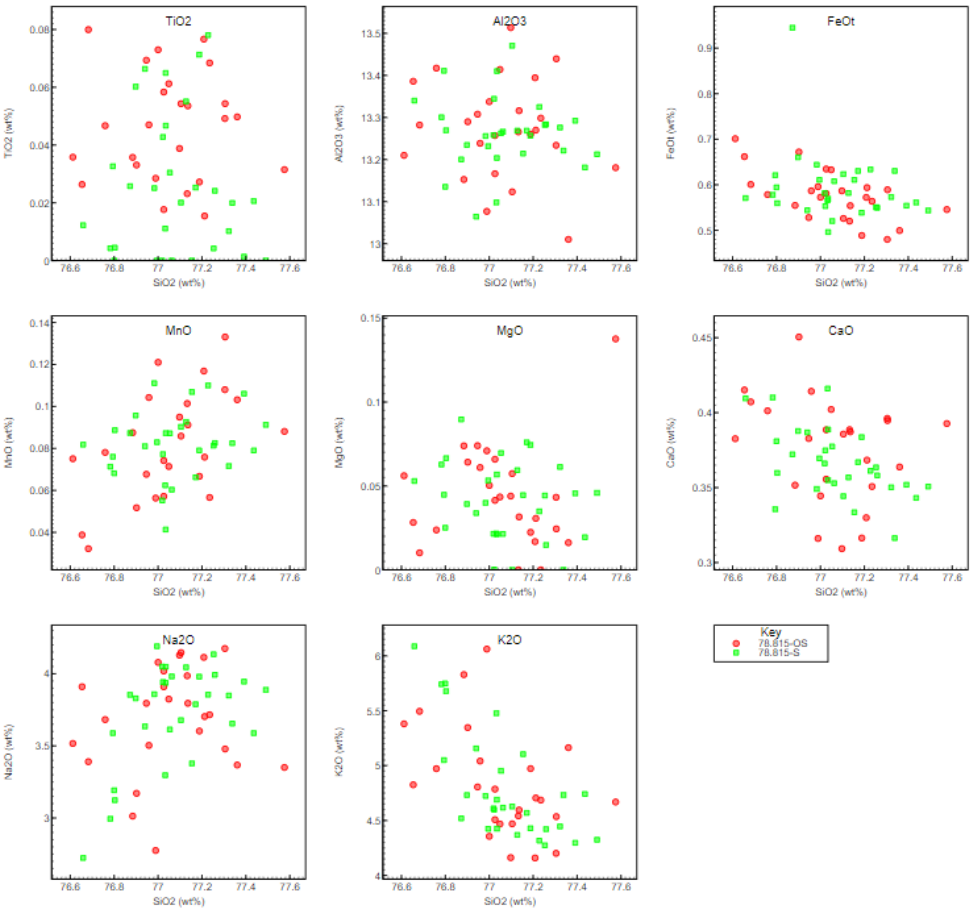
APPENDIX E2

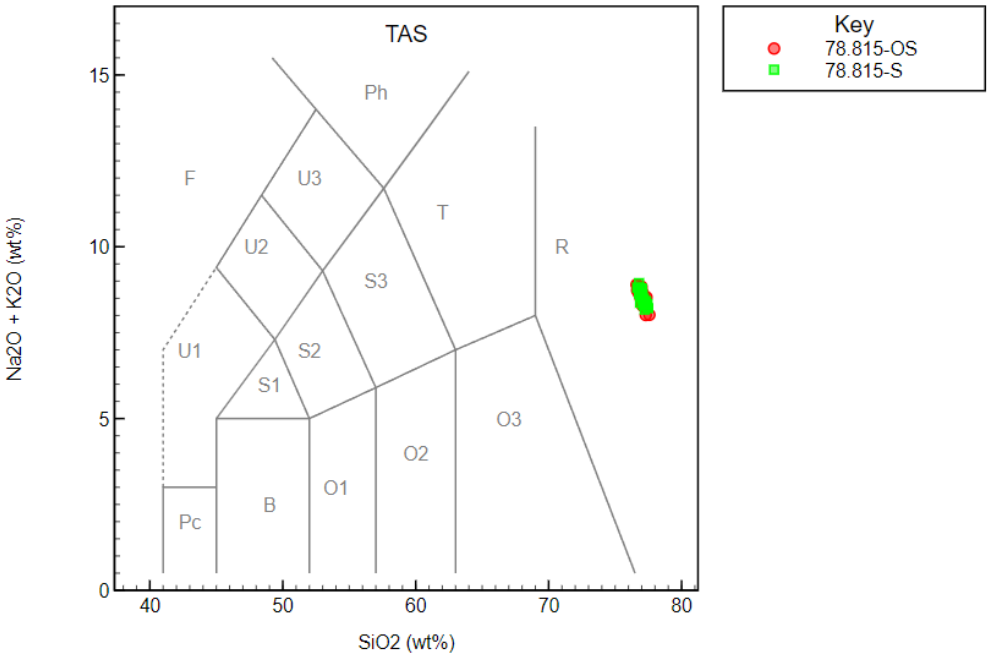
Tephra 15.113



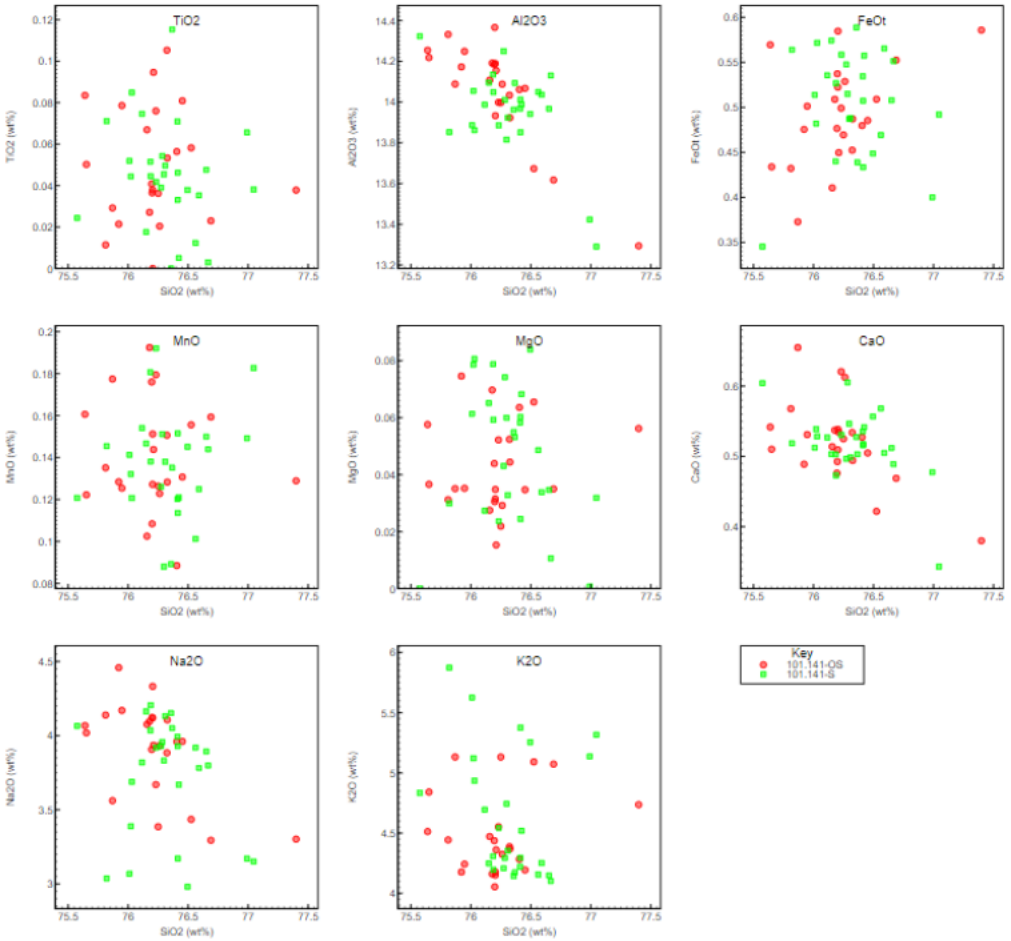


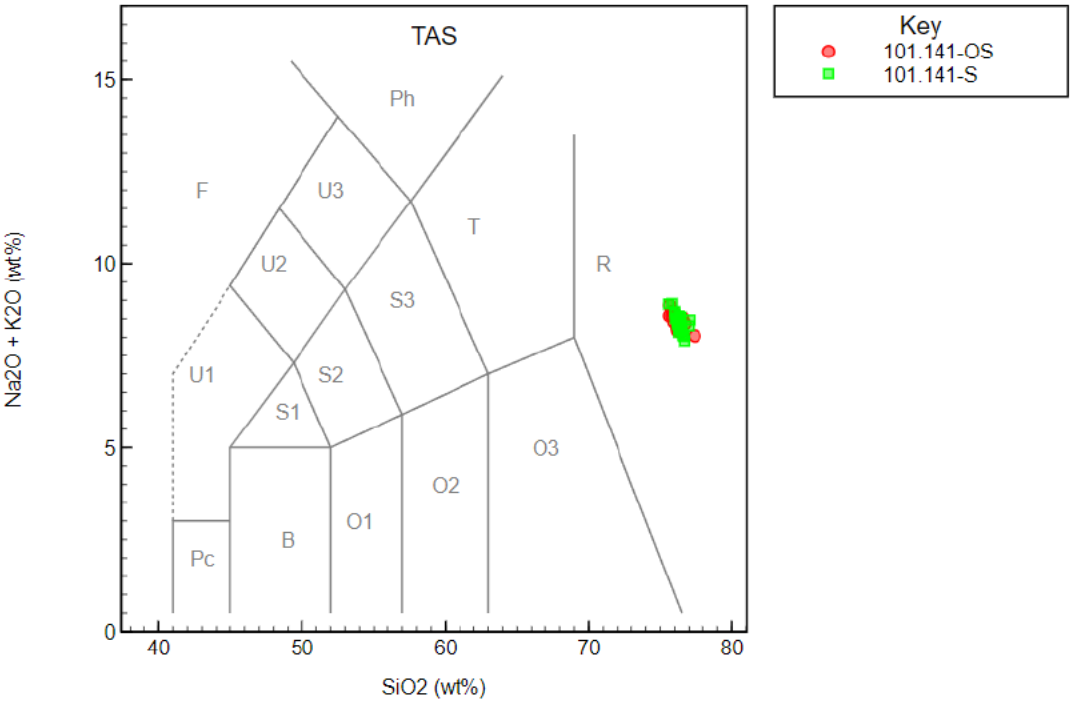
Tephra 78.815



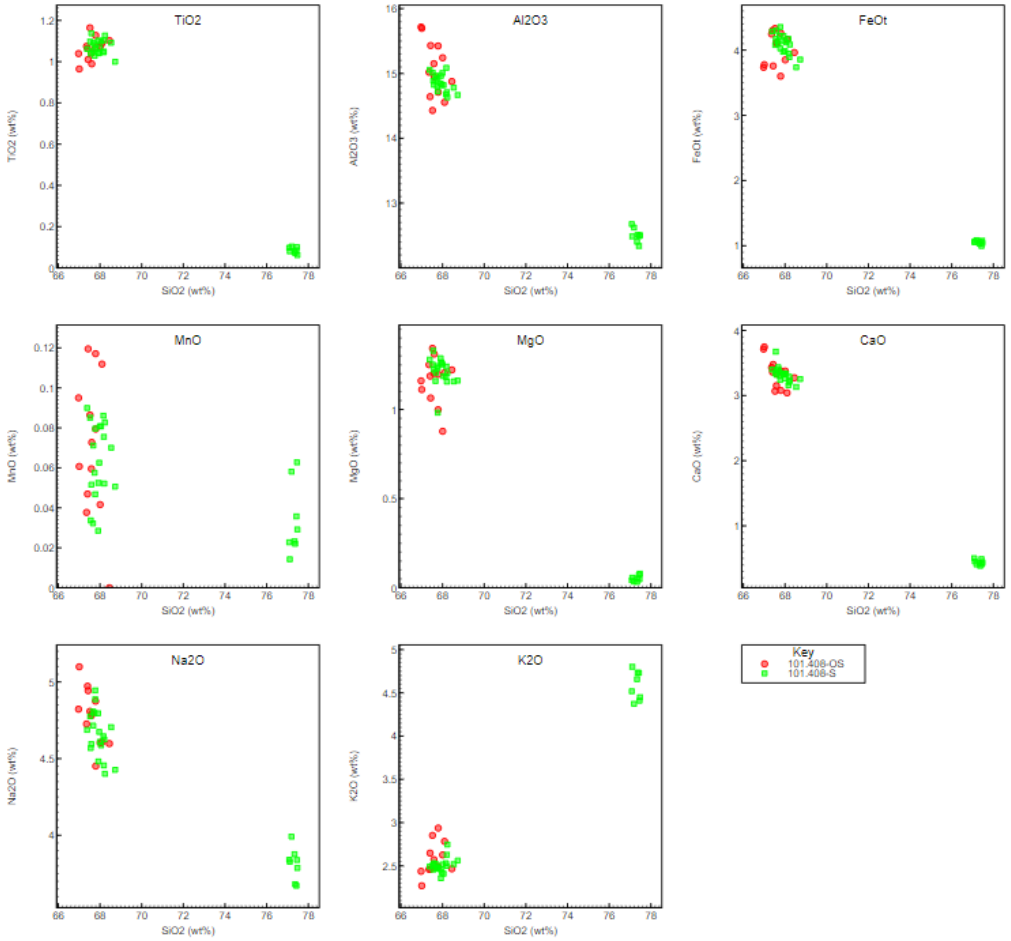


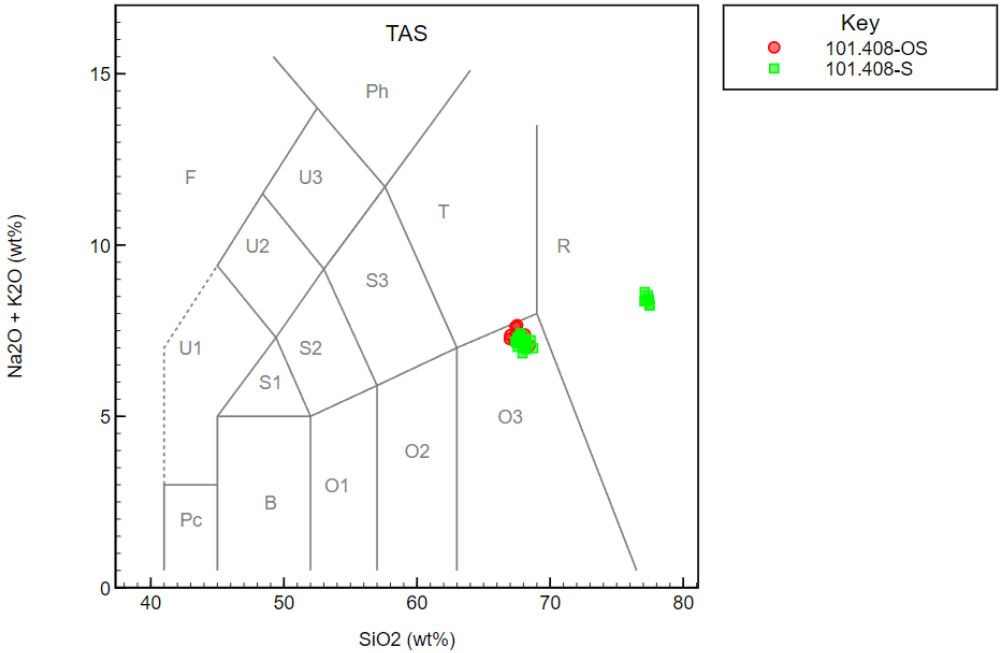
Tephra 101.141



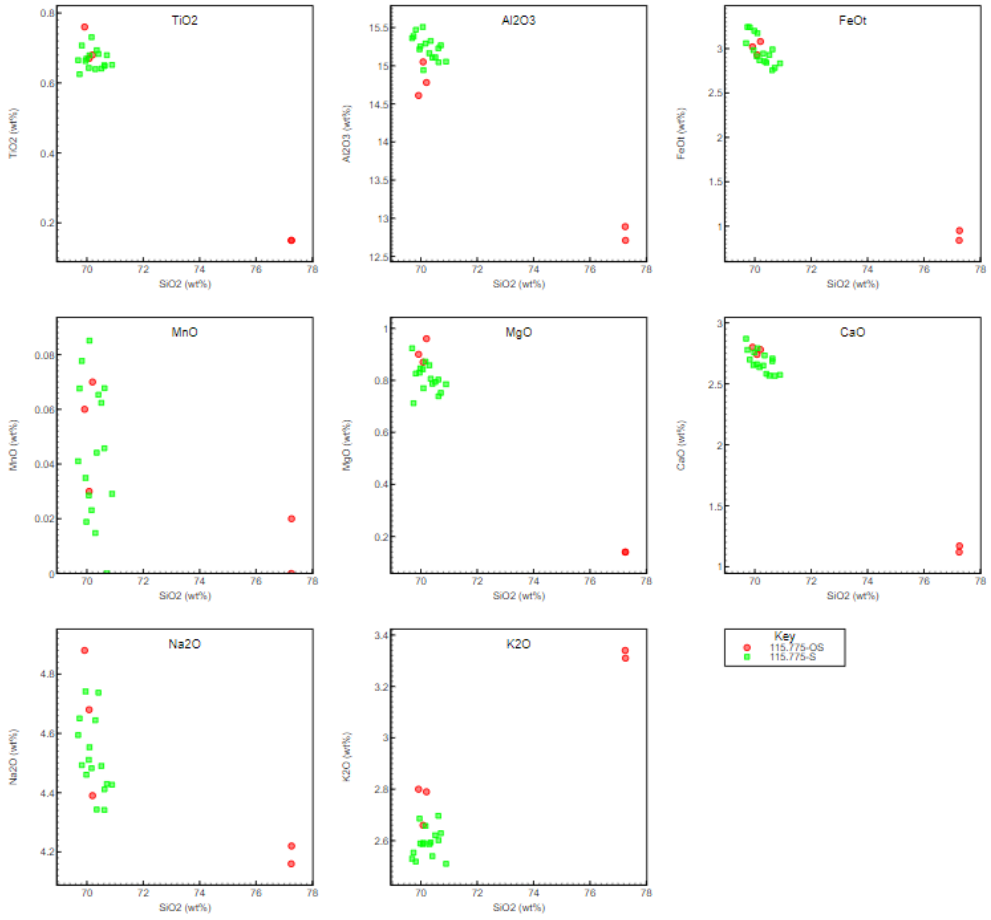


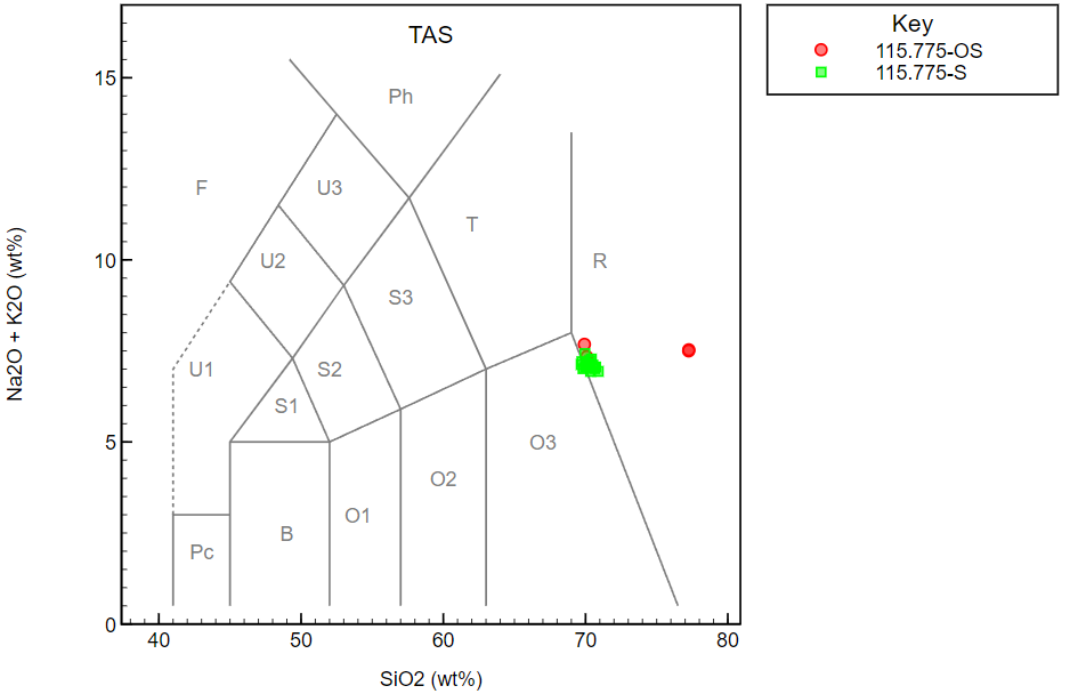
Tephra 101.408



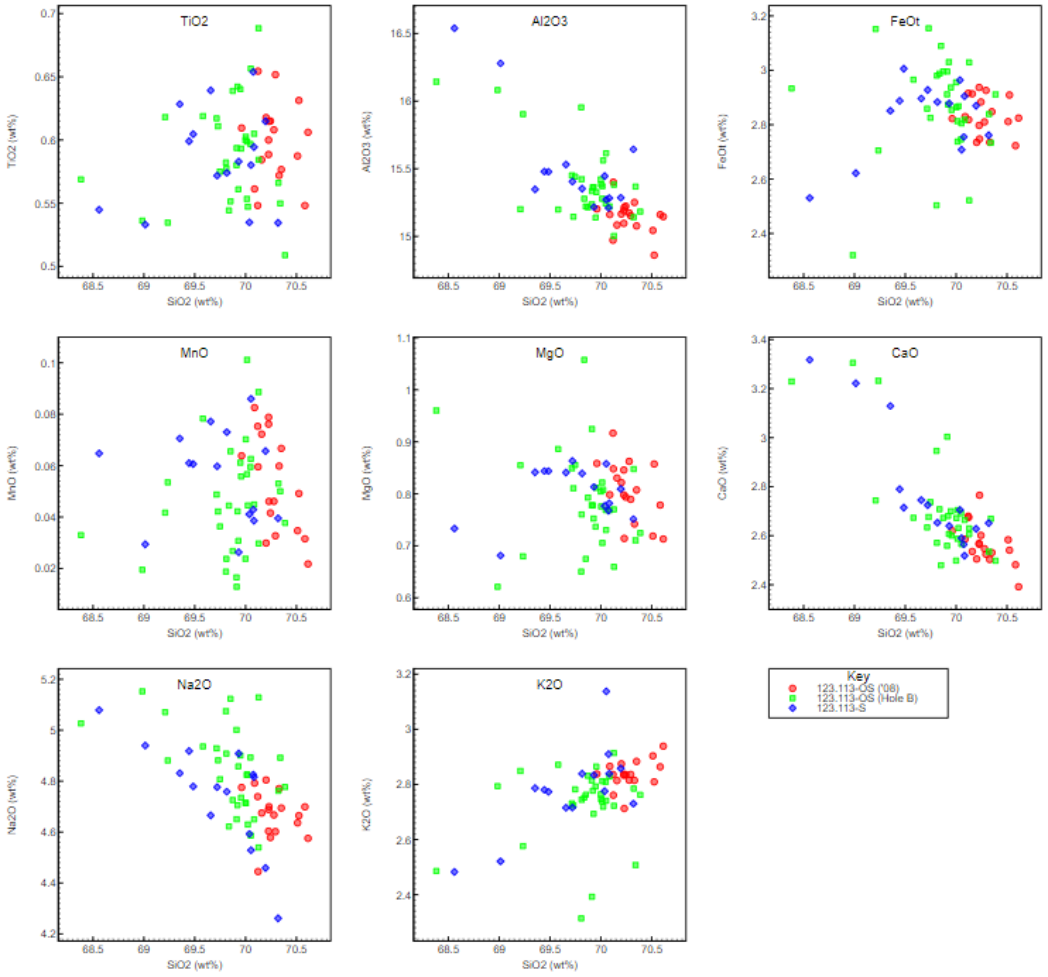


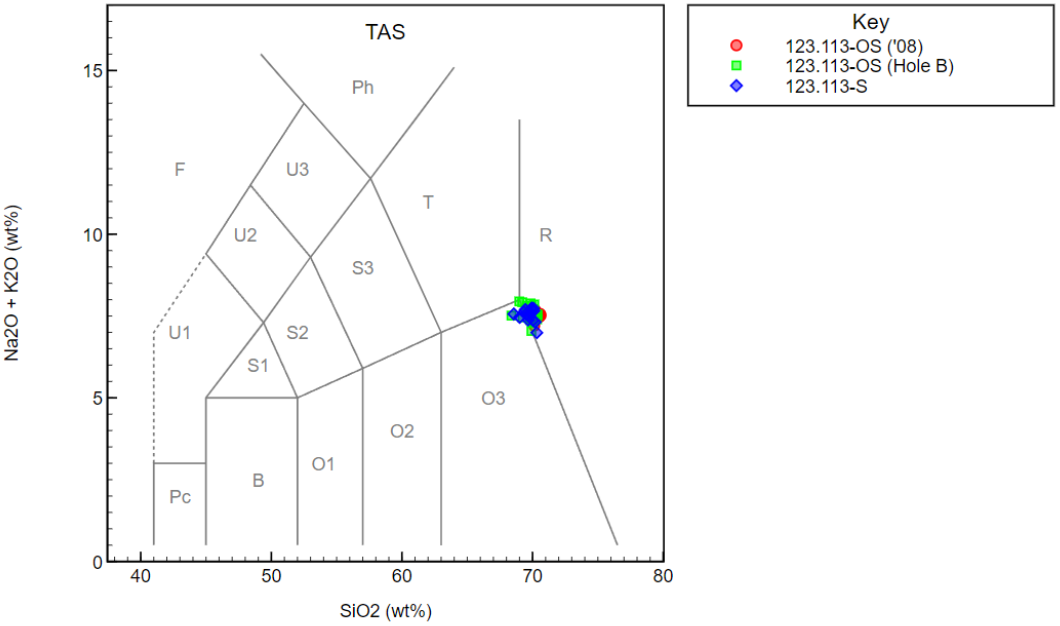
Tephra 115.75



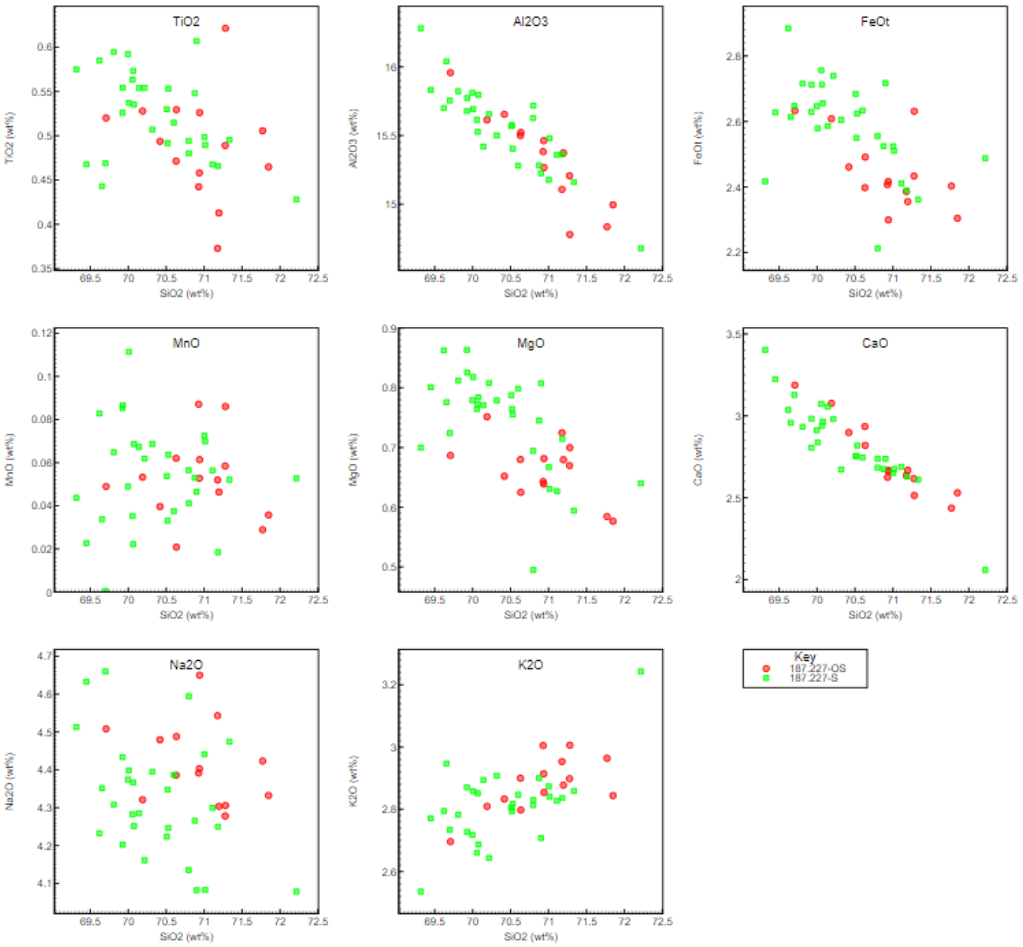


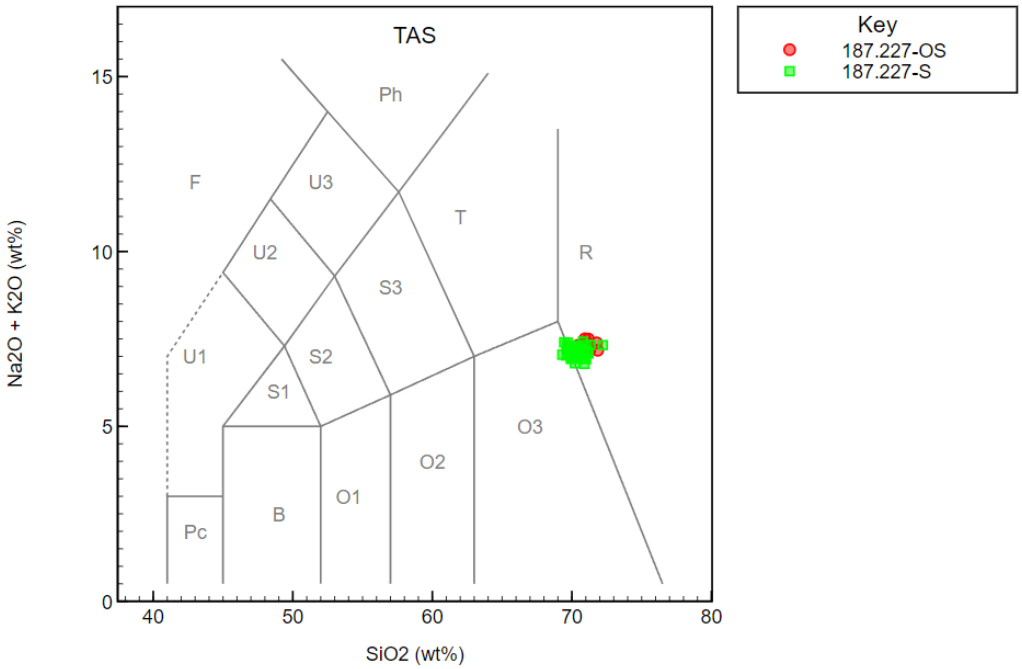
Tephra 123.113



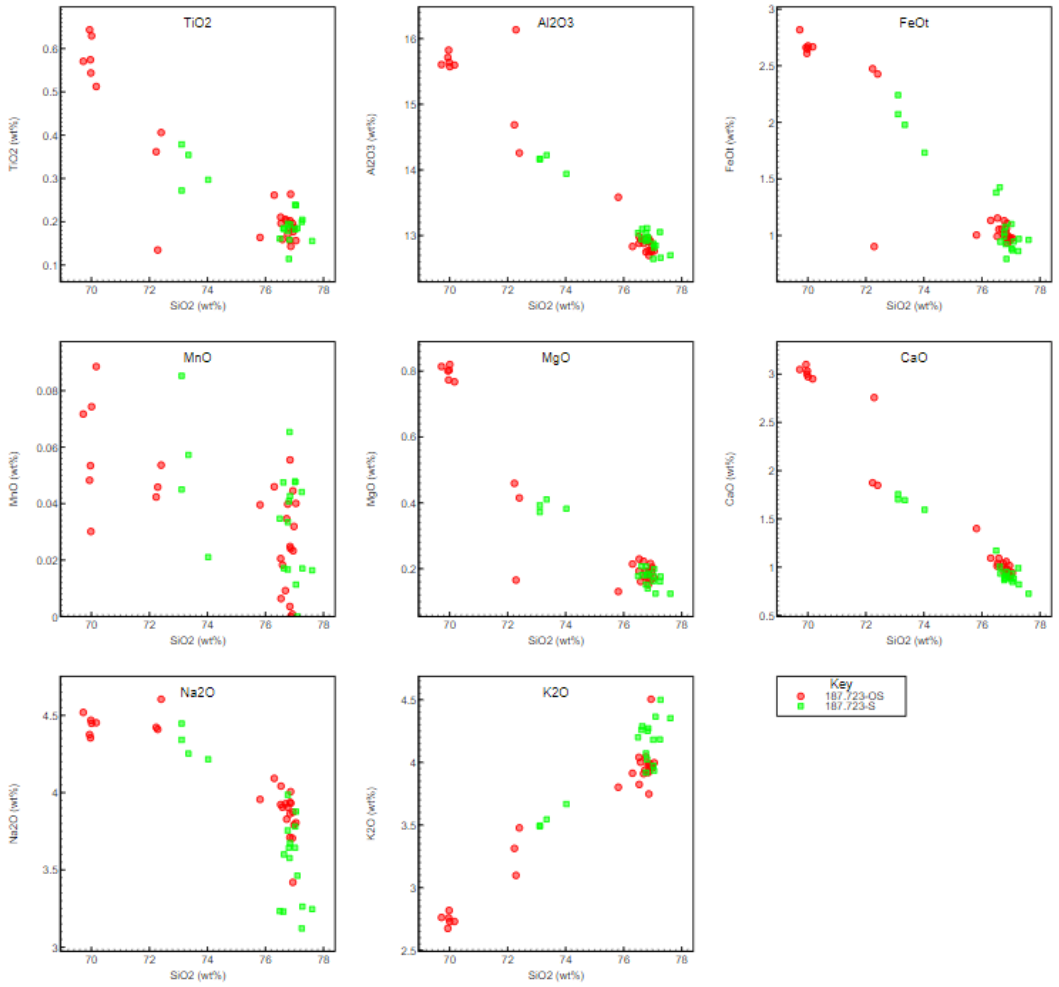


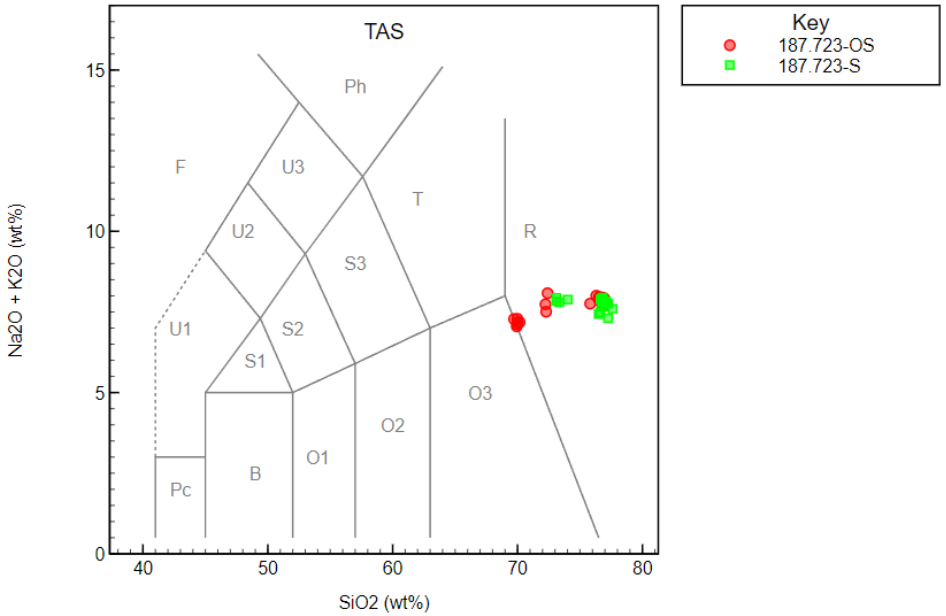
Tephra 187.227



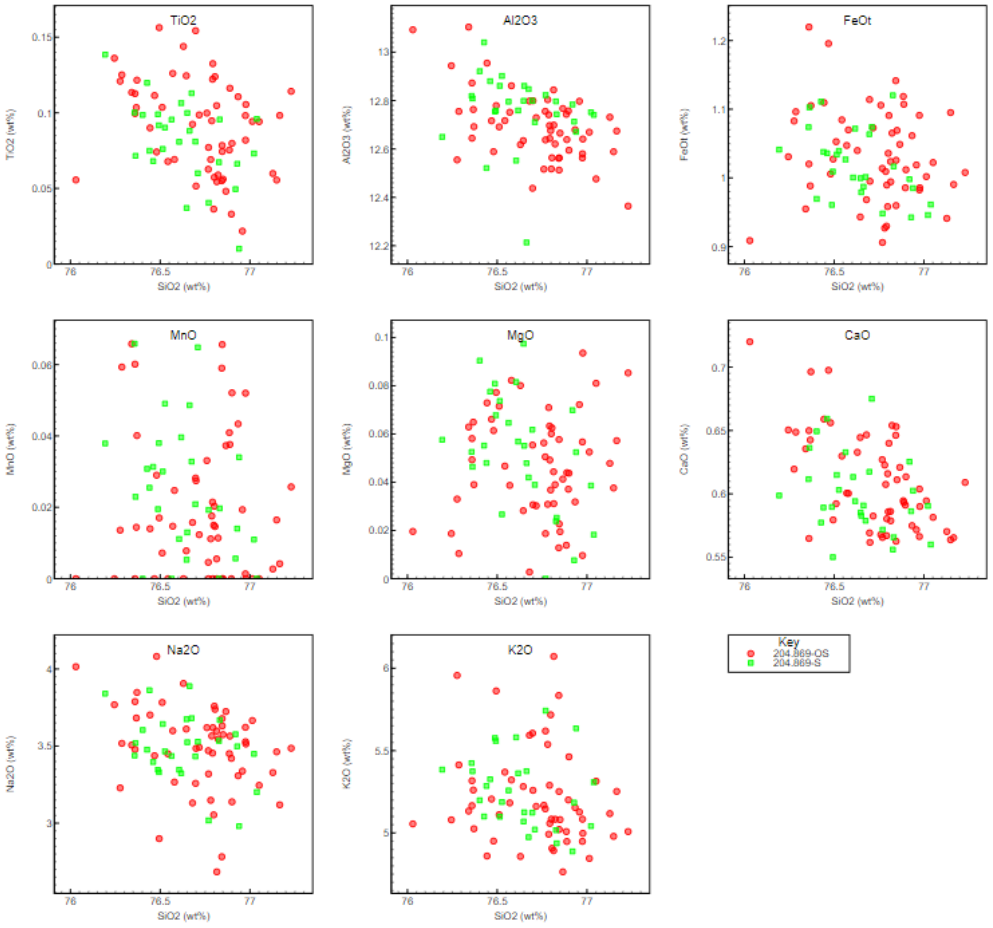


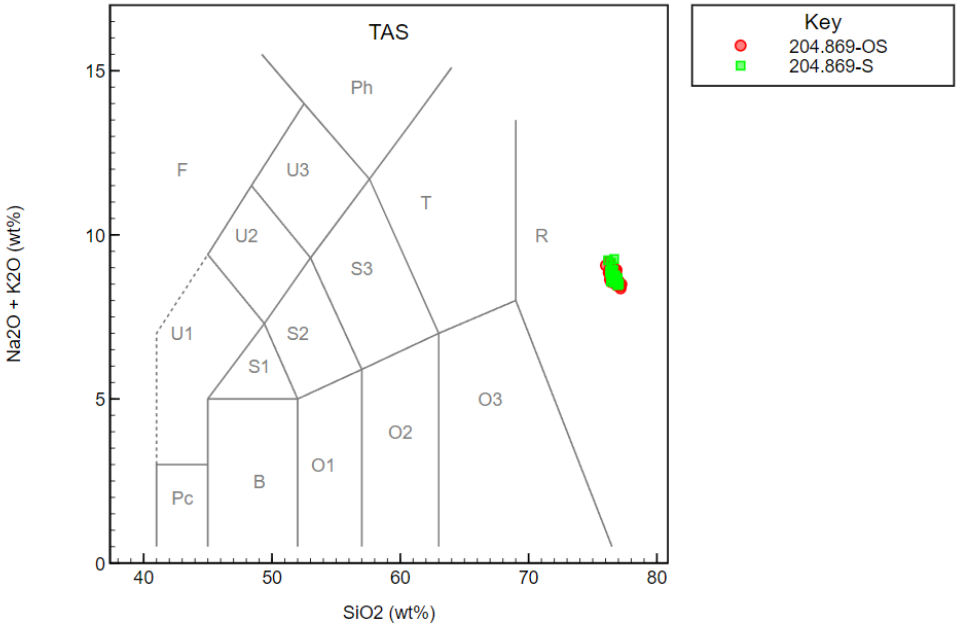
Tephra 187.723



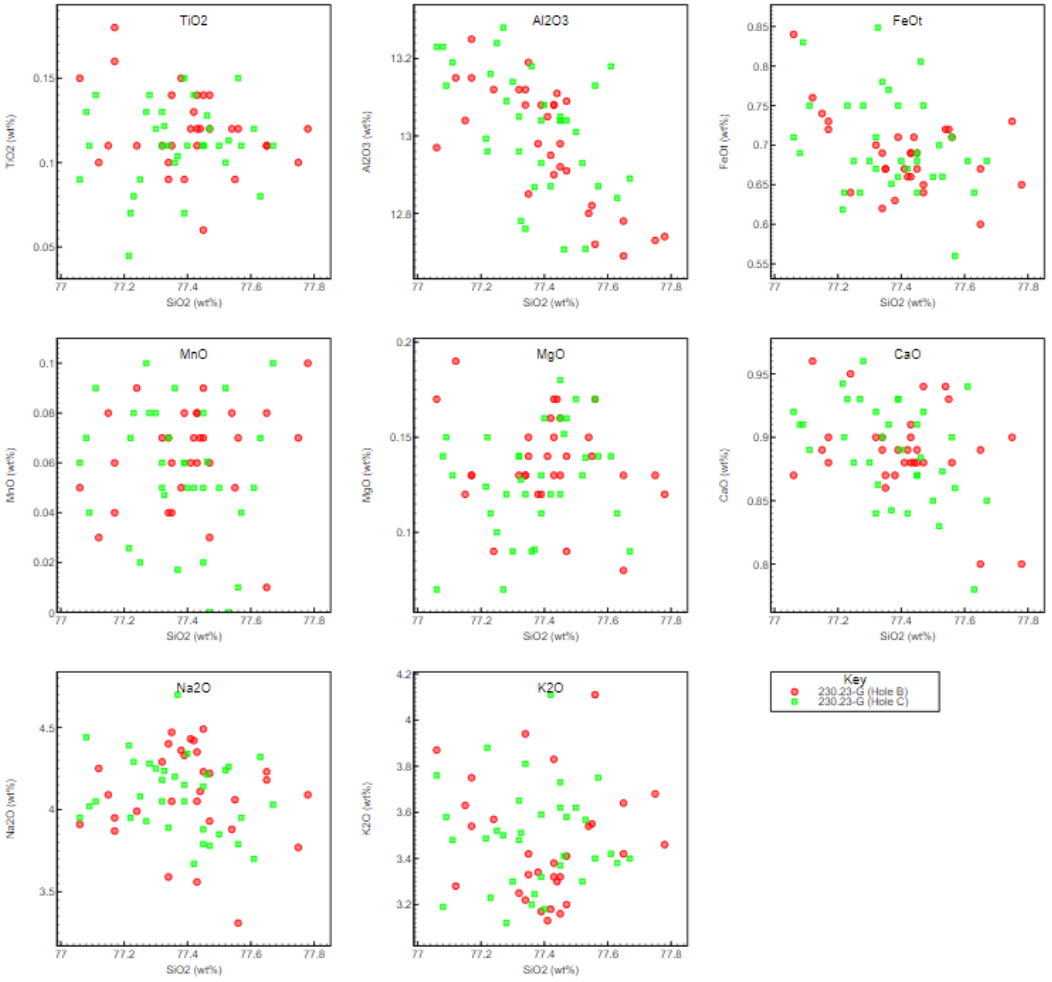


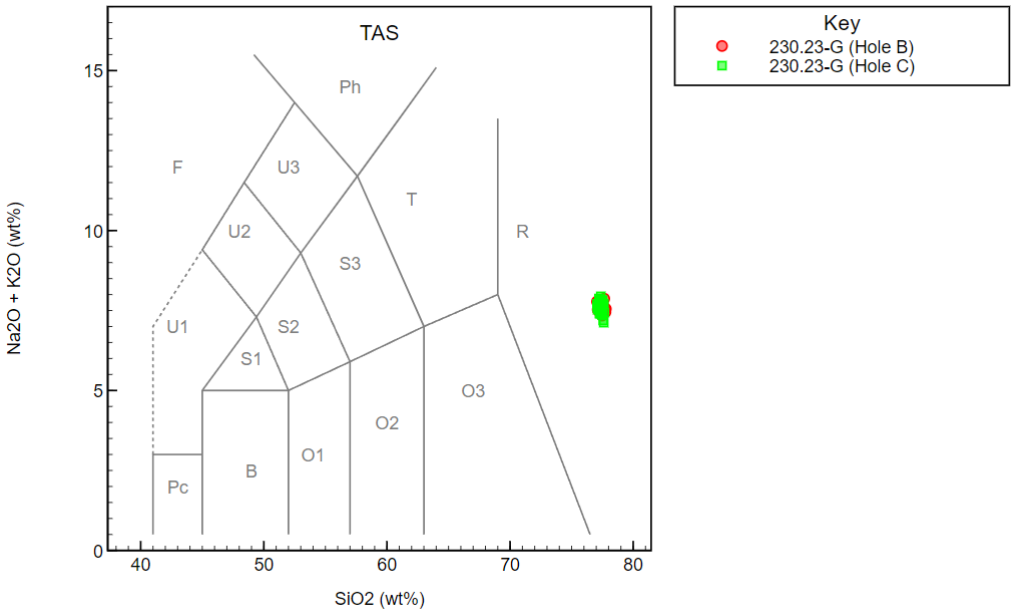
Tephra 204.869



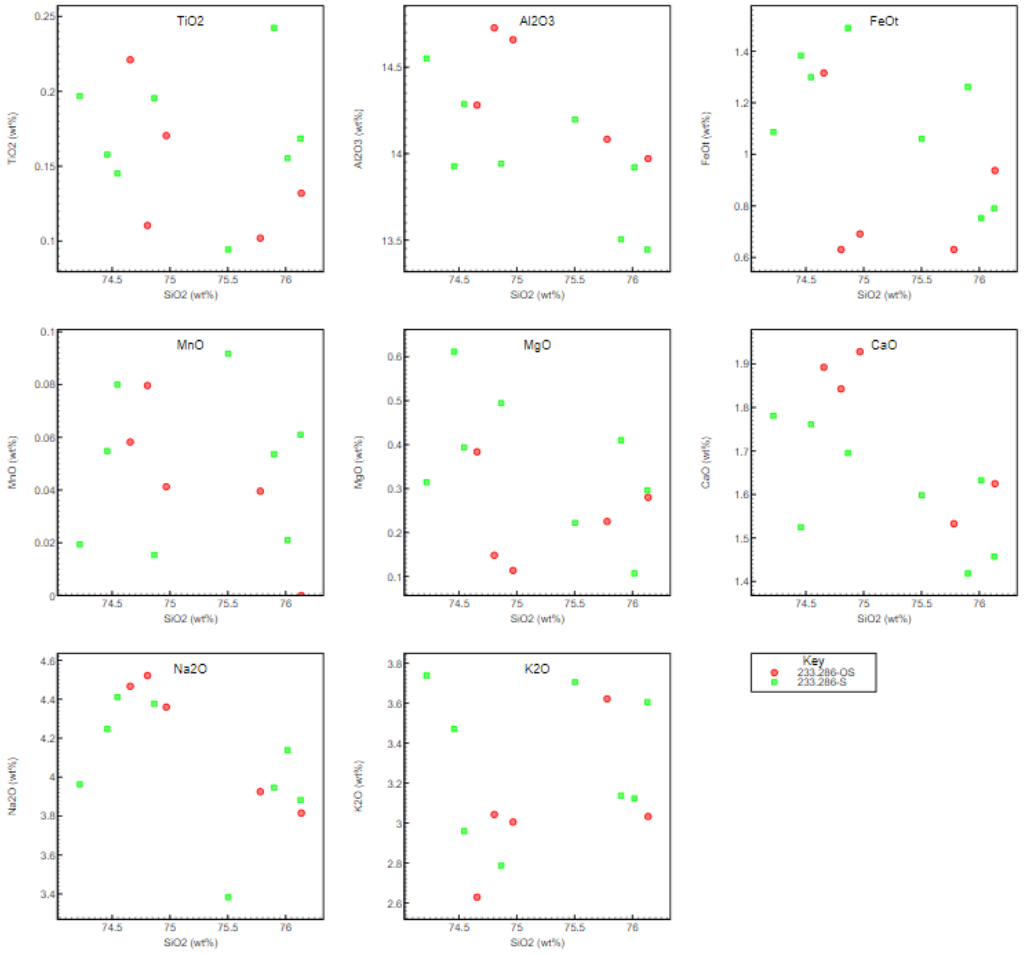


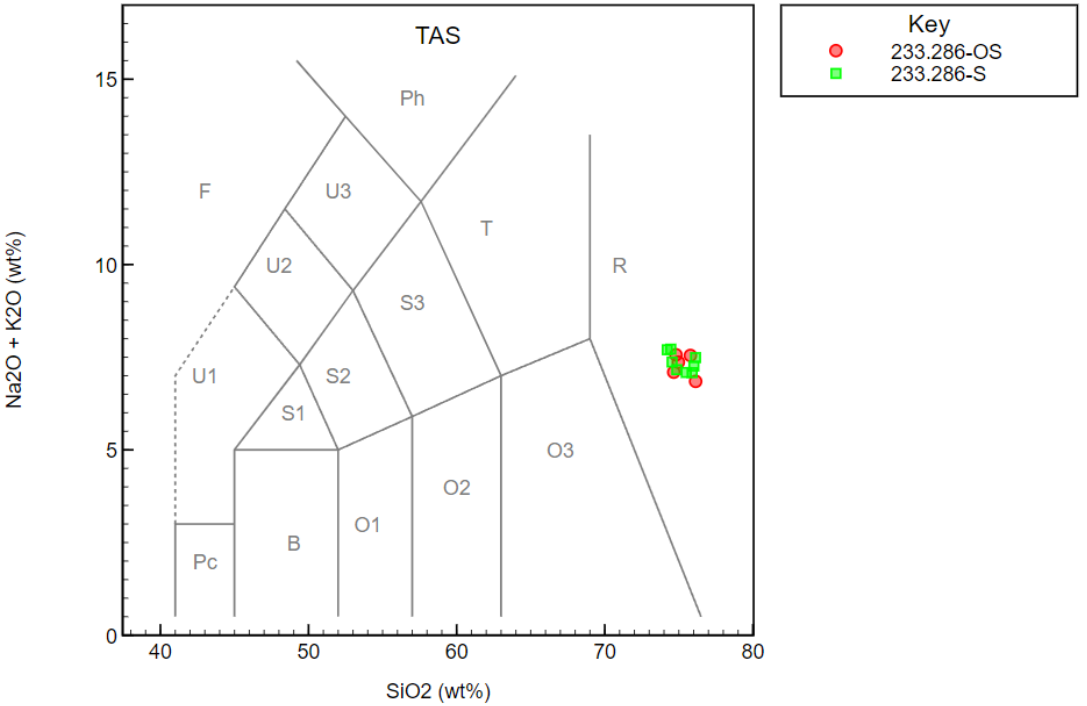
Tephra 230.23



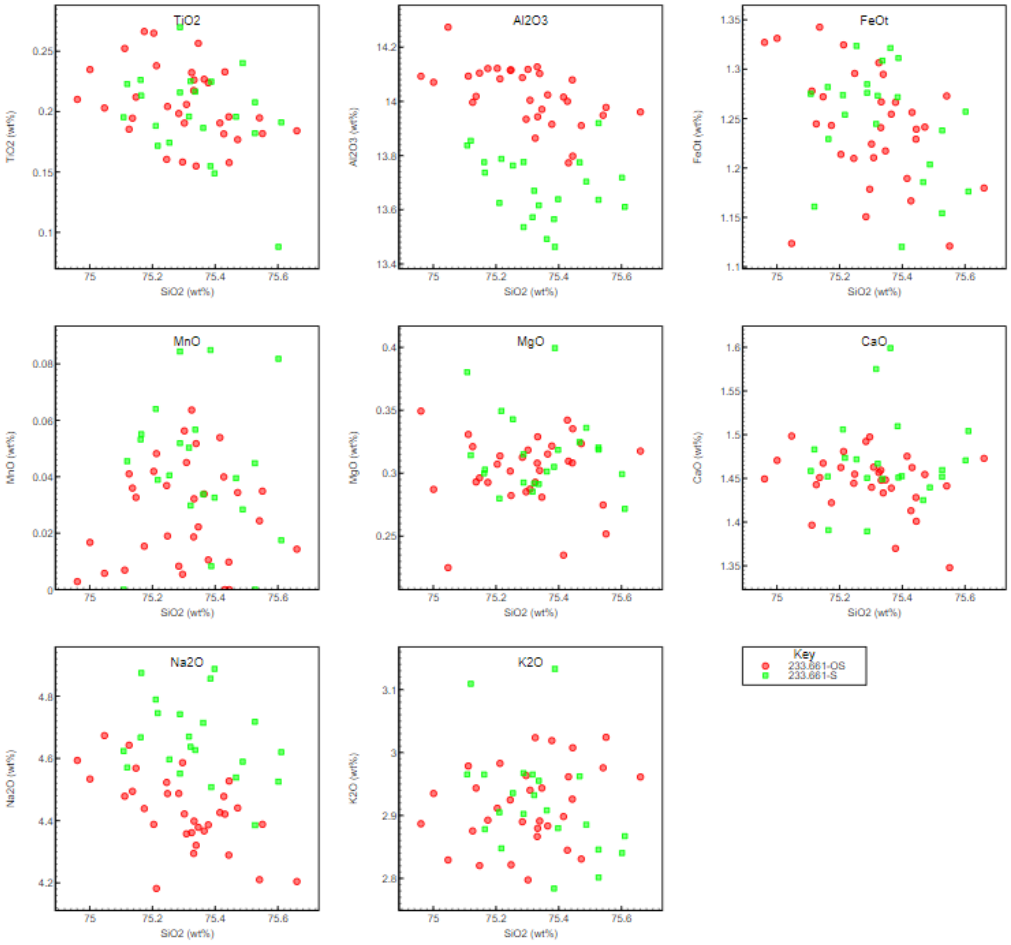


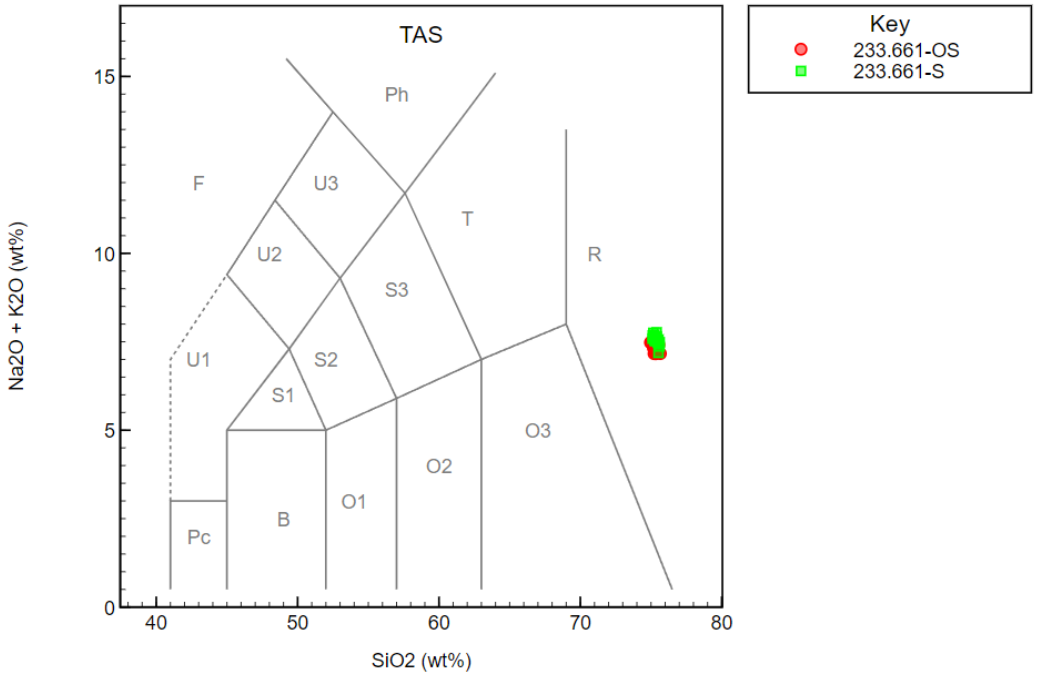
Tephra 233.286



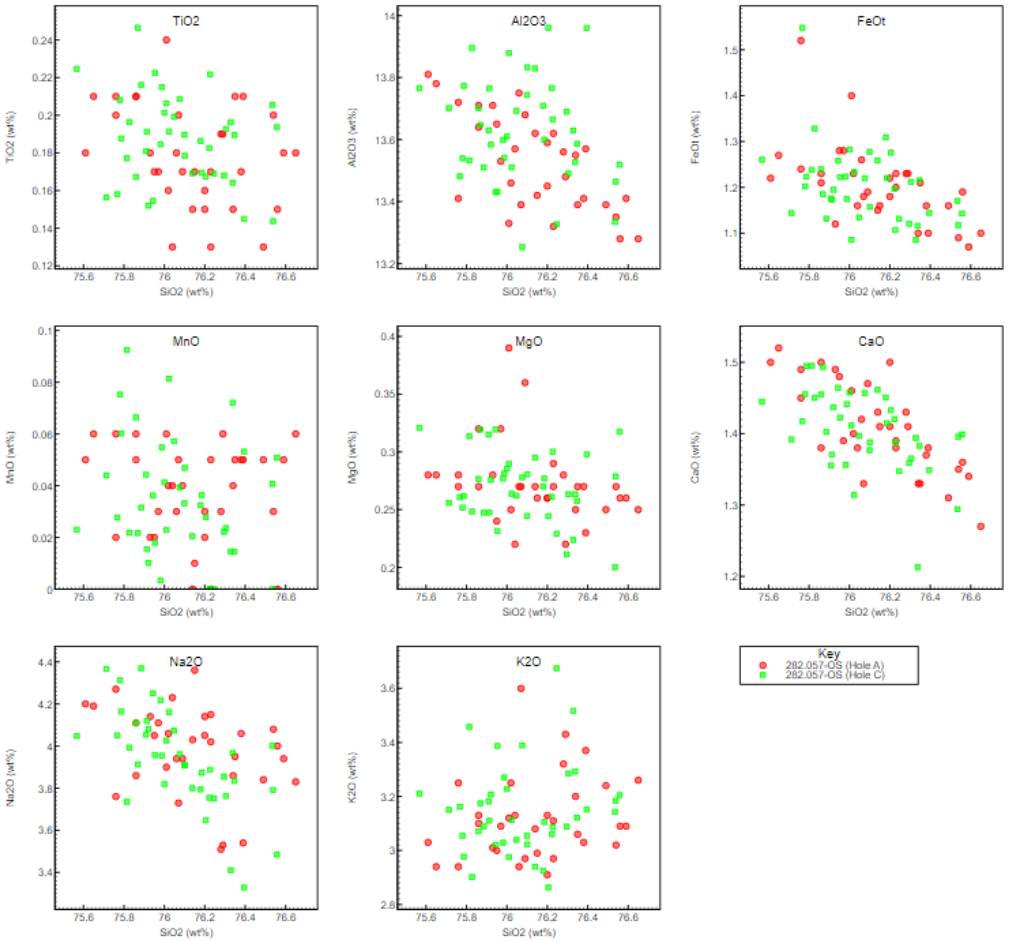


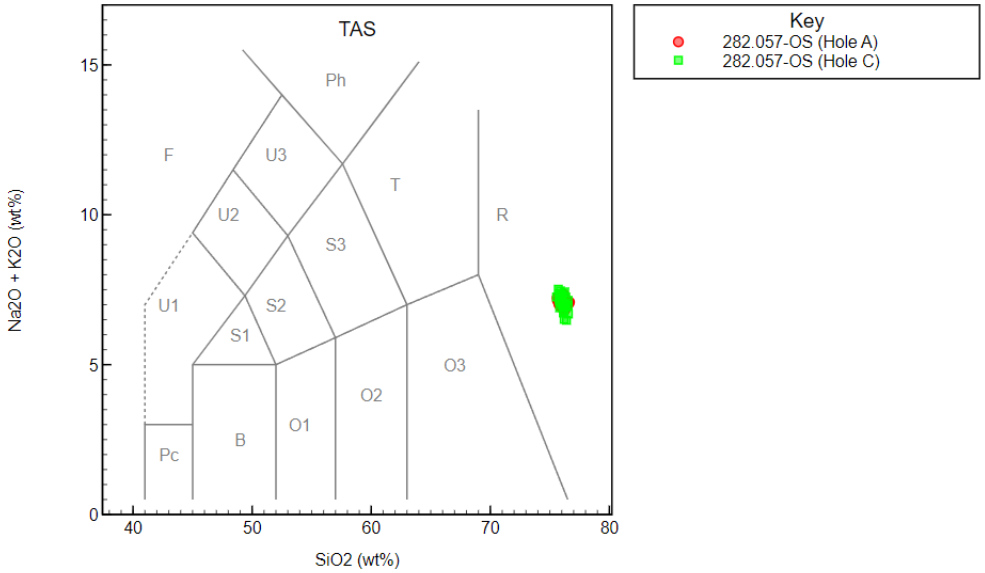
Tephra 233.661



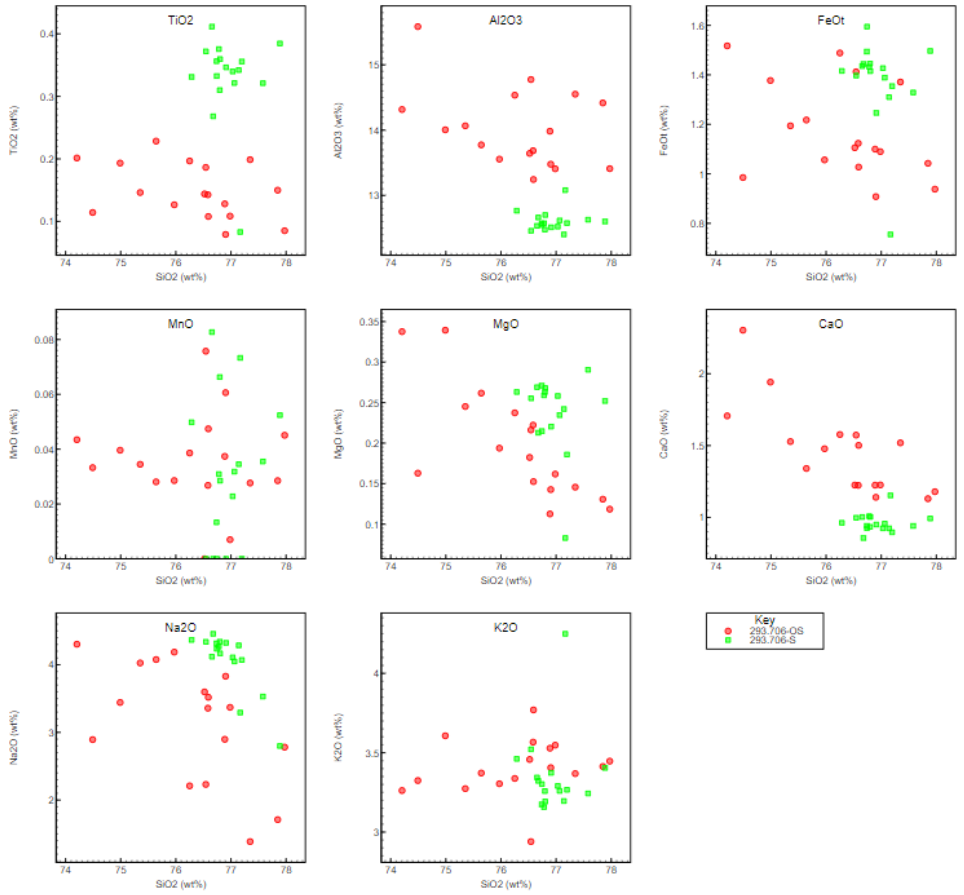


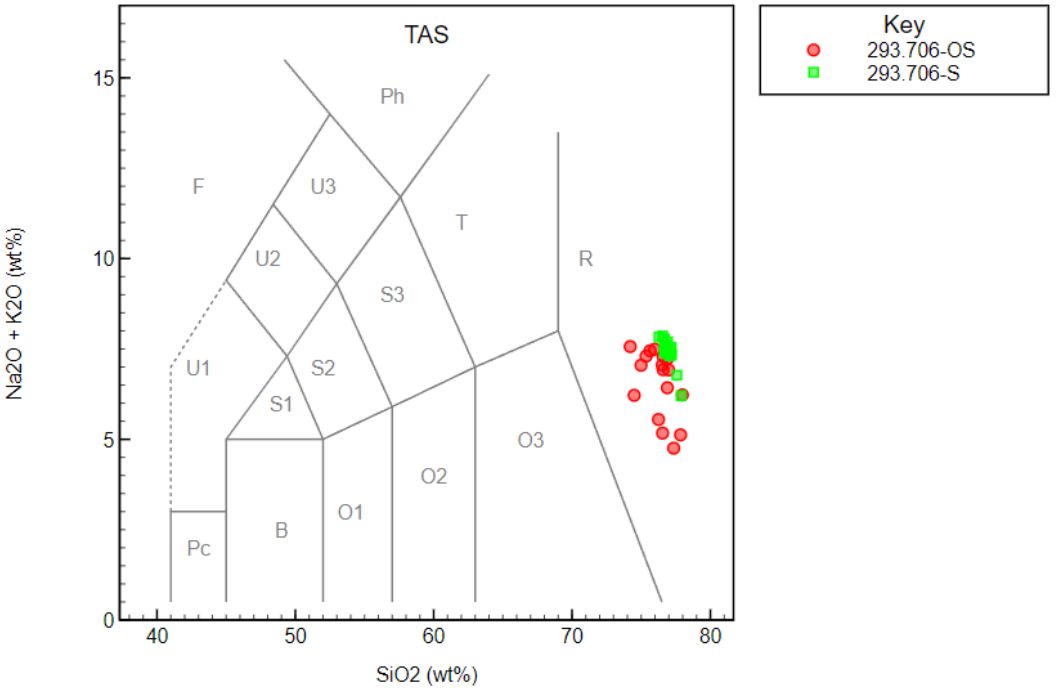
Tephra 282.057





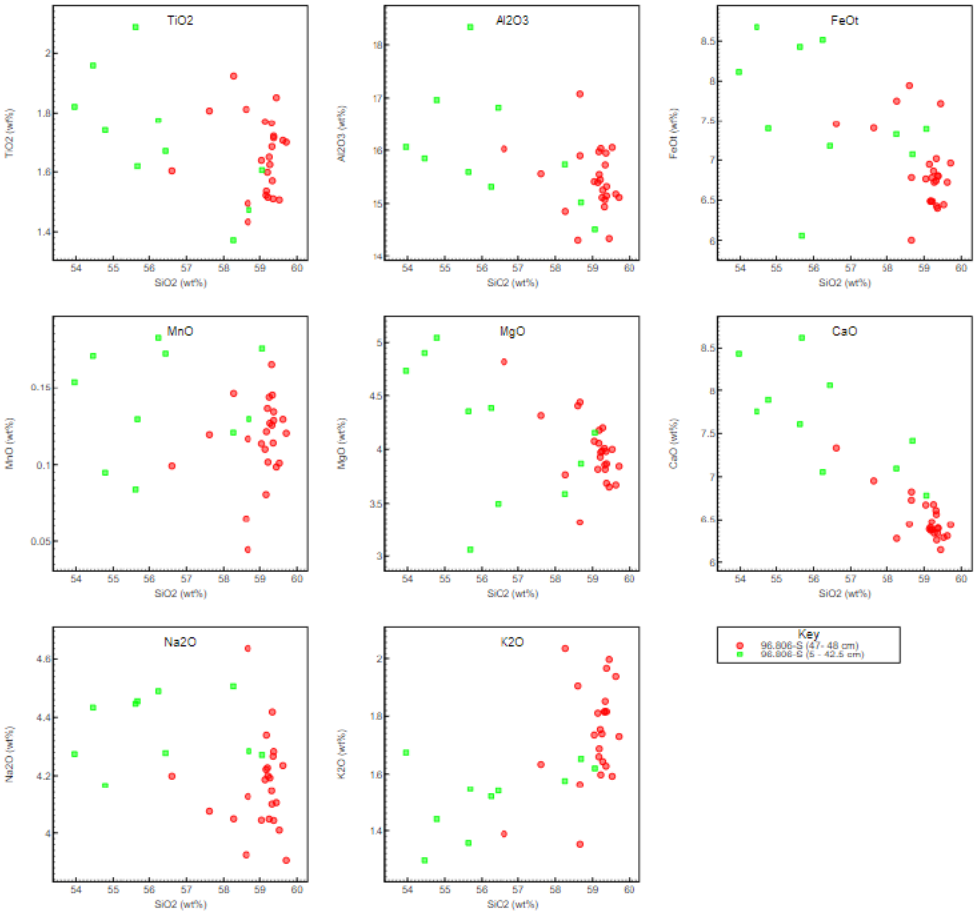
Tephra 293.706

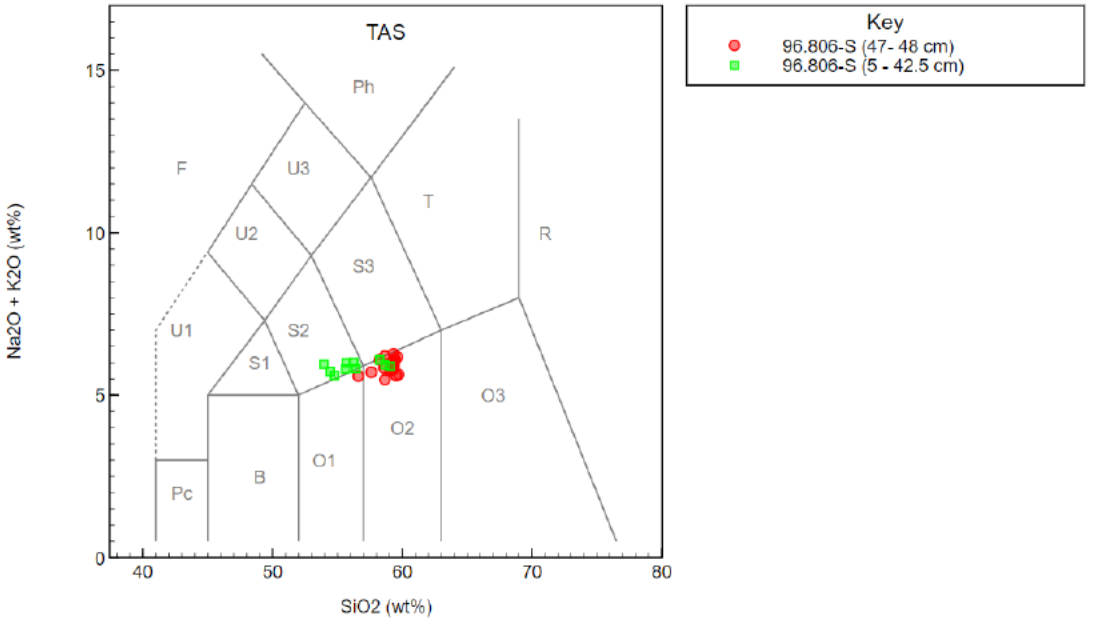




APPENDIX E3

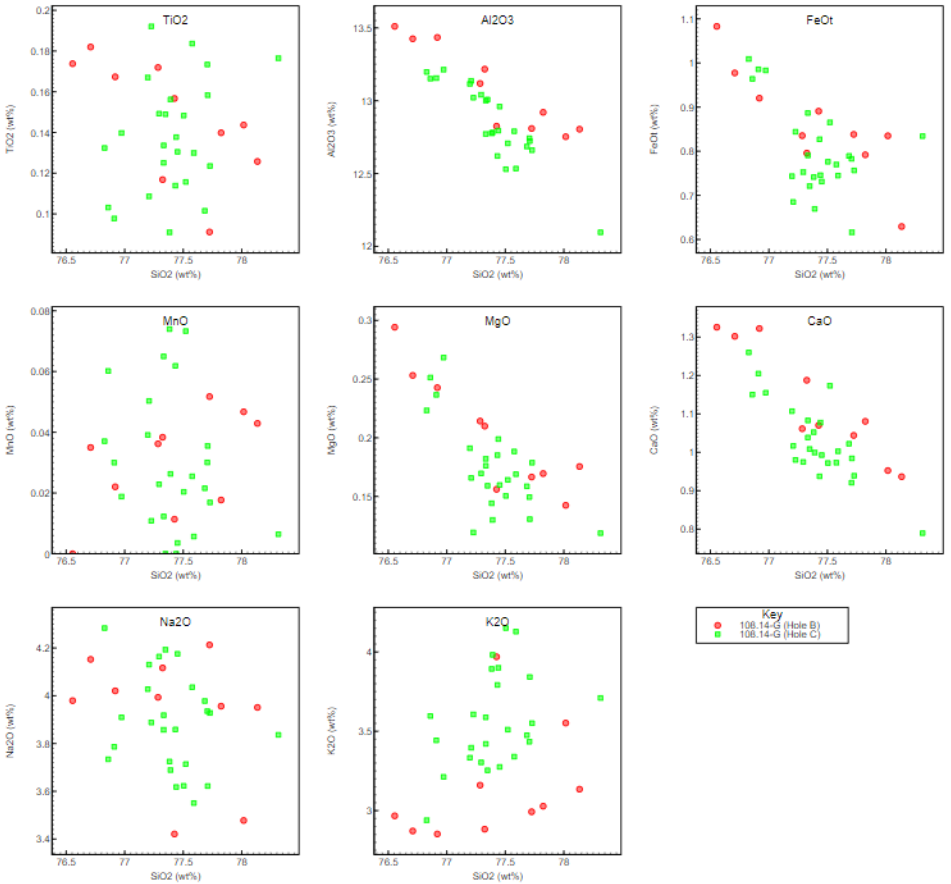
Tephra 96.806

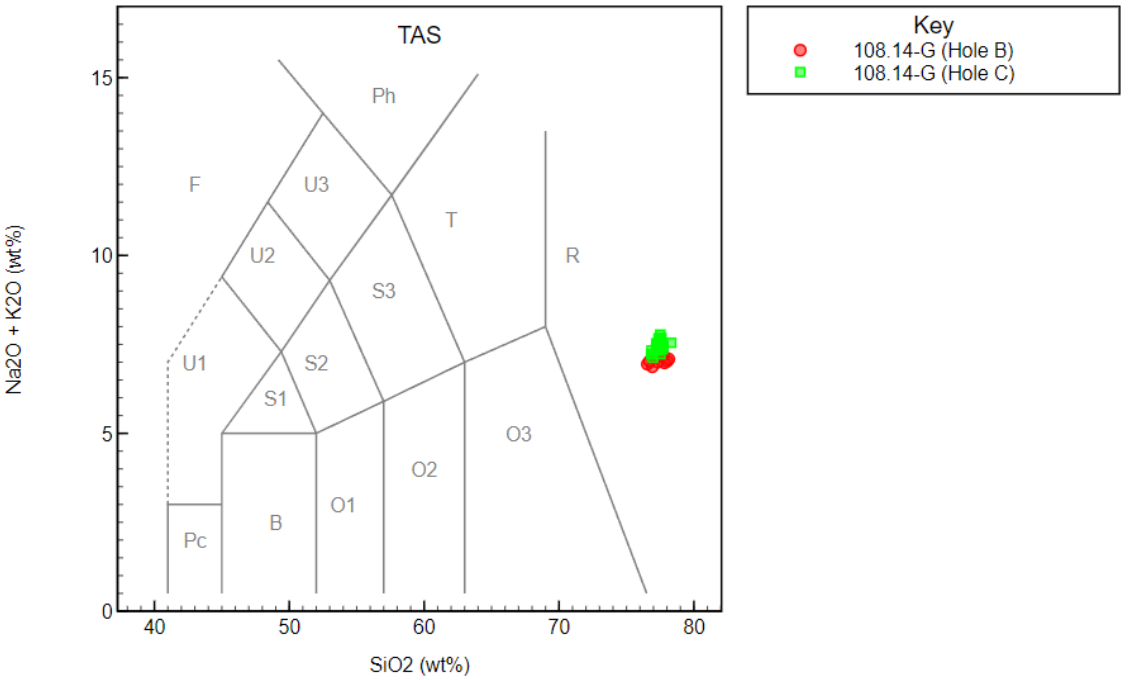




APPENDIX E4

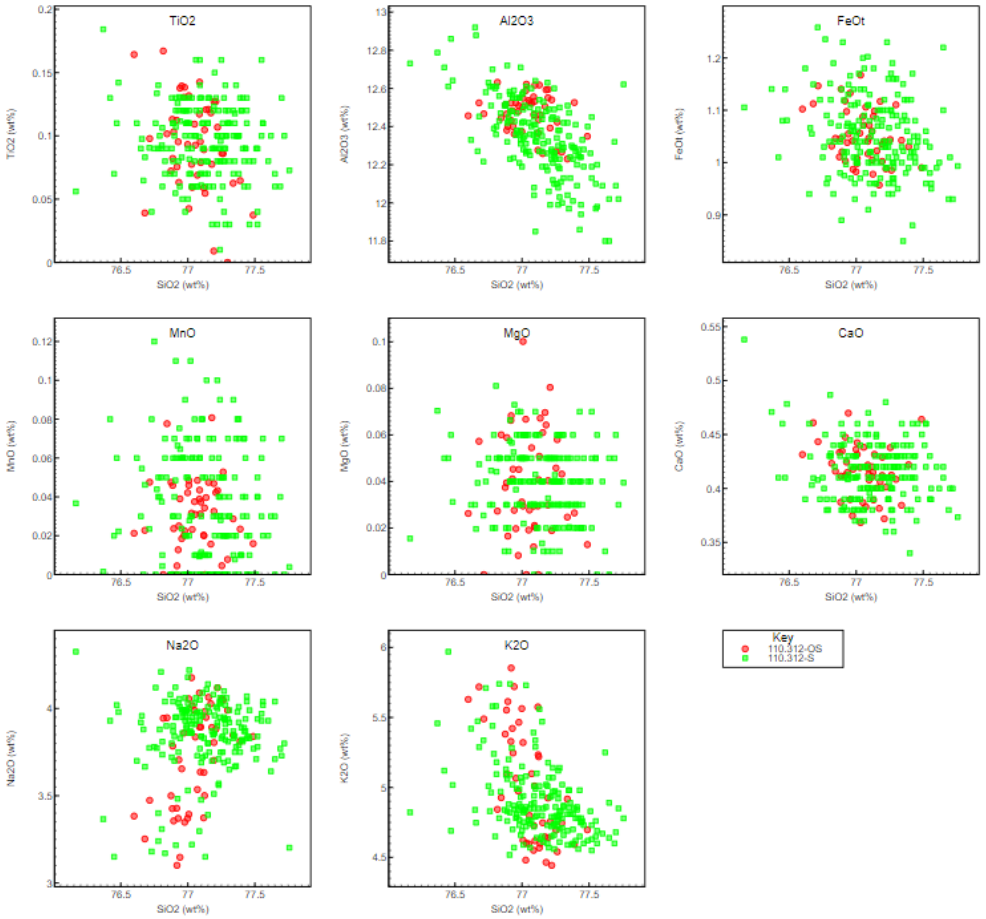
Tephra 108.14 (Ghost)

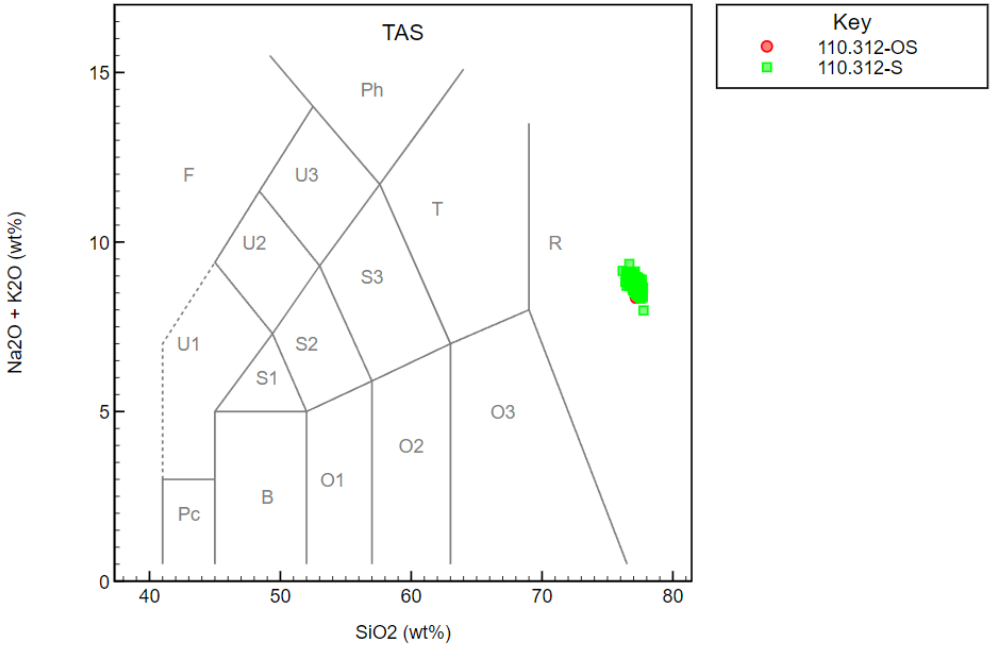




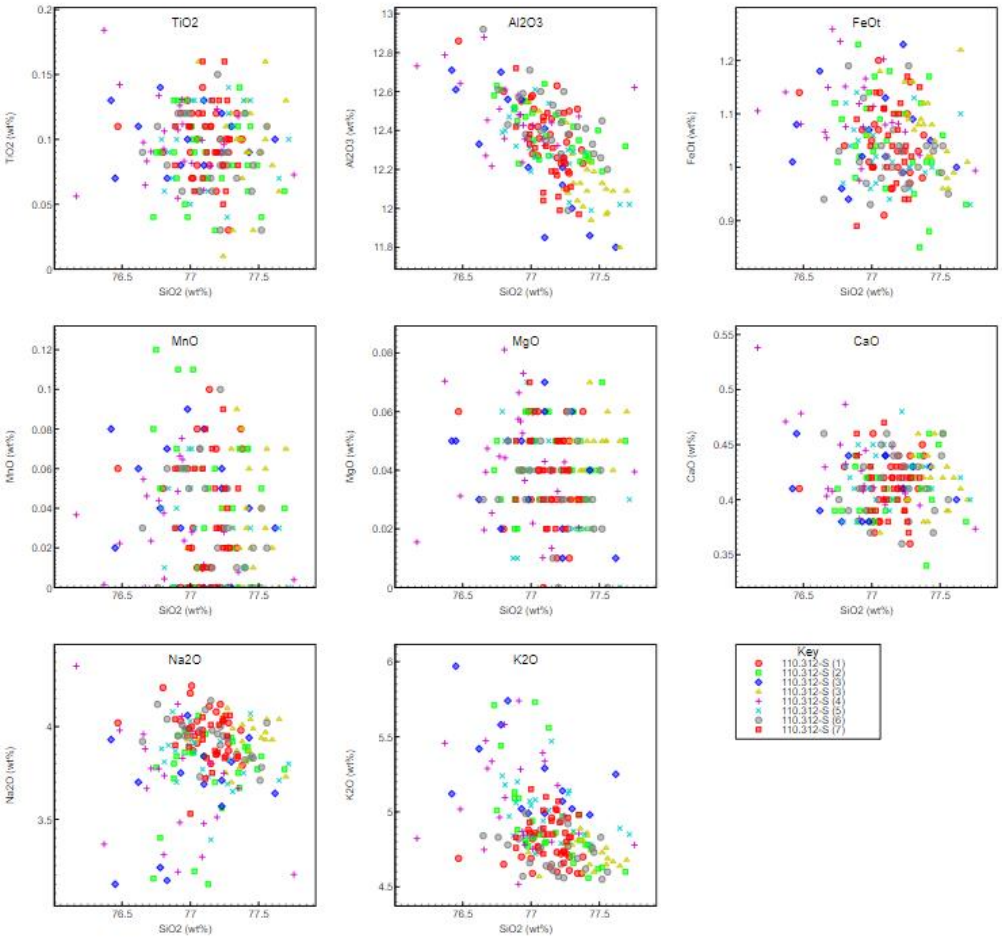
APPENDIX E5

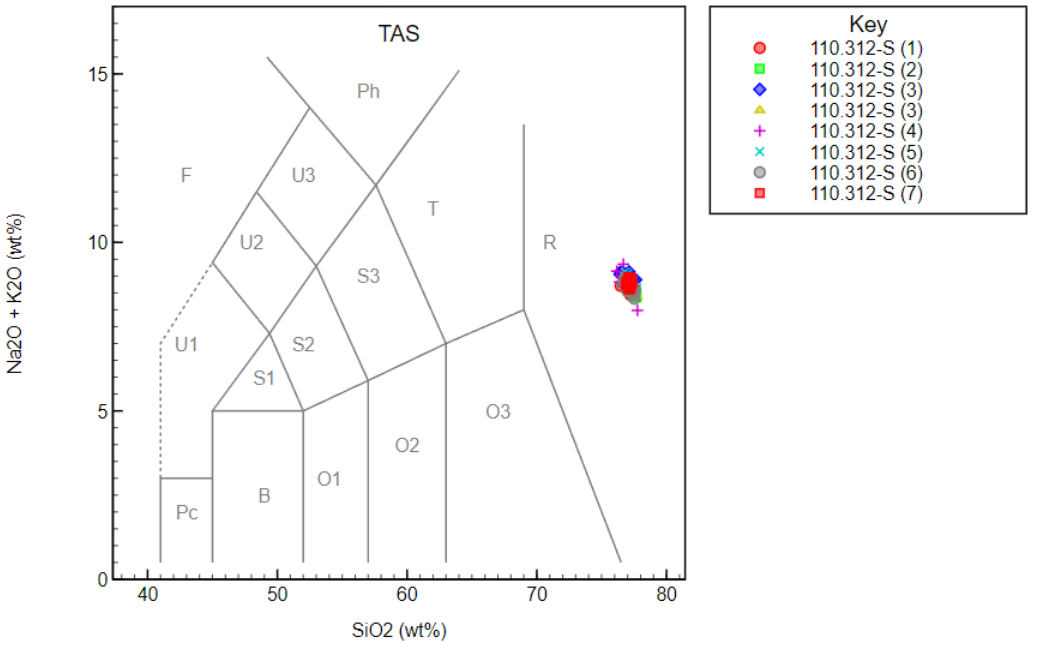
Tephra 110.312





Variation in Tephra 110.312





APPENDIX P1

International Journal of Earth Sciences
https://doi.org/10.1007/s00531-020-01964-z

ORIGINAL PAPER

Sedimentary stratigraphy of Lake Chalco (Central Mexico) during its formative stages

Rodrigo Martínez-Abarca[1] · Beatriz Ortega-Guerrero[2] · Socorro Lozano-García[3] · Margarita Caballero[2] · Blas Valero-Garcés[4] · David McGee[5] · Erik T. Brown[6] · Mona Stockhecke[6] · Alastair G. E. Hodgetts[7]

Received: 30 April 2020 / Accepted: 9 November 2020
© Geologische Vereinigung e.V. (GV) 2021

Abstract

Lake Chalco lies south of the Basin of Mexico and has been the subject of studies related to Late Quaternary climate variability. In 2016, the International Continental Scientific Drilling Program "MexiDrill Project" recovered a 520-m sediment record from Lake Chalco. Magnetic susceptibility measurements revealed substantial changes in sediment physical properties between 343 and 285 m depth, suggesting changes in composition associated with fluctuations in the depositional environment. We targeted sediments in the 343–285 m interval for high-resolution facies analysis, to develop a model of Lake Chalco formation. We identified three facies associations, using sediment composition, texture, mineralogy and micro-morphological characteristics: (1) detrital facies, consisting of laminated silt, massive sand, stratified silty sand, clast-supported gravel and matrix-supported gravel; (2) biogenic facies, which include diatom ooze and bivalve coquina; and (3) volcaniclastic facies, represented by clast-supported pumice deposits. We propose that formation of Lake Chalco occurred in four stages, which we identified by changes in sediment characteristics. The first stage was an alluvial delta environment, in which debris and hyper-concentrated flows were the main sediment transport agents. The second was characterized by turbulent flows in a fluvial deltaic environment, which alternated with laminar flows associated with floodplains. The third stage was a time of fluvio-lacustrine transition in the basin, with formation of the previously identified Paleo-Chalco-I Lake, in response to wet conditions. During the fourth stage, a deep eutrophic lake formed (Paleo-Chalco-II), with an origin that appears to have been related to regional volcanism. Our working age-depth model indicates establishment of the lake at ca. 400 ± 46 ka. This paper presents the only available record of the transition from alluvial to lacustrine sedimentation of Lake Chalco. Our results allow us to establish (1) how the lake was formed and what the phases of its development were, (2) how a major volcanic event altered and transformed the lacustrine sedimentation, and (3) which climatic conditions dominated during the lake formation. The age for the onset of the lacustrine sedimentation in Chalco is for the first time constrained to around 400 ka. This enables to expand our knowledge of the climate for a time for which there is no information from terrestrial records of tropical North America.

Keywords MexiDrill Chalco · Basin of Mexico · Lake formation · Facies analysis · Fluvial-lacustrine system · Volcanism and lakes

✉ [redacted]

[1] Posgrado en Ciencias de La Tierra, Universidad Nacional Autónoma de México, CP. 04510 Mexico City, Mexico

[2] Instituto de Geofísica, Universidad Nacional Autónoma de México, CP. 04510 Mexico City, Mexico

[3] Instituto de Geología, Universidad Nacional Autónoma de México, CP. 04510 Mexico City, Mexico

[4] Instituto Pirenaico de Ecología – CSIC, Apdo 13034, 50080 Zaragoza, Spain

[5] Department of Earth, Atmospheric and Planetary Sciences, Massachusetts Institute of Technology, Cambridge 02139, MA, USA

[6] Large Lakes Observatory & Dept. of Earth and Environmental Sciences, University of Minnesota Duluth, Duluth, MN 55812, USA

[7] School of Geography, Earth and Environmental Sciences, University of Birmingham, Edgbaston, Birmingham B15 2TT, UK

Published online: 07 January 2021

Introduction

Lake Chalco (Central Mexico) occupies the south-eastern part of the Basin of Mexico, where Mexico City is located (Fig. 1). Previous drilling recovered the upper 122 m of the sequence, whose analyses yielded stratigraphic, paleoclimatic and paleolimnological data that provided insights into the history of Lake Chalco over the past 140 ka (Lozano-Garcia et al. 1993, 2015; Caballero and Ortega 1998; Ortega-Guerrero and Newton 1998; Torres-Rodríguez et al. 2015; Ortega-Guerrero et al. 2017, 2020; Avendaño-Villeda et al. 2018; Martínez-Abarca et al. 2019; Caballero et al. 2019). It was not until recently, however, that deep cores (520 m) were drilled in this basin (Lozano-García et al. 2017), enabling investigation into the origin of the lake.

It is widely accepted that the Basin of Mexico was an exorheic fluvial system that drained southward and whose closure occurred as a consequence of the accumulation of volcanic deposits in the south during the Pleistocene (Mooser 1963). Subsequent studies reported closure of the basin between 1300 and 600 ka (Martin del Pozzo 1982; Macias et al. 2012; Arce et al. 2013), determined from the age of the volcanic deposits that outcrop in the Basin today. Nevertheless, because of the inaccessibility of the oldest sediments, which are covered by younger geologic deposits, it had not been possible to explore what geological processes led to basin closure or when they occurred.

In 2016, the ICDP-supported (International Continental Scientific Drilling Program) MexiDrill Project retrieved four

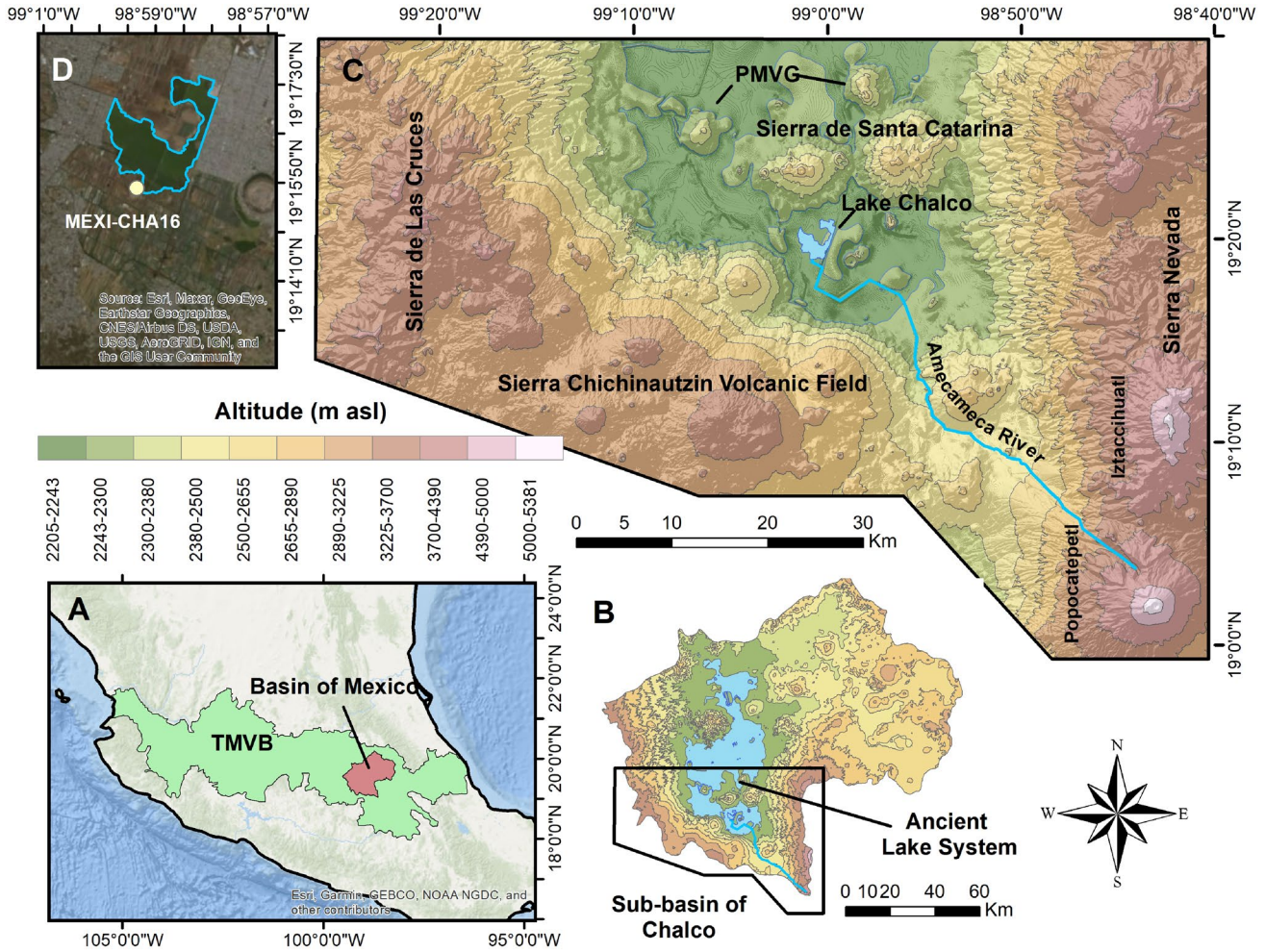


Fig. 1 Location of Lake Chalco. **A** Extent of the Transmexican Volcanic Belt (TMVB) and the Basin of Mexico. **B** Basin of Mexico, the ancient lake system is indicated. **C** Close view to the sub-basin of Chalco, the major ranges are indicated: **a** Sierra Nevada in the east, **b** Sierra de Las Cruces in the west, **c** the Chichinautzin volcanic field in the south and d Sierra de Santa Catarina to the north. Additional structures are indicated: Amecameca River and Peñon Monogenetic Volcanic Group (PMVG). **D** Location of the MEXI-CHA16 core. (Geological data obtained from INEGI 2020; satellite image from Google Earth Pro 2020)

cores from Lake Chalco, recovering a composite sequence that extended to a maximum depth of 520 m (Lozano-Garcia et al. 2017; Brown et al. 2019). The initial stratigraphic description of the MexiDrill Chalco composite sequence revealed that the upper 300 m are composed of fine-grained lacustrine sediments, and the lower section is comprised of > 200 m of alluvial and fluvial deposits, as well as lavas (Brown et al. 2019; Romero-Vera 2019).

We utilized facies analysis of the deposits between 343 and 285 m depth in Lake Chalco, which record the transition from a fluvial-alluvial phase to a lacustrine phase, to infer the environmental conditions under which the lake formed and to characterize the processes that led to its development. Analysis of the formative stages of Lake Chalco is relevant to our understanding of the geologic evolution of Central Mexico and contributes information about broader questions related to lake formation in volcanically and tectonically active regions.

Study area

The Basin of Mexico, located in the east-central part of the Trans-Mexican Volcanic Belt (TMVB) (19°15′N, 98°58′W), is an endorheic depression with a lacustrine plain at 2240 m above sea level (m asl). Lake Chalco is the southeasternmost water body of an ancient vast lacustrine system that developed in the Basin of Mexico during pre-Hispanic times. This lake system has recently undergone massive transformations and has a long history of human occupation (Niederberger 1987; Sanders et al. 1979). Today, Lake Chalco is reduced into a shallow, subsaline marsh ($z_{max} < 3$ m), with an area of ~ 5.5 km^2, and is located next to Mexico City, a megalopolis with > 25 million inhabitants (INEGI 2010). The current water body is the depocenter of the sub-basin of Chalco, which is morphologically delimited by the following volcanic ranges: (1) the Sierra de Las Cruces to the west, (2) Sierra de Santa Catarina to the north, (3) the Sierra Nevada to the east, and (4) the Sierra Chichinautzin Volcanic Field to the south (Fig. 1). Other volcanic structures with ages around 1300 ka are found north of the Sierra de Santa Catarina and Jaimes-Viera et al. (2018) called them "Peñon Monogenetic Volcanic Complex (PMVG)".

The Sierra de Las Cruces is composed of lava flows, pyroclastic and lahar deposits that are aligned NW–SE (Mora-Álvarez et al. 1991). The bulk of its volcanic activity occurred during the late Miocene (Mooser et al. 1974; Osete et al. 2000). The Sierra Nevada is composed of a chain of stratovolcanoes that include: (a) Tlaloc-Telapon (1.8 Ma); (b) Iztaccihuatl volcanic complex (0.9–0.08 Ma); and (c) Popocatepetl, whose current cone was formed 0.23 Ma ago (Nixon 1989; Macias et al. 2012; Siebe et al. 2017). At least 220 monogenetic volcanoes constitute the Sierra Chichinautzin Volcanic Field. It includes scoria cones (e.g., Xitle), shield volcanoes (e.g., Teuhtli) and lava domes (e.g. Mesa la Gloria) (Bloomfield 1975; Martin del Pozzo 1982; Marquez et al. 1999). Jaimes-Viera et al. (2018) suggested that volcanic activity in Sierra Chichinautzin occurred between ca. 1300 ka and 7 ka ago.

Methods

Drilling, initial core description and preliminary stratigraphy

The MEXI-CHA16 cores (holes 1A, 1B and 1C) were drilled near the modern lake depocenter, in the sub-basin of Chalco (19° 15′ 26″ N, 98° 58′ 32″ W) (Fig. 1c). The drilling effort yielded sediment from the surface down to 520 m depth. Drilling was carried out using a Longyear LF90 rig with standard HQ3 wireline diamond coring tools, and sediment cores were retrieved in polycarbonate liners that were 1.5-m long and 6.1 cm in diameter (Brown et al. 2019). After completion of the field program, the sections were sent to the LacCore Facility at the University of Minnesota for core measurement, scanning and description. Cores were then split lengthwise, cleaned and high-resolution color scans were acquired from each section using a DMT CoreScan digital linescan camera. Magnetic susceptibility was measured systematically at 1-cm intervals using a Bartington MS2E sensor. Stratigraphic correlation among sequences 1A, 1B and 1C was carried out by Valero-Garces et al. (In press), who used magnetic susceptibility and facies identification to develop a composite sequence that minimized the effects of gaps and artifacts from the drilling process.

Preliminary visual characterization of the MEXI-CHA16-1C core sections (color, texture, structure, thickness, sorting and boundary type) was done using high-resolution images, viewed with the free distribution software CoreWall (http://www.corewall.org/). Sediments analyzed for this study were between 343 and 285 m deep in the composite sequence.

Sediment description

Thirty-nine smear slides of samples from the MEXI-CHA16-1C core, prepared from sandy to clayey materials that represent the observed major shifts in sediment texture and composition, provided a basis for initial major component descriptions (Schnurrenberger et al. 2003). Additionally, 21 samples of undisturbed, fine-grain (clay to sand) sediment were prepared for thin sections in blocks of 4 × 5 cm. Thin-section samples were collected in aluminum trays, freeze-dried, embedded with epoxy resin and polished to 30-µm thickness in preparation for microscopic analyses. The first analysis was a petrographic micro-morphological description that included general mineralogy, geometry,

and microstructures, as well as documenting the presence of diatoms, charcoal and other biogenic material. The second analysis consisted of counting exclusively quartz (Q) and feldspar/plagioclase (F). Prior to counting, the thin sections were stained with potassium rhodizonate and barium chloride. Mineral phase percentages were estimated by counting 200 points, following the method of Gazzi-Dickinson (Ingersoll et al. 1984). The ratio Q/(Q + F) was estimated to infer the precipitation regime under which sediment could have been deposited (Picurd 1971; Weltje 1994). According to this method, sediments having a higher Q/(Q + F) ratio are indicative of wet conditions due to the loss of feldspar and plagioclase during chemical weathering (Van der Kamp 2010).

Texture analysis was carried out based on two different methods. The first one was only used for determining the grain-size distribution of coarse sand and gravel deposits, following the Rosiwal's intercepts methodology (Rosiwal 1898). This method consists on measuring clasts length intersected by parallel lines regularly spaced at 3 cm, perpendicular to core length, on scanner images where 30 clasts (minimum) were considered without repeating the same clast thrice (Sarocchi et al. 2005). Measurements were carried out with free distribution software ImageJ (Rasband 2018). The second method, applied on clay, silt and medium/fine sand, was performed on 39 samples using a Beckman Coulter Multi-Wavelength Particle Size Analyzer. Particle sizes obtained from both methods were converted to phi units, and later, sorting was inferred by estimating standard deviation (SD) based on the grain size distribution using software R version 3.5.0 (R Core Team 2018). Well-sorted material has SD values > 0.7, whereas poorly sorted material has SD values < 0.7.

Semi-quantitative diatom analysis was carried using the smear slide samples of fine-grained (sandy to clayey) deposits. We counted diatoms in two or three parallel transects on the smear slides. Diatoms were identified to genus level and at least 300 valves were counted to obtain statistically significant results (Smol and Stoermer 2010). Additionally, 21 stratigraphic samples were processed for pollen counting to estimate the relative percentages of the most common pollen taxa, following the Batten (1999) methodology.

Total nitrogen (TN), total carbon (TC) and total organic carbon (TOC) were determined on 17 samples with a Thermo Fisher Scientific NC-Soils Analyzer FLASH 2000 Series Elemental Analyzer. Total inorganic carbon (TIC) was estimated as TC-TOC. $\delta^{13}C$ and $\delta^{15}N$ were measured in organic matter with a DELTA PLUS Finnigan MAT Isotope Ratio Mass Spectrometer at the Universidade A Coruña Laboratory (Spain). Identification of aquatic/terrestrial organic matter sources was done using TN, TC, TOC and $\delta^{13}C$ data, following the scheme proposed by Meyers and Teranes (2001).

Age model

A preliminary Bayesian age-depth model was constructed using R studio and the Bacon package (Blaauw and Christen 2011). The model took 168 sections with 3.74×10^7 iterations. Depth data used for the model are referred to as "corrected composite depth (mcc)," which considers sand and volcaniclastics to be instantaneously deposited materials. The time scale for the lacustrine sequence was developed using five ^{14}C ages from the upper 36 m of sediment, collected during earlier drilling at Chalco (core CHA08; 0.5 km southwest of the MexiDrill site in the sub-basin of Chalco) (Herrera-Hernandez 2011; Ortega-Guerrero et al. 2017) (Table 1). The ^{14}C ages were calibrated using the IntCal13 calibration curve (Reimer et al. 2013). For sediments below 36 m depth, a $^{234}U/^{230}Th$ date was obtained on zircons extracted from a tephra layer in a core collected previously at Chalco (core CHA08, 0.5 km southwest of the

Table 1 Data set used for the age model

Code	Age (ka)	Error (BP ± 1σ)	Depth (m)	Composite corrected depth (mcc)	Dated material	References
Beta 287,002	24.62*	120	10.09	11.21	Pollen	Herrera-Hernandez (2011)
Beta 287,005	27.65*	140	16.50	18.03	Pollen	Herrera-Hernandez (2011)
Beta 347,492	31.74*	210	30.46	25.82	Pollen	Ortega-Guerrero et al. (2017)
Beta 347,998	34.01*	260	34.08	30.77	Pollen	Ortega-Guerrero et al. (2017)
Beta 347,499	40.46*	520	35.18	32.27	Ostracod	Ortega-Guerrero et al. (2017)
CHA08 date	76.7**	4700	63.50	69.84	Zircon	Ortega-Guerrero et al. (2017)
MIS6-5 transition	130	3000	106	106	NA	Avendaño-Villeda et al. (2018) Lisiecki and Raymo (2005)
MexiDrill date	280**	40,000	170	166.73	Lacustrine carbonates	David McGee (unpublished)

Data with asterisk (*) are uncalibrated ^{14}C dates. Data with double asterisks are $^{234}U/^{230}Th$ dates. Age-depth model was developed using composite corrected depths (mcc), which were estimated assuming sand and volcaniclastics were deposited instantaneously

MexiDrill site) (Ortega-Guerrero et al. 2017). Additionally, we employed an age of 130 ka at 106 m depth defined by Avendaño-Villeda et al. (2018), who identified the transition between Marine Isotopic Stages 6 and 5 based on diatoms analyses in Chalco, and assigned the age of this transition according to the Lisiecki and Raymo (2005) chronology. Finally, an age of 280 ± 40 ka was determined for lacustrine carbonates at 192 m (166.73 mcc), using $^{234}U/^{230}Th$. The latter is a tentative age that will likely be modified in future studies. It was estimated from four different sediment aliquots; one returned a date of 231 ± 11 ka, and another returned a date of 332 ± 14 ka (2-sigma uncertainties). Two other aliquots returned infinite ages. We used the mean of the two finite age results to provide a rough age estimate.

Results

In this section, we present facies descriptions, using the results of textural, mineralogical, compositional and stable isotope analyses from the targeted depth interval (343–285 m).

Facies description

Eight facies were defined in the sequence (Fig. 2). Using the main components, facies were grouped into three categories: (1) detrital, which includes (a) laminated silt (LS), (b) massive sand (MS), (c) stratified silty sand (STS), (d) clast-supported gravel (CSG), and (e) matrix-supported gravel (MSG) facies; (2) biogenic, composed of (a) diatom ooze (DO) and (b) bivalve coquina (CO) facies; (3) volcaniclastic, which includes clast-supported pumice (CSP) facies (Table 2).

(1) Detrital facies

The detrital facies are composed of silt, sand and gravel deposits (Fig. 3). Minor components in detrital facies include biogenic remnants such as diatoms, organic material, and charcoal. Although detrital sediment is distributed along the sequence, coarser material (gravel) is more abundant toward the base of the stratigraphic column (> 315 m). Mineralogically, sand deposits are dominated by plagioclase, feldspar, pyroxene, olivine and volcanic glass. On the other hand, gravel deposits are composed of andesite and basalt fragments. Magnetic susceptibility displays a wide range of values, with the gravel deposits showing higher values (400–1500 10^{-5} SI) than silt deposits (150–250 10^{-5} SI). Massive sand deposits have the lowest values of total nitrogen and total organic carbon (TOC*:* 0.1–0.4%; TN*:* 0.01–0.03%), whereas laminated silt and stratified silty sand have higher values (TOC*:* 0.09–1.59%; TN*:* 0.01–0.09%). In addition, the massive sand sections have low values of Q/(Q + F) ratio (< 0.4).

(2) Biogenic facies

These facies are composed mainly of diatoms, pollen, charcoal, organic material, ostracods, gastropods and vascular plant remnants. They are present between 315 and 285 m depth; with the highest abundance from 306 to 286 m depth. Magnetic susceptibility in these deposits is between 250 and 150 10^{-5} SI, the lowest in the core record. Total nitrogen varies between 0.08 and 0.52%, while total organic carbon varies between 0.61 and 5.92%, the highest values in the core record. There are two kinds of biogenic deposits: diatom ooze and bivalve coquina.

The diatom ooze is composed of 90% diatom valves and 10% feldspar-rich silt, and other components such as pollen, phytoliths, and vascular plant remains. Diatoms were divided into two associations (Fig. 4f). Association A is composed of *Staurosira*, *Rhopalodia*, *Cocconeis,* and *Navicula*, which correspond to shallow-water conditions. In contrast, association B is formed by *Stephanodiscus* cf. *minutulus* (Kütz) Cleve & Möller, and *Stephanodiscus niagarae*-Ehrenberg, as well as *Aulacoseira sp.*, which are planktonic forms that are common in eutrophic and relatively deeper-water lakes (Edlund and Kingston 2004; Bennion and Simpson 2011; Gabito et al. 2013). The diatom deposits are characterized by high values of the Q/(Q + F) ratio (> 0.4). Most of the diatom deposits are intercalated with detrital facies, particularly between 306 and 294 m depth.

The bivalve coquina is composed of bivalve, ostracod and gastropod remnants (Fig. 4g). It is present at 293 m depth as a unique deposit of 1.2 m thickness. Its palynomorph content is composed mainly of the microalga *Pediastrum*, and pollen of *Pinus, Picea, Alnus, Ambrosia* and *Quercus*.

(3) Volcaniclastic facies

Volcaniclastic facies includes four tephra deposits between 294 and 286 m depth (Fig. 5). These are well sorted, with sub-angular pumices. Based on their color and mineralogy (plagioclase, muscovite and quartz), these are from silica-rich eruptions. Magnetic susceptibility has intermediate values, between 250 and 570 10^{-5} SI. The clast-supported pumice deposits are named here to represent their stratigraphic depth: (a) Tephra CHA16-288, (b) Tephra CHA16-289a, (c) Tephra CHA16-289b and (d) Tephra CHA16-294.

Tephra CHA16-288 is located at 288.1 m depth has a thickness of 13 cm. This deposit shows inverted gradation, from ash to lapilli, and has an inferior planar contact. Tephra CHA16-289a is located at 289.6 m depth and is 24 cm thick. It is a lapilli deposit with appar-

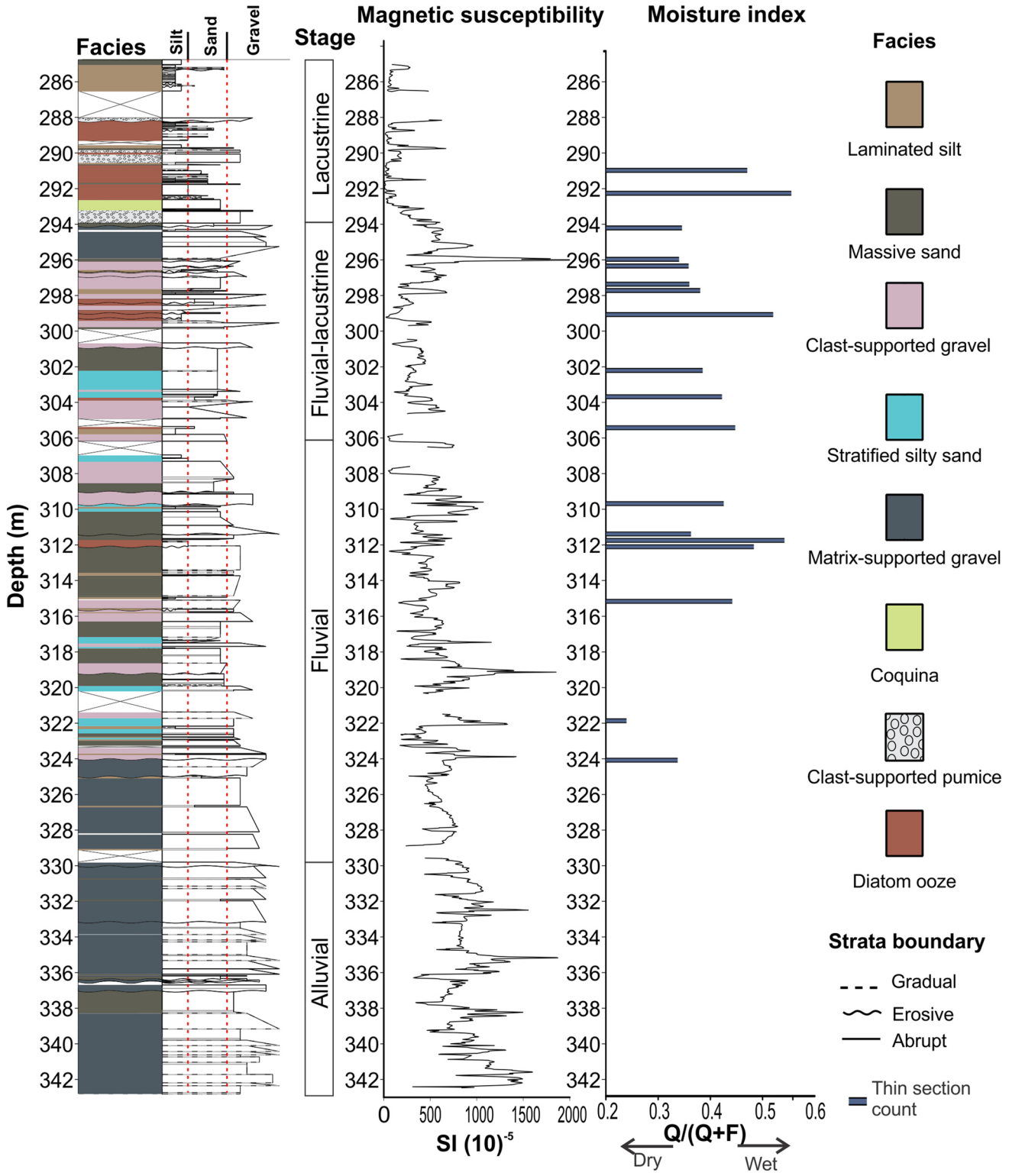


Fig. 2 Stratigraphic column for the section between 343 and 285 m depth in the MEXI-CHA16-IC core. The column is composed of the facies identified at the left and the particle size at the right. The four stages proposed: **a** Alluvial (385–330 m), **b** Fluvial (330–306.5 m), **c** Transitional Fluvial-Lacustrine (306.5–294 m), and **d** Lacustrine (294–285 m). Magnetic susceptibility and moisture index (Q/(Q + F)) ratio are shown, the latter calculated from thin section mineral counts

Table 2 Main textural, compositional, mineralogical and stable isotope features of the facies proposed in this work for Lake Chalco in the sedimentary sequence from 343 to 285 m depth

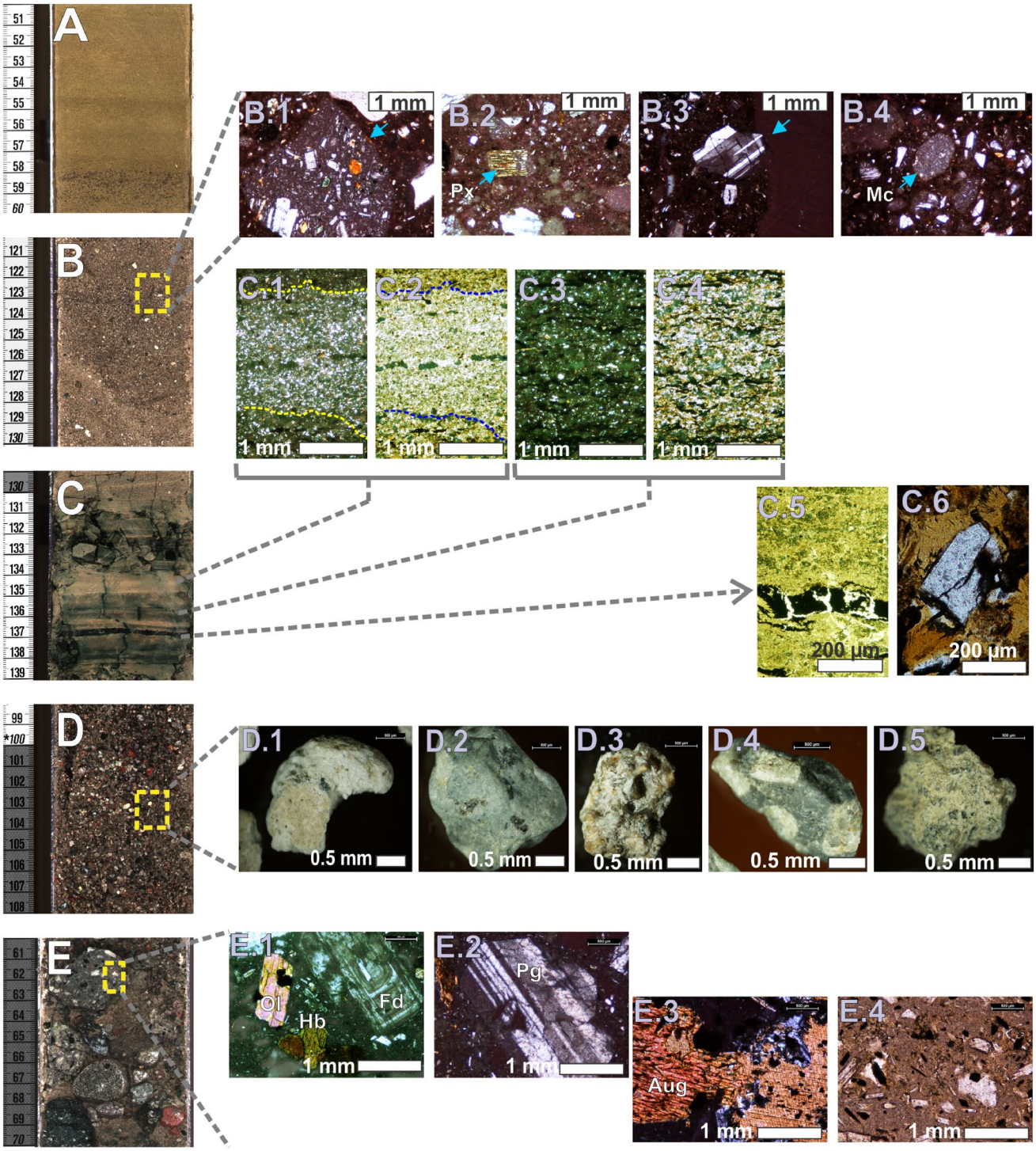
Facies	Sedimentological features	Depositional environment
Laminated silt (LS)	*Distribution:* Upper seven meters of the stratigraphic column (292–285 m depth) as strata with variable thickness (0.3–1 m) *Granulometry and sorting:* Silt (~64%), fine sand (~26%) and clay (~11%). Moderately sorted (SD = 0.72) *Mineralogy:* Feldspar (38%), pyroxene (17%), opaque minerals (11%), olivine (9%), quartz (6%) and amphibole (1%) *Biogenic rests:* organic material (1%) and siliceous remnants such as phytoliths and diatoms (9%) *Magnetic susceptibility:* 150 to 250 10^{-5}SI TOC: 0.9–1.1% / TN: 0.09–0.1% / TOC/TN: 9.1–13.1 δ^{15}N: 2.9–3.3 ‰ / δ^{13}C: – 24.4 to – 23.9 ‰	Oligotrophic lake, probably shallow
Massive sand (MS)	*Distribution:* Between 339 and 300 m depth, with the greatest occurrence between 324 and 309 m, as strata with variable thickness between 0.15 and 2 m *Granulometry and sorting:* Medium-coarse sand (72%), silt (23%) and clay (6%). poorly to moderately sorted (SD between 0.9 and 1.22) *Mineralogy:* Monocrystalline feldspar (30%), opaque minerals (12%), plagioclase on lathwortk lithic (12%), pyroxene (11%), lathwortk lithic (9%), olivine (8%), quartz (7%), biotite (4%), amphibole (2%) and microlite lithic (2%) *Biogenic rests:* Siliceous remnants such as diatoms (mainly *Cocconeis* gender; (1%) and phytoliths (4%) *Magnetic susceptibility:* 400 to 700 10^{-5}SI TOC: 0.1–0.4% / TN: 0.01–0.03% / TOC/TN: 6.4–13.9 δ^{15}N: 1.8–5 ‰ / δ^{13}C: – 33.7 to – 20.3 ‰ *Special notes:* Thin section data suggest the presence mainly of basaltic-andesite angular poorly sorting lithics (Fig. 4). Minerals show high alteration and diagenesis, such as dissolution in pyroxene and plagioclase crystals, as well as subparallel twinning in plagioclase crystals	Laminar flows in a fluvial low energy environment When MS is intercalated with MGS represents the final stage of a hyperconcentrated flow in an alluvial environment

Table 2 (continued)

Facies	Sedimentological features	Depositional environment
Stratified silty sand (STS)	*Distribution:* Between 325 and 301.5 m, with greatest recurrence between 301.5 and 307 and 318–323 m as deposits between 0.8 and 0.2 m thickness *Granulometry and sorting:* Sand (41%), silt (51%) and clay (8%) *Mineralogy:* Feldspar and plagioclase (28%), olivine (14%), pyroxene (11%), quartz (9%), plagioclase on lathwortk lithic (5%), opaque minerals (4%), clayey matrix (3%), lathwortk lithic (3%), amphibole (2%), volcanic glass (2%) and in some cases chalcedony (1%) *Biogenic rests:* Organic material and vascular plants (15%), as well as siliceous remnants such as phytoliths (3%) and diatoms (2%) *Magnetic susceptibility:* 500 to 700 10^{-5} SI TOC: 0.09–1.59% / TN: 0.01–0.09% / TOC/TN: 5.7–17.9 $\delta^{15}N$: 2.74–6.13 ‰ / $\delta^{13}C$: – 28.1 to – 22.5 ‰ *Special notes:* Micromorfologic analyzes suggest the presence of laminations associated with changes on sorting, roundness and diameter. We observed light layers associated with coarse (coarse sand), angular and poorly sorting sediment; and dark layers associated with fine (fine sand), subrounded and moderate sorting sediment. We observed charcoal and olivine phenocrystals horizontally aligned as well as a high concentration of organic material on dark layers. In addition, we observed angular crystals of quartz and plagioclase with no orientation on light layers. In some cases, there are coal layer up to 1 cm thick (Fig. 5)	Laminar flows in a flood plain environment
Clast supported gravel (CSG)	*Distribution:* Between 321 and 295 m as strata with variable thickness between 1 and 1.5 m *Granulometry and sorting:* Gravel (100%). Subangular-rounded clasts with diameters between 4 and 2 mm. Very well sorted (SD between 0.25 and 0.43) *Mineralogy:* Deposits are composed of: (1) white pumice fragments with biotite, pyroxene, plagioclase and quartz crystals (35%); (2) basalt and andesite fragments with pyroxene, feldspar and olivine (33%); (3) conglomerate fragments composed of basaltic lithics and olivine, pyroxene and plagioclase crystal on a sandy matrix (17%); (4) orange pumice fragments with plagioclase, quartz and pyroxene crystals (5%); (5) rock fragments with calcite crystals (5%); (6) plagioclase individual crystals (3%); (7) olivine individual crystals (1%); and (7) black scoria fragments (2%) (Fig. 6) *Biogenic rests:* NA *Magnetic susceptibility:* 180 to 1200 10^{-5}SI TOC: NA $\delta^{15}N$: NA / $\delta^{13}C$: NA *Special notes:* Deposits are massive and occasionally show normal gradation. Clast supported gravel facies (CGS) is composed of massive clast supported gravel deposits that occasionally show normal gradation	Streamflows with high energy in a fluvial environment

Table 2 (continued)

Facies	Sedimentological features	Depositional environment
Matrix supported gravel (MSG)	*Distribution:* Between 343 and 324 m depth, it is also present between 295 and 293.5 m. The strata have variable thickness from 1–1.5 m *Granulometry and sorting:* Gravel (100%). Subangular-rounded clasts with diameters between lower than 10 cm. Poorly sorted (SD between 1.5 and 2.5) *Mineralogy:* Clasts are angular and they have basaltic-andesitic composition with plagioclase, orthopyroxene (enstatite), clinopyroxene, opaque minerals and amphibole (hornblende) (Fig. 7) *Biogenic rests:* NA *Magnetic susceptibility:* 400 to 1500 10^{-5} SI TOC: NA $\delta^{15}N$: NA / $\delta^{13}C$: NA *Special notes:* Deposits have two types of fabric: (1) massive gravel and (2) gravel with normal gradation followed by coarse sand with plane parallel stratification	Debris flows in an alluvial environment
Diatom ooze (DO)	*Distribution:* Between 316 and 285 m depth and it has greatest recurrence between 307 and 286.5 m. Strata of 0.3–1.5 m thickness *Biogenic rests:* Biogenic fraction constitutes 90% and it is composed of siliceous remnants such as sponge spicules and diatoms *Granulometry and sorting (detrital fraction):* Silt (63%), fine sand (25%) and clay (11.7%). Fine sand grains are well sorting (SD between 0.65 and 0.85) *Mineralogy:* Feldspar (40%), quartz (12%), olivine (11%), pyroxene (9%), augite (7%) and opaque minerals (6%) *Magnetic susceptibility:* 150 to 250 10^{-5} SI TOC: 0.61–5.92% / TN: 0.08–0.52% / TOC/TN: 8–14.3 $\delta^{15}N$: 5.61–9.13 ‰ / $\delta^{13}C$: – 28.1 to – 24.8 ‰	Relatively deep (few meters), cold to temperate fresh water lake
Coquina (CO)	*Distribution:* Deposit with 1.2 m thick at 293 m depth *Biogenic rests:* The 68% of the components are oval carbonated organism's remains such as ostracods and bivalves (90%) and gastropods (10%) (Fig. 10). The 30% of components are diatoms remains (4%), sponge spicules (16%), organic material (9%) and charcoal (1%). Diatoms are mostly composed of *S. minutulus*. 76% algae (principally *Pediastrum*), 21% arborous pollen, 3% herbaceous pollen and 0.3% subaquatic plants characterize palynomorphic content *Granulometry and sorting (Detrital fraction):* Sand (49%), silt (48%) and clay (3%). Sand grains are well sorting *Mineralogy:* Aragonite (47%) and calcite (42%) *Magnetic susceptibility:* less than 150 10^{-5} SI TOC: 3.1% / TN: 0.2% / TOC/TN: 15.5 $\delta^{15}N$: 8.2 ‰ / $\delta^{13}C$: – 25.2 ‰	Shallow and eutrophic lake
Clast supported pumice (CSP)	Four deposits located at 294, 289.9, 289.6 and 288.1 m depth. Magnetic susceptibility: between 250 and 570 10^{-5} SI. The strata thickness vary between 12 and 85 cm	Pyroclastic fall deposits probably from the Iztaccihuatl volcanic complex



ent lamination and an inferior planar contact. Tephra CHA16-289b is located at 289.9 m depth and is 45 cm thick. It is a massive lapilli deposit with an inferior planar contact. Tephra CHA16-294, located at 294 m depth, is 85 cm thick, and the largest volcanic deposit in the sequence (Fig. 5H.4). This deposit is divided in two units. The first, at the bottom, is composed of massive lapilli with an inferior planar contact, whereas the second unit overlies the first one and is a massive ash deposit with an inferior sharp contact.

◂**Fig. 3** Core images of detrital facies; vertical scale in cm. **A** Laminated silt (MEXI-CHA16-1C-170Y-1). **B** Massive sand (MEXI-CHA16-1C-189Y-1), and the different kind of clasts in this facies: B.1 Lithic type lathwortk with plagioclase phenocrysts. B.2 Pyroxene phenocrystal with high degree of weathering. B.3 plagioclase monocrystal with hacksaw twinning. B.4 Lithic microlith type in a crystalline matrix. **C** Stratified silty sand (MEXI-CHA16-1C-185Y-1): C.1 and C.2 cross-polarized and plane-polarized light microphotographs, respectively, of a light layer, plagioclase crystals are observed without alignment. C.3 and C.4 Cross-polarized and plane-polarized light microphotographs, respectively, of a dark layer; the alignment of the layers can be observed on plagioclase crystals and charcoal. C.5 Coal layer intercalated between the light layers; and C.6 chalcedony (red color) enveloping a quartz crystal. **D** Clast-supported gravel (MEXI-CHA16-IC-189Y-1): D.1 white pumice fragments; D.2 and D.4 andesitic fragments. D.3 Calcite fragment. D.5 detrital rock fragment. **E** Matrix-supported gravel (MEXI-CHA16-IC-203Y-1): E.1 Olivine (Ol), feldspar (Fd) and hornblende (Hb). E.2 Fragment of plagioclase (Pg). E.3 Fragment of augite (Aug) with high degree of weathering. E.4 Opaque minerals in a hypocrystalline matrix of plagioclase and glass

Age model

The Bayesian age-depth model suggests that the upper 343 m of the MexiDrill Chalco sequence spans the last 408 ± 47 ka (Fig. 6). Eighty-nine percent of the ages obtained in the age-depth model are within the 95% confidence range (uncertainties < 44 ka). The model provides a preliminary estimate for the age of the deepest lacustrine deposits in the MexiDrill core. As discussed below, deposits associated with the establishment of a permanent lake are at 293.1 m depth (236 mcc), and have a model age of 400 ± 46 ka. The age-depth model indicates that the section analyzed in this work (343–285 m; 240–229 mcc) spans ~ 21 ka of the depositional evolution before and during the formation of Lake Chalco.

Discussion

Formative history of Lake Chalco

We divided the stratigraphic column from Lake Chalco into four phases using the stratigraphy, magnetic susceptibility data, and the Q/(Q + F) ratio. These stages are, from deepest to shallowest: (a) alluvial, (b) fluvial, (c) transitional fluvial-lacustrine, and (d) lacustrine (Fig. 2). In this section, we describe the characteristics of each stage and its associated environmental processes.

Alluvial stage

Deposits associated with this phase are located between 343 and 330 m depth. They are characterized for the most part by MSG facies. The main features of this stage are the absence of organic material and high magnetic susceptibility values (Table 2). Angularity in clasts could indicate active collision between clasts during the sediment transport. Particle size is > 2 cm, indicating high-energy transport.

There are two types of features in the MSG facies. The first is dominated by massive, poorly sorted and ungraded gravel, suggesting the presence of debris flows. They are gravity-driven flows of highly concentrated mixtures of sediment and water (> 80 wt% [percentage of total dry mass]), whose deposition occurs abruptly (Sohn et al. 1999). The second feature consists of moderately sorted, usually graded gravel, with gradual coarsening upward contacts at the bottom, and stratified sand at the top. These characteristics suggest the presence of hyper-concentrated flows (Cao and Qian 1990; Cronin et al. 1999). These are gravity-driven flows, but unlike debris flows, they have a suspended sand sediment content between 20 and 60 wt% (Beverage and Culbertson 1964) and their deposition can generate graded deposits (Pierson 2005). Presence of both hyper-concentrated and debris flow deposits leads us to propose that this section corresponds to an alluvial environment (Lowe 1982; Smith 1986).

According to our preliminary chronology, sediments in this stage may have been deposited around 408 ± 46 ka. Additionally, presence of rock fragments rich in plagioclase, orthopyroxene, clinopyroxene and amphibole in both types of deposits suggests that the material came from ranges in the basin with basalt-andesite composition, such as the Chichinautzin, Santa Catarina, Las Cruces and Nevada ranges (Fig. 3e).

Effusive volcanic activity younger than 250 ka has been recorded in the Chichinautzin and Santa Catarina Volcanic Fields (Lugo-Hubp et al. 1994; Marquez et al. 1999; Arce et al. 2015; Ortiz-Enriquez 2017; Jaimes-Viera et al. 2018), which make them unlikely sources of the MGS deposits of the alluvial stage. Volcanic activity around the basin, which is older than 400 ka and could have been the source of the MGS deposits, occurred in the Sierra de Las Cruces (Osete et al. 2000; Aguirre-Diaz et al. 2006; Arce et al. 2008), Peñon Monogenetic Volcanic Group (Jaimes-Viera et al. 2018) and Sierra Nevada (Nixon 1989).

Fluvial stage

CSG, MS, and STS facies constitute the fluvial stage deposits from 330 to 306.5 m depth. The main characteristic of this core interval is the first appearance in the record of organic materials including vascular plant remains, amorphous organic matter, and charcoal layers. These sediments, however, are devoid of remains of aquatic organisms. According to our age model, sediments of this stage are likely older than 407 ± 46 ka.

Results of the Rosiwal method show that clasts in the CSG facies are > 2 mm, but < 2 cm, suggesting a high-energy

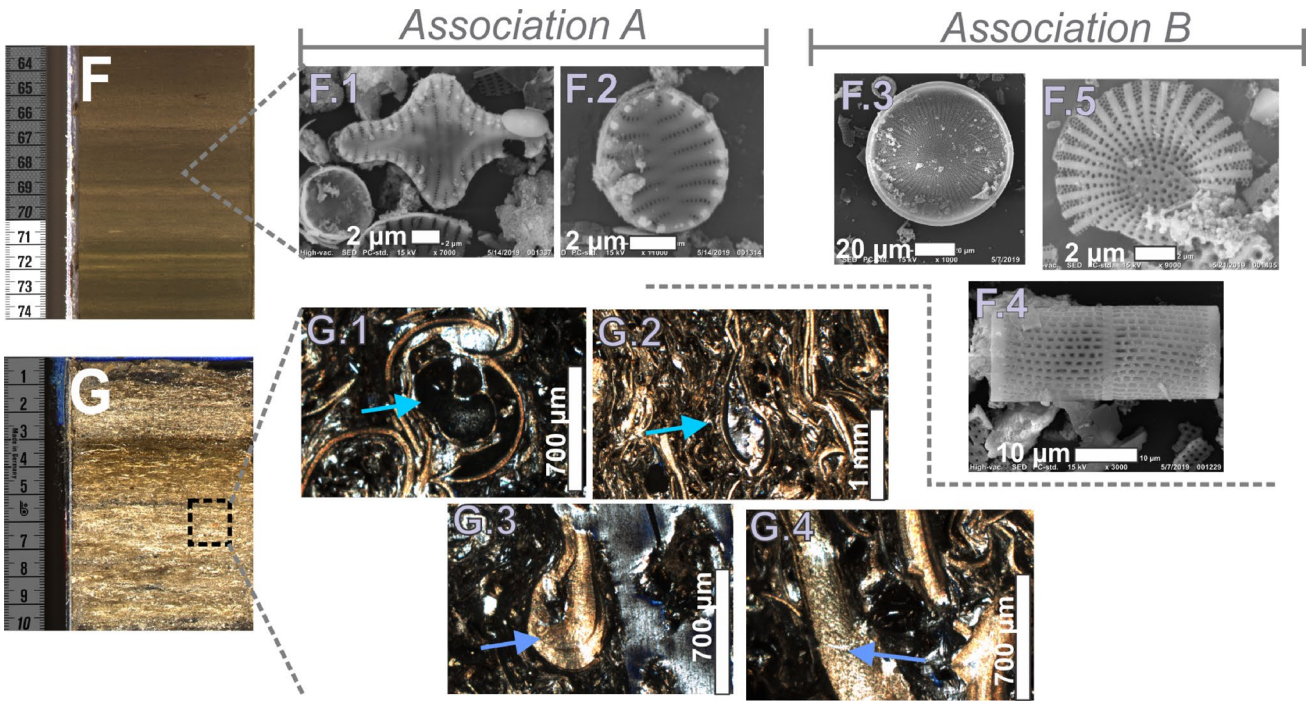


Fig. 4 Core images of biogenic facies. Vertical scale in cm. **F** Diatom ooze (MEXI-CHA16-IC-174Y-1): (F.1 and F.2) Representative diatoms from association A (*Staurosira sp.*); (F.3, F.4 and F.5) Representative diatoms from association B *(Stephanodiscus niagarae, Aulacoseira sp.,* and *Stephanodiscus minutula,* respectively). **G** Coquina (MEXI-CHA16-IC-175Y-1): (G.1) Gastropod; (G.2) Ostracod, (G.3 and G.4) Bivalve (the arrow indicates the lamellae that allowed their identification)

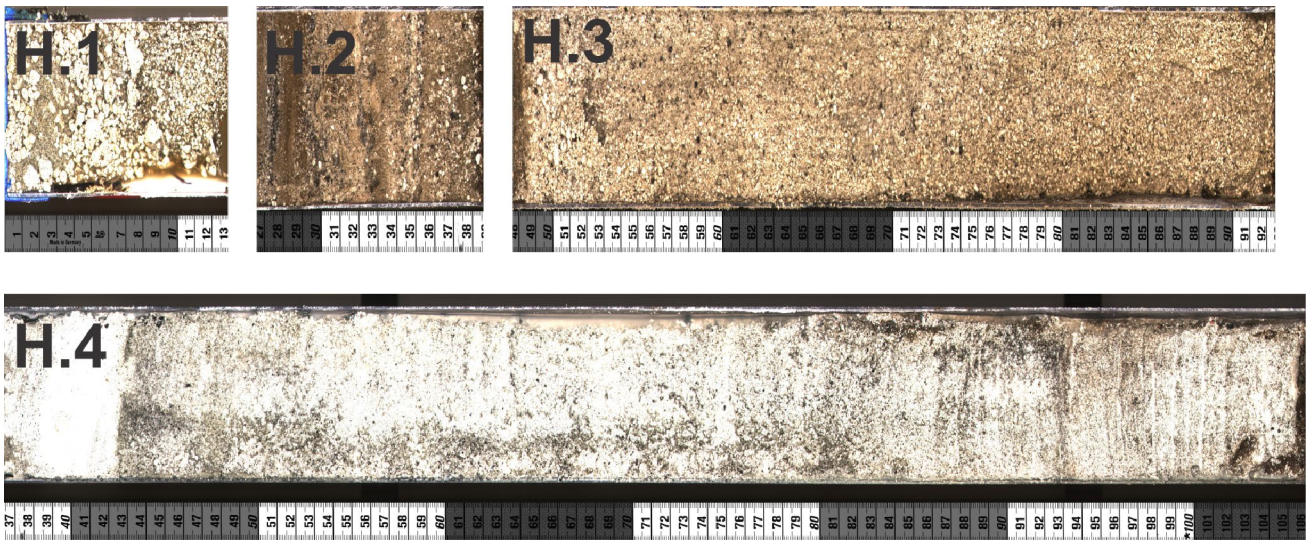


Fig. 5 Core images of volcaniclastic facies; horizontal scale in cm. **H.1** Tephra CHA16-261 (MEXI-CHA16-IC-172Y-1); **H.2** Tephra CHA16-263a (MEXI-CHA16-IC-173Y-1); **H.3** Tephra CHA16-263b (MEXI-CHA16-IC-173Y-1); **H.4** Tephra CHA16-294 (MEXI-CHA16-IC-175Y-1)

transport into the water body such as a streamflow, but with lower energy than during the alluvial stage. Also, textural and compositional sediment characteristics of the CSG, such as subangular-rounded and very well-sorted clastic deposits, in the absence of lacustrine organisms, suggest reworking (Beverage and Culbertson 1964; Smith 1986). These lithological characteristics have been recognized on the ancient lake Chalco shoreline, along with sorted sand and mud associated with recent sediments from the Amecameca River (Fig. 1b) (Frederick and Cordoba 2019).

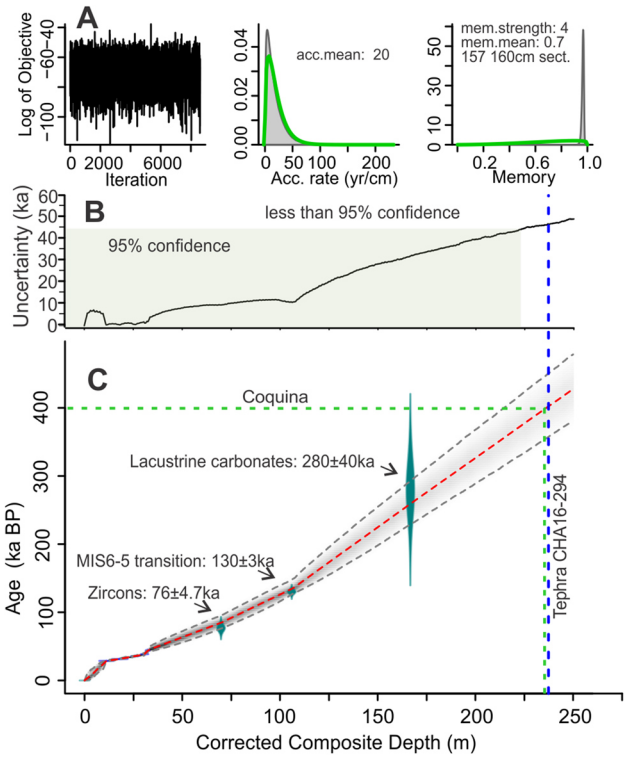


Fig. 6 Bayesian age-depth model for the upper 343 m (240 mcc) of the MEXI-CHA16-1C core. **a** Parameters obtained during model development. **b** Uncertainty along the sequence; 95% confidence range is marked in a green square. **c** Age-depth model; depth data correspond to the corrected composite depth that considers deposition of sand and volcaniclastic material as instantaneous events. Some specific dates referred to in this study are indicated. Additionally, stratigraphic markers are shown: Coquina (green dotted point line) and Tephra CHA16-294 (blue dotted point line)

Lithological heterogeneity in CSG clasts, such as pumice, basalt, and andesite fragments, suggests that the sediment came from multiple sources (Fig. 3d). A sediment source located > 30 km from the drill site could significantly rework and sort the clasts. The pumice fragments present in the CSG facies (Fig. 3D1), products of silica-rich explosive volcanism, are unlikely to have come from the Sierra Chichinautzin Volcanic Field, as their products are associated more with effusive to explosive materials of basaltic to andesitic composition (Siebe et al. 2005).

SM facies are intercalated with CSG facies and the transition between the two facies is sometimes characterized by gravel deposits, which gradually are replaced by sand. This change may be associated with low-energy periods in streamflow during which fine suspended sand was deposited in standing ponds (Lespez et al. 2011; Miall 2012). Erosive contacts in the transition from sand to gravel deposits may have been associated with an increase in the streamflow energy. SM deposits show low %N and %C org values (TOC: 0.1–0.4%; TN: 0.01–0.03%), indicating low quantities of organic material, both terrestrial and aquatic (Fig. 7c).

Grain size and mineralogical analyses on STS facies show that the sedimentation pattern consists of an alternation between light quartz-plagioclase massive coarse sand layers and dark silty-sand layers rich in charcoal and plagioclase, with parallel laminations. The light layers are characterized by poorly sorted crystals and have erosive lower contacts. These characteristics may be associated with relatively short-distance transport, which precluded sorting of the sediment, but its energy could have eroded underlying sediments (Fig. 3 C1 and C2). In contrast, dark layers are composed of plagioclase crystals with horizontal alignment, charcoal particles, and gradual lower contacts, suggesting settling in still waters of shallow (cm) ponds (Fig. 3 C3 and C4). Lespez et al. (2011) described laminated silty sand with numerous charcoal and vegetal remains on thin sections similar to STS facies from a Holocene fluvial record in West Africa. Those deposits seem to be associated with periodic occurrence of fluvial inputs (floods) to a floodplain. We suggest that STS facies are associated with channel abandonment and the development of a floodplain, where light layers may represent flooding periods. Reduction of the ratio Q/(Q + F) in dark-layer deposits suggests dry periods between 322 and 311 m depth (Van der Kamp 2010), and explains the presence of 0.5-cm charcoal layers associated with fires in the region (Fig. 3 C5). We suggest that during dark layer deposition, the floodplain level and energy declined because of dry conditions in the region.

Characteristics of the terrestrial organic matter deposited during the fluvial stage were explored using the TOC, $\delta^{13}C$ and TOC/TN values. Data were divided into two groups, the first corresponding to samples from greater depths (> 307 m) and the second corresponding to samples from depths < 307 m (Fig. 7a). Older samples have lower $\delta^{13}C$ (−33.7 to −25.3 ‰) and TOC/TN (4.4–6.9) than younger ones ($\delta^{13}C$: −23.7 to −19.8 ‰; TOC/TN: 14.4–18.3). We would expect a post-burial diagenesis effect in the organic matter in samples under 307 m depth. Meyers et al. (1995) showed that selective degradation of terrestrial organic matter during post-burial diagenesis can diminish the TOC/TN ratios in sedimentary samples. The latest is associated with a selective degradation of carbon-rich sugars and lipids in plant matter buried. In this way, younger organic matter samples are generally higher in TOC/TN than the older ones (Hodell and Schelske 1998). In absence of post-burial processes, the $\delta^{13}C$ and TOC/TN values suggest a greater input of terrestrial organic matter towards the end of this fluvial stage (Meyers and Teranes 2002) (Fig. 7a). In addition, the presence of vascular plant remains and amorphous organic matter suggest the development of soil and vegetation around the water body.

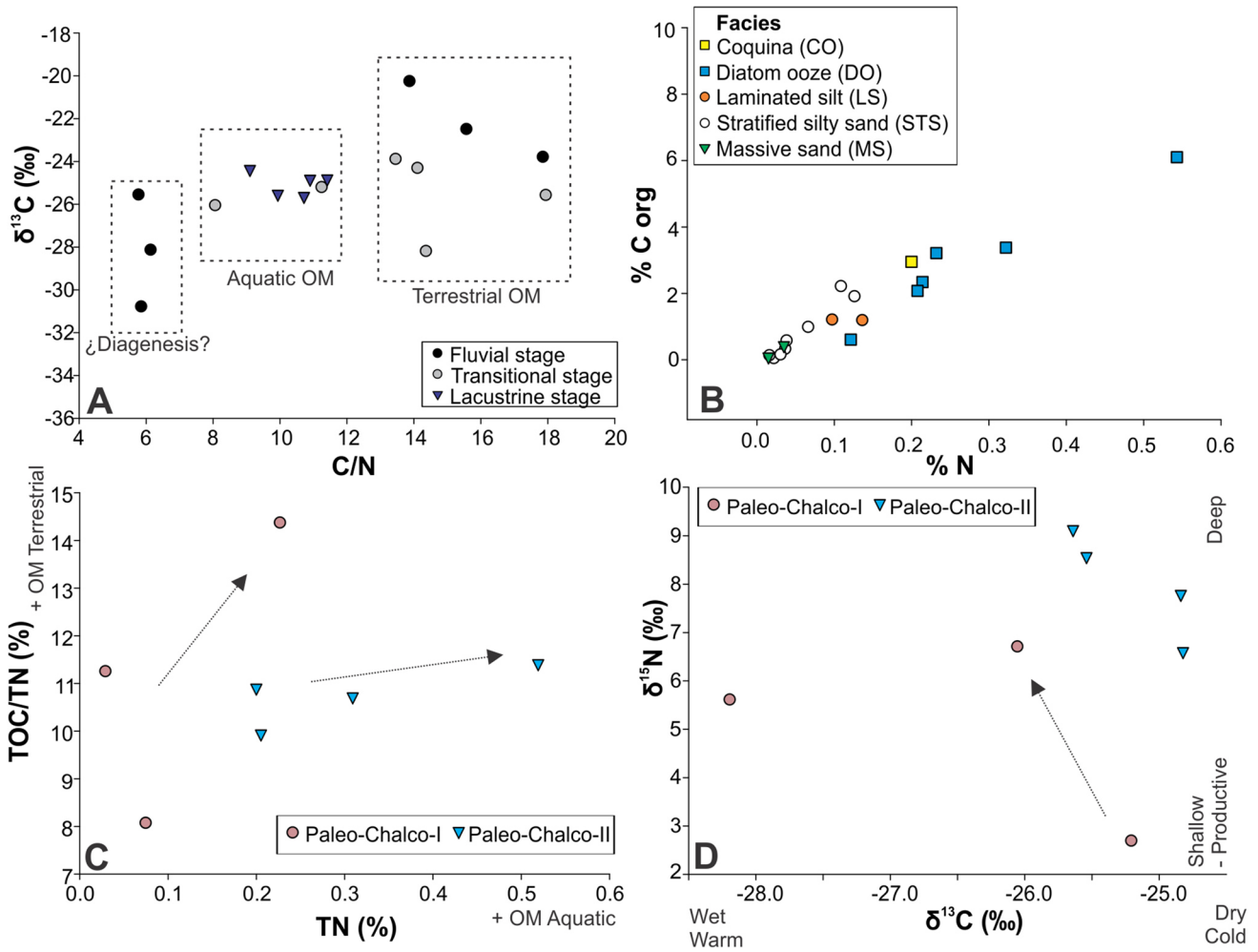


Fig. 7 **a** Relation between $\delta^{13}C$ and TOC/TN, illustrating the main origin of incoming organic material among the different stages of Lake Chalco. Envelopes (rectangles) for source types come from Meyers and Teranes (2001). **b** Percent total organic carbon (TOC) and total nitrogen (TN) that shows the main source of organic material among the sedimentary facies. **c** TN versus TOC/TN ratio that shows the main source of organic material in Paleo-Chalco-I and Paleo-Chalco-II. Arrows indicate the evolution of the paleolake. **d** Relation between $\delta^{13}C$ and $\delta^{15}N$ that shows limnological conditions in Paleo-Chalco-I and Paleo-Chalco-II. Arrow indicates the evolution of Paleo-Chalco-I

Fluvial-lacustrine transition stage

From 306.5 to 294 m depth, the facies are constituted by MS, CSG, LS, STS, DO and MSG. The principal characteristic of this stage is the novel presence of diatoms (Fig. 8). Our age model suggests that these sediments are older than 400 ± 46 ka. This interval was divided into three sub-stages.

Sub-stage 1 (Sub1)

The first sub-stage deposits span from 306.5 to 302.8 m depth. The interval is characterized by a transitional fining upward contact from CGS to LS facies that suggests a decrease in the transport energy.

There are intercalations of laminated sediments of DO facies, which have high diatom content (90%) and a minor proportion of well-sorted silt (10%). Diatoms from association A (*Staurosira*, *Rhopalodia* and *Cocconeis*), are present between 306.8 and 302.8 m depth (Fig. 8). Several authors have observed that small species of the family Fragilariaceae, such as *Staurosira,* are facultative planktonic taxa that can be fast colonizers after environmental disruptions (Vos and de Wolf 1988; Gell et al. 2002; Augustinus et al. 2008). Both *Cocconeis* and *Rhopalodia* are epiphytic forms that suggest shallow-water conditions (Gasse et al. 1997).

Multiple factors control the $\delta^{15}N$ of bulk lacustrine organic matter, such as source, depositional environment and diagenetic changes. However, an increasing number of study suggests that lower values of $\delta^{15}N$ show more intense

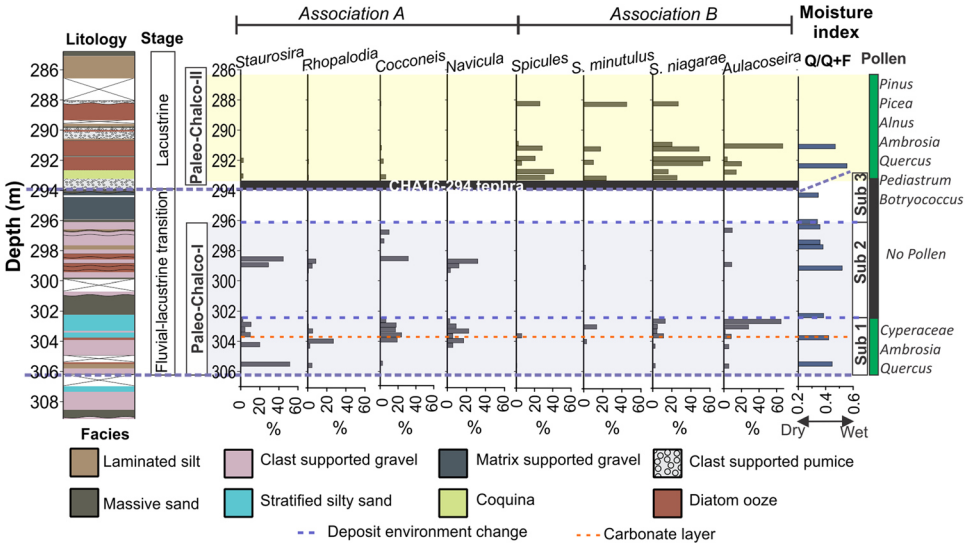


Fig. 8 Most abundant siliceous remnants observed in the smear slide samples. On the left is the stratigraphic column for the section between 308 and 285 m depth. On the right, bars of different colors indicate the representative pollen families, a range of samples without pollen content is observed. With blue dotted lines point the different sub-stages that composed the transitional stage. Orange dotted line indicates the carbonate layer location at 303.8 m depth. The regions on the record that correspond with Paleo-Chalco-I (blue) and Paleo-Chalco-II (yellow) lakes, and the tephra CHA16-294 are indicated

denitrification processes and point to more oxic environments (Hollander et al. 1992; Brenner et al. 1999; Talbot and Lædak 2000; Talbot 2001; Zhong et al. 2017). The limited $\delta^{15}N$ results ($\delta^{15}N$: 2.8–3.0‰) are coherent with a relatively shallow and oligotrophic lake (Fig. 7d). Characteristics of this sub-stage indicate fluctuating conditions, but a trend from proximal littoral facies toward the formation of a shallow, oligotrophic and probable oxic lake, which we call "Paleo-Chalco-I" (Fig. 8).

Presence of a 10-cm carbonate layer (aragonite and calcite) at 303.8 m depth suggests that Paleo-Chalco-I became a highly concentrated shallow water body. Deposits overlying the carbonate layer (303.8–302.8 m depth) are characterized by an increase in *Cocconeis* and *Navicula*, and later rise in planktonic species characteristic of diatom association B (*Stephanodiscus* and *Aulacoseira*) (Fig. 8). This shift in diatom assemblages suggests evolution to a deeper eutrophic lake (Edlund and Kingston 2004; Bennion and Simpson 2011; Gabito et al. 2013). Additionally, TN data (0.01–0.08%) and the TOC/TN ratio (8.0–11.2) indicate a mix of terrestrial and aquatic organic material input (Fig. 7c).

Sub-stage 2 (Sub2)

A second sub-stage, between 302.8 and 296.2 m depth, is characterized by a transitional coarsening upward from the DO deposit to the CSG facies. The DO facies is dominated by diatoms of association A (*Staurosira* and *Cocconeis*), which are indicative of shallow-water conditions, particularly between 299.3 and 298.3 m depth (Fig. 8). The presence of rounded and well-sorted gravel in CSG, as well as transitional changes between CSG and DO facies, indicate periodic changes in lake level and in-lake migration of littoral facies. Our Q/(Q + F) data indicate wet conditions during this sub-stage. However, because of limited data resolution, we cannot correlate changes in humidity with littoral facies migration. A recent geomorphological study of abandoned Chalco shorelines revealed large sand and gravel deposits associated with river deltas during the last 7000 years (Frederick and Cordova 2019), suggesting that there is no simple correlation between climate and sedimentation. The evidence indicates that Paleo-Chalco-I had a lower lake level during sub-stage 2, and that littoral facies were deposited at the drill site, dominated by well-sorted and rounded coarse size fractions (gravels and sands), as result of wave action in the lake. During this generally low lake period, an intermittent shallow and oligotrophic lake developed.

Sub-stage 3 (Sub3)

A third sub-stage, between 296.2 and 294.0 m depth, is characterized by high values of magnetic susceptibility (600–1800 10^{-5} SI) and the presence of subangular to rounded and poorly sorted clasts, 2–10 cm in diameter, in the MSG facies. These characteristics suggest deposition of volcaniclastic material by debris and hyper-concentrated flows that reached the Paleo-Chalco-I, at least at the location of the drill site (Lowe 1982; Smith 1986).

Lacustrine stage

The last stage is characterized by a substantial increase in diatom content of the sediments, as well as the presence of tephra layers in the analyzed sequence and a bivalve coquina deposit. This stage is constituted by DO, CSP, CO, and LS facies. The 85-cm-thick white pumice deposit at 294 m

depth, which we name "Tephra CHA16-294," is overlain by the CO facies, which in turn is covered by the DO and LS facies (Fig. 5H4).

The thickness of CHA16-294 tephra had not previously been observed in the Chalco lacustrine sequence. The thickest tephra layer (35 cm) recorded in the younger sediments of Lake Chalco is a deposit from a Plinian eruption that occurred ca. 17 cal ka BP and came from Popocatepetl (50 km from the drill site), whose major dispersion axes was in the direction of Chalco (Sosa-Ceballos et al. 2012; Ortega-Guerrero et al. 2018). The source of tephra CHA16-294 is unknown, but its thickness and mineralogy suggest it came from eruption of nearby stratovolcanoes. Based on the estimated age for the CHA16-294 tephra (400 ± 46 ka) and known regional volcanic activity (Table 3), we suggest that it may be associated with activity in the Iztaccihuatl volcanic complex, related to the collapse of the Los Pies cone (Garcia-Tenorio 2008; Macias et al. 2012). Regardless of the mechanism and source that produced the CHA16-294 tephra, it is clear that the hydrographic features of the basin changed as a consequence of this volcanic activity and helped establish a second lacustrine phase after ca. 400 ka, which we name "Paleo-Chalco-II".

Above the CHA16-294 tephra (293.1 m depth), there is a gradual change to a unique coquina deposit that is composed of bivalve, ostracod, and gastropod remains, which indicate that these organisms were abundant in the lake during its initial filling (Fig. 4g). Presence of gastropods and bivalves suggests that Paleo-Chalco-II was initially a carbonate-rich shallow lake (Tavares et al. 2015).

Microalgae such as *Pediastrum* and *Coelastrum* were found at the top of the coquina facies deposit (291.9 m). *Pediastrum* and *Coelastrum* have been reported as indicators of eutrophic conditions (Janssen and Ijzermans-Lutgerhorst 1973; Whitney and Mayle 2012; Acosta-Noriega 2019). These algae suggest that after the deposition of the coquina, water level in Paleo-Chalco-II rose and the water body became eutrophic. This inference is supported by the $\delta^{15}N$ (> 6.8‰) and $\delta^{13}C$ (< −25.7‰) values, which suggest a deeper and more productive lake (Fig. 7d).

From the top of the coquina deposit (291.9 m) to 285 m depth, a significant increase in association B diatoms (*Stephanodiscus niagarae* and *Aulacoseira*) suggests an increase in water depth (Fig. 8). *Stephanodiscus niagarae* is a species that was abundant in Lake Chalco during glacial stages such as Marine Isotopic Stages 2 and 6 (Avendaño-Villeda et al. 2018). This would suggest that Paleo-Chalco-II formed during a cold interval, which according to our age model, correlates with Marine Isotopic Stage 10 (374 ka) (Lisiecki and Raymo 2005). However, our chronology requires a better age control for sediments, as it is possible that the age of these deposits may be older than MIS10 even MIS12. Such old and cold periods have not yet been known in Central Mexico.

Higher diatom concentrations and TN values in Paleo-Chalco-II than Paleo-Chalco-I suggest an increase in production of aquatic organic matter as a result of large quantities of nutrients entering the water body, possibly associated with the weathering of the volcanic material from tephra CHA16-294 and subsequent ash falls (Tephras CHA16-288, CHA16-289a and CHA16-289b). Volcanic eruptions can promote changes in lacustrine systems. For instance, volcanic material in the water column could reduce available light to photosynthetic organisms, thereby lowering primary production (Barcker et al. 2000). On the other hand, input of nutrients associated with volcanic material can foster increased primary production of diatoms and other algae. This effect has been documented in Lakes Alberta (Canada) and Patzcuaro (Mexico) (Hickman and Reasoner 1994; Telford et al. 2004).

Stratigraphic correlation with previous cores

Previous information regarding the stratigraphy of the lacustrine sequence and the lower rock units in the Basin of Mexico came from deep drillings at sites north of the MexiDrill location (Fig. 9; Oviedo de Leon 1967; Arce et al. 2013). At the "San Lorenzo Tezonco" core (17.6 km northwest of Chalco), lacustrine deposits were found between the surface and 70 m depth; in addition, microalgae such as *Pediastrum* and *Botryococcus* were encountered in several samples of lacustrine clay from 604 to 590 m depth, and dated to > 250 ka (Lozano-Garcia and Sosa-Najera 2015). This was interpreted to indicate a deep and eutrophic water body. In the "Texcoco" core (24.3 km north of Chalco), lacustrine deposits were reported from 485 m depth to the surface; presence of clay layers with microalgae such as *Botryococcus*, *Pediastrum* and pollen of aquatic taxa as *Potamogeton* in several samples between 642 and 425 m depth, suggests the presence of an ancient water body in a wet environment (Lozano-Garcia and Sosa-Najera 2015). Palynological, stratigraphic and chronological data from the San Lorenzo Tezonco and Texcoco cores suggest that a correlation exists between clay deposits reported by Lozano-Garcia and Sosa-Najera (2015), and sediments from Paleo-Chalco-I (Fig. 9).

Regional implications

Lake Chalco sediments provide a unique archive of long-term record of climatic variability. Our data suggest that the formation of the lake occurred ca. 400 ka ago, which implies that the drill-core sequence recovered is the longest late Quaternary lacustrine record from the North American tropics. The analyzed section of the MexiDrill record

Table 3 Age compilation for different volcanoes from Sierra Chichinautzin volcanic field (SCVF) and Sierra Nevada (SN)

Range	Volcano	Age (ka)	Dated material	Method	References
SN	Iztaccihuatl (La Joya Andesite)	270	Whole rock	40Ar/39Ar	Nixon (1989)
SN	Popocatepetl (Nexpayantla)	270	Lava flow	40Ar/39Ar	Delgado Granados et al. (2017)
SN	Telapon (Domo Telapon)	274	Rock in matrix	40Ar/39Ar	Garcia-Tovar and Martinez-Serrano (2011)
SN	Popocatepetl (Nexpayantla)	280	Lava flow	40Ar/39Ar	Delgado Granados et al. 2017)
SN	Popocatepetl (Nexpayantla)	280	Lava flow	40Ar/39Ar	Delgado Granados et al. (2017)
SN	Popocatepetl (Nexpayantla)	306	Lava flow	40Ar/39Ar	Delgado Granados et al. (2017)
SN	Popocatepetl (Nexpayantla)	324	Lava flow	40Ar/39Ar	Delgado Granados et al. (2017)
SN	Iztaccihuatl (Pies)	340	Plagioclase	40Ar/39Ar	**Nixon (1989)**
SN	Popocatepetl (Nexpayantla)	380	Lava flow	40Ar/39Ar	**Delgado Granados et al. (2017)**
SN	Iztaccihuatl (Pies)	410	Plagioclase	40Ar/39Ar	**Nixon (1989)**
SN	Iztaccihuatl (Pies)	450	Plagioclase	40Ar/39Ar	**Macias et al. (2012)**
SN	Popocatepetl (Tlamacas)	538	Dome	40Ar/39Ar	Delgado Granados et al. (2017)
SN	Iztaccihuatl (Llano grande)	580	Whole rock	40Ar/39Ar	Nixon (1989)
SN	Tlaloc (C. Tlapanco)	685	Groundmass	40Ar/39Ar	Nixon (1989)
SCVF	C. La Estrella	765	Whole rock	40Ar/39Ar	Jaimes Viera et al. (2018)
SCVF	La Corona	820	Whole rock	40Ar/39Ar	Jaimes Viera et al. (2018)

They are ordered from younger to older. It is indicated the material which was measured, dating method and the reference. On bold are highlighted the eruptive events that could be associated with Paleo-Chalco-II formation

(343–285 m depth) allows us to study the formation of a lake in volcanic settings such as the Basin of Mexico.

Gradual changes in the sedimentary environments (alluvial and fluvial) dominated the landscape of the southern Basin of Mexico before the establishment of a lacustrine environment. Paleo-Chalco-II settlement is clearly linked to a major volcanic event, after which the lake deepened and its productivity increased. These changes in the lake could be a response to the alteration of the hydrology of the basin caused by the volcanic event. The role of volcanism in the formation of lakes has been also noted in other locations, i.e., Lake Kivu, West Africa (Pasteels et al. 1989) and Laacher See, Germany (Park and Schmincke 1997). In both cases, deposits from volcanic eruptions blocked fluvial systems and/or diverted the natural runoff in the basins.

The stratigraphy and evolution of the Basin of Mexico has been extensively studied through surficial geology and previous drill cores. Volcanic stratigraphy since the Miocene has been developed from outcrops (e.g., Enciso de la Vega 1992; Siebe et al. 2005; Jaimes-Viera et al. 2018; Arce et al. 2019), and the drill cores have provided a knowledge of the general stratigraphy of the upper 3 km (Oviedo de León 1967; Pérez-Cruz 1988; Arce et al. 2015). However, because of discontinuous sediment recovery in the drillings, as well as the lack of outcrops of fluvial and alluvial materials underlying the lacustrine deposits, the alluvial-lacustrine transition is for the first time reported in this work.

Conclusions

Sediment between 343 and 285 m depth in the MEXICHA16 1C core is composed of three facies groups: (1) Detrital (Laminated Silt [LS], Massive Sand [MS], Stratified Silty Sand [STS], Clast-Supported Gravel [CSG], Matrix-Supported Gravel [MSG]); (2) Biogenic (Diatom Ooze [DO], Coquina [CO]), and (3) Volcaniclastic (Clast-Supported Pumice [CSP]). We identified four environmental stages in the deposit: (1) alluvial (343–330 m depth), (2) fluvial (330–306.5 m depth), (3) transitional fluvial-lacustrine (306.5–294 m depth), and (4) lacustrine (294–285 m depth). During the alluvial stage, debris flows and hyper-concentrated flows dominated; streamflows and floodplain deposits characterized the fluvial stage; in the transitional stage, there were lacustrine and littoral deposits. Finally, volcanic and lacustrine deposits dominated during the lacustrine stage. During the formation of Lake Chalco, there were two lake periods: Paleo-Chalco-I, when a nutrient-poor and shallow water body prevailed, and Paleo-Chalco-II, when a eutrophic and deep lake existed.

Formation of Paleo-Chalco-II seems to have been associated with volcanic activity, which could modify the basin morphology, increased nutrient content in the lake and deposited the tephra layer CHA16-294. The thickness of CHA16-294 tephra (85 cm) is peculiar, since this is the thickest tephra known in the Chalco lacustrine sequence. It is likely that tephra CHA16-294 was the result of the collapse of Los Pies cone on the Iztaccihuatl volcanic complex. However, more studies are required to test this hypothesis.

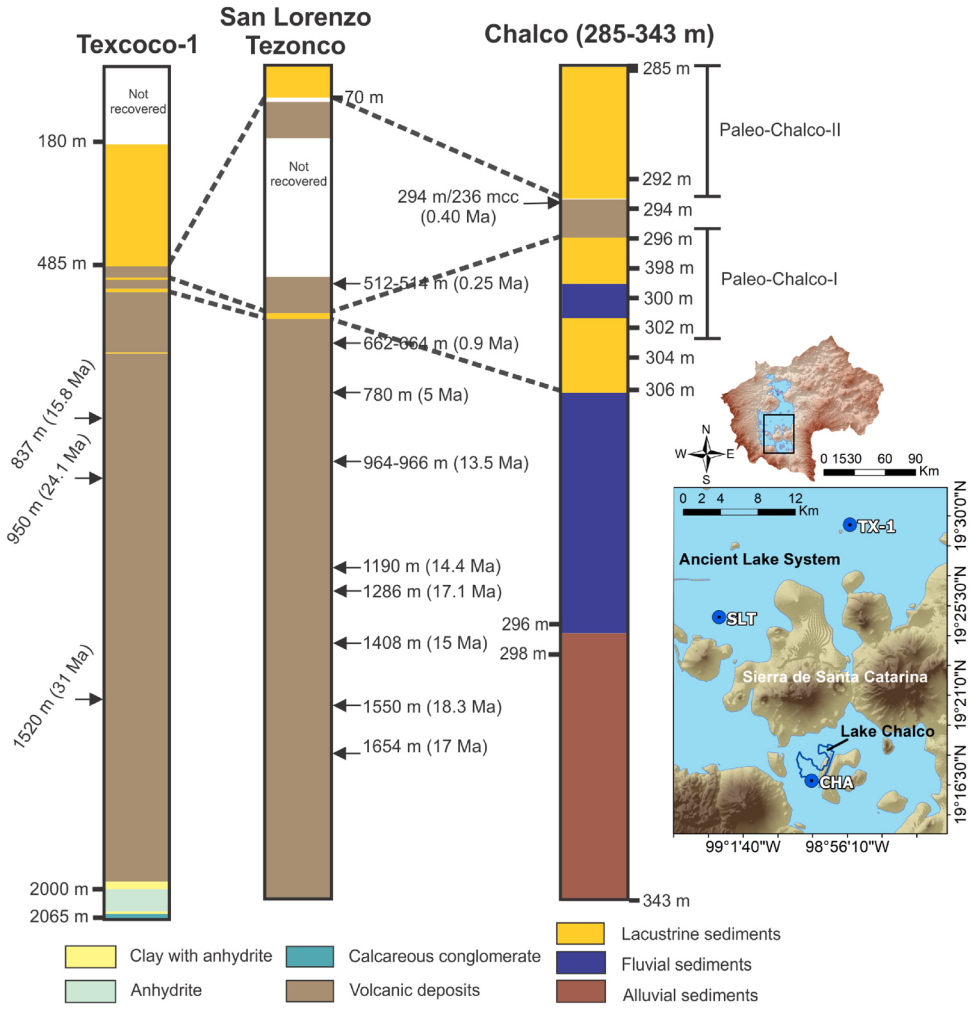


Fig. 9 Stratigraphic correlation between the San Lorenzo Tezonco (SLT) and Texcoco (TX-1) cores (Oviedo de Leon, 1967; Arce et al. 2013) and the MexiDrill (CHA) core from Chalco (this study). Gray lines point to possible correlations between Paleo-Chalco I and II lacustrine phases and lacustrine deposits reported by Lozano-García y Sosa-Nájera (2015) in TX-1 (642 and 425 m depth) and SLT (between 604 and 590 m depth). Modified from Lozano-García and Sosa-Nájera (2015). On the right is a map showing locations of the TX-1, SLT and CHA sites

Our data indicates that Lake Chalco was formed during a cold interval ~ 400 ± 46 ka ago, which could correlate with Marine Isotopic Stage 10 (374 ka). As we refine the age control for these sediments, the Chalco Basin will provide insights into global climate changes during key transitions, such as between Marine Isotope Stages 10 and 9, and even Marine Isotope Stages 12 and 11.

Although the emplacement of volcanic deposits in the Basin of Mexico since Miocene, and the recent depositional history at Lake Chalco (last 143 ka) have been widely studied, a gap of information existed between the volcanic landscape and the lacustrine onset. This work is a link between those scenarios and a clue in the recent evolution of the Basin of Mexico. Finally, this paper provides a wide range of open questions to be explored and answered in future research (e.g., refine sampling, enhance the age-depth model, describe < 285 m depth sediments, analyze tephra deposits, etc.).

Acknowledgements This work was funded by: UNAM DGAPA-PAPIIT IV100215 and IN105918, the International Continental Scientific Drilling Program (ICDP Project 05-2014), the US National Science Foundation (NSF-EAR1551311, NFS-EAR1803725), the CONACYT National Scholarship Program (CVU/Student: 854008/629653). Special thanks to the local authorities of Ejido Santiago Tulyehualco and the MexiDrill Team, who assisted with many aspects of the field work. We thank the LacCore staff and others who helped with sediment analyses: Susana Sosa Najera, Cecilia Caballero, Ana Ma. Soler, Sandra García León, Elena Royo, Raquel López, Cinta Osácar and Jaime Díaz Ortega. Rodrigo Martínez thanks UNAM's Academic Writing Program for its guidance in the preparation of this manuscript. We appreciate the comments and corrections of Dr. Mark Brenner and an anonymous reviewer that improved the early manuscript.

References

Acosta-Noriega E (2019) Análisis palinológico de una secuencia lacustre de 130,000 a 103,000 años A.P. del lago de Chalco, México. Dissertation, National Autonomous University of Mexico

Aguirre-Díaz GJ, López-Martínez M, Rendón-Márquez G (2006) La Caldera de La Catedral, Sierra de Las Cruces, una caldera al norponiente de la Ciudad de México. Reunión Anual de la

Unión Geofísica Mexicana: Puerto Vallarta, Jal. México GEOS 26:160–161

Arce JL, Macías JL, Vázquez-Selem L (2003) The 10.5 ka Plinian eruption of Nevado de Toluca volcano, Mexico: Stratigraphy and hazard implications. Geological Society of America Bulletin 115(2): 230–248. https://doi.org/10.1130/0016-7606(2003)115%3C0230:TKPEON%3E2.0.CO;2

Arce JL, Macías R, Palomo AG, Capra L, Macías JL, Layer P, Rueda H (2008) Late Pleistocene flank collapse of Zempoala Volcano (Central Mexico) and the role of fault reactivation. J Volcanol Geoth Res 177(4):944–958. https://doi.org/10.1016/j.jvolgeores.2008.07.015

Arce JL, Layer PW, Morales-Casique E, Benowitz JA, Rangel E, Escolero O (2013) New constraints on the subsurface geology of the Mexico City Basin: The San Lorenzo Tezonco deep well, on the basis of 40Ar/39Ar geochronology and whole-rock chemistry. J Volcanol Geoth Res 266:34–49. https://doi.org/10.1016/j.jvolgeores.2013.09.004

Arce JL, Layer P, Martínez I, Salinas JI, Macías-Romo MDC, Morales-Casique E, Lenhardt N (2015) Geología y estratigrafía del pozo profundo San Lorenzo Tezonco y de sus alrededores, sur de la Cuenca de México. Boletín de la Sociedad Geológica Mexicana 67(2): 123–143. Disponible en: <http://www.scielo.org.mx/scielo.php?script=sci_arttext&pid=S1405-33222015000200002&lng=es&nrm=iso>. ISSN 1405–3322.

Arce JL, Layer PW, Macías JL, Morales-Casique E, García-Palomo A, Jiménez-Domínguez FJ et al (2019) Geology and stratigraphy of the Mexico Basin (Mexico City), central Trans-Mexican Volcanic Belt. J Maps 15(2):320–332. https://doi.org/10.1080/17445647.2019.1593251

Augustinus P, Bleakley N, Deng Y, Shane P, Cochran U (2008) Rapid change in early Holocene environments inferred from lake Pupuke, Auckland city, New Zealand. J Quatern Sci 23(5):435–447. https://doi.org/10.1002/jqs.1153

Avendaño-Villeda DA, Caballero M, Ortega-Guerrero B, Lozano-García S, Brown E (2018) Condiciones ambientales a finales del Estadio Isotópico 6 (EI 6:> 130000 años) en el centro de México: caracterización de una sección de sedimentos laminados proveniente del Lago de Chalco. Revista mexicana de ciencias geológicas 35(2): 168–178. https://doi.org/10.22201/cgeo.20072902e.2018.2.649

Barker P, Telford R, Merdaci O, Williamson D, Taieb M, Vincens A, Gibert E (2000) The sensitivity of a Tanzanian crater lake to catastrophic tephra input and four millennia of climate change. Holocene 10(3): 303–310. https://doi.org/10.1191/095968300672848582

Batten DJ (1999) Small Palynomorphs. In: Jones TP, Rowe NP (eds) Fossil Plants and Spores: Modern techniques. The Geological Society, London, pp 15–19

Bennion H, Simpson GL (2011) The use of diatom records to establish reference conditions for UK lakes subject to eutrophication. J Paleolimnol 45:469–488. https://doi.org/10.1007/s10933-010-9422-8

Beverage JP, Culbertson JK (1964) Hyperconcentrations of suspended sediment. J Hydraul Div 90(6):117–128

Blaauw M, Christen JA (2011) Flexible paleoclimate age-depth models using an autoregressive gamma process. Bayesian Anal 6(3):457–474. https://doi.org/10.1214/11-BA618

Bloomfield KA (1975) Late-Quaternary monogenetic volcano field in central Mexico. Geol Rundsch 64:476–497. https://doi.org/10.1007/BF01820679

Brenner M, Whitmore TJ, Curtis JH, Hodell DA, Schelske CL (1999) Stable isotope (δ13C and δ15N) signatures of sedimented organic matter as indicators of historic lake trophic state. J Paleolimnol 22(2):205–221. https://doi.org/10.1023/A:1008078222806

Brown ET, Caballero M, Cabral Cano E, Fawcett PJ, Lozano-García S, Ortega B et al (2019) Scientific drilling of Lake Chalco, Basin of Mexico (MexiDrill). Scient Drill. https://doi.org/10.5194/sd-7-1-2019

Caballero M, Guerrero B (1998) Lake Levels since about 40,000 Years Ago at Lake Chalco, near Mexico City. Quatern Res 50(1):69–79. https://doi.org/10.1006/qres.1998.1969

Caballero M, Lozano-García S, Ortega-Guerrero B, Correa-Metrio A (2019) Quantitative estimates of orbital and millennial scale climatic variability in central Mexico during the last~ 40,000 years. Quatern Sci Rev 205:62–75. https://doi.org/10.1016/j.quascirev.2018.12.002

Cao R, Qian S (1990) Sediment transport characteristics of hyperconcentrated flow with suspended load. In: French R (ed) Hydraulics/Hydrology of Arid Lands (H^2AL). American Society of Civil Engineers, New York, pp 657–662

Cronin SJ, Neall VE, Lecointre JA, Palmer AS (1999) Dynamic interactions between lahars and stream flow: A case study from Ruapehu volcano, New Zealand. Geol Soc Am Bull 111(1):28–38. https://doi.org/10.1130/0016-7606(1999)111%3C0028:DIBLAS%3E2.3.CO;2

Delgado-Granados H, Cassatta W, Gisbert Pinto G, Paul R (2017) Historia geológica y eruptiva del volcán Popopocatepetl. In: del Pozzo M (ed) Estudios geológicos y actualización del mapa de peligros del volcán Popocatépetl, 1st edn. Instituto de Geología, Ciudad de México, pp 13–17

Edlund MB, Kingston JC (2004) Expanding sediment diatom reconstruction model to eutrophic southern Minnesota lakes. In: Heiskary S (eds) Final report to Minnesota Pollution Control Agency. CFMS Contract, Minneapolis, 32

Enciso-De la Vega S (1992) Propuesta de nomenclatura estratigráfica para la cuenca de México. Revista Geofísica Internacional 10(1):26–36

Frederick CD, Cordova CE (2019) Prehispanic and colonial landscape change and fluvial dynamics in the Chalco Region, Mexico. Geomorphology 331:107–126. https://doi.org/10.1016/j.geomorph.2018.10.009

Fries C (1960) Geología del Estado de Morelos y de partes adyacentes de México y Guerrero, región central meridional de México. Universidad Nacional Autonoma de México, Ciudad de México

Gabito L, Bonilla S, Antoniales D (2013) Paleolimnological reconstruction of change in a subtropical lake: a comparison of the subfossil record to limnological data. Limnetica 32(2): 175–188. https://doi.org/10.23818/limn.32.15

García-Palomo A, Zamorano JJ, López-Miguel C, Galván-García A, Carlos-Valerio V, Ortega R, Macías JL (2008) El arreglo morfoestructural de la Sierra de Las Cruces, México central. Revista mexicana de ciencias geológicas 25(1): 158–178. Disponible en: <http://www.scielo.org.mx/scielo.php?script=sci_arttext&pid=S1026-87742008000100010&lng=es&nrm=iso>. ISSN 2007–2902.

Garcia-Tenorio F (2008) Avalancha de escombros del Pleistoceno Tardío del cono de los Píes, Complejo Volcánico Iztaccíhuatl. Dissertation, ESIA TICOMAN–IPN

García-Tovar GP, Martínez-Serrano RG (2011) Geology and geochemistry of the Pleistocene lava flows from the Telapón stratovolcano, Sierra Nevada, México. Revista mexicana de ciencias geológicas 28(2): 301–322. Recuperado de http://www.scielo.org.mx/scielo.php?script=sci_arttext&pid=S1026-87742011000200011&lng=es&tlng=en.

Gasse F, Barker P, Gell PA, Fritz SC, Chalie F (1997) Diatom-inferred salinity in palaeolakes: an indirect tracer of climate change. Quatern Sci Rev 16(6):547–563. https://doi.org/10.1016/S0277-3791(96)00081-9

Gell P, Sluiter IR, Fluin J (2002) Seasonal and inter-annual variations in diatom assemblages in Murray River-connected wetlands in

north-west Victoria, Australia. Mar Freshw Res 53:981–992. https://doi.org/10.1071/MF01021

Google Earth Pro (2020). Fecha de imagen: 01/15/2015. Maxat Technologies Images

Hickman M, Reasoner MA (1994) Diatom responses to late Quaternary vegetation and climate change, and to deposition of two tephras in an alpine and a sub-alpine lake in Yoho National Park, British Columbia. J Paleolimnol 11:173–188. https://doi.org/10.1007/BF00686864

Hodell DA, Schelske CL (1998) Production, sedimentation, and isotopic composition of organic matter in Lake Ontario. Limnol Oceanogr 43(2):200–214. https://doi.org/10.4319/lo.1998.43.2.0200

Hollander DJ, McKenzie JA, Haven HLT (1992) A 200 year sedimentary record of progressive eutrophication in Lake Greifen (Switzerland): implications for the origin of organic-carbon-rich sediments. Geology 20(9):825–828. https://doi.org/10.1130/0091-7613(1992)020%3C0825:AYSROP%3E2.3.CO;2

INEGI (2010) Censo de población y vivienda. https://www.inegi.org.mx/programas/ccpv/2010/. Accessed 10 Jan 2020

INEGI (2020) Continuo Mexicano de Elevaciones; https://www.inegi.org.mx/app/geo2/elevacionesmex/. Accessed 1 Sep 2020

Ingersoll TF, Bullard RL, Ford JP, Grimm JD, Pickle SW, Sares (1984) The effect of grain size on detrital modes: a test of the Gazzi-Dickinson point-counting method. J Sediment Res 54(1):103–116. https://doi.org/10.1306/212F83B9-2B24-11D7-8648000102C1865D

Jaimes-Viera MC, Del Pozzo AM, Layer PW, Benowitz JA, Nieto-Torres A (2018) Timing the evolution of a monogenetic volcanic field: Sierra Chichinautzin, Central Mexico. J Volcanol Geoth Res 356:225–242. https://doi.org/10.1016/j.jvolgeores.2018.03.013

Janssen CR, Ijzermans-Lutgerhorst W (1973) A "local" late-glacial pollen diagram from Limburg, Netherlands. Acta Botanica Neerlandica 22:213–220. https://doi.org/10.1111/j.1438-8677.1973.tb00835.x

Lespez L, Le Drezen Y, Garnier A, Rasse M, Eichhorn B, Ozainne S et al (2011) High-resolution fluvial records of Holocene environmental changes in the Sahel: the Yamé River at Ounjougou (Mali, West Africa). Quatern Sci Rev 30(5–6):737–756. https://doi.org/10.1016/j.quascirev.2010.12.021

Lisiecki LE, Raymo ME (2005) A Pliocene-Pleistocene stack of 57 globally distributed benthic $\delta^{18}O$ records. Paleoceanography 20:1003. https://doi.org/10.1029/2004PA001071

Lowe D (1982) Sediment gravity flows: Depositional models with special reference to the deposits of high-density turbidity currents. J Sediment Res 52(1):279–297. https://doi.org/10.1306/212F7F31-2B24-11D7-8648000102C1865D

Lozano-García S, Sosa-Nájera S (2015) Análisis palinológico del Cenozoico de la cuenca de México: el registro polínico de los pozos Texcoco-I y San Lorenzo Tezonco. Boletín de la Sociedad Geológica Mexicana 67(2): 245–253. Recuperado en 25 de enero de 2020, de http://www.scielo.org.mx/scielo.php?script=sci_arttext&pid=S1405-33222015000200009&lng=es&tlng=es

Lozano-García S, Ortega B, Roy P, Beramendi-Orosco L, Caballero M (2015) Climatic variability in the northern sector of the American tropics since the latest MIS 3. Quatern Res 84(2):262–271. https://doi.org/10.1016/j.yqres.2015.07.002

Lozano-García S, Brown ET, Ortega B, Caballero M, Werne J, Fawcett PJ, Schwalb A, Valero-Garcés BL, Schnurrenberger D, et al (2017) Deep drilling at the Chalco lake: a technical report. Boletín de la Sociedad Geológica Mexicana 69(2): 299–311. https://doi.org/10.18268/bsgm2017v69n2a2

Lozano-García MS, Ortega-Guerrero B, Caballero-Miranda M, Urrutia-Fucugauchi J (1993) Late Pleistocene and Holocene paleoenvironments of Chalco lake, central Mexico. Quatern Res 40(3): 332-342. https://doi.org/10.1006/qres.1993.1086

Lugo-Hubp J, Mooser F, Pérez-Vega A, Zamorano-Orozco J (1994) Geomorfologia de la sierra de Santa Catarina México. Revista Mexicana de Ciencias Geológicas 11(1):13–52

Macías JL, Arce JL, García-Tenorio F, Layer PW, Rueda H, Reyes-Agustin G, López-Pizaña F, Avellán D (2012) Geology and geochronology of Tlaloc, Telapón, Iztaccíhuatl, and Popocatépetl volcanoes, Sierra Nevada, central Mexico, In: Aranda-Gómez JJ, Tolson G, Molina-Garza RS (eds) The Southern Cordillera and Beyond. Geological Society of America Field Guide 25, Mexico City, 163–193

Márquez A, Verma SP, Anguita F, Oyarzun R, Brandle JL (1999) Tectonics and volcanism of Sierra Chichinautzin: extension at the front of the Central Trans-Mexican Volcanic belt. J Volcanol Geoth Res 93(1–2):125–150. https://doi.org/10.1016/S0377-0273(99)00085-2

Martin del Pozzo AL (1982) Monogenetic vulcanism in sierra Chichinautzin Mexico. Bull Volcanol. https://doi.org/10.1007/BF02600386

Martínez-Abarca R, Lozano-García S, Ortega-Guerrero B, Caballero-Miranda M (2019) Incendios y actividad volcánica: historia de fuego en la cuenca de México en el Pleistoceno tardío con base en registros de material carbonizado en el lago de Chalco. Revista mexicana de ciencias geológicas 36(2): 259–269. https://doi.org/10.22201/cgeo.20072902e.2019.2.1090

Meyers PA, Teranes JL (2002) Sediment organic matter. In: Last WM, Smol JP (eds) and Tracking environmental change using lake sediments. Springer, Dordrech, pp 239–269

Meyers PA, Leenheer MJ, Bourboniere, (1995) Diagenesis of vascular plant organic matter components during burial in lake sediments. Aq Geochem 1:35–52. https://doi.org/10.1007/BF01025230

Miall AD (2012) The geology of fluvial deposits: sedimentary facies, basin analysis, and petroleum geology, 4th edn. Springer, New York

Mooser F (1963) Historia tectónica de la Cuenca de México. Boletín de la Asociación Mexicana de Geólogos Petroleros 15:239–245

Mooser F, Nairn AE, Negendank JF (1974) Palaeomagnetic investigations of the tertiary and quaternary igneous rocks: VIII a palaeomagnetic and petrologic study of volcanics of the valley of Mexico. Geol Rundsch 63(2):451–483

Mora Álvarez G, Caballero Miranda C, Urrutia Fucugauchi J, Uchiumi S (1991) Southward migration of volcanic activity in the Sierra de Las Cruces, basin of Mexico?-a preliminary K-Ar dating and palaeomagnetic study. Geofísica Internacional https://doi.org/10.22201/igeof.00167169p.1991.30.2.1134

Niederberger BC (1987) Paleopaysages et Archeologie PreUrbaine du Bassin de Mexico: Tome I. Collection D'Etudes Mesoamericaines, Mexico City

Nixon GT (1989) The Geology of Iztaccíhuatl volcano and adjacent areas of the Sierra Nevada and Valley of Mexico. Geolog Soc Am Special Papers 219:1–59

Ortega-Guerrero B, Newton AJ (1998) Geochemical characterization of Late Pleistocene and Holocene tephra layers from the Basin of Mexico. Central Mexico Quatern Res 50(1):90–106. https://doi.org/10.1006/qres.1998.1975

Ortega-Guerrero B, Lozano-García S, Herrera-Hernández D, Caballero M, Beramendi-Orosco L, Bernal JP et al (2017) Lithostratigraphy and physical properties of lacustrine sediments of the last ca. 150 kyr from Chalco basin, central México. J S Am Earth Sci 79:507–524. https://doi.org/10.1016/j.jsames.2017.09.003

Ortega-Guerrero B, García LC, Linares-López C (2018) Tephrostratigraphy of the late Quaternary record from Lake Chalco, central México. J S Am Earth Sci 81:122–140. https://doi.org/10.1016/j.jsames.2017.11.009

Ortega-Guerrero B, Avendaño D, Caballero M, Lozano-García S, Brown ET et al (2020) Climatic control on magnetic mineralogy

during the late MIS 6-Early MIS 3 in Lake Chalco, central Mexico. Quatern Sci Rev 230:106–163. https://doi.org/10.1016/j.quascirev.2020.106163

Ortiz-Enriquez O. (2017) Petrografía y geoquímica del vulcanismo monogenético de la Sierra de Santa Catarina, Cuenca de México. Dissertation, Autonomous University of Guerrero

Osete ML, RuizMartínez VC, Caballero C, Galindo C, UrrutiaFucugauchi J, Tarling DH (2000) Southward migration of continental volcanic activity in the Sierra de Las Cruces, Mexico: palaeomagnetic and radiometric evidence. Tectonophysics 318 (1-4): 201-215. https://doi.org/10.1016/S0040-1951(99)00312-1

Oviedo de León A (1967) Estudio geológico del subsuelo, basado en los datos obtenidos de la perforación del pozo profundo Texcoco No. 1. Instituto Mexicano de Petróleo, Departamento de Geología y Exploración, Ciudad de México

Park C, Schmincke HU (1997) Lake formation and catastrophic dam burst during the Late Pleistocene Laacher See eruption (Germany). Naturwissenschaften 84(12):521–525

Pasteels P, Villeneuve M, De Paepe P, Klerkx J (1989) Timing of the volcanism of the southern Kivu province: implications for the evolution of the western branch of the East African Rift system. Earth Planet Sci Lett 94:353–363. https://doi.org/10.1016/0012-821X(89)90152-0

Perez-Cruz GA (1988) Estudio sismológico de reflexión del subsuelo de la Ciudad de México. Seismic reflection study of the Mexico City subsoil. Dissertation, National Autonomous University of Mexico

Picard MD (1971) Petrographic criteria for recognition of lacustrine and fluvial sandstone, PR Spring oil-impregnated sandstone area, southeast Uinta Basin. Utah Survey Special Studies 36:28

Pierson TC (1982) Transformation of water flood to debris flow following the eruption-triggered transient-lake breakout from the crater on March 19, 1982. In: Pierson TC (ed) Hydrologic consequences of hot-rock/snowpack interactions at Mount St Helens volcano, U.S. Geological Survey, Information Services, Washington: 19–36

Pierson TC (2005) Hyperconcentrated flow transitional process between water flow and debris flow. In: Jackob M, Hungr O (eds) Debris-flow hazards and related phenomena. Springer, Berlin, pp 159–202

R Core Team (2018) R: A language and environment for statistical computing. R Foundation for Statistical Computing, Vienna, Austria. https://www.R-project.org/

Rasband WS (2018) ImageJ, U. S. National Institutes of Health, Bethesda, Maryland, USA, https://imagej.nih.gov/ij/

Reimer PJ, Bard E, Bayliss A, Beck JW, Blackwell PG, Ramsey CB et al (2013) IntCal13 and Marine13 radiocarbon age calibration curves 0–50,000 years cal BP. Radiocarbon 55(4):1869–1887. https://doi.org/10.2458/azu_js_rc.55.16947

Romero-Vera C (2019) Petrografía y geoquímica de los productos volcánicos de la base del pozo MexiDrill, cuenca de Chalco. Dissertation, National Autonomous University of Mexico

Rosiwal A (1898) Über geometrische Gesteinsanalysen; ein einfacher Weg zur ziffermässigen Festellung des Quantitätsverhältnisses der Mineralbestandtheile gemengter Gesteine. Verhandlungen der Kaiserlich-Koeniglichen Geologischen Reichsanstalt 5(6):143–175

Sanders WT, Parsons JR, Santley RS (1979) The Basin of Mexico: Ecological processes in the evolution of a civilization. Academic Press, New York

Sarocchi D, Borselli L, Macías JL (2005) Construcción de perfiles granulométricos de depósitos piroclásticos por métodos ópticos. Revista Mexicana de Ciencias Geológicas, 22(3): 371–382. Recuperado de http://www.scielo.org.mx/scielo.php?script=sci_arttext&pid=S1026-87742005000300371&lng=es&tlng=.

Schnurrenberger D, Russell J, Kelts K (2003) Classification of lacustrine sediments based on sedimentary components. J Paleolimnol 29(2):141–154. https://doi.org/10.1023/A:1023270324800

Siebe C, Arana-Salinas L, Abrams M (2005) Geology and radiocarbon ages of Tláloc, Tlacotenco, Cuauhtzin, Hijo del Cuauhtzin, Teuhtli, and Ocusacayo monogenetic volcanoes in the central part of the Sierra Chichinautzin, México. J Volcanol Geoth Res 141(3):225–243. https://doi.org/10.1016/j.jvolgeores.2004.10.009

Siebe C, Salinas S, Arana-Salinas L, Macías JL, Gardner J, Bonasia R (2017) The ~23,500 y 14C BP White Pumice Plinian eruption and associated debris avalanche and Tochimilco lava flow of Popocatépetl volcano, México. J Volcanol Geoth Res 133:66–95. https://doi.org/10.1016/j.jvolgeores.2017.01.011

Smith GA (1986) Coarse-grained nonmarine volcaniclastic sediment: Terminology and depositional process. Geol Soc Am Bull 97(1):1–10. https://doi.org/10.1130/0016-7606(1986)97%3C1:CNVSTA%3E2.0.CO;2

Smol JP, Stoermer EF (2010) The diatoms: applications for the environmental and earth sciences. Cambridge University Press, Cambridge

Sohn YK, Rhee CW, Kim BC (1999) Debris flow and hyperconcentrated flood-flow deposits in an alluvial fan, northwestern part of the Cretaceous Yongdong Basin Central Korea. J Geol 107(1):111–132. https://doi.org/10.1086/314334

Sosa-Ceballos G, Gardner JE, Siebe C, Macías JL (2012) A caldera-forming eruption~ 14,100 14C yr BP at Popocatépetl volcano, México: Insights from eruption dynamics and magma mixing. J Volcanol Geoth Res 213:27–40. https://doi.org/10.1016/j.jvolgeores.2011.11.001

Talbot MR (2001) Nitrogen isotopes in palaeolimnology. In: Last WM, Smol JP (eds) Tracking environmental change using lake sediments. 2nd edn: physical and geochemical methods. Kluwer, Dordrecht, 401–439

Talbot MR, Lærdal T (2000) The Late Pleistocene-Holocene palaeolimnology of Lake Victoria, East Africa, based upon elemental and isotopic analyses of sedimentary organic matter. J Paleolimnol 23(2):141–164. https://doi.org/10.1023/A:1008029400463

Tavares AC, Borghi L, Corbett P, Nobre-Lopes J, Câmara R (2015) Facies and depositional environments for the coquinas of the Morro do Chaves Formation, Sergipe-Alagoas Basin, defined by taphonomic and compositional criteria Brazilian. J Geol 45(3):415–429. https://doi.org/10.1590/2317-488920150030211

Telford RJ, Barker P, Metcalfe S, Newton A (2004) Lacustrine responses to tephra deposition: examples from Mexico. Quatern Sci Rev 23(23–24):2337–2353. https://doi.org/10.1016/j.quascirev.2004.03.014

Torres-Rodríguez E, Lozano-García S, Roy P, Ortega B, Beramendi-Orosco L, Correa-Metrio A, Caballero M (2015) Last Glacial droughts and fire regimes in the central Mexican highlands. J Quatern Sci 30(1):88–99. https://doi.org/10.1002/jqs.2761

Van de Kamp PC (2010) Arkose, subarkose, quartz sand, and associated muds derived from felsic plutonic rocks in glacial to tropical humid climates. J Sediment Res 80(10):895–905. https://doi.org/10.2110/jsr.2010.081

Vos PC, De Wolf H (1988) Methodological aspects of paleo-ecological diatom research in coastal areas of the Netherlands. Geol Mijnbouw 67(1):31–40

Weltje GJ (1994) Provenance and dispersal of sand-sized sediments: reconstruction of dispersal patterns and sources of sand-sized sediments by means of inverse modelling techniques. Utrecht University, Netherlands

Whitney BS, Mayle FE (2012) Pediastrum species as potential indicators of lake-level change in tropical South America. J Paleolimnol 47(4):601–615. https://doi.org/10.1007/s10933-012-9583-8

Zhong W, Wei Z, Chen Y, Shang S, Xue J, Ouyang J et al (2017) A 15.4-ka paleoclimate record inferred from δ 13 C and δ 15 N of organic matter in sediments from the sub-alpine Daping Swamp, western Nanling Mountains South China. J Paleolimnol 57(2):127–139. https://doi.org/10.1007/s10933-016-9935-x

APPENDIX P2

Stratigraphy and Sedimentology of the Upper Pleistocene to Holocene Lake Chalco Drill Cores (Mexico Basin)

Blas Valero-Garcés, Mona Stockhecke, Socorro Lozano-García, Beatriz Ortega, Margarita Caballero, Peter Fawcett, Josef P. Werne, Erik Brown, Susana Sosa Najera, Kristin Pearthree, David McGee, Alastair G. E. Hodgetts, and Rodrigo Martínez

Abstract The Basin of Mexico is a high elevation (2240 m asl), large (9540 km^2), tectonic endorheic basin developed in the central-eastern Trans-Mexican Volcanic Belt. In 2016, the ICDP MexiDrill project recovered a total of 1152 m of sediments from a maximum depth of 520 m in Lake Chalco, in the SW of the Basin of Mexico. The upper 309.15 m (composite sequence, mc) are composed of fine-grained lacustrine sediments alternating with discrete visible tephra layers, and the lower 200 m are primarily volcaniclastic facies and basaltic lavas with some intercalated fluvial and alluvial facies. Initial lacustrine deposition started in the Chalco Basin, after the deposition of a thick volcaniclastic sequence, and continued until the lake

B. Valero-Garcés (✉)
Instituto Pirenaico de Ecología - Consejo Superior de Investigaciones Científicas (IPE- CSIC), Zaragoza, Spain
e-mail: [redacted]

M. Stockhecke (✉)
Large Lakes Observatory and Department of Earth & Environmental Sciences, University of Minnesota Duluth, Duluth, MN, USA

Eawag, Swiss Federal Institute of Aquatic Science and Technology, Surface Waters – Research and Management, Kastanienbaum, Switzerland
e-mail: [redacted]

S. Lozano-García · S. S. Najera · R. Martínez
Instituto de Geología, Universidad Nacional Autónoma de Mexico, Ciudad Universitaria, Coyoacán, Mexico

B. Ortega · M. Caballero
Instituto de Geofísica, Universidad Nacional Autónoma de Mexico, Ciudad Universitaria, Coyoacán, Mexico

P. Fawcett · K. Pearthree
Department of Earth & Planetary Sciences, University of New Mexico, Albuquerque, NM, USA

© The Author(s), under exclusive license to Springer Nature Switzerland AG 2021

M. R. Rosen et al. (eds.), *Limnogeology: Progress, Challenges and Opportunities*, Syntheses in Limnogeology, https://doi.org/10.1007/978-3-030-66576-0_14

was drained in recent centuries. Lake Chalco has remained as a shallow lake until the present day.

Five main lithotypes throughout the core have been defined: (1) Organic, with (i) organic-rich silty clay, (ii) sapropelic silty clay, and (iii) peat; (2) Diatomaceous, with laminated, banded, and mottled diatomaceous silty clay; (3) Calcareous, with banded or massive carbonate silty clay and ostracod-rich layers; (4) Clastic, with silty clay, sand, and gravel, both clast and matrix-supported; and (5) Volcanic, as (i) volcaniclastic layers (tephras and clastic deposits) and (ii) lavas. Eighteen lithological units have been defined based on lithotypes and magnetic susceptibility values. Laminated diatomaceous facies occurred during phases with deeper depositional environments. Carbonate deposition marked more alkaline, shallower phases. Peat and organic-rich silts deposited during periods with better development of wetlands in the basin. The preliminary chronological framework suggests the lake sequence spans at least the last 367 ky. More saline diatom assemblages in diatomaceous facies and the occurrence of carbonate lithotypes and peat layers suggest relatively lower lake levels during interglacials; higher lake levels during glacial stages are indicated by more frequent freshwater diatom assemblages and the occurrence of finely laminated diatomaceous facies. The detailed stratigraphy and facies descriptions from the MexiDrill cores provide the basis for subsequent development of chronology and paleoenviromental studies of the Mexico basin record. Furthermore, the depositional model for Chalco is applicable to lakes developed in active tectonic and volcanic settings.

Keywords ICDP MexiDrill · Chalco Basin · Mexico Basin · Pleistocene · Holocene · volcanism · lake

Introduction

The pioneering work of Elizabeth Gierlowski and Kerry Kelts in the 1990s produced a global record of lake basins including some Quaternary examples (Gierlowski - Kordesch and Kelts 1994, 2001). During the last decades of the twentieth century and under the umbrella of the International Continental Scientific

J. P. Werne
Department of Geology & Environmental Science, University of Pittsburgh, Pittsburgh, PA, USA

E. Brown
Large Lakes Observatory and Department of Earth & Environmental Sciences, University of Minnesota Duluth, Duluth, MN, USA

D. McGee
Department of Earth, Atmospheric & Planetary Sciences, Massachusetts Institute of Technology, Cambridge, MA, USA

A. G. E. Hodgetts
School of Geography, Earth and Environmental Sciences, University of Birmingham, Edgbaston, Birmingham, UK

Drilling Program (ICDP, https://www.icdp-online.org/home/), a number of long Quaternary lacustrine sequences extending beyond the last glacial cycle have been made available worldwide: Lake Chad (Schuster et al. 2009), Qinghai Lake (Colman et al. 2007; An et al. 2012), Lake Baikal (Lake Baikal Paleoclimate Project Members 1992), Dead Sea (Stein et al. 2011), Bosumtwi (Koeberl et al. 2005), Lake Malawi (Scholz et al. 2007), Potrok Aike (Zolitschka et al. 2013), Lake Van (Litt et al. 2012), El'gygytgyn (Melles et al. 2012), Lake Ohrid (Wagner et al. 2014), and Towuti (Russell et al. 2016) among others. In the Americas, several lacustrine records have provided the basis for detailed reconstructions of the climate and environmental evolution in the tropical regions: e.g., Lake Titicaca (Fritz et al. 2007), Petén Itzá (Hodell et al. 2006), Chalco (Brown et al. 2012), and Junin (Rodbell and Abbott 2012). These long sequences span several glacial cycles and contain a detailed history of the origin and evolution of the lake basins, and provide reconstructions of regional vegetation, climate, and environmental change (Fig. 1a).

In this contribution, we summarize the stratigraphy of Lake Chalco in the Basin of Mexico. Investigations of lake sediments of the Valley of Mexico extend back to the 1950s (see references in Bradbury 1989) and most of the work at Lake Chalco was undertaken by researchers at the Universidad Nacional Autónoma de Mexico (UNAM) since the 1990s (see detailed references in Lozano-Garcia et al. 1993; Lozano-Garcia and Ortega-Guerrero 1994, 1998,; Caballero and Ortega Guerrero 1998; Caballero et al. 1999). These studies focused on relatively short (<25 m) cores spanning the last 40 kyr, utilized sedimentary facies, magnetic mineralogy, pollen, and diatom data and transfer functions to reconstruct paleoenvironmental conditions. They showed broadly that lake salinity was higher prior to 27 ka, decreased

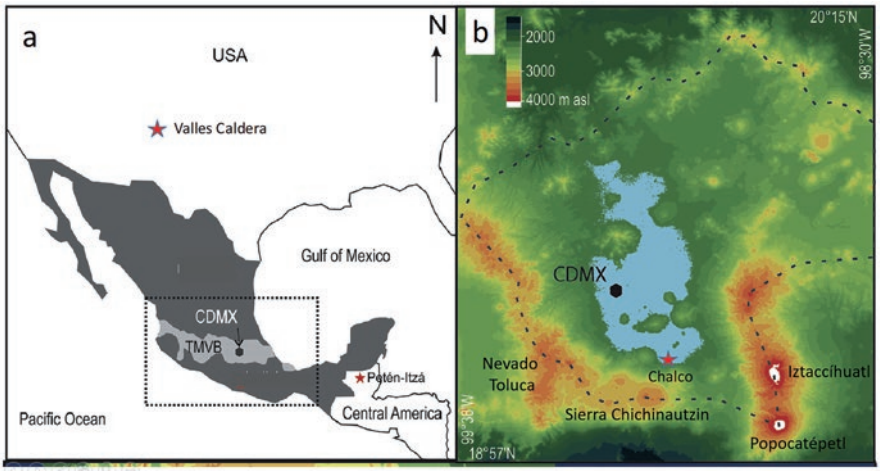


Fig. 1 (**a**) The Trans-Mexican Volcanic Belt (TMVB, light gray area), with the location of Mexico City (CDMX), and some long lacustrine records from the tropics and subtropics of North and Central America (Valles Caldera, New Mexico, USA; Lake Chalco (close to CDMX), Mexico); Petén Itza (Guatemala) (from Caballero et al. 2019). (**b**) Map of the Basin of Mexico showing maximum extent of Lake Chalco during the Pleistocene, Mexico City, and major volcanic centers within the Basin of Mexico and drill site location (red star)

during the Last Glacial Maximum and deglaciation, and increased again during the Early Holocene as temperatures increased. Several drought episodes occurred in Central Mexico during the Late Holocene and, even though human impact limits the interpretation of many records in the region, the late Classic drought (AD 600–1100) seems to have been the most important (Metcalfe et al. 2010). Longer cores from the Chalco Basin recovered in 2008 (>125 m) reached to the last interglacial and show a complex stratigraphy with numerous interbedded volcaniclastic deposits, abundant diatom-rich and laminated facies, and some carbonate-rich intervals (Avendaño 2017; Ortega et al. 2015; Lozano-García et al. 2015). In 2016, the complete lacustrine sequence of the Chalco Basin (>500 m thick) was recovered as part of the ICDP-UNAM-NSF-funded project MexiDrill-Chalco (Brown et al. 2019). In the following sections, we describe the stratigraphy and main lithotypes of the Chalco lacustrine sequence and explore some of the paleoclimate, paleoenvironmental, and basin development implications of this unique sedimentary record.

Basin of Mexico

The Trans-Mexican Volcanic Belt (TMVB) is the largest Neogene volcanic continental arc in North America (160,000 km^2 in extension, 1000 km in length) (Fig. 1) (Ferrari et al. 2012), and is built upon Cretaceous and Cenozoic magmatic provinces (Lugo-Hubp 1984; Lugo-Hubp et al. 1994) The Basin of Mexico is surrounded entirely by volcanic ranges: Sierra de las Cruces to the west includes the oldest geologic formations dated between 3.7 and 0.7 Ma (Delgado-Granados and Martin del Pozo 1993), Sierra de Pachuca and Tezontlalpan to the north (de Cserna et al. 1988), Sierra Nevada to the west (Macías et al. 2012), and Sierra Chichinautzin to the south (Martin del Pozzo 1982; Siebe et al. 2005). Several isolated volcanic structures and clusters are present on the plain, such as Sierra de Guadalupe (García-Palomo et al. 2006) and Sierra de Santa Catarina (Lugo-Hubp et al. 1994; Jaimes-Viera et al. 2018) (Fig. 1).

The Sierra Nevada consists of a chain of andesitic-dacitic stratovolcanoes in a 45 km long N–S alignment, extending from Tláloc in the North (4151 m asl.) to Popocatépetl in the South (5454 m asl.). Iztaccíhuatl (5285 m asl) sits North of Popocatépetl and is composed of a number of coalescing and superimposed edifices that began cone construction ca. 1.8 Ma ago but is now believed to be extinct (Nixon 1989; Macías et al. 2012). Popocatépetl is known to have built upon the remnants of at least three previous edifices (Siebe et al. 1995) with its oldest eruptive products dated since the last magnetic reversal ca. 750,000 years ago. Gravitational collapses, followed by subsequent rebuilding events, have been instrumental in the growth of Popocatépetl to the stratovolcano we see today. The most recent collapse has been dated between 24,000 and 29,000 cal yr BP. During the last 29,000 years, at least eight large Plinian eruptions have occurred in the volcanoes of Sierra Nevada, with seven from Popocatépetl. The Plinian fall deposit of Popocatépetl named "Pómez Tutti Frutti" (Siebe et al. 1997) erupted ca. 17,000 cal yr BP, and is currently the best

stratigraphic marker in the Basin of Mexico (Sosa-Ceballos et al. 2012). It consists of juvenile dacitic pumice and polylithologic lithic componentry making it an easily recognizable fall (Siebe et al. 1995). Since December 21, 1994, activity at Popocatépetl began again, with frequent magmatic eruptions and paroxysms occurring from January 9, 2005. Regularly, tephra and gas are emitted and are visible from the surrounding municipalities. Dome growth and ballistics also pose a significant hazard to those who live around the volcano resulting in an exclusion zones of up to 12 km being enforced by the authorities.

The Sierra Chichinautzin extends from the southern end of the Sierra Nevada to the Nevado de Toluca volcano in the Lerma basin (west of the Basin of Mexico). It is a monogenetic volcanic field with more than 220 volcanic vents consisting of scoria cones and shield volcanoes. Products from these smaller scale volcanoes include lavas and tephra deposits covering an area of ca. 2500 km^2 (Bloomfield 1975; Martin del Pozzo 1982; Lugo Hubp 1984). The compositions of these products are more basic than the nearby polygenetic volcanoes, and generally erupt as andesites with subordinate basalts and dacites defining a calc-alkaline series (e.g. Siebe et al. 2005). The oldest products are 1.2 Ma (Arce et al. 2013a), and the youngest cone is Xitle volcano of an age of 1570 cal yr BP (Siebe 2000).

Among the ranges within the Basin of Mexico, the Sierra de Santa Catarina is prominent and divides the southern Xochimilco and Chalco subbasins from the northern Texcoco subbasin. This range is composed of seven volcanoes aligned E–W, which include cones and a maar with associated lavas and domes of andesitic composition (Lugo-Hubp et al. 1994; Arce et al. 2015). Lugo-Hubp et al. (1994) suggested a Holocene age of Santa Catarina structures based on their relatively young relief; however, $^{40}Ar/^{39}Ar$ dating of its products gives an age between 132,000 and 23,000 years (Jaimes-Viera et al. 2018).

The Nevado de Toluca stratovolcano (80 km to the SW of Mexico City) has had at least one eruption which has dispersed tephra across the Basin of Mexico. This eruption, producing the Upper Toluca Pumice, was Plinian and occurred ca. 12,300 yr BP (Arce et al. 2003). These deposits have been identified and correlated across the Basin of Mexico displaying thicknesses between 12 and 30 cm (Siebe et al. 1999; Ortega-Guerrero et al. 2015).

The Basin of Mexico is a tectonic depression bound by a series of fault systems. The Sierra Chichinautzin is a topographic high of a horst oriented E–W with the Xochimilco and Xicomulco normal fault system as its northern limit and the La Pera normal fault system as its southern limit (Siebe et al. 2004; Alaniz-Álvarez and Nieto-Samaniego 2005; García-Palomo et al. 2008). These extensional faults have served as preferred pathways for frequent, small batches of ascending magma that have successively added altitude to the Sierra Chichinautzin (Siebe et al. 2004). The Sierra de las Cruces was constructed over a N–S alignment and is constituted by three blocks limited by faults oriented E–W and NE–SW (García-Palomo et al. 2008). The existence of NW–SE-oriented normal faults has been inferred from deep wells in Mexico City in the inner part of the basin, crossing most of the metropolitan area. The limestone substrate has been located at different depths at Mixhuca and Tulyehualco wells suggesting the existence of an asymmetric graben limited by

faults dipping to the SE and NW, respectively (Pérez-Cruz 1988). The closure of the ancient southward drainage of the Basin of Mexico by the Sierra Chichinautzin caused the development of a large lacustrine system that spans over the last 1.2 Ma and reached a maximum area of 1690 km^2 at an elevation of 2258 m asl (Ruiz-Angulo and López-Espinoza 2015). Continued subsidence since then has allowed accumulation of a thick sequence (~300 m) of Quaternary lacustrine sediment.

During the Quaternary, Popocatépetl and Iztaccíhuatl supported glaciers; however, a glacial chronology is only available for Iztaccíhuatl (White 1962, 1987), where six advances have been dated by ^{36}Cl between 205,000 and 1000 years ago (Vazquez-Selem and Heine 2011).

Lake Chalco

The lakes in the central Basin of Mexico were drained after the Spanish conquest for flood control, agriculture, and urban development. Documentary evidence shows that during the sixteenth century, prior to these modifications, the lake system covered an area of 1500 km^2 (Ezcurra 1990). Mexico City is built upon these lake beds. Presently, the plain of Lake Chalco is an agricultural region located in the southern subbasin of the Basin of Mexico in which the last remnant of the lake was drained during the late nineteenth and early twentieth centuries. The modern lake at Chalco covers an area less than 40 km^2 (Fig. 1b). It is a small alkaline marsh with an average depth of 3 m with turbid carbonate/bicarbonate, sodium-rich water (Lozano-García et al. 1993; Caballero et al. 2019). Although Lake Chalco falls within the administrative limits of Mexico City, it represents one of the largest remaining blocks of uninhabited land within the megalopolis and thus was identified as a target location for scientific drilling.

Surrounding vegetation has been severely affected by several thousand years of human occupation; the Basin of Mexico is one of the earliest human settlement sites in the Americas, with continuous agricultural activity since the Middle Holocene (Lozano-Garcia et al. 1993; Bhattacharya, and Byrne 2016). The lower elevation parts of the basin are used for agriculture and the foothills are covered by introduced grass and crops. *Pinus* spp. (pine) and *Quercus* spp. (oak) forests are present only in some of the highest areas. Halophytic vegetation currently dominates some of the shallow areas.

Mexico City depends on groundwater for >70% of its water supply. Since the 1950s, much of Mexico City, including the Chalco subbasin, has experienced accelerated ground subsidence with accompanying damage to urban infrastructure as a result of groundwater extraction from the regional aquifer that underlies the thick lacustrine aquitard on which the city is built. By 1991, total subsidence had reached 8 m with subsidence rates exceeding 350 mm/yr (Cabral-Cano et al. 2010). In the Chalco subbasin, these rates exceed 200 mm/yr and have favored the formation of a new lake on top of old lacustrine sediments. The extreme groundwater extraction rates and subsequent high subsidence rates pose a major challenge for a sustainable long-term water supply.

The Valley of Mexico is characterized by a high-altitude subtropical climate, with little temperature variability during the annual cycle and a rainy season from May to October, following the northward Intertropical Convergence Zone ITCZ migration during the boreal summer, although occasional polar fronts can bring precipitation during winter (Mosiño Aleman and Gracia 1974).

Coring the Chalco Basin

(a) *Geophysical surveys*

The subsurface stratigraphy of the Basin of Mexico is known from wells drilled in the metropolitan area to 2–3 km depth (Oviedo de León 1970; de Cserna et al. 1988; Pérez-Cruz 1988; Enciso-De la Vega 1992; Arce et al. 2013b, 2015). The basement rocks are Lower Cretaceous limestones and calcareous conglomerates and anhydrites, most likely of Eocene age. Overlying these deposits are volcanic rocks, which include mostly lavas and less abundant pyroclastic deposits, ages varying from Oligocene to Quaternary. Lacustrine sediments are found interlayered with lavas, breccias, conglomerates, and volcaniclastics. The older lacustrine sediments are present in most wells at depths between 750 and 300 m, although in Copilco-I well a ca. 100 m-thick lacustrine sequence was reported at 1600 m depth (Pérez-Cruz 1988).

A number of geophysical surveys were undertaken prior to the ICDP drilling campaign to characterize the sedimentary infilling of the basin (Brown et al. 2012, 2019). In the Chalco subbasin, near-surface conditions resulting from intensive agricultural development of the area complicate meaningful data collection with conventional seismic reflection surveys. Information from Bouguer gravity anomalies and passive seismic H/V spectral ratio methods, coupled with data from nearby water well logs, indicate the presence of a ca. 300 m "lacustrine sediment" package underlain by ca. 150 to 200 m of "granular material" (Ortiz-Zamora and Ortega-Guerrero 2007). This pattern has been interpreted as a graben bound to the north by the Sierra Santa Catarina and Cerro de la Estrella and to the south by a horst-shaped block composed of the Teuhtli and Xitle volcanoes (Campos-Enriquez et al. 2003). Geophysical surveys (Brown et al. 2012, 2019) provided a map of sediment thickness that was calibrated with measurements of resonance frequencies at the Santa Catarina water wells where the depth to the base of the lacustrine sediment package was known.

(b) *Previous coring campaigns and the ICDP MexiDrill*

In 2008 and 2011, six overlapping cores were drilled to different depths near the depocenter of ancient Lake Chalco: CHA08-II (1–27 m), CHA08-III (1–90 m), CHA08-IV (85–122 m), CHA08-V (29–72 m), CHA08-VI (70.8–85 and 106–122.4 m), and CHA11-VII (18 m). The cores CHA08 III to VI were drilled with a Shelby corer in 1.10 m sections with inner 10 cm diameter PVC tubes. The cores CHA08-II and CHA11-VII were drilled with a modified Livingstone piston corer in 1 and 2 m long sections.

The ICDP MexiDrill project goal was to recover the complete lake sequence of the Chalco Basin. During 6 weeks of continuous work in March–April 2016, the MexiDrill field campaign recovered more than 1000 m of drill core using wireline diamond coring techniques in four holes at a site identified by a suite of techniques as described above as the location of the thickest lacustrine sequence (Lozano-Garcia et al. 2017). The drillers, through rotational drilling techniques, reached depths of 420 m in core 1A, 310 m in 1B, and 520 m in 1C. Core 1D used a piston corer with percussion to enhance recovery of the upper soft sediments. A total of 1152 m of core sediments was recovered reaching a maximum depth of 520 m. Recovery ranged from 88% to 92% in the three cores (Fig. 2).

The upper 300 m of core 1A is composed of fine-grained lacustrine sediments alternating with discrete tephra layers, and the lower sections (ca. 300–422 m) are composed of volcaniclastics and lavas. Full downhole geophysical logs were collected from hole 1A. Cores 1B and 1C recovered the upper lacustrine sequence (313 m), and 1C continued through the volcaniclastic-lava unit reaching poorly sorted, coarse clastic deposits (ca. 512–520 m). Triple core recovery with offset core intervals in the upper 300 m lacustrine unit provides sufficient core overlap to create a composite sequence and continuous paleoenvironmental and volcanological reconstructions. In total, the project drilled 1262 m (including reamed sections) and recovered 1065 m of cores. (Fig. 2). The composite sequence is 554 mc (composite depth in meters) long including 52 m (9.4%) of gaps, mainly occurring within the lower coarse-grained volcaniclastic deposits, which were difficult to recover.

Lacustrine Facies

A number of clastic, carbonate, biogenic, chemical, and volcanic facies were defined in the Chalco 2008 cores (Herrera-Hernandez 2011). Clastic facies were composed of clay or silt with variable amounts of organic matter, varied colors (black brown, reddish), and with laminated, banded, and massive textures. Discrete occurrences of struvite (hydrated magnesium-ammonium phosphate) were identified at several levels. Biogenic facies included thin layers of diatomaceous ooze, thick layers of diatomaceous, organic-rich mud, and about 15 layers, between 5–10 cm thick, of ostracod-rich intervals. These composed more than 80% ostracod carapaces (ostracod *hash*). In the lower part of the sequence (between 113 and 122 m), up to 11 layers about 3–5 cm thick of carbonate mud mostly composed of endogenic carbonates (Mg-calcite, dolomite, and siderite) occurred. A number of tephra layers (lapilli and ash) were described and identified.

In the 2016 ICDP cores, lithotypes were defined based on lithologies and textures determined by macroscopic and microscope (smear slide) observations (Schnurrenberger et al. 2003; Table 1 and Fig. 3). In Table 1, the main features of the lithotypes are summarized and their associated depositional processes and environments interpreted. Figure 3 shows core images of selected intervals illustrating the main lithotypes identified in the MexiDrill cores.

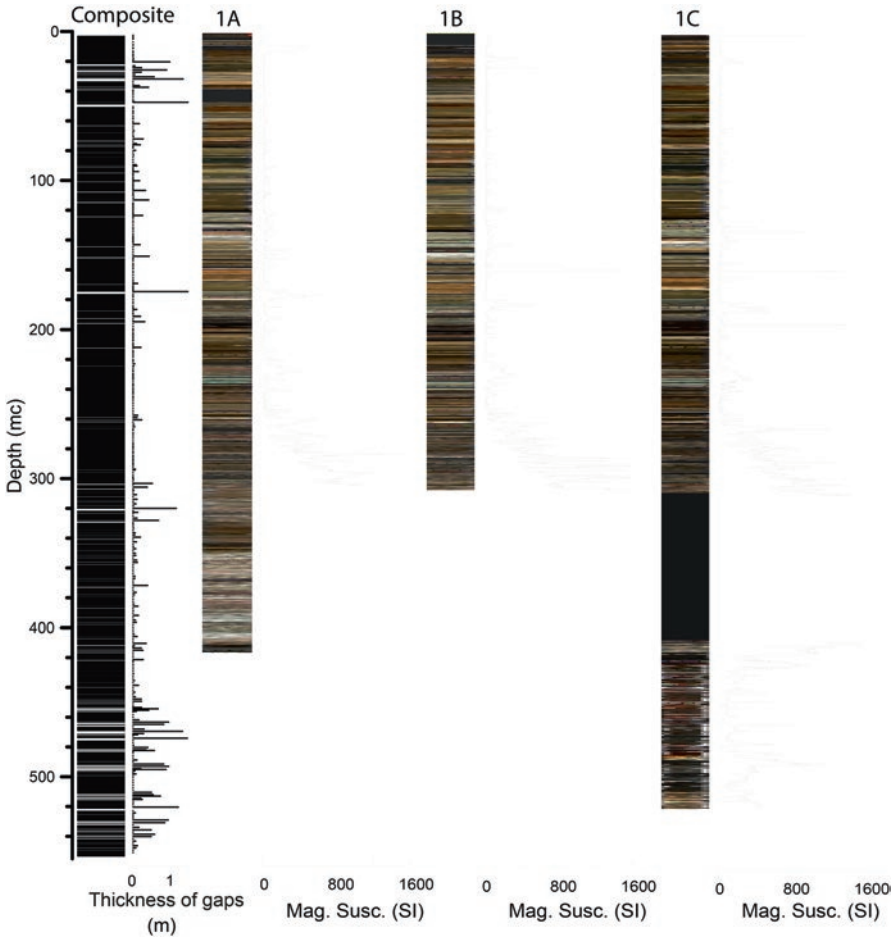


Fig. 2 Composite record from the Chalco drill cores and the ICDP MexiDrill cores including magnetic susceptibility and stacked color core images of the sections for site 1 cores (holes A, B, and C). White colored gaps of the composite record in the vertical column are given in thickness (m) by the bar chart

Total organic carbon (TOC) and inorganic carbon (TIC) analyses of selected samples are consistent with the three main types of lacustrine lithotypes: carbonate, organic, and diatomaceous (Fig. 4). The five main groups of lithotypes are:

- Organic. This includes: (i) organic-rich silty clay, (ii) sapropelic silty clay, and (iii) peat. The TOC range is quite large (up to 45%) and the TIC is below 1% in most samples.
- Diatomaceous. These are diatomaceous silty clays and include (i) laminated, (ii) banded, and (iii) "mottled" lithotypes. TIC content is generally lower than 1% and TOC reaches up to 4%.

Table 1 Chalco Basin lithotypes defined in the MexiDrill sequence: description, total thickness (in meter and percentage), and depositional processes and environments

Lithotypes	Description	Thickness	Depositional processes and environments
Organic-rich (O)	Organic-rich silty clay, banded or mottled in layers up to several dm. Organic matter includes sponge spicules, phytoliths, diatoms as well as terrestrial and amorphous aquatic OM. Lithotypes range from peaty to organic-rich silty clays. Some intervals contain abundant terrestrial OM clasts and variable amount of volcanic glass.	18 m 3.3%	Swamp/wetland to relatively shallow (and small) eutrophic lacustrine environment
Diatomaceous laminated (Dl)	Finely laminated diatomaceous silty clay with couples of light beige and dark brown laminae, light laminae (1–2 mm) contain almost only diatoms, dark laminae (2–5 mm) contain more clastic components. Thickness ranges from few cm to several dm.	44 m 7.8%	Relative deep and distal fresh-water lake undergoing strong likely seasonal changes and a at least partly anoxic water column Light laminae reflect deposition during diatom blooms Dark laminae reflect baseline deposition in the distal areas of the lake
Diatomaceous banded (Db)	Thin to medium bedded diatomaceous silty clay intercalated often by gray siliciclastic-rich 2–5 mm thin clay beds	80 m 14.4%	Distal, deep lake environments dominated by fine clastic and diatom deposition. Gray layers deposited during flood events transporting material from littoral areas and/or watershed.
Diatomaceous mottled (Dm)	Diatom-rich clayey silt with speckle of beige diatom clasts in a relatively homogenous matrix	1 m 0.2%	Distal but shallower environments with redox fluctuations responsible for mottling textures.
Carbonated banded (Cb)	Dm-thick beds composed of autochthonous carbonate minerals (Aragonite, Calcite), ostracod shells, few diatoms with etched surfaces and minor organics remains and clastic minerals; reddish intervals contain coarser carbonate grains, light gray intervals are Ostracod and Phacotus rich; dark gray intervals have more fine-grained (micritic) carbonate grains	57 m 10.4%	Shallower alkaline/ brackish environment dominated by carbonate precipitation and high biogenic productivity with fine carbonate clastic input from littoral areas

(continued)

Table 1 (continued)

Lithotypes	Description	Thickness	Depositional processes and environments
Carbonated massive (Co)	Mm to cm thick laminae composed mostly of biogenic or autochthonous carbonate material. Some dominated by ostracod shells and Phacotus (few layers almost purely of ostracod shells). Some are cemented if directly overlaying a v-layer	8 m 1.4%	Rapid carbonate deposition by endogenic processes (carbonate minerals) or biogenic accumulation (ostracods) in a highly productive system with limited detrital input
Coquina (C)	Bivalves, gastropods, and ostracods within a diatomaceous-silty clay matrix	0.6 m 0.1%	Biogenic accumulation in littoral areas
Silty clay (Sc)	Medium to thick beds of light gray silty clay dominated by silicate minerals and with variable diatom and carbonate minerals	18 m 3.2%	Distal, deep lake environments dominated by fine clastic deposition and with low bioproductivity
Sand (S)	Fine to coarse sand (carbonate, volcanic clasts) with silty clay matrix	1.4 m 0.2%	Alluvial (or close to alluvial-influenced lacustrine littoral) high-energy environment during a relatively low lake stand
Gravel (G)	Clast-supported, coarse sand matrix with rounded heterolithic pebbles, in massive, graded, and laminated layers		Alluvial /Fluvial, high-energy environment during relatively low lake stands
Tephra (T) and Lapilli (L)	Fine ash to lapilli pumice beds with sharp boundaries to over- and underlying silty clays		Reworked or fallout volcanic deposits from a volcanic source in vicinity to the lake
Volcaniclastic (V)	Coarse deposits (from gravel to sand) composed only of volcanic rock fragments and volcanic material matrix. Mostly matrix-supported; some clast-supported; massive, banded, and laminated structures. Dm to meter thick layers.	207.1 m 37.4%	Primary coarse volcaniclastic deposits and reworked volcanic materials by slope-failure, alluvial, mass wasting, and fluvial processes
Basalt (B)	Black to reddish vesicular Basalts	68.4 m 12.4%	Lava flows

- Calcareous. These are carbonate-bearing silty clay and include (i) banded and (ii) massive lithotypes. A unique lithotype is an ostracod and mollusk-rich hash or coquina at the base of the lacustrine sequence. Carbonate content covers a wide range, from 1% to almost 100% in some thin layers.
- Clastic. These include silty clay.
- Volcanic. These occur as (i) volcaniclastic layers as relatively thin tephra layers (ash and lapilli) and clastic deposits and (ii) lavas).

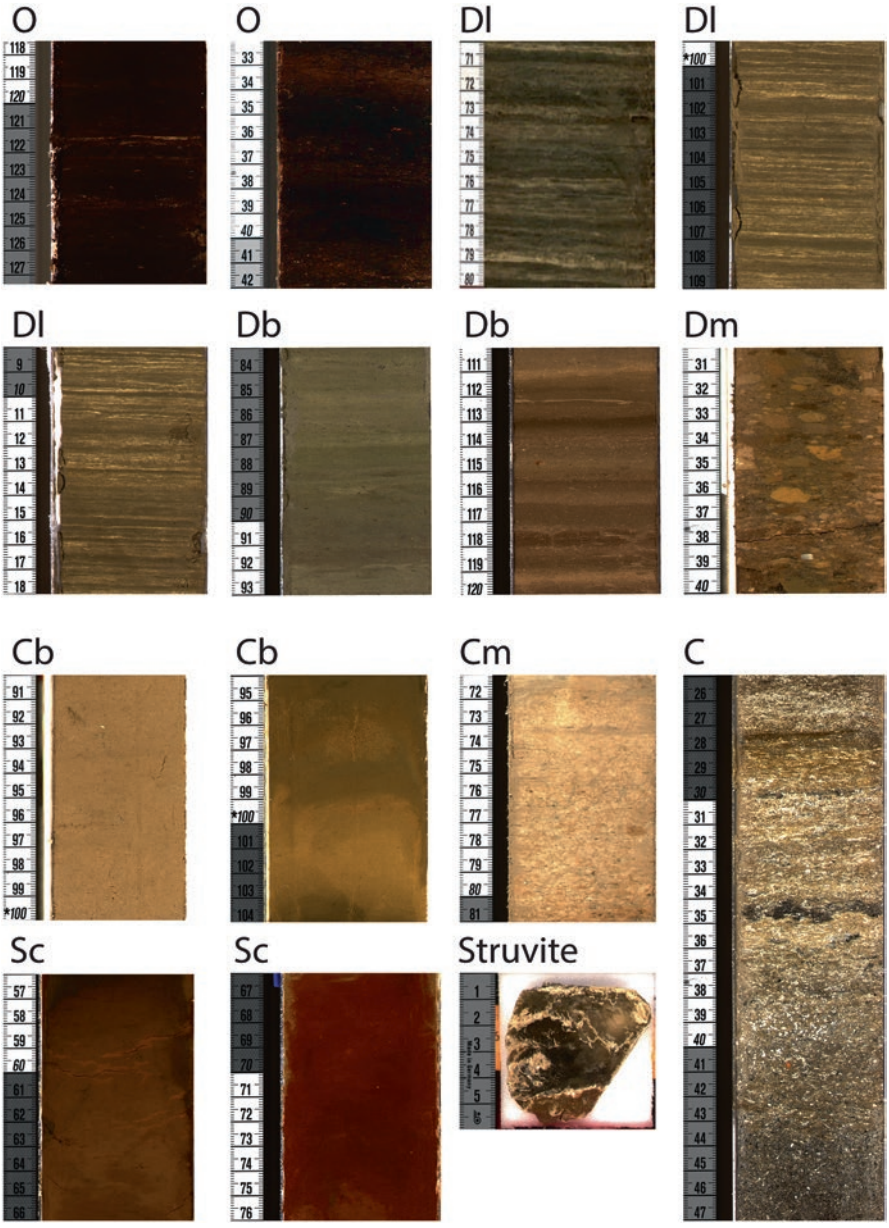


Fig. 3 (**a**) Core images of main lithotypes; vertical scale in centimeters: Organic-rich (O, MEXI-CHA16-1C-133Y-1 117.5–127.5 cm, MEXI-CHA16-1A-76Y-1 32–42 cm); Diatomaceous laminated (Dl; CHA08-VI-18 70–80 cm, MEXI-CHA16-1C-140Y-1 99–109 cm, MEXI-CHA16-1B-147Y-1 8–18 cm); Diatomaceous banded (Db, MEXI-CHA16-1A-169Y-1 83–93 cm, MEXI-CHA16-1C-167Y-1 110–120 cm); Diatomaceous mottled (Dm, MEXI-CHA16-1D-10C-2 30–40 cm); Carbonated banded (Cb, MEXI-CHA16-1D-11C-13 90–100 cm, MEXI-CHA16-1C-32Y-1 94–104 cm); Carbonated massive (Co, MEXI-CHA16-1C-174Y-1

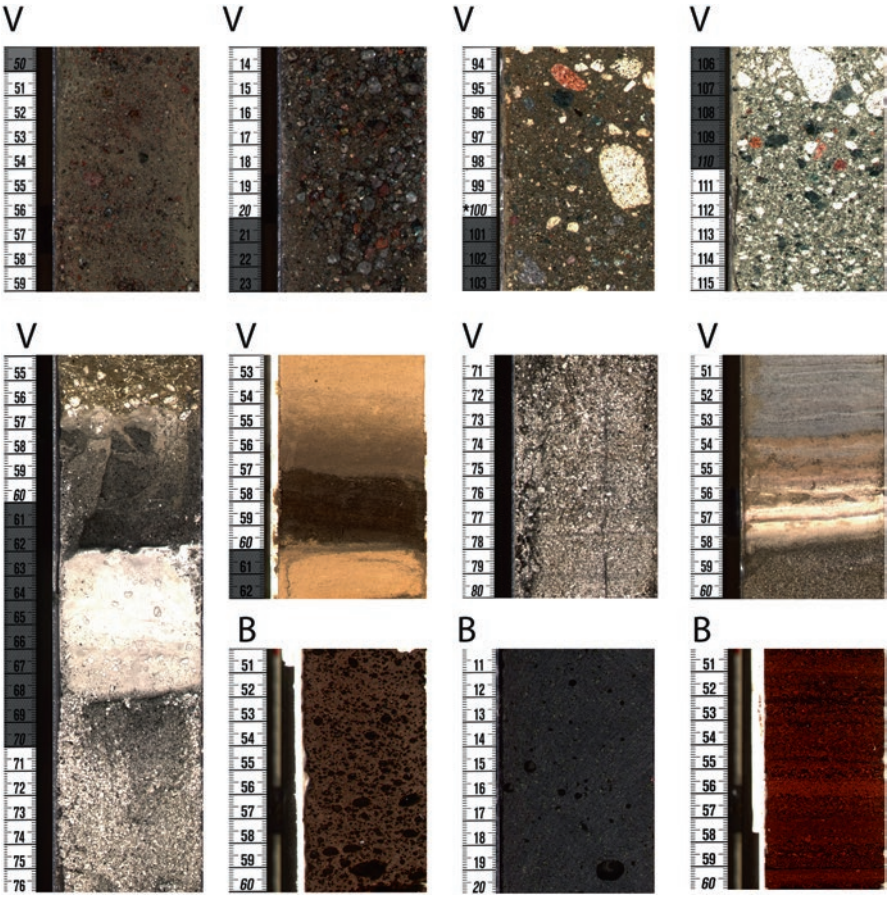


Fig. 3 (continued) 132–142 cm); Coquina (C, MEXI-CHA16-1A-175Y-1 25–47 cm); Silty clay (Sc, MEXI-CHA16-1A-27Y-1 56–66 cm, MEXI-CHA16-1A-54Y-1 66–76 cm); Struvite (MEXI-CHA16-1C-18Y-1). (**b**): Core images of main lithotypes; vertical scale in centimeters Volcaniclastic (V, MEXI-CHA16-1C-178Y-1 49–59 cm, MEXI-CHA16-1C-182Y-1 13–23 cm), MEXI-CHA16-1A-269Y-1 93–103 cm, MEXI-CHA16-1A-271Y-1 105–115 cm, MEXI-CHA16-1A-175Y-1 54–76 cm, MEXI-CHA16-1D-8C-2-A 52–62 cm, MEXI-CHA16-1B-181Y-170–80cmandMEXI-CHA16-1B-177Y-150–60cm);Basalt(B,MEXI-CHA16-1C-231Y-1 50–60 cm, MEXI-CHA16-1C-217Y-3 10–20 cm, MEXI-CHA16-1C-270Y-1-A 50–60 cm)

Along the sequence, these main lithotypes show associations at several scales. At a decimeter scale, alternation of sapropelic, diatomaceous, organic (peat), and carbonate facies are common. Lithotypes group in thicker (multimeter scale) intervals that define lithostratigraphic units (see next section) and illustrate dynamic changes of the lacustrine basin encompassing a mosaic of depositional environments: shallow alkaline carbonate-producing lakes, deeper lakes with diatomaceous

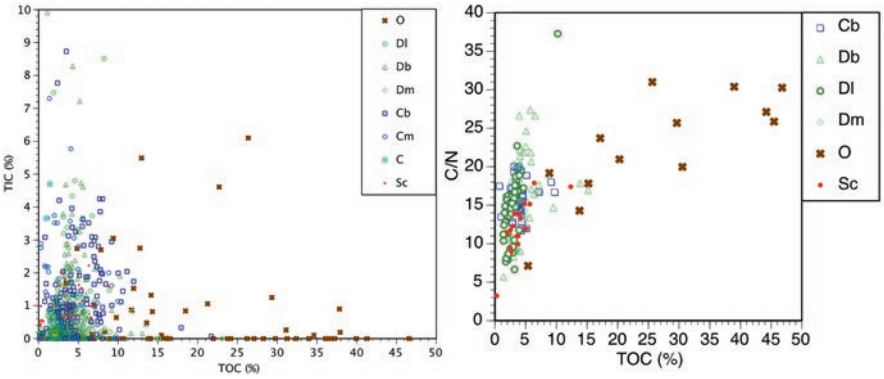


Fig. 4 (**a**) Total Inorganic Carbon (TIC) contents plotted against Total Organic Carbon (TOC) contents of main lithotypes: carbonate (blue boxes), organic (brown open circles), and diatomaceous (pink crosses) clayey silt. (**b**) TOC plotted versus C/N for the main lithotypes: carbonate (blue boxes), organic (brown open circles), and diatomaceous (pink crosses) clayey silt

deposition, wetlands with peat accumulation, and lakes dominated by organic deposition (sapropelic muds).

Stratigraphy of the Chalco Basin

Previous Stratigraphies Based on five shorter sediment cores, an initial stratigraphy was defined by Ortega-Guerrero (1992) for the upper 26 m of the sequence. The top unit 1 (0–1.8 m) is composed of brown silt with altered lapilli fragments, and more abundant ostracod and plant remains toward the base. Unit 2 (1.8–2.5 m) includes brown silt with abundant plant remains and ostracods. Unit 3 (2.5–3 m) includes diatomaceous facies with intercalated tephra intervals. Unit 4 (3–8 m) is composed of dark brown to black peat with abundant tephra layers. Brown silt dominates the lower units (5 to 7): with more plant fragments in Unit 5 (8–11 m), more gastropod shells in Unit 6 (11–16 m), and more ostracod levels and abundant lapilli layers in Unit 7 (16–26 m). The "Gran Ceniza Basáltica" at 21 m depth provides an important chronostratigraphic marker for the sequence (older than 31 ka, Ortega – Guerrero et al. 2015, 2017, 2018). Other key tephra layers are identified, including: Pómez Ocre (ca. 5 ^{14}C kyr); "Pómez Toluca Superior" or "sal y pimienta" (12,520 +/− 135 ^{14}C yr, Arce et al. 2003); "Pómez con Andesita" (ca. 14 ka) and "Pómez Tutti Frutti" (17,600 cal ka BP), Sosa Cebalos et al. 2012).

After the 2008 drill campaign, a new stratigraphy was developed for the upper 125 m with five main units (Herrera 2011): Unit 1 (0–8 m) groups organic-rich clay and silt and diatomaceous facies with several tephra layers. Unit 2 (8–68 m) is dominated by yellowish brown clayey silt (massive, banded, laminated) with more mottled intervals (subunit 2A (8–40 m)) and more frequent intercalation of gray silty clay layers (subunit 2B, 40–68 m). Unit 3 (68–90 m) contains olive brown and olive

clay-silt with some thick intervals of reddish-brown silts and the presence of struvite (Fig. 3a) at some levels. Unit 4 (90–104 m) is characterized by the occurrence of olive brown clay-silt with some diatom ooze layers. Unit 5 (104–124 m) is defined by the abundance of laminated facies with alternation of carbonate-rich layers, diatomaceous facies, brown, gray clayey silt, and olive brown clayey silt.

A. *ICDP MexiDrill lithostratigraphy*

The 2016 ICDP MexiDrill drilling campaign obtained four long drill cores in the Chalco Basin, reaching up to 553 mc (composite depth) in the volcanic basement, and recovering the entire lake sequence (upper 295 mc). Magnetic susceptibility values supported correlation of the drill cores (Fig. 2). Cores were split and imaged at LacCore/CSDCO (University of Minnesota) and further correlation was achieved by visual stratigraphy using the CoreWall software. A 554 mc long spliced sequence was generated including core section from both the 2008 and 2016 projects. Eighteen lithological units have been defined (Table 2) based on lithotypes and magnetic susceptibility values (Fig. 5). The upper five units correspond to those defined in 2008 cores. The depth boundaries are those from the spliced composite core. Furthermore, a composite corrected depth scale (mcc) was developed to reflect relatively constant background lacustrine sedimentation by collapsing volcanic layer depths to zero thickness to account for instantaneous event deposition. Similar approaches have been used within other lake drilling records facing frequent volcaniclastic input (Deino et al. 2019; Stockhecke et al. 2014). The composite-corrected sequence totals in 241.68 mcc (Fig. 6).

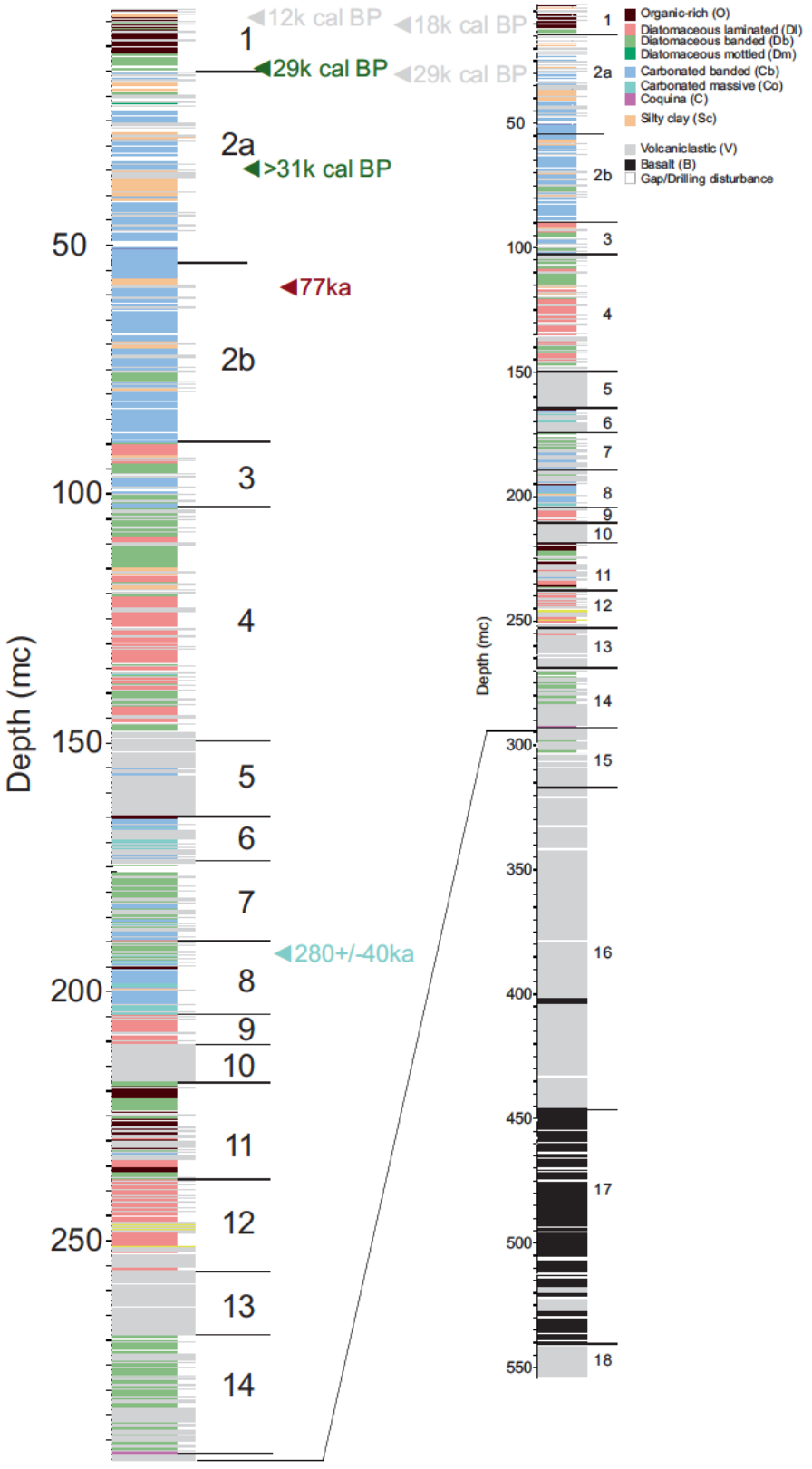
Unit 1 (0–15 m) groups organic and diatom-rich lithotypes with relatively low clastic mineral content and includes a number of volcanic tephra that are well-correlated in the basin. It corresponds to Units 1 to 4 as defined by Ortega-Guerrero (1992) and Unit 1 as defined in the 2008 cores. A conspicuous black diatomaceous interval includes the Pómez Toluca Superior (also known as "Sal y Pimienta") tephra. The laminated and silty clay and dark brown massive and banded silty clay include some peat layers, and the Tutti Frutti Tephra is present in this unit as well. The environments associated with these lithotypes are relatively shallow lacustrine settings dominated by organic and diatomaceous sedimentation.

Unit 2 (15–90 m) is characterized by carbonate lithotypes. It broadly correlates with Unit 2 in the 2008 cores. The upper unit 2A (15–53.5 m) corresponds to Units 5 through 7 (Ortega-Guerrero 1992) and is dominated by banded calcareous lithotypes. Subunit 2B (53.5–90 m) contains more grayish- and greenish-brown calcareous clayey silt and the terrigenous content is higher with common fining upward sequences. Subunit 2A groups light brown/yellowish banded diatomaceous and calcareous silty clay with plant fragments, gastropod shells, and some ostracod-rich levels and mottled intervals. It also includes the "Gran Ceniza Basáltica" tephra. Facies in Unit 2 have textures indicative of shallow lake levels with occurrence of soft clasts, subaerial cracks, and mottling. Periods of higher terrigenous content suggest higher run-off or discrete flooding episodes; more alkaline conditions were conducive to periods with more abundant ostracods. Frequent cm-thick Fe-stained intervals suggest shifting in redox conditions during early diagenesis.

Table 2 Main lithostratigraphic units (as shown in Fig. 5) defined in the composite MexiDrill sequence using corrected composite depth (mc). The thicknesses of the main units in core 1A are also indicated

Unit	Dominant lithotypes	Base of unit (mc) Splice composite	Thickness (core1A)
1	Organic and diatomaceous (laminated, massive)	15	13.02
2A	Diatomaceous and calcareous (banded)	53.5	32.36
2B	Calcareous and diatomaceous (banded), more gray silt toward the base	90	30.39
3	Diatomaceous (laminated), calcareous and diatomaceous (banded)	103	11.92
4	Diatomaceous (laminated)	150	43.42
5	Volcaniclastic (mottled)	164	10.68
6	Calcareous, volcaniclastic, diatomaceous, and organic	174	9.51
7	Diatomaceous (laminated)	190	11.99
8	Calcareous	204.5	13.56
9	Diatomaceous (laminated)	210.8	5.6
10	Volcaniclastic (with some intercalated lake sediments)	218	18.53
11	Organic, calcareous, and diatomaceous	236.6	9.73
12	Diatomaceous (laminated) and organic	256.5	18.36
13	Volcaniclastic	269	14.87
14A	Volcaniclastic and diatomaceous		5.76
14B	Calcareous/Diatomaceous (laminated)		6.59
14C	Diatomaceous (laminated) and organics	292	10.54
15	Volcaniclastic, clastic, and diatomaceous	317	22.6
16	Volcaniclastic	447	128.48
17	Basalt lava	541	92.04
18	Volcaniclastic	555	12.15

Fig. 5 The complete synthetic lithostratigraphy of the spliced sequence of MexiDrill including 2008 and 2016 cores on composite depth (mc) on the right and the magnification into the acustrine sequence covering the upper 295 mc on the left. Preliminary age constraints all transferred on the composite depth consist of correlated previously ^{14}C-dated tephras (in gray text; the "Great Basaltic Ash" (older than 34 ka) (Ortega Guerrero et al. 2015, 2017, 2018), the "Pómez Toluca Superior (PTS)" dated as 12,520 +/− 135 14C yr BP (Arce et al. 2003), the "Pómez Tutti Frutti (PTF)" as 17,670 cal ka BP (Sosa-Ceballos et al. 2012) and "White pumice (WP)" as 27,800 cal BP (Siebe et al. 2017)). Radiocarbon dates of pollen (in green text, Ortega-Guerrero et al. 2018; Lozano-García et al. 2015), a U/Th date of zircon grain selected from tephra (in red text, Ortega Guerrero et al. 2017; Torres-Rodriguez et al. 2018), and a new U/Th age from lacustrine micritic carbonate (in blue text)


12k cal BP
18k cal BP
29k cal BP
29k cal BP
>31k cal BP
77ka
280+/-40ka
Depth (mc)
50
100
150
200
250
1
2a
2b
3
4
5
6
7
8
9
10
11
12
13
14
Depth (mc)
50
100
150
200
250
300
350
400
450
500
550
1
2a
2b
3
4
5
6
7
8
9
10
11
12
13
14
15
16
17
18
Organic-rich (O)
Diatomaceous laminated (Dl)
Diatomaceous banded (Db)
Diatomaceous mottled (Dm)
Carbonated banded (Cb)
Carbonated massive (Co)
Coquina (C)
Silty clay (Sc)
Volcaniclastic (V)
Basalt (B)
Gap/Drilling disturbance

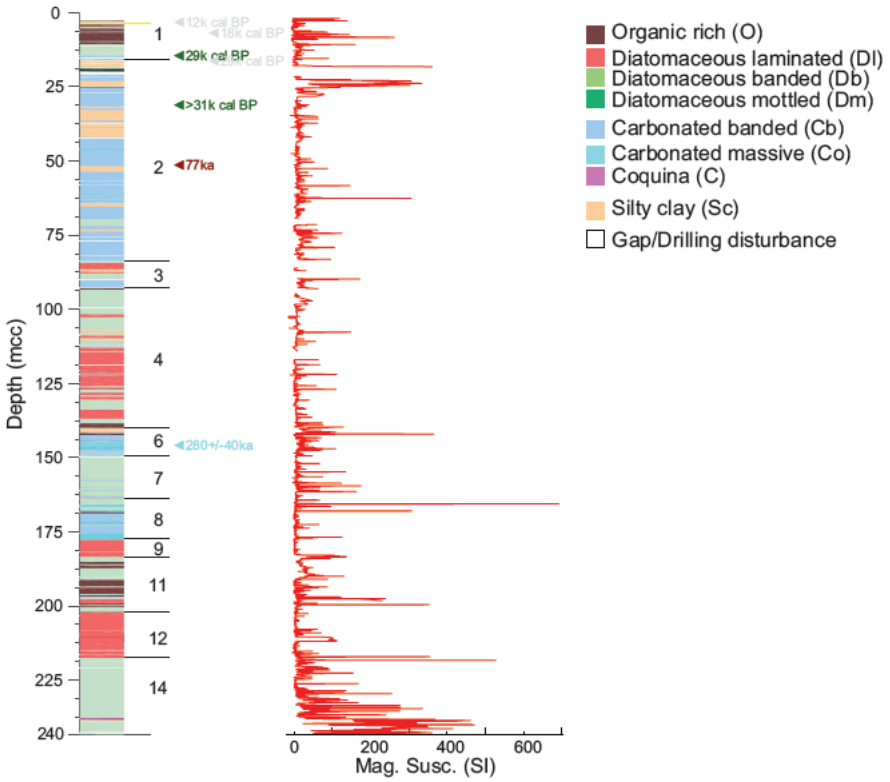


Fig. 6 The lithostratigraphy of the MexiDrill record on the composite corrected depth (mcc). Volcaniclastic layers have been collapsed in this version to show only the lacustrine sediments. Legend is shown in Fig. 5

Unit 3 (90–103 m) is characterized by the occurrence of carbonate and diatomaceous laminated lithothypes, with some reddish-brown carbonate silts. This unit presents several organic-rich levels with struvite occurrences that have been interpreted as guano accumulation during hyper-productivity phases (Pi et al. 2010). Reddish intervals have higher MS values and represent oxidized facies, likely during early diagenesis. The large facies variability (saline and freshwater diatoms, mottling, periods of high clastic input) points to significant hydrological changes during relatively low lake levels.

Unit 4 (103–150 m) is defined by the occurrence of alternations of finely laminated diatomaceous, carbonate, banded diatomaceous, and organic-rich lithotypes. Finely laminated facies are indicative of deeper lake environments and more frequent suboxic conditions. Carbonate deposition reflects periods with higher alka-

linity, but still during relatively high lake levels as suggested by the finely laminated facies.

Unit 5 (150–164 m) is a volcaniclastic unit, composed of massive volcanic material with abundant secondary textures such as nodules, cracks, and staining. This may suggest subaerial deposition and/or reworking by surface processes of pyroclastic deposits, e.g., ignimbrites or lahars. The unit is topped by a tephra layer.

Unit 6 (164–174 m) is characterized by the occurrence of calcareous lithotypes (variegated, banded to laminated). They alternate with massive brown silty clays at the top and with laminated diatomaceous and more organic-rich intervals with secondary Fe-staining toward the base. A thick volcanic interval occurs in the middle of the unit.

Unit 7 (174–190 m) groups laminated to banded greenish diatomaceous silty clay and *Unit 8 (190–204.5 m)* contains carbonate-rich, massive, and banded lithotypes, with some reddish and brownish intervals.

Unit 9 (204.5–211 m) is composed of greenish laminated diatomaceous silty clay with more dark brown intervals toward the base.

Units 6 to 9 are arranged in alternating carbonate and diatomaceous units, as Units 6 and 8 are dominated by calcareous lithotypes, while Units 7 and 9 mostly include diatomaceous ones.

Unit 10 (211–220 m) is a thick volcaniclastic unit that includes two lake sediment intervals (organic-rich and diatomaceous silty clay).

Unit 11 (224–236.5 m) and *Unit 12 (236.5–256.5 m)* are composed of alternating organic-rich lithotypes (peaty silty clay) and diatomaceous (dark brown, massive diatomaceous silty clay) with some reddish banded carbonate and silty clay. In Unit 12, diatomaceous silty clay is dominant (with some greenish/brownish, banded/laminated intervals). Banded, brownish intervals are more frequent toward the base, then grading into greenish and better laminated.

Unit 13 (256.5–269 m) is a volcaniclastic unit with intercalated diatomaceous layers and tephra at the bottom.

Unit 14 (269–292 m) includes diatomaceous lithotypes with tephra layers, more abundant at the top, brownish/reddish, banded carbonated and laminated diatomaceous lithotypes, and dark brown diatomaceous silty clay intervals in the middle and laminated diatomaceous silty clays and oozes at the bottom At the base, a unique decimeter-thick ostracod and mollusk-rich layer (coquina) is found on top of a white pumice tephra, with overlying ash.

Unit 15 (292–317 m) contains interbedded m-thick fine volcaniclastic intervals, coarse clastic lithotypes deposited by mass transport, alluvial and fluvial processes, and dm-thick laminated brownish diatomaceous silty clay. The top volcaniclastic layer is a conspicuous white, laminated, pumice-rich layer.

Units 16 to 18 are the basal volcanic and volcaniclastic units.

Unit 16 (317–447 m) is a thick volcaniclastic unit composed of m-thick subunits, displaying polylithologic clasts among a matrix of varying coarseness.

Unit 17 (447–541.7 m) is composed of lava with laminated, massive, vesicular textures.

Unit 18 (541.7–551 m) is a volcaniclastic unit, with distinct clastic horizons. Largely, the deposit appears to be fining with stratigraphic height.

Evolution of the Chalco Basin

(a) *Depositional evolution*

The lower 200 m of the Chalco sequence are composed of volcaniclastic deposits and lavas. The volcaniclastic deposits of basal unit 18 could be associated with a period of volcanic activity at the end of the volcanic-tectonic phase responsible for the formation of the modern Chalco Basin. Emplacement of nearly 100 m of lava with vesicular textures (unit 17) followed this early episode of volcanic activity. Additional volcanic events occurred leading to the deposition of a thick interval (almost 130 m) of volcaniclastic facies (unit 16) that continued with the infilling of the Chalco Basin. Thick, massive layers of coarse to fine matrix-supported clasts were deposited as alluvial activity dismantled either existing volcanic structures or deposits associated with major evolution events from nearby polygenetic volcanoes.

Unit 15 represents the onset of the infilling of the newly formed Chalco Basin by lacustrine depositional processes. This interval has been described and interpreted in detail by Martinez-Abarca (2019) and Martínez-Abarca et al. (2021). During this period, input of volcaniclastic material continued. Later on, increased efficiency of erosion is indicated by the occurrence of rounder clasts and clast-supported textures in clast-rich sections. Smaller sizes and fine lamination textures in the finer-grained layers indicate an increased influence from a hydrologic regime. A fluvial-lacustrine setting is interpreted as the depositional environment for the upper part of unit 15, followed by the final development of the Chalco Lake (Martínez-Abarca et al. 2021). The lacustrine phase in the Chalco Basin started at the top of unit 15 with deposition of banded diatomaceous silty clay intercalated with fluvial deposits. Diatom assemblages indicate freshwater conditions in this newly formed lake (Martínez-Abarca et al. 2021). The intercalation of lacustrine and alluvial facies suggests that the alluvial and fluvial drainage networks carved the volcanic watersheds and connected to the lake environment. A relatively large number of tephras interbedded with the lake sediments suggest a high frequency of explosive eruptions occurred which transported deposits to the Chalco region. The occurrence of a unique ostracod, mollusk, and gastropod coquina (Unit 14C) indicates periods of high bioproductivity in freshwater with the presence of hard substrates on the lake floor. A stepwise development with early shallow lake stages have been described in other volcanic basins (Pueyo et al. 2011; Martínez-Abarca

et al. 2021). Higher lake levels and deeper environments led to deposition of laminated diatomaceous lithotypes (unit 14 B and A). Unit 13 demonstrates volcanic activity was key producer of material here, leading to the deposition of more volcaniclastic deposits. Lake deposition continued with laminated diatomaceous and organic facies (Units 12 and 11) interrupted by deposition of another thin volcaniclastic interval (Unit 10). Fine-grained lake deposition continued with alternating diatomaceous (Units 9 and 7) and carbonate (Units 8 and 6) dominated phases. After emplacement of another volcaniclastic interval (Unit 5), the lake deepened and laminated carbonate, diatomaceous, and organic lithotypes (Unit 4) were deposited indicative of more anoxic, alkaline, and productive conditions. Deposition of banded to massive facies dominated Unit 3, suggesting relatively low lake levels. The top of this unit marks the last deposition of finely laminated diatomaceous facies.

Unit 2 is dominated by carbonate lithotypes and some silty facies which demonstrate high magnetic susceptibility. During deposition of Unit 2, lake levels continued to be relatively shallow and the lake experienced periods of higher alkalinity, conducive to precipitation of carbonates and deposition of some layers with abundant ostracods and gastropods. Terrigenous content progressively increased toward the top as indicated by higher magnetic susceptibility values and higher clastic content. The presence of intense mottling and root structures suggests multiple episodes of extremely low lake levels with subaerial exposure of the sediment at this site.

Unit 1 represents deposition in a lake dominated by sedimentation of organic-rich clay, silt, and diatomaceous facies. During this period, biogenic activity dominated over detrital watershed input.

(b) *Paleoenvironmental, paleovolcanism, and paleoclimate implications*

A preliminary chronological framework for the Chalco sequence has been established using a variety of dating techniques in several cores (Herrera 2011; Torres-Rodriguez et al. 2015, 2018; Martínez-Abarca 2019; Caballero et al. 2019) including:

- tephra layers: the Pómez Ocre (ca. 5 ^{14}C kyr), the Upper Toluca Pumice (UTP, 12,520 +/− 135 ^{14}C yr) (Arce et al. 2003), the Tutti Fruti Pumice (TFP, 17,670 cal ka BP) (Sosa-Ceballos et al. 2012), the "Great Basaltic Ash" (older than 34 ka), the "Pómez con Andesita" (ca. 14 ka) (Ortega Guerrero et al. 2015, 2017, 2018), and the White pumice (WP, 27,800 cal BP) (Siebe et al. 2017).
- Radiocarbon ages in pollen extracts from samples of the upper units (Ortega Guerrero et al. 2017; Torres-Rodriguez et al. 2018).
- U/Th date (76.74 ka) obtained from zircons collected from an ash layer at 69.84 mcc (75.28 mc in the MexiDrill-Chalco composite sequence) (Ortega Guerrero et al. 2017; Torres-Rodriguez et al. 2018).
- U/Th date obtained from a micritic carbonate sample containing few ostracods from 192.63 mc (165.73 mcc) (CHA16-1C_107Y-1 5.5 to 7.5 cm) yielding an age of 280 +/− 40 ka.

Extrapolation of sedimentation rates based on these preliminary chronological constraints suggests that onset of lacustrine deposition (top of Unit 15, 240.34 mcc, 309.15 mc) occurred between 364 and 505 ka, suggesting that the MexiDrill record will extend back to MIS 10 or MIS 13. This basal date was estimated by linear extrapolation of the two U/Th dates (zircon at 69.85 mcc and carbonate at 165.73 mcc) and considering the 40 ka error for the carbonate U/Th age. Ongoing work using 40Ar/39Ar dating of tephra and more radiocarbon dates in upper cores will refine this chronology. More saline diatom assemblages in diatomaceous facies and the occurrence of carbonate lithotypes and organic-rich layers suggest more arid conditions during interglacials, whereas higher humidity during glacial stages is indicated by freshwater diatom assemblages and the occurrence of finely laminated diatomaceous facies.

This preliminary view of glacial–interglacial conditions is consistent with the mid-Pleistocene sequence from Valles Caldera, New Mexico (Fawcett et al. 2011). In that sequence, the driest conditions occurred during the warmest phases of interglacials, with a significant reduction in summer precipitation, possibly in response to a poleward migration of the subtropical dry zone. In the South American tropics, the Lake Titicaca sequence showed a distinctive pattern during the last 400 ka of clastic, glacial-related facies deposited during wetter periods associated with glacier advances and relatively high lake level stages, and more carbonate-rich facies deposited in shallower conditions during warmer and relatively less humid interglacials (Fritz et al. 2007). In the shallow Lake Junín system, depositional variability during the last 700 ka is characterized by alternating intervals of carbonate lake-wetland facies (interglacial periods) and clastic-facies (glacial) (Cheng et al. 2020).

For the last glacial cycle, the age model is more robust. A number of studies in Lake Chalco indicate that the lake had high salinity prior to 27 ka BP and during the Last Glacial Maximum (LGM, 23 to 17 ka cal BP), and then deepened during the deglaciation, between 15 and 11 ka BP. During the Early Holocene, the lake became shallower and saline. These results suggest that lake chemistry is highly controlled by evaporation, with low evaporation periods, such as the LGM, showing lower salinity than intervals with high evaporation (end of MIS 3 and early MIS 1) which are saline. However, at Chalco, the LGM (27–15 ka cal BP) shows lower lake level conditions compared to the late glacial, consistent with lower fluxes of terrigenous material into the Cariaco Basin (Peterson et al. 2000).

In contrast, the results from the scientific drilling in Lake Peten Itza (ICDP PISDP project, Yucatan Peninsula, Guatemala) (Hodell et al. 2006) showed wet conditions during the Last Glacial Maximum, a transition to drier conditions during the late Glacial (including the Younger Dryas), and a generally wet Holocene, illustrating an opposite trend at the orbital scale. Interestingly, during the last 40,000 years at a millennial scale, the Chalco record has been interpreted to show a pattern of cold and dry conditions during colder northern hemisphere periods (stadials), comparable to other tropical northern hemisphere sites, further supporting the idea that

there is a strong coupling between tropical and North Atlantic regions (Caballero et al. 2019).

Volcanic activity has played a significant role in the origin and evolution of Lake Chalco. Multiple eruptions from a variety of source volcanoes are present within the record. Early volcanic output (Units 18 to 15, Fig. 5) was responsible for the deposition of over 200 m of volcanic and volcaniclastic material that originated and partially filled the basin. From Unit 13, over 16 m of primary and reworked tephra was deposited during a mostly stable lacustrine setting. From Unit 10, over 19 m of volcanic deposits occur within the core and from Unit 5, there is ca. 11 m of volcanically derived deposits. From Unit 2, volcaniclastic input had ceased, but many discrete tephra layers 1–50 cm can be identified; two of which are from well-documented eruptions from Popocatépetl and Nevado de Toluca volcanoes. Uplift of the Santa Catarina Sierra and the Chichinautzin Sierra volcanoes have mostly likely contributed to higher sediment input from these watersheds. Ortega-Guerrero et al. (2015) suggest that the monogenetic volcano Teuhtli, in the southwestern part of the Chalco lacustrine plain, is the origin of the so-called Gran Ceniza Basáltica tephra (dated older than 34 ka, Ortega Guerrero et al. 2015, 2017, 2018). Volcanic input occurred during the last 23 ka from Santa Catarina to the north, Xico to the east, and Teuhtli volcano to the west and are mostly likely sources of some of these tephras. Ongoing work on the tephrastratigraphy and volcanological history of the Mexico City region aims to address the volcanic contributors to the Basin of Mexico and their associated hazard implications for the region today.

Conclusions

The cores from the Basin of Mexico provide a continuous lacustrine record from tropical North America for the Upper Pleistocene and the early to mid-Holocene, including several glacial cycles and volcanic events. The >500 m long MexiDrill sequence illustrates the complex relationship between hydroclimate and volcanic activity in the evolution of lacustrine basins. The Chalco Basin originated as a result of volcanic activity and was infilled in the early stages by mostly volcaniclastic facies and lavas reworked by fluvial and alluvial processes. The thickness of this basal unit is over 200 m at the coring site and our preliminary chronology suggests a minimal age of 367 ka. Initial lacustrine deposition started in the Chalco Basin after this fluvial–alluvial phase and has continued into historic times. Deposition was dominated by alternating diatomaceous, carbonate, and organic-rich facies on scales of 10s of meters. Laminated diatomaceous facies occurred during phases with relatively deep depositional environments. Carbonate deposition marked more alkaline phases. Peat and organic-rich silt were deposited during shallow phases with development of wetlands in the basin.

The preliminary results of the MexiDrill cores show the high potential of the Chalco sequence to provide detailed information on millennial scale variability, the climate during past interglacials, and the relationships among rates of climate change, ecosystem responses, and biodiversity, as well as volcanic and tectonic evolution as the geochronology improves. The cores hold geologic, paleoenvironmental, and paleobiological information that is directly relevant to the >25 million people living in the Basin of Mexico who face challenges related to climate change, volcanic hazards, seismicity, and hydrology. Knowledge of the complex history of past environments can aid in developing policies to mitigate regional consequences of a warming world.

Acknowledgments The MexiDrill Field campaign was funded by ICDP, US National Science Foundation, and UNAM DGAPA-PAPIIT IV100215. M. S. gratefully acknowledges support from the Swiss National Science Foundation grant P300P2 158501.

References

Alaniz-Álvarez, S. A., & Nieto-Samaniego, A. F. (2005). El sistema de fallas Taxco-San Miguel de Allende y la Faja Volcánica Transmexicana, dos fronteras tectónicas del centro de Mexico activas durante el Cenozoico. *Boletín de la Sociedad Geológica Mexicana, 57*(1), 65–82.

An, Z., Colman, S. M., Zhou, W., Li, X., Brown, E. T., Jull, A. J. T., Cai, Y., Huang, Y., Lu, X., Chang, H., Song, Y., Sun, Y., Xu, H., Liu, W., Jin, Z., Liu, X., Cheng, P., Liu, Y., Ai, L., Li, X., Liu, X., Yan, L., Shi, Z., Wang, X., Wu, F., Qiang, X., Dong, J., Lu, F., & Xu, X. (2012). Interplay between the Westerlies and Asian monsoon recorded in Lake Qinghai sediments since 32 ka. *Nature Scientific Reports, 2*, 1–6.

Arce, J. L., Macías, J. L., & Vázquez-Selem, L. (2003). The 10.5 ka Plinian eruption of Nevado de Toluca volcano, Mexico: Stratigraphy and hazard implications. *Geological Society of America Bulletin, 115*, 230–248.

Arce, J. L., Layer, P. W., Lassiter, J. C., Benowitz, J. A., Macias, J. L., & Ramírez-Espinosa, J. (2013a). 40Ar/39Ar dating, geochemistry, and isotopic analyses of the Quaternary Chichinautzin volcanic field, south of Mexico City: Implications for timing, eruption rate, and distribution of volcanism. *Bulletin of Volcanology, 75*, 774.

Arce, J. L., Layer, P. W., Morales-Casique, E., Benowitz, J. A., Rangel, E., & Escolero, O. (2013b). New constraints on the subsurface geology of the Mexico City Basin: The San Lorenzo Tezonco deep well, on the basis of 40Ar/39Ar geochronology and whole-rock chemistry. *Journal of Volcanology and Geothermal Research, 266*, 34–49.

Arce, J. L., Layer, P., Martínez, I., Salinas, J. I., Macías-Romo, M. D. C., Morales-Casique, E., & Lenhardt, N. (2015). Geología and estratigrafía del pozo profundo San Lorenzo Tezonco and de sus alrededores, sur de la Cuenca de Mexico. *Boletín de la Sociedad Geológica Mexicana, 67*(2), 123–143.

Avendaño-Villeda, D. (2017). *Reconstrucción paleolimnológica en el registro del lago de Chalco durante la transición del Estadio Isotópico Marino 6 a 5 (MIS 6 a MIS 5)*, Mexico, Universidad Nacional Autónoma de Mexico, Mexico.

Bhattacharya, T., & Byrne, R. (2016). Late Holocene anthropogenic and climatic influences on the regional vegetation of Mexico's Cuenca Oriental. *Global and Planetary Change, 138*, 56–69.

Bloomfield, K. (1975). A late-quaternary monogenetic volcano field in Central Mexico. *Geologische Rundschau, 64*(1), 476–497.

Bradbury, J. P. (1989). Late Quaternary lacustrine paleoenvironments in cuenca de Mexico. *Quaternary Science Reviews, 8*, 75–100.

Brown, E. T., Werne, J. P., Lozano-García, S., Caballero, M., Ortega-Guerrero, B., Cabral-Cano, E., Valero-Garces, B. L., Schwalb, A., & Arciniega-Ceballos, A. (2012). Scientific drilling in the Basin of Mexico to evaluate climate history, hydrological resources, and seismic and volcanic hazards. *Scientific Drilling, 14*, 72–75.

Brown, E. T., Caballero, M., Fawcett, J. P. T., Lozano-García, S., Ortega, B., Pérez, L., Schwalb, A., Smith, V., Steinman, B. A., Stockhecke, M., Valero-Garcés, B., Watt, S., Wattrus, N. J., Werne, J. P., Wonik, T. H., Myrbo, A. E., Noren, A., O'Grady, R., Schnurrenburger, D., & The MexiDrill Team. (2019). Scientific drilling of Lake Chalco, Basin of Mexico (Mexidrill). *Scientific Drilling, 26*, 1–15. https://doi.org/10.5194/sd-26-1-2019.

Caballero, M., & Ortega-Guerrero, B. (1998). Lake levels since about 40,000 years ago at Lake Chalco, near Mexico City. *Quaternary Research, 50*, 69–79.

Caballero, M., Lozano, S., Ortega, B., Urrutia, J., & Macias, J. L. (1999). Environmental characteristics of Lake Tecocomulco, northern Basin of Mexico, for the last 50,000 years. *Journal of Paleolimnology, 22*, 399–411.

Caballero, M., Lozano-García, S., Ortega-Guerrero, B., & Correa-Metrio, A. (2019). Quantitative estimates of orbital and millennial scale climatic variability in Central Mexico during the last ~40,000 years. *Quaternary Science Reviews, 205*, 62–75.

Cabral-Cano, E., Osmanoglu, B., Dixon, T., Wdowinski, S., DeMets, C., Cigna, F., & Díaz-Molina, O. (2010). Subsidence and fault hazard maps using PSI and permanent GPS networks in Central Mexico. *International Association of Hydrological Sciences, Publication Series, 339*, 255–259.

Campos-Enríquez, J. O., Alatriste-Vilchis, D. R., Huizar-Álvarez, R., Marines-Campos, R., & Alatorre-Zamora, M. A. (2003). Subsurface structure of the Tecocomulco sub-basin (northeastern Mexico Basin), and its relationship to regional tectonics. *Geofísica Internacional, 42*(1), 3–24.

Chen, Ch., McGee, D., Woods, A., Pérez, L., Hatfield, R., Edwards, L. ,Cheng, H., Valero-Garcés, B., Lehmann, S., Stoner, J., Schwalb, A., Tal, I., Seltzer, G., Tapia, P., Abbott, M., Rodbell, D. (2020). U-Th dating of lake sediments: Lessons from the 700 ka sediment record of Lake Junín, Peru. *Quaternary Science Reviews, 244*, https://doi.org/10.1016/j.quascirev.2020.106422.

Colman, S. M., Yu, S.-Y., An, Z., Shen, J., & Henderson, A. C. G. (2007). Late-Cenozoic climate changes in China's western interior: A review of research on Lake Qinghai and comparison with other records. *Quaternary Science Reviews, 26*, 2281–2300.

De Cserna, Z., de la Fuente-Duch, M., Palacios-Nieto, M., Triay, L., Mitre-Salazar, L. M., & Mota-Palomino, R. (1988). Estructura geológica, gravimetría, sismicidad y relaciones neotectónicas regionales de la Cuenca de Mexico: Mexico, D.F., Universidad Nacional Autónoma de Mexico, Instituto de Geología, Boletín 104, 71 p.

Deino, A. L., Dommain, R., Keller, C. B., Potts, R., Behrensmeyer, A. K., Beverly, E. J., King, J., Heil, C. W., Stockhecke, M., Brown, E. T., Moerman, J., de Menocal, P., & Olorgesailie Drilling Project Scientific Team. (2019). Chronostratigraphic model of a high-resolution drill core record of the past million years from the Koora Basin, South Kenya Rift: Overcoming the difficulties of variable sedimentation rate and hiatuses. *Quaternary Science Reviews, 215*, 213–231.

Delgado-Granados, H., & Martín del Pozo, A. L. (1993). Pliocene to Holocene volcanic geology at the junction of Las Cruces, Chichinahutzin and Ajusco ranges southwest of Mexico City. *Geofísica Internacional, 34*, 341–351.

Enciso-De la Vega, S. (1992). Propuesta de nomenclatura estratigráfica para la cuenca de Mexico: Mexico, Universidad Nacional Autónoma de Mexico, Instituto de Geología. *Revista, 10*(1), 26–36.

Ezcurra, E. (1990). The Basin of Mexico. In B. L. Turner (Ed.), *The earth as transformed by human action, global and regional changes in the biosphere over the past 300 years* (pp. 577–588). New York: Cambridge University Press.

Fawcett, P. J., Werne, J. P., Anderson, R. S., Heikoop, J. M., Brown, E. T., Berke, M. A., Smith, S., Goff, F., Donohoo-Hurley, L. L., Cisneros-Dozal, L. M., Schouten, S., Sinninghe Damsté, J. S., Huang, Y., Toney, J., Fessenden, J., Wolde, G. G., Atudorei, V., Geissman, J. W., & Allen, C. D. (2011). Extended Megadroughts in the Southwestern United States during Pleistocene Interglacials. *Nature, 470*, 518–521. https://doi.org/10.1038/nature09839.

Ferrari, L., Orozco-Esquivel, T., Manea, V., & Manea, M. (2012). The dynamic history of the Trans-Mexican Volcanic Belt and the Mexico subduction zone. *Tectonophysics, 522–523*, 122–149.

Fritz, S., Baker, P., Seltzer, G., Ballantyne, A., Tapia, P., Cheng, H., & Edwards, L. (2007). Quaternary glaciation and hydrologic variation in the South American tropics as reconstructed from the Lake Titicaca drilling project. *Quaternary Research, 68*, 410–420.

García-Palomo, A., Carlos-Valerio, V., López-Miguel, C., Galván-García, A., & Concha-Dimas, A. (2006). Landslide inventory map of Guadalupe range, north of the Mexico Basin. *Boletín de la Sociedad Geológica Mexicana, 58*(2), 195–204.

García-Palomo, A., Zamorano, J. J., López-Miguel, C., Galván-García, A., Carlos-Valerio, V., Ortega, R., & Macías, J. L. (2008). El arreglo morfoestructural de la Sierra de Las Cruces, Mexico central. *Revista Mexicana de Ciencias Geológicas, 25*(1), 158–178.

Gierlowski-Kordesch, E., & Kelts, K. (Eds.). (1994). *Global geological record of Lake Basins* (World and regional geology series, 427 pp) (Vol. I. IGCP Project 324). Cambridge University Press.

Gierlowski-Kordesch, E., & Kelts, K. (2001). Lake Basins through space and time. *American Association of Petroleum Geologists Study Geology, 46*, 648 p.

Herrera-Hernández, D. (2011). *Estratigrafía y análisis de facies de los sedimentos lacustres del Cuaternario tardío en la cuenca de Chalco*. Mexico: Universidad Nacional Autónoma de Mexico, Ciudad de Mexico.

Hodell, D., Anselmetti, F., Brenner, M., Ariztegui, D., & the PISDP Science Party. (2006). The Lake Petén Itzá scientific drilling project. *Scientific Drilling, 3*, 25–29.

Jaimes-Viera, C., Martin del Pozzo, A. L., Layer, P. W., Benowitz, J. A., & Nieto-Torres, A. (2018). Timing the evolution of a monogenetic volcanic field: Sierra Chichinautzin, Central Mexico. *Journal of Volcanology and Geothermal Research, 356*, 225–242.

Koeberl, C., Peck, J., King, J., Milkereit, B., Overpeck, J., & Scholz, C. (2005). The ICDP lake Bosumtwi drilling project: A first report. *Scientific Drilling, 1*, 23–27.

Lake Baikal Paleoclimate Project Members. (1992). Initial results of U.S.-Soviet Paleoclimate Study of Lake Baikal. *Eos, Transactions, American Geophysical Union, 73*(43), 457–462.

Litt, T., Anselmetti, F. S., Baumgarten, H., Beer, J., Cagatay, N., Cukur, D., Damci, E., Glombitza, C., Haug, G., Heumann, G., Kallmeyer, J., Kipfer, R., Krastel, S., Kwiecien, O., Meydan, A. F., Orcen, S., Pickarski, N., Randlett, M. E., Schmincke, H.-U., Schubert, C. J., Sturm, M., Sumita, M., Stockhecke, M., Tomonaga, Y., Vigliotti, L., Wonik, T., & the PALEOVAN Scientific Team. (2012). 500,000 years of environmental history in Eastern Anatolia: The PALEOVAN drilling project. *Scientific Drilling, 14*, 18–29.

Lozano-García, M. S., & Ortega-Guerrero, B. (1994). Palynological and magnetic susceptibility records of Chalco Lake, Central Mexico. *Palaeogeography, Palaeoclimatology, Palaeoecology, 109*, 177–191.

Lozano-García, M. S., & Ortega-Guerrero, B. (1998). Late quaternary environmental changes of the central part of the Basin of Mexico; correlation between Texcoco and Chalco Basins. *Review of Paleobotany and Palynology, 99*, 77–93.

Lozano-García, S., Ortega-Guerrero, B., Caballero-Miranda, M., & Urrutia-Fucugauchi, J. (1993). Late Pleistocene and Holocene paleoenvironments of the Chalco lake, Central Mexico. *Quaternary Research, 40*, 332–342.

Lozano-García, S., Ortega, B., Roy, P. D., Beramendi-Orosco, L., & Caballero, M. (2015). Climatic variability in the northern part of the American tropics since the latest MIS 3. *Quaternary Research, 85*(2), 261–272.

Lozano-García, S., Brown, E., Ortega, B., Caballero, M., Werne, J., Fawcett, P. J., Schwalb, A., Valero-Garcés, B., Schnurrenberger, D., O'Grady, R, Stockhecke, M., Steinman, B., Cabral-Cano, E., Caballero, C., Sosa-Nájera, S., Soler, A., Pérez, L., Noren, A., Myrbo, A., Bücker, M., Wattrus, N., Arciniega, A., Wonik, T. H., Watt, S., Kumar, D., Acosta, C., Martínez, I., Cossio, R., Ferland, T., & Vergara-Huerta, F. (2017). Perforación profunda en el lago de Chalco: reporte técnico. *Boletín de la Sociedad Geológica Mexicana, 69*(2), 299–311.

Lugo-Hubp, J. (1984). Geomorfología del Sur de la Cuenca de Mexico, Instituto de Geografía, UNAM, Mexico. *Serie Varia, 1*(8), 1–95.

Lugo-Hubp, J., Mooser, F., Pérez-Vega, A., & Zamorano-Orozco, J. (1994). Geomorfología de la Sierra de Santa Catarina, D.F., Mexico. *Revista Mexicana de Ciencias Geológicas, 11*(1), 43–52.

Macías, J. L., Arce, J. L., García-Tenorio, F., Layer, P. W., Rueda, H., Reyes-Agustín, G., López-Pizaña, F., & Avellán, D. (2012). Geology and geochronology of Tlaloc, Telapón, Iztaccíhuatl and Popocatépetl volcanoes, Sierra Nevada, Central Mexico. In J. J. Aranda-Gómez, G. Tolson, & R. S. Molina-Garza (Eds.), The southern Cordillera and Beyond *Geological Society of America, field guide* (Vol. 25, pp. 163–193).

Martín del Pozzo, A. L. M. (1982). Monogenetic vulcanism in sierra Chichinautzin, Mexico. *Bulletin of Volcanology, 45*(1), 9–24.

Martínez Abarca, R. (2019). *Lago de Chalco: registro sedimentario y estratigráfico de sus etapas formativas*. Tesis de Maestria. UNAM, 128 p.

Martínez-Abarca, R., Ortega-Guerrero, B., Lozano-García, S., Caballero, M., Valero-Garcés, B., McGee, D., … Hodgetts, A. G. E. (2021). Sedimentary stratigraphy of Lake Chalco (Central Mexico) during its formative stages. International Journal of Earth Sciences, 1–21. https://doi.org/10.1007/s00531-020-01964-z

Melles, M., Brigham-Grette, J., Minyuk, P. S., Nowaczyk, N. R., Wennrich, V., DeConto, R. M., Anderson, P. A., Andreev, A. A., Coletti, A., Cook, T. L., Haltia-Hovi, E., Kukkonen, M., Lozhkin, A. V., Rosén, P., Tarasov, P. E., Vogel, H., & Wagner, B. (2012). 2.8 million years of Arctic climate change from Lake El'gygytgyn, NE Russia. *Science, 337*(6092), 315–320.

Metcalfe, S. E., Jones, M. D., Davies, S. J., Noren, A., & MacKenzie, A. (2010). Climate variability over the last two millennia in the North American monsoon region, recorded in laminated lake sediments from Laguna de Juanacatlán, Mexico. *The Holocene, 28*, 1195–1206.

Mosiño-Alemán, P. A., & García, E. (1974). The climate of Mexico. In R. A. H. Bryson & F. K. Hare (Eds.), *Climates of North America* (Vol. 2, pp. 345–405). New York: Elsevier.

Nixon, G. (1989). The geology of Iztaccíhuatl Volcano and adjacent areas of the Sierra Nevada and Valley of Mexico: Geological Society of America Special Paper 219, 58 p.

Ortega-Guerrero, B. (1992). *Paleomagnestismo, magnetoestrtifia y paleoecologia del Cuaternario tardio en el Lago de Chalco, Cuenca de Mexico (Tesis doctoral)*. Universidad Nacional Autónoma de Mexico.

Ortega-Guerrero, B., Lozano García, M., Caballero, M., & Herrera Hernández, D. A. (2015). Historia de la evolución deposicional del lago de Chalco, Mexico, desde el MIS 3. *Boletín de la Sociedad Geológica Mexicana, 67*(2), 185–201.

Ortega-Guerrero, B., Lozano-García, M. S., Herrera-Hernández, D., Caballero, M., Beramendi Orosco, L. E., Bernal, J. P., Torres-Rodríguez, E., & Avendaño-Villeda, D. (2017). Lithostratigraphy and physical properties of lacustrine sediments of the last ca. 150 kyr from Chalco Basin, Central Mexico. *Journal of South American Earth Sciences, 79*, 507–524.

Ortega-Guerrero, B., García, L. C., & Linares-López, C. (2018). Tephrostratigraphy of the late Quaternary record from Lake Chalco, Central Mexico. *Journal of South American Earth Sciences, 81*, 122–140.

Ortiz Zamora, D. D. C., & Ortega Guerrero, M. A. (2007). Origen y evolución de un nuevo lago en la planicie de Chalco: implicaciones de peligro por subsidencia e inundación de áreas urbanas en Valle de Chalco (Estado de Mexico) y Tláhuac (Distrito Federal). *Investigaciones geográficas, 64*, 26–42.

Oviedo de León, A. (1970). El Conglomerado Texcoco y el posible origen de la Cuenca de Mexico. *Revista del Instituto Mexicano del Petróleo, 2*, 5–20.

Pérez-Cruz, G. A. (1988). Estudio sismológico de reflexión del subsuelo de la Ciudad de Mexico: Mexico, D.F., Universidad Nacional Autónoma de Mexico, Tesis de Maestría, División de Estudios de Posgrado de la Facultad de Ingeniería, 83 p.

Peterson, L. C., Haug, G. H., Hughen, K. A., & Rohl, U. (2000). Rapid changes in the hydrologic cycle of the tropical Atlantic during the last glacial. *Science, 290*, 1947–1951.

Pi, T., Lozano-García, S., Caballero-Miranda, M., Ortega-Guerrero, B., & Roy, P. (2010). Discovery and characterization of a struvite layer in the Chalco paleolake, Mexico. *Revista Mexicana de Ciencias Geológicas, 27*(3), 573–580.

Pueyo, J. J., Sáez, A., Giralt, S., Valero-Garcés, B. L., Moreno, A., Bao, R., Schwalb, A., Herrera, C., Klosowska, B., & Taberner, C. (2011). Carbonate and organic matter sedimentation and isotopic signatures in Lake Chungará, Chilean Altiplano, during the last 12.3 kyr. *Palaeogeography, Palaeoclimatology, Palaeoecology, 307*, 339–355.

Ruiz-Angulo, A., & López-Espinoza, E. D. (2015). Estimación de la respuesta térmica de la cuenca lacustre del Valle de Mexico en el siglo XVI: un experimento numérico. *Boletín de la Sociedad Geológica Mexicana, 67*(2), 215–225.

Russell, J. M., Bijaksana, S., Vogel, H., Melles, M., Kallmeyer, J., Ariztegui, D., Crowe, S. A., Fajar, S. J., Hafidz, A., Haffner, D., Hasberg, A. K. M., Ivory, S. J., Kelly, C., King, J. W., Kirana, K. H., Morlock, M. A., Noren, A., O'Grady, R., & Ordonez, L. (2016). The Towuti Drilling Project: Paleoenvironments, Biological Evolution, And Geomicrobiology Of A Tropical Pacific Lake. *Scientific Drilling, 21*, 29–40.

Schnurrenberger, D., Russell, J., & Kelts, K. (2003). Classification of lacustrine sediments based on sedimentary components. *Journal of Paleolimnology, 29*, 141–154.

Scholz, C. A., Johnson, T. C., Cohen, A. S., King, J. W., Peck, J. A., Overpeck, J. T., Talbot, M. R., Brown, E. T., Kalindekafe, L., Amoako, P. Y. O., Lyons, R. P., Shanahan, T. M., Castañeda, I. S., Heil, C. W., Forman, S. L., McHargue, L. R., Beuning, K. R., Gomez, J., & Pierson, J. (2007). East African megadroughts between 135–75 kyr ago and implications for early human history. *Proceedings of the National Academy of Sciences, 104*, 16416–16421.

Schuster, M., Duringer, P., Ghienne, J.-F., Roquin, C., Sepulchre, P., Moussa, A., Lebatard, A.-E., Mackaye, H. T., Likius, A., Vignaud, P., & Brunet, M. (2009). Chad Basin: Paleoenvironments of the Sahara since the late Miocene. *Comptes Rendus Geosciences, 341*, 612–620.

Siebe, C. (2000). Age and archaeological implications of Xitle volcano, southwestern Basin of Mexico City. *Journal of Volcanology and Geothermal Research, 104*(1), 45–64.

Siebe, C., Macias, J. L., Abrams, M., Rodriguez, S., Castro, R., & Delgado, H. (1995). Quaternary explosive volcanism and pyroclastic deposits in East Central Mexico: Implications for future hazards. In *Guidebook of geological excursions: In conjunction with the annual meeting of the Geological Society of America, New Orleans, Louisiana, November 6–9, 1995* (pp. 1–48). Baton Rouge: Louisiana State University. Basin Research Institute. Center for Coastal Energy & Environmental Resources.

Siebe, C., Macías, J., Abrams, M., Rodríguez, S., & Castro, R. (1997). *Catastrophic prehistoric eruptions at Popocatépetl and Quaternary explosive volcanismin the Serdán-Oriental basin, east-central Mexico*. Pre-meeting excursion fieldtrip guidebook No 4, January 12–18: Puerto Vallarta, Mexico, International Association of Volcanology and Chemistry of the Earth's Interior (IAVCEI) General Assembly (88 pp.).

Siebe, C., Schaaf, P., & Urrutia-Fucugauchi, J. (1999). Mammoth bones embedded in a late Pleistocene lahar from Popocatépetl volcano, near Tocuila, Central Mexico. *Geological Society of America Bulletin, 111*, 1550–1562.

Siebe, C., Rodríguez-Lara, V., Schaaf, P., & Abrams, M. (2004). Geochemistry, Sr-Nd isotope composition, and tectonic setting of Holocene Pelado, Guespalapa and Chichinautzin scoria cones, south of Mexico City. *Journal of Volcanology and Geothermal Research, 130*, 197–226.

Siebe, C., Arana-Salinas, L., & Abrams, M. (2005). Geology and radiocarbon ages of Tláloc, Tlacotenco, Cuauhtzin, Hijo del Cuauhtzin, Teuhtli, and Ocusacayo monogenetic volcanoes in the central part of the Sierra Chichinautzin, Mexico. *Journal of Volcanology and Geothermal Research, 141*(3), 225–243.

Siebe, C., Salinas, S., Arana-Salinas, L., Macías, J. L., Gardner, J., y Bonasia, R. (2017). The~ 23,500 y 14C BP White Pumice Plinian eruption and associated debris avalanche and Tochimilco lava flow of Popocatépetl volcano, México. *Journal of Volcanology and Geothermal Research, 333*, 66–95.

Sosa-Ceballos, G., Gardner, J. E., Siebe, C., & Macías, J. L. (2012). A caldera-forming eruption~ 14,100 14 Cyr BP at Popocatepetl volcano, Mexico: Insights from eruption dynamics and magma mixing. *Journal of Volcanology and Geothermal Research, 213*, 27–40.

Stein, M., Ben-Avraham, Z., Goldstein, S., Agnon, A., Ariztegui, D., Brauer, A., Haug, G., Ito, E., & Yasuda, Y. (2011). Deep drilling at the dead sea. *Scientific Drilling, 11*, 46–47.

Stockhecke, M., Kwiecien, O., Vigliotti, L., Anselmetti, F. S., Beer, J., Namik Çağatay, M., Channell, J. E. T., Kipfer, R., Lachner, J., Litt, T., Pickarski, N., & Sturm, M. (2014). Chronostratigraphy of the 600,000 year old continental record of Lake Van (Turkey). *Quaternary Science Reviews, 104*, 8–17.

Torres-Rodríguez, E., Lozano-García, S., Roy, P., Ortega, B., Beramendi-Orosco, L., Correa-Metrio, A., & Caballero, M. (2015). Last glacial droughts and fire regimes in the central Mexican highlands. *Journal of Quaternary Science, 30*, 88–99.

Torres-Rodríguez, E., Lozano-García, S., Caballero-Miranda, M., Ortega-Guerrero, B., Sosa-Nájera, S. and Debajyoti-Roy, P. (2018). Pollen and non-pollen palynomorphs of Lake Chalco as indicators of paleolimnological changes in high-elevation tropical central Mexico since MIS 5. *Journal of Quaternary Science, 33*(8), 945–957.

Vazquez-Selem, L., & Heine, K. (2011). Late quaternary glaciation in Mexico. In J. E. Ehlers, P. L. Gibbard, & P. D. Hughes (Eds.), *Quaternary glaciations-extent and chronology: A closer look* (Vol. 15, pp. 849–861). Amsterdam: Elsevier.

Wagner, B., Wilke, T., Krastel, S., Zanchetta, G., Sulpizio, R., Reicherter, K., Leng, M. J., Grazhdani, A., Trajanovski, S., Levkov, Z., Reed, J., & Wonik, T. (2014). More than one million years of history in Lake Ohrid Cores. *Eos, Transactions American Geophysical Union, 95*(3), 25–26.

White, S. E. (1962). Late Pleistocene glacial sequence for the west side of Iztaccíhuatl, Mexico. *Geological Society of America Bulletin, 73*, 935–958.

White, S. E. (1987). Quaternary glacial stratigraphy and chronology of Mexico. *Quaternary Science Reviews, 5*(1–4), 201–206.

Zolitschka, B., Anselmetti, F., Ariztegui, D., Corbella, H., Francus, P., Lücke, A., Maidana, N., Ohlendorf, C., Schäbitz, F., & Wastegard, S. (2013). Environment and climate of the last 51,000 years—New insights from the Potrok Aike maar lake Sediment Archive Drilling Project (PASADO). *Quaternary Science Reviews, 71*, 1–12.

APPENDIX P3

Journal of Volcanology and Geothermal Research 421 (2022) 107413

Contents lists available at ScienceDirect

Journal of Volcanology and Geothermal Research

journal homepage: www.elsevier.com/locate/jvolgeores

Reconstructing the middle to late Pleistocene explosive eruption histories of Popocatépetl, Iztaccíhuatl and Tláloc-Telapón volcanoes in Central México

Ivan Sunyé-Puchol [a,b,*], Alastair G.E. Hodgetts [c], Sebastian F.L. Watt [c], José L. Arce [d], Dan N. Barfod [e], Darren F. Mark [e], Giovanni Sosa-Ceballos [f], Claus Siebe [g], Ross C. Dymock [e], Maarten Blaauw [h], Victoria C. Smith [a]

[a] Research Laboratory for Archaeology and the History of the Art (RLAHA), School of Archaeology, University of Oxford, Oxford, UK
[b] Department of Earth Sciences, Sapienza University of Rome, P. le Aldo Moro 5, 00185 Roma, Italy
[c] School of Geography, Earth and Environmental Sciences, University of Birmingham, Edgbaston, Birmingham, UK
[d] Instituto de Geología, Universidad Nacional Autónoma de México, Cd. de México, Mexico
[e] NEIF Argon Isotope Laboratory, Scottish Universities Environmental Research Centre (SUERC), East Kilbride, UK
[f] Unidad Michoacán del Instituto de Geofísica, Universidad Nacional Autónoma de México, Ciudad de México, Mexico
[g] Departamento de Vulcanología, Instituto de Geofísica, Universidad Nacional Autónoma de México, Cd. de México, Mexico
[h] The ^{14}CHRONO Centre for Climate, the Environment and Chronology, School of Natural and Built Environment, Queen's University Belfast, Belfast, UK

ARTICLE INFO

Article history:
Received 14 June 2021
Received in revised form 15 October 2021
Accepted 17 October 2021
Available online 26 October 2021

Keywords:
Chronostratigraphy
Glass chemistry
México
Popocatépetl
Tephra
Volcanic history

ABSTRACT

The Sierra Nevada Volcanic Range (SNVR), which includes Popocatépetl, Iztaccíhuatl and Tláloc Telapón volcanoes, has been the source of multiple large explosive eruptions that have dispersed tephra across central México. Several eruptions since 40 ka have previously been described, particularly from Popocatépetl, the southernmost volcano of the range. However, the longer term eruption history of the SNVR is poorly understood, due to challenges with correlating limited exposures of older pyroclastic sequences, and in discriminating between tephras derived from different sources. Here we describe two extensive exposures located between Popocatépetl and Iztaccíhuatl volcanoes, which provide a more complete and longer term explosive eruption record of the SNVR: the Nepopualco and Xalitzintla tephra sequences. A detailed tephrostratigraphic survey, together with new ^{40}Ar/^{39}Ar geochronological analyses and glass geochemistry, has permitted the characterization of identified eruption units further leading to the determination of geochemical fields for each volcano and the subsequent discernment of volcanic sources. Our results show that, since the collapse of the Los Pies Cone, which destroyed the Paleo Iztaccíhuatl edifice at 631 ± 44 ka (2σ), Iztaccíhuatl has produced at least 6 explosive rhyolitic eruptions. After coeval activity with Popocatépetl, between ~600 and ~500 ka, Iztaccíhuatl's explosive activity ceased while Popocatépetl's continued until present day. Popocatépetl has produced at least 27 medium to large explosive eruptions (inferred VEI 4 6), commonly of andesitic to dacitic compositions. Some of these eruptions deposited pumice fallout of >1 m thick in both the Nepopualco and Xalitzintla sequences (e.g. the 339 ± 16 ka [2σ] NT 23/WRT 7 eruption), suggesting that Popocatépetl has produced several eruptions similar in magnitude to the well known ~14 ka Tutti Frutti Pumice (a VEI 6 eruption with a ~5 km^3 tephra volume). The Popocatépetl and Iztaccíhuatl tephras are interbedded with deposits from more distal volcanoes, including some mafic to intermediate products of unknown sources (possibly from nearby monogenetic cones) and tephras related to the late Pleistocene eruptions of Tláloc Telapón (including the tephra layer produced by the San Valentin Ignimbrite, recently ^{40}Ar/^{39}Ar dated in this study at ~102 ka; 2σ). Our new chemical, stratigraphic and geochronologic investigations of these pyroclastic deposits, predominantly from Popocatépetl and Iztaccíhuatl, provide information on the scale and frequency of medium to large magnitude explosive eruptions over a longer time period than currently known and that have had potential to disperse tephra across central México since the middle to late Pleistocene. This new data can be used to determine the source of further unknown tephras in the region as well as to better assess the volcanic hazard to the densely populated megalopolis of México City.

© 2021 Elsevier B.V. All rights reserved.

* Corresponding author at: Department of Earth Sciences, Sapienza University of Rome, P. le Aldo Moro 5, 00185 Roma, Italy.
E-mail address: [redacted]

https://doi.org/10.1016/j.jvolgeores.2021.107413
0377-0273/© 2021 Elsevier B.V. All rights reserved.

1. Introduction

The metropolitan area of México City and its ~25 million inhabitants sit within the México Basin, which is surrounded by several Pleistocene Holocene volcanoes of the Trans Mexican volcanic belt (TMVB; Fig. 1). These volcanoes include Popocatépetl, Iztaccíhuatl, and Tláloc Telapón, which constitute the Sierra Nevada Volcanic Range (SNVR) to the east of the city. Their explosive activity, as well as those of volcanoes west of the México Basin, is fairly well constrained for the last 40 ka, as the associated deposits are clearly visible in some accessible exposures (e.g. Arce et al., 2003; Ortega Guerrero et al., 2018; Rueda et al., 2013; Siebe et al., 2017; Sosa Ceballos et al., 2012). However, their longer term eruption history is poorly understood, due to burial and erosion of older deposits, and challenges with correlating the available isolated exposures based on the deposit physical characteristics alone. These isolated exposures have not been studied in detail but contain valuable information that permits reconstruction of a longer and more complete record of explosive volcanism from the SNVR. This is important for evaluating the frequency of large magnitude explosive eruptions in the region, and for improving our knowledge of the temporal and spatial development of the major volcanic centres in the area.

Here we present detailed chronostratigraphic logs and the glass chemical composition of tephras recorded in two extensive exposures (Nepopualco and Xalitzintla sites), supplemented by a small number of shorter sequences, along the SNVR (Fig. 1b and c). We use these to characterize the proximal pyroclastic products of Iztaccíhuatl, Popocatépetl and Tláloc Telapón volcanoes (the three main edifices of the SNVR), and to extend and develop our understanding of their explosive eruption histories. These SNVR volcanoes have been the most active stratovolcanoes near the México basin during the middle to late Pleistocene (Cadoux et al., 2011; Macías et al., 2012). Our geochemical and geochronological data from Nepopualco and Xalitzintla constrain the range of magma compositions erupted from Popocatépetl and Iztaccíhuatl, and the timing of their eruptions over the last ~600 thousand years (ka), and constitute the first step to establishing a long term record of the medium to large explosive eruptions from the volcanoes surrounding México City.

2. Geological framework and volcanic evolution of the Sierra Nevada Volcanic Range

The México Basin (Fig. 1b) is an endorheic basin closed by the Sierra de Las Cruces Volcanic Range (SLCVR, Mora Alvarez et al., 1991; Arce et al., 2017) to the west, the SNVR to the east (Nixon, 1989; Cadoux et al., 2011; Macías et al., 2012), and the Sierra Chichinautzin Volcanic Field (SCVF, Siebe and Macías, 2004; Jaimes Viera et al., 2018) to the south. The basin closed ~1 Ma ago, when monogenetic cones and lavas of the SCVF blocked drainage to the south resulting in the lower México

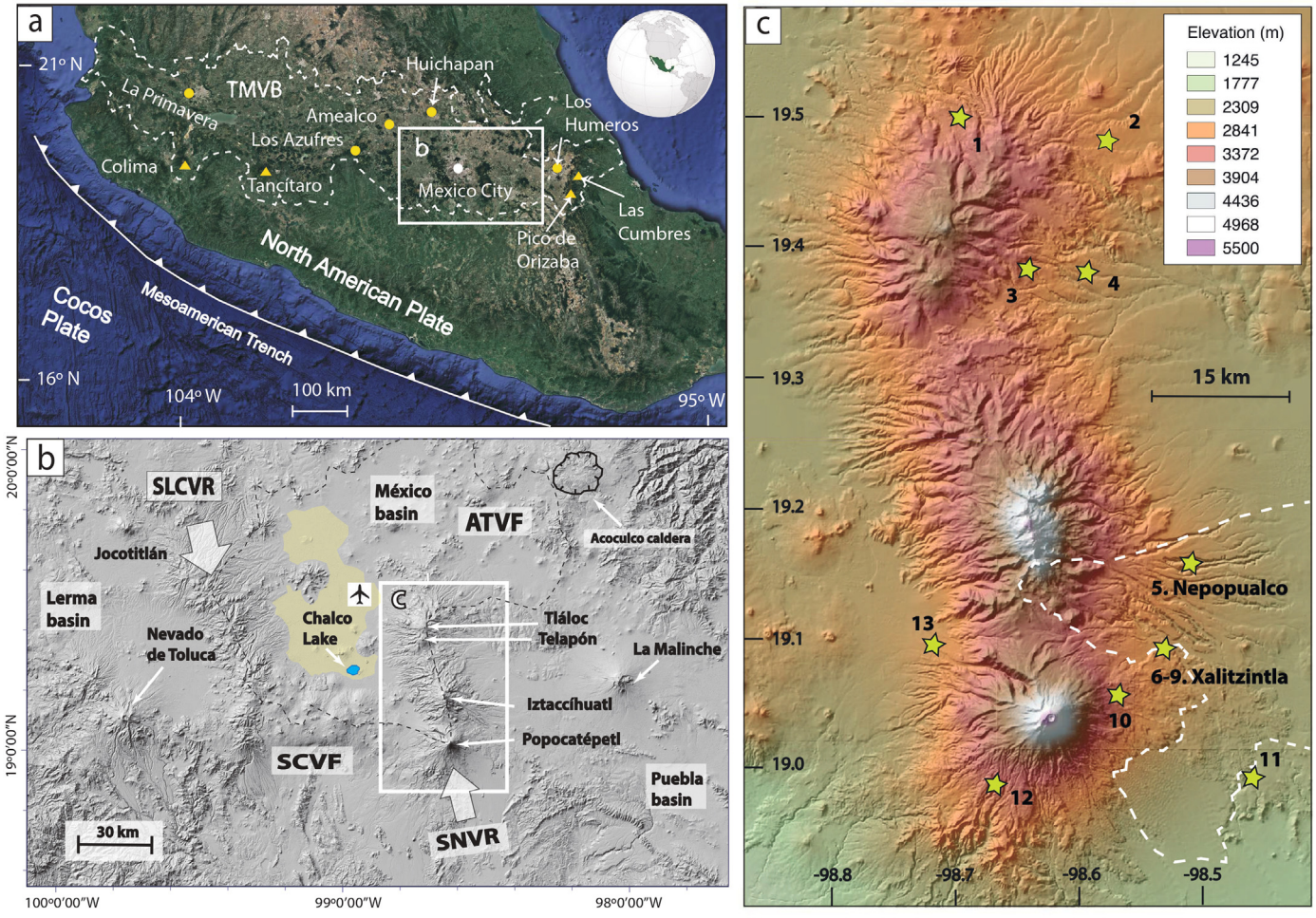


Fig. 1. a) Map of the Trans-Mexican Volcanic Belt (TMVB, area within white dashed line) showing main Quaternary stratovolcanoes (yellow triangles) and calderas (yellow dots), as well as México City (white dot); b) map of the metropolitan region of México City (yellow area) in the central TMVB, with the principal volcanic centres marked, including Popocatépetl, Iztaccíhuatl, and Tláloc-Telapón volcanoes along the Sierra Nevada Volcanic Range (SNVR). SCVF = Sierra Chichinautzin Volcanic Field, SLCVR = Sierra Las Cruces Volcanic Range, ATVF = Apan-Tezontepec Volcanic Field; and c) Digital elevation model (DEM) of the SNVR, showing the location of the studied outcrops (yellow stars; see Table 1 for outcrop locality details), including Nepopualco (n.5) and Xalitzintla sites (n.6–9). The white dashed line shows the limit of Los Pies Debris Avalanche Deposit (LPDAD; Macías et al., 2012).

Basin gradually filling with water (Mooser, 1963; Arce et al., 2013), and facilitating the rapid accumulation of lake sediments (e.g., Martínez Abarca et al., 2021). The magmatism around the México Basin is related to the 3rd phase of the TMVB (Fig. 1a), a 1000 km long Neogene continental arc related to the subduction of the Cocos and Rivera plates beneath the North American plate (Ferrari et al., 2012), active since 20 Ma. The locus of the TMVB migrated towards the trench at ~7 Ma, coinciding with an increase in silicic volcanism along the arc (Gómez Tuena et al., 2007).

2.1. Sierra Nevada Volcanic Range (SNVR)

The SNVR forms a N S oriented range (Fig. 1c) that divides drainage between the México Basin to the west and the Puebla basin to the east (Fig. 1b). There are four large volcanic edifices in the range (Fig. 1b and c); from north to south they are: Tláloc (the "Aztec's God of Rain" in the Náhuatl language), Telapón ("flat mountain" in Spanish), Iztaccíhuatl ("the woman in white" in Náhuatl), and Popocatépetl ("smoking mountain" in Náhuatl). In this paper we group Tláloc and Telapón volcanoes following the criteria of Macías et al. (2012), as they are perceived to be a single volcanic complex (i.e., compound volcano; Fig. 1c). Minor monogenetic vents are also present along the SNVR, such as El Papayo that emitted lava flows ~118 ka ago (Macías et al., 2012). The volcanic activity of the SNVR is thought to have commenced at its northern tip at Tláloc Telapón volcano at ~1.82 Ma (García Palomo et al., 2002; Cadoux et al., 2011; Macías et al., 2012). This age is based on dated lavas, which occur as blocks within pyroclastic density current (PDC) deposits, inferred to have originated from a Paleo Tláloc edifice (Cadoux et al., 2011). Subsequent activity migrated to the south and emplaced the Paleo Iztaccíhuatl volcano (Llano Grande, ~1.09 Ma; Cadoux et al., 2011) and then further south again, at the Paleo Popocatépetl volcano (Tlamacas/Nexpayantla, ~538 ka; Robin and Boudal, 1987; Conte et al., 2004; Sosa Ceballos et al., 2015; Delgado Granados et al., 2017). Although Tláloc Telapón is the site of the oldest activity of the SNVR, its eruptive history has continued until the very late Pleistocene, evidenced by deposits of ignimbrite forming eruptions that are <50 ka (e.g., Macías et al., 2012), indicating possible coeval activity with Iztaccíhuatl and Popocatépetl volcanoes (Rueda et al., 2013).

2.1.1. Tláloc Telapón

This volcanic complex comprises the lowest elevation edifices of the SNVR, at 4120 (Tláloc crater) and 4080 (Telapón crater) meters above sea level (m.a.s.l.). Located ~40 km east from the centre of México City, Tláloc Telapón is primarily composed of dacitic domes and lava flows, and surrounded by ignimbrites and lahar deposits (Cadoux et al., 2011). Radiometric dates of Paleo Tláloc lavas yield ages that extend to 1.82 Ma (Huddart and González, 2004; Rueda et al., 2007; García Tovar and Martínez Serrano, 2011; Cadoux et al., 2011 Macías et al., 2012). The modern Tláloc Telapón volcano began its construction at ~0.94 Ma by the effusion of dacitic lavas. This constructional phase ended with the extrusion of the summit lava flows and domes between 0.64 and 0.27 Ma (Cadoux et al., 2011; Macías et al., 2012). Activity at the Tláloc crater appears to have resumed at ~129 ka with the emission of rhyolitic lava flows and domes, that are distributed to the east of the present summit dome and within a 2.5 km wide horseshoe shaped collapse structure (Macías et al., 2012; Rueda et al., 2013).

Several authors have identified and characterized numerous pyroclastic deposits exposed proximally to Tláloc Telapón, which have been ascribed to that volcano (e.g., Cornwall, 1971; Huddart and González, 2004; Rueda et al., 2006; Meier et al., 2007; Macías et al., 2012). The youngest deposits include at least five Plinian eruptions that produced PDCs ranging in age from 44,000 to 21,000 ^{14}C yr BP (Macías et al., 2012). They are, from oldest to youngest: San Valentín (45,990 46,895 cal. yr BP, 95% probability [2σ]; 44,195 + 2020/−1615 yr BP), La Joya (40,668 42,807 cal. yr BP, 2σ; 37,220 ± 890 yr BP), P Mex (36,498 39,375 cal. yr BP, 2σ; 33,180 ± 550 yr BP), Multilayered White Pumice (MWP, 35,578 36,137 cal. yr BP, 2σ; 31,490 + 1995/−1595 yr BP) and Cuauhtémoc (29,909 30,065 cal. yr BP, 2σ; 25,640 + 275/−265 yr BP) ignimbrites. A relatively recent lava covers the crater at the summit of Tláloc (Rueda et al., 2013), and this is overlain by the ~5.4 cal. ka BP Ochre Pumice eruption deposit from Popocatépetl volcano (Siebe et al., 1996; Arana Salinas et al., 2010). This indicates that the last known activity at the volcano was pre 5 ka but given the occurrence of multiple late Pleistocene explosive eruptions and limited exposure in the region, Tláloc Telapón should still be considered an active volcano.

2.1.2. Iztaccíhuatl

The morphology of Iztaccíhuatl volcano has been likened to a woman lying on her back along a NNW SSE direction with her head to the north (Figs. 1c and 2a; Macías et al., 2012). This volcano is located ~47 km ESE from the international airport of México City (Fig. 1b), and consists of four peaks (Macías et al., 2012): La Cabeza (the head), El Pecho (the breast), Las Rodillas (the knees) and Los Pies (the feet). El Pecho is the highest peak and reaches 5286 m.a.s.l. The evolution of Iztaccíhuatl is divided into two main phases of cone growth: first, the Older Volcanic Series, including the activity of Paleo Iztaccíhuatl and the construction of Llano Grande, a shield volcano ~1.09 Ma (Nixon, 1989; Cadoux et al., 2011); and second, the Younger Volcanic Series, represented by lavas and domes emplaced between 600 and 80 ka (e.g., the El Solitario or Téyotl dacite flow; Nixon, 1988; Nixon, 1989; Macías et al., 2012).

A major event in the evolution of modern Iztaccíhuatl involved a sector collapse of the Los Pies cone (Siebe et al., 1995; García Tenorio, 2008). The volume of the debris avalanche deposit is estimated to be ~1.5 km^3, and the deposits cover an area of 550 km^2 on the SE flank of the volcano (Fig. 1c). Los Pies Debris Avalanche Deposit (LPDAD) is

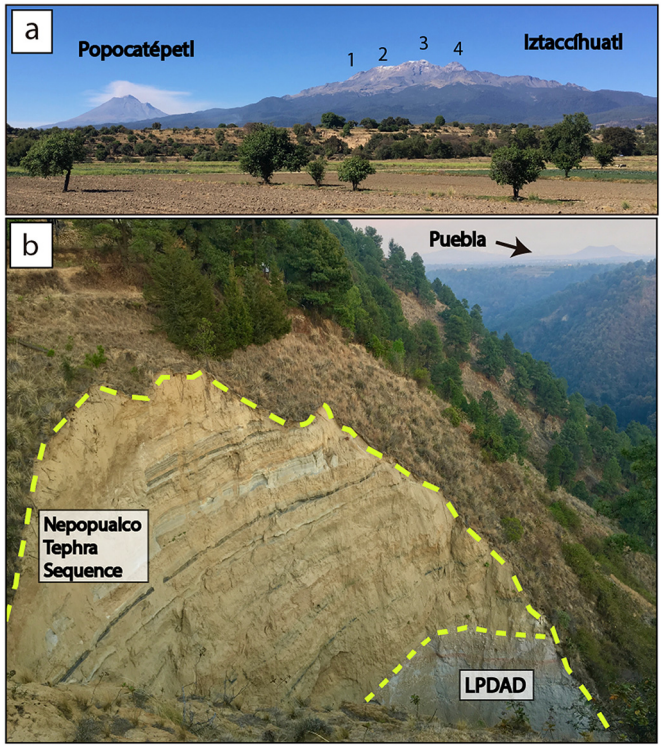


Fig. 2. a) Panoramic view of Popocatépetl and Iztaccíhuatl volcanoes (1 = Los Pies; 2 = Las Rodillas; 3 = El Pecho; and 4 = La Cabeza craters), located in the southern portion of the Sierra Nevada Volcanic Range (SNVR); b) tephra layers exposed by a landslide in the Nepopualco gully (outcrop 5 in Fig. 1c). This tephra sequence is interbedded by several remobilized volcanoclastic units and overlies the Los Pies Debris Avalanche Deposit (LPDAD) from Iztaccíhuatl volcano.

overlain by a sequence of PDCs block & ash flow type deposits associated with an eruption that followed the sector collapse (Macías et al., 2012; García Tenorio et al., 2012). An $^{40}Ar/^{39}Ar$ date on plagioclase from juvenile pumices of these PDCs yielded an age of 440 ± 190 ka for the LPDAD (Macías et al., 2012). All of these deposits are towards the base of Nepopualco gully, a key outcrop in this study and site of preliminary description by García Tenorio et al. (2015).

2.1.3. Popocatépetl

Popocatépetl is the most active volcano of the SNVR and considered one of México's most dangerous volcanoes (e.g., Macías et al., 2020), posing significant risk to the densely populated region as more than 25 million people who live within 100 km of its vent. Located ~45 km SE from México City, Popocatépetl volcano is 5452 m.a.s.l, forming the highest peak of the SNVR, and the second highest in México. After ~70 years of inactivity, Popocatépetl erupted again in 1994. This new activity typically comprises pulsating emissions of tephra and fumarolic gases (Love et al., 1998; Goff et al., 1998; Stremme et al., 2011), associated with subsequent episodes of rapid lava dome growth at the summit crater (Macías and Siebe, 2005; Gómez Vázquez et al., 2016), as well as some Vulcanian style explosions that emplace PDCs and lahar deposits (e.g., the 2001 explosion; Macías et al., 2020).

The modern edifice of Popocatépetl (Fig. 2a), which is mostly comprised of andesitic to dacitic lava flows (Robin, 1984), is constructed over the remnants of previous edifices (~538 ka; Conte et al., 2004; Sosa Ceballos et al., 2015; Delgado Granados et al., 2017). A sector collapse produced an extensive debris avalanche deposit to the south at ~27.8 cal. ka BP (~23.5 ka BP; Siebe et al., 2017). This was accompanied by the Plinian White Pumice fallout, also dispersed to the south (Robin and Boudal, 1987; Siebe et al., 1993, 1995, 2017). Since then, Popocatépetl has produced at least six Plinian eruptions, including the 16,796 18,201 cal yr BP Tutti Frutti caldera forming eruption (2σ; recalibrating dates of Siebe et al., 2017 and references) therein using the northern hemisphere calibration curve IntCal20 (Reimer et al., 2020) and OxCal (Bronk Ramsey, 2009), which is assumed to be the largest eruption from Popocatépetl based on its widespread distribution and distal thickness (e.g., 10 cm across the area in which México City is built, Siebe et al., 1999; Sosa Ceballos et al., 2012). Three Plinian eruptions have been identified during the Holocene: the 5333 5509 cal. yr BP Ochre Pumice (2σ; recalibrating dates of Robin and Boudal, 1987; Siebe et al., 1997; Arana Salinas et al., 2010), 2150 yr Lorenzo Pumice (Siebe and Macías, 2006), and 1100 yr BP Pink Pumice (Siebe et al., 1996). These eruptions had dispersal axes to the NE (Panfil et al., 1999; Siebe and Macías, 2006). Siebe et al. (1996) noted that these three Holocene eruptions began with the emplacement of dilute PDCs, followed by extensive pumice fallouts, and ended with the emplacement of dense PDCs.

2.1.4. Summary of the SNVR state of the art

The eruptive history of the SNVR, and particularly the record of the middle to late Pleistocene explosive activity of the stratovolcanoes, is still poorly constrained. For Tláloc Telapón, five late Pleistocene ignimbrites have been identified and dated (Cornwall, 1971; Huddart and González, 2004; Rueda et al., 2006; Meier et al., 2007; Macías et al., 2012), but the only radiometric ages available are radiocarbon ages, and the glass chemistry of the units have not yet been characterized. For Iztaccíhuatl, only the collapse of Los Pies Cone and its associated avalanche and ignimbrites are dated by $^{40}Ar/^{39}Ar$ (Macías et al., 2012). Other pyroclastic deposits attributed to Iztaccíhuatl have been recognised in the Nepopualco gully (Section 4.1.2; García Tenorio et al., 2012), but no chemical, stratigraphic or chronological results have been previously published. Popocatépetl has been the subject of several geological studies in the last three decades (e.g. Siebe et al., 1995, 1996, 2017; De la Cruz Reyna et al., 1995; Espinasa Pereña and Martín Del Pozzo, 2006; Arana Salinas et al., 2010; Sosa Ceballos et al., 2012), resulting in the stratigraphy of explosive eruptions for the last ~30 ka being fairly well constrained. However, there is a lack of detailed tephrostratigraphic studies, including glass chemistry, for older sequences, which are likely to date back to around 540 ka when the construction of the Paleo Popocatépetl is estimated to have commenced (e.g., Delgado Granados et al., 2017).

3. Methods

3.1. Fieldwork

Logging and sampling of the middle to late Pleistocene tephras from the SNVR volcanoes was carried out in March 2019. Published volcanological data was reviewed (e.g., Macías et al., 2012; Rueda et al., 2013; Sosa Ceballos et al., 2015; Siebe et al., 2017) and the fieldwork was supported by researchers from the National Autonomous University of México (UNAM). Fieldwork was undertaken in accessible, well exposed outcrops, near the villages of Nepopualco and Xalitzintla (Fig. 1). Roadcuts, deep gullies and quarries, that display multiple tephra units, bound by palaeosols often developed on top of reworked volcanoclastic materials (remobilized products of preceding eruptions that we have interpreted to have been redeposited by dilute lahars, or by other non volcanic processes) were the focus for this study. Thickness and grain size were estimated for each tephra layer, and the textures, colour and concentration of lithics were described. Samples of all units were taken for glass chemical analysis and thick and coarse tephras were sampled for $^{40}Ar/^{39}Ar$ dating. Localities are mapped on Fig. 1c (DEM of 15 × 20 m precision downloaded from INEGI México: https://www.inegi.org.mx), and described in Tables 1 3, including locality names and GPS coordinates. All tephra samples were given a unique sample number that was prefixed with 'MXC ' in the field, while individual eruption units (comprising a single event) were given a name that related to the specific site once determined, counting upwards from the base of the exposure (e.g., NT 1, for the oldest exposed tephra in the Nepopualco sequence).

3.2. Glass chemistry

Representative samples of multiple pumice clasts or of bulk ash were collected, depending on the grain size of the tephra layers, for glass chemical analysis. Tephras were sampled vertically across the deposit to provide a compositionally representative sample and include possible internal compositional variations. Samples were cleaned, crushed, sieved, dried, and mounted in epoxy resin. Mounts were polished and photographed with a petrographic microscope to assess shard morphology and mineralogy (Tables 1, 2, and 3). These mounts were then carbon coated prior to measuring the major element concentrations of glass shards using a JEOL JXA 8200 electron microprobe (EMP) equipped with five wavelength dispersive spectrometers at the Research Laboratory for Archaeology and the History of the Art (RLAHA), University of Oxford (UK). A beam accelerating voltage of 15 kV was used with a 6 nA current and a beam diameter of 10 μm. A narrower beam of 5 μm was used for a few highly vesicular samples. The EMP was calibrated using a suite of mineral standards. This calibration was verified using a range of secondary glass standards (ATHO G, StHs6/80 G and GOR128 G; see Supplementary Material 1; Jochum et al., 2006). Approximately 25 glass analyses, from separate glassy fragments derived from the crushed and sieved samples, were obtained for each of the 71 samples. This includes 25 previously undescribed tephra deposits from Nepopualco, 27 from Xalitzintla, and new characterization of 13 previously identified and named tephra deposits known to originate from Tláloc Telapón, Popocatépetl and Iztaccíhuatl (e.g. Macías et al., 2012; Siebe et al., 2017), sampled from other sites around the SNVR (Fig. 1c; and listed as the 13 non Nepopualco tephras in Table 1). All glass compositions were normalized to 100% for comparative purposes.

Table 1
Proximal deposits of Tláloc-Telapón, Popocatépetl, and Iztaccíhuatl volcanoes.

a) Description of some of the previous identified late Pleistocene pyroclastic deposits of Tláloc volcano

Unit		Description				Location				Age (ka)
Name	Sample	Deposit type	T (m)	Shard morphology	APCS (cm)	North	West	Locality	Outcrop	$^{14}C^{*}$ and Ar/Ar**
Cuauhtémoc Ign.	MXC-91	Poorly sorted pumice and lithics in a fine-medium ash matrix	24	PU, poor but large V	7.5	19.387378°	98.574229°	San Juan C.	4	25.6 ka BP *
MWP Ign.			33							31.5 ka BP *
	MXC-68	Large pumice and lithics-rich in a fine-medium ash matrix	4	PU, elongate V, MI	8	19.497127°	98.715072°	G. Amanalco	1	
	MXC-67	Poorly sorted pumice and lithics in a fine-medium ash matrix	25	PU, BW, elongate V	3	19.497127°	98.715072°	G. Amanalco	1	
	MXC-66	Stratified pumice fall-out/base	2.3	PU, rich in large V	2	19.497127°	98.715072°	G. Amanalco	1	
San Valentin Ign.			29.5							44.2 ka BP *
	MXC-50	Stratified pumice fall-out	2	PU, large V, BW,	1.5	19.477587°	98.575406°	Nanacamilpa	2	101 ± 2 ka **
	MXC-90	Pumice fall-out at the top of the sequence	28	PU, V, BW, CU	2	19.395989°	98.624235°	San Juan C.	3	
	MXC-88	Poorly sorted pumice and lithics in a fine-medium ash matrix	1.5	PU, large rounded V	4.5	19.396556°	98.624861°	San Juan C.	3	103 ± 3 ka **

b) Description of some of the previous identified late Pleistocene - Holocene pyroclastic deposits of Popocatépetl volcano

Unit		Description				Location				Age (ka)
Name	Sample	Deposit type	T (cm)	Shard morphology	APCS (cm)	North	West	Locality	Outcrop	C14
Pink-3 Pumice	MXC-118	Sub-unit of coarse non-graded pumice fallout with large lithics	45	SC, BW, large V, CU	2.2	18.987954°	98.453027°	Tianguismanalco	11	1.1 ka BP α
Pink-1 Pumice	MXC-114	Sub-unit of coarse angular, non-graded pumice fallout	18	SC, BW, V, CU	1.5	18.987954°	98.453027°	Tianguismanalco	11	1.1 ka BP α
Lorenzo Pumice	MXC-115	Yellowish pumice fallout of medium lapilli	80	SC, CU, V, BW, MI	1.1	19.040076°	98.563864°	Xalpilcayatl	10	2.1 ka BP β
Milky Pumice	MXC-120	Reversely graded, well-sorted, milky pumice fallout	55	PL, CU, rounded V, MI	2.1	19.075599°	98.731117°	S.P. Nexapa	13	14.3 ka BP γ
White Pumice	MXC-116	Massive whitish pumice fallout, bedded towards the top	110	SC, BW, large V, MI	1.6	18.962417°	98.663488°	Apatlahuaya	12	23.5 ka BP δ
Grey Pumice	MXC-121	Finely laminated beds of grayish pumice fallout rich in lithics	62	SC, BW, CU, large V, MI	2.4	19.075599°	98.731117°	S.P. Nexapa	13	14.3 ka BP γ

c) Description of the previous identified late Pleistocene pyroclastic deposits of Iztaccíhuatl volcano

Unit		Description				Location				Age (ka)
Name	Sample	Deposit type	T (m)	Shard morphology	APCS (cm)	North	West	Locality	Outcrop	Ar/Ar ages (2σ)
Los Pies B&A flow	MXC-02	Reverse grading pumice fall deposit	0.85	SC, rich large/rounded V	2.5	19.149749°	98.508040°	Nepopualco	5	631 ± 44 ka **
Nepopualco dry PDCs	MXC-03	Cross-Stratification ash flows (wet surges)	0.15	2 types 1 PL and 1 SC	1.5	19.149749°	98.508040°	Nepopualco	5	
Nepopualco wet PDCs	MXC-04	Interbedded medium to coarse ash flows	0.06	2 types 1 PL and 1 SC	0.1	19.149749°	98.508040°	Nepopualco	5	
Nepopualco fall	MXC-05	Block and ash flow deposit (PDC sequence)	>30	SC, PL, CU, BW, MV	5	19.149749°	98.508040°	Nepopualco	5	440 ± 190 ka ***

T = Thickness, PU = Pumiceous, PL = Platy, CU = Cuspate, BW = Bubble-Walled, F = Fluted, V = Vesicular, MV = Microvesicular, MI = Microlite Inclusions (McLean et al., 2018; and Smith et al., 2019) APCS = Average Pumice Clast Size (approximate); MWP = Multilayered White Pumice (Rueda et al., 2013); * ^{14}C ages from Macías et al., 2012; ** Ar/Ar ages from this study.*** Ar/Ar ages from Macías et al., 2012.
α = Siebe et al., 1996; β = Siebe and Macías, 2006; γ = Sosa-Ceballos et al., 2012; δ = Siebe et al., 2017.
The mineral assemblage of Tlaloc deposits is quartz + sanidine + plagioclase + biotite, with some horblende and Fe-Ti oxides.
The mineralogy content of Izta deposits is plagioclase + hornblende + pyroxene + Fe-Ti oxides and some biotites.The mineral assemblage of Popocatéptl deposits is plagioclase + pyroxene + TiFe oxides

3.3. Argon Argon geochronology

Samples for $^{40}Ar/^{39}Ar$ dating were taken from the thickest and coars est tephras with large phenocrysts (including hornblende, plagioclase and sanidine). These samples were collected from units in the Nepopualco Sequence and the various Xalitzintla outcrops. The strati graphically oldest Tláloc ignimbrite was also sampled for dating. Clean pumice clasts were separated from bulk samples and crushed to obtain juvenile hosted mineral concentrations. Crushed samples were sieved to 250 500 μm fractions then washed using an ultrasonic bath to re move adhering dust particles. Bulk feldspar was magnetically separated from amphiboles and pyroxenes and subsequently separated into sanidine and plagioclase fractions using lithium metatungstate (LMT) heavy liquid (density ~3.7 mg/l). Feldspars and amphibole were acid leached following methods of Siegburg et al. (2018) prior to being hand picked under a binocular microscope to avoid inclusion rich or al tered crystals. Samples were irradiated at the Oregon State University (OSU) Irradiation Center using the CLICIT facilities and analysis was car ried out in the NEIF Argon Isotope Laboratory at SUERC. Single crystals of sanidine were fused at ~7 W in a single step. Plagioclase and horn blendes were analysed in multigrain aliquots of ~30 crystals that were heated in two steps: a low power (0.6 W) degassing step followed by

Table 2
Description of tephras recorded in Nepopualco sequence (outcrop 5 in Fig. 1c), located 14 km East of Iztaccíhuatl and 19 NE of Popocatépetl (19.149749° N, 98.508040° W).

Tephra unit	Sample	Deposit type	T (m)	Shard morphology	Mineralogy	APCS (cm)	Volcanic Source	$^{40}Ar/^{39}Ar$ ages (2σ)
NT-25	MXC-48	Well-sorted medium ash fall rich in biotite	0.15	PU, BW, rich elongate V, F,	plag, hbl, px, ox, bi, qz	0.05	Uncertain	
NT-24	MXC-47	Well-sorted fine coignimbritic ash	0.1	PU, large V, BW,	qz, san, bi, hbl, ox	0.01	Tláloc-Telapón	
NT-23	MXC-46	White fallout unit of fine to medium lapilli pumice	1.6	PL, BW, CU, large V,	plag, px and ox	1.6	Popocatépetl	369 ± 22 ka
NT-22	MXC-45	Well-sorted orange pumice fall rich in lithics	0.77	SC, PL, CU, BW, MI	plag, hbl, px, ox	3.7	Popocatépetl	
NT-21	MXC-44	Lithic-rich orange pumice fallout of coarse lapilli	0.35	PL, CU, large V, BW, MI	plag, px and ox	3.5	Popocatépetl	
NT-20	MXC-43	Dark fallout unit of fine lapilli rich in lithics (70%)	0.08	PL, large/rounded V, MV, CU	plag, px and ox	0.5	Popocatépetl	
NT-19	MXC-42	Well-sorted white pumice fall poor in lithics	0.3	SC, BW, large V, MI	plag, hbl, px, ox	1.8	Popocatépetl	
NT-18	MXC-41	Normal graded and layered pumice and ash fall	0.9	SC, high V, CU, BW,	plag, px and ox	2.9	Popocatépetl	
NT-17	MXC-39/40	Pumice fall with two ash layers in the middle	0.51	SC, PL, elongate V, CU, rich MI	plag, px and ox	2.8	Popocatépetl	
NT-16	MXC-38	Reverse graded of white ash to fine lapilli	0.27	PU with MV, and SC, large V	plag, px and ox	0.8	Popocatépetl	
NT-15	MXC-37	Lithic-rich massive pumice fallout	0.15	PL, MV, CU, BW, MI	plag, hbl, px, ox	1.4	Popocatépetl	620 ± 52 ka
NT-14	MXC-36	Reverse grading pumice fall deposit	0.08	2 types: 1 PL and 1 SC	plag, hbl, px, ox	1.5	Popocatépetl	
NT-13	MXC-35	Normal graded pumice fall with ash fall at top	0.25	PL, BW, CU, V, MI	plag, hbl, px, ox, qz	1.2	Iztaccíhuatl	
NT-12	MXC-15	Coarse pumice fallout lithic-rich	0.55	SC, BW, rich V, MI	plag, hbl, px, ox	3	Popocatépetl	
NT-11	MXC-14	Normal graded white pumice with PDC at top	0.7	BW, CU, rich V	plag, hbl, px, ox	2.5	Iztaccíhuatl	
NT-10	MXC-13	Bedded pumice fall lithic-rich	0.9	SC, large V, CU, BW, MI	plag, px and ox	2.8	Uncertain	
NT-9	MXC-12	Mafic scoria and ochre pumice fallout	0.35	SC, PL, CU, BW, MI	plag, px and ox	2.7	Popocatépetl	
NT-8	MXC-11	Lense of PDC deposit	0.8	SC, CU, elongated V, MV	plag, hbl, px, ox, qz	3.2	Iztaccíhuatl	
NT-7	MXC-10	Bedded pumice fall rich in lithics	0.7	SC, BW, CU, rich V, MI	plag, hbl, px, ox, bi	2.8	Uncertain	
NT-6	MXC-09	Grey pumice fallout	0.18	PL, SC, large/elongated V, BW	plag, hbl, px, ox	2.4	Popocatépetl	
NT-5	MXC-08	Well-sorted dark coarse ash	0.3	PL, large/poor V, MI	plag, px and ox	0.2	Mono. Cone	
NT-4	MXC-07	Well-sorted white pumice fall	0.52	SC, PL, BW, elongated V, MI	plag, hbl, px, ox, bi, qz	1.6	Iztaccíhuatl	
NT-3	MXC-06	Well-sorted lithic-rich yellow pumice fall	0.35	SC, PL, CU, BW, high V, MI,	plag, hbl, px, ox	1.3	Iztaccíhuatl	
NT-2/ Nepopualco	MXC-05	Reverse grading pumice fall deposit	0.85	SC, rich large/rounded V,	plag, hbl, px, ox	2.5	Iztaccíhuatl	631 ± 44 ka
Ignimbrite (dry/wet	MXC-04	Cross-Stratification ash flows (wet surges)	0.15	2 types? 1 PL and 1 SC	plag, hbl, px, ox, qz	1.5	Iztaccíhuatl	
PDc's and fallout)	MXC-03	Interbedded medium to coarse ash flows	0.06	2 types? 1 PL and 1 SC	plag, hbl, px, ox	0.1	Iztaccíhuatl	
NT-1 / Los Pies B&A	MXC-02	Block and ash flow deposit (PDC sequence)	>30	SC, PL, CU, BW, MV	plag, hbl, px, ox, bi	5	Iztaccíhuatl	*440 ± 190 ka
LPDAD	MXC-01	Debris Avalanche with large blocks	>10	PL, big/poor V, MI	plag, hbl, px, ox, qz	20	Iztaccíhuatl	

PU = Pumiceous, PL = Platy, CU = Cuspate, BW = Bubble-Walled, F = Fluted, V = Vesicular, MV = Microvesicular, MI = Microlite Inclusions (McLean et al., 2018; and Smith et al., 2019)
APCS = Average Pumice Clast Size (approximative, as a guidance), LPDAD = Los Pies Debris Avalanche deposit (Macías et al., 2012), T = Thickness, * Age from Macías et al. (2012).

a fusion step at ~7 W. Sample aliquots with high age uncertainties (>100%) or negative ages were rejected; this resulted in <5% of the analyses being removed from the data set. The remaining data were then filtered principally against MSWD criteria (see Supplementary ma terial 2). Approximately 25 analyses of aliquots were plotted together (see Supplementary material 3) in order to achieve a precision of ~10% (2σ) for each sample.

4. Field tephrostratigraphy

4.1. Characterization of previously identified proximal deposits of the SNVR volcanoes

Several sites around the SNVR (Fig. 1) were visited in order to sam ple deposits of large explosive eruptions from previously identified ex posures. These samples were analysed to provide insights into the glass compositional range of each SNVR volcano, which could be used to in terpret the origin of other previously undescribed tephras from our study sites (Table 1).

4.1.1. Tláloc Telapón

The fieldwork around Tláloc Telapón was focused on sampling the deposits of previously identified late Pleistocene ignimbrites (Rueda et al., 2007; 2013; García Tovar and Martínez Serrano, 2011; Macías et al., 2012) to chemically characterize their glass chemistry (outcrops 1 to 4 in Fig. 1c). Three separate ignimbrites (MWP, San Valentín, and Cuauhtémoc) were sampled from several sites. The oldest of these, the San Valentín Ignimbrite, was sampled for both radiocarbon and $^{40}Ar/^{39}Ar$ dating to corroborate the previously published radiocarbon age of ~46 cal. ka BP (Macías et al., 2012), particularly because the age is close to the upper limit of the radiocarbon method and may thus be less reliable. Details of the Tláloc PDCs and the physical parameters of the associated eruptions (e.g., distribution, column height, and magma volume) are documented in Macías et al. (2012) and Rueda et al. (2013).

4.1.2. Popocatépetl and Iztaccíhuatl

Four previously described pumice fall deposits (Pink, Lorenzo, White and Tutti Frutti) from <30 ka Plinian explosive eruptions of Popocatépetl (e.g. Sosa Ceballos et al., 2012; Siebe et al., 2017), were sampled from four separate sites around the volcano (Fig. 1). Two subunits from the

Table 3
Description of Xalitzintla tephras by outcrops (6 to 9 in Figs. 1c and 6a): East of the Restaurant (19.078794° N, 98.506966° W), West of the Restaurant (19.080099° N, 98.507531° W), Fork in the Road (19.084910° N, 98.514919° W) and Xalitzintla Quarry (19.084671° N, 98.520788° W). Tephras and outcrops are in stratigraphic order, from oldest at the base to youngest at top.

Outcrop	Unit	Sample	Deposit type	T (m)	Shard morphology	Mineralogy	APCS (cm)	Volcanic source	$^{40}Ar/^{39}Ar$ ages (2σ)
East of Restaurant									
	ERT-7	MXC-24	Well-sorted pumice fallout of coarse lapilli	0.30	SC, BW, large V, CU	plag, px, ox	2.2	Popocatépetl	
	ERT-6	MXC-23	Fallout of medium pumice lapilli	0.35	SC, CU, rich V, BW, rich MI	plag, hbl, px, ox	1.5	Popocatépetl	
	ERT-5	MXC-22	Medium to coarse pumice fallout	0.20	BW, CU, elongate V, MI	plag, px, ox	2	Popocatépetl	
	ERT-4	MXC-21	Grey layer of coarse ash	0.05	PL, CU, rounded V, MI	plag, px, ox	0.5	Popocatépetl	
		MXC-19	Coarsest sub-unit at the base of the fallout sequence		SC, BW, CU, large V, MI	plag, px, ox	2.4	Popocatépetl	236 ± 24ka
	ERT-2	MXC-18	Uppermost sub-unit of a normal-graded pumice fallout	0.22	SC, BW, CU, large V, MI	plag, px, ox	1	Popocatépetl	
		MXC-17	Lowermost sub-unit, normal graded with a lithic-rich top	0.15	SC, large V, MI, MV	plag, px, ox	2.3	Popocatépetl	
	ERT-1	MXC-16	Normal graded orange fallout with two types of pumice	0.43	PL, CU, BW, elongate V,	plag, px, ox	1.8	Popocatépetll	
West of Restaurant									
	WRT8	MXC34	Medium to coarse fallout with a basal grey ash layer	0.55	SC, BW, rich V, large MI	plag, px, ox	2.4	Popocatépetl	
	WRT-7	MXC-33	Massive white yellowish medium lapilli	1.10	BW, CU, V, MI	plag, px, ox	1.2	Popocatépetl	354 ± 58ka
	WRT-6	MXC-32	Light-grey laminated sequence of pumice fallouts	1.20	SC, BW, large V, MI	plag, hbl, px, ox	1.3	Popocatépetl	431 ± 40 ka
	WRT-5	MXC-31	white medium lapilli pumice fallout finer at top	0.35	BW, CU, rich V, rich MI	plag, px, ox	1.9	Popocatépetl	
	WRT-4	MXC-30	Lithic-rich fallout unit of coarse grey pumice	0.35	PL, large rounded V, MV	plag, px, ox	2.8	Popocatépetl	
	WRT-3	MXC-29	Well-sorted reddish coarse ash fall	0.10	SC, BW, large V, MI, few MV	plag, px, ox	0.3	Popocatépetl	
		MXC-28	Dark-grey medium pumice lapilli fallout	0.40	SC, PU, BW, CU, large V, MI	plag, hbl, px, ox	1.4	Popocatépetl	
	WRT-2	MXC-27	Medium pumice lapilli fall with a lithic-rich basal layer	0.05	SC, BW, V, rich in MI	plag, px, ox	1.5	Popocatépetl	
		MXC-26	Reverse graded pumice medium-to-coarse lapilli	0.25	SC, BW, V, MV, MI	plag, px, hbl, ox	2	Popocatépetl	
	WRT-1	MXC-25	Scoria fallout layer	0.03	SC, BW, CU, V, rich MI	plag, px, ox	1.5	Popocatépetl	
Fork in the Road									
	FRT-6	MXC107	Coarse grey ash layer with coarse sub-rounded pumices	0.12	PL, elongate V, MI	plag, px, ox, qz	0.4	Popocatépetl	
	FRT-5	MXC-106	Reverse graded yellowish pumice fallout lithic-rich	0.23	PL, PU, large V, MV, MI	plag, px, ox	2.2	Uncertain	
	FRT-4	MXC-105	Brown pumice fallout of coarse lapilli and lithic-rich	0.10	SC, BW, V, MV, rich MI	plag, px, ox	2.7	Popocatépetl	
	FRT-3	MXC-104	Grey bedded pumice fallout sequence with granoclass.	1.20	PU, rich V, rich MI	plag, px, ox	1.2	Popocatépetl	
	FRT-2	MXC-103	Pumice fallout of medium to coarse sub-angular lapilli	0.15	SC, BW, C, large/rounded V	plag, px, ox, qz	2.1	Uncertain	
	FRT-1	MXC-102	Normallly graded pumice fallout with lithic layer at top	1.00	SC, large/rounded V, rich MI	plag, px, ox, hbl	1.5	Iztaccíhuatl	
Xalitzintla Quarry									
	XQT-7	MXC-101	Dark brown coarse pumice fallout rich in lithics	0.19	PU, rounded V, MI	plag, px, ox	2.4	Popocatépetl	
	XQT-4	MXC-100	Dark pumice fallout, granoclassified, rich in fine lithics	0.08	SC, PL, BW, larg V, rich MI	plag, px, ox	1.1	Mono. Cone	
	XQT-3	MXC-99	White pumice fallout, lithic-poor and inverse gradation	0.39	BW, large V, some MV, MI	plag, px, ox	1.8	Iztaccíhuatl	
	XQT-2	MXC-98	Dark Coarse ash fall	0.26	PL, CU, large V, MI	plag, px, ox	0.3	Uncertain	
	XQT-1	MXC-97	Dark-grey scoria of medium lapilli size	0.22	PL, CU, poor/large V , rich iMI	plag, px, ox	1.5	Mono. Cone	

PU = Pumiceous, SC = Scoriaceous, PL = Platy, CU = Cuspate, BW = Bubble-Walled, F = Fluted, V = Vesicular, MV = Microvesicular, MI = Microlite Inclusions (McLean et al., 2018; and Smith et al., 2019); APCS = Average Pumice Clast Size (aproximative, as a guidance), T = Thickness.

Tutti Frutti and Pink Pumice deposits were analysed (Pink 1 and 3 from the Pink Pumice; and the Milky and Grey Pumice units from the Tutti Frutti eruption; Table 1). Due to limited exposures, challenging access, and the close spacing between volcanic sources, only one pyroclastic deposit has been previously described and categorically ascribed to Iztaccíhuatl, the Los Pies B&A Flow (Table 1; Macías et al., 2012; García Tenorio et al., 2012, 2015). As multiple eruptions help to better classify the compositional range of the deposits of a volcano, we have included an additional, previously undescribed deposit towards the base of the Nepopualco sequence: the Nepopualco Ignimbrite (Table 1, Fig. 3). This deposit is comprised of dilute PDC deposits and a pumice fall (Nepopualco Fall, Table 1, Fig. 3), interpreted to have been produced in a single eruptive event (i.e. in conformable contact and not separated by a paleosol and/or reworked deposits). The following observations suggest Iztaccíhuatl was the source: (1) The geomorphology of the gully lies within a deep fan to the East of Iztaccíhuatl (see Section 4.2 and Fig. 1c). Topographically, due to PDCs being gravity driven currents, the location of this primary ignimbrite deposit implies emplacement from the west, and the local terrain of the Puebla basin does not feasibly support a transport direction from any other volcano in the SNVR (Fig. 1c); (2) Glass data from these deposits are similar to the underlying Los Pies B&A Flows (documented below; Fig. 10, Table 4); (3) $^{40}Ar/^{39}Ar$ Ages from the Nepopualco Ignimbrite, 631 ± 44 ka [2σ], are consistent with known activity from Iztaccíhuatl, and older than any dated deposits of Paleo Popocatépetl (~538 ka; Robin and Boudal, 1987; Conte et al., 2004; Sosa Ceballos et al., 2015; Delgado Granados et al., 2017).

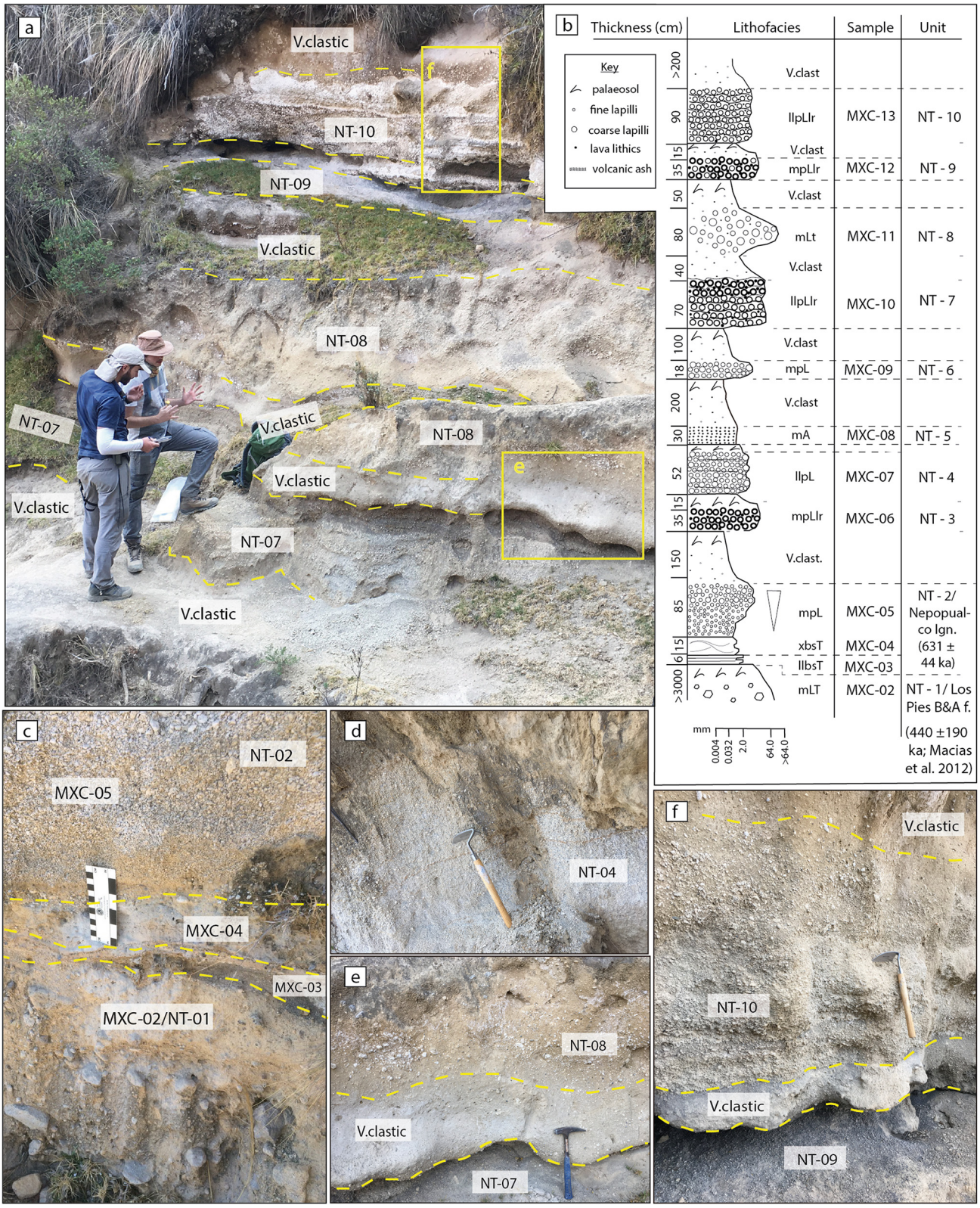


Fig. 3. a) Outcrop displaying several units of the lowermost part of the Nepopualco gully sequence. b) Stratigraphic log of the Lower Nepopualco Tephras (Legend: mLT = massive Lapilli Tuff, llsT = parallel-stratified tuff, xsT = cross-stratified tuff, mpL = massive pumice Lapilli, V.clast = volcanoclastic, mpLlr = mpL lithic-rich, llpL = parallel stratified pumice lapilli, mA = massive Ash and llpLlr = llpL lithic-rich; nomenclature based on Branney and Branney and Kokelaar, 2002). V.clast in the photographs/logs indicates a reworked (non-primary) volcanoclastic unit, bounding the units that are interpreted as primary eruption deposits. Details of: c) the first pyroclastic layers (MXC-3 to 5 of NT-2) above the Los Pies PDCs (NT-1), d) the NT-4 white fallout, e) the NT-8 above reworked volcaniclastic materials deposited on top of NT-7, and f) the layered NT-10 fallout above the mafic NT-9 fall with reworked materials in-between.

Table 4
Major element composition from the proximal deposits of Tláloc, Popocatépetl, and Iztaccíhuatl volcanoes.

a) Major element composition (average and standard deviation) of the matrix glass (anhydrous) from the Tláloc-Telapón volcano proximal deposits

Sample	MXC-91		MXC-68		MXC-67		MXC-66		MXC-50		MXC-90		MXC-88	
Eruption	Cuauhtémoc Ign.		MWP Ign.		MWP Ign.		MWP Ign.		San Valentin Ign.		San Valentin Ign.		San Valentin Ign.	
n	24		21		22		23		28		27		22	
SiO_2	77.14	*0.18*	77.07	*0.22*	77.05	*0.35*	77.09	*0.21*	77.06	*0.28*	77.16	*0.22*	77.21	*0.31*
TiO_2	0.03	*0.02*	0.03	*0.02*	0.03	*0.02*	0.03	*0.03*	0.03	*0.03*	0.02	*0.02*	0.03	*0.03*
Al_2O_3	13.45	*0.08*	13.49	*0.14*	13.47	*0.25*	13.27	*0.17*	13.55	*0.16*	13.43	*0.19*	13.42	*0.18*
FeOt	0.56	*0.05*	0.58	*0.03*	0.58	*0.05*	0.59	*0.04*	0.57	*0.04*	0.58	*0.04*	0.56	*0.04*
MnO	0.09	*0.02*	0.09	*0.02*	0.09	*0.01*	0.09	*0.02*	0.10	*0.02*	0.08	*0.02*	0.08	*0.02*
MgO	0.03	*0.02*	0.02	*0.02*	0.02	*0.02*	0.04	*0.02*	0.03	*0.02*	0.04	*0.03*	0.04	*0.02*
CaO	0.32	*0.02*	0.31	*0.02*	0.34	*0.05*	0.36	*0.03*	0.31	*0.02*	0.36	*0.03*	0.34	*0.02*
Na_2O	3.77	*0.12*	3.90	*0.13*	4.07	*0.19*	4.04	*0.14*	4.02	*0.13*	3.80	*0.25*	3.77	*0.17*
K_2O	4.56	*0.10*	4.45	*0.08*	4.31	*0.11*	4.44	*0.12*	4.26	*0.11*	4.47	*0.25*	4.49	*0.15*
P_2O_3	0.03	*0.02*	0.01	*0.01*	0.02	*0.01*	0.02	*0.02*	0.03	*0.02*	0.02	*0.02*	0.02	*0.02*
Cl	0.03	*0.01*	0.03	*0.01*	0.03	*0.01*	0.03	*0.01*	0.03	*0.02*	0.03	*0.02*	0.03	*0.02*

b) Major element composition (average and *standard deviation*) of the matrix glass (anhydrous) from the Popocatépetl volcano proximal deposits

Sample	MXC-118		MXC-114*		MXC-115		MXC-120		MXC-116		MXC-121	
Eruption	Pink-3 Pumice		Pink-1 Pumice		Lorenzo Pumice		Milky pumice		White Pumice		Grey Pumice	
n	15		18		25		17		4		18	
SiO_2	68.45	*0.57*	68.10	71.52	66.58	*0.31*	63.11	*0.54*	69.64	*0.49*	62.15	*1.92*
TiO_2	0.79	*0.03*	0.86	0.72	1.08	*0.04*	0.67	*0.04*	0.48	*0.01*	0.61	*0.17*
Al_2O_3	15.47	*0.22*	15.15	14.29	15.77	*0.11*	18.00	*0.49*	15.99	*0.55*	19.38	*2.15*
FeOt	3.26	*0.13*	3.38	2.62	3.82	*0.12*	4.23	*0.23*	2.52	*0.18*	3.44	*0.81*
MnO	0.07	*0.03*	0.05	0.06	0.05	*0.04*	0.09	*0.03*	0.06	*0.01*	0.06	*0.04*
MgO	1.00	*0.08*	1.12	0.60	1.38	*0.07*	2.01	*0.09*	0.68	*0.04*	1.58	*0.57*
CaO	3.01	*0.20*	3.07	1.90	3.70	*0.16*	5.19	*0.46*	2.66	*0.43*	5.79	*1.31*
Na_2O	4.58	*0.15*	4.87	4.35	4.74	*0.14*	4.39	*0.20*	4.47	*0.24*	4.80	*0.37*
K_2O	3.09	*0.09*	3.14	3.80	2.58	*0.05*	1.91	*0.11*	3.24	*0.21*	1.81	*0.51*
P_2O_3	0.17	*0.05*	0.15	0.05	0.21	*0.03*	0.26	*0.02*	0.12	*0.01*	0.26	*0.08*
Cl	0.10	*0.02*	0.11	0.09	0.07	*0.03*	0.16	*0.06*	0.14	*0.02*	0.13	*0.04*

c) Major element composition (average and *standard deviation*) of the matrix glass (anhydrous) from Iztaccíhuatl proximal deposits.

Sample	MXC-02		MXC-03		MXC-04		MXC-05	
Eruption	Los Pies B&A flow		Nepopualco dry PDCs		Nepopualco wet PDCs		Nepopualco fall	
n	21		15		13		21	
SiO_2	76.71	*0.20*	74.80	*2.08*	75.36	*2.44*	71.65	*0.20*
TiO_2	0.21	*0.03*	0.17	*0.03*	0.18	*0.04*	0.28	*0.04*
Al_2O_3	13.09	*0.14*	14.49	*1.38*	14.26	*1.76*	16.22	*0.14*
FeOt	0.95	*0.10*	1.14	*0.30*	0.80	*0.18*	1.69	*0.06*
MnO	0.03	*0.02*	0.05	*0.02*	0.04	*0.02*	0.05	*0.03*
MgO	0.20	*0.02*	0.32	*0.13*	0.22	*0.09*	0.51	*0.03*
CaO	1.08	*0.05*	1.67	*0.65*	1.58	*0.76*	2.54	*0.04*
Na_2O	3.58	*0.16*	4.39	*0.53*	4.24	*0.79*	4.59	*0.16*
K_2O	4.06	*0.17*	2.82	*0.54*	3.19	*0.63*	2.22	*0.04*
P_2O_3	0.02	*0.02*	0.06	*0.03*	0.06	*0.03*	0.08	*0.03*
Cl	0.08	*0.02*	0.09	*0.02*	0.07	*0.05*	0.17	*0.09*

Average and standard deviations (italics) for tephra deposits recorded through the Nepopualco sequence. Compositions in weight percent (wt%) were determined using a wavelength-dispersive EMP (see Section 5). n = number of analyses. See Supplementary material for the raw data and secondary standards. * For bimodal samples it is showed a representative composition of each group of plots instead than the general average and standard deviation.

4.2. Nepopualco and Xalitzintla sites

The remainder of our fieldwork concentrated on the numerous additional well preserved tephra units in the Nepopualco exposure, and at the additional site of Xalitzintla (outcrops 6 9 in Fig. 1c), ~10 km to the SSW. These two sites lie roughly at the same distance from Iztaccíhuatl and Popocatépetl (~20 km), so the tephra at Nepopualco and Xalitzintla outcrops could be from either volcano.

4.2.1. Nepopualco tephra sequence

The Nepopualco site is located ~14 km east of Iztaccíhuatl and 19 km NE of Popocatépetl (outcrop 5 in Fig. 1c) and preserves pyroclastic deposits of at least 25 different eruptive events within a 150 m deep gully (Table 2; Fig. 2b). The Nepopualco tephra sequence overlies the LPDAD (MXC 01, Fig. 2b), which forms an extensive, low gradient and elevated debris fan, onto which the thick pyroclastic deposits have accumulated. The fan is deeply incised by numerous gullies, and a recent landslide in the northern wall of the Nepopualco gully (triggered by the 2017 M 7.1 earthquake with an epicentre ~40 km south of Popocatépetl volcano; Mirwald et al., 2019; Fig. 2b) exposes a horizontally stratified sequence of the pyroclastic deposits. The sequence was described from several exposures observable along a footpath that goes from Nepopualco town to the river at the bottom of the gully. All tephra deposits are separated by palaeosols that have developed at the top of each tephra unit, or by layers of reworked volcanoclastic material that often overlie erosive surfaces at the top of the underlying tephra. These volcanoclastic layers commonly also display palaeosols developed at their tops (see stratigraphic logs in Fig. 3b, 4b and 5c). Apart from the stratigraphic and textural characteristics of the tephra units,

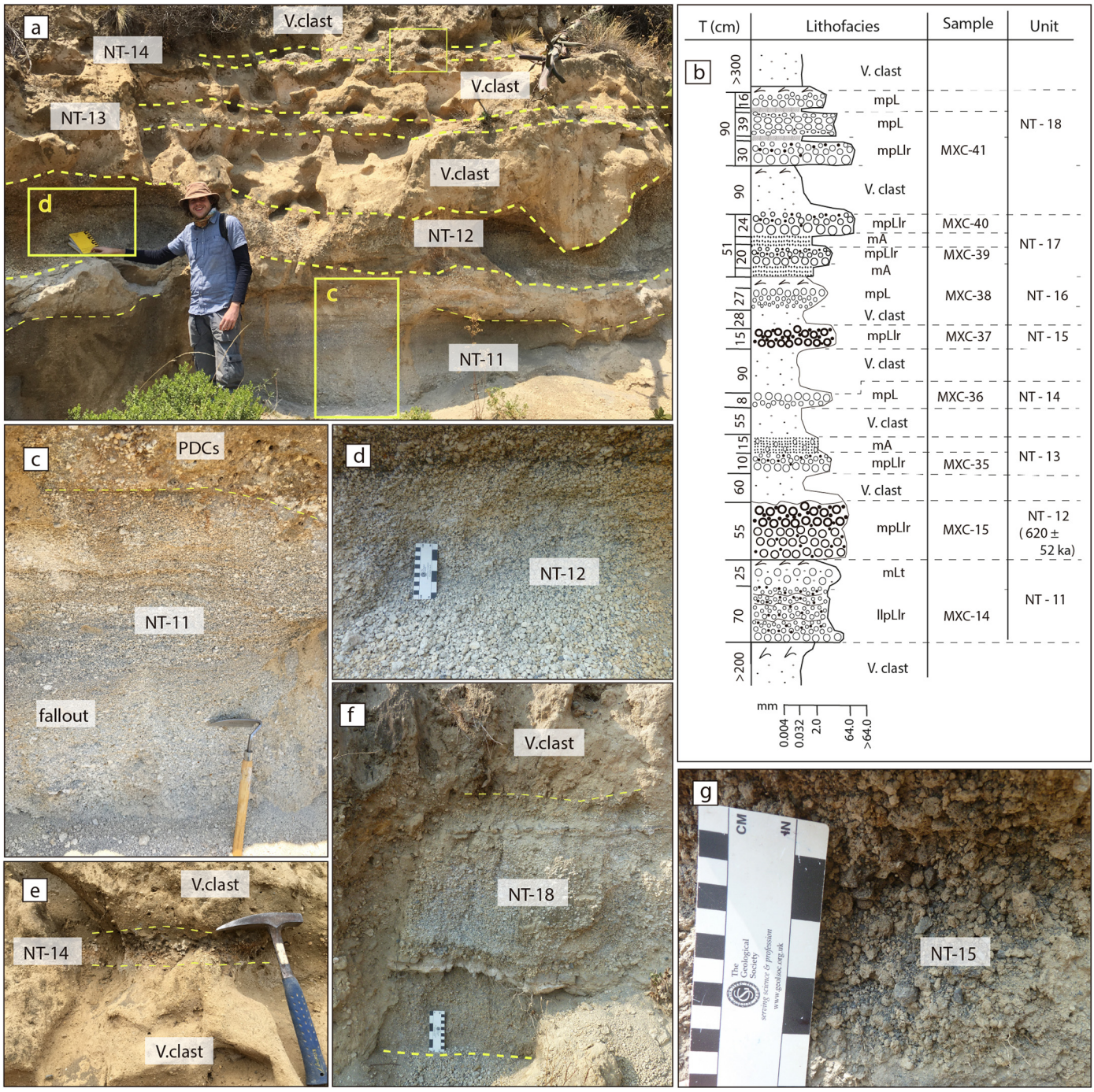


Fig. 4. a) Outcrop and b) stratigraphic log of the Middle Nepopualco Tephras (see caption of Fig. 3 for the legend). Details of: c) the thick pumice fallout at the base of NT-11 and the overlaying PDCs, d) the coarse pumice from NT-12, e) the thin NT-14 fallout interbedded within reworked volcanoclastic materials, f) the stratified NT-18 fallout with two interbedded dilute PDC deposits, and g) the lithic-rich NT-15.

the glass compositions, mineralogy and chronological information (Section 5 and 6) have been used to distinguish the tephra units. As this section is mainly focused on the hitherto undescribed Nepopualco pyroclastic deposits, we direct the reader to Figs. 3, 4 and 5 for further details regarding the reworked volcanoclastic deposits and palaeosols between tephras. Additionally, for simplicity, primary pyroclastic deposits with angular pumice, which are well sorted and clast supported, are interpreted as tephra fallouts deposits, while primary py roclastic deposits with sub angular to sub rounded pumice, poorly sorted in a matrix of volcanic ash, are interpreted as PDC deposits (ig nimbrites). Given the large number of tephra units in the Nepopualco sequence, the stratigraphy has been divided in three subgroups: Lower, Middle and Upper Nepopualco tephras. The limit between sub groups was defined by the presence of particularly thick (up to 3 m) reworked units with palaeosols developed at the top (see logs in Figs. 3, 4, and 5), possibly indicating long hiatuses of volcanic activity.

4.2.1.1. Lower Nepopualco tephras. The lowermost pyroclastic unit in the Nepopualco sequence is the Los Pies B&A Flows deposit (ignimbrite re lated to the LPDAD; Macías et al., 2012; García Tenorio et al., 2012, 2015). This thick unit (up to 30 m), is labelled as NT 1 (all tephras are numerically named with increase in stratigraphic order from base to

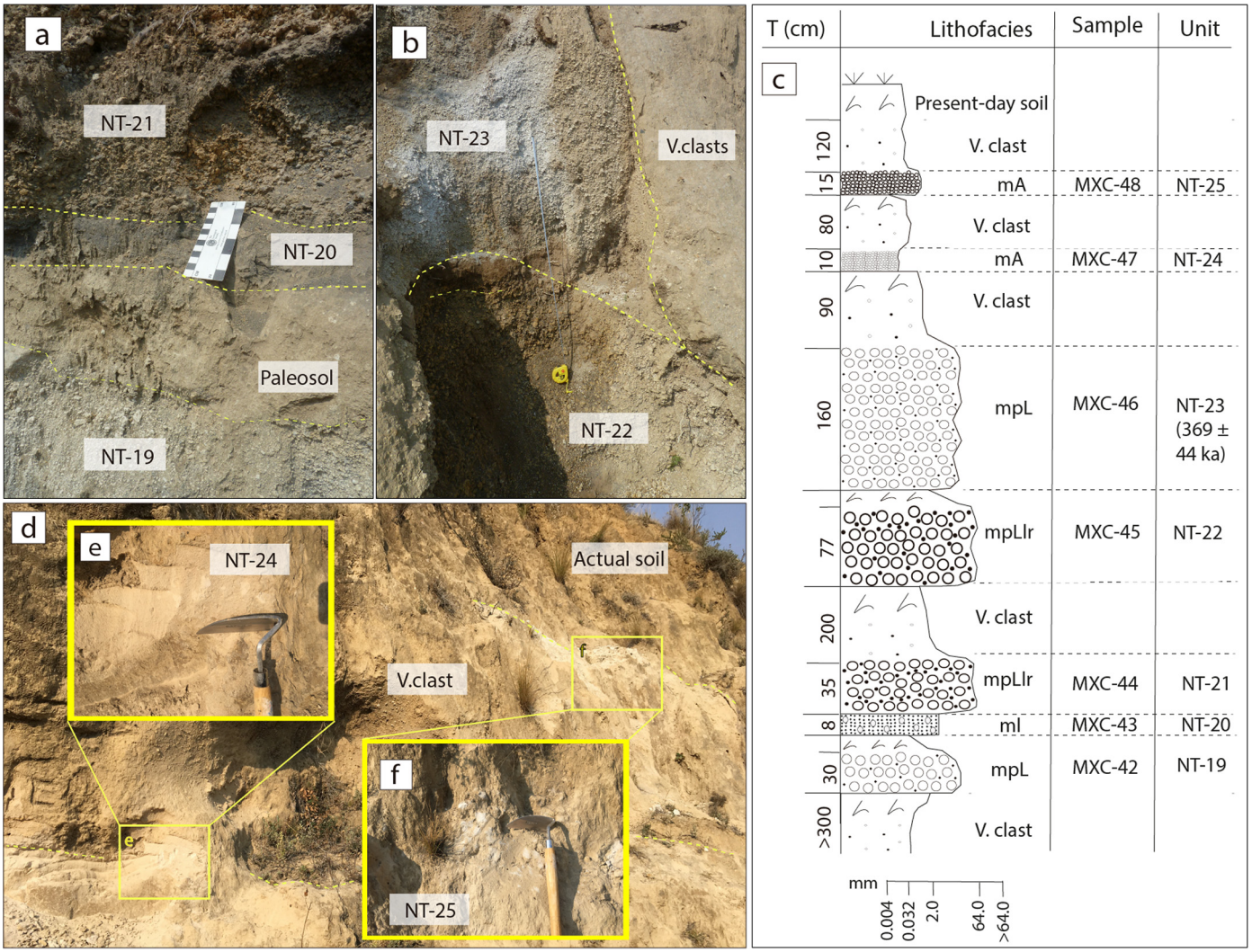


Fig. 5. Detail of: a) the mafic NT-20 and the coarse orange pumice from NT-21 above the paleosol on top of the white NT-19 pumice fallout, and b) the 1.6-m-thick NT-23 white fallout above the orange NT-22. c) Stratigraphic log of the Upper Nepopualco Tephras (see caption of Fig. 4 for the legend). d) Uppermost part of the Nepopualco sequence with two zones of fine ash pods: e) the NT-24 and f) the NT-25.

top, Fig. 3b and c; Table 2). The next unit (NT 2, which we have named here the Nepopualco Ignimbrite as described in Section 4.1.2 and attrib uted to Iztaccíhuatl volcano) is a 6 cm thick unit comprised of multiple brown laminated PDCs of coarse to medium ash (MXC 03; the Nepopualco dry PDCs), followed by 15 cm of cross stratified white PDCs (MXC 04; Nepopualco wet PDCs), and a 85 cm thick reversely graded pumice fallout of fine to medium lapilli (MXC 05; Nepopualco Fall; Fig. 3b and c). NT 3 is a 35 cm thick pumice fallout of medium la pilli that is yellowish in colour (MXC 06, Fig. 3b) and rich in lithics. NT 4 is a fallout unit that is 52 cm thick and comprised of white fine to me dium pumice lapilli (MXC 07, Fig. 3b and d), which is diffusely lami nated and crystal rich. NT 5 is a 30 cm thick fallout unit of dark grey coarse ash, and comprised of clasts that are poorly vesicular with large phenocrysts (MXC 08). NT 6 is an 18 cm thick fallout deposit of me dium to coarse grey pumice lapilli (MXC 09). NT 7 is a 70 cm thick bedded fallout deposit (MXC 10, Fig. 3a, b, and e) of grey coarse lapilli pumice and rich in lithics (especially in the upper 20 cm). NT 8 is a lens of ignimbrite up to 80 cm in thickness, with large white pumice clasts (up to 10 cm) in a brown ash matrix (MXC 11, Fig. 3b and e). NT 9 is a 35 cm thick, lithic rich fallout deposit of scoria and orange crystal rich pumice (MXC 12, Fig. 3 b and f). The uppermost tephra of this Lower Nepopualco sequence (NT 10) is a bedded 90 cm thick fallout of lithic rich, coarse pumice lapilli with darker ash layers in the uppermost part (MXC 13, Fig. 3 b and f).

4.2.1.2. Middle Nepopualco Tephras. The first tephra unit of this subgroup (NT 11) is a 70 cm thick fallout unit of a bedded white pumice that is normally graded, with clasts ranging from coarse to medium lapilli and rich in fine lithics (<0.5 mm), larger near the top, that grades into a 25 cm thick ignimbrite (MXC 14, Fig. 4a, b, and c). NT 12 is a 55 cm thick fallout deposit of coarse orange pumice lapilli (MXC 15, Fig. 4a, b, and d), rich in coarse lithics (0.5 2 cm, especially in the upper 20 cm). NT 13 is a 25 cm thick orange pumice fallout consisting of a 10 cm thick sub unit of medium lapilli with fine lithics at the base (MXC 35) and a 15 cm thick sub unit of fine lapilli in a dark matrix at the top. NT 14 is an 8 cm thick medium lapilli pumice fallout (MXC 36, Fig. 4e). NT 15 is a 15 cm thick lithic rich fallout comprised of fine to medium lapilli pumice (MXC 37, Fig. 4g). The NT 16 tephra layer is a 27 cm thick reverse graded fallout unit of white coarse ash to fine la pilli pumice (MXC 38). NT 17 is a 51 cm thick fallout sequence that starts with 4 cm of dark ash followed by 20 cm of medium to fine pum ice lapilli (normally graded) rich in lithics (MXC 39), with another 3 cm thick layer of dark ash, followed by 24 cm of coarse orange pumice with few coarse lithics (0.5 2 cm) at the top (MXC 40; Fig. 4 b). NT 18 is

a 90 cm thick pumice fallout with a couple of fine ash layers in the mid dle (Fig. 4f): the first 30 cm are a coarse orange fallout deposit (rich in lithics towards the top), followed by a thin layer (3 cm) of fine and hard ened white ash, 39 cm of bedded pumice (MXC 41), another fine ash layer (2 cm), and a 16 cm thick unit of medium to fine pumice lapilli.

4.2.1.3. Upper Nepopualco tephras. The first tephra of this subgroup (NT 19) is a 30 cm thick white pumice fallout with medium lapilli and small lithics (MXC 42, Fig. 5a and c). NT 20 is an 8 cm thick dark fallout unit comprised of lithics (>70%) and a few fine lapilli pumices and coarse ash (MXC 43, Fig. 5a and c). NT 21 is a 35 cm thick fallout of weathered

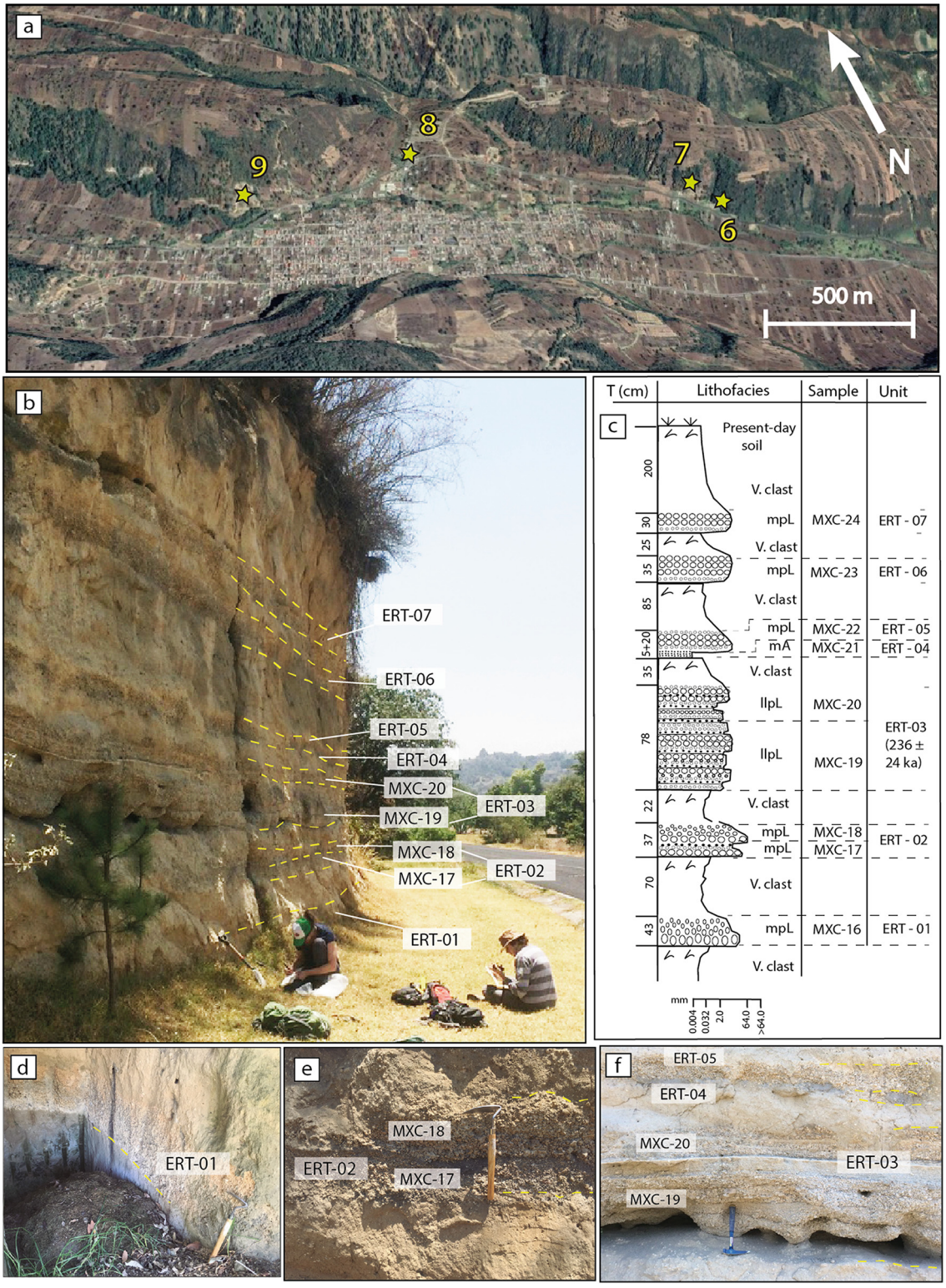


Fig. 6. a) Map of the Xalitzintla region with the location of the four study sites (yellow stars). b) East of Restaurant (ER) outcrop exposed along the Paso de Cortés road (site number 6 in a); c) stratigraphic log dislaying the seven pyroclastic units interbedded with reworked material and palaeosols (see caption of Fig. 4 for the legend); d), e) and f) field photos showing textural characteristics of tephra layers described in the text (ERT-1 to 5).

orange pumice, comprised of coarse lapilli rich in lithics (MXC 44, Fig. 5a and c). NT 22 is a 77 cm thick fallout unit of coarse orange lapilli rich in lithics (MXC 45, Fig. 5b and c). NT 23 is a 160 cm thick, medium to coarse white lapilli fallout unit (MXC 46, Fig. 5b and c). At the top of the Nepopualco outcrop are two zones of white ash pods within 2 m of soil developed in reworked deposits: the first pod (NT 24) is a fallout unit up to 10 cm thick and comprised of very fine ash (MXC 47, Fig. 5d and e), and the second fallout (NT 25) is comprised of medium ash that is rich in biotite (MXC 48, Fig. 5d and f). Overlying NT 25 is the present day soil.

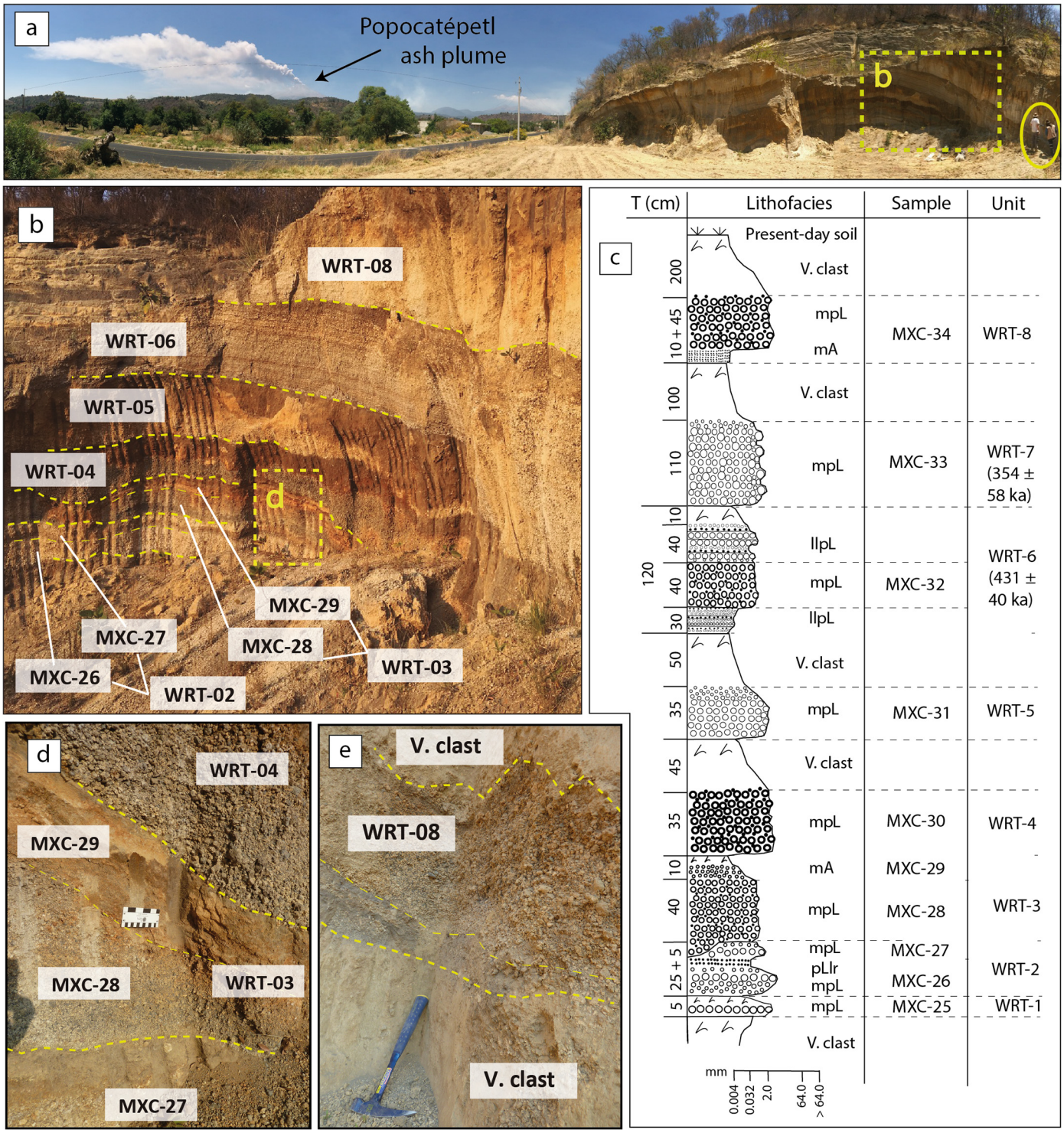


Fig. 7. a) Panoramic view of Popocatépetl volcano from the West of the Restaurant (WR) site near Xalitzintla (outcrop 7 in Fig. 6a) during a small explosive eruption (~2-km-high plume on the 5th of April 2019) with an ash cloud moving towards the SE. Note the geologist in the bottom-right of the photo (within yellow ellipsoid) for scale of the outcrop; b) tephra sequence exposed in a quarry of this WR-site; c) stratigraphic log showing the eight pyroclastic units interbedded with reworked material and palaeosols (see caption of Fig. 4 for the legend); d) and e) field photos showing textural characteristics of the tephra layers described in the text.

4.2.2. Xalitzintla

Tephra layers deposited in the Xalitzintla region are exposed in roadcuts and quarries along the Paso de Cortés road (outcrops 6 9, Fig. 1c and 6a) and within Xalitzintla town. The town is located in a wide valley between the southern margin of the LPDAD and the NE limits of Popocatépetl's flank (Fig. 1c and 6a). The Xalitzintla exposures are located on the northern side of this valley. The sequences described here are from four separate exposures (Table 3): 1) East of the Restau rant, 2) West of the Restaurant, 3) Fork in the road, and 4) Xalitzintla Quarry. The chronostratigraphic order of these sites will be discussed later in Section 7, and cannot be determined from field characteristics or topographic relationships, due to discontinuous exposures and an absence of visually correlatable horizons. The Xalitzintla tephras are all fallouts and commonly bound by reworked volcanoclastic materials with palaeosols at the top (see stratigraphic logs in Figs. 6c, 7c, 8c, and 9b).

4.2.2.1. East of the Restaurant. At least seven different pyroclastic de posits are preserved in this outcrop (ERT 1 to 7, numerically named in stratigraphic order from base to top, as in Nepopualco; Fig. 6b and c), which is located east of the Montaña Fresca Burger restaurant (point 6 in Fig. 6a). The lowermost tephra (ERT 1) is a 43 cm thick, normal graded, orange weathered pumice fallout (sample MXC 16; Fig. 6c and d) displaying coarse to medium lapilli. Two types of pumice com prise this deposit: one is grey exhibiting felsic phenocrystals and the other is pink with occasional mm sized mafic crystals. ERT 2 is a 37 cm thick, lithic rich fallout unit, which consists of two normally graded subunits of coarse pinkish pumice lapilli to coarse ash at the top (MXC 17 and 18, Fig. 6e), that are separated by a thin layer of lithics. ERT 3 is a distinctive 78 cm thick fallout sequence made up of several horizon tally bedded sub units separated by lithic rich horizons (MXC 19 and 20, Fig. 6c and f). The base of this sequence is a 7 cm thick coarse ash fall with a 0.5 cm thick lithic rich layer at the top, followed by eight ~10 cm thick (each) layers of white medium lapilli pumice. ERT 4 is a grey 5 cm thick ash fallout layer (MXC 21) and ERT 5 a 20 cm thick medium to coarse pumice lapilli fallout layer (MXC 22). ERT 6 is a 35 cm thick fallout unit of medium pumice lapilli (MXC 23). The upper most tephra of this outcrop (ERT 7) is a 30 cm thick pumice fallout of coarse lapilli (MXC 24). Lying above ERT 7 are 2 m of reworked volcanoclastic material with the present day soil developed above.

4.2.2.2. West of the Restaurant. On the western side of the restaurant (point 7 in Fig. 6a) is a small quarry where at least eight pyroclastic units are preserved (WRT 1 to 8; Fig. 7). This sequence sits on a

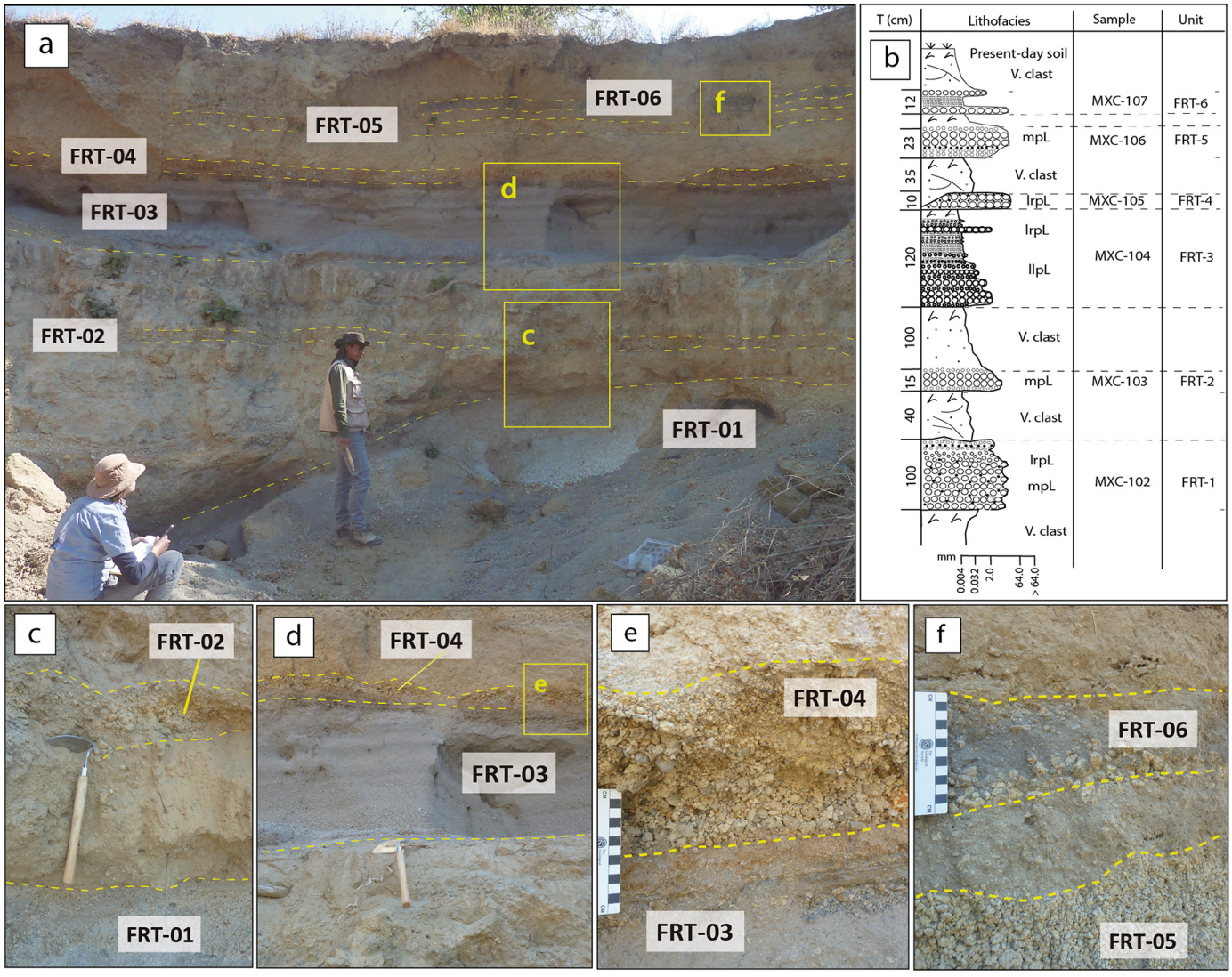


Fig. 8. a) Small quarry at the Fork in the Road (FR) site near Xalitzintla (outcrop 8 in Fig. 6a), b) stratigraphic log dislaying six identified fall layers recorded in this site, c – f) field photos showing textural characteristics of the tephra layers described in the text.

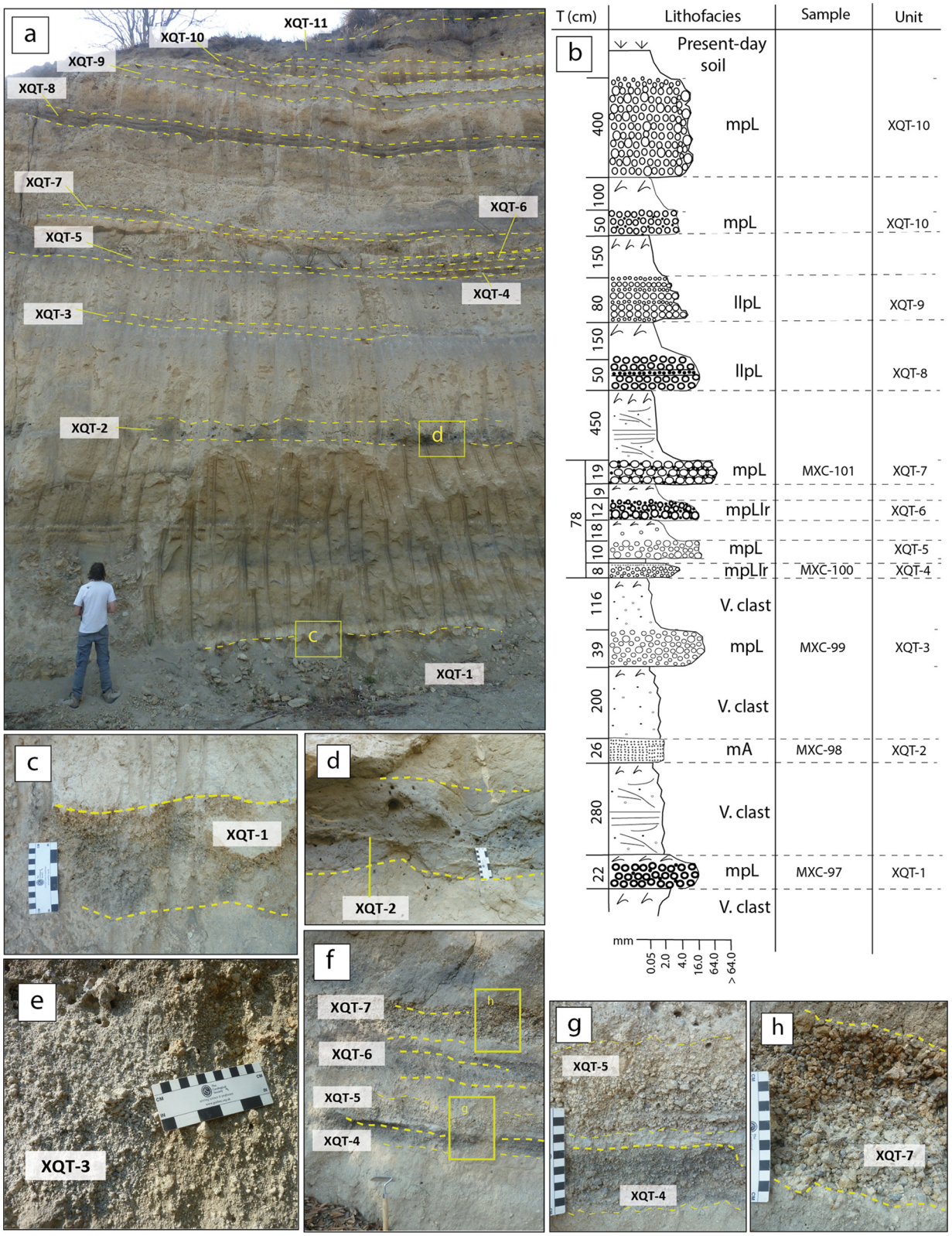


Fig. 9. b) Xalitzintla Quarry, b) stratigraphic log displaying eleven pyroclastic units recorded in this site and interbedded with thick reworked volcanoclastic material units and palaeosols, c – h) field photos showing textural characteristics of the tephra layers described in the text.

topographic high and dips ~20° towards the road, from where there is a panoramic view of Popocatépetl volcano (Fig. 7a). The lowermost tephra layer of this sequence (WRT 1) is a 3 cm thick fallout unit of dark pumice (sample MXC 25, Fig. 7b and c). WRT 2 is a 25 cm thick pinkish fallout of reversely graded medium to coarse pumice lapilli (MXC 26), which is rich in mafic crystals (orthopyroxene and horn blende) and interbedded in its upper portion with a layer of hydrother mally altered lithics. Above is an additional 5 cm of pumice lapilli fall at

the top (MXC 27), which is laterally discontinuous and eroded in some parts of the outcrop. It is discordantly overlain by WRT 3, a 40 cm thick dark fallout unit composed of grey fine to medium lapilli pumice with abundant lithics (MXC 28), which grades into a 10 cm thick fallout unit of reddish coarse ash (MXC 29). WRT 4 is a 35 cm thick lithic rich fallout of coarse grey pumice (MXC 30, Fig. 7 d). WRT 5 is a 35 cm thick white medium to coarse lapilli pumice fallout (MXC 31), which is slightly finer at the top. WRT 6 is a light grey, laminated pum ice fallout that is 120 cm thick (MXC 32). The basal sub unit of this de posit is a bedded, 30 cm thick, coarse ash to fine lapilli fall that is topped brown, lithic rich horizons. The next sub unit structureless 40 cm thick, comprising fine to medium pumice lapilli fall, with a higher con centration of lithics towards the top. The top sub unit comprises 40 cm of pumice fall interbedded with brown lithic rich horizons. WRT 7 is a 110 cm thick fallout unit, which is massive with white to yellowish me dium lapilli and pink coarse pumice clasts that are up to 4 cm in diam eter (MXC 33). The uppermost tephra of this sequence (WRT 8) starts with 10 cm of medium dark grey ash followed by 45 cm of a medium to coarse lapilli pumice fallout, which is rich in lithics (MXC 34, Fig. 7e) and grades into ~2 m of reworked volcanoclastic material with the present day soil at the top.

4.2.2.3. Fork in the road. Six more tephra layers are exposed in another small quarry along the Paso de Cortés road (FRT 1 to 6; Fig. 8; point 8 in Fig. 6a). The lowermost unit (FRT 1) is a 100 cm thick, normal graded, white pumice fallout, with clasts ranging from coarse to me dium lapilli, and a lithic rich layer at the top comprising up to 70% lithics (MXC 102, Fig. 8a, b, and c). FRT 2 is a 15 cm thick pumice fallout of medium to coarse sub angular lapilli (MXC 103, Fig. 8c). FRT 3 is a dis tinctive 120 cm thick, dark grey, normal graded and thinly bedded pumice fallout, with clasts ranging from medium to fine lapilli to coarse ash, that transitions into a lithic rich (>45%) layer with medium lapilli pumice at the top (MXC 104, Fig. 8d and e). FRT 4 is a 10 cm thick lithic rich fallout of brown pumice comprised of coarse lapilli (MXC 105; Fig. 8d and e). FRT 5 is a 23 cm thick yellowish pumice fallout in versely graded with clasts ranging from medium to coarse lapilli, with a lithic rich layer in the middle (MXC 106, Fig. 8f). FRT 6 is a 12 cm thick coarse grey ash fallout layer with sub rounded and embedded orange coarse pumice clasts (mostly at the base of the unit; MXC 107, Fig. 8f). At the top of the sequence there are 100 cm of reworked volcanoclastic material that grades into the present day soil.

4.2.2.4. Xalitzintla Quarry. At least eleven tephra layers are preserved in a large quarry located NW of Xalitzintla (point 9 in Fig. 6a). Unfortunately, the upper 4 pyroclastic units were out of reach and could not be sam pled or described in detail (Fig. 9a and b). The lowermost pyroclastic de posit of this sequence (XQT 1) is a lithic poor dark grey scoria fallout that is 22 cm thick and comprised of medium lapilli clasts (sample MXC 97, Fig. 9c). XQT 2 is a 26 cm thick fallout unit comprised of dark coarse ash (MXC 98, Fig. 9 d). XQT 3 is a 39 cm thick white pum ice fallout that is lithic poor (<5%) and slightly inversely graded, with clasts ranging from fine to medium lapilli and the occasional clast that is up to 3 cm in diameter (MXC 99, Fig. 9e). The next four tephra layers are within a 78 cm thick sequence interbedded by thin layers of reworked material (Fig. 9f). XQT 4 is a normally graded 8 cm thick dark pumice fallout, with fine to medium lapilli to coarse ash, and rich in fine to medium lava lithics (MXC 100, Fig. 9g). XQT 5 is a 10 cm thick yellowish fallout unit of medium lapilli pumice with few coarse clasts up to 2 cm in diameter. XQT 6 is a dark 12 cm thick normally graded fallout unit, from coarse to medium pumice lapilli and rich in fine to medium lithics. XQT 7 is a dark brown 19 cm thick coarse pum ice fallout rich in medium to coarse lava lithics (MXC 101, Fig. 9h). The tephra layers of the uppermost part of the outcrop could not be reached and were not sampled and include: XQT 8, a ~50 cm thick dark pumice fallout unit with a lithic rich layer; XQT 9, a ~80 cm thick light grey layered pumice fallout of fine to medium lapilli interbedded with thin layers of coarse ash (Fig. 9a and b); XQT 10, a ~50 cm thick brown pumice fallout unit; and XQT 11, the uppermost tephra recorded in this outcrop, is a ~2 m thick orange coarse pumice lapilli deposit (Fig. 9a and b) into which the present day soil has been developed.

5. Glass chemistry and tephra correlation

The glass compositions of all the tephra layers identified in the outcrops described above were analysed in order to build a tephrostratigraphy that could be used to correlate sites around the SNVR volcanoes, to identify the source of the tephras exposed at Nepopualco and Xalitzintla, and to develop the longer term explosive eruption history of the SNVR. Given that some of the units have been dated here and in other studies (e.g. Macías et al., 2012), this tephrostratigraphy can be used to constrain the chronology at other sites and help to evaluate the explosive eruptive history of the volcanoes (e.g., as marker horizons in other regional stratigraphic records; Brown et al., 2019).

5.1. Glass compositional fields of Tláloc Telapón, Iztaccíhuatl and Popocaté petl

As explained in Section 4.1, we analysed glass from pyroclastic deposits that had been previously attributed to Tláloc Telapón, Iztaccí huatl, or Popocatépetl (Table 4; secondary standards in Supplementary Material 1) in order to establish the compositional fields of the potential source volcanoes of the newly described tephras in the Nepopualco and Xalitzintla sequences.

Major element abundances displayed in a total alkali vs. silica dia gram (TAS, Fig. 10a) and bivariate plots (Fig. 10b e) show that the glass compositions of the late Pleistocene ignimbrites erupted from Tláloc Telapón are relatively K rich and rhyolitic. The deposits are com positionally homogenous and plot within a narrow cluster (green area in Fig. 10). They have 74.93 77.66 wt% SiO_2, 0.27 1.60 wt% CaO, 3.68 4.96 wt% K_2O, 12.86 14.20 wt% Al_2O_3, and up to 0.31 wt% MgO. The products of known eruptions from Iztaccíhuatl and Popocatépetl are quite variable in composition, and two slightly different evolutionary trends can be discerned (red and blue areas in Fig. 10). The middle Pleistocene Iztaccíhuatl deposits have lower K and Mg (red area in Fig. 10) and higher Ca and Al at given SiO_2 content than deposits from Popocatépetl (blue area in Fig. 10). Glass compositions of the Iztaccíhuatl deposits are rhyolitic with 71.30 78.92 wt% SiO_2, up to 0.56 wt% MgO, 0.46 2.65 wt% CaO, 2.15 4.41 wt% K_2O, and 11.68 16.61 wt% Al_2O_3. In contrast, the late Pleistocene Holocene Popocatépetl eruption deposits have glass compositions that extend from andesite to rhyolite, with ranges of 58.82 71. 84 wt% SiO_2, 0.58 2.61 wt% MgO, 1.78 8.13 wt% CaO, 0.85 3.76 wt% K_2O, and 14.05 22.73 wt% Al_2O_3.

Although Popocatépetl's products fall within a consistent linear trend, which implies that the melts have evolved along the same fractio nation trend in the past 24 ka, we cannot be certain that all melts erupted from this volcano followed the same fractionation trend during the earlier stages of its history. Our studied tephra deposits span an older time interval (Section 6), but it is notable that many of these de posits overlap compositionally with our defined post 24 ka Popocaté petl field. This suggests that magmas of a similar composition have been erupted over a long time interval from the SNVR, and in the ab sence of conflicting information, we attribute all magmas that plot along the higher K fractionation trend to the Popocatépetl source. Tem porally, our known Iztaccíhuatl samples are much closer in age to the stratigraphic interval that is being studied, but as discussed in Section 4.1.2, the limitation of these is that our compositional field is only based on two closely spaced eruptions. Nevertheless, these Iztaccí huatl samples define a distinct linear compositional trend from the post 24 ka Popocatépetl field, with lower K_2O at given SiO_2 contents, and we use this to define an Iztaccíhuatl compositional field. Although

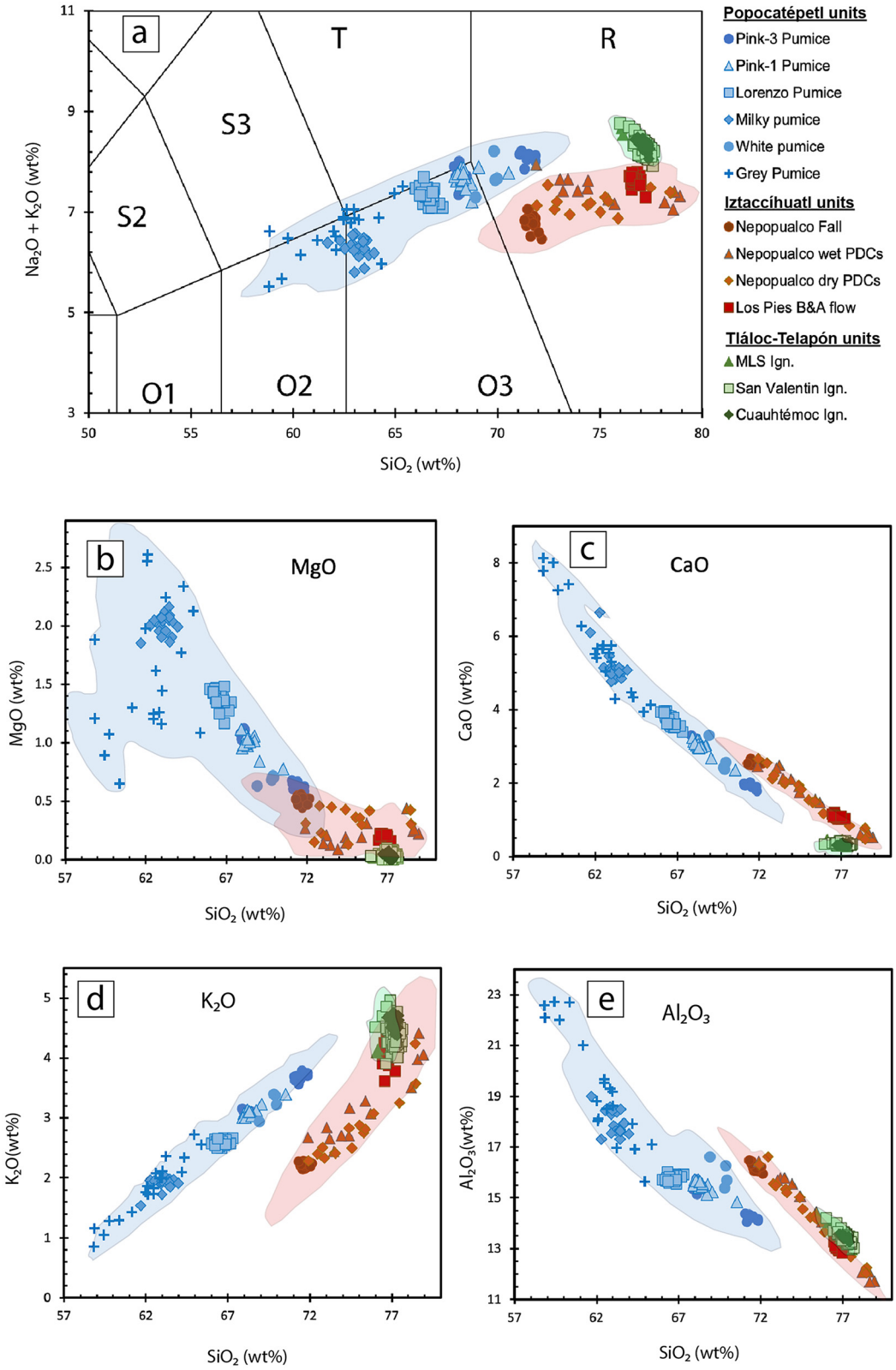


Fig. 10. Glass chemistry of previously described pyroclastic deposits erupted by Popocatépetl, Iztaccíhuatl, and Tláloc-Telapón volcanoes, with the addition of an ascribed Iztaccíhuatl deposit (see Section 4.1.2) plotted in: a) Total alkali vs silica (TAS diagram) of the tephra units; and bivariate plots of b) SiO_2 vs MgO, c) SiO_2 vs CaO, d) SiO_2 vs K_2O and e) SiO_2 vs Al_2O_3 (selected bivariate plots). Compositional fields of Popocatépetl (blue area) Iztaccíhuatl (red area), and Tláloc (green area) volcanoes estimated with OxCal/RESET software (Bronk Ramsey et al., 2015).

it is possible that the melt compositions erupted by both Popocatépetl and Iztaccíhuatl varied between these low K and high K trends over time, we do not consider this likely, given that fractionation trends at other closely spaced volcanoes are observed to be stable over prolonged periods of time (e.g. Daisen and Sambe volcanoes in Japan; (Albert et al., 2018). In the absence of further source compositional constraints, we

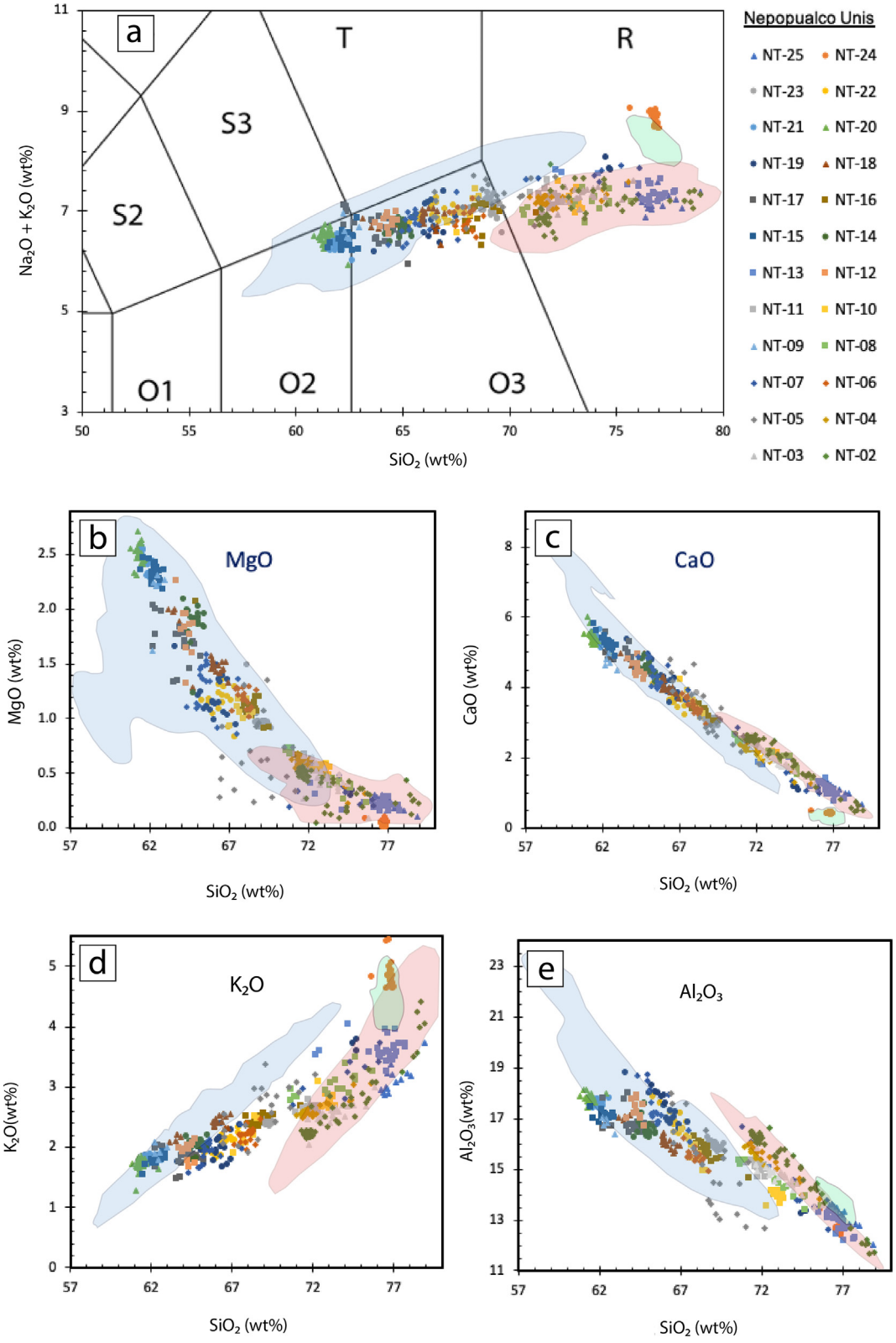


Fig. 11. a) Total alkali vs silica (TAS) of 24 analysed pyroclastic deposits through the Nepopualco gully; and bivariate plots of b) SiO_2 vs MgO, c) SiO_2 vs CaO, d) SiO_2 vs K_2O and e) SiO_2 vs Al_2O_3, displayed together with the compositional field of Popocatépetl (blue area), Iztaccíhuatl (red area), and Tláloc-Telapón (green area) volcanoes.

adopt the simplest interpretation and attribute the two low K and high K compositional types that occur within our dataset, to Iztaccíhuatl and Popocatépetl respectively.

5.2. Composition of Nepopualco tephras and correlation to their volcanic source

The tephra layers in the Nepopualco site have a wide range of sub alkaline glass compositions, from andesites to rhyolites (Fig. 11 and Table 5; secondary standards in Supplementary Material 1). These major element glass compositions of the Nepopualco tephras (Fig. 11 b e) partially plot within the two defined compositional fields of Iztac cíhuatl and Popocatépetl. For example, the andesitic to dacitic glass compositions of NT 6, 9, 12, and NT 16 to 23 (concentrations of 61.40 69.61 wt% SiO_2, 0.92 2.54 wt% MgO, 2.93 6.07 wt% CaO, 1.62 2.48 wt% K_2O, and 18.72 14.91 wt% Al_2O_3) plot within the high K Popocatépetl compositional field (blue area in Fig. 11), and most likely were sourced from Popocatépetl. The rhyolitic glasses of NT 2 to 4, and NT 8, 11 and 13 (concentrations of 70.52 78.91 wt% SiO_2, 0.12 0.75 wt % MgO, 0.46 2.85 wt% CaO, 2.28 4.46 wt% K_2O, and 11.67 16.43 wt% Al_2O_3) plot within the low K Iztaccíhuatl compositional field (red area in Fig. 11). NT 24, which is a K rich rhyolitic white fine ash fallout (75.65 77.04 wt% SiO_2, 0.36 0.47 wt% CaO, 4.63 5.43 wt% K_2O, 12.39 13.40 wt% Al_2O_3, and up to 0.09 wt% MgO), plots partially within the compositional field defined by the known Tláloc Telapón pyroclastic deposits, and is distinct from all other tephras in the Nepopualco sequence (orange dots and green area in Fig. 11).

Three tephras in Nepopualco do not plot clearly into any of our de fined compositional fields. The NT 5, 7, and 10 units (grey and blue dia monds, and yellow square in Fig. 11) have a bimodal glass composition, which overlap with both the Popocatépetl and Iztaccíhuatl fields.

5.3. Composition of Xalitzintla tephras and correlation to their volcanic source

Major element glass compositions of the tephras around Xalitzintla also span a wide range of sub alkaline compositions (Table 6; secondary standards in Supplementary Material 1), but mostly plot within the

Table 5

Sample	MXC-02		MXC-03		MXC-04		MXC-05		MXC-06		MXC-07		MXC-08		MXC-09		MXC-10*	
Eruption	NT-1 (L. P. B&A)		NT-2 (Nepopualco Ign: Dry and wet PDCs and fallout)						NT-3		NT-04		NT-05		NT-06		NT-07	
n	21		15		13		21		24		27		22		23		24	
SiO_2	76.71	*0.20*	74.80	*2.08*	75.36	*2.44*	71.65	*0.20*	73.26	*1.04*	72.13	*1.17*	69.26	*1.51*	67.94	*0.40*	73.95	66.27
TiO_2	0.21	*0.03*	0.17	*0.03*	0.18	*0.04*	0.28	*0.04*	0.31	*0.07*	0.29	*0.06*	1.04	*0.20*	0.90	*0.05*	0.18	0.50
Al_2O_3	13.09	*0.14*	14.49	*1.38*	14.26	*1.76*	16.22	*0.14*	14.65	*0.49*	15.44	*0.57*	14.51	*1.23*	15.52	*0.27*	14.56	17.95
FeOt	0.95	*0.10*	1.14	*0.30*	0.80	*0.18*	1.69	*0.06*	1.86	*0.26*	1.96	*0.28*	3.79	*0.71*	3.68	*0.19*	1.34	2.80
MnO	0.03	*0.02*	0.05	*0.02*	0.04	*0.02*	0.05	*0.03*	0.04	*0.02*	0.06	*0.02*	0.06	*0.02*	0.07	*0.02*	0.07	0.06
MgO	0.20	*0.02*	0.32	*0.13*	0.22	*0.09*	0.51	*0.03*	0.45	*0.12*	0.56	*0.11*	0.74	*0.30*	1.19	*0.09*	0.48	0.91
CaO	1.08	*0.05*	1.67	*0.65*	1.58	*0.76*	2.54	*0.04*	1.96	*0.31*	2.11	*0.31*	3.05	*0.72*	3.47	*0.22*	1.57	4.62
Na_2O	3.58	*0.16*	4.39	*0.53*	4.24	*0.79*	4.59	*0.16*	4.77	*0.22*	4.61	*0.11*	4.52	*0.24*	4.68	*0.20*	4.90	4.79
K_2O	4.06	*0.17*	2.82	*0.54*	3.19	*0.63*	2.22	*0.04*	2.56	*0.17*	2.63	*0.14*	2.75	*0.36*	2.20	*0.13*	2.80	1.85
P_2O_3	0.02	*0.02*	0.06	*0.03*	0.06	*0.03*	0.08	*0.03*	0.07	*0.03*	0.10	*0.04*	0.19	*0.07*	0.19	*0.02*	0.06	0.19
Cl	0.08	*0.02*	0.09	*0.02*	0.07	*0.05*	0.17	*0.09*	0.08	*0.04*	0.11	*0.02*	0.09	*0.07*	0.16	*0.19*	0.10	0.07

Sample	MXC-11*		MXC-12		MXC-13*		MXC-14		MXC-15		MXC-35		MXC-36		MXC-37		MXC-38	
Eruption	NT-08		NT-09		NT-10		NT-11		NT-12		NT-13		NT-14		NT-15		NT-16	
n	16		5		21		16		10		25		25		23		17	
SiO_2	74.25	70.66	62.47	*0.31*	73.15	68.22	71.86	*0.34*	64.34	*0.31*	76.30	*1.39*	64.93	*0.33*	62.36	*0.34*	68.34	*0.99*
TiO_2	0.28	0.65	1.27	*0.09*	0.53	0.83	0.41	*0.03*	0.88	*0.05*	0.30	*0.07*	1.00	*0.12*	1.08	*0.03*	0.77	*0.07*
Al_2O_3	14.39	15.35	16.80	*0.26*	13.99	15.55	15.07	*0.21*	17.32	*0.38*	13.12	*0.75*	16.57	*0.34*	17.07	*0.14*	15.82	*0.36*
FeOt	1.67	2.75	5.52	*0.11*	2.39	3.61	2.29	*0.11*	3.99	*0.26*	1.33	*0.26*	4.08	*0.23*	5.12	*0.18*	3.27	*0.17*
MnO	0.03	0.03	0.11	*0.01*	0.02	0.06	0.04	*0.02*	0.06	*0.02*	0.03	*0.02*	0.07	*0.02*	0.09	*0.02*	0.07	*0.02*
MgO	0.26	0.71	2.13	*0.29*	0.59	1.17	0.60	*0.04*	1.80	*0.24*	0.21	*0.06*	1.87	*0.16*	2.34	*0.07*	1.14	*0.25*
CaO	2.05	2.65	4.71	*0.18*	2.11	3.38	2.29	*0.09*	4.52	*0.23*	1.18	*0.31*	4.55	*0.16*	5.27	*0.19*	3.41	*0.34*
Na_2O	4.14	4.06	4.70	*0.12*	4.39	4.69	4.62	*0.13*	4.86	*0.18*	3.79	*0.18*	4.63	*0.16*	4.61	*0.13*	4.46	*0.23*
K_2O	2.88	2.94	1.94	*0.11*	2.72	2.22	2.63	*0.06*	1.93	*0.15*	3.62	*0.18*	2.02	*0.09*	1.79	*0.08*	2.42	*0.12*
P_2O_3	0.00	0.12	0.28	*0.08*	0.05	0.18	0.08	*0.03*	0.22	*0.03*	0.05	*0.03*	0.20	*0.04*	0.20	*0.04*	0.21	*0.06*
Cl	0.04	0.08	0.07	*0.03*	0.06	0.09	0.13	*0.09*	0.08	*0.01*	0.07	*0.02*	0.07	*0.03*	0.08	*0.02*	0.15	*0.08*

Sample	MXC-39		MXC-41*		MXC-42		MXC-43		MXC-44		MXC-45		MXC-46		MXC-47		MXC-48	
Eruption	NT-17		NT-18		NT-19		NT-20		NT-21		NT-22		NT-23		NT-24		NT-25	
n	20		21		22		25		20		16		23		27		15	
SiO_2	63.83	*0.93*	66.54	63.58	66.09	*0.84*	61.40	*0.30*	61.88	*0.30*	66.56	*0.59*	69.14	*0.31*	76.79	*0.25*	77.03	*0.78*
TiO_2	1.04	*0.09*	0.87	0.95	0.72	*0.04*	1.02	*0.05*	1.04	*0.04*	0.69	*0.04*	0.61	*0.04*	0.09	*0.02*	0.17	*0.03*
Al_2O_3	16.84	*0.46*	15.63	17.09	17.42	*0.62*	17.80	*0.16*	17.58	*0.12*	16.97	*0.47*	15.89	*0.18*	12.59	*0.18*	13.19	*0.45*
FeOt	4.82	*0.38*	3.97	4.36	3.33	*0.20*	5.00	*0.18*	5.04	*0.13*	3.58	*0.21*	2.93	*0.09*	1.04	*0.04*	0.87	*0.14*
MnO	0.09	*0.02*	0.05	0.06	0.05	*0.02*	0.09	*0.02*	0.08	*0.02*	0.07	*0.02*	0.06	*0.02*	0.03	*0.02*	0.04	*0.02*
MgO	1.70	*0.19*	1.51	1.99	1.20	*0.18*	2.50	*0.09*	2.43	*0.10*	1.16	*0.14*	0.97	*0.12*	0.04	*0.02*	0.22	*0.06*
CaO	4.73	*0.33*	4.01	4.82	4.16	*0.43*	5.43	*0.20*	5.37	*0.16*	3.73	*0.30*	3.07	*0.18*	0.41	*0.02*	1.16	*0.20*
Na_2O	4.83	*0.28*	4.31	4.60	4.79	*0.22*	4.79	*0.16*	4.53	*0.11*	4.90	*0.19*	4.68	*0.18*	4.01	*0.18*	4.06	*0.19*
K_2O	1.81	*0.14*	2.29	2.20	1.97	*0.22*	1.71	*0.11*	1.79	*0.05*	2.06	*0.15*	2.39	*0.04*	4.85	*0.20*	3.12	*0.23*
P_2O_3	0.22	*0.04*	0.17	0.27	0.16	*0.04*	0.20	*0.04*	0.19	*0.03*	0.21	*0.04*	0.14	*0.02*	0.01	*0.01*	0.04	*0.03*
Cl	0.09	*0.03*	0.64	0.07	0.11	*0.09*	0.07	*0.02*	0.07	*0.02*	0.08	*0.05*	0.11	*0.05*	0.12	*0.01*	0.10	*0.03*

Average and standard deviations (italics) for tephra deposits recorded through the Nepopualco sequence. Compositions in weight percent (wt%) were determined using a wavelength-dispersive EMP (see Section 5). n = number of analyses. See Supplementary material for the raw data and secondary standards. * Bimodal samples are shown as selected representative compositions for each sub-component instead of by the average and standard deviation.

Table 6
Major element composition (average and standard deviation) of the matrix glass (anhydrous) from the tephras recorded in Xalitzintla region by outcrops.

a) East of the Restaurant site

Sample	MXC-16**			MXC-17		MXC-18		MXC-19		MXC-20		MXC-21*		MXC-22		MXC-23		MXC-24	
Eruption	ERT-1			ERT-2		ERT-2		ERT-3		ERT-3		ERT-4		ERT-5		ERT-6		ERT-7	
n	29			23		14		13		13		10		21		25		26	
SiO_2	68.12	65.72	62.37	67.53	*0.26*	67.10	*0.23*	67.93	*0.28*	67.43	*0.42*	70.05	67.77	66.05	*0.27*	64.92	*0.38*	66.64	*0.32*
TiO_2	1.00	0.92	0.84	0.92	*0.05*	0.97	*0.04*	0.87	*0.03*	0.90	*0.04*	0.88	1.08	1.04	*0.03*	1.09	*0.05*	0.94	*0.03*
Al_2O_3	14.66	16.16	17.20	15.85	*0.22*	15.99	*0.13*	15.74	*0.18*	15.90	*0.13*	14.69	15.20	16.02	*0.13*	16.05	*0.13*	15.81	*0.11*
FeOt	3.75	3.81	4.66	3.35	*0.09*	3.50	*0.12*	3.30	*0.09*	3.46	*0.14*	3.22	3.94	4.01	*0.15*	4.31	*0.16*	3.73	*0.12*
MnO	0.08	0.07	0.05	0.05	*0.02*	0.05	*0.01*	0.04	*0.01*	0.05	*0.02*	0.06	0.03	0.06	*0.02*	0.08	*0.02*	0.07	*0.02*
MgO	1.11	1.52	2.53	1.21	*0.05*	1.30	*0.06*	1.08	*0.07*	1.22	*0.09*	0.92	1.21	1.44	*0.04*	1.77	*0.05*	1.54	*0.06*
CaO	2.95	4.13	5.75	3.26	*0.12*	3.42	*0.14*	3.08	*0.14*	3.29	*0.20*	2.62	3.20	3.65	*0.14*	4.23	*0.15*	3.89	*0.20*
Na_2O	4.93	4.67	4.49	4.48	*0.20*	4.45	*0.13*	4.65	*0.11*	4.55	*0.14*	4.38	4.47	4.78	*0.15*	4.93	*0.27*	4.82	*0.21*
K_2O	3.11	2.62	1.91	3.02	*0.08*	2.94	*0.07*	3.04	*0.09*	2.94	*0.07*	3.02	2.76	2.60	*0.05*	2.31	*0.04*	2.32	*0.06*
P_2O_3	0.22	0.29	0.14	0.18	*0.04*	0.18	*0.04*	0.17	*0.03*	0.17	*0.02*	0.13	0.21	0.26	*0.02*	0.23	*0.03*	0.20	*0.03*
Cl	0.07	0.09	0.06	0.16	*0.16*	0.09	*0.02*	0.09	*0.04*	0.08	*0.01*	0.03	0.11	0.09	*0.05*	0.07	*0.02*	0.05	*0.01*

b) West of the Restaurant site

Sample	MXC-25**			MXC-26		MXC-27		MXC-28		MXC-29		MXC-30		MXC-31		MXC-32		MXC-33		MXC-34	
Eruption	WRT-1			WRT-2		WRT-2		WRT-3		WRT-3		WRT-4		WRT-5		WRT-6		WRT-7		WRT-8	
n	23			14		11		26		15		21		22		12		23		12	
SiO_2	71.80	66.79	60.19	67.56	*0.36*	66.60	*0.52*	61.35	*0.34*	60.81	*0.21*	61.70	*0.23*	68.49	*0.62*	66.92	*0.41*	68.95	*0.46*	65.02	*0.59*
TiO_2	0.76	1.00	1.05	0.51	*0.04*	0.81	*0.07*	1.03	*0.04*	1.04	*0.03*	1.04	*0.03*	0.75	*0.06*	0.67	*0.04*	0.61	*0.04*	0.96	*0.11*
Al_2O_3	14.07	15.29	17.56	16.87	*0.27*	16.73	*0.49*	17.83	*0.21*	18.04	*0.16*	17.53	*0.15*	15.96	*0.31*	16.63	*0.28*	15.92	*0.34*	16.72	*0.80*
FeOt	2.86	4.85	5.95	3.13	*0.18*	3.61	*0.18*	5.00	*0.23*	5.26	*0.16*	5.19	*0.12*	3.16	*0.19*	3.65	*0.15*	2.97	*0.08*	4.02	*0.45*
MnO	0.04	0.06	0.12	0.05	*0.02*	0.06	*0.02*	0.09	*0.02*	0.08	*0.02*	0.09	*0.02*	0.05	*0.02*	0.07	*0.02*	0.05	*0.02*	0.08	*0.02*
MgO	0.55	1.65	3.62	1.06	*0.10*	1.22	*0.11*	2.54	*0.11*	2.69	*0.10*	2.46	*0.08*	1.04	*0.07*	1.19	*0.09*	0.95	*0.05*	1.53	*0.27*
CaO	2.01	3.87	6.50	3.64	*0.22*	3.66	*0.22*	5.52	*0.18*	5.55	*0.16*	5.25	*0.10*	3.20	*0.20*	3.49	*0.18*	3.11	*0.25*	4.34	*0.48*
Na_2O	4.72	3.04	3.27	4.65	*0.31*	4.86	*0.17*	4.67	*0.11*	4.59	*0.09*	4.69	*0.09*	4.55	*0.32*	4.95	*0.15*	4.78	*0.17*	4.71	*0.28*
K_2O	3.05	3.18	1.57	2.01	*0.17*	2.18	*0.20*	1.71	*0.11*	1.65	*0.06*	1.79	*0.06*	2.49	*0.11*	2.14	*0.16*	2.36	*0.09*	2.24	*0.19*
P_2O_3	0.09	0.25	0.11	0.16	*0.03*	0.17	*0.04*	0.19	*0.04*	0.21	*0.02*	0.20	*0.03*	0.16	*0.04*	0.20	*0.04*	0.14	*0.04*	0.26	*0.03*
Cl	0.06	0.03	0.06	0.34	*0.41*	0.10	*0.04*	0.06	*0.02*	0.07	*0.05*	0.07	*0.01*	0.15	*0.17*	0.09	*0.05*	0.16	*0.19*	0.12	*0.04*

c) Fork in the Road site

Sample	MXC-102		MXC-103		MXC-104		MXC-105		MXC-106*		MXC-107	
Eruption	FRT-1		FRT-2		FRT-3		FRT-4		FRT-5		FRT-6	
n	25		14		13		19		28		19	
SiO_2	72.09	*0.21*	70.80	*0.62*	63.80	0.76	63.21	*0.35*	73.21	68.09	*66.02*	*0.62*
TiO_2	0.42	*0.03*	0.78	*0.04*	0.79	0.08	0.66	*0.04*	0.49	0.91	*0.98*	*0.06*
Al_2O_3	15.14	*0.15*	14.47	*0.30*	17.51	1.08	17.96	*0.22*	14.39	15.49	15.92	0.20
FeOt	2.19	*0.09*	2.99	*0.22*	4.23	0.54	4.31	*0.18*	1.92	3.47	*3.96*	*0.13*
MnO	0.04	*0.02*	0.06	*0.02*	*0.07*	*0.02*	0.08	*0.02*	0.02	0.07	0.06	0.02
MgO	0.57	*0.03*	0.75	*0.07*	1.65	0.46	2.02	*0.08*	0.47	1.11	*1.59*	*0.13*
CaO	2.28	*0.06*	2.37	*0.18*	4.39	0.63	5.04	*0.22*	1.79	3.01	*3.93*	*0.21*
Na_2O	4.45	*0.16*	4.77	*0.12*	4.75	0.48	4.37	*0.19*	3.82	4.65	4.80	0.28
K_2O	2.63	*0.05*	2.74	*0.09*	2.38	0.37	1.91	*0.07*	3.72	2.98	2.47	0.07
P_2O_3	0.08	*0.02*	0.16	*0.11*	0.27	0.06	0.22	*0.04*	0.10	0.16	0.20	0.04
Cl	0.11	*0.07*	0.13	*0.01*	0.17	0.19	0.24	*0.25*	0.06	0.07	*0.06*	*0.02*

d) Xalitzintla Quarry site

Sample	MXC-97		MXC-98*		MXC-99		MXC-100		MXC-101	
Eruption	XQT-1		XQT-2		XQT-3		XQT-4		XQT-7	
n	20		20		22		25		11	
SiO_2	57.48	*0.65*	70.13	66.84	74.89	*0.27*	60.43	*0.46*	62.06	*0.32*
TiO_2	1.19	*0.07*	1.14	1.01	0.29	*0.04*	1.32	*0.06*	1.04	*0.04*
Al_2O_3	16.57	*0.42*	13.60	16.39	14.12	*0.22*	17.07	*0.14*	17.45	*0.25*
FeOt	6.99	*0.37*	4.31	3.61	1.42	*0.13*	6.57	*0.27*	5.70	*0.19*
MnO	0.13	*0.02*	0.08	0.04	0.03	*0.02*	0.12	*0.02*	0.11	*0.03*
MgO	4.82	*0.25*	0.79	0.77	0.34	*0.07*	2.43	*0.13*	2.04	*0.08*
CaO	8.00	*0.32*	2.67	3.95	1.62	*0.08*	5.41	*0.19*	4.89	*0.21*
Na_2O	3.44	*0.24*	5.20	4.80	4.12	*0.20*	4.33	*0.16*	4.67	*0.21*
K_2O	1.15	*0.10*	1.83	2.31	3.02	*0.06*	1.94	*0.08*	1.75	*0.13*
P_2O_3	0.18	*0.03*	0.21	0.20	0.04	*0.03*	0.29	*0.04*	0.24	*0.05*
Cl	0.05	*0.01*	0.05	0.06	0.12	*0.04*	0.08	*0.03*	0.07	*0.01*

Average and standard deviations (italics) for tephra deposits recorded through the Nepopualco sequence. Compositions in weight percent (wt%) were determined using a wavelength-dispersive EMP (see Section 5). N = number of analyses. See Supplementary material for the raw data and secondary standards. Bimodal** and trimodal*** samples are shown as selected representative compositions for each sub-component instead of by the average and standard deviation.

Popocatépetl compositional field (andesite dacite units within and close to the blue area in Fig. 12; 59.61 68.47 wt% SiO_2, 0.84 2.83 wt% MgO, 2.86 6.03 wt% CaO, 1.42 3.28 wt% K_2O, and 15.42 18.28 wt% Al_2O_3), with only two units within the Iztaccíhuatl field (XQT 3 and FRT 1 within the red area of Fig. 12; 71.38 75.34 wt% SiO_2, 0.13 0.67 wt% Mg, 1.23 2.48 wt% CaO, 2.50 3.16 wt% K_2O, and

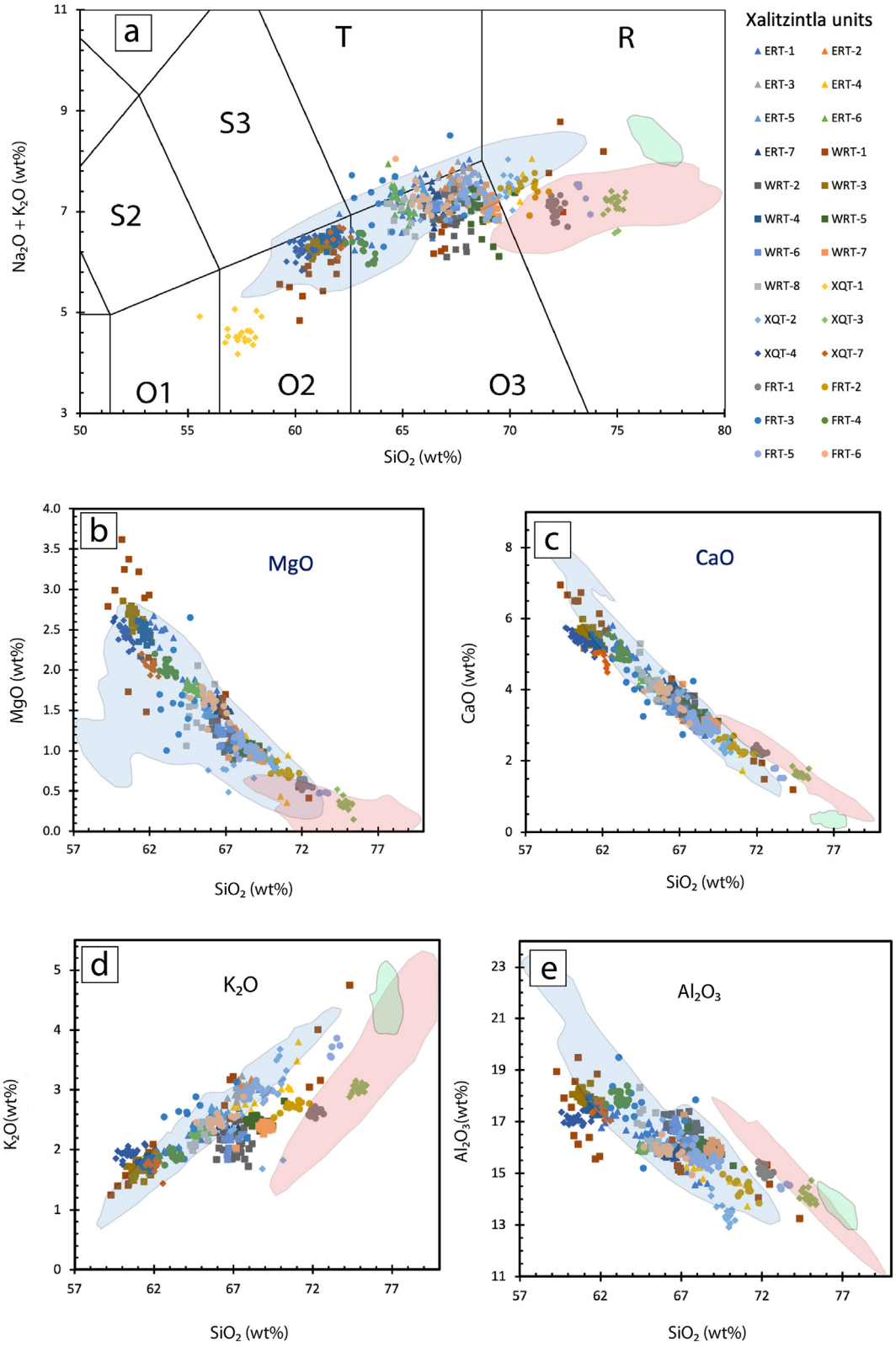


Fig. 12. a) Total alkali vs silica (TAS) of 26 tephras identified in the Xalitzintla region (shown in Fig. 6a); and bivariate plots of b) SiO_2 vs MgO, c) SiO_2 vs CaO, d) SiO_2 vs K_2O and e) SiO_2 vs Al_2O_3, displayed together with the compositional field of Popocatépetl (blue area), Iztaccíhuatl (red area), and Tláloc-Telapón (green area) volcanoes.

13.92 15.61 wt% Al_2O_3). None of the Xalitzintla tephras plot into the Tlloc Telapn compositional field (no points within green area, Fig. 12), but several tephras plot outside our defined Popocatépetl field (yellow diamonds, Fig. 12a). Other tephra layers outside the fields include XQT 4 (blue diamonds in Fig. 12) and one of the WRT 1 populations (red squares in Fig. 12), which are andesites with slightly lower CaO and Al_2O_3 glass compositions relative to the Popocatépetl trend.

6. New Argon-Argon dates

Various deposits from the studied outcrops were $^{40}Ar/^{39}Ar$ dated in this study. These new $^{40}Ar/^{39}Ar$ age ranges are reported at 2σ. From these, two analyses related to the San Valentín Ignimbrite (samples MXC 50 and MXC 88 from sites 2 and 3 respectively in Fig. 1c), that erupted from Tláloc Telapón volcano, were previously dated by radio carbon to ~46 cal. ka BP (around the limit of the technique; Rueda et al., 2007; García Tovar and Martínez Serrano, 2011; Macías et al., 2012). Analyses on single sanidine crystals yielded ages of 101 ± 2 ka (MXC 50; 2σ) and 103 ± 3 ka (MXC 88; 2σ), indicating that this ignim brite is substantially older than previously inferred from radiocarbon dating (Table 7). Moreover, new radiocarbon dates obtained from large charcoal pieces found within this deposit were beyond the upper limit of this method (>50 ka; Supplementary material 2).

Three $^{40}Ar/^{39}Ar$ ages were obtained from the Nepopualco sequence. Unfortunately, no sanidines were found in the tephras so the resulting ages were determined from plagioclase and hornblende concentrates, producing ages with larger errors. Analyses on hornblendes (sample MXC 05) from NT 2 (the Nepopualco Ignimbrite), which is the lower most tephra of this sequence, yielded an eruption age of 631 ± 44 ka (2σ). This new date is consistent with the underlying LPDAD age range but suggests that the DAD is older than the median age previously reported (440 ± 190 ka; Macías et al., 2012; Fig. 3). Analyses on plagio clase from the NT 12 fallout unit (sample MXC 15), located in the Mid dle Nepopualco Tephras (Fig. 4), yielded an eruption age of 620 ± 52 ka (2σ). This age is very similar to that of NT 2, but based on their error av erages, a time interval of up to ~100 ka could have elapsed between the NT 2 and NT 12 eruptions. At least nine additional explosive eruptions occurred during this period based on the Nepopualco stratigraphy (Table 2). Analyses on plagioclase from the NT 23 (sample MXC 46), lo cated in the Upper Nepopualco Tephras (Fig. 5), yielded an eruption age of 369 ± 22 ka (2σ). Several eruption deposits occur between the two dated horizons (NT 12 and NT 23).

Three additional reliable ages were obtained from the Xalitzintla Restaurant sites: one from a tephra exposed in the easternmost outcrop (ERT 3 unit) and two from tephras in the westernmost outcrop (WRT 6 and 7). Unfortunately, tephras from the other two Xalitzintla sites (Quarry and Fork in the road) did not yield suitable results due to the absence of appropriate minerals (e.g., sanidines or hornblendes, and inclusion free plagioclases). All $^{40}Ar/^{39}Ar$ dates for these Xalitzintla tephras were from aliquots of plagioclase crystals. ERT 2 yielded a 2σ eruption age of 236 ± 24 ka (Fig. 6), WRT 6 an age of 431 ± 40 ka (Fig. 7) and WRT 7 an age of 354 ± 58 ka (Table 7). A summary of the $^{40}Ar/^{39}Ar$ dates is reported in Table 7 (raw data and age plots in Supple mentary materials 3 and 4).

7. Tephra correlations

7.1. Tephra correlations between the Xalitzintla and Nepopualco sequences

In order to complement the chemical characterization and the correla tion of the studied tephras, we plotted the abundance of TiO_2 vs SiO_2 for the Xalitzintla and Nepopualco tephras (Fig. 13). The data are distributed into two well defined fields, which largely coincide with the defined com positional fields of Popocatépetl and Iztaccíhuatl volcanoes (blue and red areas in Fig. 13a). Because these plots do not follow a narrow trend (as generally is the case in the other bivariate plots of MgO, CaO, K_2O, and Al_2O_3; Figs. 11 and 12), but are more spatially separated, it is possible to infer some tephra correlations between these two sites. For example, the rhyolitic FRT 1 tephra (yellow triangles in Fig. 13e) recorded in Xalitzintla is very similar to the NT 11 (solid green diamonds in Fig. 13e) in its glass composition (rhyolitic), both forming tight clusters with limited overlap with any other units. Both deposits share a similar mineralogy (e.g. both contain hornblende; Tables 2 and 3) and physical characteristics, being ~1 m thick, normal graded, white pumice fallout deposits that are lithic rich at the top (see Section 4 for more details and Fig. 14). We infer that these pyroclastic deposits (FRT 1 and NT 11) are associated to the same explosive eruption and were most likely produced by Iztaccíhuatl volcano. Another rhyolitic tephra recorded in Xalitzintla, XQT 3 (empty red dia monds in Fig. 13e), partially overlaps the compositional field of NT 3, NT 4, and NT 8 (empty green triangles and diamonds, and green dashes in Fig. 13e), but based on its overall physical and sedimentological charac teristics, it could only be potentially correlative with NT 4. Both XQT 3 and NT 4 are white pumice fallouts that are 39 and 52 cm thick respectively (see Section 4 and Fig. 14), while NT 8 is an ignimbrite without any asso ciated fallout, and NT 3 is a 35 cm thick, lithic rich, coarse lapilli fallout. NT 04 is compositionally diverse and although most of the glass chemical analyses are scattered, there are some analyses that plot within the XQT 3 field, which suggests they could correlate.

Some andesite dacite tephras at Xalitzintla, which plot within the Popocatépetl compositional field (blue area in Fig. 13), are chemically similar to some Nepopualco units. WRT 7 (yellow plus sign in Fig. 13b) appears to correlate with NT 23 (solid blue diamonds in Fig. 13c), as the glass chemistry is similar. They are both thick white pumice fallout units (1.6 and 1.1 m respectively, Fig. 14) comprising medium to coarse lapilli, and the same mineralogy (plagioclase, orthopyroxene, and oxides; Tables 2 and 3). Moreover, their $^{40}Ar/^{39}Ar$ ages also support this correlation NT 23 is dated to 369 ± 11 ka and WRT 7 is 354 ± 29 ka. These data suggest that WRT 7 correlates to NT 23 and both stem from the same Popocatépetl eruption. Although less clear, there is some compositional overlap between WRT 6 (solid orange dots, Fig. 13b) and NT 19 (solid sky blue squares, Fig. 13b) as well as NT 22 (solid marine blue triangles, Fig. 13b). Differences in the

Table 7
Summary of $^{40}Ar/^{39}Ar$ dates reported in this study.

Unit	Sample	Mineral	Location		Locality	Outcrop	Age (ka;2σ)	MSWD
			North	West				
NT-2	MXC-05	Hornblende	19.149749°	98.508040°	Nepopualco	5	630 ± 44	1.49
NT-12	MXC-15	Plagioclase	19.149749°	98.508040°	Nepopualco	5	619 ± 52	1.19
ERT-3	MXC-19	Plagioclase	19.078794°	98.506966°	Xalitzintla	6	236 ± 24	1.08
WRT-6	MXC-32	Plagioclase	19.080099°	98.507531°	Xalitzintla	7	431 ± 40	1.50
WRT-7	MXC-33	Plagioclase	19.080099°	98.507531°	Xalitzintla	7	353 ± 58	1.54
NT-23	MXC-46	Plagioclase	19.149749°	98.508040°	Nepopualco	5	368 ± 22	1.35
SVI	MXC-50	Sanidine*	19.477587°	98.575406°	Nanacamilpa	2	101 ± 2	1.20
SVI	MXC-88	Sanidine*	19.396556°	98.624861°	San Juan C.	3	103 ± 3	1.30

SVI = San Valentin Ignimbrite; NT = Nepopualco Tephras; ERT = East of the Restaurant Tephras; WRT = West of the Restaurant Tephras; ka = thousand years; 2σ = two sigma; MSWD = Mean Squared Weighted Deviation.

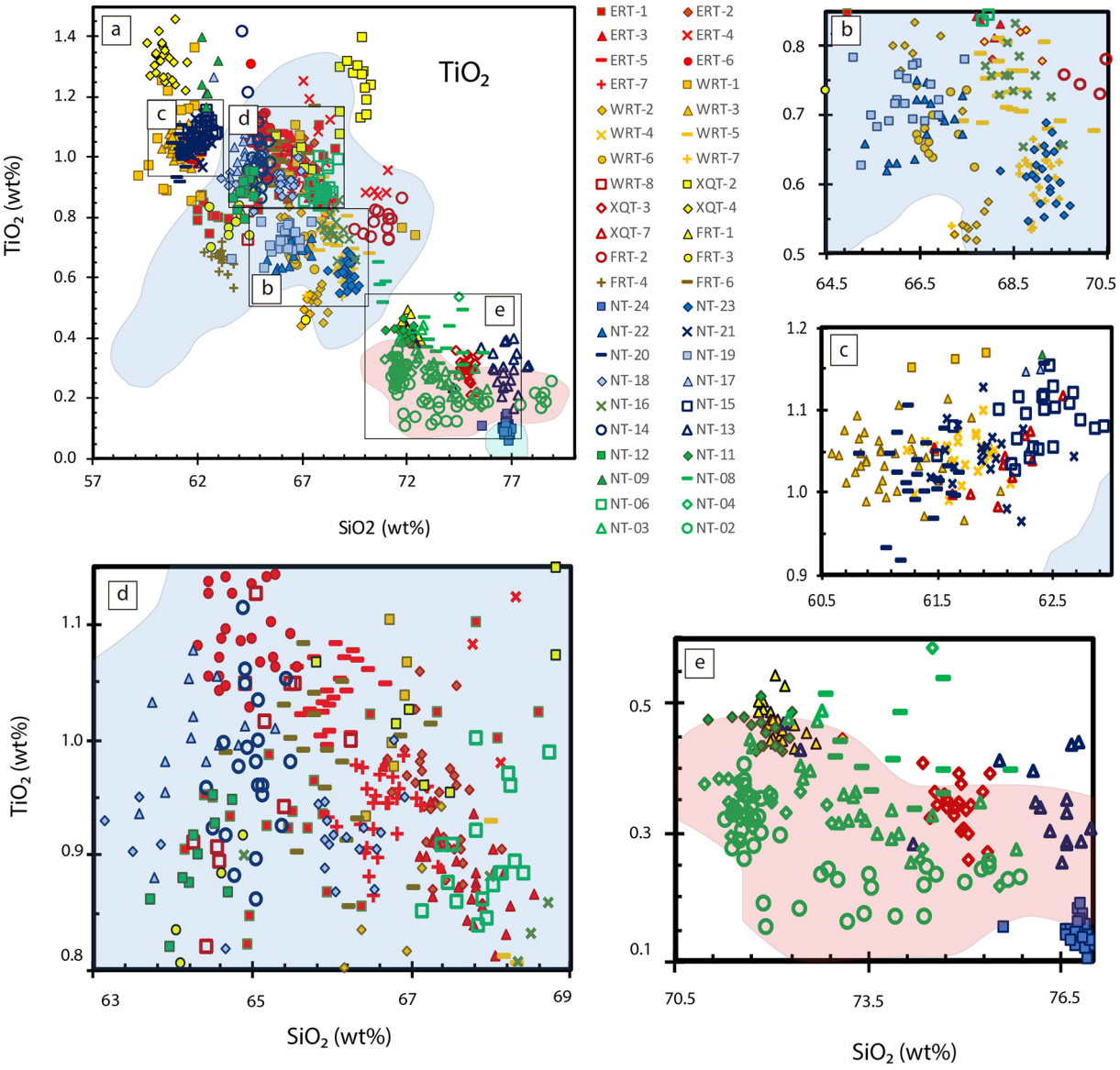
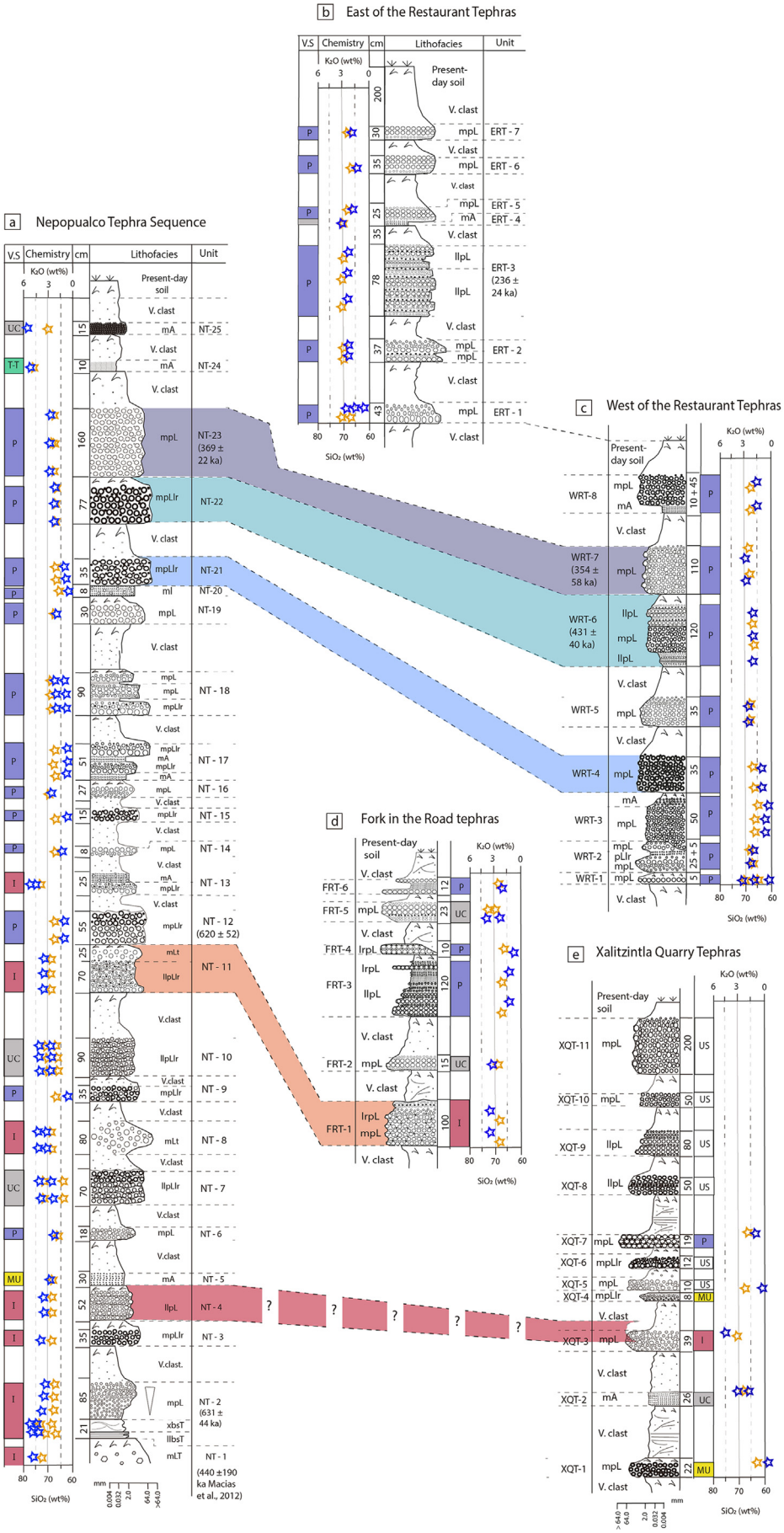


Fig. 13. TiO_2 vs SiO_2 plots of: a) tephras from East of the Restaurant (ERT, blue colours) in front of the West of the Restaurant tephras (WRT, red colours) of Xalitzintla; b) tephras from WR in front of tephras from Xalitzintla Quarry (XQ, yellow colours) and Fork in the Road tephras (green colours); c) tephras recorded in Nepopualco region (NT, green and blue colours) in front of Xalitzintla tephras (ERT, WRT, XQT and FRT, red and yellow colours), displayed together with the compositional fields of Popocatépetl (blue area), Iztaccíhuatl (red area), and Tláloc (green area) volcanoes; d) and e) details of two extended areas of the graph in c). Error bars for TiO_2 are ± 0.06 and 0.6 wt% (2s) for SiO_2 based on replicate analyses of the MPI-DING reference glasses.

deposit characteristics and stratigraphy of the deposits do not support a correlation between WRT 6 and NT 19, but a correlation with NT 22 is supported: NT 22 is a 78 cm thick pumice fallout of medium to coarse lapilli, rich in lithics and similar to the medial part of the WRT 6 deposit (Fig. 14). The mineralogy (hornblende, plagioclase, orthopyroxene, and oxides; Tables 2 and 3) and stratigraphy order further support that WRT 6 and NT 22 could have been produced by the same explosive eruption. The similar glass compositions, deposit characteristics, mineralogy, and stratigraphic positions of NT 21 (blue crosses in Fig. 13c) and WRT 4 (yellow crosses in Fig. 13c) also suggest that they correlate. Both are 35 cm thick lithic rich, coarse lapilli pumice fallout units (see Section 3 and Fig. 14). Finally, NT 20 (blue dashes in Fig. 13c) shows similarities to WRT 3 (solid orange triangles in Fig. 13c) based on the glass chemistry (Figs. 11 and 12), mineralogy (plagioclase, orthopyroxene, and oxides; Tables 2 and 3) and chronostratigraphy (Fig. 14). However, the WRT 3 deposit is a 50 cm thick dark unit composed of grey fine to medium lapilli pumice with abundant lithics, and is lithologically different from NT 20, which is an 8 cm thick dark unit of lithics (> 70%) with a few fine lapilli pumices and coarse ash. This correlation is thus less certain, although both deposits could stem from the same eruption if the Nepopualco site was located at the fallout margin with respect to the dispersal axis of the deposit. There are other units with similar glass geochemistry (Fig. 13d) but their mineralogy (see Tables 2 and 3) and chronostratigraphy (Fig. 14) do not support feasible correlations.

Despite both sequences spanning comparable age ranges, several other tephra units recorded in Xalitzintla cannot be correlated to any of the Nepopualco tephras based on glass compositions (Fig. 13a). These include: XQT 2 (solid yellow squares), XQT 4 (solid yellow diamonds), WRT 2 (solid orange diamonds), FRT 4 (brown plus signs), ERT 5 (red dashes), FRT 6 (brown dashes), and ERT 7 (red plus sign). Thus, these deposits appear to represent additional explosive eruptions to the 25 units already recorded at Nepopualco. Their absence in Nepopualco may either be related to the dispersal axis not overlapping


a Nepopualco Tephra Sequence
b East of the Restaurant Tephras
c West of the Restaurant Tephras
d Fork in the Road tephras
e Xalitzintla Quarry Tephras
V.S
Chemistry
K2O (wt%)
cm
Lithofacies
Unit
SiO2 (wt%)
Present-day soil
V. clast
mA
mpL
mpLlr
mlpL
mlt
mlT
ml
xbsT
llbsT
NT-25
NT-24
NT-23 (369 ± 22 ka)
NT-22
NT-21
NT-20
NT-19
NT - 18
NT - 17
NT - 16
NT - 15
NT - 14
NT - 13
NT - 12 (620 ± 52)
NT - 11
NT - 10
NT - 9
NT - 8
NT - 7
NT - 6
NT - 5
NT - 4
NT - 3
NT - 2 (631 ± 44 ka)
NT - 1 (440 ±190 ka Macias et al., 2012)
ERT - 7
ERT - 6
ERT - 5
ERT - 4
ERT-3 (236 ± 24 ka)
ERT - 2
ERT - 1
WRT-8
WRT-7 (354 ± 58 ka)
WRT-6 (431 ± 40 ka)
WRT-5
WRT-4
WRT-3
WRT-2
WRT-1
FRT-6
FRT-5
FRT-4
FRT-3
FRT-2
FRT-1
XQT-11
XQT-10
XQT-9
XQT-8
XQT-7
XQT-6
XQT-5
XQT-4
XQT-3
XQT-2
XQT-1
mm

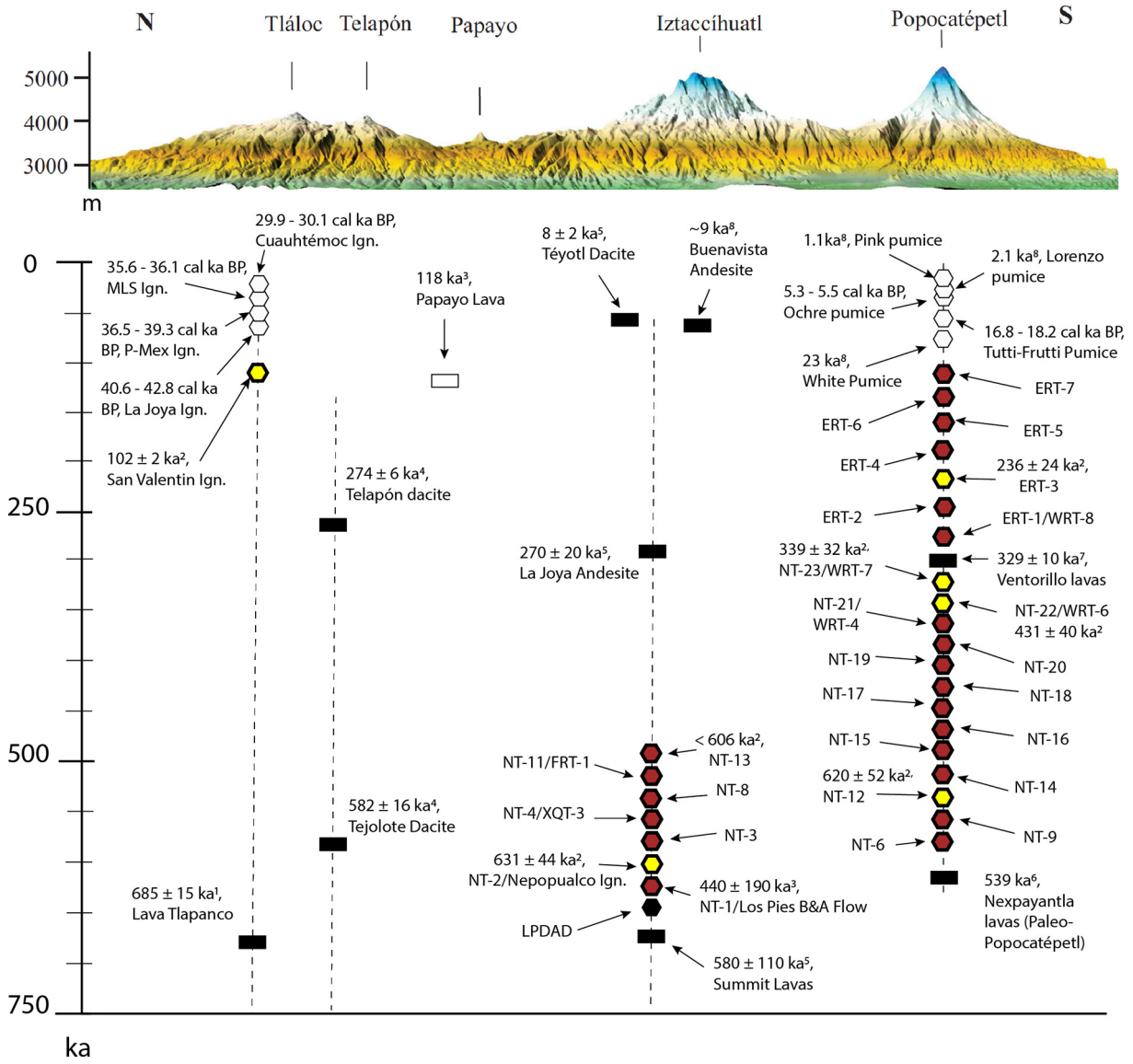


Fig. 15. Topographic profile of the Sierra Nevada Volcanic Range (SNVR), the new identified explosive eruptions from Popocatépetl and Iztaccíhuatl, as well as the new $^{40}Ar/^{39}Ar$ age for the San Valentín Ignimbrite from Tláloc-Telapón and other relevant eruptive episodes during the formation of the range (after García-Tovar and Martínez-Serrano, 2011). The dashed lines indicate the inferred time of activity for each volcano. The black rectangles are lavas with published $^{40}Ar/^{39}Ar$ or $^{40}K/^{40}Ar$ ages, the black hexagon is the debris avalanche deposit related to Los Pies collapse (LPDAD), the red and yellow hexagons are respective relative and absolute ages of the pyroclastic deposits characterized for the first time in this study, and the empty symbols are published C14 ages (rectangles for lavas and hexagons for tephras). 1 = Cadoux et al., (2011; 2σ); 2 = This study ($^{40}Ar/^{39}Ar$; 2σ); 3 = Macías et al. (2012; 1σ); 4 = García-Tovar and Martínez-Serrano (2011; 2σ); 5 = Nixon (1989; assuming 2σ); 6 = Conte et al. (2004; assuming 2σ); 7 = Sosa-Ceballos et al. (2015; 1σ); 8 = Siebe et al. (1996; assuming 2σ).

with Nepopualco, due to the primary deposits being too thin to be pre served as discrete, visible horizons. Nevertheless, the matching charac teristics of multiple tephras within a continuous stratigraphic section at both Nepopualco and Xalitzintla (particularly WRT), supported by $^{40}Ar/^{39}Ar$ ages, allow for a robust correlation between these two sites.

7.2. Chronological order of the Xalitzintla outcrops

The Xalitzintla outcrops had not been previously studied and given the limited lateral continuity of the field exposures, it was not possible to correlate any single tephra unit across all of the four sites. However, the new $^{40}Ar/^{39}Ar$ dates and glass chemical analyses provide prelimi nary chronostratigraphic constraints. ERT 3 preserved in the sequence exposed at the East of the Restaurant site (Fig. 6) has been dated to 236 ± 12 ka, and the WRT 7 tephra exposed at the West of the Restau rant (Fig. 7) has an age of 339 ± 16 ka, suggesting that the western out crop comprises an older segment of the stratigraphy. In addition, we infer that tephras exposed at the Xalitzintla Quarry and Fork in the Road (Figs. 8 and 9) are older than those at the restaurant sites (Fig. 14) because the lowermost units include rhyolitic tephras (FRT 1

Fig. 14. Stratigraphic correlation of a) Nepopualco and b) – c) Xalitzintla tephra layers (East and West of the Restaurant, Fork in the road and Xalitzintla Quarry). The blue stars indicate the average SiO_2 (wt%) composition of each population and the orange stars the K_2O (wt%). V·S = volcanic source, P = Popocatépetl (in blue), I = Iztaccíhuatl (in red), T-T = Tláloc-Telapón (in green), MU = mafic unknown (in yellow), UC = uncertain (in grey), and US = unsampled pyroclastic deposits (white).

and XQT 3, Figs. 12 and 13) that correlate to the Nepopualco Lower Tephras erupted from Iztaccíhuatl volcano (NT 4 and NT 11, Fig. 14). Iztaccíhuatl is thought to have been largely active before activity commenced at Popocatépetl ~540 ka (e.g. Cadoux et al., 2011; Delgado Granados et al., 2017; see also Section 2.1). These observations suggest the Xalitzintla exposures are separate stratigraphic sections and do not overlap (Fig. 14).

8. Chemical variations through the Nepopualco tephra sequence and its implications for the volcanic histories of Popocatépetl and Iztaccíhuatl

Considering the geochemical compositions of the tephra layers in the Nepopualco sequence, and the possible correlation of tephras to their volcanic sources using glass chemistry (see Fig. 11), we propose that Iztaccíhuatl is the source of the rhyolitic tephras recorded near the base of the gully since at least 631 ± 44 ka ($^{40}Ar/^{39}Ar$ age of Nepopualco Ignimbrite or NT 2; Fig. 3 and Table 1), while Popocatépetl started its eruptive activity later, erupting generally andesite dacite tephras (Table 2). It appears that there was a period of coeval activity between Iztaccíhuatl and Popocatépetl volcanoes, when rhyolitic and andesite dacite tephras were deposited contemporaneously. The oldest Popocatépetl unit that we recognise is NT 6. Although this is not directly dated, it lies well below NT 12 (also attributed to Popocatépetl; dated at 620 ± 52 ka). This suggests that Popocatépetl was active prior to 600 ka. Between the NT 6 and NT 14 eruptions (both attributed to Popocatépetl, and representing ~100 ka considering the new $^{40}Ar/^{39}Ar$ ages of NT 2 and NT 12; Table 2), we identify several explosive eruptions from Iztaccíhuatl, but no more after this point. This is inferred from the absence of younger pumice fallouts with glass compositions that plot along the Iztaccíhuatl fractionation trend in the younger stratigraphy. Meanwhile, most of the deposits recorded in the Middle and Upper Nepopualco Tephras plot along the Popocatépetl fractionation trend, indicating that it has continued to periodically erupt and distribute tephras over the region up until the present day (Figs. 4, 5, and 11; Table 2).

The fine ash layer (NT 24) deposited at the top of the sequence (Fig. 5) may have been produced by Tláloc Telapón (for example, from a co ignimbritic ash plume of one of the late Pleistocene Tláloc Telapón ignimbrites; Fig. 11).

The Nepopualco tephra sequence contains evidence for at least 25 explosive eruptions produced during the last ~650 ka: at least 13 are from Popocatépetl and 6 are from Iztaccíhuatl. But explosive eruptions from other sources are also recorded in Nepopualco, including one from the Tláloc Telapón and one from an unknown mafic source (possibly a nearby monogenetic cone). There are two units near the base of the Nepopualco sequence with an uncertain source, and at least three in the older Xalitzintla sequences (XQT and FRT) that we are unable to attribute. It is possible that these events, which would overlap with both the earliest stages of Popocatépetl's explosive eruption history, or the final stages of Iztaccíhuatl's explosive eruption history (based on the inferences we make above), represent more compositionally diverse magmatism during this transitional phase of SNVR development.

9. Insight into the general volcanic history, magnitudes, and tephra distribution in the México basin

The chronological, chemical, and stratigraphic correlation between Xalitzintla and Nepopualco tephras (including NT 23 to WRT 7 and WRT 8 to ERT 1, Fig. 14) allows us to establish that at least 7 explosive eruptions from Popocatépetl are recorded at Xalitzintla in addition to the 13 eruptions registered in Nepopualco. These are associated with the 7 tephras recorded in the East of the Restaurant site (ERT 1 to ERT 7, including the 236 ± 12 ka ERT 3), which is the youngest unit from Popocatépetl that we document. The late Pleistocene Holocene Plinian deposits studied previously by other authors (e.g. the Grey, White or Tutti Frutti pumices) have not been observed in these Xalitzintla tephra sequences we have studied, and fall within a younger stratigraphic interval than is exposed in our study area.

During the middle to late Pleistocene, our new observations imply that the SNVR produced widespread tephra deposits from at least 20 medium to large explosive eruptions from Popocatépetl volcano, 6 from Iztaccíhuatl, 1 from Tláloc Telapón, and 2 eruptions from nearby unknown mafic sources. At least 5 further eruptions, based on their location, physicochemical characteristics and stratigraphic position, are also likely to have been erupted from either by Popocatépetl or Iztaccíhuatl. The results of this tephrostratigraphic work considerably extend the longer term understanding of the explosive volcanic history of the Popocatépetl, Iztaccíhuatl and Tláloc Telapón volcanoes (Fig. 15).

Comparing the recorded thicknesses in these tephra sequences with those of the most recent Popocatépetl eruptions (e.g. the ~27.8 cal. ka BP White Pumice, Siebe et al., 2017; or the 16,796 18,201 cal. yr Tutti Frutti Pumice, Sosa Ceballos et al., 2012) and considering the prevailing winds of the region (Bonasia et al., 2014), most of the middle to late Pleistocene explosive eruptions identified in the Nepopualco and Xalitzintla outcrops are likely to have distributed tephra over the México and/or Puebla basins. For example, previous studies on the Tutti Frutti eruption estimated that the México City area was covered with at least 10 cm of tephra (Siebe et al., 1999; Sosa Ceballos et al., 2012), with thicknesses of ~150 cm in the Xalitzintla region (Siebe et al., 2017). If we assume that at least some of the eruptions documented above, especially those with thicknesses of ~1 m, had similar NW dispersal axies, these eruptions could have also deposited tephra across the México Basin and the area occupied today by México City. The eruption related to the WRT 7/NT 23 tephra (354 ± 29 ka), deposited 1.1 m of pyroclastic material in Xalitzintla and 1.6 m in Nepopualco (Fig. 14). It could have deposited several cm of tephra across the México Basin . If the dispersal axis for the WRT 7/NT 23 eruption was the same as that for the Tutti Frutti event, its thickness at our study sites suggests an eruption of similar magnitude (VEI ~6; involving 5 km^3 of tephra and an estimated 44 km high eruption column; Sosa Ceballos et al., 2012).

Recent studies on lacustrine sediments in Lake Chalco, which lies in the southern part of México Basin, east of SNVR (e.g., Ortega Guerrero et al., 2018) have correlated several tephra layers to eruptions of nearby stratovolcanoes, including the Tutti Frutti Pumice from Popocatépetl (Siebe et al., 1999; Sosa Ceballos et al., 2012), the MWP tephra from Tláloc (Rueda et al., 2013) and the Upper and Lower Toluca Pumice deposits from Nevado de Toluca volcano (Arce et al., 2003, 2013). However, these studies have only considered sediments from the uppermost 122 m of the Chalco sequence that spans ~140 ka (Lozano García and Ortega Guerrero, 1994; Lozano García et al., 2015; Caballero and Guerrero, 1998; Ortega Guerrero et al., 2017). Older tephras recorded in deeper sections of Lake Chalco sediment cores (520 m) drilled in 2016 by the International Continental Scientific Drilling Program (ICDP) MexiDrill project (Brown et al., 2019; Valero Garcés et al., 2021). These will provide a more complete and long term record of the explosive volcanism around the México Basin, from which eruption frequencies, styles, and magnitudes can be ascertained. The tephrostratigraphy, ages, and glass compositions presented here will be of significance in reliably correlating newly identified tephras to their volcanic sources.

10. Conclusions

This chronostratigraphic and geochemical study of the Xalitzintla and Nepopualco tephra sequences in the Sierra Nevada Volcanic Range (SNVR) provides new insights into the middle to late Pleistocene explosive history of volcanoes surrounding the México basin.

Major element glass compositions determined by electron microprobe analysis have defined glass compositional fields for Popocatépetl, Iztaccíhuatl, and Tláloc Telapón volcanoes, and permitted the correlations of tephra layers exposed in the Nepopualco and Xalitzintla

sequences to their volcanic source. The Neopopualco and Xalizintla se quences contain deposits representing 20 Popocatépetl and 6 Iztaccí huatl explosive eruptions, 5 deposits of uncertain source but likely originating from these two volcanoes, and five deposits from more dis tal vents. These include at least 2 mafic deposits from unidentified sources (possibly from nearby monogenetic cones) and 1 tephra from Tláloc Telapón volcano related to one of their 5 late Pleistocene ignim brite eruptions (including the San Valentín Ignimbrite, recently $^{40}Ar/^{39}Ar$ dated in this study at ~102 ka).

Since the lateral collapse of the Iztaccíhuatl's Los Pies Cone (LPDAD event), dated in this study to ~631 ± 44 ka (2σ), Iztaccíhuatl has pro duced at least 6 explosive eruptions that have deposited ~1 m thick py roclastic deposits, pumice fallout units and/or ignimbrites that are rhyolitic in composition (e.g., Nepopualco ignimbrite or FRT 1/NT 11 fall). After a period of coeval activity with Popocatépetl volcano, explo sive activity at Iztaccíhuatl ceased (probably between 500 and 400 ka ago) while Popocatépetl continued its explosive activity until today. In addition to the 7 known Plinian eruptions in the last ~24 ka, Popocaté petl has produced at least 20 additional explosive eruptions during the Late Pleistocene. The Popocatépetl eruption deposits identified in Nepopualco and Xalitzintla sites are consistent with Plinian to sub Plinian eruptive columns, which deposited pumice fallout units with thicknesses of up to 1.6 m. These Popocatépetl deposits are predomi nantly andesitic to dacitic in composition with a few extending to more evolved rhyolitic compositions, and plot along a fractionation trend that is displaced to higher K_2O relative to the deposits of Iztaccíhuatl. Some of these eruptions (e.g. NT 23/WRT 7) are likely to have deposited centimetres of ash on the area that is now México City. This work provides a deeper insight into the explosive volcanic histories of Popocatépetl and Iztaccíhuatl volcanoes and characterizes many pre viously unidentified Late Pleistocene pyroclastic deposits in the SNVR.

The glass compositions of the well known Popocatépetl, Iztaccíhuatl and Tláloc Telapón deposits, together with the classification of Nepopualco and Xalitzintla tephras, provides a chemical database for fu ture correlations between the Chalco tephras and their volcanic sources, and other eruption deposits.

In summary, the chemical, stratigraphic and geochronologic investi gations made on the Xalitzintla and Nepopualco tephras, provide valu able information on the long term volcanic history of the volcanoes of the SNVR, including Popocatépetl, one of the most active volcanoes in the country. These data are crucial in densely populated regions located in very active tectonic and volcanic settings, such as México City, and provide a basis to assess potential risk and design strategies to ade quately address the hazard to urban infrastructure and human lives.

CRediT authorship contribution statement

Ivan Sunyé Puchol: Conceptualization, Investigation, Methodology, Project administration, Formal analysis, Validation, Visualization, Writ ing original draft, Writing review & editing. Alastair G.E. Hodgetts: Conceptualization, Investigation, Methodology, Project administration, Validation, Formal analysis, Visualization, Writing original draft, Writ ing review & editing. Sebastian F.L. Watt: Conceptualization, Investiga tion, Funding acquisition, Methodology, Project administration, Validation, Visualization, Writing original draft, Writing review & editing. José L. Arce: Investigation, Resources, Methodology, Validation, Visualization, Writing review & editing. Dan N. Barfod: Investigation, Methodology, Resources, Formal analysis, Validation, Visualization, Writing review & editing. Darren F. Mark: Funding acquisition, Meth odology, Resources, Project administration, Validation, Visualization, Writing review & editing. Giovanni Sosa Ceballos: Investigation, Methodology, Resources, Validation, Visualization, Writing review & editing. Claus Siebe: Investigation, Methodology, Validation, Resources, Visualization, Writing review & editing. Ross C. Dymock: Methodol ogy, Validation, Visualization, Formal analysis, Writing review & editing. Maarten Blaauw: Funding acquisition, Methodology, Resources, Project administration, Formal analysis, Validation, Visualization, Writing review & editing. Victoria C. Smith: Conceptualization, Data curation, Investigation, Funding acquisition, Resources, Methodology, Project administration, Supervision, Formal analysis, Validation, Visual ization, Writing original draft, Writing review & editing.

Declaration of Competing Interest

The authors declare that they have no known competing financial interests or personal relationships that could have appeared to influ ence the work reported in this paper.

Acknowledgements

ISP and this study were funded by the Natural Environment Re search Council (NERC), UK (NE/S009035 awarded to VCS, SFLW, MB and DFM). AGEH was funded by a NERC PhD studentship awarded through the Central England NERC Training Alliance (CENTA; grant ref erence NE/L002493/1). We acknowledge fieldwork logistic support from the National Autonomous University of Mexico (UNAM) and the field assistance of undergraduate students from the Institute of Geology, UNAM, including Miguel Meza, Jesús Morales and Kai Melo. Field sup port was also provided by Ainhoa Lorenzo. ISP acknowledge also to the MSCA Individual Fellowship (European Commission Grant No. 101024337), which was funding him while working on this manuscript during the last few months.

Appendix A. Supplementary data

Supplementary data to this article can be found online at https://doi.org/10.1016/j.jvolgeores.2021.107413.

References

Albert, P.G., Smith, V.C., Suzuki, T., Tomlinson, E.L., Nakagawa, T., McLean, D., Yamada, M., Staff, R.A., Schlolaut, G., Takemura, K., Nagahashi, Y., 2018. Constraints on the frequency and dispersal of explosive eruptions at Sambe and Daisen volcanoes (South-West Japan Arc) from the distal Lake Suigetsu record (SG06 core). Earth-Science Reviews 185, 1004–1028. Earth-Science Reviews 185.

Arana-Salinas, L., Siebe, C., Macías, J.L., 2010. Dynamics of the ca. 4,965 yr. B.P. "Ochre Pumice" Plinian eruption of Popocatépetl Volcano, México. J. Volcanol. Geotherm. Res. 192, 212–231. https://doi.org/10.1016/j.jvolgeores.2010.02.022.

Arce, J.L., Macías, J.L., Vázquez-Selem, L., 2003. The 10.5 ka Plinian eruption of Nevado de Toluca volcano, Mexico: stratigraphy and hazard implications. Geol. Soc. Am. Bull. 115 (2), 230–248.

Arce, J.L., Layer, P.W., Morales-Casique, E., Benowitz, J.A., Rangel, E., Escolero, O., 2013. New constraints on the subsurface geology of the Mexico City Basin: the San Lorenzo Tezonco deep well, on the basis of 40Ar/39Ar geochronology and whole-rock chemistry. J. Volcanol. Geotherm. Res. 266, 34–49. https://doi.org/10.1016/j.jvolgeores.2013.09.004.

Arce, J.L., Cruz-Fuentes, D., Ramírez-Luna, A., Herrera-Huerta, I.A., Girón-García, P., 2017. Pómez Bosque de Tlalpan, producto de una erupción de gran magnitud en el margen suroeste de la cuenca de México. Revista Mexicana de Ciencias Geológicas 34 (3). https://doi.org/10.22201/cgeo.20072902e.2017.3.485.

Bonasia, R., Scaini, C., Capra, L., Nathenson, M., Siebe, C., Arana-Salinas, L., Folch, A., 2014. Long-Range Hazard Assessment of Volcanic Ash Dispersal for a Plinian Eruptive Scenario at Popocatépetl Volcano (Mexico): Implications for Civil Aviation Safety. https://doi.org/10.1007/s00445-013-0789-z.

Branney, M.J., Kokelaar, P., 2002. Pyroclastic density currents and the sedimentation of ignimbrites. Geol. Soc. Lond. Mem. 27 (152 pp.).

Bronk Ramsey, C., 2009. Bayesian analysis of radiocarbon dates. Radiocarbon 51 (1), 337–360.

Bronk Ramsey, C., Housley, R.A., Lane, C.S., Smith, V.C., Pollard, A.M., 2015. The RESET tephra database and associated analytical tools. Quat. Sci. Rev. 118, 33–47. https://doi.org/10.1016/j.quascirev.2014.11.008.

Brown, E.T., Caballero, M., Cabral Cano, E., Fawcett, P.J., Lozano-García, S., Ortega, B., et al., 2019. Scientific drilling of Lake Chalco, Basin of Mexico (MexiDrill). Sci. Drill. https://doi.org/10.5194/sd-7-1-2019.

Caballero, M., Guerrero, B., 1998. Lake Levels since about 40,000 years Ago at Lake Chalco, near Mexico City. Quat. Res. 50 (1), 69–79. https://doi.org/10.1006/qres.1998.1969.

Cadoux, A., Missenard, Y., Martinez-Serrano, R.G., Guillou, H., 2011. Trenchward Plio-Quaternary volcanism migration in the Trans-Mexican Volcanic Belt: the case of the Sierra Nevada range. Geol. Mag. 148, 492–506. https://doi.org/10.1017/S0016756810000993.

Conte, G., Urrutia-Fucugauchi, J., Goguitchaichvili, A., Soler-Arechalde, A.M., Morton-Bermea, O., 2004. Paleomagnetic study of lavas from the Popocatépetl volcanic region, Central Mexico. Int. Geol. Rev. 46, 210–225.

Cornwall, I.W., 1971. Geology and early man in Central Mexico. The Henry Stopes lecture. Proc. Geol. Assoc. 82 (3), 379–391 6/S0016–7878(71)80016–0.

De la Cruz-Reyna, S., Quezada, J.L., Peña, C., Zepeda, O., Sánchez, T., 1995. Historia de la Actividad del Popocatépetl (1354–1995), Volcán Popocatépetl: Estudios Realizados Durante la Crisis de 1994–1995. Centro Nacional de Prevención de Desastres, Universidad Nacional Autónoma de México, pp. 3–22.

Delgado Granados, H., Cassatta, W., Gisbert Pinto, G., Renee, P., 2017. Los edificios volcánicos antiguos. In: Martin Del Pozzo, A.L., Alatorre Ibargüengoitia, M., Arana Salinas, L., Bonasia, R., Capra Pedol, L., Cassata, W., Cordoba, G., Cortés Ramos, J., Delgado Granados, H., Ferrés López, M.D., Fonseca Álvarez, R., García Reynoso, J.A., Gisbert, G., Guerrero López, D.A., Jaimes Viera, M.C., Macías Vázquez, J.L., Nieto Obregon, J., Nieto Torres, A., Paredes Ruiz, P.A., Portocarrero Martínez, J., Renne, P., Rodríguez Espinosa, D.M., Salinas Sánchez, S., Siebe Grabach, C., Tellez Ugalde, E. (Eds.), Estudios Geológicos y Actualización del Mapa de Peligros del Volcán Popocatépel. Memoria Técnica del Mapa de Peligros del Volcán Popocatépetl. Monografías del Instituto de 846 Geofísica - UNAM. 22. Universidad Nacional Autónoma de México, México 166 p. ISBN 978–607–02–9782-3.

Espinasa-Pereña, R., Martín-Del Pozzo, A.L., 2006. Morphostratigraphic evolution of Popocatépetl volcano, México. In: Siebe, C., Macías, J.L., Aguirre-Díaz, G. (Eds.), Neogene-Quaternary Continental Margin Volcanism: A Perspective from Mexico, Geological Society of America Special Paper 402, Penrose Conference Series, pp. 115–137 https://doi.org/10.1130/2006.2402(05.

Ferrari, L., Orozco-Esquivel, T., Manea, V., Manea, M., 2012. Tectonophysics the dynamic history of the Trans-Mexican Volcanic Belt and the Mexico subduction zone. Tectonophysics 522–523, 122–149. https://doi.org/10.1016/j.tecto.2011.09.018.

García-Palomo, A., Macías, J.L., Tolson, G., Valdez, G., Mora, J.C., 2002. Volcanic stratigraphy and geologic evolution of the Apan region, east-central sector of the Trans-Mexican Volcanic Belt. Geofis. Int. 41, 133–150.

García-Tenorio, F., 2008. Avalancha de Escombros del Pleistoceno Tardío Del Cono Los Pies, Complejo Volcánico Iztaccíhuatl. [M.S. thesis]Posgrado en Geología, ESIA- IPN, p. 147.

García-Tenorio, F., Macías, J.L., Layer, P.W., 2012. Euptive History of the Iztaccíhuatl Volcanic Complex during the Past 450,000 Years, Cities on Volcanoes 7, 19–23 November 2012 (Colima Mexico).

García-Tenorio, F., Sosa-Ceballos, G., Macías, J.L., 2015. Las erupciones piroclásticas del volcán Iztaccíhuatl de los últimos 300,000 Años. Resumen de la Reunión Anual de la Unión Geofísica Mexicana, Puerto Vallarta, 2–7 Noviembre 2015.

García-Tovar, G.P., Martínez-Serrano, R.G., 2011. Geología y geoquímica de las lavas pleistocénicas del estratovolcán Telapón. Sierra Nevada: México Revista Mexicana de Ciencias Geológicas 28, 301–322.

Goff, F., Janik, C.J., Delgado, H., Werner, C., Counce, D., Stimac, J.A., Siebe, C., Love, S.P., Williams, S.N., Fischer, T., Johnson, L., 1998. Geochemical surveillance of magmatic volatiles at Popocatépetl volcano, México. Geol. Soc. Am. Bull. 110-6, 695–710. https://doi.org/10.1130/0016-7606(1998)110b0695:GSOMVAN2.3.CO;2.

Gómez-Tuena, A., Orozco-Esquivel, T., Ferrari, L., 2007. Igneous petrogenesis of the Trans-Mexican Volcanic Belt. In: Alaniz-Álvarez, S.A., Nieto-Samaniego, Á.F. (Eds.), Geology of México: Celebrating the Centenary of the Geological Society of México: Geological Society of America Special Paper. 422, pp. 1–53. https://doi.org/10.1130/2007.2422(05).

Gómez-Vázquez, A., De la Cruz-Reyna, S., Mendoza-Rosas, A.T., 2016. The ongoing dome emplacement and destruction cyclic process at Popocatépetl volcano, CentralMéxico. Bull. Volcanol. 78, 58. https://doi.org/10.1007/s00445-016-1054-z.

Huddart, D., González, S., 2004. Pyroclastic flows and associated sediments, Tláloc-Telapón, piedmont fringe of the eastern basin of Mexico. In: Aguirre-Diaz, G.J., Macías, J.L., Siebe, C. (Eds.), Penrose Conference. UNAM, Metepec, Puebla, Mexico, p. 35.

Jaimes-Viera, M.C., Martin Del Pozzo, A.L., Layer, P.W., Benowitz, J.A., Nieto-Torres, A., 2018. Timing the evolution of a monogenetic volcanic field: Sierra Chichinautzin, Central Mexico. J. Volcanol. Geotherm. Res. 356, 225–242. https://doi.org/10.1016/j.jvolgeores.2018.03.013.

Jochum, K.P., Stoll, B., Herwig, K., Willbold, M., Hofmann, A.W., Amini, M., Aarburg, S., Abouchami, W., Hellebrand, E., Mocek, B., Raczek, I., Stracke, A., Alard, O., Bouman, C., Becker, S., Dücking, M., Brätz, H., Klemd, R., de Bruin, D., Canil, D., Cornell, D., de Hoog, C., Dalpé, C., Danyushevsky, L., Eisenhauer, A., Gao, Y., Snow, J.E., Groschopf, N., Günther, D., Latkoczy, C., Guillong, M., Hauri, E., Höfer, H.E., Lahaye, Y., Horz, K., Jacob, D.E., Kasemann, S.A., Kent, A.J.R., Ludwig, T., Zack, T., Mason, P.R.D., Meixner, A., Rosner, M., Misawa, K., Nash, B.P., Pfänder, J., Premo, W.R., Sun, W.D., Tiepolo, M., Vannucci, R., Vennemann, T., Wayne, D., Woodhead, J.D., 2006. MPI-DING reference glasses for in situ microanalysis: new reference values for element concentrations and isotope ratios. Geochem. Geophys. Geosyst. 7. https://doi.org/10.1029/2005GC001060 (Q02008).

Love, S.P., Goff, F., Counce, D., Siebe, C., Delgado, H., 1998. Passive infrared spectroscopy of the eruption plume at Popocatépetl volcano, México. Nature 396, 563–567.

Lozano-García, M.S., Ortega-Guerrero, B., 1994. Palynological and magnetic susceptibility records of Lake Chalco, Central Mexico. Palaeogeogr. Palaeoclimatol. Palaeoecol. 109, 177–191.

Lozano-García, S., Ortega, B., Roy, P., Beramendi-Orosco, L., Caballero, M., 2015. Climatic variability in the northern sector of the American tropics since the latest MIS 3. Quat. Res. 84 (2), 262–271. https://doi.org/10.1016/j.yqres.2015.07.002.

Macías, J.L., Siebe, C., 2005. Popocatépetl's crater filled to the brim: significance for hazard evaluation. J. Volcanol. Geotherm. Res. 141, 327–330. https://doi.org/10.1016/j.jvolgeores.2004.10.005.

Macías, J.L., Arce, J.L., García-Tenorio, F., Layer, P.W., Rueda, H., Reyes-Agustín, G., López-Pizaña, F., Avellán, D., 2012. Geology and geochronology of Tláloc, Telapón, Iztaccíhuatl, and Popocatépetl volcanoes, Sierra Nevada, Central Mexico. Geol. Soc. Am. Field Guide 25, 163–193. https://doi.org/10.1130/2012.0025(08.

Macías, J.L., Arce, J.L., García-tenorio, F., Sosa-ceballos, G., Gardner, J.E., 2020. Source and behavior of pyroclastic density currents generated by Vulcanian-style explosions of Popocatépetl volcano (Mexico) on 22 January 2001. J. Volcanol. Geotherm. Res. 406, 107071. https://doi.org/10.1016/j.jvolgeores.2020.107071.

Martínez-Abarca, R., Ortega-Guerrero, B., Lozano-García, S., Caballero, M., Valero-Garcés, B., McGee, D., Brown, E.T., Stockhecke, M., Hodgetts, A.G.E., 2021. Sedimentary stratigraphy of Lake Chalco (Central Mexico) during its formative stages. Int. J. Earth Sci. https://doi.org/10.1007/s00531-020-01964-z.

McLean, D., Albert, P.G., Nakagawa, T., Suzuki, T., Staff, R.A, Yamada, K., Kitaba, I., Haraguchi, T., Kitagawa, J., Smith, V.C., 2018. Integrating the Holocene tephrostratigraphy for East Asia using a high-resolution cryptotephra study from Lake Suigetsu (SG14 core), Central Japan. Quat. Sci. Rev. 183, 36–58. https://doi.org/10.1016/j.quascirev.2017.12.013.

Meier, M., Grobéty, B., Arce, J.L., Rueda, H., 2007. Origin and Age of the Volcanic Rocks of Tlaloc Volcano, Sierra Nevada, Central Mexico. AGU, Joint Assembly. (#V23A-01).

Mirwald, A., Cruz-Atienza, V.M., Díaz-Mojica, J., Iglesias, A., Singh, S.K., Villafuerte, C., Tago, J., 2019. The 19 September 2017 (M_w7.1) intermediate-depth Mexican earthquake: a slow and energetically inefficient deadly shock. Geophys. Res. Lett. 46, 2054–2064. https://doi.org/10.1029/2018GL080904.

Mooser, F., 1963. Historia tectónica de la Cuenca de México. Boletín de la Asociación Mexicana de Geólogos Petroleros 15, 239–245.

Mora-Alvarez, G., Caballero, C., Urrutia-Fucugauchi, J., Uchiumi, S., 1991. Southward migration of volcanic activity in the Sierra de Las Cruces, Basin of Mexico. A preliminary K-Ar dating and paleomagnetic study. Geofis. Int. 30, 61–70.

Nixon, G.T., 1988. Petrology of the younger andesites and dacites of Iztaccíhuatl volcano, Mexico: II. Chemical stratigraphy, magma mixing, and the composition of basaltic magma influx. J. Petrol. 29, 265–303.

Nixon, G.T., 1989. The Geology of Iztaccíhuatl Volcano and Adjacent Areas of the Sierra Nevada and Valley of Mexico. Geological Society of America, Special Paper no. 219 (58 pp).

Ortega-Guerrero, B., Lozano-García, S., Herrera-Hern, D., 2017. Lithostratigraphy and physical properties of lacustrine sediments of the last ca. 150 kyr from Chalco basin, Central México. J. S. Am. Earth Sci. https://doi.org/10.1016/j.jsames.2017.09.003.

Ortega-Guerrero, B., Caballero García, L., Linares-López, C., 2018. Tephrostratigraphy of the late Quaternary record from Lake Chalco, Central México. J. S. Am. Earth Sci. 81, 122–140. https://doi.org/10.1016/j.jsames.2017.11.009.

Panfil, M.S., Gardner, T.W., Hirth, K.G., 1999. Late Holocene stratigraphy of the Tetimpa archaeological sites, northeast flank of Popocatépetl volcano, Central Mexico. Geol. Soc. Am. Bull. 111 (2), 204–218.

Reimer, P.J., Austin, W.E.N., Bard, E., Bayliss, A., Blackwell, P.G., Bronk Ramsey, C., Butzin, M., Cheng, H., Edwards, R.L., Friedrich, M., Grootes, P.M., Guilderson, T.P., Hajdas, I., Heaton, T.J., Hogg, A.G., Hughen, K.A., Kromer, B., Manning, S.W., Muscheler, R., Palmer, J.G., Pearson, C., van der Plicht, J., Reimer, R.W., Richards, D.A., Scott, E.M., Southon, J.R., Turney, C.S.M., Wacker, L., Adolphi, F., Büntgen, U., Capano, M., Fahrni, S., Fogtmann-Schulz, A., Friedrich, R., Köhler, P., Kudsk, S., Miyake, F., Olsen, J., Reinig, F., Sakamoto, M., Sookdeo, A., Talamo, S., 2020. The IntCal20 Northern Hemisphere radiocarbon age calibration curve (0-55 cal kBP). Radiocarbon 62 (4), 725–757. https://doi.org/10.1017/RDC.2020.41.

Robin, C., 1984. Le volcan Popocatépetl (Mexique): structure, evolution pétrologique et risques. Bull. Volcanol. 47, 1–23.

Robin, C., Boudal, C., 1987. A gigantic Bezymianny-type event at the begining of modern Popocatépetl. J. Volcanol. Geotherm. Res. 31, 115–130.

Rueda, H., Arce, J.L., Macías, J.L., García-Palomo, A., 2007. Pyroclastic sequences at the N-NE slopes of Tláloc Volcano, Sierra Nevada, central México. Memorias de la Conferencia Internacional Conmemorativa "Volcán Chichón 25 años después" San Cristóbal de las Casas, Chiapas, México.

Rueda, H., Arce, J.L., Macías, J.L., García-Palomo, A., 2006. ~31 ka Plinian–Subplinian Eruption at Tláloc Volcano, Sierra Nevada, México. AGU Fall Meeting, San Francisco (CA, US).

Rueda, H., Macías, J.L., Arce, J.L., Gardner, J.E., Layer, P.W., 2013. The ~ 31 ka rhyolitic Plinian to sub-Plinian eruption of Tlaloc Volcano , Sierra Nevada , central Mexico. J. Volcanol. Geotherm. Res. 252, 73–91. https://doi.org/10.1016/j.jvolgeores.2012.12.001.

Siebe, C., Macías, J.L., 2004. Volcanic hazards in the Mexico City metropolitan area from eruptions at Popocatépetl, Nevado de Toluca, and Jocotitlán stratovolcanoes and monogenetic scoria cones in the Sierra Chichinautzin volcanic field. Field Guide, Penrose Conference. Neogene-Quaternary Continental Margin Volcanism, January 2004. Geological Society of America, State of Puebla, México: Boulder, Colorado, p. 77.

Siebe, C., Macías, J.L., 2006. Volcanic hazards in the Mexico City metropolitan area from eruptions at Popocatépetl, Nevado de Toluca, and Jocotitlán stratovolcanoes and monogenetic scoria cones in the Sierra Chichinautzin Volcanic Field. In: Siebe, C., Macías, J.L., Aguirre, G. (Eds.), Neogene-Quaternary Continental Margin Volcanism: A perspective from Mexico: Geological Society of America Special Paper. 402, pp. 253–329. https://doi.org/10.1130/2004.VHITMC.SP402.

Siebe, C., Delgado, H., Abrams, M., 1993. Recurrent cone collapse of Volcán Popocatépetl, Central Mexico: implications for risk evaluation. Eos. Trans. AGU 74-43, 640.

Siebe, C., Abrams, M., Macías, J.L., 1995. Derrumbes Gigantes, Depósitos de Avalancha de Escombros y Edad del Actual Cono del Volcán Popocatépetl. Volcán Popocatépetl: Estudios Realizados Durante la Crisis de 1994–1995. SINAPROC –CENAPRED – UNAM, México D.F, pp. 195–220.

Siebe, C., Abrams, M., Macías, J.L., Obenholzner, J., 1996. Repeated volcanic disasters in Prehispanic time at Popocatépetl, Central Mexico: past key to the future? Geology 24 (5), 399–402. https://doi.org/10.1130/0091-7613(1996)024b0399:RVDIPTN2.3.CO;2.

Siebe, C., Schaaf, P., Urrutia-Fucugauchi, F., 1999. Mammoth bones embedded in a late Pleistocene lahar from Popocatépetl volcano, near Tocuila, Central Mexico. Geol. Soc. Am. Bull. 111, 1550–1562.

Siebe, C., Salinas, S., Arana-Salinas, L., Macías, J.L., Gardner, J., Bonasia, R., 2017. The ~ 23, 500 y 14 C BP White Pumice Plinian eruption and associated debris avalanche and Tochimilco lava flow of Popocatépetl volcano, México. J. Volcanol. Geotherm. Res. 333–334 (2017), 66–95 ISSN 0377-0273 https://doi.org/10.1016/j.jvolgeores.2017.01.011.

Siegburg, M., Gernon, T.M., Bull, J.M., Kier, D., Barfod, D.N., Taylor, R.N., Abebe, B., Ayele, A., 2018. Geological evolution of the Boset-Bericha Volcanic Complex, Main Ethiopian Rift: $^{40}Ar/^{39}Ar$ evidence for episodic Pleistocene to Holocene volcanism. J. Volcanol. Geotherm. Res. 351 (1), 115–133. https://doi.org/10.1016/j.jvolgeores.2017.12.014.

Smith, R.E., Smith, V.C., Fontijn, K., Gebhardt, A.C., 2019. Refining the Late Quaternary tephrochronology for southern South America using the Laguna Potrok Aike sedimentary recordQuat. Sci. Rev. 218, 137–156. https://doi.org/10.1016/j.quascirev.2019.06.001.

Sosa-Ceballos, G., Gardner, J.E., Siebe, C., Macías, J.L., 2012. A Caldera-Forming Eruption ~ 14,100 14 C yr BP at Popocatépetl Volcano , México: Insights from Eruption Dynamics and Magma Mixing. 214, pp. 27–40. https://doi.org/10.1016/j.jvolgeores.2011.11.001.

Sosa-Ceballos, G., Macías, J.L., García-Tenorio, F., Layer, P., Schaaf, P., Solís-Pichardo, G., Arce, J.L., 2015. El Ventorrillo, a paleostructure of Popocatépetl volcano: insights from geochronology and geochemistry. Bull. Volcanol. 77 (10), 1–20. https://doi.org/10.1007/s00445-015-0975-2.

Stremme, W., Ortega, I., Siebe, C., Grutter, M., 2011. Gas composition of Popocatépetl volcano between 2007 and 2008: FTIR spectroscopic measurements of an explosive event and during quiescent degassing. Earth Planet. Sci. Lett. 301, 502–510. https://doi.org/10.1016/j.epsl.2010.11.032.

Valero-Garcés, B., Stockhecke, M., Lozano-García, S., Ortega, B., Caballero, M., Fawcett, P., Werne, J.P., Brown, E., Najera, S.S., Pearthree, K., McGee, D., Hodgetts, A.G.E., Martínez, R., 2021. Stratigraphy and Sedimentology of the Upper Pleistocene to Holocene Lake Chalco Drill Cores (Mexico Basin). In: Rosen, M.R., Finkelstein, D.B., Park Boush, L., Pla-Pueyo, S. (Eds.), Limnogeology: Progress, Challenges and Opportunities : A Tribute to Elizabeth Gierlowski-Kordesch. Springer International Publishing, Cham, pp. 415–443 https://doi.org/10.1007/978-3-030-66576-0_14.